

MICROBEAM ANALYSIS

1990

J. R. Michael

Peter Ingram

Editors

Proceedings of the 25th Annual Conference
of the

Microbeam Analysis Society

Seattle, Wash., 12-18 August 1990



San Francisco Press, Inc.

Box 6800, San Francisco, CA 94101-6800

PUBLISHER'S NOTICE

The Microbeam Analysis Society (MAS) and San Francisco Press, Inc., are not responsible for the information and views presented in this volume by the several contributors.

Permission to reprint portions of this volume in professional journals published by scientific or technical societies (with suitable acknowledgment) will be given free of charge on application to the publisher; a nominal fee may be charged for reprint rights given to book publishers, commercial journals, company publications, and other media.

Copies of this volume are available to members of the Microbeam Analysis Society (MAS) and of the Electron Microscopy Society of America (EMSA) *who send prepayment by personal check* at a 20% discount from the list price. (Californians add tax.) The same discount is available to members of both societies for the MAS triennial *Analytical Electron Microscopy*, and for the *Proceedings* of the annual EMSA meeting. The following books are available (most back issues at reduced prices):

Microbeam Analysis

1975, 1977 (8th ICXOM), 1979, 1980, 1981, 1982, \$25 each
1986, 1987, \$50 each
1988, \$60
1989, \$65
1990, \$62.50

Analytical Electron Microscopy

1981, \$25
1984, \$40
1987,* \$50

Proceedings EMSA

1984, 1985, 1986, \$45 each
1987, 1988, \$65 each
1989, \$72.50

Electron Microscopy Safety Handbook, \$15

Electron Microscopy and Alzheimer's Disease (J. Metuzals, Ed.), \$10

Early History of the Electron Microscope (L. Marton), \$7.50

Electricity and Medicine: History of Their Interaction (M. Rowbottom and C. Susskind), \$30

*AEM—1987 also contains the MAS—1987 papers on surface analysis. No AEM volume was published in 1990.

Printed in the U.S.A.

ISSN 0278-1727

FOREWORD

It has been our privilege to serve as technical program chairmen for the Analytical Sciences symposia presented at the XII International Congress for Electron Microscopy held in Seattle, Washington, on 12-18 August 1990. This was the first time that the analytical sciences had been explicitly included as part of an ICEM, and indicates the growing importance and interest in microanalysis in many forms to both materials and biological studies. Papers presented in the various Analytical Sciences sessions are published in this volume. The nature of the meeting has resulted in higher visibility for the Microbeam Analysis Society in the international microscopy community, which is reflected in the larger than normal proportion of papers from overseas contributors. We extend our sincere appreciation to our colleagues who organized and chaired the various sessions.

The technical sessions presented this year were divided into Physical and Biological areas of interest. Four sessions related directly to biological microanalysis, and one dealt with radiation effects of electron beams. An attempt was made to encourage presentations that related some of the advances in research topics to clinical applications. Thus, the authors were encouraged to place considerable emphasis on the biological/medical relevance and not solely on the development of new techniques. Owing to the somewhat controversial state of the field at this juncture, we have included most of the presentations that were submitted in the hope that further interest will be generated. The physical science sessions included many of the standard MAS sessions, with the addition of a session on Electron Crystallography. The Presidential Symposium (ably organized by Al 'Taz' Romig) brought together many outstanding scientists to discuss fundamental parameters of x-ray microanalysis. This meeting would not have been the great success it was without the many contributors to the various Analytical Sciences sessions.

The XII ICEM was organized under the auspices of the International Federation of Societies for Electron Microscopy by the Electron Microscopy Society of America in association with the Microbeam Analysis Society. The efforts of the officers of these societies and of the Organizing and Program Committees are gratefully acknowledged.

Finally, we hope that those who participated in the XII ICEM found the meeting enlightening, and that those who could not attend will find this volume to be a useful source of information.

Joseph R. Michael

Peter Ingram

TABLE OF CONTENTS†

	<i>Page</i>
Foreword	iii
Officers of the Microbeam Analysis Society	viii
1989 MAS paper awards	ix
1990 MAS presidential awards	x
Sustaining members' information	xi
1. PRESIDENTIAL SYMPOSIUM: FUNDAMENTAL PARAMETERS OF X-RAY ANALYSIS	
(A. D. Romig Jr., D. B. Wittry)	
Duncumb, P., Fundamental parameters of x-ray microanalysis: An introduction	1
Shimizu, R., Ding, Z.-J., Electron scattering in solids	6
Powell, C. J., Inner-shell ionization cross section	13
Karduck, P., Ammann, N., Rehbach, W. P., ϕ (ρz) determination for advanced applications of electron probe microanalysis	21
Lábár, J. L., Nonradiative transitions in x-ray analysis	29
de Bruijn, W. C., Sorber, L. W. J., The application of bio-standards for electron energy loss analysis of biological materials	32
Serin, V., Hssein, K., Zanchi, G., Sévely, J., EXELFS studies of carbon fibers	35
Wilson, A. R., Lithium detection in aluminum-lithium alloys using PEELS	39
2. ELECTRON ENERGY LOSS SPECTROMETRY (C. Colliex, R. Leapman)	
Quandt, E., la Barré, S., Hartmann, A., Niedrig, H., Parallel detection of EELS in direct mode	43
Schattschneider, P., Hofer, F., Angle-resolved energy loss spectra of Gd_2O_3	48
Jonas, P., Schattschneider, P., Bragg-Compton and plasmon-Compton channel coupling in electron Compton scattering	51
Su, D., Schattschneider, P., Numerical problems in the deconvolution of EELS	53
Okamoto, J. K., Ahn, C. C., Fultz, B., Temperature-dependent EXELFS of Al K and Fe L_{23} edges in chemically disordered and DO_3 -ordered Fe_3Al	56
3. ADVANCES IN ANALYTICAL INSTRUMENTATION (D.E. Newbury, G. Rémond)	
Rémond, G., Campbell, J. L., Spectral Deconvolution of wavelength-dispersive x-ray spectra	59
Donovan, J. J., Rivers, M. L., PRSUPR: A PC-based automation and analysis software package for wavelength-dispersive electron-beam microanalysis	66
Wittry, D. B., Sun, S., Chang, W. Z., Stepped diffractor for point focusing of monochromatic x rays	69
Bright, D. S., Software tools for examination of microanalytical images	73
McCarthy, J. J., Ales, M. W., McMillan, D. J., High-purity germanium detectors for EDS	79
Statham, P. J., Resolution enhancement for x-ray spectroscopy at low energies	85
4. MICROPROBE MASS SPECTROMETRY (R. von Criegern, D. Simons)	
Fletcher, R. A., Etz, E. S., Hoeft, S., Complementary molecular information on phthalocyanine compounds derived from laser microprobe mass spectrometry and micro-Raman spectroscopy	89
Lampert, J. K., Koerner, G. S., Macaoy, J. M., Chabala, J. M., Levi-Setti, R., Fluid catalytic cracking catalyst microstructure as determined by a scanning ion microscope	93
Asher, S. E., SIMS studies of polycrystalline thin film CdTe/CdS solar cells	97
Lee, J.-J., Linton, R. W., Lin, W.-J., Hunter, J. L., Jr., Griffis, D. P., Three-dimensional display of secondary ion images	101
Soni, K. K., Williams, D. B., Chabala, J. M., Levi-Setti, R., Newbury, D. E., Imaging of Al-Li-Cu alloys with a scanning microscope	105

†An author index begins on p 467

5. X-RAY MICROANALYSIS (J. T. Armstrong, G. F. Bastin)

Reed, S. J. B., Fluorescence effects in quantitative microprobe analysis	109
Brown, J. D., Measurement and parameterization of ϕ (pz) curves for quantitative electron probe microanalysis	115
Pouchou, J.-L., Pichoir, F., Boivin, D., The XPP procedure applied to quantitative EDS x-ray analysis in the SEM	120
Newbury, D. E., Myklebust, R. L., Steel, E. B., Monte Carlo electron trajectory simulation of x-ray emission from films supported on substrates	127
Barkan, S., Evaluating 30mm ² detectors for light-element x-ray analysis	139
Heinrich, K. H. J., Myklebust, R. L., The effect of averaging parameters on the backscatter correction	146
Myklebust, R. L., Fiori, C. E., Newbury, D. E., A robust method for determining the Duane-Hunt energy limit from energy-dispersive spectra	147
Ammann, N., Karduck, P., A further developed Monte Carlo model for the quantitative EPMA of complex samples	150
Chambers, W. F., Chodos, A. A., Hagan, R. C., Automated mineral analyses in TASK8	155
Bastin, G. F., Heijligers, H. J. M., Dijkstra, J. M., Computer programs for the calculation of x-ray intensities emitted by elements in multilayer structures	159
Nassiopoulos, A. G., Valamontes, E., Monte Carlo calculations of the spatial resolution in x-ray microanalysis of thin overlayers in the energy range 30-100 keV	161
Mackenzie, A., A method to overcome the problem of small sample tilts in light-element EPMA	165
Yang, S. V., Wagstaff, J., McKay, G., Calibration of NIST Mineral Glass Standard K-411 and the concept of a model standard in quantitative electron microprobe analysis	167
Burilla, C. T., Quantitative EPMA of Be in Nb-Be alloys using an α -factor correction technique	169
Ogilvie, R. E., Is there a "universal" MAC equation?	174
Willich, P., Schiffman, K., EPMA of borophosphosilicate coatings	177
Reed, S. J. B., Quantitative ED analysis at high count rates	181
Ross, D. K., Heyman, R. V., Elthon, D., An empirical test of a thin film data reduction scheme for the electron microprobe: BiSrCaCu oxide thin films on Si and MgO substrates	185
Marinenko, R. B., Bright, D. S., Handwerker, C. A., Mecholsky, J. J., Jr., A study of diffusion zones with electron microprobe compositional mapping	190
Chambers, W. F., Doyle, J. H., Computer-assisted wavelength-dispersive x-ray mapping	193
Paque, J. M., Browning, R., King, P. L., Pianetta, P., Quantitative information from x-ray images of geological materials	195
Browning, R., King, P. L., Paque, J. M., Pianetta, P., EDS image classification by recursive partitioning	199
Griffin, B. J., In situ analysis of natural fluid inclusions in minerals by a cryo-stage and thin-window EDS	203
Mao, S., Characterization of occurrence and distribution of invisible gold in ore by EPMA	206
Liu, D. R., Shinozaki, S. S., Warsinski, R. G., Baird, R. J., Stoichiometry/nonstoichiometry of GaAs component in MBE grown (GaAs)Ge thin films as determined by EPMA	209
Freeman, H. A., Rabe, J. A., Microanalyses of structural defects in polymer-derived ceramic fibers	212
Henderson, C. E., A Macintosh interface for the CAMECA CAMEBAX-Microbeam electron microscope	215
Laabs, F. C., In situ ion beam cleaning in a Cambridge S-200 SEM	217

6. PHOTON BEAM ANALYSIS (P. Dhamelincoourt, E. S. Etz)

Delhay, D., Dhamelincoourt, P., A perspective of the historical developments and future trends in Raman microprobe spectroscopy	220
Pasteris, J. D., Seitz, J. C., Wopenka, B., Chou, I.-M., Recent advances in the analysis and interpretation of C-O-H-N fluids by application of laser Raman microscopy	228
Bergin, F. J., Fourier transform vibrational microscopy	235
Reffner, J. A., Wihlborg, W. T., FT-IR molecular microanalysis system	240
Etz, E. S., Schroeder, T. D., Wong-Ng, W., Raman and fluorescence spectra observed in laser microprobe measurements of several compositions in the Ln-Ba-Cu-O System	243

7. SURFACE ANALYSIS (J.A. Venables, K. Yagi)

Hembree, G. G., Luo, F. C. H., Venables, J. A., Secondary and Auger electron spectroscopy and energy-selected imaging in a UHV-STEM	249
Charbonnier, M., Romand, M. J., Gaillard, F., Low-energy electron-induced x-ray spectroscopy (LEEIXS): An emerging technique in surface and thin-film analysis	257

Koopman, M. C., Thompson, R. G., Interface segregation in a nickel base superalloy	260
Huang, M., Flora, P. S., Harland, C. J., Venables, J. A., Angular resolved electron spectroscopy with parallel recording	263
8. X-RAY MICROANALYSIS—THIN FILMS (J. R. Michael, J. Titmarch)	
Goldstein, J. I., Lyman, C. E., Zhang, J., Spatial resolution and detectability limits in thin-film x-ray microanalysis	265
Garratt-Reed, A. J., Applications of high-resolution x-ray mapping	272
Romig, A. D., Jr., Plimpton, S. J., Michael, J. R., Myklebust, R. L., Newbury, D. E., Application of parallel computing to the Monte Carlo simulation of electron scattering in solids: A rapid method for profile deconvolution ..	275
Zaluzec, N. J., Comparison of experimental and theoretical XEDS cross sections and k-factors as a function of accelerating voltage	281
L'Espérance, G., Botton, G., Caron, M., Detection and quantification problems in the analysis of light elements with UTW detectors	284
Kenik, E. A., Bentley, J., Effect of tilt angle on hole count and secondary fluorescence in x-ray microanalysis	289
Munroe, P. R., Baker, I., Application of ALCHEMI to intermetallic compounds	297
Ren, Y., Xu, Y., Sun, Z., Chen, G., Site occupation of ternary element in an AlTi compound by ALCHEMI ..	305
Zhang, J., Williams, D. B., Goldstein, J. I., Practical importance of spatial resolution and analytical sensitivity in AEM x-ray microanalysis	307
Heng, Y. M., Simon, G. T., Simultaneous evaluation of weight factors and k factors for quantitative x-ray microanalysis of thin specimens	311
Valdrè, G., Ruedl, E., Microscopy and nanoanalysis of a Cr-Mn austenitic steel α -bombarded at room and elevated temperature	318
Wakaki, Y., Otsuka, Y., Horita, Z., Nishimura, M., Sano, T., Murata, Y., Nemoto, M., Cross-sectional examination of surface layers on electropolished thin specimens	323
Rossouw, C. J., Turner, P. S., White, T. J., O'Connor, A. J., Quantitative ALCHEMI with error analysis ..	327
Zaluzec, N. J., Evolutionary developments in x-ray and EEL microanalysis instrumentation for the analytical EM	330
9. ELECTRON CRYSTALLOGRAPHY (J. A. Eades, J. Gjónnes)	
Andersen, S. J., Guo, Y. X., Høier, R., Stacking faults in the α -AlMnSi cubic phase	334
Rossouw, C. J., Miller, P. R., Allen, L. J., LACBED with qualitative anomalous absorption corrections	337
Qing, L., A group of new equations related to the operation of TEM double-tilt holder and their application to TEM ..	339
Otten, M. T., On-line measurement of specimen thickness by CBED	344
Mathinsen, K., Bakken, L. N., Høier, R., Runde, P., A strategy for quantitative determination of structure parameters by computer simulation of CBED	347
Silva, E. G., Scozia, R. A., CBED zone axis pattern map of zirconium	351
Pérez, R., Applications of CBED techniques to the structural characterization of crystalline defects	354
10. ANALYTICAL APPLICATIONS	
Ackerman, E. R., Kimmel, G., Particulate magnetic media contamination: Large defects	364
Bearman, G. H., Bradley, J. G., Davidson, S. G., Use of metal blacks for capture of low-velocity (<200 m/s) particles	367
Peeters, M. H., Antoine, J., Lamothe, V., Viala, A., Automation of gunshot-residue analysis by functional integration of an SEM and an energy-dispersive microanalysis system	369
Callender, C. A., Dawson, W. C., Funk, J. J., Correlation of permeability to pore structure by SEM-image analysis	372
Freeman, H. A., Peters, Y. A., An electron microscopical study of silicone hydrophobicity in commercial gypsum wallboard	375
Browning, R., VanZandt, T., Landolt, M., Using an iron overlayer to enhance contrast in SEMPA	377
Radzinski, Z. J., Buczkowski, A., Russ, J. C., Rozgonyi, G. A., Electron beam induced current study of multilayer structures	381
Russ, J. C., Monte Carlo modeling of secondary electron yield from rough surfaces	385

11. QUANTITATIVE MICROANALYSIS IN BIOLOGY (A. P. Somlyo, B. Walz)

Carney, M., LeFurgey, A., Hawkey, L. A., Ingram, P., Lieberman, M., Comparison of qualitative x-ray imaging and raster probing in heart cells exposed to sodium-free media	387
Zhong, C., Yu, Z., Yu, W., Ling, Y., Atrial specific granules: The intracellular calcium store	390
Spencer, A. J., Hawkey, L. A., LeFurgey, A., Dickman, K. G., Mandel, L. J., Ingram, P., Quantitative EPXMA imaging of rapidly frozen kidney proximal tubule primary cultures	393
Warner, R. R., Systematic changes in corneocyte element concentration in skin inner stratum corneum	397
Jones, K. W., Gordon, B. M., Schidlovsky, G., Spanne, P., Xue, D., Saubermann, A. J., Biomedical elemental analysis and imaging using synchrotron x-ray microscopy	401
Panessa-Warren, B. J., Tortora, G. T., Stears, R. L., Warren, J. B., Calcium imaging with monochromatic x rays	405
Kaneko, N., Teraoka, K., Horikawa, Y., Uchida, T., Matsuda, R., Hosoda, S., Nakamura, S., Pathophysiological function of the mitochondria as a calcium reservoir: Quantitative x-ray microanalysis	408
Horikawa, Y., Kaneko, N., Teraoka, K., Uchida, T., Hosoda, T., Matsuda, R., Subcellular calcium content of myocardium after ischemia and reperfusion: X-ray microanalysis	411
Sun, S., Tormet, J. M., Wittry, D. B., High-efficiency x-ray monochromator for measurement of Ca in the TEM	415
Warley, A., Ward, J. P. T., Element concentrations in cardiac myocytes isolated from control and potassium depleted rabbits studied by x-ray microanalysis	419

12. TECHNIQUES FOR MICROANALYSIS IN MEDICINE (G. M. Roomans, J. P. Shelburne)

Zglinicki, T. von, Roomans, G. M., Effects of VIP secretory stimulation on cytoplasmic ion concentration in mouse intestinal crypt cells	421
Mawn, M. P., Linton, R. W., Cross-sectional imaging of coated drug granules	423
Tvedt, K. E., Halgunset, J., Kopstad, G., Nordby, A., Preparation of freeze-dried sections of human biopsies for x-ray microanalysis	427
Kirk, R., Lee, P., Reasor, M. J., Application of x-ray microanalysis to the study of drug distributions in cultured cells	430

13. ANALYSIS OF ENVIRONMENTAL TOXICANTS (J. R. Harkema, K. U. Thiedemann)

Singh, A., Sims, D. E., Jarrell, J., Villeneuve, D. C., Hexachlorobenzene toxicity in the monkey ovary: II. Ultrastructure induced by medium (10 mg/kg) dose exposure	435
Rydzynski, K., Opalska, B., Czerczak, S., Stetkiewicz, J., Hepatotoxicity of rubber vulcanization fumes in rats	439
Reffner, J. A., Wihlborg, W. T., Microanalysis of asbestos fibers by FT-IR microscopy	442
Russell, P. A., The analyses of anthropogenic atmospheric particulates by electron microscopy	445
Warheit, D. B., Rennix, D. K., Moore, K. A., Belcher, L. A., An integrated screening method for evaluating the pulmonary toxicity of inhaled particulates: Role of microscopic techniques in assessing pulmonary macrophage clearance functions	449
Harkema, J. R., Hotchkiss, J. A., Hoover, M. D., Muggenburg, B. A., Effects of endotoxin-induced neutrophil influx on the morphology of secretory cells and intraepithelial mucosubstances in canine bronchi	453
Lee, J., Akley, N. J., Krunkosky, T. M., Adler, K. B., Methods to study interactions between inhaled substances and epithelium of the respiratory tract in vitro	457
Reffner, J. A., Wihlborg, W. T., Microanalysis of asbestos fibers by FT-IR microscopy	442

14. SPECIMEN PREPARATION METHODS FOR BIOLOGICAL AEM (P. Echlin, A. LeFurgey)

Flenniken, R. R., LeFurgey, A., Ingram, P., Kopf, D. A., Design of an ultraclean computer-controlled freeze dryer for biological specimens	454
Ahlstrand, G. G., Zeyen, R. J., Carver, T. L. W., Preparation of barley epidermis for x-ray microanalysis	463

Officers of the Microbeam Analysis Society

MAS Executive Council

President: Alton D. Romig Jr., Sandia National Laboratories, Albuquerque, N.M.

President Elect: J. T. Armstrong, California Institute of Technology, Pasadena, Calif.

Past President: David B. Wittry, University of Southern California, Los Angeles, Calif.

Treasurer: Harvey Freeman, Dow Corning Corp., Midland, Mich.

Secretary: John A. Small, National Institute of Standards and Technology 222/A121, Gaithersburg, MD 20899, (301) 975-3900

Directors

Serge Cvikevich, IBM GTD, Hopewell Junction, N.Y.

John Friel, PGT, Princeton, N.J.

Rich Lee, R. J. Lee Group, Monroeville, Pa.

Jon McCarthy, Tracor Northern, Middleton, Wis.

Ryna Marinenko, NIST, Gaithersburg, Md.

Richard Linton, University of North Carolina, Chapel Hill, N.C.

Honorary Members

L. S. Birks, Naval Research Laboratory, USA

Raymond Castaign, University of Paris (Orsay), France

A. A. Chodos, Monrovia, Calif., USA

V. E. Cosslett, University of Cambridge, Great Britain

Peter Duncumb, Tube Investment Research Laboratories, Great Britain

T. A. Hall, University of Cambridge, Great Britain

K. F. J. Heinrich, NIST, USA

R. E. Ogilvie, MIT, USA

S. J. B. Reed, University of Cambridge, Great Britain

Gunji Shinoda, Osaka University, Japan

D. B. Wittry, University of Southern California, USA

1989 MAS Paper Awards

Castaigh Award: R. Gauvin and G. L'Esperance, *The effect of fast secondary electronics on K_{AB} factors and spatial resolution*

Birks Award: D. M. Golijanin, D. B. Wittry, S. Sun, *Further developments in instrumentation for microprobe x-ray fluorescence analysis*

Macres Award: J. Pellerin, G. Shedd, D. P. Griffis, P. E. Russell, *Micro- and nanofabrication with a combined focused ion beam/scanning tunneling microscope*

Cossett Award: J. L. Batstone, *Determination of electronic properties of defects in semiconductors by cathodoluminescence*

1990 MAS Presidential Awards

Outstanding contributions to microanalysis: Thomas E. Everhart

Outstanding service to the Society: Charles E. Fiori

K F. J. Heinrich Award for outstanding young MAS scientist: Richard W. Linton

Sustaining Members' Information

ADVANCED MICROBEAM SERVICES, INC.

4217C Kings-Graves Road
Vienna, Ohio 44473

Product Contact: Donald P. Leshner (216) 394-1255

Product Line: Service of Electron Microprobes and accessories.

AMRAY, INC.

160 Middlesex Turnpike
Bedford, MA 01730

Product Contacts:

Technical Data: Dr. Sheldon Moll (617) 275-1400
Delivery & Prices: Gerald Cameron, Jr. (617) 275-1400

Product Line: Manufacturer of scanning electron microscopes

Regional Sales Offices:

George Bruno	New England	(617) 275-8310
Ed Griffith	Mid-Atlantic North	(609) 662-3922
Tom Richards	Mid-Atlantic South	(609) 662-3922
Ken Lindberg	Southeast	(305) 767-4220
Rich Lantz	Southwest	(214) 247-3542
Gerry O'Loughlin	Northern California	(408) 748-1300
John Pong	Southern California	(714) 380-0289
Fred Feuerstein	Mid-West	(312) 695-6117
Matt Gohlke	Mid-East	(216) 579-0035

CAMBRIDGE INSTRUMENTS, INC.

111 Deerlake Road
Deerfield, Ill 60015

Product Contact: Barry T. Gray (708) 405-0123

Product Line: Scanning electron microscopes, Optical Microscopes, Cryo sample prep equipment.

Regional Sales Offices:

Dr. Joseph Keegan, 111 Deerlake Rd., Deerfield, Ill. 60015 (708) 405-8130

CAMECA INSTRUMENTS, INC.

2001 West Main Street
Stamford, CT 06902-4583

Product Contact: Thomas C. Fisher (203) 348-5252

Product Line: Scanning electron microprobes and secondary ion mass spectrometers.

DAPPLE SYSTEMS

355 West Olive, Suite 100
Sunnyvale, CA 94086

Product Contact: Bill Stewart (408) 733-3283

Product Line: Microcomputer-based analytical instrumentation including automatic image analysis and energy-dispersive x-ray microanalysis.

ELECTROSCAN CORPORATION

66 Concord Street
Wilmington, MA 01887

Product Contacts: Mike Ruggiero (508) 988-0055

Product Line: Multi-environmental electron microscopes - operating up to 20 torr specimen chamber pressure. Secondary and backscattered high-resolution imaging is available throughout this pressure range (from 10 to minus 5 torr to 20 torr). Dynamic imaging provided by variable specimen chamber control and real-time (TV) imaging of any experiment irrespective of specimen's physical state.

Regional Sales Offices:
North East: Dick Harnman (914) 268-9221
Middle Atlantic: Harry Freer (703) 742-6216
California: John Treadgold (213) 207-6478
South East: Al Pick (214) 250-6663
New Jersey & New York: Roger Attle (914) 368-3935

ENERGY BEAM SCIENCES

EBTEC Corporation
P.O. Box 468
11 Bowles Road
Agawam, MA 01001

Product Contact: Linda Standrowicz (413) 786-9322

Product Line: Electron microscope filaments (tungsten, LaB6 and prototype, apertures, scintillators, SEM mounts (aluminum, carbon) and mount storage, small instruments (sputter coaters, vibratome), complete range of EM supplies.

GATAN, INC.
6678 Owens Drive
Pleasanton, CA 94588-3334

Product Contact: CA Sheri Kurland (415) 463-0200
PA Terry Donovan (412) 776-5260

Product Line: Specialized accessories for transmission electron microscopy, TV imaging systems, parallel EELS analytical systems, side entry specimen holders for TEM, specimen preparation equipment for materials scientists, & specimen preparation & TEM analysis on a service basis.

Regional Sales Office:
Eastern Region: Terry Donovan, 780 Commonwealth Dr., Warrendale, PA 15086 (412) 776-5260

GW ELECTRONICS, INC.
6981 Peachtree Industrial Boulevard
Norcross, GA 30092

Product Contact: Larry Glassman (404) 449-0707

Product Line: Electronic accessories for scanning electron microscopes and microprobes including Backscattered Electron Detectors, Specimen Current Amplifier, Signal Processor, Graphics Generator, and Microchannel Plate Detector.

HNU X-RAY SYSTEMS, INC.
160 Charlemont St.
Newton Highlands, MA 02161

Product Contact: Therese Hipple (617) 964-6690

Product Line: System 5000 Microanalysis and Imaging Instruments

INSTRUMENTS SA, INC.
6 Olsen Ave.
Edison, NJ 08820

Product Contact:
Bruce D. Perrulli (201) 494-8660

Susan Maher (201) 494-8660

Product Line: MOLE - Raman molecular microprobes, contact Bruce D. Perruli; Surface analysis microprobes, contact Susan Maher.

INTERNATIONAL SCIENTIFIC INSTRUMENTS, INC.

6940 Koll Center Parkway
Pleasanton, CA 94566

Product Contact Dr. Robert Buchanan (415) 462-2212
Mary Battle (415) 462-2212

Product Line: Scanning electron microscopes and transmission electron microscopes.

JEOL USA, INC.

11 Dearborn Road
Peabody, MA 01960

Product Contacts: Charles Nielsen, Robert Santorelli (508) 535-5900

Product Line: EPMA, Auger, SEM, TEM, NMR, Mass Spectrometers.

Regional Sales Offices:

Thayer Brickman, Jack Francis, JEOL USA, Inc., 3500 Bayshore Road, Palo Alto, CA 94303 (415) 493-2600
Robert Steiner, JEOL USA, Inc., 9801 W. Higgins St. Suite 220, Rosemont, IL 60018 (312) 825-7164
John Bonnici, JEOL USA, Inc., 23 Brunswick Woods Drive, East Brunswick, NJ 08816 (201) 254-5600

KEVEX INSTRUMENTS, INC.

355 Shoreway Road
San Carlos, CA 94070-1308

Product Contacts:

Technical Data: Tom Stark/Nancy Wolfe (415) 591-3600
Delivery & Prices: Helen J. Barker (415) 591-3600

Product Line: Energy-dispersive x-ray spectrometers for materials analysis including instrumentation for EDS, WDS, EELS, and digital image processing.

Regional Sales Offices:

Frank Mannino, 9989 Windsor Way, San Ramon, CA 94583 (415) 828-2188, Home: (415) 828-1655
Rick Cumby, P.O. Box 850820, Mesquite, TX 75185-0820 (214) 226-0182, Ans. Serv.: (214) 699-1944 Home: (214) 240-4095
Dan Polakowski, 9918 Scots Circle, Crystal Lake, IL 60014 (815) 455-8448, Home: (815) 455-8444
Vic Balmer, 7600 Primavera Way, La Costa, CA 92009 (619) 436-2932, Home: (619) 944-1063
Joe Piersante, 16 Barberry Hill Dr., Gainesville, GA 30506 (404) 887-9965, Home: (404) 889-1363
Robert Fucci, 60-C Charles Dr., Manchester, CT 06040 (203) 646-6325, Home: (203) 645-6373
Rich Fiore, Rd. 3 Box 99, Harvey's Lake, PA 18618 (717) 639-2330, Home: (717) 639-2021
Karen McGranahan, 19635 Cottonwood Trail, Strongsville, OH 44136 (216) 238-8666 Home: (216) 572-3606
Barry Weavers, 7 Valley Forge Dr., North East, MD 21901 (301) 287-3955, Home: (301) 287-5285
Rod Palmberg, P.O. Box 200, Mercer Island, WA 98040 (206) 232-3444, Home: (206) 232-6097
FAX: (206) 232-8323
Karl L.R. Mahler, P.O. Box 505, Thornhill, Ontario, Canada L3T 4A2 (416) 731-2161 Home: (416) 889-8907
FAX: (416) 731-2162
Kevex East Application Lab, 50 Valley Stream Parkway, Suite 180,
Great Valley Corporate Center, Malvern PA 19355 Office: (215) 647-4866 FAX: (215) 889-9050

R.J. LEE GROUP, INC.

350 Hochberg Road
Monroeville, PA 15146

Product Contact: Hank Beebe (412) 325-1776
FAX (412) 733-1799

Product Line: Analytical services, consulting, contract research, materials characterization, TEM, SEM, PC-based microimaging.

Regional Sales Offices:

2424 6th. Street, Berkeley, CA 94710

(415)486-8319, FAX (415)486-0927

1036 Battlevue Parkway, Manassas, VA 22110

(703)368-7800, FAX (703)368-7761

LINK ANALYTICAL INC.

Microscope Products

8017 Excelsior Drive

Madison, WI 53717

Product Contacts:

Technical Data: Paul Mainwaring (608) 836-3200

Delivery & Prices: Donald Grimes (608) 836-3200

Product Line: Advanced energy-dispersive x-ray microanalysis and imaging systems.

Regional Sales Offices:

Paul Smith, 9 Acton Road, Chelmsford, MA 01824

(508) 250-0855

Patrick Campos, 240 Twin Dolphin Dr, Suite D, Redwood City, CA 94065

(415) 595-5465

Gerald Dougherty, 1010 Huntcliff, Suite 1350, Atlanta, GA 30352

(404) 642-7666

Graham Bird, 5300 Hollister, Suite 230,, Houston, TX 77040

(713) 642-0200

Charles Lambright, 118 Hidden Tree Lane, Amherst, Ohio 44001

(216) 988-3124

McCRONE ASSOCIATES, INC.

850 Pasquinelli Drive

Westmont, IL 60559

Product Contacts:

Dr. John Gavrilovic

(708) 887-7100

Dr. Timothy Vander Wood

(404) 368-9600

Product Line: Materials characterization, surface analysis, particle characterization and identification, forensic contamination, pharmaceuticals, dust, corrosion, semiconductors, wafers, electronics. Instruments available to apply: EMA, SIMS, ESCA, Auger, Raman, SEM, AEM, ultramicrotomy, class 100 cleanroom.

Regional Sales Offices:

McCrone Associates/Atlanta, Dr. Timothy Vander Wood, 1412 Oakbrook Drive, Norcross, GA 30093, (404) 368-9600

MICRON, INC.

3815 Lancaster Pike

Wilmington, DE 19805

Product Contact: James F. Ficca, Jr. (302) 998-1184

Product Line: Analytical services including, Optical Microscopy (OM), Scanning Electron Microscopy (SEM/EDS), Transmission Electron Microscopy (TEM), Electron Probe X-Ray Microanalysis (EPA),

MICROSPEC CORPORATION

45950 Hotchkiss Street

Fremont, CA 94539

Product Contact: Joseph Carr (415) 656-8820

FAX (415) 656-8944

Product Line: WDX-3PC wavelength-dispersive x-ray spectrometer system for use on SEMs.

NISSEI SANGYO AMERICA, LTD.

HITACHI SCIENTIFIC INSTRUMENT DIVISION

460 E. Middlefield Road

Mountain View, CA 94043

Product Contact: Hideo Naito (415) 961-0461

Product Line: Scanning electron microscopes, transmission electron microscopes, field emission.

Regional Sales Offices:

Nissei Sangyo America, Ltd., 2096 Gaither Rd., Rockville, MD 20850

Nissei Sangyo America, Ltd., 2850 E. Golf Rd., Suite 200, Rolling Meadows, IL 60008

Nissei Sangyo America, Ltd., 89 Galaxy Blvd., Suite 14, Rexdale, Ontario M9W 6A4, Canada

OVONIC SYNTHETIC MATERIALS, INC.

1788 Northwood

Troy, MI 48084

Product Contact: Steven A. Flessa (313) 362-1290

(800)366-1299 FAX (313)362-4043

Product Line: The OVONIX line of multilayer x-ray monochromators are replacing natural crystals and Langmuir-Blodgett pseudocrystals for improved light-element analysis in WD/XRF and EPMA spectrometers. Increased peak intensities and suppression of higher orders improves analysis of Al-B in XRF and of F-Be in EPMA.

OXFORD INSTRUMENTS NORTH AMERICA, INC.

3A Alfred Circle

Bedford, MA 01730

Product Contact: Glenn Kinnear (617) 275-4350 FAX (617) 275-8275

Product Line: A range of accessories for scanning and transmission electron microscopes including: Cryopreparation and cryotransfer systems for SEM and TEM; Cooling (N₂ and He), heating, tensile and X Y Z stages for SEM; Cathodoluminescence detection for SEM and TEM; Cooling, heating, and analytical holders for TEM; Rapid sample freezing equipment (SEM or TEM); Freeze replication/freezing etch equipment; Digital image processing.

Regional Sales Office:

Jeremy Sutton, Oxford Instruments North America, 1050F East Duane Avenue, Sunnyvale, CA 94086, (408) 732-3002

PERKIN-ELMER

6509 Flying Cloud Dr.

Eden Prairie, MN 55344

Product Contacts:

Technical Data: Greg Carpenter (612) 828-6100,

Delivery & Prices: Customer Order Dept. (800) 328-7515

FAX: (612) 828-6322

Product Line: ESCA, Auger, SIMS and MBE instruments, vacuum products.

Regional Sales Offices:

Boston: 5 Medallion Center, Greeley St., Merrimack, NH 03054

(800)523-2310; In NH (603)424-6100, FAX: (603)424-0902

New York: 5 Progress St., Edison, NJ 08820

(201)561-6730, FAX: (201)561-0268

Wash. DC: 7310 Ritchie Hwy., Suite 520, Glen Burnie, MD 21061

(301)761-3053, FAX: (301)761-0479

Denver: 14818 W. 6th Avenue, PHI Suite, Golden, CO 80401

(303) 271-0040

San Jose: 2305 Bering Dr., San Jose, CA 95131

(408) 473-9000, FAX: (408) 434-0139

PHILIPS ELECTRONIC INSTRUMENTS

85 McKee Drive

Mahwah, N.J. 07430

Product Contact: Dr. M. N. Thompson

(201) 529-3800

Product Line: XL series Scanning Electron Microscopes, CM series Transmission Electron Microscopes, EDAX X-Ray Analysis Systems, and PHAX SCAN ultra fast microanalysis with SEM.

PRINCETON GAMMA-TECH

1200 State Rd.
Princeton, NJ 08540

Product Contacts:

Technical Data:	Doug Skinner	(609) 924-7310
Delivery and Prices:	Mark Smith	(609) 924-7310
	FAX	(609) 924-1729

Product Line: Princeton Gamma-Tech's product line consists of the PGT System 4+ microanalysis system with complete EDS x-ray analysis capabilities for SEM, TEM, and STEM. Also highlighted in our product line is PGT Imagecraft, digital image processing, enhancement, and quantitative image analysis for light microscopy as well as electron microscopy.

Regional Sales Offices:

Branch Office, 568 Weddell Drive, Suite 1, Sunnyvale, CA 94089,	(408)734-8124, FAX (408)734-8137
Western Region, Griot Group Inc., Los Altos, CA	(415)941-2533, FAX (415)941-2536
Southwest Region, Jake Brown, Euless, TX	(817)571-9075
Central West Region, Contemporary Science, Inc., Mount Prospect, IL	(312)255-3793
Central East Region, Tom Griffin, Rocky River, OH	(216)331-0120
Northeast Region, Scientific System Sales Corp, Jericho, NY,	(516)822-4880, FAX (301)822-4887
Southeast Region, Robert Green, Atlanta, GA	(404)633-3904

QBI INTERNATIONAL

2034 Golden Gate Avenue
San Francisco, CA 94115-4399

Product Contact: Quentin A. Brown (415) 929-1622

Product Line: The SEMSCAN, a wavelength dispersive spectrometer with optimum performance for the analysis of light elements and resolution of peak overlaps. SEMSCAN control and data collection are accomplished with a personal computer system.

SPECTRA-TECH, INC.

652 Glenbrook Road
P.O. Box 2190-G
Stamford, CT 06906

Product Contacts:

Technical Data:	John A. Reffner	(203) 357-7055
Delivery & Prices:	Faith Cornick	(201) 646-0421

Product Line: FT-IR microscopes and accessories

Regional Sales Offices:

Tom Driscoll, Spectra-Tech, 3 University Plaza, Hackensack, NJ 07601

SPI SUPPLIES**DIVISION OF STRUCTURE PROBE, INC.**

P.O. Box 656
West Chester, PA 19381-0656

Product Contact:

For SPI Supplies:	Ms. Sue Morris	(800) 2424-SPI, in PA (215) 436-5400, FAX (215) 436-5755
For Structure Probe, Inc.:	Ms Kim Royer	(Tel. and FAX as above)

Product Line: SPI Supplies: Complete line of sample preparation equipment, consumable supplies, standards and other accessory items for the microanalysis laboratory. Call for catalog. Structure Probe: Independent laboratory offering SEM, EDS, WDS, Auger, Metallurgical failure analysis a specialty. Accredited by American Association for Laboratory Accreditation.

Laboratories (Structure Probe, Inc.):

Ms. Kim Royer, 569 E. Gay St., West Chester, PA 19380	(215) 436-5400
Dr. A. Blackwood, 63 Unquowa Rd., Fairfield, CT 06430	(203) 254-0000
Mr. Ronald Bucari, 1015 Merrick Rd., Copiague, L.I., NY	(516) 789-0100

Regional Sales Offices:

SPI Supplies/Canada, Mrs. Pnina Rosenberg, PO Box 187, Station "T", Toronto, Ontario, Canada M6B 4A1
(416) 781-0249
Structure Probe, Inc., 230 Forrest Street, Metuchen, NJ 08840 (201) 549-9350
Structure Probe, Inc., 63 Unquowa Road, Fairfield, CT 06430, (203) 254-0000
Structure Probe, Inc., 1015 Merrick Road, Copiague, NY 11726(516) 789-0100

M.E. TAYLOR ENGINEERING, INC.

21604 Gentry Lane
Brookeville MD 20833

Product Contact: M.E. (Gene) Taylor (301) 774-6246
FAX (301) 774-6711

Product Line: Scintillators, SEM supplies, secondary and backscatter electron detectors, vacuum foreline traps, specimen stubs, filaments and related items. Precision machine work and scientific glass blowing. Repair most EDS detectors.

Regional Sales Office:

Dave Ballard, 15817 Crabbs Branch Way, Rockville, MD 20855 (301) 330-0077

TRACOR NORTHERN, INC.

2551 W. Beltline Hwy.
Middleton, WI 53562

Product Contacts:

Technical Data: Joseph Mullen (608) 831-6511
Delivery & Prices: Dennis Masaki (608) 831-6511

Product Line: Voyager Microanalysis System (new product), Series II Microanalysis System, I-2 Integrated Imaging System, TN-8502 Video Image Analysis System, and TSM Confocal Microscope.

VG INSTRUMENTS, INC.

32 Commerce Center
Cherry Hill Drive
Danvers, MA 01923

Product Contact: Bob Michael (508) 777-8034

Product Line: UHV analytical instrumentation; those pertinent to MAS include high-resolution Auger, UHV dedicated STEM, imaging SIMS.

Regional Sales Offices:

John Kadlec, 211 Mountain Way, Chan Massen, MN 55317 (612) 470-9502
Chris Macey, 5850 Cameron Run Terrace, Suite 916, Alexandria, VA 22303 (703) 960-8206
John Woods, Door #1, Lake Side Office Park, Wakefield, MA 01880 (617) 246-0040

CARL ZEISS, INC.

One Zeiss Drive
Thornwood, NY 10594

Product Contact: Paul E. Henry (914) 681-7741

Product Line: Transmission and scanning electron microscopes.

Regional Sales Offices:

Dietrich Voss, PO Box 2025, Willis, TX 77378 (409) 856-7678
Virginia Hanchett, 14870 Marie Court, San Martin, CA 95046 (408) 779-0100
Frank Coccia (301) 437-7382
Karleen Davis (513) 681-4232
Bert Grespan (416) 442-3320
Larry Williams (404) 979-2158
Steve Neptun (508) 839-3699

Presidential Symposium: Fundamental Parameters of X-ray Microanalysis

FUNDAMENTAL PARAMETERS OF X-RAY MICROANALYSIS: AN INTRODUCTION

Peter Duncumb

It is indeed fortunate that nature has provided us with such well-defined physical laws governing the generation of x rays and their interaction with matter. This benefit has given electron microprobe analysis two major advantages over many other techniques of analysis: it can be applied to almost all elements in the periodic table and it can be applied quantitatively. Nevertheless, we are continually striving for better and better quantitation over a wider range of conditions, and there is a corresponding pressure to improve our knowledge of the physics. The purpose of this paper is to identify the fundamental parameters by which these physical laws are expressed, and to explore their relative importance in determining the accuracy of which the technique is capable.

Basic Physics

What then are the physical processes taking place in microprobe analysis? Electrons focused on the sample are slowed down and scattered as they penetrate beneath the surface, some re-emerging from the surface as backscattered electrons (Fig. 1). Characteristic x-ray emission from the element to be analyzed is generated within the volume irradiated, and some of

this emission enters the spectrometer after undergoing absorption on its way out of the sample. The measured intensity may also be enhanced by secondary fluorescence generated deeper within the sample. The resultant intensity is compared with that from a known standard and the ratio corrected to give the true concentration of the analyzed element in the sample.

Some complex physical processes are thus involved as the electrons slow down, are scattered, and cause ionization, from which the resulting radiation undergoes absorption and may be enhanced by fluorescence. In principle these processes can be calculated from fundamental parameters, but are too complex to be described exactly, so that the final accuracy of the analysis may not be limited by these parameters themselves but by the physical model which embodies them.

The Physical Model

The essential link between the basic physics of microprobe analysis and its useful application is the physical model used to represent the process numerically. Many such models have been proposed in the past 40 years and are properly the subject of a separate session on quantitative analysis. However, it is too limiting to consider the basic physics in isolation for several reasons.

• The model tells us which fundamental parameters are important and which are not; in most cases, for example, it is more important to know mass absorption coefficients accurately

The author is visiting the Research Centre in Superconductivity at the University of Cambridge, having previously retired as Director of the Central Laboratories of TI Group plc. The help of Dr. Stephen Reed of the Department of Earth Sciences at Cambridge University over many years is gratefully acknowledged.

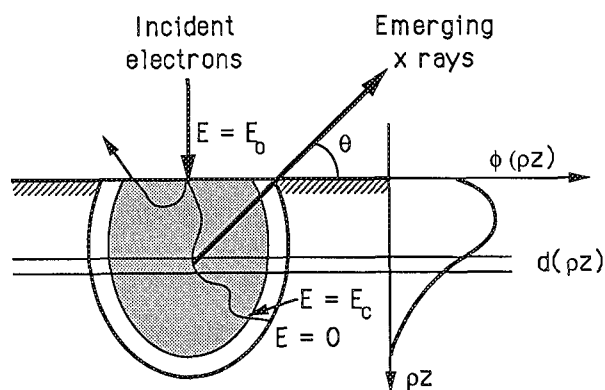


FIG. 1.--Primary x rays are generated at various depths ρz beneath surface and are collected at angle θ by the spectrometer.

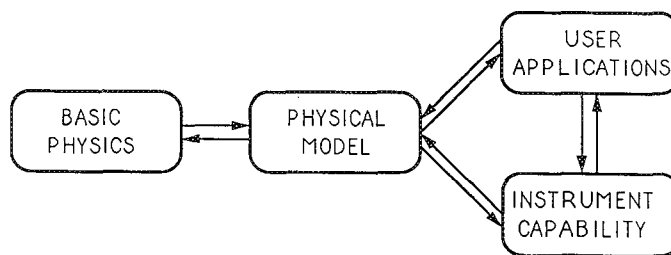


FIG. 2.--Physical model links basic physics with practical microprobe analysis.

than fluorescence yields.

- The model reflects the changing needs of the user for example in demanding better light-element analysis, for which a good knowledge of the distribution in depth of x-ray emission is important as well as of the mass absorption coefficients. The analysis of oxygen in the new superconductors is a case in point.

- The model also reflects the changing capability of the instrument, for example, the advent of multilayer monochromators has increased the popularity of light-element analysis. Improved instrument stability has also heightened demands for improved accuracy overall.

Thus, Fig. 2 indicates, the physics, instrumentation, and applications of the technique are in a continual state of interaction, and work on the fundamental parameters underpinning the physics must be part of this interaction if it is to meet the real needs of the subject. To study this relationship further we look at two main models to assess the demands that are placed on the accuracy of the fundamental parameters involved. These are the "ZAF" correction, in which effects due to atomic number, absorption, and fluorescence on the measured intensity are calculated separately; and the "Monte Carlo" approach to simulate a large number of electron trajectories in the target and hence calculate the intensity as a single process.

X-ray Absorption and the ZAF Correction

The model most widely used is the ZAF correction, which exists in a variety of forms suitable for automated correction procedures in the computer. The method had its origins in the early 1960s, as an understanding evolved first of the absorption A of the emerging primary beam, then of secondary emission due to fluorescence F , and only later of the dependence of electron penetration and backscatter on atomic number Z . Separated in this way, the absorption correction is usually the most important, and it was early shown by Castaing that the fraction $f(\chi)$ of x rays leaving the sample surface in the direction of the spectrometer may be calculated from the distribution $\phi(\rho z)$ of x-ray emission with depth ρz beneath the surface, as implied from Fig. 1. Thus

$$f(\chi) = \int \phi(\rho z) e^{-\chi \rho z} d(\rho z) / \int \phi(\rho z) d(\rho z) \quad (1)$$

where $\chi = (\mu/\rho) \csc \theta$, where μ/ρ is the mass absorption coefficient and θ the take-off angle. The first determinations of $\phi(\rho z)$, and hence $f(\chi)$, were made experimentally by Castaing and Descamps in 1955 and have since been supplemented by many others.¹ What was needed, however, was a theory that would predict $f(\chi)$ for any element and any beam energy.

A major step was made in this direction in 1962 with the proposal by Philibert of a simple quadratic expression for $f(\chi)$ in the form²

$$1/f(\chi) = 1 + a(\chi/\sigma) + b(\chi/\sigma)^2 \quad (2)$$

where a and b are functions of atomic number

and σ depends on beam energy. At about the same time Green made extensive measurements of $f(\chi)$ for various elements directly,² and, on the basis of his and other work, Duncumb and Shields proposed an expression for σ to take account of the critical excitation potential of the analyzed element as well as beam energy.³ In 1968 this expression was further improved by Heinrich but the essential quadratic relationship in $1/f(\chi)$ has been retained throughout.⁴ Much more recently Heinrich has constructed a new "f(χ) machine" for further direct measurements.⁵

A surprising result of the success of the Philibert expression was that it showed that $f(\chi)$ was relatively insensitive to the shape of $\phi(\rho z)$, a consequence of the partial cancellation of $\phi(\rho z)$ that is inherent in the form of Eq. (1). However, that is only true where absorption is not excessive. By the same token $f(\chi)$ is even less sensitive to the form of the inner shell ionization cross section, which Philibert assumed to be constant along the electron path. We shall return to this point presently. Thus the Philibert correction, appropriately modified, has been highly successful for the analysis of elements with atomic number greater than 12, but falls down when it is extended to the light elements, where these criteria may not be valid.

Mass Absorption Coefficients

In terms of the fundamental parameters required for making use of the Philibert correction, all that is thus required is a knowledge of the appropriate mass absorption coefficients, and they were first brought together for microprobe use by Heinrich in 1964.⁴ Using a derivative of the formula proposed by Kramers in 1923, Heinrich was able to fit the best experimental data then available with an expression of the form

$$\mu/\rho = C\lambda^n \quad (3)$$

where λ is the wavelength of the incident radiation and the exponent n falls in the range 2.5-2.9. The coefficient C changes abruptly at absorption edges, and is tabulated, with n , as a function of the absorbing element. More recently Heinrich revised these coefficients and extended the formula to cover the light elements,⁶ giving a consistent set of values for x-ray wavelengths up to the K emission of boron. Thus a means exists for calculating mass absorption coefficients as part of a correction procedure, rather than by storage of unwieldy tables, which can run to some 27 000 values for all combinations of emitted radiations and absorbing elements.

The main features of Heinrich's tables are summarized in Fig. 3, showing the linear contours that result from use of a logarithmic plot. There is still uncertainty in some of the values for low energies; Bastin has shown, in a careful analysis of oxygen in various known oxides, that the best way to refine these values may be to work back from the

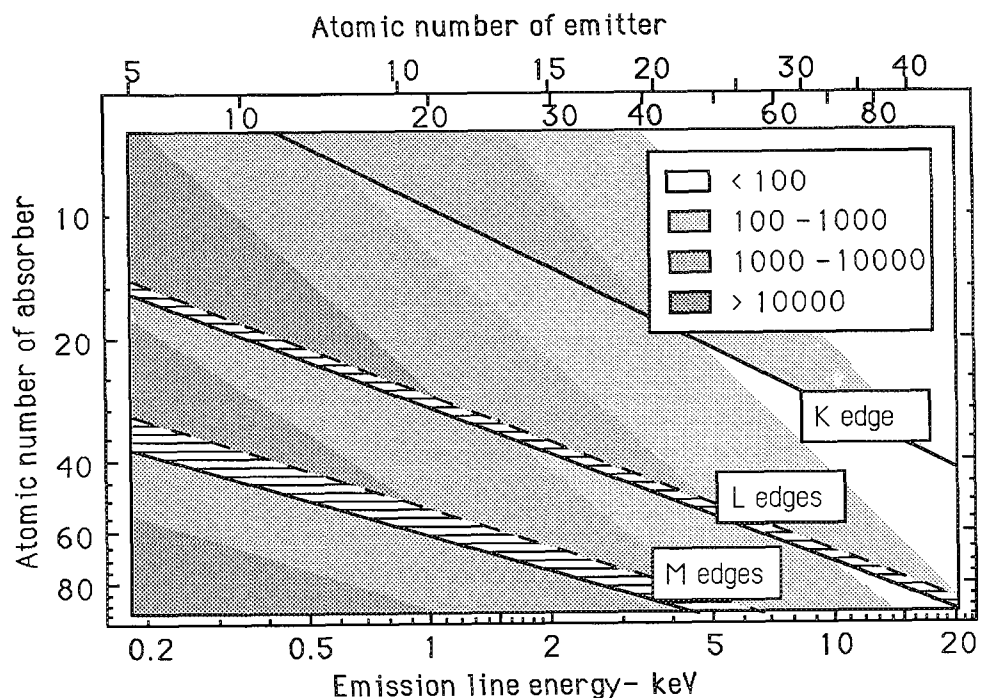


FIG. 3.--Systematic variation of mass absorption coefficient over 0.2-20keV range.

ment A in the sample, S is the electron stopping power, Q the ionization cross section and $1 - R$ the fractional loss of intensity due to backscatter. The fluorescence yield ω_A is the proportion of A ionizations that give rise to characteristic emission from a given shell, normally assumed to be the same in both sample and standard. We comment briefly on S, R, and Q as they affect the accuracy of the generated intensity.

Electron Stopping Power S. It is well known that electrons are slowed down by a series of inelastic interactions as they penetrate into the target. For most purposes this loss of energy has been well approximated by a continuous function, such as Bethe's law, which gives the rate of energy loss with mass thickness in terms of electron energy and target material. Thus

$$S = \text{const.} (Z/A) (1/E) \ln(1.166E/J) \quad (5)$$

where Z and A are the atomic number and atomic weight of the target material, and J is its mean excitation energy. This latter parameter is assumed to be a smooth function of atomic number and not dependent on chemical bonding--approximations which at some point become invalid. Likewise the Bethe expression takes no account of straggling effects which blur the deceleration process. It is relatively easy to evaluate the effect of varying the mean excitation energy, but the importance of straggling and the effect of chemical bonding are not yet fully understood.

Electron Backscatter R. The intensity loss due to backscatter can be readily calculated from a knowledge of the energy distribution of the backscattered electrons. This distribution has been determined experimentally for a number of elements and beam energies, notably by Bishop, and these measurements have been successfully interpolated by a fitted polynomial.³ The effect of inclining the beam axis away from the normal to the surface is less well known, but the Monte Carlo technique appears to be the best way of supplementing such experimental data as do exist.

Ionization Cross-section Q. To date, a knowledge of the ionization cross section as a function of electron energy has been of less importance, because of the inherent compensation between sample and standard normally used with bulk samples. That may not be the case at the high overvoltages often used for the light elements. In addition, the form of Q clearly influences the shape of $\phi(\rho z)$, which in turn must influence the absorption correction, as noted above. A further reason for knowing Q is so as to carry out thin-film analysis in the analytical electron microscope, where intensity comparisons are made among various wavelengths in a given sample. The most commonly used form of Q is given by

$$Q E_c^2 = \text{const.} (\ln U)/U^m \quad (6)$$

where E_c is the critical excitation potential, U is the overvoltage ratio E/E_c , and the index m is normally chosen to be unity. The effect of varying this index on the depth distribution $\phi(\rho z)$

K α microprobe analysis of known samples.⁷
L α The fundamental information we need here is thus not yet complete.

Electron Retardation and Backscatter

The effect of atomic number on the generated x-ray intensity can be split into two parts: that due to electron retardation, and that due to backscatter. As an integral along the track of an electron in Fig. 1, the intensity generated from element A is

$$I_g = \text{const.} \omega_A c_A R \cdot \int (Q/S) dE \quad (4)$$

where c_A is the mass concentration of element A in the sample, S is the electron stopping power, Q the ionization cross section and $1 - R$

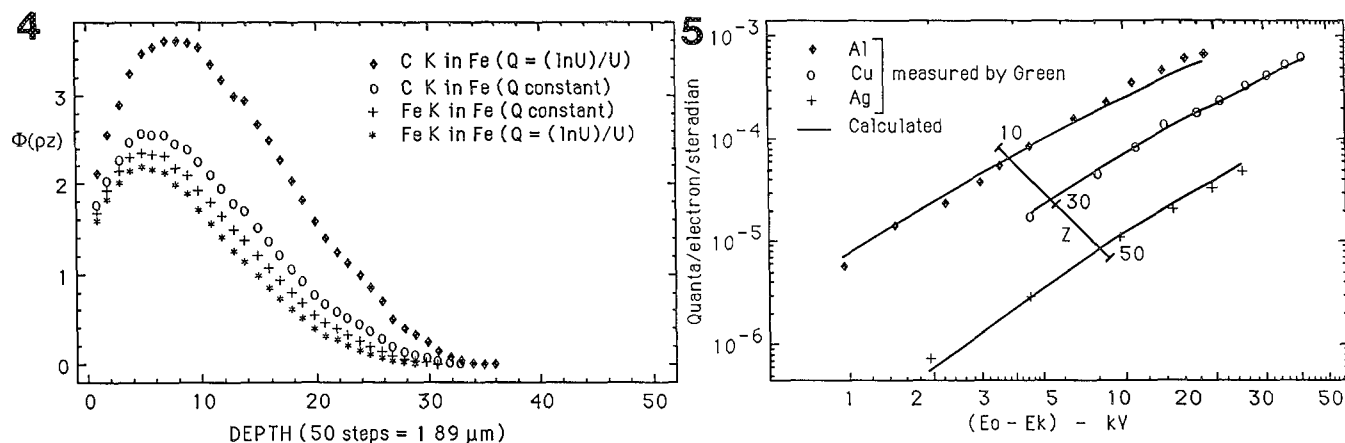


FIG. 4.--Comparison of $\phi(\rho z)$ curves for two forms of Q , by Monte Carlo calculation.

FIG. 5.--Comparison of Green's measurements of quantum efficiency with values calculated in this paper.

can be studied very effectively by the Monte Carlo technique, and we take an example now to show how it can be done.

Monte Carlo Modeling

The technique was first applied to microprobe analysis in the early 1960s by Green and by Bishop,³ and has since been revolutionized by the advent of low-cost computing. Progress was reviewed in 1975 at a special workshop organized by the NBS,⁸ and frequent advances have since been reported at the annual MAS meetings,⁵ which are reviewed in other papers in this volume.

The essence of the method is to simulate a large number of electron trajectories, each made up of a number of individual scattering events, generated at random according to an assumed law of electron scattering. These are separated by a finite step length within which the electron loses energy. As each electron slows down, the probability of causing x-ray ionization in a given layer may be summed to build up the distribution $\phi(\rho z)$ with depth ρz below the surface. The intensity emerging from the sample surface from each depth can then be calculated. Thus the measured intensity for element A is

$$I_m = \text{const. } c_A \int \phi(\rho z) e^{-\chi \rho z} d(\rho z) \quad (7)$$

The constant term allows for the units in which $\phi(\rho z)$ is expressed, and for the efficiency of detection, and disappears when I_m is related to the intensity from a standard.

The Monte Carlo method overcomes many of the difficulties with the ZAF technique in respect of the light elements, and is moreover suited to tilted or layered geometries. Because it computes $\phi(\rho z)$ directly there is no need to separate the atomic-number effect from absorption, although this is easily done for comparison if necessary. Thus Eq. (1) allows Eq. (7) to be rewritten as

$$I_m = \text{const. } c_A f(\chi) \int \phi(\rho z) d(\rho z) \quad (8)$$

in which $f(\chi)$ represents the absorption correction and the remainder is the intensity generated before absorption, as in Eq. (4). We can thus relate the absorption and atomic-number effects straight back to the fundamental laws of electron scattering, electron stopping power, and ionization cross section so that the effect of varying any of the parameters on the end result can readily be tested.

To provide an example of this ability, the technique has been used to simulate the x-ray emission from a sample containing a trace of carbon in iron. This configuration represents a real problem for the metallurgist and formed one of the first applications for light-element analysis. The calculation is based on a simple 50-step Rutherford scattering model first described by Duncumb,³ which is adequate for this purpose and easy to use.

Figure 4 shows the distribution $\phi(\rho z)$ for iron K radiation, based on the form of ionization cross section Q given on Eq. (6), and compares it with that obtained with Q set to be constant ($U > 1$), as assumed in the earlier Philibert approach. Very little difference is seen in the ϕ curves for iron, even with this extreme change in Q . However, for carbon radiation a different result is obtained, since the overvoltage ratio U for this low-energy radiation is much greater, which has a correspondingly large effect on $\phi(\rho z)$ and hence on $f(\chi)$. For light-element analysis, therefore, Q must be chosen with care, and it may be worth trimming the value of m to a value slightly lower than unity used in this illustration.

The Monte Carlo method thus offers an ideal way of exploring the effect of varying any of the fundamental parameters it embodies on $f(\chi)$ and on the total intensity generated. For day-to-day analysis, however, the method is too cumbersome, and it is more practical to replace the $\phi(\rho z)$ curves so obtained by analytical expressions fitted to the shape and total area; one such approach is described by Pouchou and Pichoir.^{5,6}

We have seen that a knowledge of the absolute intensity of emission has not been of primary importance in quantitative analysis, because of the cancellation that occurs in comparing sample with standard. However, there are several instances where that is not the case; we have referred to the fluorescence correction, to the normalization of the area under $\phi(\rho z)$ curves, and to the analysis of thin isolated films. In addition, a growing influence over the past few years has been the advent of "standardless" analysis, made possible by the relative stability of energy-dispersive detectors over crystal spectrometers. In principle, it is only necessary to calibrate the detector efficiency at one wavelength in order to calculate the count rate from a known sample at any other wavelength. To do so, it is essential to know how the intensity generated within the sample varies with beam voltage and atomic number. In practice, several reference samples are often required, but in general the exploratory analysis of a sample with many unknown elements can be greatly speeded up.

The absolute intensity of emission, in terms of x-ray quanta generated per electron, was studied early by Green and Cosslett in relation to microprobe analysis.² Using a gas proportional counter of known efficiency, they measured the intensity from a number of $K\alpha$, $L\alpha$, and $M\alpha$ emitters, and confirmed the existence of a power law variation with the overvoltage $E_0 - E_C$. Their measurements for the K emission from aluminum, copper, and silver are plotted as quantum efficiency in Fig. 5, and are here compared with the calculated efficiencies obtained by numerical integration of Eq. (4) above. Good agreement is obtained over a wide range of overvoltage and atomic number, showing a variation of three orders of magnitude in quantum efficiency. The constant terms in Eqs. (5) and (6), which form part of Eq. (4), are those given by Reed.³ Some fall-off is evident in the calculated values for high overvoltages in aluminum; this discrepancy can be reduced by lowering m in Eq. (6) from 1 to 0.8, but may possibly be explained by inaccuracy in the high absorption correction implicit in Green's reported data.

Plotted on a log-log scale, as illustrated, Green's data show a linear displacement with atomic number Z . This displacement is represented in Fig. 5 by the diagonal scale showing the plot spacing as a function of atomic number. Thus a reasonable knowledge of quantum efficiency exists for K radiation, and Green's measurements are consistent with the later theory adopted in this paper. The situation for L and M emission is not so satisfactory, and a better knowledge of ionization cross section Q and fluorescence efficiency ω_A is still needed.

Fluorescence Yield

Whereas the term for fluorescence yield appears directly in the calculation of absolute intensity (Eq. 4), it is eliminated when the

intensity measured is compared with that from a standard sample. That is not the case where secondary fluorescence is significant, since the relative enhancement in the measured intensity is directly proportional to the fluorescence yield of the exciting element. Fortunately this is well known for K radiation, where the effect may be strong, but less so for L or M emitters. The calculation of secondary fluorescence is well documented and falls outside the scope of this paper.³

Even where secondary fluorescence is not a major factor, the primary intensity may be affected by nonradiative transitions.⁴ The Auger effect is well known, but the redistribution of vacancies within L or M subshells from Coster-Kronig transitions has only recently received detailed attention.⁵ This redistribution has the effect of varying the intensity of one line relative to another; in practical terms, it can lead to a significant error in the calculation of absolute intensity, especially at low voltages. It is difficult to measure this effect directly; it may be that (as with some mass absorption coefficients) the best way forward is by the microprobe analysis of known standards.

Conclusion

We have looked at two physical models of the process of microprobe analysis, in order to assess the relative importance of the fundamental parameters on which they are based. Although there will always be scientific interest in improving our knowledge of the basic physics, we need to shape this interest toward the parameters that will improve the accuracy of the technique for the end user. In this context, the papers that follow expand the subject in more detail.

References

For brevity, these references are to books or conference proceedings, each of which includes or refers to several papers of interest. They should be taken in conjunction with the more detailed references cited by authors of succeeding papers.

1. V. D. Scott and G. Love, Eds., *Quantitative Electron-probe Analysis*, Chichester, England: Ellis Horwood, 1983.
2. H. H. Pattee, V. E. Cosslett, and A. Engstrom, Eds., *X-ray Optics and X-ray Microanalysis*, New York: Academic Press, 1963.
3. S. J. B. Reed, *Electron Microprobe Analysis*, Cambridge: Cambridge University Press, 1975.
4. K. F. J. Heinrich, *Electron Beam X-ray Microanalysis*, New York: Van Nostrand, 1981.
5. D. E. Newbury, *Microbeam Analysis--1988*.
6. J. D. Brown and R. H. Packwood, Eds., *X-ray Optics and Microanalysis*, London, Ont.: University of Western Ontario, 1987.
7. P. E. Russell, Ed., *Microbeam Analysis--1989*.
8. K. F. J. Heinrich, D. E. Newbury, and H. Yakowitz, Eds., Special Publication 460, National Bureau of Standards, 1976.

ELECTRON SCATTERING IN SOLIDS

Ryuichi Shimizu and Z.-J. Ding

We propose a practical model for the Monte Carlo simulation of electron scattering in solids. This model is based on the use of the dielectric function for describing inelastic scattering and of the differential cross sections derived by partial wave expansion method, often called Mott scattering cross section, for describing elastic scattering.

The present approach has been applied to (1) anisotropy in the angular distribution of elastically backscattered electrons in the sub-keV region; (2) simulation of $N(E)$ -spectra with secondary electrons included; (3) ultimate resolution of the SEM, leading to more comprehensive understanding of basic mechanisms in microanalysis for quantification; and (4) the calculation of escape depth for quantitative Auger electron spectroscopy (AES) and x-ray photoelectron spectrometry (XPS).

Theoretical

Elastic Scattering. According to quantum mechanics, the incident wave of an electron is scattered by a scattering center. The scattered spherical waves have their own phase shifts, and the scattering amplitude can then be obtained by the summation of these partial waves. Mott has given the relativistic representation of the differential cross section for an electron elastically scattered through an angle θ :

$$\frac{d\sigma}{d\Omega} = |f(\theta)|^2 + |g(\theta)|^2 \quad (1)$$

with the scattering amplitudes

$$f(\theta) = \frac{1}{2ik} \sum_{\ell=0}^{\infty} [(\ell+1)(e^{i2\delta_{\ell}^{+}} - 1) + \ell(e^{i2\delta_{\ell}^{-}} - 1)] P_{\ell}(\cos \theta) \quad (2)$$

$$g(\theta) = \frac{1}{2ik} \sum_{\ell=1}^{\infty} [-e^{i2\delta_{\ell}^{+}} + e^{i2\delta_{\ell}^{-}}] P_{\ell}^1(\cos \theta) \quad (3)$$

where δ_{ℓ}^{+} and δ_{ℓ}^{-} are spin "up" and spin "down" phase shifts of ℓ -th partial wave with $P_{\ell}(\cos \theta)$ and $P_{\ell}^1(\cos \theta)$ Legendre and associated Legendre functions, respectively. The atomic potentials were calculated from the analytical expression for the Thomas-Fermi-Dirac atomic potential.¹ The details of these calculations have been described elsewhere.²

The authors are at the Department of Applied Physics, Osaka University, Suita, Osaka 565, Japan.

Figure 1 shows polar plots of Mott differential cross sections calculated by the partial wave expansion method for 400eV electrons colliding with the Au-atom. The comparison with the Rutherford scattering cross section is also plotted. The marked difference between the cross sections is shown by the existence of lobes for certain directions in the Mott scattering cross section. It has already been pointed out that these lobes are directly related to lobes observed in angular distribution of elastically backscattered electrons in the sub-keV region.

Inelastic Scattering. The theoretical formulation for inelastic scattering of a penetrating electron in solid has been well established in terms of the dielectric function.³ This formulation provides the differential cross section for inelastic scattering as

$$\frac{d^2\lambda^{-1}}{d(\Delta E)dq} = \frac{1}{\pi a_0 E} \text{Im} \left\{ \frac{-1}{\epsilon(q, \omega)} \right\} \frac{1}{q} \quad (4)$$

where $\hbar q$ is momentum transfer from an incident electron of kinetic energy E to the solid, causing an energy loss of the incident electron by $\Delta E = \hbar\omega$. Even though the above equation is valid, the theoretical deviations of $\epsilon(q, \omega)$ have been made so far only for so-called free electron metals. However, recent rapid progress in synchrotron radiation facilities has enabled us to determine the database of optical dielectric constant $\epsilon(0, \omega)$ for a wide range of materials. Hence we have adopted the following excitation function for inelastic scattering,⁴

$$\frac{d\lambda^{-1}}{d(\Delta E)} = \frac{me^2}{2\pi\hbar^2} \frac{1}{E} \text{Im} \left\{ \frac{-1}{\epsilon(\omega)} \right\} \ln \frac{cE}{\Delta E} \quad (5)$$

by integrating Eq. (4); and the optical dielectric constants from the database⁵ were used for $\epsilon(\omega)$.

Derivation of Inelastic Mean Free Path and Stopping Power

Using Eq. (5) one can derive the inelastic mean free path (IMF) λ_{in} :

$$\lambda_{in}^{-1} = \int_0^{E-E_f} \frac{d\lambda^{-1}}{d(\Delta E)} d(\Delta E) \quad (6)$$

Since the experimental data on λ_{in} have been reported, Eq. (6) permits the determination of the constant c in Eq. (5) so that the λ_{in} calculated from Eq. (6) fits the experimental data. The results are shown in Fig. 2.⁶

Eq. (5) also allows one to derive the stopping power as

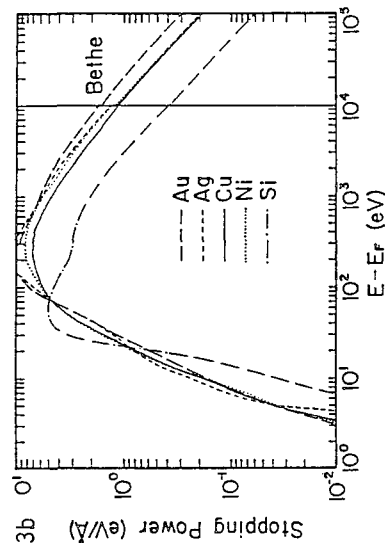
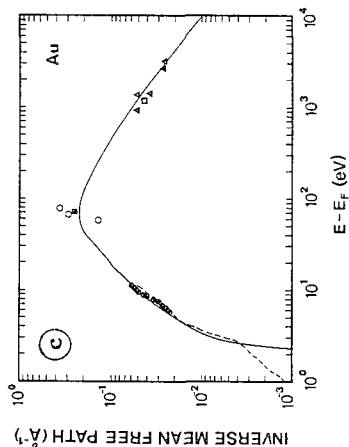
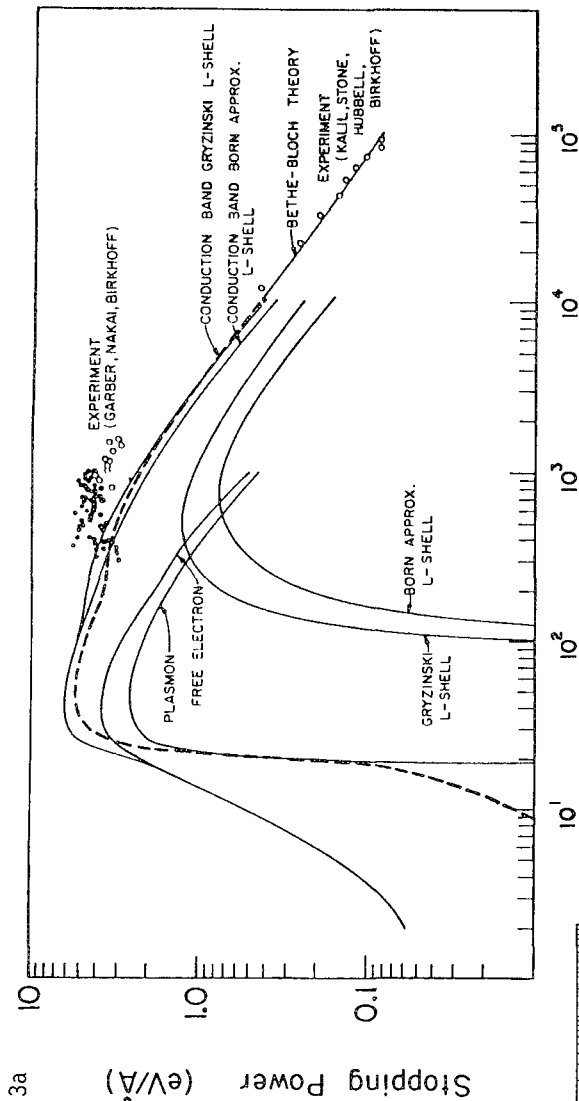
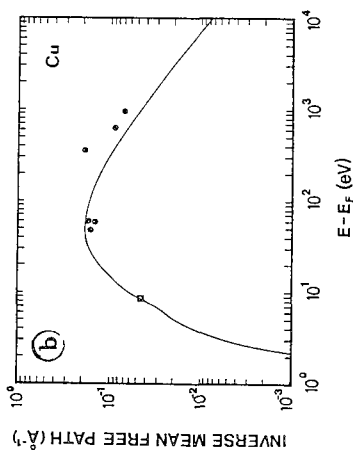
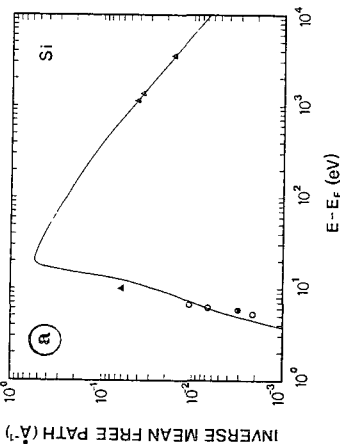
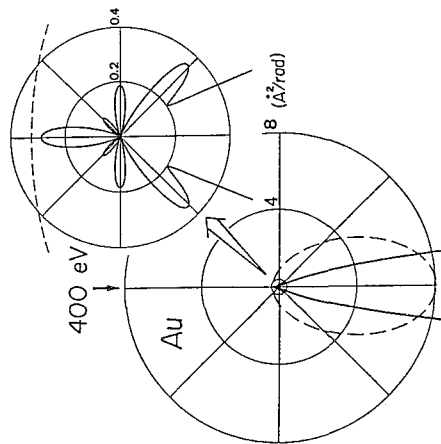


FIG. 1.--Polar plots of differential cross sections for elastic scattering of 400 eV electrons with Au atom. Thick solid line and dashed line represent Mott and Rutherford cross sections, respectively.

FIG. 2.--Energy dependence of inverse of IMPF calculated by Eq. (6) using optical dielectric data. Marks represent experimental values. (a) Si; (b) Cu; (c) Au.

FIG. 3.--Electron stopping power vs electron energy. (a) Dashed line is present calculation by Eq. (8) for Al; (b) calculated curves for several other materials. Bethe's stopping powers are shown above 10 keV.

$$-\frac{dE}{ds} = \int_0^{E-E_F} (\Delta E) \frac{d\lambda^{-1}}{d(\Delta E)} d(\Delta E) \quad (7)$$

A more direct derivation from Eq. (4) according to the definition leads to

$$-\frac{dE}{ds} = \int_0^\infty (\Delta E) \operatorname{Im} \left\{ \frac{-1}{\epsilon(\Delta E)} \right\} \ln \left(\frac{q_1}{q_2} \right) d(\Delta E) \quad (8)$$

where

$$q_1 = \sqrt{k^2 - k_F^2 - (2m\Delta E/\hbar^2)} \quad (9)$$

$$q_2 = \frac{1}{2} [(k - \sqrt{k^2 - (4m\Delta E/\hbar^2)})]$$

Comparing Eq. (8) with Bethe's stopping power one can easily see the mean ionization energy of the Bethe's stopping power defined in the present approach as

$$\ln I = \frac{2}{\pi} \left(\hbar \sqrt{\frac{4\pi N Z e^2}{m}} \right)^{-2} \cdot \int_0^\infty (\Delta E) \operatorname{Im} \left\{ \frac{-1}{\epsilon(\Delta E)} \right\} \ln(\Delta E) d(\Delta E) \quad (10)$$

In Fig. 3(a) the stopping power calculated from Eq. (8) for Al is compared to the Bethe's stopping power to determine whether it includes the wider energy region down to tens of electron volts. Figure 3(b) shows the stopping powers for various metallic materials, in which one can see that each stopping power calculated is in agreement with the relevant Bethe's stopping powers for the high-energy region.⁷

Simulation Model

The theoretical expressions for elastic scattering (Eq. 1) and inelastic scattering (Eqs. 4 or 5) enable us in principle to simulate the scattering processes of a penetrating electron in a solid, leading to the more comprehensive description of the energy loss processes from the primary energy to the slow secondary energy; i.e., covering whole $N(E)$ spectrum. However, in practical computer simulation this type of simulation based on the use of Eq. (4) for whole energy region requires huge computing times, two or three orders of magnitude larger than the conventional Monte Carlo simulation based on the use of the Rutherford scattering formula and the Bethe stopping power. Hence, we divided the whole energy region into three parts; $E_p \sim E_p - 100$ eV, $E_p - 100$ eV ~ 100 eV, and 100 eV to 0 eV. For the first and third parts, where energy loss peaks often associated with fine structures and secondary electron peaks of very large intensity appear, respectively, Eq. (5) has been used for describing the inelastic scattering processes. For the second part, which covers the major part of the energy region, we have used Gryzinski's excitation function

$$\frac{d\sigma_n}{d(\Delta E)} = \pi e^4 Z_n \frac{1}{(\Delta E)^3} \frac{E_n}{E} \left(\frac{E}{E+E_n} \right)^{3/2} \left(1 - \frac{\Delta E}{E} \right)^{E_n/(E_n+\Delta E)} \cdot \frac{\Delta E}{E_n} \left(1 - \frac{E_n}{E} \right) + \frac{4}{3} \ln \left(2.7 + \sqrt{\frac{E - \Delta E}{E_n}} \right) \quad (11)$$

which has reduced the computing times very much, accommodating practical use.

Angular Distribution of Elastically Backscattered Electrons

It has been pointed out that the angular distribution of elastically backscattered electrons in the sub-keV region reflects the atomic scattering factor rather than the structure factor for a polycrystalline sample. Hence, the lobes appearing in the angular distribution directly correspond to the lobes of the differential cross section of elastic scattering (Fig. 1), as illustrated in Fig. 4. Electrons that have undergone a single elastic collision exit from the surface as backscattered electrons while maintaining their kinetic energies. The angular distribution of those backscattered electrons therefore reflects the differential cross section (single-collision model).

To confirm this conclusion we performed the measurement of the angular-energy distribution of backscattered electrons with a rotatable sector-type energy analyzer. A schematic of the experimental arrangement is shown in Fig. 5.

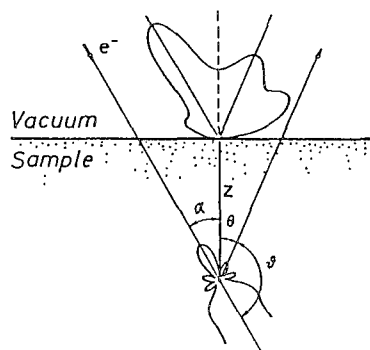
The experimental results were compared with two theoretical calculations by Monte Carlo simulation and the single-collision model, as shown in Fig. 6.⁸ The direction of the lobes of both the calculated results agree very well with those of the experiment, leading to the conclusion that the angular distribution of elastically backscattered electrons of sub-keV is mainly controlled by the differential cross-section of elastic scattering with single atoms, particularly for heavy-element materials.

$N(E)$ -spectra with Secondary Electrons Included

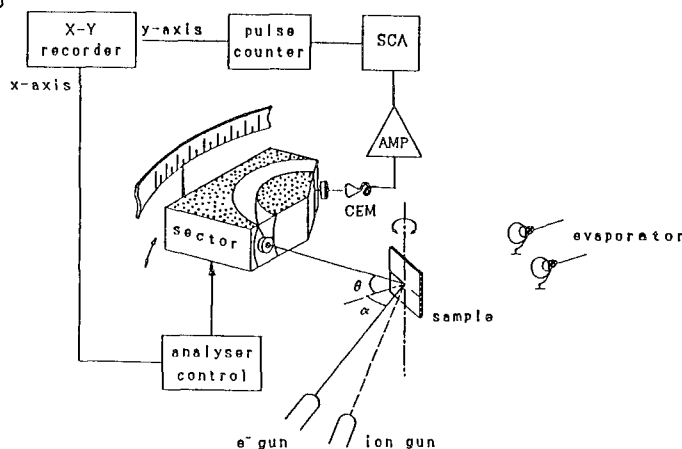
In microanalysis, considerable amounts of signal are generated by the backscattered electrons. To establish quantitative analysis with those signals, the precise knowledge of the backscattered electrons is therefore necessary, and we attempted to provide the theoretical full energy spectrum from the elastic peak to the low-energy secondary electron peak, which is another signal of SEM.

Figure 7 shows the calculated total energy distribution, $N(E)$ spectra, of all the backscattered and secondary electrons ejected from the surface into the vacuum in hemispherical solid angles.⁶ The inset figures are the energy distribution of secondary electrons and the energy loss peaks, enlarged for more detailed examination. As seen from the figures for the secondary electrons, the calculated energy distributions (plotted in a histogram) agree with the experimental ones quite satisfactorily. With respect to the energy distributions of the backscattered electrons with the loss peaks, more systematic investigations have also been performed to confirm that the present Monte Carlo simulation agrees with the experimental results.⁹

4



5



6

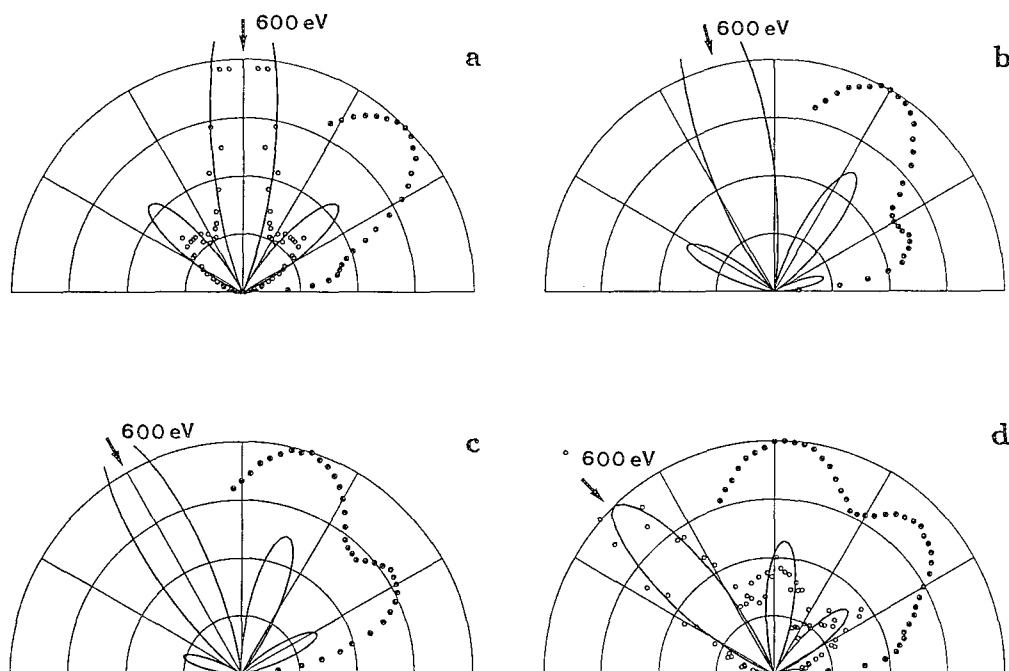


FIG. 4.--Schematic diagram of collision model.

FIG. 5.--Experimental arrangement.

FIG. 6.--Polar plots of angular distribution of elastic peak in the incidence plane for 600 eV primary energy. (O) Monte Carlo simulated results; (●) experimental data, scaled to be unity for the maximum; — calculated from single-collision model.

Ultimate Resolution of SEM

The recent development of high-brightness electron sources and progress in the electron optical design of instruments have enabled the SEM to approach its ultimate resolution. Nagatani and Saito¹⁰ demonstrated that a spatial resolution of 8 Å was attainable from the observation of Au-Pd fine particles evaporated on a carbon film substrate (Fig. 8). Modern electron optical design produces a minimum probe size of 6 Å or less, at an accelerating voltage of 30 kV; Nagatani and Saito, by obtaining a probe size of 8 Å or less, have almost attained the theoretical limit.

However, a new question has arisen: does the spatial resolution in such an SEM-observation

directly guarantee that the spot size is equal to or less than the spatial resolution? We therefore wish to examine this question by Monte Carlo simulation of their experiment, as follows. Figure 9 shows a schematic illustration of the sample used in the experiment and the model for the simulation. In the model, the Au-Pd particles on carbon film are simplified to be Au-blocklets and carbon film is neglected for convenience of simulation. Next, an electron probe of infinitesimal spot size is assumed to scan over those Au blocklets by considering the gap between them as a parameter.

Figure 10 shows the trajectories of incident electrons (top) and of secondary electrons

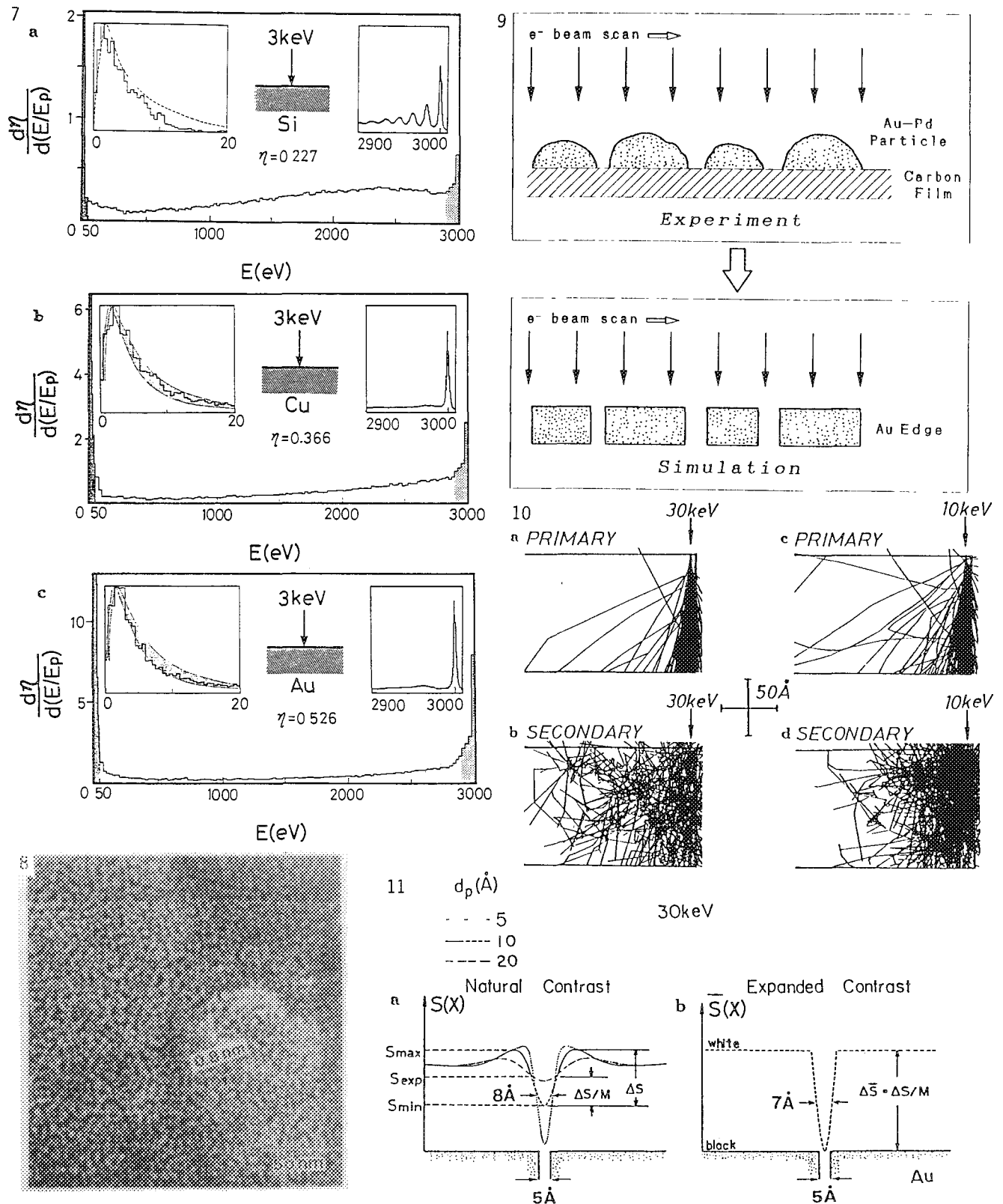


FIG. 7.--Calculated total energy distribution of backscattered electrons and secondary electrons. Left inset is for true cascade secondaries, dashed line and shaded region show experimental curves. Right inset shows low-loss energy peaks with elastic peak. (a) Si; (b) Cu; (c) Au. FIG. 8.--Secondary electron image of evaporated Au-Pd particles. FIG. 9.--(a) Schematic diagram of the sample for Fig. 6; (b) simplified model for simulation. FIG. 10.--Trajectories of electrons produced by primary beam of infinitesimal spot size incident on Au film 100 Å thick at 5 Å from the edge. FIG. 11.--Line scan profiles near edges for several diameters d_p . (a) Natural contrast; (b) expanded contrast, as shown for d_p of 10 Å with expansion constant $M = 2$.

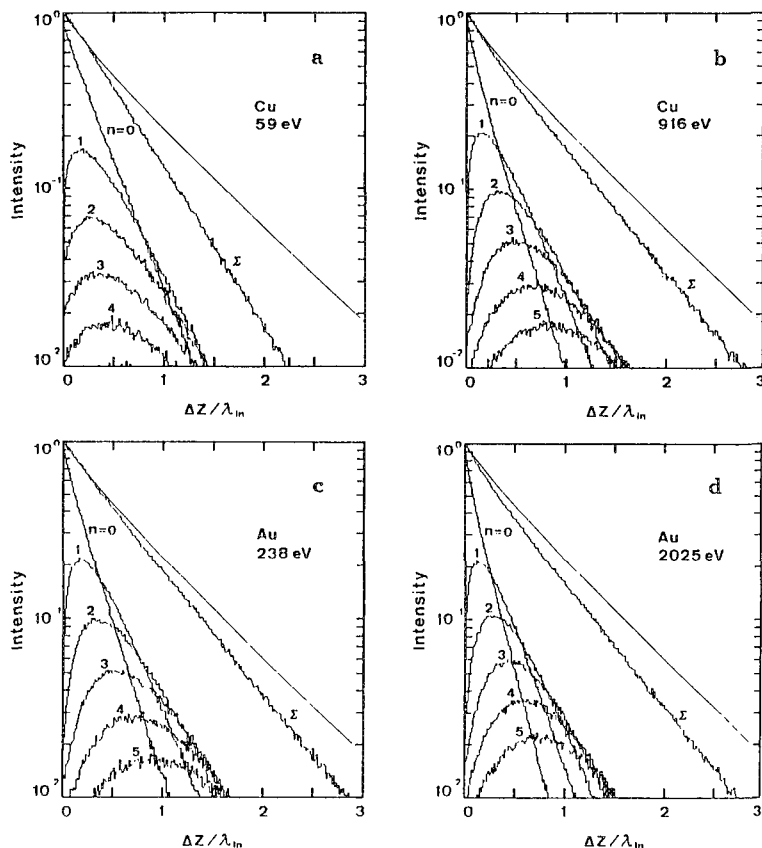


FIG. 12.--Depth distribution of Auger electron intensity measured with hemispherical solid angle. Solid line indicates case when elastic scattering is neglected. Histograms are Monte Carlo calculation results by inclusion of elastic scattering. n represents number of scattering times, Σ summation over n . (a) Cu (59 eV); (b) Cu (916 eV); (c) Au (238 eV); (d) Au (2025 eV).

suggests that the edge-to-edge resolution depends on many factors of an experiment and can be considerably improved by appropriate image processing. It is therefore strongly recommended that electron microprobists should be careful in the assessment of the probe size from SEM observation.

Elastic Scattering in Escape Processes Correction for Escape Depth

In the conventional formalism of escape depth or attenuation length, the elastic scattering of the signal electron has not been considered. However, recent calculations¹² have shown the attenuation of the signal electrons, incurring considerable error in quantitative AES and XPS. Differential cross sections for both elastic and inelastic scatterings are available from Eqs. (1) and (4). This allows for Monte Carlo simulation of the escape process of signal electrons of different kinetic energies to determine how the elastic scattering affects the assessment of escape depth, which has been conventionally assessed from the IMFP only.

Figure 12 shows Monte Carlo calculations of depth distribution of the signal electrons, i.e., the escape probability of the signal electrons generated at depth Δz .¹³ This result indicates how the elastic scattering contributes to practical reduction of the escape depth. In the case of (b)-(d), elastic scattering has resulted in the reduction of $\sim 20\%$ of the escape depth and much more for the case (a).

Consequently, the present Monte Carlo simulation has demonstrated that elastic scattering should be included in the assessment of escape depth for quantitative AES and XPS.

References

1. R. A. Bonham and T. G. Strand, *J. Chem. Phys.* 39: 2200, 1963.
2. Y. Yamazaki, Ph.D. thesis, Osaka University, 1977.
3. D. Pines, *Elementary Excitations in Solids*, New York: Benjamin, 1964, 126.
4. C. J. Powell, *Surf. Interface Anal.* 7: 263, 1985.
5. E. D. Palik, Ed., *Handbook of Optical Constants of Solids*, London: Academic Press, 1985.
6. Z.-J Ding and R. Shimizu, *Surface Sci.* 197: 539, 1988.

generated in the Au blocklet. Assuming that all those secondary electrons emitted from both surfaces, top and side, are to be detected as signal, we have obtained the line scan profiles for electron probes of various spot sizes d_p , which can easily be done by taking a convolution of the Gaussian distribution function describing the intensity distribution of the relevant electron probe, with the line scan profile for the electron probe of infinitesimal spot size obtained by the Monte Carlo simulation.

The results are shown in Fig. 11(a). Here we assumed that the gap of two Au blocklets is 5 Å. There are two possibilities to allow the observation of 8 Å edge-to-edge resolution in an SEM image. The first one is the case in which both d_p and the gap are less than 8 Å, as demonstrated by the dotted line in the figure. Another possibility for obtaining such a high edge-to-edge resolution is demonstrated in Fig. 11(b). Here we assume d_p is 10 Å. Some devices may enable the high resolution to be attained by image processing provided that S/N is sufficiently high. Taking into account the experimental conditions of the SEM observation shown in Fig. 7 and the Rose criterion, we have demonstrated that the experiment allows a contrast expansion M of at least double; i.e., $M = 2$ in Fig. 11(b), which leads to the conclusion that the edge-to-edge resolution in this case is ~ 7 Å, as discussed in more detail elsewhere.¹¹

Consequently, the present simulation suggests that the edge-to-edge resolution depends on many factors of an experiment and can be considerably improved by appropriate image processing. It is therefore strongly recommended that electron microprobists should be careful in the assessment of the probe size from SEM observation.

7. Z.-J. Ding and R. Shimizu, *Surf. Sci.* 222: 313, 1989.
8. Z.-J. Ding , H. Yoshikawa, and R. Shimizu, *Phys. Stat. Sol.* (b) (in press).
9. Z.-J. Ding, R. Shimizu, T. Sekine, and Y. Sakai, *Appl. Surface Sci.* 33/34: 99, 1988.
10. T. Nagatani, and S. Saito, *Proc. 11th ICEM*, 1986, 2101.
11. Z.-J. Ding and R. Shimizu, *J. Microscopy* 154: 193, 1989.
12. A. Jablonski, *Surf. Interface Anal.* 14: 659, 1989.
13. Z.-J. Ding, Ph.D. thesis, Osaka University, 1990.

INNER-SHELL IONIZATION CROSS SECTIONS

C. J. Powell

Values of cross sections for ionization of inner-shell electrons by electron impact are required for electron probe microanalysis, Auger electron spectroscopy, and electron energy loss spectroscopy. The author has reviewed measurements and calculations of inner-shell ionization cross sections.¹⁻⁴ This paper is an update and summary of these previous reviews with emphasis on data for total inner-shell ionization cross sections as needed for x-ray microanalysis. Information is given on the more useful formulas for ionization cross sections and the extent to which they agree with calculations and measurements for particular elements.

Bethe Theory of Inner-shell Ionization

Bethe⁵ has shown that the cross section for ionization of the n_l shell by electrons of energy E is

$$Q_{n_l} = \frac{\pi e^4}{E_{n_l}} \frac{Z_{n_l} b_{n_l}}{E} \ln(c_{n_l} E/E_{n_l}) \quad (1)$$

where Z_{n_l} is the number of electrons in the n_l shell and E_{n_l} their binding energy. The terms b_{n_l} and c_{n_l} are referred to as the Bethe parameters and are expected to be approximately unity and in the range 1-4, respectively. It has been assumed in the derivation of Eq. (1) that $E \gg E_{n_l}$; the minimum value of E to satisfy this relation will be discussed below.

Equation (1) has been written in nonrelativistic form. If $E \gtrsim 50$ keV, relativistic corrections are necessary and Eq. (1) becomes^{6,7}

$$Q_{n_l} = \frac{\pi e^4}{(m_0 v^2/2)} \frac{Z_{n_l} b_{n_l}}{E_{n_l}} [\ln(c_{n_l} m_0 v^2/2E_{n_l}) - \ln(1 - \beta^2) - \beta^2] \quad (2) \quad Q_E$$

where β is the ratio of the electron velocity v to the velocity of light and m_0 is the electron rest mass. Values of v and β for selected accelerating voltages have been tabulated.⁸

It is convenient to rewrite Eq. (1) in the form

$$Q_{n_l} E_{n_l}^2 = (\pi e^4 Z_{n_l} b_{n_l} / U_{n_l}) \ln(c_{n_l} U_{n_l}) \quad (3a)$$

where $U_{n_l} = E/E_{n_l}$. With values of constants inserted, Eq. 3(a) becomes

$$Q_{n_l} E_{n_l}^2 = 6.51 \times 10^{-14} Z_{n_l} b_{n_l} \ln(c_{n_l} U_{n_l}) / U_{n_l} \quad (3b)$$

$\text{cm}^2 \text{eV}^2$

Similarly, Eq. (2) can be written

$$Q_{n_l} E_{n_l}^2 U_{n_l}' = 6.51 \times 10^{-14} Z_{n_l} b_{n_l} \cdot (V_{n_l} + \ln c_{n_l}) \text{cm}^2 \text{eV}^2 \quad (4a)$$

$$\text{where } V_{n_l} = \ln U_{n_l}' - \ln(1 - \beta^2) - \beta^2 \quad (4b)$$

$$\text{and } U_{n_l}' = m_0 v^2 / 2E_{n_l} \quad (4c)$$

A simple yet valuable method of analyzing cross-section data is the Fano plot.^{8,10} Such plots are made by plotting $Q_{n_l} E_{n_l}^2 U_{n_l}$ vs $\ln U_{n_l}$, as suggested by Eq. (3) for the non-relativistic Bethe equation, or $Q_{n_l} E_{n_l}^2 U_{n_l}'$ vs V_{n_l} , as suggested by Eq. (4) for the relativistic case. These plots are linear if the assumptions made in the above theory are valid. Linear plots also permit ready determination of the Bethe parameters b_{n_l} and c_{n_l} . An important internal-consistency check is that the value of b_{n_l} so derived should equal (within experimental error) the value obtained from an appropriate integration of photoabsorption data.^{1,3,11}

Interpretation of Fano plots is unfortunately not generally simple since the plots often show *two* linear regions, as illustrated schematically in Fig. 1. It is only for region 2

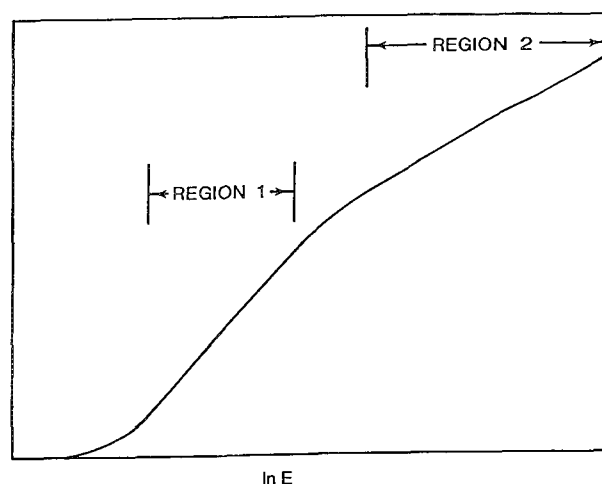


FIG. 1.--Schematic illustration of Fano plot in which product of incident energy E and a particular ionization cross section Q is plotted against logarithm of E (after Ref. 11). See text for description of regions 1 and 2.

C. J. Powell is at NIST, Surface Science Division, Gaithersburg, MD 20899. He is indebted to Drs. J. N. Chapman, T. Sato, T. Sekine, and J. A. Venables for the communication of numerical results.

in Fig. 1 that the plots show the asymptotic Bethe dependence with a slope directly related to photoabsorption data. At lower incident energies, region 1 in Fig. 1, another linear region is generally found with a slope approximately 20% greater than that for region 2. As a result, empirical values of b_{n1} for region 1 are greater than would be expected from the corresponding optical data.¹ The empirical values of c_{n1} for region 1 are similarly smaller than the corresponding values for region 2.

The values of U_{n1} that define the boundaries of regions 1 and 2 in Fig. 1 are not well known. Analyses of K- and L-shell ionization cross sections have shown that region 1 covers at least $4 < U_K < 25$ and $4 < U_{L23} < 20$.¹ Similar analyses of data for ionization of gas-phase atoms show region 1 extending from $U = 4$ to U between 25 and 50.⁹ The lower limit for region 2 is not known but is thought to be $U_{n1} \sim 50$ -200, depending on material.^{12,13}

Although the Bethe equation provides a simple, convenient, and physically based means for calculating inner-shell ionization cross section, a number of important cautions should be kept in mind when it is used.¹¹ First, the Bethe equation is only expected to be valid when the incident energy is high enough to insure the validity of the first Born approximation; that is, region 2 of Fig. 1. Second, it is only for such high energies that cross sections can be calculated from first principles. The fact that Fano plots may show linear regions at lower incident energies (region 1 of Fig. 1) is empirically useful but should not necessarily be relied on. There are several reasons¹² for the change of slope in the Fano plot from region 2 to region 1, but the most likely cause is electron-exchange effects.¹¹ It is difficult to predict slopes for region 1 and how they may change with atomic number.¹⁰ Finally, the Bethe equation cannot be expected to be even empirically useful for near-threshold incident energies ($U_{n1} < 4$). Although the calculated cross sections may become negative (since the empirical values of c_{n1} are generally less than unity), this result does not represent a "defect" of the Bethe theory because Eq. (1) is not expected to be valid at such low energies (and should not, of course, be used for energies where the Fano plot is nonlinear).

For most x-ray microanalysis applications, the incident electron energy is often at least partly in the range corresponding to region 1 of Fig. 1. Analysts should insure that the Bethe equation is applied only for conditions (elements, shells, and values of U_{n1}) for which it is expected to be valid. No equation should be used outside the parameter range for which it has been demonstrated to be valid.

It has been sometimes assumed that the Bethe parameters are "constants," independent of atomic number, for ionization of a given shell. Such a result has not been proved for either region 1 or region 2 of Fig. 1. Values of b_{n1} for region 2 can be derived independently from photoabsorption data, and it has been shown that such values of b_K and b_{L23} do not vary appreciably with Z .^{1,14}

Values of the Bethe Parameters

Since the Bethe equation has been applied extensively in x-ray microanalysis, we shall comment here on measurements and calculations of the Bethe parameters in Eq. (1).

The present author¹ analyzed measured K-shell and L_{23} -shell ionization cross sections and found that Eq. (1) described most measurements. Linear Fano plots were obtained from $6 \leq Z \leq 28$ and $4 \lesssim U_K \lesssim 25$ for which $b_K \approx 0.9$ and $c_K \approx 0.65$. There was no evidence for a significant variation of the Bethe parameters with Z . The limited L_{23} -shell ionization data available were then similarly analyzed for $15 \leq Z \leq 18$ and $4 \lesssim U_L \lesssim 20$ to give $b_{L23} \approx 0.5 - 0.9$ and $c_{L23} \approx 0.6$. The variation of the derived b_{L23} values with Z , however, was not consistent with the trend expected from photoabsorption data.

Rez¹⁵ and Batchelor et al.¹⁶ have reported calculations for ionization of K-, L-, and M-shell electrons in a range of atoms using first-order perturbation theory and Hartree-Slater wave functions. Rez fitted his calculated cross sections to the Bethe equation and found values of the Bethe parameters in the following ranges: $0.71 \leq b_K \leq 1.20$ and $0.71 \leq c_K \leq 1.11$ for $13 \leq Z \leq 39$; $0.96 \leq b_{L23} \leq 1.09$ and $0.74 \leq c_{L23} \leq 0.86$ for $40 \leq Z \leq 64$; and $1.21 \leq b_{M4} \leq 1.25$ and $0.69 \leq c_{M4} \leq 0.72$ for $74 \leq Z \leq 92$. The Rez values of b_K show a larger variation with Z than found experimentally.³

Paterson et al.¹⁷ have measured the ratios of characteristic $K\alpha$ x-ray to nearby bremsstrahlung intensities for Si, Cr, Fe, Co, Ni, Cu, Ge, Mo, Ag, and Sn at electron energies between 80 and 200 keV. Since cross sections for the production of bremsstrahlung are reasonably well known, it was possible for Paterson et al. to derive K-shell ionization cross sections. Figures 2 and 3 show Fano plots for their data using the nonrelativistic and relativistic Bethe equations, respectively. Surprisingly, they found good linear fits, within the experimental scatter, for both equations over the range $3 < U_K < 55$; however, the values of b_K and c_K were different for each case (0.62 and 0.90 for the nonrelativistic and 0.43 and 1.26 for the relativistic equations, respectively). The same data are shown in Fig. 4 in a plot of $Q_K E_K^2$ vs U_K , as suggested by Eq. (3); from Figs. 2-4, there is no evidence of a significant variation of the Bethe parameters with Z . Figure 4 also indicates that the cross sections of Paterson et al. are about 20% lower than would be expected from the earlier analysis.¹

Some authors¹⁸⁻²⁰ have proposed that certain parameters in the Bethe equation be empirically fitted to limited data sets in order to provide convenient representations of the data. Although the expressions so derived may be useful for some purposes, there is a risk in more general use because of the potential or actual conflict with other data. For example, Hoefft and Schwaab²⁰ derived empirical expressions for

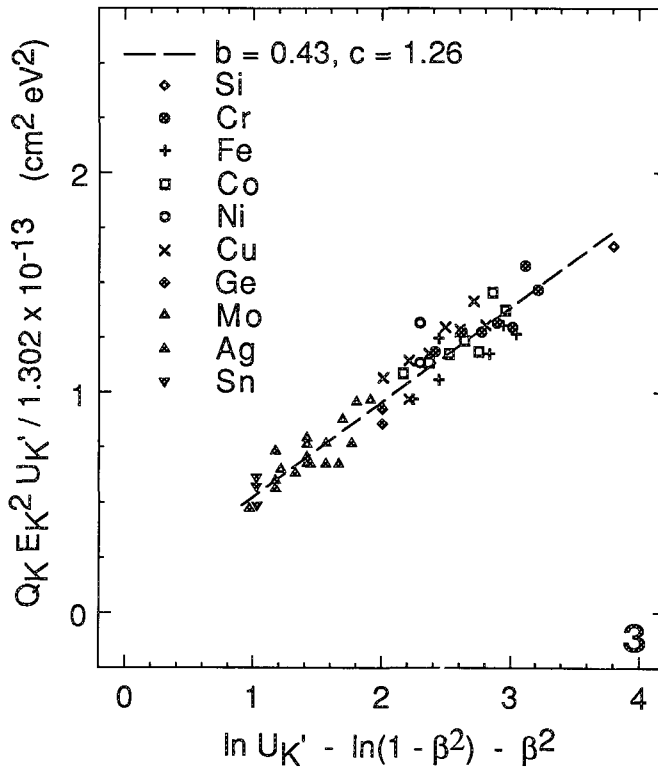
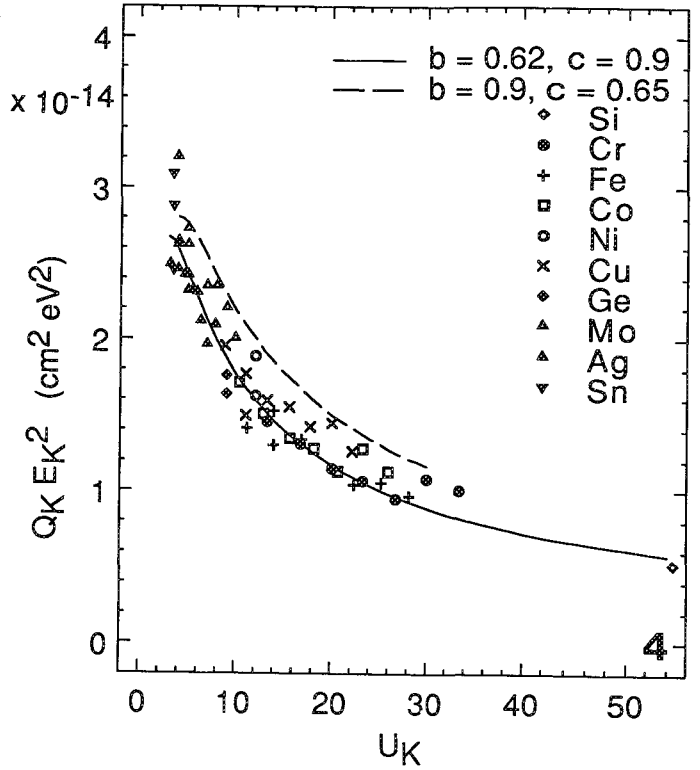
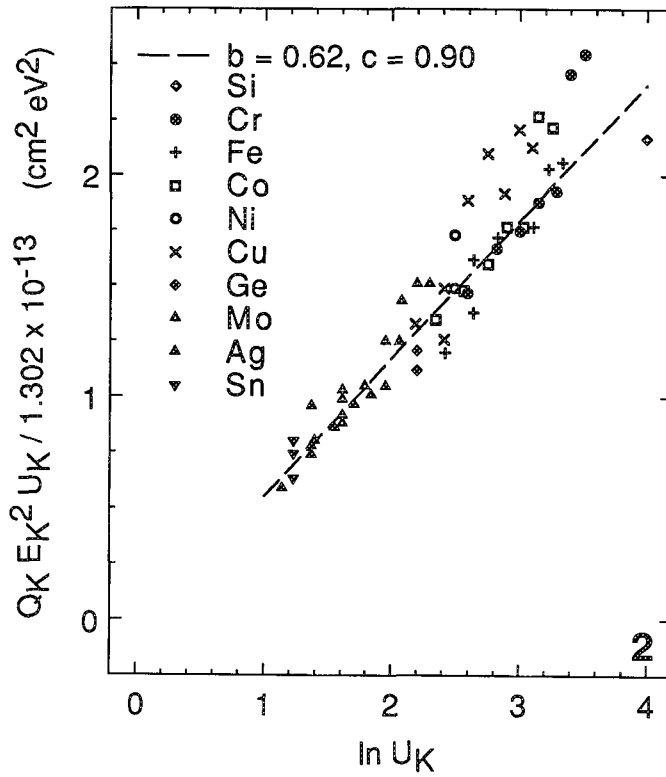


FIG. 2.--Fano plot using nonrelativistic Bethe equation (Eq. 3) and data of Paterson et al.¹⁷ Dashed line is linear fit with $b_K = 0.62$ and $c_K = 0.90$.

FIG. 3.--Fano plot using relativistic Bethe (Eq. 4) and data of Paterson et al.¹⁷ Dashed line is linear fit with $b_K = 0.43$ and $c_K = 1.26$.

FIG. 4.--Plot of $Q_K E_K^2$ vs U_K as suggested by Eq. (3b) using data of Paterson et al.¹⁷ Dashed line is for Bethe parameters given in Ref. 1.

the dependence of b_K , b_L , and b_M on atomic number; their results for incident energies between 35 and 200 keV and for a wide range of atomic numbers showed large variations of the "effective" Bethe parameters for low Z that appear to be in conflict with other measurements.¹

Other Cross-section Formulas and Calculations

We mention here several cross-section formulas that have been found to be useful. Gryzinski²¹ developed a classical theory of atomic ionization and excitation that has been widely applied largely because of its simplicity and general utility. His expression for the inner-shell ionization cross section is

$$Q_{n1} E_{n1}^{-2} = 6.51 \times 10^{-14} Z_{n1}^2 g(U_{n1}) \text{ cm}^2 \text{ eV}^2 \quad (5a)$$

$$\text{where } g(U) = \frac{1}{U} \left[\frac{U-1}{U+1} \right]^{3/2} \{ 1 + (2/3) [1 - (1/2U)] \ln [2.7 + (U-1)^{1/2}] \} \quad (5b)$$

Equation (5) agrees closely with measured K-shell cross sections;^{2,3} some additional comments are given below.

Experimental K-shell cross-section measurements have been fitted recently to empirical expressions by two groups.^{22,23} Casnati et al.²² derived the following formula:

$$Q_K E_K^2 = (Z_K a_0^2 F R^2 \psi \phi \ln U) / U \quad (6a)$$

$$\text{where } \psi = (E_K / R)^d \quad (6b)$$

$$d = -0.0318 + (0.3160/U) - (0.1135/U^2) \quad (6c)$$

$$\phi = 10.57 \exp[(-1.736/U) + (0.317/U^2)] \quad (6d)$$

a_0 is the Bohr radius, R is the Rydberg energy (13.606 eV), and F is a relativistic correction factor given by Quarles²⁴ as

$$F = \left[\frac{2+I}{2+T} \right] \left[\frac{1+T}{1+I} \right]^2 \left[\frac{(1+T)(2+T)(1+I)^2}{T(2+T)(1+I)^2 + I(2+I)} \right]^{3/2} \quad (6e)$$

$$I = E_K / mc^2 \quad (6f)$$

$$T = E / mc^2 \quad (6g)$$

Equation (6) was found to fit cross-section data to typically better than $\pm 10\%$ over the range $1 \leq U_K \leq 20$ and $6 \leq Z \leq 79$.

Jakoby et al.²³ analyzed some 600 measurements of K-shell cross sections for elements with $6 \leq Z \leq 92$ and for $E_K \leq E \leq 2$ GeV. Their formula is

$$Q_K = aF_1(F_2 + bF_3 + F_4F_5^C) \text{ cm}^2 \quad (7a)$$

$$\text{where } F_1(Z, \beta) = 2.549 \times 10^{-19} / E_K \beta^2 \quad (7b)$$

$$F_2(\beta) = \ln[\beta^2 / (1 - \beta^2)] - \beta^2 \quad (7c)$$

$$F_3(Z, \beta) = 1 - (\beta_0^2 / \beta^2) \quad (7d)$$

$$F_4(Z) = \ln(1 / \beta_0^2) \quad (7e)$$

$$F_5(Z, \beta) = \beta_0^2 / \beta^2 \quad (7f)$$

$$\beta^2 = 1 - [1 + (E / mc^2)]^{-2} \quad (7g)$$

$$\beta_0^2 = 1 - [1 + E_K / mc^2]^{-2} \quad (7h)$$

$$a = 5.14Z^{-0.48} \quad (7i)$$

$$b = 5.76 - 0.04Z \quad (7j)$$

$$c = 0.72 + 0.039Z - 0.0006Z^2 \quad (7k)$$

The term E_K in Eq. (6b) is expressed in electron volts. Equation (7) was found to fit measured cross sections to an accuracy of $\pm 13\%$.

Figures 5 and 6 show plots of Eqs. (6) and (7) calculated for aluminum ($Z = 13$, $E_K = 1,560$ eV).⁴ The solid line in each figure is the Bethe equation (Eqs. 1 and 3) with $b_K = 0.9$ and $c_K = 0.65$, values that provide a good fit to the K-shell cross-section data for low- Z atoms over the overvoltage range $4 \lesssim U_K \lesssim 25$.^{1,3} The three curves in Fig. 5 agree to better than 10% over this range of U_K . In the near-threshold region, shown in Fig. 6, the Bethe equation is not expected to be valid and, not surprisingly,

it does not represent the experimental data.²⁵⁻²⁷ Equations (6) and (7) both agree well with the near-threshold results ($U_K < 4$) and appear to be superior to the Gryzinski equation (Eq. 5) in this region.³ Figure 7 shows a comparison of the Gryzinski equation (Eq. 5) with the results of the Bethe equation (Eq. 3) using parameter values from Refs. 1 and 17.

Scofield²⁸ has calculated K-shell and L-shell ionization cross sections by high-energy electrons. He gives values for nine elements with atomic numbers between 18 and 92 and for incident energies between 50 keV and 1 GeV. Recent measurements²⁹ of L-shell ionization cross sections for Cu, Sr, Ag, Sn, Sm, Ta, and Au by 50-200keV electrons are in good agreement with Scofield's results.

Recent Auger-yield Experiments

Two papers have been published recently that report values of inner-shell ionization cross sections derived from measurements of Auger-electron yields from solid elements as a function of electron energy.^{30,31} Measurements of Auger-electron yields are attractive in that it is not necessary to know fluorescence yields, as is required for the corresponding x-ray yield measurements. Nevertheless, such measurements for solid targets are difficult in that a significant correction is required for the additional inner-shell ionizations produced by backscattered electrons. Batchelor et al.³⁰ made this correction using transport calculations of backscattered-electron energy distributions while Sato et al.³¹ developed an experimental method for comparison with the Monte Carlo results and other formulas.

Batchelor et al.³⁰ report the energy-dependence of cross sections for K-shell ionizations of Si, L₃-shell ionization of Cu, and M₅-shell ionization of Ag and W with incident energies from 3 to 30 keV. Comparison was made with the energy dependence of calculated cross sections;¹⁶ good agreement was found for Si and less good agreement for the other elements. The Bethe equation with this author's parameter values¹ provided a good fit to the Cu and W data but deviations were observed for Si and Ag. The Si results were the only data to agree well with Gryzinski's equation.

Sato et al.³¹ have determined cross-section dependence on energy for K-shell ionization of C, Al and Si, L-shell ionization of Ti and Cu, and M-shell ionization of Au in the overvoltage range 1.1-15. Their data showed generally good agreement with the energy dependence of Gryzinski's equation, although there were deviations of up to 15% for Si. Fano plots based on the Sato et al. data are shown in Fig. 8. Since only relative cross sections were measured, the data have been normalized to the results of Paterson et al.¹⁷ for K-shell ionization at $\ln U = 2$. It is seen that essentially linear plots are obtained for all six elements and that the slopes

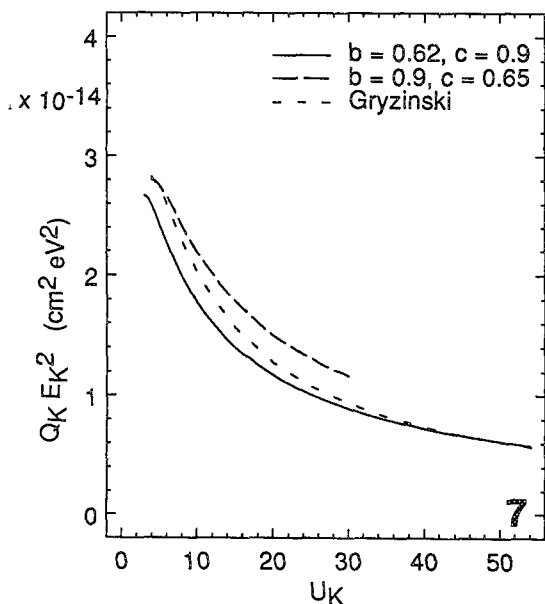
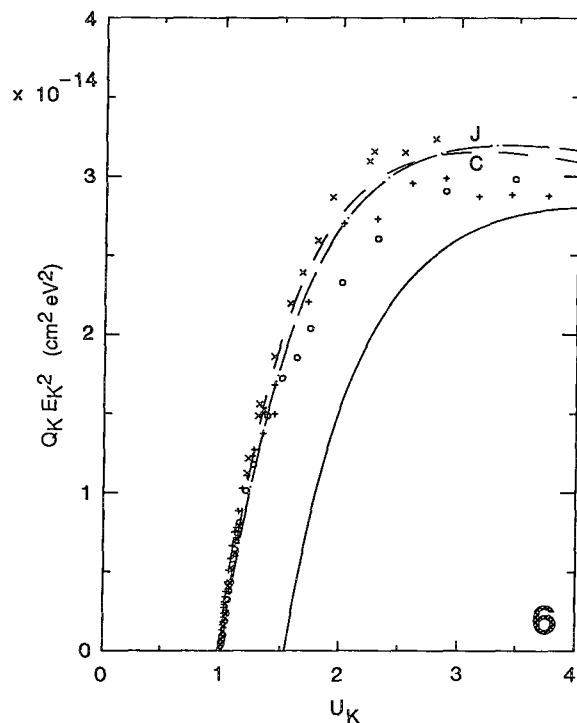


FIG. 6.--Plots of $Q_K E_K^2$ vs U_K in near-threshold region. Solid line is Bethe equation as for Fig. 5, dashed curve C is Casnati et al.²² equation, and dot-dashed curve is Jakoby et al.²³ equation, both evaluated for aluminum. Points show measurements of Hink et al.²⁵ for Ne(o), Hippler et al.²⁶ for Ar (+), and Shima et al.²⁷ for Cu (x).

FIG. 7.--Comparison of predicted K-shell cross sections predicted by Gryzinski equation (Eq. 5, short-dashed line) and Bethe equation (Eq. 3) with $b_K = 0.62$ and $c_K = 0.90$ (Ref. 17, solid line) and with $b_K = 0.9$ and $c_K = 0.65$ (Ref. 11, long-dashed line).

energy-loss intensity over a range of about 100 eV commencing at the threshold energy loss corresponding to the binding energy of an electron in a particular shell for a detected element.

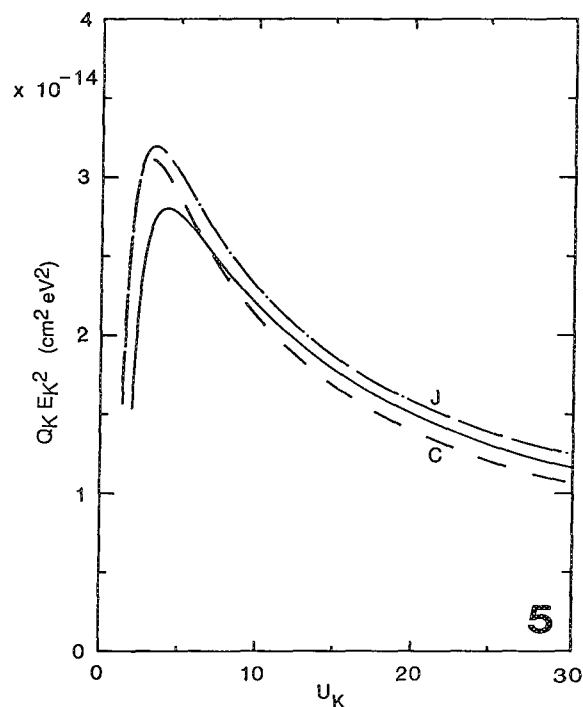


FIG. 5.--Plot of $Q_K E_K^2$ vs U_K . Solid line is Bethe equation (Eq. 3) with $b_K = 0.9$ and $c_K = 0.65$, values that provide a good fit to experimental cross-section data for low-Z elements over overvoltage range $4 \lesssim U_K \lesssim 25$.^{1,3} Dashed curve C is Casnati et al.²² equation (Eq. 6) and dot-dashed curve J is Jakoby et al.²³ equation (Eq. 7), both evaluated for aluminum.

are similar to that found for K-shell ionization by Paterson et al.¹⁷

Cross Sections for Microanalysis

Several authors³²⁻³⁴ have applied different expressions for inner-shell ionization cross sections to the calculation and evaluation of k_{AB} factors that are needed in the widely used Cliff-Lorimer approach to microanalysis.³⁵ Cross-section values obtained from the various formulas may differ considerably, but the ratios of cross sections needed for the calculation of k_{AB} factors do not vary nearly as much.

Partial Inner-shell Ionization Cross Sections

For microanalysis by electron energy-loss spectroscopy, it is necessary to determine partial ionization cross sections corresponding to a limited range of excitation energies and scattering angles of the incident electrons. It is customary to measure the total

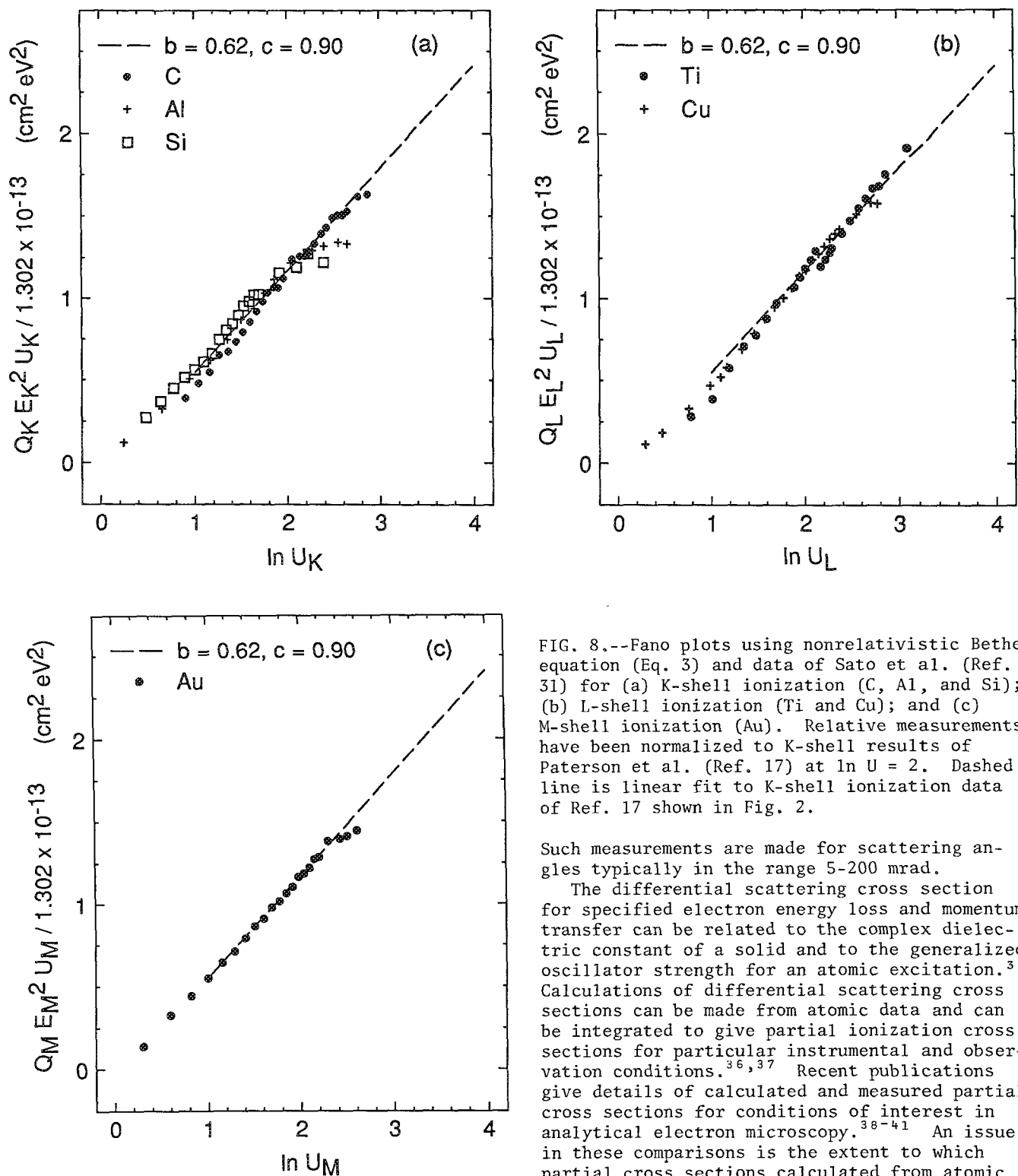


FIG. 8.--Fano plots using nonrelativistic Bethe equation (Eq. 3) and data of Sato et al. (Ref. 31) for (a) K-shell ionization (C, Al, and Si); (b) L-shell ionization (Ti and Cu); and (c) M-shell ionization (Au). Relative measurements have been normalized to K-shell results of Paterson et al. (Ref. 17) at $\ln U = 2$. Dashed line is linear fit to K-shell ionization data of Ref. 17 shown in Fig. 2.

Such measurements are made for scattering angles typically in the range 5-200 mrad.

The differential scattering cross section for specified electron energy loss and momentum transfer can be related to the complex dielectric constant of a solid and to the generalized oscillator strength for an atomic excitation.³ Calculations of differential scattering cross sections can be made from atomic data and can be integrated to give partial ionization cross sections for particular instrumental and observation conditions.^{36,37} Recent publications give details of calculated and measured partial cross sections for conditions of interest in analytical electron microscopy.³⁸⁻⁴¹ An issue in these comparisons is the extent to which partial cross sections calculated from atomic data may differ from measured cross sections due to so-called solid-state effects.^{3,37}

Summary

The Bethe equation for inner-shell ionization cross sections has been frequently used in x-ray microanalysis. Although it is a simple and convenient means for estimating cross sections, considerable care has to be exercised to insure that reliable values are obtained. This

equation is only valid over limited regions of overvoltage and should not be applied in conditions where its validity has not been established.

The regions of validity of the Bethe equation can be identified readily with the use of a Fano plot. Such plots typically have two linear regions, as illustrated in Fig. 1. Values of the two Bethe parameters for each linear segment should not be used to estimate cross sections for overvoltages outside the particular segment. The Bethe parameters for a given linear region and for ionization of a given shell may not be independent of atomic number but such variations are expected to be smaller than about 20%.

It is possible to modify the Bethe equation or to introduce functional forms for the parameters so that this familiar equation can thereby empirically represent a limited set of cross-section data over a wider range of overvoltage and atomic numbers than would otherwise be the case. For example, a simple expedient could be to use a single straight line in Fig. 1 to represent the cross-section values in some average sense. Alternately, one or another of the Bethe parameters could become functions of atomic number. Such steps may be expedient for interpolation amongst the data set, but the parameterization may lead to conflicts with other data.

The x-ray microanalysis literature contains many different equations or parameter values that have been proposed to represent ionization cross-section data.¹⁻⁴ Many of these equations were proposed when the available cross-section data literature was much smaller than it is now. These equations should not be used unless they have been validated for particular conditions.

Information is given above on situations where the Bethe equation can be used. The empirical equations for K-shell ionization developed by Casnati et al.²² and Jakoby et al.²³ appear to be suitable for x-ray microanalysis. The formula developed by Gryzinski²⁴ from classical theory fits a wide range of cross-section data except close to threshold ($U < 4$). The cross sections calculated by Scofield²⁸ for K-shell and L-shell ionization appear to be useful for relativistic energies. A compilation of measured K-shell ionization cross sections has been recently published by Long et al.⁴²

References

1. C. J. Powell, *Rev. Mod. Phys.* 48: 33, 1976.
2. C. J. Powell, in K. F. J. Heinrich, D. E. Newbury, and H. Yakowitz, Eds., *Proceedings of a Workshop in the Use of Monte Carlo Calculations in Electron Probe Microanalysis and Scanning Electron Microscopy*. NBS Spec. Publ. 460, 1976, 97.
3. C. J. Powell, in T. D. Märk and G. H. Dunn, Eds., *Electron Impact Ionization*. New York: Springer-Verlag, 1985, 198.
4. C. J. Powell, *Ultramicroscopy* 28: 24, 1989.
5. H. Bethe, *Ann. Physik* 5: 325, 1930.
6. E. J. Williams, *Proc. Roy. Soc.* A139: 163, 1933.
7. D. B. Williams, D. E. Newbury, J. I. Goldstein, and C. E. Fiori, *J. Microscopy* 136: 209, 1984.
8. L. Marton, C. Marton, and W. G. Hall, *Electron Physics Tables*, Washington: NBS Circular 571, 1956.
9. U. Fano, *Phys. Rev.* 95: 1198, 1954.
10. M. Inokuti, *Rev. Mod. Phys.* 43: 297, 1971.
11. F. J. de Heer and M. Inokuti, in T. D. Märk and G. H. Dunn, Eds., *Electron Impact Ionization*, New York: Springer-Verlag, 1985, 232.
12. Y.-K. Kim and M. Inokuti, *Phys. Rev.* A3: 665, 1971.
13. S. Tanuma, C. J. Powell, and D. R. Penn, *Surf. Interface Anal.* 11: 577, 1988.
14. S. P. Khare and S. Prakash, *Phys. Rev.* A39: 6591, 1989.
15. P. Rez, *X-ray Spectrometry* 13: 55, 1984.
16. D. R. Batchelor, P. Rez, D. J. Fathers, and J. A. Venables, *Surf. Interface Anal.* 13: 193, 1988.
17. J. H. Paterson, J. N. Chapman, W. A. P. Nicholson, and J. M. Titchmarsh, *J. Microscopy* 154: 1, 1989.
18. T. P. Schreiber and A. M. Wims, *Ultramicroscopy* 6: 323, 1981.
19. P. Schwaab, *Scanning* 9: 1, 1987.
20. H. Hoefft and P. Schwaab, *X-ray Spectrometry* 17: 201, 1988.
21. M. Gryzinski, *Phys. Rev.* 138: A336, 1965.
22. E. Casnati, A. Tartari, and C. Baraldi, *J. Phys.* B15: 155, 1982.
23. C. Jakoby, H. Genz, and A. Richter, *J. Physique Colloq.* 48: C9-487, 1987.
24. C. A. Quarles, *Phys. Rev.* A13: 1278, 1976.
25. W. Hink, L. Kees, H.-P. Schmitt, and A. Wolf, in D. J. Fabian, H. Kleinpoppen and L. M. Watson, Eds., *Inner-shell and X-ray Physics of Atoms and Solids*, New York: Plenum, 1981, 327.
26. R. Hippler, K. Zaeed, I. McGregor, and H. Kleinpoppen, *Z. Physik* A307: 83, 1982; R. Hippler, H. Klar, K. Saeed, I. McGregor, A. J. Duncan, and H. Kleinpoppen, *J. Phys.* B16: L617, 1983.
27. K. Shima, T. Nakagawa, K. Umetani, and T. Mikumo, *Phys. Rev.* A24: 72, 1981.
28. J. H. Scofield, *Phys. Rev.* A18: 963, 1978.
29. S. Reusch, H. Genz, W. Löw, and A. Richter, *Z. Phys.* D3: 379, 1986.
30. D. R. Batchelor, H. E. Bishop, and J. A. Venables, *Surf. Interface Anal.* 14: 700, 1989.
31. T. Sato, Y. Nagasawa, T. Sekine, Y. Sakai, and A. D. Buonaquisti, *Surf. Interface Anal.* 14: 787, 1989.
32. J. E. Wood, D. B. Williams, and J. I. Goldstein, *J. Microscopy* 133: 255, 1984.
33. Z. Horita, T. Sano, and M. Nemoto, *J. Electron Microscopy* 35: 324, 1986.
34. P. J. Sheridan, *J. Electron Microscopy Technique* 11: 41, 1989.
35. G. Cliff and G. W. Lorimer, *J. Micros-*

copy 103: 203, 1975.

36. R. F. Egerton, *Electron Energy Loss Spectroscopy in the Electron Microscope*, New York: Plenum, 1986.

37. P. Rez, *Ultramicroscopy* 28: 16, 1989.

38. F. Hofer and P. Golob, *Micron and Microscopica Acta* 19: 73, 1988.

39. J. Auerhammer, P. Rez, and F. Hofer, *Ultramicroscopy* 30: 365, 1989.

40. R. F. Egerton, *Ultramicroscopy* 28: 215, 1989.

41. P. A. Crozier, *Phil. Mag.* B61: 311, 1990.

42. X. Long, M. Liu, F. Ho, and X. Peng. *Atomic Data and Nuclear Data Tables* 45: 353, 1990.

$\phi(\rho z)$ DETERMINATION FOR ADVANCED APPLICATIONS OF ELECTRON PROBE MICROANALYSIS

Peter Karduck, Norbert Ammann, and W. P. Rehbach

Electron probe microanalysis (EPMA) has developed to a versatile technique for the quantitative analysis of microvolumes in solids. Particularly in the last ten years, important progress in the accuracy of quantification, as well as in the variety of possible applications, has to be noted. For example, the matrix correction techniques have been improved significantly by the introduction of new models. Although the application of EPMA to thin-film analysis had been proposed very early, it could only really be translated into practical quantitative analysis in recent years. In all cases, these developments have been supported essentially by systematic investigations of $\phi(\rho z)$, the so-called depth distribution of generated x-ray intensities, and by the introduction of new and improved analytical expressions to describe $\phi(\rho z)$ as accurately as possible.

From the beginning of EPMA, it was understood and accepted that the knowledge of $\phi(\rho z)$ was the essential key to an accurate matrix correction. Nevertheless, for more than 20 years rather simple and crude models for $\phi(\rho z)$ have been used for the absorption correction because at that time most of the x-ray lines of the light elements suffering high absorption could be barely analyzed. With the increasing efficiency of microprobe analyzers, the demand for better and more correct $\phi(\rho z)$ models increased and diverse attempts of $\phi(\rho z)$ determinations were initiated.

The present paper is a short review of several techniques of experimental $\phi(\rho z)$ determination. The suitability of Monte Carlo simulations for the calculation of $\phi(\rho z)$ is discussed and the results of both techniques are assessed as to their reliability. Finally, possible requirements on future $\phi(\rho z)$ studies are discussed with respect to new applications of EPMA such as quantitative thin-film analysis and others.

Significance of $\phi(\rho z)$ for Quantitative EPMA

Definition of $\phi(\rho z)$. In the literature, $\phi(\rho z)$ is denoted as the depth distribution of x-ray production excited by a monoenergetic electron beam in a solid target. Following the definition of Castaing and Descamps,¹ $\phi(\rho z)$ describes the x-ray intensity generated in an infinitesimally thin depth element between ρz and $\rho z + d\rho z$, normalized by the intensity emitted from a thin unsupported film of the same material with the same thickness $d\rho z$.

This definition can be generalized if the

distribution of the primary electrons is regarded as stationary inside the excitation volume.² With this stationary electron distribution $N(E, \rho z)$, with E as the corresponding energy of each electron in the depth ρz , the relative intensity emerging from depth ρz_i is

$$\phi(\rho z_i) = \frac{1}{Q_{n1}(E_0)} \int_{E_{n1}}^{E_0} Q_{n1}(E) N(E, \rho z_i) dE \quad (1)$$

The intensity from the infinitesimally thin tracer is represented in this equation by $Q_{n1}(E_0)$, i.e., the ionization cross section of the shell with quantum numbers n and l . Since the ionization cross section depends only on the primary electron energy E_0 and the critical excitation energy E_{n1} , $N(E, \rho z)$ describes the effect of the target composition as well as that of E_0 on the depth distribution of generated x-ray intensities. The concentration of the ionized element in question is only included implicitly in $N(E, \rho z)$. Similarly, $\phi(\rho z)$ can be defined for compounds or alloys: $N(E, \rho z)$ gives the effect of the target composition c_i on the depth distribution, whereas Q_{n1} is not (or only slightly) dependent on c_i .³ From here, it easily follows that in the case of stratified specimen, Eq. (1) is also valid; in this case $N(E, \rho z)$ contributes the effect of rapid changes of the compositions $c_i(\rho z)$ at interfaces. But $\phi(\rho z)$ shows no steps at interfaces, although the concentration profile $c_i(\rho z)$ may change gradually. That is the case only for the depth distribution $cQ(E_0)\phi(\rho z)$ of the generated intensity. Furthermore, it can be deduced that $\phi(\rho z)$ also exists for the characteristic radiation of an element that is not present in the target. Thus it seems reasonable to denote $\phi(\rho z)$ also as an ionization probability.

Role of $\phi(\rho z)$ in Quantitative EPMA. From the definition of $\phi(\rho z)$, a full matrix correction of EPMA data (except fluorescence effects) can be calculated if reliable data for $\phi(\rho z)$ are available for the whole range of experimental conditions and possible sample compositions.

For example, the atomic number effect, i.e., the ratio of the generated x-ray intensity in the unknown to that in the corresponding standard, can be calculated for both from the integrals of $\phi(\rho z)$, which by definition also includes the intensity loss due to electron backscattering. But following historical development, $\phi(\rho z)$ was first applied exclusively to the correction of the absorption effect, i.e., different degree of absorption of the respective radiation in the unknown sample and in the standard.¹ In this application, only relative

The authors are with the Gemeinschaftslabor für Elektronenmikroskopie der RWTH Aachen, D-5100 Aachen, Ahornstr. 55, Federal Republic of Germany.

$\phi(\rho z)$ values are needed for the calculation of the absorption factor $f(\chi)$ given by

$$f(\chi) = \frac{\int_0^\infty \phi(\rho z) \exp(-\chi \rho z) d\rho z}{\int_0^\infty \phi(\rho z) d\rho z} \quad (2)$$

where $\chi = (\mu/\rho)/\sin \theta$, μ/ρ = mass absorption coefficient, and θ = take-off angle. Nevertheless, as the absorption correction considers the ratio $f(\chi)/f(\chi)_{\text{standard}}$, a knowledge of $\phi(0)$, the so-called surface ionization, as well as the precise description of $\phi(\rho z)$ with depth, are basic prerequisites for a good correction of medium-to-strong absorption effects. Therefore, models based on simplified expressions for $\phi(\rho z)$ clearly fail in this range.^{4,5}

Determination of $\phi(\rho z)$

Direct Experimental Techniques. (a) *Tracer technique.* The first experimental determination of $\phi(\rho z)$ was made by Castaing and Descamps.¹ They used the so-called sandwich-sample technique, as described schematically in Fig. 1, in which a thin tracer of element B is deposited at various depths of a matrix element A by an appropriate evaporation technique. The characteristic x-ray intensity of element B from the various depths of the tracer can be measured and transferred into the intensity generated from depth ρz_i by correction for absorption by the factor $\exp(\chi \rho z_i)$. By relating these intensities to the intensity emitted from the same but unsupported tracer one obtains the absolute depth distribution of x-ray production (ionizations) according to the definition given above. It follows that $\phi(0)$ is always larger than unity, due to the additional ionizations produced in the surface layer by backscattered electrons. Castaing and Descamps produced a series of reliable $\phi(\rho z)$ curves for Al, Cu, and Au matrices and calculated the absorption factors $f(\chi)$. Later, other authors adopted this method of using tracer and matrix materials with closely matching atomic numbers to study mainly the absorption effect.⁶⁻⁸ Beginning in the early 1960s some authors successfully extended this tracer technique for tracer and matrix elements to a wider range of atomic numbers Z in order to study the atomic-number effect as well.⁹⁻¹² If tracers of identical thickness of one element Z are combined with matrices of different atomic numbers, the measured $\phi(\rho z)$ curves show differences in the shape and as well as in the magnitude of the integral over $\phi(\rho z)$ (total intensity generated) for various matrix elements. These changes could be attributed to differences in backscattering, stopping power, and electron scattering. An example is given in Fig. 2, in which the $\phi(\rho z)$ curves for B_i L α are shown for various matrix materials at 25 keV. The experimental data from Brown and Parobek are compared with MC results from the model of Ammann and Karduck,² and show satisfactory agreement.

(b) *The wedge specimen technique.* A slightly different approach was proposed by Schmitz et al.¹³ and has been pursued by Büchner.¹⁴ These

authors used a shallow wedge-shaped tracer (3-5°) deposited on a matrix of an atomic number lower than that of the tracer ($\delta Z = 1$) to avoid characteristic fluorescence. Measurement of a characteristic x-ray line of the tracer along a line across the wedge as a function of distance x yields the integral of $\phi(\rho z) \exp(-\chi \rho z)$ as a function of the wedge thickness ρz . Differentiation of the integral curve then yields the normalized depth distribution $\phi(\rho z)/F(\chi)$, where $F(\chi)$ equals the numerator in Eq. (2). This technique is illustrated in Fig. 3. Büchner and Pitsch used these $\phi(\rho z)$ experiments to propose their own absorption correction model, which (like the simplified model of Philibert) fails for strongly absorbing systems, mainly because of its very crude representation of the depth distribution and because the model sets $\phi(0) = 0$.⁵

The advantages of the wedge method are possible use of alloys as tracers and the fairly good determination of tracer thickness by means of the precisely known wedge angle. But the following drawbacks of the wedge technique more than offset the advantages: restriction to tracer and matrix materials of similar Z , and difficulties in the accurate determination of $\phi(0)$.

(c) *Tracer technique applied to soft x rays.* The tracer experiments reported up to 1985 had Si K α as the lowest x-ray energy and the minimum primary electron energy E_0 was 6 keV. Thus there was still a lack of $\phi(\rho z)$ data for soft or even ultrasoft x rays like B to O K α lines, which are needed for a further optimization of existing $\phi(\rho z)$ expressions for use in matrix correction procedures.¹⁵ Karduck and Rehbach^{16,17} were the first to carry out an extensive investigation devoted to $\phi(\rho z)$ of x-ray lines with critical energies E_c below 1 keV. They also used the tracer technique, which in the case of soft x rays raises particular problems for the experimenter:

- due to high absorption of the lines in use (B to O K α lines, L lines of Ti to Co) in almost all matrix materials and with regard to their low x-ray yield accurate intensity measurements could only succeed for absorption coefficients of the matrix material of much less than 10 000 cm²/g
- the maximum depth from which x rays are still detectable with sufficient confidence is limited by strong absorption to 200-300 $\mu\text{m}/\text{cm}^2/\mu\text{g}$
- to satisfy the condition that tracer thickness should be thin enough so that no significant electron scattering takes place in it, tracers of 2.4-5.8 $\mu\text{g}/\text{cm}^2$ were used, which in any case yield only low intensities

All these negative factors required a very accurate specimen preparation and microprobe measurements with long counting times. The authors applied four independent techniques to determine the thicknesses of tracer and matrix layers giving only deviations of less than 5%.¹⁶ Some examples of their results are shown in Figs. 8-11 and are discussed later.

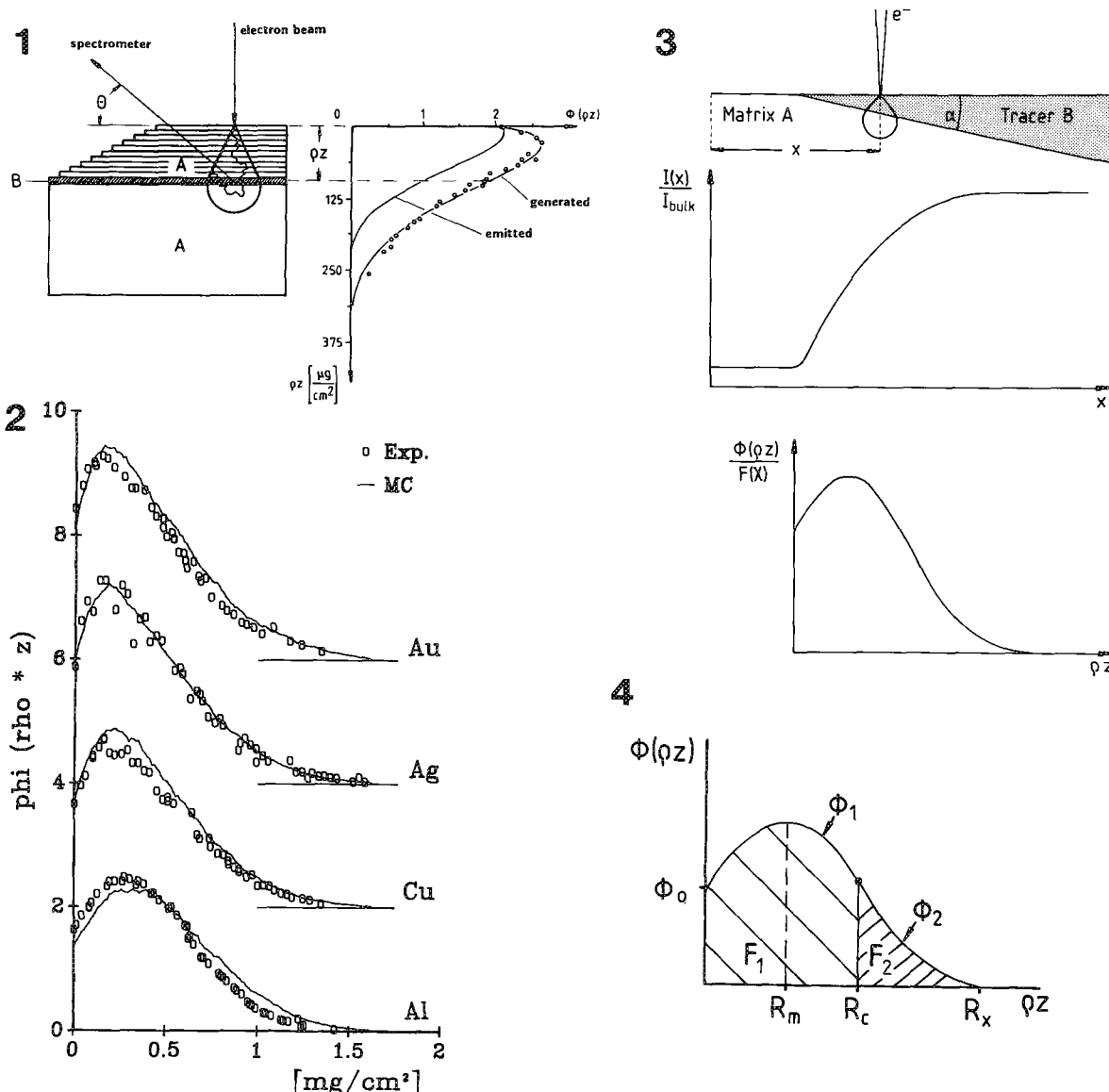


FIG. 1--Schematic representation of tracer technique for $\phi(\rho z)$ determination.

FIG. 2.--Experimental $\phi(\rho z)$ data for Bi $L\alpha$ in various matrices at 25 keV showing effect of atomic number;⁹ comparison with Monte Carlo results.

FIG. 3.--Wedge specimen technique, schematic presentation of resulting $\phi(\rho z)$.

FIG. 4.--Parabolic $\phi(\rho z)$ model according to Pouchou and Pichoir.¹⁸

A Combined Technique to Determine $\phi(\rho z)$ Indirectly. In the following the well-known and established model of Pouchou and Pichoir (called PAP) for the "ZAF" correction of bulk as well as stratified samples shall be examined from a somewhat different point of view.¹⁸ Aiming to establish a new, more versatile matrix correction procedure, the authors carried out an extensive investigation of $\phi(\rho z)$. Their model was conceived not only as an operative matrix correction procedure, but also as a tool for the investigation of mass absorption coefficients, especially of stratified specimens. To achieve this goal, the "heart" of the model had to be a $\phi(\rho z)$ description as realistic and reliable as possible with a good parameterization of the form of $\phi(\rho z)$ and the condition of providing first of all correct values of the generated primary x-ray intensity. In other words, Pouchou and Pichoir strictly obeyed the definition of Castaing and Descamps that the integral of $\phi(\rho z)$ equals the total generated intensity.

It is astonishing that the PAP model was the first strictly to obey this condition; none of the existing $\phi(\rho z)$ models up to that time did so, not even the Gaussian $\phi(\rho z)$ model of Packwood and Brown, although it calculates both the absorption and the atomic-number correction from its mathematical parameterization of $\phi(\rho z)$.¹⁵ As a mathematical expression, Pouchou and Pichoir chose a very simple and flexible combination of two parabolic branches with a common point of equal value and slope at a certain mass thickness, as shown in Fig. 4. The conditions for the parameterization were:

- the integral has to be equal to the total generated primary intensity
- at the surface ϕ must be the surface ionization function $\phi(0)$
- the maximum of ϕ must be positioned at a certain depth
- the curve must become zero at a certain value for the maximum range of ionization

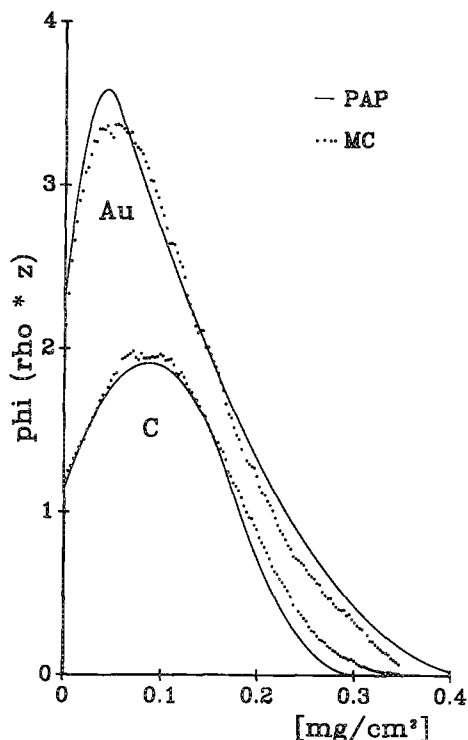


FIG. 5.-- $\phi(\rho z)$ of Cu L α in carbon and gold at 10 keV. Results of PAP model compared with Monte Carlo results.

To fulfill all these conditions the authors used a variety of data for several purposes:

- $\phi(\rho z)$ -distributions obtained by the tracer technique and Monte Carlo simulations, both to find a good fit for the shape of $\phi(\rho z)$ at all boundary conditions

- measurements of intensities or k-ratios at variable E_0 (electron energy) from known specimen or layers of known compositions and thickness on known substrates, first to find an accurate expression for the total generated intensity and second to normalize $\phi(\rho z)$ to this value for both bulk and layered samples

- further analysis data from binary specimen have been used to optimize the performance in matrix correction

With this extensive set of data, Pouchou and Pichoir elaborated a consistent description of $\phi(\rho z)$, as demonstrated by the authors with many examples comparing experimental data with those calculated by the PAP model. Figure 5 shows Monte Carlo results of Ammann and Karduck² compared with $\phi(\rho z)$ curves calculated by PAP. In both cases, excellent agreement is found. Therefore it seems to classify the work of Pouchou and Pichoir as a useful technique for the indirect determination of realistic $\phi(\rho z)$ values.

$\phi(\rho z)$ Determination by Monte Carlo Simulation of Electron Trajectories. A Monte Carlo technique simulates three-dimensional electron trajectories of parallel incident primary electrons in a sample. The solid target is treated as a body with a density ρ and randomly distributed atoms. Each electron trajectory itself is divided into several straight-line segments, i.e.,

free paths of the electron between two collisions. Random numbers are used to select the particular scattering angle of each elastic collision or the energy loss after an inelastic collision according to equations describing the appropriate probability distributions. The main application of Monte Carlo simulations is to calculate data that are quite intractable by analytical solutions and by experimental treatment. To achieve good results for microscopic quantities (like x-ray data or values for backscattered or transmitted electron intensities) with statistical confidence, large numbers of individual trajectories must be calculated.

It is not the intent of this paper to review the development of Monte Carlo simulations in EPMA. A large body of literature deals with this topic with respect to a variety of purposes, including x-ray generation, and summarizes the development of about 20 years.^{19,20} Surprising that the examination of the literature shows that only a few investigations were aimed at the systematic collection of $\phi(\rho z)$ data for EPMA. Most of the reported research deals with the details of optimizing the basic concepts of the simulations. The results are usually examined by comparison with experimental electron backscatter or transmission data, with $f(\chi)$ values, and to a minor extent with $\phi(\rho z)$ data. For the quantification of x-ray data, MC simulations were of use mostly as a rough guideline for the modeling of $\phi(\rho z)$ so as to give the tentative behavior of $\phi(\rho z)$ with changing electron energy E_0 , excitation energy E_{n1} , or atomic number Z of the target. For example, Love et al.²¹ did so to obtain data for the mean depth of x-ray generation used in their absorption correction model.²²

All MC models that need multiple scattering approaches, or screened Rutherford cross sections, for elastic scattering provided $\phi(\rho z)$ results with deviations from experimental data too large for quantitative purposes. As an example, in 1972 Shimizu et al.²³ applied their MC model to the quantitative EPMA of various binary aluminum alloys with fairly high absorption corrections for Al K α . Their results became very unsatisfactory with an increasing absorption correction, indicating uncertainties in the $\phi(\rho z)$ predictions by their MC model. Krefting and Reimer²⁴ have improved the agreement of MC data with experiment greatly by introducing Mott elastic cross sections in a single-scattering approach. They also treated the energy loss partly in a single-scattering mode by using the theory of Gryzinski for the differential cross sections.²⁵ In so doing, they could improve two shortcomings of the former models. The poor approximation of elastic scattering by Rutherford cross sections affected the results, particularly in the energy range of importance for EPMA and particularly for heavier elements. As demonstrated in Ref. 24, $\phi(\rho z)$ data of these elements are strongly affected.²⁴ Second, the effect of electron straggling could be considered as well as the contribution of fast secondary electrons to

backscattering. By a similar model Kotera et al. obtained reasonable $\phi(\rho z)$ results even for low E_0 and high atomic numbers.²⁶ Nevertheless, remaining discrepancies between their MC data and experimental results could not be convincingly explained by the authors. The reason may be that the extensive set of experimental $\phi(\rho z)$ data available up to that time has not been systematically used to study the performance of existing MC models. The first who did so were Karduck and Rehbach,²⁷ using an MC model similar to the one of Reimer and Krefting. Fairly good agreement between their MC data and experimental $\phi(\rho z)$ data could be found over a wide range of boundary conditions, including soft x-ray lines like B and C K α . Nevertheless, there were systematic deviations between experiment and MC, especially at low primary electron energies, for several critical energies E_{n1} . From their results the authors concluded that MC results were to be preferred to experimental ones for use in $\phi(\rho z)$ modeling. They were able to confirm this conclusion by obtaining a full agreement between measured and MC-determined x-ray intensities at 4 to 30 keV for C, Si, Cu K α and Cu L α lines, each from the pure element standard. This result shows that their MC model produces $\phi(\rho z)$ curves close to reality for the whole range of E_0 .

In the present paper several results of $\phi(\rho z)$ determinations are compared with those of a new MC model presented by Ammann and Karduck in this volume.² This model is an extension of the previous one, which now considers multielement samples with up to 20 elements as well as layered structures. The details of the model can be summarized as follows:

- single-scattering model for $\theta > 10^\circ$ with Mott cross section according to the tabulated values of Reimer and Lødding²⁸; interpolation between tabulated values for variable energy and atomic number
- multiple scattering for $\theta < 10^\circ$
- to obtain a consistent model the differential Gryzinski cross sections²⁵ have been corrected by $\langle dE/ds \rangle_{\text{Bethe}} / \langle dE/ds \rangle_{\text{Gryzinski}}$ to give the mean energy loss according to Bethe
- single inelastic scattering for energy loss $E > E_{n1} + 200$ eV are simulated based on these differential cross sections
- the residual energy losses are treated as continuous according to Bethe
- the ionization cross sections are also calculated on the basis of the corrected inelastic cross sections of Gryzinski

This procedure thus introduces the consideration of the conservation of energy into the whole simulation; i.e., the description of energy dissipation as well as the conversion of it into ionizations and subsequent x-ray emissions are obtained from the same theory.

It was the intention of this work to develop a MC model especially for the calculation of reliable x-ray data for boundary conditions that do not lend themselves to experimental investigations. In the following all experimental $\phi(\rho z)$ results are discussed in comparison with

MC values obtained by the model of Ammann and Karduck.²

Results

Verification of the MC Model. Ammann and Karduck² have demonstrated the agreement of their MC results by means of a variety of experimental data. As an example, Fig. 6 gives a comparison of MC data for relative intensities of C K α in SiC and Ga L α in GaAs with the experimental values of Pouchou.²⁹ There is excellent agreement over a wide range of E_0 from 2 to 40 keV. Together with similar tests based on data from thin layers on substrates, the present MC model is shown to produce $\phi(\rho z)$ data very close to reality, which are certainly suitable for both optimization of analytical expressions for $\phi(\rho z)$ and for direct application to the correction of atomic number and absorption effects. An example of the latter is given in Fig. 7 for carbon in carbides applied to k-values obtained by Bastin and Heijligers at electron energies from 4 to 30 keV.³⁰ Compared with the result of the $\phi(\rho z)$ -correction procedure of Bastin and Heijligers, the MC-based ZA-correction produces more consistent and accurate results for SiC and B₄C.

Effect of Tracer Thickness on Experimental $\phi(\rho z)$ Curves. Tracer thickness can strongly affect the shape of experimental $\phi(\rho z)$ curves, as Castaing and Descamps pointed out in their early work.¹ This relationship is demonstrated quantitatively in Fig. 8 with chromium tracers 4 and 12 $\mu\text{g}/\text{cm}^2$ thick, respectively, in an aluminum matrix at 12 keV. With the thick tracer the value of the maximum of $\phi(\rho z)$ is reduced by more than 10% compared to the curve obtained with a thin tracer, whereas the value of $\phi(0)$ remains largely unaffected. The solid line shows the results of an MC simulation that matches the experimental values of the thin tracer very well.² The reason for the deviation is that owing to electron scattering in the tracer, the intensity from the unsupported tracer layer increases the value $Q(E_0)d\rho z$ by a factor of $1/\langle \cos \theta \rangle$ where $\langle \cos \theta \rangle$ is the mean angular deflection of the electrons in the tracer. By relating the other intensities from greater depth to that intensity, the curve is compressed to lower values. This explanation of the effect can be substantiated by Fig. 9, in which results of tracer experiments with 4 $\mu\text{g}/\text{cm}^2$ Cr in Al and 15 $\mu\text{g}/\text{cm}^2$ Cr in Cu and Au are compared with MC results (solid lines). In addition, the tracer experiments have been simulated by MC with the corresponding tracer layers at various depths of the matrix material. These results, depicted by the filled symbols, are in close agreement with the experimental ones, but both deviate strongly from the MC results calculated according to the definition of $\phi(\rho z)$ and representing more realistic curves. The deviation of the experimental results becomes more serious with increasing Z of the matrix and obviously with decreasing E_0 , as can be seen from Fig. 10 for a carbon tracer of 5-10 $\mu\text{g}/\text{cm}^2$ (20-40 nm) in a silver matrix.

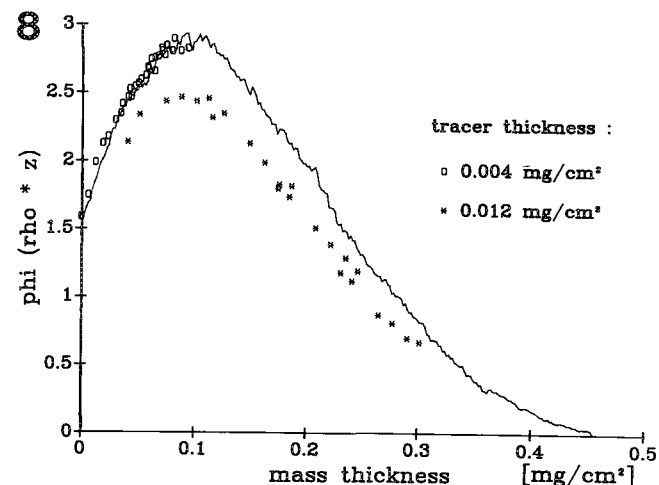
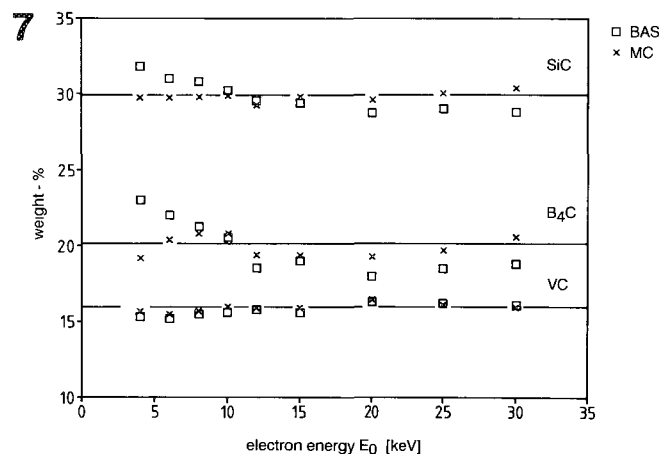
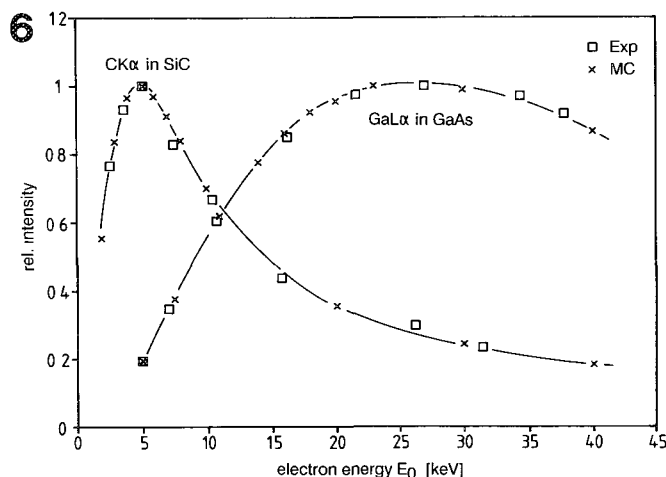


FIG. 6.--Comparison of measured x-ray intensities of C K α in SiC and Ga L α in GaAs with Monte Carlo results.

FIG. 7.--Results of quantitative carbon analyses in binary carbides with matrix corrections³⁰ and ZA-corrections by Monte Carlo; solid line equals nominal composition of compounds.

FIG. 8.--Effect of tracer thickness on shape of $\phi(\rho z)$ curves, Cr L α in Al, 12 keV; solid line gives Monte Carlo results.

From this behavior it can be concluded empirically that the tracer thickness should be less than 1% of the electron range at the corresponding electron energy E_0 . But this conclusion also seems to depend on the difference be-

tween the atomic number of the tracer and the matrix, as could be concluded from Fig. 9, where the effect is stronger for larger differences.

X-ray Generation of Fast Secondary Electrons. The probability of fast secondary electrons (FSE) by ionization is very small. Most of the energy losses of the primary electrons are below 200 eV. From these circumstances it has been concluded in the literature that the role of secondary electrons in x-ray production is negligible, except with a low fraction at low critical energies E_{n1} . Karduck and Rehbach²⁷ were the first to investigate the role of FSE in x-ray production systematically. They were able to show, by comparison of MC and experimental $\phi(\rho z)$ data of soft x rays, that FSE indeed contribute to the total x-ray production, but only in cases where the critical excitation energy E_{n1} is small. Effects could be observed for $E_{n1} < 1$ keV and at high overvoltages. A clear contribution is shown in Fig. 11 by comparison of experimental data of B K α in silver with MC data simulated with and without secondary electrons. The authors also found a marked effect on the surface ionization $\phi(0)$, for which they proposed a new expression that takes the contribution of FSE into account by introducing a dependence on E_{n1} .^{12,31}

$\phi(\rho z)$ of Layered Structures on Substrates. Little detailed information is available at present about $\phi(\rho z)$ of thin layers or multilayers on substrates, since these data are not directly accessible by experiment. A surprisingly small number of investigations have been carried out by MC, most aimed toward the solution of specific analytical problems; there has been no detailed $\phi(\rho z)$ investigation by MC simulation. Several authors have carried out thin-layer analyses by an MC-based evaluation of x-ray data and have achieved reasonable results.³²⁻³⁴ The first detailed study of $\phi(\rho z)$ of layered structures was carried out by Ammann and Karduck² by the MC model briefly discussed before. The essential results can be summarized as follows: $\phi(\rho z)$ curves of x rays from layered structures deviate from those of the pure layer or the pure target material if the atomic numbers of the two differ significantly. The changes of $\phi(\rho z)$ of layers on substrates are somewhat unexpected but may be largely explained by the different elastic scattering and energy losses in the two materials. Two extreme examples are shown in Figs. 12 and 13. In Fig. 12 $\phi(\rho z)$ curves of B K α in fictitious layers of light compounds on a heavy substrate demonstrate that the maximum of $\phi(\rho z)$ curves is the farther shifted toward the substrate the smaller the average Z of the layer. With increasing Z of the layer, as in the case of TiC, a new maximum appears in the layers itself. This behavior is caused by the "transparency" of the light materials due to a small fraction of high-angle scattering. Conversely, the maxima increase compared with $\phi(\rho z)$ of the bulk layer material because of extensive electron

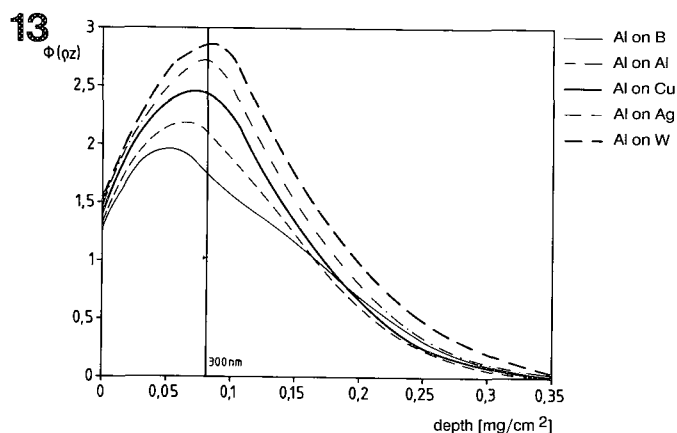
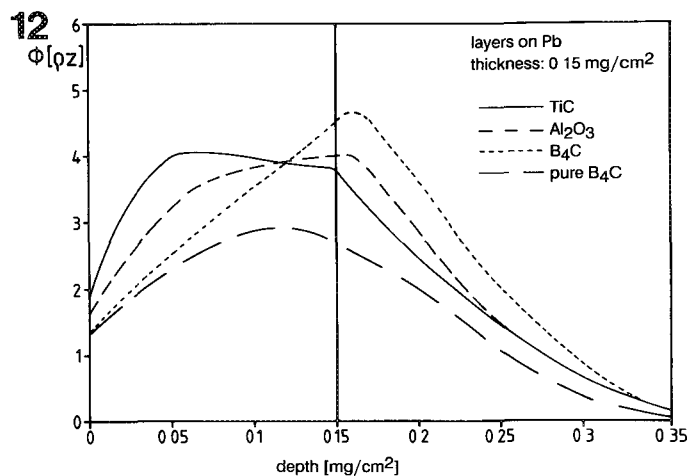
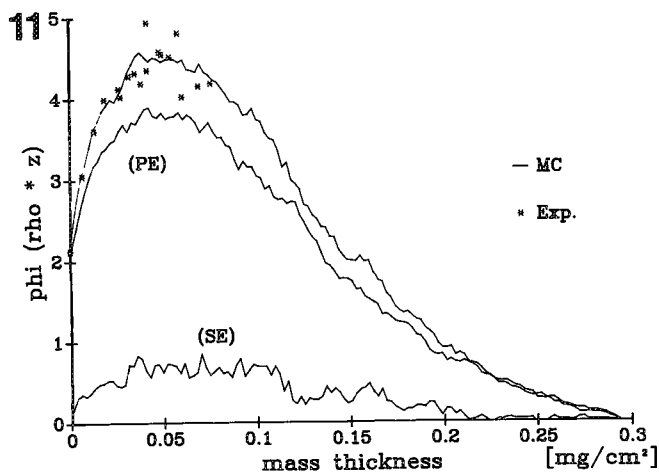
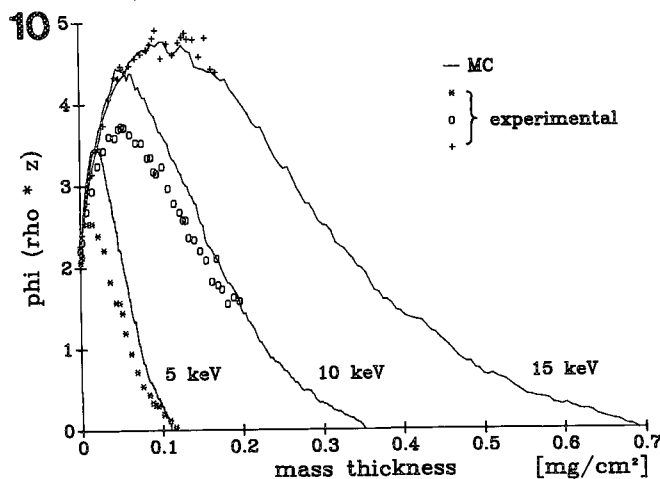
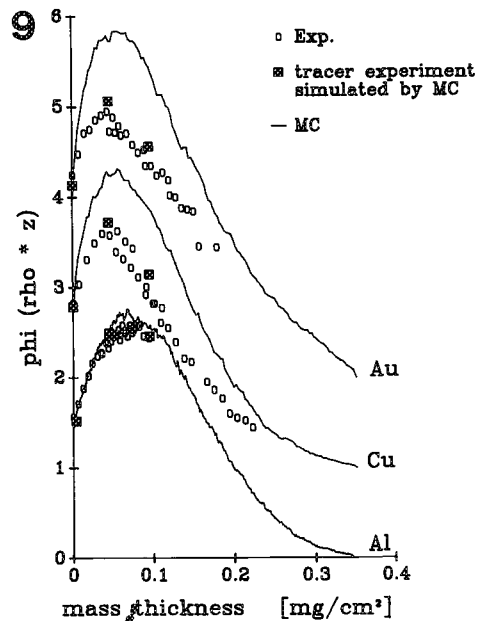


FIG. 9.-- $\phi(\rho z)$ of Cr $L\alpha$ in Al, Cu and Au at 10 keV. Comparison of tracer experiments with Monte Carlo simulations. Thickness of Cr tracer: in aluminum $4 \mu\text{g}/\text{cm}^2$, in copper and gold $15 \mu\text{g}/\text{cm}^2$.

FIG. 10.-- $\phi(\rho z)$ of C $K\alpha$ in silver at various electron energies. Comparison of tracer experiments with Monte Carlo simulations; thickness of carbon tracer $5\text{--}10 \mu\text{g}/\text{cm}^2$.

FIG. 11.--Contribution of fast secondary electrons to $\phi(\rho z)$, B $K\alpha$ in silver, 9 keV; comparison of experiment with Monte Carlo results.

FIG. 12.-- $\phi(\rho z)$ of B $K\alpha$ from fictitious layers on lead substrate at 10 keV, obtained by Monte Carlo simulation.

FIG. 13.-- $\phi(\rho z)$ of Al $K\alpha$ from 300nm film of aluminum on various substrates obtained by Monte Carlo simulation.

back diffusion from the heavy substrate inducing extra ionizations in the layer, as can be seen in the case of B_4C .

Figure 13 gives examples for an aluminum layer on light-to-heavy substrates. The maxima behave opposite to those of $\phi(\rho z)$ in the pure uncoated substrate materials, in which the maxima shifts toward the surface with increasing atomic number of the target. This result is in contradiction to the assumptions of Pouchou and

Pichoir that the maxima would behave similarly to those in the pure substrates.^{3,5}

Discussion

Tracer experiments have been of great importance in the development of quantitative EPMA, although the experimental techniques are very complicated and susceptible to errors. But the continuing experimental $\phi(\rho z)$ work of the

last 35 years was the basis for the proposal of successful correction procedures like the Gaussian $\phi(\rho z)$ approach of Packwood and Brown¹⁵ or the quadrilateral model of Sewell et al.³⁶ Nevertheless, both models, as well as an attempt by Rehbach and Karduck³¹ to improve the Gaussian $\phi(\rho z)$ for light-element analysis, needed further optimization treatments by fitting of the $\phi(\rho z)$ expressions to special data sets of binary compounds, as Bastin and Heijligers were able to realize for the model of Packwood and Brown.³⁰

From the results of the present assessment it can be assumed that the effect of using tracers that are too thick has caused systematic deviations in the E_0 dependence of the corresponding parameterizations of $\phi(\rho z)$. A rough estimate reveals that about 20-30% of all existing $\phi(\rho z)$ data is more or less distorted by this tracer effect. That is probably the reason the model of Packwood and Brown¹⁵ had to be modified to provide better results.³⁰ A similar doubt exists in the case of the absorption correction model of Sewell et al.³⁶ Their description of the maximum point of $\phi(\rho z)$ is also related to tracer experiments at low over-voltage ratios, which in comparison to MC data also suffer from the tracer effect. Unfortunately these authors gave no values of the tracer thicknesses used,¹¹ so that this dependence could not be proved by MC simulations. At the moment an improvement of the existing correction models by means of further experimental $\phi(\rho z)$ measurement is not to be expected. But the new Monte Carlo approach of Ammann and Karduck² promises to be suitable for future $\phi(\rho z)$ investigations. They are to be expected in the following fields of application:

1. Thin-layer and multilayer analysis. The strong effect of inhomogeneous compositions of stratified samples on $\phi(\rho z)$ produces unconventional curves that cannot be parameterized easily. There is no other tool for studying $\phi(\rho z)$ in such samples but a reliable MC model. We may therefore assume that accurate MC simulations can be used as a routine tool for the matrix correction of such complicated samples, especially with respect to the increasing computer capacities.

2. Analysis of tilted specimens. The improvement of matrix corrections in the case of tilted samples also seems to be promising, with the aid of MC investigations. The application of tracer experiments can be excluded for the reasons discussed above. Thus it may be concluded that direct experimental $\phi(\rho z)$ studies cannot fulfill the requirements of the future applications of EPMA. Nevertheless, the promising Monte Carlo model of Ammann and Karduck is also suitable for investigating $\phi(\rho z)$ in samples with complex composition or geometry with satisfying results for down to electron energies as low as 2 keV.

References

1. R. Castaing and J. Descamps, *J. Phys. et de Radium* 16: 304, 1955.
2. N. Ammann and P. Karduck, this volume.
3. C. J. Powell, in D. F. Kyser, H.

Niedrig, D. E. Newbury, and R. Shimizu, Eds., *Electron Beam Interaction with Solids for Microanalysis, and Microlithography*, Chicago: SEM, Inc., 1982, 19.

4. J. Philibert, in H. H. Pattee et al., Eds., *X-ray Optics and X-ray Microanalysis*, New York: Academic Press, 1963, 379.

5. A. R. Büchner and W. Pitsch, *Z. Metallkunde* 62: 392, 1971.

6. A. Vignes and G. Dez, *Brit. J. Appl. Phys.* 1: 1309, 1968.

7. R. Castaing and J. Henoc, *4th ICXOM*, Paris, 1966, 139.

8. J. D. Brown, Ph.D. thesis, University of Maryland, 1966.

9. J. D. Brown and L. Parobek, *6th ICXOM*, 1972, 163.

10. L. Parobek and J. D. Brown, *X-ray Spectrom.* 7: 26, 1978.

11. D. A. Sewell, G. Love, and V. D. Scott, *J. Phys.* D18: 1233, 1985.

12. W. Rehbach, Doctoral thesis, Aachen, 1988.

13. U. Schmitz, P. L. Ryder, and W. Pitsch, *5th ICXOM*, Berlin, 1969, 104.

14. A. R. Büchner, Doctoral thesis, Aachen, 1971.

15. R. H. Packwood and J. D. Brown, *X-ray Spectrom.* 10: 138, 1981.

16. P. Karduck and W. P. Rehbach, *Microchim. Acta Suppl.* 11: 289, 1985.

17. P. Karduck and W. P. Rehbach, *11th ICXOM*, London, Ont., 1987, 244.

18. J. L. Pouchou and F. Pichoir, *La Recherche Aerospatiale* 167 and 349, 1984.

19. K. F. J. Heinrich, D. E. Newbury, and H. Yakowitz, Eds., *Use of Monte Carlo Calculations in Electron-probe Microanalysis and Scanning Electron Microscopy*, NBS Spec. Publ. 460, 1976.

20. Ref. 3.

21. G. Love, M. G. C. Cox, and V. D. Scott, *J. Phys.* D10: 7, 1977.

22. G. Love, M. G. C. Cox, and V. D. Scott, *J. Phys.* D9: 7, 1976.

23. R. Shimizu, N. Nishigori and K. Murata, *6th ICXOM*, 1972, 95.

24. L. Reimer and E. R. Krefting, Ref. 19, 45.

25. M. Gryzinski, *Phys. Rev.* 2A 138: 337, 1965.

26. M. Kotera, K. Murata, and K. Nagami, *J. Appl. Phys.* 52: 997, 1981.

27. P. Karduck and W. P. Rehbach, *Microbeam Analysis--1988*, 277.

28. L. Reimer and B. Lødding, *Scanning* 6: 128, 1984.

29. J. L. Pouchou, personal communication.

30. G. F. Bastin and H. J. M. Heijligers, *X-ray Spectr.* 15: 135-150, 1986.

31. W. P. Rehbach and P. Karduck, *Microbeam Analysis--1988*, 285.

32. D. F. Kyser and K. Murata, *NBS Spec. Publ.* 460: 129, 1976.

33. A. Desalvo and R. Rosa, *Mat. Chemistry* 4: 495, 1979.

34. K. Murata, S. Cvičevich, and J. D. Kuptsis, *J. de Physique* 45: 13, 1984.

35. J. L. Pouchou and F. Pichoir, *NIST Spec. Publ.* (in preparation).

36. Ref. 11, p. 1245.

37. P. Karduck and W. P. Rehbach, *NIST Spec. Publ.* (in preparation).

NONRADIATIVE TRANSITIONS IN X-RAY ANALYSIS

J. L. Lábár

Changes in the measured x-ray intensities caused by the presence of nonradiative transitions are not taken into account in the correction procedures used in electron probe x-ray microanalysis (EPMA). Of course it is known that nonradiative transitions compete with radiative ones, and they together determine both the absolute and the relative intensities of the generated x rays.^{1,2} Textbooks elaborate these effects in connection with x-ray excitation (fluorescence), and introduce the notion of "effective fluorescence yield" to describe the enhanced absolute intensity of the $L\alpha$ line.³ In the present paper we review for L lines which physical quantities are affected by the nonradiative transitions, how conventional EPMA can be successful without incorporating these effects, when the introduction of an effective fluorescence yield is an exact solution, and in which cases the subshells are to be calculated separately and the nonradiative transitions are to be explicitly incorporated.

Absolute X-ray Intensities

The initial state for x-ray emission is an atom ionized in one of its inner (sub)shells. Since the lifetime of such an excited state is relatively long, excitation and deexcitation can be treated separately. Three successive steps can be distinguished in that approach.

1. The beam of primary radiation (e.g., charged particles or photons) ionize an atom of the sample to be examined. The ionization caused directly by an outer particle (without the interactions of the bound electrons of the atom) will be called direct ionizations. They correspond to the ionizations of an atom with electronic (sub)shells independent of each other.

2. A rearrangement of electrons and empty electron states may occur. Most common of these processes is the Auger effect, which leaves the atom in a doubly ionized state. The primary empty state is shifted to another (sub)shell with lower binding energy and an outer electron is ejected at the same time due to the interaction of the electrons of the atomic shells. From our point of view, the most interesting is the so-called Coster-Kronig effect, which denotes a special case of the Auger effect. In that case the empty state is shifted to another subshell (e.g., to L_3) of the same shell in which the direct ionization took place (e.g., in the L_1 or L_2 subshells). These indirect ionizations produce empty states

additional to the directly generated ones. That means that when the L_2 or L_3 subshells are to be considered as initial states for the later x-ray emission, the total number of empty states originates from two sources: the direct ionizations and the indirect ionizations.

3. The deexcitation of the atom occurs and serves to fill the empty state, which is the initial state for the x-ray emission under consideration. The possibility that the deexcitation may result in an x-ray emission is called the fluorescence yield of the (sub)shell. To the extent that the above steps can be treated separately, the transition rates of both the radiative and nonradiative transitions can be considered as atomic constants and the total number of generated x rays can be computed from the ionization possibilities for the direct ionizations of the various subshells in a straightforward manner.

For a given ionizing radiation a ratio of the total generated x rays to those generated by direct ionization can be computed as a function of atomic number. This ratio can be regarded as a correction factor necessary to convert the number of x rays generated directly to the number of total x rays. If this correction factor were a function of both sample composition and experimental conditions, there would be no point in this formulation. Figure 1 presents the above correction factor for electron excitation. Both bulk and thin samples are shown for experimental conditions usual for the analysis by L lines of elements in the given range of atomic numbers. The Coster-Kronig rates are taken from Krause and for the single electron ionization cross sections that functional form was selected for all three subshells as used by Pouchou for the total L shell.^{5,6} The relativistic correction depends only on the energy of the bombarding electron and is independent of the energies of the subshells. Therefore it affects the ionizations of all the three subshells to the same extent and consequently does not affect the value of the correction factor in Fig. 1. Three conclusions can be drawn from Fig. 1.

1. The shape of the plot resembles the atomic number dependence of the $f_{1,3}$ Coster-Kronig rates reflecting the latter's significance in the deduction of the correction factor. That correction factor is almost independent of the type of the sample (i.e., bulk or thin). The main factor determining its value for a given element is not the thickness of the sample but the E_0 energy of the primary electron beam (and consequently the overvoltage for the given element). Because the correction factor is practically independent of both sample type and

J. L. Lábár is at the Research Institute for Technical Physics of the Hungarian Academy of Sciences.

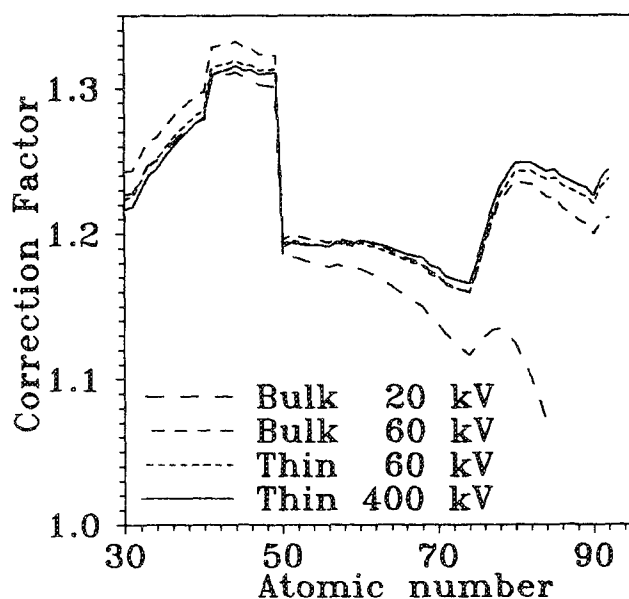


FIG. 1.--Correction factor to convert number of direct ionizations to number of total ionizations. Enhancement is caused by nonradiative rearrangements of electrons.

composition, it is almost cancelled in the course of the calculation of the k-ratio in conventional EPMA where standards are used.

2. For high E_0 [e.g., analysis in a transmission electron microscope (TEM)], the correction factor is independent of the excitation conditions. It can be seen that no significant change in the correction factor appears when E_0 is increased through the excitation energy of the K level of an element. That is so because the ionization probability is proportional to $1/E_c^2$ for electron excitation, where E_c is the energy level of the atomic subshell to be ionized. The independence of the excitation conditions means that the correction factor in Fig. 1, multiplied by the fluorescence yield for the L_3 subshell, can be treated as an effective fluorescence yield and there is no need for the separate computation of the ionizations of the three subshells.

3. It is absolutely necessary to compute the direct ionizations of the three L subshells separately and calculate the total number of generated x rays from them by use of the Coster-Kronig rates as weight factors for the summation if standardless analysis is performed with low overvoltage for at least one element of the sample.

For x-ray excitation, the introduction of an effective fluorescence yield is also correct if the energy of the primary x-ray photon is between the energies of the K and L_1 levels of the atom.⁴ These effective fluorescence yields (rather than the normal fluorescence yields) are to be used in the calculated secondary x-ray intensities; that applies to both x-ray fluorescence analysis (XRF) and the fluorescence correction in EPMA. If the primary photon energy

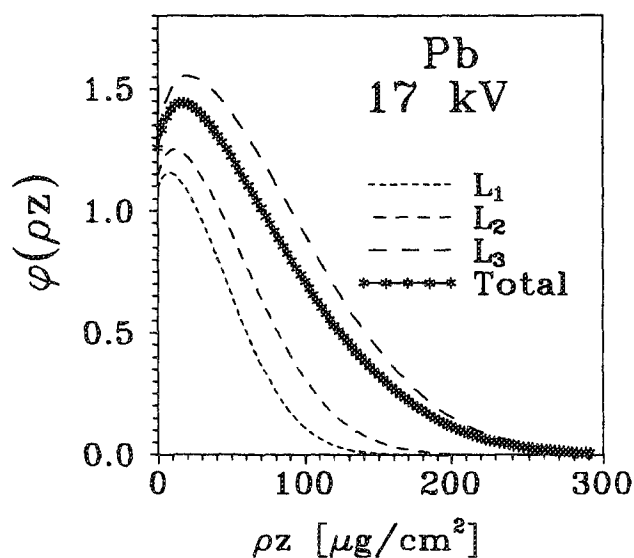


FIG. 2.--Depth distributions of ionizations within sample. Distributions of direct ionizations of the three L subshells are compared with distribution of total ionizations. Enhanced intensity in thin layer, used by definition for normalization, resolves virtual contradiction between plots labeled " L_3 " and "Total."

is above the K level, a new set of effective fluorescence yields must be calculated, because the K to L transitions play an important role in the indirect ionizations of the L subshells. That is so because the ionization probability is proportional to E_c^2 for x-ray excitation. Its practical importance is limited by the low direct ionization efficiency of the L shell for such high primary photon energies.

Depth Distribution of Generated X Rays

The probability of ionizations by electrons is a function of the electron energy and of the energy of the atomic level to be ionized. Since the energy of the electrons is changed during their course in the sample, the depth distribution of the direct ionizations is not determined only by the ionization probability function, but also by the stopping power of the sample and is unique to the subshell. Because the nonradiative rearrangements take place within the atom, the indirect ionizations in the L_3 subshell happen at the same depths within the sample where the direct ionizations of the L_1 and L_2 subshells originally took place. Consequently the depth distributions of the direct and of the indirect ionizations differ from each other. Since the shape of the ionization function is a slowly varying function of the overvoltage (calculated for a particular subshell), the depth distributions of ionizations of the three subshells converges if E_0 is increased, and so the relative differences between the three overvoltages are de-

creased. It follows that a noticeable deviation of the three depth distributions is observed at low primary beam energies compared with the ionization energies of the L subshells. At such an E_0 the depth distribution of the total ionizations (to the L_3 subshell) deviates from the depth distributions due to direct ionization (to the L_3) only. Figure 2 shows the depth distributions of both the direct and indirect ionizations for lead at $E_0 = 17$ keV. The absolute height of the curves can be misleading at first sight because the plot of the total ionizations is below the plot of the direct L_3 ionizations and seems to contradict the fact that the absolute number of total ionizations is higher than the number of direct ionizations. This virtual contradiction is a consequence of the definition of the depth distribution function. That definition contains a normalization to the intensity measured from an infinitely thin stand-alone layer of the same composition as the sample. The virtual contradiction is resolved if the higher normalization factor for the total ionizations in that layer is taken into account.

The incorporation of that effect into the Monte Carlo calculations of the emitted x-ray intensities is anticipated to shift the peak of the depth distribution slightly to the surface.

Sources of Atomic Data

As far as the K shell is concerned, theoretical fluorescence yield data are in excellent agreement with experimental values and a fitted polynomial is available for reliable and quick calculation of these data.^{7,8}

For the L shell *ab initio* relativistic calculations are only partly in agreement with experimental subshell fluorescence yield and Coster-Kronig transition data.⁹ A semi-empirical set of self-consistent tabulated data for the same atomic data is generally used, although 10-20% uncertainties can occur in problem areas.⁵ Fluorescence yields for the L_3 and L_2 subshells and the $f_{2,3}$ Coster-Kronig rates are measured by the coincidence technique with low (one to few percent) uncertainties.¹⁰ The uncertainties are the worst for the L_1 subshell for which both experimental and theoretical problems hinder the determination of the exact values.¹¹ It is especially inconvenient because contribution from the L_1 subshell is the major factor in the calculation of the x-ray intensity modified by the nonradiative transitions with excitations common in x-ray analysis. New experimental data obtained by the synchrotron photoionization technique seem to be the most reliable.¹¹

The M shell is even more problematic. Reliability of subshell fluorescence yields seems to be no better than 20%.¹² Theoretical calculations show that relativistic many-body effects play a significant role in nonradiative transitions and discrepancies between theory and experiment can be as high as 50%.^{13 14} Paucity of reliable experimental data is conspicuous.

Conclusions

1. The effect of nonradiative transitions cannot be omitted if the absolute $L\alpha$ x-ray intensities are to be calculated. The enhancement due to the Coster-Kronig transitions is up to 30%.

2. The "effective fluorescence yield" approach is justified for XRF and for EPMA with high E_0 , as is usual in a TEM.

3. Direct ionizations of the three L subshells are to be calculated separately in order to incorporate the effect of nonradiative transitions if standardless EPMA is performed with low E_0 .

4. A deviation in the shape of the depth distribution for the total ionizations from that of the direct ionizations of the L_3 subshell is predicted. Users of Monte Carlo calculations are encouraged to incorporate this effect in order to see a shift of the peak in the depth distribution of ionizations to the surface.

References

1. W. Bambynek et al., *Rev. Mod. Phys.* 44: 716, 1972.
2. T. P. Schreiber and A. M. Wims, *Microbeam Analysis--1982*, 161.
3. K. F. J. Heinrich, *Electron Beam X-ray Analysis*, New York: Van Nostrand Reinhold, 1981.
4. J. L. Lábár, *Proc. 12th IXCOM*, Cracow, 1989, 185; XRS to be published.
5. M. O. Krause, *J. Phys. Chem. Ref. Data* 8: 307, 1979.
6. J. L. Pouchou and F. Pichoir, *10th IXCOM*, London, Ont., 1987, 249.
7. M. H. Chen, B. Crasemen, and H. Mark, *Phys. Rev. A* 21: 436, 1980.
8. W. Bambynek, *X-ray and Inner Shell Processes in Atoms, Molecules and Solids*, Leipzig, 1984, 1.
9. M. H. Chen, B. Crasemen, and H. Mark, *Phys. Rev. A* 24: 177, 1981.
10. A. L. Catz, *Phys. Rev. A* 36: 3155, 1987; P. L. McGhee, J. L. Campbell et al., *J. Phys. B* 21: 2295, 1988.
11. U. Werner and W. Jitchin, *J. de Physique, Colloque C9, Suppl. 12*, 48: 559, 1987; U. Werner and W. Jitchin, *Phys. Rev. A* 38: 4009, 1988; W. Jitchin, G. Grosse, and P. Rohl, *Phys. Rev. A* 39: 103, 1989.
12. E. J. McGuire, *Phys. Rev. A* 5: 1043, 1972.
13. M. H. Chen, B. Crasemen, and H. Mark, *Phys. Rev. A* 21: 449, 1980.
14. M. H. Chen, B. Crasemen, and H. Mark, *Phys. Rev. A* 27: 2989, 1983.

THE APPLICATION OF BIO-STANDARDS FOR ELECTRON ENERGY LOSS ANALYSIS OF BIOLOGICAL MATERIALS

W. C. de Bruijn and L. W. J. Sorber

The application of standards, with a known externally determined element concentration, for the determination of unknown concentrations in cell organelles and tissue is a well-known practice in x-ray microanalysis.¹⁻³ The conditions to be met for a good standard have been formulated earlier.² Pure-element standards and standards made from PVP-films have been proposed for electron energy loss spectroscopic (EELS) analysis.^{4,5} In this presentation we investigate the use for EELS analysis of Chelex¹⁰⁰-type ion-exchange beads, which will be called Bio-standard. Such Bio-standards have been applied successfully for x-ray microanalysis previously.³

Experimental

Bio-standards can be loaded with a variety of cations. The ion-exchange characteristics, the methods of loading, and the matrix composition have been described previously.² Bio-standards are stored as a dry powder and can be co-embedded with the tissue to be analyzed, by adding it to the final embedding monomer prior to curing. In that way the standard is present in each ultrathin section, at an (assumed) thickness equal to that of the cells or tissue, containing the unknown concentration of that element.

Here we shall concentrate on the aspect of the ultrathin-sectioned standard material as test material:

- (1) to acquire reliable EELS-spectra;
- (2) to standardize some of the instrumental conditions;
- (3) for the implication of a computer program for EELS analysis;
- (4) to calibrate EELS-spectra; and
- (5) to compare fitting programs.

The electron microscope is a Zeiss EM902, in which the photomultiplier is coupled, via a selector, amplifier, and analog/digital converter to an Olivetti M280 AT-type computer. This acquisition chain is shown schematically in Fig. 1.

Results

In Fig. 2(a) part of a spectrum is shown from a cerium-containing Bio-standard showing the $M_{4,5}$ edge at 883 eV. In Fig. 2(b), the first derivative is used to find objectively the ionization edge, indicated by the vertical line. The dotted horizontal line above the

base line is $3\times$ standard deviation. In Fig. 2(a) a curve-fitting procedure is shown, known as the two-area method, which is applied to the 100eV-wide pre-ionization zone according to Egerton.⁶ In Fig. 3(a) the total spectrum of this cerium Bio-standard is shown from 100 to 1100 eV. In Fig. 3(a) another fitting procedure is applied to the same $M_{4,5}$ preionization region, the so-called Simplex method.⁷ After extrapolation beyond the edge, which is shown by the dark area, the I_B -part of the spectrum is subtracted; the resultant edge is shown in Fig. 3(b). In the meantime the ratio I_M/I_B or $I_M/(I_M + I_B)$ is determined for a 50eV range beyond the edge.

This procedure is repeated twice to calibrate the spectrum, once at the ionization edge of carbon, where the first derivative is used to find the edge (284 eV), shown in Fig. 4(a); and once in the region of the cerium $N_{4,5}$ edge (at about 120 eV, not shown). In Fig. 4(b) the resultant carbon edge is shown after subtraction of the extrapolated background (I_B).

Fitting procedures are similarly applied to iron-containing Bio-standards (11.5wt%) and calcium-containing Bio-standards (6.13wt%) leading to similar ratios for $I_L/(I_L + I_B)$ for iron and calcium.

In Figs. 5 and 6 the ratios are called relative concentrations. In these two figures results are accumulated in which the influence of the application of the two fitting procedures mentioned above (two-area or Simplex method) are applied to a set of Bio-standard-spectra from 25 cross sections in one ultrathin section and acquired with three different objective-lens diaphragms installed (30, 60, and 90 μ m). The columns represent the mean values, the bars the standard deviation.

Results from experiments in which (with the use of spectra from the calcium Bio-standard) 10 cross-sectioned beads in one section are measured in five time sequences to show the influence of mass loss expressed as the I_L/I_B ratio changes are given elsewhere.⁸

It is evident that by application of cross-sectioned standards of known externally determined concentration of the element involved in the tissue (in this case, by neutron activation analysis), quality EELS-spectra are acquired for multiple purposes.

References

1. G. M. Roomans, "Problems in quantitative x-ray microanalysis of biological specimens," *SEM/1980 II*, 309.
2. W. C. de Bruijn, "Ideal standards for x-ray microanalysis of biological specimens,"

The authors are at the AEM-unit, Clinical Pathology I, Erasmus University, Medical Faculty, P.O. Box 1738, NL-3000 DR Rotterdam, The Netherlands.

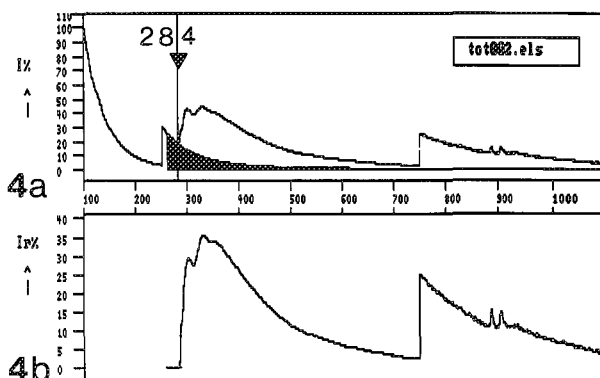
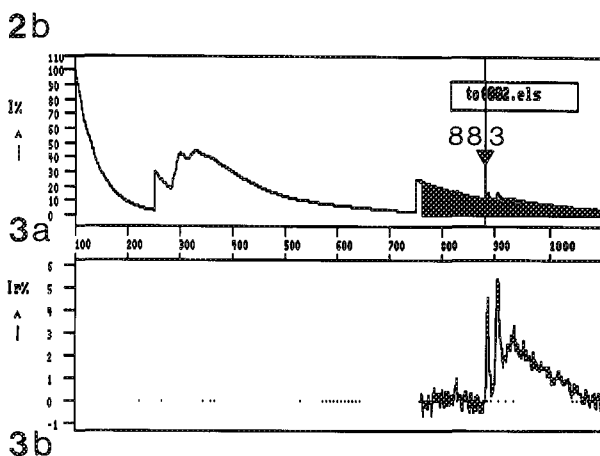
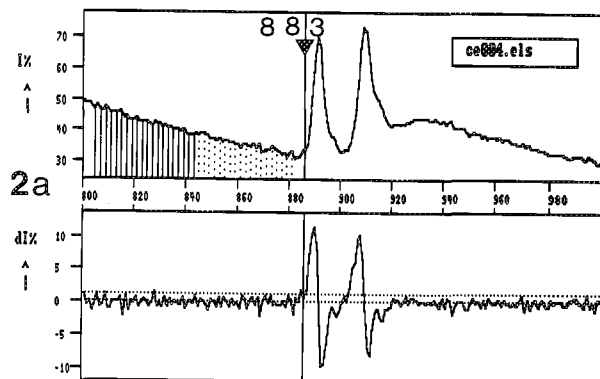
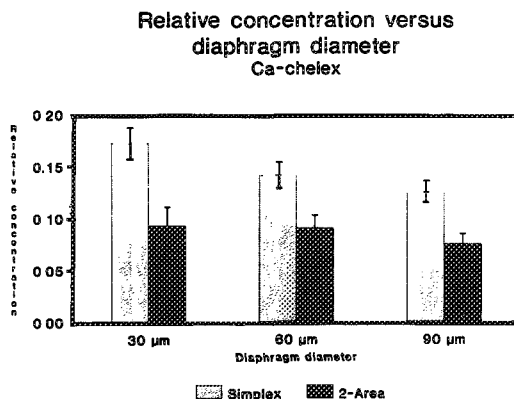
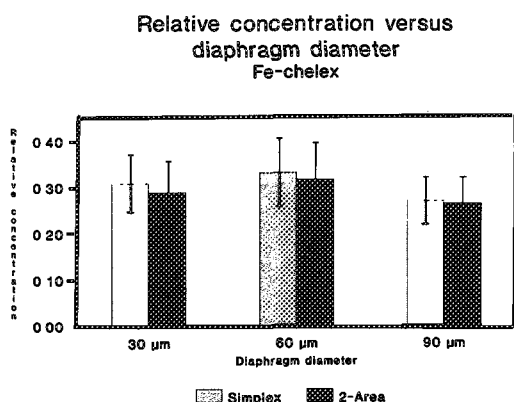
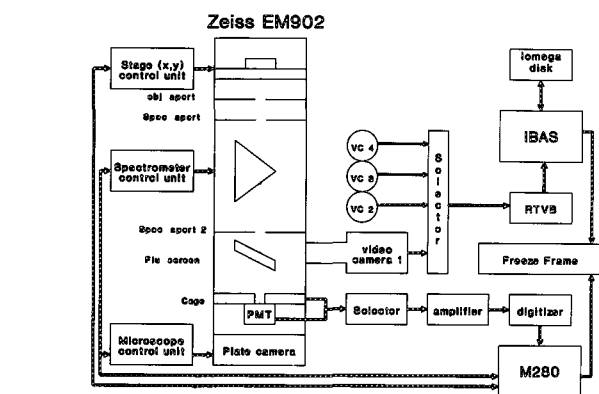


FIG. 1.--Schematic representation of spectrum-acquisition chain connecting Zeiss EM902 to Olivetti M280 computer.

FIG. 2.--Two phases of spectrum processing according to the two-area method: (a) rough Ce-standard spectrum, 2(b) first derivative to find ionization edge.

FIGS. 3 and 4 demonstrate the use of a large spectrum for calibration: 3(a) at Ce ($M_{4,5}$) edge; 3(b) after fitting according to Simplex method and subtraction of background (I_B) 4(a) fitting at carbon edge; 4(b) subtracted spectrum.

FIGS. 5 and 6 show the variation in the relative concentration when both the fitting procedure and the objective-lens diaphragm are changed during acquisition of 25 Ca or Fe Bio-standard cross sections in one ultrathin section.

SEM/1981 II, 357.

3. W. C. de Bruijn and M. I. Cleton, "Application of Chelex Standard beads in integrated morphometric and x-ray microanalysis," *SEM/1985* II, 715.

4. R. D. Leapman and R. L. Ornberg, "Quantitative electron energy loss spectroscopy in biology," *Ultramicroscopy* 24: 251, 1988.

5. H. Shuman and A. P. Somlyo, "EELS analysis of near-trace-element concentrations of calcium," *Ultramicroscopy* 21: 23, 1987.

6. R. F. Egerton, *Energy Loss-spectroscopy in the Electron Microscope*, New York: Plenum Press, 1986, 257.

7. K. W. C. Burton and G. Nickless, *Optimization via Simplex, Chemometrics and Intelligent Laboratory Systems*, 1987, 1, 135.

8. C. W. J. Sorber, G. A. M. Ketelaars, E. F. Gelsema, J. F. Jongkind, and W. C. de Bruijn, "Quantitative analysis of EELS-spectra for ultrathin sectioned biological material," *J. Microsc.* (in press). (a) I. Optimization of the background-fit with the use of Bio-standards, (b) II. The application of Bio-standards for quantitative analysis.

EXELFS STUDIES OF CARBON FIBERS

V. Serin, K. Hssein, G. Zanchi, and J. Sévely

The present developments of electron energy loss spectroscopy (EELS) in the microscope allow the spectra and their different complex structures corresponding to inner shell electron excitation by the incident electrons to be recorded accurately.¹ Among these structures, the extended energy loss fine structures (EXELFS) are of particular interest. They are equivalent to the well-known EXAFS oscillations widely processed in x-ray absorption spectroscopy.² Due to the specificity of EELS, the Fourier analysis of the EXELFS signal appears to be a promising technique for the characterization of composite materials, the major constituents of which are low-Z elements. By processing the EXELFS signal, we have studied the microstructure of carbon fibers. This analysis is performed beyond the carbon K edge, which appears in the spectra at 285 eV. The purpose of the paper is to compare the local short-range order, determined in this way for various types of high tensile strength (HTS) and high modulus (HM) carbon fibers.

Since 1970 the carbon fiber has come into the spotlight as a reinforcing constituent in composite materials for structural usage. Imaging by electron microscopy (high-resolution or moiré figures) has shown the structural differences between high tensile strength and high modulus carbon fibers.^{3,4} From these studies, models for the microstructure of these two kinds of fibers have been proposed. High modulus carbon fibers are made of basic structural units, which are almost isometric in shape but folded and entangled parallel to the fiber axis. Their diameter varies from 20 to 70 nm and their radius of curvature can vary from 2 to 13 nm. In the case of high tensile strength carbon fibers, the aromatic structural units are less than 1 nm in size. They are associated edge to edge in parallel to form larger wrinkled aromatic sheets. The sheets are crumpled parallel to the fiber axis and their folds are entangled.³ Elemental characterization of the fibers has shown that high tensile strength properties are closely connected with strong bonding between aromatic structural units inside the basic planes.⁵ This bonding is achieved during the processing route of the carbon fibers and is due to nitrogen release. On the contrary, the high modulus properties of carbon fibers are related to sufficient bonding between aromatic sheets, which is to say between basis planes. By using EXELFS technique, we have tried to evaluate the local short-range order in the two kinds of fibers and its connection with their mechanical properties.

The authors are at CEMES LOE, BP4347, F-31055 Toulouse Cédex, France.

Experimental

Within the dipole approximation appropriate to this case, the analytical expression describing the extended fine structure due to the backscattering of ejected electrons from near-neighbor atoms can be written in the same way as for EXAFS:⁶⁻⁸

$$\chi(k) = \sum_j \frac{N_j}{k R_j^2} \exp(-2\sigma_j^2 k^2) \exp\left[\frac{2R_j}{\lambda(k)}\right] \cdot |f_j(\pi, k)| \sin[2kR_j + \phi(k)]$$

where k is the magnitude of the ejected core-electron wave vector; R_j the distance from atoms in the j th shell to the central atom; N_j the number of atoms in this shell at the radius R_j ; σ_j^2 the mean-square amplitude of displacement due either to thermal motion or to disorder; λ the mean-free path of the ejected electron; and $\phi(k)$ the ejected electron wave phase shift due to both the excited atom and the j th backscatterer.

For the processing of the spectra, it has been shown that this equation is accurate only up to the thickness $t/\lambda_p < 0.3$ (where t is the thickness of the sample and λ_p is the mean free path for inelastic scattering of the incident electrons in the sample).⁹ Beyond this value, due to multiple scattering effects of the electrons in the sample, the shape of the characteristic excitation profiles changes when the thickness t increases.

Thin sections of carbon fibers were observed with a Philips EM 400 microscope equipped with a VG (ELS 80) electron spectrometer used in the sequential mode. In the case of 100-120 keV incident electrons, λ_p is of the order of 100-150 nm. That means a 30-50 nm maximum thickness for the specimen. Such thin sections are obtained either by ultramicrotomy of fibers correctly embedded in an epon resin or by grinding. The thickness of the sample was accurately controlled by modeling of the EELS spectra.¹⁰

For the studies on the carbon K edge, the associated spectra are recorded in the 200-700 keV energy loss range (Figs. 1a and 2a). The treatment of the EXELFS signal requires a sufficient signal-to-noise ratio (SNR), which is achieved with a counting rate higher than 10 000 counts per channel. In the energy loss range in question, the spectra are recorded with a 0.2 s per channel counting time. The probe size of the electron beam on the sample (30 nm) defines the selected area. The accuracy of the analysis in distance is about 5×10^{-3} nm; this value is mainly limited by the $[3.6, 9] \text{ \AA}^{-1}$ k window range.

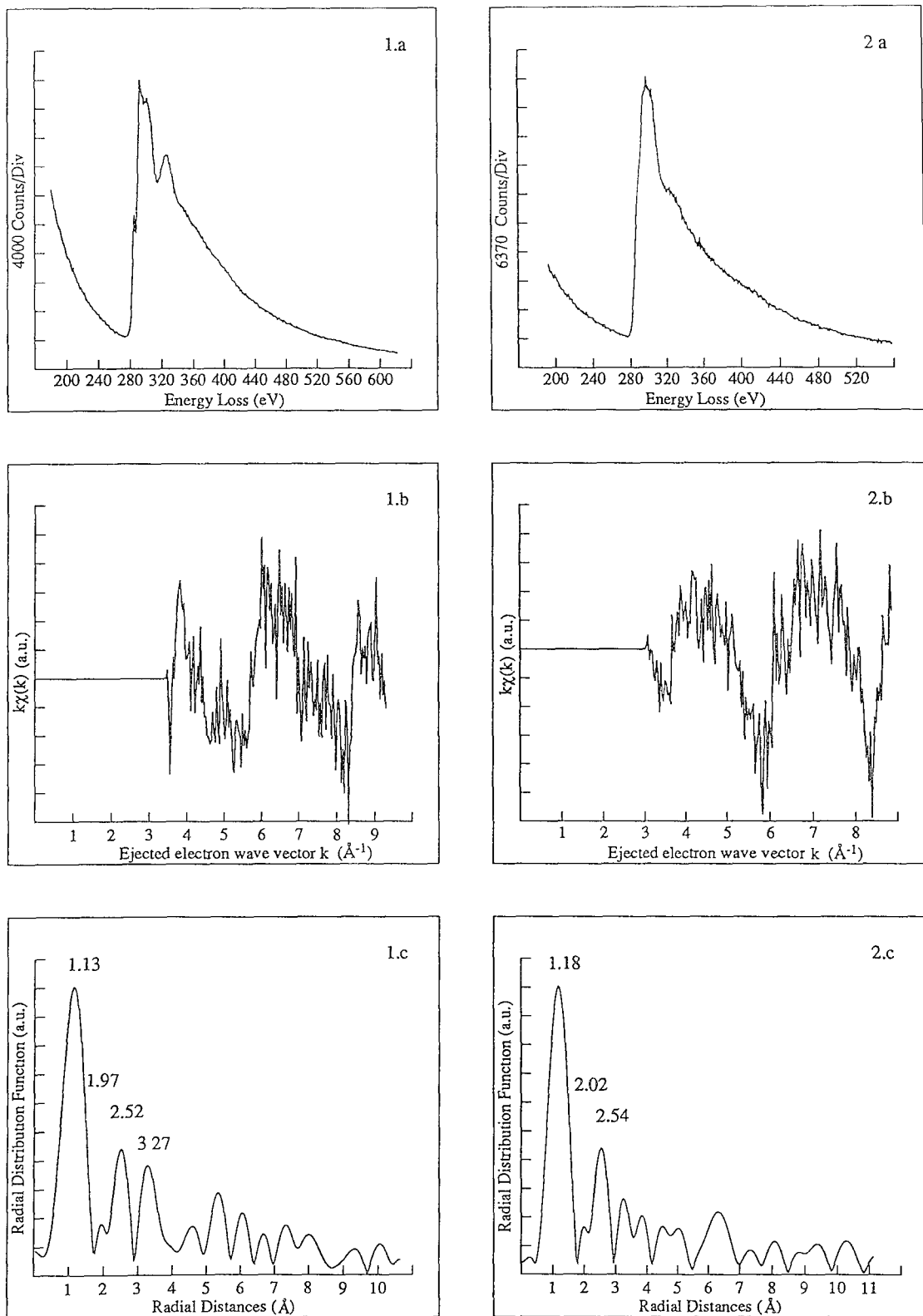


FIG. 1.--(a) Carbon K edge at 120 kV with high modulus GY70 carbon fiber; (b) EXELFS modulations $\chi(k)$ multiplied by k ; (c) corresponding RDF. Values are not corrected for phase shift, which is 0.36 \AA for C-C spacing.

FIG. 2.--(a) Carbon K edge at 120 kV with high tensile strength Courtaulds HTS carbon fiber; (b) EXELFS modulations $\chi(k)$ multiplied by k ; (c) relative RDF. Values are not corrected for phase shift, which is 0.36 \AA for C-C spacing.

TABLE 1.--Radial distances R_j deduced from EXELFS treatment on carbon K' edge obtained with pyrographite, high tensile strength carbon fibers, and high modulus carbon fibers. Results are compared with theoretical distances in graphite; (these distances are corrected for phase shift value, 0.36 Å).

a							
Theoretical	$R_j(\text{Å})$	1.42	2.45	2.85	3.35	3.63	3.76
Graphite	N_j	3	6	3	0 or 2	12 or 6	6
	N/R_j^2	1.49	0.99	0.37	0.09	0.68	0.42
Experimental	$R_j(\text{Å})$	1.42	2.20	2.88		3.60	
Pyrographite							
b							
High modulus carbon fibers							
M40		1.49	2.35	2.87		3.61	
P100		1.52	2.30	2.88		3.59	
GY70		1.49	2.33	2.88		3.63	
Endo		1.50	2.25	2.84		3.51	
Teijin		1.44	2.21	2.86		3.68	
c							
High tensile strength carbon fibers							
T1000		1.44	2.31	2.96			3.74
C HTS		1.54	2.38	2.90			
T300 1700°		1.52	2.26	2.95			
P25		1.61	2.51	3.23			

Table 1

Results and Discussion

In a first step, the EXELFS technique was applied to samples of cleaved monocrystalline pyrographite. The results of the EXELFS treatment were compared to the theoretical interatomic distances of the hexagonal structure of graphite (Table 1a). In the radial distribution function (RDF) of the pyrographite, four maxima appear at 1.42, 2.20, 2.88, and 3.60 Å. These values are corrected for a 0.36 Å phase shift value, obtained from the calculations of Teo and Lee in the $[3.6, 9] \text{Å}^{-1}$ k window range.¹¹ These maxima can be associated with four interatomic distances: three inside the 0002 plane for the 1.42, 2.45, 2.85 Å distances and one at 3.63 Å between 0002 planes. However, due to its small coordination number, the 3.35 Å distance is not resolved. These results confirm that the hexagonal structure of graphite is recovered by the EXELFS technique.

The experimental phase shift value confirms the theoretical calculations of Teo and Lee for carbon. From these conclusions, it looks worthwhile to extend the technique to more complex carbon structures, such as that observed in carbon fibers. The results are given in Table 1, and can be related to the mechanical properties of the fibers given in Table 2.

In HM carbon fibers (Fig. 1 shows the treatment on the GY 70 carbon fiber) four major contributions in the RDF are measured for the M40, P100, GY 70 and Teijin carbon fibers (see Table 1b). As compared to the hexagonal structure of graphite, the first three values can be attributed to distances between atoms inside the 0002 plane (1.42, 2.45, and 2.85 Å). As to the fourth distance, it can be identified with an interlayer spacing contribution (distance at 3.36 Å in graphite). This result reveals a quite closed-packed structure, the local order

TABLE 2.--Comparison of mechanical properties of sampling of carbon fibers.

Fibers	Precursor	Density (g/cm ³)	Modulus (Gpa)	Tensile Strength (Gpa)
Toray M40	Pan-Based	1.81	392	2.74
Union Carbide P100	Pitch-Based	2.15	724	2
Celanese GY70	Pan-Based	1.96	517	1.86
Endo (experimental fiber)	Ex-benzene	-	-	-
Teijin	Pitch-Based	2.16	650	5.85
Toray 1000	Pan-Based	1.82	294	7.06
Courtaulds HTS	Pan-Based	1.82	237	2.99
Toray 300 1700°	Pan-Based	-	-	-
Union Carbide P25	Pitch-Based	1.90	160	1.40

Table 2

tending toward the three-dimensional organization of graphite. The interlayer bonding due to the π electrons is consistent with the high modulus properties of this type of fiber.

In the case of HTS carbon fibers: T1000, Courtaulds HTS and T300 1700° (Table 1c), only three major contributions are deduced from the processing of the EXELFS modulations; an example corresponding to the treatment of Courtaulds HTS fiber is shown in Fig. 2. As for the HM fiber, these values correspond to the first three interatomic distances between the atoms inside the 0002 plane. In that case, due to a higher spacing, the interlayer distance is not detected. From this result we concluded that any interlayer bondings are weak or nonexistent, which suggests a two-dimensional structure for this type of fiber.

This conclusion is confirmed by the results on the Toray 1000 carbon fibers. This fiber corresponds to a new generation of high tensile strength fibers. It is characterized by more extended basis structural units, as confirmed by the electron diffraction pattern from which it is possible to measure the diameter of the basis structural units.¹² For this fiber, the EXELFS treatments show a fourth maximum at 3.74 Å, which corresponds to a distance inside the 0002 basis plane (i.e., at 3.76 Å in the graphite structure). This result reveals a two-dimensional order in this fiber with a more extended local order inside the carbon sheets, consistent with the known structural properties of this fiber. The RDF achieved from the EXELFS signal is in good agreement with the established turbostratic structure for these fibers. It also coincides with their high tensile strength behavior in connection with the weak bondings between carbon sheets.

In the same way, the results of the analysis on P25 carbon fiber can be considered as coherent with its moderate tensile strength behavior. They reveal three distances, but with about 10% larger values. This finding is consistent with the poor degree of atomic order in this type of fiber.

Conclusions

These studies reveal a systematic difference in the stacking of carbon sheets when the structures of the HTS and HM carbon fibers are compared. For the HTS fibers they allow us to characterize an increase in the interlayer distance,

which is in good agreement with the high tensile strength properties of the fibers. These results provide a new example of the potentialities of the EXELFS technique for the structural investigation of low-Z materials.

References

1. R. F. Egerton, *Electron Energy Loss Spectroscopy in the Electron Microscope*, New York: Plenum Press, 1986.
2. R. D. Leapman, L. A. Grunes, P. L. Fejes, and J. Silcox, in B. K. Teo and D. C. Joy, Eds., *EXAFS Spectroscopy Techniques and Application*, New York: Plenum Press, 1981.
3. M. Guigon, A. Oberlin, and G. Desarmot, *Fibre Science and Technology* 20: 55 and 177, 1984.
4. E. Fitzer and D. J. Muller, *Carbon* 13: 63, 1975.
5. V. Serin, R. Fourmeaux, Y. Kihn, J. Sévely, and M. Guigon, *Carbon* 28: 573, 1990.
6. S. Csillag, D. E. Johnson, and E. A. Stern, in B. K. Teo and D. C. Joy, Eds., *EXAFS Spectroscopy Techniques and Application*, New York: Plenum Press, 1986.
7. S. M. Heald and E. A. Stern, *Phys. Rev.* B17: 4069, 1978.
8. E. A. Stern, D. E. Sayers, and F. W. Lytle, *Phys. Rev.* B11: 4836, 1975.
9. J. Sévely, G. Zanchi, Y. Kihn, and K. Hssein, *Scanning Microscopy*, suppl. 1: 179-187, 1987.
10. G. Zanchi, Y. Kihn, J. Sévely, and B. Jouffrey, in R. M. Fisher, R. Gronsky, and K. H. Westmacott, Eds., *Proc. of the 7th Intern. Conf. High Voltage Electron Microscopy*, 1983, 85.
11. B. K. Teo and P. A. Lee, *J. Am. Chem. Soc.* 101: 2815, 1979.
12. M. Guigon, Thesis, Compiègne, France, 1985.

LITHIUM DETECTION IN ALUMINUM-LITHIUM ALLOYS USING PEELS

A. R. Wilson

Aluminum-lithium (Al-Li) alloys are important alloys for the aerospace industry because of their good strength-to-weight properties. However, these alloys suffer from poor short-transverse fracture toughness. Segregation of Li onto the grain boundaries is one mechanism proposed to account for this poor toughness.¹ The present work considers the use of parallel electron energy loss spectroscopy (PEELS) for quantifying, with high spatial resolution, the Li concentrations in these alloys.

Theoretical Considerations

Table 1 shows that the composition of two typical Al-Li alloys is around 11 at.% of Li. Figure 1 shows a theoretical spectrum for a binary alloy of 11 at.% Li dispersed in Al. The Li K and Al $L_{2,3}$ edges in Fig. 1 were calculated by use of Egerton's results based on the hydrogenic model,² as implemented in the electron energy loss software developed by Gatan Inc. (called "EL/P"), and were then smoothed to simulate the finite resolution of the electron energy loss (EEL) spectrometer. The detection of Li is difficult owing to a combination of factors: (1) the very low Li K edge jump ratio in Fig. 1, (2) the proximity of both the Al plasmon and Al $L_{2,3}$ edge, and (3) the deviation of the Li K edge from the ideal sharp Fermi step.

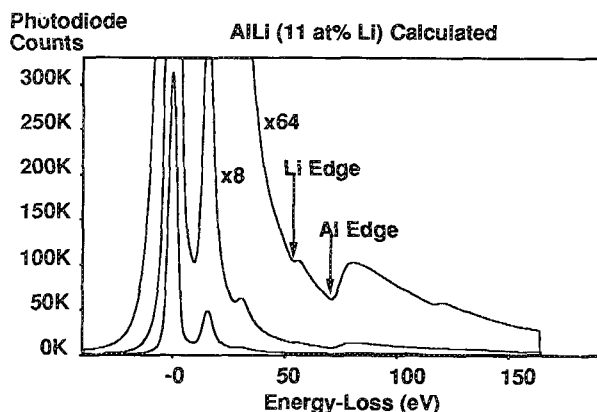


FIG. 1.--Calculated Li K edge and Al $L_{2,3}$ edge EEL spectrum for 11 at.% Li in Al with edge broadening resolution effects included. Li K edge is visible but with very low jump ratio.

The Li edge is seen more clearly if the second difference of the spectrum is obtained (Fig. 2) by convolution of the spectrum with a top-hat filter. Figure 3 illustrates the effects of

A. R. Wilson is at the Aircraft Materials Division, Aeronautical Research Laboratory, DSTO, 8506 Lorimer St., Fishermens Bend 3207 Victoria, Australia.

TABLE 1.--Nominal compositions of two Al-Li alloys.

8090 Al-Li Alloy		
Element	Weight %	Atomic %
Al	95.2	87.6
Li	2.5	11.7
Cu	1.3	0.36
Mg	0.12	0.17
Zr	0.1	0.04
Fe	0.1	0.03
Si	0.05	0.05

2090 Al-Li Alloy		
Al	95.0	88.7
Li	2.2	10.5
Cu	2.7	0.76
Zr	0.12	0.05

various top-hat filter widths on the second-difference result for abrupt spectral edges. The zero crossings in the second-difference result correspond to the edge on-set energies. If the top-hat filter width is the same as the resolution of the spectrum the minima on the low-energy side of the zero crossing points correspond to the energy at which the resolution broadened edge commences, which is the energy that should be chosen for the determination of integrated counts under the edge. Choice of a wider top-hat filter does not affect the zero crossing energy but does move the preceding minimum to lower energy. This movement does not affect the integrated edge count result since background subtraction gives zero counts in the extra energy region included. Use of a narrower top-hat filter does not affect the energies for the zero crossing point but broadens the preceding minimum. Thus selection of the top-hat filter width is not critical for the determination of the energy at which edge count integration should commence.

Experimental Considerations

Figure 4 shows a spectrum obtained from a grain boundary in a 2090 Al-Li alloy. Even though the dark-current and readout noise associated with the electron detection system has been removed from this spectrum the Li edge is still only just visible. Figure 5 is the second-difference curve obtained from the spectrum in Fig. 4 and both the presence and position of the Li edge are now more easily determined. The presence of Li edges can easily be overlooked if these processing steps are not

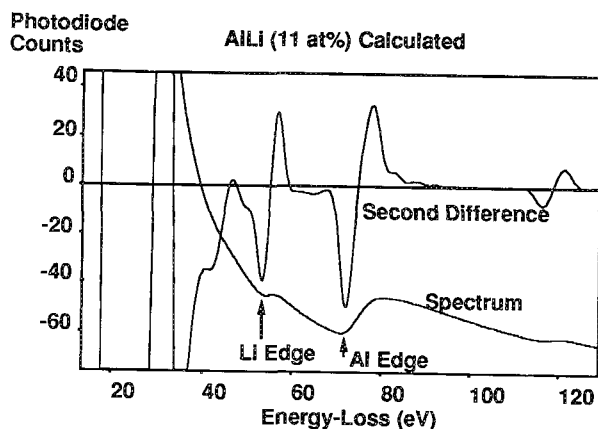


FIG. 2.--Second-difference result for spectrum in Fig. 1 showing improved visibility of Li edge.

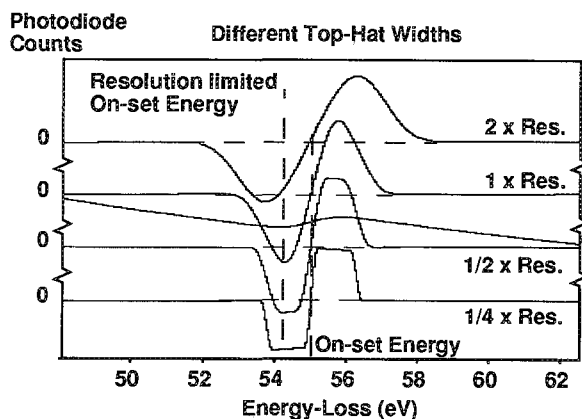


FIG. 3.--Examples of effect of top-hat filter widths of twice to a quarter of spectrum resolution on resulting second-difference spectrum. Spectra have been vertically displaced. Vertical dashed lines correspond to Li edge onset energy at 55 eV and onset energy after experimental resolution limiting effects are included.

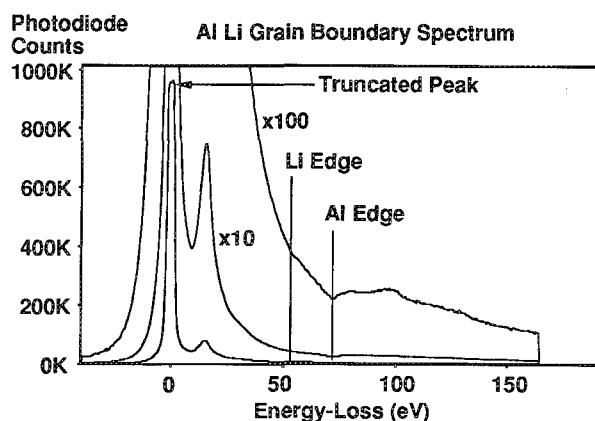


FIG. 4.--Typical spectrum obtained from grain boundary in Al-Li alloy that showed Li segregation. The $\times 1$ spectrum shows saturated zero loss peak; Li signal is just visible in $\times 100$ spectrum. Before background and noise subtraction, Li edge was even less visible.

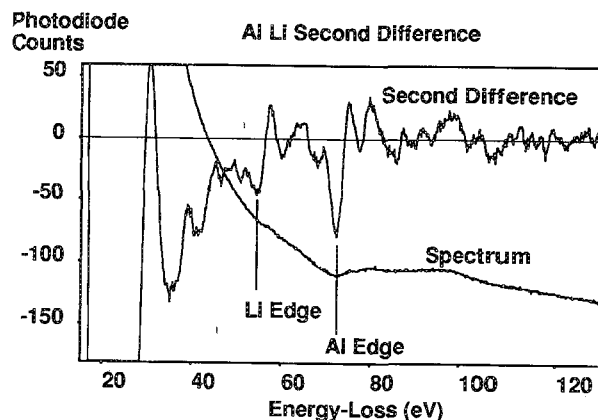


FIG. 5.--Same spectrum as in Fig. 4 after second difference (top-hat filter) has been performed. Presence and threshold energy of Li edge are much more apparent.

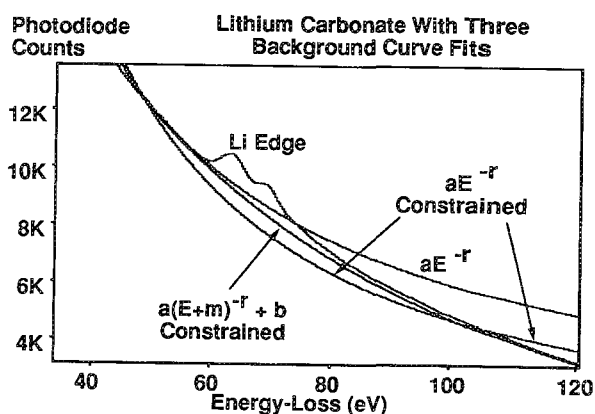


FIG. 6.--Low-energy region of Li_2CO_3 spectrum, showing clearly visible Li edge, with three different background fitting curves. Both standard and constrained aE^{-r} curves give poor fits, whereas $a(E+m)^{-r} + b$ gives much better fit.

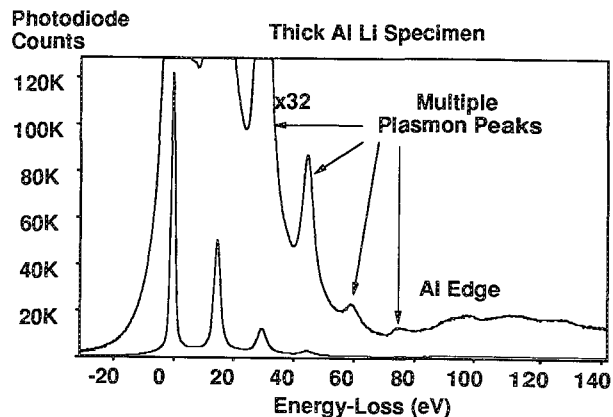


FIG. 7.--PEEL spectrum obtained from thick region of Al-Li specimen as generally used for metallurgical microstructure investigations. Multiple energy loss scattering severely broadens Al $L_{2,3}$ edge and masks any Li K edge information.

TABLE 2.--Li concentration with the electron beam placed progressively across the grain boundary. Specimen 2 is a simple grain boundary, specimen 1 is on an inclined boundary. The plasmon results were obtained from the measurements of the plasmon peak energy.

Beam Position	Spec. 1 Li at. %	Spec. 2 Li At. %	Spec. 2 Li at. % (Plasmon)
1	<1	3.1	2
2	4.0	2.7	0
3	2.8	2.4	0
4	3.1	3.5	0
5	5.0	9.3	0
6	1.4	8.2	12
7	-	5.5	11
8	-	0.4	0

routinely performed.

Figure 4 also shows that the conditions necessary to obtain sufficient counts above the background noise level in the Li edge often result in saturation of the zero loss peak (ZLP). Spectral deconvolution to extract the single scattering result requires an unsaturated ZLP for the determination of the incident electron intensity. A suitable ZLP can be obtained by scaling of an unsaturated ZLP from a spectrum collected with lower electron beam current or lower detector integration time but with all other experimental conditions the same.

Concentration Determinations

Electrochemically polished Al-Li alloys were examined in a cold holder (operating at a temperature of typically -170 C) in a scanning transmission electron microscope operating at 200kV acceleration voltage. Analyses using the techniques above and the standard aE^{-1} background fit indicate that Li segregation occurs in the region of some of the grain boundaries studies. Two examples of these analyses are shown in Table 2. The Li concentrations obtained are lower than would be expected from the nominal concentrations of the alloys. One explanation is that the Li is highly concentrated onto the thin grain boundary and hence the sampling region of around 6 nm diameter includes regions of low Li concentration found in the precipitate-free zone on each side of the grain boundary. A simplistic area ratio calculation that assumes that the Li all occurs on a 2nm-wide strip indicates that the Li concentration could be underestimated by a factor of 2.5. This would adjust the concentrations in Table 2 to levels above the average bulk levels on the grain boundary with the concentration in the region next to the grain boundary remaining below the average bulk concentration as would be expected if the Li is diffusing to the grain boundary.

The possibility of incorrect background subtraction due to the use of an aE^{-1} fit at low energies must also be considered. Spectra were collected from Li_2CO_3 samples to calibrate the Li response and to check the background sub-

traction. An example of one of these spectra is shown in Fig. 6, together with various background fits. The aE^{-1} fit results in an underestimate of the Li counts giving a Li:C:O ratio of 0.8:1:2.9. The good C:O ratio indicates that the standard curve fit is adequate at energies above 250 eV. This result implies that the Li concentrations determined for the Al-Li alloys could be underestimated by up to a factor of 2.5 if the standard aE^{-1} background fit is used.

The determination of the background at low energy with the aE^{-1} curve constrained to fit the spectrum at higher energies results in a very poor fit to the background for the Li_2CO_3 spectrum in Fig. 6. A more complicated $a(E + m)^{-1} + b$ curve (Fig. 6), constrained to fit at higher energies, gives a much better fit to the background. The Li:C:O ratio is improved to give 1.5:1.0:2.9 but is still too low by 25% for the Li concentration. More work on background modeling at low energies needs to be done before any reliable quantitative results can be obtained. Modeling the plasmon peak may lead to better background subtraction at low energies and is currently under investigation.

Other Considerations

Not all the specimens examined gave measurable amounts of Li. The absence of Li might be due to leaching of Li during specimen preparation since some specimens exhibited signs of preferential etching along the grain boundaries. Also, Li diffusion through Al may be a problem especially diffusion along grain boundaries to the surface of specimens. Secondary ion imaging (SIM) studies³ conducted on bulk specimens at room temperature over several months have shown that Li diffuses readily along grain boundaries. The diffusion rate indicated is of the order of nanometers per hour, sufficient to result in redistribution of Li in thin (10-30nm) TEM specimens. Some ultramicrotomed specimens have also been examined; however, they have not shown the microstructural detail expected with evidence of severe distortion around grain boundaries. No Li at all was detected in these specimens.

A further problem with EELS is the need for thin specimens to reduce the number of multiple energy loss scattering events. It is very difficult to obtain images from thin specimens with the same microstructural detail as observed in thicker regions of the specimen. A PEELS spectrum obtained from a wide area of a thick region of an Al-Li alloy is shown in Fig. 7. The Al edge in this spectrum is extremely broad and the multiple plasmon peak obscures the presence of any Li edge. Such a spectrum is not amenable to the current deconvolution techniques used to obtain the single scattering result. However, measurement of the plasmon peak energy can also be related to the Li concentration (strictly true only for binary alloys).^{4,5} The plasmon energy of 14.0 ± 0.1 eV in Fig. 7 corresponds to a Li concentration of 9 ± 3 at.% for an alloy with a nominal Li con-

tration of 10.5 at.%. Calibrated measurements of the plasmon energy for a spectrum collected from a large area not near a grain boundary in another specimen gave a Li concentration of 12.5 ± 3 at.%. Measurement of the plasmon energy may give better absolute measurements of concentration than the edge analysis technique; however, the requirements on the spectrometer are more stringent with a 0.1 eV shift in energy corresponding to a change of 2.6 at.% in the Li concentration. This problem may be overcome to some extent if curves are fitted to the zero loss and plasmon peaks and the peak energy is determined by interpolation to a higher resolution than the intrinsic resolution of the EEL spectrometer. Included in Table 2 are the results obtained if this method is applied to the same spectra that were used to give the Li edge analysis concentrations, collected with 0.2 eV energy steps and a resolution of around 2.5 eV. The Li concentrations determined by the plasmon technique are not underestimated due to background subtraction inherent in the Li edge analysis. However, the possibility of underestimation by a factor of 2.5 on the grain boundary due to the finite beam diameter is the same as in the Li edge calculation. There is only rough correspondence between the plasmon and the integrated edge count results; however, the technique shows some promise and is also under further investigation although it will require accurately calibrated energy loss scales.

Conclusions

The routine use of dark current and readout noise subtraction and the calculation of the second difference spectrum greatly enhances the chances of observing the Li K edge in EEL spectra of Al-Li alloys. Some success has been gained in observing Li segregation to grain boundaries in these alloys although the absolute quantitation is unsure owing to inadequate background models at low energy losses. Measurement of the plasmon peak energy may offer an alternative method for determining Li concentrations, especially for thick (> 30 nm) regions of a specimen.

References

1. W. S. Miller, M. P. Thomas, D. J. Lloyd, and D. Creber, "Aluminium-lithium alloys III," *Proc. Third Intern. Al-Li Conf.*, London: The Institute of Metals, 1986, 584.
2. R. F. Egerton, *Electron Energy Loss Spectroscopy in the Electron Microscope*, New York: Plenum Press, 1986, 184 and 357.
3. D. B. Williams, R. Levi-Setti, J. M. Chabala, and D. E. Newbury, "High spatial resolution secondary ion imaging and secondary ion mass spectrometry of aluminium-lithium alloys," *J. Microscopy* 148: 241, 1987.
4. D. B. Williams and J. W. Edington, *Metal Science* 9: 529, 1975.
5. C. M. Sung, H. M. Chan, and D. B. Williams, Ref. 1, 337.

Electron Energy Loss Spectrometry

PARALLEL DETECTION OF ELECTRON ENERGY LOSS SPECTRA IN DIRECT MODE

Eckhard Quandt, Stephan Ia Barré, Andreas Hartmann, and Heinz Niedrig

Due to the development of cellular semiconductor--e.g. charge coupled devices (CCDs) or photodiode arrays (PDAs)--the parallel detection of electron energy loss spectra (EELS) has become an important alternative to serial registration because of the improved detection efficiency. In designing a detection system one has to consider indirect or direct exposure with both types of arrays. The best choice among these four parallel detection realizations certainly depends on the kind of experiment to be carried out.¹ When parallel detection is used to record energy spectroscopic large angle convergent-beam-like patterns (LACBPs),² special selected scattering vectors and small detection apertures lead to very low intensities. Therefore, the very sensitive direct irradiation of a cooled linear PDA in place of the common combination of scintillator, fiber optic, and semiconductor³ has been investigated. In addition, the whole parallel detection system consists of a quadrupole lens system to improve the energy resolution by magnifying the spectra. Figure 1 is a schematic drawing of the sectorfield spectrometer, the quadruplet, and the parallel detection device.

Parallel Detection Device

The detector is a Hamamatsu S2304-512Q linear PDA with 512 diodes and removed quartz-glass window. Diode arrays with 256 or 1024 diodes can be used as well. The individual active surface of each diode measures $13\ \mu\text{m} \times 2.5\text{mm}$ with an element spacing of $25\ \mu\text{m}$. The detector is mounted on a small sheet bar in the image plane of the quadrupole lens system and can be adjusted in the nondispersive direction by manual operation of a ram.

The reset noise of the videoline as well as the charge-sensitive amplifier noise is associated with the videoline capacitance. Therefore, the driver/amplifier board of the PDA is placed within the vacuum chamber close to the detector to reduce the videoline length.

The dark current of the PDA decreases by two orders of magnitude when the PDA is cooled with LN_2 to -100 C (Fig. 2). In addition, the cooling increases the dynamic range (DR) and reduces the radiation damage. The reduction of radiation damage by cooling the array increases

the lifetime by a factor of about 20.

As a second important feature, the direct registration efficiency was investigated as a function of the primary energy. The theoretical value for direct exposure can be calculated by dividing the primary energy by the electron-hole-pair generation energy of 3.64 eV for silicon. The lower experimental value can be explained by the geometrical structure of the diodes. The aspect ratio of the photodiode array halves the reachable value. Moreover, the layer structure of the p-n junction leads to electron-hole-pair production outside the depletion zone. Electrons with energies lower than about 8 keV are readily absorbed in the SiO_2 passivating layer, whereas faster electrons partly produce electron-hole-pairs below the depletion area. With the help of Monte Carlo simulations, we were able to confirm the experimental values (Fig. 3). The lower calculated values for energies higher than 30 keV result from the use of the dead-layer model for the depletion area.⁴

The overall performance of the parallel detector in direct mode is closely related to its DR and the detection quantum efficiency (DQE), both of which depend on the incident electron dose, the integration time, and the number of readouts.⁵ A consequence of the high gain even for low intensities is that high DQEs are attainable. A comparison of DQE for a PDA operated in direct and indirect mode for different numbers of incident electrons and readouts show a superior performance of the PDA in direct mode when the signal on the detector is low. The detection efficiency for the direct mode ($\eta = 3700$, 40keV electrons) was determined experimentally (Fig. 4) and was compared to a typical value for the indirect mode ($\eta = 64$, 40 keV electrons) derived from data given by Krivanek.³ The DQE in the direct mode is very close to unity over a wide range of incident electron doses and decreases with the number of readouts. Single electron detection appears to be possible. The DR for a single readout is about 7000 and increases with the number of readouts. In Fig. 5 the DR of a PDA and a CCD is shown. The CCD has a very small active surface of $13 \times 13\ \mu\text{m}$ and therefore the saturation charge is about two magnitudes lower than for the PDA.

The driver/amplifier circuit is operated by external clock and start pulses provided by a microprocessor. This computer controls the STEM and allows the acquisition, representation and evaluation of the measured data with 16-bit resolution. The output voltage of the PDA is A/D-converted with 14-bit resolution and with $8\mu\text{s}$ conversion time so that the data can be converted, stored, and displayed online

The authors are at the Optisches Institute (Sehr. P11), Technische Universität Berlin, Strasse des 17. Juni 135, D-1000 Berlin 12, Germany. They thank E. Zeitler and H. Pätzold (FHI Berlin) for helpful suggestions on the design and manufacture of the quadrupole lenses, and C. P. Scott (University of Glasgow) for the use of his quadrupole-analysis programs.

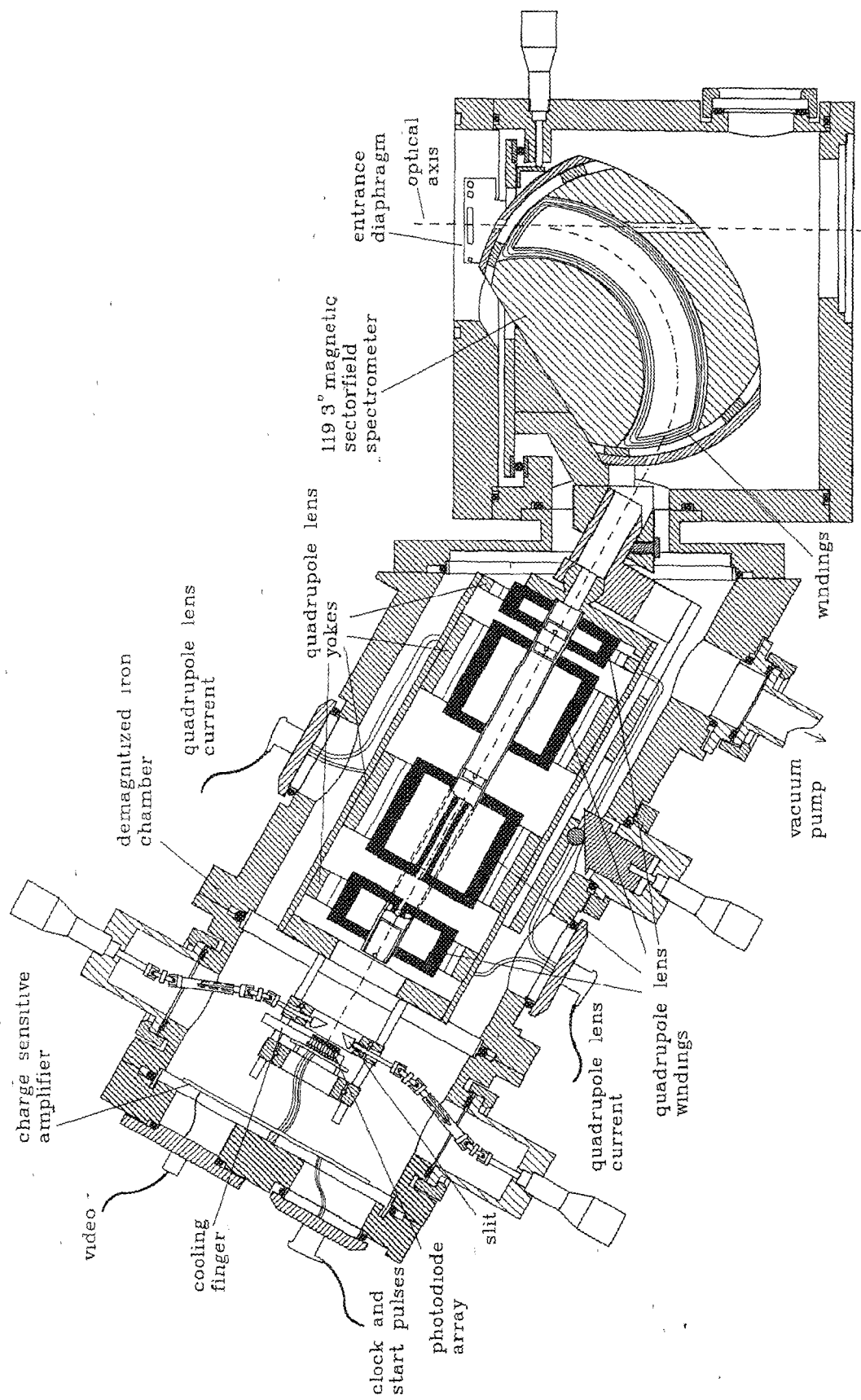


FIG. 1.--Survey diagram of double-focusing sector field spectrometer combined with quadrupole lens system and parallel detector.

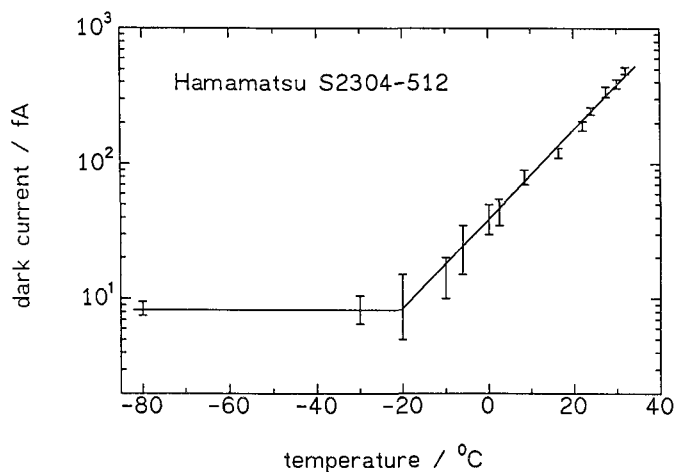


FIG. 2.--Dark current of Hamamatsu S2304-512Q PDA as a function of temperature.

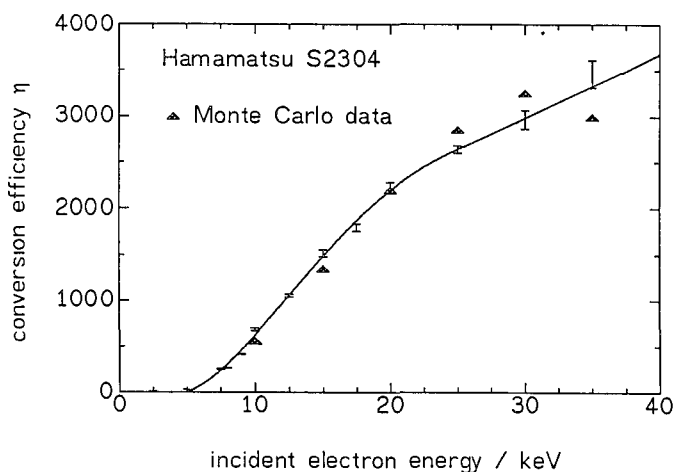


FIG. 3.--Measured conversion efficiency η per incident electron vs electron energy compared to Monte Carlo data; simulation is based on a dead-layer model with the assumptions of a 0.4 m SiO₂ passivating layer and estimated 3 m depletion zone.

at all usable clock frequencies up to 62.5 kHz. The integration time can be varied from 10 ms to about 600 s, whereas the lower limit represents the minimum readout time and the upper limit represents the discharge time of the array by the dark current. A block diagram of the detector is shown in Fig. 6.

Quadrupole Lens System

The quadrupole optics was designed according to a proposal of C. P. Scott⁶ and has been attached to a double-focusing 119.3° magnetic sector field spectrometer.⁷ Experimental conditions require the possibility of shifting the whole spectrometer against the optical axis--a translation that the quadruplet and the detector have to follow, so that all three parts had to be rigidly connected (Fig. 1).

The magnification system consists of four magnetic quadrupole lenses and uses the disper-

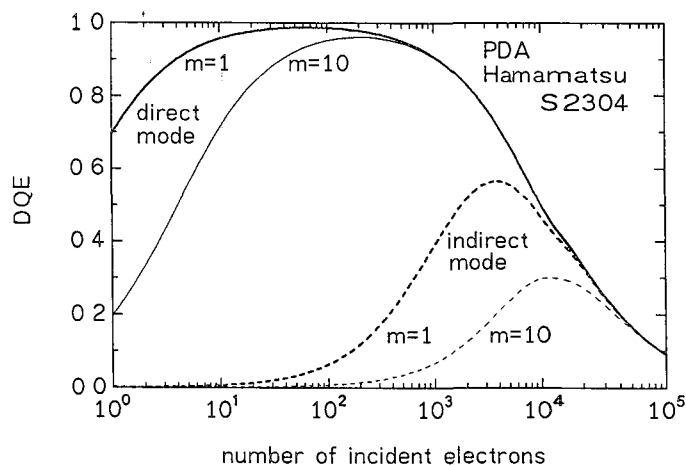


FIG. 4.--Detective quantum efficiency (DQE) as function of number of incident electrons for direct and indirect mode and various numbers of readouts.

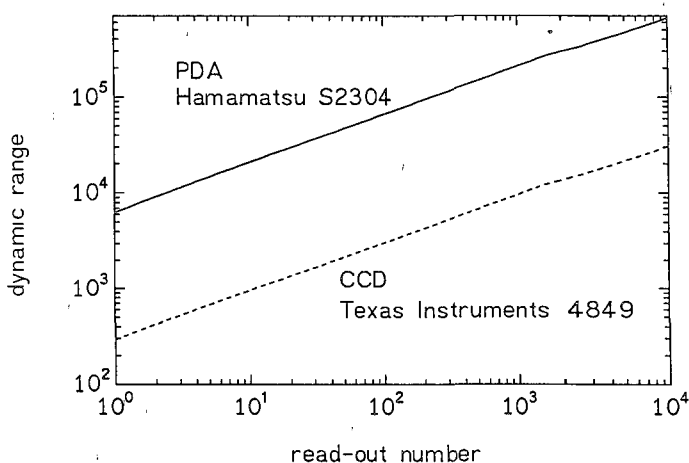


FIG. 5.--Dynamic Range (DR) as a function of readout number for PDA with active area of 13 × 2.5 mm and CCD with active area of 13 × 13 μm.

sion plane as a real object--a design that does not affect the optical properties of the spectrometer.⁸ To minimize the inaccuracy of the manufacture and the effort of the adjustment, the pole shoes and the yokes are made as one-piece by spark erosion and are fixed in relation to the optical axis by a tube that contains the diaphragms of each lens. The system allows a variable magnification in the dispersive direction, whereas the nondispersive direction is almost constantly demagnifying (0.2×). As the position of the crossover is nearly independent of the magnification, fixed slits can be attached to minimize the effect of stray scattering. The two central lenses lead to a magnification of 12×, which can be increased or decreased by the last lens according to the direction of the excitation (high-mag-mode or low-mag-mode, respectively). In Fig. 7 schematic electron trajectories for the low-

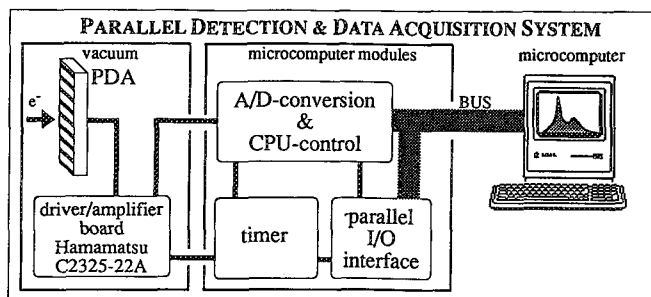


FIG. 6.--Outline of computer-controlled parallel detection and data-acquisition system.

and high-magnification mode in the dispersive plane are shown. The attainable magnification is about $4\times$ to $15\times$ in low-mag-mode and $20\times$ to $90\times$ in the high-mag-mode, determined by a measurement of the distances between primary peak and plasmon losses of aluminum (Fig. 8) for various lens excitations. These values agree well with calculated data derived by programs from C. P. Scott (Fig. 9).⁶ Considering a dispersion of $3.5 \mu\text{m}/\text{eV}$ for 40keV electrons, the quadruplet enables an increase in this value in the range from 14 to $315 \mu\text{m}/\text{eV}$. As the spatial resolution of the parallel detector is $25 \mu\text{m}$ in direct mode, the maximum magnification allows a theoretical limit of 80 meV for the energy resolution with a parallel detected energy range of 900 to 40 eV . The reached energy resolution of the parallel detection spectrometer was determined to be 1.1 eV (Fig. 10)--a value that agrees well with the energy spread of the thermionic tungsten cathode operated at about 3000 K .

The spectrum of TiO_2 (Fig. 10) was measured at about maximum magnification ($85\times$) in the high-mag-mode, whereas the spectrum of MoSe_2 (Fig. 11), recorded with a scattering vector of $q = g_{100}/2$, is an example for the low-mag-mode (magnification $12\times$).

Conclusion

For low electron doses and primary electron energies in the range from 20 to 40 keV , the direct exposure of a cooled linear PDA seems to be the best compromise between high DQE, DR, and sensitivity if cellular semiconductors are considered. The spectra obtained by a double-focusing magnetic sector field spectrometer were magnified in the range of $4\times$ to $90\times$ by an attached quadrupole lens system, which uses the image plane of the spectrometer as a real object. The microprocessor-controlled operation provides on-line representation of the converted data with 14-bit resolution and allows standard evaluation of the data. With this parallel-detection electron-energy-loss spectrometer we have reached an energy resolution of 1.1 eV using a thermionic cathode.

References

1. J. N. Chapman, A. J. Craven, and C. P. Scott, "Electron detection in analytical electron microscopy," *Ultramicroscopy* 28: 108, 1989.

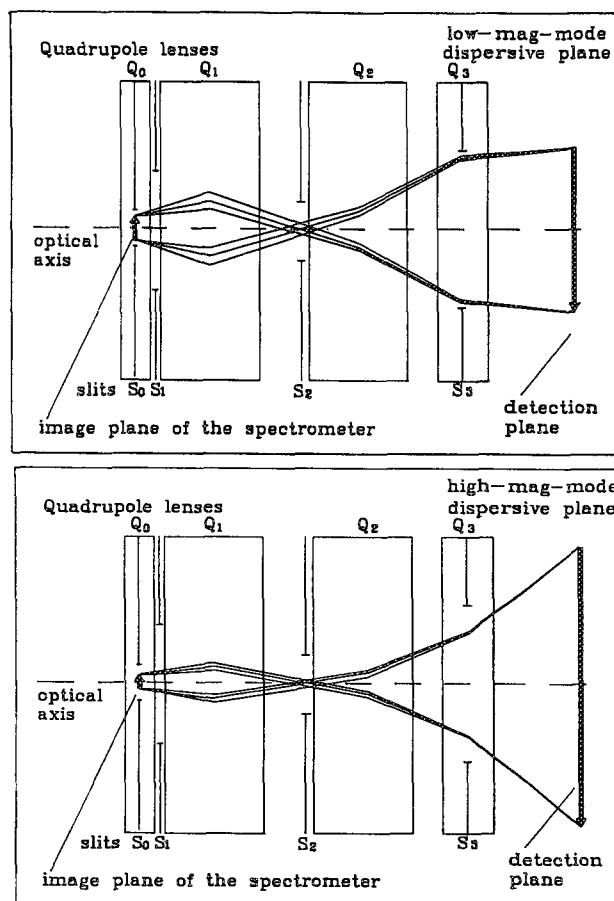


FIG. 7.--Schematic electron trajectories in dispersive plane for (a) low and (b) high-magnification mode.

2. E. Quandt, S. la Barré, and H. Niedrig, "Direct parallel detection of energy-resolved large-angle convergent-beam patterns," *Ultramicroscopy* 33: 15, 1990.

3. O. L. Krivanek, C. C. Ahn, and R. B. Keeney, "Parallel detection electron spectrometer using quadrupole lenses," *Ultramicroscopy* 22: 103, 1987.

4. D. G. Stearns and J. D. Wiedwald, "Response of charge-coupled devices to direct electron bombardment," *Rev. Sci. Instr.* 60: 1095, 1989.

5. R. F. Egerton, *Electron Energy Loss Spectroscopy in Electron Microscope*, New York: Plenum Press, 1986, 106.

6. C. P. Scott, *A Quadrupole Lens System for Use in the Recording of Electron Energy Loss Spectroscopy*, Thesis, University of Glasgow, 1988.

7. A. V. Crewe, M. Isaacson, and D. Johnson, "High resolution electron spectrometer for use in transmission scanning electron microscopy," *Rev. Sci. Instr.* 42: 411, 1971.

8. C. P. Scott and A. J. Craven, "A quadrupole lens system for use in a parallel recording system for electron energy loss spectroscopy," *Ultramicroscopy* 28: 126, 1989.

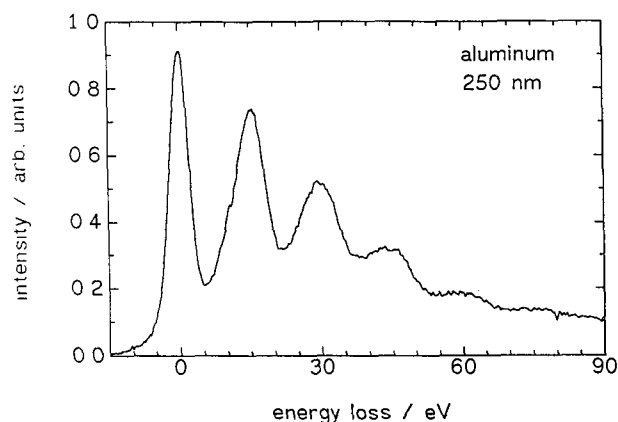


FIG. 8.--EELS showing primary beam and plasmon losses of aluminum foil 250 μm thick (electron energy 40 keV, detection aperture 2 mrad, magnification 30 \times).

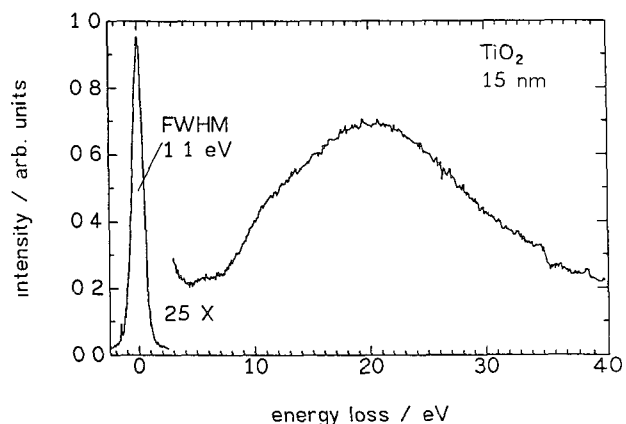


FIG. 10.--EELS of TiO_2 recorded in the high-magnification mode of quadrupole lens system. FWHM of primary beam is 1.1 eV and determines energy resolution of system (electron energy 40 keV, detection aperture 2 mrad, magnification 85 \times).

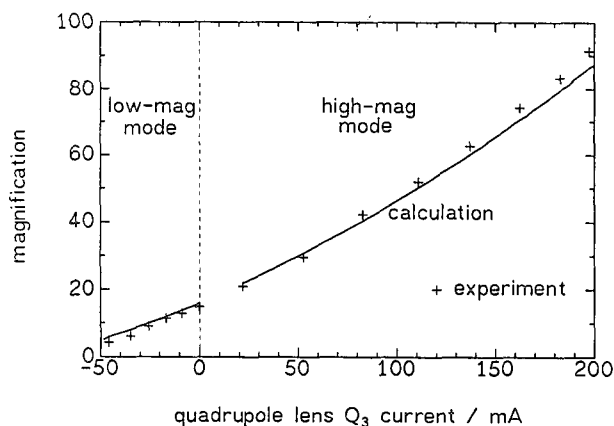


FIG. 9.--Measured and calculated magnification of quadrupole lens system vs current of lens Q_3 for the low- and high-mag mode.

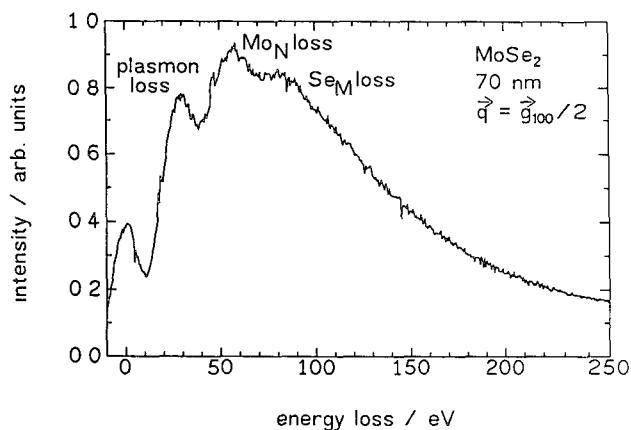


FIG. 11.--EELS of MoSe_2 recorded with scattering vector $\vec{q} = \vec{g}/2$ in low magnification mode of quadrupole lens system (electron energy 40 keV, detection aperture 2 mrad, magnification 12 \times).

ANGLE-RESOLVED ENERGY LOSS SPECTRA OF Gd_2O_3

Peter Schattschneider and Ferdinand Hofer

Energy loss spectra of heavy rare earth oxides show two well-defined plasmon-like peaks below 40 eV and some intensity variation beyond. Since the high-energy maximum is at about twice the energy of the low-energy maximum, double scattering contributions may mask the former. This effect induces artifacts when one attempts to determine the dielectric function $\epsilon(\omega)$ from Kramers-Kronig-analysis (KKA) of the loss spectrum. Knowledge of $\epsilon(\omega)$ allows one to assign heuristically interband transitions or plasma excitations to particular maxima. Measurements in diffraction mode allow detection of dispersive features in $\epsilon(\omega, q)$.

Experiment

Polycrystalline Gd_2O_3 films 40nm thick were investigated at 120 kV in a Philips EM420, equipped with a Gatan 607 energy spectrometer. Spectra were taken in diffraction mode (image coupling) at 8 scattering angles with a q -resolution of $\sim 0.03 \text{ \AA}^{-1}$ and an energy resolution of $\sim 2 \text{ eV}$. After aperture correction² the spectra were combined to give a q -dependent loss function. Channel coupling between quasi-elastic and inelastic events was removed by subtraction of a weighted image mode spectrum.³ Angle-resolved plural-scattering deconvolution was subsequently applied.⁴ For KKA, spectra were extrapolated to zero below 5 eV.

Results

Figure 1 shows q -dependent loss functions before (dotted) and after the corrections mentioned above. The plural scattering is negligible at small q , but contributes more than 70% of the total intensity at higher q , in the high-energy tail. The broad background at $\sim 70 \text{ eV}$, which is removed by the method, is the self-convolution of the double-maximum structure.

The shape of the spectra up to $\sim 35 \text{ eV}$ is not much altered by deconvolution. The contribution of the 16eV maximum, convoluted by itself, act so as to increase the measured intensity between ~ 30 and 35 eV slightly. Consequently, deconvolution reduces the second maximum relative to the first one. The multiple scattering intensity is shown in Fig. 2, together with the image mode spectrum, obtained with the full aperture of the objective polepiece.

The maxima in image mode are at 15 and 36.5 eV,

in agreement with reported values.⁵ The slight increase of intensity to the far right of the figure is the onset of the Gd-N edge.

Figures 3 and 4 show $Re[\epsilon(\omega, q)]$ for two scattering angles. The position of zeroes is 13 eV for both spectra, causing the plasmon-like resonance in Figs. 1 and 2. The fact that there is no detectable shift in the zero as a function of momentum indicates that the corresponding maximum in the loss spectrum is not much plasmon-like but is strongly influenced by interband transitions. They show up in $Im[\epsilon(\omega, q)]$ (Fig. 5). The 22 eV-maximum is assigned to the $0 - 2s \rightarrow 5d + 6s$ transition,⁵ which is optically forbidden. (Note the increase of oscillator strength with q .) A transition at 30 eV is optically allowed, giving rise to a rather constant structure. At this energy, the $5p \rightarrow 5d + 6s$ transition is located.⁵ Shifts in the peak position and faint structure beyond 30 eV indicate that the 5d-band is no more flat because of hybridizing with the 6s band.

Figure 6 shows the influence of deconvolution on $Im[\epsilon(\omega, q)]$. As can be seen, multiple scattering changes the spectra in a way that does not seriously affect the outcomes of a Kramers-Kronig analysis. That is not true in general. Application of KKA to (for example) energy loss spectra of aluminum, without prior deconvolution, causes spurious peaks in $Im[\epsilon(\omega, q)]$ at multiples of the plasma loss.¹ The relative insensitivity of KKA to deconvolution is due to the smooth appearance of the double scattering contribution in Gd_2O_3 (Fig. 2).

References

1. P. Schattschneider and D.-S. Su, *Ultramicrosc.* 28: 47, 1989.
2. A. J. Craven, T. W. Buggy, and R. P. Ferrier, *Quantitative Microanalysis with High Spatial Resolution*, London: Metals Soc., 1981.
3. P. Batson and J. Silcox, *Phys. Rev.* B27: 5224, 1983.
4. P. Schattschneider, F. Födermayr, and D.-S. Su, *Scanning Microsc.* 2: 255, 1988.
5. C. Colliex, M. Gasgnier, and P. Trebbia, *J. de Physique* 37: 397, 1976.

Peter Schattschneider is at the Institut für Angewandte und Technische Physik, TU Wien, A-1040 Wien, Austria; Ferdinand Hofer is at the Zentrum für Elektronenmikroskopie, A-8010 Graz, Austria. The former gratefully acknowledges the financial support of the Hochschuljubiläumstiftung der Stadt Wien.

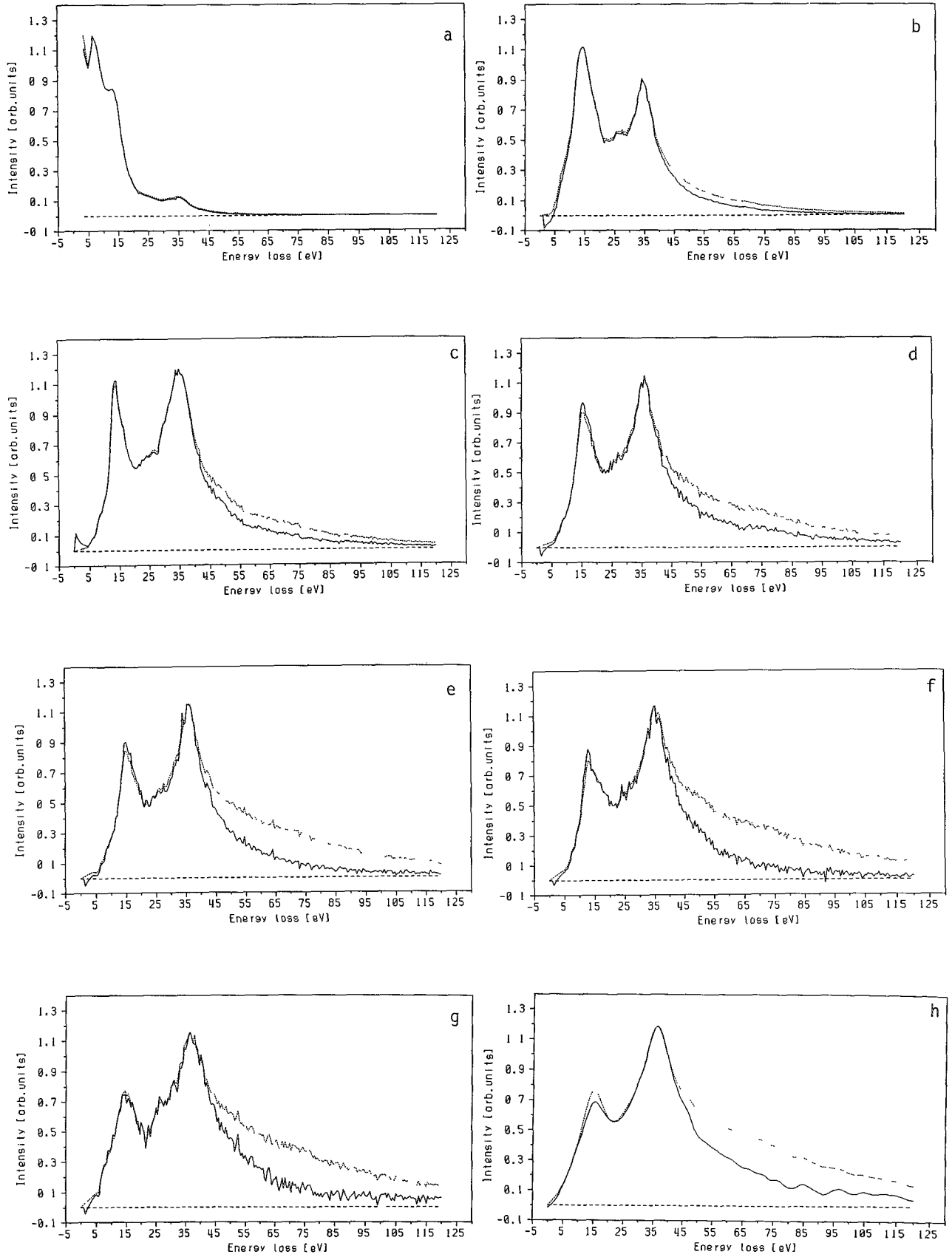


FIG. 1.--(a-h) Loss spectra (dotted) of Gd_2O_3 at scattering angles $\theta = 0, 0.31, 0.62, 1.24, 2.49, 3.74, 4.98$, and 6.23 mrad, respectively. (Full line: single loss.)

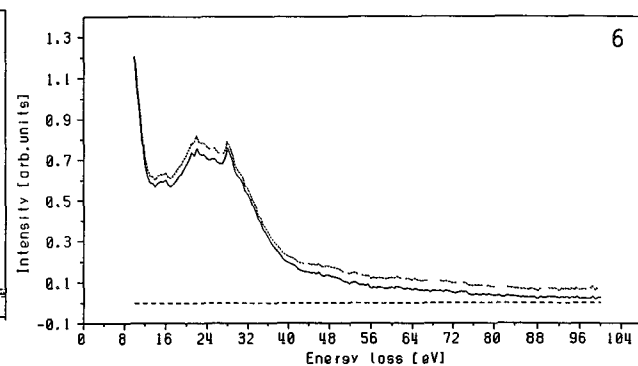
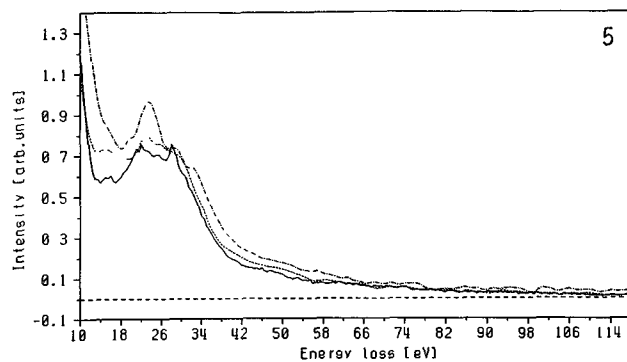
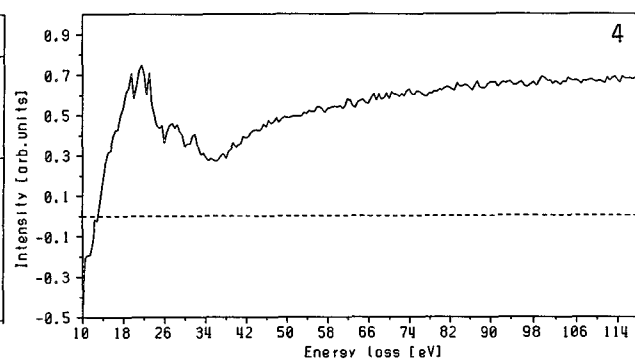
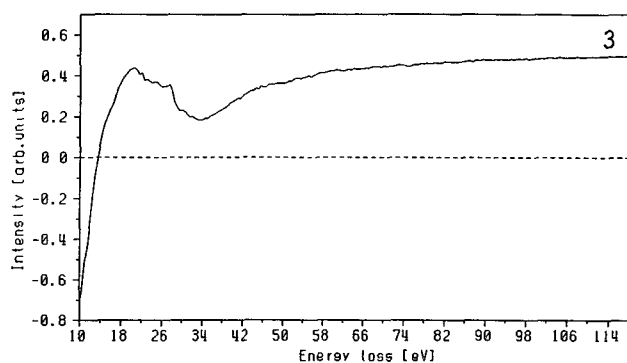
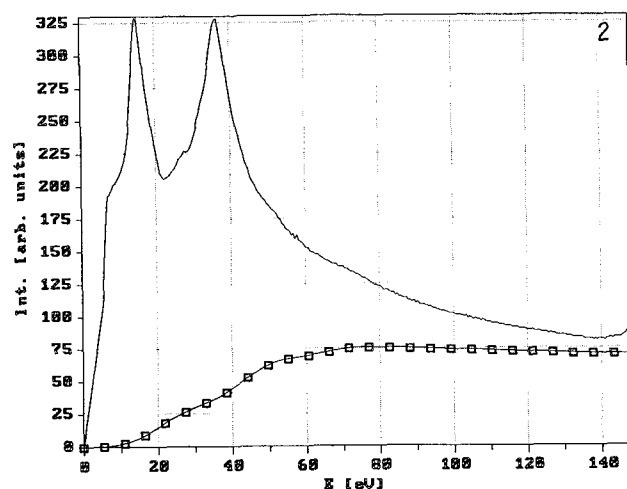


FIG. 2.--Image mode spectrum of Gd_2O_3 and double scattering contribution (squares).
 FIG. 3.-- $\text{Re}[\varepsilon(\omega, q)]$ at 0.62 mrad.
 FIG. 4.-- $\text{Re}[\varepsilon(\omega, q)]$ at 4.98 mrad.
 FIG. 5.-- $\text{Im}[\varepsilon(\omega, q)]$ at 0.62 (full line), 3.7 (dotted) and 4.98 mrad (dash-dotted).
 FIG. 6.-- $\text{Im}[\varepsilon(\omega, q)]$ at 0.62 mrad (full line), and the same obtained from plural scattering data (dotted).

BRAGG-COMPTON AND PLASMON-COMPTON CHANNEL COUPLING IN ELECTRON COMPTON SCATTERING

Peter Jonas and Peter Schattschneider

Electron Compton scattering is inelastic scattering of fast electrons at large angles off core or valence electrons. The energy of the scattered electron is increasingly lowered with scattering angle; the energy distribution can be shown to an image of the electron momentum density distribution in the ground state.¹

Besides the Compton effect, other electronic excitations within the solid must be considered. Low-angle scattering off valence electrons gives rise to plasmon excitation peaking in the low-energy-loss region. Such a plasmon excitation can be followed by a Compton event. An equally dominant contribution to multiple scattering arises from combined Bragg-Compton scattering.

The Bragg spots and plasmon peaks can be considered as new sources for Compton events. Since these Compton events correspond to various scattering angles a number of Compton profiles with different maximum and width are superimposed in a measurement.²

Bragg Scattering

We may write the total measured intensity M at a particular energy loss E as a linear combination of coupled Bragg-Compton events. In the case of a systematic row reflection with i excited beams it is always possible to choose $n = 2 * (i - 1)$ angles $\vec{\Omega}_k$ such that the system of linear equations

$$M(\vec{\Omega}_k', E) = \sum_{j=1}^n P_j I(\vec{\Omega}_j, E) \quad 1 \leq k \leq n \quad (1)$$

can be solved with respect to I , P_j is the intensity of the j -th Bragg (elastically scattered) beam, and $I(\vec{\Omega}_j)$ is the intensity of the Compton scattering coming from the j -th Bragg spot. This relationship holds under the assumption that the Compton profile is centrosymmetric, $I(\vec{\Omega}, E) = I(-\vec{\Omega}, E)$ and the P_j are all different from each other.

A free electron model was used for calculation of the valence electrons Compton profiles of aluminum. For the L-shell electrons a hydrogenic expression for the respective ionization cross section was used.³ The P_j were calculated and averaged over a thickness of 20 nm with the EMS-Software Package.⁴

For a five-beam case, eight measurements are necessary to deconvolute the spectra exactly

The authors are at the Institut für Angewandte und Technische Physik, TU Wien, A-1040 Wien, Austria. This work was sponsored by the Austrian Fonds zur Förderung der wissenschaftlichen Forschung.

(Fig. 1). To test the abilities of our algorithm under experiment-like conditions, a random noise was added to the simulated M such that the statistical significance $\Delta I/I = 0.03$ at the Compton peak (Fig. 2). Figures 3 and 4 show 2 of 8 Compton profiles calculated from the simulated noisy total profiles compared with the theoretical ones. We are able to reconstruct four profiles with very high accuracy, but get no useful information about the remaining four. The first ones are the Compton profiles which represent a direct scattering event from the (0,0,0) beam to the spectrometer aperture. The quality of the profile of Fig. 4 improves significantly when the noise is reduced.

Plasmon Scattering

Because of plasmon scattering each $I(\vec{\Omega}, E)$ in Eq. (1) should be exactly written as (considering only the first and the second plasmon)

$$I_{ges}(\vec{\Omega}, E) = I(\vec{\Omega}, E) + \int d\vec{\Omega}_p I_{p1}(\vec{\Omega}_p) I(\vec{\Omega} - \vec{\Omega}_p, E - E_p) + \int d\vec{\Omega}_p I_{p2}(\vec{\Omega}_p) I(\vec{\Omega} - \vec{\Omega}_p, E - 2E_p) \quad (2)$$

$I(\vec{\Omega}, E)$ is the normalized single-scattering profile; I_{p1} and I_{p2} are the intensities of the first and second plasmon peaks, relative to the intensity of the zero loss peak; and E_p is the plasmon energy, which is about 15 eV for aluminum. The angular distribution of the plasmons follows a simple law⁵:

$$I_{p1}(\theta) \sim \frac{\theta_E^2}{\theta_E^2 + \theta^2} \quad (3a)$$

where $\theta_E = E_p/2E_0$, which is 0.075 mrad for electrons with $E_0 = 200$ keV. Plasmon scattering therefore is concentrated in the forward direction, and for $\theta_E \ll \theta$ we have a good approximation

$$I_{p1} \doteq \tilde{I}_{p1} \delta(\vec{\Omega}_p) \quad (3b)$$

Equation (2) then simplifies to

$$I_{ges}(\vec{\Omega}, E) = I(\vec{\Omega}, E) + \tilde{I}_{p1} I(\vec{\Omega}, E - E_p) + \tilde{I}_{p2} I(\vec{\Omega}, E - 2E_p) \quad (4)$$

We simulated Compton profiles following Eqs. (2)

and (4) to prove Eq. (3b); the plasmon intensities were determined assuming that the scattering obeys Poisson statistics. Figures 5 and 6 show that for a specimen thickness much smaller than the mean free path (for 200 keV in aluminum about 157 nm),⁶ plasmon scattering could be regarded as scattering in forward direction.

In general, energy-loss spectra are available in discrete form. Equation (4) can be written in a matrix formulation:

$$\vec{I}_{ges} = (\mathbf{1} + \mathbf{A}\vec{I}_{p1} + \mathbf{B}\vec{I}_{p2})\vec{I} \quad (5)$$

$\mathbf{1}$ is the unity matrix and \mathbf{A} and \mathbf{B} are, for an energy resolution of 5 eV, of the following form:

$$A_{ij} = \begin{cases} 1 & \text{for } j = i + 3 \\ 0 & \text{otherwise} \end{cases} \quad B_{ij} = \begin{cases} 1 & \text{for } j = i + 6 \\ 0 & \text{otherwise} \end{cases} \quad (6)$$

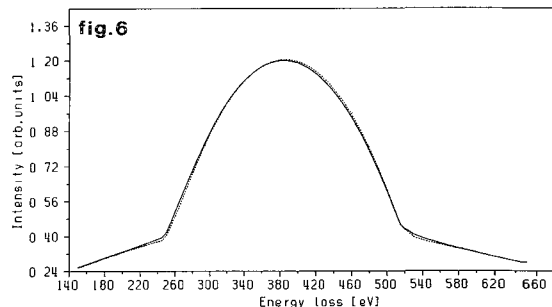
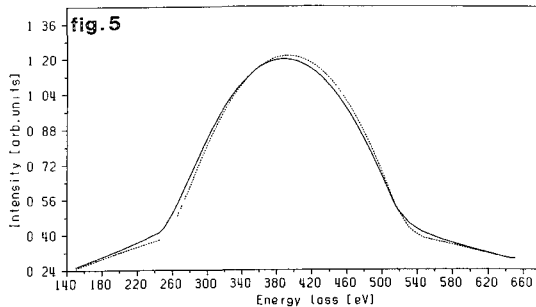
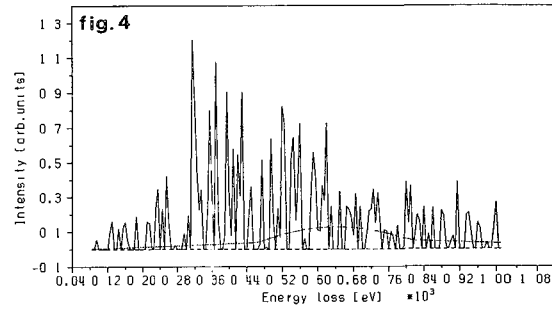
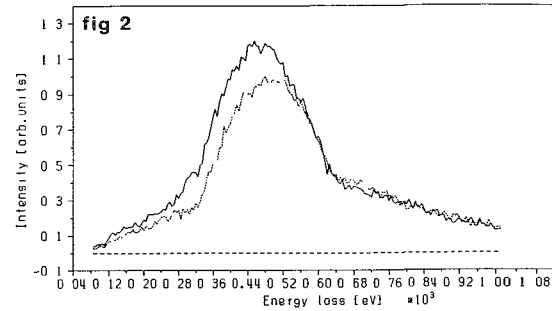
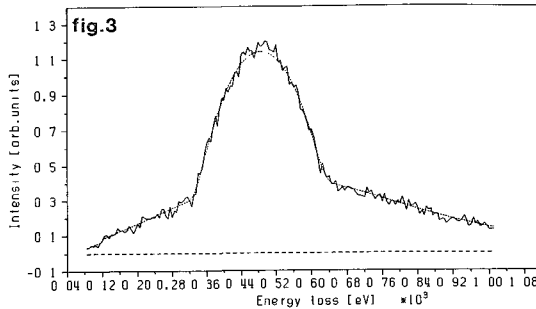
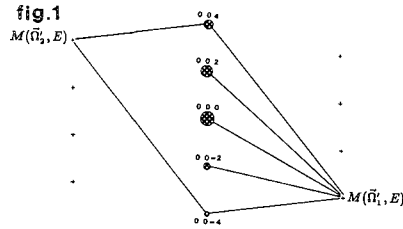


FIG. 1.--Spot pattern, points for measurements for a five-beam systematic row reflection

$P_{0,0,0} = 1$, $P_{0,0,2} = 0.213$, $P_{0,0,4} = 0.038$, $P_{0,0,-2} = 0.0037$, $P_{0,0,-4} = 0.0007$.

FIG. 2.--Total spectra $M(\vec{r}_1, E)$ (dotted line), $M(\vec{r}_2, E)$ (full line).

FIGS. 3 and 4.--Compton profiles deconvoluted from eight total spectra (full line), exact Compton profiles (dotted line).

FIG. 5.--Compton profiles for scattering angle $k = 10 \text{ \AA}^{-1}$ for specimen thickness $t = 150 \text{ nm}$ following Eq. 2 (full line), Eq. 4 (dotted line).

FIG. 6.--Compton profiles for scattering angle $k = 10 \text{ \AA}^{-1}$ for a specimen thickness $t = 50 \text{ nm}$ following Eq. 2 (full line), Eq. 4 (dotted line).

Equation (5) can be solved straight via recursion; it holds exactly only for an infinite energy interval. The error that we are making by truncation of the energy loss to within the Compton profile vanishes after a few steps of the recursion provided I_{p1} and I_{p2} are less than 1 (i.e., specimen thickness is less than the mean free path).

References

1. P. Schattschneider et al., *Analytical Electron Microscopy--1987*, 270-274.
2. B. G. Williams et al., *Proc. Roy. Soc. A409*: 161-176, 1987.
3. R. F. Egerton, *Energy-loss Spectroscopy*, New York: Plenum Press, 1986, 359.
4. P. Stadelmann, *Ultramicroscopy* 21: 131-146, 1987.
5. R. Ferrel, *Phys. Rev.* 101: 554-563, 1956.
6. H. Raether, *Excitation of Plasmons*, Berlin: Springer Verlag, 1980, 40.

NUMERICAL PROBLEMS IN THE DECONVOLUTION OF ELECTRON ENERGY LOSS SPECTRA

Dangsheng Su and Peter Schattschneider

A measured energy loss spectrum is not suited for an immediate theoretical analysis because some incident electrons are scattered inelastically more than once when passing through a specimen. This multiple process results in a plural scattering contribution to the energy loss spectrum, which changes the shape of the spectrum and tends to hide characteristic spectral features. Therefore an exact analysis of energy loss spectra requires the removal of plural scattering from the measured spectrum in order to yield a single scattering distribution. Several methods available for calculating the single scattering distribution have been reported.¹⁻⁴ However, only the Fourier-log deconvolution seems to be very well developed and widely used.^{5,6}

We show that the Fourier log deconvolution depends very strongly on the choice of the interval for Fourier transform, if the thickness of the specimen d is very large. We also make a study of the effect of truncation on the calculated single loss distribution. For thick specimens the Fourier log deconvolution is strongly limited by the truncation errors. Other methods have been described.^{3,6} They can be shown to be less sensitive to the effect of interval truncation to be discussed in the following.⁷

Theory

Assuming independent scattering events, the measured inelastic scattering probability P

$$P(E) = \exp(-D) \sum_{n=0}^{\infty} \frac{D^n}{n!} p^{(n)}(E) \quad (1)$$

where E is the energy loss, $D = d/\lambda$ is the thickness of the specimen given in units of mean free path length λ of the fast electron $[(1/\lambda) = \sum (1/\lambda_i)]$, where i denotes the various energy loss mechanisms in the medium such as plasmon, phonon, core losses, etc., and $p^{(n)}(E)$ is the n -fold scattering distribution which is the n -fold self-convolution of the single scattering distribution $p(E)$,

$$p^{(n)}(E) = \int_0^{\infty} p^{(n-1)}(E - E') p(E') dE' \quad (2)$$

After Fourier transforming of Eqs. (1) and (2) we have

$$\tilde{P}(j) = \exp(-D) \exp[D\tilde{p}(j)] \quad (3)$$

where $\tilde{P}(j)$ and $\tilde{p}(j)$ are the Fourier transform

of $P(E)$ and $p(E)$, respectively. The Fourier transform of the single scattering distribution is then obtained as

$$\tilde{p}(j) = \frac{1}{D} [\ln \tilde{P}(j) + D] \quad (4)$$

We can calculate the single scattering distribution from Eq. (4) by taking the inverse Fourier transform. Because we are concerned with multiple scattering deconvolution and use simulated spectra in the following, we make no attempt to discuss the effect of noise and energy resolution and neglect any instrumental broadening effect. Otherwise, an instrumental function $Z(E)$ ought to be used, as in Ref. 5.

Although the measured and the single scattering distribution are never complex, their Fourier transform could be. Let $\tilde{P}(j) = r(j)e^{i\theta(j)}$ and $\tilde{p}(j) = \text{Re}[\tilde{p}(j)] + i \cdot \text{Im}[\tilde{p}(j)]$ where $r(j)$ is the modulus of Fourier transform of plural scattering distribution and $\theta(j)$ is its phase, and Re and Im denote the real and imaginary parts of the single loss distribution in Fourier space. From Eq. (4) we have

$$\ln r = D \cdot [\text{Re}(\tilde{p}(j)) - 1] \quad (5)$$

$$\theta = D \cdot \text{Im}[\tilde{p}(j)] + n\pi, \quad n = 0, 1, 2, \dots \quad (6)$$

$$|\theta| < \frac{\pi}{2} \quad (7)$$

The normal Fourier deconvolution routine is by a fast Fourier transform (FFT) to calculate $\ln r$ and θ , by Eq. (5) and (6) to obtain $\text{Re}[\tilde{p}(j)]$ and $\text{Im}[\tilde{p}(j)]$, and then by an inverse FFT to retrieve the single scattering distribution. If the spectra were normalized, then for all j $|\text{Im}[\tilde{p}(j)]| < 1$, which means that the Fourier-log deconvolution can only be applied to specimens with $D < \pi/2$. For $D > \pi/2$, due to the possible discontinuities in phase as shown in Fig. 1, there will be difficulty in retrieval of the correct phase and therefore of the single loss spectrum.⁶

Some methods have been proposed to cope with this difficulty. A simple way is to evaluate θ from Eq. (6) but instruct the computer to correct for each discontinuity in the array by adding or subtracting multiples of π .⁵ This correction does not work for any thickness, as expected, because the correction is based on the assumption that the difference between two adjacent $\theta(j)$ must be smaller than $\pi/2$. If j were a continuous variable one could immediately pick up the discontinuity in phase and correct it. But for discrete j the phase difference is given by

$$\begin{aligned} \Delta\theta &= \theta(j+1) - \theta(j) \\ &= D \cdot \{\text{Im}[\tilde{p}(j+1)] - \text{Im}[\tilde{p}(j)]\} \end{aligned}$$

and for large enough D it is quite possible

The authors are at the Institut für Angewandte und Technische Physik, TU Wien, A-1040 Wien, Austria.

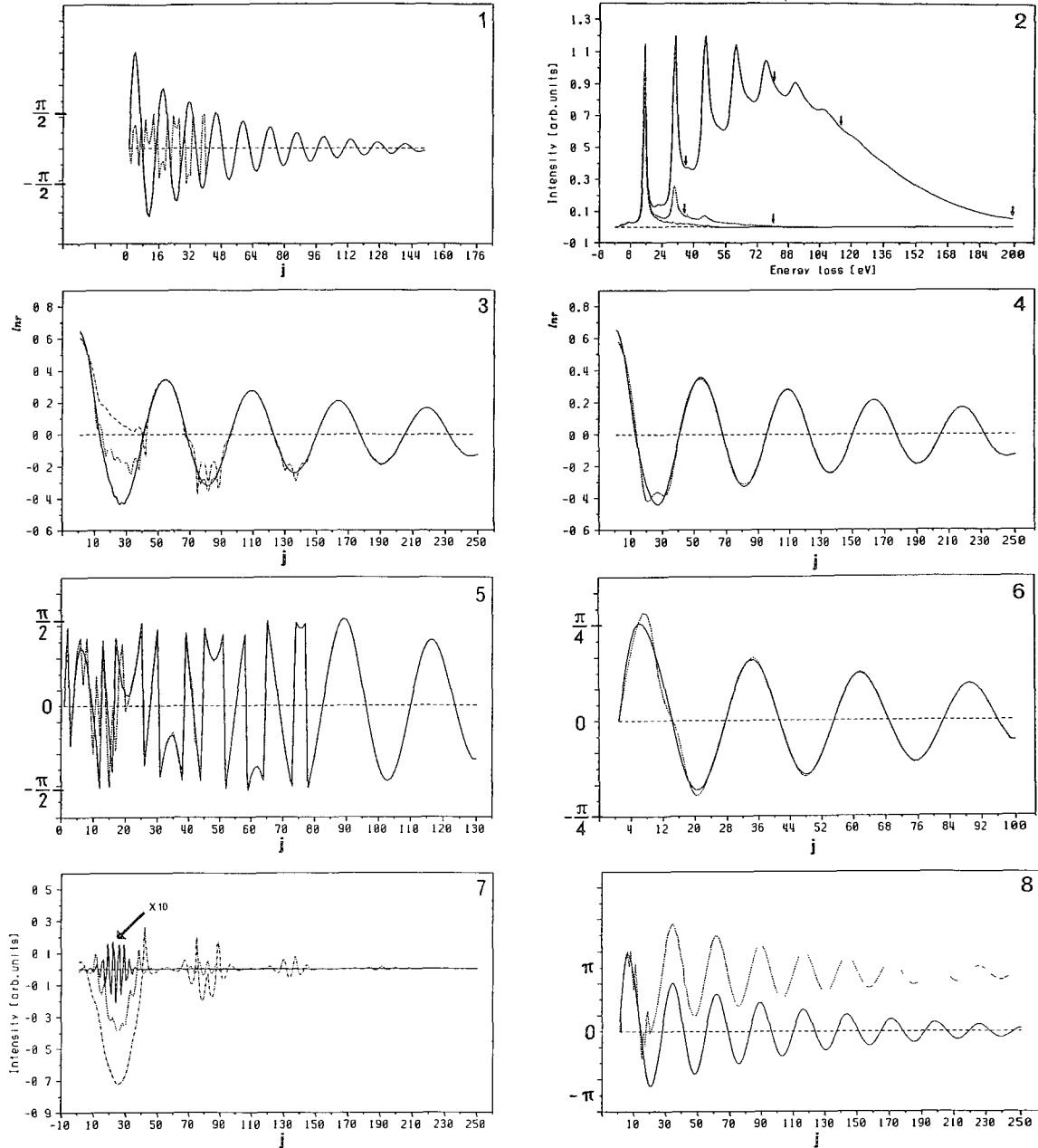


FIG. 1.--Dotted line, retrieved phase with Eq. (5); full line, true phase.
FIG. 2.--Simulated spectrum: full line, $D = 5$; dotted line $D = 1$; dash-dotted line, single loss. Arrows show where spectra were truncated.
FIG. 3.--Effect of truncation on $\ln r$ for $D = 5$: full line, $E_c = 200$ eV; dotted line, $E_c = 110$ eV; dash-dotted line, $E_c = 80$ eV.
FIG. 4.--Effect of truncation on $\ln r$ for $D = 1$: full line, $E_c = 80$ eV; dotted line, $E_c = 35$ eV.
FIG. 5.--Effect of truncation on retrieved phase of P for $D = 5$: dotted line, $E_c = 110$ eV; full line, $E_c = 200$ eV. Number of points for FFT is 2048.
FIG. 6.--Effect of truncation on retrieved phase of P for $D = 1$: full line, $E_c = 80$ eV; dotted line, $E_c = 35$ eV.
FIG. 7.--Amplitude of truncation errors for various cutoff energies: full line, $E_c = 200$ eV, dotted line, $E_c = 110$ eV; dash-dotted line, $E_c = 80$ eV. $D = 5$.
FIG. 8.--Wrong phase of P corrected as in Ref. 5. Full line shows true phase. $D = 5$.

that $\Delta\theta > \pi/2$. That means that we have to enlarge the interval for Fourier transform to increase the number of transform points, so as to insure that $\Delta\theta < \pi/2$. For FFT this amounts to double the energy interval n times, where n is not known in advance.

Truncation Errors

The use of Fourier coefficient means that one has chosen a fundamental interval for the energy loss spectrum which is certainly not specific. It is therefore important to ask how we can choose a period length for this nonperiodic spectrum without introducing any artifact. We see intuitively that the larger the fundamental interval, the better the results, which means that we must measure the energy loss spectrum in a very large energy region, which may not be feasible for practical reasons.

The measured spectrum will therefore be extrapolated to zero up from the last measured energy channel E_C to a very large energy value. A commonly used method is making use of an exponential function AE^{-r} , where the parameters A and r will be determined from the measured spectrum. If we define the function $\Delta P(E)$ as the difference between the real spectrum $P(E)$ and the extrapolated spectrum $P'(E)$

$$\Delta P(E) = P(E) - P'(E) \quad (8)$$

$$\Delta P(E) = 0 \quad E < E_C$$

$$\Delta P(E) = \exp(-D) \sum_n \frac{D^n}{n!} P_n(E) - AE^{-r} \quad E \geq E_C.$$

Taking the Fourier transform of Eq. (8) and using Eq. (3), we get

$$\tilde{p}'(j) = \tilde{p}(j) + \frac{1}{D} \ln \left(\left| 1 - \frac{\Delta \tilde{p}(j)}{\tilde{p}(j)} \right| \right) + \frac{i}{D} \Delta \theta \quad (9)$$

and Eqs. (3) and (4) become

$$\ln r = D \cdot [\operatorname{Re}(\tilde{p}(j)) - 1] - \ln \left(\left| 1 - \frac{\Delta \tilde{p}(j)}{\tilde{p}(j)} \right| \right) \quad (10)$$

$$\theta = D \cdot \operatorname{Im}[\tilde{p}(j)] + \Delta \theta \quad (11)$$

where $\Delta\theta$ is the phase error induced by the truncation and extrapolation.

As can be seen, unless $\Delta \tilde{p}(j) = 0$, the Fourier-log deconvolution can only give an approximate result. In order to analyze how the truncation and extrapolation affect the calculated single scattering distribution, we simulated energy loss spectra with different D (Fig. 2). The spectra were truncated at various energies and extrapolated to zero by the power law $P \sim AE^{-r}$. The results are shown in Figs. 3-10. Figures 3 and 4 show the effect of truncation on $\ln r$ for various D . Figures 5 and 6 show the effect of truncation on θ . For $D = 1$ this effect is very small and the calculated single loss distribution is exactly as the original one. The relative error in the area under the main maximum of the retrieved single spectrum is less than 0.001%, even if the spectrum was truncated at energy $E = 35$ eV. Conversely, for $D = 5$, the relative error is 20% at $E = 110$ eV

and reduces to 0.002% at $E = 200$ eV. Figure 7 shows the amplitude of the truncation errors for various cutoff energies for $D = 5$. Figure 8 shows that the phase correction given in Ref. 5 is also affected by the truncation which leads to unphysical results, as shown in Figs. 9 and 10. It is evident that for large D the Fourier log deconvolution is very sensitive to the truncation, but for small D it is less sensitive.

References

1. D. W. Johnson and J. C. H. Spence, *J. Phys.* D7: 771-780, 1974.
2. R. F. Egerton, *Ultramicroscopy* 28: 215-225, 1989.
3. P. Schattschneider, *Phil. Mag.* B47: 555-560, 1983.
4. P. Schattschneider and G. Sölkner, *J. Microscopy* 134: 73-87, 1984.
5. R. F. Egerton and P. A. Crozier, *Scanning Microscopy Suppl.* 2: 245-254, 1988.
6. J. Spence, *Ultramicroscopy* 4: 9-12, 1988.
7. D. S. Su, thesis, Technische Universität Wien, Vienna, 1990.

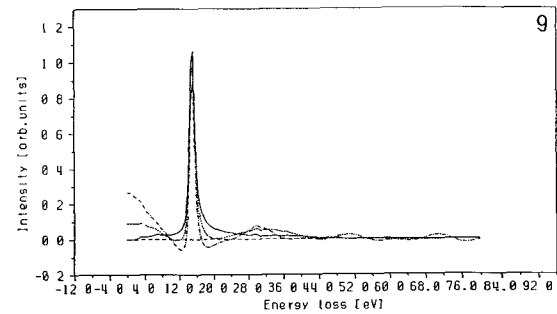


FIG. 9.--Retrieved single loss distribution from $D = 5$: full line, $E_C = 200$ eV; dotted line, $E_C = 110$ eV; dash-dotted line, $E_C = 80$ eV.

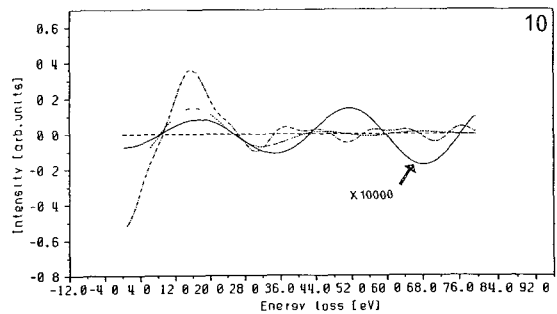


FIG. 10.--Absolute errors introduced by truncation: full line, $E_C = 200$ eV; dotted line, $E_C = 110$ eV; dash-dotted line, $E_C = 200$ eV. $D = 5$.

TEMPERATURE-DEPENDENT EXELFS OF Al K and Fe L₂₃ EDGES IN CHEMICALLY DISORDERED AND DO₃-ORDERED Fe₃Al

J. K. Okamoto, C. C. Ahn, and B. Fultz

A parallel detection system makes extended electron energy-loss fine structure (EXELFS) in the electron microscope a viable structural probe. We are using EXELFS to study the short-range chemical order and local thermal vibrations of the Al atoms and the Fe atoms in chemically disordered and ordered Fe₃Al. We are particularly interested in the changes in lattice vibrations that accompany the order-disorder transformations in Fe₃Al because knowledge of these changes will further our understanding of the thermodynamics of order-disorder transformations. Al K edge and Fe L₂₃ edge data were taken from pure Al, pure Fe, chemically disordered Fe₃Al and DO₃-ordered Fe₃Al at temperatures ranging from 96 to 423 K. The average number of Fe atoms in the first nearest-neighbor (1nn) shell surrounding the Al and Fe atoms in chemically disordered and DO₃-ordered materials are determined approximately by comparison of our data with *ab initio* EXAFS calculations.¹ The mean-square relative thermal displacements between the Al and Fe atoms and their 1nn shell are determined from the damping of the first shell EXELFS oscillations as a function of temperature.² Using these mean-square relative thermal displacements, we can estimate the vibrational entropy difference between chemically disordered and DO₃-ordered Fe₃Al.

Experimental

Chemically disordered Fe-25at.%Al samples were prepared by piston-anvil quenching. Some samples were annealed at 300 C for over a day to develop DO₃ order. Al K edge and Fe L₂₃ edge electron energy-loss spectra were acquired with a Gatan 666 parallel detection magnetic prism spectrometer attached to a Philips EM 430 transmission electron microscope. Figure 1 shows the Al K edge and the Fe L₂₃ edge from Fe₃Al. The energy resolution at the detector was about 4 eV with a dispersion of 1.07 eV per channel. Spectra were obtained at temperatures ranging from 96 K to 423 K at a collection angle of 10 mrad. To minimize any possible effect of electron beam heating, these spectra were collected from regions ~4 μm diameter with 200keV electrons and a beam current of about 10 nA. In comparison, Disko et al.³ obtained their data illuminating a submicron-diameter region with 300keV electrons and a beam current of 5 nA, and concluded from their data that the temperature measured at the edge of their thin aluminum foil was reasonably accurate even in the presence of the intense elec-

tron beam they used. Gain fluctuations in our detector system were removed by a two-step process that Shuman and Kruit showed to be effective in extracting useful data from parallel recorded energy-loss spectra with low signal-to-background ratios. First, each spectrum was divided by a gain-calibration spectrum obtained in the so-called "uniform illumination mode" of the Gatan 666. Second, gain-averaging was performed over several spectra, each repositioned by about 3 detector elements. Ten spectra were gain-averaged for the Al K edge data; twenty for the Fe L₂₃ edge data. Dividing by the gain-calibration spectrum should reduce the element-to-element variation of the array detector, but may add variations in detector response due to nonuniformities in the illumination of the detector array when collecting the calibration spectrum. The larger the energy range over which gain is averaged, the greater the distance in k-space one can go and still detect useful EXELFS oscillations. To remove the smoothly varying portion of the energy-loss data, cubic spline fits with knots approximately evenly spaced in k-space were used. The EXELFS oscillations were normalized to the edge jumps.

Results

Figure 2(a) shows the Al K edge EXELFS weighted by the first power of k for the ordered Fe₃Al sample. Fourier transforms were performed on the Al K edge data in the range $4 < k < 9 \text{ \AA}^{-1}$ because of plural scattering at lower k and long-range detector gain fluctuations at higher k. Analysis of the extended fine structure of L edges in use of the standard EXAFS formula is possible because the matrix element of the p-to-s transition is insignificantly small in comparison to the matrix element of the p-to-d transition.⁵ With the 10mrad collection angle, the Fe L₁ edge was unobservably small in the energy-loss spectra. The Fe L₃ and L₂ edges are 13 eV apart with an intensity ratio of 2:1. To reduce the effect of the 13eV difference between L₃ and L₂ edges, and to eliminate the L₁ edge jump from the EXELFS data, only Fe L edge data more than 170 eV past the L₃ edge jump (which corresponds to $k > 6.5 \text{ \AA}^{-1}$) were Fourier transformed. At higher k, long-range detector gain fluctuations limited the useful data to $k < 12 \text{ \AA}^{-1}$. Figure 2(b) shows the Fe L₂₃ edge EXELFS weighted by the first power of k for the ordered Fe₃Al sample. Figure 3 shows the Fourier transforms of the Al K and Fe L₂₃ EXELFS weighted by k for the ordered Fe₃Al sample at 96 K and 348 K. The peaks near 1.3 \AA are due to the presence of surface oxide and/or residual low-frequency oscillations from the spline fits. The combined 1nn and 2nn shells were isolated by back-transformation of the data in the range

The authors are at the Keck Laboratory of Engineering Materials of the California Institute of Technology, Pasadena, CA 91125. This research was supported by the U.S. Department of Energy under contract DE-FG03-86ER45270.

$1.7 < r < 2.8 \text{ \AA}$ for the Al K edges and $1.8 < r < 2.7 \text{ \AA}$ for the Fe $L_{2,3}$ edges. By comparing our data to *ab initio* plane wave EXAFS calculations¹ and by neglecting the effect of the 2nn shell, we can extract approximate 1nn shell distances that agree to within $\pm 0.05 \text{ \AA}$ with 1nn distances determined from x-ray crystallography. The uncertainty in the proper choice of edge onset energy E_0 contributes to the error in the absolute determination of 1nn shell distances from our EXELFS data.

The difference in chemical short-range order between the piston-anvil quenched and DO_3 -ordered Fe_3Al samples can be determined from our EXELFS data. In going from an ideally disordered Fe_3Al sample to one with perfect DO_3 order, the number of Fe-Al bonds would increase by 33%. By comparing our data with *ab initio* EXAFS calculations,¹ we can determine that Al atoms in the DO_3 -ordered sample have on average 5 to 25% more Fe atoms in their 1nn shell than have Al atoms in the piston-anvil quenched sample. Similarly, Fe atoms in the DO_3 -ordered sample have on average 3 to 25% more Al atoms in its 1nn shell than have Fe atoms in the piston-anvil quenched sample. These results are consistent with Mössbauer spectrometry studies, which show that our piston-anvil quenched Fe_3Al is nearly a disordered solid solution.⁶ The relatively large uncertainties assigned to these EXELFS results are due to the uncertainties in the normalization of the EXELFS oscillations because of differences in sample thickness and surface oxide between piston-anvil quenched and DO_3 -ordered samples. One can eliminate these sources of error by annealing the piston-anvil quenched sample in situ within the electron microscope.

Experimental mean-square relative displacements (MSRD) were determined relative to the lowest-temperature data. Neglecting the 2nn shell contribution, these 1nn MSRD data are presented in Fig. 4, which also includes 1nn MSRD data from pure Al metal and from pure Fe metal. The scatter in the data can be attributed to slight sample drift in the electron microscope. The experimental data were fit to Einstein models⁷ with "local" Einstein temperatures given in the captions of Fig. 4. As the number of Fe-Al bonds increases (as in going from piston-anvil quenched Fe_3Al to DO_3 -ordered Fe_3Al), the MSRD becomes smaller. The local Einstein temperatures of 315 K for pure aluminum and 300 K for pure iron correspond to local Debye temperatures of 430 K and 415 K, respectively. These local Debye temperatures can be compared with Debye temperatures from heat-capacity measurements of 394 K for bulk aluminum and 420 K for bulk iron.⁸ Although the expected trends are shown in our present MSRD data, our confidence in their accuracy will be improved by gain-averaging over a larger energy range and by acquiring more counts to reduce statistical noise.

A fundamental interest in the disorder-order transformation has motivated us to make these measurements of local Einstein temperatures. The free-energy difference of the disordered and ordered phases, which sets the critical tempera-

ture of the transformation, depends on the entropy difference between the ordered and disordered phases. Present interpretations of the critical temperature are based on an entropy difference that is configurational in origin. However, the greater number of vibrational states available to the disordered alloy may increase sufficiently the entropy of the disordered state to suppress the critical temperature of the disorder-order transformation. Approximately, neglecting the zero point vibrations, the vibrational entropy per atom is

$$S_V \approx 3 k_B \ln(T/\theta_E)$$

With our measured difference in θ_E for the disordered and DO_3 -ordered phases, the difference in vibrational entropy is $0.4 k_B$ per atom at the critical temperature. In comparison, the difference in configurational entropy calculated in the mean-field approximation is $0.56 k_B$ per atom. The present temperature-dependent EXELFS measurements suggest that vibrational entropy is nearly as important as configurational entropy in the thermodynamics of the order-disorder transformation in Fe_3Al .

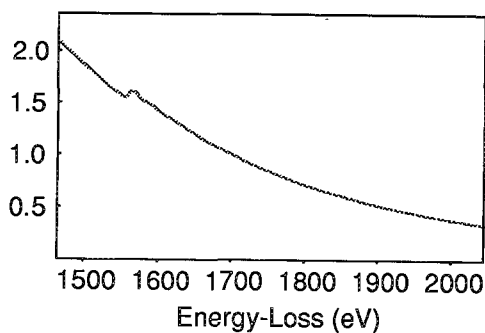
Conclusions

A parallel detection system makes quantitative studies of EXELFS in the electron microscope possible. In addition to nearest-neighbor distances, short-range chemical order and local thermal vibrations can be measured by EXELFS and its temperature dependence. Finally, and most significant, our MSRD data indicate that the vibrational entropy contribution to the critical temperature of the order-disorder transformation in Fe_3Al is of the same order of magnitude as the configurational entropy contribution.

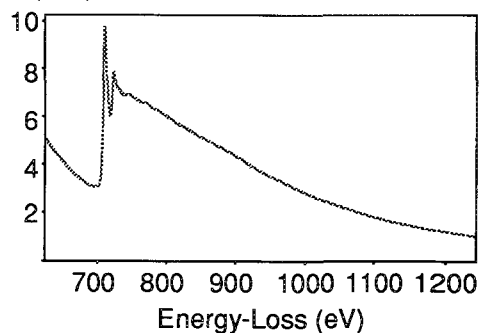
References

1. B. K. Teo and P. A. Lee, "Ab initio calculations of amplitude and phase functions for extended x-ray absorption fine-structure," *J. Am. Chem. Soc.* 101: 2815, 1979. (Software implemented by R. A. Scott et al.)
2. G. Beni and P. M. Platzman, "Temperature and polarization dependence of extended x-ray absorption fine-structure spectra," *Phys. Rev. B* 14: 1514, 1976.
3. M. M. Disko et al., "Temperature-dependent transmission extended electron energy-loss fine-structure of aluminum," *J. Appl. Phys.* 65: 3295, 1989.
4. H. Shuman and P. Kruit, "Quantitative data processing of parallel recorded energy-loss spectra with low signal to background," *Rev. Sci. Instrum.* 56: 231, 1985.
5. U. Fano and J. W. Cooper, "Spectral distribution of atomic oscillator strengths," *Rev. Mod. Phys.* 40: 441, 1968.
6. B. Fultz, Z-Q. Gao, and H. H. Hamdeh, "Short range ordering in undercooled Fe_3Al ," *Hyperfine Interactions* 54: 521, 1990.
7. E. A. Stern, "Theory of EXAFS," in D. C. Konigsberger and R. Prins, Eds., *X-ray Absorp-*

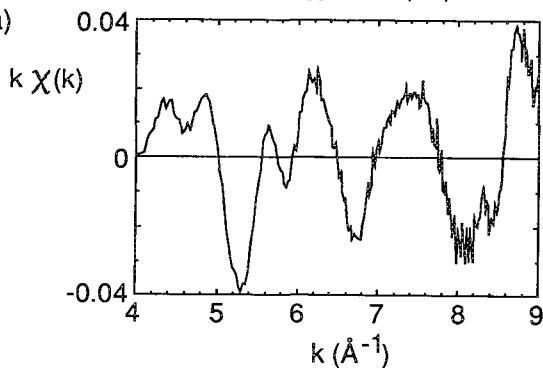
(a) Counts (10^6)



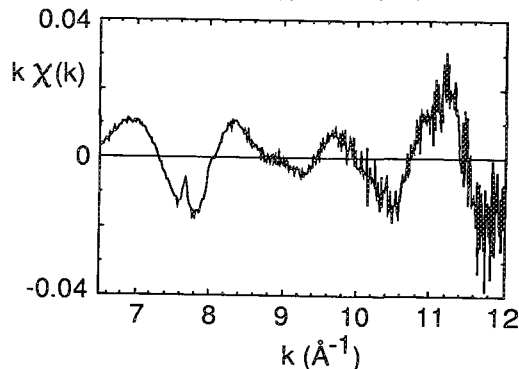
(b) Counts (10^6)



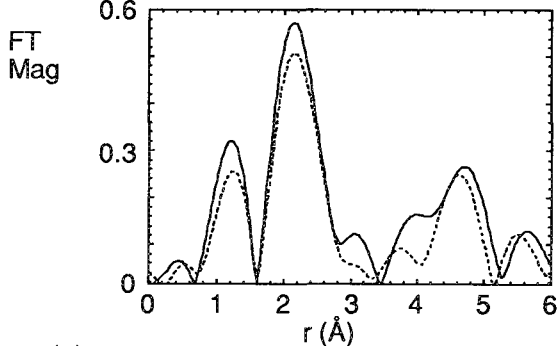
(a)



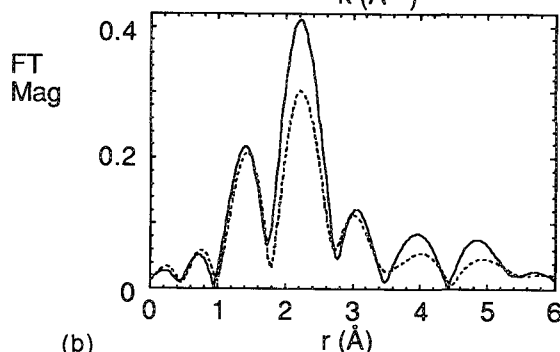
(b)



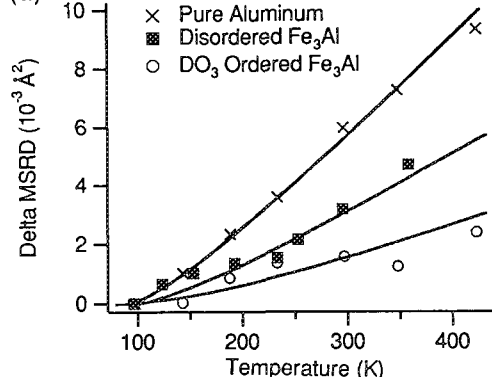
(a)



(b)



(a)



(b)

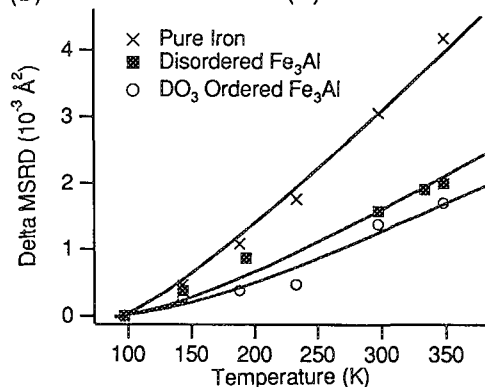


FIG. 1.--(a) Al K edge from Fe_3Al ; (b) Fe L_{23} edge from Fe_3Al .

FIG. 2.--(a) Al K and (b) Fe L_{23} EXELFS weighted by k for DO_3 -ordered Fe_3Al at 295 K.

FIG. 3.--Magnitude of Fourier transform of (a) Al K; (b) Fe L_{23} EXELFS weighted by k for DO_3 -ordered Fe_3Al at 96 K (solid line) and 348 K (dashed line).

FIG. 4.--(a) Experimental MSRD between Al atoms and their 1nn shell relative to data at 96 K. Lines are theoretical MSRD with local Einstein temperatures of 315 K for pure Al, 350 K for Al in piston-anvil quenched Fe_3Al , and 460 K for Al in DO_3 -ordered Fe_3Al . (b) Experimental MSRD between Fe atoms and their 1nn shell relative to data at 96 K. Lines are theoretical MSRD with local Einstein temperatures of 300 K for pure Fe, 400 K for Fe in piston-anvil quenched Fe_3Al , and 440 K for Fe in DO_3 -ordered Fe_3Al .

SPECTRAL DECONVOLUTION OF WAVELENGTH-DISPERSIVE X-RAY SPECTRA

Guy Rémond and J. L. Campbell

X-ray peaks frequently exhibit asymmetrical shape resulting from instrumental spectral distortions and from the existence of nondiagram lines. In order to account for a possible non-proportionality between the peak height and the peak area in quantitative analysis, an analytical description is used to process x-ray peaks obtained by means of wavelength-dispersive spectrometry (WDS). The observed peak width must be expressed in terms of the instrumental resolution and the natural width of the emission line in order to avoid artifacts in spectra processing. The effect of the matrix composition on the intensity of high-energy satellites resulting from double ionization mechanisms and Coster-Kronig transitions is illustrated for the case of gold-bearing compounds.

Experimental

The computer-and-microprocessor controlled electron probe microanalyzer (EPMA) equipped with four WDSs and installed at the joint Bureau de Recherches Géologiques et Minières - Centre National de la Recherche Scientifique laboratory at Orléans was used. An interval corresponding to a variation of ± 0.00075 of the $\sin \theta$ value around the peak maximum was analyzed by moving the monochromator step by step. Each step was equal to a variation of $\sin \theta = 3 \times 10^{-5}$, so that each analyzed domain contained 500 channels. For each channel the counting time was 1 s.

The observed photon energy distribution $P(\lambda)$ within an x-ray emission line is the convolution product of the Lorentzian physical energy distribution with the instrumental response function of the spectrometer. The observed shape of an x-ray line analyzed by WDS is controlled by the entrance slit of the spectrometer, the intrinsic properties of the monochromator, and its geometrical arrangement within the spectrometer.¹ Thus, the WDS peak profile is intermediate between a Gaussian and a Lorentzian distribution. For practical application in quantitative processing of complex x-ray spectra by means of least-squares fitting techniques, Huang and Lim suggested the use of the equation²

$$P(\lambda) = C_g G(\lambda) + C_l L(\lambda) \quad (1)$$

where $0 \leq C_g \leq 1$ and $C_l = 1 - C_g$ are the con-

tributions of a Gaussian $G(\lambda)$ and Lorentzian $L(\lambda)$ of same width and centered at the same maximum position.

Equation (1) has been used to process WDS x-ray spectra acquired by EPMA.^{3,4} In order to correct for departure from symmetry of peaks, Gaussian offsets were empirically added to the above equation.^{3,4} In the fitting procedure, each parameter can be fixed, released, or coupled to others to insure a proper modeling of the peak, taking into account its known physical properties.

Results

In order to illustrate the change in the peak shape as a function of the analyzed radiative transitions, the S $K\alpha$, Nb $L\alpha$ and Au $M\alpha$ emission lines, whose energies are similar, were digitally recorded and processed (Fig. 1). These x-ray peaks were analyzed by a PET monochromator ($2d = 0.874$ nm). The corresponding Bragg angles were located approximately midway within the Bragg angle domain imposed by the mechanical limitations of the monochromator displacement within the spectrometer. The following observations were made.

- The unresolved S $K\alpha_1, K\alpha_2$ doublet is accompanied by two high-energy nondiagram lines labeled S KL and S KM (Fig. 1a). The separation distances between the satellite peaks and the parent S $K\alpha_1$ peak were S $K\alpha_1$ - S KL = 0.00348 nm (15 eV) and S KM - S $K\alpha_1$ = 0.000865 nm (3.7 eV), respectively.

- The unresolved Nb $L\alpha_1, L\alpha_2$ peaks also exhibited a high-energy nondiagram line Nb $L\alpha$ S (Fig. 1b). This satellite was asymmetrical and described as the sum of two Gaussian offsets. The separation distance of the satellite maximum from the Nb $L\alpha_1$ peak was 0.00206 nm (7.8 eV) with an intensity ratio $I(\text{Nb } L\alpha\text{S})/I(\text{Nb } L\alpha)$ equal to 15%. The Nb $L\beta$ peak was also found to be asymmetrical. The intensity of the high-energy satellite was only 6% with respect to that of the Nb $L\beta$ parent peak.

- The Au $M\alpha$ emission peak exhibited a pronounced high-energy tail, which was resolved as that of the Nb $L\alpha$ parent peak.

Low energy nondiagram lines were also observed for the case of some emission peaks of the lanthanide elements (Fig. 2) and for the case of $K\alpha$ and $K\beta$ peaks of the transition analyzed by means of a LiF monochromator.^{3,4}

Discussion

The peaks being corrected for asymmetry, the calculated half-width at half maximum (HWHM) values Γ , are effective values accounting for the instrumental resolution Γ_1 , and the

G. Rémond is at the Bureau de Recherches Géologiques et Minières, Service Géologique National (Département Géologie), BP 6009, F-45060 Orléans Cedex 2, France; J. L. Campbell is at the University of Guelph, College of Physical and Engineering Science, Guelph, Ont., Canada N1G 2W1.

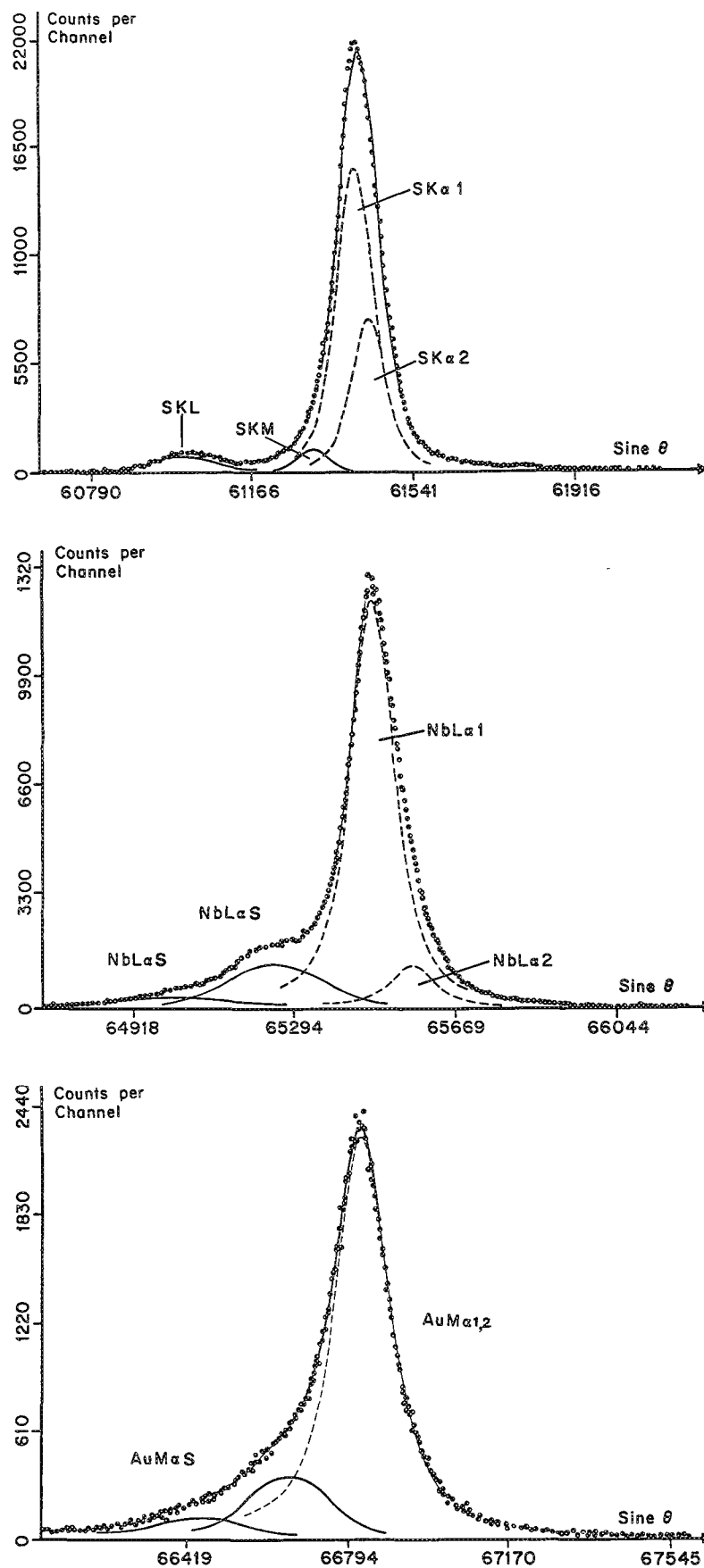


FIG. 1.--Results of fit to experimental WDS x-ray peaks made with PET monochromator. Each analyzed wavelength domain contains 500 channels. Distance between two successive steps is 3×10^{-5} of the $\sin \theta$ value. (a) S $K\alpha_1, K\alpha_2$ peaks; (b) Nb $L\alpha_1, L\alpha_2$ peaks; (c) Au $M\alpha_{1,2}$ peaks.

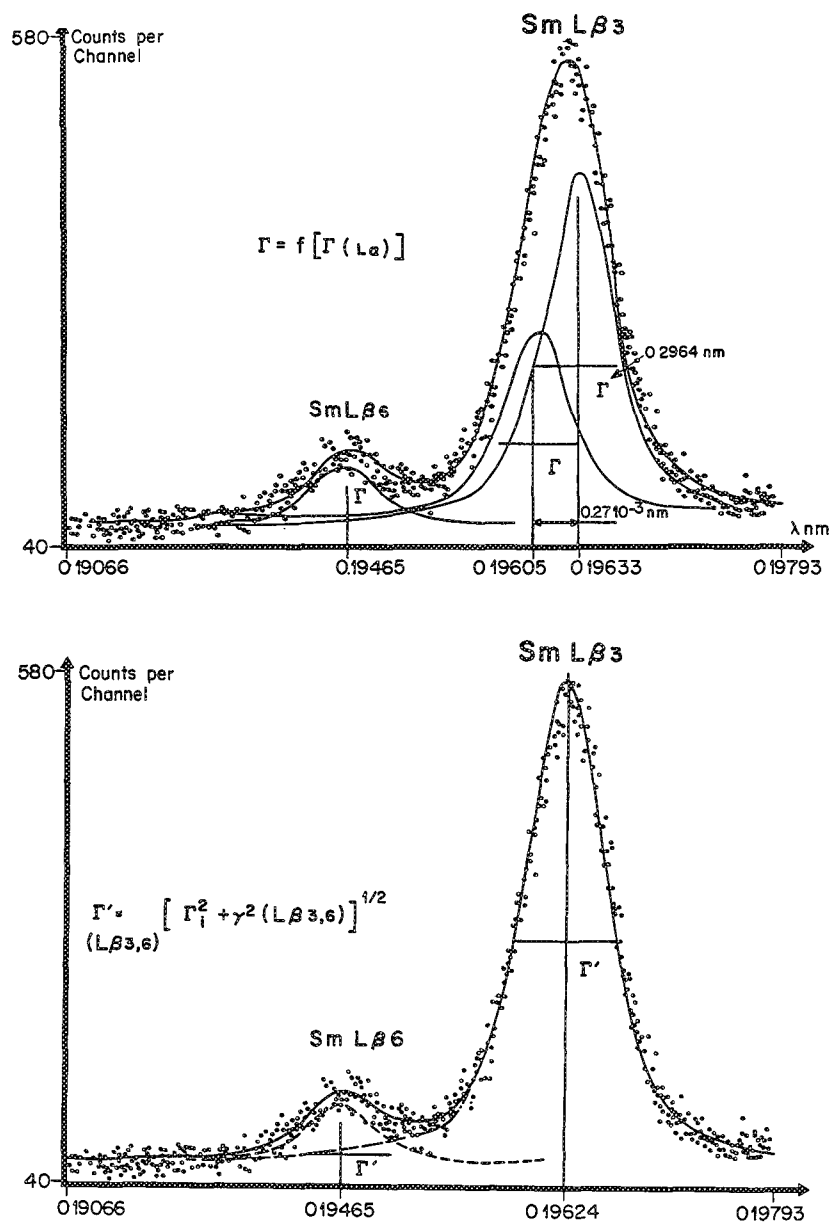


FIG. 2.--Results of fit to the Sm Lβ₃ peak with Eq. (1) used as fitting function and peak width derived from (a) calibration curve expressing width of Lα peaks as a function of wavelengths, (b) Eq. (2).

natural width of the analyzed x-ray emission γ . The observed Γ values were expressed by quadrature addition of the Γ_1 and γ values³:

$$\Gamma_{jk} = [(\Gamma_1)^2 + (\gamma_{jk})^2]^{1/2} \quad (2)$$

where Γ_{jk} is the observed HWHM of the peak resulting from the radiative transition between the j and k levels, respectively, Γ_1 is the HWHM value resulting from the instrumental resolution, and γ_{jk} is the natural half-width of the jk x-ray emission line.

Equation (2) is a sufficient approximation to explain the observed difference in peak widths. Since the natural width of the S Kα emission line is only a few tenths of an electron-volt, the 3.7eV calculated value derived from the S Kα₁, Kα₂ peak processing (Fig. 1a) is indicative of the PET resolution within a narrow en-

ergy domain containing the S Kα emission peaks. With the 1.77eV natural width of the Nb Lα line taken into account, Eq. (2) led to a predicted 4.1eV width, consistent with the measured width, which we found to be 3.97 eV.

The natural width of the Lβ₃ emission lines of the lanthanide elements ($57 \leq Z \leq 71$) is almost twice that of the Lα emission lines. This difference is responsible for the difference in peak width as shown in Table 1.

In addition, setting the Lβ₃ peak width to the value derived from the calibration curve for the Lα peak width led to the detection of a spurious peak (Fig. 2a); the Lβ₃ peak was solved as a single peak when the width was corrected for the natural width (Fig. 2b).³

TABLE 1.--Observed and predicted HWHM values (nm) for $L\alpha_3$ emission peak of some lanthanide elements.

	La	Pr	Nd	Eu
$(L\beta_3)$ (nm)	0.2411	0.2218	0.2127	0.1887
$\Gamma_1 = f(\Gamma(L\alpha))$ (nm)	$0.255 \cdot 10^{-3}$	$0.273 \cdot 10^{-3}$	$0.280 \cdot 10^{-3}$	$0.302 \cdot 10^{-3}$
$\Gamma_2 = (\sqrt{T_4^2 + \gamma^2})^{1/2}$ (nm)	$0.326 \cdot 10^{-3}$	$0.327 \cdot 10^{-3}$	$0.330 \cdot 10^{-3}$	$0.340 \cdot 10^{-3}$
Γ_{obs} (nm)	$0.330 \cdot 10^{-3}$	$0.320 \cdot 10^{-3}$	$0.328 \cdot 10^{-3}$	$0.338 \cdot 10^{-3}$

Significant low-energy satellites were found to accompany the $L\beta_2$, $L\gamma_1$, and $L\gamma_{2,3}$ emission lines of the lanthanide elements; i.e., transitions originating from the incompletely filled 4f shell of these elements. The result of a fit to the Nd $L\gamma_1$ emission is shown in Fig. 3. A linear relationship was observed for the wavelength separation distance between the nondiagram and the parent diagram line as a function of wavelengths (Fig. 4). The separation distances derived from spectra processing according to Eqs. (1) and (2) were found to be in fairly good agreement with data published by other authors.⁶⁻⁸ These low-energy satellites are similar to those accompanying the $K\beta_{1,3}$ emission peaks of transition metals.⁹⁻¹¹

High-energy satellites have been shown to exist on $K\alpha$, $L\alpha$, and $M\alpha$ peaks (Fig. 1). The separation distance between the S KL satellite and S $K\alpha_{1,2}$ peak (Fig. 1a) is consistent with x-ray spectra modifications resulting from a de-excitation process of the K shell in presence of simultaneous 2p vacancy.¹² When 1s and 2p vacancies are created simultaneously, the 2p vacancy has a longer lifetime than that of the 1s hole. Thus, the inner vacancy de-excites in presence of an outer vacancy which produces a change in the electrostatic potential leading to shifts in the energy levels. These shifts were kindly calculated for us by B. Crasemann.¹³ Because of the large numbers of atomic levels involved in each case, the satellite consists of a number of transitions closely spaced, and we observed their envelope. The S KM satellite (Fig. 1a) is tentatively assigned to simultaneous vacancies on the K and M levels. A linear increase of the energy separation distance $Z KL - Z K\alpha$ as a function of the atomic number Z was observed accompanied by a simultaneous linear decrease of the intensity ratio $I(Z KL)/I(Z K\alpha)$ as a function of Z.⁴ The energy separation distance $Z KM - Z K\alpha$ also linearly increased as a function of Z, but the intensity ratio $I(Z KM)/I(Z K\alpha)$ increased when Z was increased.⁴

The separation distance of ~ 8 eV we measured between the Nb $L\alpha S$ satellite and the Nb $L\alpha$ dia-

gram line (Fig. 1b) is consistent with the calculated data by Crasemann and with the energy shift for Sn L x rays resulting from additional electron vacancies.^{13,14} A separation distance of ~ 8 eV was also observed between the Nb $L\alpha S$ satellite and Nb $L\beta$ emission line. The intensity ratios $I(Nb L\alpha S)/I(Nb L\alpha)$ and $I(Nb L\beta S)/I(Nb L\beta_1)$ are in proportion, consistent with the measured and calculated relative satellite intensity of the $L\alpha$ and $L\beta_1$ x-rays produced by 2.5 MeV proton bombardment of elements within the $37 \leq Z \leq 56$ atomic number domain.¹⁵

Besides direct simultaneous ionization of inner and outer shells, the emission process in a double-hole configuration may also result from Coster-Kronig (CK) decay mechanisms of the L and M shells; i.e., Auger decay within the same shell.

The CK transitions are not energetically allowed for all elements and the relative satellite intensities exhibit a cutoff threshold for some specific atomic numbers. As an example, the $L_1 - L_3 M_{4,5}$ CK transition becomes forbidden for $Z \geq 50$, which explains the low satellite-to- $L\alpha$ intensity ratio that we measured as 1.7% for the case of Ba ($Z = 56$), compared with the value of 15% we obtained for Nb ($Z = 41$).

When permitted, the CK transitions dominate the other decay processes and are responsible for the satellites we measured on the high-energy side of the $L\alpha$ peaks for Hg, Au, Pt, and W. The tailing effects we observed on the high-energy side of the $M\alpha$ peaks for Au (Fig. 1c), Hg, Pt, and W are also more likely to be due to emission in double-vacancy configuration created by CK transitions of the M shell. The Au $M\alpha$ peak width induced by a 20 keV electron beam energy was 2.7 eV (Fig. 1c), leading to a value for the intensity ratio between the satellite and the Au $M\alpha$ peak of 0.2. An intrinsic width of 2.5 eV and a 0.5 intensity ratio were obtained for the Au $M\alpha$ emission induced by a Cr x-ray fluorescence tube.¹⁶ The difference in the ionization cross section as a function of the excitation energy may explain the variations of the Au $M\alpha S$ and Cu $L\alpha S$ satellite intensities associated to the Au $M\alpha$ and Cu $L\alpha$ intensities measured at the surface of several Au-Cu alloys (Fig. 5). The intensity of the Au $M\alpha S$ satellite was independent of the Au and Cu concentrations. The Cu $L\alpha S$ satellite intensity increased when the Au concentration within the Au-Cu alloys increased; i.e., when the secondary fluorescence of the Cu $L\alpha$ (928 eV) induced by the generated Au $M\alpha$ photons (2123 eV) also increased, leading to simultaneous CK transitions induced by electrons and x-ray photons.

Practical Considerations

There is a need to extend the available database for the prediction of the intensity of any x-ray emission line. Most of the available data are derived from x-ray emission in thin targets induced by heavy particles of monoenergetic photons. Accurate quantitative

3

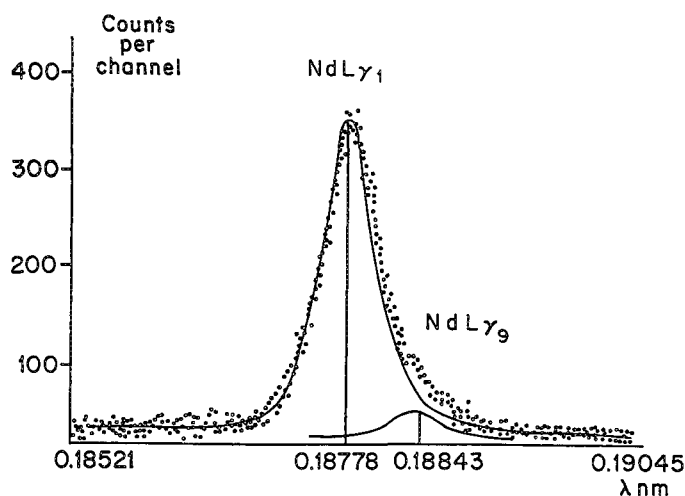
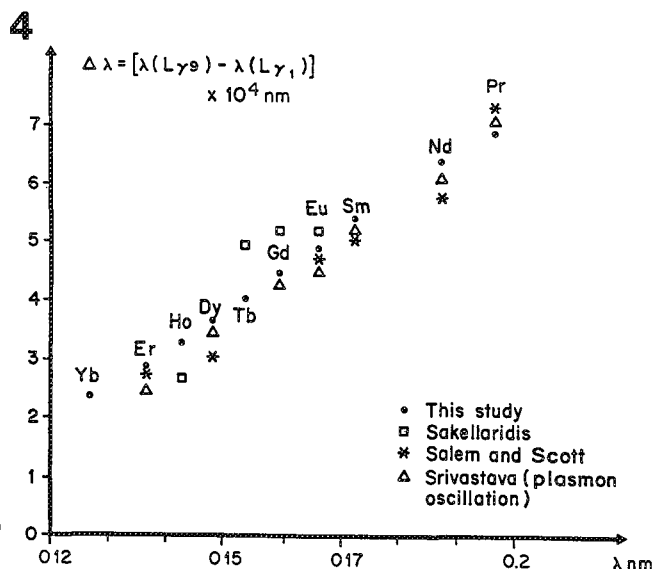


FIG. 3.--Results of fit to experimental Nd $L\gamma_1$ emission peak with a LiF monochromator.

FIG. 4.--Comparison of wavelength separation distances between the nondiagram $L\gamma_9$ and diagram $L\gamma_1$ lines of lanthanide elements as a function of wavelengths derived from experimental measurements (this study) and from published data.⁶⁻⁸



processing of high-resolution wavelength-dispersive of x-ray peaks combined with the analysis the in-depth distribution of the ionizations would probably contribute to the determination of physical parameters involved in the mechanisms of x-ray emission induced by electron bombardment of thick targets.

For practical use, spectral deconvolution must be applied when peak area is used for x-ray intensity measurement in quantitative analysis by means of the EPMA, as illustrated by the two examples given in Table 2 and Fig. 6.

For the case of the analysis of Au-Cu alloys, results obtained either by the usual peak height measurement and peak areas derived from Au $M\alpha$ and Cu $L\alpha$ peak deconvolution were found to be in a good agreement. An excess in the calculated Cu concentrations was observed when the total peak and satellite areas were used for quantification (Table 2) consistent with the data in Fig. 5.¹⁷

For quantitative purposes, peak deconvolution must be used rather than total peak integration when spectral distortions occur on both the peak and the underlying continuum (Fig. 6). The high-energy tailing of the Au $L\alpha$ peak is the sum of CK transitions and of spectral distortion resulting from the Johann mounting type of the LiF monochromator.¹⁷ The sharp decrease of the continuum intensity within the Au $L\alpha$ wavelength domain has been explained in terms of diffraction from crystallographic planes other than those corresponding to the monochromator type.¹⁸ It is obvious from Fig. 6 that both spectral distortion in the peak and continuous shape must be corrected to obtain reliable peak areas.

TABLE 2.--Comparisons of quantitative analysis of Au-Cu alloys as a function of Au $M\alpha$ and Cu $L\alpha$ intensity measurements. Pure Au and Cu were used as standards. The experimental concentrations were processed according to the PAP correction procedure.

Alloy	1 wt %		2 wt %		3 wt %	
	Cu	Au	Cu	Au	Cu	Au
80 Cu - 20 Au	.805	.197	.801	.201	.815	.200
60 Cu - 40 Au	.606	.405	.602	.402	.612	.399
40 Cu - 60 Au	.409	.611	.403	.615	.422	.612
20 Cu - 80 Au	.206	.816	.205	.817	.219	.815

1. Peak height measurements as monochromator is moved away from the Bragg angle of maximum emission Au $M\alpha$ and Cu $L\alpha$ peaks.

2. Peak area of Au $M\alpha$ and Cu $L\alpha$ emission peaks derived from fit to experimental data.

3. Peak areas corresponding to total number of photons within Au $M\alpha$ and Cu $L\alpha$ emission lines and high-energy satellites.

Conclusion

The shape of wavelength x-ray peaks has been shown to be correctly described by a pseudo-Voigt function; i.e., a linear combination of a Gaussian distribution and a Lorentzian distribution having the same width and amplitude and centered at the same wavelength. The peak-width calculated by quadrature addition of the instrumental resolution and the natural width of an x-ray emission line led to an approximation that was sufficient to predict the width of any x-ray peaks and to detect the presence of low-energy and high-energy nondiagram lines. Spectral deconvolution of wavelength-dispersive

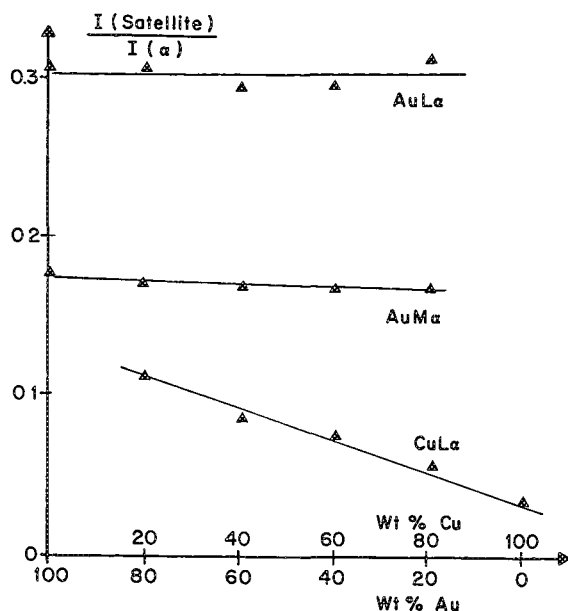


FIG. 5.--Variations of intensity ratios between high-energy satellites Au $M\alpha$, Cu $L\alpha S$ and their parent lines Au $M\alpha$, Cu $L\alpha$, respectively, as a function of composition of Au-Cu alloys.

x-ray spectra using the simplified pseudo-Voigt function can be applied to quantitative analysis of complex spectra exhibiting peak overlaps, nondiagram lines, or any spectral distortion leading to a nonproportionality peak height vs peak area. In addition, physical parameters such as Coster-Kronig yields and double ionization cross sections for electron bombardment are also obtained from the K and L high-energy satellites. These data, derived from the analysis of thick targets by means of the EPMA, complement the available data derived from x rays induced by heavy particles or photons in thin targets.

References

1. S. I. Salem and P. L. Lee, "Width of the L x-ray lines of the rare-earth elements," *Phys. Rev.* A10: 2033, 1974.
2. T. C. Huang and G. Lim, "Resolution of overlapping x-ray fluorescence peaks with the pseudo-Voigt function," *X-ray Anal.* 29: 461, 1986.
3. G. Rémond et al., "Analytical description of x-ray peaks: Application to L x-ray spectra processing of lanthanide elements by means of the electron probe micro-analyzer," *Scanning Microscopy* 3: 1059, 1989.
4. G. Rémond and J. L. Campbell, "Spectral deconvolution of wavelength-dispersive x-ray spectra: Part I. Diagram and non-diagram lines" (submitted to *Scanning Microscopy*).
5. S. I. Salem and P. L. Lee, in R. C. Weast and M. J. Astle, Eds., *CRC Handbook of Chemistry and Physics*, Boca Raton, Fla.: CRC Press, 1979, E207.
6. P. Sakellariadis, "Multiplets caractéristiques des terres rares dans leur spectre d'émission X," *J. de Physique et le Radium* 16: 422, 1955.
7. S. J. Salem and B. L. Scott, "Splitting of the $4d^{3/2}$ and $4d^{5/2}$ levels in rare-earth elements and their oxides," *Phys. Rev.* A9: 690, 1974.
8. K. S. Srivastava et al., "Electron-electron interaction in the x-ray emission spectra of rare-earth element and their oxides," *Pure and Appl. Phys.* 21: 256, 1983.
9. S. J. Salem, G. M. Hockney, and P. L. Lee, "Splitting of the 3p levels in the transition elements and their oxides," *Phys. Rev.* A13: 330, 1976.
10. K. S. Srivastava et al., "Electron-electron interaction in transition metal spectra," *Phys. Rev.* A25: 2838, 1982.
11. K. Tsutsumi, H. Nakamori, and K. Ichikawa, "X-ray Mn K β emission spectra of manganese oxides and manganates," *Phys. Rev.* B13: 929, 1976.
12. J. Bhattacharya, U. Laka, and B. Talukdar, "Model for x-ray energy shifts for additional atomic vacancies," *Phys. Rev.* A37: 3162, 1988.
13. B. Crasemann, Department of Physics, University of Oregon, Eugene, OR 97403 (private communication).
14. D. K. Olsen, C. F. Moore, and P. Richard, "Characteristic L x-ray spectra from proton, α particle and oxygen bombardment of Sn," *Phys. Rev.* A7: 1244, 1973.
15. B. L. Doyle and S. M. Shafroth, " $L_{1-2,3} M_{4,5}$ Coster-Kronig transitions thresholds in the region $37 \leq Z \leq 56$," *Phys. Rev.* A19: 1433, 1979.
16. A. Kaakkonen and G. Graeffe, "M x-ray linewidths of gold," *J. de Physique, Colloque C9, Suppl. 12*, 48: C9-605, 1987.
17. G. Rémond et al., "Deconvolution of wavelength dispersive x-ray spectra: Part II. Peak height versus peak area in quantitative analysis" (submitted to *Scanning Microscopy*).
18. P. G. Self et al., "Holes in the background in XRS," *X-ray Spectrometry* 19: 59, 1990.

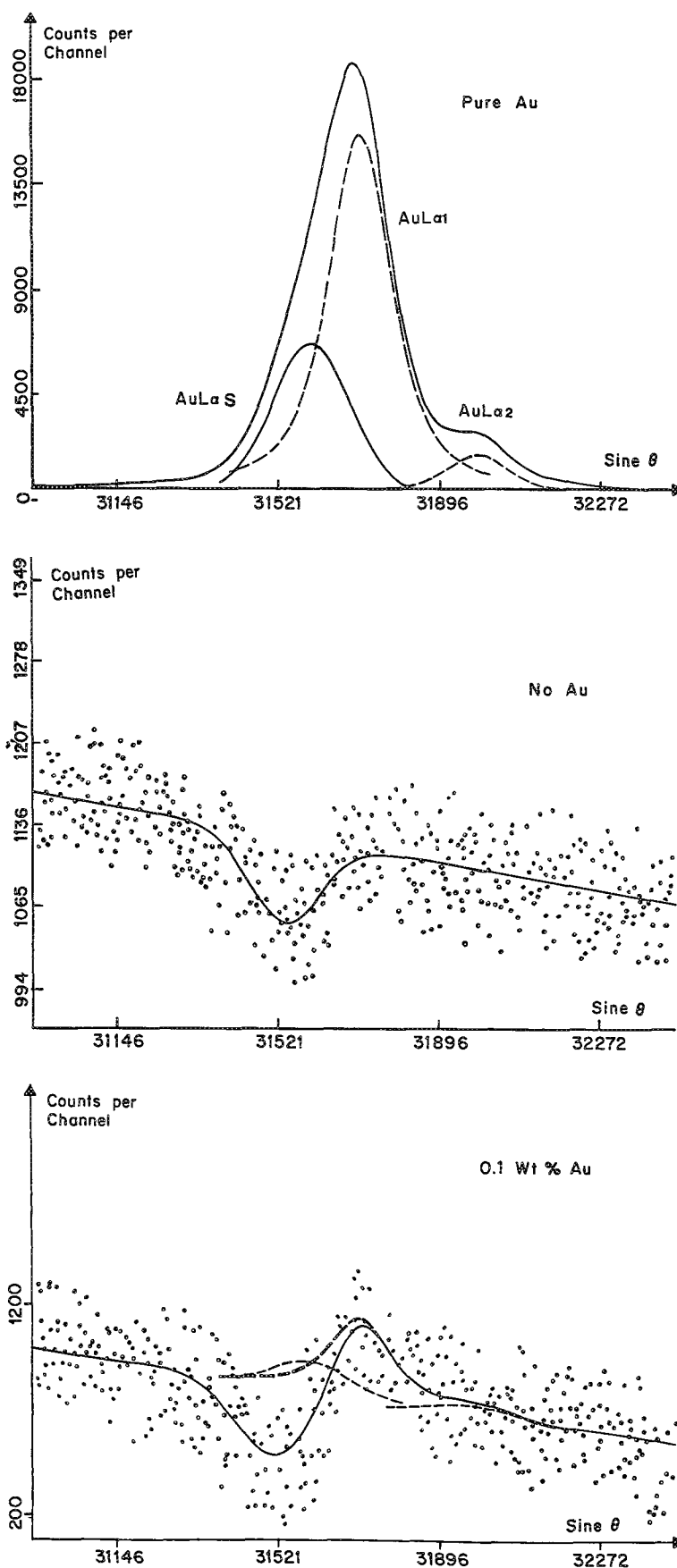


FIG. 6.--Effect of spectral distortions of Au La peak and associated continuum emission on observed x-ray peak characteristic of gold present at trace level: (a) Au La of a pure gold specimen, (b) anomalous distribution of continuum distribution observed at surface of any target, (c) observed Au La peak observed at surface of specimen containing ~ 1000 ppm gold.

PRSUPR: A PC-BASED AUTOMATION AND ANALYSIS SOFTWARE PACKAGE FOR WAVELENGTH-DISPERSIVE ELECTRON-BEAM MICROANALYSIS

J. J. Donovan and M. L. Rivers

An acquisition, automation, and quantitative analysis program for wavelength-dispersive electron-beam microprobes is presented. The developmental considerations and analytical capabilities of the program are described. Hardware independence and state-of-the-art matrix corrections, plus the ability to run on an IBM PC or compatible are specifically addressed. The entire source code (24 000 lines of FORTRAN and Assembler) is available free as shareware for distribution to individuals and institutions. The program may be registered; registration includes free updates and telephone consultation.

Objectives

Several commercial software packages are available for the acquisition, automation, and data reduction of microanalytical x-ray fluorescence data. Many of these programs provide useful capabilities and features for users of electron microbeam equipment. We feel that among the most important of these capabilities are the hardware independence and portability of the software platform. Of equal importance is the quality of the matrix correction software. In addition, the ability to run on an inexpensive and readily available microcomputer should also be a consideration. Specifically, the following criteria were applied in our development of an acquisition, automation and analysis software package.

1. Enough hardware independence to run data acquisition and automation on a wide variety of microprobes with any configuration of stage and/or spectrometer components, which means a software package that can be configured easily to support various microprobes of unusual or unique arrangements for a variety of analytical requirements.

2. Portability to acquire x-ray data when running on-line connected to a microprobe and also to reduce and reprocess x-ray data on another microcomputer when not acquiring data in real-time; that is, the ability to use the same analytical software off-line to examine one's previously acquired data without using up valuable time on the microprobe.

3. The ability to produce quantitative results of the highest accuracy over the entire analytical range of the microprobe using the

most advanced matrix correction software available. This feature is absolutely essential for modern quantitative microanalysis.

Description

With the above objectives in mind we have developed and written a complete software package called PRSUPR for data acquisition, automation, and data reduction that runs under DOS on any IBM PC or compatible XT, AT, or 386 with 640Kb RAM, a hard disk, and a math coprocessor. Real-time multitasking for running automated analyses in "background" is supported with a 386 or 486 CPU under a suitable multitasking environment. No special graphics card or monitor is required to run the package.

Program PRSUPR accommodates up to 16 analyzed elements and 8 fixed concentration elements in a single run for a total of 24 matrix corrected elements. Each analyzed element may be automatically corrected for up to two interfering elements. Both nonlinear MAN (mean atomic number) and automated off-peak background corrections are available. The program automatically corrects for linear standard count drift using up to ten separate restandardizations.

The program utilizes a simple yet versatile user interface that makes extensive use of multiple choice menus and defaulted experimental parameters for exceptional ease of use. The program can save analytical setups to disk for use in setting up new analytical runs. The software includes complete documentation for users and for programmers who wish to modify the hardware interface. Figure 1 reveals the basic structure of the PRSUPR acquisition and user interface routines.

The program contains just four hardware-dependent routines for interfacing to the microprobe hardware for on-line data acquisition and automation. No modifications to the source code are necessary when the suggested commercially available motion control and digital I/O components are used. Other hardware can be supported with minor changes to the specific hardware-dependent routines.

PRSUPR includes an extensive set of capabilities for microprobe stage and spectrometer automation as well as a complete collection of ZAF and $\phi(\rho z)$ expressions for fully quantitative analysis from the well-known CITZAF matrix correction library written by John Armstrong at the California Institute of Technology. The following is a brief description of these automation and analysis features in the PRSUPR software package and how they can be used.

The authors are with the University of California (Department of Geology), Berkeley, CA 94720. M. L. Rivers is now at Brookhaven National Laboratory. The assistance of Dr. John Armstrong of the California Institute of Technology is gratefully acknowledged.

1. *Automated standard data acquisition for unattended operation using predigitized standard samples referenced to calibrated fiducial marks or user-defined locations from a previous standardization.* The program can input and spatially transform coordinate files of digitized standard mounts, containing any number of individual standards, for use in fully automated standardizations. These standard mounts can be digitized in three dimensions (X, Y, and Z), a feature that provides extremely consistent reproducibility of standard analyses. The program allows the user to adjust the standard analysis coordinate positions while running in an automated mode and can save any user adjustments for future restandardization.

The program also supports manual acquisition of standards and automatically saves the coordinates positions selected by the user for use in fully automatic restandardizations, if desired. The user can also specify that the program must automatically offset its position when restandardizing to avoid analyzing the exact same position repeatedly when analyzing for volatile elements such as sodium, potassium, and chlorine.

2. *Automation for unknown sample specimens using random selected points, line traverses, and x-y stage step scanning from user-defined Cartesian or irregular polygon grids input using a digitizing device such as a mouse or trackball.* Any combination of random points, line traverses, or step scans can be run fully automated. Again all coordinates can be digitized in three dimensions and referenced to physical fiducial reference marks on the sample and recorded to disk for purposes of relocating any or all unknown analyzed coordinates. In addition, the program can input digitized coordinate files from previously analyzed samples or independently generated data files (e.g., from a digitizing microscope). These digitized files may also be spatially transformed for exact relocation, in the microprobe, of selected points of interest. The digitized points from the coordinate file may also be run in a completely automated fashion.

The automation of unknown samples also includes the ability to specify that any or all of the standards be rerun automatically at user-defined intervals during the analysis of unknown samples. This feature allows the program to correct for drift in the standard counts when the analysis of unknown samples requires extended periods of time. In this way, the program can run completely unattended without the user's attention for days at a time.

3. *Spectrometer automation routines can perform a number of automated functions for microbeam analysis as well.* Most important, is the ability to analyze automatically multiple elements on each scanning spectrometer, which is essential for microprobes with a limited number of spectrometers. The program allows up to 16 elements to be analyzed using as few as one scanning spectrometer.

Full support of automated off-peak measure-

ments are included, as well as automatic wavelength scanning for qualitative analysis or peak shift and shape studies. In addition, the program can perform spectrometer peak alignments at user-defined analysis intervals for light elements that exhibit serious peak shift problems.

4. *The matrix correction software used in the analysis routines is another very important aspect of microprobe analysis.* Extensive quantitative matrix corrections for ZAF, $\phi(\rho z)$, and nonlinear fit Bence-Albee methods¹ are totally integrated into the PRSUPR acquisition and analysis package.

The CITZAF² ZAF analysis library contained in the PRSUPR acquisition and analysis package performs on-line and off-line analyses. The quality of the analyses produced by this set of matrix corrections is unsurpassed for the quantitative analysis of oxide, silicate, and metallic compounds and for minerals, glasses, and alloys.

The specific correction used in the analysis of samples may be selected from nine different absorption models, three atomic number corrections, two backscatter models, two mean ionization equations, and--for the $\phi(\rho z)$ absorption models--two different $\phi(\rho z)$ expressions. The traditional FRAME ZAF expressions are included for comparison purposes.

In addition to the ZAF correction factors, both the traditional constant Bence-Albee expression,³ the linear UCB expression, and John Armstrong's nonlinear fit α -factors can be calculated and utilized in the analysis of data. The program also supports the use of empirically measured calibration curves using k-ratios from literature or user-supplied measurements. The ability to use a modern Bence-Albee type of correction such as John Armstrong's nonlinear fit α -factors is especially useful when one is reducing large amounts of data from step scans or x-ray images.

Summary

The combination of on- and off-line processing capability, along with the extensive automation features, makes the PRSUPR software analysis package a useful and flexible environment for electron-beam microanalysis. This package is an ideal upgrade for any wavelength-dispersive microprobe that lacks a modern automation and analysis system.

References

1. J. T. Armstrong, "Bence-Albee after 20 years: Review of the accuracy of the α -factor correction for silicate and oxide minerals," *Microbeam Analysis--1988*, 239.
2. J. T. Armstrong, "Quantitative analysis of silicate and oxide materials: Comparison of Monte Carlo, ZAF, and $\phi(\rho z)$ procedures," *Microbeam Analysis--1988*, 239.
3. A. L. Albee and L. Ray, "Correction factors for electron probe microanalysis of silicates, oxides, carbonates, phosphates, and sulfates," *Analyt. Chem.* 42: 1408, 1970.

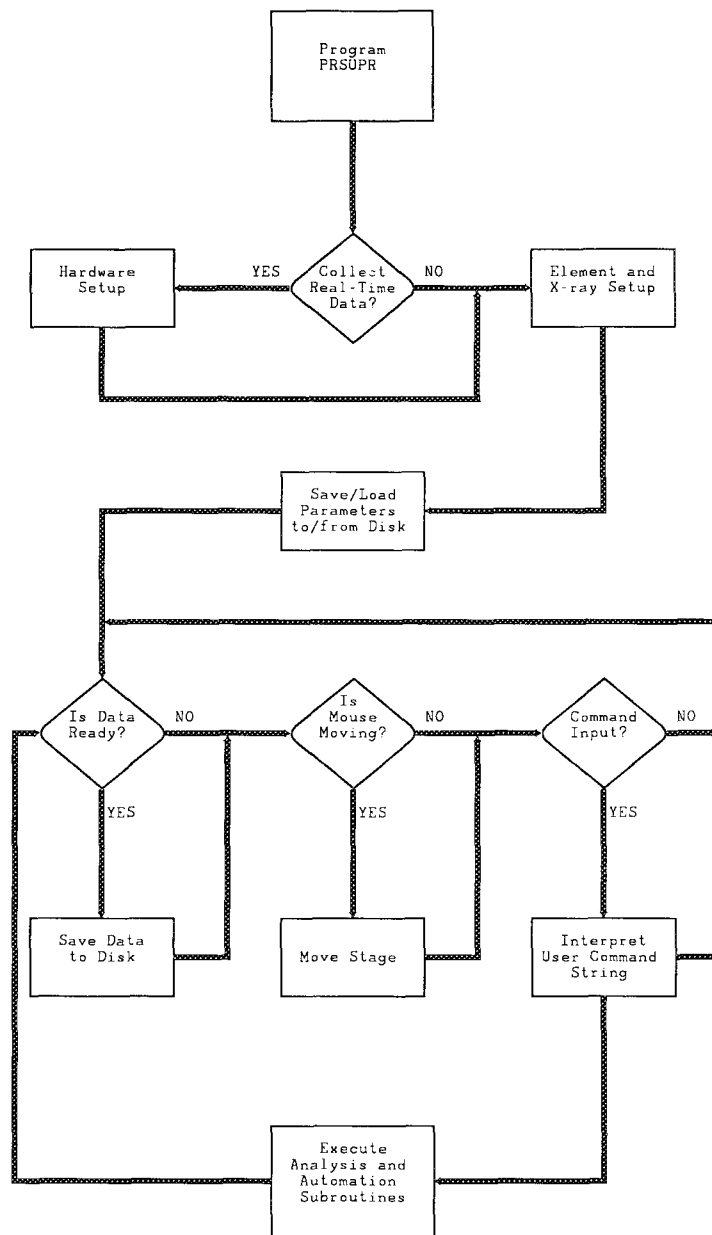


FIG. 1.--Program PRSUPR block flow diagram.

STEPPED DIFFRACTOR FOR POINT FOCUSING OF MONOCHROMATIC X RAYS

D. B. Wittry, S. Sun, and W. Z. Chang

X-ray diffractors with a high collection efficiency for point focusing monochromators or for scanning monochromators have doubly curved surfaces and doubly curved planes.¹ Because of the difficulties of fabricating these diffractors from single crystals, we have explored the possibility of making better doubly curved diffractors by using a stepped diffractor structure in which pieces of the diffracting material are elastically instead of plastically deformed. In this paper we discuss the design considerations for diffractors with doubly curved surface steps, describe the fabrication of these diffractors, and show experimental results for a diffractor approximating the Wittry geometry that was made with mica as the diffracting material.

Design of Stepped Diffractors

The objective of a stepped diffractor structure that would have high collection efficiency is to provide a geometry similar to that which results from rotating the Johansson geometry about a line lying in the plane of the focal circle. In the Johansson geometry, the diffracting planes are cylindrically curved to a radius twice the radius of the focal circle and the surface is cylindrically curved to the same radius as the focal circle. For rays that lie in the plane of the focal circle, monochromatic x rays from a point source are focused exactly to a point image. The first consideration for the stepped diffractor is therefore to select a stepped diffractor structure that approximates the Johansson geometry in the plane of the focal circle.^{2,3} The steps should have a curved surface in the plane of the focal circle parallel to the planes of the Johansson geometry, i.e., curved to a radius of $\sim 2r$ in this plane. For ease of construction and theoretical analysis, we consider that the steps are of equal height, as shown in Fig. 1.

If the midpoint of the steps lie on the focal circle the equation for the intercept of the surfaces of the steps and the focal circle is:

$$\cos \phi_N = 1 - NE + E \quad (1)$$

In this equation, the radius of the focal circle is taken as unity (the coordinates of the actual diffractor are divided by $2r$ to obtain dimensionless equations), ϕ_N is an angular coordinate about a point on the focal circle diametrically opposite the center of a symmetri-

cal diffractor, $\Delta\phi_N$ is an angular coordinate expressing the position of a point on the N th step, E is the step height, and N is the number of the step where N ranges from 1 to M with M equal to the total number of steps on one side of the diffractor.

If the focal circle passes through the step height at half the step height, the edges of the steps are given by

$$\cos \phi_N' = 1 - NE + (E/2) \quad (2)$$

For a ray from the source S incident on the N th step at a point P , the angle of incidence of the ray on the curved surface of the step differs from the Bragg angle θ_B by $\Delta\theta$, where θ_B is the angle of incidence at the point where the step coincides with the focal circle. It may be shown from the law of sines that $\Delta\theta$ is given by

$$\Delta\theta \cong \frac{\Delta\phi_N \tan \phi_N}{\tan \theta_B - \tan \phi_N} \quad (3)$$

One condition on the design of a stepped diffractor is that the steps must have sufficiently small width so that the entire surface of the diffractor can be used, i.e., $\Delta\theta \leq w/2$ where w is the width of the rocking curve of the diffractor material.

A second condition that is important relates to the focusing properties of the rays after diffraction. If we neglect any deviation in the diffracted ray due to irregularities (or mosaic character) of the diffracting planes, the difference between the focal point in the image plane for the ray diffracted at P from the position of the correct image point is given in Fig. 1 by

$$H = \frac{\cos(\theta_B + \Delta\theta) \cos \phi_N}{\cos(\phi_N + \Delta\phi + \Delta\theta)} - \cos \theta_B \quad (4)$$

For applications in which the focusing aberration is important, the maximum number of steps required would be that number which would make the focusing aberration less than a given value.

Equations (3) and (4) can be expressed in terms of the number of steps M for a diffractor of width corresponding to a maximum angle ϕ_M by noting that

$$E = \frac{1 - \cos \phi_M}{M - 1} \quad (5)$$

The largest values for the deviation from the Bragg angle and the focusing aberration are obtained for the rays striking the diffractor at the greatest distance from the midpoint. Examples of these two values as a function of

D. B. Wittry is in the Departments of Materials Science and Electrical Engineering and S. Sun and W. Z. Chang are in the Department of Materials Science at the University of Southern California, Los Angeles, CA 90089-0241.

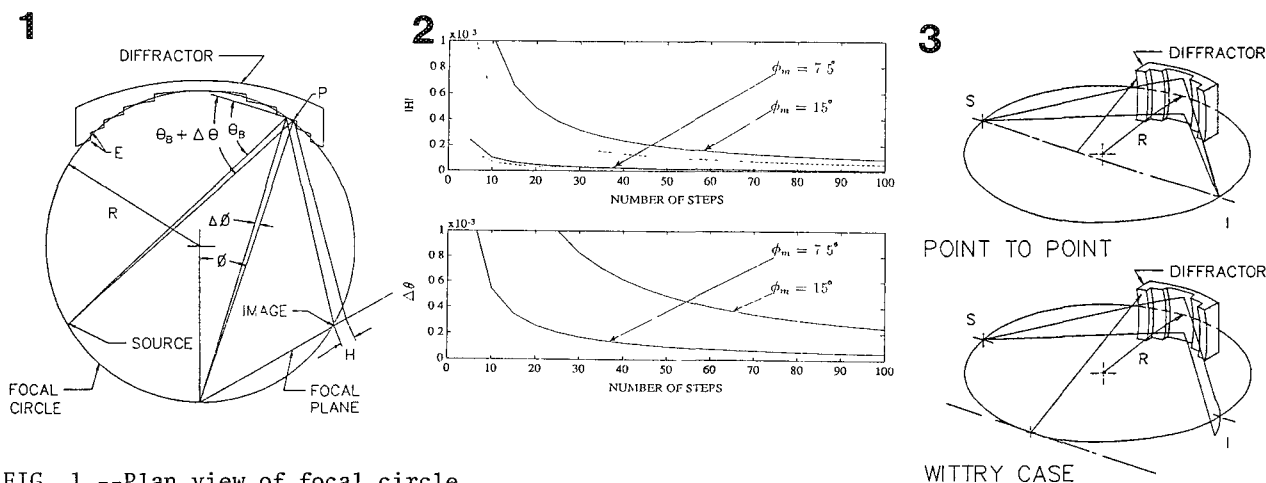


FIG. 1.--Plan view of focal circle.

FIG. 2.-- $|H|$ and $\Delta\theta$ vs number of steps.

FIG. 3.--Two important diffractor geometries.

the number of steps is shown in Fig. 4 for a Bragg angle of 45° . Since Eq. (4) is not symmetrical in ϕ_N , two plots are shown for H ; the solid lines correspond to positive values of ϕ_N , the dashed lines for negative values.

Diffractors with Doubly Curved Steps⁴

As shown by Wittry and Sun,¹ high-efficiency diffractors can be obtained by a geometry that corresponds to rotating the Johansson geometry about a line that lies in the plane of the focal circle. Two cases are important, as shown in Fig. 3. In the first case, the point-to-point focusing geometry is obtained by rotation of the section of the diffractor lying in the plane of the focal circle about a line passing through the source and image points. In the second case, which provides a diffractor with a high efficiency over a wide range of Bragg angles, the geometry corresponds to rotating the section about a line passing through a point diametrically opposite the midpoint of a symmetrical diffractor and parallel to the line between the source and image points. This configuration is analogous to the diffractor with continuous surface that was first described by Wittry.⁵

For both the point-to-point case and the Wittry case, the width of the diffracting material's rocking curve imposes a fundamental limitation on the spectral resolution when the diffractor is used as a monochromator. In other words, the spectral resolution of the diffractor with doubly curved steps can be better than that of a diffractor of less optimal geometry (e.g., the Johann geometry) but it will not be better than a corresponding diffractor with continuous surface. A similar conclusion also applies with regard to the fraction of the diffractor's surface over which the angle of incidence lies within $\theta_B \pm \Delta\theta$; as the number of steps on the stepped diffractor increases, the effective area increases, but it will not exceed the effective area of the corresponding diffractor with continuous surface. The latter result has been confirmed by detailed calculations taking

account of rays striking the diffractor's surface at points ranging over the entire surface.⁶

Understanding of the effect of the diffracting material's rocking curve on the focusing properties of the diffractor requires a detailed knowledge of the physical basis of the rocking curve. If the diffracting planes are ideally smooth and have uniform spacing, reflection of x rays by the diffracting material is like reflection of light by a mirror; no angular spreading takes place (even though there may be wavelength spreading due to the use of a small number of diffracting planes). On the other hand, if the diffracting material has a mosaic or wavy structure, reflection of x rays by the material is like reflection of light by an imperfect mirror; in this case, the wavelength dispersion is accompanied by a spreading of the reflected beam even though the incident beam has the correct directions.

From the foregoing considerations it can be seen that there is no significant advantage in a stepped diffractor geometry with respect to spectral resolution or collection solid angle when the corresponding diffractor with a continuous surface can be fabricated. The real advantage of the stepped diffractor is that it is possible to fabricate this type of diffractor from materials that could not otherwise be used and that it is possible to fabricate diffractors with large area and/or small radii of curvature.

Fabrication of Diffractors with Doubly Curved Steps

A large number of possibilities exist for fabricating diffractors having steps with doubly curved surfaces. The diffracting material may consist of single crystal material stacked together, thin sheets of single crystal material mounted on the doubly curved surfaces of steps on a substrate, small pieces or flakes of single-crystal material mounted on the doubly curved surfaces of the steps, or layered structures deposited on the doubly curved surfaces of the steps. For the present work, we used sheets of

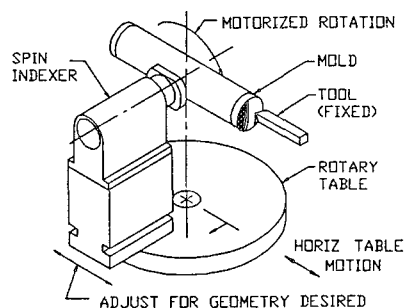


FIG. 4.--Schematic diagram showing fabrication of molds.
mica mounted on a suitably contoured substrate.

For testing the possibilities of fabricating material on the steps of a substrate, we decided to use the stepped approximation to the Wittry geometry because the substrate configuration is the same for all Bragg angles, whereas the point-to-point case requires a different substrate configuration for each Bragg angle and hence for each diffracting material.¹

The substrate was made by first preparing a concave mold in a modified milling-drilling machine and its x-y table motion along with a "spin indexer" mounted on a rotary table to provide two perpendicular axes of rotation. The arrangement is shown schematically in Fig. 4. To approximate the Wittry geometry, the two rotation axes are adjusted to intersect since the desired surfaces of the steps are spherically curved. For the point-to-point focusing case, the two axes would be offset from each other because the desired surfaces of the steps are toroidally curved. The steps are machined with a single point tool clamped in a fixed position and the rotary table motion is used to machine each step after setting the depth of cut by use of the x motion of the x-y table.

The mold was machined from aluminum rod 3.8 cm in diameter. Aluminum was used for ease of fabrication, although stainless steel would be preferred. Five steps 0.15 mm high with surfaces with a radius of curvature of 10 cm were machined on each side of the central portion; this corresponds to the Wittry geometry for a 5cm radius focal circle. The concave substrate was cast over the mold using a two-part polyester resin. After hardening, the casting was milled to 2.5 cm square. Mica was split into a sheet approximately 0.02 mm thick and 11 pieces ranging from 1.24 to 7.84 mm in width and matching the shape of the steps were cut from the same mica sheet with a razor blade. These pieces were attached to the steps on the substrate one at a time with acrylic lacquer. After each piece was mounted, the substrate and mold were quickly clamped together in a vise to shape the mica to the surface of the step. Although this may seem like a laborious procedure, it is actually much easier to carry out than the procedures that have been used for fabricating corresponding diffractors from single crystals.^{7,8} For fabricating diffractors with a significantly larger number of steps, photoli-

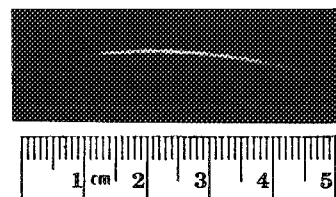


FIG. 5.--Image of focus form mica diffractor with five steps 0.15 mm high on each side of central portion (Wittry case, 2.5×2.5 cm diffractor on 5cm-radius focal circle, Cu K α radiation).

thography could be used to increase the speed and accuracy of forming the small pieces of diffracting material required.

The completed diffractor was tested using Cu K α radiation from a microfocus source and Polaroid type 57 film to record the focus formed by the 5th order diffraction from the mica ($\theta_B = 22.76^\circ$). Figure 5 shows the image obtained in 1 min with the x-ray source operating at 20 kV and 50 μ A. An x-ray topograph that results when the film is placed near the diffractor showed separate lines from the individual pieces of mica; these lines had some small irregularities along their length, presumably due to imperfect bending. However, as can be seen in Fig. 5, the focus from all of the steps merge into a single line focus. The result shown was obtained with the first stepped diffractor that was made; it is expected that better results can be obtained with refinements of the fabrication procedures and more careful consideration of the materials used for the mold, substrate, and cement.

Summary and Conclusions

Equations and criteria were established for the design of stepped diffractors and a mica diffractor was constructed and tested. The preliminary results indicate that the stepped diffractor structure may be an important solution to the problem of fabricating high-efficiency diffractors for use with point sources of radiation.

These diffractors have important applications to instruments for materials characterization techniques, such as microprobe x-ray fluorescence (MXRF), scanning electron microscopy (SEM), transmission electron microscopy (TEM), x-ray photoelectron spectroscopy (XPS), proton-induced x-ray emission (PIXE), etc. These diffractors may also be useful as x-ray optical elements, for example in x-ray astronomy or in x-ray scattering experiments. The advantages include economical fabrication and the possibility of making diffractors of virtually unlimited size.

References

1. D. B. Wittry and S. Sun, *J. Appl. Phys.* 67: 1633-1638, 1990.
2. Stepped diffractors approximating the

Johanson geometry and using multiple monomolecular films were proposed by H. Okano (U.S. Patent 3,469,098, 19 September 1969). However, Okano did not take into account the large width of the rocking curve for these materials.

3. Stepped diffractors approximating the Johanson geometry based on single crystal lamellae were proposed by D. B. Wittry (U.S. Patent 3,927,319, 16 December 1975) with the idea that the collection efficiency would be greater than that of an ordinary Johann diffractor. This idea was based on an oversimplification of the diffracting properties of the Johann case.

4. D. B. Wittry, patent pending.

5. D. B. Wittry, U.S. Patents 4,807,268, (21 February 1989) and 4,882,780 (21 November 1989).

6. D. B. Wittry and S. Sun, *J. Appl. Phys.* (in press).

7. D. M. Golijanin et al., *Microbeam Analysis--1989*, 186-190.

8. D. B. Wittry et al., *XII ICXOM* (in press).

D. S. Bright

Digital image processing is used to enhance and interpret micrographs. Software tools, now available for desk top computers at reasonable cost, allow animation of short image sequences, real-time rotation of three-dimensional graphs, and manipulation of the color look-up table or palette of the display device. These capabilities help to visualize microscope stage drift, the spatial relationships of two or three chemical constituents in elemental images, and the concentration relationships of three and four constituents in x-ray maps. These uses are illustrated as much as possible with still black and white images.

The software tools discussed in this paper are programs written for a Macintosh* computer. The tools augment the image acquisition and processing done on minicomputers having operating systems with virtual memory. The minicomputers are connected to our microscopes and support the LISPIX image processing system,¹ which is written in FORTRAN and LISP. Because LISPIX works in the traditional minicomputer environment where commands are entered via the keyboard, it lacks capability for certain functions that are done easily with the tools discussed in this paper. A computer network is used heavily to transfer images between the minicomputers and the desktop computers.

The Tools

NIH IMAGE^{2,3} is a program for displaying and processing images, and for measuring images under direct operator control. NIH IMAGE is useful for examining images because it has functions to zoom, scroll, smooth, and sharpen the images and to modify the color palette for contrast enhancement. Threshold settings can be tested, and particles counted and measured. This program also displays histograms and shows intensity profiles. Parts of images are easily selected and annotated for making illustrations.

MaxSpin⁴ is used to display three-dimensional graphics and perform rotations in real time.

NCSA PalEdit⁵ is a palette editor and display utility. The palette diagrams for this paper were made with this utility.

The following examples show how these tools have been useful in our microanalysis applications.

The author is with the Microanalysis Research Group, Center for Analytical Chemistry, National Institute of Standards and Technology, Gaithersburg, MD 20899. Macintosh is a registered trademark of Apple Computer, Inc. Certain commercial equipment, instruments, or materials are identified in this report to specify adequately the experimental procedure. Such identification does not imply recommendation or endorsement by NIST, nor does it imply that the materials or equipment identified are necessarily the best available for the purpose.

Image Sequences

NIH IMAGE can animate or show short image sequences in rapid succession. Many images can be loaded at once, and the animation can be enhanced by modifying the palette of just one of the images. The images can be animated at variable speed forward or backward, and can be "flipped through" with keystrokes.

Visualizing Stage Drift of Electron Microscope. Short image sequences are useful for showing dynamic effects such as the drift of an electron microscope stage. TEM images at approximately 400 \times were taken at 12min intervals for a little over 2 h. The first frame (Fig. 1) was taken shortly after the microscope was turned on.

In the animation, the stage drift appears initially as rapid motion of the particles to the lower right. The movement slows down and almost stops after the 2h interval; thus, for automated analysis at this magnification, the warm-up period for the microscope should be at least 2 h.

A mosaic of the sequence (Fig. 2) shows the upper left portion of every other frame. It is harder to gauge the motion of the stage from this mosaic.

Six of the frames in Fig. 2 are superimposed in Fig. 3. Since these images are bright field with small dark particles, we made the superimposition (with the LISPIX image processing system) by taking the minimum value for each pixel location, over all six images. The positions of the small particles show the asymptotic slowing of the stage drift.

Depth Profiling with Ion Microscope. The ion microscope erodes the sample by sputtering as it collects images. A series of images thus shows the interior of a sample as if it were being sectioned. Fifty-eight O¹⁸ images were taken in sequence as the ion beam eroded a single crystal of Ba-Y-Cu, ceramic superconductor. The images are 256 \times 256 pixels, the field width is 150 μ m, and about 1 mm of material was eroded between each frame. Every fifth image appears in the mosaic (Fig. 4). Animation of these images has the effect of time averaging the noise, so that faint blobs become more visible than when one still frame is viewed. The erosion and thus the O¹⁸ depth profile of the crystal area can be seen as well.

Determination of Refractive Index with Light Microscope. When particles are immersed in a matching refractive index fluid, the edges of the particles have least contrast at the wavelength and temperature at which the index of the fluid matches that of the particles. Figure 5 is a typical transmission light micrograph of glass particles and Fig. 6 is a series of images showing different amounts of grain contrast at different temperatures. Figure 6

shows changes between the frames, but it is easier to view the full-sized images with NIH IMAGE and either animate or rapidly switch from one frame to another to see the effect of temperature on the visibility of the edges of the particles. The stage shifted a small amount in the middle of the sequence, which is much easier to notice from the animation than from the mosaic.

Concentration Histogram Image (CHI)

The values of the pixels of registered images or x-ray maps can be accumulated in a multidimensional histogram (Concentration Histogram Image or CHI⁶). These concentration histogram images provide an easy method for viewing the intensity or concentration information of registered x-ray maps and searching, for example, for clusters that might represent phases in the material. The number of registered maps determines the dimension of the histogram; two, three, and four components can be viewed at once with two-, three-, and four-dimensional CHIs. Two-dimensional histograms are viewed as scatter diagrams^{7,8} or as suitably pseudo-colored images⁵ in which the bins appear as pixels colored with a thermal scale to show counts (e.g., Fig. 7).

3-D Real-time Rotation. Three-dimensional CHIs are rendered with $256 \times 256 \times 256$ bin resolution as two-dimensional perspective projections with LISPIX. This representation is useful once the general shape of the CHI is known. Since the CHI can be an arbitrary pattern of points that is unfamiliar, it must be examined from several viewpoints to ascertain its shape. With MacSpin, the CHI can be plotted and pseudo-colored to match the LISPIX display, and then rotated in real time.

To review the CHI with MacSpin, the CHI is transferred to the Macintosh by first generating the three-dimensional histogram (with LISPIX) but at reduced resolution; there is space for a $64 \times 64 \times 64$ array in LISPIX but not for a $256 \times 256 \times 256$ array. Also, the reduced resolution results in fewer bins to be sent to MacSpin. LISPIX writes a text file with a specified number of populated bins, one per line, as x, y, and count. These data are in turn read by MacSpin. LISPIX changes the resolution or bin size until the number of populated bins is no greater than that specified. A file with a few thousand populated bins is satisfactory for viewing the shape of the CHI.

Two examples of three-dimensional CHIs appear with two orientations each in Figs. 8 and 9. Figure 8 is the three-dimensional CHI for the Al-Li-Cu alloy that is in two-dimensional form in Fig. 7. The left view is similar in perspective to the views usually plotted with LISPIX. The CHI was checked for planarity simply by slow rotation about a vertical axis. At some point, the plane will be seen on edge, as in the right view (Fig. 8). The planarity of the CHI suggests that the two-dimensional CHI of Fig. 7 can be used for further study, with no risk of missing information.

Fig. 9 shows a CHI for a Mg-Co-V ceramic that is not planar, so that projections of the CHI must be used with care. The left view might suggest a planar shape much like the CHI in Fig. 8, but the rotated view shows that the cloud of points extends back to the origin as well as extending parallel to the Co axis.

The two- and three-dimensional CHIs are used with what we call the "traceback" function, where regions of points in the CHI are outlined and the corresponding pixels in the original maps are highlighted. To outline a region in three dimensions, a closed region is drawn with a mouse on a two-dimensional projection. This loop defines a cylinder extending back along the line of sight. When outlining in this way, rotation helps to select the best viewpoint, so that there are few points that appear to be in the outlined cluster that are really distant along the line of sight.

4-D Image Sequence. Four-dimensional CHIs are rendered by showing a sequence of three-dimensional CHIs corresponding to a threshold steadily moving along the fourth CHI axis. The clustering of bins along this axis stands out in the animation, but it is also evident after study of the mosaic in Fig. 10.

Palette Manipulation for Displaying Volcano Plot

The palette on most common display devices has 256 entries. Each entry specifies the brightness level for red, green, and blue, and therefore the color, for one numeric value of the 8-bit pixels in the display memory. With NIH IMAGE, the palette in the Macintosh can be stretched or shifted in real time, and the resulting contrast enhancement of the image can be observed simultaneously. With a palette that can be shifted, images of the direction of the gradient⁴ can be displayed in a more flexible and simpler way than by showing specially processed⁴ images but with a normal palette.

The direction of the gradient (volcano plot) is useful for such things as visualizing objects (or edges of objects) with low brightness in the presence of objects with high brightness. Figure 11 shows an ion microscope barium image of particles, with blooming due to various components in the imaging system. Signal from bright pixels bleeds into neighboring pixels that would otherwise be background. (Better imaging systems that reduce blooming are now available.) The particles gradually fade out so that it is difficult to tell what regions of the image represent background. The volcano plot shows the background regions clearly.

Initially, the volcano plot has values ranging from 0° to 360° . Since the pixel values in such a plot represent direction or angle, a gray ramp would not be a reasonable representation because 0° and 360° , which would be displayed as black and white, are really the same direction. A palette that varies smoothly and that gives 0° and 360° the same brightness

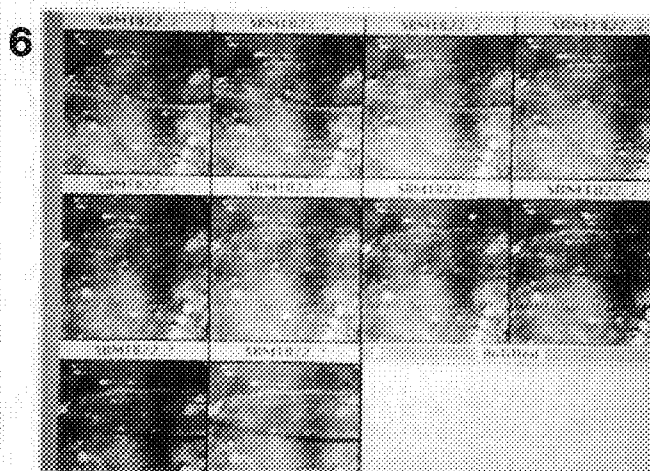
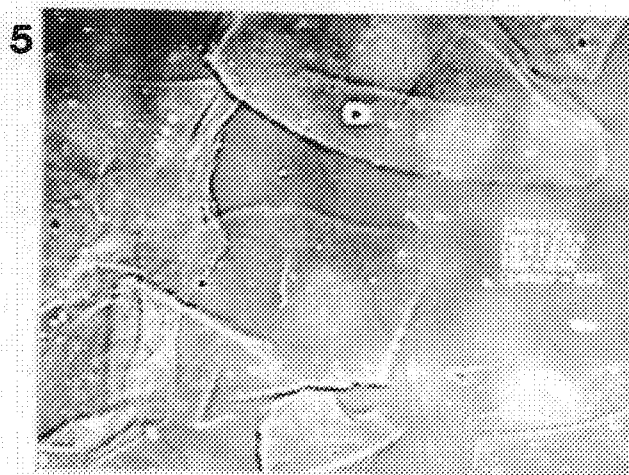
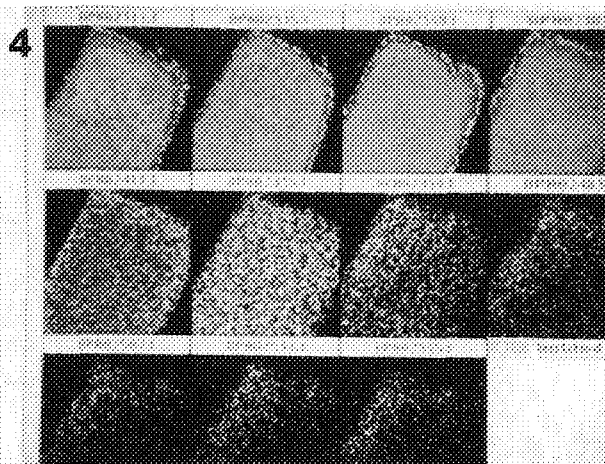
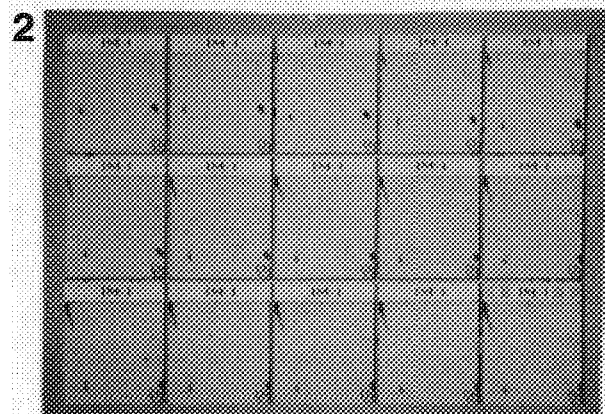


FIG. 1.--Electron micrograph of particles, analytical electron microscope, STEM mode, 50µm field width. Particles used to mark stage position.

FIG. 2.--Mosaic of time series of images. Only upper left part of each image shown.

FIG. 3.--Superposition of frames in Fig. 2. Motion seen as downwards and to right.

FIG. 4.--Mosaic of representative frames in a 60-image sequence. Ba-Y-Cu ceramic superconductor single crystal, ion microscope, O^{18} image, resistive anode encoder detector. Image width 250 µm. About 50 Å depth increment between frames in this mosaic. Image pseudocolored before black-and-white photograph to improve contrast between signal levels. Images courtesy of Greg Gillen, Microanalysis Group, Center for Analytical Chemistry, NIST.

FIG. 5.--Transmission light micrograph of glass fragments (approximately 2 mm across) in an index matching fluid. Image width 5 mm. Micrographs taken by Eric Steel, Microanalysis Group, Center for Analytical Chemistry, NIST.

FIG. 6.--Mosaic of series of frames like Fig. 5; only upper left part shown.

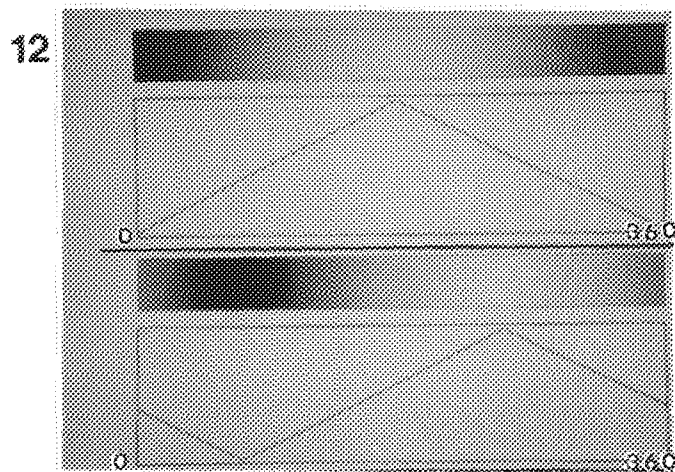
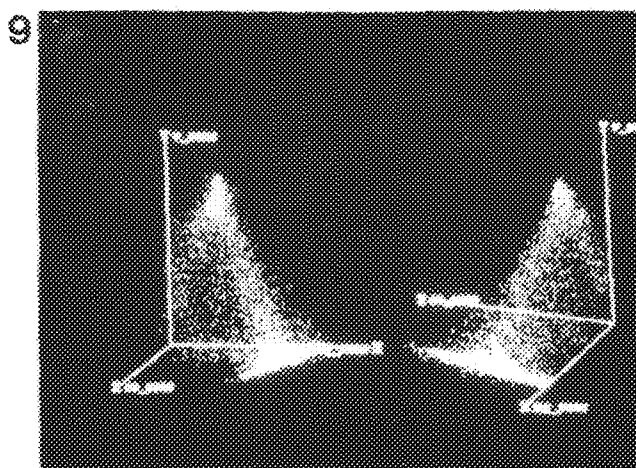
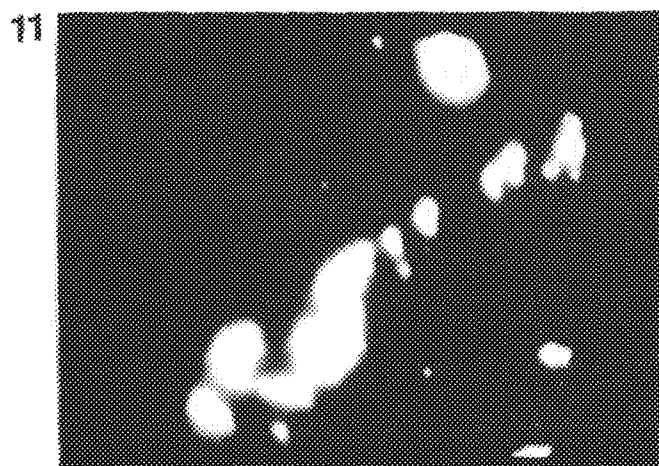
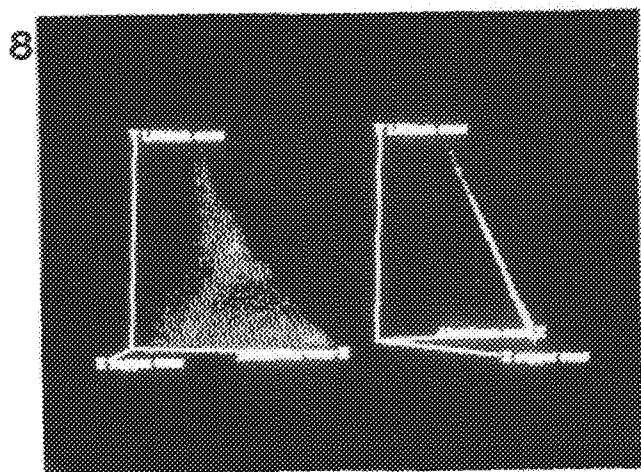
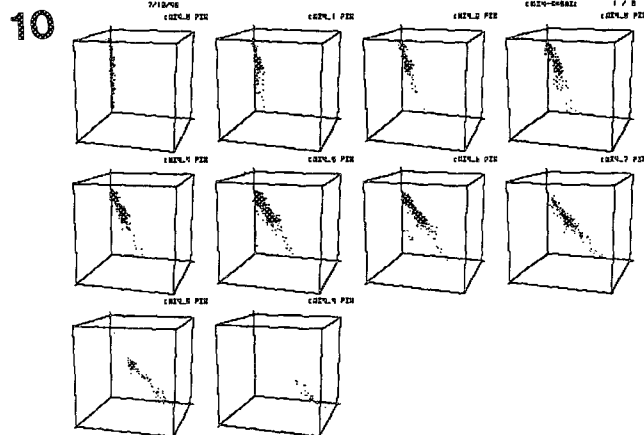
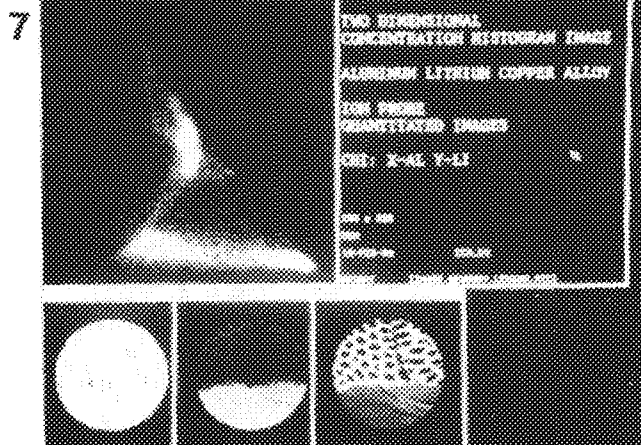


FIG. 7.--Example of two-dimensional CHI, Al-Li-Cu alloy: x axis, Al (0-80 at.%); y axis, Li (0-50 at.%) Projection of planar three-dimensional CHI (Fig. 8). Ion microscope images along bottom; Al, Li, Cu: 150 μ m field width.

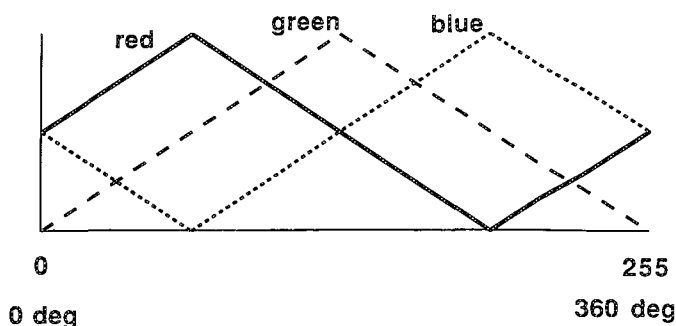
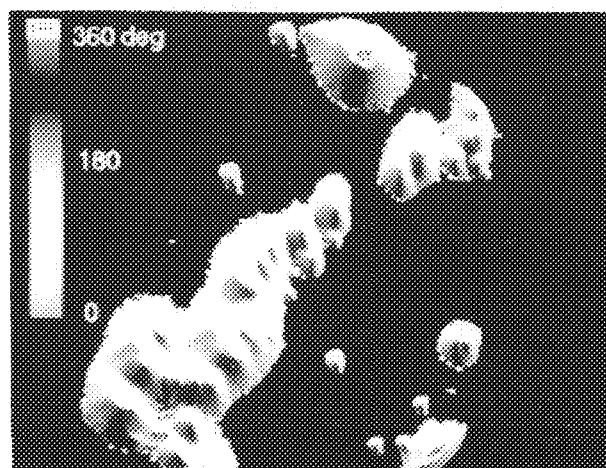
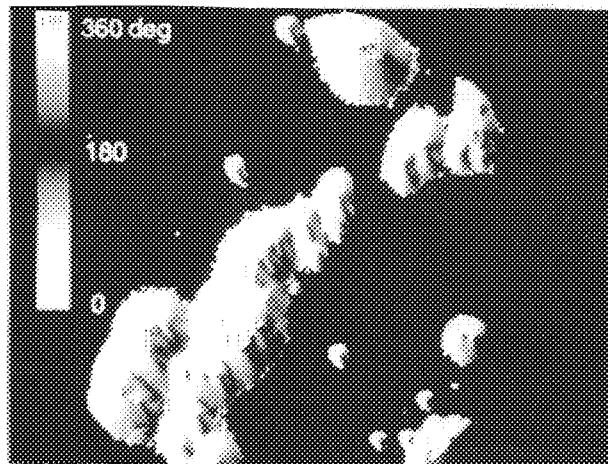
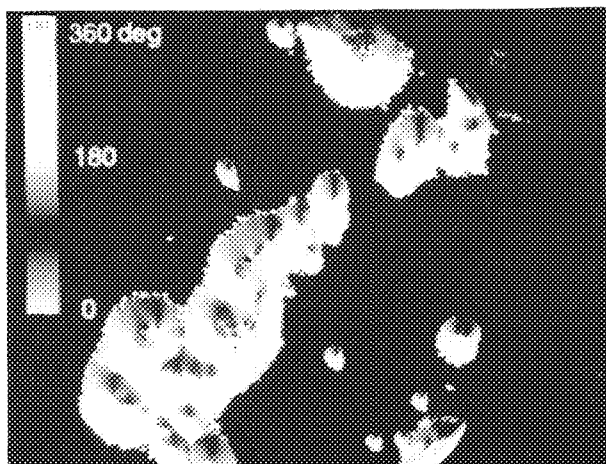
FIG. 8.--Three-dimensional CHI, Al-Li-Cu alloy, two views. CHI is planar.

FIG. 9.--Three-dimensional CHI, Mg-Co-V ceramic, two views. CHI is not planar.

FIG. 10.--Four-dimensional CHI, Raney Nickel; horizontal axes, 2 background regions of EDS spectrum; vertical axis, Al. Three-dimensional CHIs sequenced along Ni axis.

FIG. 11.--Ion microscope barium image of particles. Blooming caused by imaging system. 150 μ m field.

FIG. 12.--Palette diagrams for display of volcano plot. One palette shifted with respect to other. Upper gray level bands show display intensity. Graphs below them show display intensity (0-255) vs pixel value (0-255).



FIGS. 13-15.--Volcano plots showing direction of gradient for Fig. 11, using palette in Fig. 12 shifted by various amounts. Band at left shows palette.
FIG. 16.--Palette diagram for color display of volcano plot.

is shown in Fig. 12, top. Figure 12, bottom, shows a shifted version of the same palette. Figures 13, 14, and 15 show the volcano plot with the palette shifted various amounts. The effect of shifting the pallet is to change the apparent illumination direction.

Reading of angles from the image by use of the gray scale can be ambiguous because of the two gray ramps back to back that cover different ranges of angle. If the ambiguity should be a problem, ramping the red, green, and blue colors separately, as in Fig. 16, removes the ambiguity and has the effect of illuminating the peaks with red, green, and blue lights spread 120° apart.

Conclusion

Special purpose real time image processing tools available for the Macintosh along with computer networking for image transfer, help solve image analysis problems. The tools can animate image sequences, display and rotate three-dimensional graphics, and manipulate the palette. The tools save time: it took longer to make the illustrations than it took to use the tools to explore the problems.

References

1. D. S. Bright, "A Lisp-based Image Analysis with Applications to Microscopy," *J. Microscopy* 148(Pt. 1):51-87, 1987.
2. R. R. O'Neill, L. G. Mitchell, C. R. Merrill, and W. S. Rasband, "Use of image analysis to quantitate changes in form of mitochondrial DNA after x-irradiation," *Applied and Theoretical Electrophoresis* 1: 163-167, 1989.
3. W. Rasband, NIH IMAGE: An image processing software package for the Macintosh II. Available free of charge from Wayne Rasband, NIH, Bldg. 36, Rm. 2A03, Bethesda, MD 20892.
4. A. W. Donoho, and C. W. Olson, MacSpin V. 2.0, Graphical Data Analysis Software, D² Software, Inc., Box 9545, Austin, TX 78766-9546.
5. National Center for Supercomputing Applications, University of Illinois, NCSA Software Development-PalEdit, 152 Computing Applications Bldg., 605 E. Springfield Ave., Champaign, IL 61820.
6. D. S. Bright, D. E. Newbury, and R. B. Marinenko, "Concentration-Concentration Histograms: Scatter diagrams applied to quantitative compositional maps," *Microbeam Analysis--1988*, 18-24.

7. R. Browning, "New methods for image collection and analysis in scanning Auger microscopy," *J. Vac. Sci. Technol.* A3(3): 1959-1964, 1985.

8. R. Browning, "Materials analysis by scanning Auger microscopy: Why the information crunch is needed," *Microbeam Analysis--1987*, 311-316.

HIGH-PURITY GERMANIUM DETECTORS FOR EDS

J. J. McCarthy, M. W. Ales, and D. J. McMillan

High-purity germanium (HPGe) detectors offer multiple advantages for x-ray microanalysis in electron microscopes. These advantages include improved detector efficiency at photon energies above 20 keV and higher energy resolution than can be obtained with a lithium drifted silicon detector [Si(Li)]. In the past, the use of HPGe detectors for energy-dispersive spectroscopy (EDS) at photon energies below about 2 keV was impossible due to severe distortions of peak shapes and large shifts in peak positions. These effects are the result of incomplete charge collection and are most pronounced at energies just above the energy of the germanium L absorption edges (1.2 to 1.4 keV).¹⁻³ Using new processing techniques, we have manufactured 30mm² HPGe detectors that do not exhibit significant spectral peak distortion from incomplete charge collection. These detectors have been used for EDS applications in transmission electron microscopy (TEM) and scanning electron microscopy (SEM). In this paper we review the properties of these detectors and comment on their use for microanalysis.

HPGe Detector Performance

Several factors contribute to peak shape and resolution of HPGe detectors. The shape of the peak is primarily distorted by the effect of incomplete charge collection in the detector. The major causes attributed to incomplete charge collection are trapping of charge carriers in the bulk material of the sensitive volume or at the surfaces of the detector. In particular, the front surface with its associated "dead layer" (a region of minimal charge collection) was thought to be the limiting factor in previous HPGe detectors. These phenomena are also present in Si(Li) detectors. Several measurements have been adopted that indicate quality of the charge collection in a detector. These measurements include the ratio of full-width-tenth-maximum (FWTM) to the full-width-half-maximum (FWHM), the statistical broadening or dispersion (D) of spectral peaks (measured peak resolution (FWHM) less the electronic noise subtracted in quadrature), peak-to-background ratios, and estimates of the dead-layer thickness. The resolution of a peak is determined by the dispersion D and the electronic noise of the entire spectrometer. D is defined by

$$D = \sqrt{5.52F\epsilon E}$$

where E is the energy of the peak, F is the Fano factor, and ϵ is the mean number of elec-

tron-hole pairs produced per unit energy.

Given that the Fano factor has been shown to be roughly equal for Ge and Si,⁴ and that ϵ_{Ge} is 27% less than ϵ_{Si} , the resolution of an HPGe detector is better than the resolution of a Si(Li) detector. The difference in ϵ also leads to improved signal-to-noise ratio for HPGe, which reduces the noise linewidth. These predictions are confirmed by measurements on actual devices. In detectors we have produced to date, these factors have led to typical resolutions at Mn in the range ($\pm 1\sigma$) of 127 eV to 137 eV for a 30mm² detector which employs a standard FET in the head amplifier. Resolutions as low as 122 eV have been achieved. This resolution is 10 to 20 eV better than premium Si(Li) detectors of the same size.

Figure 1 presents a comparison of the peak shapes obtained from an HPGe detector produced by a previous method and a new detector produced with our current process. The data in this figure were collected with a small portable source-excited x-ray fluorescence system (XRF) in order to obtain peak profiles with minimum background. During these experiments the same detector cryostat was used and only the detecting element changed. Figure 1(a) presents a series of peaks, collected with a detector produced by the prior techniques, that approach the energy of the Ge L edge from the high side. The distortion increases as the edge energy is approached until it would be difficult to resolve the adjacent Al and Si peaks in a spectrum containing both. Figure 1(b) presents the same peaks collected with an improved detector. These peaks exhibit symmetrical shapes and peak centroids at the proper position. Figure 1(c) compares Al peak shapes for the two detectors. The theoretical FWTM/FWHM ratio for a Gaussian peak shape is 1.82. The FWTM/FWHM for the Al peak from the improved detector is 1.89, which indicates a nearly Gaussian shape.

We have also made measurements of dispersion, FWTM/FWHM, and dead layers to characterize the charge collection of these devices. Table 1 summarizes measurements of charge-collection-related quantities for both a HPGe and a Si(Li) detector. Both devices were 30 mm² in area; the HPGe device was 4 mm thick, the Si(Li) device 3 mm thick. Both detectors exhibit Gaussian peak shapes as indicated by the FWTM/FWHM ratios. The dispersion values indicate Fano factors in the range of 0.11 for both detectors, in good agreement with values cited by other researchers.^{3,4} The values for the HPGe detector are equal to or less than those for the Si(Li), in general agreement with the predictions made above. As a result, for equal

The authors are at Tracor Northern, Inc.,
2551 West Beltline Highway, Middleton, WI
53562.

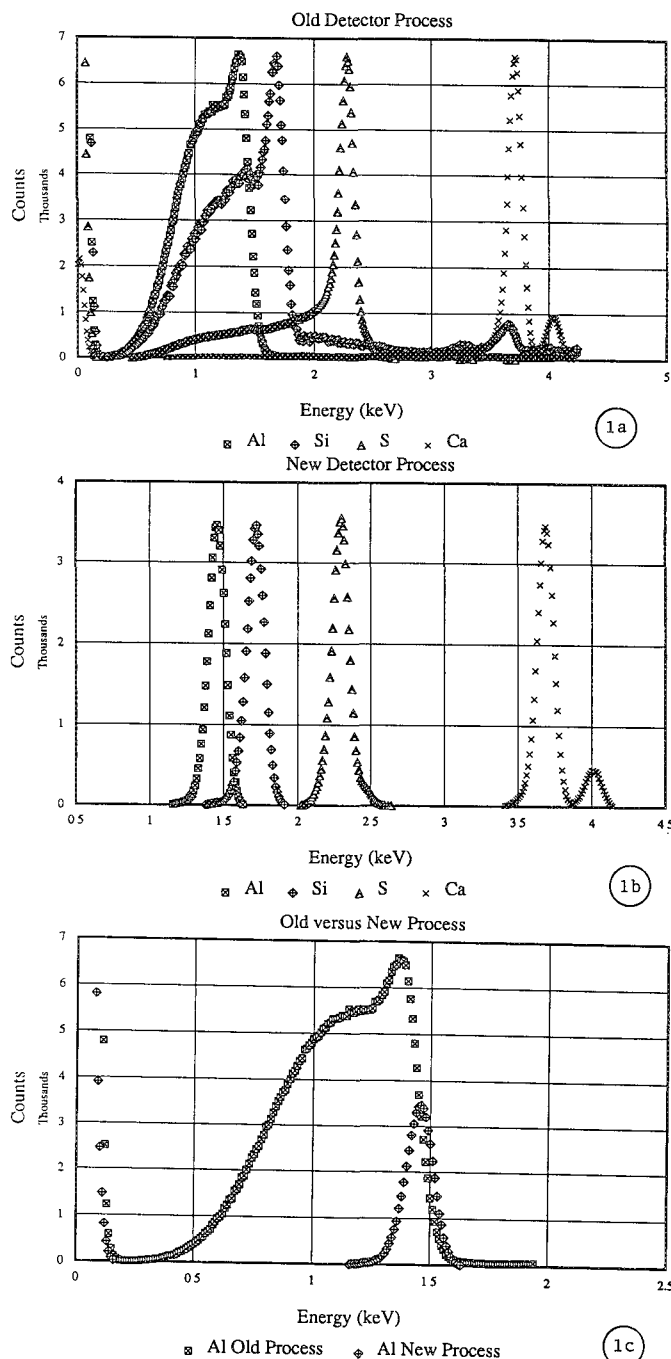


FIG. 1.--Comparison of peak shaped of Al, Si, S, and Ca. Detector fabricated by (a) previous methods, (b) new process. Peak distortions increase as energy of peak approaches energy of Ge L edge. In (b) peaks are symmetrical and at proper energy in spectra from new detector. Figure 1(c) compares only Al peaks from both detectors. All peaks have been arbitrarily scaled to provide better visual comparison and peak height is not related to detector performance.

TABLE 1.--Comparison of charge collection properties for premium 30mm² HPGe and Si(Li) detectors. (Td is the measured dead layer thickness for a single device.)

device.)

	HPGe			Si		
Parameter	C	Na	Mn	C	Na	Mn
FWTM/FWHM	1.84	1.87	1.85	1.84	1.84	1.85
Dispersion (eV)	39.5	53.4	105.6	68.0	51.9	119.6
FWHM @ 60 eV noise width	72	80	121	92	79	134
FWHM @ 75 eV noise width	85	92	130	102	91	141
P/B @ 1 keV	6500:1 to 14000:1			4000:1 to 8000:1		
Td (μm)	0.12 ± 0.02			0.20 ± 0.03		

contributions from electronic noise, the HPGe detector provides superior peak resolution. The impact of this improvement on microanalysis is discussed below. The Na values for HPGe are elevated due to the proximity of the Ge L edge. We have observed increases of the FWTM/ FWHM ratio and D of the order of 10% in the vicinity of absorption edges in both HPGe and Si(Li) detectors. Such increases can lead to slight peak tails and modest shifts of peak centroids to lower energies.

The higher stopping power of germanium leads to increased detection efficiency relative to silicon at x-ray energies above about 20 keV. This improvement is illustrated in Fig. 2, based on 3mm-thick detectors. In the 50-80keV range, germanium is more than 5 times as efficient as silicon. In addition, because of increased absorption the HPGe detector has a much smaller background from Compton-scattered photons of high energy lines that enter the detector, which leads to improved detection sensitivity at low energies. These properties have been compared for HPGe and Si(Li) by use of an Am²⁴¹ source mounted in a fixed configuration on the end of the detector tube. In order to minimize geometric changes, the two devices were swapped into the same cryostat assembly. The result is shown in Figs. 3 and 4. Figure 3 compares the peaks due to the 59.5keV gamma line. The measured peak ratio improvement of the 59.5keV line relative to the 26.4keV gamma line is 9.7, which is even better than the computed improvement value of 8.8. The difference may be caused by errors in mass absorption coefficients. Figure 4 displays the lower-energy portion of the same spectrum and illustrates the reduced Compton background in the HPGe detector. The ratio of backgrounds at 2.5 keV is roughly 10:1.

Considerations for Microanalysis

Extended Energy Range. The high-energy photon detection efficiency and the improved dispersion discussed above suggest that the HPGe detector should be preferred in TEM applica-

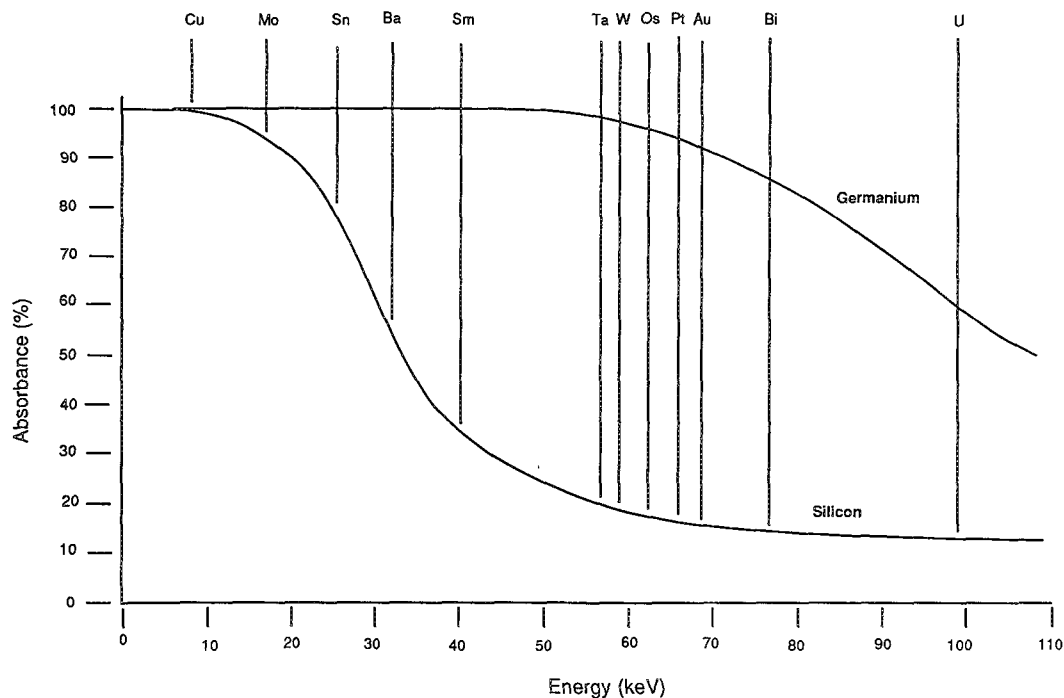


FIG. 2.--Photon absorption in % of 3mm-thick slices of silicon and germanium. Energies of $K\alpha$ lines for select elements are indicated by vertical bars.

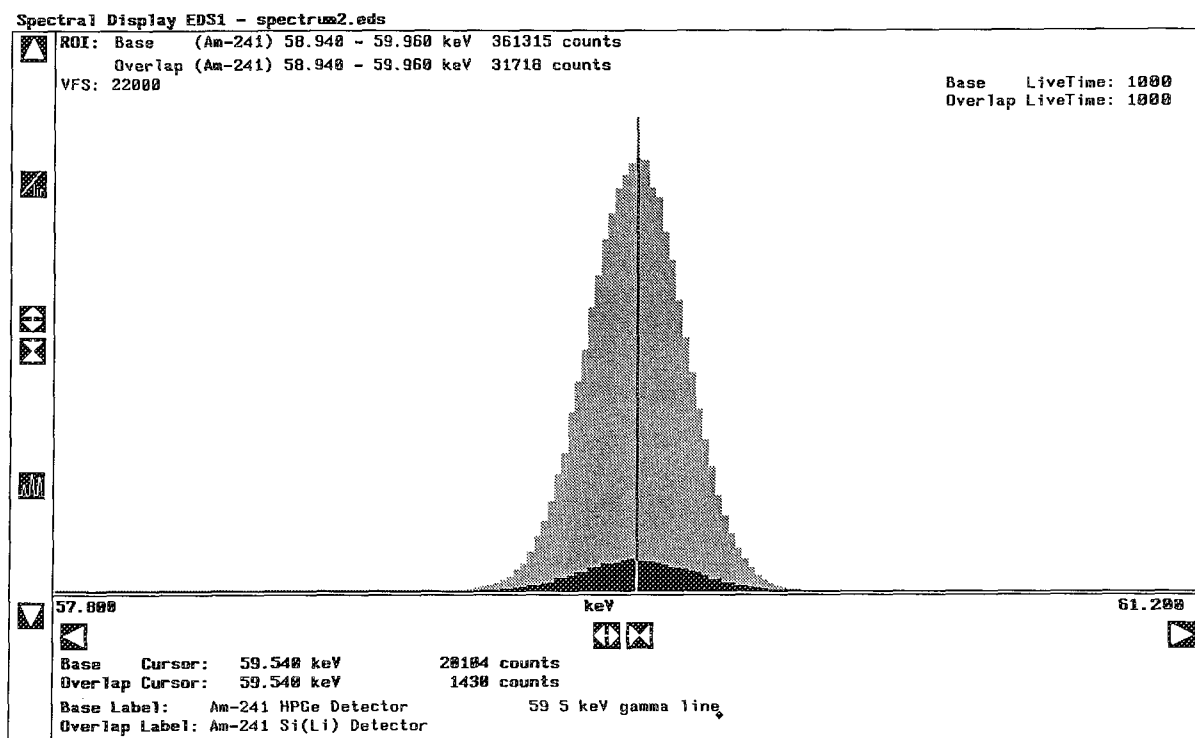


FIG. 3.--Comparison of 59.6keV peaks from HPGc (gray) and Si(Li) (black) detectors. Spectra were produced by Am^{241} source. Identical excitation conditions were obtained by swapping of detector crystals into the same spectrometer housing. Am^{241} source was attached to spectrometer so as to yield reproducible geometry for excitation.

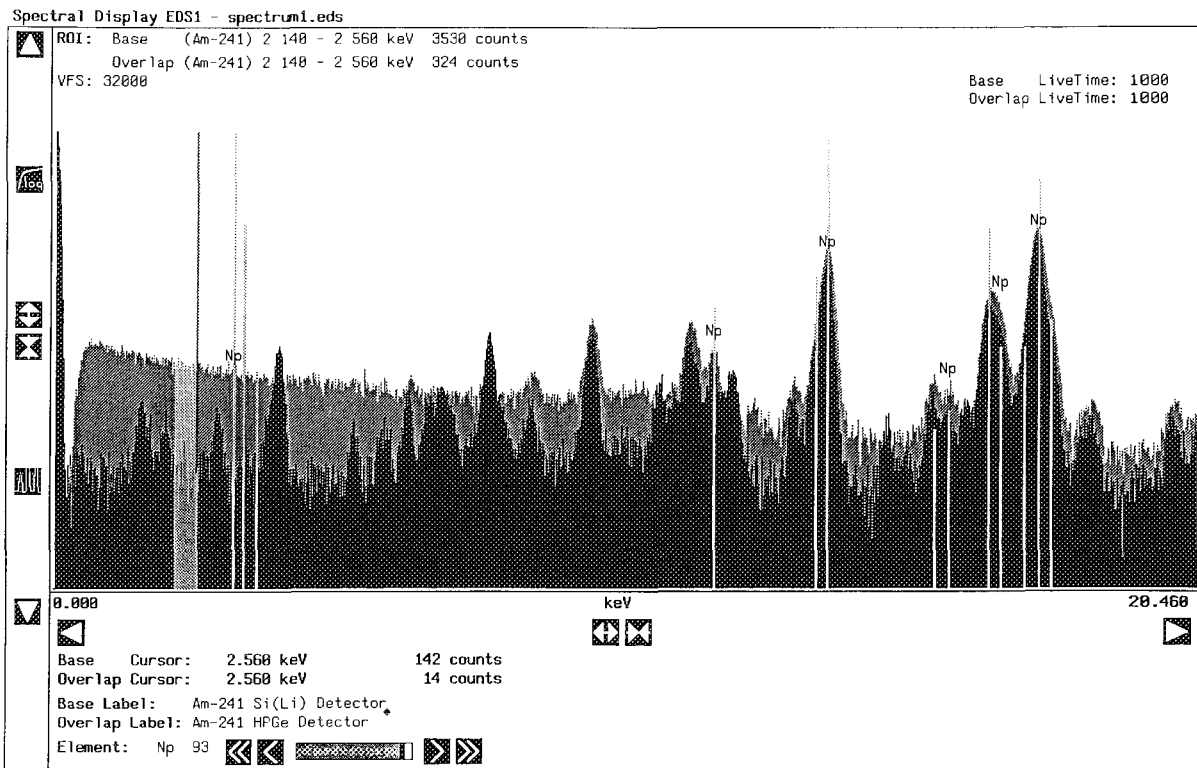


FIG. 4.--Comparison of low-energy spectrum from an HPGe detector (black) with same spectrum from Si(Li) detector (gray) collected under the conditions given in Fig. 3. Background from Compton scattering of high-energy lines in HPGe spectrum is about one-tenth that in Si(Li) spectrum.

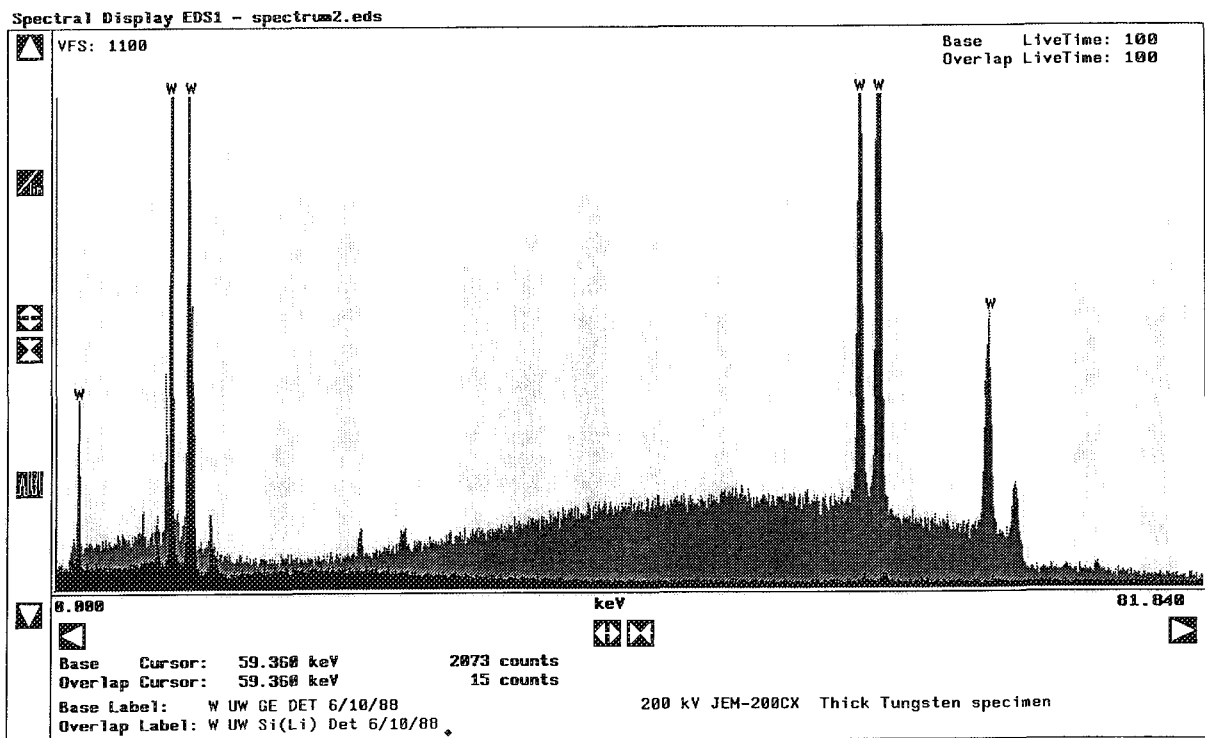


FIG. 5.--Comparison of W spectrum from HPGe (gray) and Si(Li) (black) detector collected under similar conditions on the same TEM. Specimen was relatively thick and HPGe spectrum clearly shows broad background below W K lines due to Compton scattering of photons in specimen.

tions. Figure 5 presents a comparison of the spectra from a relatively thick W specimen collected on the same 200kV TEM with HPGe and Si(Li) detectors under similar excitation conditions. The two spectra were normalized at the W L α peaks. The W K α and K β lines are well resolved and prominent in the HPGe spectrum, but barely visible in the Si(Li) spectrum. In addition, the large shoulder (due to Compton scattering in the specimen) below the K-lines is prominent in the HPGe spectrum, but is only weakly seen at much lower energy in the Si(Li) spectrum.

Escape Peak Removal. Due to the Ge K edge at 11.103 keV, the escape peaks from higher-energy lines can complicate analysis of the low-energy spectrum. A current example is the analysis of the yttrium barium copper superconductors. The K escape peaks from Y appear right in the midst of the Ba L lines! Unfortunately the commonly used channel-by-channel escape peak removal algorithms employed to the Si(Li) detector may fail when applied to Ge escape peaks, because the large energy separation from the main peak leads to a difference in resolution such that simple subtraction leaves prominent residuals in the spectrum if the escape peak is large. We have found that the straightforward inclusion of fitting references for the escape peaks can be used to fit and remove peaks for spectral analysis. Work is under way to develop a more automatic means of removing escape peaks.

Improved Detection Limits. As illustrated above, the lower dispersion of the HPGe detector leads to improved peak resolution values over those from a Si(Li) detector. In devices we have made to date, that is particularly true for low-Z elements, where the dispersion of the Si(Li) detector is increased due to dead layer and proximity to the Si L edge. It can be shown that improved resolution leads directly to lower elemental detection limits, which results in enhanced detection sensitivity in cases of overlapped peaks, or when the relative peak heights are significantly different. This correspondence is easily established by consideration of the expression of Ziebold,⁵ which estimates the minimum detectable concentration of an element in a given specimen to be

$$C_{DL} = 3.29\alpha / [(P/B)Pt]^{1/2}$$

where P/B is the peak-to-background ratio, P is the peak intensity in counts per second per nA, t is the total counting time in seconds, and the parameter α depends on the specimen composition. For a given beam current and counting time, the factor $F_{DL} = 1/[(P/B)Pt]^{1/2}$ can be used to compare two detectors. Two important conclusions can be immediately drawn from this equation.

First, since the P/B ratio increases as peak resolution decreases (FWHM), the detection limit decreases as the FWHM decreases. Since the resolution of an HPGe device is generally better than that of an Si(Li) of the same size,

TABLE 2.--Comparison of C_{DL} for overlapped peak vs peak FWHM for two values of relative peak height. Calculations assume a fixed peak separation of 100 eV and a P/B ratio of 20:1.

FWHM (eV)	Overlap Factor	F_{DL} Peak Ratio (1:1)	F_{DL} Peak Ratio (10:1)
80	.039	.298/ \sqrt{P}	.67/ \sqrt{P}
100	.119	.408/ \sqrt{P}	1.114/ \sqrt{P}
$C_{DL}^{80} / C_{DL}^{100}$		1.37	1.67

better detection limits will be the rule with HPGe, particularly for light elements, and especially in a TEM, considering the reduction in Compton scattering background at low energies. For a 20% improvement in FWHM, an improvement in C_{DL} of about 10% is expected. Although an exact calculation is difficult, an approximation of the impact of overlaps can be calculated from a few assumptions and calculations of peak overlap factors, as suggested by Statham and Nashashibi.⁶ We have calculated the relative change in detection limit as a function of FWHM and peak-to-peak ratio from the Ziebold equation assuming a P/B ratio of 20:1 and a fixed peak separation of 100 eV (Table 2). For a 10:1 peak ratio, C_{DL} for the smaller peak is decreased by a factor of 1.7 for a 20% change in FWHM. This is an idealized case, and one should expect that actual spectral measurements may not show such a large improvement in the detection limit.

The second conclusion, from Table 1, is that the same resolution can be obtained from a 30mm² HPGe as from the best premium 10mm² Si(Li). It follows that for the same beam current and counting time, the 30mm² HPGe provides a C_{DL}^{Si} that is 1.73 times lower than C_{DL}^{Si} from the 10mm² Si(Li) detector! Alternately, the beam current may be reduced on sensitive specimens by the same factor, with no sacrifice of analytical sensitivity.

These results present a strong argument for the use of HPGe detectors on SEMs as well as TEMs. Figure 6 is an example of the excellent performance of an HPGe detector for light-element detection. The spectrum was obtained from a unit installed in the field on a JSM 6400. The noise peak has been suppressed by setting the threshold discriminator. The detector was equipped with a diamond thin window and shows good nitrogen sensitivity. Detector resolution at Mn was measured to be 130 eV. The peak-to-valley ratio for boron measured at the factory was 13:1 for this detector.

Conclusions

HPGe detectors with improved charge collection properties offer several advantages over Si(Li) detectors for EDS applications. The HPGe detector offers improved detection efficiency at photon energies above 20 keV, and also provides reduced background at lower ener-

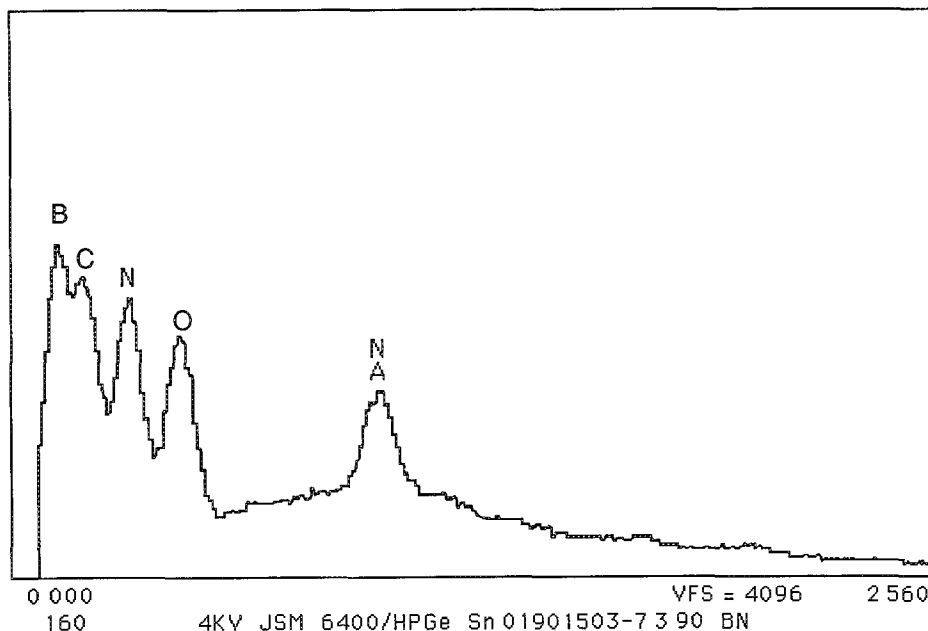


FIG. 6.--SEM spectrum illustrating excellent peak resolution and detection sensitivity of HPGe detector with 1 at. diamond window. Noise peak at zero energy has been suppressed with threshold setting. At the factory, resolution at Mn was measured at 130 eV and a boron peak-to-valley of 13:1 was obtained.

gies from Compton-scattered radiation. These properties alone suggest that the HPGe detector may become the preferred x-ray detector for TEM where good light-element resolution and high detection efficiency at higher x-ray energies are required. The improvement in peak resolution offered by the HPGe detector enhances elemental detection sensitivity in both SEM and TEM applications, by lowering detection limits and allowing larger solid angle detectors to be used with no resolution penalty. As a result, we expect that in the future the HPGe detector will be used in a broad range of microanalysis applications.

References

1. J. Llacer et al., "Entrance windows in germanium low-energy x-ray detectors," *IEEE Trans. NS-24*: 53-60, 1977.
2. N. C. Barbi and D. B. Lister, *A Comparison of Silicon and Germanium X-ray Detectors*, NBS Spec. Publ. 604, 1981, 35.
3. C. E. Cox et al., "Small area high purity germanium detectors for use in the energy range 100 eV to 100 keV," *IEEE Trans. NS-35*: 28-32, 1988.
4. R. W. Fink, *Properties of Silicon and Germanium Semiconductor Detectors for X-ray Spectrometry*, NBS Spec. Publ. 604, 1981, 5.
5. T. O. Ziebold, "Precision and sensitivity in electron microprobe analysis," *Anal. Chem.* 39: 858, 1967.
6. P. J. Statham and T. Nashashibi, "The impact of low-noise design on x-ray microanalytical performance," *Microbeam Analysis--1988*, 50.

RESOLUTION ENHANCEMENT FOR X-RAY SPECTROSCOPY AT LOW ENERGIES

P. J. Statham

Interpretation of the low-energy x-ray spectrum below 1 keV is complicated by a number of factors that can be regarded either as causes of error or as potential sources of new information about the sample. Chemical bonding effects produce line energy shifts of a few eV and band shape changes over as much as 15 eV. L series lines separated by a few tens of eV are often subject to severe differential absorption in the sample; furthermore, tabulated line-intensity ratios are often not adequate to provide conclusive identification of a particular emission. For a typical EDX system with 145eV resolution at 5.9 keV, these effects will only be seen as subtle changes in the form of the spectrum, whereas a Bragg crystal spectrometer (WDX) can resolve most of the detail. EDX has the advantage of increased efficiency that is more reproducible and predictable as a function of energy, and for most routine applications, the resolution limitation has traditionally been overcome by data processing. Therefore, an interesting question to pose is thus "is there any way we can dramatically improve EDX resolution to enable investigation of the precise form of spectra at low energies?"

Instrumental Improvements

The detector response function due to the Si(Li) crystal is further degraded by electronic noise. Thus, monochromatic radiation of energy E keV produces a peak with full width at half maximum (FWHM) "resolution" given by

$$\text{fwhm}^2 = \text{fwhm}_0^2 + \text{fwhm}_d^2 \quad (1)$$

where fwhm_0 is due to electronic noise and fwhm_d the detector contribution in eV. The noise distribution is Gaussian and in most Si(Li) detectors, for energies above about 4 keV, the detector contribution is also Gaussian, with $\text{fwhm}_d = 2550\text{E}$. Incomplete charge collection may occur, particularly for x rays that are absorbed strongly in silicon and therefore liberate charge closer to the front surface of the detector. As a result, the fwhm may be broadened beyond 2550E and additional tailing may make the detector contribution markedly non-Gaussian at low energies.

Recent developments¹ have pushed the attainable fwhm_0 as low as 41 eV. For example, Fig. 1(a) shows the sulfur L1 line clearly visible in a system where $\text{fwhm}_0 = 41$ eV. Not only does S Li not usually appear on EDX "slide rules," but the intensity is sufficient to cause problems of interpretation and overlap with Be, B, and C.

P. J. Statham is with Link Analytical Ltd, Halifax Road, High Wycombe, Bucks, England HP12 3SE.

Figure 1(b) shows that the same system can resolve Be K clearly from the noise tail. Indeed, if there were no electronic noise, Eq. (1) would suggest that we could see a Be peak with fwhm of only 16 eV.

Digital Filtering

Clearly, reduction of electronic noise fwhm_0 is a practical way of improving low-energy resolution, but we can attempt to go further by digital filtering. If we consider the digital Fourier transform (DFT) of the data we find that any slowly varying background contributes most of the low frequencies, peaks include higher frequency components, and statistical fluctuations have components at all frequencies. Convolution by a Gaussian instrumental function is equivalent to attenuating high-frequency components. Unfortunately, reversing this process accentuates the high-frequency statistical components, so that a compromise is involved between resolution enhancement and increasing amplitude of statistical artifacts. We can experiment to our heart's content with various types of linear filter (many of them reviewed in Ref. 2, including equivalent iterative techniques) but it is possible to calculate what is the best we can hope to achieve by such methods. For an x-ray energy histogram, the coefficients of a real filter that will provide the best possible restoration in a least-sum-of-squares sense are given by

$$H_k = (1/G_k) |S_k|^2 / (|S_k|^2 + N_0) \quad (2)$$

where G_k represents the DFT of the instrument function; S_k is the transform of the data if there were no statistical fluctuations; and N_0 is expectation of the noise power, which can be shown to be equal to the area in counts of the spectral data. (A full derivation is given in Ref. 3.) If we have only one set of data to work from, we can only estimate S_k , but one can achieve a close to optimal result by scanning the power spectrum and fitting a Gaussian function to the region where the signal dominates.³

Limitations of Linear Methods

The fundamental problem with all linear methods is that they do not separate statistical fluctuations from the data; they only attenuate the highest frequencies where the signal is weak. After the filter is applied, all the low-frequency components of statistical noise still remain "interwoven" with low-frequency signal components. Furthermore, what was formerly "white noise" is molded by the filter into peak-like artifacts and any attempt to enhance the resolution simply exaggerates

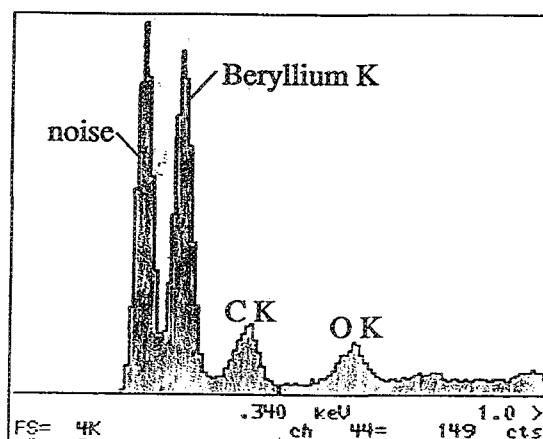
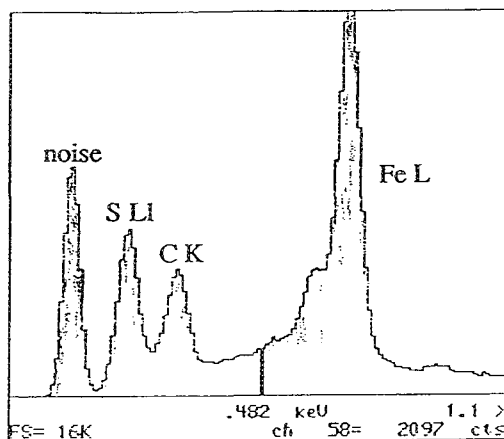


FIG. 1.--EDX spectra for a system with noise fwhm = 41 eV. (a) Carbon-coated iron sulphide specimen, SEM, 5 kV. (b) Be foil, SEM, 10 kV.

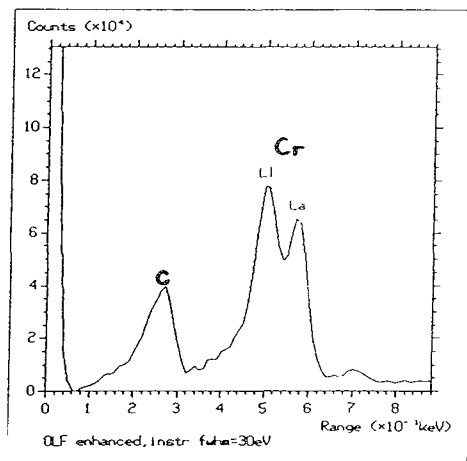
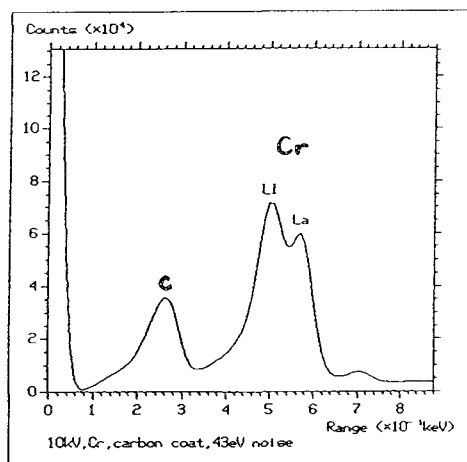


FIG. 2.--(a) EDX spectrum from carbon-coated chromium specimen, SEM, 10 kV. Noise fwhm = 43 eV. (b) Data from 2(a) processed with estimate of optimal linear filter, enhanced according to instrumental function, fwhm = 30 eV

these spurious ripples. This limitation is demonstrated by Fig. 2, which shows the results of optimum linear enhancement. Although the Cr L peaks in Fig. 2(b) are better resolved, the effective gain in resolution is slight. Attempts to deconvolve further with an instrument function of 40eV fwhm simply produce much greater ripple artifacts. Although increasing the number of counts could improve the signal-to-noise ratio and allow more sharpening before ripples become objectionable, theoretical calculations for a wide range of conditions suggest that such gains are slight³; for example, even with 10^6 counts in a single peak, about 20% improvement is the most we can achieve if spurious ripples are to be kept below 1%.³ To do any better, we have to look toward nonlinear procedures and carefully analyze the deconvolution process.

Nonlinear and Maximum Entropy Methods

If channel i contains y_i counts, deconvolution involves seeking a solution s which, when convolved with an instrumental function g , represents the original data to within a residual r which is consistent with the expected statistical fluctuation. In shorthand notation we have for each channel i

$$y_i = (g * s)_i + r_i \quad (3)$$

where the $*$ represents the convolution operation. In linear methods, s has to be obtained by filtering of the original data vector y , but nonlinear methods release this restriction and a wide variety of techniques can be used to select a suitable solution s . Many of these techniques are reviewed by Jansson,² but perhaps the best known are the so-called "maximum entropy" techniques. If we divide s_i by the total of s_j over all channels, we get a normalized value p_i . One approach is to define an entropy expression,

$$H = - \sum_i p_i \ln p_i \quad (4)$$

and use a numerical search procedure to find the solution s_i , which gives the maximum value of H , subject to the constraint that the resid-

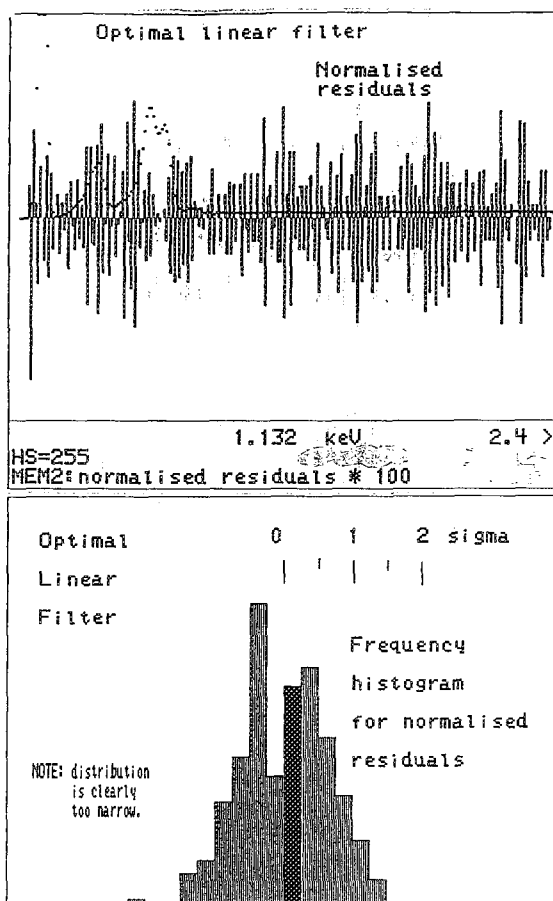


FIG. 3.--Result of convolving 2(b) with a Gaussian fwhm = 30 eV, subtracting from 2(a) and scaling by the square root of this result. (a) scaled residuals, full scale ± 2.5 . (b) Histogram showing frequencies of amplitudes.

duals r_i are consistent with the data. For example, if $y_i > 10$, the variance in channel count is close to y_i , so we would expect the sum

$$\chi^2 = \sum_i r_i^2 / y_i \quad (5)$$

to obey a χ^2 statistic and take a value close to n , where n is the number of channels.

Within the constraints imposed by Eq. (5), maximization of H forces the search toward s_i values which are all positive and as close as possible to the same mean level; although this procedure favors a solution that is smooth, there is a tendency toward solutions with lower peaks and higher backgrounds than the ideal. Ponman⁴ demonstrates three further entropy expressions and shows how, based on exactly the same data, the characteristics of the solution s can be biased by the formula used for H . Thus, although there are some interesting arguments for ascribing physical significance to the entropy expression, they often hide the fact that seeking a solution with maximum entropy is simply a mathematical trick to inject some prior knowledge of the answer we really expect! Frieden² emphasizes that introducing such prior knowledge via some modification of the en-

tropy expression only produces a *tendency* toward a particular solution; the main influence still comes from the original data. Unfortunately, for x-ray data, statistical fluctuations reduce this controlling influence and permit a wide range of solutions that still give an acceptable value for χ^2 .

Nonlinear Least-squares Fitting

The problem of alternative solutions has also been demonstrated in nonlinear least-squares fitting.⁵ Even with good prior knowledge of peak shape and with low background levels, statistical noise can be sufficient to permit alternative solutions with radically different values for relative peak heights that produce equivalent "goodness of fit" by a criterion similar to Eq. (5).

Improved Statistical Tests

The χ^2 measure as given by Eq. (5) is a rather crude indication of the goodness of fit. If we ever found the true solution s , the scaled residuals $r_i / (g * s)_i^{0.5}$ would be distributed according to a normal distribution with zero mean and unity variance. Furthermore, they would be independent so that there would be no correlation, particularly between one channel and the next. Thus, we can improve the fitting constraint (i) by using a test such as χ^2 or Kolmogorov-Smirnov to confirm that scaled residuals are distributed appropriately; and (ii) by computing and testing the serial correlation coefficient SCC, using scaled residuals from pairs $r_i r_{i+1}$ of adjacent channels.⁶ A test very similar to the latter has been used to reveal systematic errors when fitting spectral peaks with modified Gaussians⁷ and the distribution test is clearly related to an "order statistic" which has also been reported.⁸

Experimental Verification

To illustrate how these tests can be useful, consider again the restoration in Fig. 2. Calculating from Eq. (5) gives $\chi^2/n = 0.4$ and the mean residual is -0.004 so we obviously have a good fit to the data. Even the histogram of residuals in 3(b) looks symmetric and Gaussian in appearance. However, when the scaled residuals are viewed in Fig. 3(a), it is clear that they are not wholly random and look more like modulated high-frequency oscillations. That is shown up by, SSC which takes a value of -0.76 , far below the minimum value of -0.12 which could be explained by statistics alone.⁶ Inspection of Fig. 3(b) shows that the residual distribution, though symmetric, is much narrower than would be expected for unity variance.

When the same tests are applied to the nonlinear fitting simulations, the "correct" solution gives $\chi^2/n = 1.08$ and $\text{SCC} = -0.22$, whereas we might expect values as low as -0.41 . The best fit solution (fit 3)⁵, which happens to give completely incorrect parameters, gives $\chi^2/n = 0.86$ and $\text{SCC} = -0.36$. Even though we

could not reject fit 3 on the basis of SCC alone, selection of the solution with the smallest absolute value of SCC does favor the correct solution over all the other fits, even though it gives the largest χ^2 !

Conclusion

Although this study has not produced a method for guaranteeing satisfactory resolution enhancement, it has revealed a better method of assessing whether a given solution is realistic. In future, the following recipe can be adopted:

- a. Select a possible solution s to represent the true underlying spectrum.
- b. Convolve s with a Gaussian fwhm_0 .
- c. If χ^2/n is less than 1 and SCC is large and negative, low-frequency statistical fluctuations are still likely to be present in the solution. If χ^2/n is greater than 1 and SCC is positive, there is evidence of systematic departure from the correct signal. If a choice of s is available, favor the solution with the smallest value of SCC provided χ^2/n is close to 1.

References

1. P. Statham and T. Nashashibi, *Microbeam Analysis--1988*, 50.
2. P. A. Jansson, Ed., *Deconvolution*, New York: Academic Press, 1984.
3. P. Statham, "Resolution enhancement of x-ray spectra," *Proc. 8th ICXOM*, Boston, 1977, 136.
4. T. J. Ponman, *Nucl. Instrum. & Meth.* 221: 72, 1984.
5. P. J. Statham, *X-ray Spectrometry* 7(3): 132, 1978.
6. D. E. Knuth, *Seminumerical Algorithms*, Reading, Mass.: Addison Wesley, 1969.
7. A. Aarnio et al., *Nucl. Instrum. & Meth.* 184: 487, 1981.
8. R. K. Bryan and J. Skilling, *Mon. Not. R. Ast. Soc.* 191: 69, 1980.

Microprobe Mass Spectrometry

COMPLEMENTARY MOLECULAR INFORMATION ON PHTHALOCYANINE COMPOUNDS DERIVED FROM LASER MICROPROBE MASS SPECTROMETRY AND MICRO-RAMAN SPECTROSCOPY

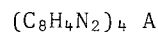
R. A. Fletcher, E. S. Etz, and Stephen Hoeft

In this work we show the complementary information about molecular structure provided by laser microprobe mass spectrometry (LAMMS) and micro-Raman spectroscopy. The vibrational frequencies observed in micro-Raman spectroscopy indicate molecular structure, whereas mass spectrometry often indicates the mass (m/z value) of the molecule. Characteristic fragment ion peaks found in the mass spectrum can contain additional structural information about the molecular species being analyzed.

Phthalocyanines (Pc's) belong to the class of porphyrin compounds (e.g., chlorophyll); in particular they are tetraazaporphyrins in which there is a fused aromatic ring(s).¹ Their semiconductor properties result from the abundance of π -bonded electrons in the molecule.² The metal-free phthalocyanines are symmetric molecules with planar geometry (Fig. 1). The H_2Pc (m/z 514) is a true planar molecule, but the metal complexes are slightly nonplanar because the metal ion puckers the molecule. Metal coordinate covalent bonding in the center helps to stabilize the Pc structure.

Phthalocyanines have come under study because of their diverse applications. One application related to their semiconductor and optoelectronic properties makes the Pc's attractive materials for fabrication of ultrafast molecular electronic devices.²⁻⁷ Various Pc's can be deposited as ultra thin films, essential for the construction of organic molecular electronics. Ionic attachments (e.g., halogens) alter the conductivity of some metallated Pc's; hence Pc materials are being evaluated as candidates for micro gas sensors.⁸ The orientation and optical absorption of thin metal Pc films have also been studied.^{9,10} Vanadyl phthalocyanine (VOPc) has been extensively investigated regarding its potential use as an active medium in optical storage devices, and has been shown to be a photoconductor in the infrared.^{2-6,11}

Several methods have been used to explain the relationship between molecular structure and the optical and electronic properties of Pc's.^{5,12} Early studies used heated-probe electron impact mass spectrometry.¹³ The thermal stability of the Pc molecules makes them well suited for LAMMS characterization. In fact, LAMMS can be applied directly to the as-prepared Pc thin films. Although the compounds used in this



where $A = VO^{2+}$, $AlCl^{2+}$, Cu^{2+} , or $2H^+$

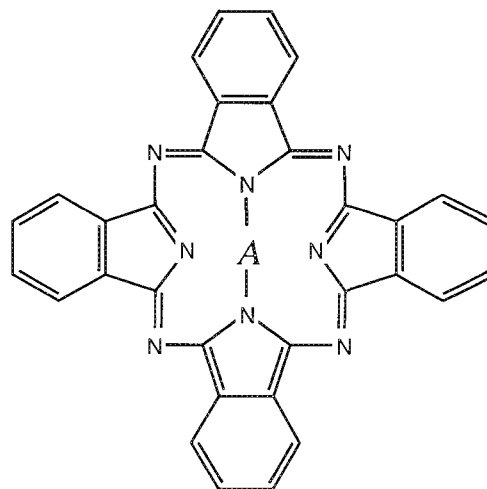


FIG. 1.--Molecular structure of phthalocyanine complexes characterized by the two techniques.

study have been characterized by conventional (i.e., bulk) Raman spectroscopy,^{5,12,14} no investigations of these metal Pc's have been made by micro-Raman spectroscopy or LAMMS. We have studied the metal-free Pc (H_2Pc) and derivatives containing Cu^{2+} , $AlCl^{2+}$, VO^{2+} , Fe^{2+} , and Zn^{2+} . In this paper we are presenting work only on the first four compounds, but the spectral information for all the compounds is similar, except for the $AlPcCl$.

Experimental

A laser microprobe having transmission optics with respect to the time-of-flight mass spectrometer was employed in this study. The focused 266nm laser beam provides 2-4 μm spatial resolution and is useful for the analysis of thin film samples or particles. The samples analyzed were reagent-grade powders. At least 10 positive ion mass spectra and multiple negative ion spectra were collected for each compound. The LAMMS data are presented in histogram representation of m/z vs integrated peak areas.

The measurements by Raman microprobe spectroscopy were performed with a laboratory-constructed system based on spectrographic dispersion. It employs a multichannel optical detec-

R. A. Fletcher and E. S. Etz are at the Center for Analytical Chemistry, National Institute of Standards and Technology, Gaithersburg, MD 20899; S. Hoeft is at the Chemistry Department, Washington University, St. Louis, MO 63130.

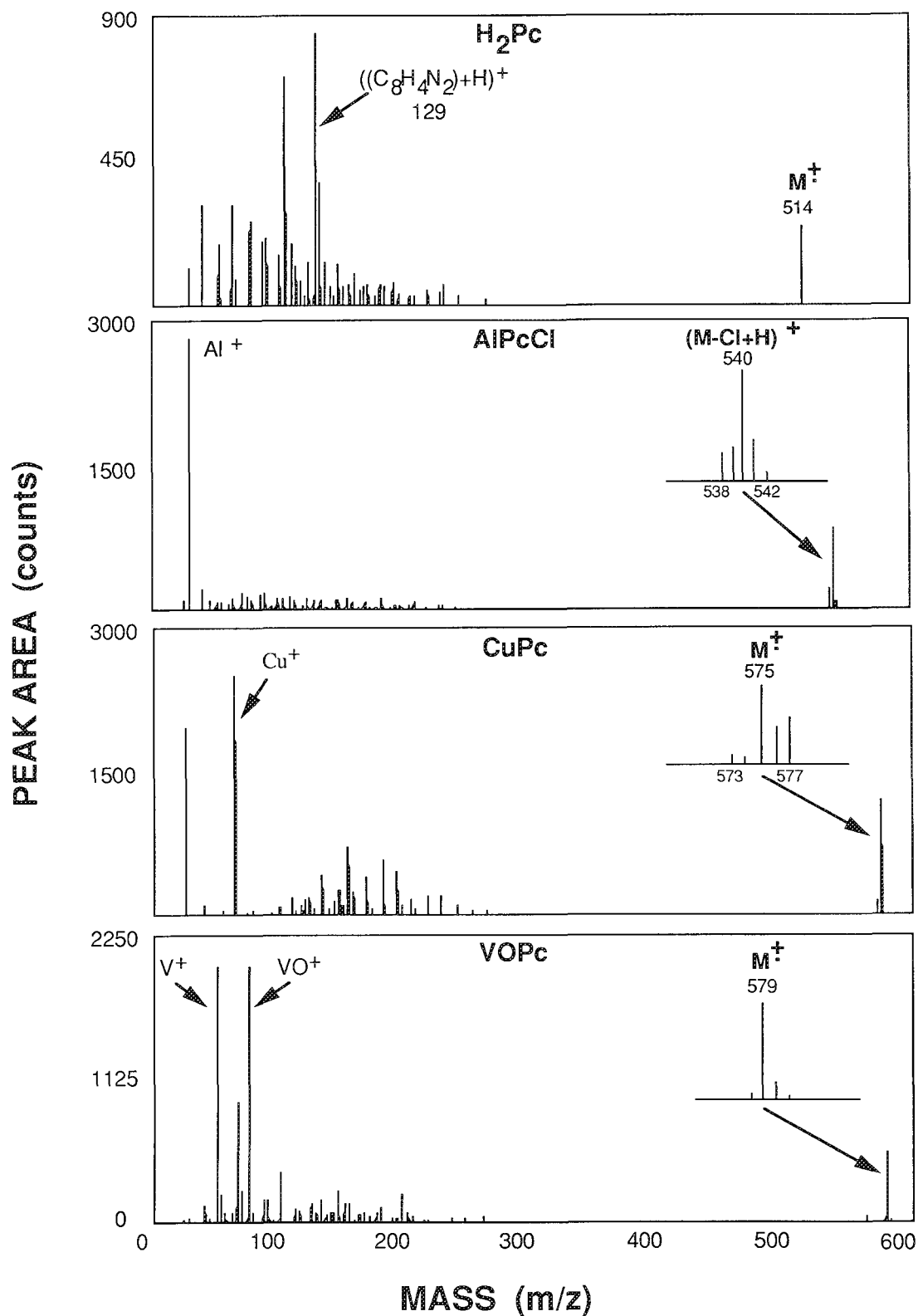


FIG. 2.--Positive-ion laser microprobe mass histograms of peak areas for Pc's examined. Molecular ions are designated by M^+ .

tion system that has an intensified diode array as the detector. The spectra of the Pc's are pre-resonance Raman spectra excited by the 514.5nm Ar⁺ laser line that falls at the absorption minimum formed by two electronic absorption bands centered at 350 and 620 nm.

Results and Discussion

The aromatic ring structure most likely contributes to the molecular ion production in laser mass spectrometry by producing what appears to be an odd electron ion, M^+ ; other highly

TABLE 1.--Principal bands observed in the micro-Raman spectra of H₂Pc and VOPc with their vibrational assignments (spectra excited at 514.5 nm).

Raman Shift (cm ⁻¹)		Vibrational Mode Description
H ₂ Pc	VOPc	
183 m	185 m	in-phase motion of isoindole groups
229 m	221 w	
absent	256 m	isoindole ring deformation
482 vw	485 w	V-N stretching
570 m	591 s	isoindole ring deformation
682 vs	679 vs	benzene ring deformation
795 s	absent	macrocycle breathing
absent	835 s	macrocycle deformation
1010 w	1002 m	macrocycle ring stretching
1024 w	1032 m	C-H bend
1104 m	1106 m	C-H bend
1140 m	1141 m	C-H bend
1337 vs	1338 vs	pyrrole ring breathing
1425 m	1428 w	pyrrole ring stretching
1450 w	1447 m/1479 m	isoindole ring stretching
1515 s	1526 vs	isoindole ring stretching
1534 vs	1548 w	C-N pyrrole stretching
1615 m	1589 m/1612 m	C-C isoindole stretching
		benzene ring stretching

conjugated ring structures (e.g., polycyclic aromatic hydrocarbons) also give a M⁺ peak. The stability of this molecular ion is evident from the lack of fragmentation found in the mass spectra, as shown in the representative positive ion mass histograms of four Pc's in Fig. 2.

The VOPc compound was the most studied compound in our work, and will be thus used in the discussion of the general features of the other metal Pc's. The peak at m/z 579 indicates the molecular weight of the compound. Oxygen remains bound in the molecular ion. The largest peaks are V⁺ and VO⁺ at m/z values of 51 and 67. There are small peaks at m/z of 179 (C₈H₄N₂V)⁺ and 195 (C₈H₄N₂VO)⁺ that correspond to one-fourth of the VOPc molecule with the vanadium and the vanadyl attached, respectively. This fragmentation pattern is similar to the LAMMS spectra reported for CoPc, but in that case the authors report a proton adduct as the highest m/z peak in the spectrum.¹⁵

The CuPc spectrum follows a pattern similar to that of VOPc showing a large amount of free Cu⁺ and Na⁺ (sodium is most likely a contaminant). The isotope pattern of Cu is clearly present in the CuPc spectrum with molecular ion peaks at m/z of 575 and 577. The H₂Pc compound (m/z 514) fragments yield a peak at m/z 129 that corresponds to the addition of a proton to one-fourth of the aromatic structure. The chemical formula for this fragment would be (C₈H₄N₂ + H)⁺.

The AlPcCl salt behaves differently: the spectra do not contain pronounced, identifiable molecular ions. There are small peaks at m/z 574 and 576 that correspond to correct m/z values for a molecular ion, but they are too small to be useful for compound identification. The strongest fragment ion peak is at m/z = 540, which corresponds to (M-Cl+H)⁺. The ionically bound Cl⁻ appears to be readily liberated from this aluminum chloride salt. Why the fragment apparently contains an added proton is not yet understood, given that the trivalent aluminum

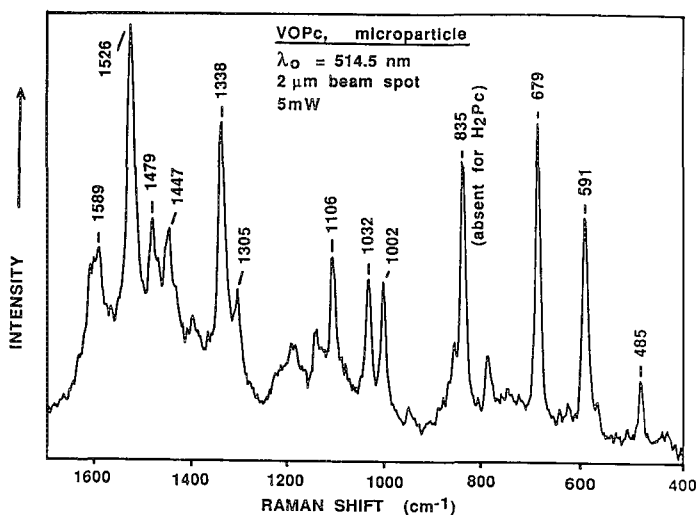


FIG. 3.--Micro-Raman spectrum of VOPc.

species should carry a positive charge after Cl⁻ liberation. Free Al³⁺ is abundant in the AlPcCl spectra.

The negative ion laser microprobe mass spectra are primarily composed of carbon and carbon-nitrogen clusters. Although the laser intensity is well below the threshold for forming carbon clusters in the positive ion spectra, carbon clusters are for the most part the only ions in the negative ion spectra. The energy threshold for negative ion cluster formation is lower than for positive ion cluster formation. The negative ion clustering of these Pc compounds reveals that an interesting process is occurring. In a Pc molecule the C to N ratio is 32 to 8, which suggests that N is readily available for clustering, yet the cluster pattern contains only C_n⁻ and NC_n⁻, not N_mC_n⁻. For some reason, possibly due to the stability of the clusters that are formed, N is not extensively incorporated. One other expected observation is the detection of Cl⁻ in the negative ion spectra of the AlPcCl.

All published Raman spectra of metal-free Pc¹⁶ and of several metal complexes^{12,13,17} indicate characteristic Raman frequencies of the Pc molecule. Complete vibrational assignments have been made for these compounds. The vibrational spectra are commonly described in terms of group frequencies. Group frequencies and their intensities provide information on structural differences (e.g., distortions of the normally planar macrocycle, as in H₂Pc) and on the various forms of a given Pc. A comparison of the observed Raman shifts is presented in Table 1 for H₂Pc and VOPc. Our data for the low frequency region, <400 cm⁻¹ (Table 1), show there are subtle differences in spectra of Pc's due to specific metal ions or coordination. VOPc has a characteristic band at 256 cm⁻¹ associated with the V-N stretching vibration that is not present in the H₂Pc. Other spectral differences arise from differences in bond energies for most of the Raman-allowed vibrational modes. The micro-Raman spectrum (Fig. 3) is that of the VOPc over the range of

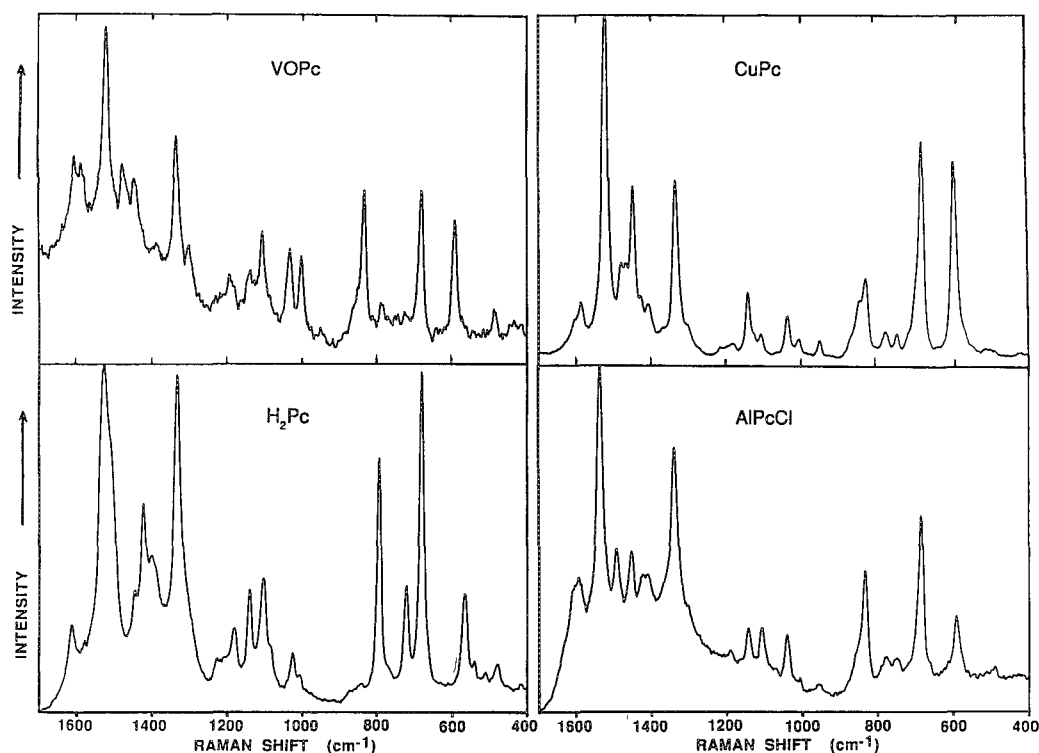


FIG. 4.--Micro-Raman spectra of VOPc, ALPcCl, H₂Pc, and CuPc.

400-1700 cm⁻¹. Some of the major band frequencies are indicated; they can all be related to fundamental vibrational modes of the molecule. Figure 4 shows the Raman spectra of four metal-Pc complexes discussed with the LAMMS results. The spectra are similar, but there are sufficient differences due to variations in vibrational structure to allow unequivocal identification of these compounds.

In summary, we present LAMMS and micro-Raman spectra of four different Pc's. All of the Pc's that we have analyzed by LAMMS (except ALPcCl) furnished a molecular ion useful for identification of the compound. The mass (*m/z* values) of the molecular species, and the fragment ion patterns obtained by LAMMS, complement the structural information obtained through the vibrational micro-Raman spectra of the same compounds.

References

1. F. H. Moser and A. L. Thomas, *Phthalocyanine Compounds*, New York, London: Reinhold, 1963, 8.
2. D. D. Eley, *Mol. Cryst. Liq. Cryst.* 171: 1, 1989.
3. B. N. Achar et al., *J. Polymer Science* A25: 443, 1987.
4. S. J. Chang et al., *Appl. Phys. Lett.* 54: 1040, 1989.
5. T. D. Sims et al., *Chemistry of Materials* 1: 26, 1984.
6. S. Yamada et al., *Proc. IEEE EMB Soc. 10th Annual Conf.* (IEEE Cat. No. 88CH2566-8), 1988, 999.
7. S. Grammatica and J. Mort, *Appl. Phys.*

Lett. 38: 445, 1981.

8. S. Kurosawa et al., *Anal. Chem.* 62: 353, 1990.

9. A. J. Dann et al., *J. Appl. Phys.* 67: 1371, 1990.

10. H. Hoshi et al., *J. Appl. Phys.* 67: 1845, 1990.

11. P. Kivitis et al., *Appl. Phys.* A26: 101, 1981.

12. D. Battish et al., *Chemistry of Materials* 1: 124, 1989.

13. F. H. Moser and A. L. Thomas, *The Phthalocyanines*, Boca Raton, Fla.: CRC Press, 1983, vol. 1.

14. R. Aroca and R. O. Loutfy, *Spectrochim. Acta* 39A: 847, 1983.

15. S. W. Graham et al., *Anal. Chem.* 54: 649, 1982.

16. R. Aroca et al., *J. Phys. Chem. Solids* 43: 707, 1982.

17. C. Jennings et al., *Spectrochim. Acta* 41A: 1095, 1985.

FLUID CATALYTIC CRACKING CATALYST MICROSTRUCTURE AS DETERMINED BY A SCANNING ION MICROPROBE

J. K. Lampert, G. S. Koermer, J. M. Macaoay, J. M. Chabala, and R. Levi-Setti

Fluid catalytic cracking (FCC) catalysts are used by the refining industry to convert heavy hydrocarbon fractions into high-quality gasoline and fuel oil by cracking hydrocarbon molecules into smaller species. Modern cracking catalysts are approximately 70 μ m-diameter microspheres consisting of crystalline zeolite Y, a synthetic faujasite type of zeolite, in a matrix such as amorphous silica alumina.¹ Ion-exchanged (e.g., H⁺, La³⁺) zeolite Y is responsible for most of the catalytic activity. The matrix functions as a diffusion medium, dilution medium, heat transfer agent, a scavenger for catalyst poisons, and a contributor to heavy molecule cracking.^{2,3}

Commercial cracking catalyst manufacture follows two main procedures, using either "incorporation" or "in situ" techniques.³ The more common incorporation methods involve spray-drying cation-exchanged zeolite Y with a silica alumina sol or gel binder to form microspheres. The silica alumina binder is considered to be the matrix.

For this report, we analyzed catalysts produced by the in situ method, in which microspheres are preformed by spray drying a kaolin clay slurry. These microspheres are then calcined at high temperature and the zeolite is crystallized in the resulting porous bead. The portion of the microsphere not transformed into zeolite is the matrix.

Regardless of the manufacturing method, the zeolite phase has a higher silicon-to-aluminum ratio and higher sodium content than the matrix. Microsphere sodium content and location are important catalyst issues because sodium affects FCC catalyst activity, stability, and selectivity.⁴ Sodium is present in the microspheres from the manufacturing process and is a catalyst contaminant present in oil feedstocks.

Kugler and Leta used a CAMECA IMS-3F ion microprobe/microscope to collect ion images of catalyst particles from FCC cracking units containing both incorporation and in situ catalysts.⁵⁻⁷ Secondary ion mass spectrometry (SIMS) elemental distribution images (maps) exhibiting minor La⁺, Al⁺, and Si⁺ ion intensity variations were attributed to catalysts prepared by the in situ procedure. Mineral phases

comprising in situ catalysts are well dispersed within the microspheres and in size ranges below the 0.5 μ m resolution of the CAMECA 3F, necessitating the use of an imaging SIMS instrument with a higher resolution.

In this study, we present high lateral resolution SIMS images of in situ FCC catalysts obtained with the University of Chicago Scanning Ion Microprobe (UC SIM). The UC SIM employs a tightly focused Ga⁺ beam extracted from a liquid metal ion source; a 40nm FWHM diameter probe was used during this experiment. The secondary ion maps clearly differentiate zeolite and matrix phases by differences in their stoichiometries. We investigated zeolitic sodium migration in the microsphere for hydrothermally treated (steamed) catalysts. We show that zeolite growth in the in situ catalyst preparations is uniform throughout the microsphere, with zeolite intimately associated with matrix phases. A significant increase in matrix sodium is observed after catalyst steaming, which suggests that hydrothermal conditions result not only in loss of zeolite crystallinity, but also zeolitic debris migration to the catalyst matrix.

Experimental

Detailed descriptions of the UC SIM and its performance have been presented previously.⁸⁻¹⁰ Briefly, the instrument is composed of a two-lens primary ion column, an efficient secondary ion energy analyzer and transport system, and an RF quadrupole mass filter for SIMS analysis. A channel electron multiplier detector operating in pulse-counting mode collects the transmitted ions. The resulting one-detected-ion to one-pulse signal is stored directly in digital memory in a KONTRON image analysis computer. These maps can be processed and analyzed retrospectively to derive quantitative information from chosen subareas of an image. Images are displayed on a high-resolution CRT and hard copies are produced with a video printer. Image acquisition time is adjusted to obtain adequate signal statistics. For this study, the microprobe was operated with a 40keV, 10pA Ga⁺ primary ion probe focused to a 40nm FWHM spot; images were constructed from scans containing 512 \times 512 probe settings. Elemental SIMS maps were obtained from 10 \times 10 μ m² areas in times not exceeding 524 s. The signal-to-noise ratio was better than 1000 for all secondary ion signals recorded during this experiment. Two additional channel electron multipliers, overlooking the target region at a shallow angle, detect ion-induced secondary electrons (ISE) or

J. K. Lampert, G. S. Koermer, and J. M. Macaoay are at the Engelhard Corp., Menlo Park CN28, Edison, NJ 08818; J. M. Chabala and R. Levi-Setti are at the Enrico Fermi Institute and Department of Physics at the University of Chicago, Chicago, IL 69637. The work at the University of Chicago was supported by a grant from Engelhard Corp. The authors wish to thank F. M. Allen for devising the sample preparation procedure for SIM analysis.

non-mass-resolved ions (ISI) for imaging of the surface topography and material contrast of a sample.

Zeolite was grown in calcined kaolin microspheres as described previously.¹¹ For these experiments, sodium levels in the microspheres were reduced to approximately 1% Na₂O by standard NH₄NO₃ exchange procedure.¹² The catalyst was then calcined at 540 C for 2 h to facilitate further sodium removal. Ammonium nitrate exchange was continued to generate microspheres with "intrinsic" Na₂O levels of 0.7%. A portion of this catalyst was hydrothermally treated with 100% steam at 790 C for 4.5 h.

Specimens were prepared for UC SIM analysis by potting of the microspheres in LR-White epoxy and microtoming to obtain a smooth surface. Because these samples otherwise displayed extreme charging artifacts, a thick layer of gold (approximately 30 nm) was sputter-deposited on the analytical surface. This coating is rapidly sputtered away from the region being scanned and does not contaminate the SIMS signals. The gold lying on the surface surrounding the scanned area and the metallic Ga⁺ primary ion implant are sufficient to insure charge dissipation.

Results

Catalyst microstructure is readily apparent in Si⁺, Na⁺, Al⁺, and ISI images obtained from 10 × 10 μm² areas of the samples (Figs. 1 and 2). Two distinct mineralogical phases are apparent: one characterized by high Na⁺ and Si⁺ ion intensities and low Al⁺ intensities; the other, by low Na⁺ and Si⁺ and higher Al⁺ intensities. In general, Na⁺ and Si⁺ images correspond directly, and the Al⁺ image is their complement.

The observed elemental distributions correspond to the zeolite and silica-alumina matrix phases of the microsphere. For both the non-steamed and steamed samples, zeolite and matrix are distinguishable by differences in aluminum and silicon ion intensities between the phases. The relative ion intensities agree with the relative atomic fractions of the elements in each phase; Al⁺ is more intense in the matrix, and Si⁺ is more intense in the zeolite. Two or more phases are discernible within the matrix of the nonsteamed microspheres, as evidenced by close examination of the Si and O maps (Figs. 1a and d, respectively). It is not clear whether these phases form during the calcination or zeolite crystallization steps. Differences in phase stoichiometry may not completely account for the relative intensities observed, because sputter yields and secondary ion fractions may be phase dependent (matrix effects).

For the nonsteamed sample, sodium is associated predominantly with the zeolite material (Fig. 1c). Matrix sodium signals are recorded in the image computer, but at levels too low to be displayed conveniently adjacent to the intense zeolite signals in a black-and-white micrograph. Matrix sodium is more perceptible after the microspheres are steamed (Fig. 2c). After the intrinsic sodium sample is steamed, a

larger sodium signal is observed in areas corresponding to matrix stoichiometry (that is, in areas with higher aluminum and lower silicon signals): the zeolite-matrix Na contrast is reduced (compare Figs. 1c and 2c).

Oxygen-bearing species are strongly adsorbed by the zeolite phase and are thermally desorbed following hydrothermal conditioning. The ¹⁶O⁻ SIMS map (Fig. 1d) shows higher secondary ion intensity from the zeolite than from the surrounding matrix before hydrothermal treatment. The O⁻ SIMS contrast between the matrix and zeolites in the steamed sample (not shown) is significantly reduced. The O⁻ ion originates from both water and silicon/aluminum oxide fragmentation. High O⁻ intensities from the zeolite in the nonsteamed sample are probably due to zeolitic water that is desorbed after steaming.

Topographical features in the non-mass-resolved ion induced secondary ion (ISI) images reflect features of the SIMS maps for each sample. As an example, Fig. 2d is the ISI image of the same area of the steamed sample mapped in Figs. 2a-c. Regions with zeolite, as determined from the SIMS maps, correspond to the recessed, bumpy areas and troughs, with plateaus of smoother matrix rising between them. These pits and folds are indicative of differential sputtering from the various microsphere phases under ion bombardment.

Discussion

Mineral phases in the catalyst microsphere are distinguished by differences in the component elements' secondary ion yields, where both stoichiometry and SIMS matrix effects may play roles in determining the yields. Attributing the high-Si⁺, low-Al⁺ intensity regions to zeolite and the complementary areas to matrix is based on known stoichiometries for these phases. X-ray diffraction unambiguously detects the presence of zeolite Y (2Na₂O 2Al₂O₃ 9SiO₂) after the zeolite crystallization step of catalyst synthesis. The microsphere matrix is composed of a completely dehydroxylated kaolin that has undergone the phase transition to mullite (3Al₂O₃ 2SiO₂) at 980 C and is known to be poorly crystalline.¹³

We can quantitatively compare the relative ion intensities for the phases with the values expected from phase stoichiometry. The recorded ion signals from several thousand pixels in regions corresponding to zeolite and matrix are acquired from the digitized images, and zeolite-to-matrix intensity ratios for each element are compared with the theoretical values (Fig. 3). Ion intensity ratios between the two regions for aluminum and silicon are in fairly good agreement with the ratios calculated from matrix and zeolite stoichiometry for both the nonsteamed and steamed samples. The values for both ions are systematically higher than expected, which shows that SIMS matrix effects may modify secondary ion yields. There is visual evidence that the microsphere matrix actually consists of more than one phase, as

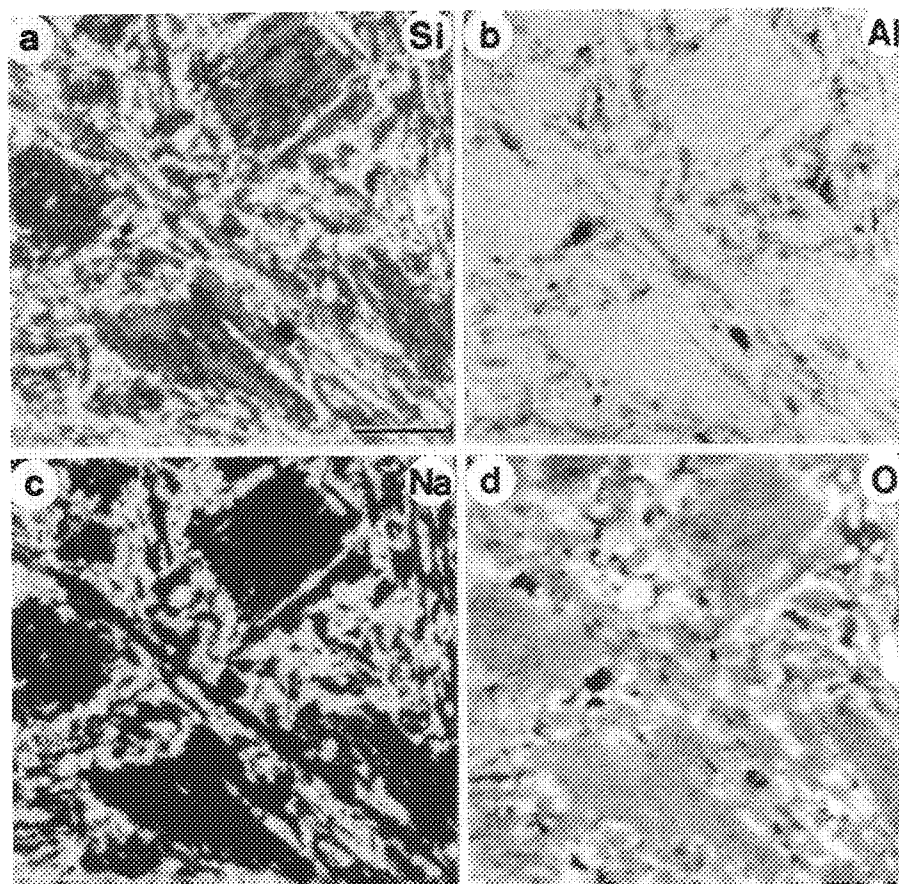


FIG. 1.--SIMS elemental distribution maps of one area of nonsteamed 0.7% intrinsic Na_2O FCC catalyst microsphere. (Bar = 2 μm .) (a) Si distribution. Zones of higher intensity correspond to zeolite. At least two distinct Si concentrations are discernible in matrix regions. Log gray scale is used to display image, enhancing features in low-intensity regions. 3.9×10^6 counts recorded in 262s exposure. (b) Al distribution, indicating higher Al concentration in matrix areas; 11.3×10^6 counts recorded in 262s, log display. (c) Na, log display; 9.2×10^6 counts recorded in 262 s. (d) O, linear gray scale; 8.5×10^6 counts recorded in 524 s.

mentioned above. These phases were not differentiated during this quantitative measurement, which may have contributed to the variability in the silicon intensity ratios.

Agreement between theoretical and experienced aluminum and silicon relative intensities does not necessarily mean that the high silicon/low aluminum regions of the microsphere contain zeolite. Catalyst steaming causes zeolite crystallinity loss and a reduction in zeolite unit cell size due to dealumination as measured by x-ray diffraction and a decrease in zeolite pore volume as measured by N_2 adsorption.¹⁴ The resulting zeolite debris remains predominantly in the zeolite regions as observed in Si^+ and Al^+ images from steamed catalysts (Fig. 2a and b), or it can migrate to the catalyst matrix. Increases in sodium concentrations observed after catalyst steaming are evidence for zeolite debris migration to the matrix (Fig. 3). Sodium can be present in the matrix regions as a salt, oxide, or hydroxide, or as the counter ion to a matrix negative charge site. Matrix sodium concentrations are very low prior to catalyst hydrothermal treatment, which shows that these species are not present in the matrix prior to catalyst

steaming to a significant degree (Fig. 1c). Steaming is accompanied by an increase in matrix sodium either as a zeolite debris counter ion or through zeolite-matrix Na^+ exchange.¹⁵

Conclusion

With a high-lateral-resolution scanning ion microprobe comprising a finely focused nanometer-scale beam, it is now possible to resolve FCC catalyst microstructure not distinguishable with conventional ion microscopes and microprobes. We observe the aluminosilicate phases that comprise catalysts synthesized by in situ methods. Microsphere analytical ion images show that zeolite growth in the in situ catalysts is uniform throughout the microsphere, with zeolite intimately associated with matrix phases. Zeolite and matrix are distinguishable by differences in aluminum and silicon secondary ion intensities resulting from phase stoichiometry. Ion intensity ratios between the two regions for aluminum and silicon obtained from microquantization of digitized scans are in good agreement with theoretical values. We show that the zeolite-to-matrix Na^+ ratio decreases after catalyst hydrothermal

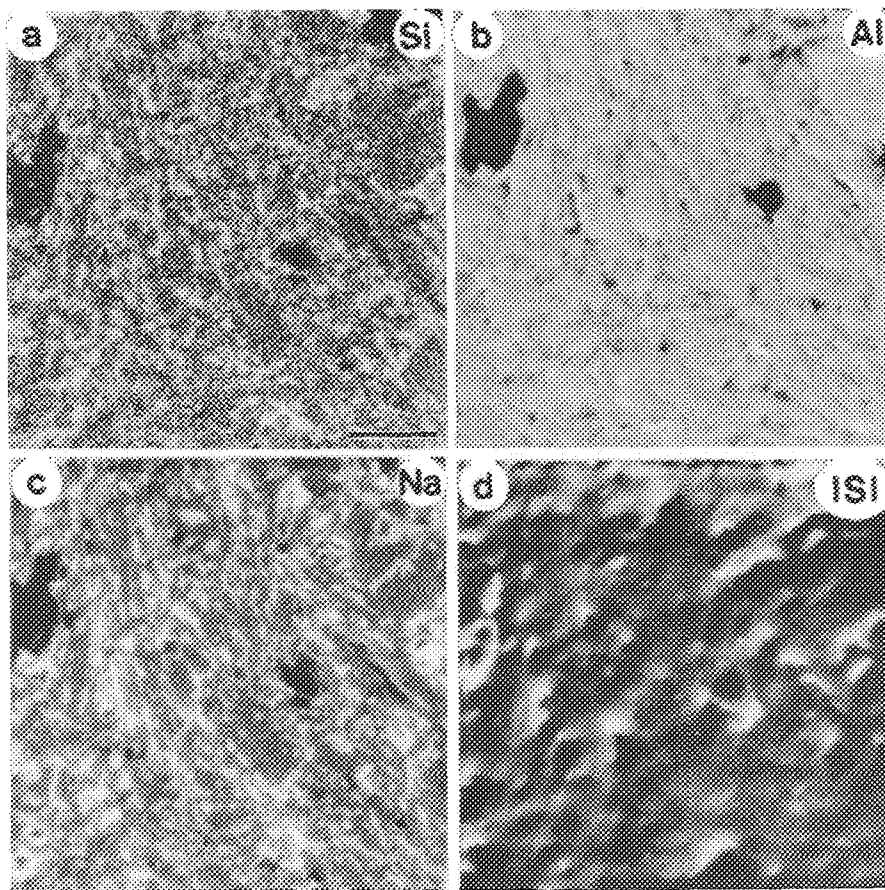


FIG. 2.--SIMS distribution maps of one area of steamed 0.7% intrinsic Na_2O FFC catalyst microsphere. All images are displayed on log gray scale. (Bar = 2 μm .) (a) Si distribution. Areas of higher intensity correspond to zeolite; 1.3×10^6 counts collected in 524 s. (b) Al, 8.7×10^6 counts recorded in 157 s. (c) Na distribution. Measured zeolite/matrix Na ratio is much lower than that found in nonsteamed sample; 5.1×10^6 counts collected in 262 s. (d) ISI image of surface topography.

treatment, which means that zeolite dealumination is accompanied by zeolite debris migration to the catalyst matrix. A future publication will discuss the results of imaging SIMS analyses of catalysts subjected to additional processing steps.

References

1. B. W. Wojciechowski and A. Corma, *Catalytic Cracking*, New York: Marcel Dekker, 1986.
2. A. Oblad, *Oil and Gas J.* 70: 84, 1976
3. J. Scherzer, *Catal. Rev.—Sci. Eng.* 31: 215, 1989.
4. P. B. Venuto and E. T. Habib, *Fluid Catalytic Cracking with Zeolite Catalysts*, New York: Marcel Dekker, 1979.
5. E. L. Kugler and D. P. Leta, *J. Catal.* 109: 387, 1988.
6. D. P. Leta and E. L. Kugler, *ACS Div. Pet. Chem.* 33: 636, 1988.
7. D. P. Leta and E. L. Kugler, *Proc. Sixth Intern. Conf. on Sec. Ion Mass Spectrom.*, New York: Wiley, 1987, 373.
8. R. Levi-Setti et al., *Appl. Surf. Sci.* 26: 1986, 249.
9. R. Levi-Setti et al., *Microbeam Analysis --1989*, 17.
10. J. M. Chabala et al., *Microbeam Analysis --1989*, 586.
11. W. L. Haden and F. J. Dzierzanowski, U.S. Patent 3,657,154 (1972).
12. C. R. Altomare et al., *Chem. of Materials* 1: 459, 1989.
13. D. W. Breck, *Zeolite Molecular Sieves*, R. E. Krieger Publishing Co., 1984.
14. M. F. L. Johnson, *J. Catal.* 52: 425, 1978.
15. S. C. Eastwood et al., *Proc. 8th Intern. World Pet. Cong.* 4: 246, 1971.

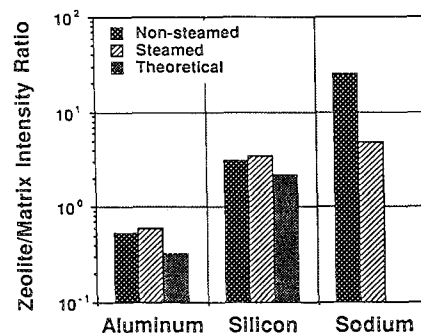


FIG. 3.--Secondary ion intensity ratios for Al, Si, and Na, derived retrospectively by measurement of subareas within digitally stored SIMS images.

SECONDARY ION MASS SPECTROMETRY STUDIES OF POLYCRYSTALLINE THIN FILM CdTe/CdS SOLAR CELLS

S. E. Asher

Polycrystalline thin films of CdTe deposited on CdS represent one of the promising materials systems currently being investigated for the fabrication of low-cost, large-area, high-efficiency photovoltaic devices. One of the attractive features of this materials system is the number of techniques available for CdTe deposition.¹ However, many of the deposition processes being used to fabricate these thin-film materials have not yet been well characterized. In particular, the interdiffusion of Te and S has not been studied. The CdTe/CdS structure must be annealed to produce a device with a high efficiency.² It is thus important to study the extent of any interdiffusion that occurs as a result of this processing step.

Secondary ion mass spectrometry (SIMS) is a useful technique for the study of interfacial quality and elemental interdiffusion. In this paper, SIMS is used to follow the interdiffusion of S and Te at the CdTe/CdS heterointerface. The analysis of structures grown by electroplating and spray processing is discussed. Scanning electron microscopy (SEM) images reveal significant differences in the sputtering behavior of the CdTe surface depending on the initial film morphology. S diffusion is clearly observed by SIMS in an annealed electroplated film; however, spray-processed films develop severe sputter cones and S diffusion cannot be ascertained by SIMS. Electron probe microanalysis (EPMA), x-ray diffraction, and SIMS images are investigated as methods to resolve this problem.

Experimental

Polycrystalline thin films of CdTe on CdS were fabricated by two different methods. CdTe films made by the first method were deposited by electroplating from solution onto CdS/SnO_x/glass to a thickness of approximately 2 μm . CdTe films made by the second method were deposited by spray processing onto CdS/SnO_x/glass to a thickness of approximately 6 μm . In both cases CdS was deposited by spray processing, to a thickness of approximately 0.15 μm and 6 μm , respectively.

SIMS analyses were performed by a Cameca IMS-3f with a 10.8keV Cs⁺ primary ion beam with detection of negative secondary ions. The energy bandpass of the spectrometer was 130 eV. The analyzed area was 22 μm^2 for the spray pro-

cessed films and 60 μm^2 for the electroplated films. Primary ion currents were 100-550 nA (beam spots 90-130 μm). EPMA with x-ray wavelength dispersive spectroscopy (WDS) was used to compare the bulk compositions of the films. X-ray diffraction measurements were performed with a powder diffractometer equipped with a rotating anode source using Cu K α radiation.

Results and Discussion

The intent of this study was to find the extent of interdiffusion occurring in the CdTe/CdS heterostructure. A SIMS profile obtained from the as-deposited electroplated film (Fig. 1) shows that within the limits of resolution for a polycrystalline film, there has been no diffusion in this structure during the initial steps of deposition. However, in order to produce device-quality material, it is necessary to heat treat the structure in an oxygen-containing atmosphere. To observe the effect of this postdeposition anneal, the film shown in Fig. 1 was divided into pieces that were annealed at 375, 390, 410, and 425 C for 1 h each. Figure 2 shows a montage of the SIMS depth profile data obtained for S and Te from these samples. It is clear that even at the lowest temperature used in this study there has been a significant amount of diffusion of S into the CdTe layer. The Te profile has not been significantly changed by the annealing process. Films that had been fabricated by the spray-processing method were also examined by SIMS. A depth profile obtained from one of these samples is shown in Fig. 3. This profile shows that a significant amount of diffusion has occurred in the as-deposited film. Measurements of the SIMS crater depths in these samples found that the bottoms of the sputtered craters were extremely rough. The surface topography of both types of films were examined by SEM.

SEM images of the surface morphology visible on the films used in this study are shown in Figs. 4(a)-(c). Each figure shows the surface of the film before (a,c,e) and after (b,d,f) sputtering with an ion beam. The surfaces of the electroplated films are relatively smooth and are not significantly altered by the ion beam. However, the surface of the spray-processed film is extremely rough and the original topography is greatly changed by the ion beam. Although not shown here, similar changes in the morphology were observed in the spray-processed film after sputtering with an O₂⁺ primary beam. The micrographs show that the depth resolution is adequate for the SIMS analyses of the electroplated films but that SIMS analysis of the

S. E. Asher is at the Solar Energy Research Institute, 1616 Cole Boulevard, Golden, CO 80401. This work was supported by the U.S. Department of Energy under contract DE-AC02-83CH10093.

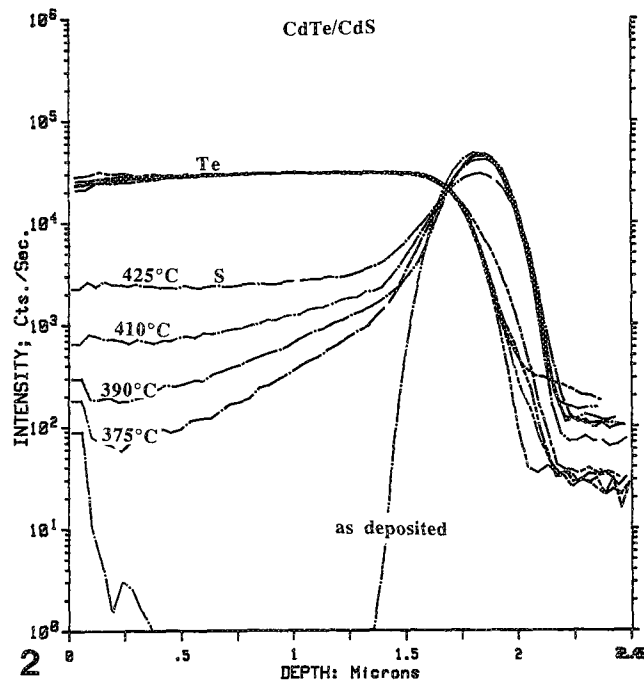
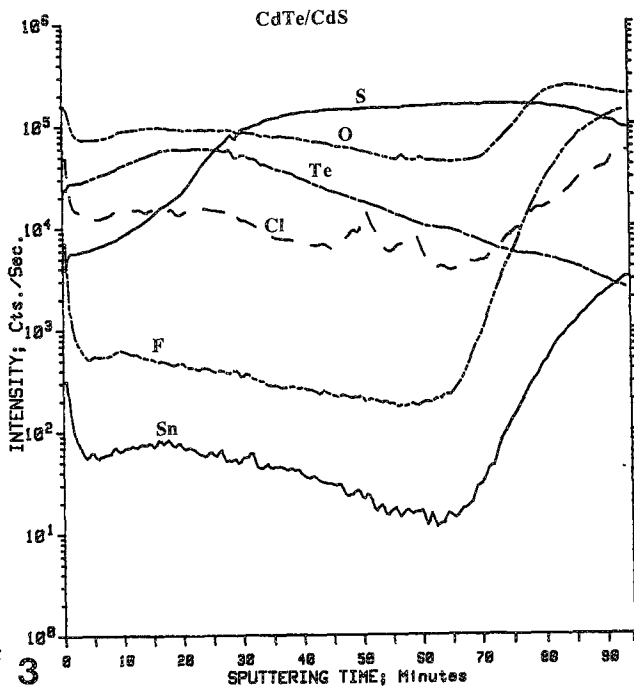
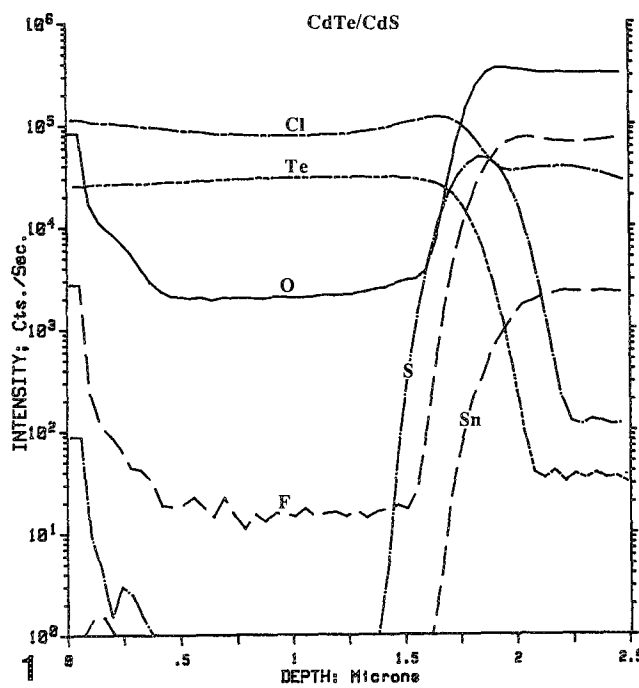


FIG. 1.--SIMS depth profile of as-deposited electroplated CdTe/CdS/SnO_x structure showing no apparent S or Te interdiffusion.

FIG. 2.--Effect of postdeposition annealing on S and Te interdiffusion. Montage of S and Te SIMS depth profiles generated by overlaying data from four different anneal temperatures on-to the profiles from the as-deposited sample. Annealing temperatures were 375, 390, 410, and 425 C for 1 h each.

FIG. 3.--SIMS depth profile of as-deposited spray processed CdTe/CdS/SnO_x structure showing apparent S and Te interdiffusion.

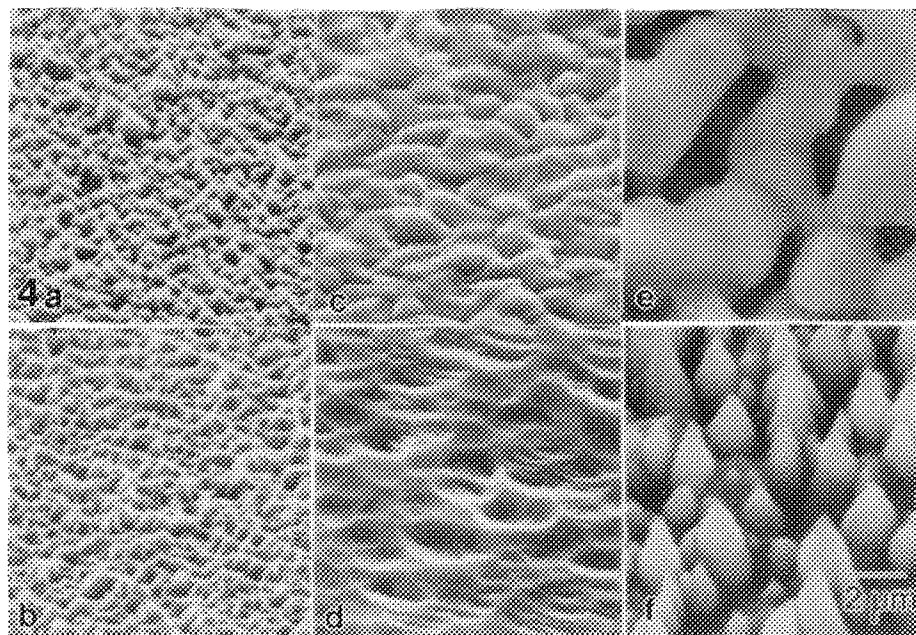


FIG. 4.--SEM micrographs of as-deposited electroplated CdTe surface (a) before and (b) after ion beam sputtering; electroplated CdTe surface annealed at 425 C for 1 h (c) before and (d) after ion beam sputtering; spray-processed CdTe surface (3) before and (f) after ion beam sputtering.

spray-processed films is severely limited by the surface topography.

The origin of the cones on the spray-processed film was investigated further in an attempt to determine how the polycrystalline nature of the film affected the ion-sputtering process. It is known that polycrystalline metals often exhibit surface roughening under ion bombardment.³ X-ray diffraction was used in this study to determine the extent of crystallinity in these films. The diffraction spectra for the three films shown in Figs. 4(a), (b), and (e) are shown in Fig. 5(a)-(c). The diffraction spectrum from the as-deposited electroplated film (Fig. 5a) shows that the film is cubic and highly oriented along the (111) direction. This is also evidenced in the SEM micrograph, which shows the surface of this film to be uniformly covered with a highly faceted, cone-like topography (Fig. 4a). The diffraction spectrum from the electroplated film annealed at 425 C (Fig. 5b) shows that a significant change in the crystallinity has occurred. The diffraction spectrum contains all the significant peaks from a randomly distributed cubic polycrystalline film with no preferred orientation. In addition, a broad low-angle peak is visible, which shows that some amorphous material is also present. A systematic decrease in the d-spacings is also observed, which is consistent with the incorporation of S into the Te sublattice. The SEM micrograph of this film (Fig. 4b) does not exhibit the highly faceted structure observed in the as-deposited film. The diffraction spectrum in Fig. 5(c) is from the spray-processed film. This spectrum is almost identical to the one obtained from the 425 C annealed film (Fig. 5b). It also contains the peaks expected from a randomly distributed cubic material; however, no

low-angle amorphous peak is present. This film also exhibits the same systematic decrease in the d-spacings observed in the 425 C annealed film. Thus, from x-ray diffraction, both the annealed electroplated film and the spray-processed film are randomly oriented polycrystalline grains with a distorted crystal lattice that is smaller than pure CdTe.

As an independent check of the S contents of these films, bulk compositional analysis was performed by EPMA. The S contents of the electroplated films were found to be 0.1 at.% for the as-fabricated sample, and 1.9 at.% for the 425 C annealed sample. SIMS did not detect any S in the CdTe layer of the former film, which leads to the conclusion that the electron beam may have penetrated to the CdS layer even though only a 10keV electron beam was used for analysis. However, there is a significant difference in the S concentration between the as-deposited and the annealed sample, showing that it did diffuse during the annealing cycle. The spray-processed film was found to contain a bulk S concentration of 3.5 at.%. This result was consistent across each sample and for all the films that were measured. It is unlikely that the electron beam was analyzing through the film and into the CdS substrate. The spray-processed film was also examined by ion microscopy to determine the emission of S. If the CdS substrate were visible through the CdTe film, the ion image for S and Te should be different. The resulting images for S and Te were almost identical, which shows that S was emitted uniformly from all areas of the sample that also contained Te, and provides further proof that S had indeed diffused into the CdTe layer.

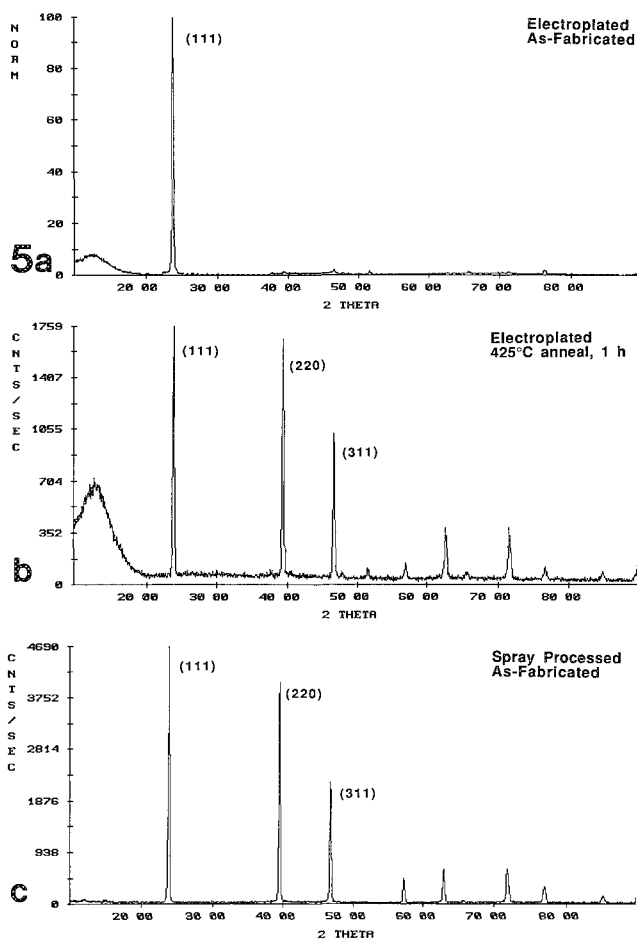


FIG. 5.--X-ray diffraction spectra from polycrystalline CdTe (a) as-deposited electroplated film, (b) 425 C annealed electroplated film, (c) as-deposited spray-processed film. Indices for major cubic lattice peaks are labeled.

Conclusions

SIMS has been successfully used to study the interdiffusion of S and Te in electroplated polycrystalline thin films of CdTe on CdS. After annealing at 425 C at 1 h, the concentration of S in this film was found to be uniform throughout the CdTe layer (by SIMS) at a level of 1.9 at.% (by EPMA). The as-deposited film was found to be highly oriented along (111); the annealed film was found to consist of randomly oriented polycrystalline grains. The SIMS investigation of the spray-processed film was obstructed by the extreme topography of the CdTe layer and further hindered by the polycrystalline morphology of the film. The ion beam caused the development of large sputter cones, which obscured any diffusion effects. S diffusion in this film was confirmed by a combination of EPMA, x-ray diffraction, and ion imaging. The S content of the spray-processed film was found to be 3.5 at.%.

References

1. P. V. Meyers, *Solar Cells* 23: 59, 1988.
2. R. W. Birkmire, B. E. McCandless, and W. N. Shafarman, *Solar Cells* 23: 115, 1988.
3. G. Carter, B. Navinsek, and J. L. Whitton, "Heavy ion sputtering induced surface topography development," in R. Berisch, Ed., *Sputtering by Particle Bombardment II* (Topics in Applied Physics, vol. 52: 231-269), New York: Springer-Verlag, 1983.

THREE-DIMENSIONAL DISPLAY OF SECONDARY ION IMAGES

J.-J. Lee, R. W. Linton, W.-J. Lin, J. L. Hunter Jr., D. P. Griffis

Although three-dimensional (3D) microscopic imaging of solid material surfaces has become increasingly common, few imaging techniques provide detailed chemical information. Secondary ion mass spectrometry (SIMS), with the use of ion microprobe or microscope instrumentation, couples lateral imaging and dynamic ion beam sputtering to provide 3D compositional maps (image depth profiles). A typical data set acquired with an ion microscope involves about 100 mass-resolved ion images, each containing at least 256×256 pixels, with lateral and depth resolutions at the order of $1 \mu\text{m}$ and 10 nm , respectively. An effective methodology for data presentation is required to assist in the qualitative evaluation of these 3D SIMS images.

The recent evolution of efficient computerized visualization techniques holds much promise for the display of 3D microscopic data such as intuitive view of large data arrays. The descriptive information available in a 3D image is many times that of related numerical data. In addition to simplifying data analysis, the images may be used as effective feedback in the experimental correction of SIMS analytical artifacts such as surface topography, sample matrix effects and atomic mixing. Correlation algorithms and complementary information from other surface imaging techniques also may be incorporated to facilitate the correlation of physical and chemical microstructure.

Several types of 3D visualization techniques have been developed to generate realistic projections of 3D data sets.¹ The three basic types are surface rendering, binary voxels, and volume rendering. A comparison of the three techniques suggests that volume rendering is most appropriate for 3D SIMS imaging studies.

Surface rendering involves edge detection algorithms or binary intensity classification (thresholding) to define the surfaces in the

J.-J. Lee, R. W. Linton, and J. L. Hunter Jr. are with the Department of Chemistry, University of North Carolina, Chapel Hill, NC 27599-3290; W.-J. Lin is with the Department of Computer Science, University of North Carolina, Chapel Hill; and J. L. Hunter Jr. and D. P. Griffis are with the Analytical Instrumentation Facility at North Carolina State University. We are grateful to M. Levoy, H. Fuchs, and V. Interrante at the UNC Computer Science Department for access to volume-rendering techniques; J. Shelburne, J. Burchette, A. Sanfilippo at Duke University Medical Center for help with specimen preparation; V. Guarisco and M. Mawn at UNC-CH for assistance with electron microscopy; and K. Mar for very useful discussions. The research was supported in part by UNC-CH and NCSU.

Ray Tracing Technique

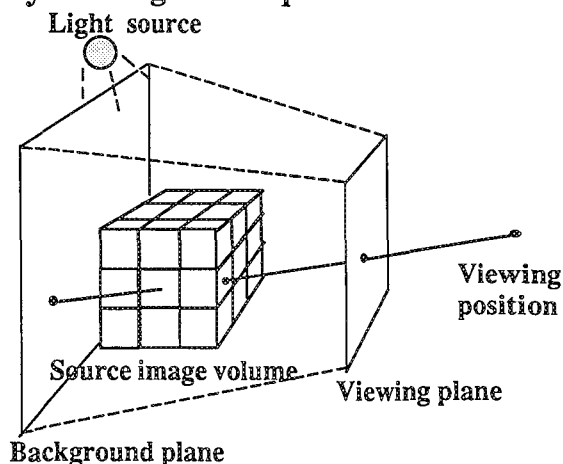


FIG. 1.--Ray tracing technique used in volume rendering.

data set. The algorithm then finds the best way of fitting geometric polygons to the defined surfaces. Shading and hidden surface removal techniques are applied to display 3D features on a 2D screen. Shading requires an imaginarily positioned light source and a known observer position. The light intensity reflected from the feature surface is then computed based on the way the object is positioned relative to the light source. In addition to shading, hidden lines are removed based on the position of the observer, providing a perspective image. Surface rendering has been previously applied in SIMS image depth profiling, as well as in microscopic techniques such as confocal microscopy.^{2,3} However, surface rendering is not always reliable for complex features. Binary classification of the raw data often generates flawed images, especially for images containing small or poorly defined structures.

Binary voxel techniques apply binary thresholding to generate a 3D binary data array. Ray tracing, in which imaginary rays approaching from the observer's viewing position stop at the positions of data volume elements (voxels) with a value of 1, then produces a projected image on the 2D screen. Although this simple binary classification requires relatively little computation, the image produced is very crude in quality.

Finally, volume rendering is a more sophisticated technique that encompasses ray tracing, shading, and classification procedures.³⁻⁵ It is based on an algorithm that computes a

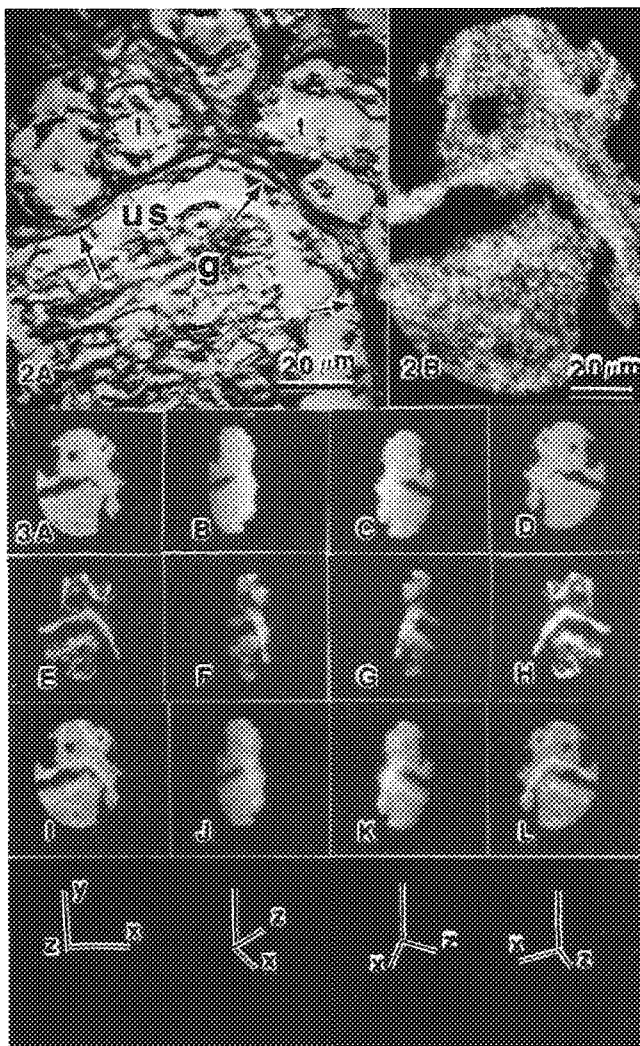


FIG. 2.--(A) Secondary electron micrograph: g = glomerulus, us = urinary space, t = tubules, arrows = basement membrane. (B) Overlay of CN^- and Ag^- volume-rendered images. FIG. 3.--(A)-(D) CN^- volume-rendered images, (E)-(H) Ag^- volume-rendered images, (I)-(L) Overlay of CN^- and Ag^- volume-rendered images. Bottom row shows the corresponding coordinate frames representing the viewing angles for each column of images, in order, 0° , 80° , 120° , and 160° from the surface normal.

color from shading and then determines a partial transparency for each voxel from its intensity value and spatial position by means of a classification procedure. By use of the ray tracing concept, images are formed by blending together contributions made by voxels projecting to the same picture element (pixel) on a 2D viewing screen (Fig. 1). One important advantage is the ability greatly to improve the characterization of small or poorly defined features by elimination of the simple binary classification of the data.

In the volume-rendering algorithm used for this work, a shading procedure is first applied to the sample data to generate a 3D array of voxel color values. In this shading routine, the local data gradient and the light vectors

are combined to give a color value. In a separate step, a classification procedure, which involves a multiple thresholding algorithm, is used to achieve an array of opacity (negative transparency) values. The color value and the opacity value are combined by means of a transformation function to give the final contribution of the voxel to the 3D image. This work presents the first application of this volume-rendering technique to 3D SIMS image depth profiles.

Experimental

Both a biological tissue and a microelectronics device were used to illustrate the display of 3D SIMS images by the volume-rendering technique.

A human kidney tissue section, treated by an immunocytochemical staining technique, served as the biological sample.⁶ The staining technique involves selective binding of antibodies to antigenic sites on the basement membranes (Fig. 2A). The antibodies are bound to Ag-coated Au particles, which provide a contrasting medium in the 3D SIMS image. The SIMS images were obtained with a Cameca IMS-3f microscope with a magnetically filtered Cs^+ beam and a digital secondary ion imaging system.⁷ Negative secondary ion detection in conjunction with energy filtering, achieved by off-setting of the sample potential (122V), was confirmed to provide adequate detection of Ag^- without molecular interferences. Previous results indicated the Ag stain is confined to the near surface of the tissue section. The sputtering rate of 20 to 30 nm/min was achieved with a 10nA, 9.5keV Cs^+ beam rastered over a $250 \times 250 \mu\text{m}$ area. The analytical area was confined within a circle, 150 μm in diameter, centered in the sputtered area. During 20 min of acquisition, approximately 0.4 μm was sputtered from the sample. The CN^- image was used to define the areas containing tissue components and established the overall tissue morphology. Since the tissue structure was relatively constant throughout the sputtered depth profile, only one CN^- ion image was required between every nine successive Ag^- ion images. A secondary electron micrograph was obtained with an ISI DS-130 scanning electron microscope to substantiate the tissue distribution indicated CN^- -image.

The same raster and image field conditions were used for the SIMS image depth profiling of a random access memory (RAM) chip. The primary ion beam utilized was 15 keV O_2^+ . The Al metallization lines in the RAM chip are approximately 1 μm thick, and the SiO_2 regions are raised about 300 nm above the surface regions containing only Si. The total sputtered depth was approximately 2 μm . Image depth profiles of Al^+ and Si^+ were used to identify the major regions. Al^+ ions emanated from the regions containing the metallization lines. A larger Si ion yield from SiO_2 caused a higher intensity for this component in the Si^+ ion images. This contrasting effect was used to extract

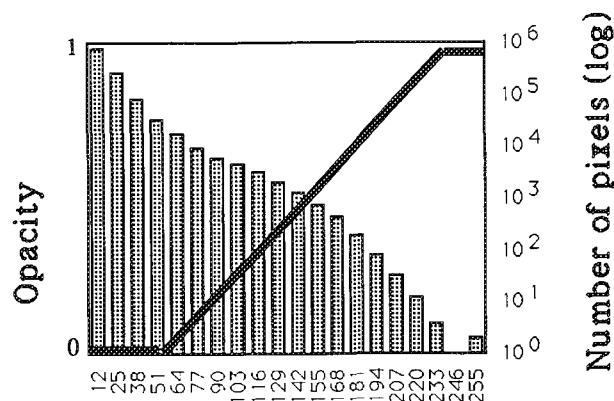


FIG. 4.--Bar graph representing the intensity histogram of Ag⁻ ion images (Y axis is number of pixels). The line graph shows classification function (Y axis is opacity) used to render Ag⁻ images in Figs. 2 and 3.

chemical-state-specific maps to distinguish Si and SiO₂ regions in the same Si⁺ ion image. The high sensitivity of SIMS also allowed 3D imaging of B⁺ to monitor the distribution of this p-type dopant. The image files acquired on the SIMS imaging system were stored on floppy disks in the MS-DOS format and uploaded to a workstation file server. Programs were written in the C language to convert the image file format and to normalize the image intensity for the variable image acquisition times used to optimize the inter-image dynamic range. The volume-rendering algorithm was implemented on a DEC 3100 workstation.

Results and Discussion

The electron micrograph in Fig. 2(A) shows a portion of a glomerulus, including some tubules with membranes stained by antibody-bound Ag particles. A series of Ag⁻ and CN⁻ SIMS images used in the volume-rendering scheme were obtained in the same area shown in the electron micrograph. Examples of volume rendered images with different viewing angles are shown in Fig. 3. Figures 3(A)-(D) are rendered CN⁻ images; the second row (E-H) shows Ag⁻ ion images, and the third row (I-L) shows composite CN⁻ and Ag⁻ images. If the sample surface is defined as the X-Y plane, Figs. 3(A), (E) and (I) in the first column are from a viewing angle normal to the sample surface. For each column of images, a coordinate frame is drawn at the bottom of the column to show the relative viewing angles, which are 0°, 80°, 120°, and 160°, in order, from the surface normal.

The variation of the Ag particle distribution with depth is revealed, which shows that the immunolabeling reaction is largely confined

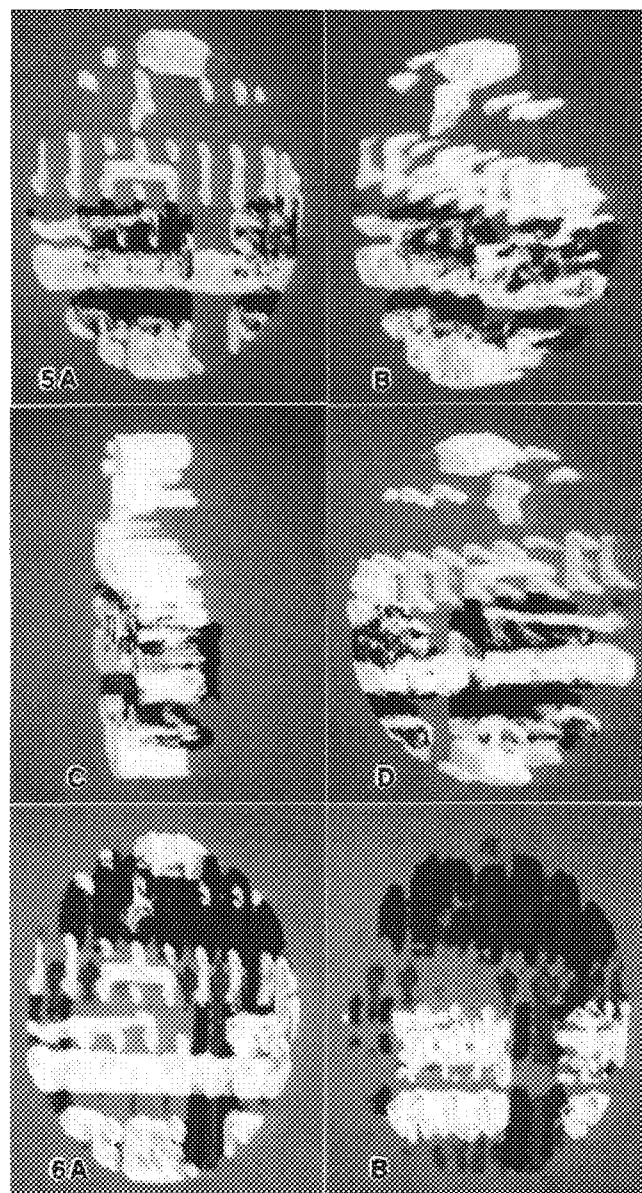


FIG. 5.--Overlay of Al (bright color) and B (dark color) volume-rendered images for a RAM chip at 0°, 40°, 80°, and 160° from the surface normal in (A), (B), (C), and (D), respectively. The background is shown by medium gray color. FIG. 6.--(A) Overlay of Al (bright color) and SiO₂ (dark color) volume-rendered images. (B) Overlay of B (bright color) and SiO₂ (dark color) volume-rendered images.

to membranes in the outermost region of the tissue section. By use of various gray levels and transparencies, 3D CN⁻ ion images are overlaid onto the Ag⁻ images to substantiate further the relative distribution of the labeled antigenic sites (Figs. 2B and 3I-L).⁶

From Figs. 3(E)-(H), diffusely or nonspecifically stained Ag particles are rendered as partially transparent features. In the 2D images, the heavily stained membrane regions have an intensity greater than 230 in a gray scale range of 0 to 255, with background inten-

ties below 50. However, nonspecific Ag staining occasionally exists at the pixels with intensity between 50 and 230. As indicated in the histogram shown in Fig. 4, the classification function is linearly varied for the transition region from 50 to 230. A voxel array of opacity values is generated by application of this classification function to the sample data set. By use of a ray tracing algorithm, a perspective picture is composed on the 2D viewing screen from both the voxel color and opacity arrays. Based on the transparency concept, the voxels within the 50-230 intensity region are shown as more transparent features that represent less concentrated or nonspecific Ag staining (Fig. 3E-H).

To illustrate briefly the result for the RAM device, Fig. 5 shows the overlay of Al^+ and B^+ volume rendered images viewed at 0° , 40° , 80° , and 160° from the surface normal. The bright areas represent Al^+ ion images; the dark areas show B^+ ions. These pictures reveal the 3D localization of the Al metallization lines relative to the B dopant distribution in the complex device structure. Figures 6(A) and (B) are overlays of $\text{Al} + \text{SiO}_2$ and $\text{B} + \text{SiO}_2$, respectively. The dark regions in both images represent the SiO_2 features. They were extracted from the Si^+ ion images by the classification process, which was adjusted to render only the intensity range of Si^+ ions from SiO_2 .

By comparison of various mass-resolved ion images, the volume-rendering technique applied to the SIMS data provides the ability to visualize the device structure, both physically and chemically. Other visualization techniques are also being explored to extract more quantitative analytical information. One possibility is the rendering of iso-intensity contour surfaces, which may provide quantitative indications of the concentration distribution of ions, e.g., B^+ ions from the dopant. Rendered SIMS images also will be used as a tool to assess methodologies for correction of matrix effects, topographic variations, and differential sputtering rates that hinder quantitation.

References

1. Henry Fuchs et al., *Computer*, Aug. 1989, 46.
2. S. R. Bryan et al., *Proc. SIMS VI*, 1987, 360.
3. J. J. McCarthy et al., *Microbeam Analysis --1989*, 381.
4. M. S. Levoy, *Trans. IEEE Computer Graphics & Applications*, May 1988, 29.
5. M. S. Levoy, Ph.D. thesis, Computer Science Department, University of North Carolina at Chapel Hill, 1989.
6. J.-J. Lee et al., Ref. 3, 45.
7. J. L. Hunger et al., Ref. 3, 597.

IMAGING OF Al-Li-Cu ALLOYS WITH A SCANNING ION MICROPROBE

K. K. Soni, D. B. Williams, J. M. Chabala, R. Levi-Setti and D. E. Newbury

Al-Li base alloys are being introduced as next-generation materials for aerospace structures because of their high strength-to-weight ratio. Although the microstructure of these alloys has been extensively characterized, relatively little is known about their microchemistry, especially Li distribution. Two principal techniques capable of detecting Li at the submicrometer level are electron energy loss spectrometry (EELS) and secondary ion mass spectrometry (SIMS). EELS can provide standardless quantitative analysis of Li and other light elements with a spatial resolution $< \sim 50$ nm, but has several drawbacks: poor signal-to-noise ratio (< 1), stringent specimen requirements, and complex quantification and imaging procedures.¹ On the other hand, SIMS generates strong signals for most elements (which results in very high sensitivity) and can be conveniently exploited to produce chemical images of bulk specimens. Recently SIMS was applied to the study of Al-Li alloys in conjunction with transmission electron microscopy (TEM).^{2,3} The goal of the present study was to correlate the microstructure of Al-Li-Cu alloys with corresponding elemental composition images obtained with a high-resolution scanning ion microprobe (SIM) utilizing secondary ion mass spectroscopy.

Most Al-Li base commercial alloys contain Cu, often with the addition of Mg. The Al-Li-Cu phase diagram is crucial to the understanding of the constitution of commercial alloys such as 2090 (Al-Li-Cu) and 8090 (Al-Li-Cu-Mg). However, relatively little work has been done regarding the phase equilibria in this system since the seminal study performed by Hardy and Silcock.⁴ They identified the ternary phases and determined isothermal sections at 350 and 500 C using metallography and x-ray diffraction work on a large number of alloys. In the Al-Li-Cu system, two phases of major importance are T_1 and T_2 , with nominal compositions of Al_2LiCu and Al_6Li_3Cu , respectively. In commercial alloys, containing ~ 2 wt.% Cu, T_1 develops a plate-like structure with a thickness $< \sim 2$ nm and contributes to the alloy strength by dispersion of planar slip. However, it cannot be analyzed in this form by the

available microanalytical techniques. T_2 is the equilibrium phase with a controversial icosahedral structure; its presence is undesirable in the industrial alloys. The phase equilibria between T_1 and T_2 were studied in this work by casting Al alloys with high contents of Li and Cu.

Experimental Procedure

Two alloys A (Al-23.4at.%Li-17.1at.%Cu) and B (Al-18.7at.%Li-11.6at.%Cu), were studied here, cast close to the stoichiometry of T_1 and T_2 , respectively, in order to have phases large enough to microanalyze by imaging SIMS. The alloys were heat treated at 500 C for 7 days. Bulk specimens were prepared by conventional metallographic procedures with final stages of preparation including polishing with 1 μ m diamond paste and 0.3 μ m Al_2O_3 suspension in ethylene glycol. Specimen contact with water was avoided as it may alter the surface chemistry by leaching out Li. Polished specimens were sputter-coated with a thin layer of Au-Pd to protect the surface from atmospheric oxidation.

SIMS work was performed on the high-resolution scanning ion microprobe (SIM) at the University of Chicago (UC). In the UC SIM, a primary ion beam is extracted from a liquid Ga source and is accelerated by 40 kV. The beam can be focused to ~ 20 nm FWHM. For this experiment, the instrument was operated with a 70nm-diameter, 40pA probe, which was scanned over a 512×512 raster encompassing areas up to $160 \times 160 \mu m^2$. The specimen was held at 2×10^{-8} Torr during the analysis. The secondary ions are energy filtered and analyzed according to their mass-to-charge ratio in an RF quadrupole mass spectrometer. By a rapid peak-switching procedure, the UC SIM can acquire up to four signals/images simultaneously, which originate from the same depth in the specimen.⁵ Topographic images of the sample surface can also be constructed by collection of either the ion-induced secondary electrons (ISE) or the non-mass-resolved secondary ions (ISI). Secondary ion images are recorded on a KONTRON IBAS image processing workstation interfaced to the UC SIM. The digitally stored images can be processed and analyzed in retrospect to obtain quantitative information from selected areas of the image such as precipitates. Image acquisition times range from ~ 1 -9 min.

Because of high Li content, these alloys underwent surface oxidation during preparation and subsequent storage, and it was necessary to clean the surface by sputtering with Ar^+ ions in the antechamber of the UC SIM. Images

K. K. Soni and D. B. Williams are with the Department of Materials Science and Engineering, Lehigh University, Bethlehem, PA 18015. J. M. Chabala and R. Levi-Setti are with the Enrico Fermi Institute and Department of Physics, The University of Chicago, Chicago, IL 60637; D. E. Newbury is at the National Institute of Standards and Technology, Gaithersburg, MD 20899. This material is based on work funded by National Science Foundation grant DMR 86-12254.

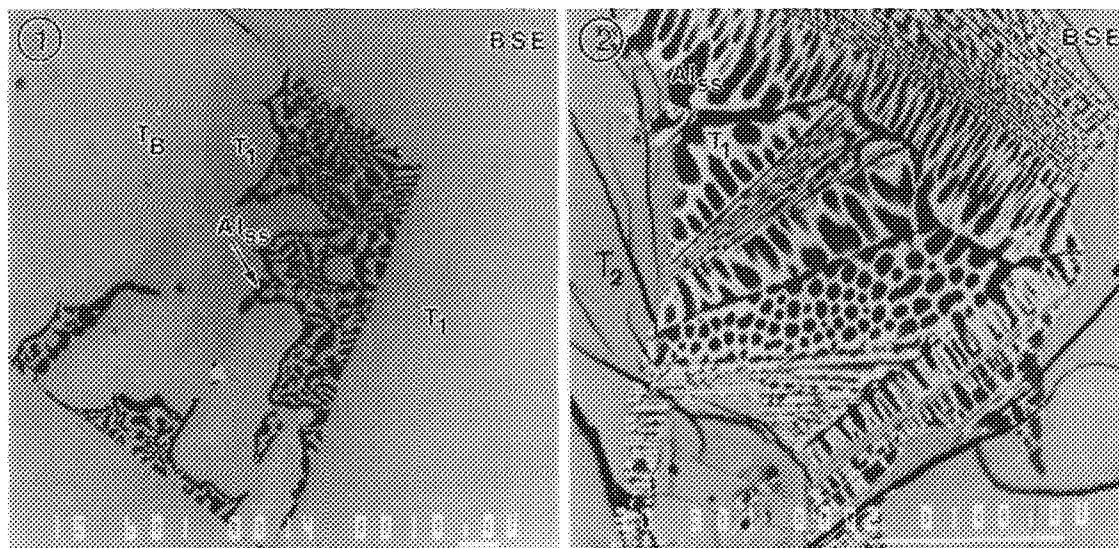


FIG. 1.--Backscattered electron micrograph of alloy A (Al-23.4 at.% Li-27.1 at.% Cu), showing presence of large primary T_1 and phase mixture of T_B , α (or Al_{ss} , aluminum solid solution) and secondary T_1 .

FIG. 2.--Backscattered electron micrograph of alloy B (Al-18.7 at.% Li-11.6 at.% Cu), showing large primary T_2 and eutectic mixture of T_1 (light) and α (dark).

were acquired only after the secondary ion signals had become stable.⁷

Results and Discussion

Alloy Microstructures. *Alloy A.* Alloy A was cast close to the nominal stoichiometry of the T_1 (Al_2LiCu) phase. This composition can be located in the $T_1 + T_B + \alpha$ phase field of the 500 C isotherm as determined by Hardy and Silcock.⁴ Figure 1 is an SEM backscattered electron micrograph and shows the large primary phase T_1 and a mixture of T_B , α and secondary T_1 as indicated. T_B is the ternary phase with a nominal stoichiometry $Al_{7.5}Cu_4Li$. T_B appears brighter than T_1 because of its slightly higher average atomic number. The darkest constituent is aluminum solid-solution, α .

Alloy B. Alloy B was slightly off the nominal stoichiometry of the T_2 phase and its composition lies in the $T_2 + T_1 + \alpha$ phase field of the 500 C isotherm.⁴ Figure 2 shows a backscattered electron micrograph of this alloy; the large primary phase is T_2 and the eutectic mixture is composed of T_1 (light) and α (dark) as indicated.

SIMS Imaging

Alloy A. Figures 3(a-d) show Al^+ , Li^+ , Cu^+ , and O^- distribution maps of the same specimen area in alloy A. The individual phases are marked. It is evident that α (aluminum solid solution) dominates in the Al^+ image, but it contains the least amounts of Li and Cu, as expected. T_1 can be identified as the phase richest in Li (Fig. 3b). T_1 and T_B contain roughly equal amounts of Al and Cu and therefore cannot be discerned from each other in Al and Cu maps. These images represent the distributions of secondary ion intensities, not of true concen-

trations, which requires empirical calibration to account for the well known "matrix-effects" and "instrumental factors." Such calibration was carried out for the binary Al-Li system for the UC SIM and indicated a linear relationship between the ratio of Li^+ and Al^+ signals and Li content.² A similar calibration approach for the Al-Li-Cu system will be the subject of a future publication. Nevertheless, the secondary ion images are useful in demonstrating the relative trends in elemental distributions. The feature in the top left corner is Li-oxide contamination. The O^- image (Fig. 3d) displays the same distribution as in the Li^+ map (Fig. 3b). This similarity suggests that the oxygen segregation is directly related to the Li content of the individual phases. The traces of oxygen are assumed to arise from the oxidation of the liquid alloy during casting, reaction of Li with oxygen in the specimen chamber, or surface oxidation during specimen preparation and storage. The last factor is unlikely as the specimens were sputter-cleaned with an Ar^+ gun, as described earlier in the experimental section.

A subtle effect in the Li map is highlighted in Fig. 3(e). There is a Li diffusion zone between T_1 and T_B indicating diffusion of Li from the former (Li-rich) to the latter (Li-poor). The T_B precipitates are deficient in Li in the central region compared to the particle periphery. Figure 3(f) is the Li intensity profile across the horizontal line shown in Fig. 3(e) which clearly displays the Li intensity levels corresponding to T_1 and T_B and their interdiffusion zone. A possible explanation for this phenomenon is that the T_B phase forms by a peritectic reaction between liquid and T_1 , which involves solute diffusion through the growing solid and consequently seldom reaches equilib-

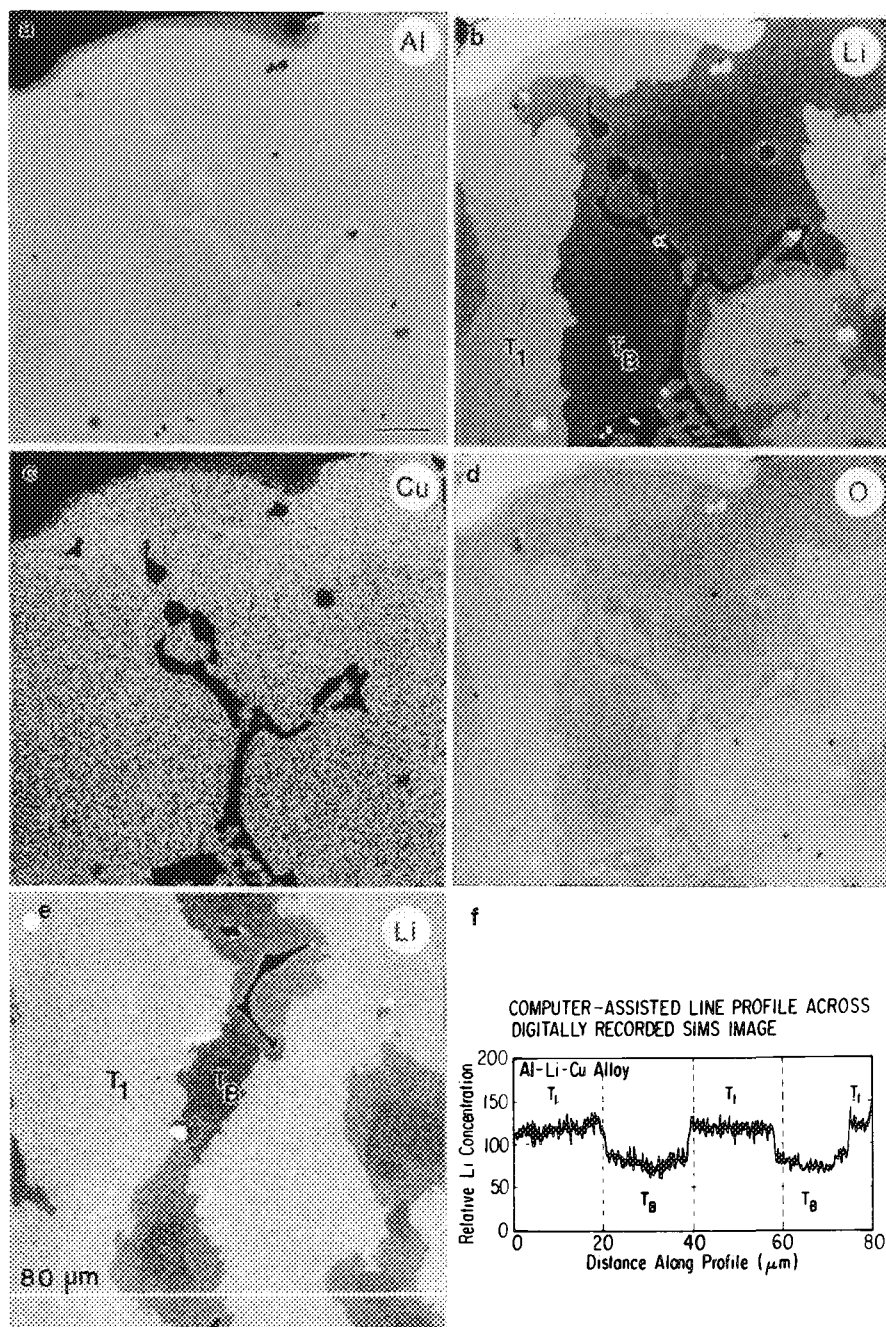


FIG. 3.--SIMS maps of alloy A described in Fig. 1: (a) Al⁺, (b) Li⁺, (c) Cu⁺, (d) O⁻. These images are displayed with logarithmic gray scale to enhance brightness in low-intensity areas. Individual phases are marked. Bar in (a) = 10 μm. (e) Li⁺ map of alloy A. Diffusion of Li is seen from T₁ (light) to T_B (dark) and diffusion zone is of intermediate intensity. (f) Profile of Li intensity across horizontal line indicated in (e).

LiF⁻) in the eutectic matrix and it is clearly evident that these elements are completely segregated to the T₁ plates. This segregation tendency is associated with the strong affinity of oxygen and fluorine for lithium. Oxygen is likely to be introduced by oxidation of the liquid alloy during casting. Fluorine is thought to be left over from the cryolite used in the aluminum extraction process, but to the authors' knowledge its presence in commercial aluminum-base alloys has never been examined.

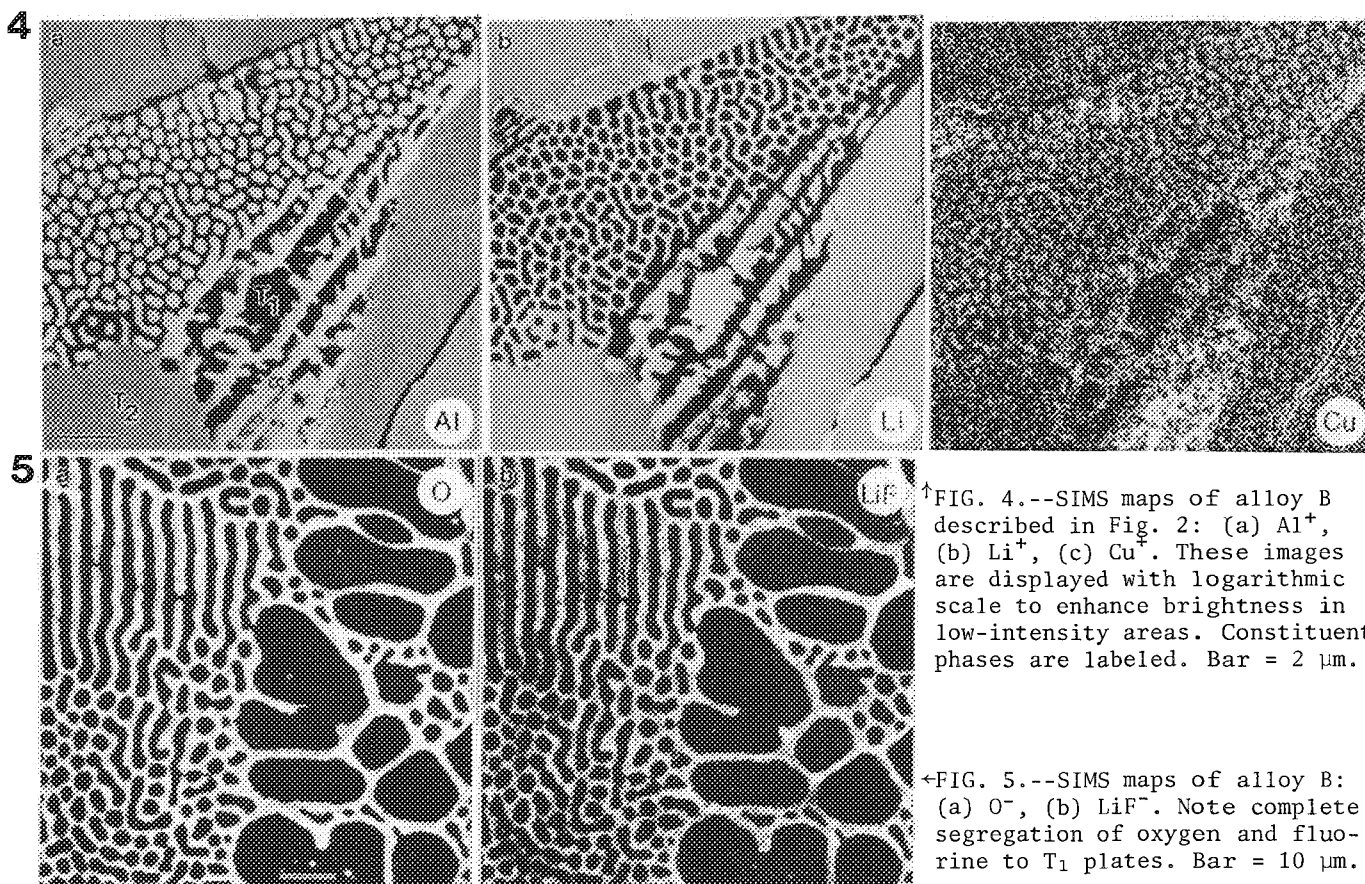
Conclusions

Two alloys with compositions close to the stoichiometry of T₁ (Al₂LiCu) and T₂ (Al₆Li₃Cu) were studied by scanning electron microscopy and secondary ion mass spectrometry. Chemical images were acquired by a high-resolution scanning ion microprobe in order to improve the understanding

rium state. Formation of T_B by a peritectic reaction was also mentioned by Dubost et al.,⁸ who characterized the phase equilibria in the Al-Li-Cu system. This Li profile could not be seen in the backscattered electron micrograph of this alloy (Fig. 1) as the resulting change in the average atomic mass is too small to detect.

Alloy B. Figures 4(a-c) show Al⁺, Li⁺, and Cu⁺ distribution maps of the alloy B. The large Li-rich phase is T₂ and the honeycomb-shaped eutectic mixture consists of T₁ (Cu-rich) and α (Al-rich). The Cu⁺ signal was much weaker than Al⁺ and Li⁺ signals. This poor signal is a consequence of the intrinsically low secondary ion yield of Cu. In addition, the UC SIM is operated at high vacuum (2 × 10⁻⁸ Torr) without any introduction of oxygen, which is known to enhance positive ion emission. Consequently, the poor signal statistics in the Cu⁺ map result in an inferior image contrast and probe-size resolution cannot be attained. The Cu distribution is very inhomogeneous especially in the T₁ phase and is a consequence of the slow diffusion rate of Cu and the mode of formation of T₁ in this alloy, i.e., by a eutectic reaction. This inhomogeneity at a sub-micrometer level could not be detected by backscattered electron imaging (e.g., Figs. 1 and 2) or by x-ray mapping (e.g., the Cu and Al x-ray maps in Fig. 4 of Ref. 10).

A negative ion mass spectrum of this alloy was taken which revealed the presence of oxygen and fluorine in these alloys, estimated to be at ppm levels, which is not expected. Figures 5(a,b) show the distribution maps of O and F (as



↑FIG. 4.--SIMS maps of alloy B described in Fig. 2: (a) Al⁺, (b) Li⁺, (c) Cu⁺. These images are displayed with logarithmic scale to enhance brightness in low-intensity areas. Constituent phases are labeled. Bar = 2 μm.

←FIG. 5.--SIMS maps of alloy B: (a) O⁻, (b) LiF⁻. Note complete segregation of oxygen and fluorine to T₁ plates. Bar = 10 μm.

of the alloy chemistry and to aid in the interpretation of the microstructure. Cu was found to be inhomogeneously distributed, manifesting the slow diffusion rate of Cu relative to that of Al and Li. Also, traces of oxygen and fluorine were detected in the Li-rich T₁ phase. Li distributions revealed the difficulty in attaining equilibrium between T_B and T₁ as T_B forms peritectically.

References

1. D. R. Liu and D. B. Williams, "Accurate quantification of lithium in aluminium-lithium alloys with electron energy-loss spectrometry," *Proc. Roy. Soc. Lond.* A425: 91-111, 1989.
2. D. B. Williams, R. Levi-Setti, J. M. Chabala, Y. L. Wang, and D. E. Newbury, "Microanalysis of precipitates in aluminium-lithium alloys with a scanning ion microprobe," *Appl. Surf. Sci.* 37: 78-94, 1989.
3. D. B. Williams, R. Levi-Setti, J. M. Chabala, Y. L. Wang, D. E. Newbury, and K. K. Soni, "SIMS studies of binary Al-Li alloys," *Proc. 5th Inter. Aluminum-Lithium Conf.*, Williamsburg, Va., Birmingham (U.K.): M.A.C.E. Publications, 1989, 605.
4. H. K. Hardy and J. M. Silcock, "The phase sections at 500°C and 350°C of aluminium-rich aluminium-copper-lithium alloys," *J. Inst. Metals* 84: 423-428, 1955-56.
5. R. Levi-Setti, J. M. Chabala, C. Girod, P. Hallegot, and Y. L. Wang, "The use of focused heavy-ion beams for submicrometer imaging microanalysis," *Microbeam Analysis--1989*, 17-22.
6. J. M. Chabala, R. Levi-Setti, and Y. L. Wang, "Advanced imaging techniques with a scanning ion microprobe," *Microbeam Analysis--1989*, 586-590.
7. D. B. Williams, R. Levi-Setti, J. M. Chabala, Y. L. Wang, and D. E. Newbury, "High spatial resolution secondary ion imaging and secondary ion mass spectrometry of aluminium-lithium alloys," *J. Microsc.* 148: 241-252, 1987.
8. B. Dubost, C. Colinet, and I. Ansara, "An experimental and thermodynamic study of the Al-Li-Cu equilibrium phase diagram," *Ref. 3*, 605.
9. K. S. Vecchio and D. B. Williams, "Convergent beam electron diffraction analysis of the T₁ (Al₂CuLi) phase in Al-Li-Cu alloys," *Met. Trans.* 19A: 2885-2891, 1988.
10. K. S. Vecchio and D. B. Williams, "The apparent 'five-fold' nature of large T₂ (Al₆Li₃Cu) crystals," *ibid.*, 2875-2884.

FLUORESCENCE EFFECTS IN QUANTITATIVE MICROPROBE ANALYSIS

S. J. B. Reed

The most important form of fluorescence is that involving excitation by characteristic radiation. The standard method of calculating corrections for this effect is that derived by Castaing¹ and modified by Reed.² The approximations used in the derivation are reconsidered here; the effect of substituting new data for fluorescence yields, etc., is also discussed. Peak intensities measured with a Si(Li) detector are used to check the intensity expression in the fluorescence formula. Results obtained after updating of the correction procedure are compared with those given by the original version. The difference is greatest for low atomic numbers (e.g., 11-15), for which, however, the absolute size of the correction is small.

Fluorescence excitation by the continuum is usually ignored, but can be quite significant. The factors governing the size of the correction are considered, by use of the formula given by Springer.³ Measurements of peak and continuum intensities are used to test the validity of this formula.

Characteristic Fluorescence

The expression obtained by Castaing¹ for the fluorescence intensity I_f emitted by element A as a result of excitation by the characteristic radiation of element B is

$$I_f = 0.5C_A \frac{\mu_B^A}{\mu_B} \frac{r_A - 1}{r_A} \omega_A I_B f_{abs} \quad (1)$$

where C_A = mass concentration of A, μ_B^A = mass absorption coefficient (m.a.c.) of pure A for B radiation, μ_B = m.a.c. of the sample for B radiation, r_A = absorption edge jump ratio of A, ω_A = fluorescence yield of A, I_B = intensity of B radiation, and f_{abs} = correction factor for absorption of emerging fluorescence radiation. Dividing both sides of Eq. (1) by I_A (the intensity of A radiation excited by electron bombardment) and assuming $I_A = C_A I_A^A$ and $I_B = C_B I_B^B$, where I_A^A and I_B^B are the intensities from pure A and B respectively, we have:

$$\frac{I_f}{I_A} = 0.5C_B \frac{\mu_B^A}{\mu_B} \frac{r_A - 1}{r_A} \omega_A \frac{I_B^B}{I_A^A} f_{abs} \quad (2)$$

In the usual form of the correction procedure the following version of the intensity expression given by Green and Cosslett⁴ is used:

$$I_A^A = K \frac{\omega_A}{A} (U_A - 1)^{1.67} \quad (3)$$

S. J. B. Reed is with the Department of Earth Sciences, University of Cambridge, Cambridge, England, CB2 3EQ.

where A_A is the atomic number of A, U_A is the overvoltage ratio for A (the incident electron energy E_0 divided by the critical excitation energy of A, E_A^c) and K is a constant. Substitution of the G-C expression in Eq. (2) gives:

$$\frac{I_f}{I_A} = 0.5C_B \frac{\mu_B^A}{\mu_B} \frac{r_A - 1}{r_A} \omega_B \frac{A_A}{A_B} \left(\frac{U_B - 1}{U_A - 1} \right)^{1.67} f_{abs} \quad (4)$$

The J(A) Approximation

A simplification originally introduced to facilitate the calculation of corrections by hand involves combining several parameters in Eq. (4) into a single variable $J(A)$, equal to $0.5[(r_A - 1)/r_A] \cdot \omega_B (A_A/A_B)$. For a given A, $J(A)$ is assumed to be constant and can be obtained from a table.² Although this approximation is valid when A and B are close in atomic number, significant errors occur for larger atomic number differences. It is therefore suggested that the use of $J(A)$ should be discontinued, and Eq. (4) be used in full.

The Absorption Factor

In deriving an expression for the absorption factor f_{abs} , Castaign used an exponential function to represent the depth distribution of primary x-ray production.¹ Although this approximation is satisfactory in most cases, it has been found to underestimate f_{abs} for elements such as Mg, Al, and Si by ~10%.⁵ A more realistic function would be preferable, but it is not proposed to address this question further here.

Input Data

For calculating fluorescence corrections, values are required for mass absorption coefficients, absorption edge jump ratios, and fluorescence yields. For m.a.c.s it is desirable to use the more recent data of Heinrich⁶ rather than earlier values: the effect is not dramatic but is sometimes significant. As regards the K edge jump ratio, Reed² assumed a constant value of 0.88 for $(r - 1)/r$, which is too small in the low-Z region. The following polynomial is suggested as a preferable alternative:

$$(r - 1)/r = 1.024 - 9.098 \times 10^{-3}Z + 1.268 \times 10^{-4}Z^2 \quad (5)$$

For the K-shell fluorescence yield, Reed² used the following expression: $\omega = Z^4/(10^6 + Z^4)$. This underestimates ω , especially for low Z, and the following polynomial (fitted to data from Ref. 7) is suggested:

$$\begin{aligned} \omega = & -2.6436 \times 10^{-2} + 1.0288 \times 10^{-2}Z \\ & - 1.4625 \times 10^{-3}Z^2 + 1.0123 \times 10^{-4}Z^3 \\ & - 1.5137 \times 10^{-6}Z^4 \end{aligned} \quad (6)$$

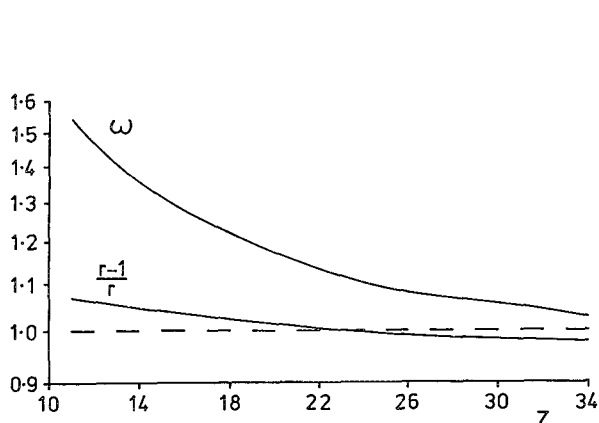


FIG. 1.--Ratio of new to old values of fluorescence yield ω and absorption edge jump ratio factor $(r - 1)/r$.

The new values of ω and $(r - 1)/r$ are compared with those used previously in Fig. 1. For $Z > 23$ the difference is $< 10\%$ and therefore is not very serious. However, the discrepancy becomes quite large for low Z (though the absolute size of the correction in this region is small).

The U-dependent Term

The $(U - 1)^{1.67}$ term in the Green-Cosslett (G-C) intensity formula (Eq. 3) is an approximation for the expression $U \ln U - U + 1$ and there is no valid reason for not using the latter, more rigorous, form. In relation to fluorescence corrections, the difference is usually minor but is significant for values of U that are either small or large. As shown in Fig. 2, this difference becomes important for low atomic numbers, especially with a high accelerating voltage (and hence high U). The slope of the curve in this region is such as to make the correction larger than given by the original G-C formula. There is also considerable divergence for high atomic numbers and low accelerating voltages (low U), which in this case leads to a reduction in the fluorescence correction.

The Atomic Number Effect

In deriving the expression for the x-ray intensity emitted by a pure element given in Eq. (3), Green and Cosslett⁴ used a simplified form of stopping power in order to obtain an integrable function. This deficiency can be remedied if the intensity is multiplied by $1/S$, where S is the Bethe stopping power factor⁸ given by $S = (Z/A) \ln(1166\bar{E}/J)$, in which \bar{E} is the mean electron energy, equal to $(E_0 + E_c)/2$, and J is the mean ionization energy. It is also desirable to include the factor R , which allows for the effect of electron backscattering. (A polynomial such as that in the NBS 'COR 2' program can be used for calculating R .) These factors are identical to those involved in the part of the ZAF correction procedure concerned with the "atomic number effect."

With the incorporation of the R and S factors and the preferred form of U -dependent function, Eq. (3) becomes:

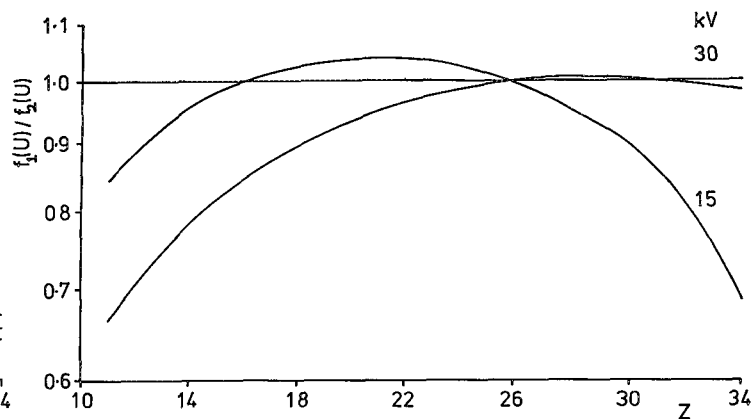


FIG. 2.--Ratio of U -dependent functions in intensity expression, for accelerating voltages of 15 and 30 kV; $f_1(U) = U \ln U - U + 1$, $f_2(U) = (U - 1)^{1.67}$.

$$I_A^A = K \frac{\omega_A}{A_A} \frac{R_A}{S_A} (U_A \ln U_A - U_A + 1) \quad (7)$$

where R_A^A and S_A^A are the backscatter and stopping power factors for A radiation in a pure A target. The S factor has the effect of changing the dependence of the intensity on Z for a given E_0 and on E_0 for a given Z . These trends are modified by the variation of R , but the effect of S is predominant.

Intensity Ratio in a Common Matrix

For fluorescence corrections the ratio of B and A intensities for the same matrix (the analyzed sample) is required, hence it is not strictly correct to use pure element intensities. We can easily take that into account by substituting in the fluorescence formula intensities I_A^X and I_B^X , which are the pure element intensities corrected for matrix X, given by

$$I_A^X = K \frac{\omega_A}{A_A} \frac{R_A^X}{S_A^X} (U_A \ln U_A - U_A + 1) \quad (8)$$

where R_A^X and S_A^X are the backscattering and stopping power factors for A in matrix X. An analogous expression may be used for I_B^X . However, this factor varies only very slowly with Z_A (e.g., by $< 3\%$ for $Z_A = 11 - 34$), hence for the purpose of fluorescence calculations the R/S term can be dropped. It follows that the only modification required to Eq. (4) is to replace $[(U_B - 1)/(U_A - 1)]^{1.67}$ by $(U_B \ln U_B - U_B + 1)/(U_A \ln U_A - U_A + 1)$.

Because the R and S factors are neglected in Eq. (3), this equation (preferably with the above modification) is well suited to the calculation of relative intensities in a common matrix. However, if it is to be used for its original purpose, namely predicting pure element intensities, then the R and S factors should be included, as in Eq. (8).

Experimental Intensity Data

Various studies (e.g., Ref. 10) have shown that the detection efficiency of a Si(Li) de-

TABLE 1.--Measured total K intensities for pure elements (photons/s/na/msterad).

	accelerating voltage (kV)			
	15	20	25	30
22	1230	2290	3540	4860
23	1040	2010	3260	4390
24	870	1760	2790	3990
25	730	1510	2470	3540
26	610	1310	2170	3140
27	470	1100	1900	2820
28	373	950	1620	2440
29	289	760	1380	2130
30	213	610	1140	1810
31	152	500	980	1570
32	100	402	820	1360
33	64	301	670	1110

tector is close to 100% over the range of energies that is of most importance for fluorescence corrections (4-12 keV). Such a detector has therefore been used to measure the intensities of the characteristic peaks of pure elements for the purpose of testing intensity expressions such as those already discussed. In order to define the solid angle of acceptance and avoid possible edge effects, a 1mm aperture was placed in front of the detector. Integrated intensities of the $K\alpha$ and $K\beta$ peaks of pure elements from Ti ($Z = 22$) to As ($Z = 33$) were measured, with accelerating voltages of 15, 20, 25, and 30 kV. These values were corrected for background by linear interpolation. The small correction required for window absorption was calculated from nominal values for the thickness of the Be window, etc. Corrections for self-absorption and continuum fluorescence were also applied. The results are given in Table 1. The estimated relative accuracy is about $\pm 5\%$. The absolute accuracy may be somewhat worse, owing to uncertainty in the solid angle.

Comparison Between Experimental and Theoretical Intensities

As has been found in other studies (e.g., Ref. 11), the exponent of 1.67 requires amendment in order to yield good agreement between the G-C expression and experimental data for a given element at different accelerating voltages. For the data in Table 1 the "best fit" values of the exponent depend systematically on Z , rising from 1.56 for $Z = 22$ to 1.70 for $Z = 33$. The "constant" also varies somewhat with Z . These observations confirm the shortcomings of the G-C expression in its original form when used to predict pure element intensities and can be explained by the neglect of the R/S term (which modifies the dependence on E_0) and to some extent the substitution of $(U - 1)^{1.67}$ for $U \ln U - U + 1$.

For fluorescence corrections the important question is the dependence of the intensity on Z for a given E_0 , in a constant matrix. In Fig. 3 experimental pure element intensities (for $E_0 = 20$ keV), normalized to a matrix of Fe by the application of R and S factors, are com-

pared with the G-C expression in its original form and with $U \ln U - U + 1$ instead of $(U - 1)^{1.67}$. For $Z > 20$ the difference between these forms is small and both agree with experiment quite adequately for present purposes. For $Z < 20$ the two forms diverge, but direct experimental evidence is lacking in this region.

Intensity Expression for Low Z

For $Z < 20$ it becomes increasingly difficult to obtain reliable intensity data because of uncertainty in the detection efficiency. However, it is possible to determine the dependence of the intensity for a given element on accelerating voltage (assuming that an accurate absorption correction is used). Armstrong⁵ measured intensities for a number of elements at 15 and 20 kV. An increasing divergence from the $(U - 1)^{1.67}$ relationship was observed for $Z < 20$, on the basis of which Armstrong proposed a new U -dependent function. However, the validity of this new function for use in fluorescence corrections is unproved and is questionable because it does not tend to 1 as Z_B approaches Z_A . The discrepancy between the experimental data for low atomic numbers and the G-C expression is partly attributable to the divergence between $(U - 1)^{1.67}$ and $U \ln U - U + 1$ for large U values, and partly to the effect of the R/S term. As shown in Fig. 4, quite good agreement is obtained between the modified expression (Eq. 7) and Armstrong's experimental data. Hence there is no reason to use a different intensity expression for low atomic numbers.

Comparison of Old and New Correction Methods

The effect of the changes to the correction procedure outlined above can be evaluated by a comparison of the factor $1 + (I_f/I_A)$ (by which uncorrected concentrations are divided) as calculated by the old and new methods. The old method is defined as that put forward in 1965,² based on tabulated $J(A)$ values (though this last is not an essential part of this method). The new method is as defined above [not using $J(A)$, but using $U \ln U - U + 1$ and new data for fluorescence yields, etc.]

Figure 5 shows the comparison between old and new methods for a trace of Ti in pure elements of atomic number 24-32. The new method gives larger corrections but the maximum difference is only about 2.5% of the Ti concentration, which is not very significant given that the concentration concerned is low. (The correction gets smaller as the concentration increases.) The main cause of the underestimation of the correction by the old method is the $J(A)$ approximation.

Figure 6 shows the comparison between old and new methods for a trace of Al in pure elements of atomic number 14-20. The new method again gives a larger correction. In this case the main cause is the higher fluorescence yield values used. The maximum difference is about 3% of the Al concentration, which increases to

nearly 4% if the underestimation of the absorption factor noted by Armstrong⁵ is taken into account.

The K β Line

So far it has been assumed that the K spectrum consists solely of the K α ($\alpha_1 + \alpha_2$) line, whereas fluorescence calculations strictly should be divided into separate parts for K α and K β (consisting mainly of β_1 , but including minor β lines). For this purpose data for relative intensities are required (e.g., from Ref. 12). Since the K β intensity does not exceed about 14% of the total K intensity, the effect of separate calculation is negligible unless there is a significant absorption edge between the K α and K β lines.

Summary--Characteristic Fluorescence

The following measures are proposed to improve the accuracy of characteristic fluorescence corrections:

1. Use the full formula (Eq. 4) rather than the simplified version with $J(A) = \text{constant}$.
2. Substitute more recent data for fluorescence yields and absorption edge jump ratios, as given by Eqs. (5) and (6).
3. Replace $(U - 1)^{1.67}$ by $U \ln U - U + 1$ in Eq. (4).

The effect of these changes is generally small when the correction is large ($Z_A > 20$). For low atomic numbers ($Z_A < 20$) where the absolute size of the correction is small, the relative difference is greater and is caused mainly by the change in the fluorescence yield values.

Continuum Fluorescence

Springer³ derived the following expression for the continuum fluorescence intensity for element A in a sample of mean atomic number \bar{Z} :

$$\frac{I_f}{I_A} = G \frac{r_A - 1}{r_A} A_A \bar{Z} E_A^A \frac{\mu_C^A}{\mu_C} f_{\text{abs}} \quad (9)$$

where μ_C^A and μ_C are the m.a.c. values of pure A and the sample, respectively, on the high-energy side of the absorption edge of A. (For details of the absorption factor f_{abs} , see Ref. 3.) Equation (9) refers to the simple case where there are no absorption edges between E_0 and E_A^A : if such edges are present, the calculation is divided into separate parts for each inter-edge region.¹³

The constant G incorporates terms that originate from expressions used for stopping power, ionization cross section, and continuum intensity. Springer proposes the value 4.34×10^{-6} for K radiation (with E_0 in keV). Using the same formulas for stopping power, etc., one can express the ratio of continuum to characteristic intensity for a pure element thus:

$$\frac{I_c}{I_A} = \frac{2G A_A Z_A \Delta E(E_0 - E)}{\omega_A (U_A \ln U_A - U_A + 1) E} \quad (10)$$

where ΔE is the width of the band of continuum radiation concerned and E is the mean energy of this band (both in keV). Measuring I_c/I_A thus provides an independent means of verifying the value of G.

Total K intensities ($\alpha + \beta$) and continuum intensities were measured on samples of pure Ti, Fe, and Zn with accelerating voltages of 20 and 30 kV. The continuum was integrated over 1 keV bands between 5 and 12 keV. Only regions free from characteristic peaks were included. All intensities were corrected for absorption in the detector window and the sample itself. Values of G calculated by Eq. (10) are plotted in Fig. 7. The slight downward trend with continuum energy is consistent with previously observed divergences from Kramers's law. The mean experimental G value of 3.85×10^{-6} is considerably closer to the Springer value than to that of 2.9×10^{-6} used by Hénoc in his version of the continuum fluorescence correction.¹⁴

Factors Controlling Continuum Fluorescence

The calculated continuum fluorescence intensity for a trace of Zn in samples consisting of otherwise pure elements of atomic number 6-42 is plotted in Fig. 8. The continuum fluorescence intensity is controlled predominantly by the ratio μ_C^A/μ_C . For a trace of A in B this ratio varies almost as the inverse cube of Z_B , thereby overriding the effect of Z_B on the continuum intensity. In a "light" matrix, A atoms absorb a disproportionate fraction of the continuum, owing to the low m.a.c. of B. This effect decreases as $Z_B \rightarrow 30$. The jump at 29 occurs because the emerging A radiation is no longer strongly absorbed by B. The further jump at 31 is caused by the sudden decrease in μ_C^B which occurs when the energy of the B absorption edge becomes greater than that of the A edge and differential absorption by A enhances I_f .

For $Z_B > 30$, the absorption edge of B lies within the band of continuum responsible for fluorescing A. Strong differential absorption by A occurs in the section between the A and B edges, but not above the B edge. The increase in the width of the interedge region with increasing Z_B causes I_f to increase, but is counteracted by a simultaneous decrease in the differential absorption effect, so that I_f/I_A passes through a maximum, as shown in Fig. 8.

Summary--Continuum Fluorescence

The continuum fluorescence correction is unjustifiably neglected--it commonly exceeds 1% and can rise above 10% in cases where there is strong differential absorption by the fluoresced element. The correction should be therefore included in quantitative analysis programs.

References

1. R. Castaing, Ph.D. thesis, Univ. of Paris, 1951.

2. S. J. B. Reed, *Brit. J. Appl. Phys.* 16: 913, 1965.
3. G. Springer, *N. Jahrb. Miner. Abh.* 106: 241, 1967.
4. M. Green and V. E. Cosslett, *Proc. Phys. Soc.* 78: 1206, 1961.
5. J. T. Armstrong, *Microbeam Analysis--1988*, 239.
6. K. F. J. Heinrich, *Proc. 11th ICXOM*, 1987, 67.
7. M. O. Krause, *J. Phys. Chem. Ref. Data* 8: 307, 1979.
8. H. A. Bethe and J. Ashkin, *Experimental Nuclear Physics*, New York: Wiley, 1953.
9. J. Hénoc, K. F. J. Heinrich, and R. L. Myklebust, *A Rigorous Correction Procedure for Quantitative Electron Probe Microanalysis (COR 2)*, NBS Tech. Note 769, 1973.
10. H. D. Keith and T. C. Loomis, *X-ray Spectrom.* 5: 93, 1976.
11. E. Lifshin, M. F. Ciccarelli, and R. Bolon, *Proc. 8th ICXOM*, 1980, 141.
12. M. R. Khan and M. Karimi, *X-ray Spectrom.* 9: 32, 1980.
13. G. Springer, *Proc. 6th ICXOM*, 1972, 141.
14. J. Hénoc, in K. F. J. Heinrich, Ed., *Quantitative Electron Probe Microanalysis*, NBS Spec. Publ. 298, 1968, 197.

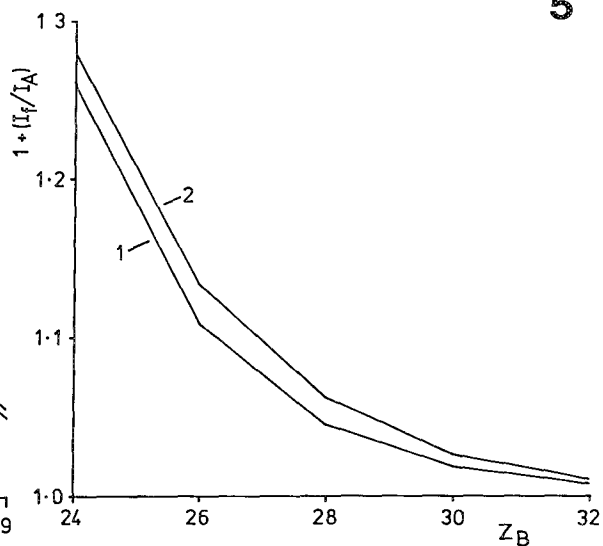
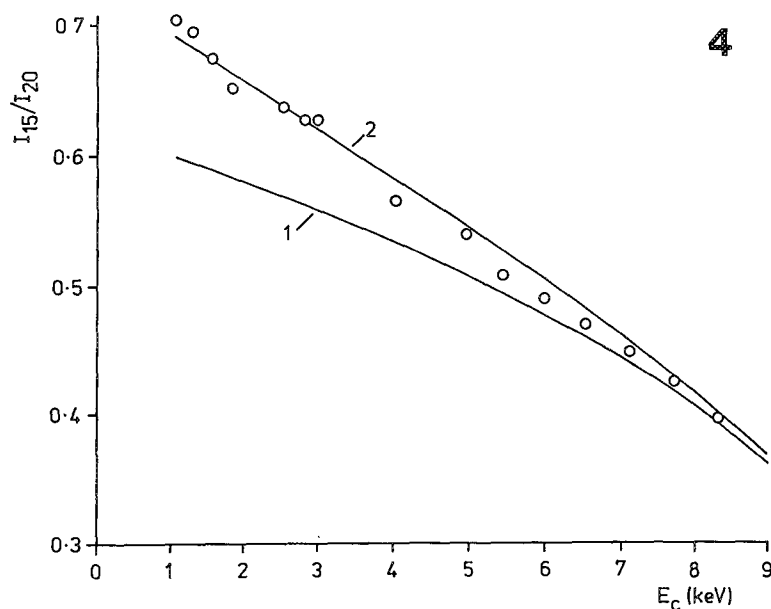
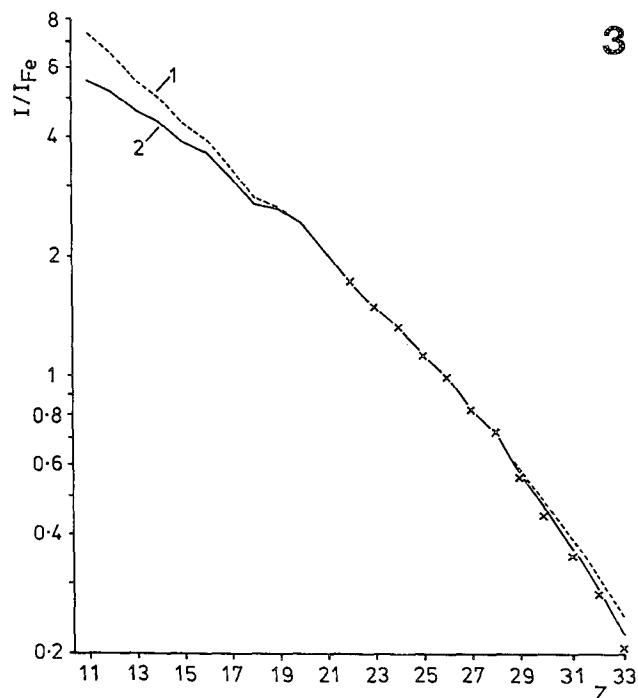


FIG. 3.--Pure element intensities relative to Fe (corrected for Z effect): x, experimental points; 1, Green-Cosslett equation (original form); 2, ditto with $U \ln U - U + 1$ in place of $(U - 1)^{1.67}$.

FIG. 4.--Ratio of pure element intensities for 15 and 20 kV accelerating voltages, as a function of critical excitation energy: o, experimental points from Ref. 5; 1, Green-Cosslett equation (original form); 2, ditto with $U \ln U - U + 1$ in place of $(U - 1)^{1.67}$, multiplied by R/S.

FIG. 5.--Characteristic fluorescence enhancement factor for trace of Ti in element B, calculated by old (1) and new (2) methods (accelerating voltage 20 kV, x-ray take-off angle 40°).

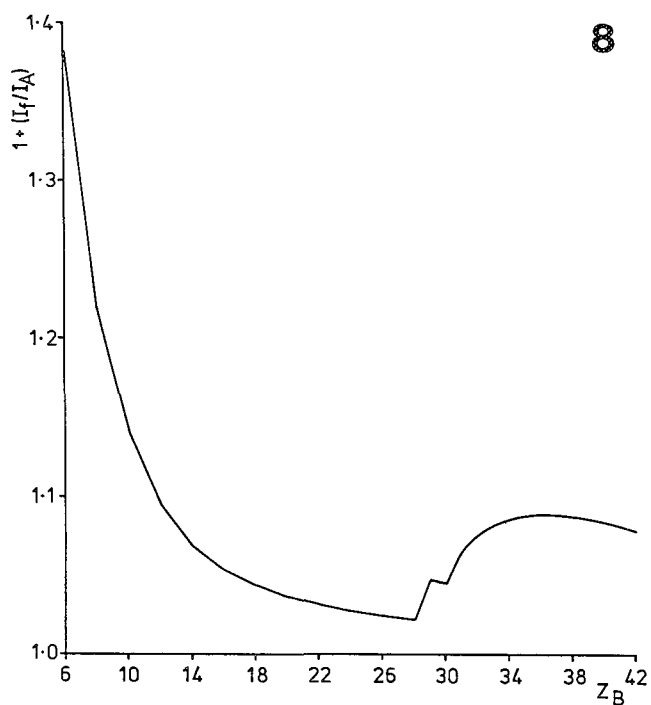
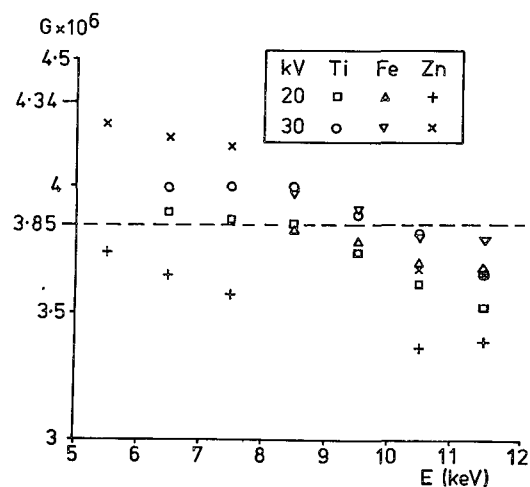
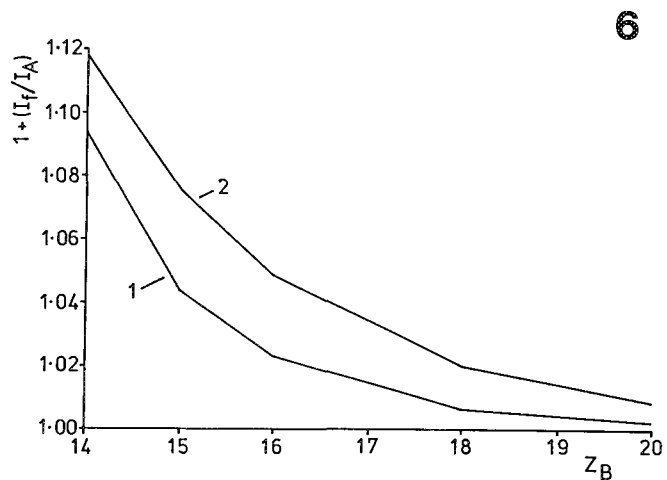


FIG. 6.--Characteristic fluorescence enhancement factor for Al (otherwise as Fig. 5).

FIG. 7.--Experimental values of continuum constant G (mean value, 3.85×10^{-6} ; Springer¹⁴ value, 4.34×10^{-6}).

FIG. 8.--Continuum fluorescence enhancement factor for trace of Zn in pure B; 30 kV accelerating voltage, 40° x-ray take-off angle (derived from Springer¹⁴).

MEASUREMENT AND PARAMETERIZATION OF $\phi(\rho z)$ CURVES FOR QUANTITATIVE ELECTRON PROBE MICROANALYSIS

J. D. Brown

Writing correction equations in terms of $\phi(\rho z)$ curves (x-ray generation curves) has the very attractive attributes of being simple to understand, as exact as the curves can be approximated, and amenable to several different methods of improvement from experimental measurement to the use of theory relating electron interaction with atoms. The origin of $\phi(\rho z)$ curves goes back to the original work of Castaing.¹ He recognized that the x-ray emission from a solid could be written in terms of the $\phi(\rho z)$ curves. Later, during the 1960s and 1970s, lack of data on $\phi(\rho z)$ curves and limitations imposed by computing power at that time forced researchers into simple approximations for the corrections. A resurgence of the $\phi(\rho z)$ approach has occurred as computing power and measured data have increased. More and more routine electron microprobe analyses are carried out by use of $\phi(\rho z)$ correction equations.

The three corrections that have been identified as necessary for conversion of measured characteristic x-ray k-ratios to composition can be exactly expressed in terms of $\phi(\rho z)$ curves. The absorption correction, which is the fraction of generated x rays that escape from the specimen, is expressed in terms of $\phi(\rho z)$ curves as

$$f(\chi) = \frac{\int_0^\infty \phi(\rho z) \exp(-\mu \rho z \csc \psi) d\rho z}{\int_0^\infty \phi(\rho z) d\rho z}$$

in which the numerator represents the number of x rays that escape from the specimen at take-off angle ψ , and the denominator represents the total number of x rays generated in the specimen. The atomic number effect recognizes that the number of x rays generated in the specimen per unit concentration of a given element is larger in matrices of higher atomic number. In terms of $\phi(\rho z)$ curves, the atomic number effect can be written

$$\frac{I_{\text{un}}}{I_{\text{std}}} = \frac{\int_0^\infty \phi_{\text{un}}(\rho z) d\rho z}{\int_0^\infty \phi_{\text{std}}(\rho z) d\rho z}$$

in which the area under $\phi(\rho z)$ curves is the total number of x rays generated in the specimen and standard per unit current and unit concentration. The correction for fluorescence by absorption of characteristic x rays can also be written in terms of $\phi(\rho z)$ curves as

J. D. Brown is with the Department of Materials Engineering, The University of Western Ontario, London, Ont., Canada N6A 5B9. This work was supported by a grant from the Natural Sciences and Engineering Research Council of Canada.

$$\frac{I_{fA}}{I_A} = \frac{KW \int_0^\infty \int_0^\infty \phi_B(\rho z) \int_{s-x}^\infty [\exp(-x)/x] dx d\rho s d\rho z}{\int_0^\infty \phi_A(\rho z) d\rho z} \cdot \frac{W_A \int_0^\infty \phi_A(\rho z) d\rho z}{W_B \int_0^\infty \phi_B(\rho z) d\rho z} \frac{I_A^0}{I_B^0}$$

In this equation, the primary radiation from element B is emitted at depth ρz , the fluorescent radiation from element A at depth ρs . The constant K includes fluorescence yields, jump ratios, etc.; the integral of $\exp(x)/x$ is the exponential integral, and W_A and W_B are weight fractions. The first term in the equation gives the fluorescent radiation of element A in terms of the directly excited radiation of B. The second term is the ratio of directly excited x rays of A to B, and the third term is the ratio of intensities from thin layers of A and B that are used in the normalization of the $\phi(\rho z)$ curves. Although such an expression can be written, this approach has rarely been used on the rationale that the fluorescence is adequately represented by simpler expressions.

Measurement of $\phi(\rho z)$ Curves

Castaing and Descamps² first suggested the sandwich sample method for the determination of $\phi(\rho z)$ curves. In this method, a "tracer" layer is deposited on a polished block of a pure element and is then covered, area by area, by successively thicker layers of the same pure element. The consequence is a specimen in which a thin layer of the tracer element is found at various depths in the pure element substrate. Intensities are measured for a characteristic x-ray line of the tracer element from the various depths in the specimen. After correction for dead time and subtraction of background, the intensities are corrected for absorption by the pure element layer to obtain the generated intensity. To normalize the curves and to make them independent of the tracer layer thickness, Castaing and Descamps proposed comparing these intensities to that from the same tracer layer thickness isolated in space. This procedure was accomplished by evaporation of a layer of tracer on a thin carbon substrate at the same time as the tracer layer was evaporated on the pure element substrates. The ratio of corrected intensities from the tracer layer deposited on the substrate to the intensity from the same thickness of tracer on the carbon film (isolated in space) is termed the $\phi(0)$ value. An alternate method of determining $\phi(0)$ values is to deposit the same thickness of tracer layer on substrates composed of pure element of differing atomic number, measure the

intensities from these substrates, and then extrapolate to atomic number 0 for which the $\phi(0)$ value must be unity.

The choice of the tracer layer is quite crucial. To mimic the properties of the matrix material, the tracer should be close in atomic number but not suffer any characteristic fluorescence. Originally Castaing and Descamps chose bismuth as a tracer in gold, zinc as a tracer in copper, and copper as a tracer in aluminum. This last choice was criticized as inappropriate and a later curve measured with a magnesium tracer showed significant differences.³ Parobek and Brown showed that the sandwich sample technique could be used more generally to look at the atomic-number effect.⁴ They deposited identical thicknesses of tracer layer in specimens of different atomic number. The consequence of measuring the same characteristic line from the same tracer on matrices of different atomic number is that these intensities reflect the differences in electron scattering and stopping power for the different elements, exactly the atomic-number effect.

The layer must also satisfy several criteria if a successful and accurate measurement of $\phi(\rho z)$ curves is to be obtained. The layer must be thick enough to yield sufficient intensity in a reasonable count time. At the same time, the layer must be thin enough so that the $\phi(\rho z)$ curve is not distorted by the layer. In practice for electron-beam energies in the range 15-30 keV, layer thicknesses of 5-10 $\mu\text{g}/\text{cm}^2$ are appropriate. If the electron energy and absorption edge energy become small, the layer thickness must decrease accordingly so that it becomes difficult if not impossible to maintain measurable intensities without distorting the $\phi(\rho z)$ curve. An example of this effect of the tracer layer has been explored by Karduck and Rehbach.⁵

An alternate method to measure $\phi(\rho z)$ curves is the wedge specimen technique of Büchner and Pitsch.⁶ A specimen consisting of two materials placed against each other is taper-sectioned at a small angle through the interface. The result is a layer of increasing thickness of one material over a substrate material. The thickness of the overlayer can be calculated if the distance from the interface on the surface is measured and the angle of the taper section is known. Characteristic x-ray intensities are measured as a function of distance from the interface yielding the integral of the $\phi(\rho z)$ curve. By differentiation of this curve, the $\phi(\rho z)$ curve itself is obtained. A relatively large number of $\phi(\rho z)$ curves have now been measured for a range of electron energies and a variety of tracers and matrix materials. This body of data is now sufficient to develop generalized expressions for $\phi(\rho z)$ that can predict the shape and area of curves for any composition and analysis conditions.

Modeling of $\phi(\rho z)$ Curves

The general shape of a typical $\phi(\rho z)$ curve can be seen in Fig. 1. The curve rises from a value at the surface which is greater than 1, passes through a maximum at some depth into the

specimen, and then decays to zero at some greater depth. The details of the shape of the curve are important in obtaining an accurate absorption correction; the area under the curve must be accurately modeled for a good atomic-number correction.

The early workers in the field argued that accurate modeling of the shape of the $\phi(\rho z)$ curve was not important in quantitative analysis and indeed almost any shape was used from a constant intensity as a function of depth (the quadrilateral model of Belk⁷) to an exponential decay from the surface (the thin-film model of Duncumb⁸). Of course in the limit of no absorption of the x rays on leaving the specimen, the shape is indeed immaterial; only the total areas need be accurate. On the other hand, as the absorption increases, the accuracy of the shape of the $\phi(\rho z)$ curves becomes more and more critical. The rule of thumb that $f(x)$ should not be less than 0.9 (i.e., 90% of the x rays which are generated escape from the specimen) when Philibert's simple expression is used is just an admission of the inadequacies of the implied $\phi(\rho z)$ curves in that model.

The earliest attempt to model accurately the shape of the $\phi(\rho z)$ curve was due to Criss,¹⁰ who used a multiorder polynomial to describe the shape of the existing measured curves of Castaing and Descamps.² Brown and Parobek¹¹ and Büchner and Pitsch⁶ used an empirical expression which was extended to higher electron energies by Brown and Robinson.¹² Wittry¹³ used a Gaussian expression centered at the maximum of the $\phi(\rho z)$ distribution and Kyser¹⁴ later introduced an asymmetric term in recognition of the obvious asymmetry about the maximum. Pichou and Pichoir¹⁵ have used a pair of parabolas to model the shape of the $\phi(\rho z)$ curve in their correction model. The disadvantage of all these approaches is that improvements to accuracy can only be made on the basis of comparison to experimental measurements.

Figure 2 shows a plot of $\ln[\phi(\rho z)]$ vs square of depth which reveals the nature of the $\phi(\rho z)$ curves, a Gaussian-centered at the surface of the specimen. Such dependence has been observed for more than a hundred measured $\phi(\rho z)$ curves with the only variation a consequence of continuum fluorescence that can be seen in the measured curve with a high matrix atomic number such as shown in Fig. 3. The deviation from the linear dependence at high depths is due to that cause. Near the surface, the curve falls away from the Gaussian because the electrons enter the specimen in a specific direction and the Gaussian dependence is not achieved until the electrons are traveling in random directions. The equation that Packwood and Brown¹⁶ used to describe the curves is

$$\phi(\rho z) = \gamma_0 [1 - q \exp(-\beta \rho z)] \exp[-(\alpha \rho z)^2]$$

where $q = [\gamma_0 - \phi(0)]/\gamma_0$. Four parameters, γ_0 , α , β , and $\phi(0)$, are needed to calculate the $\phi(\rho z)$ curve for any particular analysis. The regions of importance for each of the parameters is shown in Fig. 4. The α value establishes the rate at which the $\phi(\rho z)$ decays from

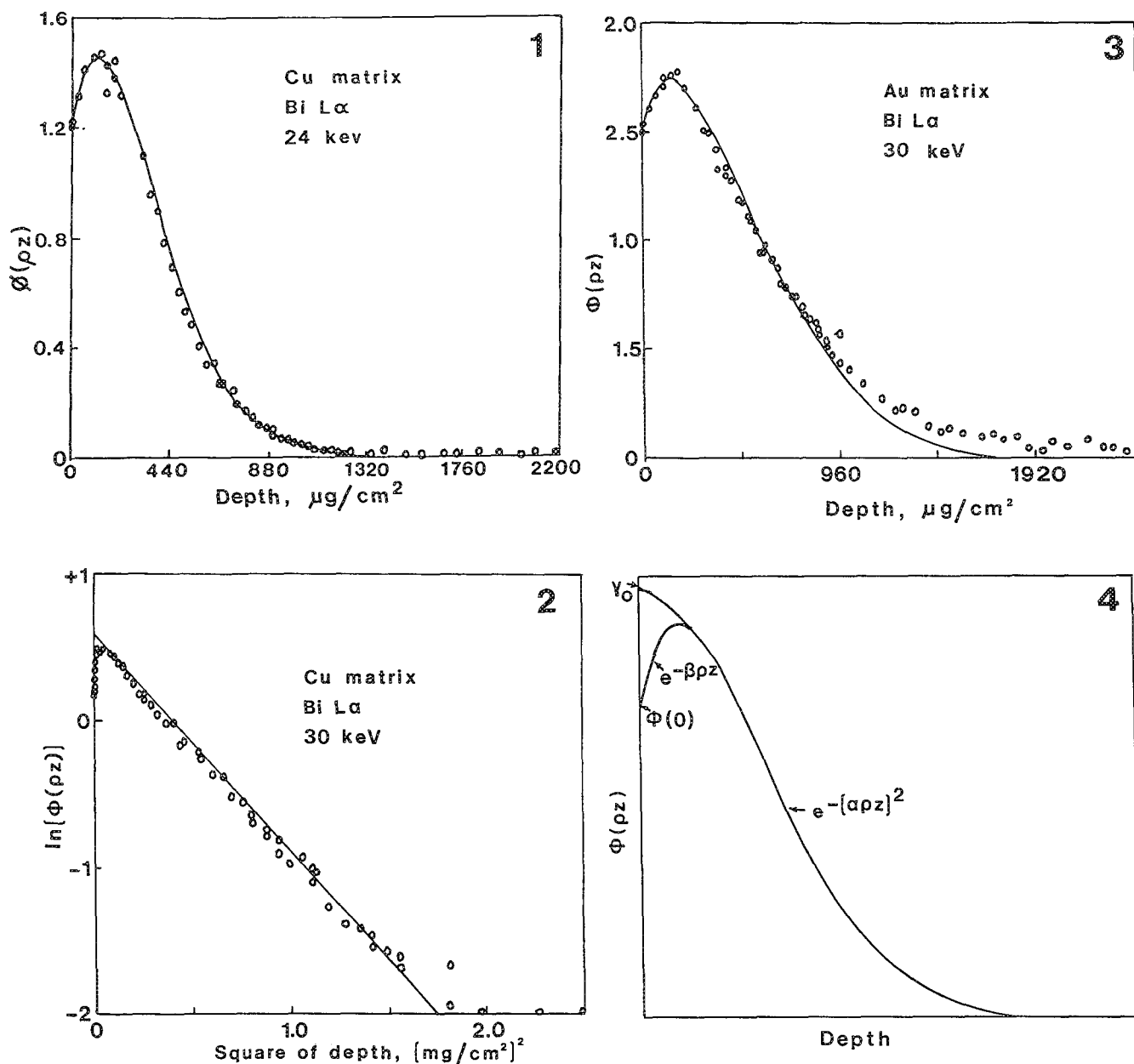


FIG. 1.--Typical $\phi(\rho z)$ curve showing general shape.

FIG. 2.-- $\phi(\rho z)$ curve plotted to show Gaussian behavior.

FIG. 3.-- $\phi(\rho z)$ curve for Bi L α in Au matrix showing continuum fluorescence contribution at large depths.

FIG. 4.--Gaussian used to model $\phi(\rho z)$ curves showing significance of parameters.

the maximum in the curve. There is a very strong dependence on electron energy and absorption edge energy but only a small dependence on atomic number. It is interesting that as the specimen is tilted from normal electron incidence, the value of β remains unchanged. The β value is determined by how quickly the electrons that originally travel in a specific direction become randomized by interactions with the atoms of the solid. Since interactions are much larger for elements of higher atomic number, there is a large dependence on atomic number as well as on electron energy. The $\phi(0)$ value is given

by the ratio of the intensity from a thin tracer layer on a substrate to the intensity of the same thickness of tracer layer isolated in space. In addition to measurements made when $\phi(\rho z)$ curves are measured, a number of alternate measurements and calculations of $\phi(0)$ have been made and a number of expressions published.¹⁷⁻²⁰ The $\phi(0)$ value is important in that in the measurement of $\phi(\rho z)$ curves using the sandwich sample method, the $\phi(0)$ value determines the magnitude of the curve and hence the area under the curve--obviously of great importance in the atomic-number effect. The γ_0

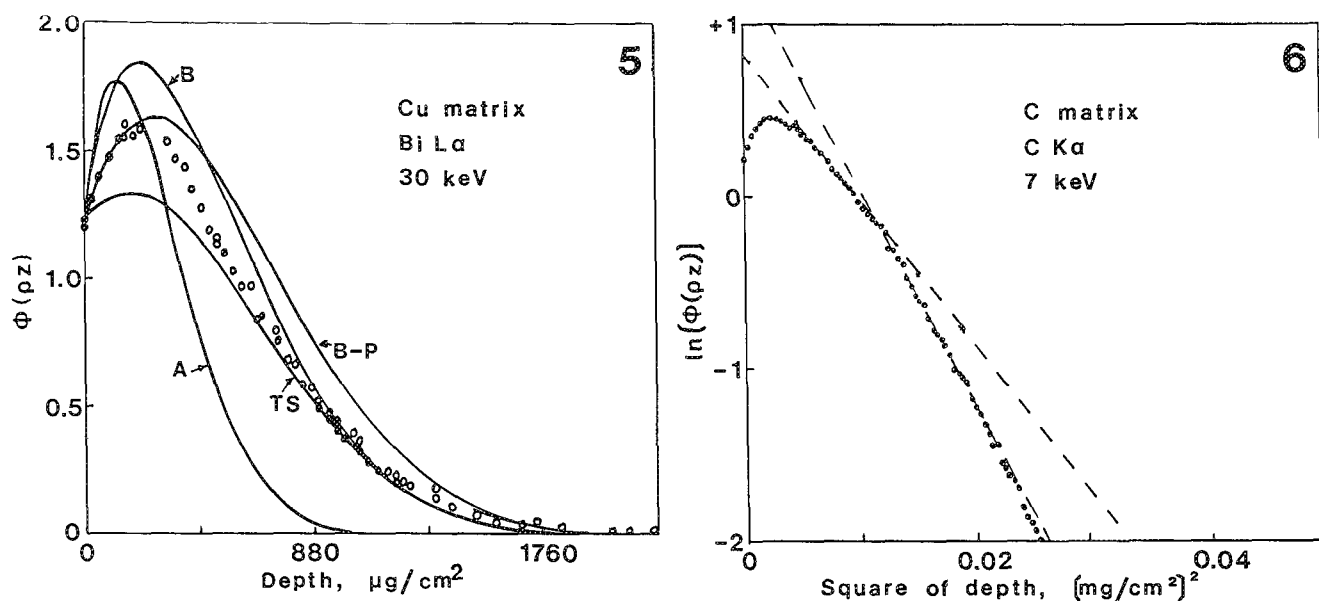


FIG. 5.--A comparison of calculated curves with experimental data. Cu matrix, Bi L α line, 30 keV. B-P, Brown and Packwood²¹; B. Bastin et al.²²; A. Armstrong²³; TS, Tirira Saa et al.^{25,26}
 FIG. 6.--A replot of the data of Rehbach and Karduck²⁶ for C K α in C at 7 keV.

value is equivalent to the $\phi(0)$ value except that one should imagine the incident electrons as coming from random directions. To a first approximation, one would expect γ_0 and $\phi(0)$ to be related by a simple factor.

Comparison of Parameters

The various published values for the parameters used in the $\phi(\rho z)$ equation have been generated by different criteria of optimization, either on the basis of a different set of experimental data or for a specific purpose. Brown and Packwood²¹ started from parameters fitted to measured $\phi(\rho z)$ curves and then modified them to improve performance in quantitative analysis. Bastin et al.²² optimized the parameters for low-atomic-number analyses, and Armstrong²³ was concerned with the analysis of minerals. More recently Tirira Saa et al.^{24,25} have used theoretical arguments in proposing new values. Recent measurements of $\phi(\rho z)$ curves with a JEOL Superprobe have been compared to curves calculated on the basis of the published equations from the four papers mentioned above. A typical result is shown in Fig. 5. It is dangerous to draw definite conclusions on the basis of only a few comparisons, but some comments can be made. None of the predicted curves fit the experimental data particularly well. The maximum in the Brown and Parobek curve occurs at too great a depth in the specimen, which would tend to indicate that too large an absorption correction will result. The maxima for the Bastin et al. and Tirira Saa et al. expressions occur at almost the same depth as the experimental data but the areas under the curves are very different. For an accurate absorption correction it is certainly very important in modeling $\phi(\rho z)$ curves

to get the depth of maximum production correctly; and since ratios are taken for the atomic number effect, the performance of these equations in quantitative analysis is quite good. The Armstrong parameters predict a very shallow x-ray generation. Since his parameters were generated specifically for mineral analysis, for which very good results have been obtained, does the small depth of x-ray production reflect charge build up in the insulating specimens? This issue needs to be resolved.

Recently Karduck and Rehbach²⁶ have suggested the Gaussian form for the $\phi(\rho z)$ curve breaks down for matrices of low atomic number and for low-energy characteristic lines based on $\phi(\rho z)$ curves generated by Monte Carlo calculations. It appears from these curves that too few x rays are generated at very great depths. Their curve for C K α in carbon at 7 keV was blown up and then replotted as $\ln[\phi(\rho z)]$ vs the square of the depth. If one uses the portion of the curve in which 90% of the x rays are generated, the plot of Fig. 6 results. The plotted points are taken as well as possible from their curve. This result suggests that a perfectly acceptable Gaussian fit is possible, although there appear to be two straight line portions with different slopes. It may be that some parameter used in the Gaussian, for example the ionization cross section near the absorption edge, leads to this effect. Further work needs to be done.

Conclusions

The description of $\phi(\rho z)$ curves using a Gaussian equation for quantitative electron probe microanalysis is now well established. Several authors have published parameters that give excellent results for a wide range of ex-

perimental conditions and specimen types. Comparison with measured curves would suggest that further improvements can be made. Examination of the parameters that are successful for mineral analysis would suggest that some evidence exists for a decrease in depth of x-ray generation in insulating specimens. For low-energy characteristic lines, some deviation from the Gaussian shape may occur at large depths in the specimen. Further work needs to be done in all these areas.

References

1. R. Castaing, *Advances in Electronics and Electronic Physics*, New York: Academic Press, 13: 317, 1960.
2. R. Castaing and J. Descamps, *J. Phys. et Radium*. 16: 304, 1955.
3. R. Castaing and J. Henoc, *Proc. 4th ICXOM*, Paris, 1966, 120.
4. L. Parobek and J. D. Brown, *Adv. X-ray Anal.* 17: 479, 1974.
5. P. Karduck and W. Rehbach, *Microbeam Analysis--1988*, 277.
6. A. R. Büchner and W. Pitsch, *Z. Metallkunde* 62: 392, 1971.
7. J. A. Belk, Ref. 3, p. 214.
8. P. Duncumb and P. A. Melford, Ref. 3, p. 240.
9. J. Philibert, *Proc. 3rd ICXOM*, New York, 1963, 379.
10. J. Criss, *Electron Probe Microanalysis*, NBS Special Publ. 298, 1968, 53.
11. L. Parobek and J. D. Brown, *X-ray Spectrometry* 7: 26, 1978.
12. J. D. Brown and W. H. Robinson, *Microbeam Analysis--1979*, 238.
13. D. B. Wittry, Ph.D. thesis, California Institute of Technology, 1957.
14. D. F. Kyser, *Proc. 6th ICXOM*, Tokyo, 1972, 147.
15. J. L. Pouchou and F. Pichoir, *Proc. 11th ICXOM*, London, Ont., 1987, 249.
16. R. H. Packwood and J. D. Brown, *X-ray Spectrometry* 10: 138, 1981.
17. G. A. Hutchins, in T. D. McKinley et al., Eds., *The Electron Microprobe*, New York: Wiley, 1966, 390.
18. Ref. 14, 121.
19. S. B. Hale and R. H. Packwood, *Microbeam Analysis--1983*, 97.
20. G. Love, M. G. Scott, and V. D. Scott, *J. Phys. D11*: 23, 1978.
21. J. D. Brown and R. H. Packwood, *X-ray Spectrometry* 11: 187, 1982.
22. G. F. Bastin et al., *X-ray Spectrometry* 13: 91, 1984.
23. J. T. Armstrong, *Microbeam Analysis--1982*, 175.
24. J. H. Tirira Saa et al., *X-ray Spectrometry* 16: 243, 1987.
25. J. H. Tirira Saa and J. A. Riveros, *X-ray Spectrometry* 16: 27, 1987.
26. W. Rehbach and P. Karduck, *Microbeam Analysis--1988*, 285.

THE XPP PROCEDURE APPLIED TO QUANTITATIVE EDS X-RAY ANALYSIS IN THE SEM

Jean-Louis Pouchou, Françoise Pichoir, and Denis Boivin

During the past few years, the energy dispersive x-ray detectors (EDS) have undergone significant improvements with regard to the spectral resolution and the sensitivity to low-energy photons. Detectors with thin atmospheric windows now make it possible to detect soft radiations without any danger of contaminating the detector crystal, and consequently with an efficiency that should not vary with time. However, we feel that during the same period, less attention has been paid to improve the efficiency and the reliability of the software provided for quantitative EDS analysis in scanning electron microscopes (SEM).

Considering from our previous experience with the electron microprobe that noticeable progress could also be expected in quantitative SEM/EDS analysis, we have spent some time to implement our recent $\phi(\rho z)$ model called XPP¹ into the KEVEX system,² and using a Quantum detector to perform the first experimental checks which will permit the control of the various elements of the software with a view to optimizing it.

Several aspects of SEM/EDS analysis of bulk specimens are considered here: analysis with or without standards, analysis at normal or oblique beam incidence, analysis of very light elements (e.g., oxygen), and analysis of layered specimens (STRATA program).

The Basic XPP Model

The XPP model is a $\phi(\rho z)$ model that has been especially designed for SEM/EDS quantitative analysis, with the goal of yielding:

- (1) realistic $\phi(\rho z)$ distribution in depth of the ionization, on the basis of a simple mathematical model able to accept the integral F of $\phi(\rho z)$ as a basic parameter;
- (2) distributions with a high degree of flexibility, so that they can be strongly distorted to account for the effects of tilting the specimen; and
- (3) $\phi(\rho z)$ functions that could be easily used for surface-film or layered-specimen analysis.

These criteria led us^{1,3} to combine exponential and linear functions of the mass depth ρz :

$$\phi(\rho z) = A \exp(-a\rho z) + (B\rho z + \phi(0) - A) \exp(-b\rho z) \quad (1)$$

The coefficients A , B , a , and b are deduced from the four parameters selected to characterize the distribution, as follows:

Area F of $\phi(\rho z)$. As in our previous PAP model,^{3,4} and in agreement with the definition of $\phi(\rho z)$ by Castaing,⁵ the area F is proportional to N_j , the number of vacancies produced at level j of atoms A (critical energy E_c) per incident electron (initial energy E_0):

$$N_j = C_A(N/A)Q_j(E_0)F \text{ with } F = \int_0^\infty \phi(\rho z) d\rho z \quad (2)$$

where N = Avogadro's number, $Q_j(E_0)$ = ionization cross section of level j , A = atomic mass of element A , and C_A = weight fraction of element A . In practice, the number N_j of ionizations is computed from the usual formula

$$N_j = C_A(N/A)R/S \text{ with } 1/S = \int_{E_0}^{E_c} Q_j(E) dE/d\rho s \quad (3)$$

From Eqs. (2) and (3), it is obvious that the area F represents the usual atomic-number effect

$$FQ_j(E_0) = R/S \quad (4)$$

In the XPP model, the backscattering factor R is expressed as a function of the backscattering coefficient η and of the mean reduced energy \bar{W} of the backscattered electrons (BSE):^{3,4}

$$R = 1 - \eta\bar{W}[1 - G(U_0)] \quad (5)$$

The efficiency factor $1 - G(U_0)$ is computed by assimilating the energy distribution of BSE to a simple power function.

For the electron energy loss $dE/d\rho s$, a semi-empirical law, more adequate in the low energy range than the usual Bethe's expression, is used:^{3,4}

$$dE/d\rho s = - (M/J) [1/f(V)], \quad \text{with} \quad (6)$$

$$f(V) = \sum_{k=1}^3 D_k V^{Pk}, \quad M = \sum_i C_i Z_i / A_i, \quad V = E/J$$

J = mean ionization potential of the target. It has been shown previously^{3,4} that when an ionization cross section proportional to $\ln(U)/U^{0.5} E_c^2$ is used, the R/S ratio can be written:

The authors are at the Office National d'Etudes et Recherches Aéronautiques (ONERA), 29 Avenue Division Leclerc, F-92320 Chatillon, France.

$$R/S = R(U_0/V_0/M)$$

$$\cdot \sum_{k=1}^3 D_k (V_0/U_0)^{P_k} (T_k U_0^{T_k} \ln U_0 - U_0^{T_{k+1}})/T_k^2$$

where $T_k = 1 + P_k - m$. In this relation, all proportionality factors that are not useful in analysis with standards are omitted. For standardless analysis, some of these factors can be no longer ignored to get the effective number of ionizations:

(1) The shell factor b_j (usually assumed to be constant for a given level) and the number Zn_l of electrons in the excited subshell have to be incorporated into the expression of the ionization cross section

$$Q_j(U) = b_j z_{n_l} \ln(U)/U^m E_c^2 \quad (8)$$

(2) In the case of L and M lines, the Coster-Kronig transitions increase the effective number of vacancies in the level of interest (L_3 level for $L\alpha$ line, M_5 for $M\alpha$ line) by a factor f_{ck} . In the case of the $L\alpha$ line, which can be used to analyze many elements, f_{ck} can be written as

$$f_{ck} = 1 + f_{13}N_{13}S_{13} + f_{23}N_{23}(1 + f_{12}N_{12}S_{12})S_{23} \quad (9)$$

where f_{ij} is the probability of vacancy transition from subshell i to subshell j ; N_{ij} is the ratio of the number of electrons in the subshells ($N_{12} = 1$; $N_{13} = N_{23} = \frac{1}{2}$); and S_{ij} is the ratio of the $1/S$ factor of subshell i to that of subshell j . (S_{ij} tends to 1 at high over-voltage.)

Mean Depth of X-ray Generation. This important parameter has been related to F in order to match our previous model:¹

$$\bar{\rho z} = F/K_1, \text{ where } K_1 \text{ is a function of } Z \text{ \& } U_0 \quad (10)$$

Surface Ionization. The expression of $\phi(0)$ is unchanged:^{3,4}

$$\phi(0) = 1 + 3.3 [1 - (1/U_0 g)] n^{1.2} \quad (11)$$

where $g = 2 - 2.3\eta$.

Initial Slope. This parameter is related to the previous ones by^{1,3}

$$\phi'(0) = K_2 F/(\bar{\rho z})^2 \quad (12)$$

where K_2 is a function of Z and U_0 .

Adaptation of the XPP Model to Tilted Specimens

It is frequent in SEM practice to tilt the specimens in order to increase secondary electron emission and consequently to improve the imaging capability. Advantage can also be taken of tilting the specimen toward the EDs crystal to obtain a higher x-ray take-off angle and also a smaller mean depth of x-ray generation, so that the emerging intensity of the soft radiations (the most strongly absorbed) can rise by a significant amount.

Let θ_0 be the take-off angle at normal incidence and ψ be the azimuth defining the orientation of the detector port with respect to the

tilt axis. When the specimen is tilted by β , the effective take-off θ becomes

$$\cos \theta = \cos \theta_0 [1 - 2 \sin \beta \cos \beta \cos \psi \tan \theta_0 - \sin^2 \beta (\cos^2 \psi - \tan^2 \theta_0)]^{1/2} \quad (13)$$

Obviously, the highest increase of the emerging intensity with tilt can be achieved with a horizontal detector; but interesting enhancements can also be obtained with an inclined detector, as shown by the spectra of Figs. 1 and 2. The definition of $\phi(\rho z)$ can be extended to the case of oblique incidence by considering that the elementary self-supported layer which is the reference in the tracer scheme is tilted by the same angle β as the specimen itself. Hence, the electron path length in that layer is increased by $1/\cos \beta$, so that the area below the $\phi(\rho z)$ curve becomes

$$F_\beta = N_j \cos \beta / [C_A (N/A) Q_j(E_0)] \quad (14)$$

When $\phi(\rho z)$ is defined in this way, its area F_β decreases when the specimen is tilted, since N_j and $\cos \beta$ are decreasing functions of η (Fig. 3); and N_j decreases like the backscattering factor R , because of the increase of and \bar{W} with β . From Monte Carlo results, simple power laws have been proposed for the variation of n and \bar{W} with β .¹

Figure 3 shows that the ultimate depth of ionization does not change significantly with the conditions of beam incidence. On the contrary, the mean depth for x-ray generation $\bar{\rho z}$ varies noticeably and has in practice the major effect on the absorption correction. Monte Carlo simulations have shown that the ratio $\bar{\rho z}_\beta/\bar{\rho z}_0$ varies almost linearly with $(\cos \beta)^{3/2}$. Figure 4 shows that the slope s of this linear relationship depends strongly on the atomic number of the target. The variation of $\bar{\rho z}$ is hence described as follows:¹

$$\bar{\rho z}_\beta = \bar{\rho z}_0 [1 - s + s(\cos \beta)^{3/2}] \quad (15)$$

where s is a function of Z and U_0 .

Although our Monte Carlo program, based on a multiple scattering scheme, is not adequate to yield very accurate information about the surface ionization $\phi(0)$, it predicts a weak variation of this parameter with tilt angle.¹ Similarly, the initial slope $\phi'(0)$ is not strongly sensitive to β , except at very high tilt angles where it suddenly becomes negative.¹ All the expressions needed to adapt the parameters of $\phi(\rho z)$ to oblique incidence are given elsewhere.¹

Additional Features of the XPP Procedure

The XPP procedure is not constituted by the $\phi(\rho z)$ model solely, but also includes additional routines, used either for spectra processing or for the quantification itself.

Background Subtraction. One of the major problems in EDS analysis, mainly in the soft x-ray region, is the modeling and subtraction of the background. In the Kevex system used in the present work, the shape of the background is modeled theoretically, and its

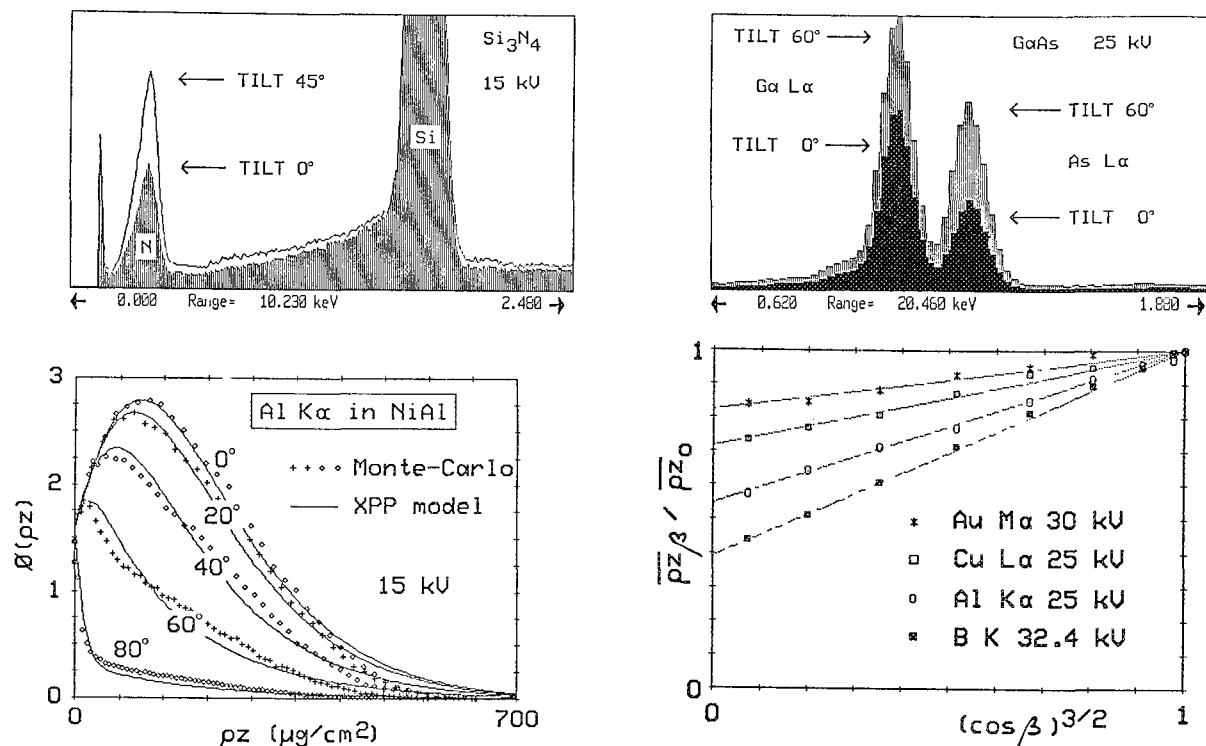


FIG. 1.--Increase of N K intensity of Si_3N_4 tilted by 45° at 15 kV. Quantum detector; $\theta = 30^\circ$; $\phi = 30^\circ$.

FIG. 2.--Increase of Ga L and As L intensities as GaAs is tilted by 60° at 25 kV; same detector as in Fig. 1.

FIG. 3.--Variation of $\phi(\rho z)$ with tilt predicted by Monte Carlo simulation and by XPP model. Al K line in NiAl at 15 kV.

FIG. 4.--Plot of $(\rho z)\beta/(\rho z)_0$ against $(\cos \beta)^{3/2}$ at high overvoltage in various targets, from Monte Carlo simulations.

TABLE 1.--Parameters defining a typical Quantum detector (the parameters followed by * are ratios to nominal data).

Quantum detector	Yes
Hardened detector	Yes
Detector thickness	2 mm
Dead layer	0.1 μm
Gold layer	200 Å
Al coating thickness	1000 Å
Window thickness ratio *	1.000
Deposition factor *	1.000
Etching factor	1.000

amplitude is automatically adjusted to the experimental amount of continuous radiation. Our first action in this field has been to include into the software the computation of the efficiency of the Quantum detector, by properly describing this detector and its atmospheric window. New parameters, given in Table 1, have been included in the menu. Because the characteristics of the Quantum window have not yet been revealed by the manufacturer, the corresponding parameters of this new menu refer to nominal data defined in the program.

Many empirical expressions of the spectral distribution of the continuum are proposed in the literature. From the contradictions reported, it may be suspected that most of them could be valid only for the particular detector

and the particular geometry used by every author. In fact it is really difficult to get an accurate description of the generated bremsstrahlung, in a wide energy range, for several reasons:

(a) The conversion of the observed spectral intensity into an emerging intensity is strongly influenced by the uncertainties on the characteristics of the window, the dead layer and the coating of the detector.

(b) The generated continuum is usually deduced from the emerging intensity by the assumption that the distribution in depth of a radiation of the continuum is identical to that of a characteristic photon with the same energy. In fact, it is easy to verify, for example with pure titanium at a sufficient voltage, that the amplitude of the absorption jump computed at the K edge with this assumption is significantly smaller than the measured one.

(c) The backscattered electrons can add some spurious contribution to the continuum: in conventional detectors, they can generate some extra intensity of bremsstrahlung in the window itself; in detectors for light elements, some residual backscattered electrons can reach the detector crystal in spite of the magnetic trap, and produce some spurious contribution that can noticeably modify the shape of the background, mainly in the high-energy region.

These difficulties led us to describe tempo-

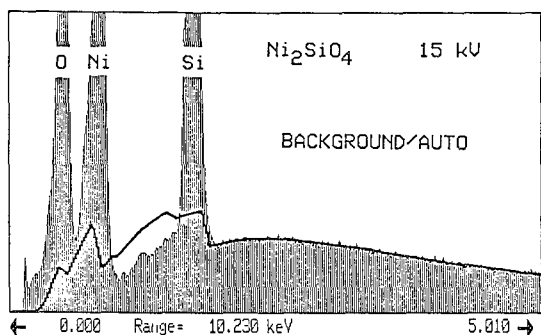


FIG. 5.--Background modeling with rough estimate of concentrations; Quantum detector; Ni_2SiO_4 at 15 kV.

rarily the generated background as $I_{BG} \propto (E_0 - E)^n$ user-definable. In practice, the appropriate values of n at usual accelerating voltages range from 0.8 (heavy targets) to 1.2 (light targets).

Another problem with background modeling is that the target composition must be known before the emerging continuum can be computed. In principle, background modeling should be integrated into the iterative scheme of quantification. But this procedure would be unacceptably time consuming and is not done in practice. In the original Keve software, the composition of the target is crudely estimated from the height ratios of the major lines, without any correction. Sometimes this approach can produce strong alterations of the computed background. Figure 5 shows that in the low-energy region of the Ni_2SiO_4 spectrum recorded at 15 kV, the computed background is far from the experimental one between the Ni L and the Si K absorption edges, because the crude estimate of the composition gives rise in that case to an excess of Si relative to Ni. To avoid such inadequacies, we have added the /OPTIMIZE option to the process, which corresponds one first to getting very quickly (after digital filtering and matrix correction) a reasonable estimate of the concentration of the major elements; and then, after having recalled the gross spectrum, uses this first approximation to model the background properly. The improvement obtained is demonstrated on Fig. 6.

As can be noticed on Figs. 5 and 6, some residual problems still limit the capability of automatic computation of the background in the very low-energy region (below ~ 600 eV), because of extra sources of noise (electronic noise, leakage current, incomplete charge collection, etc.) that contribute strongly to the real background in this domain. At present, we must be content ourselves with improving the background in this region by "manual" adjustment.

Deconvolution. The original software of Keve contains a Gaussian deconvolution procedure that is easy to use and has the advantage of being insensitive to small variations of the calibration of the analyzer. However, such a

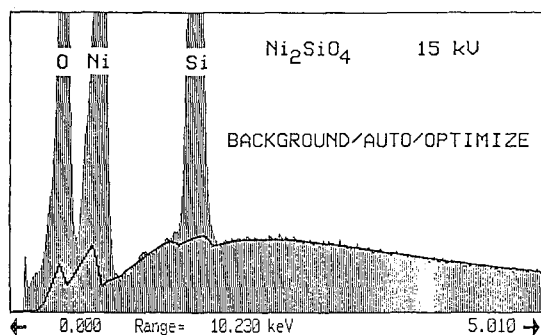


FIG. 6.--Background modeling with optimized estimate of concentrations; Quantum detector; Ni_2SiO_4 at 15 kV.

procedure must be applied as properly as possible. Therefore, we have improved the computation of the synthetic Gaussians by taking into account, on the one hand, the variation of the line width with energy; and on the other hand, the influence of the overvoltage on the excitation efficiency of the various lines in a series. After this first improvement, it became evident that some revision had to be made in the original data⁶ giving the relative weights of the L lines. For the future, we think that the incorporation of a /OPTIMIZE option that permits the differences in the absorption of the various lines to be taken into account would be effective.

Mass Absorption Coefficients. The XPP model uses tabulated absorption coefficients for quantification. The values of the tables can be modified by the user if necessary. Originally, the table is filled with the coefficients computed with the most recent model of Heinrich,⁷ except for very light emitters ($Z < 10$) and in particular cases (in the vicinity of an edge) for which more adequate values are proposed.^{3,8,9}

First Assessment

Analyses with Standards. It has already been shown,^{1,3} on the basis of a large file built up with microprobe measurements at a normal incidence, that the XPP model was one of the most reliable models for matrix corrections, even in the case of very-light-element analysis. Microprobe measurements on tilted specimens, with respect to untilted standards, have also shown¹ that no significant loss of accuracy was occurring in the range -30° to $+50^\circ$ tilt.

Therefore, we have not spent too much time checking the analyses with standards in the SEM, since the accuracy of the results is most often governed by the stability of the microscope. In the present work, a Cambridge S100 microscope was used, providing a 30° take-off angle at normal incidence. Although this SEM is not equipped with a beam-current stabilizer, careful measurements make it possible to get satisfactory results up to 60° tilt, even in the unfavorable case where the standards are

TABLE 2.--Analyses of Co₃Ti (nominal 21.1 wt%) at 15 kV from 0° to 60° tilt. Untilted pure standards. Quantum detector; $\theta_0 = 30^\circ$; $\psi = 30^\circ$.

	0°	10°	20°	30°	40°	50°	60°	m	σ
Ti wt%	21.32	21.01	20.96	21.00	21.31	21.51	22.02	21.30	0.35
Co wt%	78.68	78.16	77.64	77.85	78.91	79.98	79.44	78.67	0.79
Total	100.00	99.17	98.60	98.85	100.22	101.49	101.46	99.97	1.09
Ti at%	25.00	24.85	24.93	24.92	24.94	24.86	25.43	24.99	0.19
Co at%	75.00	75.15	75.07	75.08	75.06	75.14	74.43	75.01	0.23

TABLE 3.--Ratio of experimental to nominal concentration obtained by standardless analyses of binary compounds; 0° to 60° tilt; Quantum detector.

Target	kV	Line	0°	10°	20°	30°	40°	50°	60°	m	σ
NiAl	25	Ni K α	0.990	1.014	1.008	1.000	0.994	0.990	0.990	0.998	0.009
		Al K α	1.023	0.969	0.983	1.001	1.013	1.021	1.023	1.005	0.020
GaP	25	Ga K α	0.994	1.022	1.002	0.995	0.986	0.987	0.969	0.994	0.015
		P K α	1.006	0.978	0.998	1.005	1.014	1.014	1.023	1.005	0.015
Co ₃ Ti	15	Co K α	1.008	1.007	1.007	1.008	1.007	1.008	1.001	1.006	0.002
		Ti K α	0.981	0.978	0.978	0.977	0.978	0.975	0.993	0.981	0.007
Co ₃ Ti	25	Co K α	1.004	1.006	1.004	1.005	1.003	1.004	1.001	1.004	0.002
		Ti K α	0.987	0.981	0.978	0.986	0.989	0.987	0.997	0.988	0.004
NiO	25	Ni K α	1.003	--	0.977	--	0.946	--	0.960	0.972	0.021
		O K	0.997	--	1.023	--	1.054	--	1.040	1.028	0.021
Cu ₂ O	25	Cu K α	0.969	1.010	--	1.000	0.977	0.969	0.982	0.985	0.016
		O K	1.063	0.980	--	1.000	1.046	1.062	1.036	1.031	0.031

TABLE 4.--Ratio of experimental to nominal concentration obtained by standardless analyses of binary compounds; 0° to 60° tilt; Quantum detector.

Target	kV	Line	0°	10°	20°	30°	40°	50°	60°	m	σ
AgY	25	Ag L α	1.006	1.009	1.002	0.998	0.996	0.997	0.990	1.000	0.006
		Y L α	0.994	0.991	0.998	1.002	1.004	1.003	1.010	1.000	0.006
W-Re 26.4 wt%	25	W L α	0.997	0.999	0.993	1.001	0.998	0.999	0.987	0.996	0.004
		Re L α	1.009	1.002	1.019	0.999	1.007	1.003	1.037	1.011	0.012
GaAs	25	Ga L α	1.002	1.022	1.023	1.024	1.029	1.033	1.036	1.024	0.010
		As L α	0.998	0.978	0.977	0.976	0.971	0.968	0.964	0.976	0.010
InP	25	In L α	0.992	0.996	0.992	0.979	0.980	0.977	0.975	0.985	0.008
		P K α	1.008	1.004	1.008	1.021	1.020	1.023	1.025	1.015	0.008
GaP	25	Ga L α	1.004	1.018	1.018	1.023	1.025	1.032	1.037	1.023	0.010
		P K α	0.996	0.982	0.982	0.977	0.975	0.968	0.962	0.977	0.010
Cu ₃ Pd	25	Cu K α	1.008	0.999	0.996	0.997	1.015	0.991	0.985	0.999	0.009
		Pd L α	0.971	1.003	1.013	1.010	0.944	1.034	1.056	1.004	0.030
Cu ₃ Pd	15	Cu K α	1.004	1.021	1.018	1.009	1.015	1.007	1.015	1.013	0.008
		Pd L α	0.987	0.924	0.932	0.968	0.946	0.974	0.946	0.954	0.021
PtV	25	Pt L α	1.001	0.990	0.988	0.990	0.985	0.999	0.992	0.992	0.005
		V K α	0.999	1.010	1.012	1.010	1.015	1.001	1.008	1.008	0.005
Cu-Au 30 wt%	25	Cu K α	0.995	1.003	0.988	0.985	0.982	0.987	0.996	0.991	0.007
		Au L α	1.011	0.993	1.028	1.034	1.042	1.030	1.009	1.021	0.016
Cu-Au 50.8 wt%	25	Cu K α	0.999	0.978	0.995	0.979	0.983	0.983	0.994	0.987	0.008
		Au L α	1.001	1.022	1.005	1.021	1.016	1.016	1.006	1.012	0.008

not tilted, as shown in the example of Table 2.

Analyses Without Standards. It is clear that most SEM/EDS users are mainly interested in standardless analysis, because of its speed and its nonsensitivity to the fluctuations of the beam current. It would be a very powerful tool indeed that could perform standardless analyses in routine work with an accuracy of a few percent for the major elements. To reach such a level of performance, it is clear that the window as well as the layers at the surface of the detector have to be described precisely, to get accurate values of the detection efficiency. In the case of our Quantum detector all the parameters have been set equal to the nominal values (Table 1), except the so-called etching factor, which has been set to 1.13 in order to give satisfactory results for the analysis of NiAl at 25 kV, used as a reference.

Analyses involving K lines only. Several conductive binary compounds with known compositions have been analyzed by the K lines between 0° and 60° tilt. It can be seen from Table 3 that the results are globally fairly good, with maximum errors of the order of 2%.

The capability of standardless analysis applied to a very light element (oxygen) has also been evaluated. To perform this test, we have restricted ourselves to the conductive oxides NiO and Cu₂O for the following reasons.

(a) Coated insulators could not be analyzed directly by a standardless procedures without the effect of the coating on the emitted intensities being taken into account.

(b) The accumulation of charge in nonconductive specimens (even surface coated) might produce noticeable deviations from the laws of quantification valid for conductive materials.

(c) Since we were constrained to perform a "manual" quadratic modeling of the background in the vicinity of the O K line, it was necessary to avoid specimens in which overlapping with the oxygen line could occur.

The results of Table 3 indicate that, in cases where the background can be reasonably evaluated, standardless analyses of oxygen gives quite meaningful information.

Analyses involving L lines. As mentioned before, a correct approach for L lines implies computation of the effect of the Coster-Kronig transitions and its application to the ratio $L\alpha_{12}/\Sigma L_3$, where ΣL_3 = sum of the intensities of the lines corresponding to the L α level. This feature has been added to the Kevex software, on the basis of the coefficients calculated by Lábar.¹⁰

When K and L lines are used simultaneously, the results of standardless analyses depend on the shell factors used in Eq. (8). For the K shell, we have set b_K equal to $1.4 \times 10^{-20} \text{ m} \cdot \exp(1)$, in order to scale the maximum of $Q_K E_K^2$ at $2.8 \times 10^{-20} \text{ cm}^2 \text{ keV}^2$. Since the situation is more muddled for L lines, we have temporarily set b_L equal to $1.42 \times 10^{-20} \text{ m} \cdot \exp(1)$. With these coefficients, the resulting program gives

globally better results than the original one, but in particular cases, some discrepancies up to 20% can be found. Hence, we began quite recently to look for the factors that should be applied to the number N_j of direct ionizations produced by electron impact in order to get the correct compositions for a number of known compounds. The first factors obtained are plotted in Fig. 7 vs the atomic number, and can be compared to the graphs of the Coster-Kronig effect f_{ck} , as given by Lábar¹⁰ or as computed from the tables.¹¹ Clearly, the apparent scattering of the experimental points is strongly correlated with the discontinuities of the theoretical curves, but the measured effect has a greater amplitude than the calculated one. The difficult question will be whether this means that the theoretical jumps are underestimated or that the shell factor b_L changes from one element to another.

Using the adjusted coefficient of Fig. 7, the stability of the analytical results has been checked for tilt angles varying from 0° to 60°. Table 4 shows that the deviations are only a few percent.

Analyses of Layered Specimens. A new program named STRATA has been written for the Kevex software. This user-friendly program, based on the $\phi(\rho z)$ functions of the XPP model, makes it possible to analyze layered specimens (up to 5 layers on top of a substrate). It enables the simultaneous determination of the composition and the mass thickness of the layers by a method that depends on the nature and the complexity of the problem, as follows.

(a) If the number of strata is known, as well as the localization of the elements in each of them, and if no element is in unknown concentration in more than one stratum, the compositions and the mass thicknesses are obtained very quickly by application of an automatic iterative procedure to the experimental K-ratios, the progress of which can be checked graphically.

(b) If the specimen structure is more complex or undefined, the program switches to a procedure by trial and error, in which calculated curves of K-ratio vs the accelerating voltage have to be adjusted to the experiments.

In addition, STRATA also permits the display of the $\phi(\rho z)$ curves of the XPP model.

At present, the effects of fluorescence by the characteristic and the continuous radiations³ occurring in the layered structure are neglected. The implementation of the appropriate routines is planned for the near future.

Conclusions

The XPP procedure implemented with the Kevex system has been shown to be effective in the improvement and the extension of the quantitative capability of SEM/EDS x-ray analysis. The first results presented here demonstrate that quantitative analysis can be performed on tilted specimens without significant loss of accu-

racy whatever the analytical mode (with or without standards). In the favorable cases in which the background can be subtracted without noticeable error, even the standardless analysis of oxygen in particular oxides has been found to be meaningful. When L lines are used for standardless analysis, one has to take into account the effect of the Coster-Kronig transitions, but other phenomena could also influence the variation with Z of the intensity of the L lines; further experiments are required in this domain.

For the future, a sharper optimization of the XPP parameters is planned, to be realized by a careful examination of the present results associated with the conclusions that will be drawn from the application of the new STRATA program to synthetic layered specimens.

References

1. J. L. Pouchou, F. Pichoir, and D. Boivin, *Proc. 12th ICXOM*, Cracow, 1989; ONERA Report TP 157, 1989.
2. The implementation of the XPP procedure into the Kevex software was done in cooperation with J. F. Thiot (SAMx-Kevex Europe).
3. J. L. Pouchou and F. Pichoir, *NBS Workshop on Quantitative Microanalysis*, Gaithersburg, Md., 1988 (in press).
4. J. L. Pouchou and F. Pichoir, *Proc. 11th ICXOM*, London, Ont., Canada, 1987, 249.
5. T. P. Schreiber and A. M. Wims, *Microbeam Analysis--1982*, 181.
6. K. F. J. Heinrich, Ref. 4, 67.
7. J. L. Pouchou and F. Pichoir, *J. Microspectr. Electron.* 11: 229, 1986.
8. J. L. Pouchou and F. Pichoir, *Microbeam Analysis--1988*, 319.
9. J. L. Lábár, *Microbeam Analysis--1988*, 253.
10. W. Bambynek, B. Craseman, et al., *Rev. Modern Physics* 44: 716, 1972.

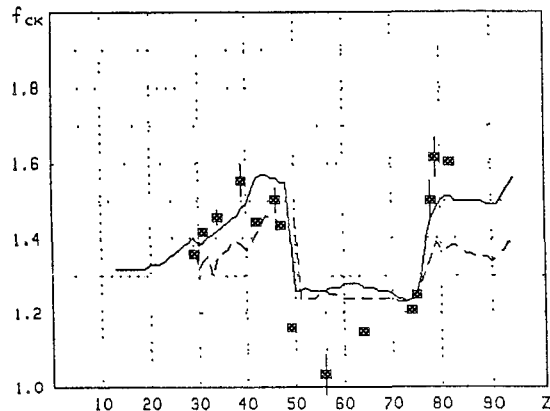


FIG. 7.--Experimental adjustment factors for $L\alpha$ lines (■) compared to Coster-Kronig factors from Ref. 10 (—) and Ref. 11 (- - -).

MONTE CARLO ELECTRON TRAJECTORY SIMULATION OF X-RAY EMISSION FROM FILMS SUPPORTED ON SUBSTRATES

D. E. Newbury, R. L. Myklebust, and E. B. Steel

Monte Carlo electron trajectory simulation provides a powerful tool for theoretical studies of electron and x-ray interactions in solid targets. A broad range of conditions encountered in electron probe microanalysis and scanning electron microscopy can be studied.^{1,2} The great power of the Monte Carlo technique arises from the stepwise treatment used to construct each electron trajectory in the target; this approach provides a continuous record of electron position, velocity, and kinetic energy. Such a treatment is capable of dealing with the unusual geometric boundary conditions imposed by irregular specimens that differ from an ideal flat, semi-infinite slab specimen, for which analytic expressions of x-ray generation and propagation can be written to form the basis of quantitative x-ray microanalysis. X-ray emission from special specimens of interest, such as randomly tilted surfaces, particles, thin foils, and films supported on substrates, can be simulated by a Monte Carlo procedure to provide appropriate corrections for quantitative analysis.

It is proper to speak of "a" rather than "the" Monte Carlo procedure because no single formulation of the simulation is in universal use. Several possible choices exist for the treatment of the electron scattering and energy loss processes. A general convention in constructing a Monte Carlo code for bulk specimens is to assign all the angular deviation of the trajectory to elastic scattering and to ignore any angular deviation contribution from inelastic scattering. The basic repetitive step of the calculation therefore depends on the elastic mean free path. For treating elastic scattering, the main choices are the screened Rutherford cross section and the Mott cross section. Because a convenient analytic formula exists for the screened Rutherford cross section, it is mathematically simple to implement in a Monte Carlo simulation; the cross section can be calculated for any electron energy and scattering atom of interest. However, the cross section suffers from inaccuracies at low scattering angles, low energies, and high atomic numbers.³ The exact Mott cross section provides the needed accuracy for these parameters, but no analytic function exists for ease in implementing the Mott cross section in the Monte Carlo simulation. Rather, the cross section must be tabulated over a range of scattering angles, atomic numbers, and electron energies, and interpolation

is then used to supply other values as needed in the simulation.^{4,5}

Approaches to simulating inelastic scattering also vary. Most simulations consider inelastic scattering by means of a continuous energy loss approximation rather than by modeling the discrete inelastic processes. The Bethe expression is applied at high electron energies (> 3 keV), but several different choices are now proposed for the treatment of energy loss in the low energy range (< 3 keV) where the Bethe model actually gives incorrect values.⁶⁻⁸ Some simulations use a combination of the continuous energy loss approximation supplemented by a discrete treatment of fast secondary electron generation.^{9,10} Such an approach is important in the treatment of thin foils and films because fast secondary electrons are generated with scattering angles nearly at right angles to the propagation of the primary beam. For situations where the primary electrons undergo little elastic scattering, as in passing through a thin foil, fast secondaries thus deposit energy laterally in planar targets, which can affect the distribution of ionization and subsequent x-ray production.¹⁰

Finally, the calculation of secondary radiation products such as characteristic x rays is also subject to a variety of choices for the cross sections.¹¹ The choice of a proper cross section for inner shell ionization for determination of characteristic x-ray generation is particularly difficult. Most experimental and theoretical discussions of inner shell ionization do not consider the region of low overvoltage near the threshold for excitation, $U = 1$ ($U = E/E_c$, where E is the beam energy and E_c is the critical excitation energy). However, in electron probe x-ray microanalysis of bulk samples, it is just in this region that we must operate.

In this work, the NIST Microanalysis Monte Carlo Simulation was employed.¹² This Monte Carlo formulation makes use of the screened Rutherford cross section for elastic scattering with the Kyser-Murata correction to the elastic path length; for energy loss, the Bethe expression is used down to energies of approximately 3 keV, and the Rao-Sahib/Wittry expression is used below 3 keV to the low energy cutoff of 1 keV. For a multielement target, mass concentration weighting is used for the elastic scattering and energy loss expressions. As an option, fast secondary electrons can be included in the simulation.

The authors are with the Microanalysis Research Group, Center for Analytical Chemistry, National Institute of Standards and Technology Gaithersburg, MD 20899.

TABLE 1.--Standard reference material K2063: microanalysis thin film Mg-Si-Ca-Fe.

Element	Certified concentration % by weight	Uncertainty % by weight
Mg	8.04	±0.24
Si	23.89	±0.27
Ca	12.89	±0.67
Fe	12.43	±0.82
Ar	(0.8)	
O	(41.95)	

Thickness = 101 nm (\pm 5nm at 95% confidence level)

Density = 3.0 g/cm³ (\pm 0.3 g/cm³ at 95% confidence level)

Values in parentheses are not certified; oxygen is calculated from assumed stoichiometry

Testing a Monte Carlo Simulation

When a Monte Carlo simulation is formulated, it must be evaluated critically against experimental data to establish the level of achievable accuracy. A common choice for an initial test is the behavior of the electron backscattering coefficient as a function of atomic number. Often the limitations in the scattering and energy loss models lead to inaccuracies in calculated backscatter coefficients. Empirical adjustments to the scattering model, for example to the elastic mean free path, can compensate and give good accuracy.¹³ Once this empirical adjustment has been applied, the simulation should be tested against other experimental data with no further empirical adjustments applied. Suitable test data include electron backscattering from tilted bulk targets, backscattering and transmission of electrons through unsupported thin films, backscattering and x-ray production in thin films supported on bulk substrates, and x-ray depth distribution functions from bulk targets.

Unfortunately, most of these experimental data have been measured exclusively on pure-element targets, including bulk and thin-film forms. Although highly useful, such data provide only a first level of testing and do not address the issue of how to model a mixed element target accurately. In formulating a Monte Carlo simulation for mixed-element targets, several possibilities exist for calculating the relative contributions of the constituents to the various scattering processes. The weighting of the cross sections is typically done on the basis of mass (weight) concentrations rather than atomic concentrations because of the dimensionability of the cross-section formulation, but it is not so obvious that this approach is appropriate for inelastic stopping power.¹⁴ An alternative weighting could be calculated on the basis of a mean atomic number, atomic weight, and density for the mixed targets.

To test Monte Carlo simulations for mixed element targets, only a limited database of binary thin film data exists, primarily due to the work of Kyser and Murata.¹³ The need for

TABLE 2.--Standard reference material 470 (glass K411): mineral glasses for microanalysis.

Element	Certified concentration % by weight	Uncertainty % by weight
Mg	8.85	±0.12
Si	25.38	±0.09
Ca	11.05	±0.14
Fe	11.21	±0.15
O	(42.36)	

more rigorous testing and possible modification of Monte Carlo simulations for the analysis of supported thin films was recently suggested by Lifshin et al., who reported anomalous deviations between Monte Carlo calculations and experimentally measured intensity k-ratios (the ratio of x-ray intensity from the film/x-ray intensity from a bulk standard).¹⁵ Their measurements of supported films of Y-Ba-Cu-O high T_c superconductors provide a new database of multicomponent films suitable for testing Monte Carlo simulations. Unfortunately, crystallographic effects on the growth of these films make thickness measurements difficult, and the density can only be estimated.

Development of a New Multielement Film Database

Further extension of this database for supported multielement films is an objective of this work. An interesting series of supported multielement films has become available as a result of the development of NIST Standard Reference Material (SRM) 2063 and related materials.^{16,17} SRM 2063, described in Table 1, is a five component film (containing O, Mg, Si, Ca, and Fe) produced by ion sputtering of glass targets to deposit layers of uniform composition and thickness. SRM 2063 is intended to be used in transmission, so that it is deposited on a thin (20nm) carbon film carried on a transmission electron microscope grid. For an accurate measurement of the thickness by stylus profilometry, the glass film is simultaneously deposited on polished silicon wafers. The mass per unit area is determined gravimetrically from film simultaneously deposited on polycarbonate filters. Combining these values provides a measurement of the density of the deposited film; ρ = 3.0 g/cm³, with an uncertainty of 10%. In subsequent deposition runs, glass films will be deposited on other substrates (e.g., carbon and gold) with different atomic numbers to provide a wide range of backscattering conditions.

Results

X-ray measurements of the supported films were made by wavelength-dispersive x-ray spectrometry in the electron probe microanalyzer. Measurements of k-values (element intensity in the film/intensity from a standard) were made under a variety of beam energies. The beam energies were determined by measurement of the Duane-Hunt limit with a calibrated energy-

TABLE 3.--X-ray k-values measured from SRM 2063 (101 nm) on Si (relative to SRM 470, glass K-411).

Element (keV)	5.14	10.42	15.20	20.99
Mg K α	0.514	0.148	0.0871	0.0649
(rsd)	(0.8%)	(1.0%)	(1.0%)	(0.9%)
Ca K α	1.08	0.192	0.0833	0.0430
(rsd)	(2.0%)	(0.8%)	(0.9%)	(0.5%)
Fe K α		0.277	0.0950	0.0441
(rsd)		(1.5%)	(1.5%)	(1.5%)

rsd = relative standard deviation for 10 measurements at different locations on the specimen.

dispersive x-ray spectrum and application of the fitting method of Myklebust et al.¹⁸ Standard Reference Material 470 (Glass K411), the composition of which is listed in Table 2, was used as the standard. The background was measured at the spectrometer peak position by use of a silicon wafer identical to the substrate beneath the film. Ten locations were measured on both the film and the bulk standards for each beam condition. The results for four different beam energies are listed in Table 3. The relative standard deviation of the 10 measurements was 2% relative or less in all cases. Silicon in the film was not measured because of the obvious interference from the substrate. Because of its thin nature and the conducting substrate, the film did not charge during electron bombardment and was therefore examined without coating. By necessity, the bulk glass K411 standard was coated with a thin (nominal 20 nm) carbon film.

A comparison of the experimental results with calculations performed with the NIST Microanalysis Monte Carlo Simulation to a precision of 0.6% (25 000 trajectories) is shown in Fig. 1. Reasonable agreement, within 5% relative at higher beam energies, but a systematic deviation of approximately 15% above the experimental results is observed at the lowest beam energies (lowest x-ray overvoltages) for all three characteristic x-ray lines measured, Mg K α (1.25 keV) and Ca K α (3.69 keV) at E = 5 keV, and Fe K α (6.40 keV) at E = 10 keV.

Discussion

The deviation between the Monte Carlo calculations and the experimental measurements at low beam energy and low overvoltage can arise from several possible sources. The limitations of the elastic scattering model and the energy loss model formulation as well as the cross section for inner shell ionization utilized in the Monte Carlo have been mentioned previously. These limitations are expected to manifest themselves most strongly at either low beam energy or low overvoltage. In the experimental measurements, the need to coat the standard for conductivity could potentially lead to differences with the calculations. Coating the target will lead to some loss in generated intensity due to the loss in energy by the beam electrons while penetrating the coating; the magnitude of

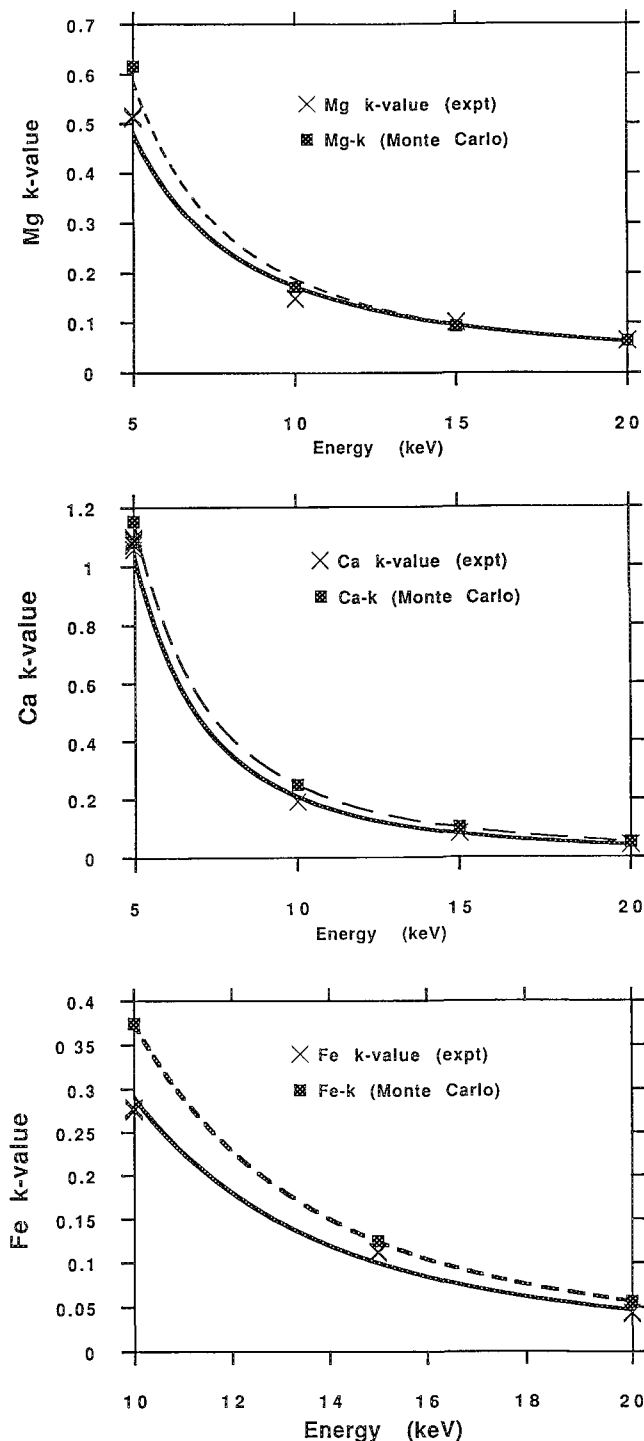


FIG. 1.--Measured and calculated k-values vs beam energy for SRM 2063, 101nm-thick glass film on Si substrate; standard is SRM 470 (glass K 411). (a) Magnesium, (b) calcium, (c) iron.

this effect is greatest at low overvoltage. Loss due to x-ray absorption is also possible, but should not be significant for the x-ray energies measured and the thickness of the coating. Moreover, both of these losses in the intensity measured from the standard have the effect of raising the experimentally measured k-value, since the standard intensity appears

in the denominator of the ratio, which would tend to bring the experimental values closer to the Monte Carlo calculations. To resolve the differences further work, including a more extensive experimental database, will be needed.

References

1. K. F. J. Heinrich, D. E. Newbury, and H. Yakowitz, Eds., *Use of Monte Carlo Calculations in Electron Probe Microanalysis and Scanning Electron Microscopy*, NBS Spec. Publ. 400, 1976.
2. D. E. Newbury, D. C. Joy, P. Echlin, C. E. Fiori, and J. I. Goldstein, *Advanced Scanning Electron Microscopy and X-ray Microanalysis*, New York: Plenum, 1986, 1.
3. L. Reimer and E. R. Krefting, "The effects of scattering models on the results of Monte Carlo calculations," Ref. 1, 45.
4. L. Reimer and B. Lodding, *Scanning* 6: 128, 1984.
5. Z. Czyzewski and D. C. Joy, *Microbeam Analysis--1989*, 396.
6. H. Bethe, *Ann. Phys.* 5: 325, 1930.
7. T. S. Rao-Sahib and D. B. Wittry, *J. Appl. Phys.* 45: 5060, 1974.
8. D. C. Joy and S. Luo, *Scanning* 11: 176, 1989.
9. K. Murata, D. F. Kyser, and C. H. Ting, *J. Appl. Phys.* 52: 4396, 1981.
10. D. C. Joy, D. E. Newbury, and R. L. Myklebust, *J. Microsc.* RP1, 1982.
11. D. E. Newbury and R. L. Myklebust, "Monte Carlo electron trajectory calculations of electron interactions in samples with special geometries," *SEM 1984*, 153.
12. C. J. Powell, "Evaluation of formulas for inner shell ionization cross sections," in Ref. 1, 97.
13. D. F. Kyser and K. Murata, *IBM J. Res. Dev.* 18: 352, 1974.
14. D. E. Newbury and E. B. Steel, *Microbeam Analysis--1989*, 216.
15. E. Lifshin, L. A. Peluso, A. Mogro-Campero, and L. G. Turner, *Microbeam Analysis--1989*, 243.
16. National Institute of Standards and Technology (formerly National Bureau of Standards) Standard Reference Material, available from Office of Standard Reference Materials, NIST, Gaithersburg, MD 20899.
17. E. Steel, D. Newbury, and P. Pella, *Analytical Electron Microscopy-1981*, 65.
18. R. L. Myklebust, C. E. Fiori, and D. E. Newbury, *Microbeam Analysis--1990*.

MEASUREMENT OF THE FLUORESCENCE OF Si K X RAYS by Au M X RAYS

J. A. Small, S. A. Wight, R. L. Myklebust, and D. E. Newbury

List of Symbols¹

b	fluorescing element
a	fluoresced element
I'_{fa}	emitted α intensity excited by b x rays
I'_{pa}	emitted α intensity excited by the primary electron beam
C_i	weight fraction of element i in the sample
A_i	elemental atomic weight for element i
U_i	overvoltage for element i
$\mu(ab)$	mass absorption coefficient for element a x rays in element b
$\mu(*b)$	mass absorption coefficient for element b x rays in the sample
r_{qa}	absorption jump ratio per edge q for element a
ω_b	fluorescence yield for b radiation
P_{ij}	Reed fluorescence factor
$\ln(1+u)/u$	downward fluorescence term
$\ln(1+v)/v$	upward fluorescence term
$I'_{f(Si)}$	measured fluoresced Si intensity corrected for continuum excitation and geometry
$I'_{f(meas)}$	experimentally measured Si intensity
I_{con}	continuum fluorescence intensity
I_{char}	characteristic fluorescence intensity
G	geometry correction
N_{Si}	fluoresced Si intensity
Ω	detector solid angle
E	term dependent on the fluorescence yield and jump ratio which is constant for a given element
μ_λ	mass absorption coefficient for a given wavelength x ray in Si
μ_{Si}	mass absorption coefficient of Si in Si
$N_0(\lambda)$	the intensity of the fluorescing radiation at wavelength λ
ϕ	the entrance angle for the fluorescing radiation (assumed to be 90°)
ψ	the emergence angle for the fluoresced radiation
λ	x-ray wavelength

The characteristic fluorescence correction is used in electron probe microanalysis to account for the additional x-ray intensity, beyond that produced by direct electron excitation, generated in an element by the characteristic x rays of another element. This correction can be significant particularly when the fluorescing element b is a major component of

The authors are at the Microanalysis Research Group, Center for Analytical Chemistry, National Institute of Standards and Technology, Gaithersburg, MD 20899.

the sample and the characteristic line for element b is slightly higher in energy than the critical excitation energy for the excited line of fluoresced a .

A formulation of the fluorescence correction that is commonly used in data reduction

$$\frac{I'_{fa}}{I'_{pa}} = \frac{C_b}{2} \times \frac{A_a}{A_b} \times \left(\frac{U_b - 1}{U_a - 1} \right)^{1.67} \frac{\mu(ab)}{\mu(*b)} \times \frac{r_{qa} - 1}{r_{qa}} \times \omega_b P_{ij} \times \left[\frac{\ln(1+u)}{u} + \frac{\ln(1+v)}{v} \right] \quad (1)$$

Several parameters in this equation are accurately known only for the K x-ray lines, with limited or no information available for the M x-ray lines. Most of the existing analytical procedures assume that the fluorescence of analytical lines induced by M x rays is insignificant and therefore do not include it in their quantitative calculations. The few analytical procedures that do include M line fluorescence make use of several untested assumptions in determining the magnitude of the correction.²

In 1988 Marinenko et al. reported on the analysis of Pb silicate glasses, which were analyzed by electron probe using a variety of standards.³ A summary of the results which, do not include a characteristic fluorescence correction for the excitation of Si by the Pb M lines, are reported in Table 1. In general, when light element standards such as the SRM mineral glass K-411 or SiO₂ are used, the Si analyses are higher than the certified value by about 7-8% relative. However, when the Pb silicate glass K-227 is used as the Si standard, the relative error is greatly reduced.

TABLE 1.--Analysis of silicon in lead silicate glasses.

		Certified			
		Wt. %	K-227	SiO ₂	K-411
Glass K-456	13.30	13.31	14.41	14.19	
Glass K-493	13.00	12.92	14.26	13.90	
Glass K-523	12.81	12.97	14.46	13.90	

Possible sources for the anomalous Si values

are inaccuracies in the atomic number, absorption, or fluorescence factors used in the correction procedures for quantitative electron probe analysis. In this experiment, we address the possible influence of the fluorescence factor; i.e., an increase in the Si intensity as a result of excitation by the Pb M lines. The electron optical bench at NIST⁴ was used to determine experimentally the Si x-ray intensity emitted from a Si target as a result of excitation by Au M radiation. The x-ray-excited Si intensity was divided by the electron-excited Si intensity to obtain the value for $I'_f(\text{Si})/I'_p(\text{Si})$, which was then compared to the value calculated with Eq. (1). Au was selected as the fluorescing element rather than Pb since it is easy to prepare as a foil with the thickness needed for the experiment. In addition, the Au M lines are closer than the Pb M lines to the critical excitation energy E_q for Si and yield a larger, more easily measured fluorescence effect.

Experimental

The fluorescence correction for electron probe analysis assumes a homogeneous mixture of atoms from both the fluoresced and the fluorescing elements. However, in a homogeneous mixture it is not possible to separate the x-ray intensity generated by electrons from that generated by secondary x-ray fluorescence. In order to make independent measurements of the electron and x-ray contributions to the Si intensity, we have physically separated the M x-ray source and fluoresced target (Fig. 1). In this configuration, the Au foil can be positioned in the electron-beam path for the measurement of the electron-generated Si spectrum. In addition, the x-ray detector can be moved relative to the electron beam and sample. The detector was placed at a take-off angle of 45° to measure the emission from the Si target. To eliminate the need for an accurate determination of the Au foil thickness, the detector was used in the transmission position, with the sample removed, to measure directly the spectrum emitted from the Au foil.

A detailed drawing of the Au foil assembly is shown in Fig. 2. The electron-opaque Au foil was made by vacuum evaporation of approximately $1\ \mu\text{m}$ of Au onto a $2.5\ \mu\text{m}$ -thick mylar film. The Au foil was positioned, with the Au facing the electron beam, over a 0.5cm -diameter hole in a $10 \times 15\text{cm}$ sheet of 2mm -thick carbon foil. A Mo aperture, C coated on the side facing the Au foil and an additional C collimator with a 2mm -diameter opening were placed on the side of the film facing the electron beam to minimize the possibility of electron excitation of the Si target by backscattered electrons. The beam current was independently monitored at both the Si target and the Au-foil assembly to insure that the excitation of the Si by scattered electrons was negligible. With the Au-foil placed in the path of the electron beam, we measured a residual current at the Si target of less than $3 \times 10^{-13}\ \text{A}$ compared to a beam

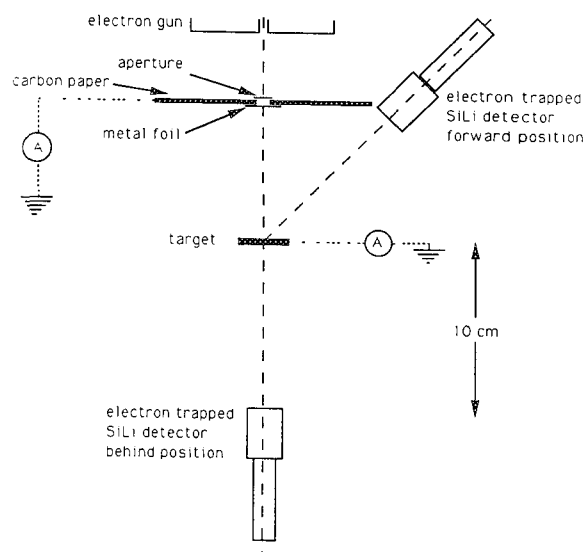


FIG. 1.--Experimental set-up for fluorescence measurements.

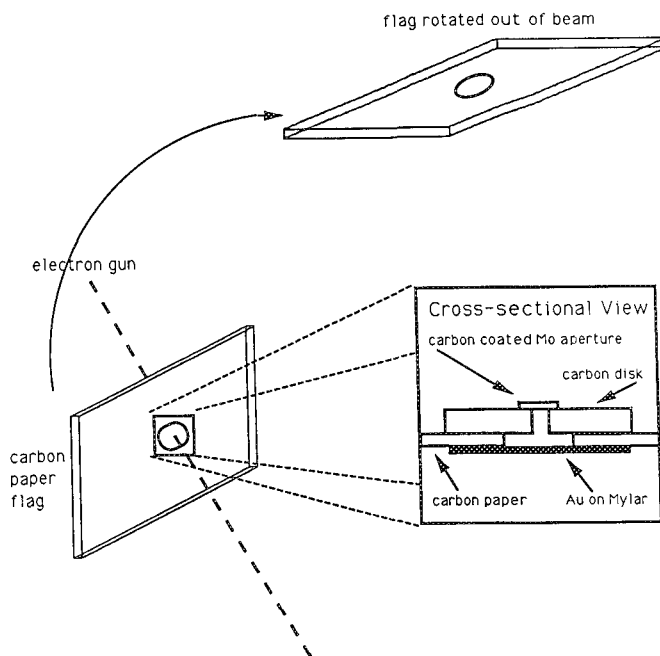


FIG. 2.--Detailed drawing of Au foil assembly.

current of $50\ \text{nA}$ at the Au foil. The maximum Si intensity produced as a result of this residual current, assuming that all the electrons were energetic enough to excite Si, is less than 2% of the measured fluoresced Si intensity and was therefore ignored.

The accelerating potential of the electron beam was $8\ \text{keV}$, so that only the Au M lines and the associated continuum were available for Si excitation. The detector was a $10\ \text{mm}^2$ Si(Li) detector equipped with an $8\ \mu\text{m}$ -thick Be window. The beam currents were $50\ \text{nA}$, measured on the Au foil, for the fluorescence measurements; $10\ \text{nA}$, measured on the Au foil, for the transmitted Au measurements; and $25\ \text{nA}$,

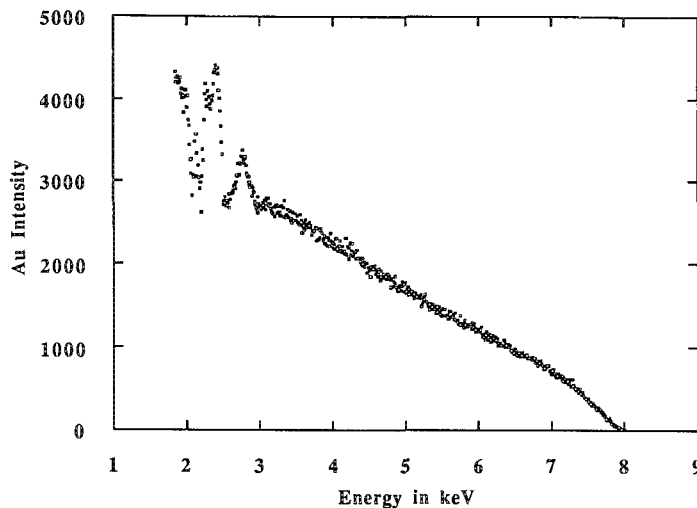


FIG. 3.--Au foil continuum spectrum.

measured on the Si, for the electron-generated Si spectrum. Prior to data reduction all spectra were normalized to a target current of 50 nA and an analysis time of 2000 live-time seconds.

Data Reduction

To compare the experimental measurements with the fluorescence values calculated from the literature it was necessary to correct the experimental data for continuum fluorescence, and geometry as described in Eq. (2).

$$I'_{f(Si)} = \left[I'_{f(meas)} - I'_{f(meas)} \times \left(1 - \frac{I_{con}}{I_{char}} \right) \right] \times G \quad (2)$$

Continuum Excitation. In addition to the fluorescence of Si K by the Au M x rays, Si K x rays can also be excited by the continuum x rays generated in the Au film. To estimate the Si intensity generated by the Au continuum we used the measured spectrum from the Au foil. The Au M peaks were stripped from the spectrum with a sequential simplex procedure.⁵ The x-ray intensities as a function of x-ray wavelength given in the residual spectrum (Fig. 3) were then used to obtain a calculated value for I_{con} from Eq. (3).⁶ Similarly, the intensities and wavelengths of the stripped M lines were used to calculate I_{char} . The calculated value for I_{con}/I_{char} was 0.011 for the Si-Au system.

$$N_{Si} = \frac{\Omega}{\sin \phi} E \int_{\lambda_0}^{\lambda_c} \frac{\mu_{\lambda} N_{Au} d\lambda}{\mu_{\lambda} / \sin \phi + \mu_{\alpha} / \sin \psi} \quad (3)$$

Geometry Corrections. Since the fluorescing and fluoresced targets were separated for this

experiment, it was necessary to make two different geometry corrections. In the case of a true homogeneous Au-Si target, the Au x rays generated in 2π steradians are available for secondary fluorescence, which is not the case in this experiment with physically separated targets. For this experiment only the Au M x rays contained in the area defined by the solid angle of the Si target (Fig. 4) are available to excite measurable Si x rays. The first correction scales the measured x-ray fluoresced Si intensity for the I/r^2 loss of Au x rays, where r is the distance from the Au foil to the center of the Si target. For this calculation we assumed that the Au M x rays are emitted as a point source from the Au foil and that this point source is equidistant from all points on the Si target.

The separation of the Au and Si targets results in the entire Si target surface being exposed to Au M x rays, whereas the direct electron-excited Si arises from a point source. A second correction accounts for the fact that only a portion of the Si target surface that is excited by Au M radiation is viewed by the detector chip. Figure 5 is a schematic representation of the area of the sample and collection efficiency as viewed by the detector for a sample with a TOA of 45° . The inner shaded oval representing the sample area falls within the solid angle of the detector chip. The outer oval represents the area in which only a portion of the detector chip area is available for x-ray collection due to shielding by the detector collimator. In the outer oval, the available detector area decreases nonlinearly from 100% at the border with the inner oval to 0% at the border of the outer oval. The superimposed shaded circle represents the actual sample area. To estimate the loss in the Si x-ray intensity as a result of the partial shielding of the detector, we modeled the change in the Si x-ray intensity by a parabolic function. The intensity loss was then determined from the numerical integration of the parabolic function, using the sample dimensions as the limits of integration. Combining the two geometry corrections results in a value of 89.3 for the G factor in Eq. (2).

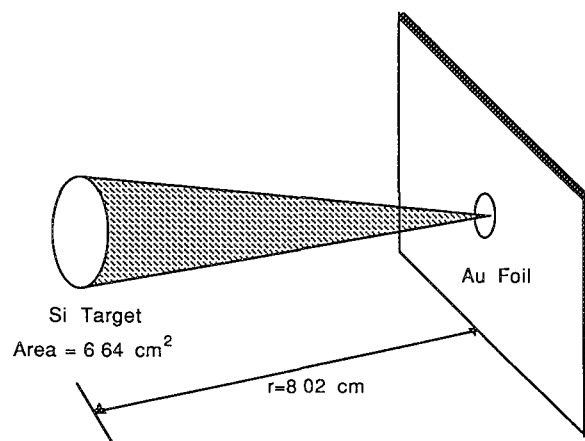
Results

In making the comparison of experimental results with those calculated from Eq. (1) we have made the following assumptions:

1. The Si intensity resulting from fluorescence by the Au radiation generated below the specimen surface and radiating upward, described by the $\ln(1 - v)/v$ term in Eq. (1), is negligible.

2. The Au x-ray intensity from the foil, corrected for solid angle, is equivalent to the intensity generated in the electron probe by Au target containing a trace of Si.

3. The experimentally determined value for $I'_{f(Si)}/I'_{p(Si)}$ is equivalent to the maximum value for $I'_{f(Si)}/I'_{p(Si)}$ calculated from Eq. (1).



$$\text{corr} = 6.64 / 2\pi(r)^2 = 0.016$$

FIG. 4.--Solid angle of Si target used in geometry correction.

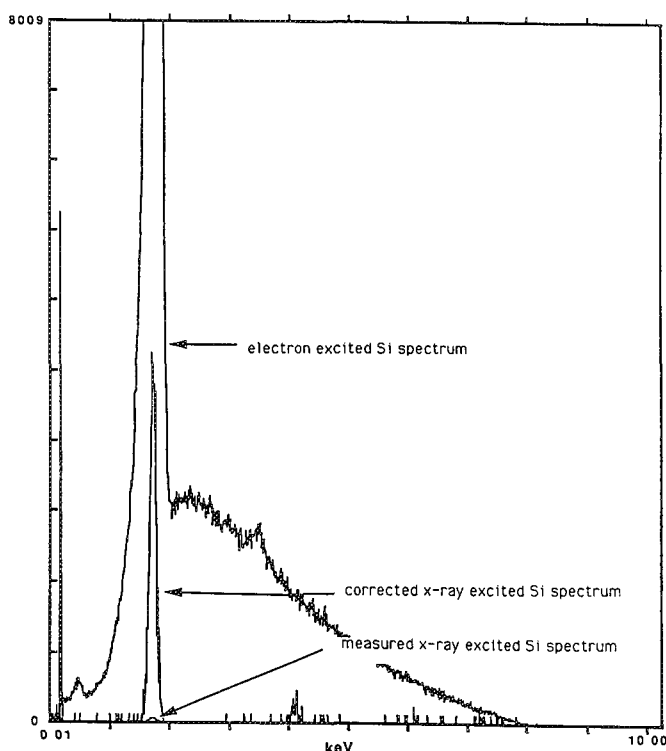


FIG. 6.--Measured x-ray excited Si spectrum, corrected x-ray excited Si spectrum, and electron-excited Si spectrum.

The measured x-ray fluoresced spectrum from the Si target is shown in Fig. 6 along with the corrected fluorescence Si spectrum and the electron-excited Si spectrum. In addition, Table 2 lists the relative intensity of $I'_f(\text{Si})$ and $I'_p(\text{Si})$, along with the experimental values of $I'_f(\text{Si})/I'_p(\text{Si})$ and the values calculated from Eq. (1).

Our preliminary experimental results suggest that there is a significant difference between the experimental measurements and the calculated values from Eq. (1). Despite this large discrepancy, our experimental measurements suggest that M-line fluorescence accounts for only about 0.13 wt% of the roughly 1.3 wt%

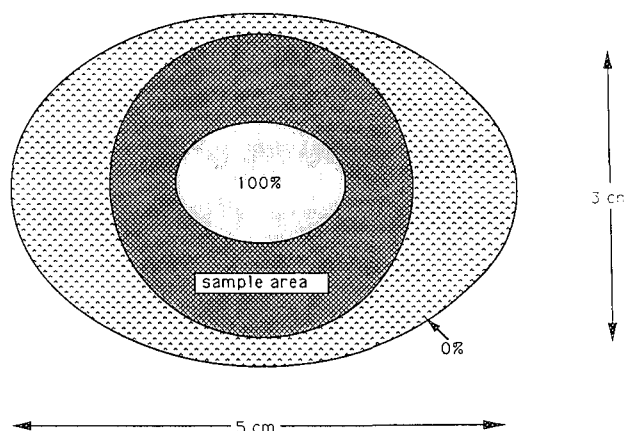


FIG. 5.--Sample area and collection efficiency for Si detector.

TABLE 2.--Secondary fluorescence results for the Si-Au system.

	$I'_f(\text{Si})$	$I'_p(\text{Si})$	$I'_f(\text{Si})/I'_p(\text{Si})$
Experimental*	6.05×10^4	8.03×10^6	0.0097
Eq. (1)	--	--	0.0064

*Experimental counts corrected for current, time, and solid angle.

excess Si. It is therefore unlikely that secondary fluorescence is the source of the discrepancies observed in the glass analyses reported in Table 1.

Future work in this area will include additional measurements on the Si-Au and other M-line fluorescence systems. In addition, measurements will be made on the Fe-Ni system, for which the fluorescence has been extensively studied and is well known. The experimental measurements on the Ni-Fe system will be compared with the literature values and used to verify the various assumptions, calculations, and corrections applied to experimental data.

References

1. K. F. J. Heinrich, *Electron Beam X-ray Microanalysis*, New York: Van Nostrand, 1981, 327.
2. J. Henoc et al., *A Rigorous Correction Procedure for Quantitative Electron Probe Microanalysis*, NBS Technical Note 769, 1973.
3. R. B. Marinenko, D. H. Blackburn, and J. B. Bodkin, *Glasses for Microanalysis: SRMs 1871-1875*, NIST Special Publ. 260-112, 1990.
4. J. A. Small et al., *Microbeam Analysis--1988*, 263.
5. C. E. Fiori, C. R. Swyt, and K. E. Golen, *Microbeam Analysis--1981*, 320.
6. R. O. Muller and K. Keil, *Spectrochemical Analysis by X-ray Fluorescence*, New York: Plenum Press, 1972, 47-52.

CONTRIBUTION OF X-RAY TOTAL REFLECTION TO THE BACKGROUND IN THE WAVELENGTH-DISPERSIVE ANALYSIS AT SMALL DEFLECTION ANGLES

W. P. Rehbach and Peter Karduck

In the wavelength dispersive analysis of soft x rays anomalies in the background are found for several target elements. In the literature extremely high backgrounds in the wavelength range of the O K α line are reported for C, Al, Si, Mo, and Zr.¹ This feature results in problems in analyzing oxygen and nitrogen, as the anomaly depends strongly on the target material. We also found the same effect for boron (Fig. 1). For small deflection angles θ , the background measured by a LdSte crystal from boron is significantly higher than the ones from boron nitride and from carbon, although the latter are of higher atomic number. In this paper the origin of the anomalies is investigated. It is found that totally reflected soft x rays cause this effect.

The Continuous Background

The background is that part of the signal which is not due to line emission.² It is caused by continuous radiation (bremsstrahlung, i.e., deceleration radiation). This radiation is produced when an electron passes through the Coulomb field of the nucleus of an atom. The electron is deflected and decelerated, and therefore loses energy. This energy is emitted as an x-ray photon. The energy of the emitted photons varies continuously from zero to the energy of the exciting electron.

Kramers³ derived a theoretical equation for the intensity of the generated continuous radiation as a function of the observed frequency.

$$I(\nu) d\nu = h^2 k Z (\nu - \nu_0) d\nu$$

As the measured quantity in electron probe microanalysis is not the intensity but the number of photons with the frequency ν , the equation must be divided by the electron energy $E = h\nu$:

$$N(\nu) d\nu = h k Z \frac{\nu - \nu_0}{\nu} d\nu$$

Rewritten in units of wavelength this equation results in:

$$N(\lambda) d\lambda = h k Z \left(\frac{1}{\lambda^2} - \frac{1}{\lambda \lambda_0} \right) d\lambda$$

with a maximum at $\lambda = 2\lambda_0$.

In further investigations Rao-Sahib and Wittry⁴ found a dependency with Z^n , where n varies between 1.12 and 1.38, depending on Z , λ , and λ_0 . In all cases $N(\lambda)$ should increase with the atomic number Z . The anomalous backgrounds we

reported and measured do not show this expected dependency on Z .

Moreau and Calais⁵ found that the continuum changes proportionally to the weight fraction of the constituent elements. Moreover, this dependency is not found in some cases (see, for example, B and BN in Fig. 1). In order to elucidate the effect, further measurements were carried out systematically with a LdSte crystal in the region $\theta = 12-24^\circ$ ($n\lambda = 20-40\text{\AA}$) at a large number of pure elements and compounds. Some examples are shown in Fig. 2. Figure 2(a) shows that, compared with Mg and Fe, Al and Si have very high backgrounds especially for small values of θ . Similar behavior is shown in Fig. 2(b) for Zr, Nb, and Mo, which have high backgrounds compared with Ta. This phenomenon cannot be described by lines of higher order. Nor can backscattered electrons reaching the counter at small θ values explain the extraordinary behavior for specific elements. The backscatter coefficient η increases monotonously with Z , so that the effect should also increase with Z in the same manner, which is not found. Nor does different absorption of continuous radiation cause the effect.

The fact that the anomaly is the more remarkable the smaller θ gives cause for the presumption that total reflection of x rays at the surface of the analyzing crystal is the reason.

Total Reflection

Total reflection can occur if radiation arrives from an optically denser medium and impinges on an optically thinner medium. For x rays, any medium is thinner than vacuum, so total reflection is generally possible (Fig. 3).

According to Ref. 6, the refractive index for photons is

$$n = 1 - 2\pi N_a r_0 \left(\frac{\hbar c}{E} \right)^2 \frac{\rho}{A} f$$

where N_a is Avogadro's number, $r_0 = e^2/mc^2$ (the classical electron radius), and f is the atomic scattering factor. Far from the absorption edges f nearly equals Z . In the vicinity of absorption edges, dispersion and absorption must be considered and results in an atomic scattering factor

$$f = Z + f' + if''$$

The refractive index becomes complex and may be written as:

$$n = 1 - \delta - i\beta$$

The authors are with the Gemeinschaftslabor für Elektronenmikroskopie der RWTH Aachen, Ahornstr. 55, D-5100 Aachen, Federal Republic of Germany.

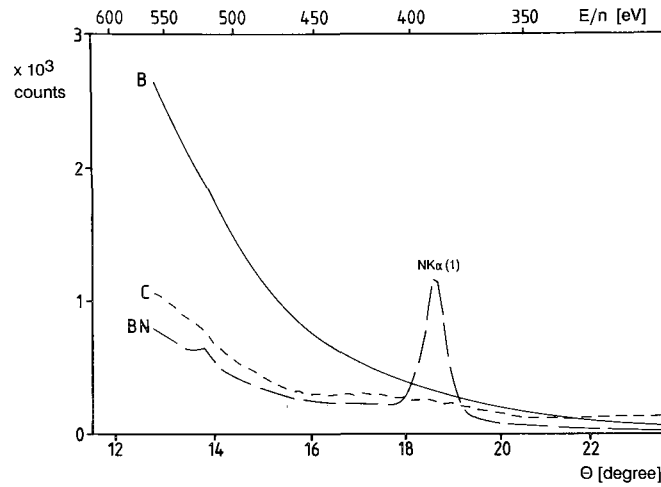


FIG. 1.--LdSte spectrometer scan on pure boron, boron nitride, and vitreous carbon, discriminator settings for N K α .

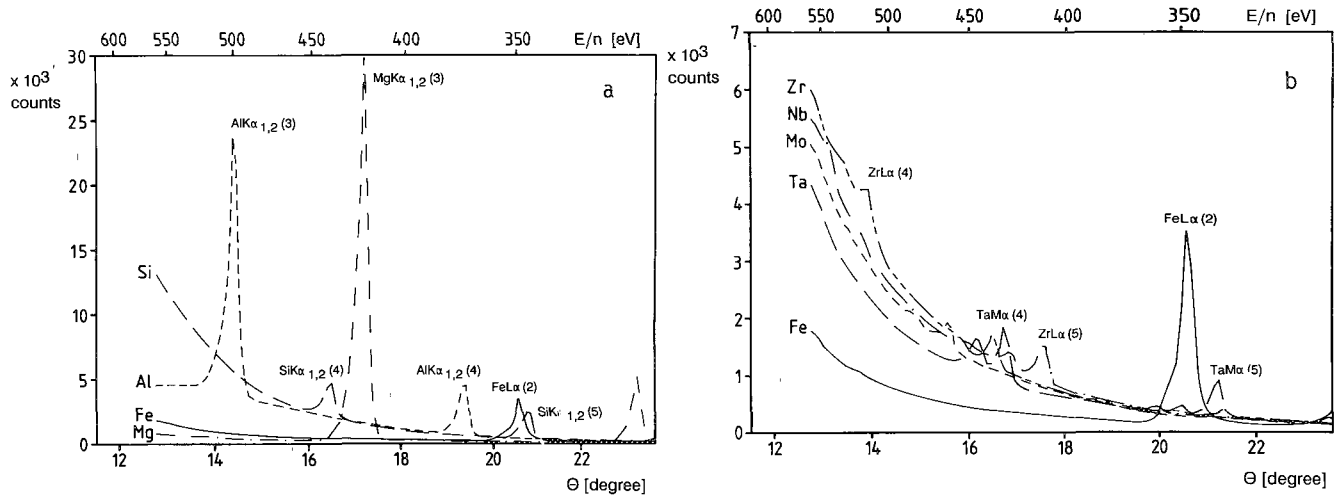


FIG. 2.--(a) LdSte spectrometer scan on Mg, Al, Si, and Fe, discriminator settings for O K α ; (b) LdSte spectrometer scan on Fe, Zr, Nb, and Mo, discriminator settings for O K α .

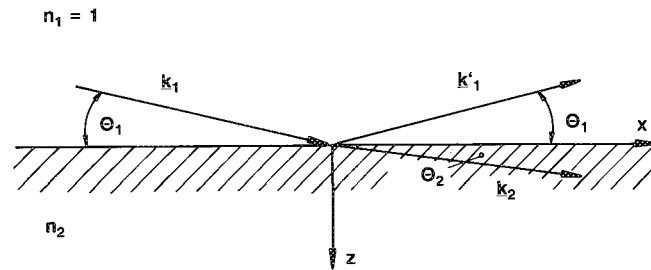


FIG. 3.--Refraction and reflection of x-ray photons impinging from vacuum into a medium of refractive index n_2

where $\delta = 2\pi N_a r_0 \left(\frac{\hbar c}{E} \right)^2 \frac{\rho}{A} (Z + f')$

and $\beta = 2\pi N_a r_0 \left(\frac{\hbar c}{E} \right)^2 \frac{\rho}{A} f''$

The absorptive part may be simply expressed by the linear absorption coefficient μ :

$$\beta = \mu \frac{\lambda}{4\pi}$$

For x rays δ and β are positive and small, which results in reflection indexes that are below unity, i.e., x rays are deflected away from the normal. Snell's law of deflection is (Fig. 3):

$$n_1 \cos \theta_1 = n_2 \cos \theta_2 \quad (n_1 = 1)$$

There exists a critical angle of total reflection θ_{1c} , with $\theta_{2c} = 0$ and therefore $\theta_{2c} = 1$ (Fig. 4):

$$\cos \theta_{1c} = n_2$$

Neglecting absorption and expanding the cosine in a power series, we obtain for small angles θ in:

$$\theta_1 = \sqrt{2\delta_2} \approx \sqrt{\frac{N_a r_0}{\pi} \frac{\rho Z}{A}} \cdot \lambda$$

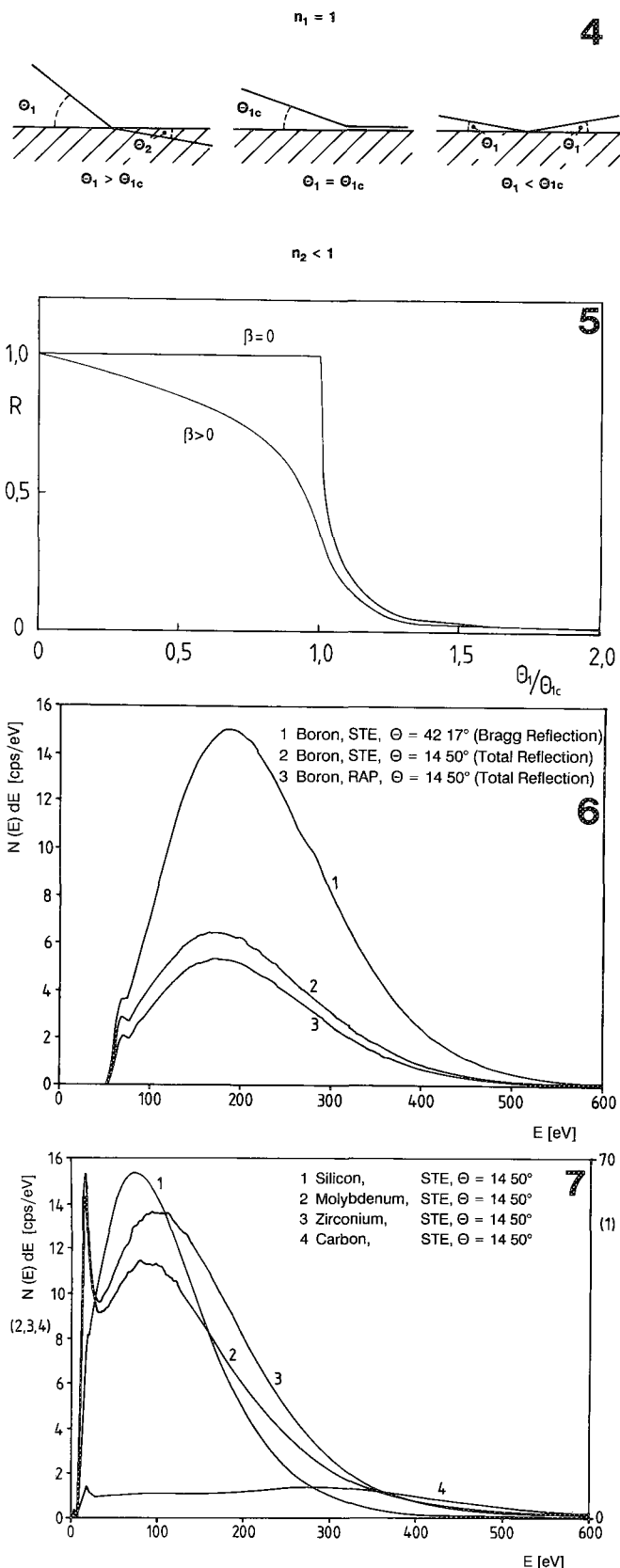


FIG. 4.--Schematic representation of the critical angle of total reflection θ_{1c} .

FIG. 5.--Reflection coefficient of x-ray photons vs θ/θ_{1c} .

FIG. 6.--Pulse height distributions for boron.

FIG. 7.--Pulse height distributions for C, Si, Zr, and Mo.

TABLE 1.--Energies and critical angles of total reflection for several low-energy lines.

X-line	E [eV]	θ_c [°]
Be K α	108.5	15.18
B K α	183.3	9.00
C K α	277.0	5.95
Na L $_{2,3}$ M	30.5	54.22
Mg L $_{2,3}$ M	49.3	33.49
Al L $_{2,3}$ M	72.4	22.83
Si L $_{2,3}$ M	91.5	18.05
Zr M ζ	151.1	10.93
Nb M ζ	171.7	9.61
Mo M ζ	192.6	8.58

Hence the critical angle is proportional to the wavelength of the photons. Table 1 shows values of the critical angle θ_{1c} of some characteristic x lines, assuming $\rho Z/A = 1$.

Taken absorption into account, no sharp limit of total reflection exists. For increasing θ a decreasing reflectivity is to be found also for $\theta < \theta_{1c}$, and in the region $\theta_{1c} < \theta < 2\theta_{1c}$ the reflectivity is not negligible (Fig. 5).⁷ Hence for some lines in Table 1 total reflection should be possible in the θ region, as shown in Figs. 1 and 2. These lines should produce a pulse height distribution in the proportional counter similar to the distribution produced by the same line at the Bragg-reflection position. This assumption is proved in Fig. 6 for the B K α line. The Bragg-reflected photons, just like those totally reflected at a LdSte crystal, produce qualitatively similar pulse-height distributions. Photons reflected at an RAP crystal at the same angle also show this behavior. Thus it is clearly demonstrated that the Bragg-reflected as well as the totally reflected signals are of the same nature, but are deflected by two different mechanisms.

It can also be shown for other elements (e.g., Si, Zr, Mo; Fig. 7) that the high background at small θ values is caused by total reflection of low-energy L and M lines.

Now it is also clear why the effect vanishes in carbides, nitrides, and oxides: The severe absorption of the lines in question in the compound reduces the emission to a large extent. It was observed that even a very thin layer of an oxide, e.g., on Si, results in a strong diminution of the background.¹

To avoid uncertainties in the evaluation of the background in the case of total reflection it is advisable to avoid the region of small θ angles, which may be achieved by use of synthetic multilayer

rystals. They may also show total reflection at small angles, but suitable 2θ values may be chosen to avoid this region. If measurement at small deflection angles is unavoidable, one should prefer off-peak measurements of the background on the specimen to peak measurements on a reference specimen. Only by doing so may the true background be determined.

References

1. J. Betzold, *Beitr. elektronenmikroskop. Direktabb. Oberfl.* 19: 7, 1986.
2. K. F. J. Heinrich, *Electron Beam Microanalysis*, New York, 1981.
3. H. A. Kramers, *Phil. Mag.* 46: 836, 1923.
4. T. S. Rao-Sahib and D. B. Wittry, *J. Appl. Physics* 45: 5060, 1974.
5. G. Moreau and D. Calais, *J. Phys.* 25 (Suppl. 6), 83, 1964.
6. R. W. James, *The Optical Principles of Diffraction of X-rays*, London, 1962.
7. B. Lengeler, in *Synchrotronstrahlung in der Festkörperforschung*, Jülich, 1987.

EVALUATING 30mm² Si(Li) DETECTORS FOR LIGHT-ELEMENT X-RAY ANALYSIS

Shaul Barkan

Light-element x-ray microanalysis with the Si(Li) detector depends on two important detector characteristics. One is *resolution*, traditionally standardized as FWHM at Mn K α . The other is *efficiency*, primarily, but not entirely, established by the detector area. These two factors affect light-element sensitivity in an inverse manner. A detector with premium resolution can be produced by minimization of the area of the detector window, but its efficiency is directly proportional to the detector area.

A special effect of efficiency degradation exists in the very-low-energy end of the spectrum, where the x-ray energy pulses are only slightly greater than the electronic noise level. The detector dead layer plays an important role in low-energy detection efficiency, since low-energy efficiency is far more important than good Mn or electronic noise resolution for obtaining superior light-element sensitivity.

For this experiment, two Kevex Quantum detectors (a 10mm² and a 30mm²) were tested and compared. By analysis of their Fe source spectrum, both were found to have about the same dead-layer thickness. The detectors were then installed on an SEM. The boron results revealed that both detectors demonstrate the same peak-to-valley ratio when the 10mm² detector is specified to be 135 eV (Mn K α resolution); the 30mm² detector's resolution specification is 142 eV.

Resolution and Electronic Noise

From a pool of 10mm² Kevex Mark V Quantum detectors (typically displaying about 135 eV resolution at Mn) one detector was chosen. The electronic noise resolution measured 62 eV, which results in a Fano factor of 0.118:

$$\text{FWHM} = [(2.35 \sqrt{FE\epsilon})^2 + (\text{EN})^2]^{1/2}$$

where F = Fano factor, E = incident energy in eV, ϵ = energy per electron hole [3.76 eV @ 77K for Si (Ref. 1)], and EN = electronic noise in eV.

The author is with Kevex Instruments, Inc., Box 3008, San Carlos, CA 94070-1308. He wishes to thank Dr. Daniel Bartell for his constructive observations; Nancy Wolfe, Galen Sapp, and Willi Lebhertz for their help on the SEM work; George Jung for the use of his laboratory in collecting Fe⁵⁵ and pulser spectra; Garry Baerwaldt for supplying the Si(Li) crystals; and Gideon Kramer and Tom Stark for editing this paper.

Dead-layer Thickness Model

The silicon dead layer of a detector affects the background level. This dead layer, approximately 2000-4000 Å thick, is located on the detector-window side of the crystal. In this region of the detector charge collection is incomplete and may diminish to zero. The absorption formula for the detector material is

$$I_x = I_0 e^{-\rho\mu x} \quad (2)$$

where ρ = density (g/cm³), I_x = radiation intensity at depth x (photon/s-cm²), I_0 = radiation intensity impact on crystal (photon/s-cm²), and μ = mass absorption coefficient (cm²/g).

Let us assume that the dead layer (thickness d) is defined as a region that collects only a part of the charge. If the photoelectric event occurs inside this layer ($x < d$), it causes a count in the tail of the peak. If the photoelectric event occurs in the completely sensitive region ($x > d$), the system identifies this count as a peak count (Fig. 1).

The radiation absorbed in the dead layer is

$$\Delta I = I_0 - I_d = I_0(1 - e^{-\rho\mu d}) \quad (3)$$

The radiation remaining beyond the dead layer is $I_0 e^{-\rho\mu d}$, and is counted in the peak. Furthermore,

$$\begin{aligned} \frac{P}{B} &= \frac{\text{Peak area}}{\text{Background area}} = \frac{I_0 e^{-\rho\mu d}}{I_0(1 - e^{-\rho\mu d})} \quad \text{or} \\ \frac{B}{P} &= e^{\rho\mu d} - 1 \rightarrow \rho\mu d = [1 + (B/P)] \\ d &= \frac{\ln[1 + (B/P)]}{\rho\mu} \end{aligned} \quad (4)$$

where B = number of counts in background, P = number of counts in peak, ρ = density (2.33 g/cm³ for Si), μ = mass absorption coefficient [for Si @ 5.9 keV is 145 cm²/g (Ref. 2)], and d = dead-layer thickness. Therefore, the same peak-to-background ratio indicates the same dead-layer thickness.

The Experimental Process

To determine whether the 30mm² detector can demonstrate low-end performance equal to that of the 10mm² detector, we shall define *low-end performance* as the ability of a detector to resolve boron from noise and measure it by examining the peak-to-valley ratio. All factors affecting detector performance shall remain the same, including:

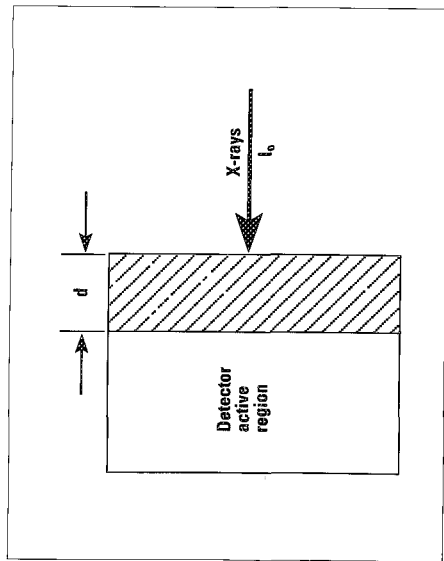


FIG. 1.--Schematic cross section of Si(Li) detector showing dead layer on detector window side (d).

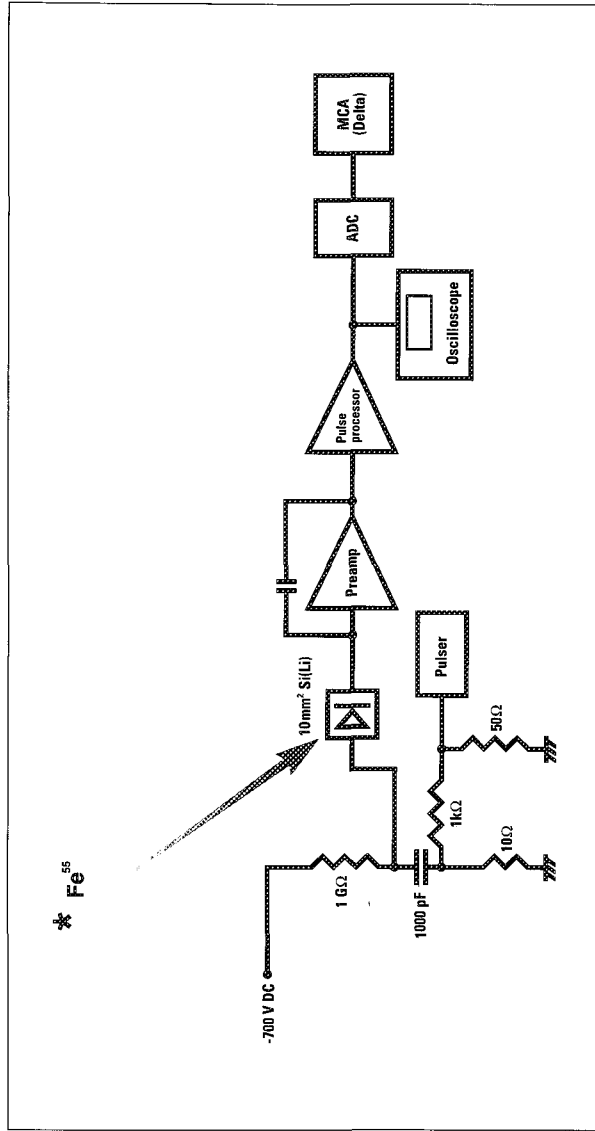


FIG. 2.--Experimental system for dead-layer calculation and simulation of boron peak with 10mm^2 detector.

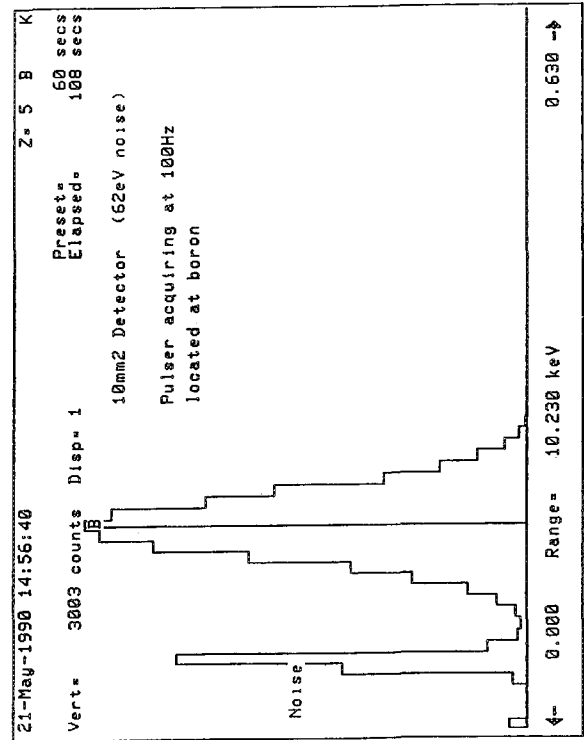


FIG. 3.--Pulsar at 100 Hz located at boron.

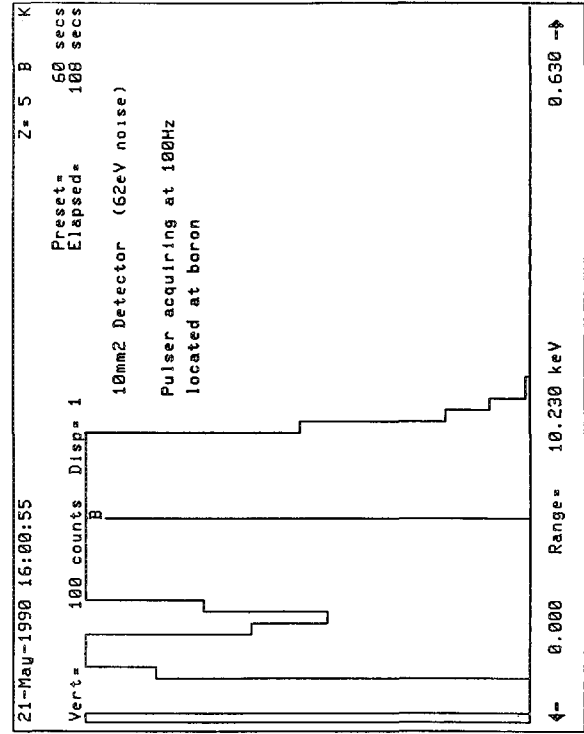


FIG. 4.--Figure 3, expanded vertical scale.

- sample
- dead-layer thickness
- Fano factor
- SEM electron beam current
- SEM geometry
- Quantum detector window

An identical dead layer is achieved by choosing two detectors (10mm² and 30mm²) with the same peak-to-background ratio as produced from an Fe⁵⁵ source, in accordance with Eq. (4). The same Fano factor is achieved by choosing a Kevex 10mm² detector with a Mn K α resolution of 135 eV (electronic resolution of 62 eV), and a typical 30mm² detector with 142 Mn K α (74 eV electronic resolution). From the resolution formula (Eq. 1), we can calculate that the Fano factor is approximately 0.118 for both detectors (assuming $\epsilon = 3.76$ eV per electron hole¹ and $E = 5900$ eV at Mn K α). For the following experiment, the Kevex 10mm² Si(Li) detector with 135 eV resolution at Mn K α was chosen. The electronic resolution was measured and found to be 62 eV. Step 1 involves simulating a boron peak by injecting pulses into the 10mm² detector system with an established frequency, then acquiring the spectrum. Step 2 involves multiplying the pulser frequency by 3 (assuming the 30mm² detector is triply efficient), and by using higher gain, simulating higher noise than normally exists (as expected from a 30mm² detector), until one gets the same peak-to-valley ratio. The experimental procedure is as follows:

1. Set the pulser frequency at 100 Hz and the pulse amplitude at the boron peak (185 eV). The pulser spectrum collected is shown in Figs. 3 and 4.

2. Set the pulser frequency at 300 Hz. Start increasing the amplifier gain while reducing pulse amplitude to keep the peak in the same position (185 eV) until the same peak-to valley ratio is reached as in step 1 (when 62 eV pulser resolution and 100 Hz count rate are used). The data collected are shown in Figs. 5 and 6. One calculates the new noise resolution, 74 eV, by moving the peak to the right using gain changes in the pulser (Fig. 7). Assuming identical dead layers, the results show that one obtains a boron peak with the same peak-to-valley ratio using a 10mm² detector with Mn K α of 135 eV as with a 30mm² with noise resolution of 74 eV. This procedure yields a FWHM Mn K α resolution of 141 eV, common for new Kevex Super-Quantum 30mm² detectors.

Peak-to-background Calculation

As shown Eq. (4), the peak-to-background (P/B) ratio is directly proportional to dead-layer thickness. A problem arises when one is counting the background and the peak precisely while the peak and the background overlap. In this example (Figs. 8-10), different vertical scales are used for the same spectrum to demonstrate the level of the background counts.

The regular scale spectrum is shown in Fig. 10. Clearly, it is difficult to detect any

background. Assuming that in a common Si(Li) detector this background does not significantly affect FWHM, one could theoretically calculate the peak area. The theoretical peak shape is a normal distribution:

$$Y_x = Y_m e^{-(x-m)^2/2\sigma^2} \quad (5)$$

where σ is the standard deviation and m is the mean measured value as shown in Fig. 11.

Knowing the relationship between standard deviation and FWHM ($= 2\sigma\sqrt{2\ln 2}$), one can calculate the peak area from peak height and FWHM, which can be readily measured.

$$A = \int_{-\infty}^{\infty} Y_x dx = Y_m \sigma \sqrt{2\pi} = Y_m \frac{\text{FWHM} \sqrt{2\pi}}{2\sqrt{2\ln 2}} \quad (6)$$

$$A = 1.065 Y_m \text{ FWHM} \quad (7)$$

For our purposes, we shall use the reasonably accurate figure obtained from the highest point in the peak centroid and an FWHM value as calculated in the half-height of the peak. The K β peak area is calculated similarly. (The K β peak should have sufficient height from a statistical perspective.)

The escape peak area is added back to the K α and K β peaks, contribution of only 0.4% of the peak area. But subtracting that same value from the net background is not negligible, and the operation may not be omitted. Thus, the peak-to-background ratio is calculated as follows:

$$\frac{B}{P} = \frac{(\text{INT})}{1.065 [(Y_m \text{ FWHM}) 1.004 + (Y_m \text{ FWHM})_{K\beta} 1.003]} - 1 \quad (8)$$

The result is placed in the dead-layer formula (Eq. 4).

The dead layer for the 10mm² detector can be calculated from the data collected and shown in Figs. 8-10.

FWHM K α = 135.5 eV FWHM K β = 150.1 eV
 $Y_{mK\alpha}$ = 20 000 $Y_{mK\beta}$ = 3660
 INT = 353494 10 = 3534940
 $d = \ln(1.0145)/2.33 \times 145 = 42 \times 10^{-6}$ cm
 The dead layer for the 10mm² detector is 0.42 μ m

The 10mm² Quantum detector was mounted on a JEOL JSM 6400 SEM, and from a boron metal sample, the spectrum in Fig. 13 was acquired using a count rate of 1000 counts per second. In the penultimate step, the 30mm² SuperQuantum detector was chosen and tested for boron performance. The 30mm² detector was also tested on the same SEM and in the same manner. The results, shown in Figs. 14-16, are similar to those for the simulated 30mm² detector, produced by the pulser method. The boron spectrum is shown in Fig. 17. From the collected data, one may calculate the p/b ratio and the dead layer.

FWHM K α = 142.0 eV FWHM K β = 151.2 eV
 $Y_{mK\alpha}$ = 20 000 $Y_{mK\beta}$ = 3649

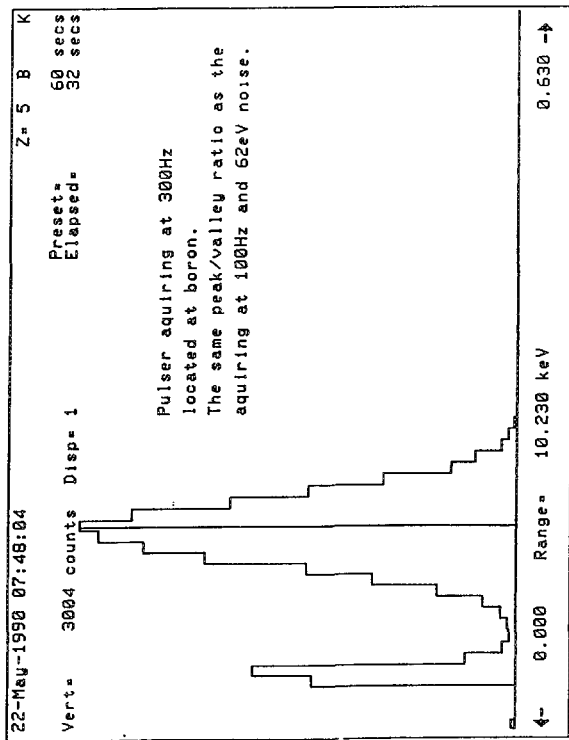


FIG. 5.--Pulser spectrum at 300 Hz, located at boron peak energy. FIG. 6.--Figure 5, expanded vertical scale.

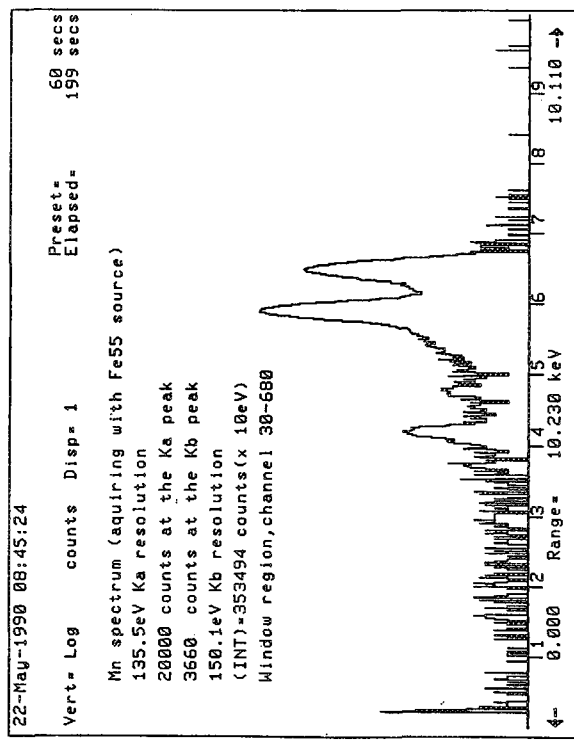


FIG. 7.--Log scale display of Mn spectrum obtained with 10mm² detector with resolution of 135.5 eV.

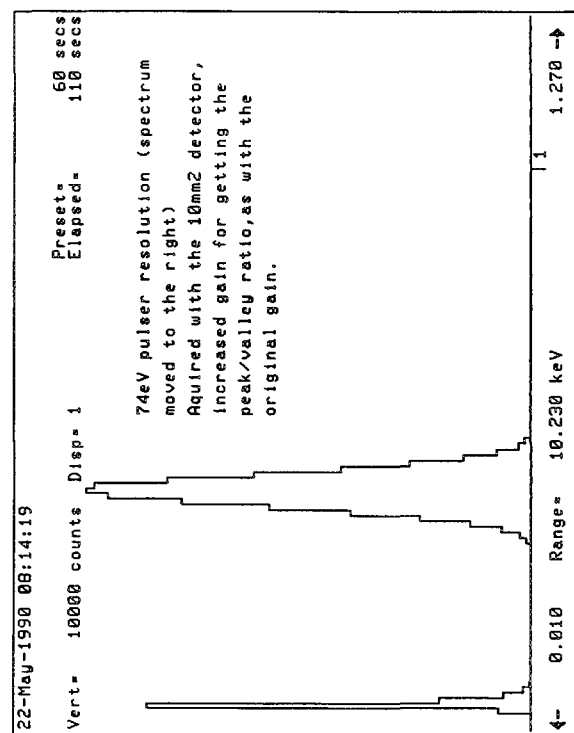
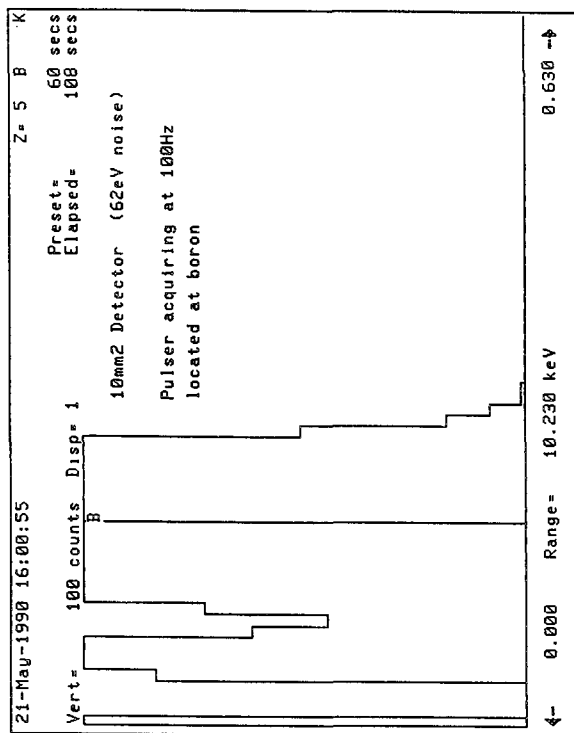


FIG. 8.--Pulser resolution spectrum for simulated 30mm² detector.

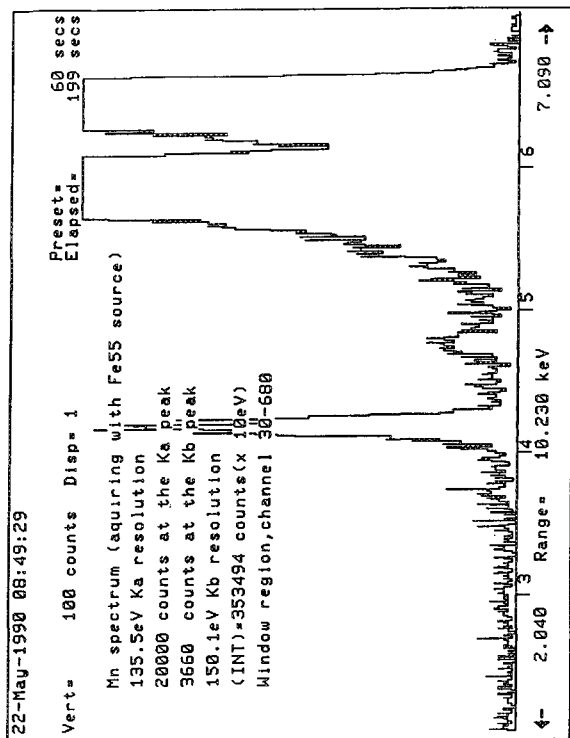


FIG. 9.--Expanded vertical scaling of MN spectrum obtained with 10mm² detector with resolution of 135.5 eV.

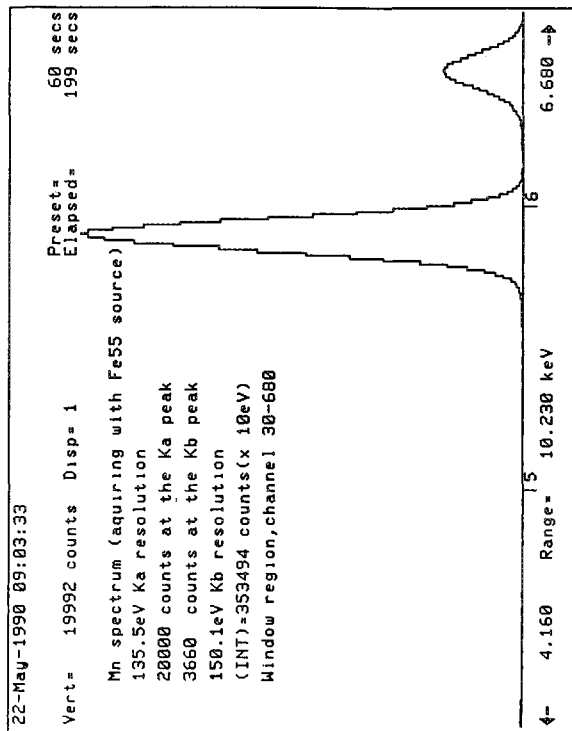


FIG. 10.--Regular scaling of Mn spectrum obtained with 10mm² detector with resolution of 135.5 eV.

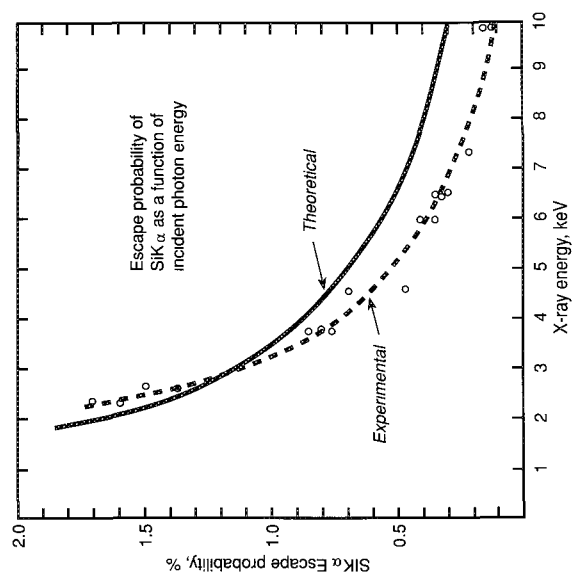


FIG. 11.--Percent escape probability of Si K_α vs "full-energy" deposit (parent energy).

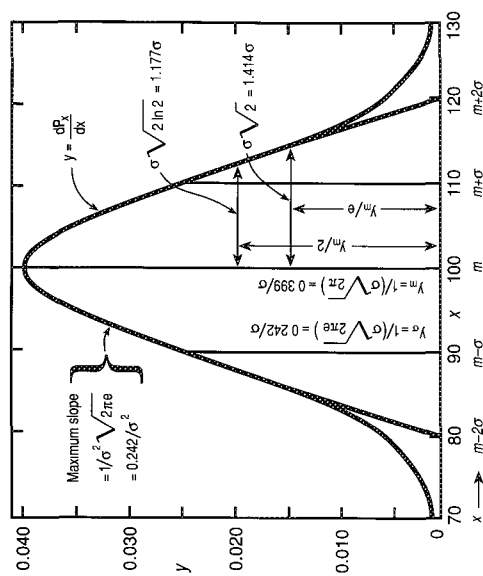


FIG. 12.--Normal distribution for special case of mean value $m = 100$ and standard deviation $\sigma = 10$.

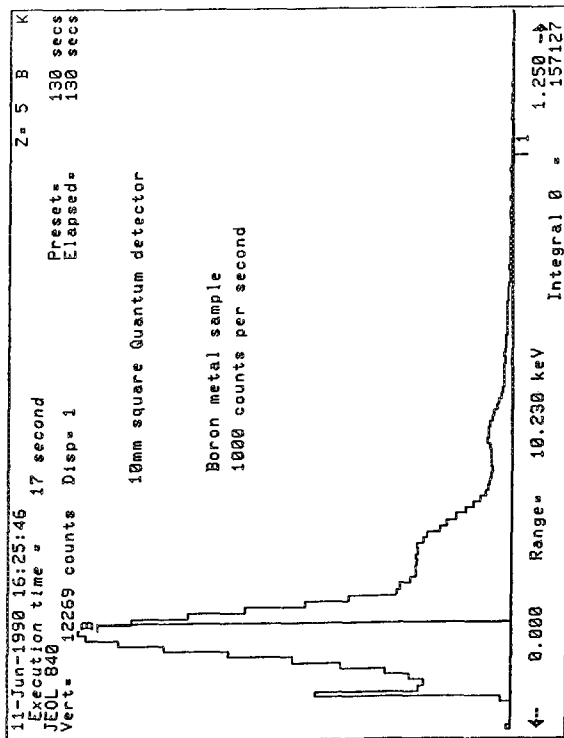


FIG. 13.--Boron peak collected with 10mm² detector on JEOL 6400 SEM.

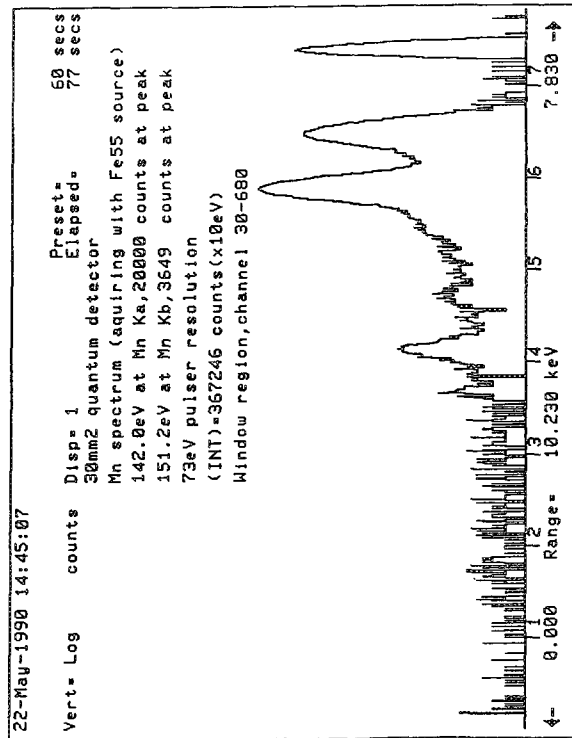


FIG. 15.--Figure 14, log scale display.

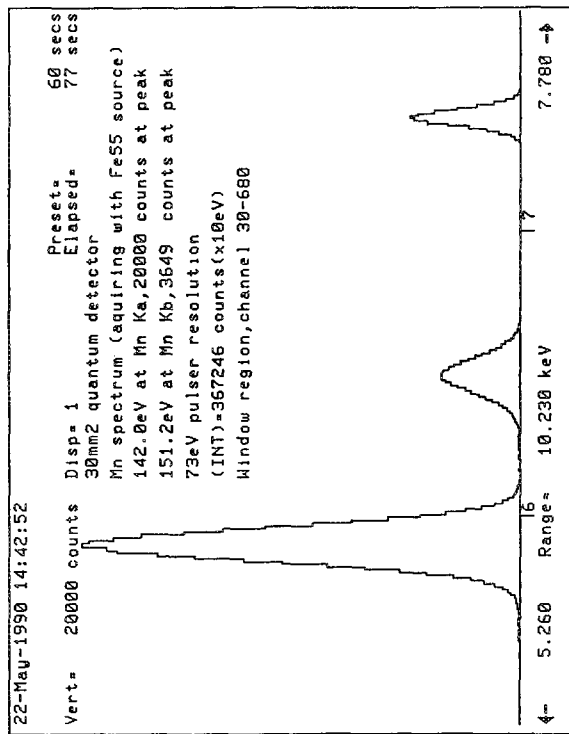


FIG. 14.--Manganese spectrum acquired with 30mm² detector and Fe⁵⁵ source.

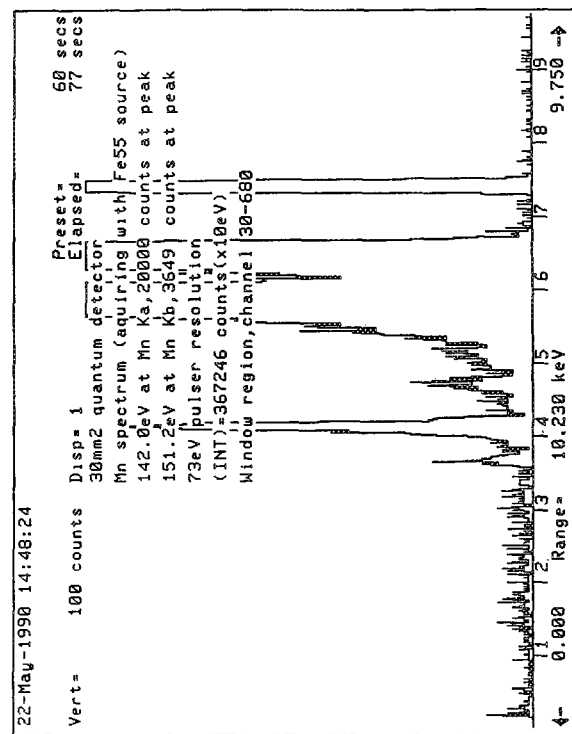


FIG. 16.--Figure 14, expanded scale display.

$$\text{INT} = 367\,246 \times 10 = 3\,672\,460$$

$$\frac{B}{P} = \frac{3\,672\,460}{1.065[20\,000 \times 142.0]1.004 (3649 \times 151.2)1.003} - 1$$

$$= 0.0128 \quad (9)$$

$$d = \ln(1.0128)/2.33 \times 145 = 38 \times 10^{-6} \text{ cm}$$

The dead layer for the 30mm² detector is 0.38 μm .

Although the results are not truly identical, they are sufficiently close to allow us to conclude that the dead layers of the 10mm² and 30mm² detectors are approximately equal.

Conclusion

From these test results, it is clear that a 30mm² detector with resolution of 142 eV is superior to a 10mm² detector with 135eV resolution, assuming an identical dead layer. The 30mm² detector resolves boron as well as the 10mm² detector because it is three times more efficient than the 10mm² detector. Although the electronic noise component is greater with a 30mm² detector, its effects are more than compensated by the improvement in efficiency.

References

1. G. F. Knoll, *Radiation Detection and Measurements*, Sec. D, 363.
2. J. I. Goldstein, *Scanning Electron Microscopy and X-ray Microanalysis*, 626.
3. R. Woldseth, *X-ray Energy Spectrometry*, Kevex Instruments, 1973.
4. J. Llacer and E. E. Haller, "Entrance windows in germanium low-energy x-ray detectors," *Trans. IEEE* NS-24: 1977.
5. H. L. Malm, "Properties of metal surface barriers on high purity germanium," *Trans. IEEE* NS-22, 140, 1975.

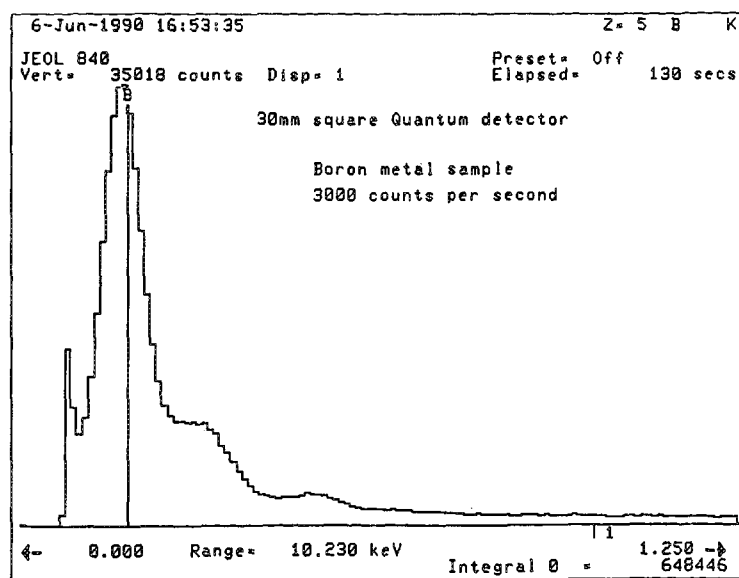


FIG. 17.--Boron peak collected with 30mm² detector on JEOL JSM-6400 SEM.

THE EFFECT OF AVERAGING PARAMETERS ON THE BACKSCATTER CORRECTION

K. F. J. Heinrich and R. L. Myklebust

The backscatter correction, together with the stopping-power calculation, is represented in the Z term of the conventional ZAF scheme. The present work is part of a systematic study of the errors committed in reducing a set of more than 1800 measurements of binary specimens of known composition with various correction procedures. It is impossible to assess the accuracy of the stopping-power calculation until a reasonable estimate of the accuracy of the backscatter correction is established.

The backscatter correction is derived from the knowledge of the backscatter factor, which indicates the number of backscattered electrons, and from the energy distribution of the backscattered electrons. The effect of variations in the energy distribution on the accuracy of data reduction is minor.¹ Unlike the procedure of Duncumb,² newer approaches^{3,4} include the backscatter coefficient numerically. Since this parameter has been determined experimentally by various investigators,^{5,6} this approach lends itself to a more detailed study of its effects on the correction procedure.

The backscatter coefficient varies strongly with atomic number of the specimen, and less so with the operating voltage and the atomic weight of the elemental target. The effect of atomic weight⁷ is always neglected; that of energy is taken into account in the procedure of Scott et al.³

The method of averaging the components of a multielement target can have a significant effect on the result when major components differ considerably in the atomic number and element standards are used. Castaing⁸ proposed adding backscatter coefficients in weight proportions, and this procedure is followed in most ZAF procedures. The recent PAP procedure of Pouchou and Pichoir⁴ uses an "average atomic number"

$$\text{ave. } Z = (\sum C_i \sqrt{Z_i})^2$$

to calculate the backscatter coefficient, and then the backscatter correction. The proposed averaging procedures can be tested against experimental data.^{5,6,9} The comparison of calculated and measured backscatter

1. When elements of high atomic number are major components of the specimen, it is advisable to take into account the variation of backscatter with the operating voltage, as done by Scott et al.

2. The averaging procedure of Castaing leads

K. F. J. Heinrich's address is 804 Blossom Drive, Rockville, MD 20850; R. L. Myklebust is with the Center for Analytic Chemistry, National Institutes of Standards and Technology, Gaithersburg, MD 20899.

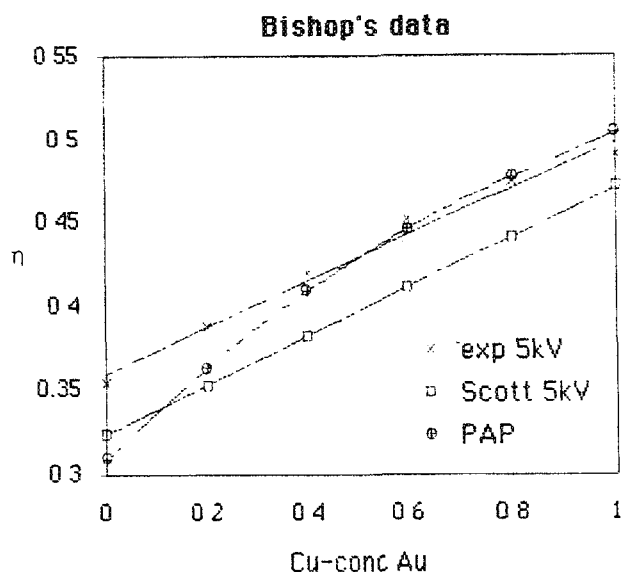


FIG. 1.--Comparison of experimentally obtained backscatter coefficients on Cu-Au alloy set (Ref. 5) with calculations according to Scott and to PAP method.

to minor deviations in backscatter coefficients of multielement targets, which do not significantly affect the analytical result.

3. The agreement between the experimental data and those predicted by the PAP procedure is less satisfactory and may effect the accuracy of the analysis if the standard is of composition substantially different from that of the specimen.

References

1. R. L. Myklebust and D. F. Newbury, *Microbeam Analysis*--1988, 261.
2. P. Duncumb and S. J. B. Reed, *NBS Special Publ.* 298, 1968, 133.
3. G. Love and V. D. Scott, *J. Phys.* D11: 1369, 1978.
4. J. L. Pouchou and F. Pichoir, *11th ICXOM*, London, Ont., 1978, 249.
5. A. E. Bishop, *4th ICXOM*, Paris, 1966, 153.
6. K. F. J. Heinrich, *4th ICXOM*, Paris, 1966, 159.
7. K. F. J. Heinrich, *NBS Special Publ.* 298, 1968, 8.
8. R. Castaing, *Adv. Electr. Electron Phys.*, vol. 13, New York: Academic Press, 1960, 317.
9. J. W. Colby, *The Electron Microprobe* New York: Wiley, 1966, 96.

A ROBUST METHOD FOR DETERMINING THE DUANE-HUNT ENERGY LIMIT FROM ENERGY-DISPERSIVE SPECTRA

R. L. Myklebust, C. E. Fiori, and D. E. Newbury

The electron beam energy is a parameter required for quantitative electron probe microanalysis. It occurs in all parts of the ZAF-type matrix correction procedure as well as in all of the other matrix correction procedures. Recently, there has been much interest in analyzing materials at lower beam voltages. The correction procedures use the so-called "over-voltage" term (beam energy/excitation energy). Uncertainties in the beam voltage generate larger errors at low overvoltage than at high overvoltage. The user may well be faced with an instrument that does not have a very precise voltmeter to measure the beam voltage, or the reported voltage may not actually represent the potential drop from the filament to ground (specimen). The true beam energy may differ from the measured potential drop by several hundred volts.

It is difficult and potentially exciting to measure the beam voltage with a calibrated voltmeter; however, the physics of the beam-specimen interaction provides a method that is built into the energy-dispersive x-ray detector. Continuum x rays are generated up to the incident energy of the electron beam (the Duane-Hunt limit). The beam voltage can then be determined with a calibrated energy dispersive spectrometer (EDS) by examining the high-energy portion of the spectrum. Although one can get an approximate answer by simply looking at the spectrum, the action of the detector response function distorts the apparent Duane-Hunt limit from the true value. We propose a method that we hope provides consistently unbiased values.

The intensity of the continuum x rays at a given energy E can be described with an equation derived by Kramers¹:

$$I(E)dE = kZ(E_0 - E)\frac{dE}{E} \quad (1)$$

where Z is the atomic number, k is a constant, E_0 is the beam voltage, dE is the energy interval and $I(E)dE$ is the x-ray intensity per energy interval. A plot of the high-energy end of the x-ray continuum of copper is shown in Fig. 1. The solid line represents the generated x rays as defined by Eq. (1), and crosses the x-axis at exactly the energy of the electron beam, E_0 . When this continuum is convolved with the Gaussian detector function, the dashed line in Fig. 1 is produced, which intercepts the x-axis about 100 eV higher in energy than the original expression. This distorts the shape

of the curve at the Duane-Hunt limit and makes it more difficult to fit the data accurately. Because of the $1/E$ term in Eq. (1), the plot of intensity vs energy is slightly curved near the Duane-Hunt limit (Fig. 2 is a plot of the continuum tails for carbon, copper, and gold) and one would expect that a least-squares fit to a second-degree polynomial expression would produce good results. In some cases results from a quadratic fit appear to be satisfactory; in other cases (when the spectrum is from a low-atomic-number element or there is pulse pile-up close to the Duane-Hunt limit), the fit produces only imaginary roots. Least-squares methods also have undesired sensitivity to outlying points, a serious problem, since data points beyond the Duane-Hunt limit introduced by the spectrometer resolution function (as shown in Fig. 1) need to be eliminated from the fit. Figures 3 and 4 are plots of quadratic fits to copper spectra at 15 and 20 keV beam energies, respectively. In Fig. 3, the pulse pile-up above the Duane-Hunt limit tends to pull the intercept to a higher energy and even though the quadratic fit shown in Fig. 4 appears to be a good model of the data, it only produces imaginary roots.

Another difficulty to be reckoned with is the statistical noise associated with the x-ray spectrum. For the most part, this noise can be modeled by a normal distribution; however, near the Duane-Hunt limit the normal distribution is not valid. A basis for the method of least squares is that the data be normally distributed. Therefore, it would be mathematically naive to attempt to use a method for the modeling of normally distributed data to model a Poisson process in which the data go from relatively large numbers (where the normal approximation is valid) to zero.

We have chosen to use a robust estimator and fit a straight line by minimizing the sum of the absolute deviations instead of the sum of the squares of the deviations.² The function to be minimized is therefore

$$\sum_{i=1}^N |y_i - a - bx_i| \quad (2)$$

instead of χ^2 as required for least squares. Figure 7 is a dramatic example of the effectiveness of the robust estimator where the presence of the gold peak does not significantly influence the quality of the fit through the continuum. If we multiply the x-ray intensities in Eq. (1) by their energies, the result should be a straight line, the x-intercept of which is the Duane-Hunt limit. Experimentally, a slight deviation from a straight line arises

The authors are at the Microanalysis Research Group, Center for Analytical Chemistry, National Institute of Standards and Technology, Gaithersburg, MD 20899.

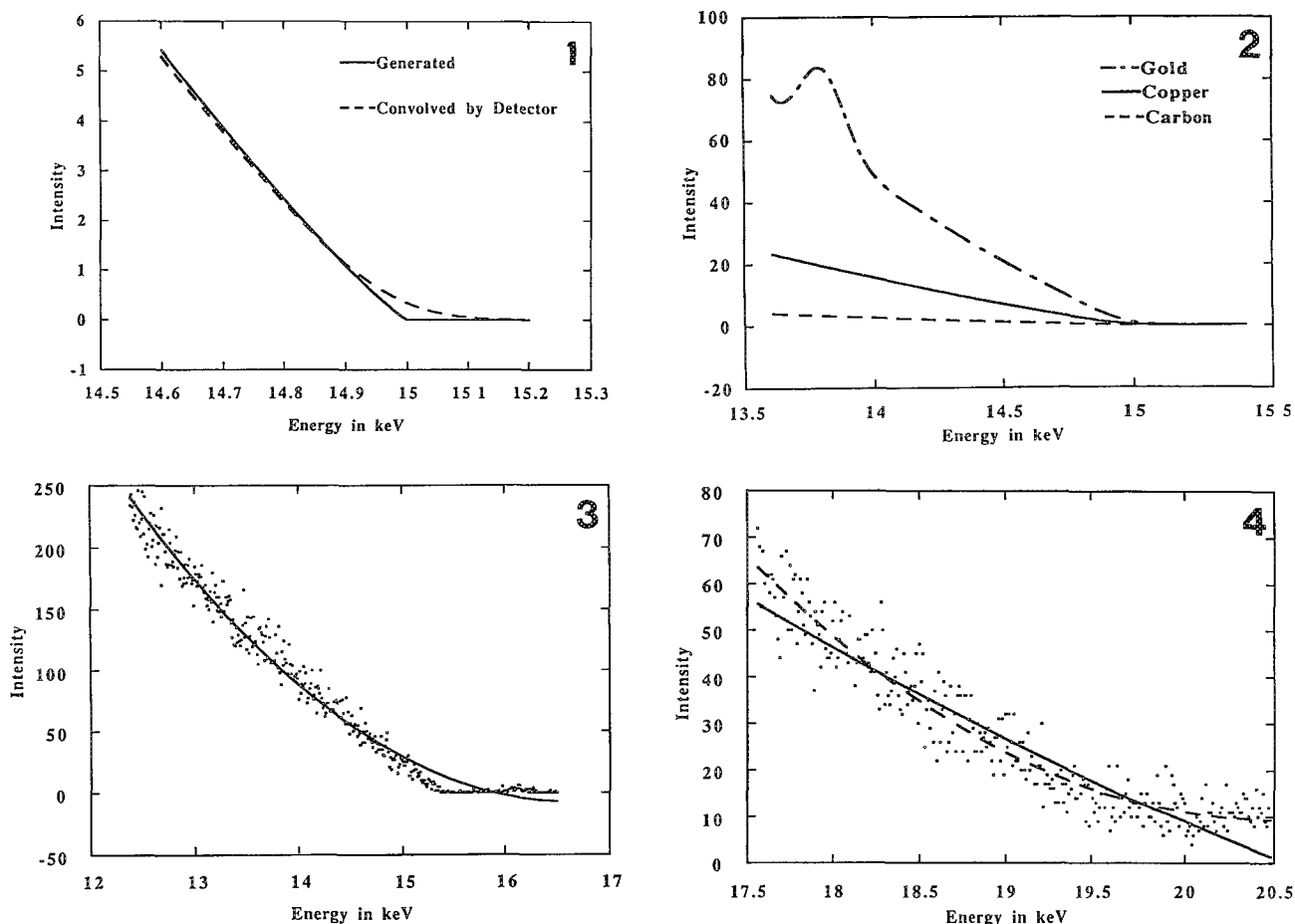


FIG. 1.--Segment of synthetic copper spectrum measured with beam voltage set at nominal value of 15 keV. Solid line is generated x rays computed with Eq. (1). Dashed line is generated x rays convolved with Gaussian detector function. Data have all been transformed back to intensity by dividing by E.

FIG. 2.--Segments of synthetic spectra of gold, copper, and carbon at 15 keV. Data have all been transformed back to intensity by dividing by E.

FIG. 3.--Segment of experimental spectrum of copper at nominal value beam voltage of 15 keV together with least-squares fit a second-degree polynomial. Data have all been transformed back to intensity by dividing by E.

FIG. 4.--Segment of experimental spectrum of copper at nominal beam voltage of 20 keV together with least-squares fit to second-degree polynomial (dashed line) and fit using robust estimation method described here (solid line). Data have all been transformed back to intensity by dividing by E.

because of imperfections in Kramers's equation and the Gaussian response shown in Fig. 1. Because it is physically impossible to have non-zero intensities beyond the Duane-Hunt limit, the next step is to eliminate all the data beyond the root from the fitting procedure and refit the data. An iterative procedure has been devised to eliminate systematically data points with energies higher than the value of the root of the equation. The procedure always uses 300 channels (a channel is defined as an energy interval and is usually 5, 10, or 20 eV) on the low-energy side of the best estimate of the root and a number of channels on the high-energy side that is reduced with each iteration. At the start, 150 channels on the high-energy side are used. On successive iterations, this

number is reduced to 50 channels, then 10, 7, 5, 3, and finally 1 channel. The program is not allowed to terminate until after the number of channels on the high-energy side is reduced to 1. The resulting expression is used to compute predicted values of the intensities which are then plotted with the measured values (Fig. 5). To test the fitting method, energy-dispersive spectra are synthesized with Eq. (1) so that the "true" Duane-Hunt limit can be defined. For this test case, the proposed fitting method is exact. When specimen absorption, detector efficiency, spectrometer broadening, and Poisson noise are added to a synthesized copper spectrum, the fit is still within 0.33% of the "true" value for 10 repeated syntheses with random noise.

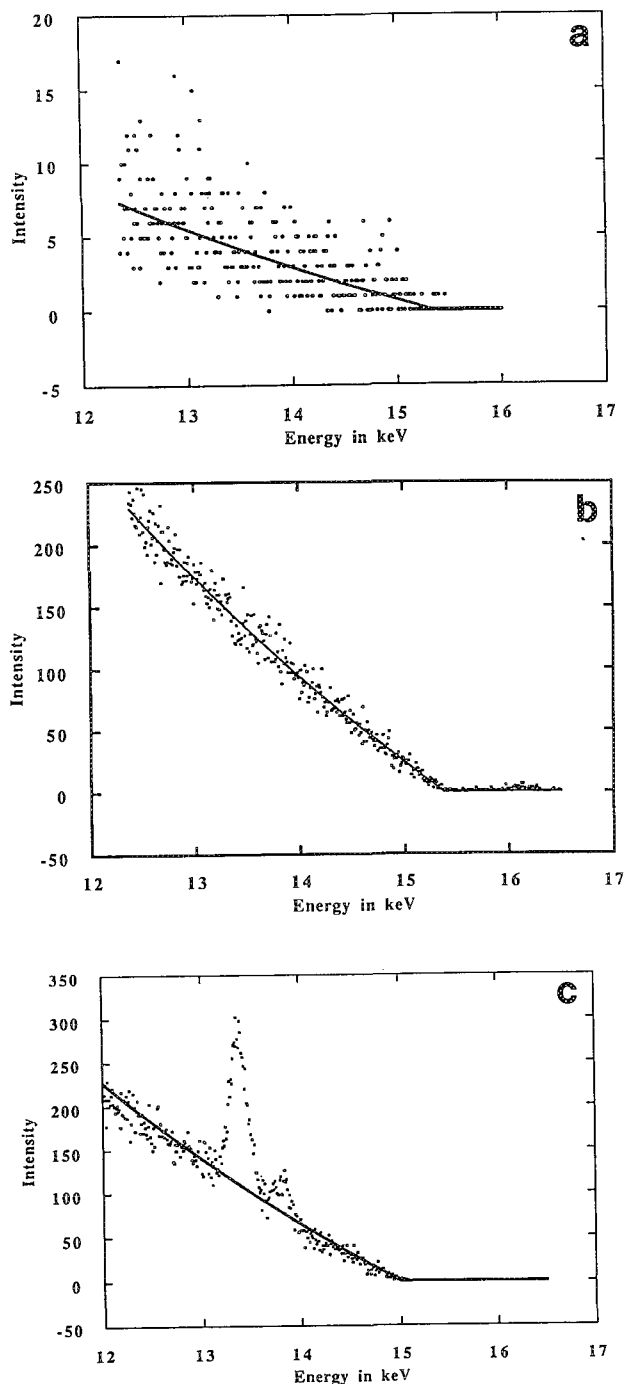


FIG. 5.--Segment of experimental spectrum at nominal beam voltage of 15 keV together with fit using robust estimation method described here. Data have all been transformed back to intensity by dividing by E . (a) carbon, (b) copper, (c) gold.

An examination of Figs. 2 and 5 demonstrates why the results are better with high-atomic-number targets than with low. Since the continuum intensity increases with atomic number, the higher atomic number targets provide more x-ray counts in the spectrum and therefore bet-

ter statistics. Also, the higher number of counts the method more robust, as is demonstrated by the fit shown in Fig 5(c). Here two of the gold L-series x-ray lines occur within the range of the data to be fit. Note that the fitted line is still a good estimation of the data regardless of the peaks present. In fact, if the peaks are stripped from the spectrum and the fit is repeated, the Duane-Hunt limit is only lowered by 4 channels (40 eV).

As with any procedure of this type, the results depend on the information supplied by the user. The spectrum should be accumulated for a sufficient length of time and at a low enough detector dead-time to insure good statistics and to minimize any pulse pile-up. It is necessary that the detector be properly calibrated to avoid miscalibration errors propagating through to the final result. Further testing of the method will be carried out to identify any possible systematic errors that might arise from the deviation in linearity from the assumed response given by Eq. (1). In addition, we intend to evaluate other fitting procedures such as a quadratic fit where the discriminant ($b^2 - 4ac$) is constrained to be greater than or equal to zero.

References

1. H. A. Kramers, *Phil. Mag.* 46 (6th ser): 836, 1923.
2. W. H. Press et al., *Numerical Recipes*, New York: Cambridge University Press, 1986, 539-545.

A FURTHER DEVELOPED MONTE CARLO MODEL FOR THE QUANTITATIVE EPMA OF COMPLEX SAMPLES

Norbert Ammann and Peter Karduck

An universal Monte Carlo (MC) program has been developed in order to calculate the ionization probabilities $\Phi_{n1}(z)$ in layered specimens. Having started with a model for pure elements,¹ the new program now simulates the EPMA of any sample consisting of up to 20 different elements from hydrogen to uranium in up to 10 layers on substrates. The cross sections for inelastic scattering have been revised completely in order to obtain a realistic model.

The present program works without any adjusting parameter. With the new ionization cross sections, the results of the MC simulations agree closely with experiments. Significant deviations of $\Phi_{n1}(z)$ in coated samples from those in homogeneous specimens have been found and could be explained.

Definitions

The depth coordinate relevant for the electron diffusion is the mass depth expressed in units of mass per area. For simplicity the mass depth is denoted by z , whereas z' is the symbol for the geometrical depth. z is often defined by the product of the density ρ and z' , but in general the density at depth z' is the derivative of z with respect to z' :

$$dz = \rho(z')dz' \quad z = 0 \Leftrightarrow z' = 0 \quad (1)$$

Any result of EPMA concerning the depth is a mass per area or, when divided by the atomic weight, a number of atoms per area.

The electron bombardment establishes a stationary electron (flux) density $N(E, z)$ in the region near the sample surface. $N(E, z) dE dz$ is the mean number of electrons with energies between E and $E + dE$ in the depth interval $(z, z + dz)$, related to a beam current of one electron per time unit. The electron density is determined by the sample composition, the beam energy E_0 , and the tilt angle.

Equation (2) is a physical definition of the ionization probability $\Phi_{n1}(z)$ by the electron density. Q_{n1} is the ionization cross section and E_{n1} the binding energy of the atomic sub-shell characterized by the quantum numbers n and l .

$$\Phi_{n1}(z) = \frac{1}{Q_{n1}(E_0)} \int_{E_{n1}}^{E_0} Q_{n1}(E) N(E, z) dE \quad (2)$$

It can be shown that Eq. (2) is consistent

The authors are with the Gemeinschaftslabor für Elektronenmikroskopie der RWTH Aachen, Ahornstr. 55, D-5100 Aachen, Germany.

with the experimental definition of Castaing and Descamps.²

Any relative emitted x-ray intensity I_λ can be calculated by Eq. (3) once $N(E, z)$ is known, where $\langle \mu_\lambda(z) \rangle$ is the mass absorption coefficient averaged from the surface to depth z , θ_t is the x-ray take-off angle, and λ is the wavelength:

$$I_\lambda = Q_{n1}(E_0) \int_0^\infty c(z) \exp[-\langle \mu_\lambda(z) \rangle z / \sin(\theta_t)] \cdot \Phi_{n1}(z) dz \quad (3)$$

Equation (3) demonstrates the common problem of EPMA, the determination of the concentrations $c(z)$ from the measured intensities and the corresponding set of (coupled) intensity equations. Obviously the knowledge of the $\Phi_{n1}(z)$ curves is prerequisite to exact calculations, but up to now these curves have been rather unknown even for samples with thin coatings.

The trajectories $[E_{i,j}(s); z_{i,j}(s)]$ of N beam electrons (index $i, 0$) and those of the produced secondary electrons ($i, j > 0$) are related to the electron density by Eq. (4); $\delta(x)$ is the Dirac function, and s is the path length.

$$N(E, z) = \lim_{N \rightarrow \infty} \frac{1}{N} \sum_{i=1}^N \sum_{j=0}^\infty \int_0^\infty \delta(E - E_{i,j}(s)) \cdot \delta(z - z_{i,j}(s)) ds \quad (4)$$

The present program calculates $N(E, z)$ from Eq. (4) by approximating $\delta(x)$.

Finally, the quantity g_Z is defined by Eq. (5), where c_Z is the weight fraction of element Z at point of space X , A_Z its atomic weight, and N_A is Avogadro's number:

$$g_Z(X) = c_Z(X) N_A / A_Z \quad (5)$$

Here g_Z is used as the weighting factor for the cross sections in compounds.

Cross Sections

The MC simulation is a numerical method to calculate the predictions of atomic cross sections. The cross sections determine the accuracy of the simulations and therefore the values used have to be explained prior to the presentation of results.

The elastical scattering is described completely by the differential cross sections $d\sigma_{e1}/d\theta$. Normalized, $d\sigma_{e1}/d\theta$ represents the distribution of scattering angles θ due to a single event. The integral of $d\sigma_{e1}/d\theta$ from $\theta = 0$ to π is the total elastic cross section

σ_{e1} ; summation of $g_Z \sigma_{e1,Z}$ over the atom numbers Z results in the mean number of elastical scatterings per unit path length in a compound.

The present program uses Mott cross sections, which are published for 13 elements.³ Approximated values for the remaining elements have been calculated by linear interpolation of the R values, which are the ratios of Mott to Rutherford cross sections. For the interpolation to low Z , $R(Z = 0)$ has been set to unity.

Inelastic scattering is completely described by the differential cross sections $d\sigma_{n1}/dW$.⁴ The fundamental relations between $d\sigma_{n1}/dW$, the ionization cross section, and the stopping power lead to the main difference between the present and previous models. Normalized, $d\sigma_{n1}/dW$ is the distribution of the primary electron energy loss W after an ionization of the $n1$ shell. Integration of $d\sigma_{n1}/dW$ from $W = E_{n1}$ to the electron energy E gives the ionization cross section $Q_{n1}(E)$:

$$Q_{n1}(E) = \int_{E_{n1}}^E (d\sigma_{n1}/dW) dW \quad (6)$$

With the occupancy N_{n1} , the mean number of $n1$ -shell ionizations per unit path length is given by the product $g_Z \cdot N_{n1} \cdot Q_{n1}$. The integral $W \cdot d\sigma_{n1}/dW$ over W is the stopping power S_{n1} and at least the mean energy loss $\langle dE/ds \rangle$ is given by summarizing $g_Z \cdot N_{n1} \cdot S_{n1}$ over all elements and their shells.

$$\langle dE/ds \rangle = \sum_Z g_Z \cdot \left[\sum_{n1} N_{n1} \int_{E_{n1}}^E W (d\sigma_{n1}/dW) dW \right]_Z \quad (7)$$

Obviously neither the energy loss nor the ionization cross sections are independent of the differential cross sections. A reasonable input for the simulation has to obey these relations to avoid contradictions. For example, an ionization cross section greater than that of Eq. (6) would predict more energy converted to ionizations than the electron has lost. A systematic deviation of the calculated intensities may be the consequence of using an ionization cross section that systematically deviates from Eq. (6). Therefore, the leading idea was to find a reasonable input for the simulation program which obeys Eqs. (6) and (7). The formulas of previous models could not be adopted because none of them satisfies this condition.

The cross section formulas of Gryzinski⁴ are suitable for MC simulations because they provide $d\sigma_{n1}/dW$, Q_{n1} , and S_{n1} in a closed form. The energy variation of the ionization cross sections shows satisfying agreement with experimental values.⁵ Yet the mean energy loss predicted by the same formulas differs up to 20% from experience and there seems to be only the choice of realizing either consistent equations or an experienced energy loss.

But use of the Gryzinski cross sections

modified according to Eq. (8) allows even the realization of any mean energy loss $\langle dE/ds \rangle$ without violating Eqs. (6) and (7):

$$d\sigma_{n1}/dW = (d\sigma_{n1}/dW)_{Gryz} \frac{\langle dE/ds \rangle}{\langle dE/ds \rangle_{Gryz}} \quad (8)$$

$\langle dE/ds \rangle$ has been calculated by the Bethe formula with the mean ionization potential of Sternheimer⁶ and the extrapolation to low energies proposed by Rao Sahib and Wittry.⁷ The binding energies of Sevier⁸ have been used to calculate the Gryzinski formulas. Contrary to earlier models,¹ the shells of each model atom are occupied by all Z electrons.

An accurate simulation in layered specimen has to consider the effect of interfaces on the free-path distributions.⁹ The general relation for the simulation of free paths Λ in samples with any inhomogeneity is Eq. (9). The integrand represents the scattering probability per unit path length, possibly different at any point in space X ; R is a random number.

$$\int_0^{\Lambda(R)} \sum_Z g_Z [X(s)] [\sigma_{e1} + \sum_{n1} N_{n1} Q_{n1}]_Z ds = -\ln(1 - R) \quad (9)$$

The present program provides an exact simulation of the free paths. Suppose an electron is at point X_0 in the sample. The next free path has to be simulated. At first any inhomogeneity is ignored and $\Lambda^{(0)}$ is simulated by Eq. (10). $\langle \Lambda_0 \rangle$ is the mean free path in the material surrounding X_0 .

$$\Lambda^{(0)} = \langle \Lambda_0 \rangle \ln(1 - R) \quad (10)$$

Interfaces are assumed at distances D_1, D_2, \dots from the starting point X_0 . Each time the electron strikes an interface, the free path is recalculated by multiplication of the remaining path by the ratio of the mean free paths of the materials after and before the interface, $\langle \Lambda_k \rangle$ and $\langle \Lambda_{k-1} \rangle$, respectively.

$$\Lambda^{(k)} = D_k + \frac{\langle \Lambda_k \rangle}{\langle \Lambda_{k-1} \rangle} (\Lambda^{(k-1)} - D_k) \quad k > 0 \quad (11)$$

The real number of scattering events per beam electron is of the order of 10^4 to 10^6 , too high for a pure single scattering model. Similar to previous hybrid models, the present program simulates elastical interactions with scattering angles higher than $\pi/18$ ($=10^\circ$), and ionizations with secondary electrons of more than 200 eV energy explicitly. These ionizations represent approximately 1% of the physical scattering events and 1/3 of the total energy loss. The remaining energy loss, given by Eq. (12), is continuously subtracted along the trajectories.

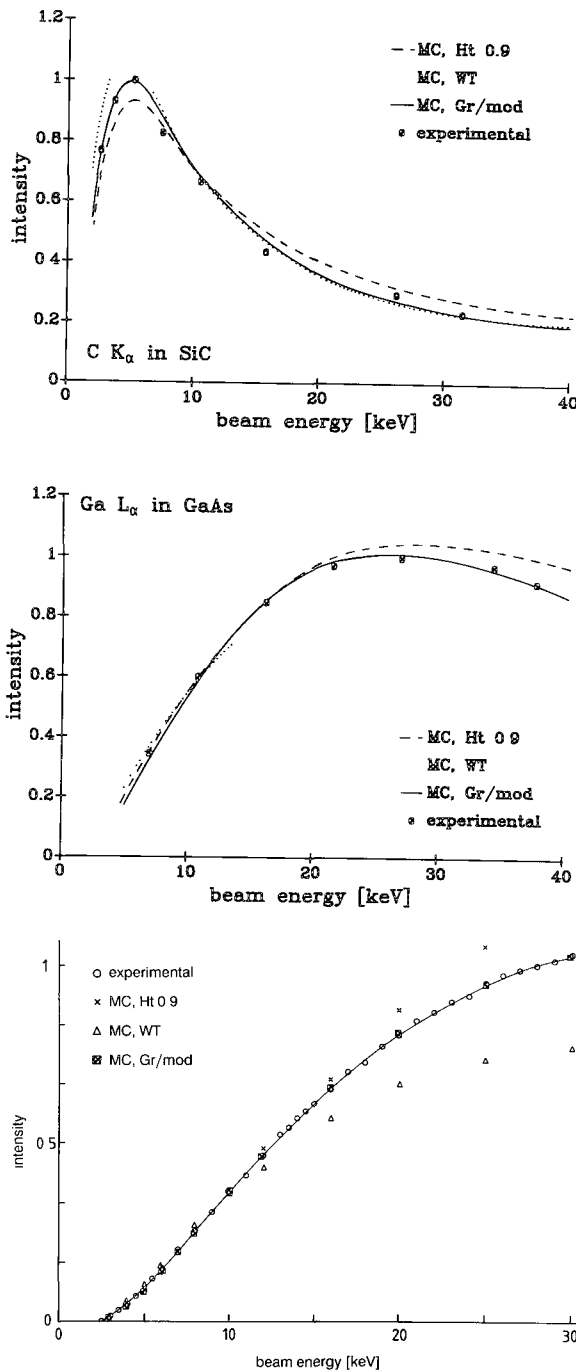


FIG. 1.--Relative intensities, calculated for various ionization cross sections and experimental values.¹¹ (a) C K α intensities of SiC, (b) Ga L α intensities of GaAs, (c) Pt M α intensities of Pt.

$$\langle dE/ds \rangle_{\text{rem}} = \sum_Z g_Z \left[\sum_{n1} N_{n1} \cdot \int_{E_{n1}}^{E_{n1}+200\text{eV}} W(d\sigma_{n1}/dW) dW \right]_Z \quad (12)$$

The remaining scattering is taken into account by artificial scatterings at the half of each simulated free path.¹ The remaining

elastic but also the inelastic events are considered by the calculation of the mean scattering angle on the simulated free path.

Results

Previous MC programs have used Mott cross sections for elastic scattering and simulated single ionizations, as well as secondary electrons. But they could not accurately reproduce the measured x-ray intensities with the ionization cross sections known from the literature.¹⁰ If the ionization cross sections given by Eqs. (6) and (8) (Gr/mod) are used, the calculated intensities of K, L, and M lines agree with those measured^{11,12} within experimental error. Systematic deviations occur if the ionization cross sections of Hutchins¹³ (Ht 0.9) or Worthington and Tomlin¹⁴ (WT) are used (Fig. 1).

Simulated intensity ratios (k-ratios) of layer and substrate elements in coated samples agree closely with experimental values¹⁵ (Fig. 2). This finding shows that the Φ_{n1} curves are accurate in the film and in the substrate.

Using the simulated electron densities, we have calculated the compositions of Ni-Cr on Gd-Fe-Pt double layers on silicon from measured intensities independently at 20, 25, and 30 kV (Fig. 3). Within experimental error agreement with values from RBS analysis¹⁶ is obtained. A further application of the present program, quantification of a:C/B-H layers, has been reported elsewhere.¹⁷

The present program has been used to investigate the effect of inhomogeneities on the shape and amplitude of ionization probabilities Φ_{n1} . In films with low atomic numbers on substrates of high Z ("light on heavy"), the maximum of $\Phi_{n1}(z)$ shifts to greater depths with growing film thickness. It is well known that the maximum of Φ_{n1} in homogeneous specimen lies the deeper the lower the atomic number of the material. Therefore this shift has to be expected. But the B K α ionization probability in NiCr coated with BC shows that the maximum can lie even deeper than in the pure film material. Not until the film thickness becomes more than half the electron penetration depth does the maximum position shifts rapidly back to that of the pure film material. Furthermore, the amplitude of Φ_{n1} behind the interface is considerably higher than it would be in the same depth of the pure substrate material (Fig. 4).

The integral of $N(E, z)$ from E_{n1} to E_0 represents the pure number of the electrons capable of ionizing the $n1$ shell. The comparison of this electron density with the corresponding $\Phi_{n1}(z)$ curves demonstrates that the shape deformations are mainly due to the pure number of electrons in depth.

In the opposite case of heavy layers on light substrates the maximum shifts rapidly toward the surface with increasing film thickness. Similar to the case of "light on heavy," the position of the maximum is not restricted

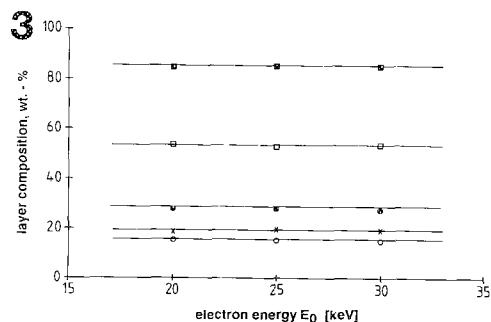
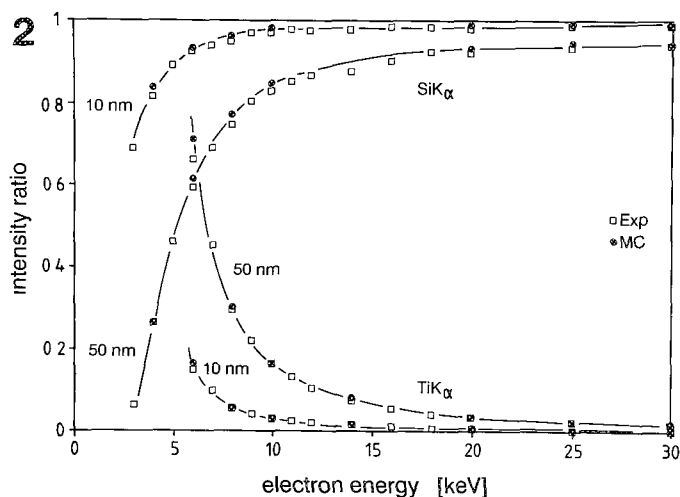


FIG. 2.--Calculated and experimental¹⁵ Ti K α and Si K α k-ratios of silicon coated with titanium (10 and 50 nm).
FIG. 3.--Layer compositions of a NiCr on GdFePt double layer on silicon. RBS results¹⁶ (solid lines) and values obtained by MC-based matrix correction of measured k-ratios (at three different beam energies).

to the region between the maxima of the ϕ_{n1} curves in the homogeneous materials. The position can be much closer to the surface than that of the pure film material. Above a relatively low critical film thickness, the effect is reversed and the maximum shifts to the position of the pure film material. The amplitude of ϕ_{n1} in the substrate is damped by strong backscattering in the film, although deep in the substrate $\phi_{n1}(z)$ is nearly unaffected even at thicknesses half the penetration depth (Fig. 6).

Conclusions

Accurate results concerning ϕ_{n1} curves, intensities, and k-ratios can be calculated by the present MC program if the modified cross section formulas are used. Although the direct verification of the calculated ionization probabilities in complex specimens seems nearly impossible, the overall agreement with the experiments confirm that the simulated curves are very close to reality. Nevertheless, one cannot assume that Eq. (8) represents the exact cross sections; it must be concluded that

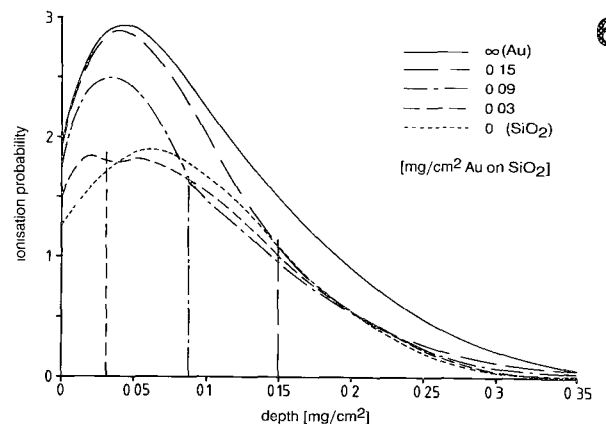
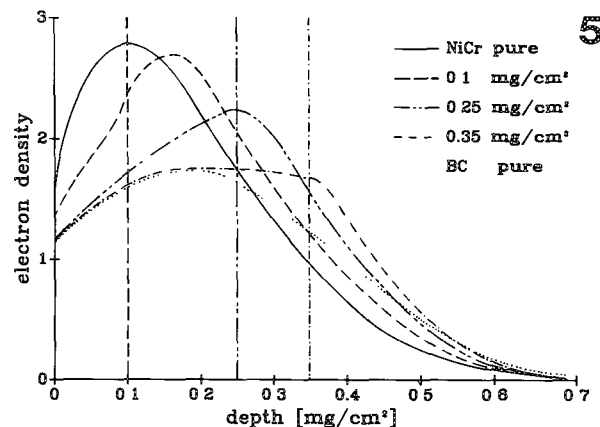
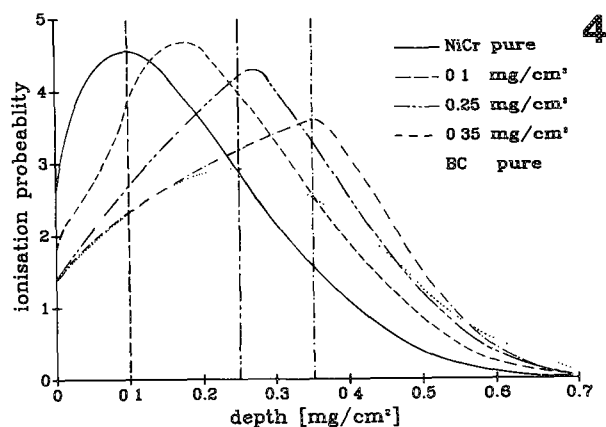


FIG. 4.--Simulated $\phi_{n1}(z)$ curves for B K α in a NiCr alloy coated with BC layers of various thicknesses.

FIG. 5.--Densities of electrons with $E > 188$ eV in the samples shown in Fig. 4.

FIG. 6.--Simulated $\phi_{n1}(z)$ curves for O K α in SiO₂ coated with Au layers of various thicknesses.

the most important quality of MC models is the realization of the fundamental physical relations.

Even simulations of EPMA in samples coated with single films reveal how manifold the $\phi_{n1}(z)$ curves in nonhomogeneous specimen are.

Such Φ_{n1} curves deviate in shape and amplitude from those in homogeneous samples. Only the MC simulation is flexible enough to provide all these curves. Therefore, this method seems to be an irreplaceable tool for accurate analysis of inhomogeneous specimens. Nevertheless, thin-film data evaluation programs, based on parametrized Φ_{n1} curves, are already available and work fairly well.¹⁸

References

1. L. Reimer and D. Stelter, *Scanning* 8: 265, 1986.
2. R. Castaing et J. Descamps, *J. Phys. Radium* 16: 304, 1955.
3. L. Reimer and B. Lödding, *Scanning* 6: 128, 1984.
4. M. Gryzinski, *Phys. Rev. A* 138: 305, 1965.
5. C. J. Powell, *NBS Spec. Publ.* 460, 1975, 97.
6. R. M. Sternheimer, *Phys. Rev.* 145: 247, 1966.
7. T. S. Rao-Sahib and D. W. Wittry, *J. Appl. Phys.* 45: 5060, 1974.
8. K. D. Sevier, *At. Data. Nucl. Tables*, Vol. 24, No. 4, 1979, 323.
9. S. Horigushi, M. Suzuki, T. Kobayashi, H. Yoshino, and Y. Sakakibara, *Appl. Phys. Lett.* 39: 512, 1981.
10. K. Murata, S. Cvikevich, and J. D. Kuptsis, *IXCOM 10*, 1983, C2-13.
11. J. L. Pouchou, private communication.
12. W. Reuter, J. D. Kuptsis, A. Lurio, and D. F. Kyser, *J. Phys. D* 11: 2633, 1978.
13. G. A. Hutchins, *Characterization of Solid Surfaces*, New York: Plenum Press, 1974, 441.
14. C. R. Worthington and S. G. Tomlin, *Proc. Phys. Soc.* A69: 401, 1956.
15. G. F. Bastin, private communication.
16. P. Willich and D. Obertop, *Surf. Int. Anal.* 13: 20, 1988.
17. P. Karduck, N. Ammann, H. G. Esser, and J. Winter, *Fresenius Z. Chem.* (in press).
18. J. L. Pouchou and F. Pichoir, *Rech. Aerosp.* 5: 47, 1984.

AUTOMATED MINERAL ANALYSES IN TASK8

W. F. Chambers, A. A. Chodos, and R. C. Hagan

TASK8 was designed as an electron microprobe control program with maximum flexibility and versatility, lending itself to a wide variety of applications.¹ One of the quantitative analysis routines available under TASK8 is a Bence-Albee program, BA85, capable of analyzing up to 45 oxides,² and normally used in the microprobe laboratories of the Sandia and Los Alamos National Laboratories for geologic analyses. While using TASK8 and BA85, we decided to incorporate the capability of using subroutines which perform specific calculations for nearly any type of mineral phase that might be analyzed in the laboratory. This minimizes the need for post-processing of the data to perform such calculations as element ratios or end-member or formula proportions. It also allows real time assessment of each data point.

The use of unique "mineral codes" to specify the list of elements to be measured and the type of calculation to perform on the results was first used in the microprobe laboratory at the California Institute of Technology to optimize the analysis of mineral phases.³ A similar approach was used to create files that are matrices of mineral codes for TASK8 that can be called via three letter codes. Each mineral code specifies the number and identity of the significant elements to be analyzed for in a particular mineral type, the standards to be used, and constants such as the number of oxygen atoms and the number of cations in the mineral formula. An end-member subroutine tailored for that particular mineral type can also be called by the mineral code.

The strength of this method is the versatility that it provides in creating mineral codes. Three files are used to create mineral codes: an alpha table, the "mineral code" matrix (MCM), and the TASK8 elemental table. The alpha table has $\phi(\rho z)$ calculated alpha factors for 90 compounds, including nearly every component found in minerals. Several of the table entries are for different valence states of common elements (e.g., both FeO and Fe₂O₃ are represented although only one would be used for any one analysis). The MCM is in an essay-to-edit file that assigns a three-letter mnemonic that identifies the Chemical Instrumentation Research Division 1821, Sandia National Laboratories, Albuquerque, NM 87185. He is now in the Repository Performance Assessments Division 6312. A. A. Chodos is at the Geological and Planetary Sciences Division, California Institute of Technology, Pasadena, CA 91125. R. C. Hagan is at the Earth and Environmental Sciences Division, Los Alamos National Laboratory, Los Alamos, NM 87544. This work was supported by the U.S. Department of Energy under Contracts DE-AC04-76DP00789 and W-7405-ENG-36.

the mineral and defines the compounds, the elemental references with their standards, the stoichiometry, and the number of oxygens and cations. Flags are set in the MCM to indicate if any element is present in a fixed concentration or is to be calculated by difference and to indicate which end-member subroutine should be associated with each mnemonic. Up to 25 mineral codes can be defined in a single MCM file and up to 200 MCMs are permitted in the TASK8 system. Tables 1 and 2 present summaries of MCM entries for a feldspar and a zeolite. Note that Fe is analyzed as FeO in FEL but as Fe₂O₃ in ZEO, and the two systems use different references. As shown in Table 3, the TASK8 element table associates elements with calibration data collected from standards and provides necessary data collection information (e.g., analysis crystal and spectrometer, peak and background locations, detector bias, maximum counting time, and analysis priority). The CF column in the element table relates the intensity collected from the standard to that which would have been collected from a pure oxide of the element in question.

Having the end-member calculation printed at the time of the analysis permits an evaluation of the quality of the analysis by the geochemist in a real-time sense. A geochemist is usually studying a suite of samples with a particular goal in mind, for example the effects of magma mixing on crystallite growth. Often only a few of the parameters printed from the end-member calculation will be pertinent to the particular problem under study; however, having extra parameters is not a burden. The ease of addition of new criteria to the end-member calculations means that as new problems are encountered additional evaluation parameters are included. Our philosophy has been to add to the existing criteria whenever a geochemist requires a new piece of information but to leave all the previous information available.

To perform an analysis, the quantitative routine is initiated from TASK8 after an element table has been loaded and the references are calibrated. The routine requests the numbers of the alpha table and MCM that are to be used. Once they are loaded, entering the mnemonic for a mineral code will cause the machine to perform a full quantitative analysis of the selected point and will use this information to perform an end-member calculation. Acceptable analyses are stored to disk and may be simultaneously output to a database on a separate computer. Analysis points can be selected interactively via a joystick or preselected and entered in a points table. If points are preselected, any available mineral

code may be independently associated with each point when it is set. The system permits over 20 000 preselected points.

Representative quantitative analyses and end-member calculation using the FEL and ZEO codes are presented in Tables 4 and 5. The "Beta" factor is the correction factor applied to the measured k-ratio. MDL is the minimum detection limit of the oxide based on counting statistics for the experimental conditions utilized. To date, the 21 end-member subroutines shown in Table 6 have been incorporated in the TASK8 system. The associated documentation describes in detail the workings of each subroutine and gives procedures both for modifying existing subroutines and writing new ones.³

References

1. W. F. Chambers and J. H. Doyle, *SANDIA TASK8, Version C: A Subroutined Electron Microprobe Automation System*, Sandia Report SAND90-1703, 1990.
2. W. F. Chambers, *BA85: A Bence-Albee Oxide Analysis Routine with Mineral Code Capabilities*, Sandia Report SAND90-1702, 1990.
3. A. A. Chodos et al., "Optimization of computer-controlled quantitative analysis of minerals," *Proc. Eighth National Conference on Electron Probe Analysis*, 1973, 45.

TABLE 1.--Feldspar (FEL) entry for mineral code matrix.

Code	1 FEL	Use end-member subroutine # 1. Use 8 Oxygens and 5 Catatoms for stoichiometry. There are 9 entries for this code. 0 of these are fixed. None are by difference.
The oxides and their references are:		
SiO2	uses ref SI1	TiO2 uses ref TI1
Al2O3	uses ref AL1	FeO uses ref FE1
MgO	uses ref MG1	CaO uses ref CA1
BaO	uses ref BA1	Na2O uses ref NA1
K2O	uses ref K1	SrO uses ref SR2

TABLE 2.--Zeolite (ZEO) entry for mineral code matrix.

Code	20 ZEO	Use end-member subroutine # 20. Use 36 Oxygens and 10 Catatoms for stoichiometry. There are 11 entries for this code. 0 of these are fixed. One is by difference. The oxides and their references are:
SiO2	uses ref SI1	TiO2 uses ref TI1
Al2O3	uses ref AL1	Fe2O3 uses ref FE2
MnO	uses ref MN1	MgO uses ref MG1
CaO	uses ref CA1	Na2O uses ref NA1
K2O	uses ref K1	BaO uses ref BA1
H2O	by diff.	

TABLE 3.--Selected element table items relating reference names to standards and collection parameters

EL	Sp	Xtal	Pri	Position	Bkg	Offsets	KV	Max time	Bias	Standard-intensity	CF	STD
NA1	2	TAP	1	0.46357	0.013	0.013	15	20	1249	12.69 +- 0.7%	0.609	FEL1
SI1	2	TAP	0	0.27745	0.022	0.022	15	20	1198	299.85 +- 0.3%	0.588	FEL2
CA1	4	PET	0	0.38370	0.018	0.018	15	20	1867	91.79 +- 0.3%	0.178	FEL6
BA1	4	PET	0	0.31742	0.015	0.015	15	20	1844	152.77 +- 0.5%	0.581	BAR1
FE1	3	LIF	0	0.48099	0.018	0.018	15	30	1842	19.21 +- 0.5%	0.137	OP14
FE2	3	LIF	0	0.48098	0.018	0.018	15	30	1842	128.33 +- 0.5%	1.000	HEMA
TI1	3	LIF	0	0.68304	0.018	0.018	15	30	1842	53.63 +- 0.3%	1.000	RUT1

TABLE 4.--Results of typical FEL code analysis.

Point # 1	MAS Demo		20-Feb-90		9:23 AM						
BA8, File # 2	X= 35.454		Y= 36.573		FEL						
Refs:	SI1	TI1	AL1	FE1	MG1	CA1	BA1	NA1	K1	SR2	
Oxide	K-ratio	Beta	MDL	Norm'd	Calc'd Wt%	Stoic: (8 Ox)			(5 Cat)		
SiO2	0.5754	1.1285	0.048	65.33	64.94 +- 0.38	SI-	2.9134	2.9045			
TiO2	0.0006	1.0932	0.084	0.06	0.06 +- 0.04	TI-	0.0021	0.0021			
Al2O3	0.1922	1.0605	0.038	20.51	20.39 +- 0.14	AL-	1.0781	1.0748			
FeO	0.0013	1.1158	0.077	0.14	0.14 +- 0.04	FE-	0.0053	0.0053			
MgO	0.0000	1.0000	0.038	0.00	0.00 +- 0.00	MG-	0.0000	0.0000			
CaO	0.0110	1.0748	0.028	1.19	1.18 +- 0.03	CA-	0.0568	0.0567			
BAO	0.0012	1.3019	0.145	0.15	0.15 +- 0.12	BA-	0.0026	0.0026			
Na2O	0.0665	1.3118	0.064	8.78	8.72 +- 0.15	NA-	0.7590	0.7566			
K2O	0.0283	1.1164	0.022	3.18	3.16 +- 0.05	K-	0.1810	0.1805			
SrO	0.0052	1.2258	0.115	0.64	0.64 +- 0.06	SR-	0.0166	0.0165			
Total=	0.8817					99.39					
K Fe3+ Si3 O8		0.000	K Al Si3 O8		18.112	Na Al Si3 O8		75.905			
Ba Al2 Si2 O8		0.274	Ca Al2 Si2 O8		5.148	FM Al2 Si2 O8		0.000			
Ca FM Si3 O8		0.544	() Si4 O8		0.018						
AB	75.918	AN	5.693	OR	18.115	CN	0.274				
Na + K + Ca + Ba + Sr (BASED ON 8 OXYGEN) = 1.016											
(Na + K + 2(Mg + Ca + Ba + Sr)) / (Al + Fe) = 1.008											

TABLE 5.--Results of typical ZEO code analysis.

Point # 2	MAS Demo		20-Feb-90		9:27 AM							
BA8, File # 2		X= 12.752		Y= 12.388		ZEO						
Refs:	SI1	TI1	AL1	FE2	MN1	MG1	CA1	NA1	K1	BA1	4 Iterations	
Oxide	K-ratio	Beta	MDL	Norm'd	Calc'd Wt%			Stoic: (36 Ox)		(10 Cat)		
SiO2	0.4743	1.1682	0.038	55.41	55.41	+-	0.39	SI-	12.2299	5.1341		
TiO2	0.0000	1.0000	0.064	0.00	0.00	+-	0.00	TI-	0.0000	0.0000		
Al2O3	0.1995	1.1059	0.030	22.06	22.06	+-	0.16	AL-	5.7390	2.4092		
Fe2O3	0.0002	1.1145	0.061	0.02	0.02	+-	0.03	FE-	0.0036	0.0015		
MnO	0.0002	1.1463	0.049	0.02	0.02	+-	0.02	MN-	0.0038	0.0015		
MgO	0.0000	1.0000	0.026	0.00	0.00	+-	0.00	MG-	0.0000	0.0000		
CaO	0.0000	1.0000	0.021	0.00	0.00	+-	0.00	CA-	0.0000	0.0000		
Na2O	0.1047	1.3047	0.047	13.66	13.66	+-	0.20	NA-	5.8444	2.4535		
K2O	0.0000	1.0000	0.014	0.00	0.00	+-	0.00	K-	0.0000	0.0000		
BAO	0.0000	1.0000	0.118	0.00	0.00	+-	0.00	BA-	0.0000	0.0000		
H2O				8.88	8.88	(Diff)		H	12.9945	5.4550		
Total=	0.7789					100.00						
Si + Ti + Al + Fe3+ 17.4725 Ti + Al + Fe3+ 5.7426 Mg + Ca + Mn + Ba + Na + K 5.8482												
Ti, Fe, Mn Omitted: Al/Na + K +2*(Ca + Mg + Ba) 0.9819 Si + Al 17.9680 Si/Al 2.13101												

TABLE 6.--End-member subroutines provided with BA85.

MINERAL	SUB	FORMULA	# Ox	# Cat	Elements
Feldspar	1	(Na,K,Ca) Si ₃ O ₈	16		Na Mg Al Si K Ca Sr Fe Ba
Feldspar	101	(1-oxygen norm) (Na,K,Ca) Si ₃ O ₈	16		Na Mg Al Si K Ca Sr Fe Ba
Pyroxene	2	(Fe,Mg,Ca) ₂ Si ₂ O ₆		4	Na Mg Al Si Ca Ti Cr Mn Fe
Olivine	3	(Mg,Fe) ₂ SiO ₄		3	Mg Al Si Ca Ti Cr Mn Fe Ni
Garnet	4	(Mg,Ca,Fe) ₃ Al ₂ (SiO ₄) ₃		8	Mg Al Si Ca Ti Cr Mn Fe
Opaque	5	(Fe,Mg) Al ₂ O ₄		2	Mg Al Si Ti Cr Mn Fe Zr
Biotite - Muscovite	6	K(Fe,Mg) ₃ (Al,Fe)Si ₃ O ₁₀ (OH,F) ₂			Mg Al Si Ti Cr Mn Fe Zr
Sphene	7	CaTiSiO ₅		3	F Mg Al Si Ca Ti Mn Fe Ce
Amphibole	8	(Ca,Na) ₂₋₃ (Mg,Fe ₂₊ ,Fe ₃₊ ,Al) ₅ (Al,Si) ₈ O ₂₂ (OH) ₂		15	F Na Mg Al Si Cl K Ca Ti Cr Mn Fe
Kyanite - Sillimanite - Andalusite	9	Al ₂ SiO ₅		3	F Na Mg Al Si Cl K Ca Ti Mn Fe
Stilpnomelane	10	Mg ₂ (Fe,Mn) ₆ Al ₂ Si ₁₂ O ₃₀ (OH) ₁₀		15	F Na Mg Al Si Cl K Ca Ti Mn Fe Ba
Carbonate	11	none			C Na Mg Ca Mn Fe Ba Sr
Apatite	12	Ca ₅ (PO ₄) ₃ (F,Cl,OH)			F Na Mg Al Si P Cl Ca Fe Ce
Whitlockite	12	Ca ₃ P ₂ O ₈			F Na Mg Al Si P Cl Ca Fe Ce
Magnetite	13				Mg Al Si Ti Cr Mn Fe Zr
Glass	14	none			Na Mg Al Si P S K Ca Ti Cr Mn Fe Ni Zr Ba
Cordierite	15	Mg ₂ Al ₄ Si ₅ O ₁₈		11	Na Mg Al Si K Ca Ti Mn Fe
Chlorite	16	(Mg,Fe,Al) ₆ (Al,Si) ₄ O ₁₀ (OH) ₈		10	F Mg Al Si Cl Ca Ti Mn Fe
Chloritoid	17	(Fe,Mn) ₂ Al ₄ Si ₂ O ₁₀ (OH) ₄			F Mg Al Si Ca Ti Mn Fe
Staurolite	17	(Fe,Mg,Zn) ₂ Al Si ₄ O ₂₃ (OH)			F Ng Al Si Ca Ti Mn Fe
Hematite	18				Mg Al Si Ti Cr Mn Fe Zr
Epidote & Clinozoisite	19	Ca ₂ (Al,Fe) ₃ Si ₃ O ₁₂ (OH)		13	F Mg Al Si Ca Ti Mn Fe Ce
Zeolite	20			36	Na Mg Al Si K Ca Ti Mn Fe Ba

Unless otherwise mentioned, all norms are to 1 catatom.

COMPUTER PROGRAMS FOR THE CALCULATION OF X-RAY INTENSITIES EMITTED BY ELEMENTS IN MULTILAYER STRUCTURES

G. F. Bastin, H. J. M. Heijligers, and J. M. Dijkstra

Almost immediately after the introduction of the first electron probe microanalyzer by Castaing¹ it was realized that the technique would be eminently suited to the analysis of thin films and the determination of concentration profiles in depth. The basic requirement for this specific application of the technique is that an accurate knowledge is available about the x-ray production as a function of depth in the specimen, a knowledge that is usually expressed in terms of so-called $\phi(\rho z)$ curves (ϕ is the number of photons and ρz is the product of density and linear depth in the specimen). Unfortunately, it has taken up to the beginning of the 1980s before a number of $\phi(\rho z)$ models^{2,3} became available on which a successful thin film approach could be based. Our own bulk matrix correction program "PROZA",^{4,5} with its proven excellent performance for a wide variety of applications (e.g., ultralight-element analysis and extremes in operating conditions) has been used as the basis for the development of the thin-film software package discussed here. The PROZA bulk-correction program is based on a combination of our own modifications of the surface-centered Gaussian $\phi(\rho z)$ approach, originally introduced by Packwood and Brown,³ and the atomic-number correction of Pouchou and Pichoir.⁶ Like in the Pouchou and Pichoir model, this approach guarantees that the integral of $\phi(\rho z)$ has at all times the value dictated by the atomic-number correction and that the $\phi(\rho z)$ curve displays the proper distribution. Contrary to the conventional "ZAF" approaches, this method makes it possible not only to integrate the $\phi(\rho z)$ curve between 0 and infinity (for bulk correction) but also between distinct limits, which is essential for thin-film applications. However, it is clear that for the extension of a bulk matrix correction program toward thin-film applications it is necessary to take the film/substrate interactions into account, and this aspect will now be discussed.

Basic Procedures

The surface-centered Gaussian $\phi(\rho z)$ approach is based on the use of four parameters, α , β , γ and $\phi(0)$ ³ with which the $\phi(\rho z)$ curves are modeled. For an element in a film on a substrate one must determine how the four Gaussian parameters vary with film thickness and the nature of the substrate. In dealing with this problem the following strategy (for a single-

film case) has been used.

- a. The ρz scale in each $\phi(\rho z)$ curve is continuous across the interface.
- b. The $\phi(\rho z)$ curves of the elements in the film are affected by the nature of the substrate; the curves for the substrate elements are not influenced by the presence of the film.
- c. The Gaussian parameters for a particular element in the film vary between two extremes typical for either extremely thin or extremely thick layers. In the latter case the bulk parameters P_b will have to be approached; in the former case the parameters can be approximated if one considers the element as being solved in the substrate P_s . In all intermediate cases the parameters will have to vary in a smooth and consistent way between these extremes. For the single-film case this goal has been accomplished by the use of simple exponential functions of the general form

$$P = P_b + (P_s - P_b)\exp(-ax^n)$$

in which the main parameter $x = 0.5\alpha\rho T \times 10^{-6}$ and T is the layer thickness in ρz units of $\mu\text{g}/\text{cm}^2$. The exponent n is unity for β and equal to 2 for the others. The constant a has the value of 6, 3, 8, or 10 for the parameters α , β , γ , and $\phi(0)$, respectively. This empirical weighting procedure insures a smooth variation of the parameters and does justice to the fact that the backscattering of the substrate has a different effect on the various film parameters; the shortest distance of interaction is on $\phi(0)$.

For the case of a multilayer system a more complex procedure has to be followed. One obtains the composed parameters for each element by assigning specific weights to the parameters in each of the films and in the substrate, depending on the distance from the particular film examined, and finally integrating these contributions according to a fourth-degree polynomial, not unlike in the procedure followed by Pouchou and Pichoir.⁷ Once the four Gaussian parameters for each element in a particular film are available the generated and emitted intensities are calculated by partial integration⁸ of the $\phi(\rho z)$ curve.

Basic Structure of the Programs

The software package developed consists of two programs: one for a single film either on a substrate or unsupported ("TFA"), the other for up to 7 films ("MLA"). Basically, each program contains four options.

With the first option it is possible to calculate the emitted intensities from a layer

The authors are with the Laboratory for Solid State Chemistry and Materials Science, University of Technology, P. O. Box 513, NL-5600 MB Eindhoven, The Netherlands. "PROZA" is a trademark of Tracor Northern, USA.

system with given thicknesses and compositions as a function of accelerating voltage. This option is very important to exploratory calculations to find the highest sensitivity of the system and determine the best measuring strategy.

In the second option the voltage is fixed and the calculations are performed as a function of layer thickness of (one of) the layer(s).

The third option enables the determination of layer thicknesses (for supposedly known compositions) from measured k-ratios at a fixed voltage in a single iterative and fully automatic way.

The fourth option provides the possibility of establishing both thicknesses as well as compositions from measured k-ratios at a fixed voltage in a double iterative and fully automatic way, with the obvious restriction that each element occurs only once in the system.

Performance of the Programs

The programs were extensively tested on the available thin-film data in literature and found to perform highly satisfactorily, as demonstrated in Fig. 1 on a number of measurements by Reuter et al.⁹ on two Pt films deposited on Au and Si. The agreement between the calculations (solid curves) and the measurements is excellent, which shows that the effect of the nature of the substrate is properly accounted for. The results of some of our own measurements on two Ti films on Si are shown in Fig. 2. Again the agreement between calculations and measurements is excellent, this time not only for the film but also for the substrate elements. Recently our software has been successfully used for the determination of concentration profiles in 1000 and 2500 Å-thick $\text{YBa}_2\text{Cu}_3\text{O}_{7-x}$ films on SrTiO_3 substrates and the determination of N, O, and Si concentration profiles in implanted Si specimens (doses 10^{17} – 10^{18} at/cm²). In the latter cases one can find the concentration profiles in an interactive way by simulating the geometry in 5–7 sublayers of the same compound with different thicknesses and compositions and comparing the calculations with the measurements, which must be available over the widest possible range in accelerating voltages.

In summary, we believe that thin-film analysis with a scanning electron microscope or microprobe is an elegant and powerful technique for nondestructive (sub)surface analysis that can now be carried out with relatively cheap and widely available equipment. Once the necessary software is commercially available the technique certainly deserves a widespread application.

References

1. R. Castaing, Application des sondes électroniques à une méthode d'analyse ponctuelle chimique et cristallographique, Ph.D. thesis, University of Paris, 1952.
2. J. L. Pouchou and F. Pichoir, "A new model

for quantitative x-ray microanalysis: Part I. Application to the analysis of homogeneous samples," *Réch. Aéropat.* 1984-83, 13-37.

3. R. H. Packwood and J. D. Brown, "A Gaussian expression to describe $\phi(\rho z)$ curves for quantitative electron probe microanalysis," *X-ray Spec.* 10: 138-146, 1981.

4. G. F. Bastin and H. J. M. Heijligers, "Quantitative electron probe microanalysis of ultra-light elements (boron-oxygen)," *Proc. NBS Workshop*, August 1988, NBS Spec. Publ. (in press).

5. G. F. Bastin and H. J. M. Heijligers, "Quantitative electron probe microanalysis of ultra-light elements (boron-oxygen)," *Proc. First Workshop of European Microbeam Analysis Society*, Antwerp, 1989, 81. (To be published in *Scanning*.)

6. J. L. Pouchou and F. Pichoir, "Basic expression of 'PAP' computation for quantitative EPMA," *Proc. 11th ICXOM*, London, Ont., 1987, 249-253.

7. J. L. Pouchou and F. Pichoir, "A new model for quantitative x-ray microanalysis," Part II. Application to in-depth analysis of heterogeneous samples," *Réch. Aéropat.*, 1984-85, 47-65.

8. R. H. Packwood and K. S. Milliken, "A general equation for predicting x-ray intensities from stratified samples in the electron microprobe," *CANMET Report*, PMRL 85-25 (TR), 1985.

9. W. Reuter, J. D. Kuptsis, A. Lurio, and D. F. Kyser, *J. Phys.* D11: 2633, 1978.

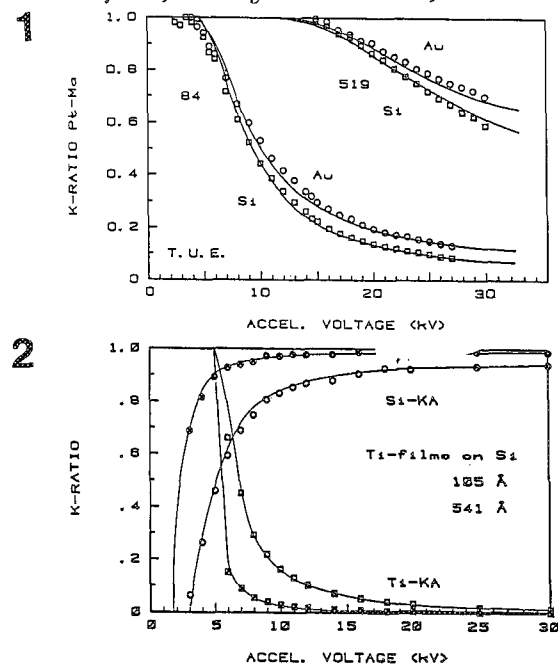


FIG. 1.--Agreement between predictions of our program and experimental data of Reuter et al. for two Pt films of 84 and 519 $\mu\text{g}/\text{cm}^2$ (392 and 2420 Å), once on Au and once on Si. X-ray take-off angle 52.5°.

FIG. 2.--Agreement between predictions of our program and our own measurements on two Ti films of 4.75 and 24.35 $\mu\text{g}/\text{cm}^2$ (105 and 541 Å) on Si. X-ray take-off angle 40°.

MONTE CARLO CALCULATIONS OF THE SPATIAL RESOLUTION IN X-RAY MICROANALYSIS OF THIN OVERLAYERS IN THE ENERGY RANGE 20-100keV

A. G. Nassiopoulos and Evangelos Valamontes

Monte Carlo simulations have been used in order to calculate the lateral extent of the x-ray signal in x-ray microanalysis of thin overlayers. Various primary beam energies in the range 20-100 keV and various film thicknesses (400-5000 Å) have been used for incident beam sizes of $\sigma_0 = 40$ Å and $\sigma_0 = 1000$ Å. The case of a Cu film on an Au substrate has been considered; the analyzed x-ray line was Cu K α . In this case, at high primary beam energies, the total enhancement signal due to backscattering and characteristic or continuous x rays from the substrate is larger than the primary-beam-induced signal. However, when the film thickness is small, this signal is distributed over a large area and contributes to the total signal as a low background superimposed on the sharp change of the incident-beam-induced signal. The conditions for which this signal must be taken into account in the spatial resolution are discussed below.

Total Enhancement Factor and Spatial Resolution

Monte Carlo simulations have been used for the calculation of the enhancement factor due to backscattering, characteristic, and continuous x rays from the substrate in x-ray microanalysis of thin overlayers. Results published elsewhere¹⁻³ show that this signal enhancement can rise to values greater than a 100% of the primary beam-induced signal in cases where the substrate is of a high-Z material and the analysis is made at high primary beam energies ($E_0 > 30$ keV).

The most important enhancement signal is due to backscattering, but the contribution of characteristic and continuous x rays may not be negligible in some cases in the signal quantification. The contribution of characteristic x rays may attain 16-18% of the primary-beam-induced signal and the contribution of continuous x rays 12-14%, at 40 keV for substrates of a high-Z material.¹⁻³ These results are confirmed experimentally by a comparison of the x-ray signal from a thin unsupported film to that from a film of the same material supported by a bulk substrate. Some experimental results for 400Å-thick overlayers are found in the literature.^{1,2,4}

Figures 1 and 2 show further experimental results obtained from a series of Cu films on various substrates for film thicknesses of 400 and 1500 Å. Full lines indicate results from Monte

Carlo calculations (see Ref. 1 for details on the Monte Carlo program) and the points show the experimental results. The agreement between calculations and experimental results is quite good in all cases within the limits of experimental and calculation errors.

But although the enhancement of the primary-beam-induced signal due to the three factors enumerated above is very important, its influence on the spatial resolution depends strongly on film thickness. The two extreme situations are the case of a bulk material, where the spatial resolution is principally governed by the diffusion of the primary beam into the sample and is in the micron range; and the case of a very thin overlayer (some tens or hundreds of Angstroms), where the situation is analogous to that of Auger electron spectroscopy. In the latter case, it is now well established⁵⁻⁹ that the spatial resolution is governed by the lateral extent of the primary-beam-induced signal.

A general consideration of the problem of the spatial resolution in x-ray microanalysis of thin coatings has been made in a recent paper by Cazaux et al.⁴ The radial distribution of the x-ray emission from the sample (point spread function) has been considered to be the sum of two Gaussian functions, one related to the primary-beam-induced signal and the other related to the contribution of backscattered electrons. Assumptions have been made concerning the standard deviations σ_p and σ_R of these two functions.

In this paper, the radial distribution of the total x-ray signal is calculated by Monte Carlo simulations for primary beam energies ranging from 20 to 100 keV at normal incidence and various film thicknesses. All factors contributing to the x-ray signal are considered: primary electron beam, backscattered electrons, and characteristic and continuous x rays from the substrate.

The calculated point spread function is then divided into two terms. The first describes the primary-beam contribution, the second the sum of the other three contributions. The calculated results show that the first function is easily approximated by a Gaussian curve. The second function shows a maximum at a point different from zero on the R axis. It may thus be approximated by a Gaussian curve at radial distances greater than the distance to this point.

Results and Discussion

The Monte Carlo program has been described in detail elsewhere.¹ It is based on a general formalism proposed by Love et al.¹⁰

The primary beam is considered to enter the

The authors are at the Microelectronics Institute, NCSR "Demokritos," P.O. Box 60228, 153 10 Aghia Paraskevi, Attikis, Athens, Greece.

sample at normal incidence and the detection angle is 25.5° from the surface of the sample. The radial distribution of the analyzed x-ray signal is calculated by consideration of the escape position of each photon. Intervals of 20 Å are used in the R axis.

The radial distribution of the total x-ray signal is first calculated and the contribution of the enhancement signal is obtained by subtraction of the primary-beam-induced signal from the total signal. The primary-beam-induced signal is easily obtained by calculation of the signal from a thin unsupported film. This approximation is good when backscattering within the film is negligible. It is valid for the film thicknesses and primary beam energies used.

Figure 3 shows the radial distribution of the primary-beam-induced signal I_p for the case of a Cu film (thickness 400 Å) on an Au substrate at various primary beam energies. The incident beam, at normal incidence, was taken to have a Gaussian distribution with $\sigma_0 = 40$ Å. The inset of Fig. 3 shows the radial distribution of the primary-beam-induced signal I_p of the same film for an incident beam of a larger spot size ($\sigma_0 = 1000$ Å). In the first case (when σ_0 is small), σ_p is of the order of $2\sigma_0$, but it approaches σ_0 in the second case ($\sigma_p = 1.3-1.5\sigma_0$; see Table 1).

The lateral extent of the enhancement signal is, in the above case (film thickness 400 Å), very large compared with that of the primary-beam-induced signal. It is also decalated with respect to the point of incidence of the primary beam. Its maximum intensity for all primary beam energies is smaller than 5% of the maximum intensity of the primary-beam-induced signal. This result is illustrated in Fig. 4, where I_p is the primary-beam-induced signal and $I(R + U + V)$ is the sum of the x-ray signals induced by (a) backscattering ($R = I_b/I_p$, where I_b is the x-ray signal from backscattered electrons), (b) by characteristic x rays ($U = I_{ch}/I_p$), and (c) by continuous x rays ($V = I_{con}/I_p$) from the bulk. The same arbitrary units are used for I_p and $I(R + U + V)$. The inset of Fig. 4 shows the radial distribution of $I(R + U + V)$ for various primary energies in the range of 20-100 keV. This signal is approximated by a Gaussian curve after the maximum in intensity and the standard deviation σ_E of this Gaussian is calculated from this approximate Gaussian curve ($\text{FWHM} = 1.66\sigma_E$). On the other hand, the maximum intensity $I(R + U + V)_{\text{max}}$ is decreased with respect to $I_{p\text{max}}$ when E_0 is increased.

When the film thickness is increased (from $t = 400$ Å to $t = 2000$ Å and $t = 5000$ Å) the lateral extent of the signal is increased (σ_p becomes greater than $10\sigma_0$; a smaller increase is observed in σ_E). Also, the ratio $I(R + U + V)/I_{p\text{max}}$ increases rapidly with the increase in the film thickness (Table 2) and becomes important for thicker overlayers, especially for small primary-beam energies. These results are illustrated in Figs. 5 and 6. The case of a bulk material is shown in Fig. 7 for

comparison. The spatial resolution in this case is mainly governed by the lateral extent of the enhancement signal; σ_E is in the range $\frac{1}{2}R_0$ to $\sigma_E > R_0$ depending on the primary-beam energy (Tables 1 and 2) and is approximately equal to the lateral extent of backscattered electrons.¹¹⁻¹⁴

Conclusion

The radial distribution of the x-ray signal in the case of thin overlayers (Cu coatings on an Au substrate) has been calculated by Monte Carlo simulations for primary-beam energies in the range 20-100 keV for various film thicknesses. All factors contributing to the x-ray signal creation are taken into account. A point spread function equal to the sum of two Gaussian curves is considered; the first describes the primary-beam-induced signal, the second the other three enhancement factors (backscattering and characteristic and continuous x-rays from the bulk). The standard deviations of these two Gaussian curves have been calculated for energies in the range of 20-100 keV for film thicknesses 400, 2000, and 5000 Å.

It is shown that for a film thickness $t = 400$ Å the enhancement signal creates a low background superimposed on the primary-beam-induced signal and does not affect the spatial resolution. This result is analogous to that obtained in Auger electron spectroscopy. The same behavior is found for film thicknesses $t = 2000$ Å and 5000 Å for primary-beam energies greater than 50 keV. For smaller energies the enhancement signal maximum becomes important.

The use of high primary-beam energies (50-100 keV) is thus more advantageous than energies of 10-20 keV. Focusing of the primary beam is easier and the spatial resolution is not limited by backscattering and x rays from the bulk, even for film thicknesses of some thousands of Ångströms.

References

1. A. G. Nassiopoulou and E. Valamontes, *Surf. Interface Anal.* 15: 405, 1990.
2. J. Cazaux, O. Jbara, A. G. Nassiopoulou, and E. Valamontes, *12th ICXOM*, 1989, 201.
3. A. G. Nassiopoulou and E. Valamontes, *Proc. III Balkan Congress on Electron Microscopy*, Athens, 1989, 188.
4. J. Cazaux, O. Jbara, and X. Thomas, *Surf. Interface Anal.* 15: 567, 1990.
5. J. Cazaux, *Surf. Science* 125: 335, 1983.
6. M. Tholomier, D. Dogmane, and E. Vicario, *J. Microsc. Spectrosc. Electr.* 13: 119, 1988.
7. M. M. El Gomati and M. Prutton, *Surf. Science* 72: 485, 1978.
8. J. Cazaux, *J. Microscopy*, 145(Pt3): 257, 1987.
9. J. Cazaux, J. Chazelas, M. N. Charasse, and J. P. Hirtz, *Ultramicroscopy* 25: 31, 1988.
10. G. Love, M. G. Cox, and V. D. Scott, *J. Phys.* D10: 7, 1977.
11. H. Niedrig, *Inst. Phys. Conf. Ser.* 93(1):

225, 1988 (paper presented at EUREM 88).
 12. A. E. Grun, *Z. Naturf.* 12A: 89, 1957.
 13. H. Seiler, *SEM I/1976*, 9.

14. *Proc. Electron Microscopy*, EUREM 84,
 Budapest, I: 563, 1984.

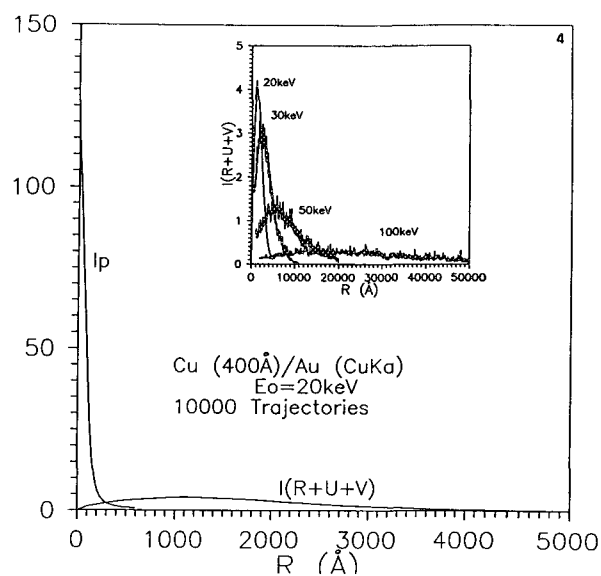
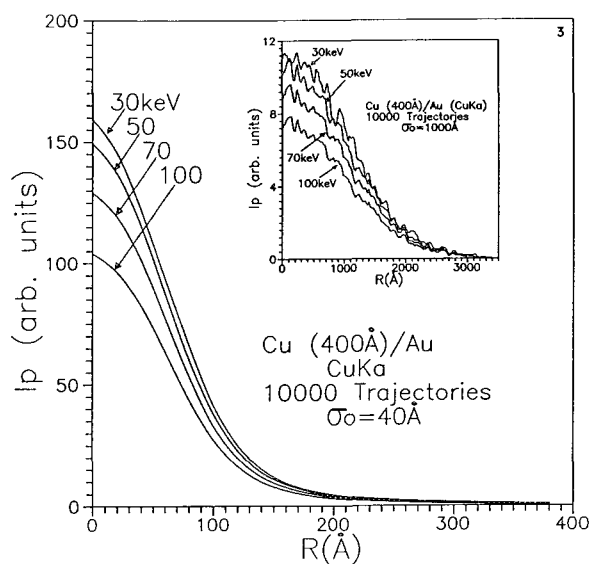
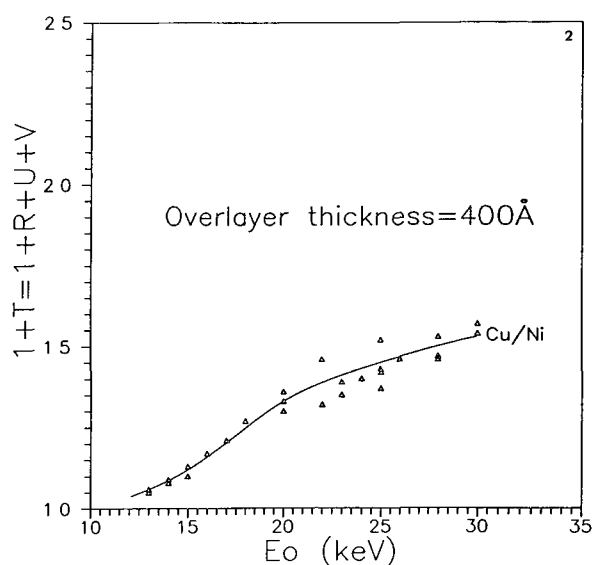
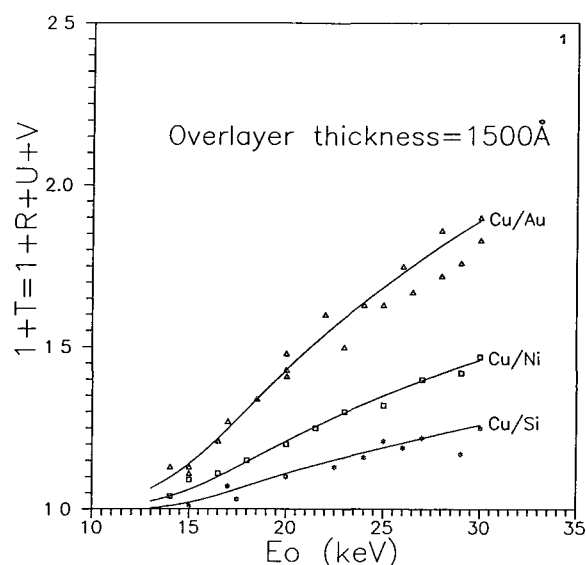


FIG. 1.--Total x-ray signal from Cu overlayer (1500 Å thick) on different substrates, normalized to primary-beam-induced signal (from a thin unsupported Cu film). T is the total enhancement of the signal due to backscattering ($R = I_b/I_p$, where I_b is backscattering-induced signal; I_p is primary-beam-induced signal), to characteristic x rays ($U = I_{ch}/I_p$), and to continuous x rays ($V = I_{co}/I_p$) from the substrate. Full lines, Monte Carlo results; points, experimental results, detection of Cu K α (Cu/Au) and (Cu/Si) or Cu K β (Cu/Ni).

FIG. 2.--Same as Fig. 1 for Cu layer, 400 Å thick.

FIG. 3.--Monte Carlo results of radial distribution of primary-beam-induced x-ray signal for Cu film (thickness 400 Å) on Au for various primary energies in 30-100 keV range. Primary electron beam, at normal incidence, is considered to be Gaussian distributed with $\sigma_0 = 40$ Å. Inset: Same as in main figure, for a Gaussian primary beam with $\sigma_0 = 1000$ Å.

FIG. 4.--Radial distribution of enhancement signal $I(R + U + V)$ compared to primary-beam-induced signal shown in same arbitrary units. Primary energy $E_0 = 20$ keV, $\sigma_0 = 40$ Å. Inset: Lateral extent of enhancement signal at various primary beam energies ($\sigma_0 = 40$ Å).

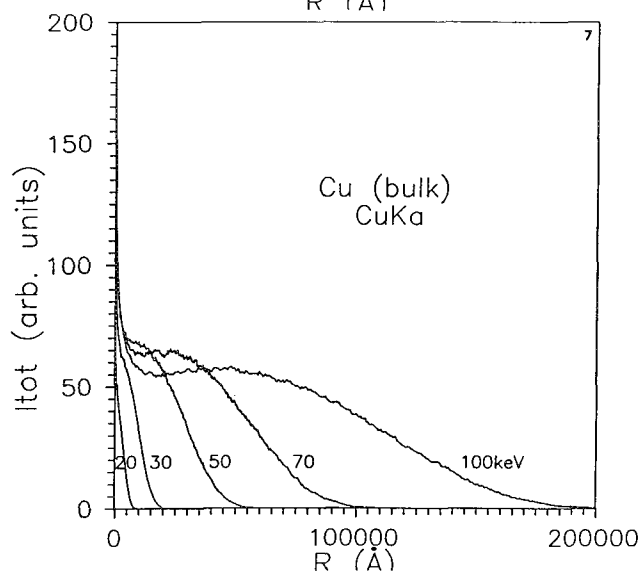
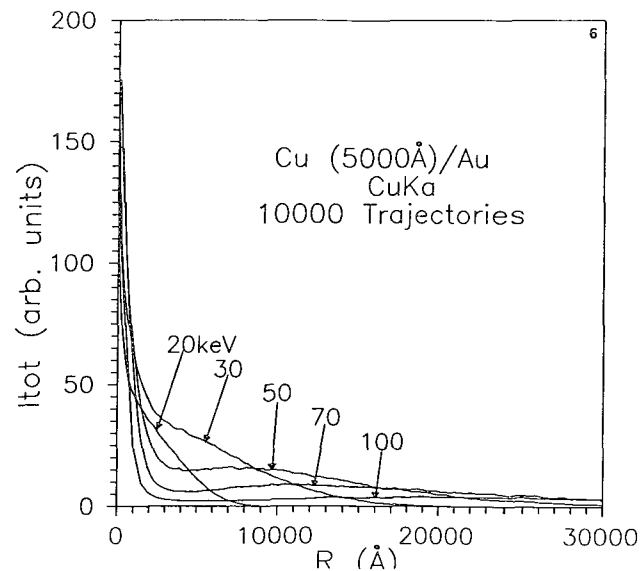
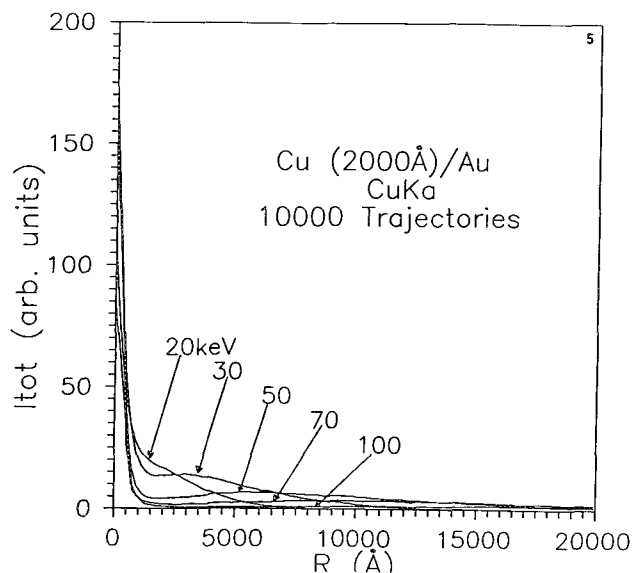


FIG. 5.--Radial distribution of total x-ray signal from Cu film (2000 Å thick) on Au at various primary-beam energies ($\sigma_0 = 40$ Å).

FIG. 6.--Same as in Fig. 5 for Cu film (5000 Å thick).

FIG. 7.--Radial distribution of total x-ray signal from bulk Cu material at various primary-beam energies in 20-100keV range ($\sigma_0 = 40$ Å).

TABLE 1

Thickness $t=400\text{Å}$ (Cu/Au)					
E_0 (keV)	R_e (μm) Au	$\sigma_0=40\text{Å}$			$\sigma_0=1000\text{Å}$
		σ_p (Å)	σ_E (μm)	$I(R+U+V)_{\text{max}}/I_{p\text{max}}$	σ_p (Å)
20	1.32	96	0.27	3.51%	1650
30	2.58	84	0.52	2.02%	1450
50	6.08	84	1.20	1.06%	1360
70	10.79	84	2.30	0.69%	1360
100	19.97	84	4.30	0.45%	1360

TABLE 2

Thickness $t=2000\text{Å}$ (Cu/Au) $\sigma_0=40\text{Å}$				Thickness $t=5000\text{Å}$ (Cu/Au) $\sigma_0=40\text{Å}$			Cu Bulk
E_0 (keV)	σ_p (Å)	σ_E (μm)	$I(R+U+V)_{\text{max}}/I_{p\text{max}}$	σ_p (Å)	σ_E (μm)	$I(R+U+V)_{\text{max}}/I_{p\text{max}}$	
20	520	0.57	16.39%	980	0.64	32.24%	0.44
30	480	1.00	9.13%	840	1.50	18.88%	1.20
50	450	2.40	4.08%	720	2.70	9.36%	3.55
70	420	3.80	2.45%	600	4.70	6.16%	6.26
100	420	7.20	1.85%	480	7.40	3.40%	12.65

A METHOD TO OVERCOME THE PROBLEM OF SMALL SAMPLE TILTS IN LIGHT-ELEMENT ELECTRON PROBE MICROANALYSIS

Andrew Mackenzie

The technique of Electron Probe Microanalysis (EPMA) is extremely useful in the rapidly advancing field of high-temperature superconductivity. Since the properties of the oxide superconductors depend strongly on the oxygen concentration, it is important to be able to measure oxygen as accurately as possible. It is particularly useful to know unambiguously the composition of small single crystals, which either grow with good smooth surfaces (for example, in the Y-Ba-Cu-O system) or can be easily cleaved (for example, in the Bi-Sr-Cu-O system) to provide excellent surface quality without polishing. The $\text{Bi}_{2+x}\text{Sr}_{2-x}\text{CuO}_{6+z}$ crystals are extremely soft and layer like, which makes polishing difficult; another advantage of cleaving is that the crystal need not be embedded in epoxy, and can thus be relatively easily removed from its mount for subsequent annealing treatments or other experiments. The disadvantage of mounting in this manner is the inevitable existence of small tilt angles, because the thin crystals bend a little when they are cleaved. The method outlined below was developed to overcome this problem for small tilts. Applying it to a wide range of specimens has shown that tilting is a problem even in conventionally mounted specimens, and that a significant improvement in data quality is often obtained by correction for the tilt.

The effect of a small tilt angle θ on the x-ray path length to the surface of the specimen is shown in Fig. 1. For small angle tilts of less than 3° the change in absorption is assumed to dominate the change in the distribution [commonly referred to as the $\phi(\rho z)$ function] describing the primary x-ray production. In the notation of Fig. 1, the increased path length in the case of a positive tilt is given by

$$\rho z^+ = \frac{\rho x}{\sin \psi} \left(1 + \frac{\sin \theta \cos \psi}{\sin (\psi - \theta)} \right)$$

where ρz^+ is the increased path length due to the tilt, $\rho z / \sin \psi$ is the path length at zero tilt, ψ is the x ray takeoff angle, and θ is the tilt angle. The expression for ρz^- is

$$\rho z^- = \frac{z}{\sin \psi} \left(1 - \frac{\sin \theta \cos \psi}{\sin (\psi + \theta)} \right)$$

Since the problem is one-dimensional for each spectrometer, defined by the plane containing the electron optic axis and the center of the

analyzing crystal, the idea is to calculate the ratio I_{\max}/I_{\min} expected for two sample orientations rotated by 180° . This calculation is made by use of the calculated path lengths of ρz^- and ρz^+ , respectively, in a program based on a good $\phi(\rho z)$ model (in this case based on the "PAP" model,¹ since these modern procedures have been shown to produce reliable absorption corrections for light-element analysis.^{2,3}

Figure 2 shows the I_{\max}/I_{\min} ratio vs θ for a sample of $\text{Bi}_{2+x}\text{Sr}_{2-x}\text{CuO}_{6+z}$ at 30 kV. As expected, the higher the mass absorption coefficients, the more severe the effect, although this relationship also depends on the parameters of the $\phi(\rho z)$ curve at the accelerating voltage concerned. Back calculation from I_{\max} to the intensity expected for zero tilt is performed once the angle θ is known. In fact, once this is done it is seen that simply averaging I_{\max} and I_{\min} gives negligible errors.

In a real experiment this procedure is dangerous, because there could be many reasons for measuring intensities that differ by more than counting statistics at the two orientations which would have nothing to do with sample tilting. These reasons could include surface roughness, spectrometer defocus, current drift or changes to the detection efficiency of the proportional counters. Calculation of the tilt angle permits important consistency checks to be made. For example, if the correct mass absorption coefficient is used, the angle measured at any point should remain constant as the accelerating voltage is changed, and the same angle can be checked by consideration of data taken from two different x-ray lines with the same spectrometer. Once the angle has been confirmed as genuine, the data can be safely averaged and should show improved consistency even in a sample where a variety of tilt angles are present.

Experimental measurements to demonstrate the usefulness of the technique were performed with a Cameca SX-50 microprobe. The 180° change in orientation was achieved by removing the specimen mounting block and rotating and replacing it. The center of the coordinate system was redefined carefully by realigning engraved crosshairs on the mounting block, using the light optics. This procedure allowed each analysis point to be relocated by a move to the negative of the original coordinates. A high-magnification electron image was used for realignment to an accuracy of $\pm 2 \mu\text{m}$. With practice, the whole operation took around 10 min for a run on 20 analysis points. The $K\alpha$ x-ray lines of O, Fe, Cu, and Y, the $L\alpha$ lines of Y and Sr, and the $M\alpha$ line of Bi were studied

Andrew Mackenzie is at the Cavendish Laboratory and Interdisciplinary Research Center in Superconductivity, Madingley Road, Cambridge, England. He acknowledges the help of Dr. S. Reed, Prof. L. M. Brown, and Dr. G. G. Lonzarich.

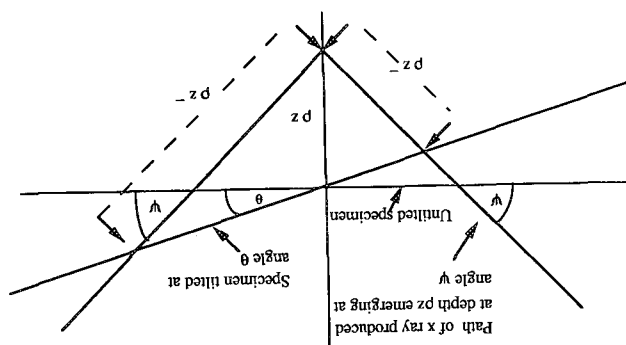


FIG. 1.--Geometry of path-length changes for tilted specimen.

in a range of samples, either cleaved superconducting $\text{Bi}_{2-x}\text{Sr}_{2-x}\text{CuO}_{6\pm z}$ crystals or polished specimens of Fe_2O_3 , Cu, Bi, Bi_2Se_3 , CuO, SrTiO_3 and YAG (yttrium aluminum garnet). Accelerating voltages between 10 and 40 kV were used, and a database of consistency checks such as those mentioned above was set up. Counting precisions were around 0.3%, and the current was stabilized to better than 0.1%. The spectrometers were not moved while peak data were taken, and a separate run was used for the backgrounds.

The results of over 40 consistency checks indicated that angles of less than 3° can be measured to a precision of 0.14° . More important, data that passed the angle consistency checks were consistent within any one sample to better than 1% for all x-ray lines including oxygen, and it is this figure, not the counting precision, that should be always used to estimate the real precision of the experimental data from homogeneous samples. The use of single crystals for all the oxide samples increased confidence that they were homogeneous. The figure of 1% compares very favorably to the single orientation measurements, where consistency for oxygen was as poor as 3% in polished samples and worse still in the small crystals.

Although the problem of surface tilts is most severe when light-element data are taken from unusually mounted specimens, it is by no means restricted to this situation. The angles measured in the course of this work were up to 2.5° in the crystals and, surprisingly, up to 2° even in polished samples. These 2° angles occurred at the edges, where rounding effects due to the polishing process were evident in a light microscope. Smaller angles of 0.5° were often measured and confirmed from the center of the samples, where none was suspected from the light optics. Figure 2 shows that even a 0.3° tilt angle affects Bi M α line (2.42 keV) data taken at 30 kV by $\sim 1\%$, so that the importance of dual orientation measurements is seen to have a far wider scope than just improving oxygen data from cleaved superconducting samples. In addition, one of the worst affected polished

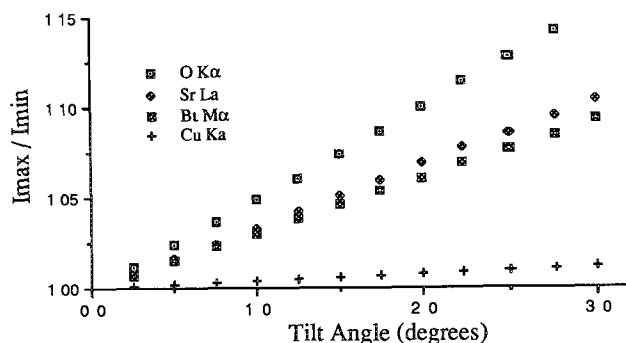


FIG. 2.-- I_{\max}/I_{\min} ratio vs tilt angle θ in $\text{Bi}_{2-x}\text{Sr}_{2-x}\text{CuO}_{6\pm z}$ at 30 kV.

samples (YAG) was commercially provided, showing that the problem is not restricted to deficiencies in the polishing process used in our laboratory.

Another advantage of the dual-orientation method of data taking is that even local tilts may be measured and corrected, whereas any angles measured by the light optics of a microprobe instrument are global to the whole sample. As long as the consistency checks described above are used, it is possible to verify that the local tilt angle that is measured is genuine.

In conclusion, the technique developed for measuring and correcting small angle specimen tilts has been shown to work well, and its use extends the range of sample mounting procedures that can be used to provide reliable raw data for microanalysis. In the case of light-element analysis especially an improvement is seen when dual orientation measurements are used on almost any type of specimen.

References

1. J. L. Pouchou and F. M. A. Pichoir, *Proc. IXXOM*, 1986, 249-253.
2. G. F. Bastin and H. J. M. Heijligers, *Microbeam Analysis--1989*, 207.
3. J. L. Pouchou and F. M. A. Pichoir, *Microbeam Analysis--1988*, 319.

CALIBRATION OF NIST MINERAL GLASS STANDARD K-411 AND THE CONCEPT OF A MODEL STANDARD IN QUANTITATIVE ELECTRON MICROPROBE ANALYSIS

S. V. Yang, J. Wagstaff, and G. McKay

The concept of a "model standard" is introduced in this study. A model standard has had its composition calibrated by the backward-ZAF-calculation method described by Yang and McKay.¹ The reported and the calibrated compositions of the NIST microanalytical mineral glass standard K-411 are listed in Table 1 for comparison. This study emphasizes methodology and concept rather than pursuing numerical precision.

Procedures

The National Institute of Standards and Technology (NIST, formerly NBS) offers a wide spectrum of high-quality analytical standards. For microanalytical standards, NIST mineral glass standards SRM470 (K-411 and K-412) "provide a highly homogeneous material at microscopic spatial resolution."² Other advantages of these NIST mineral glass standards are their availability and their stable compositions.³ At NASA Johnson Space Center, NIST mineral glass standard K-411 was evaluated along with several other local microprobe standards by the backward-ZAF-calculation method. These standards were not analyzed against a reference standard in the usual manner. Instead, our CAMECA MBX electron microprobe was used to collect standard data records (peak intensity in counts per second per nanoamp) for each element of the several different standards being evaluated. These peak intensity data for each standard record were then transformed to their respective pure elemental standard intensities by three different ZAF procedures (CAMECA ZAF,⁴ CAMECA PAP⁵, and DUST⁶). The resulting transformed pure elemental standard intensities for Si are plotted in Fig. 1 for comparison.

First, compare the NIST certified Si data for the K-411 (point A, Fig. 1) composition, of which the oxygen concentration is calculated stoichiometrically and the total Fe is reported as FeO, with the calculated pure element standard peak intensities as transformed from the standard data records. This comparison reveals an apparent undercorrection of Si by all three ZAF procedures. (In Fig. 1, data points plotted below the average line are considered to be relatively undercorrected.) Similar apparent undercorrections for the K-411 composition are associated with Ca and Mg data as well. Undercorrected standards trend to give systematically high analytical totals, and vice versa.

S. V. Yang and J. Wagstaff are with Lockheed Engineering and Science Co., 2400 NASA Rd. 1, C23, Houston, TX 77258; G. McKay is at the NASA Johnson Space Center (JSC), SN2, Houston, TX 77058.

Some of the major factors which can cause such errors are (1) inaccurately reported compositions, (2) ZAF correction errors, (3) instrumental errors, and (4) analytical errors.

We modified the stoichiometric oxygen data of K-411 to account for the extra O₂ in Fe₂O₃, based on the FeO/Fe₂O₃ weight ratio of 0.342.⁶ In addition, we incorporated an uncertified Mn value⁷ (see Table 1) into the backward-ZAF calculation. These modifications reduced but did not eliminate the undercorrection problem of Si in K-411 (see point B in Fig. 1 and Table 1).

In principle, a probe sample can be analyzed a number of independent times with several standards with the results of these analyses averaged to reduce the errors from the ZAF correction and from inaccurately reported standard compositions. Unfortunately, this procedure is tedious and impractical for routine analyses. An alternative and much more practical method is to adopt this backward-ZAF conversion procedure and calibrate the composition of the chosen standard by the amount it is off the standard average (e.g., point B to point C in Fig. 1). Table 1 shows the calibrated compositions of K-411 (C to E), in which the Si concentration was calibrated by 14 Si standards. Here we define the standard with the calibrated composition as a MODEL STANDARD. In reality, the composition of a model standard may not necessarily reflect its true composition. However, using a model standard is technically equivalent to performing a probe analysis with use of multiple standards for each individual element. Plots similar to Fig. 1 will help the analyst identify which probe standards that have their natural quantities closest to the qualities of a model standard.

Discussion

This study quantitatively demonstrates the fact that a small inaccuracy or ambiguity of the reported concentration value of a nonanalyzed element such as oxygen can affect the overall quality of data reduced by use of that concentration as a standard value. To avoid similar future problems, the composition of all electron microprobe standards should be reported in the form of elements instead of oxides or other compounds.

Many electron microprobe analysts believe the myth that to minimize the ZAF correction error, one should choose the standards with the composition close to that of the unknown. In reality, it is very difficult to do so. In Fig. 1, both JSC standards CP19 and IRPX are pyroxenes that have similar compositions. Un-

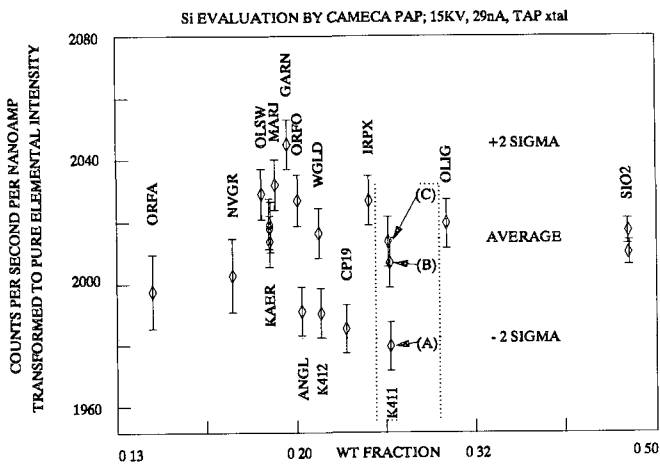


FIG. 1.--Evaluation of Si in K-411 by CAMECA pap. See Table 1 for data points (A) to (C). Multiple symbols for the same standard represent supplemental calibrations of that standard.

fortunately, the analyzed Si concentration of IRPX will be higher than the reported value if one uses CP19 as the Si standard. On the other hand, there is no statistical difference between the analyzed and the reported Si values of IRPX if either JSC standard OLSW (Mg-Fe olivine) or ORFO (Mg olivine) is used as the Si standard.

Data points in Fig. 1 show that JSC standards KAER, WGLD, OLIG, and SIO2 are all qualified to be model standards for Si analyses. One can minimize the analytical error for Si in quantitative electron microprobe analysis by use of one of these model standards as the Si standard. This error minimization is the single most important advantage of the above procedure. Such error minimization is particularly important when the composition of the target is totally unknown or when several different phases are to be analyzed with the same standard. In theory, the composition of any homogeneous microprobe standard can be calibrated to be that of a model standard by application of the backward-ZAF-calculation procedure. This calibration can be easily performed in a user-designed spreadsheet on a personal computer. This method not only shortens the calculation time, it also makes routine calibrations of new standards possible.

References

1. S. V. Yang and G. A. McKay, *Microbeam Analysis--1988*, 477.
2. NIST Standard Reference Materials Catalog, 1990-1991.
3. R. B. Marinenko et al., *Microbeam Analysis--1989*, 254.
4. From CAMECA Instruments, Inc., 2001 W. Main, Stamford, CT 06902.
5. From John Armstrong, Caltech.
6. FeO and Fe₂O₃ data from Pennsylvania State University.
7. NASA-JSC probe lab data.

TABLE 1.--Composition of K-411. Oxygen calculated from stoichiometry. Total Fe as FeO in A; FeO/Fe₂O₃ = 0.342 and MnO = 0.13 in B to E. Total normalized to 100 in C to E. A: NIST certified data. B: NIST certified data with modified Mn and O compositions. C: Composition calibrated by CAMECA PAP. D: Composition calibrated by CAMECA ZAF. E: Composition calibrated by DUST.

	Si	Fe	Mg	Ca	Mn	O	Total
A	25.38	11.21	8.85	11.06	-	42.37	98.86
B	25.38	11.21	8.85	11.06	0.10	43.56	100.15
C	25.26	11.17	8.90	11.11	0.10	43.46	100.00
D	25.33	11.24	8.75	11.11	0.10	43.47	100.00
E	25.28	11.12	8.80	11.12	0.10	43.45	100.00

QUANTITATIVE ELECTRON PROBE MICROANALYSIS OF Be IN Nb-Be ALLOYS USING AN α -FACTOR CORRECTION TECHNIQUE

C. T. Burilla

With the advent of multilayered dispersion elements (MLDE) it is now possible routinely to detect beryllium with the electron microprobe.¹ Because of the ultralight nature of the Be x-ray emission, and the attending absorption problems that are characteristic of all light-element analyses by EPMA, it is prudent to expect that the majority of the Be radiation excited in Be-containing binary alloys will be significantly absorbed by the companion element and never reach the detector. The end result will be very low count rates and correspondingly poor detection levels. When the binary companion element is much heavier than Be, this absorption problem can become so pronounced that the applicability of the electron probe method itself has to be questioned.

The application of EPMA to the analysis of Be in Nb-Be binary alloys represents a unique case—one that involves a relatively uncommon occurrence in light-element analysis in a heavy-element matrix. In these alloys the Be x-ray yield is extraordinarily high and the count rates are substantial enough to allow Be to be easily detected, even in low concentrations. To take advantage of this phenomenon, a method that allows direct quantitative analysis of Be in Nb-Be binaries has been developed. Through the use of an empirical correction technique,² in conjunction with the area-peak factor concept³ and well-characterized Nb-Be standards, Be intensities can be accurately and efficiently converted into concentrations. The procedure is straightforward and permits the lightest element detectable with the electron microprobe to be quantified in moderately heavy Nb matrices.

Method

A series of Nb-Be binary alloys, consisting of Nb₃Be₂, NbBe₂, NbBe₃, Nb₂Be₁₇, and Be and Nb metal were examined with a Cameca MBX electron microprobe. Both detector and column windows were fitted with stretched polypropylene. P-10 gas was used in the detector. Various acceleration voltages, between 5 and 30 keV, and a beam current of 100 nA were used in the study. Beam current was maintained at 100 nA at each acceleration voltage via Cameca's feedback-regulation system and was measured by a Faraday cup. Beam current was reset to 100 nA each time the acceleration voltage was changed, since it was found that the regulation system, though maintaining a stable current at any one acceleration voltage, did not hold the current

to the preset value when the voltage was changed. A boron carbide/molybdenum MLDE (Ovonics Synthetic Materials) with a spacing of $2d = 203.6 \text{ \AA}$ was installed in an inclined spectrometer on the MBX. The Be and Nb metal standards as well as the analysis specimens were diamond polished in an environmentally contained rig (for safety and oxidation-preventive purposes) and inserted into the microprobe immediately afterwards.

Beryllium Intensity Observations

One of the novel findings of this study was the substantial Be K α x-ray yield in the moderately heavy Nb-rich matrices. When the experiment Be K α k-ratios for the Nb-Be binaries are plotted as a function of weight fraction Be it is seen that the k/C ratio is greater than unity over the whole concentration range for all acceleration voltages (Fig. 1). For acceleration voltages greater than 20 keV there is the strong suggestion that the maximum in the curve $k = f(C)$ is above 1 for high Be concentrations (45-100 wt% Be). This result suggests that either the mass absorption coefficient of Be K α radiation is lower in Nb than it is in Be itself, or that the combination of Z effects and absorption effects is responsible for this behavior. A similar phenomenon was observed for boron K α radiation in LaB₆.⁷ Evidence reported in that work attributed the cause to the proximity of the La N_{III} absorption edge to the B K α line. It was proposed that the values for the mass absorption coefficients of B K α radiation in lanthanum and B K α radiation in boron were 2500 and 3471 cm²/g, respectively (i.e., the mac of B K α is lower in La than in B itself). (A similar situation may also be present in the Nb-Be binaries, but we are unable to draw any conclusions at this time.) Other factors such as chemical bonding and crystallographic effects, as well as the surface physics of emission from the Be metal standard and the niobium beryllides, must be investigated more fully before the enhancement origin can be understood. Nonetheless, the fortuitousness of the situation allows for very favorable Be K α peak intensities and P/B ratios to be obtained from Nb-Be binary alloys. Table 1 shows these values as obtained with the B₄C/Mo MLDE.

Experimental

Wavelength scans obtained at an acceleration voltage of 10 keV for Be and the Nb-Be binaries are shown in Fig. 2. There is a measurable wavelength shift between each of the alloys and the Be metal, with the peaks shifting toward

C. T. Burilla is at the United Technologies Research Center, East Hartford, CT 06108.

TABLE 1.--Beryllium $K\alpha$ peak intensities and P/B ratios obtained with a boron carbide/molybdenum MLDE (beam current, 100 nA).

FIG. 2.--Area-peak factors for Be $K\alpha$ radiation in the niobium beryllides relative to a Be metal standard.

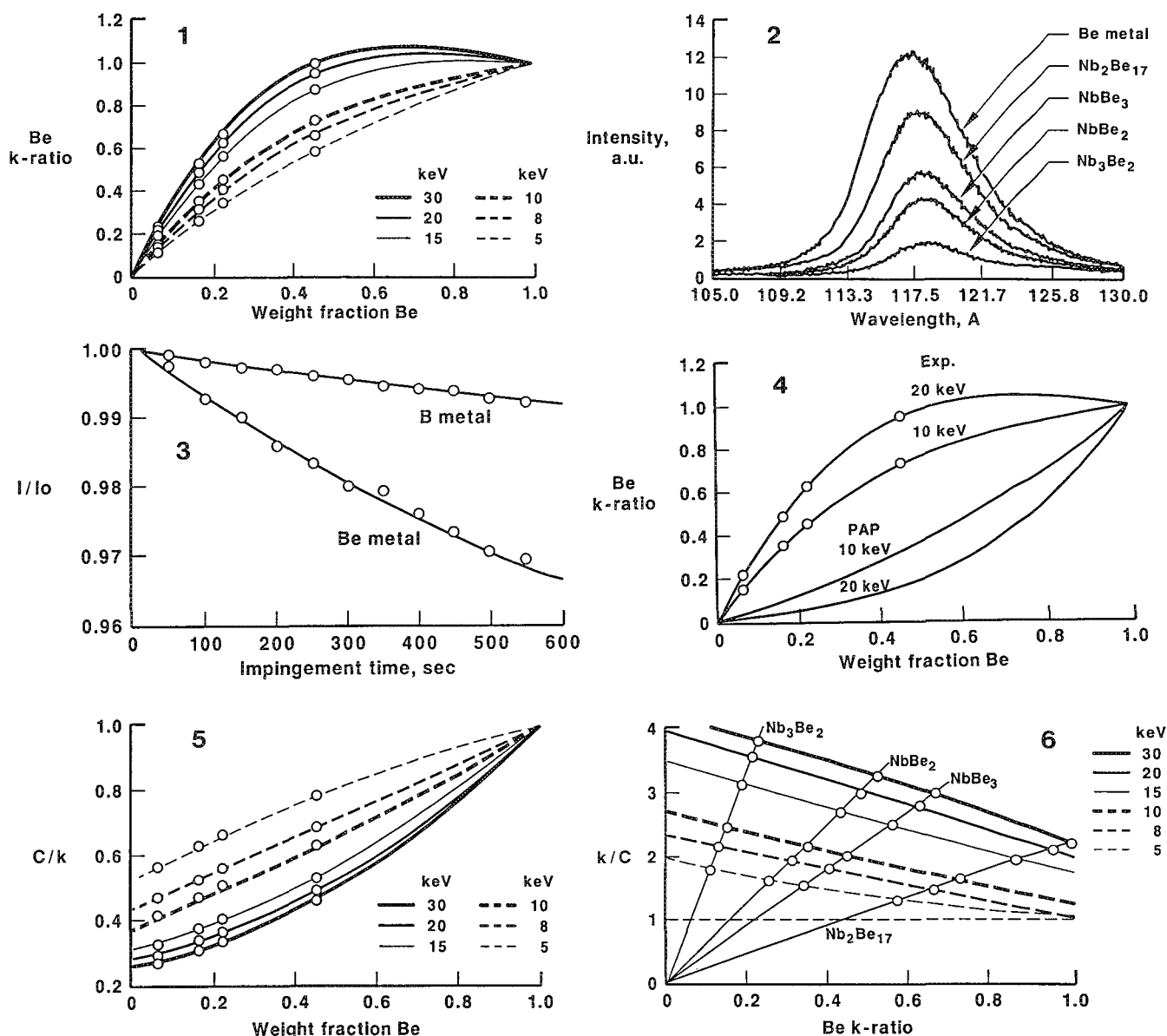


FIG. 1.--Curves of $k = f(C)$ for four niobium beryllides obtained at several acceleration voltages. Standard is pure Be metal.

FIG. 2.--Wavelength scans of Be metal and Nb-Be binaries at 10 keV.

FIG. 3.--Decrease in Be intensity from pure Be metal as a function of electron beam impingement time: 10 keV, 100 nA, focused beam (spot mode). Boron metal shown under identical conditions for comparison purposes.

FIG. 4.--Comparison of "Cameca-PAP" predicted k-ratios with measured k-ratios for 10 and 20 keV acceleration voltages.

FIG. 5.--Relationship between C/k and C at several acceleration voltages. Linear relation is apparent at approximately 8 keV.

FIG. 6.--Occurrence of linearity between k/C and k at acceleration voltage identical to the one where linearity develops between C/k and C in Fig. 5.

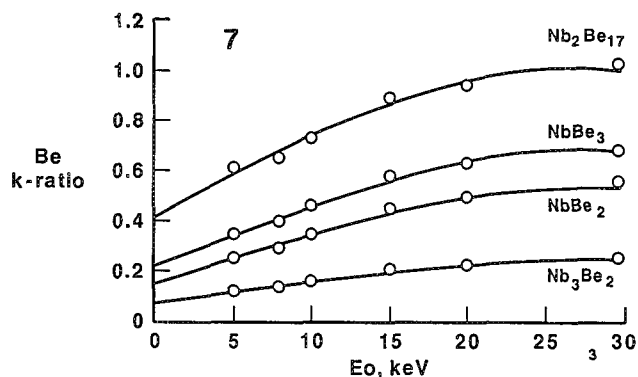


FIG. 7.--Be k-ratio as a function of accelerating voltage. Trend is clearly toward confluence of k C as E_0 approaches E_c .

higher wavelengths at decreasing Be concentration. Similar scans at the other acceleration voltages produced analogous shifts. Aside from this peak shifting, each of the Be peaks shows very similar peak shapes, including a skewing on the high wavelength side.

In x-ray microanalysis it is customary to calculate k-ratios by ratioing the background-corrected peak intensity of the unknown to that of a standard. This method is valid only when the areas under the peaks are proportional to the peak heights, as is usually the case. However, when dealing with light elements, the proportionality between area and peak height is often disturbed because excitation of the light-element K radiation takes place through transitions of electrons involved in the chemical bond. This phenomenon results in appreciable peak shifting and significant peak shape alterations,³⁻⁶ and one must resort to measuring peak areas rather than peak heights in order to establish an accurate k-ratio. Because of the peak shifting and peak asymmetry observed in the Nb-Be system (Fig. 2) it is to be expected that the Be K peak heights will not be precisely proportional to peak areas. To determine whether this is the case, the concept of area-peak factor (APF)³⁻⁶ was employed. The APF is defined as the ratio between the correct area (integral) k-ratio and the peak k-ratio.

The APFs (relative to Be metal) for each of the Nb-Be binaries were measured between 5 and 30 keV. The measurement of peak areas involved scanning the spectrometer through the region of interest and recording the intensities in a data file. The actual range covered was from 104.0 to 133.0 Å, with a step size corresponding to 0.040 Å. In each interval the intensity was measured for 1000 ms. After the scan was completed the data were dumped to a hard disk and then transferred for later processing to a microcomputer, where the background-subtracted integral and peak k-ratios were extracted and the corresponding APFs were obtained.

The resulting APF values were found to be essentially independent of acceleration voltage. This APF independence on acceleration voltage was reported earlier for C and B binary com-

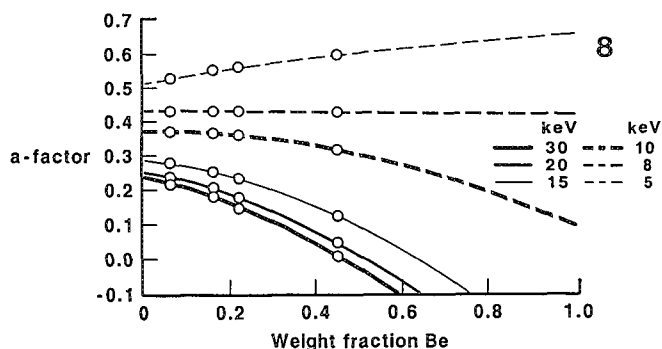


FIG. 8.--Linear relation between a-factor and Be concentration at the same unique acceleration voltage found in Figs. 5 and 6.

pounds.⁴ Table 2 shows the APFs obtained for each Nb-Be binary. Because of the APF deviations from unity, errors are introduced if the concentration is calculated from peak k-ratios, especially for lower Be compositions. Therefore, in order to acquire accurate k-ratio measurements, the APFs obtained in Table 2 were applied to all measured Be peak k-ratios.

When dealing with light-element (and especially with ultralight element) analysis by electron-beam methods, one must be concerned with the potential of surface contamination attenuating the emitted signal. In the microprobe, with its relatively poor vacuum and associated oil pumping system, the specimen is gradually covered with a contamination layer of organic matter in the vicinity of the electron bombarded layer.⁸ Under other than long-wavelength situations this effect is not very troublesome, since the emitted x rays are not significantly absorbed by the deposit. Beryllium, the lightest element detectable with the electron microprobe, was expected to exhibit substantial attenuation of its x-ray emission due to this undesirable contamination layer. In an effort to determine the magnitude of this potential problem, a highly polished specimen of pure Be metal was introduced into the microprobe within minutes after the polishing operation. The specimen was bombarded with 10keV electrons and the emerging Be K α intensity was measured as a function of electron beam impingement time. The beam current was set at 100 nA and the electron beam was focused as finely as possible (spot mode). A specimen of pure B metal was bombarded under identical conditions for comparison purposes. Figure 3 shows the relative attenuation of the Be K α and B K α x rays over a period of 10 min. It is obvious that the analyst must consider this contamination-induced attenuation as a source of error in any light-element analysis procedure. The simplest way to avoid significant errors in long-wavelength intensity determinations is to keep dwell time to a minimum. This approach is often not feasible if the counting rates are low due to either low concentrations or low x-ray yields (counting statistics considera-

tions) or when one is attempting to determine accurate peak shapes and shift observations (Fig. 2) that by definition involve longer dwell times. In these situations the slope of the intensity decrease vs impingement time function (Fig. 3) can be applied to correct the measured intensities for dwell time aberrations in a straightforward fashion. In the present situation this correction can be avoided in Be peak k-ratio determinations since, once the APFs are obtained, the dwell times can be kept relatively short and a statistically sufficient number of Be counts can be acquired on the peak in under 50 s. Under these conditions electron-beam-induced contamination attenuations do not add significant error (less than a 0.2% relative reduction in Be K α counts in 50 s). For a 50s counting time more than 47 000 counts were accumulated in the worst case (the Nb₂Be₃ 6.1 wt% binary at 30 keV). Since the standard deviation for x-ray counting purposes is defined by the square root of the mean number of counts ($\sigma = N^{1/2}$) and the variation in percent of total counts by $(\sigma/N)100$, the variation calculated for the 6.1 wt% alloy is less than 0.5%.

Application of the Empirical Correction Method

Because of many factors, including the uncertainty of the mass absorption coefficients and the huge overvoltages, traditional correction procedures such as ZAF can be expected to fail. Also, the recently developed PAP correction program (CAMECA-PAP version),⁹ shown to be suitable for other light-element analyses, was unsuccessful when applied to the determination of Be and Nb matrices (Fig. 4). In order to quantify Be in Nb-Be binary alloys, an α -factor technique has been employed to correct the Be intensities successfully. It has been shown previously that empirical α -factors can be used to correct electron-probe analyses in binary metal alloys.² This correction is based on the assumption that there is a hyperbolic relationship between concentration and intensity such that

$$C_{AB}^A/k_{AB}^A = \alpha_{AB}^A + (1 - \alpha_{AB}^A)C_{AB}^A \quad (1)$$

where C_{AB}^A is the concentration of A in the binary, k_{AB}^A is the ratio of the background-subtracted x-ray intensity of A in the binary relative to the standard, and α_{AB}^A is the α -factor. When this relation exists a plot of C/k vs C yields a straight line whose y-intercept is the α -factor. Parenthetically, when a series of alloys is examined, a plot of k/C vs k must also result in a straight line.¹⁰ If both of these factors do not occur simultaneously then a hyperbolic relationship between concentration and intensity does not exist. In Fig. 5 a plot of C/k vs C for the Nb-Be alloys clearly shows that a linear relation exists near an acceleration voltage of 8 keV. However, it is obvious that this is *not* the case at any other voltage. As stated, it is also necessary for the $k/C = f(k)$ function to result in a straight line if a hyperbolic relation exists. Figure 6 shows

that this is also true for the acceleration voltage identical to the one that exhibits linearity in Fig. 5. The curves in Figs. 5 and 6 were calculated from second-order polynomial fits of the data points.

When one examines the k-ratio vs concentration curves (Fig. 1), it is apparent that they become more and more linear as E_0 decreases. In fact as E_0 decreases the value of the Be k-ratio approaches the actual Be concentration. Figure 7 graphically depicts this observation. Here it is evident that as E_0 decreases the Be k-ratio for each binary gets closer and closer to the binaries' respective concentration. In the vicinity of $E_0 = E_C$ (0.117 keV) the curves for each of the binaries, which have been generated by a polynomial fit of the data points, intersect the k-ratio axis close to the position where the k-ratio equals the concentration. Because of the absence of data in the region $E_C < E_0 < 5$ keV it is not possible to ascertain this intersection with high reliability. However, based on these results it is evident that the data are consistent and the convergence of k-ratios with concentration in the region $E_0 = E_C$ adds credence to this fact.

The relationship between α -factors and Be concentration is shown in Fig. 8. Here it is obvious that the α -factors depend functionally on concentration for all of the acceleration voltages considered but that they are *consistent* and *independent* of concentration only for an acceleration voltage near 8 keV, where the hyperbolic requirements stated above were fulfilled. Therefore, by choosing an acceleration voltage around 8 keV, where all of the criteria for hyperbolicity are satisfied, one should be able to use the well-known α -factor technique for converting the Be intensities obtained from Nb-Be binaries into concentrations. By deploying the α -factor thus obtained one can solve Eq. (1) for C after acquiring the Be k-ratio for the Nb-Be unknown.

Conclusions

A boron carbide/molybdenum MLDE can be used in an electron microprobe to quantify beryllium in niobium matrices accurately. Due to the high apparent Be K α x-ray yield in Nb, it is obvious that either the mass absorption coefficient for Be K α x-rays in Nb matrices is fairly low (possibly lower than the mac of Be K α x-rays in Be itself), or that a combination of Z effects and absorption effects is responsible for the behavior. Also, since the excitation of the ultralight Be K α radiation takes place through the transitions of the very electrons involved in chemical bonding, chemical effects must be considered in any plausible enhancement explanation. Regardless of the source of this enhancement, it has been shown that statistically acceptable k-ratio can be obtained in relatively short counting times. Since the Be K α line is subject to peak-shift and peak-shape alterations, it is imperative that integral k-ratios be used in

all calculations. Peak k-ratios can be substituted for integral k-ratios once the area-peak factors are calculated for the niobium beryllide being measured. A quantitative α -factor correction technique was successfully applied to the Be-Nb system. This technique produced favorable results that were not obtainable by other matrix correction schemes. The procedure, although it requires several well-characterized binary standards, is relatively easy to apply. Since the method relies only on the experimentally determined k-ratios and does not require any theoretical correction scheme, the errors usually associated with such corrections are conspicuously absent.

By applying the α -factor method and choosing an operating voltage close to 8 keV, one can take advantage of the linearities of the system and the only measurements necessary to characterize the beryllides are those involving the determination of peak and background intensities on pure Be metal and on the unknowns. This procedure permits the straightforward, direct quantitative determination of the lightest element detectable with the electron microprobe in moderately heavy Nb matrices.

References

1. D. A. Sentner and H. I. Heitur, "Electron probe microanalysis of Be in Cu-Be alloys," *Microbeam Analysis--1987*, 65.
2. T. O. Ziebold and R. E. Ogilvie, "An empirical method for electron microanalysis," *Analyt. Chem.* 36: 322, 1964.
3. G. F. Bastin and H. J. M. Heijligers, "Quantitative electron probe microanalysis of carbon in binary carbides," *Microbeam Analysis--1984*, 291.
4. G. F. Bastin and H. J. M. Heijligers, "Quantitative electron probe microanalysis of very light elements," *Microbeam Analysis--1985*, 1.
5. G. F. Bastin and H. J. M. Heijligers, "Quantitative electron probe microanalysis of carbon in binary carbides," *X-ray Spect.*, 135, 1986.
6. G. F. Bastin and H. M. M. Heijligers, "Quantitative electron probe microanalysis of boron in some binary borides," *Microbeam Analysis--1986*, 285.
7. J. L. Pouchou and F. M. A. Pichoir, "Determination of mass absorption coefficients for soft x rays by the use of the electron microprobe," *Microbeam Analysis--1988*, 319.
8. R. Castaing, *Advances in Electronics and Electron Physics*, New York: Academic Press, 1960, 317.
9. Available from CAMECA Instruments, Inc., 2001 W. Main St., Stamford, CT 08902
10. A. E. Bence and A. L. Albee, "Empirical correction factors for the electron microanalysis of silicates and oxides," *J. Geol.*, 382, 1968.

IS THERE A "UNIVERSAL" MAC EQUATION?

R. E. Ogilvie

The search for an empirical attenuation equation begins with the work of Siegbahn¹ in 1914. At that time Siegbahn showed that the value of μ/ρ for a given element could be expressed as a function of the wavelength λ of the x-ray photon by

$$(\mu/\rho) = C\lambda^n \quad (1)$$

where C is a constant for a given material, which will have sudden jumps in value at critical absorption limits. Siegbahn found that n varied from 2.66 to 2.71 for various solids, and from 2.66 to 2.94 for various gases.

Bragg and Pierce,² at this same time period, showed that their results on materials ranging from Al(13) to Au(79) could be represented by

$$\mu_a = CZ^p\lambda^{2.5} \quad (2)$$

where μ_a is the atomic attenuation coefficient and Z the atomic number. Today Eq. (2) is known as the "Bragg-Pierce" law. The value of the exponent, $5/2$, was questioned by many investigators, who felt that n should be closer to 3. The work of Wingardh³ showed that the exponent of Z should also be much lower, $p = 2.95$; however, this value is much lower than that found by most investigators.

One of the most extensive studies on absorption was carried out by Jönsson,⁴ in his thesis at Uppsala. He tabulated almost 600 measured attenuation coefficients. However, the most interesting part of his thesis is the "Universal" absorption curve. Jönsson introduces a new true absorption coefficient, which may be called the electronic true absorption coefficient τ_e :

$$\tau_e = \tau_a/Z = (\tau/\rho)A/NZ \quad (3)$$

where A is the atomic weight, N is Avogadro's number, and τ/ρ is the normal true absorption coefficient. Jönsson proposed that τ_e is a function of $Z\lambda$ only. The $\log(\tau_e N)$ was plotted against $\log(Z\lambda)$.

$$\tau/\rho = CZ^{n+1}\lambda^n/A \quad (4)$$

where n decreases as $Z\lambda$ increases. Equation (4) has not proved to be in agreement with most experimental data; however, it will be shown that τ/ρ is the value that should be used in electron microanalysis.

There is no question that the best analytical fit to the experimental data of μ/ρ as a function of Z and E has been developed by Heinrich:⁵

$$\mu/\rho = CZ^n(12398/E)^n \{1 - \exp[(-E + b)/a]\}/A \quad (5)$$

where E (ev) is the photon energy and C , n , a , and b are functions of Z . These functions are

$$C = \sum C_i Z^i, n = \sum n_i Z^i, a = \sum a_i Z^i, b = \sum b_i Z^i$$

The number of terms in the summation will vary, as indicated in his tables. It is unfortunate that p was assumed to be equal to 4, since a lot of data show that p is less than 4.

Procedure

It has been assumed that Heinrich's data are the best representation of the mass attenuation coefficients (MAC); with these data, the values of C , p , and n have been evaluated by the method of least squares for the following equation:

$$\mu/\rho = CZ^p(12398/E)^n/A \quad (6)$$

The data used were for the energy range from 5 to 20 keV and the atomic number varied from 20 to 92. The atomic number was determined by the zone; that is, zone 1 through zone 5 is determined by the following energy values:

$$E > EK, EL_1 < E < EK, EL_2 < E < EL_1,$$

$$EL_3 < E < EL_2, EM_1 < E < EL_3$$

The use of Eq. (6) assumes that, when $\log(\text{MAC} \cdot A)$ is plotted versus the $\log(E)$ and $\log(Z)$, the resulting surface is a plane. Heinrich's data do not fall on a plane; however, it is very close. Such a plot is illustrated in Fig. 1 for the energy range of 1-20 keV and $Z = 5-90$. Since the Heinrich's data did not produce a plane, it was decided to fit a quadratic equation to his data of the form

$$A1 \cdot X^2 + A2 \cdot X + A3 \cdot Y^2 + A4 \cdot Y + A5 \cdot M^2 + A6 \cdot M + A7 = 0 \quad (7)$$

where $X = \log(E)$, $Y = \log(Z)$, and $M = \log(\text{MAC} \cdot A)$.

The seven coefficients were evaluated by the method of least squares by Newton's method. The coefficients were then normalized by division through by $A7$. The solution for M is then done by the normal quadratic technique, which has two solutions, but it is easy to determine the correct one.

Results

The coefficients evaluated for Eq. (6) are listed in Table 1. For zones 1, 2, and 5 the MACs were calculated and compared with those

R. E. Ogilvie is at the MIT Department of Materials Science and Engineering, Cambridge, MA 02139.

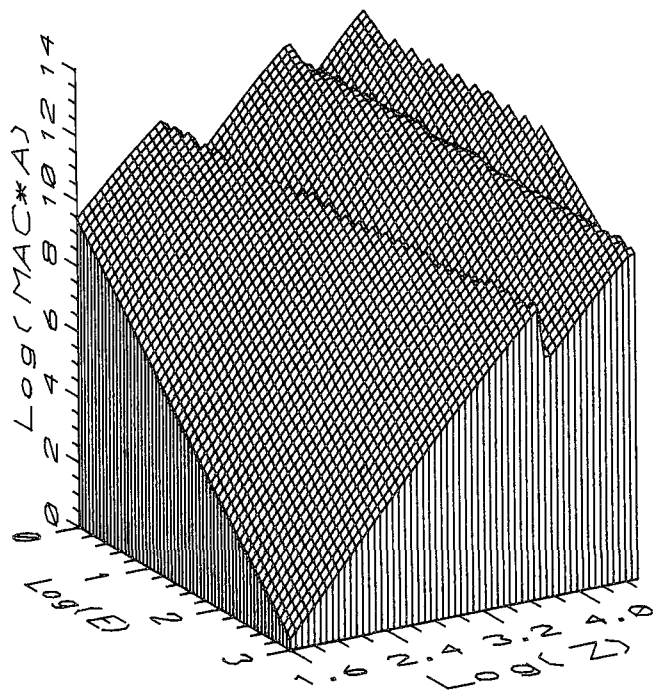


FIG. 1.--Plot of $\log(\text{MAC} \cdot A)$ vs $\log(E)$ and $\log(Z)$ of Heinrich's data. Surfaces are very close to a plane.

TABLE 1.--Values of the coefficients used in Eq. (6).

Zone	C	p	n
Zone-1	3.2405E-2	3.6869	2.7502
Zone-2	1.7365E-3	3.9590	2.6940
Zone-3	1.5494E-4	4.4710	2.8976
Zone-4	8.1414E-5	3.4869	2.4710
Zone-5	1.3411E-4	4.2155	2.6277

calculated from Eq. (5). The percent difference was calculated for the particular element for the energy range between edges, in steps from 200 to 1000 eV. These results are illustrated in Fig. 2. The use of Eq. (6) gives values of MAC that are closer to Heinrich's values than those of many other tabulated sets of data. It is also my opinion that Heinrich's values are too low near edges. The same procedure was used for Eq. (7), and the seven coefficients are given in Table 2. The percent difference plotted versus Z for zones 1, 2, and 5 are shown in Fig. 3. A positive difference is where Eqs. (6) or (7) give higher values than those obtained using Eq. (5). This is the case near edges, but if we consult the data of Del Grande and Oliver,¹ we see that the values are indeed higher near the K-edges than those given by Eq. (5). For the energy range 5-20 keV, Eq. (7) gives excellent agreement for the five zones studied.

It has been assumed that μ/ρ is the value

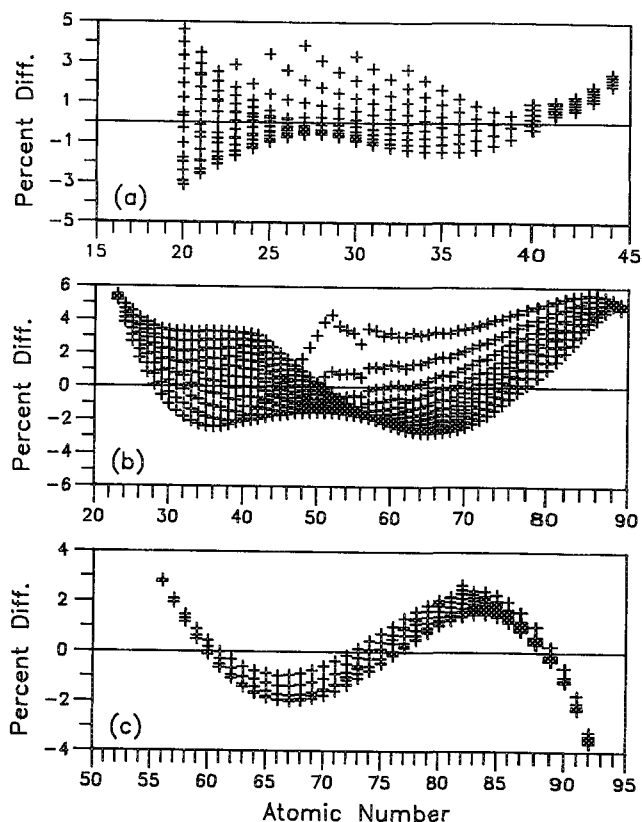


FIG. 2.--Percent difference of Eqs. (6) and (5) for (a) Zone 1, (b) Zone 2, (c) Zone 5, as a function of Z .

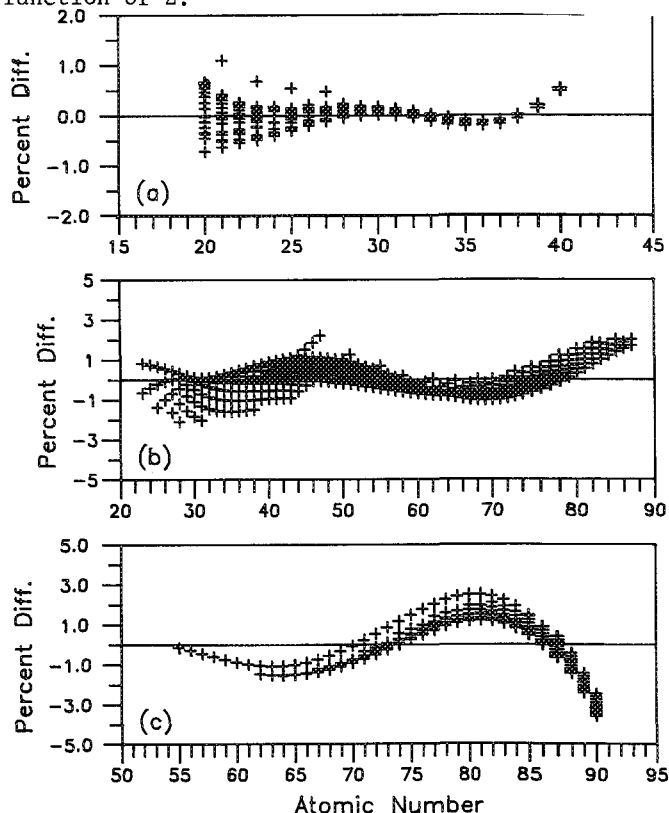


FIG. 3.--Percent difference of Eqs. (7) and (5) for (a) Zone 1, (b) Zone 2, (c) Zone 5, as a function of Z .

TABLE 2.--Values of the coefficients used in Eq. (7).

Zone	A1	A2	A3	A4	A5	A6	A7
Zone-1	2.0328E-2	9.7845E-1	1.6480E-2	-9.2133E-1	-6.1938E-3	-2.0161E-1	1
Zone-2	5.9893E-2	-2.0840	-1.4885E-2	1.1729	4.0993E-3	6.3174E-1	1
Zone-5	4.4408E-2	-6.5621E-1	-3.3778E-3	1.8561E-1	4.0009E-4	5.6558E-2	1

from μ/ρ data. I hope that Heinrich will continue with this problem.

References

1. M. Siegbahn, *Physikalische Zeitschrift* 15: 753, 1914.
2. W. H. Bragg and S. E. Pierce, *Phil. Mag.* 28: 626, 1914.
3. K. A. Wingardh, *Zeitschr. f. Physik* 8: 363, 1922.
4. E. Jönsson, Thesis, Uppsala, 1928.
5. K. Heinrich, *XI ICOM*, 1986, 67.
6. N. Del Grande and A. Oliver, UCRL-73923, 1972.
7. W. McMaster et al., UCRL-50174, 1969.

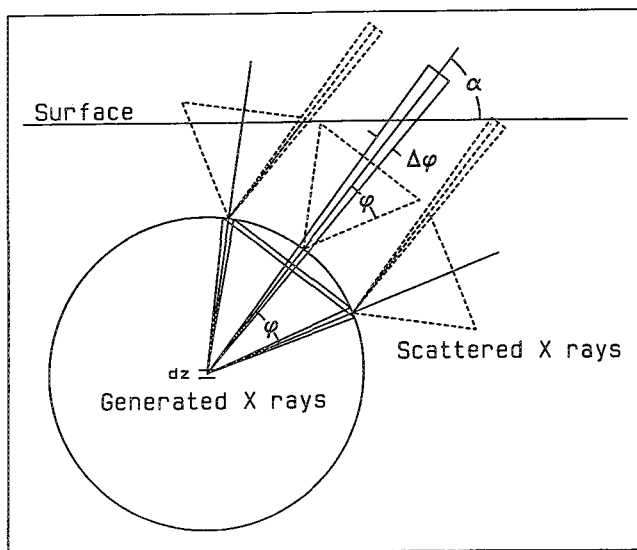


FIG. 4.--Illustration of how scattered x rays from a cone, with semi-angle ϕ , compensate for scattered x rays from direction of detector.

that should be used in electron microanalysis; however, it can be shown that τ/ρ is closer to the truth. The reason is that when a photon is emitted from the layer dz at a depth z at the take-off angle, there is a finite probability that it will be absorbed (τ/ρ), or it may be scattered (coherent or incoherent) at some angle ϕ , but there is a cone of emitted radiation with a semiangle ϕ about the direction of the take-off angle. One of the photons in this cone has the same probability of being scattered in the direction of the take-off angle to the x-ray detector. This process is illustrated in Fig. 4. If the direction to the detector is perpendicular to the surface of the specimen, the ratio of photons scattered from the cone to the detector to those scattered from the direction of the detector is greater than 1. In normal use the ratio is a little less than 1.

Conclusion

It is clear that Eqs. (6) and (7) must be evaluated with measured data from the literature, and that the values near edges should be carefully examined. It is obvious that more work is necessary--new measurements of μ/ρ and new analytical expressions. It is also important to evaluate the τ/ρ values as tabulated by McMaster et al., which have been calculated

ELECTRON PROBE MICROANALYSIS OF BOROPHOSPHOSILICATE COATINGS

Peter Willich and Kirsten Schiffmann

It has been demonstrated that quantitative electron probe microanalysis (EPMA) of ultralight elements (B, C, N, O) is possible with surprisingly high accuracy.¹⁻³ This finding is a consequence of refined experimental procedures in combination with sufficiently accurate models of data reduction available at present. Quantitative EPMA applied to ultralight elements opens a wide range of practical applications, e.g., analysis of thin films deposited on a substrate where the film is composed of a metal in combination with one or several of the ultralight elements.⁴⁻⁶ In this context coatings of borophosphosilicate glass (BPSG) are discussed as an example of considerable technological interest. The material is frequently applied to low-temperature planarization and passivation of integrated circuits. BPSG is prepared by chemical vapor deposition (CVD) and mainly consists of silicon and oxygen, but low-temperature flow properties depend on the relatively low concentrations (1-5 wt%) of boron and phosphorus. Some fundamental aspects of EPMA applied to ultralight elements can be demonstrated by the example of BPSG, including an estimate of the analytical accuracy for the determination of boron in comparison with the results of chemical analysis. Moreover, EPMA is used to control the film thickness (0.3-1.5 μm) of BPSG deposited on silicon. Determination of the film thickness is based on thin-film data processing,⁷ without the need for thin-film standards.

Experimental

EPMA was carried out by a CAMECA SX50 microprobe based on wavelength-dispersive spectrometry. Synthetic multilayer monochromators of Ni-C (2d = 9.50 nm) and W-Si (2d = 6.05 nm) were used to measure the intensities of B K α and O K α . This procedure results in x-ray intensities of boron and oxygen that are about 4 times higher than with a conventional monochromator of Pb-stearate. Calibration was performed by standards of pure boron (B K α), FeBO₃ (B K α), Ca₅F(PO₄)₃ (P K α), and Mg₂SiO₄ (Si K α , O K α). A set of BPSG test samples was available for which the concentrations of boron and phosphorus were defined by inductively coupled plasma-optical emission spectrometry (ICP-OES), a destructive method based on dissolving the film material in a mixture of H₂O/HF. Ellipsometry

was used to determine the film thickness. For EPMA, standards (besides pure boron) and samples were coated with carbon film 10-40 nm thick. For all points of analysis the intensity of C K α (monochromator of Pb-stearate) was simultaneously recorded as a measure of the local carbon-coating thickness. Relative intensities (k-ratios) of C K α were obtained by use of vitreous carbon as a standard.

Results and Discussion

Coating with carbon is essential to the performance of reproducible measurements on insulating BPSG and the corresponding oxide standards. A comparison of the C K α intensities shows significant differences between the carbon-coating thickness on standards and samples and even within a set of samples that was coated simultaneously. Analytical errors up to 10% can be due to the influence of carbon coating. This estimation takes into account that EPMA has to be performed by use of soft x rays in combination with low electron energies (E_0 = 4-10 keV) to enable "bulk" analysis of BPSG coatings only 0.3-1.5 μm thick. After the x ray intensities of a coated BPSG sample and the corresponding k-ratio of carbon originating from the coating have been determined, correction functions (as given in Fig. 1) can be used to derive the intensities of the BPSG elements representing the sample without coating. Correction functions for BPSG (Fig. 1) and the composition of the standards were calculated by the thin-film model of Pouchou and Pichoir (PAP).⁷ This model enables one to describe the relation between the thickness of a surface coating (represented by its k-ratio) and the k-ratios of the underlying material. The accuracy of the calculations was tested by measurements at various thicknesses of the surface coating.⁸ It can be shown that even an identical carbon coating of, for example, 20 nm on BPSG and FeBO₃ (standard) leads to a k-ratio of boron that is about 6% too high in comparison with the k-ratio expected for measurements on corresponding uncoated materials.

A further refinement of the k-ratios concerns the influence of peak shift and peak shape alterations. These effects are clearly visible when spectra of B K α on BPSG, boron, and FeBO₃ are recorded (Fig. 2). A comparison of peak area (Fig. 2) and peak height k-ratios leads to area/peak factors^{1,2} of 1.43 (BPSG relative to boron) and 1.28 (BPSG relative to FeBO₃). For the BPSG samples studied so far the area/peak factors proved to be independent of the individual composition. This result makes it possible to perform routine analysis of BPSG based on conventional peak height

The authors are at Philips Research Laboratories Hamburg, P. O. Box 54 08 40, Hamburg, Federal Republic of Germany. Samples of BPSG were kindly provided by J. J. M. Borstrok, Philips Research Laboratories Eindhoven, The Netherlands.

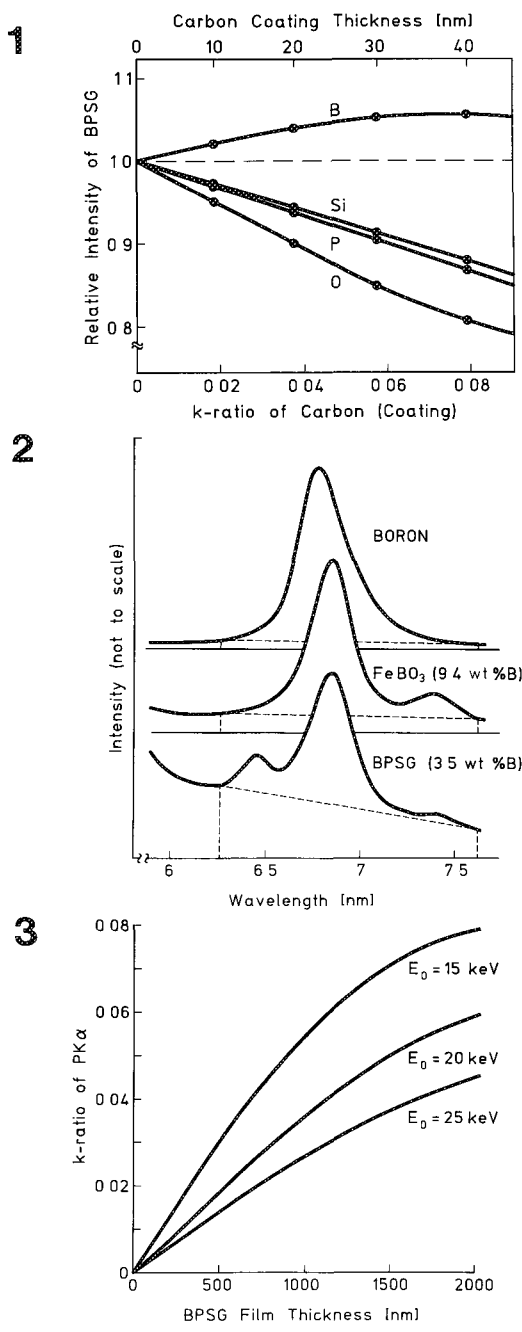


FIG. 1.--Calculated correction functions (PAP thin-film model) to derive x-ray intensities representing uncoated BPSG from EPMA of carbon-coated material. $E_0 = 6$ keV.
 FIG. 2.--B $K\alpha$ spectra and conditions of peak area intensity measurements. Peak maximum intensity of B $K\alpha$ on boron is 24 000 cps (6 keV, 100 nA) by use of Ni-C multilayer monochromator.
 FIG. 3.--Calibration curves calculated by PAP thin film model to determine film thickness of BPSG on silicon substrate by use of P K intensity. Curves refer to BPSG containing 2 wt% of phosphorus. Standard for P $K\alpha$ is $\text{Ca}_5\text{F}(\text{PO}_4)_3$.

k-ratios, the multiplication of which by the area/peak factor gives the corresponding values of peak area k-ratios. Also, a small effect of peak broadening on BPSG relative to Mg_2SiO_4 (standard) is visible for O- $K\alpha$. In

this case the k-ratios (peak height) must be multiplied by an area/peak factor of 1.06.

After the k-ratios were refined with respect to carbon coating and chemical shift of B $K\alpha$ and O $K\alpha$, the concentrations were calculated by the PAP model, a model which proved to be sufficiently accurate when applied to the analysis of boron in various borides.¹⁰ Absorption correction for boron in BPSG is extreme due to the very high mass absorption coefficient of 84 000 for B $K\alpha$ in silicon.^{2, 10} Table 1 demonstrates the consistency of EPMA performed at various electron energies and calibration of boron by various materials. The concentrations of boron established by use of the metal as a standard are slightly (0.1-0.2 wt%) lower than the results based on FeBO_3 . The concentrations of oxygen agree within 2% rel. to the results calculated by assuming the formation of the nominal oxides (B_2O_3 , SiO_2 , $\text{P}_2\text{O}_3/\text{P}_2\text{O}_5$). In general the concentrations of EPMA are in good agreement in comparison with those obtained by chemical analysis based on ICP-OES (Table 2). Sample 1 of Table 2 shows a relatively large deviation due to the fact that 0.1 wt% of boron is close to the detectability limit of EPMA for boron in BPSG. The average relative deviation between EPMA and chemical analysis is 3.6% for boron and 1.4% for phosphorus. On this level of accuracy it is difficult to decide whether the deviations are a problem of EPMA or caused by analytical errors of the reference method.

EPMA of BPSG coatings performed at sufficiently high electron energies ($E_0 > 15$ keV) represents the situation of "thin-film" analysis where the film thickness (0.3-1.5 μm) is only a fraction of the x-ray emission depth. In this case the x-ray intensities of a BPSG sample depend on the composition as well as on the film (mass) thickness. The soft x rays of oxygen and particularly of boron, as a consequence of the high mass absorption, always originate from a depth very close to the surface and a practically useful sensitivity to the film thickness is limited to very thin coatings. The measurement of the P $K\alpha$ intensity proved to be the most sensitive way to determine the thickness of BPSG deposited on silicon. In Fig. 3 the intensity of P $K\alpha$ relative to $\text{Ca}_5\text{F}(\text{PO}_4)_3$ is plotted as a function of the BPSG film thickness. Calibration functions as given in Fig. 3 can be calculated by the PAP thin-film model,⁷ provided that the concentration of phosphorus in the film is known from "bulk" analysis carried out at a sufficiently low electron energy. The computation of calibration curves for each individual phosphorus concentration is avoided when the k-ratios of phosphorus are normalized to an average concentration of, say, 2 wt%, assuming a linear relationship between concentration and intensity over the narrow range (1-4 wt%) of typical phosphorus concentrations. On the average the film thicknesses determined by EPMA are about 5% too high in comparison with the results of ellipsometry (Table 2). Thin film EPMA is related to the mass thickness and conversion to

TABLE 1.--EPMA of BPSG sample at various electron energies E_0 . PAP matrix correction based on k-ratios corrected for carbon coating and chemical shift (B $K\alpha$, O $K\alpha$). Result of ICP-OES chemical analysis: 3.5 wt% B, 2.2 wt% P.

E_0 [keV]		B ^a	B ^a	P	Si	O ^a
4	k wt%	0.0131 3.63	0.198 3.68	0.1067 2.12	2.081 40.1	1.186 54.1
6	k wt%	0.0069 3.48	0.160 3.76	0.1070 2.17	2.125 39.8	1.170 54.2
8	k wt%	0.0043 3.35	0.137 3.64	0.1003 2.09	2.202 40.0	1.148 54.3
10	k wt%	0.0034 3.49	0.130 3.62	0.1007 2.18	2.267 39.7	1.129 54.5
Standard		B	FeBO ₃	Ca ₅ F(PO ₄) ₃	Mg ₂ SiO ₄	

^aPeak area measurements

TABLE 2.--EPMA of BPSG samples in comparison with results of ICP-OES (composition) and ellipsometry (film thickness).

Sample	Composition ^a [wt%]				Film Thickness ^b [nm]	
	Boron ^c		Phosphorus ^d			
	EPMA	ICP-OES	EPMA	ICP-OES	EPMA	Ellipsometry
1	0.07	0.10	0.54	0.52	510	530
2	0.92	0.99	5.58	5.50	650	647
3	2.12	2.18	4.86	4.90	990	920
4	2.48	2.33	5.12	5.10	610	600
5	3.48	3.50	2.17	2.20	1150	1110
6	4.25	4.20	3.20	3.19	330	295

^a $E_0 = 6$ keV. ^b $E_0 = 20$ keV (P- $K\alpha$). ^cStandard B-metal. ^dStandard Ca₅F(PO₄)₃

the geometrical film thickness as given in Table 2 was done by assuming a global value of 2.2 g/ccm for the density of BPSG. An accuracy for the determination of the BPSG film thickness of the order of 5% is acceptable throughout in view of possible density fluctuations. Moreover, EPMA and ellipsometry were carried out on different parts of a large wafer and local variations of the film thickness cannot be excluded.

Conclusions

EPMA proves to be a sensitive and accurate technique for the nondestructive characterization of BPSG coatings with respect of composition and film thickness. The practical use of EPMA may be that of a reference method to support production control of BPSG by use of more convenient "relative" techniques, e.g., x-ray fluorescence or IR absorption spectrometry. Moreover, local analysis by EPMA enables one to study the lateral uniformity of composition and film thickness. An accuracy of about 3.6% for

the determination of boron confirms that quantitative EPMA of ultralight elements is feasible, although BPSG represents an extremely difficult example owing to the problems arising from low concentrations, conductive coating, chemical shift, and extremely high absorption correction.

References

1. G. F. Bastin and H. J. M. Heijligers, "Quantitative electron-probe microanalysis of carbon in binary carbides," *X-ray Spectrom.* 15: 135, 1986.
2. G. F. Bastin and H. J. M. Heijligers, "Quantitative electron-probe microanalysis of boron in some binary borides," *Microbeam Analysis--1986*, 285.
3. G. F. Bastin and H. J. M. Heijligers, "Quantitative EPMA of oxygen," *Microbeam Analysis--1989*, 207.
4. P. Willich, "Determination of chemical state and composition of metal-carbon films

by use of EPMA," in J. D. Brown and R. H. Packwood, Eds., *Proc. 11th ICXOM*, London, Ont., 1987, 238.

5. P. Willich, D. Obertop, and J. P. Krumme, "Quantitative electron-probe microanalysis of oxygen in Y-Ba-Cu-O superconducting materials," *Microbeam Analysis--1988*, 307.

6. P. Willich and D. Obertop, "Quantitative electron-probe microanalysis of light elements: Determination of a Si:C:N:O:H insulating films," *Mikrochim. Acta (Wien)*, 233, 1989.

7. J. L. Pouchou and F. Pichoir, "A new model for quantitative x-ray microanalysis: Part II. Application to in-depth analysis of heterogeneous samples," *Rech. Aérop.* 5: 47, 1984.

8. P. Willich and D. Obertop, "Quantitative EPMA of ultra-light elements in non-conducting materials," in S. Jasieńska & L. J. Maksymowicz, Eds., *Proc. 12th ICXOM*, Cracow, Poland, 1990, 100.

9. J. L. Pouchou and F. Pichoir, "A new model for quantitative x-ray microanalysis: Part I. Application to the analysis of homogeneous samples," *Rech. Aérop.* 3: 14, 1984.

10. J. L. Pouchou and F. Pichoir, "A simplified version of the PAP model for matrix corrections in EPMA," *Microbeam Analysis--1988*, 315.

11. B. L. Henke et al., "Low energy x-ray interaction coefficients: Photo absorption, scattering and reflection," *Atomic Data and Nuclear Data Tables* 27: 1-144, 1982.

QUANTITATIVE ED ANALYSIS AT HIGH COUNT RATES

S. J. B. Reed

For quantitative energy-dispersive analysis a spectrum accumulation rate of 3-5 kHz is commonly used, with a live time of around 100 s. There are significant advantages, however, in using the higher acquisition rates that are possible with current ED systems. One benefit is a reduction in the time required per analysis, with a consequent enhancement in productivity. Alternatively, more counts can be accumulated in a given time, thereby increasing the precision of the results and lowering the detection limits. Furthermore, for combined ED and WD analysis, relatively high beam currents are often used and flexibility as to the ED count rate is useful. It is therefore of interest to investigate the extent to which high acquisition rates (~ 10 kHz and above) can be used for quantitative analysis without compromising the quality of the results. Factors that have to be considered include the effect of the broadening of the peaks under these conditions, as well as dead time and pulse pile-up. The present study refers to a particular system (Link detector, with XP2 pulse processor). Other types of system may, of course, differ in their performance at high count rates, but the same criteria are applicable. Test results at acquisition rates up to 30 kHz are reported here.

Description of the System

The ED system was manufactured by Link Analytical Ltd. The detector (type 5812) has a nominal area of 10 mm^2 and is fitted with a Be window of $8\text{ }\mu\text{m}$ stated thickness. The specified energy resolution is 138 eV for Mn K α (at a count-rate of ~ 1 kHz). The detector is fitted to a Cameca SX50 electron microprobe, with a detector-specimen distance of about 60 mm. The pulse processor is of the type described by Kandiah et al.,¹ which differs from most others in using time-variant pulse-shaping parameters and having a strobed noise peak that appears in the spectrum at zero energy. There is a choice of 6 "process times," equivalent to the time constants in a conventional system, of which No. 1 is the shortest. The p.t. can be changed rapidly via the keyboard; the required adjustment to the calibration of the spectrum is carried out automatically.

The "ZAF4" quantitative analysis software provided with this system utilizes the well-known "top hat" filter function to remove background and least-squares fitting of stored elemental peak profiles to determine peak areas.² All spectra (including stored profiles) are ad-

justed to a constant energy resolution in order to eliminate the effects of differences in peak widths in different spectra. It is assumed that such differences are caused exclusively by changes in the contribution of noise to the total peak width. Each recorded spectrum is modified to make the noise peak width equal to a predetermined value, known as the "system resolution," which is slightly greater than the maximum noise peak width observed for the process time in use. All peak intensities are normalized relative to the spectrum of a calibration element (usually Co), allowing freedom in the choice of beam current, provided the same current is used for specimens and standards.

Performance of the System at High Count Rates

The rate at which pulses can be recorded (the "acquisition rate," which also equals the output rate of the pulse processor) is a function of the dead time of the system, defined as the time taken to complete the processing of each pulse. This is related to, though not numerically the same as, the process time (which refers to only one part of the processing operation). Figure 1 shows the relationship between input and output (or acquisition) rates for different process times. The observed behavior is typical of a system with extendable dead time, in that the output rate increases with input rate at first, levels off, and then decreases at very high input rates. A maximum output rate of 32 kHz is obtained with p.t. 1, the dead time per pulse being 12 μs . For other p.t.s of interest the corresponding figures are: p.t. 2, 20 kHz, 20 μs ; p.t. 3, 12 kHz, 32 μs . The "% dead time" as displayed on the screen (the fraction of "real" time for which the system is "dead") is about 65% at the maximum of the output rate curve.

The high acquisition rate obtainable with short process times is gained at the expense of broadening of the noise peak (Fig. 2). The energy resolution is thus worsened, though for x-ray peaks the effect is somewhat smaller because the contribution of ionization statistics is independent of the process time.

An important characteristic of the pulse processor is the variation in energy resolution with count rate. As shown in Fig. 2, this variation is small: for all p.t.s except 1 the change in noise peak width is about 1.5 eV for a range of count rates corresponding to 15-50% dead time. For p.t. 1 the broadening is worse: 3.8 eV for the same range. The Fano factor as calculated from the Co K α peak width is constant at 0.120 except in the case of p.t.1,

S. J. B. Reed is with the Department of Earth Sciences, University of Cambridge, Cambridge, England CB2 3EQ.

for which it is both larger and somewhat dependent on count rate (owing to nonideal behavior of the system).

Pulse pile-up at high count rates causes pulses to be lost from peaks and spurious sum peaks to appear in the spectrum; both phenomena are liable to create problems in quantitative analysis at high count rates unless appropriate countermeasures are applied. Sum peaks can be minimized by pile-up rejection circuitry in the pulse processor. In the present system the arrival of incoming pulses is detected by two fast "recognition channels" (optimized for various parts of the energy spectrum). Pulse processing is aborted when the arrival of a pulse within the process time of the previous one is recognized. This procedure greatly reduces the size of the sum peaks, but owing to the finite resolving time of the recognition system they are not totally eliminated. Measurements of sum/parent peak ratios were carried out and the inferred resolving times were 0.28 and 0.39 μ s for Mg and Co $K\alpha$, respectively. (The difference is presumably related to the smaller height of the Mg $K\alpha$ peak relative to the threshold of the recognition channel discriminator.) The resolving time is independent of the process time.

The loss of pulses caused by pile-up rejection is compensated electronically by extension of the live time. However, when a second pulse arrives within a time interval smaller than the resolving time and is therefore unrecognized, the combined pulse, though not rejected, appears in the "wrong" place in the spectrum and is thus lost from the peak. This effect was investigated by determining the Co $K\alpha$ peak area for a range of beam currents and plotting (peak area)/(current) vs input count rate. The value obtained for the resolving time was 0.4 μ s, similar to that deduced from the size of the sum peaks.

Operating at High % Dead Time

A modest increase in throughput rate can be achieved by extension of the working range beyond the upper limit of 50% dead time recommended by the manufacturers. There is even some benefit in exceeding 65% (at which throughput is at its maximum) for samples that give higher than average count rates, in order to maximize the mean acquisition rate for a set of samples of varying composition. Table 1 shows the results of olivine analyses carried out at different count rates, with up to 85% dead time (up to 94% for the Co standard). Operating with such high dead time has very little ill effect: the concentrations obtained decrease slightly at the highest count rates, but only by about 1% (relative). An upper limit of 50% therefore appears to be an unnecessary restriction.

The Effect of Broader Peaks

The broadening of peaks for short process times (see above) might be expected to have an adverse effect on the accuracy of quantitative

analysis. However, the peaks of Na, Mg, Al, and Si are still quite well resolved with p.t. 2, or even 1. Results of olivine analyses using process times 2 and 5 (Table 2) are not significantly different, even though the noise peak is 42 eV wider in the former case. The lack of spurious Al concentrations, despite the close proximity of large Mg and Si peaks, shows that the spectrum fitting process is effective even for the broader peaks obtained with p.t.2.

Count-rate Dependent Broadening

The count rates for different specimens and standards vary considerably: a range of at least 2:1 is typical. The spectrum processing procedure is quite sensitive to differences in peak width, hence count-rate dependent broadening is a potential source of error in quantitative analysis. (Note, though, that with the present system such broadening is no worse for short process times, except p.t.1.) The procedure used in ZAF4, whereby all spectra are modified to give a constant noise peak width, depends on determining the width W of the noise peak in each recorded spectrum. The theoretical standard deviation of W is given by $\sigma = (0.866/N^2)W$, where N is the total number of counts in the peak.⁴ For short counting times the broadening correction may be ineffective because the statistical error in W is larger than the original variations. In order to improve the statistical precision, the noise strobe rate was raised from 0.6 to 2.5 kHz. However, the broadening correction is still of marginal value for short counting times, given the small amount of variation in peak widths encountered in practice.

The Use of Variable Beam Current

A possible strategy for avoiding count-rate dependent effects is to keep the count rate constant by varying the beam current for different samples and standards. With the present system there is little to be gained by adopting this strategy other than possibly with p.t.1, which is less well behaved than the longer p.t.s. However, the time taken to change the current must be taken into account when the usefulness of this procedure is assessed.

Sum Peak Interferences

The size of a sum peak relative to the parent peak (or peaks) is a linear function of the input count rate and such peaks are thus more important at high count rates than at "normal" rates. (Note that in this context it is the count rate of the parent peak or peaks that is important, rather than the total spectrum count rate.) Possible interferences between sum peaks and $K\alpha$ lines are listed in Table 3. Figure 3 shows exaggerated sum peaks recorded at a very high input count rate.

This problem can be solved by treating the sum peak as if it were a "real" peak. A profile of the peak obtained from a spectrum such as that in Fig. 3 can be "stripped" in the

TABLE 1.--Analyses of olivine at various count rates (process time 3).

beam curr. (nA)	olivine		cobalt		concentrations (wt%)		
	input count rate (kHz)	dead time (%)	input count rate (kHz)	dead time (%)	Mg	Si	Fe
2	5.7	22	10.4	33	30.13	18.84	7.75
4	11.4	35	20.8	50	30.11	18.68	7.72
6	17.2	45	31.1	63	30.19	18.85	7.80
8	22.8	53	41.5	72	30.09	18.72	7.70
11	31.4	63	56.7	82	29.99	18.72	7.78
15	43.0	74	77.6	89	29.86	18.62	7.72
20	57.3	82	102.8	94	29.78	18.56	7.73

Note: Al was included in the analysis (though not present): the amount recorded was below the detection limit (0.05%) in all cases.

TABLE 2.--Analyses of olivine with different process times (5 nA beam current, 1 mm detector aperture, 2 kHz input count rate, 200 s live time).

proc. time	system res.	Mg	Al	Si	Mn	Fe	Ni
2	107	30.14	n.d. (<0.08)	18.59	0.12	7.52	0.31
5	65	30.21	n.d. (<0.05)	18.54	0.15	7.49	0.35

TABLE 3.--Sum peak interferences

K α peak	sum peak	energy diff. (eV)
V	MgCa	6
Cr	SiCa	18
Ti	MgK	57
K	AlSi	87
Ni	CaCa	91

usual way, which removes its influence on the overlapped elemental peak. An example of the application of this technique is given in Table 4. Here the spurious Cr concentration in wollastonite (CaSiO_3) caused by the SiCa sum peak is completely eliminated by stripping.

Pile-up Losses

A pulse is lost from a peak due to pile-up if it is preceded or followed by another pulse (of any size) within the resolving time of the pulse recognition circuits; hence the loss is a function of the total spectrum count rate. For example, with the present system a loss of 7% occurs at an input rate of 86 kHz (corresponding to the maximum acquisition rate for p.t. 1). The resolving time depends somewhat on energy, but for moderate corrections can be assumed to be the same for all peaks in the spectrum. An example of the application of the correction for pile-up loss is given in Table 5.

Rapid Quantitative Analysis

The analysis in Table 5 illustrates the use of a high acquisition rate to obtain a quantita-

TABLE 4.--Analysis of wollastonite: effect of SiCa sum peak (44 kHz input count rate, process time 2).

sum peak stripping	concentrations (wt.%)			
	Si	Ca	Cr	Fe
no	24.07	34.27	0.48	0.36
yes	24.05	34.30	n.d. (<0.07)	0.32

TABLE 5.--Analysis of olivine at 30 kHz acquisition rate (process time 1, 25 nA beam current, 5 s live time).

	concentrations (wt%)		
	Mg	Si	Fe
mean of 10 analyses	30.32	19.73	8.26
standard deviation	0.27	0.26	0.06
corrected for pile-up losses	30.38	19.15	7.90
typical result at low count rate	30.10	18.80	7.80

tive analysis in a short time (10 s "real" time in this case). The reproducibility of the major elements is around 1% relative (1 s.d.), which is satisfactory for most purposes. This result illustrates the possibility of obtaining large numbers of analyses (e.g., for "quantitative mapping") in a reasonable time.

Conclusions

There are no insuperable objections to considerably higher acquisition rates for quantitative ED analysis than the typical rate of ~ 5 kHz commonly used, subject to adequate performance of the pulse processing electronics. Above 10 kHz it becomes desirable to introduce certain measures such as stripping sum peaks from the spectrum where interferences occur and correcting for the loss of counts from peaks caused by pulse pile-up. Increase in the acquisition rate enables the time per analysis to be reduced or better precision and lower detection limits to be obtained in a given time.

References

1. K. Kandiah, A. J. Smith, and G. White, *IEEE Trans. Nucl. Sci.* 22: 2058, 1975.
2. F. Schamber, in T. G. Dzubay, Ed., *X-ray Fluorescence Analysis of Environmental Samples*, Michigan: Ann Arbor Sci. Publ., 1977, 241.
3. P. Statham, *X-ray Spectrom.* 49: 2149, 1977.
4. V. V. Raznikov, A. F. Dodonov, and E. V. Lanin, *Int. J. Mass Spectrom. Ion Phys.* 25: 295, 1977.

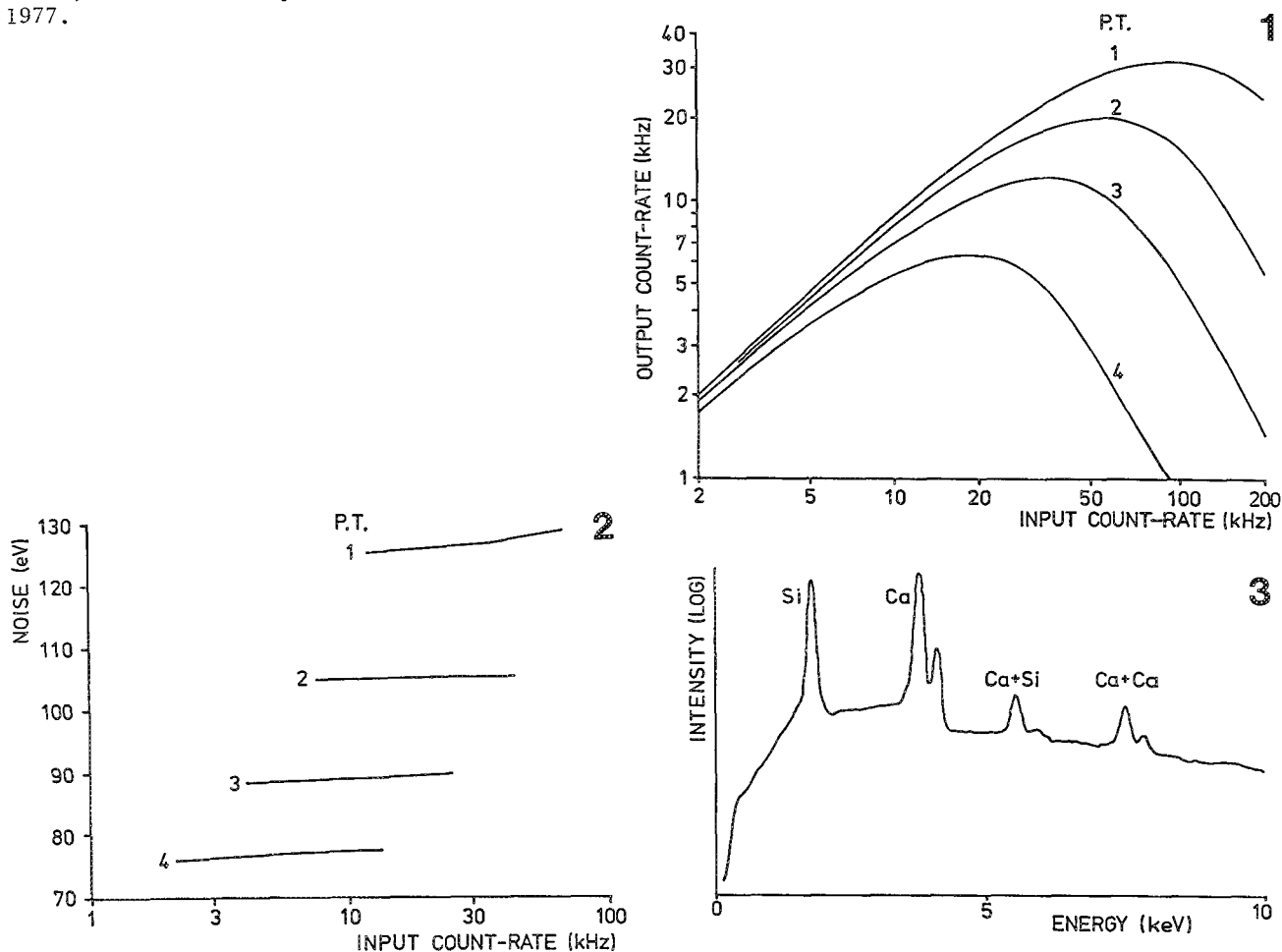


FIG. 1.--Output count rate as a function of input count rate for Link XP2 pulse processor, with various process times.
 FIG. 2.--Noise (FWHM of strobed noise peak) vs input count rate for various process times (Link XP2 pulse processor).
 FIG. 3.--Sum peaks in spectrum of wollastonite (CaSiO₃) recorded at 150 kHz input count rate.

AN EMPIRICAL TEST OF A THIN FILM DATA REDUCTION SCHEME FOR THE ELECTRON MICROPROBE: BiSrCaCu OXIDE THIN FILMS ON Si AND MgO SUBSTRATES

D. K. Ross, R. V. Heyman, and Don Elthon

Electron microprobe analysis is a mature technique for high-quality chemical analysis of solid materials. Accuracy and precision of 1% relative errors for major element components can be attained without great difficulty. One assumption on which this technique is based is that standards and samples are both of "infinite" thickness. That is, that the excited volume (x-ray emitting region) is entirely contained within the material analyzed for both standard and unknown. This assumption of "infinite" thickness is of course violated in the case of thin films. Attempts to analyze thin films must include equations for determining film thickness from observed x-ray production in order to permit quantitative solutions for film composition. Algorithms that solve for film thickness and composition, provide full

matrix corrections, and include light elements such as oxygen have only recently become available.¹

In this paper, we report our results of a test of a thin-film data reduction scheme by Waldo.¹ We have analyzed several BiSrCaCuO thin films at 15 kV accelerating potential. Substrate penetration was minimal, and ZAF matrix corrections yielded analyses with sums of 98 to 102%, indicating that these films can be treated effectively as bulk samples at 15 kV. The same films were re-analyzed using a beam energy of 30 kV. At this energy the substrate was strongly penetrated, based on high x-ray count rates for elements found only in the substrate and low totals for the film composition. This penetration permits comparison of results obtained with the film reduction scheme vs those obtained with ZAF and $\phi(\rho z)$ matrix corrections. Such a comparison makes it possible to assess the quality of results of the film reduction scheme. Use of the 15kV analyses as the known compositions of the films is justified because these analyses yielded good totals, low substrate count rates were observed, and $\phi(\rho z)$ modeling of the depth of x-ray generation

The authors are at the Texas Center for Superconductivity, University of Houston, Houston, TX 77204. Don Elthon is also at the UH Department of Chemistry, and D. K. Ross is also at the UH Department of Geosciences. This work was supported by DARPA under prime grant MDA 972-88-G-0002 and by the State of Texas

TABLE 1.--Conditions for analyses of thin films. Peak positions and background offsets (Bkgd.) are given in millimeters. Peak position is the distance from the x-ray source to the analyzing crystal⁹ and background offset is added or subtracted from this value.

Analytical Conditions - 30 kV

Element	Line	Order	Crystal	Peak Pos.	Bkgd.	Standard
Bi	L α	1	LIF	79 49	+6/-5	Bi ₁₂ GeO ₂₀
Sr	L α	1	PET	219 99	+4/-6	SrTiO ₃
Ca	K α	1	PET	107 63	+4/-4	CaMgSi ₂ O ₆
Cu	K α	1	LIF	107 23	+6/-4	Cu ₂ O
Pb	L α	1	LIF	81 77	+5/-5	PbCrO ₄
O	K α	1	LDE1	110 34	+20/-10	CaMgSi ₂ O ₆
Si	K α	1	TAP	77 28	+3/-2	CaMgSi ₂ O ₆
Mg	K α	2	TAP	215 07	+4/-4	CaMgSi ₂ O ₆

Analytical Conditions - 15 kV

Bi	M α	1	PET	164 21	14/-12	Bi ₁₂ GeO ₂₀
Sr	L α	1	PET	220 00	+4/-6	SrTiO ₃
Ca	K α	1	PET	107 63	+4/-4	CaMgSi ₂ O ₆
Cu	K α	1	LIF	107 41	+6/-4	Cu ₂ O
Pb	M α	1	PET	169 59	+2/-2	PbCrO ₄
O	K α	1	LDE1	110 30	+20/-10	CaMgSi ₂ O ₆
Si	K α	1	TAP	77 38	+15/-15	CaMgSi ₂ O ₆
Mg	K α	2	TAP	215 07	+3/-3	(Mg,Fe) ₂ SiO ₄

TABLE 2.--Compositions of thin films analyzed. For each sample 15kV composition (using the ZAF method and treating the film as a bulk sample) and 30kV composition (using the Waldo film routine and $\phi(\rho z)$ option B⁵) are given. Beam energy is given in kV. In column two, n is the number of points analyzed for each sample. Thickness is given in microns. Compositions are reported in weight %. Standard deviations quoted were calculated based on the variability in replicate analyses of each sample, not on single-measurement counting statistics alone.

Sample	n	beam energy	correction scheme	Bi	Sr	Ca	Cu	Pb	O	Total	Thickness Calculated
62989-1	7	15	ZAF	29.19	23.87	8.97	14.15	1.11	20.62	97.91	1.29
			1 s.d.	0.17	0.13	0.03	0.15	0.13	0.04		
	10	30	Waldo	28.31	25.30	7.37	14.53	1.56	22.99	100.06	
			1 s.d.	1.26	0.46	0.29	0.89	0.11	0.95		
62989-2	7	15	ZAF	29.02	23.84	8.63	14.58	1.05	20.92	98.04	1.11
			1 s.d.	0.15	0.11	0.04	0.08	0.04	0.16		
	10	30	Waldo	29.05	25.66	7.07	15.60	1.71	20.94	100.03	
			1 s.d.	1.31	0.53	0.10	0.55	0.09	0.83		
62989-3	7	15	ZAF	30.75	23.86	8.34	15.49	1.09	20.86	100.39	0.95
			1 s.d.	1.30	0.53	0.07	0.21	0.07	0.73		
	8	30	Waldo	30.68	23.83	6.75	15.13	2.21	21.43	100.03	
			1 s.d.	1.69	1.20	0.70	1.40	0.15	1.07		
62989-4	6	15	ZAF	31.33	21.18	7.93	16.72	2.56	20.12	99.84	0.78
			1 s.d.	0.35	0.27	0.03	0.17	0.20	0.46		
	10	30	Waldo	32.72	19.86	6.82	16.51	3.05	20.97	100.03	
			1 s.d.	0.41	0.27	0.10	0.35	0.10	0.36		
62989-5	7	15	ZAF	33.79	18.05	7.61	17.97	2.48	19.57	99.47	0.64
			1 s.d.	0.49	0.37	0.11	0.28	0.34	0.34		
	9	30	Waldo	31.38	18.39	6.49	16.16	2.95	24.65	100.02	
			1 s.d.	2.83	1.23	0.84	3.02	0.27	1.30		
62989-7	6	15	ZAF	32.63	17.30	9.91	15.93	2.84	19.02	97.63	0.61
			1 s.d.	0.18	0.18	0.15	0.07	0.10	0.14		
	8	30	Waldo	32.07	18.57	7.99	18.28	3.64	19.45	100.00	
			1 s.d.	1.82	0.53	0.74	1.62	0.19	1.99		
706Bd2	6	15	ZAF	49.16	16.32	5.27	14.02	0.46	14.73	99.96	1.00
			1 s.d.	0.76	1.39	0.21	0.14	0.26	1.46		
	8	30	Waldo	47.92	17.01	5.83	14.75	0.31	14.21	100.03	
			1 s.d.	1.98	1.23	0.41	0.47	0.24	3.20		

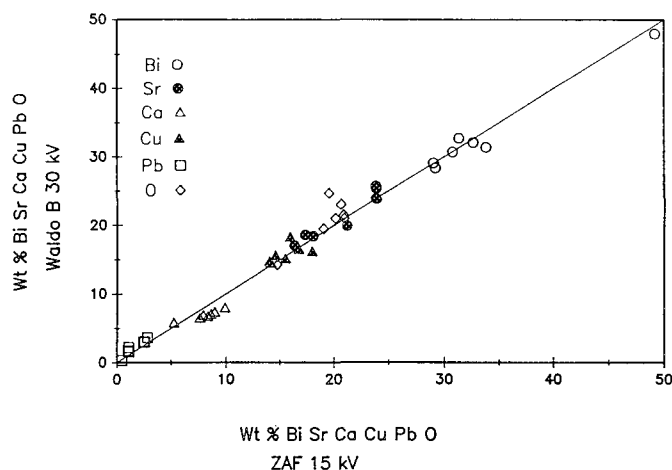


FIG. 1.--Thin film analysis results: 15kV analyses with ZAF matrix corrections (films treated as bulk samples) vs 30kV compositions with Waldo film reduction using $\phi(\rho z)$ option B⁵. Diagonal line is one-to-one line, along which data should lie if perfect agreement between the two data sets were achieved. These data and standard deviations for each element are shown in Table 2.

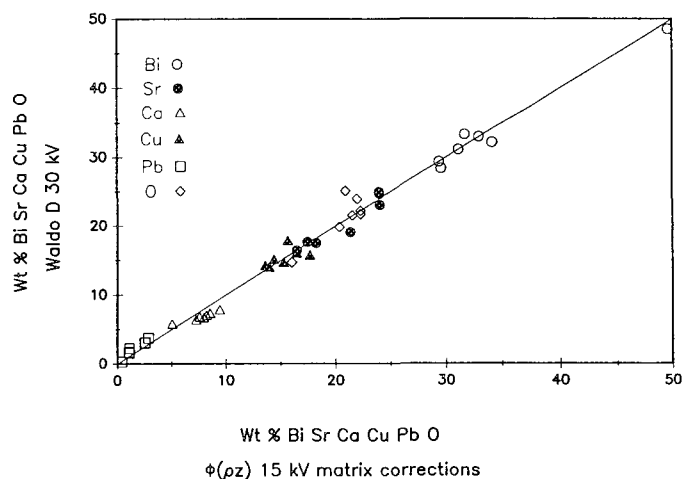


FIG. 2.--Same as Fig. 1 but with 15kV data using $\phi(\rho z)$ matrix corrections (again treating films as bulk samples) and 30kV data reduced with Waldo using $\phi(\rho z)$ option D⁵. In this case both data sets have been reduced with identical methods for calculating depth of x-ray generation. Agreement between the two data sets is slightly better than in Fig. 1. These data are shown in Table 3.

TABLE 3.--Compositions of films, based on the same set of observations as in Table 2, but with different matrix correction methods. PRZ is the $\phi(\rho z)$ method, again treating films as bulk samples at 15 kV. At 30 kV, the Waldo film routine was again used but with $\phi(\rho z)$ option D⁵.

Sample	beam energy	correction scheme	Bi	Sr	Ca	Cu	Pb	O	Total	Thickness Calculated
62989-1	15	PRZ	29 56	23 98	8.55	13.93	1.12	21.95	99 09	1 38
	30	Waldo D	28.42	24.70	7.36	14.04	1.58	23 95	100 05	
62989-2	15	PRZ	29 39	23 96	8.23	14.36	1.07	22 26	99.27	1 17
	30	Waldo D	29 38	24 97	7.07	15 15	1.74	21.72	100 03	
62989-3	15	PRZ	31 14	23.99	7.96	15.25	1.10	22.25	101.69	1 01
	30	Waldo D	31 15	23.06	6.72	14 71	2.26	22 21	100.11	
62989-4	15	PRZ	31.71	21 31	7 57	16 43	2.59	21 49	101 10	0 86
	30	Waldo D	33 36	19 08	6.85	16 06	3 13	21 53	100 01	
62989-5	15	PRZ	34 17	18 19	7 26	17.63	2.51	20.92	100 68	0 68
	30	Waldo D	32 21	17.47	6 39	15 77	3 05	25 12	100 01	
62989-7	15	PRZ	32 98	17.42	9 44	15.63	2 87	20 33	98 67	0 65
	30	Waldo D	33 02	17.64	7 88	17.88	3 77	19 82	100 01	
706Bd2	15	PRZ	49 59	16.44	5 06	13.59	0 40	16.01	101 09	1 05
	30	Waldo D	48 52	16 41	5 80	14.30	0.30	14 69	100 02	

in these films at 15 kV indicates that they are thick enough so that over 95% of the excited volume is contained within the film.

The Waldo thin film routine¹ allows a choice from among several $\phi(\rho z)$ models.²⁻⁶ All these models have been used to reduce the observed x-ray intensities from these films. We can say for these materials which of the various $\phi(\rho z)$ options best reproduces the 15kV results.

Experimental Methods

The results reported here were obtained with a JEOL JXA-8600 Superprobe equipped with four wavelength-dispersive spectrometers (WDS) and one energy-dispersive spectrometer (EDS). Quantitative results on thin films were all obtained by WDS analysis. Both 15 and 30kV data were obtained with a beam current of 20 nA. Peak intensities were measured for 100 s for all elements. The films analyzed were reasonably smooth and flat. These films are conducting so that no conductive coating was necessary. However, all standards are carbon coated. This is a possible source of error, although the same uncoated films were analyzed at 15 and 30 kV so that the test attempted here should not be affected. On-line data reduction by ZAF matrix corrections was used for the 15kV data. The 15kV data were also reduced by the $\phi(\rho z)$ technique off line. The version of $\phi(\rho z)$ available from Tracor Northern⁵ is also available in the Waldo program, so that a direct comparison of results with identical methods of calculating depth of x-ray generation was possible. The Waldo film reduction scheme was used to convert

x-ray k-ratios into compositions off line. The Tracor Northern reduction routines utilize the Henke et al.⁷ calculation of mass-absorption coefficients for x-ray energies below 1 kV and the Heinrich⁸ method for energies above 1 kV. (Waldo uses Heinrich.)

A total of ten films were analyzed during this project, seven of which were thick enough to be treated as bulk samples at 15 kV. Of the ten samples, three were deposited on MgO substrates, seven on Si metal substrates. The films deposited on Si substrates were made as superconductor precursors and would require annealing to form superconducting compounds. The films deposited on MgO substrates had been annealed. Analytical conditions for 30 and 15kV measurements are summarized in Table 1. Substrate x rays were monitored in order to gauge the extent of substrate excitation.

Results

The films investigated in this report are composed of Bi, Sr, Ca, Cu, Pb, and O. Compositions of thin films are tabulated in Tables 2 and 3. These data are plotted in Figs. 1 and 2. In Fig. 1, 15kV ZAF compositions are plotted against 30kV Waldo reduced compositions. The 30kV data shown in Fig. 1 were calculated from $\phi(\rho z)$ option B⁵, one of the five included in the Waldo film routine. The data resulting from this option are tabulated in Table 2. This option is used because it provided the closest match to the 15kV ZAF bulk analyses. The 15kV data were also reduced using the $\phi(\rho z)$ method (again treating the films as bulk

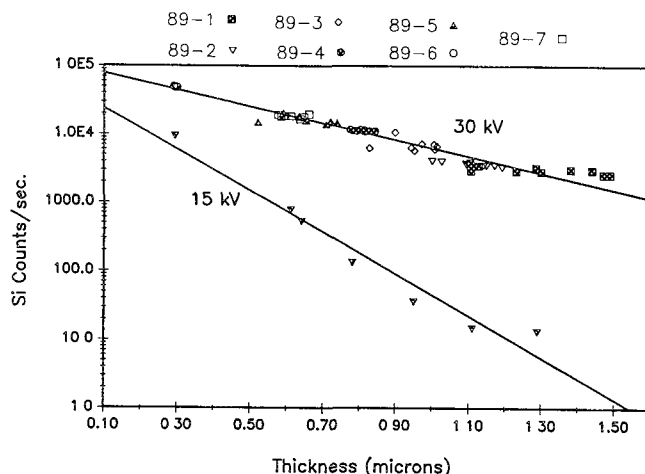


FIG. 3.--Substrate count rate vs film thickness for films on Si metal substrates (as calculated by Waldo program using $\phi(\rho z)$ option B³). Thickness was calculated from 30kV data. Average thickness was plotted against average substrate count rate for 15kV data. Note logarithmic scale on y axis.

samples). These data are plotted in Fig. 2 vs 30kV Waldo compositions, based on $\phi(\rho z)$ option D⁵, which provided the best match in this case.

The closeness of the match between the two data sets was determined by summing of the absolute value of the deviations of 30kV data from 15kV data, for each of the five $\phi(\rho z)$ options. The option that gave the smallest sum was chosen as the best match. The diagonal lines in Figs. 1 and 2 are the one-to-one lines along which all data would fall if there were perfect agreement between the two data sets. The largest relative errors in these data occur for Ca and Pb. Ca tends to be consistently low at 30 kV and Pb consistently high relative to the 15kV results. The differences in these two elements are often outside of uncertainties. For the remaining elements the differences are generally within uncertainties. Standard deviations calculated from repeated analyses of each film are reported in Table 2. The quoted standard deviations are often much larger in the 30kV results. Films were analyzed at 15 kV first and it is believed that degradation in the quality of the film surfaces due to exposure to the atmosphere and/or the electron beam is the cause of the much greater variability seen in the 30kV data set.

Film thicknesses as calculated by the Waldo routine are reported in Table 2 and in Table 3. The different thicknesses for samples shown in Table 2 vs Table 3 result from use of different $\phi(\rho z)$ models. These models yield differences in thickness of approximately 5 to 10%. The films have thicknesses that range from about 0.60 to 1.4 μm . Modeling of the depth of x-ray generation using $\phi(\rho z)$ methods shows that over 95% of x rays for all elements in the films occurs in the upper 0.60 μm at 15 kV, which supports the treatment of these films as bulk samples at this energy.

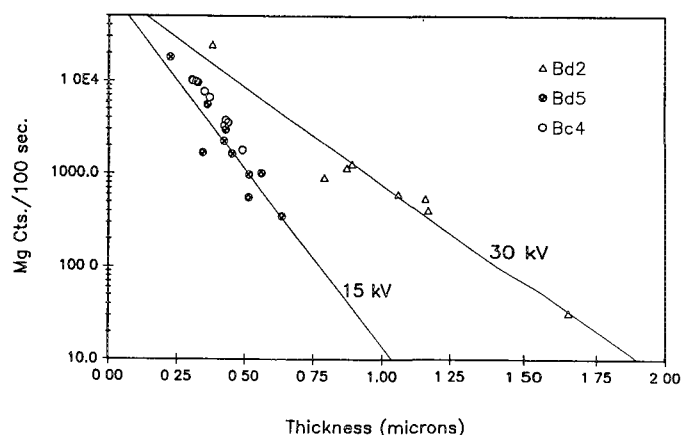


FIG. 4.--Substrate counts vs calculated thickness for three films on MgO substrate. Sample Bd2 alone was thick enough to permit treatment as bulk sample at 15 kV. Mg substrate counts were measured at 2nd-order Mg K α position in order to avoid Bi overlap at the 1st-order position.

Figure 3 shows the intensity of x rays emitted by Si from the substrate vs film thickness as calculated by the Waldo routine. Si intensity is negatively correlated with film thickness, as one would expect. Electron energy is progressively dissipated as the film is penetrated, decreasing the likelihood of exciting the substrate in thicker films. In addition, as film thickness increases the likelihood of absorbing substrate x rays increases. Si intensity increases as beam energy increases because the ability of electrons to penetrate and excite the film increases with beam energy. Similar features are seen in Fig. 4, a plot of Mg intensity vs film thickness for films deposited on MgO substrates.

Discussion

Examination of Figs. 1 and 2 shows that good agreement was achieved between the 15 and 30kV measurements. This result provides some measure of confidence that the film routine used here can be used to analyze other thin-film samples with the electron microprobe, and that results obtained are reasonably accurate. However, it is clear that more tests of this sort must be completed and published to provide greater confidence in film analyses of complex materials with the microprobe. In the study reported here, only one of the samples has any elements in both the film and the substrate. Sample 706Bd2 has oxygen in the film and the substrate (MgO). The thickness of this sample was great enough so that no oxygen x rays generated in the substrate could escape from the film because of strong absorption. This is shown by $\phi(\rho z)$ modeling of the depth of x-ray generation for the elements in this sample. Oxygen is so strongly absorbed that it is emitted only if it is generated in the upper

0.35 μm of the sample. This film has an average thickness of 1.0 μm . In the case of a much thinner film, with elements in common with the substrate, the data reduction becomes more complicated; this situation has not been tested in the study reported here.

References

1. R. A. Waldo, "An iteration procedure to calculate film compositions and thicknesses in electron-probe microanalysis," *Microbeam Analysis--1988*, 310.
2. G. F. Bastin, F. J. J. van Loo, and H. J. M. Heijligers, "Evaluation of the use of Gaussian $\phi(\rho z)$ curves in quantitative electron probe microanalysis: A new optimization," *X-ray Spectrometry* 13: 91, 1984.
3. G. F. Bastin, H. J. M. Heijligers, and F. J. J. van Loo, "A further improvement in the Gaussian $\phi(\rho z)$ approach for matrix correction in quantitative electron probe microanalysis," *Scanning* 8: 45, 1986.
4. G. F. Bastin and H. J. M. Heijligers, "Quantitative electron probe microanalysis of ultra-light elements (boron-oxygen)," NBS workshop, Gaithersburg, Md., 1988.
5. G. F. Bastin and H. J. M. Heijligers, *Quantitative Electron Probe Microanalysis of Boron in Binary Borides*, Internal report, University of Technology, Eindhoven, Netherlands, 1986.
6. R. Packwood, "Electron probe quantitation and automation," *Microbeam Analysis--1986*, 268.
7. B. L. Henke, P. Lee, T. J. Tanaka, R. L. Shimabukuro, and B. K. Fujikawa, "Low energy x-ray interaction coefficients: Photoabsorption, scattering and reflection," *Atomic and Nuclear Data Tables* 27: 1, 1982.
8. K. F. J. Heinrich, "Mass absorption coefficients for electron probe microanalysis," *Proc. 11th IXCOM* 67: 1, 1982.
9. *X-ray Emission and Absorption Wavelengths and I-value Tables*, JEOL.

A STUDY OF DIFFUSION ZONES WITH ELECTRON MICROPROBE COMPOSITIONAL MAPPING

R. B. Marinenko, D. S. Bright, C. A. Handwerker, and J. J. Mecholsky Jr.

Electron microprobe x-ray compositional mapping has been used to study diffusion zones between metal-metal and glass-metal interfaces. Image analysis techniques including gray-level enhancement, product and quotient images, and concentration-histogram images have proved to be extremely useful in visualizing the extent of diffusion. The qualitative and quantitative information provided by these digital acquisition and display techniques far exceeds what conventional line-scan and x-ray dot maps could provide.

Metal-metal Interface

As part of a study of the ancient fabrication techniques¹ used by the Esmeraldas-Tumaco Pacific coast people of present-day Ecuador and Colombia to make platinum-gold objects and adornments, some gold-platinum diffusion couples were fabricated and studied with electron microprobe x-ray compositional mapping. The first of these specimens was prepared by sandwiching of a gold sheet about 40 μm wide between two platinum sheets. The specimen was annealed for 3 min at 1350 C, then quenched. The wavelength-dispersive (WDS) concentration map^{2,3} for gold in this specimen is shown in Fig. 1(a). Because of the high background from the high gold concentration, the diffusion of the platinum into the gold is hardly visible in a conventional image presentation when a linear ramp (in which pixel intensity corresponds linearly to concentration) is used to display this image. To enhance the visibility of the diffusion zone, a dual ramp was applied (Fig. 1(b)). This image-display technique expands the gray-level range of the display scale of the low-intensity pixels and decreases the range for the high-intensity pixels. Most of the pixels in the diffusion zone are then displayed at a lower gray-level intensity, leaving only the few pixels corresponding to the highest gold concentrations to be displayed at the highest gray-level intensities. The gold region into which the platinum has diffused now becomes clear.

The annealing temperature (1350 C) used for

this sandwich specimen was sufficient to melt the gold (m.p. 1064 C) but not the platinum (m.p. 1769 C). Figures 2(a) and (b) are the concentration maps for gold and platinum, respectively; Figs. 2(c) and (d) are the product and quotient images of the concentration maps. Figure 2(c) is a scaled image obtained after the corresponding pixels of the two elemental images are multiplied; Fig. 2(d) is formed by division of the corresponding pixels of the gold by the platinum image. The product image (Fig. 2c) defines the regions where both elements coexist at the highest concentrations, i.e., where the greatest amount of diffusion has occurred; the quotient image (Fig. 2d) defines the region where the gold concentration is highest. From Fig. 2(c) platinum appears to have diffused up to 15 μm into the gold layer during the heating process. The average concentration of gold in the center region is about 79.6 wt% and the platinum in this region is about 19.4 wt%. These values were obtained by sampling of several randomly selected pixels in this region of the gold and platinum maps. (The total is slightly less than 100% because no attempt was made to sample corresponding pixels in this inhomogeneous region.) Since up to 20 wt% platinum is soluble in liquid gold at 1350 C, the hypothesis is that the platinum diffused into the molten gold during the annealing process and that the excess platinum, which is adjacent to the pure platinum, precipitated during the cooling process.

Two other Au-Pt alloys were formed by the wrapping of gold wires around platinum wires. The overall composition on an atomic basis was 15% platinum and 85% gold. The first of these specimens was heated from room temperature to 1100 C in 2 min, then held at 1100 C for 3 min before water quenching. The second specimen was heated to 1200 C in 2 min, held at that temperature for 7 min, then water quenched. The resulting alloys can be seen in Figs. 3 and 4, respectively. The two processes have produced different microstructures and composition distributions that are particularly visible in the lower images (c and d) of each figure. These lower images are histogram equalized.^{4,5} Rather than using a linear ramp such as is used in the top images (a and b) of each figure, we adjusted the pixel intensities up or down (still keeping them in order) to create the intensity histogram of the pixels as flat as possible, so that equal brightness intervals (regardless of location) correspond to equal areas of the image. Histogram equalization is a good method for bringing out visual detail when contrast is low over much of the image area. We achieved histogram equalization by calculating the cumulative histogram; scaling

R. B. Marinenko and D. S. Bright are at the Center for Analytical Chemistry and C. A. Handwerker is at the Materials Science and Engineering Laboratory, National Institute of Standards and Technology, Gaithersburg, MD 20899; J. J. Mecholsky Jr. is at the Department of Material Science and Engineering, University of Florida, Gainesville, FL 32611. Thanks to W. Anokye and H. Schaeffer for preparing the glass-metal specimens for analysis. The glass-metal interface research was supported in part by an Army Research Office grant DAAL03-86-K-0123.

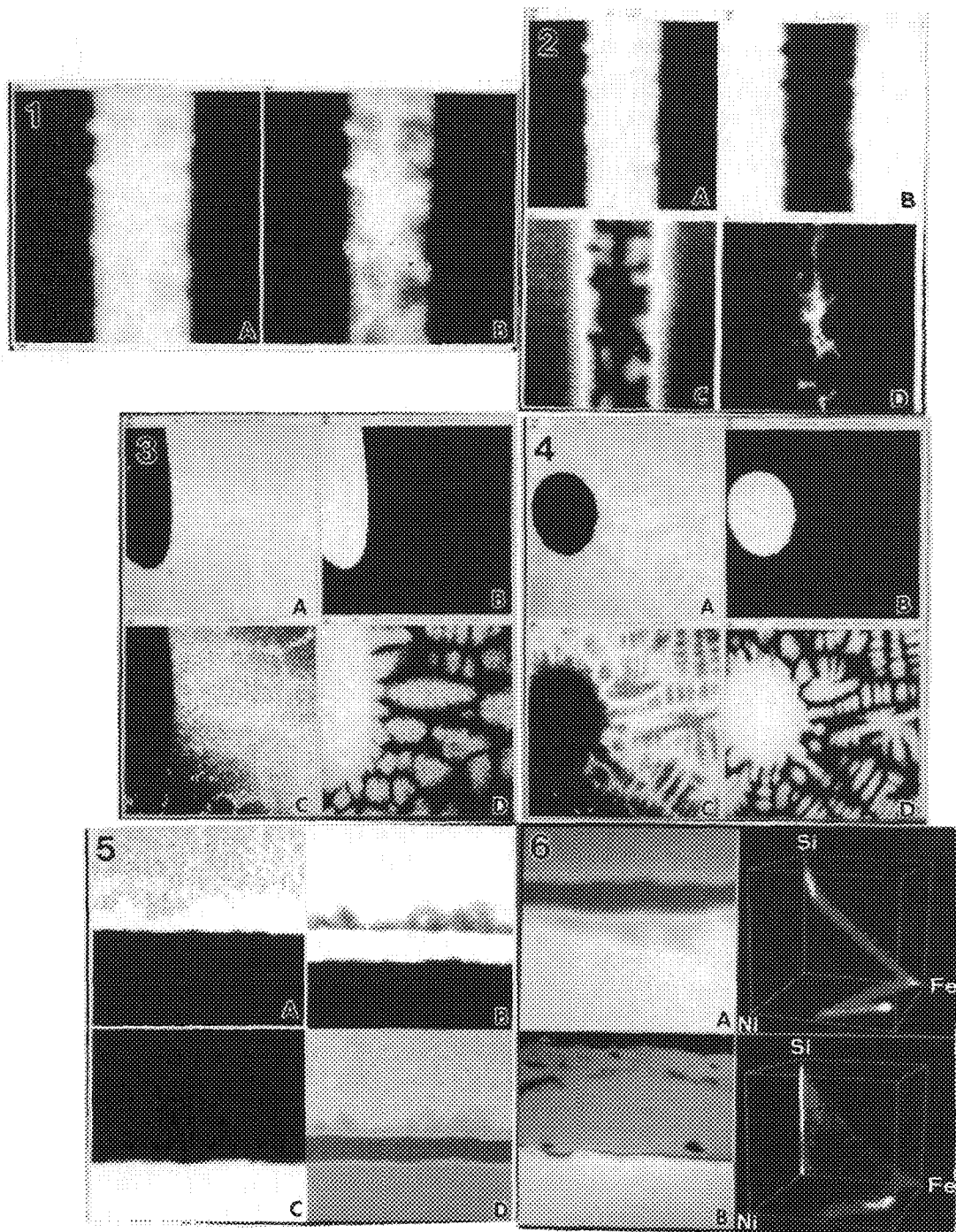


FIG. 1.--WDS concentration map of Au sandwiched between two Pt sheets, 107 μm wide: (a) Au $\text{M}\alpha$ concentration map, (b) enhanced dual-ramp image of (a). Maps taken at 15 kV, 15 nA, 64×64 pixels.

FIG. 2.--(a) Au $\text{M}\alpha$ concentration map as in Fig. 1, (b) Pt $\text{M}\alpha$ concentration map, (c) the product of maps (a) and (b), (d) quotient of maps (a) and (b).

FIG. 3.--15Pt-85Au alloy annealed at 1100 C. Concentration map for (a) Au $\text{M}\alpha$, (b) Pt $\text{M}\alpha$. Histogram-equalized images of (c) Pt, (d) Au. Maps taken at 15 kV, 125 nA, 128×128 pixels, 240 μm wide.

FIG. 4.--15Pt-85Au alloy annealed at 1200 C, same as in Fig. 4.

FIG. 5.--Glass-metal interface, original EDS maps, 23 μm wide. (a) Ni $\text{K}\alpha$, (b) Fe $\text{K}\alpha$, (c) Si $\text{K}\alpha$, (d) overlay of all three element maps.

FIG. 6.--Original WDS maps of glass-metal interface: overlays of Ni, Fe, and Si. (a) 25 μm wide, (b) 125 μm wide. To the right of each map is corresponding concentration histogram image (CHI).

these values linearly as is normally done with pixel values, using the original image pixel values as indices to the histogram; and applying the scale values of the histogram as pixel values in the equalized image. The brightness values are not linear with pixel number, but they are monotonic; that is, if area A is brighter than area B in the original image, it will also be brighter in the equalized image, but not necessarily by the same amount. Such a transformation is qualitatively useful for image enhancement, but the original unmodified concentrations must be used for quantitative comparisons.

Metal-glass Interface

The interface region between a Kovar metal alloy and a borosilicate glass (Corning Glass 7056) is being studied to determine whether diffusion across the boundary of the two different materials occurs and whether the extent of diffusion has any effect on the bonding strength of the two materials. The nominal compositions of the Kovar alloy and the Corning glass are listed in Table 1.

The metal in the specimen studied here (Figs 5 and 6) was preoxidized in a nitrogen-oxygen atmosphere at 800 C for 30 min, forming an oxide layer on the metal surface. Sealing of the metal to the glass was done at 800 C for 10 min. Original (uncorrected) energy-dispersive (EDS) maps were obtained for nickel (Fig. 4a), iron (Fig. 5b), and silicon (Fig. 5c). The map in Fig. 5(d) is an overlay of the three element maps. These maps show that iron has diffused from the Kovar alloy toward the metal-glass interface, leaving behind a region high in nickel, while forming an iron-rich zone at the interface of the two materials. Maps for cobalt, aluminum, and potassium were recorded simultaneously but are not displayed here. The cobalt distribution is similar to nickel (i.e., a region enriched in cobalt remains in the Kovar alloy), and aluminum and potassium appear to be homogeneously distributed in the glass similar to silicon. The remaining elements (oxygen, boron, lithium, and sodium) were not mapped because of sensitivity limitations in EDS.

Concentration histogram images (CHI) are used to show the frequency distribution of pixel values (or concentrations) in a map.⁶ The maps in Figs. 6(a) and (b) are WDS overlays of nickel, iron, and silicon. Map (a) is about 25 μ m on an edge, map (b) is about 125 μ m on an edge. The corresponding CHIs are to the right of each image. The iron is plotted along the horizontal (y) axis; silicon along the vertical (z) axis; and nickel along the (x) axis, perpendicular to the image plane. The white regions in the CHIs correspond to a high pixel frequencies, i.e., regions where there are a lot of pixels in that concentration range. In these images, the silicon-rich pixels along the z axis correspond to the silicon in the glass. Iron is associated with silicon across the back plane, which corresponds to the diffusion zone ending in an iron-rich region at the bottom right corner.

TABLE 1.--Nominal compositions (weight percent).

Kovar Fe-Ni-Co, alloy		Corning 7056 Borosilicate glass	
Fe	53.48	SiO ₂	68
Ni	29	B ₂ O ₃	18
Co	17	Al ₂ O ₃	3
Mn	0.3	Li ₂ O	1
Si	0.2	Na ₂ O	1
C	0.02	K ₂ O	9

Iron is also associated with nickel on the bottom plane, where the highest density for both elements corresponds to the Kovar alloy. The highest nickel concentration in this plane is low in iron (corresponding to the iron-depleted zone in the Kovar alloy), and the part of the trace going to the iron-rich back plane corresponds to the iron-enriched zone adjacent to the glass. Nickel has apparently not diffused and shows no association with silicon. Quantitation of the maps showed that the iron and nickel concentrations are 51-53 wt% and 27-30 wt%, respectively, in the Kovar alloy; in the iron-depleted zone the iron concentration is 29-33 wt% and nickel is 38-43 wt%.

Conclusion

Compositional mapping with the electron microprobe is a useful technique for the study of diffusion zones. With digital map storage and subsequent image analysis, qualitative and quantitative information about the diffusion zones becomes readily available. Enhancement techniques using dual ramp images, product and quotient images, and histogram-equalized images are helpful for visualizing the extent of diffusion, especially when the effect of diffusion is a small signal above a high background signal. The CHIs give a clear visualization of the frequency distribution of pixel intensities or concentrations as well as the relationship between elements.

References

1. C. A. Handwerker et al., "Fabrication of Pt-Au alloys in pre-Hispanic South America: Issues of temperature and microstructure control," *Mat. Issues in Art and Arch.* (in press).
2. R. B. Marinenko et al., "Digital x-ray compositional mapping with 'standard map' correction for wavelength dispersive spectrometer defocussing," *J. Microsc.* 145 (pt 2): 207, 1987.
3. R. B. Marinenko et al., "Defocus modeling correction for wavelength-dispersive digital compositional mapping with the electron microprobe," *J. Microsc.* 155 (pt 2): 183, 1989.
4. J. C. Russ, *Practical Stereology*, New York: Plenum Press, 1986.
5. A. Rosenfeld and A. C. Kak, *Digital Picture Processing*, New York: Academic Press, 2d ed., 1982, vol. 1, 2.
6. D. S. Bright et al., *Microbeam Analysis --1988*, 18.

COMPUTER-ASSISTED WAVELENGTH-DISPERSIVE X-RAY MAPPING

W. F. Chambers and J. H. Doyle

Elemental x-ray maps frequently provide one of the best ways to display compositional gradients and inhomogeneities in a sample. Two problems consistently plague the effective use of elemental x-ray mapping: proper exposure and the maintenance of x-ray focus. Solutions applicable to Cameca MBX microprobes have been previously reported.^{1,2} These solutions involve aligning the X axis of the electron beam raster parallel to the insensitive axis of the analyzing crystal and synchronously scanning the spectrometer with the Y axis of the electron beam raster to maintain x-ray focus. The capability of the Cameca to set the beam current via an external computer was also utilized.

We have recently needed to duplicate these capabilities on JEOL microprobes. JEOL and MBX instruments differ in three important aspects relating to their x-ray mapping capability. First, although JEOL instruments can read the beam current, they lack the capability of setting it via an external computer. Second, the lowest magnification available on an MBX is 100×; the lowest available on a JEOL is 40×. Third, Cameca uses no slits on its x-ray detectors, whereas JEOL increases its spectrometer resolution by using slits.

The problem of determining acceptable beam current-exposure setting combinations has been resolved by having the computer calculate the beam current that would be required for each of the possible scan speeds to give a predetermined number of counts on the image if the specified element is uniformly present in the sample at the indicated concentration. The desired number of counts (normally 600 000 or 1 000 000) and the possible scan times are constants that are input at configuration time for the operating program, TASK8.³ Since the TASK8 element table contains the count rate expected from pure elements or oxides of the element or oxide of interest, calculating the required beam current for a given scan time reduces to

$$I = C / (SI * ST * k)$$

where I is the required beam current in nanoamperes, C is the desired number of counts, SI is

W. F. Chambers performed this work while at The Chemical Instrumentation Research Division 1821, Sandia National Laboratories, Albuquerque, NM 87185. (He is now in the Repository Performance Assessments Division 6312.) J. H. Doyle, now at Materials and Process Reliability Group, Storage Technology Corp., Louisville, CO 80028-2166, was at Physical Metallurgy Research Division, EG&G Rocky Flats Plant, Golden, CO 80401. This work was supported by U.S. Department of Energy under Contracts DE-AC04-76DP00789 and DE-AC04-76DP03533.

JEOL Low Mag Mapping Setup PUSH CANCEL TO PROCEED

Element name = **SI3**
 Magnification = **50 X**
 Desired exposure setting is **100 %**
 Exposure time = **60 sec**
 Set current to **7.46 nA**
 For 30 sec. exposure use *14.92 nA*
 For 60 sec. exposure use *7.46 nA*
 For 120 sec. exposure use *3.73 nA*
 For 360 sec. exposure use *1.24 nA*
 Mag. cutoff for rotation **500 X**
 % on CRT is **ENABLED**

Computer control using STAGE Z-AXIS

FIG. 1.--Menu used to set parameters for low-magnification x-ray mapping. Bold values are user specified, *italic* values are program calculated

the count rate in counts/s-nA for a 100% standard of the element or oxide of interest, ST is the scan time in seconds, and k is the desired k-ratio. The possible beam currents are displayed in menu form along with the element to be mapped, the desired magnification, the desired k-ratio to produce the optimum exposure, and the selected exposure time (Fig. 1). The command to initiate the menu is PHOTO SI3, which indicates that a map of Si should be taken by use of spectrometer No. 3. Possible beam current--exposure time combinations are color coded. White indicates an acceptable combination that does not correspond to the present beam-current setting of the instrument. Blue indicates a combination corresponding to the present beam current. Yellow indicates a potentially usable beam current but one that is high enough so that it should be used with extreme caution. Red beam currents are high enough so that the system will have difficulty focusing and may damage the sample. The menu also offers an option of displaying the exposure setting on the image and of selecting computer control by either spectrometer or stage z-axis motion.

In our early low-magnification x-ray mapping attempts on the JEOLs, we duplicated the synchronously scanned spectrometer techniques developed on the Camecas. We found that the spectrometer slits limited our capability to maps of greater than 100× magnification. In an attempt to lower this limit we decided to investigate the possibility of maintaining x-ray focus by driving the z axis, thereby dynamically altering the sample height. As in the case

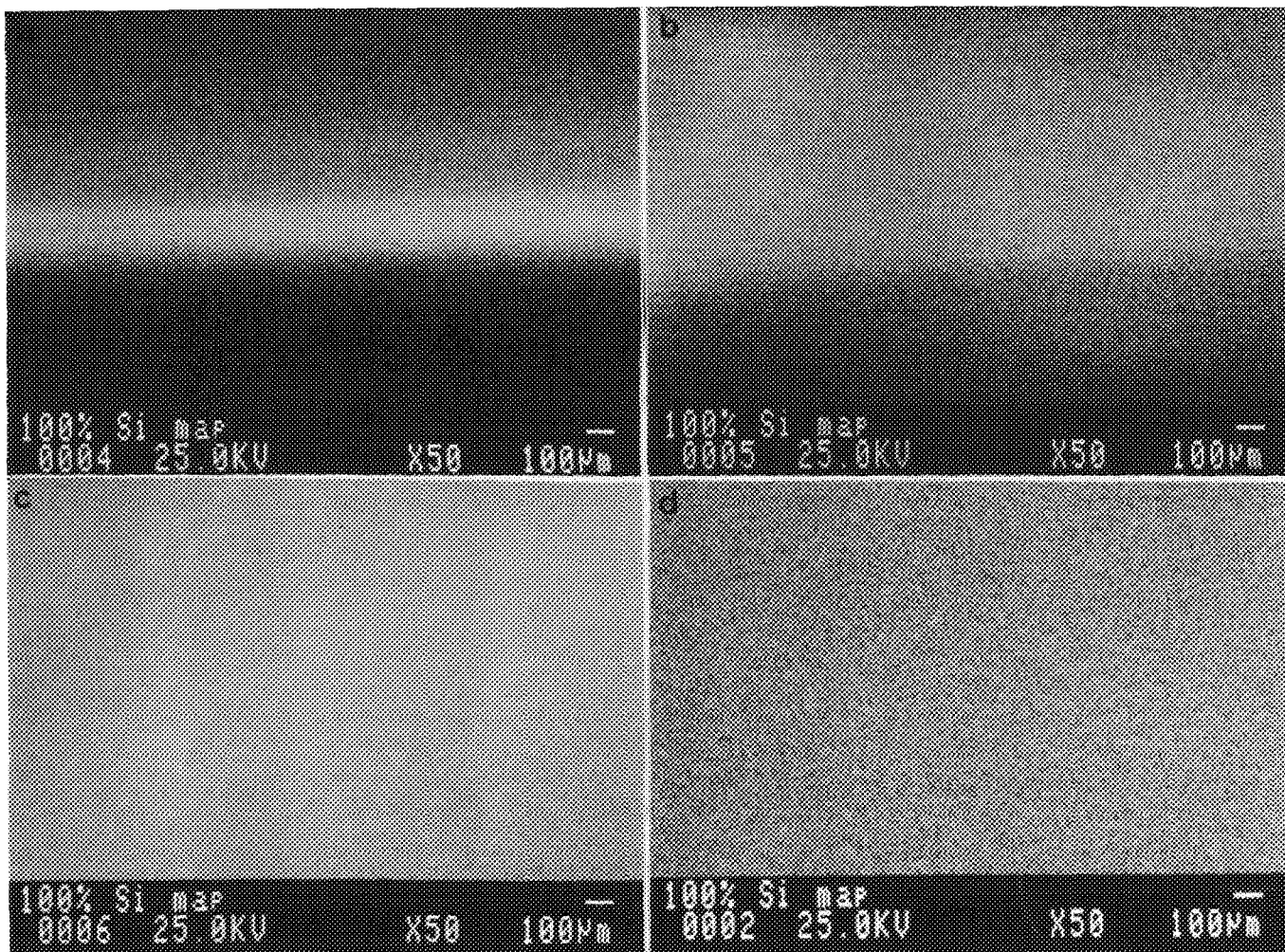


FIG. 2.--Low-magnification Si x-ray map, original magnification 50 \times . (a) No computer control, 550 μ m detector slits; (b) computer control of spectrometer, 550 μ m detector slits; (c) complete control of stage z axis, 550 μ m detector slits; (d) computer control of spectrometer, no detector slits.

of the spectrometer drive, the x axis of the electron beam raster was oriented parallel to the insensitive axis of the crystal. We were pleased to find that usable x-ray maps were obtainable down to magnifications as low as 40 even when the detector slits were inserted. Furthermore, the simple equation

$$Z = Z_0 + 40 [1 - (2T/ST)]M \quad M \geq 40$$

where Z_0 is the initial position of the stage, M is the magnification, T is time, and ST is the total scan time, satisfactorily describes the required offset of the stage z-axis as a function of the scan time. We found that effects of the crystal position in the spectrometer were secondary and did not include them in our equation.

In operation, once the magnification, desired exposure setting, and exposure time are input and the beam current and scan rotation are set, the computer positions the spectrometer, sets detector bias and pulse height analyzer baseline and window values, sets the magnification and labels the map with the element name if column automation is present, lowers the stage, starts the scan, and dynamically raises the z axis of the stage during the scan.

Once the map is complete, the stage is repositioned to its normal optical focus point. Figs. 2 (a)-(c) provide a comparison of the results of using no computer control, spectrometer scanning, and stage z-axis scanning. Each figure is an Si x-ray map collected at an original magnification of 50 \times , using a 550 μ m slit with the detector. If the slit is removed, the image from the spectrometer scan is usable as shown in Fig. 2(d); however, the image shows a periodic variation that is due to imperfectly tracking the narrow Si x-ray peak. Although the technique described here uses the analog scan circuitry of the JEOL, a similar technique has been developed that uses digital scanning circuitry.

References

1. W. F. Chambers, *Microbeam Analysis--1978*, 87.
2. W. F. Chambers and J. H. Doyle, *J. Physique* 45 (Suppl. 2): C2-223, 1948.
3. W. F. Chambers and J. H. Doyle, *SANDIA TASK8, Version C: A Subroutined Electron Microprobe Automation System*, Sandia Report SAND90-1703, 1990.

QUANTITATIVE INFORMATION FROM X-RAY IMAGES OF GEOLOGICAL MATERIALS

J. M. Paque, Ray Browning, P. L. King, and Pierro Pianetta

Geologists are commonly confronted with samples containing many minerals (phases), each mineral with a multiple element composition. To answer question such as the origin and evolution of the earth, the genesis of ore deposits, or the source regions of petroleum products, researchers require knowledge of the chemical characteristics of rock samples and their constituent minerals.

This paper presents a method of obtaining quantitative chemical information rapidly from multiple x-ray elemental images. Scatter plots and principal-component analysis quickly yields quantitative information concerning the composition and spatial location of minerals in a sample.

A complete analytical description of a geological sample should give the number of phases present, the volume occupied by each phase in the bulk sample, and the average and range of composition of each phase.¹ Existing quantitative methods do not permit this information to be obtained easily and accurately through a single analytical method. A practical approach to providing such a complete description is from analysis of multi-elemental x-ray images. An example is given to illustrate the procedure.

Conventional Approach

Several methods can be used to obtain bulk compositions of samples. The sample can be pulverized and analyzed by wet chemistry or x-ray fluorescence, but once it is ground up, information on the individual constituents is lost. Another method involves analyses of large areas on a sample by use of the electron microprobe ("defocused beam"). However, matrix correction procedures are based on homogeneous samples and often cannot be applied to these analyses.²

One procedure commonly employed by geologists involves preparation of a 30 μ m thin section of the sample to be examined. The sample is viewed with a polarizing microscope and mineral identification is done over a grid pattern, by a tally of the total number of occurrences of each mineral. Once the percentage of each mineral is ascertained, point analyses on the electron microprobe permit calculation of the bulk composition. This procedure suffers several drawbacks: (1) it is very time consuming and hard on the eyes; (2) the results depend heavily on the operator's expertise in optical mineralogy; (3)

(3) the statistical errors are large because the time involved to identify points on a finely spaced grid is prohibitive; and (4) the system breaks down if any of the minerals is not homogeneous, a common situation in natural materials. In addition, one can get information on the range of composition of an individual phase only through numerous individual point analyses using the electron microprobe. This point-counting procedure can also be automated through the use of the electron microprobe, with identification of phases determined from short-count-time energy-dispersive analysis.¹

X-ray Image Processing Approach

With recent advances in the speed and storage capabilities of personal and laboratory computers, large quantities of data can be efficiently manipulated. Commercial software and hardware available at present allow simultaneous collection and storage of multiple x-ray images from a sample (up to 15 for the Kevex Delta system). Thus, x-ray images of most or all of the detectable elements in a sample can be collected.

Simple examination of the x-ray images can provide a lot of information about a sample. However, an element such as Si may be present in several minerals, sometimes with a different concentration in each mineral, or else similar concentrations in two phases. Graphical and statistical techniques, including histograms, scatter plots, and principal-component analysis (PCA) can yield insight into mineral phase composition and the distribution of minerals within a sample.

Obtaining quantitative information from x-ray images is not a new approach;³⁻⁵ however, previous methods have focused on performing the matrix correction at each individual picture element (pixel) in the image. To improve signal-to-background ratios, some researchers have used wavelength-dispersive spectrometry (WDS) rather than EDS for this work.^{3,4}

Procedure

The x-ray system used in the experiment described below is a Kevex Delta System that can collect up to 15 images simultaneously and include either a backscatter or secondary electron image. The image size collected was 128 by 128 pixels.

The elements present in the sample are determined by energy-dispersive x-ray spectroscopy (EDS), and multiple x-ray maps are then collected for the elements of interest. EDS and/or WDS can be used, with the parameters of dwell time at each pixel and count rate determining the precision in the analysis. The

J. M. Paque is with the Center for Materials Research and Geology Department; Ray Browning, Center for Integrated Systems; and P. L. King and Pierro Pianetta, Stanford Synchrotron Radiation Laboratory; all at Stanford University, Stanford, CA 94305.

file with the raw data is transferred to a personal computer via a communication program by the Kermit file transfer protocol. A PC-DOS computer (IBM AT class) with a 80386 processor (20 MHz), 1 megabyte of random access memory (RAM), and an EGA monitor is used to process the data. (Computers with an 80286 processor are also fast enough to run the software.) Data files produced by the Kevex Advanced Imaging program are read directly by the software without any modification.

The software on the PC-DOS computer displays the original x-ray (or backscatter or secondary electron) images, histograms of intensity vs counts, and scatter plots of the intensity of element vs the intensity of another for each pixel. For statistical manipulation (principal-component analysis) and phase partitioning, data are currently transferred to another computer that only handles a matrix of 64×64 pixels; every other pixel is discarded. Work is proceeding to integrate all aspects of the image analysis process except data acquisition onto a single personal computer.

To illustrate what data can be obtained we present an example from the carbonaceous chondritic meteorite Efremovka. The backscatter electron image of the area studied is shown in Fig. 1. The minerals in this sample (Table 1) have also been characterized by point analyses using the microprobe. This fairly simple sample consists of five major minerals and one minor mineral in the system $\text{CaO-MgO-Al}_2\text{O}_3\text{-SiO}_2\text{-TiO}_2$. Sodium and iron, although analyzed, are near or below the detection limit in this sample, and are not considered in the analysis.

Data Analysis

Plot of intensities of one element versus another, for each pixel in the image,⁶ produces clusters of points that represent the various minerals. Although there are five major mineral phases in this sample, only four clusters are apparent on the scatter plot of Al vs Si (Fig. 2). The scatter of points within a cluster is a result of both the precision (counting error) inherent in the analysis and the actual range of composition (heterogeneity) of the mineral. Scatter resulting from the counting error approximates a Gaussian distribution that can be seen by a thermographic color scale incorporated into the software; i.e., the denser the concentration of points, the "hotter" the color (red \rightarrow orange \rightarrow yellow \rightarrow white). The scatter of points between the clusters results from pixels that overlap more than one mineral; minor phases; and cracks, holes, or voids in the sample.

Various combinations of elements could be used for scatter plots in an attempt to determine the major phases. However, with geological samples (which often contain 10 or more elements), this process can result in over 40 scatter plots. Extracting the pertinent data from these scatter plots is time consuming and not very efficient. Minerals that are not homogeneous, perhaps with varying proportions of end-

member compositions, complicate this procedure.

Principal-component Analysis

A quicker and more general method is to apply principal-component analysis (PCA) to the data to extract the most information. PCA is a statistical technique used on large data sets to find the combination of variables that provide the greatest variance in the data.⁷ The same number of principal-component images are calculated as the number of elemental images in the original data set, but pertinent data are condensed into fewer images; the remaining images contain mainly noise, or are the product of a few pixels far out of the range of most of the data. The equations formed by PCA yield the contribution each element made to each principal-component map.

Scatter plots of one principal-component image versus another often delineate additional phases (Fig. 3). Although for many samples the same information can be obtained eventually by choice of the correct elements to plot on a scatter plot, or use of several scatter plots concurrently, use of PCA produces the result more rapidly and does not rely on the selection of elements by the analyst.

The next step is to group pixels into various phases based on the clusters in the scatter plot(s). Areas on the scatter plot can be selected, and the image points within the selected area colored. Display of the selected points as an image shows the spatial location of the mineral (Fig. 4). This process is repeated for each of the phases present in the sample. Segregation of pixels into phases depends on the decisions made by the analyst. If the goal is to obtain a highly accurate bulk composition, all the pixels should be partitioned into various phases, as was done for this example. If the goal is to obtain very accurate values for the composition of individual minerals, pixels that lie along phase boundaries should be discarded, lest they contaminate the analysis.

Standardless Analysis

From a count of the number of pixels within selected areas we can calculate the area percentage of each mineral and the average intensity of elements within each area (Table 2). These intensities, after background correction, can be used to calculate the average composition of each mineral by use of matrix corrections and standardless analyses.

For this example, background values were estimated manually by measurement of the backgrounds at representative points on the sample scaled to the same conditions as image collection. Backgrounds were subtracted from the total intensities in Table 2 to obtain net peak intensities. The background for a single element on various minerals is very similar in this sample, since all the minerals are oxides of a restricted set of elements and are similar in atomic weight. This similarity would be absent in many other samples, and other methods

TABLE 1.--Minerals in area sampled.

Mineral	Area percent	Average intensity (counts)						
		Al	Si	Mg	Ca	Ti	Fe	Na
Melilite	27	107	78	8.5	230	8.7	3.1	5.0
Pyroxene	16	30	173	26	146	16	3.4	5.0
Spinel	40	163	31	43	51	15	4.4	4.9
Hibonite	3	108	139	10	120	9.2	2.9	4.9
Anorthite	13	227	20	10	75	29	3.3	4.7
Perovskite	1	106	15	30	125	101	3.9	5.9
Background		8	11	8	18	13	4.0	5.2

TABLE 2.--Statistics obtained from image data.

Mineral	Abbreviation	Chemical Formula
Melilite	mel	$\text{Ca}_2(\text{Mg,Al})(\text{Al,Si})\text{O}_7$
Pyroxene	pyx	$\text{Ca}(\text{Mg,Ti,Al})(\text{Al,Si})_2\text{O}_6$
Spinel	sp	MgAl_2O_4
Hibonite	hib	$\text{CaAl}_{12}\text{O}_{19}$
Anorthite	an	$\text{CaAl}_2\text{Si}_2\text{O}_8$
Perovskite	pv	CaTiO_3

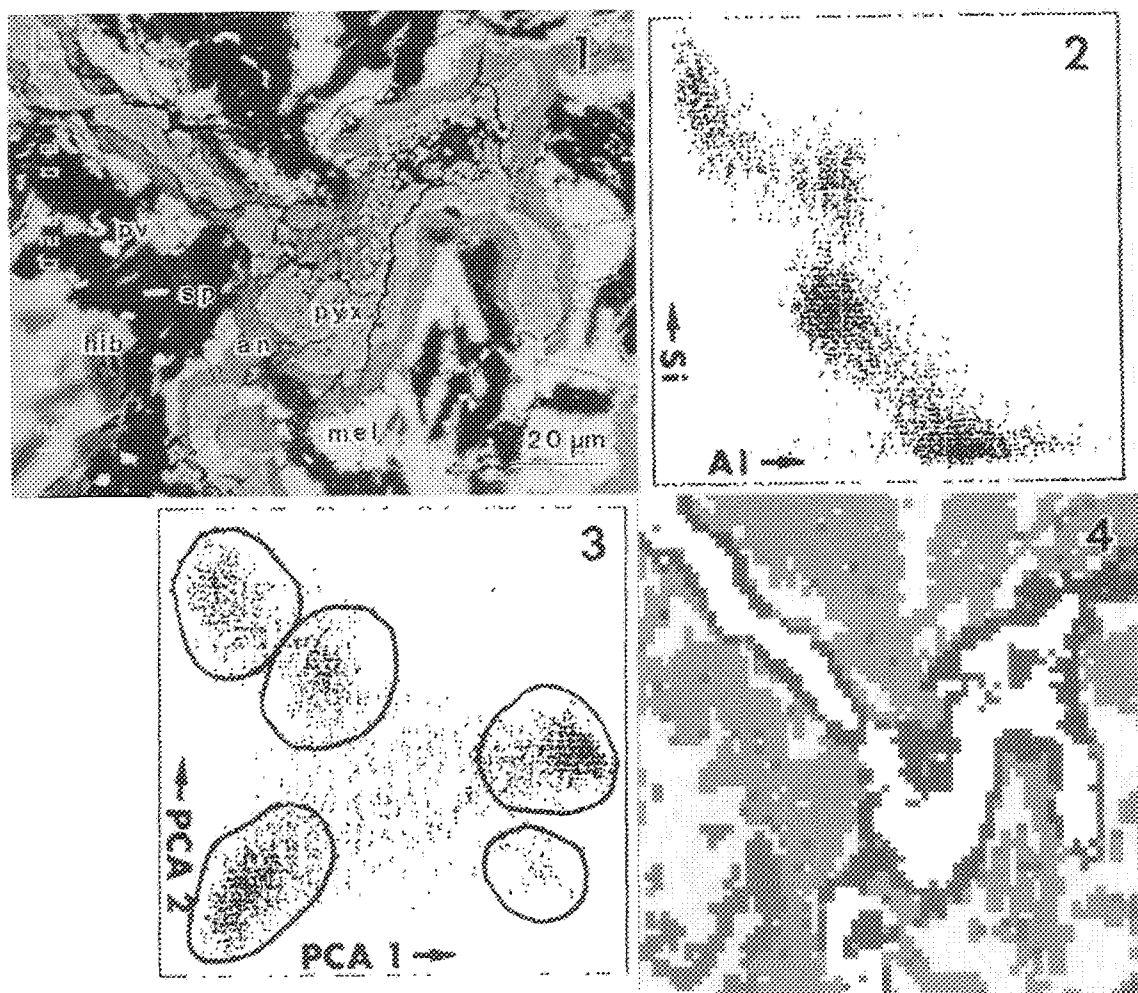


FIG. 1.--Backscatter electron image of area sampled (mineral abbreviations in Table 1).

FIG. 2.--Scatter plot of Al vs Si for all pixels in image.

FIG. 3.--Scatter plot of principal component 1 (PCA 1) vs principal component 2 (PCA 2). Outlined areas encompass various phases. Remaining points are minor phases, mixtures of two or more phases, or holes and voids.

FIG. 4.--Spatial location of minerals as determined from scatter plot in Fig. 3. Computer program discards half of the pixels.

TABLE 3.--Comparison of standardless analyses of data obtained from x-ray imaging, with electron microprobe analyses. (All values are in wt.%)

		MgO	Al ₂ O ₃	SiO ₂	CaO	TiO ₂
Melilite	standardless	0.2	31.0	27.9	41.0	0.0
	microprobe	0.4	32.1	21.2	40.8	0.0
Pyroxene	standardless	5.6	7.4	59.3	26.7	1.0
	microprobe	15.3	6.9	48.9	26.5	3.1
Spinel	standardless	11.0	64.3	15.4	8.5	0.8
	microprobe	27.7	70.2	0.6	0.5	0.2
Anorthite	standardless	0.6	28.3	51.2	20.0	0.0
	microprobe	0.1	35.5	40.5	23.4	0.0
Hibonite	standardless	2.1	73.9	6.0	13.2	4.8
	microprobe	4.0	80.0	0.4	9.1	7.3
Perovskite	standardless	8.5	41.2	2.3	22.5	25.6
	microprobe	0.5	4.6	3.0	40.0	44.7
Calculated bulk composition		5.6	41.6	30.0	22.0	0.9

of background subtraction are under consideration. One possible method is to acquire a background map at a nearby portion of the spectrum, concurrently with the elemental map of interest. Given the present software limitation of 15 elements, this approach would restrict the analyst to 7 each of elemental and background subtraction in situations where the background varies considerably with different phases in the sample. Ideally, the peak and background values for each pixel would be subtracted before storage of the value in the data file, but that might lead to inaccurate results in regions of the spectrum where the slope of the background deviates significantly from zero.

The net peak intensities obtained after background subtraction are next normalized to one for each mineral. These values are used as k-ratios for the purpose of standardless analysis via the MAGIC V matrix recalculation program. Table 3 compares the values obtained by this method with those from a representative conventional microprobe analysis. Considering that the pixel segregation into phases was optimized for the bulk composition, the analyses agree fairly well for melilite and anorthite. Pyroxene is present as a solid solution of several different components, so that one cannot choose a representative analysis that agrees well with the standardless analysis, although the standardless analysis results are within the range of the microprobe analyses for all oxides except MgO, which is low.

The variance found for spinel, hibonite, and perovskite can be accounted for by the high percentage of pixels that are at the edge of these smaller grains, particularly in perovskite (bright phases in Fig. 1), as the grain size is generally less than 5 μ m. The perovskite is associated spatially with spinel, a phase rich in Mg and Al, which is reflected in the high MgO and Al₂O₃ contents of perovskite as calculated by standardless analysis.

Total bulk composition of the sample can also be calculated by weighting of the individual phase analyses by the percentages in Table 2, and is consistent with values expected for a

sample of this type. The bulk composition is considered more accurate than the individual phase compositions calculated by standardless analysis, as discussed earlier.

Summary

The above analysis illustrates that multiple x-ray image techniques, including the use of principal-component analysis and scatter plots, can give a lot of information about the mineral compositions and distributions in geological samples. The methods and procedures used can be readily extended to other nongeological samples.

References

1. A. L. Albee, D. W. Beaty, A. A. Chodos, and J. E. Quick, "Quantitative analysis of petrographic properties and of mineral compositions with a computer-controlled energy-dispersive system," *Proc. 8th ICXOM*, 1977, 526.
2. A. L. Albee, J. E. Quick, and A. A. Chodos, "Source and magnitude of errors in 'Broad-Beam Analysis' (BBA) with the electron probe," *Lunar Science VIII*, 7.
3. R. L. Myklebust, D. E. Newbury, R. B. Marinenko, and D. S. Bright, "Background correction in electron microprobe compositional mapping with wavelength-dispersive x-ray spectrometry," *Microbeam Analysis--1987*, 27.
4. R. L. Myklebust, R. B. Marinenko, D. E. Newbury, and D. S. Bright, "Quantitative calculations for compositional mapping techniques in electron probe microanalysis," *Microbeam Analysis--1985*, 101.
5. J. J. Friel, T. J. Juzwak, and P. F. Johnson, "Quantitative EDS mapping of a ceramic superconductor," *Microbeam Analysis--1988*, 41.
6. D. S. Bright, D. E. Newbury, and R. B. Marinenko, "Concentration-concentration histograms: Scatter diagrams applied to quantitative compositional maps," *Microbeam Analysis--1988*, 18.
7. B. F. J. Manly, *Multivariate Statistical Methods*, New York: Chapman and Hall, 1986, 159.

EDS IMAGE CLASSIFICATION BY RECURSIVE PARTITIONING

Raymond Browning, P. L. King, J. M. Paque, and Pierro Pianetta

Recent instrumental developments in x-ray imaging open up some very exciting possibilities for the analysis of complex multiphase materials. X-ray microanalysis systems are now configured to collect multiple images simultaneously; the maximum number of images is limited only by computer memory size rather than any intrinsic limits. The multispectral technique offers both quantitative analysis of relative quantities in mixtures of elemental phase systems and the semiquantitative analysis of highly dispersed or inhomogeneous phases.¹⁻³ However, the success of the multispectral imaging approach depends on the ability to extract information from the very large data sets that are produced.

Image Analysis

When analyzing multispectral images it becomes quickly apparent that any a priori approach may be insufficient to cover the variation in data. This variation might be due not only to meaningful signal that contains information about "real" processes such as elemental concentration, but also random occurrences such as digital dropout, or nonrandom variations such as the large change in signal that might be seen on a physical crack in the sample.

A common method used to reduce large multispectral data sets is principal-component analysis (PCA).⁴ The PCA procedure is straightforward to implement and often gives a very useful reduction in the number of images with significant signal variance. In the example described below, the first two principal components contain 90% of the image information originally contained in 12 x-ray images. PCA is also used because it gives an automatic view of most of the complexity in the data with little operator intervention or prior knowledge. However, when PCA is used in the analysis of multispectral x-ray dispersive images of geological minerals,¹ it is found that the large number of mineral phases typically present leads to a large number of significant principal component images. This large dimensionality produces difficulties in graphic presentation of the data and interactive partitioning of the image. A further problem is in the nature of the mineral-phase distribution. Some phases are well separated in at least one projection direction; other phases are continuous mixtures with two or more end points. Both types of mineral-phase distributions can

be found intimately mixed in a geological sample. The very different types of these distributions means that a first-level approach to partitioning the images could lead to overlooking significant aspects of the signal.

Recursive Partitioning

A multistep image analysis procedure that circumvents the above problem promises to be a convenient and relatively simple extension of PCA. The analysis method relies on the fact that there is very often some clear separation of an image after PCA and that this clear separation can be readily observed in the first few principal-component images. Thus the information in the first few principal-component scatter diagrams can be partitioned interactively into regions that are well separated from each other, but may be individually complex. PCA can then be applied to the data subsets and the process can be repeated until a meaningful projection of the data can be viewed in a low-dimensional scatter diagram. The real image can then be formed by either density or false-color imaging, depending on which is appropriate for the subset alone. Use of PCA recursively on subsets of an image also discriminates heavily against outliers, and the distinction between the projections based on either the covariance or correlation matrices is less important.

The recursive use of the PCA transform is illustrated by the partitioning of a 12-component multispectral energy dispersive spectroscopy (EDS) image.⁵ In this analysis we treat the data simply as a partitioning problem, to find information in the image without prior knowledge about the system. The 12-elemental components are listed in Table 1. The real-space image of the backscatter image (channel 12) and two elemental images Ce and Nd are shown in Fig. 1 as a monochrome reproduction of a color image. The scatter diagrams for the first against the second and third principal components for each pixel in the image are plotted in Fig. 2. The principal components are derived from the covariance matrix; the first three components have 74.3%, 15.3%, and 4.0% of the signal variance, respectively. The three histograms show how the relative variance divides the image. It can be seen from the scatter diagrams in Figs. 2(b) and (c) that the image has clustered into four main regions of interest, but there is some structure in the larger phase distribution at the top of the scatter diagrams. The four major phases can be separated, and a false-color image of the phase's spatial distribution can be displayed by windowing of the clusters. In this case the

Raymond Browning is at the Center for Integrated Systems, J. M. Paque is at the Center for Materials Research, and P. L. King and Pierro Pianetta are with the Stanford Synchrotron Radiation Laboratory, Stanford, CA 94305.

TABLE 1.--Elemental maps collected in "smithx.map."

1-Al, 2-Si, 3-Mg, 4-Ca, 5-Ag, 6-K, 7-Ti 8-Gd, 9-Fe, 10-Ce, 11-Nd, 12-Backscatter

software used an oval window. A monochrome reproduction of this false-color image is shown at the bottom left of Fig. 2.

By windowing of the clusters to form the false-color image the data have been partitioned and the larger phase with structure can then be treated separately with PCA. This larger cluster only appears complex when the covariance matrix is used. Use of the correlation matrix produces a more rounded cluster, so that it is quite possible to miss information if just one choice of projections is used. Just as important is the fact that even as far out as the ninth principal component image significant (although small) signal can be seen in the real image (0.15%). Figure 3 shows the data from the first two principal-component images from the structured phase alone. The phase now looks like a V in the first and second principal-component scatter diagram. Thus at least four significant image components are needed to give a description of the data to this point in the analysis. In fact the data in this phase are even more complex. With the phase isolated by the windowing, it becomes apparent that associated with this phase alone are a group of high-variance outliers that dominate the PCA; a very different result can be obtained by removing them. However, the scatter diagram of Fig. 3 can still be usefully partitioned into four regions to show the spatial distribution of the signal around the V. In the false-color image of Fig. 3, there is also some spatial grouping within the partitioned cluster, so that a spatial smooth of the image data would be useful.

From the partitioned image of Fig. 3 an additional type of information can be obtained. As the images are collected from various parts of the x-ray spectrum, a crude spectrum (11 data points) of the individual parts of the image can be generated. From this spectral data it can be readily seen that the components determining the variation in the phase are largely Si, Ca, and K. The (anti)correlation between the Si and Ca signals, and the Si and K signals, are shown in Fig. 4. Thus partitioning the full image, and then subsequent PCA, allows the details of the subset to be extracted in isolation. Observing the Si/Ca and Si/K correlation within the complex phase would be very difficult otherwise.

Conclusions

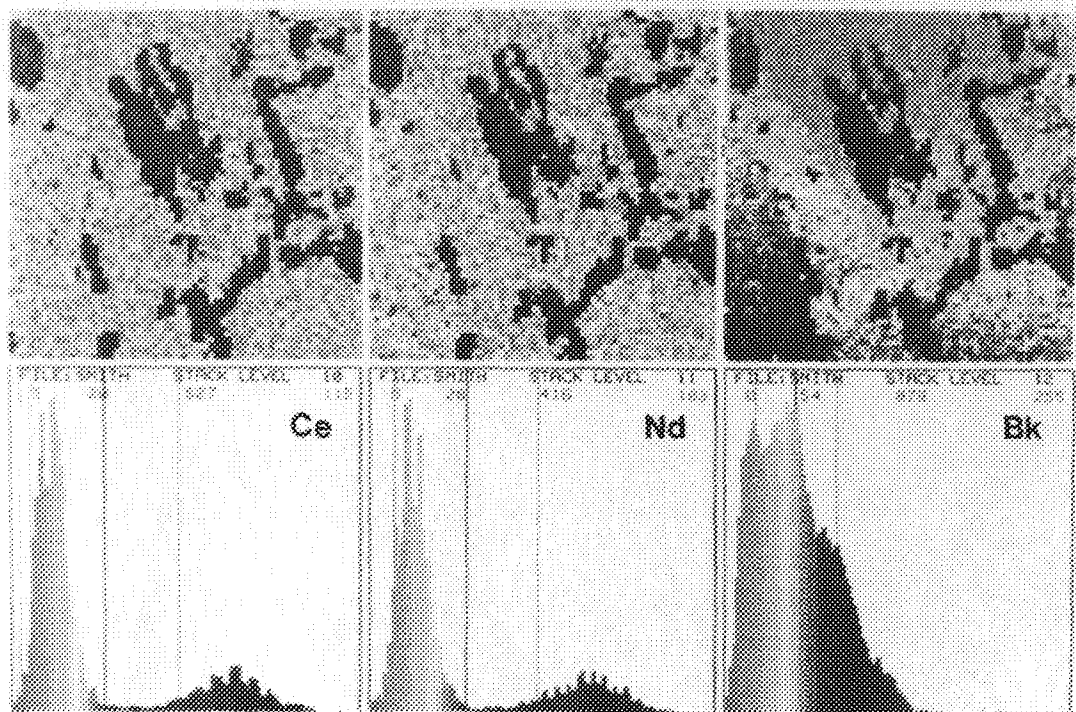
The above analysis shows that a great deal of information can be extracted from a complex multispectral image by recursive application of the principal-component transform to subsets of the data. It also shows that a first-level approach to partitioning the data might overlook significant information unless high-order prin-

cipal components are considered. Recursive application of PCA can separate out dominant signals and allow signals with smaller variance to be analyzed.

References

1. J. M. Paque et al., "Quantitative analysis of x-ray images from geological materials," *ICEM--1990*, vol. 2, 244, and this proceedings.
2. D. S. Bright, D. E. Newbury, and R. B. Marienko, "Concentration-concentration histograms: Scatter diagrams applied to quantitative compositional maps," *Microbeam Analysis--1988*, 18.
3. R. B. Marienko, D. S. Bright, C. A. Handwerker, and J. J. Mecholsky Jr., "A study of diffusion zones with electron microprobe compositional mapping," Ref. 1, p. 242.
4. P. J. Ready and P. A. Wintz, "Information extraction, SNR improvement, and data compression in multispectral imagery," *IEEE Trans. Comm.* 21: 1123, 1973.
5. Obtained from KeveX Corp., San Carlos, Calif. (Data File "smithx.map").

1



2

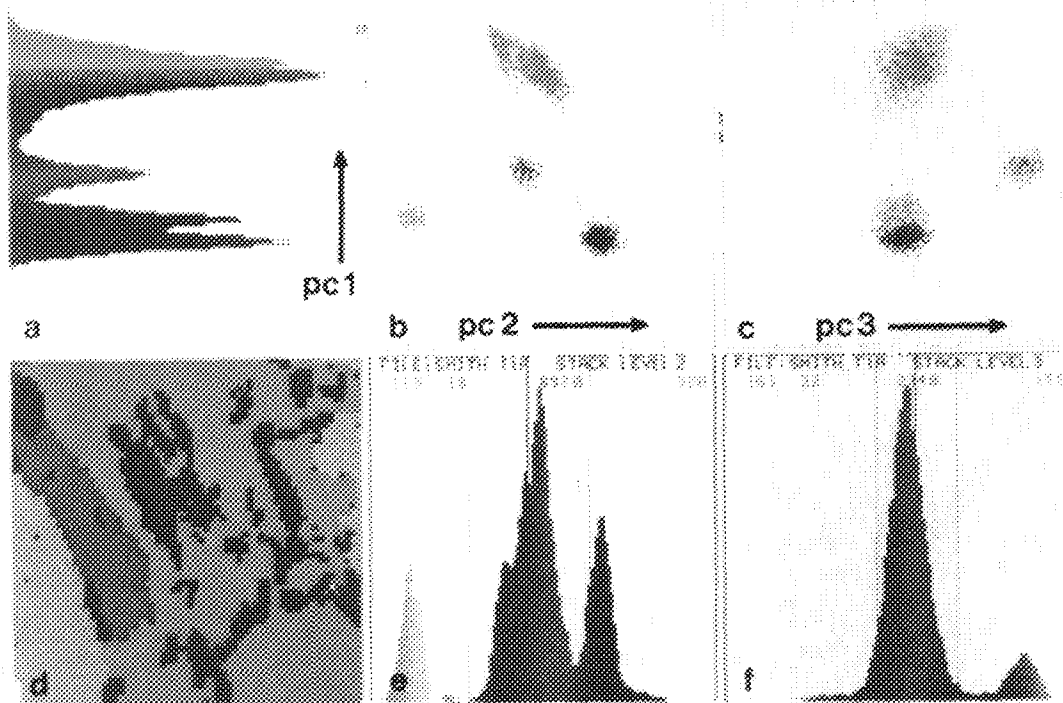
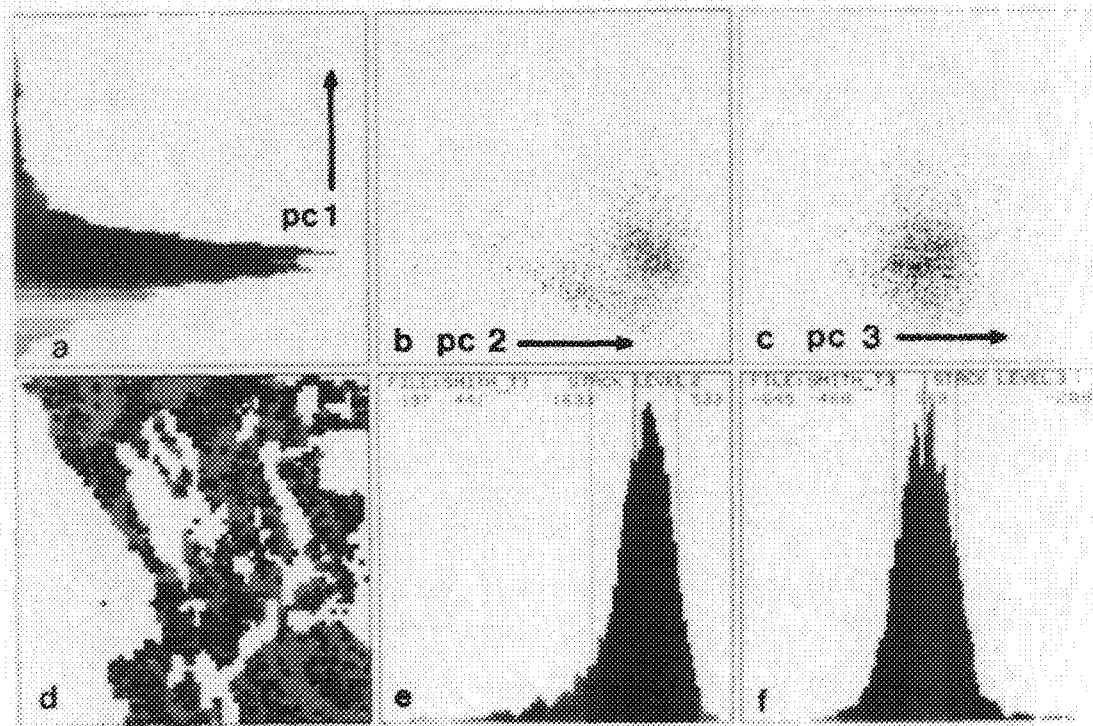


FIG. 1.--64x64 pixel images of signal channels 10(Ce), 11(Nd) and 12(backscatter) images with respective signal histograms.
 FIG. 2.--Principal-component image data. (a) PC-1 histogram, (b) PC-1 vs PC-2 scatter diagram, (c) PC-1 vs PC-3 scatter diagram, (d) false-color phase image, (e) PC-2 histogram, (f) PC-3 histogram.

3



4

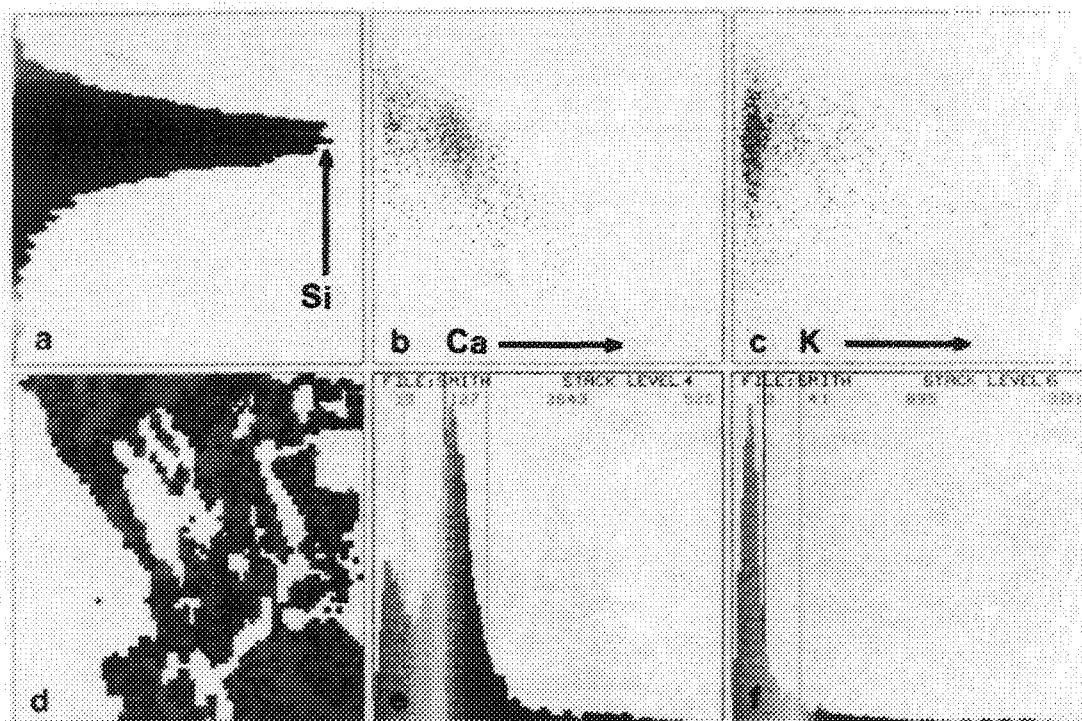


FIG. 3.--Principal-component image data from complex phase. (a) PC-histogram, (b) PC-1 vs PC-2 scatter diagram, (c) PC-1 vs PC-3 scatter diagram, (d) false-color image, (e) PC-2 histogram, (f) PC-3 histogram.

FIG. 4.--X-ray elemental image data from complex phase. (a) Si signal histogram, (b) Si vs Ca scatter diagram, (c) Si vs K scatter diagram, (d) false color phase image, (e) Ca signal histogram, (f) K signal histogram.

IN SITU ANALYSIS OF NATURAL FLUID INCLUSIONS IN MINERALS BY A CRYO-STAGE AND THIN-WINDOW EDS

B. J. Griffin

Fluid inclusions (Fig. 1) are samples of solutions parent to the host phases. They are trapped during crystallization and thereby preserve a record of conditions present during mineralization. Knowledge of fluid compositions allows modeling of mineralizing events and consequently prediction of the possible siting of further mineral deposits. Measurement of fluid composition by conventional optical techniques^{1,2} is based on analogy to "model" brines, usually NaCl-rich. Bulk analytical methods only provide averaged data. More sophisticated spectroscopic techniques (e.g., laser Raman) are not easily quantified.³

Decrepitation of near-surface inclusions by heating through exposure to high electron beam intensities has been used to qualitatively analyze nonvolatile residues.⁴ The potential of cryogenic stages on scanning electron microscopes (SEMs) has been recognized.⁵ Results are presented here on the chemistry of some Cl brine-filled fluid inclusions and gas-filled fluid inclusions. The data demonstrate the increased information available from fluid inclusions by the application of thin-window energy dispersive spectrometry (EDS) and cryo-SEM techniques.

Experimental

Fluid inclusion-rich samples of fluorite (CaF₂) and sphalerite (Zn,Fe S) from the Black Flag Deposit, and quartz (SiO₂) from the Lawlers Deposit in Western Australia have been examined. The samples were slabbed into 1mm-thick sections and polished on both sides. A range of fluid inclusion populations have been identified optically in the Black Flag samples. Conventional microthermometric measurements indicate two fluid compositions present with 3-8 equivalent wt.% and 8-12 equivalent wt.% NaCl, respectively.⁶ The fluid composition of the Lawlers sample was suspected to be carbon dioxide.⁷

Samples were examined in a Philips 505 SEM equipped with a Hexland cryo-stage and accessories. X-ray spectra were collected in a turreted EDAX ECON IV and PV9900 EDS with a spot size of 200 nm, 100-200s live counting time, and 15kV accelerating voltage.

The sphalerite slabs were mounted vertically in slotted carbon stubs, glued in with a carbon-based adhesive and snap frozen by being plunged into liquid nitrogen slush. The exposed section of slab was fractured within the cryo-chamber, coated with approximately 10 nm of carbon, and

transferred to the SEM stage. A range of NaCl, KCl, and CaCl₂ standard fluids, 4-20 total wt.% in water, were similarly snap frozen on carbon stubs in droplet form.

Fluid inclusions exposed on horizontal fracture surfaces of the sphalerite were located by using backscattered electron imaging (Fig. 2) and analyzed. Reference x-ray spectra from the sphalerite host were also collected. Standard solutions were analyzed by both spot and raster (50 × 100µm) electron beam modes. X-ray spectra from the carbon stub were used to monitor electron beam intensity variations. The fluorite and quartz samples were similarly examined except that no coating was applied to the quartz sample as carbon dioxide was suspected to be the fluid phase (Fig. 3).

Qualitative Results

The spectra from inclusions in the sphalerite and fluorite consistently contain peaks corresponding to Ca, K, and Cl in addition to the host elements. Superimposition of the reference sphalerite spectrum on the inclusion spectrum demonstrates the additional presence of Na (Fig. 4), initially masked by the Zn Lα peak.

The spectra from inclusions in the quartz contained no characteristic x-ray peaks, in conventional Be-window mode. Spectra collected by use of the thin-window mode contain oxygen and carbon peaks (Fig. 5). The absence of a silicon peak confirmed the lack of interference from the quartz host. The frozen fluid was subsequently observed to sublime at -78 C, confirming its identity as carbon dioxide.

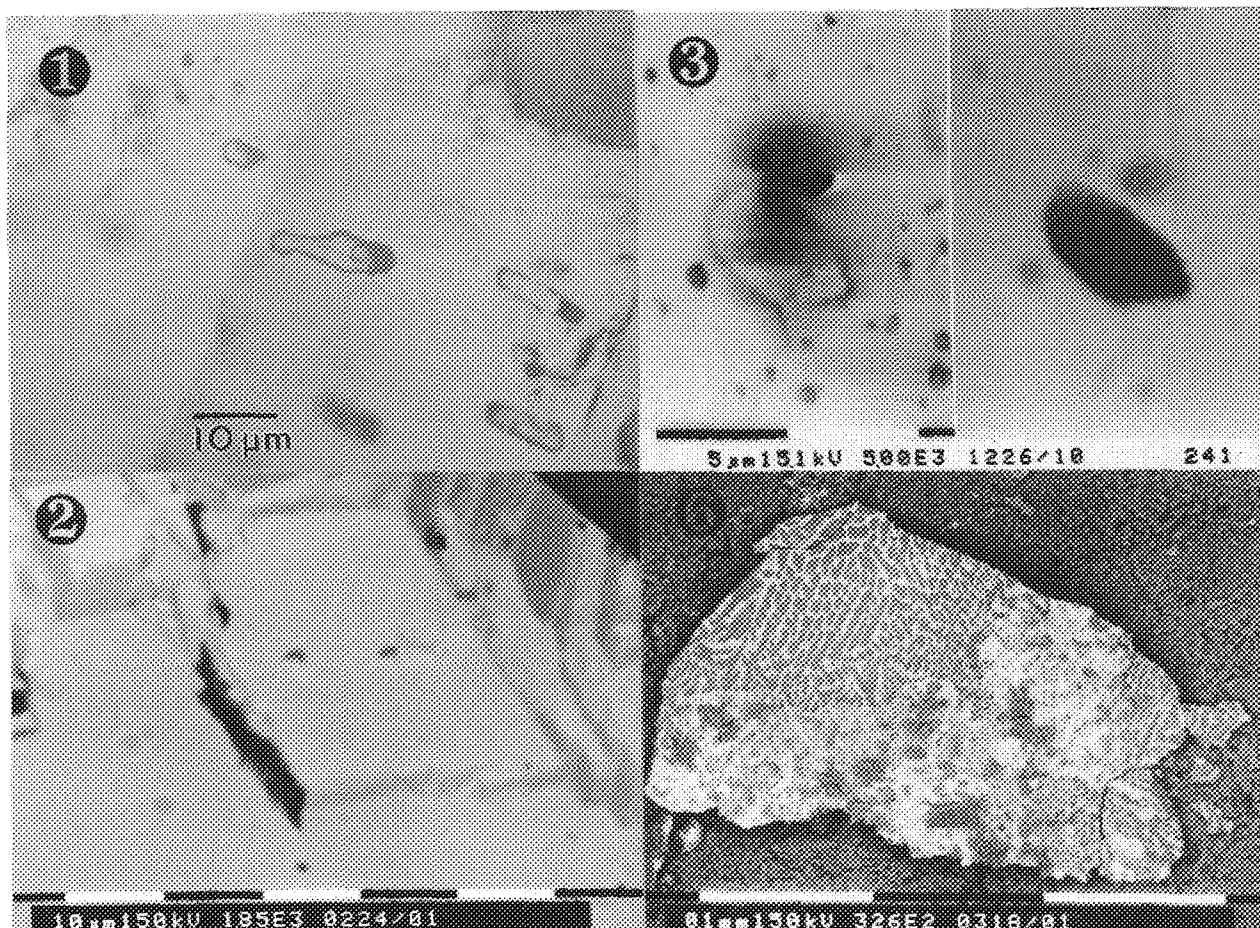
Quantitative Results

Spectra initially obtained from the standard solution droplets gave no consistent data. This result was recognized to be due to the presence of a contaminant ice layer on the surface. Attempts to cut flat surfaces on the frozen droplets by a metal cutter produce inconsistent results. An important result was that shattered fragments of the droplets were observed to be inhomogeneous crystalline composites of ice crystals and an interstitial chloride mixture (Fig. 6).

Conclusions

The qualitative results show the fluid inclusions in the Black Flag sphalerite and fluorite to contain sodium, calcium, and potassium chloride species and are therefore more complex than suggested by conventional techniques. The fluid included in the Lawlers

B. J. Griffin is at the EM Centre, University of Western Australia, Nedlands, W.A., Australia 6009.



FS = 497 / 3612 PRST = 200LSEC
 AB = inclusion : host sphalerite

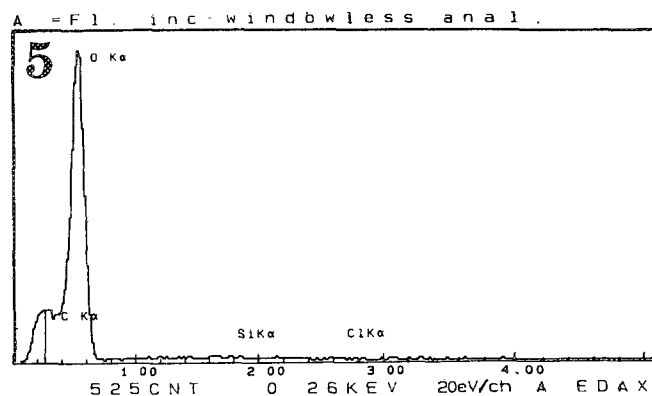
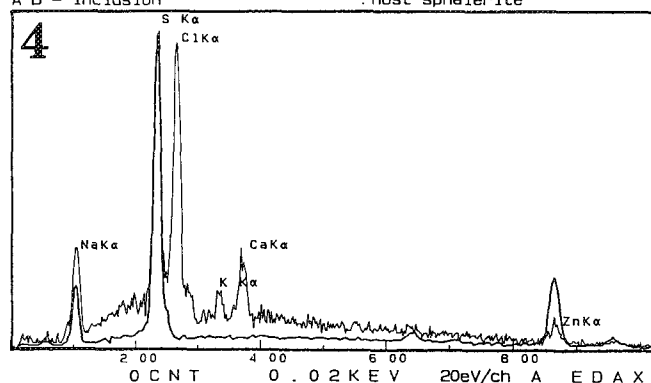


FIG. 1.--Composite fluid, gas, and daughter salt-rich inclusions in Black Flag sphalerite.

FIG. 2.--Backscattered electron (BE) image showing cleavage control on location of inclusions in sphalerite.

FIG. 3.--Secondary electron (SE) and BE images of frozen CO₂ inclusion in quartz. Sample was not coated, as indicated by charging in SE image.

FIG. 4.--Overlayed x-ray spectra from frozen inclusion and host sphalerite (black). Inclusion is Na, K, Ca, and Cl rich.

FIG. 5.--Overlayed x-ray spectra from frozen carbon dioxide inclusion and quartz host. Inclusion spectrum was collected with thin-window mode of EDS. Carbon and oxygen peaks are clear.

FIG. 6.--BE image showing presence of ice crystals (dark) and interstitial Na, Ca, K chlorides in frozen "standard solution" droplet.

quartz is carbon dioxide.

The quantification of these data requires more sophisticated techniques than those used here. Snap freezing in liquid nitrogen slurry is too slow to prevent inhomogeneity in the droplets. This may become a minimal problem if spectra are collected from sufficiently large areas of the droplet, after ice removal. The application of cryo-SEM and EDS analysis does provide new qualitative information. Quantification of the data is more difficult.

References

1. E. Roedder, *Min. Soc. Am. Reviews in Mineralogy* 12: 644, 1984.
2. T. J. Shepherd, A. H. Rankin, and D. H. M. Alderton, *A Practical Guide to Fluid Inclusion Studies*, Glasgow: Blackie & Sons, 1985.
3. I.-M. Chou, J. D. Pasteris, and J. J. Freeman, *Geochim. Cosmochim. Acta*, 54: 535, 1990.
4. Y. Bone and B. J. Griffin, *Seventh Australian Geological Convention Ext. Abstracts*, 1984, 67.
5. W. C. Kelly and P. A. Burgio, *Econ. Geology* 78: 1262, 1983.
6. J. M. Bennett, in S. E. Ho, D. I. Groves, and Julie Bennett, Eds., *Gold of the Yilgarn Craton, Western Australia: Nature, Genesis and Exploration Guides*, Geology Department and University Extension, University of Western Australia, Publ. 20 (in press).
7. K. F. Cassidy, in S. E. Ho and D. I. Groves, Eds., *Advances in Understanding Precambrian Gold Deposits*, vol. II, Geology Department and University Extension, University of Western Australia, Publ. 12: 165, 1988.

CHARACTERIZATION OF OCCURRENCE AND DISTRIBUTION OF INVISIBLE GOLD IN ORE BY EPMA

Shuihe Mao

There is a particular type of gold-bearing ore in which the Au tenor is quite high--sometimes even up to tens of ppm--but the gold in the ore is not visible by examination of a great number of polished sections under an optical microscope at high magnification. Generally, this kind of gold is called "invisible gold," "ultramicro gold," or "submicron gold." Owing to the invisibility of ultramicro gold in "Carlin type" gold ore, it is extremely difficult to investigate its occurrence and distribution by conventional determining means. EPMA has been proved to be a very powerful instrument for doing research on this subject because it has the advantages of high space resolution, being nondestructive, getting in situ quantitative analysis results, observing various kinds of images continuously with the same equipment, etc. Therefore, using the electron-probe micro-analyzer (EPMA) and scanning electron microscope (SEM) as the main instruments, we have investigated the distribution characteristics and concentration of invisible gold at various locations in gold-bearing minerals of various grain sizes, crystal forms, and paragenetic stages.

Experimental

The unoxidized (primary) ore sample from a "Carlin type" gold deposit in Southwest China consists of drill cuttings with gold tenor of 31.02 ppm and weight of 2438 g. Chemical analysis gave 2.40% S, 3.41% Fe, 2.59% Al, and 1.63% K in bulk ore. The main sulfides are pyrite and arsenopyrite; the other common minerals are quartz, illite, kaolinite, calcite, dolomite, apatite, and barite. Modal analysis by optical microscope and point counting gave 4.7% pyrite (including a small quantity of some other sulfides), 68.7% quartz and some carbonates, and 26.6% clay minerals. The operating conditions of EPMA are: accelerating voltage 25 kV, beam current 1×10^{-8} A, beam diameter about 1 μ m. Au $L\alpha$ but not Au $M\alpha$ is preferably chosen as the analyzed x-ray line because Au $M\alpha_1$ (5.840 Å) overlaps with the 3rd-order line of Fe $K\alpha$ (5.812 Å) to some extent and iron is the main component of the pyrite matrix. According to the expression of detection limit^{1,2} the calculated value of C_{DL} under the circumstances is 0.038%. Considering some uncertainties, such as instrumental instability, sample

imperfection, and so on, the C_{DL} value for detecting trace gold in pyrite is estimated to be 0.05% in practice. Another point to be noted is that the common method for measuring background is unsuitable here. In the present work, pure pyrite and other minerals that have been shown to contain no gold are employed as standards for measuring background when the spectrometer is located at the peak position of Au $L\alpha$. In this way, the precision for detecting trace gold in pyrite and other minerals is improved. The instrument in this work is the JEOL 733 electron probe equipped with a TN5500 EDS system and a TN5600 automation system. One of the wavelength-dispersive spectrometers (WDS) is exclusively arranged to determine the gold content; this spectrometer is kept at the peak position of Au $L\alpha$ throughout the measurement procedure without any movement to eliminate mechanical error. At the same time, the EDS system is used to analyze the contents of sulfur, iron, arsenic, etc., to monitor that the spot selected for analyzing is correct.

Results and Conclusions

On the basis of results of electron-probe microanalysis on various kinds of minerals of which the ore is composed (Table 1), SEM observation, and chemical dissolving experiments on pyrite, the following conclusions have been drawn.

1. Pyrite is the most important gold-bearing mineral. More than 95% of the pyrite grains occur as anhedral granules that consist of euhedral crystal cores formed earlier containing little Au and As, and rims formed later notably enriched in Au and As. There is little or no Au in the euhedral pyrite crystals. The average Au content in pyrite is 257.6 ppm. The average content of Au in rims of anhedral pyrite is 599.8 ppm; in their interiors, less than 81 ppm.

2. Usually there is no way for observing and displaying the invisible gold in pyrite grains because of its trace content. Fortunately, in the present circumstances the distribution characteristic of the invisible gold in pyrite can be displayed and examined according to that of arsenic in SEM images (Fig. 1) and in EPMA data (Table 1), because there is almost a positive correlation between the Au and As contents.

3. In chemical dissolution experiments on pyrite, the gold liberated from dissolved pyrite is not in the HNO₃ solution; it is in the residue, together with the undissolved pyrite and will later go into the KI + I₂ gold-

Shuihe Mao is at the Institute of Comprehensive Utilization of Mineral Resources, Emei, Sichuan 614200, People's Republic of China. This work was supported by the Chinese Academy of Geological Sciences.

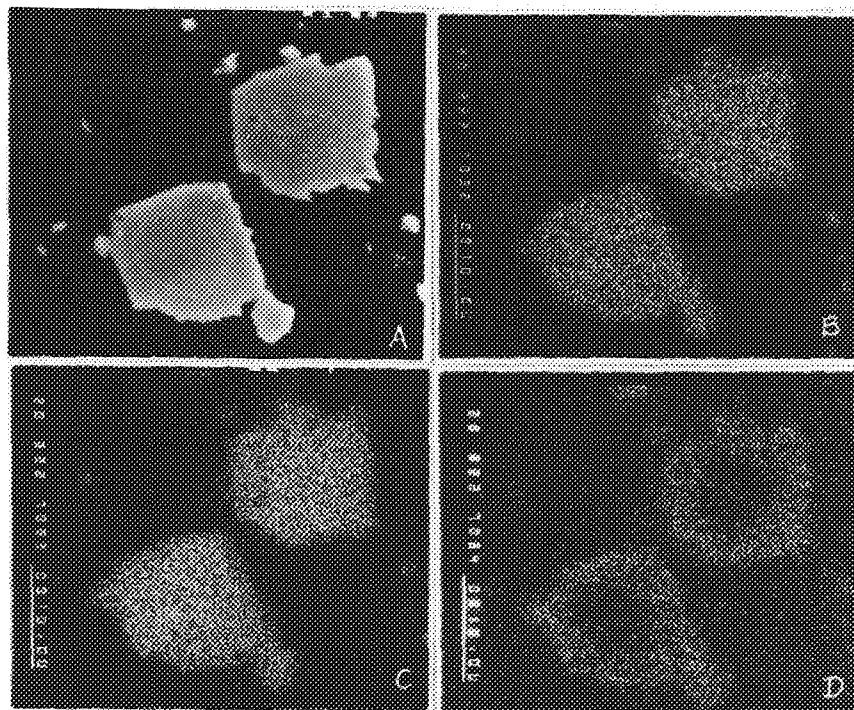


FIG. 1.--Electron beam scanning images on anhedral pyrite grain: A. SEI, B. Fe K α , C. S K α , D. As L α .

TABLE 1.--Contents of Au and As in minerals analyzed by EPMA.

	Ana. sp.	Spots with Au cont. ($>0.05\%$)					Spots with Au cont. ($<0.05\%$)		
		Sp.	Au (%)		As (%)		Sp.	As (%)	
			Range	Ave.	Range	Ave.		Range	Ave.
Py. ($<10\mu\text{m}$)	120	92	0.05-0.34	0.15	1.60-9.29	5.22	28	0-5.64	2.05
Int. of py.*	73	10	0.05-0.11	0.08	0-9.13	2.67	63	0-3.77	0.81
Rims of anh. py.*	57	44	0.05-0.46	0.18	0.85-7.37	5.61	13	0-4.51	0.76
Rims of euh. py.*	18	0					18	0-0.49	0.12
Arsenopyrite	22	1	0.15	0.15			21		
Quartz	59	5	0.05-0.09	0.07			54		
calcite	40	2	0.05-0.06	0.06			38		
Barite	26	1	0.05	0.05			25		

Note: Only gold contents are determined in arsenopyrite, quartz, calcite, barite.
 * = pyrite grains with size $>10\mu\text{m}$. Ana. = Analysed, anh. = anhedral, Ave. = Average,
 cont. = contents, euh. = euhedral, Int. = Interiors, Py. = Pyrite, Sp. = Spots

leaching solution. In addition, EPMA results indicate that gold contents at different spots in the gold-rich rim within the same pyrite grain are remarkably different. These facts confirm that the invisible gold in pyrite occurs as ultramicro native gold inclusions, not as isomorphous substitution.

4. The gold content in other minerals, such as arsenopyrite, quartz, calcite, and barite, are all below the detection limit of EPMA (0.05%). In association with the results of chemical assays of mineral separates, it is believed that these minerals are not gold-bearing bodies.

5. More than 60% of the gold content given by chemical assay of clay minerals occurs in micro pyrite inclusions ($<1\ \mu\text{m}$) in which gold is noticeably enriched.

6. The main features of the ore sample studied in the present work are very similar to those of the ore from Carlin and Cortez gold mines, Nevada, USA, in the following ways: the manner of occurrence and distribution characteristics of the invisible gold, the positive correlation between Au and As contents, the microstructure of the main gold-bearing minerals, the mineralogical composition of the ore, and so on.³ That shows that the "Carlin type" gold deposits have their own common and specific features.

7. The special mode of occurrence and distribution characteristic of the invisible gold in such ores is favorable to the process design for oxidizing-roasting, chloridizing, and cyanide-leaching. In this case, sufficient oxidation and leaching of the pyrite surface produces satisfactory gold recovery. As a result it will bring the advantage of saving time, reagents, and energy.

References

1. M. G. C. Cox, in V. D. Scott and G. Love, Eds., *Quantitative Electron-probe Microanalysis*, New York: Wiley, 1983, 141.
2. T. O. Ziebold, "Precision and sensitivity in electron microprobe analysis," *Anal. Chem.* 39: 858-861, 1967.
3. J. D. Wells and T. E. Mullens, "Gold-bearing arsenian pyrite determined by microprobe analysis, Cortez and Carlin gold mines, Nevada," *Economic Geology* 68: 187-201, 1973.

STOICHIOMETRY/NONSTOICHIOMETRY OF GaAs COMPONENT IN MBE GROWN (GaAs)Ge THIN FILMS AS DETERMINED BY ELECTRON PROBE MICROANALYSIS

D. R. Liu, S. S. Shinozaki, R. G. Warsinski, and R. J. Baird

(GaAs)Ge thin films have been grown by molecular beam epitaxy (MBE) on (100)-oriented GaAs substrate to form metastable alloys. These films are of interest because they are possible candidates for optoelectronic applications.¹ It is important to be able to determine accurately the composition of the film, and particularly to determine whether the GaAs component can be made in stoichiometry and/or nonstoichiometry. However, the K α peaks from these elements cannot be used for chemical analysis of these films. The thickness of the film is usually about 0.5–1.5 μm . If K α peaks of the elements are used for quantification, the accelerating voltage E must be more than 10 kV so that the overvoltage $U = E/E_c$ could be larger than one and the K α peaks sufficiently excited. Under this voltage E , the depth within which some generated x-ray photons can emerge from the sample is already more than 0.5 μm . For example, when a sample of a Ge layer 0.51 μm -thick grown on a GaAs substrate was analyzed in the electron microprobe under $E = 12$ kV, the apparent Ga content was about 5%, whereas the apparent As content was almost zero. Thus, for an accelerating voltage of 12 kV, the generation depth of Ga K α x-ray photons is more than 0.5 μm , whereas that of As K α is less than 0.5 μm . More experimental results on this aspect will be discussed later. If a lower voltage is used to reduce the generation depth, the L peaks have to be used, in spite of the fact that there will be some interference among the L peaks and heavy absorption of the generated L x-ray photons. This paper demonstrates that, after taking care of the various L line x-ray signal interference, we were able to determine the presence of stoichiometric and nonstoichiometric composition of the GaAs component in the films prepared at various epitaxial growth conditions.

Experimental

The samples were (GaAs)Ge thin films MBE grown on (100)-oriented GaAs substrate. Several samples grown under various conditions were mounted on a single 1 in. metal disk, along with pure Ge and GaAs reference standards on the same disk. A CAMECA SX50 electron microprobe was used for the present work, and two wavelength spectrometers each equipped with a TAP crystal were set to collect L α peak signals.

* The authors are with the Research Staff, Ford Motor Co., SRL, Box 2053, Dearborn, MI 48121. They thank Dr. H. Holloway for useful discussions and Mr. M. D. Hurley for sample preparation.

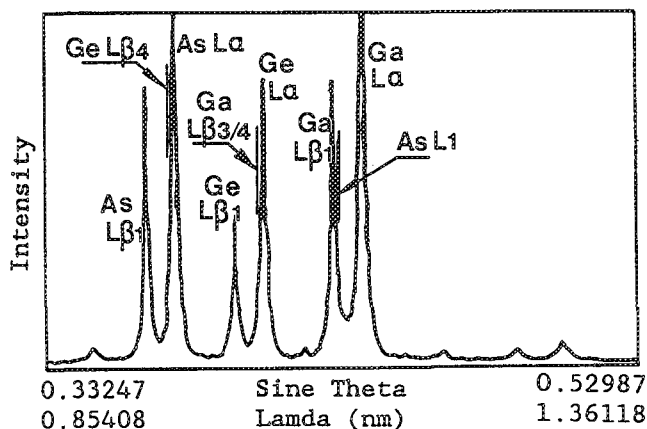


FIG. 1.--WDS spectrum from typical (GaAs)Ge sample collected with TAP crystal. Relevant L peaks discussed in text are marked.

with one TAP crystal used twice to collect signals of the Ga and Ge L peaks. The acceleration voltage was 8 kV. Prior to the signal collection, an x-ray wavelength scan of wide range was performed separately on the Ge, GaAs, and InAs reference materials and a typical (GaAs)Ge sample in order to investigate the interference between various x-ray peaks, but only the spectrum of a typical (GaAs)Ge film is shown in Fig. 1. Proper background offsets were set to extract the peak signals for subsequent quantification.

Results and Discussions

Stoichiometry Determination. Because the Ga, As, and Ge L α peaks are at low energy (slightly higher than 1 keV), and there are many L peaks for each element, these peaks may interfere with one another. Therefore, we have to examine them very carefully. For the purpose of clarity, only the L peaks relevant to the present discussion are marked in Fig. 1. Normally the L α peaks are used for quantification. However, if we examine the situation near the As L α peak and the Ge L α peak, we find that there is a Ge L β_4 peak close to the As L α peak with a wavelength difference of 0.003 nm and a Ga L $\beta_{3/4}$ peak close to the Ge L α peak with a wavelength difference of 0.008 nm. If L α peaks are used for quantification of the (GaAs)Ge films, the error is mainly overestimation of the As content due to the intrusion of the tail of the Ge L β_4 peak into the As L α peak. Now we may examine the possibility to use alternatively L β_1 peaks for quantification. In general, the mass absorption coefficient μ/ρ of an L α line

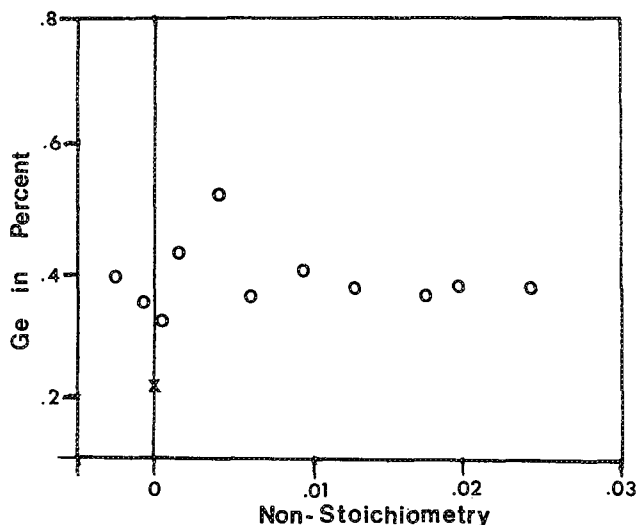


FIG. 2.--Presence of stoichiometry (x) and non-stoichiometry (o) of GaAs component in (GaAs)Ge MBE films discussed in text. Nonstoichiometry is expressed with difference of percentage of As minus percentage of Ga.

is much higher than that of the $L\alpha$ line of the same element. For example, the μ/ρ of Ga $L\beta$ in Ga is 7338, whereas the μ/ρ of Ga $L\alpha$ by Ga is 1355. The so-called PAP procedure for the ZAF correction used in the present instrumentation reportedly can handle L lines of medium Z elements reasonably well.² More important, the result of the present microprobe work is consistent with the results obtained on the same samples with other instrumentation.³ Therefore, we may assume that the absorption correction did not introduce large errors in the determination of stoichiometry/nonstoichiometry for the samples studied here.

It is evident from the L peak markings in Fig. 1 that the only concern with the $L\beta_1$ peak is the proximity of the As L_1 peak at 1.107 nm to the Ga $L\beta_1$ peak at 1.102 nm. Calibration of the Ga and As $L\beta_1$ peaks was accomplished with a single compound standard GaAs. Our purpose was to determine the presence of stoichiometry in the (GaAs)Ge films, and we therefore realized that it was still advantageous to use $L\beta_1$ peaks for quantification because now the influence of the tail of the As L_1 peak on the Ga $L\beta_1$ signal was almost the same as that when they were calibrated. The percentage of the As L_1 peak tail under the Ga $L\beta_1$ peak was thus the same. As for the As $L\beta_1$ and Ge $L\beta_1$ peaks, the interference from nearby L peaks is almost negligible. Therefore, the selection of $L\beta_1$ lines for quantification instead of $L\alpha$ lines should improve the accuracy of stoichiometry determination. This gain is at the expense of the peak-to-background ratio by about a factor 2 because, in general, a reduction in the intensity of an $L\beta_1$ peak is about half of that of an $L\alpha_1$ peak; that was not the problem here since none of the three elements in the samples of our interest

was near the detectability limit. The $L\beta_1$ lines were used for analysis of a typical (GaAs)Ge sample with a nominal 30at% Ge. The results of five analyses from this sample are Ge/Ga/As = 22.73/38.68/38.60, 22.86/38.57/38.58, 22.68/38.83/38.49, 22.81/38.43/38.77, and 22.59/38.93/38.48. Therefore, we are reasonably confident that the GaAs component in this sample is near the stoichiometric composition.⁴

Presence of Nonstoichiometry of the GaAs Component. When the question whether nonstoichiometry of the GaAs component in some films could exist was investigated, it seemed that the $L\alpha$ peaks might serve the purpose better, as discussed below. It was noted (Fig. 1) that, although the As L_1 peak is slightly farther away from the Ga $L\beta_1$ peak (by $\Delta\lambda = 0.005$ nm) than is the Ge $L\beta_4$ peak from the As $L\alpha$ peak (by $\Delta\lambda = 0.003$ nm), the intensity of the tail of the As L_1 peak under the position of the Ga $L\beta_1$ (1.10205 nm) was equivalent to 1.02% of the As $L\alpha$ peak intensity, as could be directly measured from the recorded InAs spectrum. Also, the intensity of the tail of the Ge $L\beta_4$ peak under the position of the As $L\alpha$ was equivalent to 0.531% of the Ge $L\alpha$ peak intensity, as could also be measured directly from the recorded Ge spectrum. In the present work, we have investigated a group of (GaAs)Ge films where the contents of the Ga, As, and Ge elements were roughly the same in terms of atomic percentage. If the x-ray generation cross sections of the three elements are about the same, the Ga $L\beta_1$ peak apparently contains slightly more interference intensity from other elements than does the As $L\alpha$ peak. Since the Ga and As peaks were calibrated with a single GaAs compound standard, the intrusion of the As L_1 tail into the Ga $L\beta_1$ peak would not be a problem, if the GaAs component in the sample is in good stoichiometry. However, the error of using $L\beta$ lines to deal with nonstoichiometric compositions would increase as the nonstoichiometry increases.

On the other hand, we might still use $L\alpha$ peaks for quantification, if additional data processing is considered, as shown below. We have noticed that the intensity of the tail of the Ge $L\beta_4$ peak under the position of the As $L\alpha$ peak is equivalent to 0.531% the Ge $L\alpha$ peak intensity. If an equivalent amount of 0.531% Ge $L\alpha$ peak signal intensity is subtracted from the collected As $L\alpha$ peak intensity (after the background subtraction), the correct As content could be obtained. Shown in Fig. 2 is the result for a group of samples under discussion whose x-ray signal data had been collected with respect to the $L\alpha$ peaks, with all the As $L\alpha$ peak intensities then subtracted by an equivalent amount of 0.531% Ge $L\alpha$ peak intensities. From this figure, we see that the GaAs component in this group of (GaAs)Ge MBE films clearly shows deviation from stoichiometry. This nonstoichiometry was achieved during the film growth by variation of the ratio of fluxes of Ga and As and changing the substrate tempera-

ture.³ The correlation between the degree of nonstoichiometry and the growth conditions will be discussed in a separate publication.

X-ray Emergence Depth. In the present work, we were dealing with thin films 0.5-1.5 μ thick, so that we had to use an accelerating voltage below 10 kV. The effect of the acceleration voltage on the x-ray emergence depth can be seen from the following experiments. The 8kV voltage was applied to a sample consisting of a Ge film 0.51 μ m thick deposited on a GaAs substrate. The computed composition of this sample on the average was approximately Ge/Ga/As = 98.6/0.7/0.7 in atomic percentage. The tiny amount of x-ray signal from the substrate which had reached the spectrometers could affect the actual composition determination of a film if its thickness approaches 0.5 μ m. Therefore, the acceleration voltage should be further reduced for films of this thickness. The same voltage was also applied to a thin film of pure Ge 1.07 μ m thick deposited on a GaAs wafer, and the nominal amount of Ga and As in the film was computed to be less than 0.1at%. However, when a voltage of 12 kV was applied to the same sample and $K\alpha$ peaks were used for quantification, the nominal amount of Ga in the film was computed to be about 6% and the As content was zero.

Conclusions

In this work, we were working on thin (GaAs)Ge films 0.5-1.5 μ thick. In order to avoid the interference of the x rays generated from the substrate, we had to employ a low accelerating voltage. From experiments, we realized that the voltage had to be lower than 10 kV, and therefore the L peaks of the three elements had to be used for quantification. The next important consideration was how to reduce or eliminate the influence of the interference between various L line x-ray signals. To determine the stoichiometry of the GaAs component in the films, we argued that it was best to use the $L\beta_1$ peaks for the purpose if the Ga and As peaks were calibrated with a single GaAs compound standard. To determine the nonstoichiometry of the GaAs component in some MBE films, we showed that the $L\alpha$ peaks could serve the purpose better provided that the interference of the Ge $L\beta_4$ peak to the As $L\alpha$ peak was accounted for by subtraction of an equivalent amount of 0.531% Ge $L\alpha$ peak intensity from the As $L\alpha$ peak intensity.

Therefore, in the present electron microprobe work, we were able for the first time to demonstrate that the GaAs component in the (GaAs)Ge films can be made either in stoichiometric composition or in nonstoichiometric composition, by a change in the epitaxial growth conditions.

References

1. L. C. Davis and H. Holloway, "Properties of $(\text{GaAs})_{1-x}\text{Ge}_2\text{x}$ and $(\text{GaSb})_{1-x}\text{Ge}_2\text{x}$: Consequences of a stochastic growth process," *Phys. Rev. B* 35: 2767, 1987.

2. J. L. Pouchou and F. Pichoir, "PAP $\phi(\rho z)$ procedure for improved quantitative microanalysis," *Microbeam Analysis--1985*, 104.

3. R. J. Baird et al., "Germanium/gallium arsenide alloys grown by molecular beam epitaxy," *Phys. Rev.* (in press).

4. D. R. Liu, S. S. Shinozaki, and R. J. Baird, "Determination of stoichiometry of GaAs component in (GaAs)Ge epitaxially grown thin films by electron microprobe x-ray analysis," *Proc. XII ICEM*, 1990, 264.

MICROANALYSES OF STRUCTURAL DEFECTS IN POLYMER-DERIVED CERAMIC FIBERS

H. A. Freeman and J. A. Rabe

Fiber-reinforced ceramic matrix composites are undergoing investigation as candidate materials for demanding structural high-temperature applications. When properly fabricated, these composites are not expected to exhibit the brittle, catastrophic failure mode typical of traditional ceramics and they should be far more resistant to oxidation than carbon/carbon composites. High fiber strength is necessary to provide the desired reinforcement and toughening. Retention of these properties and overall stability of the composite in specific environments assure the best performance. Unfortunately, commercially available ceramic fibers often degrade during fabrication steps or subsequent use.¹ For example, fibers with a primarily Si-C-O composition may evolve CO and SiO in certain circumstances,² which leads to SiC grain growth and porosity development that act as critical flaws to weaken the fiber.

An Si-N-C-O fiber has now been developed through the pyrolysis of a hydridopolysilazane (HPZ) polymer precursor. It displays significantly improved high-temperature compositional and microstructural stability. However, the tensile strength of early versions declined in a manner similar to that of Si-C-O fibers even under conditions where the HPZ fiber suffered no other detectable changes. Since the full benefit of the improved bulk stability was not being realized, a program has begun to understand and eliminate causes of this strength loss.

Experimental

HPZ fibers were exposed in a tube furnace to temperatures of 1400 C or more for varying times under atmospheres of argon or nitrogen. Primary fracture surfaces from single-filament tensile test specimens were then captured³ and examined individually. Scanning electron images showed all critical defects to be small localized sites of degradation or structural change in otherwise unaltered fibers that were typically 12 μm in diameter. Three general defect types were found: roughly spherical inclusions in the fiber interior (Figs. 1-4), surface pits sometimes associated with granular aggregates (Fig. 5), and single crystals or

clusters of crystals growing from the fiber surface (Figs. 6 and 7).

Microanalyses were performed on these defects with a Cameca MBX scanning electron microprobe and a JEOL JEM 2000FX analytical electron microscope equipped with a Noran Instruments Micro-ZHV ultrathin window detector (EDS) and TN 5500 system. Electron diffraction analyses were also conducted.

Results

The roughly spherical internal inclusions located in fracture planes of a series of HPZ fibers were found to contain a small amount of Pb in addition to the usual Si, C, N, O, and minor Cl (Fig. 1). Others, in addition, contained Sn (Fig. 2). Seen in profile (Fig. 3), one such Pb-containing inclusion exhibited a somewhat irregular surface with small protruding crystals identified as SiC by electron diffraction (Fig. 4).

A second type of defect responsible for the initiation of fracture showed a pit containing a minute particle and surrounded by a slightly granular halo (Fig. 5). Energy dispersive x-ray analyses (insets in Fig. 5) revealed a small amount of Ca, possibly some Al, and a level of O higher than that typical of the fiber surface. Granular aggregates contained within other surface depressions were found to contain Fe and Cr.

Fine growths of single crystals and whisker aggregates at discrete sites on the HPZ surface also initiated tension fracture. Some of them were identified as silicon oxynitride by electron diffraction (Fig. 6). Clusters of crystalline Si_3N_4 whiskers on other fiber specimens (Fig. 7a) contained Fe and Ni at their somewhat enlarged tips (Fig. 7b). These whiskers were apparently formed via a VLS whisker growth mechanism⁴ where Fe/Ni particulates were present at the fiber surface.

Conclusions

The evidence suggested that the defects were induced by concentrations of catalytic species introduced in the form of particulate impurities. Many of the detected impurities have been reported to degrade ceramic fibers⁵ or profoundly to affect the course of nitridation and other processes^{6,7} related to Si-N-C-O ceramic degradation reactions. Microscopical analyses performed on the polymer precursors traced back some of the impurities to specific process stages (Fig. 8) and suggested ways of minimizing their occurrence. Ceramic fibers with lower impurity levels have now been produced that retain their strength better after elevated temperature exposure.

The authors are with the Research Division of Dow Corning Corporation in Midland, MI 48640. They appreciate the assistance provided by L. K. Frevel, C. T. Li, J. Lipowitz, and N. R. Langley as well as support under DARPA funding, U.S. Air Force Contract F33615-83-C-5006, administered by the USAF Wright Research and Development Center Materials Laboratory, Dr. Allan Katz.

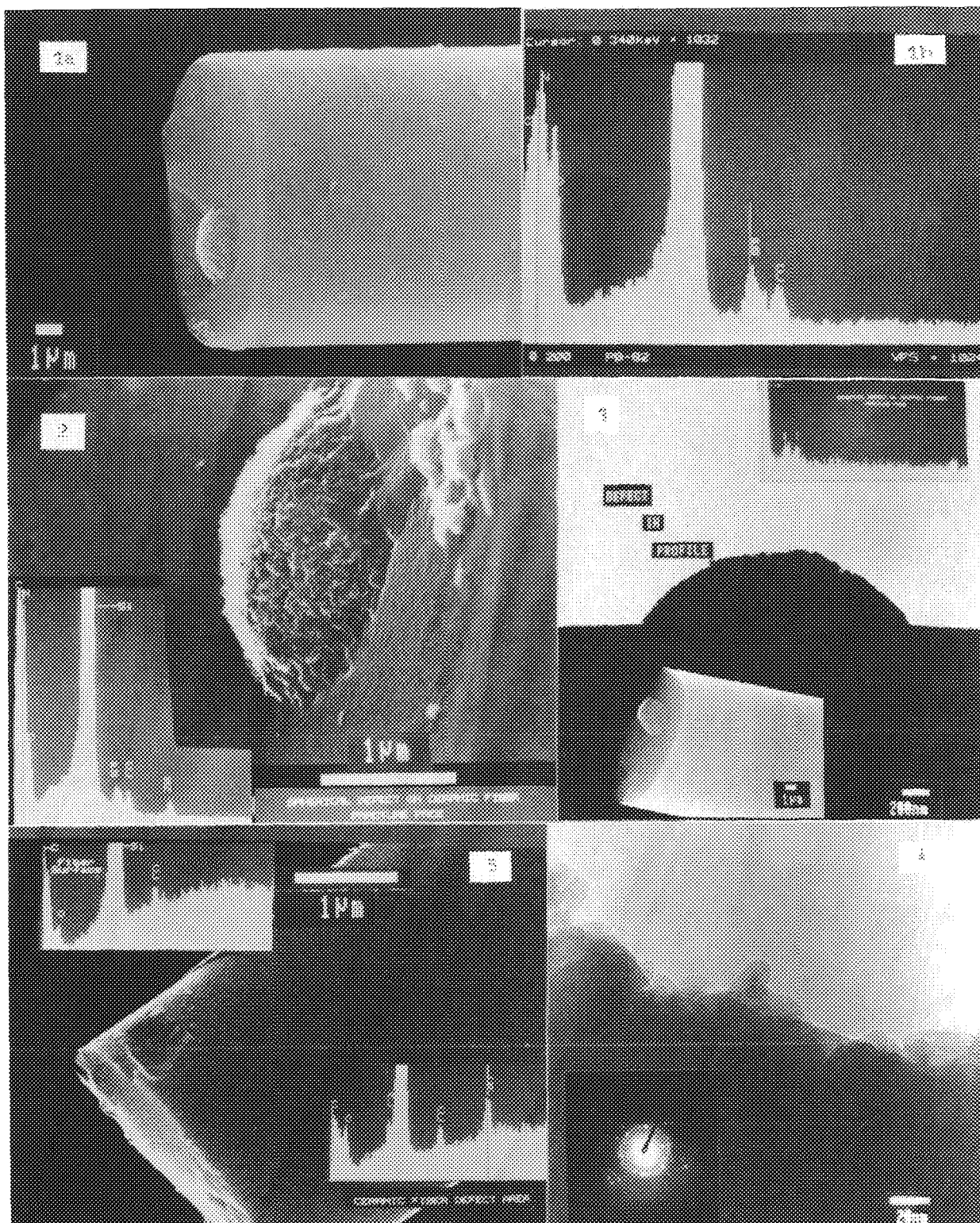


FIG. 1.--Interior spherical inclusion flaw on primary tensile fracture surface of HPZ fiber: (a) fractured end with flaw, (b) EDS spectrum from the flaw.
 FIG. 2.--Spherical inclusion containing Pb and Sn (inset EDS analysis).
 FIG. 3.--Transmitted image of spherical inclusion profile from tensile fracture fiber surface (lower inset), EDS spectrum (upper inset).
 FIG. 4.--Spherical inclusion from Fig. 1, electron diffraction pattern (inset)
 FIG. 5.--Surface pit with central particle, EDS spectrum of pit (lower inset), typical spectrum from fiber surface (upper inset).

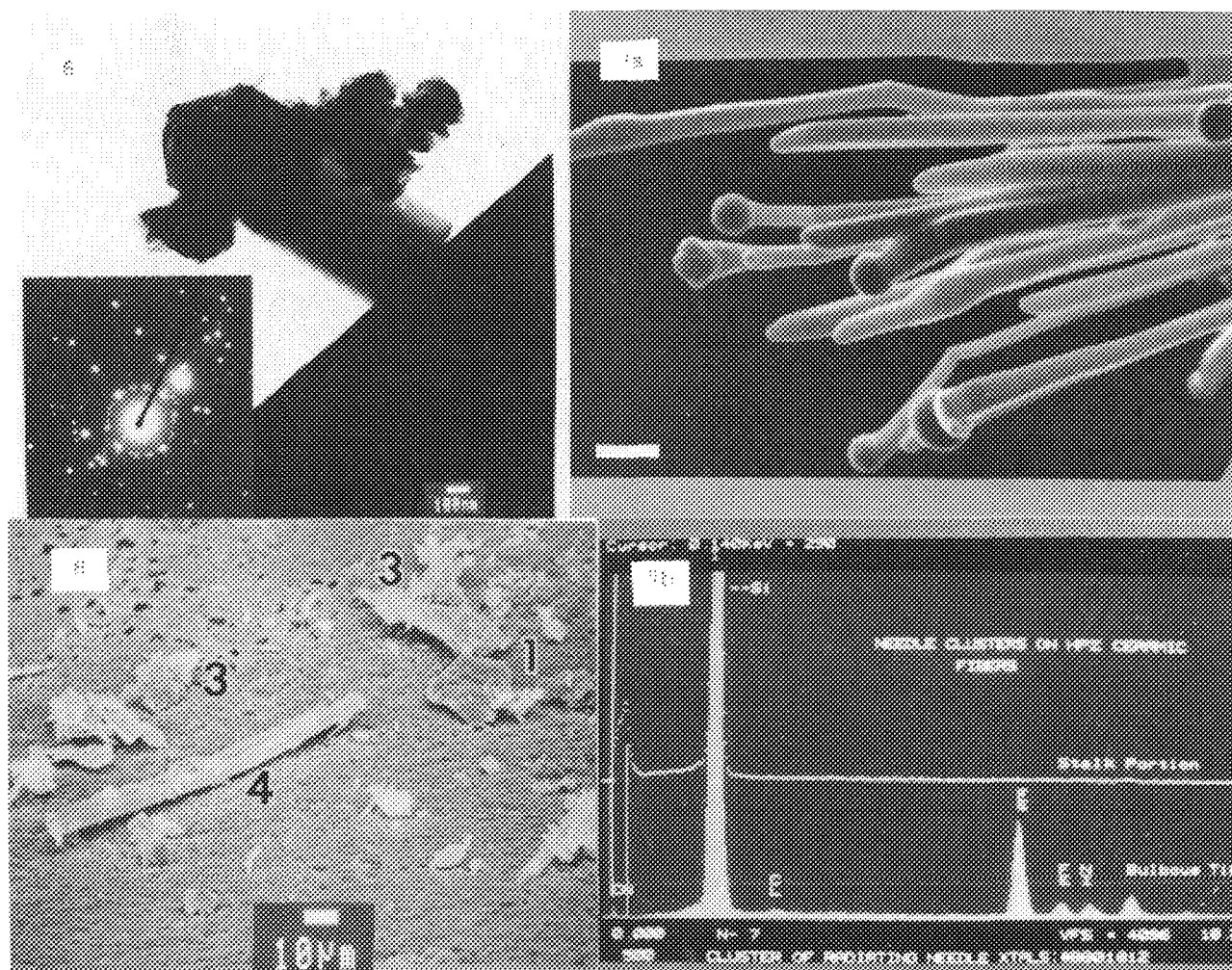


FIG. 6.--Silicon oxynitride whisker aggregate on fiber surface, electron diffractogram (inset).
 FIG. 7.--VLS whisker growths, (a) extending from fiber, (b) EDS spectra of silicon nitride stalk and bulbous tips containing Fe and Ni. Bar scale = 10 μ m.
 FIG. 8.--Particles isolated from polymer precursor: #1-diatomite; #3-silicates containing Fe and Ca; #4-Fe, Cr, Ni metal particle.

References

1. T. Mah, M. G. Mendiratta, A. P. Katz, and K. S. Mazdiasni, "Recent developments in fiber-reinforced high temperature ceramic composites," *Ceram. Bull.* 66: 304, 1987.
2. J. Lipowitz, J. A. Rabe, N. R. Langley, and H. A. Freeman, "Thermal behavior of polymer-derived Si-N-C-O ceramic fibers," *Proc. Elect. Chem. Soc.* (in press).
3. C. T. Li, "A simplified method for capturing primary fracture surfaces for fractographic analysis," *J. Mater. Sci. Letters* 9: 233, 1990.
4. J. V. Milewski, F. D. Gac, J. J. Petrovic, and S. R. Skaggs, "Growth of beta-silicon carbide whiskers by the VLS process," *J. Mater. Sci.* 20: 1160, 1985.
5. S. M. Johnson, R. D. Brittain, R. H. Lamoreaux, and D. J. Rowcliffe, "Degradation mechanisms of silicon carbide fibers," *J. Am. Ceram. Soc.* 71: C-132, 1988.
6. S. A. Siddiqi and A. Hendry, "The influence of iron on the preparation of silicon nitride from silica," *J. Mater. Sci.* 20: 3230, 1985.
7. W. R. Moser, D. S. Briere, R. Correia, and G. A. Rossetti, "Kinetics of iron-promoted silicon nitridation," *J. Mater. Res.* 1: 797, 1986.

A MACINTOSH INTERFACE FOR THE CAMECA CAMEBAX-MICROBEAM ELECTRON MICROPROBE

C. E. Henderson

Over the past few years it has become apparent in our multi-user facility that the computer system and software supplied in 1984 with our CAMECA CAMEBAX-MICROBEAM electron microprobe analyzer has the greatest potential for improvement and updating of any component of the instrument. Although the standard CAMECA software running on a DEC (Digital Equipment Corporation) PDP-11/23+ computer under the RSX-11M operating system can perform almost any task required of the instrument, the commands are not always intuitive and can be difficult to remember and frustrating for the casual user (of which our laboratory has many). Given the widespread and growing use of other microcomputers (such as PCs and Macintoshes) by users of the microprobe, the PDP has become the "oddball" and has also fallen behind the state of the art in terms of processing speed and disk storage capabilities. Upgrade paths within products available from DEC are considered to be too expensive for the benefits received. After using a Macintosh for other tasks in the laboratory, such as instrument use and billing records, word processing, and graphics display, its unique and "friendly" user interface suggested an easier-to-use system for computer control of the electron microprobe automation. Specifically a Macintosh IIx was chosen for its capacity for third-party add-on cards used in instrument control.

Hardware

An RS-232 serial line from the Macintosh computer to the built-in CAMECA microprocessor controls the stage and spectrometer automation. In addition there are four 16-bit parallel lines for electron beam control and video signal digitizing. These input/output (I/O) functions are performed by the addition of a Creative Solutions Hurdler-HQS quad port serial board and two National Instruments NB-DIO-32F parallel I/O boards into three of the Macintosh's NuBus slots.^{1,2} Custom cables were fabricated to connect the new cards to the existing cabling of the microprobe. Changeover between the Macintosh and the older PDP-11 computer systems takes about 5 min; only one minor and reversible modification to the CAMECA automation electronics is necessary.

Software

Software source code supplied with the CAMECA probe was written in FORTRAN-IV and PDP-11 assembly language. For ease of software conver-

sion, FORTRAN was chosen as the programming language on the Macintosh; specifically the FORTRAN-77 compiler supplied by Language Systems Corporation was selected for its ability to be used in the Macintosh Programmer's Workshop (MPW) programming environment.^{3,4} MPW will link subroutines written in several languages, such as Pascal, C, or FORTRAN, to allow for greater flexibility in future software modification. Initial programming efforts concentrated on the emulation of the PDP-11-based system. Original assembly language routines for input and output of control data to the microprobe automation were rewritten in FORTRAN and carefully tested. The CAMECA program, CMB, which contains many small subroutines to control all aspects of the instrument automation, was also successfully converted to the Macintosh and correctly operated the microprobe stage, spectrometer, and beam control automation.

The next phase of programming involves the implementation of a true Macintosh user interface and the integration of instrument control and data reduction into three distinct applications: qualitative analysis, quantitative analysis, and instrument setup/testing. As an aid to implementing the Macintosh interface, a commercial package of precompiled resources (FaceWare Pack) is being used to control interface items such as pull-down menus and dialog boxes for user data entry. The Macintosh program MBX (qualitative analysis) has been written and includes many features that make the use of the microprobe more intuitive to the average user. We hope that controlling the microprobe with programs such as MBX will allow users to concentrate less on specific software commands and more on the methods and results of microanalysis. Next, applications will be written to handle quantitative analysis and instrument testing. Other applications, such as image acquisition/processing and special data reduction routines, should follow.

Advantages and Disadvantages of the Macintosh-based System

Advantages

1. Ease of use by different users due to the "friendlier" Macintosh user interface.
2. Greatly increased processor and disk speed over the PDP-11-based system. Hardware upgrades are available to increase processor speeds further.
3. Availability of a wide variety of third-party hardware and software.
4. Relatively low cost, as compared to other minicomputers and workstations. Cost to equip a Macintosh II series computer with the neces-

C. E. Henderson is at the Electron Microbeam Analysis Laboratory, 1006 C. C. Little Bldg., University of Michigan, Ann Arbor, MI 48109-1063.

sary communications boards is approximately \$1600.

5. Ease of connectivity with other computers, printers, and networks through Appletalk and Ethernet. Data can be easily shared in a local network of Macintoshes and PCs.

6. Since the source code has been completely reworked and updated, future programming should be less difficult.

7. Dedicating the existing PDP-11/23+ to the Kevex 8000 analyzer allows the latest Kevex RT-11 software for EDS analysis and digital imaging to be used concurrently with probe automation software.

Disadvantages

1. Loss of combined EDS-WDS analysis capability. Perhaps the Kevex EDS system could be interfaced to the Macintosh at some later date.

2. Loss of the multi-user, multitasking capabilities of the DEC RSX-11M operating system. With other networked computers that can share data from the microprobe computer, this feature becomes less important.

References

1. Creative Solutions, Inc., 4701 Randolph Rd., Suite 12, Rockville, MD 20852.

2. National Instruments Corp. 12109 Technology Blvd., Austin, TX 78727-6204.

3. Language Systems Corp., 441 Carlisle Dr., Herndon, VA 22070.

4. Apple Computer, Inc., 20525 Mariani Ave., Cupertino, CA 95014.

5. FaceWare, 1310 N. Broadway, Urbana, IL 61801.

IN SITU ION BEAM CLEANING IN A CAMBRIDGE S-200 SEM

F. C. Laabs

The increased use of the scanning electron microscope as a flexible analytical tool has resulted in its application to a variety of problems based on signals that originate or are controlled by surface properties, including crystallographic orientation, contamination, and structural deformation of the surface layer. This paper describes results and observations of efforts to control and remove that layer by energetic argon ion bombardment.

Experimental

A Kratos Mini-Beam I ion gun was attached to a Cambridge Model S-200 scanning electron microscope; the horizontal port normally occupied by an energy-dispersive spectrometer was used (Fig. 1). The EDS spectrometer was moved to a position 35° above the port position. This configuration results in the ion gun lying in a plane perpendicular to the electron beam and 45° to the tilt axis, necessitating tilting the sample toward the ion beam during ion bombardment and, more important, sputtered material is directed away from the EDS detector. No auxiliary or differential pumping of the ion gun was found necessary in that only marginal vacuum degradation was experienced (4×10^{-6} rather than 2×10^{-6} Torr) with ion beam conditions of $3 \mu\text{A}$ at 2.5 kV.

A thin film sandwich of 1150Å Ni on a 590Å SiO_2 film on a pure Si substrate was used to establish an erosion rate of $\sim 120\text{Å}/\text{min}$ under the aforementioned operating conditions. Figure 2 shows the size and shape of the resulting crater at a 45° sample tilt and an ion exposure time of 5 min.

Originally the SEM operation and ion cleaning operation were separated, since ion bombardment generates great numbers of secondary electrons that in turn flood the secondary electron detector system. However, during the examination of native oxides on aluminum it was observed that a residual level of oxygen was reached that could not be further diminished. Subsequently, experiments were conducted in which the electron beam and EDS spectral collection continued simultaneously with ion-beam bombardment. Figure 3 shows the results of this examination. The oxygen concentration dropped to zero and the ion beam was shut off, whereupon the oxygen concentration rose to the resid-

ual level previously observed. The likely explanation is that at the vacuum level of 3×10^{-6} Torr there is enough partial pressure to allow the development of an oxide layer that passivates the surface and reduces further oxide growth.

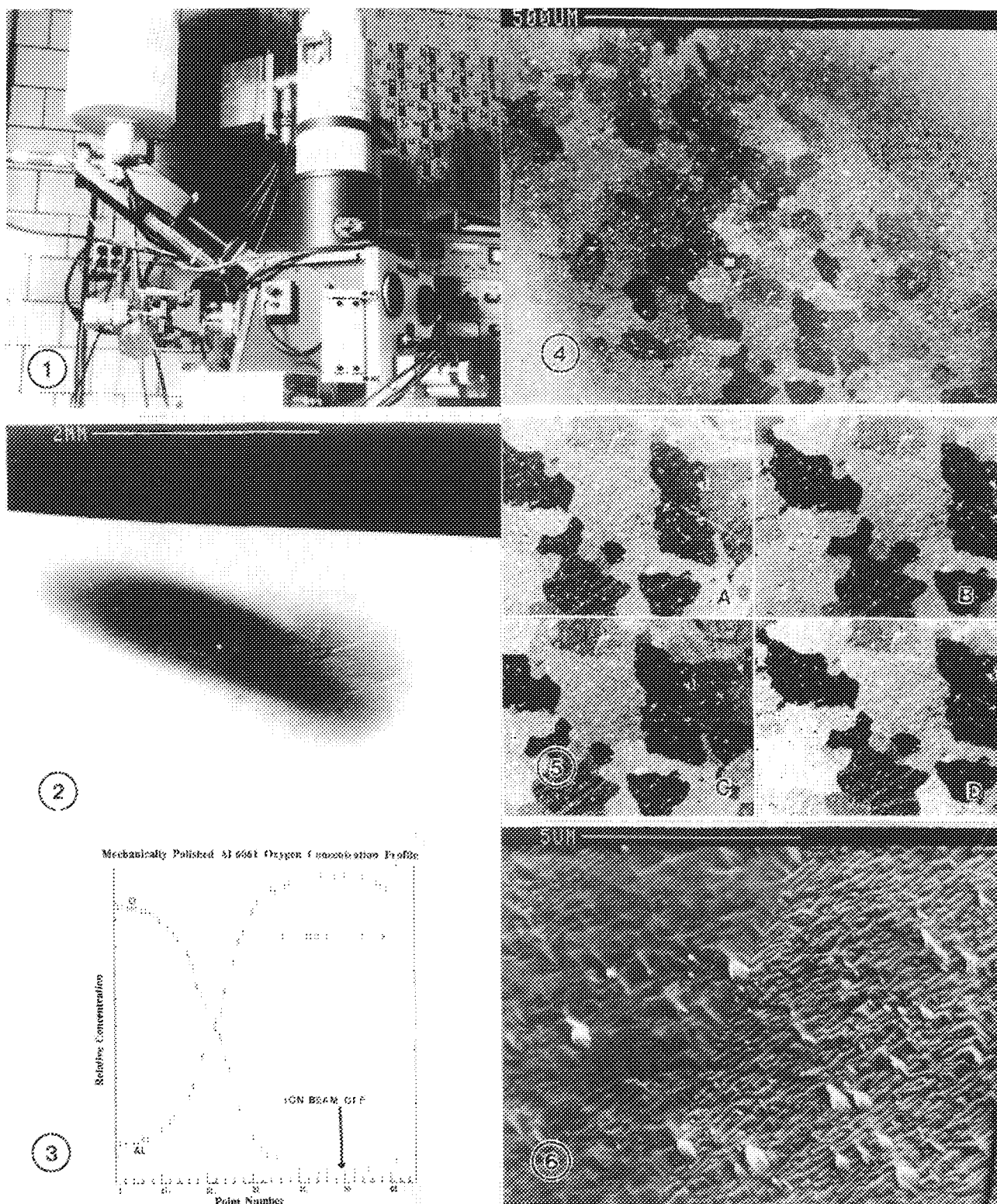
Figure 4 shows a typical SEM-SEI micrograph of an ion cleaned region of a 6061 Al sample. Upon casual examination one might conclude that it exhibits classical diffraction contrast, especially in that the grain structure is clearly visible. However, tilting the specimen as shown in Fig. 5 (in which each micrograph differs from the next by 10° of tilt) causes no change in relative contrast of the various grains, which suggests that the contrast mechanism must be something other than diffraction. Figure 6 shows a higher magnification micrograph of a grain boundary shown in Fig. 5. It can be seen that the contrast mechanism is in fact a "textural" change due to the variability of ion beam erosion with respect to crystallographic orientation. Figure 6 also suggests that surface deformation might in fact be severe enough to negate use of the diffraction contrast mechanisms in the imaging mode. To check on this possibility the sample was electrolytically repolished and reexamined under conditions more optimum for diffraction contrast. Figure 7 shows both backscattered electron images and selected area electron channeling patterns both in the ion-cratered area and in the adjacent electrolytically polished area. It is immediately apparent that the region within the ion crater does not exhibit clear SACP or images showing crystallographic orientation, which suggests relatively severe surface deformation within the first few microns.

6061 aluminum normally contains a variety of precipitates; one is Mg_2O , which is sensitive to pH of routine polishing solutions and slurries and is often lost before it can be analytically examined. To this end numerous precipitates, both in the mechanically polished and electrolytically polished sample, were examined by ultrathin-window EDS techniques and were compared to precipitates in the ion-etched regions of the same sample. Specimens prepared by the traditional mechanical polishing methods showed large variations and inconsistent composition of the observed precipitates. In the case of electrolytic polishing all traces of the Mg_2O precipitate were gone, whereas precipitates detected in the ion crater region clustered consistently into expected compositions.

Conclusions

The use of in situ ion milling for analytical EDS examinations adds considerably to the accuracy of EDS results and can enable x-ray

F. C. Laabs is at Ames Laboratory, Iowa State University, Ames, IA 50011. He wishes to acknowledge the help of his colleagues and of the Ames Laboratory, operated for the U.S. Department of Energy by Iowa State University under Contract W-7405-ENG-82. This research was supported by the Director for Energy Research, Office of Basic Energy Sciences.



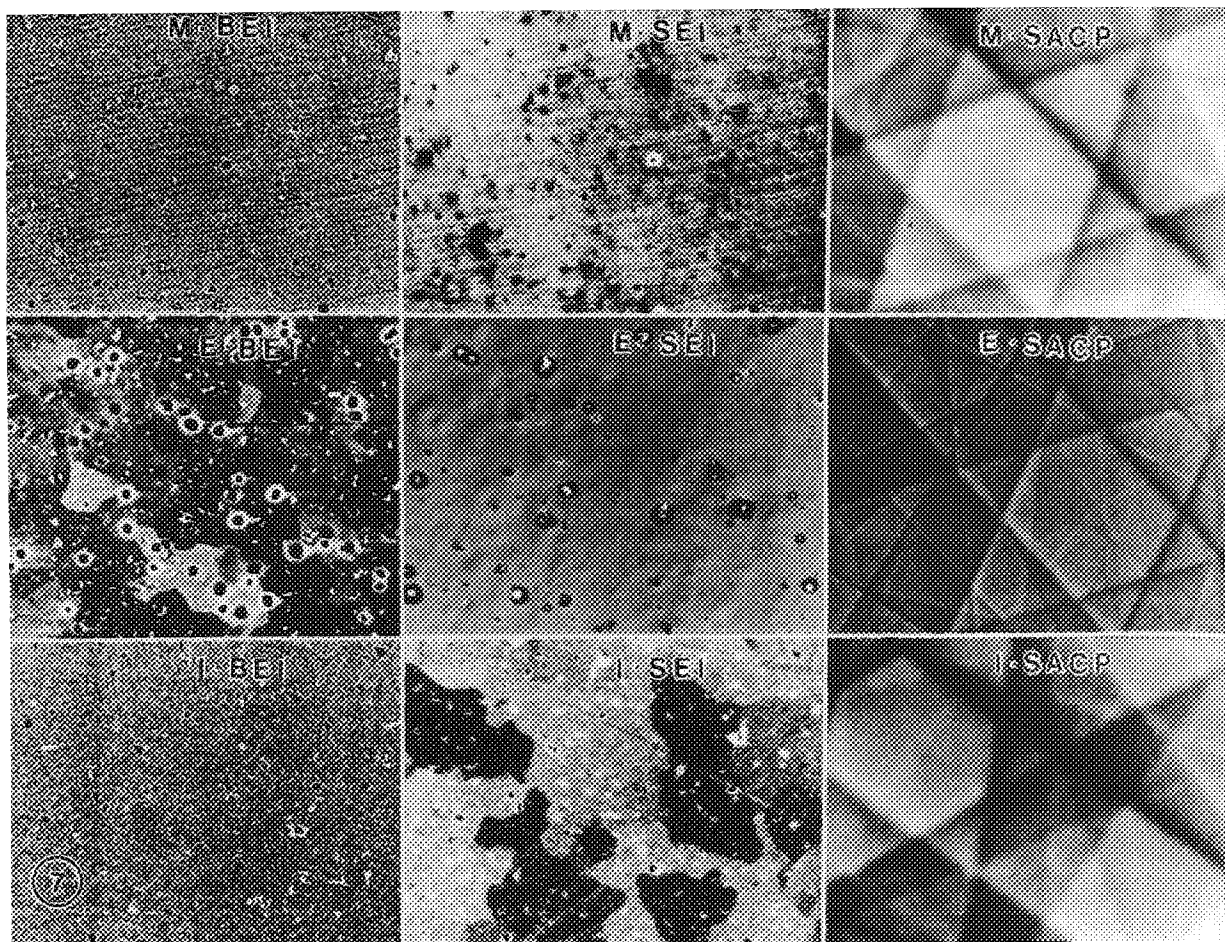


FIG. 7.--Signal response vs polishing technique comparison (M = standard mechanical polishing; E = electrolytic polishing; I = in situ ion milling).

emission studies in depth profiling with results similar to SIMS and Auger. However, it can introduce morphological artifacts that can mask and in some cases completely suppress signals that depend on electron channeling mechanisms. In cases where this could be an adverse effect one can minimize the ion milling time to the smallest amount necessary to remove normal surface contaminants, thereby minimizing substrate deformation.

A PERSPECTIVE OF THE HISTORICAL DEVELOPMENTS AND FUTURE TRENDS IN RAMAN
MICROPROBE SPECTROSCOPY

M. Delhaye and P. Dhamelincourt

The Historical Evolution of Raman "Microsampling"

Immediately following the discovery of the Raman effect, the usefulness of recording Raman spectra for applications in chemical microanalysis was widely recognized. But the early instruments that photographically recorded the Raman spectra excited with a mercury lamp were at that point time consuming and cumbersome. The relatively low level of illumination generated by such incoherent monochromatic light sources required the sample volume to be at least of the order a few milliliters in size.

A very notable advance was achieved in the 1950s with the introduction of photoelectric, direct-recording Raman instruments. For example, the Cary Model 81 Raman spectrometer,¹ introduced in 1953, constituted a decisive advance because of its relative ease of operation, sensitivity, and reproducibility. The use of image slicers, which made it possible to use the light coming from a large area of the Raman cell instead of only a strip in the center, increased the sample light efficiency. Another important advance was the introduction of capillary cells only a few tenths of a milliliter in diameter.

The first Raman experiments that used a laser source (ruby emitting at 6943 Å, He-Ne at 6328 Å) were reported by Porto and Wood² in 1962 and Kogelnik and Porto³ in 1963. They still used a large cell in order to take advantage of total internal reflections at the cell walls. The first commercial laser Raman spectrometer, LRI, was proposed by Perkin Elmer⁴ and used a nonfocused 4mW He-Ne laser and a double-pass Littrow monochromator. A smaller probed volume of 0.2 ml was reported in 1965 by R. C. Hawes⁵ using the modified Cary 81 Raman spectrometer equipped with an He-Ne laser.

In 1966 two papers^{6,7} clearly established the interest of focusing the laser beam to a small waist in a microsample. By considering the conservation of beam spread through the use of coupling optics between the irradiated sample volume and the monochromator or spectrograph, it proved the feasibility of microsampling down to microliter-size volumes. As early as 1967, through the use of glass capillaries, it became possible to obtain useful spectra from an effective scattering volume of 0.04 microliter⁸ and, in 1969, 7 nanoliters.⁹ B. Schrader proposed the use of highaperture aspherical objectives coupled to interference prefilters in 1972.¹⁰

In 1973, T. Hirschfeld¹¹ first published the

The authors are at the Laboratoire de Spectrochimie Infrarouge et Raman (LASIR, CNRS, UPR A 2631L), Université de Lille I, Bât. C.5, F-59655 Villeneuve d'Ascq Cédex, France

revolutionary idea he had proposed in a private communication several years earlier: the laser power contained in a diffraction-limited spot should be sufficient to enable the measurement of the Raman spectrum from a $1\mu\text{m}^3$ sample volume (femtoliter). This statement was first verified independently at NBS (USA) and at CNRS (University of Lille). Abstracts of papers related to real micro-Raman spectroscopy were presented at the Fourth International Conference on Raman Spectroscopy in 1974.^{12,13} The instrument developed at NBS¹⁴ was especially designed to analyze single micrometer-size particles. Briefly, it was a conventional laser Raman Spectrometer, HG 2 S (I.S.A.), in which the sample holder had been replaced by a state-of-the-art fore optical system with components designed to focus the laser beam tightly, in backscattering geometry, on the particle to be analyzed and to collect the scattered light efficiently by means of a high-numerical aperture ellipsoidal mirror with an extremely sophisticated micropositioning system.

In our laboratory at Lille, we more specifically attempted to benefit from the excellent characterization offered by Raman spectra to map out the distribution of chemical substances in a heterogeneous sample.

From our experience in many techniques and applications of Raman studies, including multichannel detection, we decided to create a new instrument we called "MOL," for molecular microprobe, combining both local nondestructive Raman microanalysis and sample mapping. We started out with the tool of the microscopist--the optical microscope--to take advantage of all existing capabilities of optical microscopy (dark- and bright-field sample illumination, large field, and high-quality images). We proposed both point illumination by a diffraction-limited laser beam using the existing beamsplitter and global illumination of the whole field by use of dark-field annular illuminators. As a result, we published the first Raman micrographic images taken in monochromatic light corresponding to a given vibrational mode, in combination with multichannel spectra characterizing micrometer-sized areas.¹⁵

An industrial prototype was shown at the Fifth ICORS in 1976 and the commercial Raman microprobe (MOLE) was constructed under licence by I.S.A. between 1977 and 1980. The U-1000 spectrometer that followed no longer possesses the imaging capability. By the time, Raman microprobing techniques had matured and a large number of applications were described mainly by the two pioneering

laboratories mentioned above.

The next boost to Raman techniques and particularly to micro-Raman was given by the appearance on the market of efficient multi-channel detectors (i.e., silicon diode array, C.C.D.). As emphasized by Bridoux and coworkers in 1963,¹⁶ multichannel detectors offer great advantages over scanning techniques in terms of sensitivity and recording time. Thus, in 1980, again in close collaboration with French industry (the DILOR company), we developed a new Raman microprobe employing spectrographic dispersion using an intensified Reticon diode array as the detector. In this instrument, the entire optical system has been redesigned to optimize the coupling between the sample and the multichannel detector together with improved stray light rejection. Approximately at the time, micro-Raman instruments using commercial multiplex detection systems were developed by various companies (Spex Industries, Instruments SA, Jasco, and others) or assembled by researchers in laboratories.^{17,18}

The Raman microprobing instruments available at present have achieved a high degree of sophistication. More particularly, the acquisition and handling of data by the computer that controls the instruments permit a quasi-automation of the analysis. A perspective of Raman microanalysis in terms of optical microscopy, polarization measurements, coupling with other microbeam analysis techniques, etc., has recently been presented in *Microbeam Analysis--1987-88*.^{19,20} We shall emphasize Raman mapping and imaging techniques which, due to the emergence of very sensitive two-dimensional multichannel detectors and lower stray light monochromators, should become a more widely used technique of heterogeneous sample analysis.

Summary of the Principles of Raman Microprobing

In a very general form the total intensity of Raman light scattered from a volume V of homogeneous sample matter is given by:

$$I_R = \int_V \int_{\Omega} [E_{\text{exc}} \alpha_{XYZ} E_{\text{Sc}}]^2 dv d\Omega$$

where E_{exc} and E_{Sc} are the electric vectors for the exciting radiation and the scattered radiation, respectively.

Complete calculations of the distribution of the electric field E_{exc} in the region of the waist of a polarized laser beam have been published.²¹ A good theoretical basis is also available on the scattering tensor α_{XYZ} , related to the polarizability tensor of the molecules, and the electric vector E_{Sc} . Particularly, their angular dependences, which are theoretically established from the molecular orientations, are characterized in Raman polarization measurements.²² However, in a given experimental configuration, the most difficult task is to evaluate the integrals $\int_V \int_{\Omega}$, which

have to be calculated for the whole observed volume V and the whole solid angle of collection Ω .

Several levels of possible approximations have been proposed. For instance, the following expression is most often used:

$$I_R \approx I_0 \frac{\partial \sigma}{\partial \Omega} \Omega N$$

where N is the number of molecules observed, I_0 is the irradiance of the exciting light at the sample (Watts per unit area), and $\partial \sigma / \partial \Omega$ is the differential cross section for a given Raman band (of the order of $10^{-30} \text{ cm}^2 \text{ sterad}^{-1} \text{ molecule}^{-1}$), assuming that the irradiance I_0 is uniform in the volume V and the scattering is also uniform over the angle Ω . This useful approximation often results in the erroneous conclusion that the Raman signal I_R , proportional to the number of molecules N , is then strictly proportional to the observed volume V . In fact the volume and the angle of collection are not independent. We demonstrated in early papers^{6,7} that focusing the laser beam to a small spot dramatically increases the local irradiance I_0 and enables a much wider angle of collection by means of an optical system coupled to the spectrometer, which compensates for the decrease of the number of molecules N .

A more complete calculation of the Raman signal has to take into account two factors of prime importance: (a) the shape of the laser beam around the focal region; and (b) the optimized optical coupling from the scattering sample to the photoelectric detector, via the collection optics and the monochromator and/or spectrograph.

The Raman Microprobe as a "Confocal Laser Microscope"

The equations governing the properties of focused laser beams were published as early as 1965.²³ More recently, the interest in the results of such calculations has been renewed by the development of "confocal optical microscopes," which improve both the lateral resolution and the optical tomography capabilities.²⁴

The Raman microprobe was really conceived, at its origin, as a "confocal microscope" and demonstrated clearly the potentialities of such instruments. Unfortunately, most instrument makers seemed to ignore this intrinsic feature of the original Raman microprobe, and were happy enough offering the market an approximate association of an existing microscope, through an existing monochromator, to an existing photodetector system.

In fact, a real confocal configuration requires a very accurate optical alignment and a high degree of stability and reproducibility of the mechanical and optical adjustments. These qualities are only encountered in the instruments specially designed for this purpose, and the demonstration of confocal performance constitutes a good test of the excellence of a Raman microprobe.

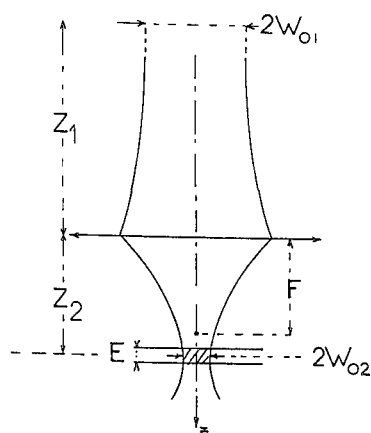


FIG. 1.--Geometry of Gaussian TEM_{00} laser beam focused by convergent system of focal length F . Z_1 and Z_2 are the distances of the optical center of the system to laser cavity waist and focal zone, respectively. $2W_{01}$ and $2W_{02}$ are beam waists inside laser cavity and at focal zone, respectively. E is thickness of sample positioned at focal zone.

The shape of the beam generated in the laser cavity is a hyperboloid characterized by the "waist" diameter $2W_{01}$ corresponding to a plane wavefront, and by the asymptotic divergence angle 2α defined at $1/e^2$ intensity for the Gaussian mode TEM_{00} propagating as a spherical wavefront. Typically, the waist diameter of an argon laser is of the order of 3000λ , which corresponds to a divergence angle $\alpha = 1/3000 \approx 3 \times 10^{-4}$ rad.

The laser beam, received by a convergent aberration-free optical system, made of lenses or mirrors, is focused again to a "waist" $2W_{02}$ where the wavefront becomes plane again, according to the equation

$$\frac{1}{W_{02}^2} = \frac{1}{W_{01}^2} \left(1 - \frac{Z^2}{F^2} \right) + \frac{1}{F^2} \frac{\pi W_{01}^2}{\lambda}$$

where Z is the distance on the optical axis and F is the focal length of the convergent system (Fig. 1).

Use of any of the now available excellent microscope objectives, with short focal length (1 to 5 mm) and high numerical aperture (N.A. = $n \sin \theta$) ranging from 0.5 to 0.95 in air or 1.40 in homogeneous immersion liquids, results in a diffraction-limited laser waist $2W_{02} \approx 1.22\lambda/(n \sin \theta)$ of the order of $0.6 \mu m$ for the visible radiation of an argon laser. The local irradiance in this section of the beam, a fraction of a square micrometer, reaches an extremely high value, even for moderate laser power. For example, 1 mW of laser power focused on a $0.6 \mu m$ circular area corresponds to a local irradiance of $I \approx 300 \text{ kW cm}^{-2}$.

With the use of a beam splitter, the same microscope objective can collect the scattered Raman radiation (Fig. 2). This configuration takes advantage of the wide solid angle Ω to collect a large part of the available Raman

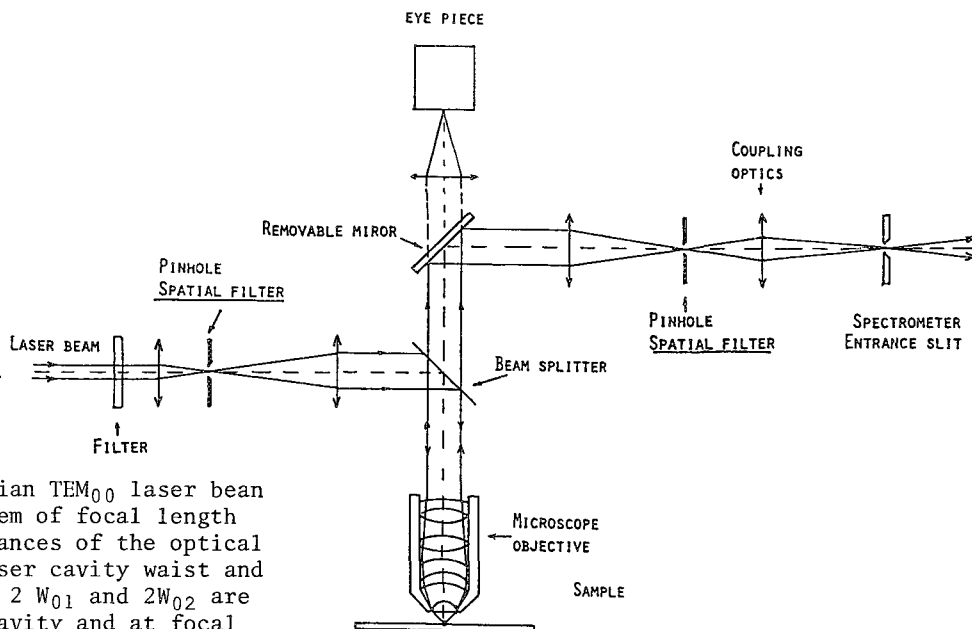


FIG. 2.--Schematic diagram of widely adopted laser-focusing, sample viewing, and scattered light collection geometries for Raman microprobing.

signal. For example, the collected fraction of the energy, assuming a uniform scattering in 4π steradian, is given in Table 1, for various photographic or microscope objectives.

TABLE 1.--Fraction of collected energy as a function of objective numerical aperture (NA).

Fraction ^a of collected energy ($\Omega/4\pi$)	Objective	
	Photographic F number	Numerical aperture ^b (NA = $n \sin \theta$)
$2.5 \cdot 10^{-3}$	F/5	0.099
$1.5 \cdot 10^{-2}$	F/2	0.124
$5.3 \cdot 10^{-2}$	F/1	0.447
$8.4 \cdot 10^{-2}$		0.55
0.2		0.80
0.34		0.95

$$^a \Omega \text{ (steradian)} = 2\pi(1 - \sqrt{1 - NA^2}).$$

$$B_0 = \text{half-angle of collection.}$$

Axial and Lateral Resolutions

The confocal optical configuration, shown in Fig. 2 for a typical Raman microprobe arrangement, requires both excellent focusing properties of the microscope objective and imaging of the observed sample zone on a pinhole diaphragm optically conjugated with the waist $2W_{02}$ (Fig. 3). The incident beam is coherent, whereas the scattered beam is incoherent, which implies different calculations in the optical computing of the beam paths.

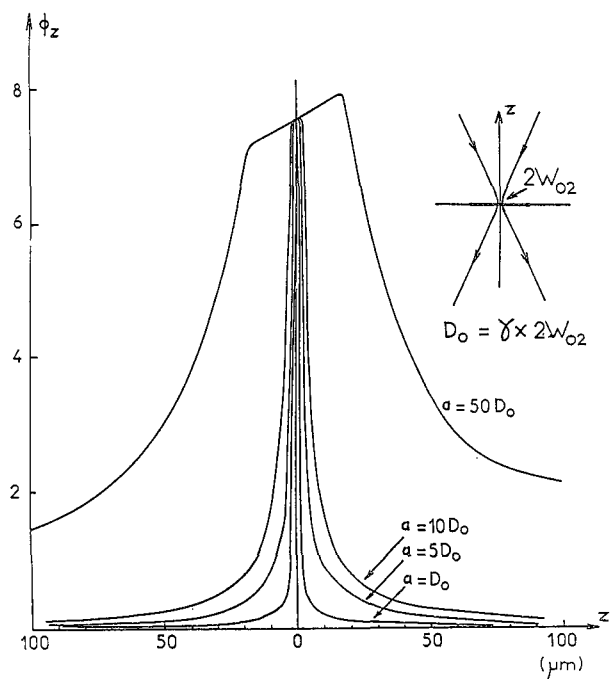


FIG. 3.--Magnitude of scattered light flux (arbitrary units) collected after exit pinhole (cf. Fig. 2) from very thin slice of sample as a function of its vertical position. The $Z = 0$ value is for slice positioned at laser beam waist ($2W_{02}$). D_0 and a are diameters of image of laser beam waist as given by objective and pinhole, respectively. Calculations were made for Leitz objective ($\gamma = 100\times$, $NA = 0.9$). Reduction of pinhole diameter results in decrease of depth of field.

Even for the widest angle of collection by means of a high-aperture objective, the beam geometrical spread $U = (s \times S)/L^2$, where s is the pinhole area, S the pupil or exit aperture top of the microscope objective, and L is the distance between the pinhole and aperture top, is always much smaller than the geometrical spread of a conventional grating monochromator (and obviously of that of a Michelson interferometer, such as those used for FT Raman experiments in the near IR).

The role of intermediate coupling optics is essentially properly to cover the aperture of the grating dispersor so as to insure the desired spectral resolution. As a consequence of the conservation of geometrical spread U along the whole optical system, this coupling optics reduces the total magnification of the microscope system, giving a reduced image on the slit compared to the direct image given by the objective. Another obvious consequence of the invariance of U is that the use of a high-aperture collimator in the spectrometer is unwarranted and does not improve the luminosity.

The axial and lateral resolutions thus depend both on the quality of laser focusing and on the spatial filtering of the incoherent scattered light path. This last factor, implemented by an image-field iris diaphragm

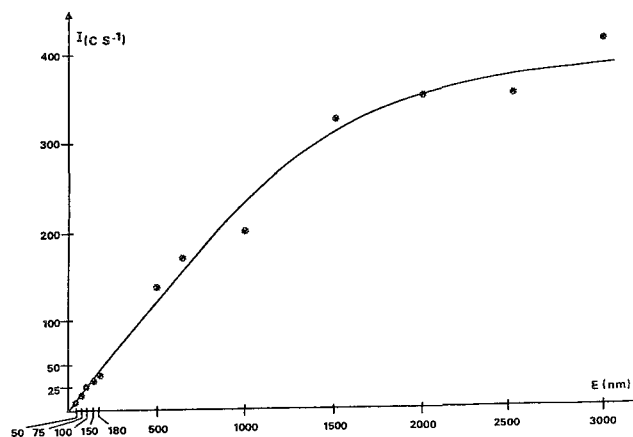


FIG. 4.--Measured intensity of Raman band at 998 cm^{-1} vs thickness of polystyrene sections. Pinhole diameter (cf. Fig. 3) was chosen to insure $a = D_0$. The change in curve slope observed at $2\text{ }\mu\text{m}$ is in good agreement with axial resolution estimated from Fig. 3.

placed in the image plane of the sample, improves the axial resolution. With M. Truchet²⁵ and the Dilor company, we have made a series of experimental verifications of the calculated axial resolution, using as test samples very thin sections of polystyrene. These specimens were obtained by use of a mechanical microtome giving reproducible thickness in the range from several micrometers down to 50 nm. A plot of the measured Raman intensities vs the sample thickness is shown in Fig. 4 and clearly confirms the calculated axial resolution. Figure 5 gives the nonresonant Raman spectrum of the thinnest section (50 nanometers = $500\text{ }\text{\AA} \approx \lambda/10$) obtained with a commercial microprobe system (DILOR XY) without any data treatment.²⁵ The total amount of polystyrene observed in this experiment is of the order of 3×10^{-14} gram.

Raman Mapping and Imaging

For most applications it is sufficient to sample a limited number of selected points over the sample surface (or below) and to relate identified chemical species to the image, as viewed in white-light illumination through the optical microscope. However, in many cases there is no obvious relation between the optical image (color, morphology, reflectivity, etc.) and the distribution of chemical species. Sometimes there is no visual change at all over the observed area (e.g., stress in materials). For all these cases, sampling a few points is not sufficient, and Raman mapping or imaging at several characteristic wave-numbers is needed for an understanding of the nature of the species distribution across the sample.

If the sample area is uniformly illuminated by the laser radiation, all the spatial and spectral information concerning the species is

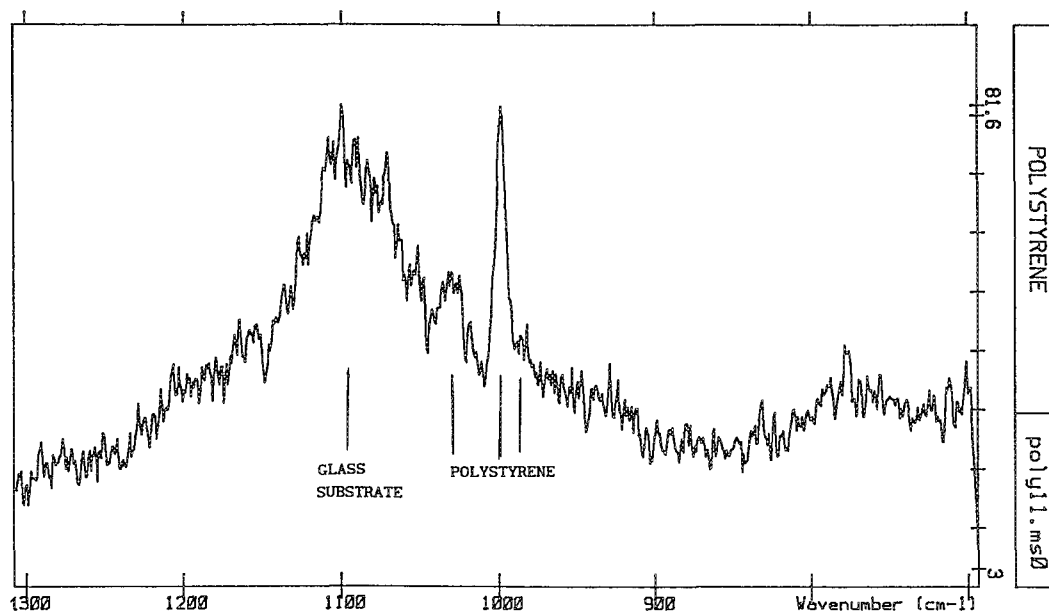


FIG. 5.--Nonresonant Raman spectrum of thin section of polystyrene (thickness = 50 nm = 500 Å $\approx \lambda/10$). Effective amount of matter analyzed is a few femtograms (argon laser = Spectra Physics Model 164, $\lambda_{\text{exc}} = 514.5$ nm, Raman microprobe is the XY DILOR). Prediction made in 1973 by T. Hirschfeld (see text) is at last realized.

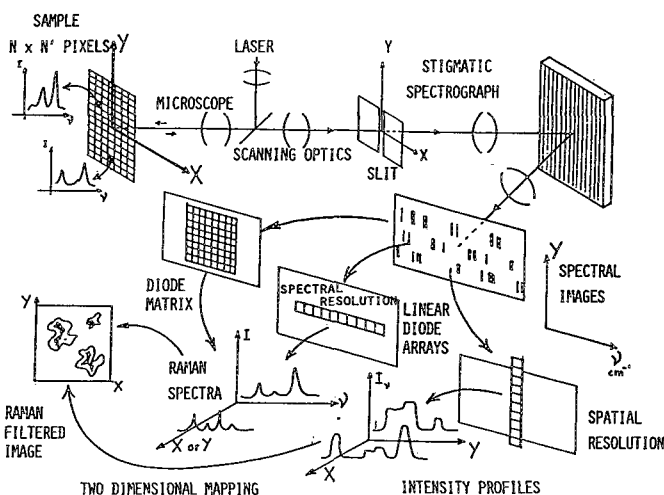


FIG. 6.--Schematic representation of methods employed for obtaining images of samples from characteristic Raman lines.

simultaneously available in the image space of the microscope objective under which the sample is being examined. But it is obvious that it is not feasible to deal with this total information in order to produce direct Raman maps. As early as 1975 we proposed three methods of sample laser illumination and instrument configurations to perform Raman mapping¹⁵ (Fig. 6), as follows.

Point Illumination. The basic design of the instrument is that of a classical Raman microprobe equipped with an intensified diode-array detector with the sample moved beneath

the microscope, by stepping motors. Ideally, in dealing with an unknown sample, a complete spectrum should be recorded for each point analyzed from which spectral information of interest is extracted subsequently for Raman image reconstruction.

This point-by-point complete analysis is, as is obvious, exceedingly time consuming even if the mapping system runs unattended. Moreover, the computer would require a memory of several hundred megabytes to store the data.

Nevertheless, the point illumination method is of great interest because, on the one hand, there is no need to modify an existing instrument; and, on the other hand, because in the conventional instrument configuration the Raman microprobe works like a confocal microscope with a well-defined axial resolution and the best stray light rejection capability. This method permits, for example, the generation of Raman "tomographies" through transparent materials with an axial resolution on the order of a few micrometers, or the analysis of highly reflective materials. In fact, few samples analyzed are totally unknown and it is sufficient to extract a limited number of useful spectral data (e.g., band positions, net integrated intensities, etc.) in order to reconstruct Raman images. Successful maps²⁶ (400 points, providing 4 μm lateral resolution) of methane inclusions in a quartz host have been built up in less than 1 h from net integrated intensities of lines at 2910 cm^{-1} (CH_4) and 464 cm^{-1} (quartz).

Line Illumination. A narrow rectangular area is formed on the sample, either by cylindrical optics or by scanning the laser

beam, and then focused on the entrance slit of the monochromator. In the spectrograph objective focal plane, where the detector has to be placed, and if the monochromator has been corrected for astigmatism, data in the x direction are related to wavenumber, and data in the y direction are related to species position on the sample surface (scanned line).

With a monodimensional multichannel detector, the best instrument configuration results by positioning of the detector parallel to the scanned line y direction. Intensity profiles at a given wavenumber are thus directly obtained. If a reticon diode array is used (2.5mm pixel height), the size of the intermediate slit of the fore monochromator must be adjusted in order to maintain spectral resolution.

With a two-dimensional detector, spectral and spatial data are simultaneously recorded and intensity profiles at several characteristic wavenumbers are generated.

For both detectors, the size of the detector pixel along the y direction insures that the axial resolution is maintained (spatial filtering), but the stray-light rejection is poorer than in point illumination because the total height of the entrance slit is illuminated.

Whatever type of detector is employed, Raman maps can be built up from intensity profiles by a succession of scanned lines in the x directions.

With 2D detectors, the binning process along the y direction commonly used to improve the signal-to-noise-ratio and to reduce integration time impairs spatial, lateral, and axial resolutions. This approach of exploration of the sample was employed by Veirs et al.²⁷ in a macro-Raman experiment (40 μ m lateral resolution), and by S. Kudo et al.²⁸ and M. Bowden et al.²⁹ in micro-Raman experiments (few micrometers lateral resolution).

Global Illumination. We reported in 1974 the results of the first experiments on Raman micrography in which the entire sample was illuminated by laser radiation.¹³ A holographic grating monochromator was modified so as to form an enlarged image of the sample on the grating and beyond on the photocathode of an intensified phototube. The axial and lateral resolutions of the optical microscope were conserved. This set-up was integrated in the first generation of the commercial MOLE microprobe, but a limitation of the instrument's performance was that it lacked sufficient sensitivity and spectral resolution to reveal weak lines and to discriminate Raman features from spectral background. Indeed, in this configuration the aperture stop of the microscope objective was imaged onto the widely opened slits in order not to impair the lateral resolution of the image.

This Raman global imaging method is restricted in that it only gives information about the band selected by the filter, whereas information from the rest of the spectrum is lost. Nevertheless, with sensitive 2D detectors (CCD, CID)

and recent spectrometers with high dispersion and virtually no stray light (e.g., five-stage monochromators developed by the DILOR company), this method acquires a renewed interest because it is the only one that permits quasi real-time imaging capability.

Perspectives

Minimization of Fluorescence Interference. Fluorescence interference is still by far one of the greatest limitations encountered in Raman microanalysis. It is generally less severe than in conventional Raman spectroscopy, because most of the time one can select a part of the sample that fluoresces less. Nevertheless, it is still hindering some sample analyse. Near-infrared (NIR) excitation permits one to minimize or suppress fluorescence interference because most of the samples are not fluorescent when excited with radiation of wavelength of the order of 1 μ m, but that is done at the expense of a far lower sensitivity. Indeed, this last consequence is caused, on the one hand, by the intrinsic $1/\lambda^4$ law for scattering efficiency and, on the other hand, by a lower sensitivity of the available detectors. The multiplex advantage of FT spectroscopy may partially compensate for weaker Raman signals, but the low-frequency range ($< 200 \text{ cm}^{-1}$) is always lost because of the filter used to cut off the Rayleigh line. Moreover, coupling a microscope with a Michelson interferometer is not straightforward and cannot be done without loss of performance. For example, the Raman results reported by R. G. Messerschmidt and B. Chase³⁰ in the analysis of a single Kevlar fiber by means of a commercial IR microscope correspond to a $12 \times 20 \mu\text{m}$ analyzed area. That is very far from the spatial limit imposed by diffraction when samples are excited with near-IR radiation whose wavelength is around 1 μ m. Moreover, even for relatively large samples, a loss of sensitivity of the IR microscope coupled to the FT interferometer compared to a macrosampling system is observed, probably because the optical coupling to the entrance aperture of the Michelson interferometer is unfavorable and causes a loss of the "Jacquinot" throughput advantage. A potential future advance should be the use of the new NIR-sensitive linear-array detectors that have recently appeared on the market. Indeed, efficient conventional NIR spectrographs exist and there is no limitation on the throughput by coupling of these instruments with microscopes. Another approach is the use of Hadamar spectroscopy,³¹ which also uses conventional spectrometers or spectrographs; moreover, the encoding mask can effectively remove the Rayleigh line. However, only a few experiments have been reported so far.

Coupling with Other Techniques. *Separation techniques.* Coupling Raman microprobing with thin-layer chromatography has already been described. With the use of capillaries to deposit the analyte of interest, spots with

areas of the order of hundreds of square micrometers are easily attained and analyzed because of easy sample positioning.³²

Electron microprobe. The successful implementation of a Raman system has been recently described by Delhaye and Truchet.³³

Laser microprobes based on ion mass analysis (LAMMA or LIMA) should be the next ones amenable to coupling with Raman microprobing.

Tunneling Optical Microscopy. Lewis et al.³⁴ described a method that permits the resolution to be extended below the limit imposed by diffraction. The principle, first introduced in microwave experiments, is in the "near-field" effects of an electromagnetic wave propagating through a hole whose dimension is much smaller than the wavelength. Laser light is sent into a metal-coated glass pipette of inner diameter down to several tens of nanometers. With a tunneling-microscope type of device, the pipette tip scans over the surface of the sample within the near-field condition. The authors reported not only super-resolution optical microscopy capabilities, but also the detection of fluorescence excited in this manner. The extension to vibrational microspectroscopy should be feasible in the near future, including perhaps Raman spectroscopy in situations where a strong enhancement by resonance excitation or by surface-enhanced Raman scattering (SERS) compensates for the inherent weakness of Raman phenomena.

References

1. H. Cary, W. S. Galloway, and K. P. George, *Molecular Spectroscopy Symposium*, Ohio State University, Columbus, Ohio, 1953.
2. S. P. S. Porto, and D. L. Wood, *J. Opt. Soc. Am.* 52: 251, 1962.
3. H. Kogelnik and S. P. S. Porto, *J. Opt. Soc. Am.* 53: 1446, 1963.
4. E. H. Siegler, C. D. Hinman, and A. F. Slomba, *Molecular Spectroscopy Symposium*, Ohio State University, Columbus, Ohio, 1964.
5. R. C. Hawes, *Pittsburgh Conference*, 1965.
6. M. Delhaye and M. Migeon, "Calcul du gain apporté par un dispositif optique de concentration du faisceau laser pour l'étude de l'effet Raman," *C. R. Acad. Sci. Paris*, 262: 702, 1966.
7. M. Delhaye and M. Migeon, "Intérêt de la concentration d'un faisceau Laser pour l'excitation de l'effet Raman," *C. R. Acad. Sci. Paris*, 262: 1513, 1966.
8. G. F. Bailey et al., "A new Raman microsampling technique," *Anal. Chem.* 39: 1040, 1967.
9. M. Deporcq-Stratmains and R. Demol, "Spectroscopie Raman-Laser de petite échantillons," *Revue Gams* 3: 234, 1969.
10. W. Meier, B. Schrader, and M. Pisarcik, "Einfaches, lichtstarkes Ramanspektrometer mit Laser-Lichtquelle," *Messtechnik* 5: 119, 1972.
11. T. Hirschfeld, "Vibrational spectroscopy in the femtogram range" (abstract), *J. Opt. Soc. Am.* 63: 476, 1973.
12. G. J. Rosasco, E. S. Etz, and W. A. Cassat, "Investigation of the Raman spectra of individual micron-sized particles," *Proc. 4th ICORS*, 1974.
13. M. Delhaye and P. Dhamelincoirt, "Laser Raman microprobe and microscope," *ibid.*
14. G. J. Rosasco and E. S. Etz, "A new microanalytical tool: The Raman microprobe," *Research and Development* 28: 20, 1977.
15. M. Delhaye and P. Dhamelincoirt, "Raman microprobe and microscope with laser excitation," *J. Raman Spectrosc.* 3: 33, 1975.
16. M. Bridoux et al., "Photographie rapide du spectre Raman," *Rev. Gams* 4: 309, 1963.
17. P. Milanovich et al., "The Lawrence Livermore National Laboratory Raman microprobe," *Microbeam Analysis--1982*, 270.
18. F. J. Purcell and E. S. Etz, "A new spectrograph with a multichannel optical detector for the Raman characterization of microparticles," *ibid.*, 301.
19. P. Dhamelincoirt and M. Delhaye, "Evolution and prospects of Raman microprobing techniques," *Microbeam Analysis--1987*, 119.
20. M. Delhaye, P. Dhamelincoirt, and J. Barbillat, "The evolution and perspective of Raman microanalysis," *Microbeam Analysis--1988*, 153.
21. B. Richards and E. Wolf, *Proc. R. Soc. London* A253: 358, 1959.
22. G. Turrell, "Analysis of polarization measurements in Raman microspectroscopy," *J. Raman Spectrosc.* 15: 103, 1985.
23. G. D. Boyd and H. Kogelnik, *Bell. Syst. Tech. J.* 41: 1347, 1962.
24. T. Wilson and C. Sheppard, *Theory and Practice of Scanning Optical Microscopy*, New York: Academic Press, 1984.
25. P. Dhamelincoirt et al., "Etude en microspectrométrie Raman de l'efficacité de détection en fonction de l'épaisseur des échantillons: Détermination de la profondeur de champ et conséquences pour le couplage avec un microscope électronique à transmission," *J. Raman Spectrosc.* (in press).
26. DILOR Company technical sheet C1011, 1989.
27. D. K. Veirs et al., *Microbeam Analysis--1988*, 179.
28. S. Kudo, J. Mizuno, and H. Hasegawa, *Adv. Ceramics* 24: 103, 1988.
29. M. Bowden et al., "Line-scanned micro-Raman spectroscopy using a cooled CCD imaging detector," *J. Raman Spectrosc.* 21: 37, 1990.
30. R. G. Messerschmidt and D. B. Chase, "FT-Raman microscopy: Discussion and preliminary results," *Appl. Spectrosc.* 43: 11, 1989.
31. P. J. Treado and M. D. Morris, "A thousand points of light: The Hadamard transform in chemical analysis and instrument instrumentation," *Anal. Chem.* 61: 723 A, 1989.
32. J. P. Ebanga, *Contribution à l'étude des pesticides par spectrométrie Raman*, Thesis, University of Lille, 1982.

33. M. Truchet and M. Delhayé, "Couplage d'une sonde Raman laser et d'une sonde de Castaing dans un microscope électronique," *J. Microsc. Spectrosc. Electron.* 13: 167, 1988.

34. A. Lewis et al., "Near-field optics: Application of microbeams of light with wavelength-independent resolution beyond the diffraction limit," *Microbeam Analysis--1988*, 164.

RECENT ADVANCES IN THE ANALYSIS AND INTERPRETATION OF C-O-H-N FLUIDS BY APPLICATION OF LASER RAMAN MICROSCOPY

J. D. Pasteris, J. C. Seitz, Brigitte Wopenka, and I-Ming Chou

The initial goal of Raman spectroscopic studies of fluids by physicists and chemists was a better understanding of molecular structure and intermolecular forces.¹⁻³ Beginning in the mid-1970s, geologists and other applied scientists became interested in laser Raman microspectroscopy (LRM)⁴⁻⁷ as a means of nondestructive analysis of fluid inclusions, which are minute volumes (tens of cubic micrometers) of fluids (with various densities) trapped in minerals. This paper briefly summarizes the application of LRM to the analysis of fluid inclusions, some of the existing Raman spectroscopic data on gases, and the need for more data on C-O-H-N gas mixtures at elevated pressures (up to about 1000 bars). Some of our recently acquired experimental data illustrate the kinds of quantitative information that can be extracted from Raman spectra of fluid inclusions.

Background

A major goal of geologists is to use field and laboratory observations to infer the temperature, pressure, and composition of a given system during rock formation or ore deposition. Because fluids are actively involved in many rock-forming processes, fluid inclusions trapped within minerals are studied as direct evidence of the pertinent system parameters. Due to the complex histories of many geological environments, individual minerals may contain several generations of fluid inclusions. Micro-analytical techniques therefore are required for the measurement of small quantities of materials in individual inclusions, some of which are supercritical fluids at hundreds of bars pressure.

Raman microspectroscopy has long been recognized as a qualitative technique for the identification of covalently bonded dissolved aqueous species (e.g., sulfate and carbonate) and volatile components (e.g., CO₂, CH₄, N₂) in fluid inclusions.^{6,7} More recent LRM studies have explored means of improving *quantitative* analysis by examining the accuracy, reproducibility, and detection limits of the method via

studies of natural samples and synthetic mixtures.⁸⁻¹² The application of numerous LRM studies has provided data that are essential to the interpretation of geologic processes and that cannot, in many cases, be derived by other analytical techniques.^{6,10-18} Dubessy et al.¹⁸ summarized some of the advances that have been made in the understanding of C-O-H-N-S fluid geochemistry based on the Raman microspectroscopic analysis of fluid inclusions.

Three aspects of quantitative Raman microspectroscopic analysis that are particularly significant to geologists are the measurement of composition, density, and isotopic ratios. The ease in making accurate and reproducible isotopic determinations by LRM analysis for fluid inclusions and solid phases has improved markedly with the introduction of triple-mono-chromator systems with multichannel analyzers,^{6,19} but will not be discussed here. This paper focuses on compositional and density determinations of fluids in the C-O-H-N system, which encompasses most volatile species of geologic interest.

The compositional analysis of volatile-bearing fluid inclusions by LRM appears quite straightforward, in that only ratios, or molar proportions, of species are determined. According to Placzek's theory,²⁰ the intensity of Raman scattered radiation from a species Y (in an inclusion) is proportional to the intensity of the incident radiation, the number of molecules of species Y in the irradiation volume, and the Raman scattering efficiency of species Y (σ_Y). The Raman scattering efficiencies of pure gases of geological interest are tabulated in the literature,^{18,21} as analyzed at 1 bar pressure, relative to the scattering efficiency of nitrogen (defined as $\sigma^0 = 1$). Given the integrated peak intensities (i.e., areas A) of two species Y and Z in the same phase of a fluid inclusion, the ratio of their molar concentrations X can be calculated from

$$(X_Y/X_Z) = (A_Y/A_Z) (\sigma_Z/\sigma_Y) (\eta_Z/\eta_Y) \quad (1)$$

where η is the instrumental efficiency for the wavelength and polarization of light that is scattered from the species. In principle, quantitative analysis also can be achieved in a similar manner by comparison of the relative intensities (peak heights) of the species.

Methodologies for Raman Analysis of Multicomponent Fluids

Among the complexities in applying Eq. (1) to a compositional analysis are the derivations of η (instrumental efficiency) and σ (Raman

The authors are at the Department of Earth and Planetary Sciences, Washington University, Campus Box 1169, St. Louis, MO 63130, except Chou, who is at the U.S. Geological Survey, MS 959, Reston, VA 22092. J. C. Seitz's present address is Department of Geological Sciences, VPI&SU, Blacksburg, VA 24061.) This work was supported in part by NSF grant EAR 8708123 to JDP and BW. The authors thank Harvey Belkin, John Freeman, and George Morgan for comments on a previous version of this paper.

scattering efficiency) values appropriate for fluid-inclusion analysis. The evaluation of η requires, among other measurements, the determination of the wavelength response of the instrument by use of a lamp calibrated for spectral radiance. In addition, the optical throughput of spectrometer gratings is also very sensitive to the orientation of the plane of polarization of the incident light. In the past, spectroscopists using Raman *macrospectrometers* to make measurements on low-pressure gases have accounted for this polarization effect either by placing a polarization scrambler between the sampling chamber and the monochromator to randomize the polarization of light entering the monochromator, or by using a polarizer that transmits only one plane of polarization. The former technique requires knowledge of the wavelength-dependent transmission of the scrambler. For the latter technique, since simple gases are strongly polarized at low pressure, their small but well-defined depolarization ratios have been used to *calculate* the intensities that *should* result if all directions of vibration could be measured (i.e., simulating polarization insensitivity of the gratings).²¹ [Note: Some spectrometers require use of a half-wave plate before the monochromator to rotate the Raman scattered radiation to the most favorable orientation with respect to the gratings.] Thus, the σ^0 's published in the literature are derived values.

However, in Raman *microspectrometers* the small diameter of the focused beam of scattered radiation precludes effective implementation of a scrambler between the microsampling device and the monochromator, as discussed in the first technique above. Unfortunately, problems also arise with the second technique, because depolarization occurs in fluids at elevated pressures.²²⁻²⁴

Due to the preceding uncertainties associated with *macro*- and, particularly, *micro*-Raman spectroscopic analysis of gases, considerable attention must be given to the appropriate choice of σ values for quantitative analysis. Three basic approaches to deriving a molar compositional ratio from the Raman spectrum of a multicomponent fluid inclusion are currently used: (a) assume that the *ratios* of σ^0 values at 1 bar are valid at all pressures and for all mixtures of interest; (b) apply calculated or experimentally determined pressure corrections to the σ^0 values of the pure gases, and assume that these values are valid in gas mixtures; and (c) do Raman analyses of the pure gases and gas mixtures over the pressure range of interest, and interpret the spectra of inclusions based on these calibrations.

Approach (a) is the simplest, and the one implicitly recommended by Dubessy et al.,¹⁸ who suggest that Eq. (1) can be calculated readily, that the uncertainties in the values of the Raman scattering efficiencies are of the same order as the uncertainties in the fluid models to which the Raman data will be applied, and that the resulting compositional analyses are sufficiently accurate for most geological applications. Dubessy et al.¹⁸ also point out that

for years many laboratories have published Raman analyses of fluid inclusions based on *normalized* differential Raman scattering cross sections listed by Schrötter and Klöckner,²¹ but that these tabulated values must be recalculated for the specific wavelength of excitation used in an analysis. Their recalculation of the scattering efficiencies¹⁸ brought the σ -values considerably closer to our published experimental Raman "quantification factors" (product of σ and η), which were derived by analysis of known gas mixtures in capillaries.⁹ The similarity of our values is fortuitous, in that the quantification factors account for both the pressure dependence (up to 16 bars) and composition dependence of σ , as well as for the instrument function η .

In addition to the instrumental uncertainties in the published values of σ^0 , additional complications are involved with their application in Eq. (1). The scattering efficiencies were derived for pure gases at 1 bar, and their use for gas mixtures at 10s to 100s of bars pressure involves numerous (some testable) assumptions, as discussed in previous publications^{8,9,24} and examined in this work.

Approach (b) is based on calculated pressure corrections for 1-bar Raman scattering efficiencies (σ^0). "High-pressure scattering efficiency values" (σ_p) incorporate a correction for the internal field effect (L), according to the definition that σ_p is equal to $(\sigma^0)(L)$ (Fig. 1). Calculation of the internal field effect is based on the refractive index of a fluid as a function of pressure and wavelength, and is hampered by the scarcity of data.²⁴ Moreover, these correction procedures do not account for additional effects, such as specific intermolecular interactions, which would be enhanced in mixtures and at elevated pressure^{21,25} (Fig. 1). In addition, some consequent complexities in the measurement of band intensities arise at elevated pressures. For example, spectral depolarization in compressed gases affects the efficiency of propagation of the signal through the spectrometer due to polarization sensitivity of the gratings.

We believe that approach (c), spectroscopic analysis of both pure gases and gas mixtures at elevated pressures, is required to determine the true spectral responses of species in natural multicomponent fluid inclusions. Although obtaining the parameters necessary for accurate calculation of Eq. (1) is time consuming, the resulting compositional data are significantly more useful than those determined from indiscriminant application of literature values. Moreover, as discussed in this work, other (geologically) valuable information can be derived from the necessary Raman experiments on high-pressure gas mixtures.

Approach (c), either directly or indirectly, involves the determination of effective scattering efficiencies σ^* , through monitoring of the spectral response of each species in the pure gas and gas mixtures of interest as a function of pressure. The goal of many spectroscopic studies is to derive information on fundamental parameters such as Raman scattering

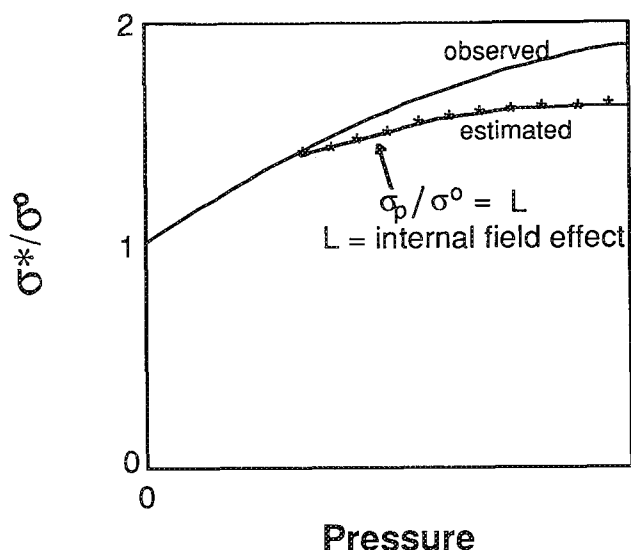


FIG. 1.--Schematic representation of pressure dependence of σ^*/σ^0 for a gas, showing possible relation between observed measurements (σ^*) and calculated values (σ_p); $\sigma_p = (\sigma^0)(L)$, σ^0 is relative (to nitrogen) Raman scattering efficiency at 1 bar, L is internal field effect. Based on actual data²⁵ for ν_1 of N_2 .

efficiency or intermolecular forces. This process requires the determination of peak areas, application of accepted corrections for wavelength and polarization effects in the instrument, and calculation of fundamental parameters of the gas molecules. In the absence of intermolecular interactions, the measured value of σ^* equals the calculated value of σ_p .²⁵ The spectroscopic research group of Fabre et al.²⁵ has investigated the Q branch of pure nitrogen ($\approx 2327 \text{ cm}^{-1}$) at room temperature up to 3000 bars, using a Raman macrospectrometer. They determined that at pressures above about 500 bars σ^*/σ^0 for N_2 gas begins to deviate appreciably from the calculated value of L (internal field correction, based on refractive index; cf. Fig. 1).

For application to fluid inclusions, there is also a need to translate the peak areas obtained on multicomponent fluids into compositional analyses. This need leads to two principal questions. If Raman spectra are obtained at various pressures on a single gas mixture of known composition, (1) does application of published σ values yield the correct compositional analysis, and (2) is the peak-area ratio of the species constant over all pressures? If all gases of geological interest behaved as predictably as N_2 up to several hundred bars pressure, if the refractive index measurements required to calculate the internal field effect were available, and if molecular interactions among unlike molecules in mixtures were negligible, then it would be possible to calculate accurately compositions of multicomponent fluid inclusions based on σ^0 values in the literature (approach b). At present, however, there are not sufficient experimental data to evaluate the

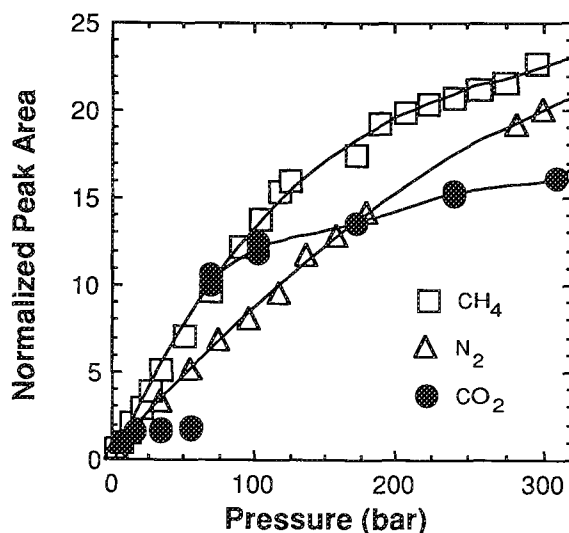


FIG. 2.--Relation between peak area and pressure for pure CH_4 , N_2 , and CO_2 . Each peak area normalized to respective peak area measured at 6.9 bars pressure. Discontinuity in CO_2 data is due to gas-liquid phase change. Differences in normalized spectral responses (i.e., trajectories) are due to differences in pressure sensitivity of scattering efficiencies of individual species and possibly to changes in polarization state of fluid, which affects efficiency of signal propagation through spectrometer. Uncertainty in measurement of pressure is ± 1 bar; uncertainty in measurement of area ratios is approximately ± 2.5 -5 relative %.

relation between σ^* and pressure for pure CO_2 and CH_4 , or for binary mixtures of CO_2 , CH_4 , and N_2 . We have thus begun an applications-oriented Raman investigation of the endmember gases and binary gas mixtures in the system N_2 - CH_4 - CO_2 at room temperature and at pressures up to about 700 bars. The spectral data can be used directly to derive instrument-specific calibration curves for the accurate compositional (and density) analysis of fluid inclusions (approach c). Moreover, the data provide spectroscopic information on the intermolecular dynamics of gas species as a function of gas pressure and composition.

Experimental Methods

All analyses were done with a 1983 model RAMANOR U-1000 laser Raman microprobe (Instruments SA) outfitted with a modified Olympus BH-2 microscope. The scanning spectrometer system consists of double one-meter monochromators in additive configuration. A 5W Ar-ion laser (514.5 nm) was used to deliver about 10 mW excitation at the surface of the optical cell, as transmitted by an Olympus 50 \times ultra-long-working-distance objective with a numerical aperture of 0.55. The photon detector is an RCA C31034 photomultiplier tube. Most analyses were done using a 0.5 cm^{-1} stepping interval, 5-10 s dwell time per point, and a spectral resolution of about 5 cm^{-1} . In some

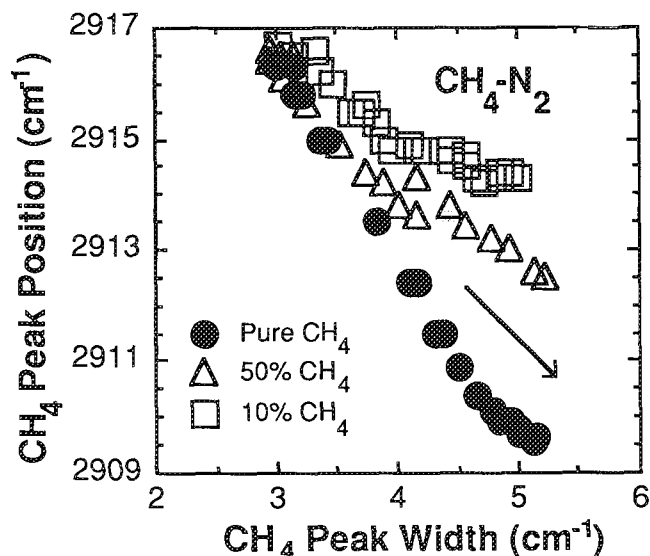


FIG. 3.--Relation between position and full width at half height for ν_1 band of CH_4 in pure CH_4 and in CH_4 - N_2 mixtures (listed in mole %). Arrow indicates direction of increasing pressure. Uncertainty in measurement of peak position is less than $\pm 0.2 \text{ cm}^{-1}$.

cases, multiple scans were summed to increase the signal-to-noise ratio. In our instrument, the grating grooves are horizontal, as is the plane of polarization of light exiting the microscope after scattering by strongly polarized samples. A half-wave plate is therefore inserted between the microscope and the monochromator to maximize spectral throughput. The optical cell consists of a fused quartz tube 3 mm OD \times 1 mm ID into which known gas mixtures are introduced. The gas is pressurized by a mechanical piston, and monitored by an on-line pressure transducer.²⁶

The analytical set-up and scanning procedure used in the gas experiments are very similar to those routinely applied to fluid inclusions analyzed in our laboratory. The spectral resolution is much lower (about 5 cm^{-1}) than that required by most Raman *macro*spectroscopic studies of gases that were done in the past. The main reason for analyzing the gas standards under these conditions is to ascertain exactly which spectral parameters can be measured and quantified in a fluid inclusion. However, this optical configuration is not desirable for determining the absolute values of spectroscopic parameters whose measurements require high spectral resolution or vary as a function of the polarization state of the sample.

The parameters measured in our study include the spectral peak positions and both the absolute values and the ratios of Raman peak intensities, areas, and widths. These experimentally derived parameters can be used to characterize both the composition and internal pressure of fluids in inclusions. For CO_2 , the spectral separation of the two bands of the Fermi diad also was monitored. Some similar data, derived by Raman *macro*spectroscopy, are available for

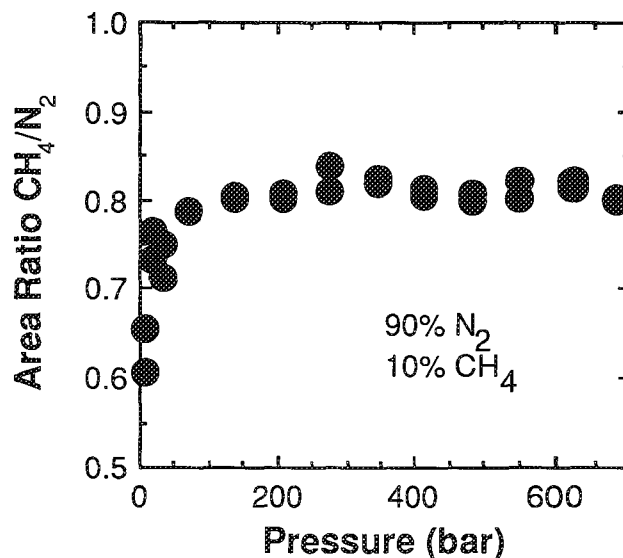


FIG. 4.--Ratio of areas of ν_1 bands of N_2 and CH_4 in 90:10 (molar) N_2 : CH_4 gas mixture as a function of pressure. Uncertainty in measurement of pressure is about ± 1 bar, in measurement of peak area ratios is about ± 3 relative %.

pure CH_4 , CO_2 , and N_2 ,^{23,25,27-29} but we have concentrated on mixtures at pressures applicable to fluid-inclusion analysis.

Experimental Results and Discussion

Peak areas of pure CH_4 , N_2 , and CO_2 (normalized to their respective areas at 6.9 bars) as a function of pressure are shown in Fig. 2. The relations among the normalized peak areas result primarily from differences in the pressure sensitivity of their Raman-scattering efficiencies. Given our analytical conditions, it is not possible to evaluate for these individual gases whether the relation between σ^*/σ^0 and pressure is accurately modeled by L (approach b). However, the data in Fig. 2 do suggest that the application of ratios of uncorrected σ^0 values to high-density fluid inclusions (approach a) will produce considerable inaccuracies. These data on the endmember gases furthermore suggest that use of a *constant* σ ratio (derived at low pressure) for CH_4 - N_2 mixtures with a range in density will result in errors in compositional determination, because the curves for the pure gases do not exactly covary.

Although the spectroscopic investigation of endmember compositions is useful for interpreting fluid-phase systematics, the data most necessary for the analysis of multicomponent fluid inclusions are calibration spectra of gas mixtures. The concern is how the effective Raman scattering efficiencies (σ^*) of individual species respond to the internal field effect and intermolecular interactions imposed by both like and unlike molecules in a gas mixture. These effects are reflected in the band shapes and positions. The spectral parameters derived during calibration experiments on the various

gas mixtures may be applied to the Raman spectra of inclusion fluids without regard to the theoretical significance of the calibration spectra. The experimental data may be also used to investigate some aspects of the spectroscopic behavior of gas species in mixtures.

One test of the effect of adding species Z to species Y is to monitor the relation between peak width and peak position for a Raman band of Y, as a function of pressure, both in the presence and absence of species Z. The relation between peak position, peak width, and pressure for the ν_1 band of CH_4 is well documented in the literature,²⁷ and has been reproduced in our own experiments. Figure 3 shows how the relation between spectral width and position for the ν_1 band of CH_4 is affected by the addition of nitrogen. As might be expected, increasing deviation from the behavior of pure CH_4 is observed as the proportion of N_2 is increased. Our experiments on 50-50 mixtures of CH_4 with N_2 , H_2 , and Ar all show different extents of decoupling (compared to pure CH_4) of the relation between spectral width and position for the ν_1 band of CH_4 .

Another test of the effect of mixing of the components is illustrated in Fig. 4. The ratio of the peak areas for the ν_1 bands of CH_4 and N_2 mixture changes as a function of pressure (up to about 75 bars). The relation between the peak area ratio and pressure is not what one would expect from an investigation of the pure endmembers (cf. Fig. 2). This finding illustrates the need to investigate actual gas mixtures in order to calibrate a Raman microprobe for quantitative analyses of fluid inclusions.

An additional benefit of such experiments is the ability to calibrate the positions of Raman bands for individual species as functions of gas pressure and composition. As the relations in Figs. 2 and 4 indicate, an independent measurement of pressure is required in order for the Raman peak area ratios to provide compositional analyses. Our data on peak positions agree with similar data for pure CH_4 , N_2 , and CO_2 available in the literature,^{25,27-29} but we have extended our studies to gas mixtures. Calibration curves derived through these experiments enable the estimation of both internal pressure (density) and composition in the same fluid inclusion, in many cases with an accuracy that exceeds that of the classically accepted and only other viable technique, microthermometric analysis. (The latter involves freezing the fluid inclusion and monitoring the temperatures at which it melts and subsequently homogenizes to a one-phase fluid. Given sufficient information, these phase changes can be interpreted in terms of a composition and density of the fluid.) Furthermore, by documenting the co-variation of spectral peak positions, intensities, areas, and widths, the most sensitive parameter with respect to some property, such as pressure, can be identified and selected for closer examination in natural and synthetic fluids.

Why Are Experimental Calibrations Necessary?

The geologist uses the compositional and density data from a suite of fluid inclusions to model the physicochemical conditions and changes that pertained during the evolution of a rock. Clearly, the more accurate the analyses are, the more accurate the model results will be. The experimental Raman data presented above demonstrate the usefulness of investigating the actual spectral response of gas species in high-pressure gas mixtures like those occurring in natural fluid inclusions. Only in this way can one evaluate the inaccuracies produced by reliance on σ^0 ratios.

In their review paper on the application of Raman microspectroscopy to C-O-H-N-S fluid geochemistry, Dubessy et al.¹⁸ correctly emphasize the usefulness of even semiquantitative Raman analyses of fluid inclusions. They investigate some of the ramifications of the estimated uncertainties in the published σ^0 values. Their conclusion is that the uncertainty in the models, to which fluid-inclusion data are applied, would not be reduced significantly by further Raman quantification. Our response is that (1) the inaccuracies introduced by use of σ^0 values are not known, and indeed may be very different depending on the specific chemical system and the pressure of the fluid under pressure; and (2) increased accuracy in the determination of fluid compositions would significantly affect some geochemical models.

Differential spectral response of certain fluids could lead to the misleading appearance of compositional trends, based on the very assumption of constancy of σ ratios. For instance, our data suggest that fluid inclusions of the same composition can yield different Raman peak area ratios for different internal pressures. Disregard for this effect could lead to the incorrect conclusion that changes had occurred in the composition and oxygen pressure of a fluid during the evolution of a particular rock system or that two rock systems had evolved differently.

Of particular concern are the increases in the uncertainties due to *coupling* of measurements. For instance, Raman analyses of fluid-inclusion composition in some cases are paired with microthermometric measurements from which density can be inferred (given accurate knowledge of the fluid composition). Although the predicted uncertainties in the σ^0 values employed may not cause intolerably large uncertainties in the fluid compositional analysis, use of these inferred compositions may produce considerably larger uncertainties in the density determinations. The end result can be unacceptably large uncertainties in the inferred temperature and pressure of fluid trapping in the rock (uncertainties on the order of 100s of °C and 1000s of bars pressure).

Conclusions

For years many geologists involved in Raman microspectroscopy have used approach (a), assuming that the *ratios* of the σ^0 values deter-

mined for species at 1 bar are the same as ratios of the σ^* values for the same species in high-density inclusions. Our contention remains that this relation is not known *a priori*. Only after the appropriate experiments have been done, will it be possible to evaluate how closely the actual data are reproduced by various models, over the pressure range of interest.

Our recent work has shown that the discrepancies between published scattering efficiencies, σ^0 , and individually calibrated quantification parameters are in large part due to actual molecular interactions in gas mixtures of geological interest, whereas we previously had concentrated on such discrepancies as a function of the inability to account for instrumental (primarily optical) effects in Raman microprobes. Although the need for calibration of individual Raman microspectrometers may be debated, an observation that remains undisputed is that the Raman spectrum of a volatile species is sensitive to its physical and chemical environments (e.g., pressure), presence of other gas species, and dissolution in an aqueous solvent. One can take advantage of this spectral sensitivity in the study of fluid inclusions, so as to derive accurate data not only for composition but also for density.

Raman microspectroscopic analyses of fluid inclusions, even at a semiquantitative level, have constrained models of the geologic history of a wide variety of rock systems. However, considerable analytical improvement is possible. The spectral variations revealed in our ongoing Raman microspectroscopic studies on pure gases and gas mixtures as a function of pressure make it clear why calibration is essential to the derivation of accurate compositional analyses. Furthermore, with such calibration, Raman spectroscopy is one of only two nondestructive microanalytical techniques for the accurate determination of both composition and density of individual fluid inclusions. For a wide range of gas compositions and pressures of geological interest, calibrated Raman microspectroscopy can provide more accurate data than microthermometry.

References

1. A. D. May et al., "The Raman effect in gaseous hydrogen at high pressures," *Can. J. Phys.* 39: 1769, 1961.
2. A. D. May et al., "Vibrational frequency perturbations in the Raman spectrum of compressed gaseous hydrogen," *Can. J. Phys.* 42: 1058, 1964.
3. R. P. Srivastava and H. R. Zaidi, "Intermolecular forces revealed by Raman scattering," in A. Weber, Ed., *Raman Spectroscopy of Gases and Liquids*, New York: Springer-Verlag, 1979, 167 (and references therein).
4. M. Delhaye and P. Dhamelincourt, "Raman microprobe and microscope with laser excitation," *J. Raman Spec.* 3: 33, 1975.
5. G. J. Rosasco et al., "The analysis of discrete fine particles by Raman spectroscopy," *Appl. Spec.* 29: 396, 1975.
6. P. Dhamelincourt et al., "Analysis d'inclusions fluides à la microsonde MOLE à effet Raman," *Bull. Minéral* 102: 600, 1979.
7. E. S. Etz, "Raman microprobe analysis: Principles and applications," *SEM/1979* 1: 67.
8. B. Wopenka and J. D. Pasteris, "Limitations to the quantitative analysis of fluid inclusions in geological samples by laser Raman microprobe spectroscopy," *Appl. Spectrosc.* 40: 144, 1986.
9. B. Wopenka and J. D. Pasteris, "Raman intensities and detection limits of geochemically relevant gas mixtures for a laser Raman microprobe," *Anal. Chem.* 59: 2165, 1987.
10. G. J. Rosasco and E. Roedder, "Application of a new Raman microprobe spectrometer to nondestructive analysis of sulfate and other ions in individual phases in fluid inclusions in minerals," *Geochim. Cosmochim. Acta* 43: 1907, 1979.
11. J. Dubessy et al., "The determination of sulphate in fluid inclusions using the MOLE Raman microprobe: Application to a Keuper halite and geochemical consequences," *Geochim. Cosmochim. Acta* 47: 1, 1983.
12. T. P. Mernagh and A. R. Wilde, "The use of the laser Raman microprobe for the determination of salinity in fluid inclusions," *Geochim. Cosmochim. Acta* 53: 765, 1989.
13. J. Dubessy et al., "The use of the Raman microprobe MOLE in the determination of the electrolytes dissolved in the aqueous phase of fluid inclusions," *Chem. Geol.* 37: 137, 1982.
14. N. Guilhaumou et al., "Raman microprobe analysis of gaseous inclusions in diagenetically recrystallized calcites," *Bull. Minéral* 107: 193, 1984.
15. C. Ramboz et al., "The P-V-T-X- fO_2 evolution of H_2O - CO_2 - CH_4 -bearing fluid in a wolframite vein: Reconstruction from fluid inclusion studies," *Geochim. Cosmochim. Acta* 49: 205, 1985.
16. T. Andersen et al., "Nitrogen-bearing, aqueous fluid inclusions in some eclogites from the Western Gneiss region of the Norwegian Caledonides," *Contrib. Mineral. Petrol.* 103: 153, 1989.
17. J. D. Pasteris and B. J. Wanamaker, "Laser Raman microprobe analysis of experimentally re-equilibrated fluid inclusions in olivine: Some implications for mantle fluids," *Amer. Mineral.* 73: 1074, 1988.
18. J. Dubessy et al., "Advances in C-O-H-N-S fluid geochemistry based on micro-Raman spectrometric analysis of fluid inclusions," *Eur. J. Mineral.* 1: 517, 1989.
19. R. C. Burruss et al., "Raman microprobe observations of carbon and oxygen stable isotopes in geologic materials," *Microbeam Analysis--1989*, 173.
20. G. Placzek, "Rayleigh-Streuung und Ramaneffekt," in E. Marx, Ed., *Handbuch der Radiologie*, part 2 of volume VI, Leipzig: Akademische Verlagsgesellschaft, 1934, 205.
21. H. W. Schrötter and H. W. Klöckner, "Raman scattering cross sections in gases and liquids," in A. Weber, Ed., *Raman Spectroscopy*

of Gases and Liquids, New York: Springer-Verlag, 1979, 122.

22. C. H. Wang and R. B. Wright, "Raman studies of the effect of density on the Fermi resonance in CO_2 ," *Chem. Phys. Lett.* 23: 241, 1973.

23. C. H. Wang and R. B. Wright, "Effect of density on the Raman scattering of molecular fluids: I. A detailed study of the scattering polarization, intensity, frequency shift, and spectral shape in gaseous N_2 ," *J. Chem. Phys.* 59: 1706, 1973.

24. J. D. Pasteris et al., "Practical aspects of quantitative laser Raman microprobe spectroscopy for the study of fluid inclusions," *Geochim. Cosmochim. Acta* 52: 979, 1988.

25. D. Fabre et al., "Dependance en pression de la section efficace de diffusion Raman de la bande vibrationnelle de N_2 ," *Symposium GEORAMAN 89* (Toulouse, May, 1989), Soc. Franc. Miner. Crist., unpaginated abstract.

26. I.-M. Chou et al., "High-density volatiles in the system C-O-H-N for the calibration of a laser Raman microprobe," *Geochim. Cosmochim. Acta* 54: 535, 1990.

27. D. Fabre and R. Couty, "Etude par spectroscopie Raman, du methane comprimé jusqu'à 3 kbar: Application à la mesure de pression dans les inclusions fluides contenues dans les minéraux," *Acad. Sci. Comptes Rendus*, ser. II, no. 14, 303: 1305, 1986.

28. R. B. Wright and C. H. Wang, "Effect of density on the Raman scattering of molecular fluids: II. Study of intermolecular interaction in CO_2 ," *J. Chem. Phys.* 61: 2707, 1974.

29. J. F. Bertran, "Study of Fermi doublet $\nu_1-2\nu_2$ in the Raman spectra of CO_2 in different phases," *Spectrochim. Acta* 39A: 119, 1983, and references therein.

FOURIER TRANSFORM VIBRATIONAL MICROSCOPY

F. J. Bergin

Recent developments in the performance of Fourier transform (FT) instruments, coupled with the considerable advancement in associated computational power, have led to many exciting changes in optical spectroscopy. Among the most exciting have been the developments in areas such as FT-IR microscopy, FT-Raman spectroscopy, modulation techniques, and many more. Over the past few years there has been an enormous increase in the number of applications of the infrared microscope, including applications in textiles,¹ polymers,² forensic science,³ and lubrication science,⁴ for example. The IR microscope has also been particularly useful when used in conjunction with separation techniques such as HPLC, GPC, and SFC.⁵ This interest in IR microscopy has been mirrored by developments in conventional Raman microscopy.⁶ Indeed, the drive to examine smaller amounts of material, to carry out vibrational mapping of surfaces, or to analyze with ever higher spatial resolutions, has initiated work on other forms of vibrational microscopy such as near infrared microscopy,⁷ FT-Raman microscopy,^{8,9} and Hadamard transform microscopy.¹⁰ In this paper some more novel applications of the infrared microscope and recent developments in FT-Raman microscopy are discussed.

FT-IR Microscopy

Although the IR microscope was developed for analyses requiring high spatial resolution, it can also serve as an extremely useful and versatile sampling accessory. We have not only made extensive use of its high spatial resolution, we have also been exploring its potential for the analysis of bulk polymeric materials and thin films on nonmetallic substrates.

It is well known that when radiation impinges on a material, the reflected light consists of two components: a front surface, specular component and a diffusely reflected component. In general, the nature of the surface determines which of the two dominates, with the specular component tending to dominate with the smoother, more polished surfaces. Both components contain molecular/vibrational information about the material. In the case of diffuse reflectance, the radiation penetrates the sample and undergoes multiple reflection, refraction, absorption, etc., within the sample before re-emerging from the surface. This reflected light R is related to the absorption and scattering within the sample via the Kubelka-Munk equation

$$f(R) \approx (1-R)^2/2R = k/s$$

where k and s denote absorption and scattering coefficients of the material.

In the case of specular reflectance, the situation is more complex. The reflectivity at near normal incidence is given by

$$R = (m - 1)^2 / (m + 1)^2$$

where the complex refractive index $m = n - ik$. The term k , the absorption index, is related to the absorption coefficient $\alpha(\omega)$, which is normally measured in conventional absorption experiment by

$$\alpha(\omega) = 4\pi\omega k(\omega)$$

Hence an absorption-like spectrum can be extracted from the measured reflectivity spectrum. The advances in dedicated computers associated with IR instruments mean that most instruments can run the software necessary for this extraction/analysis.

In these FT-IR studies, a Perkin-Elmer Model 1760-X FT-IR instrument was used, with a Spectra-Tech IR-Plan microscope fitted to the external port. The microscope was fitted with a narrow-band MCT detector and a 15× Cassegrainian objective. Data storage and manipulation were carried out by means of a Perkin Elmer 7700 Series data station.

Diffuse Reflectance

To illustrate some of the applications of the microscope in the analysis of bulk polymeric materials, Fig. 1(a) shows the diffuse reflectance spectrum of a foamed polymeric material. The sample was simply mounted under the microscope and brought into focus, and its reflectivity spectrum was measured; a gold mirror was used as a background or reference spectrum. Figure 1(b) shows a spectrum of the same material after storage in water at 95 °C and a pressure of 1.6 MPa for 8 days. Among the changes that have occurred is the clear loss of the isocyanate-based foaming material. (The changes in the CH₂/CH₃ region are a result of some contamination from the oil used to produce the required pressure.) In this case, the analysis area was approximately 1 mm in diameter and hence the high resolving power of the microscope was not used. The power of this approach lies in its speed and simplicity and, perhaps more important, in that it is non-destructive.

Specular Reflectance

The above example nicely illustrates a

F. J. Bergin is at Shell Research Ltd., Thornton Research Centre, P.O. Box 1, Chester, England CH1 3SH.

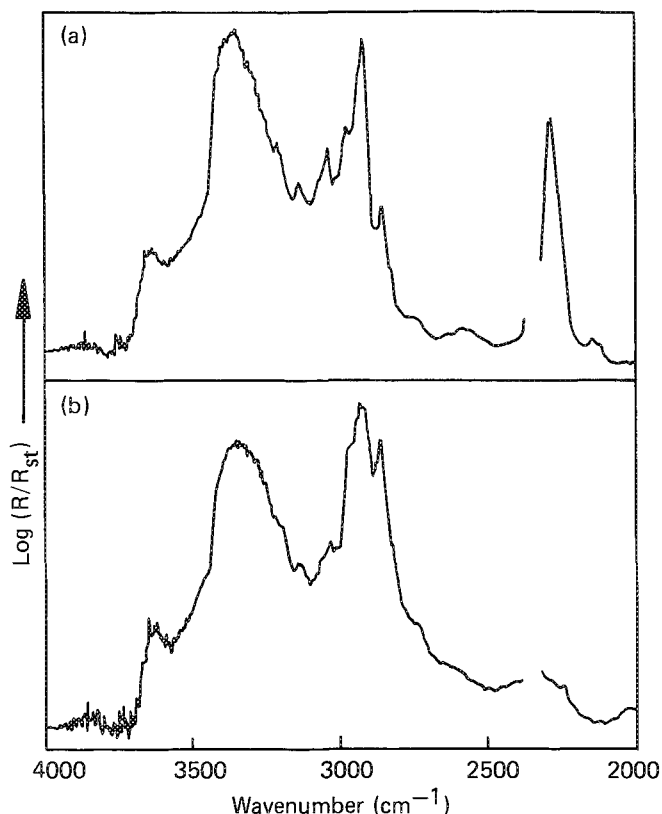


FIG. 1.--(a) Diffuse reflectance spectrum of foamed polymeric material recorded through microscope; (b) diffuse reflectance spectrum of same material after storage in water at 95°C and 1.6 MPa for 8 days.

system in which diffuse reflectance is the dominant component of the measured reflectivity spectrum. When specular reflectance dominates, the recorded spectrum is more complex, taking on the appearance of a first-derivative-like spectrum. As an example, Fig. 2(a) shows the recorded spectrum for a black polymeric material--a pipette sucker bulb. This derivative nature is a consequence of the behavior of the real component of the refractive index in the region of an absorption band. The absorption index or extinction coefficient spectrum can be extracted from this spectrum by use of the appropriate software (Fig. 2b) which allows the material to be readily identified as a phthalate-based polyester.

In many cases the extracted spectrum closely resembles that observed in a more conventional approach such as KBr disk, solvent thin films, etc., but in some instances measurable differences have been noted. Fig. 3(a) shows the spectrum of a polyurethane elastomer recorded by the casting of a thin film from solution onto a KBr window. Several castings were made, yielding very similar results. Figure 3(b) shows the extracted extinction coefficient spectrum for the same material. In the fingerprint region (2000-600 cm^{-1}), the two materials are similar, with similar band positions but

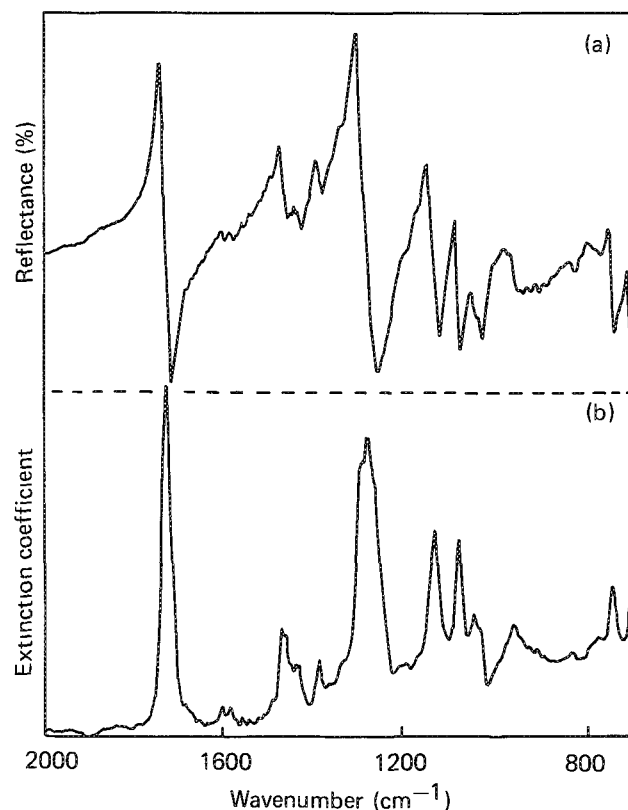


FIG. 2.--(a) Observed reflectivity spectrum for black pipette sucker bulb; (b) extracted extinction coefficient spectrum for Fig. 2(a).

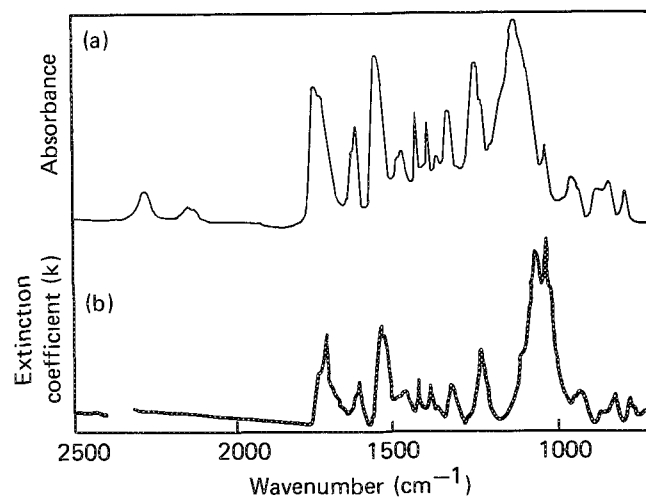


FIG. 3.--(a) IR transmission spectrum of polyurethane elastomer, thin film cast from solvent on KBr disk; (b) extracted extinction coefficient spectrum of same material taken from observed reflectivity spectrum.

with differing relative intensities. In the region 2500-2000 cm^{-1} , the reflectivity spectrum differs considerably from that of the more conventional spectrum. These differences

may arise because this specular reflectance approach is effectively a surface--sensitive technique with an effective depth of penetration of the order of tens of micrometers.

In the above examples, the spectra were dominated either by diffuse or specular reflectance with little mixing. However, frequently the observed spectrum is a combination of the two components and it is difficult to extract a clear vibrational spectrum. As noted earlier the strength of this type of approach, when applicable, lies in its speed, simplicity, non-destructive nature, and, in the case of specular reflectance, its surface sensitivity. Finally, the concept of using the IR microscope for reflectance measurements has been developed further by Claybourn and Colombel, who have illustrated that reflectance measurements can also be made from bulk liquid samples.¹¹

Reflection-absorption from Nonmetallic Substrates

The above analysis illustrates how the microscope can be a simple, versatile, sampling accessory that readily allows spectroscopic data to be obtained from bulk materials. The microscope can also be used to examine thin films on nonmetallic substrates. Some recent publications have indicated that IR spectroscopic data can be obtained from monomolecular films spread on aqueous substrates.^{12,13} In contrast to the situation for thin films on metallic surfaces, where the angle of incidence should lie between 70° and 82° to the normal, for aqueous substrates the optimum angle lies between 0 and 30°. The objective lens of the IR-Plan microscope provides such an optical configuration and we have shown previously that molecular, spectroscopic data can be obtained from such monomolecular films.¹⁴ Although the throughput, or optical power at the sample, is more than an order of magnitude lower than that observed in the macro chamber of an IR instrument, the data are of sufficient quality to allow some analyses to be performed.

As a further example, we have used the microscope to aid in determining the origin of a slight bloom that occurred on some transfer optics of a plasma emission spectrometer. Here a glass lens had been used to seal the plasma chamber, at atmospheric pressure, from an evacuated monochromator. Over a period of time a slight bloom, the image of the plasma, had appeared on the lens, thereby reducing the sensitivity of the instrument. Some discussion followed on whether this image was a result of some impurities being deposited onto the lens in the evacuated monochromator or whether it was a result of a hydrocarbon deposit caused by solvent being introduced into the plasma. Simply placing the lens under the microscope and recording the reflectivity spectrum showed that the bloom was in fact on the side of the monochromator. Figure 4(a) shows the spectrum recorded from the monochromator side of the lens in the region of the bloom, Fig. 4(b) shows the spectrum from the plasma side of the lens, and Fig. 4(c) shows a 100% line. The

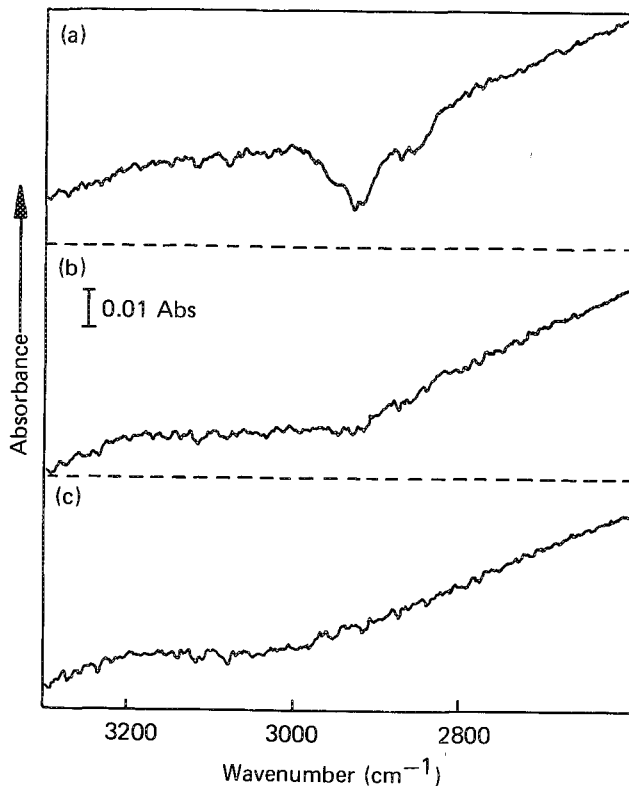


FIG. 4.--(a) Reflection-absorption spectrum of bloom on glass lens, evacuated side; (b) observed spectrum from plasma side of lens; (c) 100% line from glass lens.

observed absorption bands are negative here, similar to those observed for thin films on aqueous substrates.

FT-Raman Microscopy

One of the other areas of vibrational spectroscopy to benefit considerably from the developments in FT-IR instrumentation and improvements in associated computers is that of Fourier transform Raman (FT-Raman) spectroscopy. In the four years since the first publication on this topic, the number of papers reporting developments in instruments, filters, detectors, etc., has been considerable and the range of applications continues to grow. Indeed, recently a special issue of *Spectrochimica Acta* was devoted to this topic and at present several books on the subject are being compiled. Most of the publications have focused on the general application of the technique and until recently little attention has been paid to the development of FT-Raman microscopy. Although we have concentrated on applications of the IR microscope where high spatial resolution was not required, our interest in this section lies in the ability to clearly identify the region of the sample being analyzed and to explore the potential of the microscope for the analysis of small contaminants, inhomogeneities, fibers, etc.

In the first paper on FT-Raman microscopy,

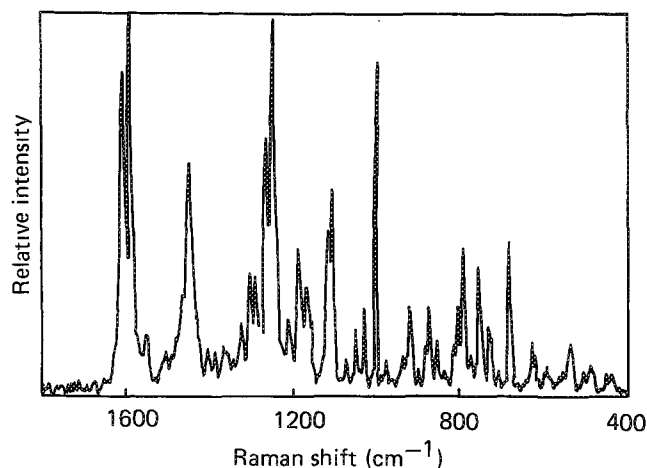


FIG. 5.--FT-Raman spectrum of n-benzyl 3, 7, biocetyl phenothiazine recorded from solid pellet with microscope.

Messerschmidt and Chase⁷ used an IR-Plan microscope with reflective optics and obtained results that "argue for the development and commercialization of combined FT-IR/FT-Raman microscope instruments for the successive analysis of the same specimen." We have taken a different approach to the reflective optics of Messerschmidt and Chase and have explored the potential of a simple metallurgical glass optics microscope.

Experimental

The essential components of our experimental system included a Perkin-Elmer model 1760 near-infrared spectrometer equipped with a liquid-nitrogen-cooled germanium detector. The Nd:YAG laser was supplied by Spectron Lasers and the Rayleigh rejection was achieved by use of two dielectric-coated filters. (A more detailed description is given in Ref. 15.) These filters had a combined optical density of 6 at 1.06 μm and the combined system of detector, filters, and instrument meant that Raman data could be collected only between 3100 and $\sim 400\text{ cm}^{-1}$. The microscope was a Nikon Optiphot metallurgical microscope. The laser was focused on the sample by means of a 40 \times glass objective, which also collected the scattered Raman signal. This scattered radiation was directed toward the spectrometer by a glass prism and a single lens, positioned at the Jacquinot stop of the instrument. This lens was positioned on an X-Y-Z stage to allow for fine tuning.

Results and Discussion

As with the IR microscope, one of the benefits accrued from this microscope system is the simplicity of sampling. In the Raman system the sample is just placed under the microscope objective and brought into focus, and the spectrum is recorded. As an example, Fig. 5 shows the FT-Raman spectrum of a crystalline solid (a phenathiazine-based material). A small amount of the material was

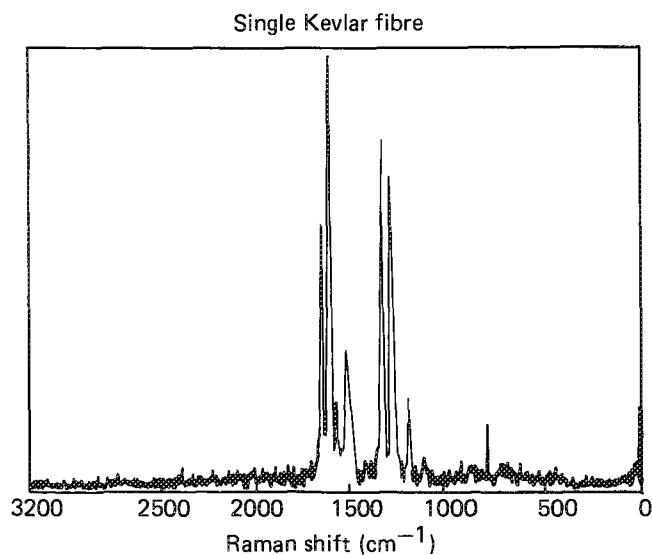


FIG. 6.--FT-Raman spectrum of single Kevlar fiber, 12 μm in diameter. Laser power 350 mW, data collection time 7.5 min.

poured onto a glass slide and the spectrum was recorded. However, our main interest in FT-Raman microscopy was not so much the simplicity but the ability to analyze small amounts of material, fibers, etc.

Figure 6 shows the FT-Raman spectrum of a 12 μm -diameter Kevlar fiber recorded with 350 mW at the sample and a data collection time of 7.5 min. As a final example, Fig. 7(a) shows the FT-Raman spectrum of a sample (50 \times 100 μm) of an antidepressant drug recorded with the microscope. For comparison, Fig. 7(b) shows the FT-Raman spectrum of the same material when the more conventional macro optics is used.

The above examples illustrate that spectra with reasonable signal-to-noise ratios can be obtained from some single fibers and small quantities of material. However, one of the difficulties with this system is inherent to the optics. Assuming a spot size of approximately 5-10 μm and a magnification of 40 produces a primary image at most 400 μm in size. This image is formed approximately 200 mm from the objective lens, with the sample only 3-4 mm from the lens. Thus, the microscope produces a narrow, almost parallel beam going into the spectrometer. Alternatively, we can consider this problem in terms of f numbers, with an f number of 0.77 for the microscope objective and an f number of 8-10 for the spectrometer. This mismatch of f numbers is partially compensated by suitable coupling optics, but the microscope still forms a throughput-limiting stop in the system. This limitation means that when the microscope is used, one of the main advantages of the FT-Raman technique, that of high throughput, is lost. This restriction may well limit the general application of the microscope. Since our FT-Raman system was purchased,

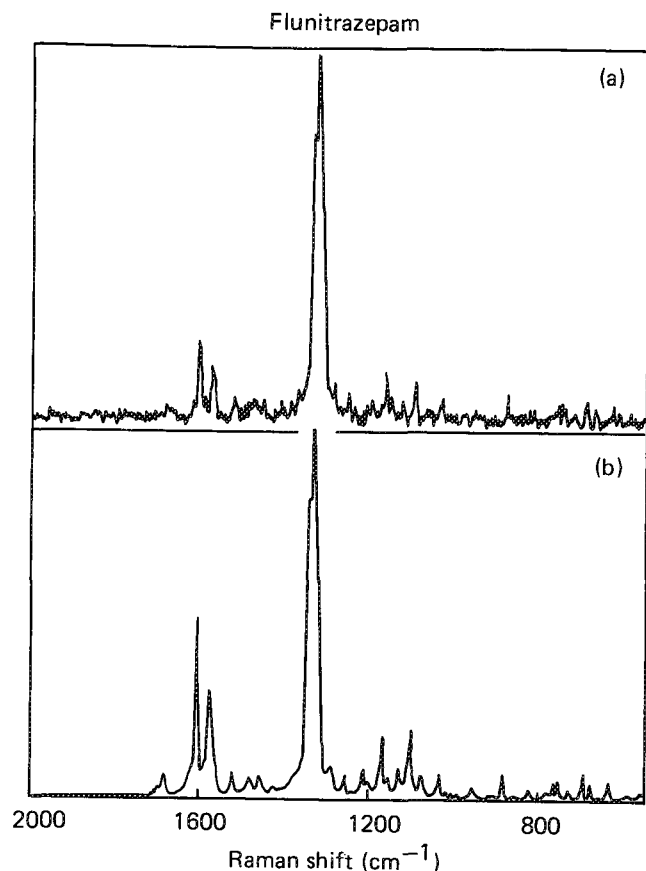


FIG. 7.--FT-Raman spectrum of antidepressant drug (Flunitrazepam) taken (a) with microscope, (b) with conventional macro optics.

there have been many improvements in detectors, filters, beam-splitters, etc., which yield an improvement of approximately 4-5 over our current instrument. Indeed, at present one of the infrared instrument manufacturers has developed an FT-Raman microscope, with at least one other company following suit.

Conclusion

In summary, the recent advances in FT-IR instrumentation and the developments in dedicated computers have considerably broadened the range and nature of materials amenable to vibrational analysis. In particular these advances have stimulated the development of Fourier-transform vibrational microscopy. In addition to the considerable benefits accruing from its high spatial resolution, the infrared microscope is also a very versatile sampling accessory that allows spectroscopic data to be recorded nondestructively from bulk polymeric materials and from thin films on nonmetallic substrates. Initial results suggest that despite the limitations inherent to the optics of the FT-Raman microscope, it may well play a major role in the years to come.

References

1. D. Griebble and S. Gardner, *Text. Chem. Color.* 21: 11-13, 1989.
2. J. B. Beauchaine and R. J. Rosenthal, "Applications of FT-IR microscopy in polymer analysis," *Microbeam Analysis--1987*, 185-186.
3. J. B. Beauchaine, K. D. Kempfert, M. P. Fuller, and R. J. Rosenthal, "Application of FT-IR microscopy in forensic analysis," *Microbeam Analysis--1987*, 218-220.
4. P. M. Cann, R. W. M. Wardle, R. C. Coy, and H. A. Spikes, "Automotive lubrication," *Proc. 7th Intern. Colloquium on Tribology*, Esslingen, 1990.
5. M. W. Raynor, K. D. Bartle, I. L. Davies, A. Williams, A. A. Clifford, J. M. Chalmers, and B. W. Cook, *Anal. Chem.* 60: 427-433, 1988.
6. D. J. Gardiner, C. J. Littleton, and M. Bowden, *Appl. Spectrosc.* 42: 15, 1988.
7. M. J. Smith and R. T. Carl, *Appl. Spectrosc.* 43: 865, 1989.
8. R. G. Messerschmidt and D. B. Chase, *Appl. Spectrosc.* 43: 11, 1989.
9. F. J. Bergin and H. F. Shurvell, *Appl. Spectrosc.* 43: 516, 1989.
10. P. J. Treado and M. D. Morris, *Appl. Spectrosc.* 44: 1, 1990.
11. M. Claybourn and P. Colombel, *Bruker Report* 1: 8-12, 1990.
12. R. D. Dluhy and R. Mendelson, *Anal. Chem.* 60: 269A, 1988.
13. R. D. Dluhy, N. A. Wright, and P. R. Griffiths, *Appl. Spectrosc.* 42: 138, 1988.
14. F. J. Bergin, *Appl. Spectrosc.* 43: 511, 1989.
15. F. J. Bergin, *Spectrochimica Acta* 46A: 153, 1990.

FT-IR MOLECULAR MICROANALYSIS SYSTEM

J. A. Reffner and W. T. Wihlborg

The evolution of FT-IR microscopy has advanced from an extension of infrared microanalysis to a microbeam analysis system with expanded functions for materials and biological scientists. The combination of light microscopy for morphological examination with infrared spectroscopy for chemical identification of microscopic samples or domains has become an important microbeam analytical technique.¹ Although use of mid-infrared radiation limits spatial resolution, its advantages for molecular analysis diminishes this loss. Dual masking technology has maximized spatial resolution. The IR_μs™ is the first fully integrated system for Fourier transform infrared (FT-IR) microscopy and its optical, mechanical, and system design are described to illustrate the state of development of molecular microanalysis.

The Evolution of IR Microbeam Analysis

Infrared spectral analysis of microscopic samples is not a new idea; it dates back to 1949, with the first commercial instrument offered in 1953.² These early efforts showed promise but failed the test of practicality. It was not until the advances in computer science were applied that infrared microspectrometry emerged as a useful technique. Microscopes designed as accessories for Fourier transform infrared spectrometers have been commercially available since 1983. These accessory microscopes provide the best means for analytical spectroscopists to analyze microscopic samples without interfering with the FT-IR spectrometer's normal functions.

The microscopist's needs for molecular microanalysis have led to the development of the IR_μs integrated system. Microscopists relate morphology with chemical composition. The expanding use in electron microscopy of x-ray emission spectral analysis, electron diffraction, and energy loss spectroscopy is testimony to the enhancement that chemical analysis adds to morphological investigations. Infrared microanalysis is unique because it provides direct data about the molecular bonding within a sample. This feature is of primary importance in the examination of organic materials, since electron microbeam techniques often fail to yield analytical data on low-atomic-number complex organic materials. For the microscopist, spectral analysis must be an integral part of the examination, easily accessed and easily interpreted. Mapping molecular compositions is also required to relate the sample's chemistry to its morphology.

The authors are at Spectra-Tech Inc., Stamford, CT 06906.

Instrument Design Factors

The Resolution Problem. Resolution is a major concern of any microscopical technique; use of infrared radiation for molecular spectral analysis limits spatial resolution. For practical infrared microanalysis, masks are placed in remote image planes to define the area of the field for spectral analysis. Dual remote image masks provide improved resolution for infrared sample definition in the same way that they function in confocal microscopy. With dual masks it is possible to obtain resolution approaching the diffraction limit of one-half wavelength. Since the mid-infrared spectral region extends from 2.5 to 16.7 μm (4000 to 600 cm^{-1}), the minimum area of the sample for spectral measurement is 1.25 to 8.4 μm in its smallest dimensions.

The resolution effect is illustrated in Fig. 1. A polystyrene film 12 μm thick was mounted in Nujol brand mineral oil, between two barium fluoride windows, which created a sharp, low-contrast edge. This edge was then mapped by use of dual remote apertures that produce a 6 μm -wide slit. IR spectra were sequentially collected at every 2 μm over a line 60 μm long. The normalized peak absorbance for the 3030 cm^{-1} (3.3 μm) and the 1601 cm^{-1} (6.25 μm) polystyrene bands are plotted as a function of distance. The sharper edge profile is seen for the shorter-wavelength (3030 cm^{-1}) band.

Spectral measurements at the microscopic level demand greater resolution than just spatial separation by a minimum contrast between two points; there must be a minimum of spectral mixing from adjacent areas. The use of dual remote apertures minimizes the diffraction and leads to higher resolution for the spectral measurements. This improved spectral purity is shown in Fig. 2. The spectra shown were collected by use of a 6 μm slit located at the edge of the polystyrene/Nujol interface. Seen by light microscopy, the slit is totally within the Nujol phase. The 1601 cm^{-1} band of the styrene is present in single-apertured data and is nearly absent in the dual-apertured spectrum.

A minimum photon flux is needed to generate spectra with sufficient signal-to-noise for detection, which also limits spatial definition. The energy throughput is a critical consideration in the optical design of an infrared microanalysis system. A high numerical aperture, all reflecting optical system with the highest possible efficiency is essential. The infrared source must be of high intrinsic brightness and the interferometer efficiently optimized for the desired spectral range. Liquid-nitrogen-cooled mercury cadmium telluride (MCT) detectors are used, since they have the highest

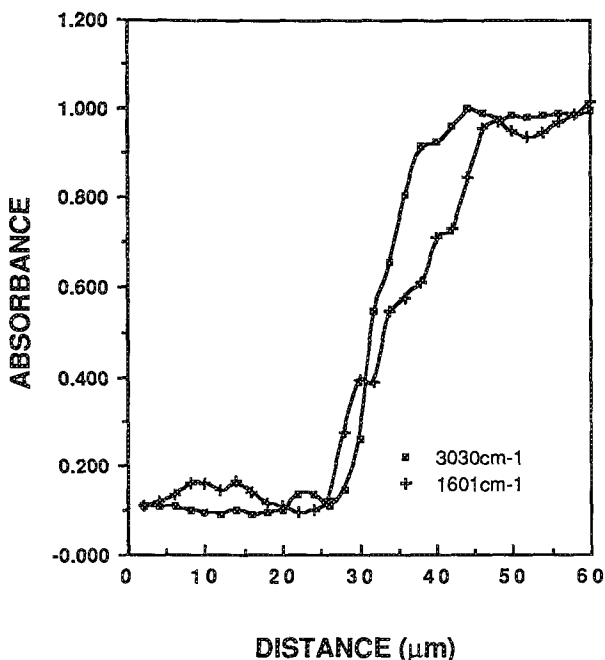


FIG. 1.--Edge profile map of polystyrene/Nujol interface made with 6 μ m-wide slit produced by dual remote apertures. Normalized peak absorbance for 3030 cm^{-1} (3.3 μ m) and 1601 cm^{-1} (6.25 μ m) polystyrene bands are plotted as a function of distance.

signal-to-noise values ($D^* = 3 \times 10^{10} \text{ cm Hz}^{1/2} \text{ W}^{-1}$) through the mid-infrared region.

Dual Optical Functions. In FT-IR microanalysis the microscope must function for both visible light and for infrared spectroscopy. Reflecting elements are used for both spectral ranges, but the optics of the infrared spectrometer are significantly different from the optics for imaging with visible light. For example, Koehler illumination, imaging of the source in the objective lens Fourier plane, is preferred for visible light imaging, since it provides uniform illumination over a large field. However, for infrared spectroscopy the source, after passing through a Michelson interferometer, is imaged in the object field and is concentrated in the central area seen by the detector. When the 15 \times , N.A. 0.58 reflection objective is used, the eye can see a field 1.25 mm in diameter, but the MCT detector "sees" only a 0.25+ mm field. It is critical that the infrared and visible radiation are coaxial and parfocal, and it is also necessary that each be optimized for their function. Figure 3 shows the optical layout of the two radiation paths. The optical elements are arranged to minimize the overall path length.

Data Collection and Analysis. The computer architecture and software are the key elements that make molecular microanalysis a viable technology. Automated sequential data collection makes it possible to collect the arrays of data needed for molecular mapping. Libraries of molecular spectra and the need for computer-assisted searches of libraries are critical. What

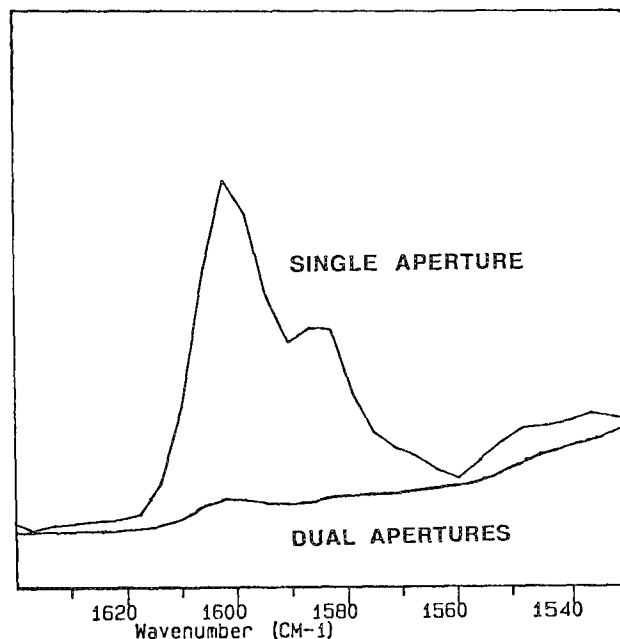


FIG. 2.--Spectra collected using a 6 μ m slit located at the edge of polystyrene/Nujol interface. Seen by light microscopy, slit is totally within Nujol phase. The 1601 cm^{-1} band of the styrene is present in single-apertured data, but is nearly absent in dual-apertured spectrum.

good is it having the ability to collect data that are not interpretable? Energy-dispersive x-ray microanalysis required the microscopist to identify fewer than fifty elements; infrared microanalysis can produce unique spectra of many thousands of materials.

There are several types of spectral data that can be collected with the FT-IR microbeam analysis system, including specular and diffuse reflection spectra. These reflection spectra require special data reduction in order to be interpreted. Quantitative analysis also places special demands on both the spectral data collection and on the mathematical analysis software. The software for FT-IR molecular microanalysis is pivotal to a system's performance.

Results

Although visible and infrared radiation limit resolution, these photons provide distinct advantages for molecular microanalysis. A major advantage is that analyses can be made at ambient conditions. Water and carbon dioxide gases present in the atmosphere have infrared absorptions that can cause interference, but they can be eliminated by purging of the IR μ s system with dry air or nitrogen. FT-IR microanalysis of aqueous suspensions or biological tissues can be made without special sample preparation.³ For example, the molecular chemistry of single human red blood cells has been studied.

The integration of the light microscope and FT-IR spectrometer has resulted in a total sys-

IR μ sTM Molecular Microspectroscopy System

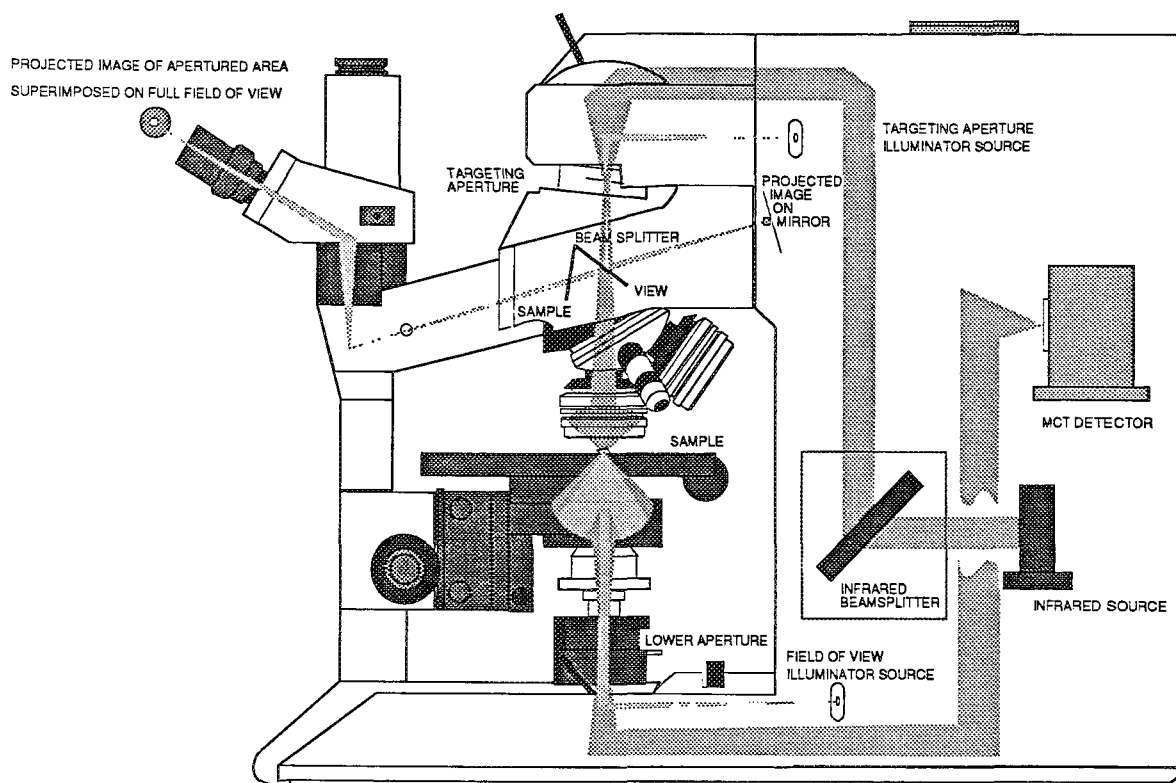


FIG. 3.--Optical ray diagram of integrated FT-IR microbeam spectrometer.

tem for molecular microanalysis. This total system yields greater efficiencies in both utility and performance. Subnanogram samples can be routinely studied and spatial resolutions are at the diffraction limits.

Conclusions

FT-IR spectroscopy has been integrated into a microbeam analysis system for molecular microanalysis. The advantages of molecular microbeam analytical data outweigh the limits of spatial resolution. This system fills a vital need for the analysis of organic materials.

References

1. R. G. Messerschmidt and M. A. Harthcock, Eds., *Infrared Microspectroscopy Theories and Applications*, New York: Marcel Dekker, 1988.
2. J. A. Reffner et al., *American Lab.* April 1987, 86.
3. A. Dong et al., *Biophys. Res. Comm.* 156: 752, 1988.

RAMAN AND FLUORESCENCE SPECTRA OBSERVED IN LASER MICROPROBE MEASUREMENTS OF SEVERAL COMPOSITIONS IN THE Ln-Ba-Cu-O SYSTEM

E. S. Etz, T. D. Schroeder, and Winnie Wong-Ng

We have used Raman microprobe measurements to investigate the superconducting and related phases in the $\text{LnBa}_2\text{Cu}_3\text{O}_{7-x}$ system (for $x = 0$ to 1), where yttrium has been replaced by one of the lanthanide (Ln = Nd, Sm, Eu, Ho, Er) or rare earth elements. The aim is to relate the observed optical spectra (Raman and fluorescence) to the compositional and structural properties of these solids as part of a comprehensive materials characterization. The results are then correlated with the methods of synthesis, the processing procedures of these materials, and their superconducting properties. Of interest is the substitutional chemistry of these isostructural systems, the differences in the spectra, and their microanalytical usefulness for the detection of impurity phases and the assessment of compositional homogeneity.

In an earlier paper, we reported on the investigation by Raman microprobe spectroscopy of high- T_c superconductors in the Y-Ba-Cu-O (YBCO) system.¹ In that study we discussed the micro-Raman spectra of three types of YBCO materials (ceramic powders, ceramic pellets, and single-crystal preparations), which are primarily composed of the (orthorhombic) superconducting phase of composition $\text{YBa}_2\text{Cu}_3\text{O}_{7-x}$, and the (tetragonal) insulating phase close to $\text{YBa}_2\text{Cu}_3\text{O}_6$ stoichiometry.

The present communication is an extension of our earlier studies in which we examine both the Raman and fluorescence spectra from the broader YBCO system of compositionally and structurally analogous compounds containing various rare earth ions, substituted for yttrium. Specifically, we are examining a series of compositions from which we expect to observe highly diagnostic, structure-specific optical spectra. It is now thoroughly documented that yttrium can be substituted for, partly or fully, by other trivalent lanthanide (Ln^{3+}) ions, with little effect either on the transition temperature or the crystal structure.²⁻⁴ The already extensive literature on Raman and infrared spectroscopy in this field demonstrates the usefulness of vibrational spectroscopy in the characterization of all classes of high- T_c superconductors.⁵⁻⁸

Lanthanide ions can be sensitive fluorescent

probes in a variety of host matrices, and rare earth ion spectroscopy has previously been applied to the study of high- T_c superconductors.⁹⁻¹¹ In these cases, the Ln^{3+} fluorescence emissions become sensitive indicators of molecular/crystallographic structure, bonding, and charge environment. In the Ln-Ba-Cu-O system, the microprobe spectra consist principally of three types of signatures: (1) the normal Raman emissions from allowed vibrational modes,⁵⁻⁸ (2) structure and site-specific fluorescence emissions of Ln^{3+} ions in yttrium sites,⁹⁻¹² and (3) electronic Raman scattering from certain electronic states of Cu(II) .¹³

Experimental

The materials examined here are all ceramic powders prepared by solid-state reactions by conventional ceramic processing techniques.¹⁴ The nominally single-phase materials of the various indicated compositions were prepared from stoichiometric mixtures of the respective trivalent lanthanide oxides, Ln_2O_3 , BaCO_3 , and CuO . In all cases, commercial starting materials of the highest available purity were used for preparing the various compositions in the phase diagram. For example, in the yttrium system, yttrium oxide of either 99.99% or 99.999% certified purity was used in conjunction with nominally 99.99% cupric oxide and 99.99% barium carbonate. The erbium- and europium-bearing compositions are based on the use of oxides of 99.99% stated purity. Details on the synthesis and processing of these ceramics have been presented elsewhere.^{3,14,15}

Several compositions are of interest in the phase compatibility diagram for the Y_2O_3 (or Ln_2O_3)- $\text{BaO}(\text{BaCO}_3)$ - CuO system in air, which we treat as a pseudo-ternary system.¹⁵ Among the materials investigated were the starting materials (Ln_2O_3 , BaCO_3 , CuO), and the compounds of composition BaCuO_2 , Y_2BaO_4 , $\text{Y}_2\text{Cu}_2\text{O}_5$, Y_2BaCuO_5 , with the corresponding erbium and europium analogs, in addition to the orthorhombic and tetragonal phases of $\text{LnBa}_2\text{Cu}_3\text{O}_{7-x}$.¹ We employed mainly powder x-ray diffraction (and for some samples neutron diffraction) for the bulk structural characterization of these ceramic powders.

Finely ground portions of each of these compositions (generally polycrystalline materials) were examined in the Raman microprobe. We acquired the spectra of single particles and agglomerates ranging in size from ~ 3 to ~ 40 μm . Often two or three spectra were obtained from different probe spots on a relatively large single particle (~ 20 μm and larger), to examine the material for microscopic compositional homogeneity.

E. S. Etz is with the Center for Analytical Chemistry and W. Wong-Ng is with the Ceramics Division of the National Institute of Standards and Technology, Gaithersburg, MD 20899. T. D. Schroeder is a summer guest scientist at NIST, from the Department of Chemistry, Shippensburg University of Pennsylvania, Shippensburg, PA 17257.

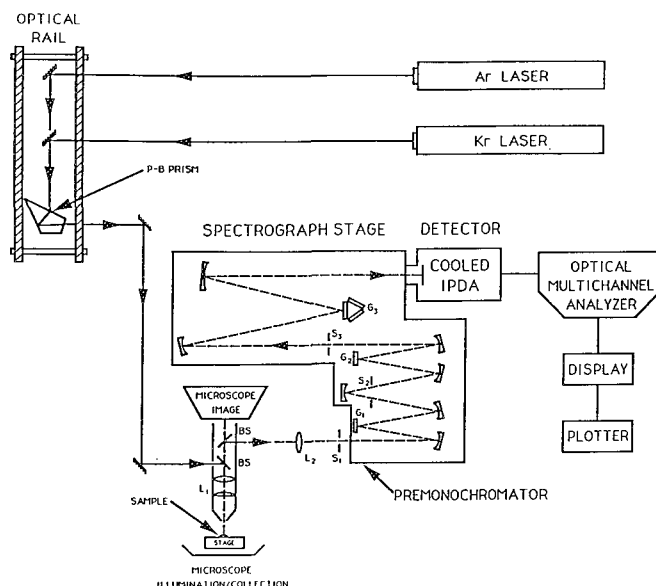


FIG. 1.--Schematic of the multichannel detection Raman microprobe used in obtaining optical spectra (Raman and fluorescence) of compounds in Ln-Ba-Cu-O system.

The spectra were obtained with a multichannel Raman microprobe constructed from commercially available components. A simplified schematic of the microprobe system is shown in Fig. 1. The instrument is designed around a modified research microscope that is optically coupled to a conventional medium-resolution Raman spectrograph, and is interfaced with an optical multichannel analyzer with an intensified diode array detector. Separate Ar⁺ and Kr⁺ cw gas lasers deliver several excitation lines from the blue (478.2 nm) to the red (647.1 nm) that are convenient for distinguishing fluorescence emissions from Raman emissions. A conventional focusing objective of large numerical aperture is employed to provide a focused beam spot at the sample of about 2-3 μm in diameter. With 514.5 nm excitation, laser powers directed at the sample in the probe spot typically vary from 20 mW for the less optically absorbing white (i.e., colorless), pink, and green phases of these materials, down to 1 mW for the highly absorbing dark (i.e., black) phases. The optically less absorbing solids (e.g., Y_2O_3 , Er_2O_3 , Eu_2O_3 , and even the green phases $\text{Ln}_2\text{BaCuO}_5$) are all strong Raman scatterers. For these samples, under moderate (typically 5mW) laser irradiation, spectra can be acquired with integration times of less than 1 min. On the other hand, Raman signals of the black compositions (e.g., CuO , superconducting $\text{LnBa}_2\text{Cu}_3\text{O}_{7-x}$), irradiated at power levels not exceeding 2-3 mW, are extremely weak and require integration times of 30 to 45 min. These weak signals can be detected only with the diode array detector cooled to typically -38 C for effective lowering of the photo-

cathode dark background.^{1,16} For the most part, the spectra are excited with the 514.5nm line of the Ar laser and are obtained with a spectral resolution of 5 cm^{-1} . We examined principally two spectral regions, the region of normal Raman emissions (i.e., from the exciting line to $\sim 800 \text{ cm}^{-1}$ Raman shift), and the region(s) in which we expect to observe characteristic lanthanide ion fluorescence emissions. For the Er^{3+} -system, the latter region extends from the green to the yellow, covering the range from 535 nm (800 cm^{-1} Raman shift) to $\sim 573 \text{ nm}$ ($\sim 2000 \text{ cm}^{-1}$ Raman shift, with 514.5 nm excitation), as reported earlier from the study of the fluorescence in the Raman spectra of Er_2O_3 and Er^{3+} -bearing silicate and phosphate glasses.¹⁷ A second spectral region of Er^{3+} fluorescence exists at longer wavelengths in the red, covering the range from $\sim 644 \text{ nm}$ ($\sim 3900 \text{ cm}^{-1}$ Raman shift) to $\sim 692 \text{ nm}$ ($\sim 5000 \text{ cm}^{-1}$ Raman shift, from 514.5 nm), as reported earlier.¹⁷ The region of fluorescence of Eu^{3+} , as observed in our micro-Raman spectra of Eu_2O_3 and several europium-bearing glasses, is in the range from ~ 575 to $\sim 640 \text{ nm}$ (or Raman shift 2000 to 3800 cm^{-1} , from 514.5 nm). Thus, for a 1 wt% Eu_2O_3 silicate glass, the major fluorescence band is centered at around 610 nm.¹⁸

Results and Discussion

Our earlier work centered on the vibrational Raman spectra of the high- T_C Y-Ba-Cu-O superconductor.¹ We have since examined the analogous Er and Eu compounds of this composition, and their spectra closely resemble those of the yttrium 1:2:3 compound. This similarity is consistent with the recognition that the observed bands are mostly due to Cu-O vibrations.⁴ We focus in this paper on the spectra of some of the pertinent stable compositions prepared in the Y, Er, and Eu based systems, especially those in the vicinity of $\text{LnBa}_2\text{Cu}_3\text{O}_{7-x}$. Among these compositions, the 2:1:1 compound (orthorhombic green phase, $\text{Ln}_2\text{BaCuO}_5$) is probably the second most extensively studied, next to the 1:2:3 superconducting phase. It is widely recognized as a potentially troublesome insulating phase, and is often undetected by the conventional bulk methods of analysis.^{1,7,19} Another common impurity phase reported to be present at inter-grain boundaries of polycrystalline YBCO is the barium cuprate of composition BaCuO_2 .²⁰

Lanthanide ion luminescence is based on the electronic configuration of these elements. The usual excitation wavelengths from gas lasers used in Raman spectroscopy excite many of the electronic transitions within a given $4f^n$ configuration, causing very specific Ln^{3+} luminescence emissions to be observed. These emissions can be quite intense, and are frequently quite sharp and narrow. In the case of the Er^{3+} -substituted materials, we are looking for the laser-excited green and red fluorescence emissions which, if they are present, originate from the $^4S_{3/2}$ (electronic

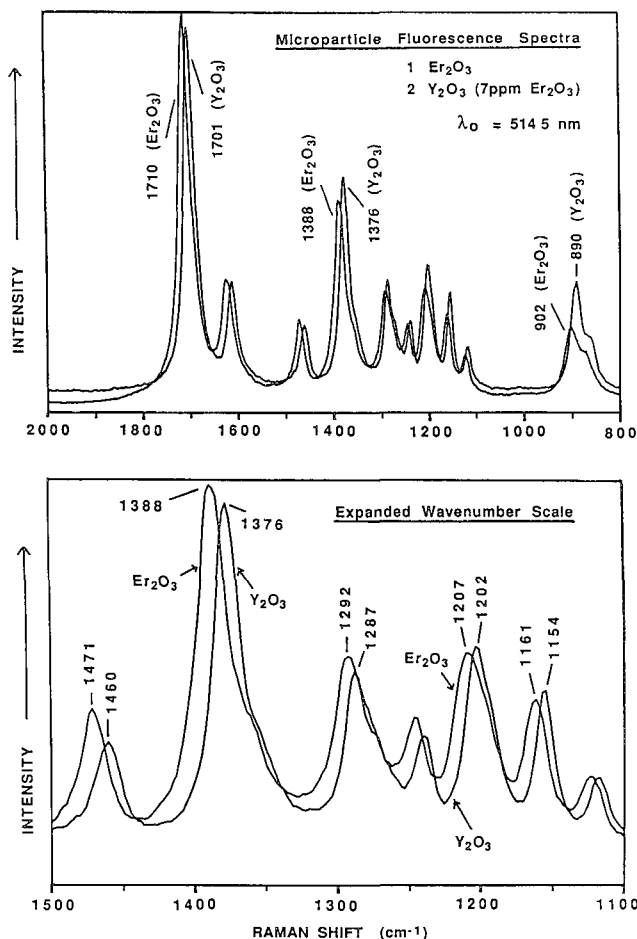


FIG. 2.--Fluorescence emissions observed in the micro-Raman spectra of particles of (1) erbium oxide (purity 99.99%) and (2) yttrium oxide (purity 99.99%, with 7 ppm Er_2O_3). Expanded wavenumber shift scale shows displacements of peak positions more clearly.

transition $^4\text{I}_{15/2} - ^4\text{S}_{3/2}$) and $^4\text{F}_{9/2}$ (transition $^4\text{I}_{15/2} - ^4\text{F}_{9/2}$) emissive states, respectively. In the case of the Eu^{3+} -substituted materials, we are examining the spectra for the presence of the red fluorescence emissions, which we attribute to the $^5\text{D}_0 - ^7\text{F}_2$ transition.

These relationships provide the basis for the present investigations to examine the micro-Raman/fluorescence spectra of the Ln^{3+} -substituted YBCO compounds for their analytical usefulness in the characterization of these materials. Figures 2-5 show some of the results from this work. Figure 2 shows the superposition of the microparticle spectra of two of the lanthanide oxides, Y_2O_3 and Er_2O_3 , that have been used as starting materials for the preparation of various compositions in the $\text{BaO}(\text{BaCO}_3) - \text{Ln}_2\text{O}_3 - \text{CuO}$ phase diagram. They are recorded beyond the range of the Raman emissions of these oxides, and therefore represent true fluorescence spectra excited at 514.5 nm. Both oxides are of certified 99.99% purity, with the Y_2O_3 containing a certified bulk Er_2O_3 impurity of 7 ppm. It is evident that this trace Er^{3+} impurity gives rise to a "modified," or shifted, fluorescence spectrum of Er_2O_3 that is moderate-

ly intense and easily detected. The spectra of the two samples are identical (if we disregard the vast differences in scattering intensities), except for a frequency shift of all bands, which moves the $\text{Y}_2\text{O}_3:\text{Er}^{3+}$, or europium-doped, yttrium oxide spectrum to lower wavenumbers. This shift amounts to a Raman shift displacement of from 5 to 13 cm^{-1} for the bands. We surmise that this spectral shift arises from a different electronic environment of the Er^{3+} ion in some of the yttrium sites of the Y_2O_3 lattice. This interpretation would then be consistent with other observations from lanthanide ion spectroscopy¹², e.g., that different close-by environments of the Ln^{3+} ion can, in principle, yield transitions at slightly different frequencies. Thus, this Y_2O_3 sample of 99.99% purity does not appear to contain Er_2O_3 in a separate phase. By comparison, a maximum purity commercial sample of Y_2O_3 (99.999% with 0.4 ppm Er_2O_3) yielded a clean Raman spectrum with low spectral background, where any evidence of fluorescence emissions from ultratrace Er_2O_3 was totally confined to the ripple of the spectral background.

The spectrum observed in the Raman microprobe of the compound of composition $\text{Er}_2\text{Cu}_2\text{O}_5$ (a blue-green phase) is shown in Fig. 3, superimposed on the spectrum of erbium oxide, Er_2O_3 , from which it was prepared. The erbium cuprate ceramic had provided a good powder x-ray diffraction pattern, with some indication of small amounts of unreacted starting material (Er_2O_3). In the measurements of numerous particles and aggregates of this material, consistent spectra were obtained that showed only the Er^{3+} fluorescence emissions of the unreacted oxide. All the erbium cuprate spectra also exhibit a rising spectral

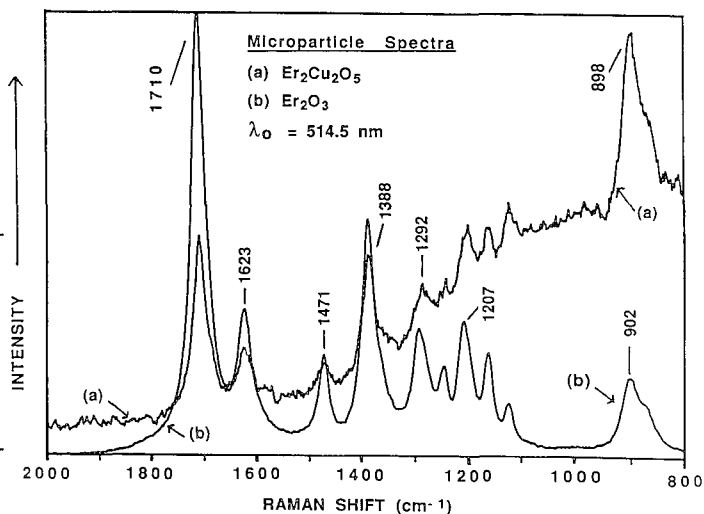


FIG. 3.--Erbium fluorescence emissions, attributed to low concentration impurity by Er_2O_3 , observed in study of phase of composition $\text{Er}_2\text{Cu}_2\text{O}_5$ (trace a). Spectrum of erbium oxide (trace b) is superimposed to facilitate recognition of this impurity in sample.

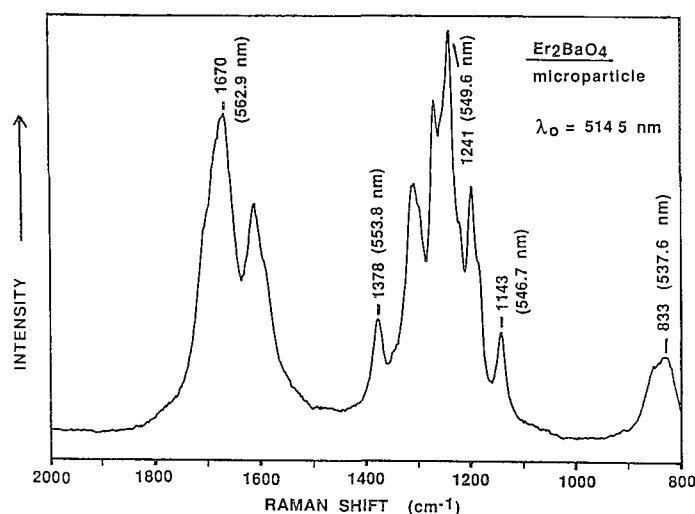


FIG. 4.--Fluorescence emissions excited in Raman microprobe measurements of particle of Er_2BaO_4 . Raman spectrum of this compound, excited at 514.5 nm, is swamped by fluorescent emissions.

background toward lower wavenumbers, thereby obscuring the expected Raman emissions below 800 cm^{-1} . Additional studies on other preparations of this compound, with detailed x-ray diffraction analysis, will be required to elucidate further the intrinsic fluorescence and Raman scattering properties of this phase. However, this example illustrates the sensitive detection of unreacted starting material, results often difficult to establish by XRD. RD.

Er_2BaO_4 (a pink phase) is also a composition derived from the phase diagram relations considered here. The intense fluorescence of this phase within the 800 to 2000 cm^{-1} range (shift from 514.5 nm) is shown in Fig. 4. Fluorescence emissions of lower intensity overwhelm the Raman spectrum below 800 cm^{-1} with 514.5 nm excitation. The fluorescence emissions of Er^{3+} in this compound are similar to the erbium green emissions, when they are compared with the spectrum of Er_2O_3 .¹⁷ This oxide has a large number of sharp-line intense bands, with the most intense feature centered at 1712 cm^{-1} (564.2 nm), and two other fairly intense bands centered at 1387 cm^{-1} (554.1 nm) and 902 cm^{-1} (539.6 nm). Lower-frequency fluorescence emissions make the detection of the strong Raman line at 378 cm^{-1} barely possible with 514.5 nm excitation. The intensity of the fluorescence spectrum of Er_2BaO_4 permits easy microprobe detection and identification of this potential impurity phase.

Nearly as extensively studied as the superconducting compound $\text{YBa}_2\text{Cu}_3\text{O}_{7-x}$ has been the commonly observed principal impurity phase Y_2BaCuO_5 .^{1,2,7,8} Almost all the phases that tend to form in the YBCO system have complicated the spectroscopic study of the superconducting 1:2:3 compound.⁸ Regarding these secondary phases, there is still in many cases no clear-cut consensus on the unique assignments of Raman bands. Yet it seems certain that a band

often seen around 640 cm^{-1} is probably best ascribed to the most intense phonon of BaCuO_2 , also rated a major impurity phase. Similarly, a fairly intense Raman band around 600 cm^{-1} , which is often accompanied by a band in the vicinity of 390 cm^{-1} , is generally attributed to the green-phase 2:1:1 compound (Y_2BaCuO_5). We have examined the green-phase compositions in the Ln-Ba-Cu-O system to obtain their Raman spectra, which are thought to be actually resonantly enhanced by 514 nm excitation. Figure 5 shows the spectra of the Y, Er, and Eu based green-phase compositions, obtained from single particles which, in each case, were about $5\text{ }\mu\text{m}$ in size. Excellent scattering in-

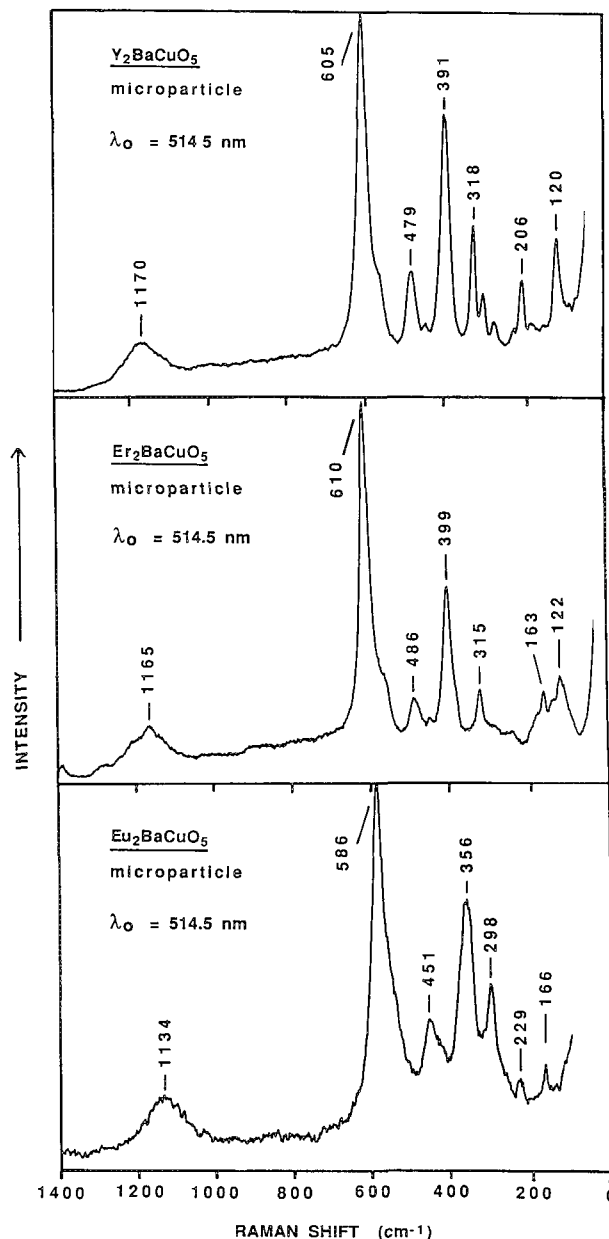


FIG. 5.--Micro-Raman spectra of green-phase compositions in Ln-Ba-Cu-O system (where Ln = Y, Er, Eu). Fluorescence is observed from none of these compounds.

tensities are observed from these compounds, even at moderate irradiance levels. Indeed, the signal intensities are much greater, possibly by a factor of 40, compared to those of the black superconductor, so that this parasitic green phase is easily detected in microprobe measurements. The broad and relatively weak feature observed in the spectrum of Y_2BaCuO_5 centered at 1170 cm^{-1} has been assigned to electronic Raman scattering, originating from an electronic excitation in the Cu(II) atom.¹³ Although reported so far only for the yttrium green phase material, we feel that the corresponding broad bands, observed close to that same frequency for the Er and Eu analogs, can be similarly explained.

If we consider these results from the green phase materials, and also the other examples discussed earlier, a key implication emerges from these findings. The results show that impurity-phase concentrations below the detection limit of x-ray diffraction (e.g., in the 1-2% range) can still produce micro-Raman spectra, and fluorescence spectra, as it may apply, with bands comparable in intensity to the Raman features observed for the high- T_c 1:2:3 phase. Clearly, the 1:2:3 compound (tetragonal and orthorhombic phase) has a much lower Raman scattering cross section than many of the secondary phases that are commonly present as impurities in even the best preparations of YBCO.

References

1. E. S. Etz et al., "Micro-Raman spectroscopy of high- T_c superconductors in the Y-Ba-Cu-O system," *Microbeam Analysis--1988*, 187-192.
2. Y. Morioka et al., "Raman scattering from high- T_c superconductor $\text{YBa}_2\text{Cu}_3\text{O}_{7-x}$ and its analogs," *Jpn. J. Appl. Phys.* 26: L1499-L-1501, 1987.
3. W. Wong-Ng et al., "Structural phase transition study of $\text{YBa}_2\text{Cu}_3\text{O}_{6+x}$ in air," *J. Mater. Res.* 3: 832-839, 1988.
4. M. Cardona et al., "Infrared and Raman spectra of the new superconducting cuprate perovskites $\text{MBa}_2\text{Cu}_3\text{O}_7$, $M = \text{Nd, Dy, Er, Tm}$," *Solid State Commun.* 65: 71-75, 1988.
5. Z. Iqbal, "Raman scattering studies of the copper-oxygen vibrations and oxygen order in La, Y-Ba, Sr-Cu oxides," in C. N. R. Rao, Ed., *Chemistry of Oxide Superconductors*, International Union of Pure and Applied Chemistry, Oxford: Blackwell, 1988, 163-174.
6. R. Feile, "Lattice vibrations in high- T_c superconductors: Optical spectroscopy and lattice dynamics," *Physica C* 159: 1-32, 1989.
7. H. D. Bist et al., "High critical temperature superconductors and Raman spectra," in H. D. Bist, J. R. Durig, and J. F. Sullivan, Eds., "Raman Spectroscopy, Sixty Years On," *Vibrational Spectra and Structure*, vol. 17A, Amsterdam: Elsevier, 1989, 167-194.
8. J. R. Ferraro and V. A. Maroni, "The characterization of high-critical temperature ceramic superconductors by vibrational spectroscopy," *Appl. Spectrosc.* 44: 351-366, 1990.
9. B. M. Tissue and J. C. Wright, "Observation of sharp-line lanthanide fluorescence in high temperature superconductors," *J. Lumin.* 37: 117-121, 1987.
10. B. M. Tissue and J. C. Wright, "Identification of fluorescing phases in Eu^{3+} doped $\text{La}_{1.85}\text{Sr}_{0.15}\text{CuO}_4$ superconductors," *J. Lumin.* 42: 173-180, 1988.
11. N. I. Agladze et al., "Optical spectra of high- T_c superconductor Er-Ba-Cu-O in the region of $^4I_{15/2} - ^4I_{13/2}$ transition in Er^{3+} ion," *Solid State Commun.* 69: 385-386, 1989.
12. J. P. Hessler and W. T. Carnall, "Optical properties of actinide and lanthanide ions," in N. M. Edelstein, Ed., *Lanthanide and Actinide Chemistry and Spectroscopy*, ACS Symposium Series 131, American Chemical Society, Washington, D.C., 1980, Chap. 17, pp. 349-368.
13. W. R. Flavell and R. G. Egdell, "Observation of electronic Raman scattering in Y_2BaCuO_5 ," *Solid State Commun.* 69: 631-633, 1989.
14. J. E. Blendell et al., "Processing-property relations for $\text{YBa}_2\text{Cu}_3\text{O}_{7-x}$ high- T_c superconductors," *Adv. Ceram. Mater.* 2: 512-529, 1987.
15. Winnie Wong-Ng et al., "Crystal chemistry and phase equilibria studies of the $\text{BaO}(\text{BaCO}_3)\text{-R}_2\text{O}_3\text{-CuO}$ systems, $R = \text{lanthanides}$, Part IV," *J. Solid State Chem.* 85: 117-132, 1990.
16. N. E. Schlotter et al., "Low signal-level Raman spectroscopy with an intensified optical multichannel array detector," *Appl. Spectrosc.* 42: 748-753, 1988.
17. E. S. Etz and J. C. Travis, "Stokes and anti-Stokes fluorescence of Er^{3+} in the Raman spectra of erbium oxide and erbium glasses," *Proc. of the Tenth Int'l. Conf. Raman Spectrosc.*, Eugene, Ore.: University of Oregon, 1986, 11-67.
18. E. S. Etz and T. R. Lettieri, "Observation of sharp resonances in the spectra of spherical microparticles examined in the Raman microprobe," *Proc. of the 11th Int'l. Conf. Raman Spectrosc.*, Chichester, England: Wiley, 1988, 931.
19. Z. Y. Popovic et al., "Optical phonons in Y_2BaCuO_5 ," *Solid State Commun.* 66: 43-47, 1988.
20. A. Erle et al., "Characterization of the intergrain properties of $\text{YBa}_2\text{Cu}_3\text{O}_{7-x}$ by Raman spectroscopy," *Solid State Commun.* 73: 753-757, 1990.



SECONDARY AND AUGER ELECTRON SPECTROSCOPY AND ENERGY-SELECTED IMAGING IN A UHV-STEM

G. G. Hembree, F. C. H. Luo, and J. A. Venables

High-spatial-resolution secondary-electron spectroscopy and energy-selected imaging are powerful tools for the investigation of surface properties on a nanometer scale, especially when they are applied to the Auger electron signal. A new UHV-STEM (ultra-high vacuum scanning transmission electron microscope) which incorporated these tools has been developed for the National Science Foundation High Resolution Electron Microscope Facility at Arizona State University.¹ In this instrument low energy (0-2keV) electrons can be collected through the objective lens either from both sides of thin samples, or from the input side of bulk samples. After collection, the slow electron beams are separated from the high-energy beam and deflected off axis by electrostatic optics for subsequent energy analysis. Examples will be given of both spectroscopy and imaging applications, obtained by two types of detectors, at high spatial resolution.

Magnetic parallelizers are used to control the angular compression of the emitted secondary and Auger electrons, which spiral around the magnetic field lines as they travel away from the specimen.² The parallelizers have axial fields of about 100 Gauss and compress all these emitted electrons into a cone of less than 6°. The sample may be biased negatively up to 700 V, which enables us to compress the cone angle further and to observe the sample using biased secondary electron imaging (b-SEI).³ A magnetic aperture is used to terminate the parallelizer field over a distance that is short in comparison with the pitch of the spiraling secondary electrons. This action forms the slow electron beam. After the exit aperture of the parallelizer the low-energy electrons are deflected slightly off axis by a Wien ($E \times B$) deflector to separate them from the 100keV beam. Figure 1 is a photograph of one of the two deflector assemblies. By switching the signs of the fields in this deflector the secondary electrons can be either energy analyzed for spectroscopy and energy-filtered imaging or collected by an Everhart-Thornley detector for high-efficiency b-SEI. For spectroscopy this deflector is followed by a gridless cylindrical mirror analyzer (CMA) sector (Fig. 2), which provides additional deflection to bend the slow electron beam normal to the optical axis of the microscopy.⁴ At the present stage of development the probe position drifts

The authors are at the Department of Physics, Arizona State University, Tempe AZ 85287; J. A. Venables is also at the School of MaPS, University of Sussex, Brighton, England BN1 9QH. Support was provided by NSF, ONR, ASU, and Shell Development Corp.

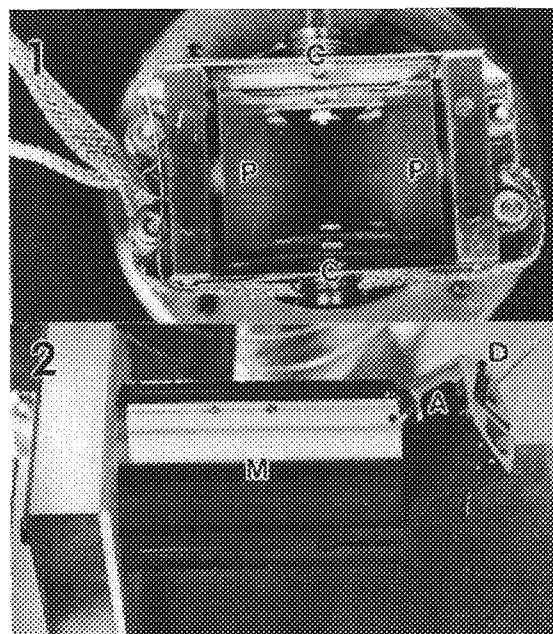


FIG. 1.--View from 100keV beam entrance side of Wien deflector assembly. Note coils at C perpendicular to electric plates at P. FIG. 2.--Side view of CMA sector showing entrance aperture at A and drift tube for high energy beam at D. Large tube at M is for mounting and stray flux shielding.

somewhat during an energy scan due to imperfect compensation in the Wien filter. We are experimenting with additional compensation coils placed before the deflector to correct this drift.

We have used two detectors at the line focus following the CMA (F on diagrams in Ref. 4) to obtain secondary-electron spectra and energy selected images. The first detector is a 2mm-wide slit mounted in front of an electron multiplier, which produces spectra with an energy resolution of around 3%.⁴ A secondary-electron spectrum obtained by this detector is displayed in Fig. 3. Collection efficiencies approaching 100% for secondary electrons can be obtained with larger slit sizes, provided that the parallelizer field has been optimized for a given sample bias and collected electron energy. The second detector is a concentric hemispherical analyzer (CHA) with a 100mm mean radius (VSW HA100). With this analyzer the energy resolution can be varied over a fairly wide range, simply by choosing a combination of slit size and electron pass energy consistent with the other parameters of a particular experiment. Typically the CHA has been operated in the fixed-retard-ratio 5 mode with a 4×10 mm

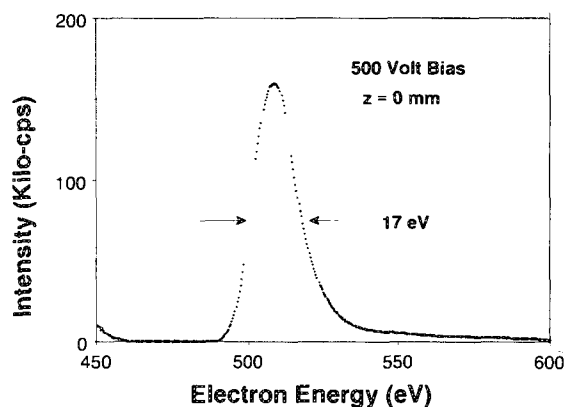


FIG. 3.--Secondary-electron spectrum obtained from upper surface of thin silicon sample by slit detector with current-to-frequency converter output.

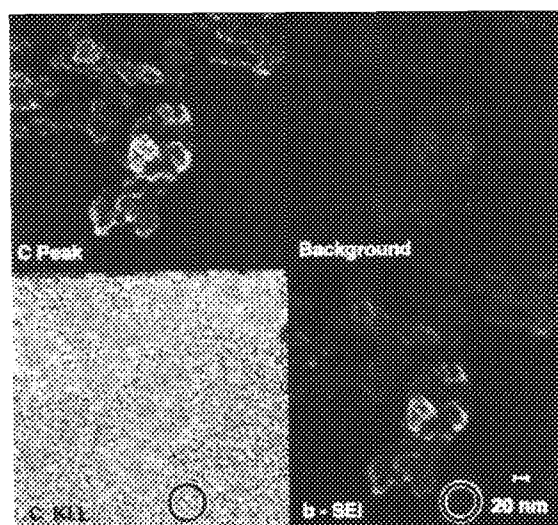


FIG. 4.--Secondary-electron images of graphitized carbon particles lying on gold decorated carbon film. Peak and background images obtained by slit detector with CMA set at and just above carbon KLL Auger peak, respectively. C KLL image obtained by $(A - B)/(A + B)$ normalization technique.

slit size which produces an energy resolution better than 1% full width at half-maximum (FWHM).

An application of the slit detector to energy-selected imaging is illustrated by Fig. 4, which shows micrographs of a composite sample of graphitized-carbon particles on a gold-decorated carbon film biased to ~ 100 V. The 256-pixel by 240-line digital images were obtained from the input side of the sample by means of a nominally 3nm-diameter, 0.3nA probe in about 80 s. The b-SE image was obtained with the

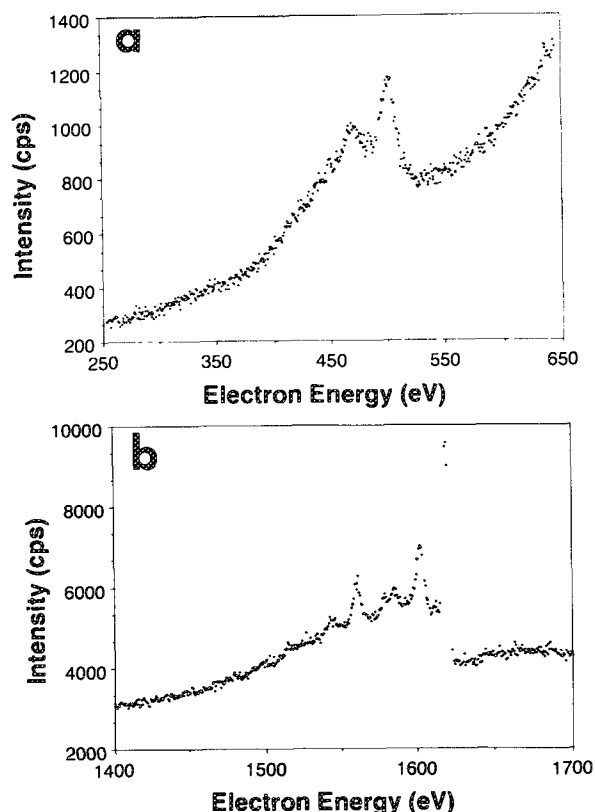


FIG. 5.--(a) Oxygen Auger electron spectrum from oxide-passivated silicon sample: 100keV, 0.2nA incident probe with 5nm diameter; 512 point spectra with 0.1s dwell collected in multiple sweeps over 20 min by CHA. (b) High-energy resolution silicon KLL Auger electron spectrum from silicon surface cleaned in situ by 1200 C flash heating. Conditions as in previous spectrum except 2nA, 10nm electron beam and 10min acquisition time.

Everhart-Thornley detector collecting all the low-energy electrons emitted from the parallelizer exit aperture. The peak and background images were formed by selection of 350eV and 400eV secondary electrons, respectively, with the CMA, which correspond to energies at and just after the carbon KLL Auger electron peak. The principal difference between the latter two images is simply variation of the amount of topographic contrast due to the total number of electrons collected in each energy range. The overall increase in signal at the carbon Auger peak can be converted into an element specific map by image subtraction and normalization procedures that have been explored previously. In the examples shown here the algorithm $(A - B)/(A + B)$ was used, where A is the image at the Auger energy and B is the background image at an energy 50 eV higher. Image processing was done off line on a work station with commercially available software. The result of this processing is the carbon KLL map in Fig. 4. One can obtain an indication of the resulting image resolution by observing the relative contrast of the gold islands and their supporting carbon film in the circled area of

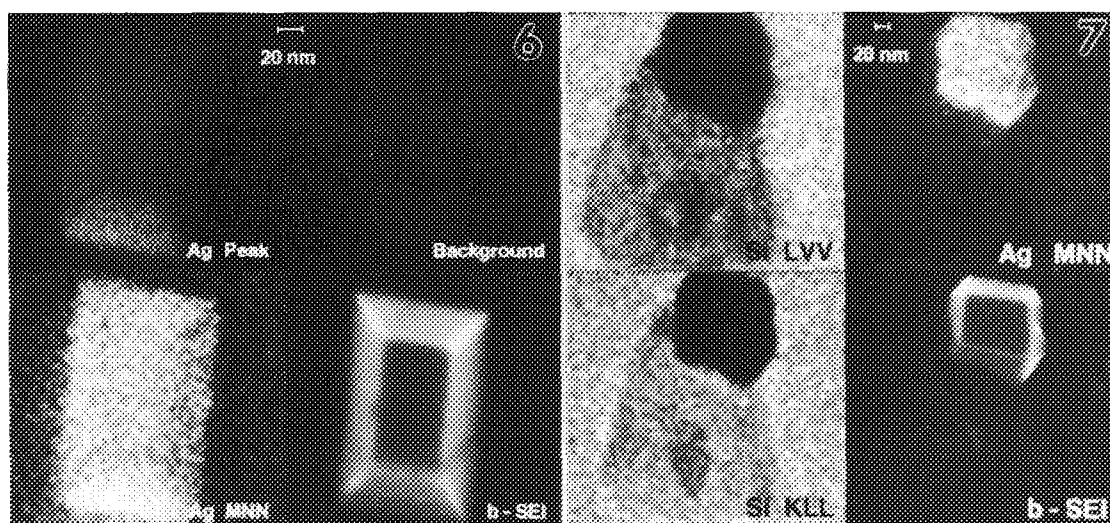


FIG. 6.--Silver crystal grown on Si(100) surface at 500 C. 1.5nA beam current, 20min acquisition time, by CHA, except for b-SEI.

FIG. 7.--Silver crystal grown on SiC(?) particle on Si(100) surface. Conditions as in Fig. 6.

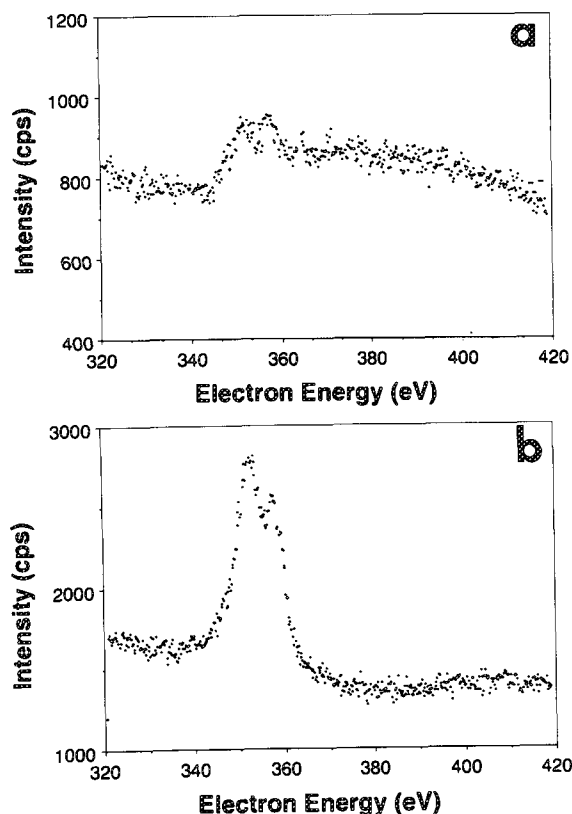


FIG. 8.--(a) Silver MNN Auger electron spectrum from 0.3 monolayer high-temperature intermediate layer on Si(100) surface; 20min acquisition by CHA. (b) Ag MNN Auger spectrum from surface of 100nm-wide silver crystal; 10min acquisition by CHA. Beam current 1.57 nA for both spectra.

the C KLL and b-SE images.

A typical application of Auger electron spectroscopy and mapping is the determination of film thickness and element distribution after a foreign species has been deposited on a

semiconductor surface. We have chosen a test system from this application, Ag/Si(100), to evaluate the capabilities of our spectroscopy instrumentation. In situ UHV specimen preparation is a prerequisite to obtaining consistent data in these studies. As an example, the CHA was used to acquire the high-resolution Auger electron spectra shown in Fig. 5 from an oxide-passivated bulk silicon sample, both before and after the oxide was desorbed by flash heating to 1200 C. The sample was biased to -700 V and -400 V for the oxygen and silicon spectra, respectively. The energy scales were shifted by postcollection processing. Carbon and oxygen Auger peaks were undetectable after the silicon was flash-heated.

When silver is deposited on a silicon (100) surface, which is held at temperatures near 450 C, an intermediate layer of around 0.3 monolayer thickness is grown between epitaxial silver crystals.⁶ A typical silver crystal grown on Si(100) at 500 C can be seen in Fig. 6. The Ag MNN image clearly demonstrates that better than 5nm edge resolution has been achieved in the well-focused regions. Another silver island, grown on a presumably SiC contaminant, is imaged at lower resolution in Fig. 7. In both of the Si Auger maps the silver crystal is black, whereas the SiC particle is at different intensities relative to the substrate. This difference may be due to the deeper escape depth of the Si KLL Auger signal. A relative indication of the sensitivity of the spectroscopy system can be gained by comparison of the signal strengths produced by the intermediate layer and the silver islands. The spectra in Fig. 8 provide these data, which show that 0.3 monolayer deposits of silver are clearly detected. Similar work on the Ge/Si(100) system is described elsewhere.⁷

To summarize, a new electron spectroscopy system has been developed for a UHV-STEM. We have demonstrated the capability for high-

resolution Auger imaging and spectroscopy with 100keV electrons at nanoampere currents. The example of Ag/Si(100) has shown the potential for detailed analytical work with sub-monolayer sensitivity on surface systems.

References

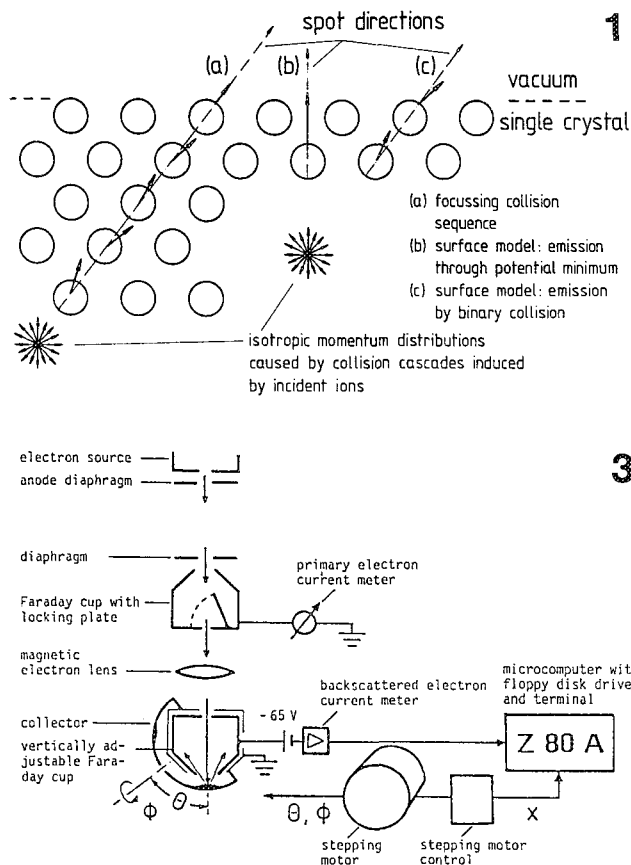
1. J. A. Venables, J. M. Cowley, and H. S. von Harrach, *Inst. Phys. Conf. Series* 90: 85, 1987.
2. P. Kruit and J. A. Venables, *Ultramicroscopy* 25: 183, 1988.
3. G. G. Hembree, P. A. Crozier, J. S. Drucker, M. Krishnamurthy, J. A. Venables, and J. M. Cowley, *Ultramicroscopy* 31: 111, 1989.
4. G. G. Hembree, Luo Chuan Hong, P. A. Bennett, and J. A. Venables, *Proc. EMSA* 46: 666, 1988; J. S. Drucker, M. Krishnamurthy, G. G. Hembree, Luo Chuan Hong, and J. A. Venables, *ibid.*, 47: 208, 1989.
5. C. J. Harland and J. A. Venables, *Ultramicroscopy* 17: 9, 1985 and references quoted.
6. M. Hanbuecken, M. Futamoto, and J. A. Venables, *Surface Science* 147: 433, 1984.
7. M. Krishnamurthy, J. S. Drucker, and J. A. Venables, *Proc. ICEM XII*, 1990, 308; G. G. Hembree, J. S. Drucker, F. C. H. Luo, M. Krishnamurthy, and J. A. Venables, *Applied Physics Letters* (submitted).

INVESTIGATION OF ION BEAM SPUTTER MECHANISMS BY ELECTRON BEAM TECHNIQUES

Thomas Guerlin, Heinz Niedrig, and Martin Sternberg

The observation of atomic emission maxima in low-indexed lattice directions (Wehner spots or ejection spot patterns) in single-crystal sputtering indicates that besides isotropic energy transfer, momentum transfer along preferred crystal directions also plays an important role in the sputter process.¹ This contribution is concerned with the investigation of the physics of the anisotropic emission of atoms from single-crystal surfaces under ion-beam bombardment.

sion sequence in a chain of hard spheres, representing the atoms in a crystal. In this model it is assumed that the incident ions produce an approximately isotropic momentum distribution in the depth of the crystal as a result of multiple scattering processes and of the induced statistical collision cascades. A momentum transferred to an atom in a close-packed atomic chain (left part of Fig. 1) produces a series of binary collisions in which the direc-



Atomic Emission Mechanisms in the Sputter Process

According to Silsbee² one possibility of explaining these ejection spots is the assumption of momentum focusing along chains of close-packed atoms within the crystal: focused collision sequences or "focusons." The *focuson model* was calculated in detail by Nelson and Thompson.³ Figure 1(a) shows a focused colli-

The authors are at the Optisches Institut, Technische Universität Berlin, D-1000 Berlin 12, Germany.

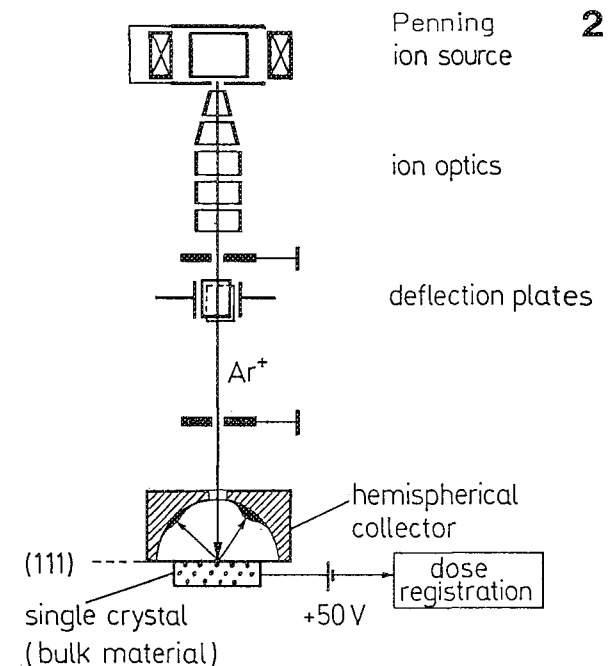


FIG. 1.--Mechanisms of anisotropic atomic emission from ion bombarded single crystals.
 FIG. 2.--Deposition of sputtered spot pattern on hemispherical collector.
 FIG. 3.--Digital recording of electron backscattering from spot pattern on hemispherical collector.

tion of the transferred moments successively approximates the direction of the atomic chain. If the finally transferred energy is high enough, the atom at the surface end of the chain is ejected along the chain direction. The focusing condition is fulfilled if the distance between the centers of two neighboring atoms in the chain is less than twice the atomic diameter; for example, this is the case for the $\langle 110 \rangle$ direction.

A preferential ejection can also arise from binary collisions within the two atomic planes at the surface (Fig. 1c) or by emission of subsurface atoms through potential minima between surface atoms (Fig. 1b): the surface model of

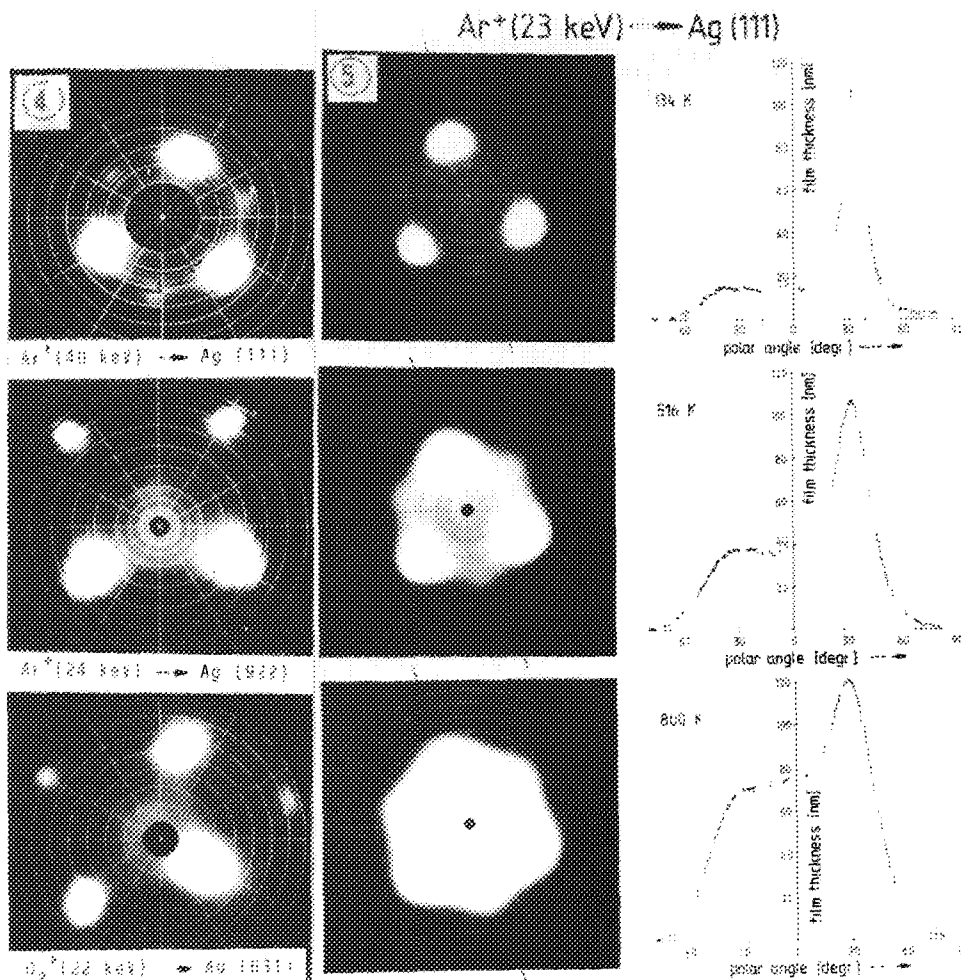


FIG. 4.--Brightness modulated ejection spot diagrams of different oriented crystal surfaces.¹⁰

FIG. 5.--Effect of target temperature on sputter emission spot pattern.¹²

Lehmann and Sigmund.⁴ The necessity of this model followed from the observation of Wehner spots at ion energies below 1 keV, where the penetration depth is of the order of the lattice distance and therefore focused collision sequences cannot develop. Furthermore, spots have been observed in directions in which the focusing condition is strongly violated and therefore a preferential emission can only be explained by the surface model.

A further hypothetical mechanism for preferential directions of atomic emission may be given by direct momentum transfers from the incident ions to the surface atoms of the target. This process might be observed for oblique incidence of the ion beam by increased atomic emission in the direction of reflection.

A possibility for discrimination among various emission mechanisms is to measure the angular spread of the spot emission as a function of the target temperature. Because a collision sequence will be more affected by thermal vibrations of the atoms in a chain than a binary collision, the theory predicts a stronger temperature dependence of the angular spread for the focuson model than for the surface model.^{5,6}

Experimental Arrangement

The total angular atomic emission distribution from a flat single-crystal target can be determined by scanning of the thickness distribution of the film sputter deposited on the in-

ner surface of a hemispherical collector with the target in its center (Fig. 2). The cooled metal collector has a bore for the incident Ar^+ ion beam of 5 to 25 keV energy. The atomic number of its material has to be chosen as different as possible from the atomic number of the target material. Then the thickness distribution of the film sputter deposited on the collector (10-100 nm thick) and in consequence the angular atomic emission distribution from the target can be determined from the backscattering ratio of an electron beam scanned over the inner surface of the collector hemisphere.⁷⁻⁹ Digital storage and processing of the backscattering data (Fig. 3) permits various display modes of the angular atomic emission distribution. As an example Fig. 4 shows brightness-modulated ejection-spot diagrams of variously oriented fcc crystal surfaces. The main spots are always $\langle 110 \rangle$ directions, whereas the weak spots in the $\text{Ag}(111)$ diagram correspond to $\langle 100 \rangle$ directions.¹⁰

Results

Temperature Dependence of Ejection Spot Patterns. Figure 5 exhibits the strong dependence of both the spot height and the angular spread on the temperature of the sputtered single crystal, in this case a silver (111) surface. A quantitative evaluation of such measurements is shown in Fig. 6. Whereas the observed temperature dependence of the angular spread for

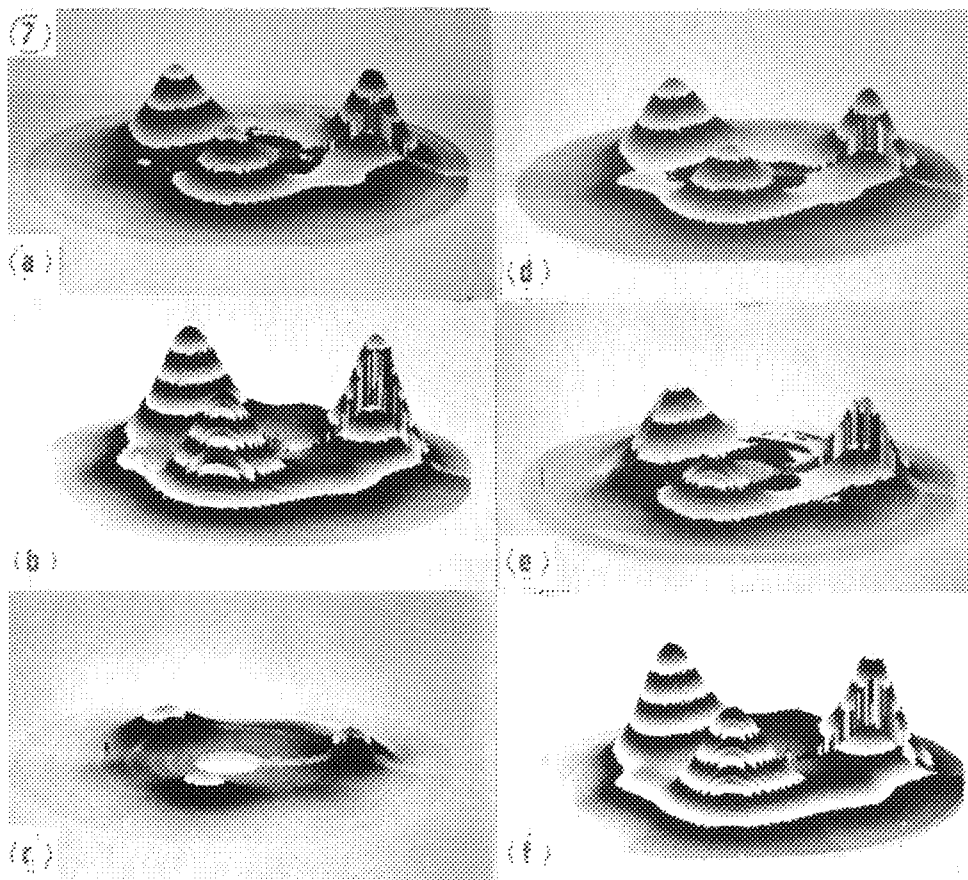
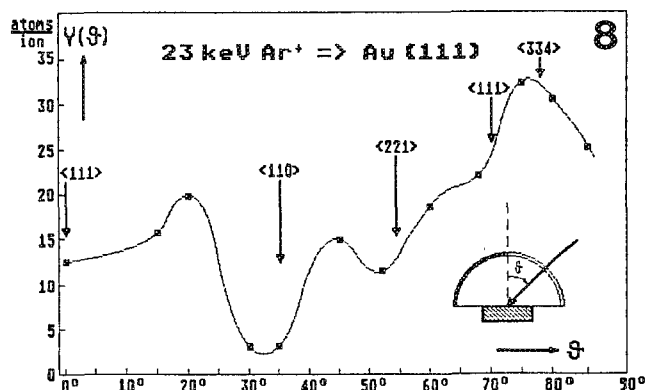
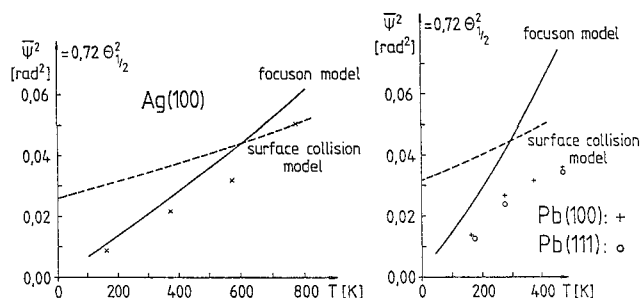


FIG. 6.--Angular spread of atomic emission into (110) spots vs temperature of crystal target: Comparison experiment - theory.^{11,12}

FIG. 7.--Y-modulation representations of angular atomic emission distributions from Au(111) surfaces for oblique incidence of 23 keV Ar⁺ ion beam:¹³ a: $\theta = 0^\circ$, b: $\theta = 20^\circ$, c: $\theta = 35^\circ$, d: $\theta = 45^\circ$, e: $\theta = 52^\circ$, f: $\theta = 68^\circ$.
FIG. 8.--Sputter rate vs incidence angle of Ar⁺ ion beam.

Ag favors the focuson model due to Nelson, for Pb the surface model due to Sigmund also appears to play an important role, at least at higher temperatures.^{11,12}

Dependence on Incidence Angle of Ion Beam. Oblique incidence of the ion beam may affect the angular distribution of the emitted atoms. For instance, the spot intensities near the reflection direction may be increased by direct momentum transfers from the incident ions to near-surface target atoms. For investigating this hypothetical emission mechanism, spot patterns from Au (111) surfaces have been recorded for oblique incidence of 23keV Ar ions with angular steps of 5° to 10°. The ion dose has been kept constant for each recording.¹³

Total two-dimensional angular distributions

of the atomic emission for different incidence angles θ are shown in a y-modulation representation in Fig. 7. For normal incidence ($\theta = 0^\circ$, Fig. 7a) the heights of the three <110> spots are approximately equal and correspond to a differential sputter rate of about 20 atoms per ion and sterad. No background subtraction was made.

For $\theta = 20^\circ$ the spot heights remain approximately symmetric around the surface normal, whereas the sputter rate increases (Fig. 7b). The increase can be understood if one considers that the inclined path within the penetration depth of the incident ions is more close to the surface than for normal incidence. A preferential emission caused by the inclined incidence cannot be observed within the measuring accuracy.

With further increasing incidence angle the sputter rate strongly decreases (Fig. 7c) with a minimum at $\theta = 32^\circ$. The spot heights remain symmetric. The decrease of the sputter rate is caused by channeling effects: the incidence direction of the ions coincides with the direction of open channels in the target crystal. The ions then penetrate deep into the crystal and the collision energy guided back to the surface is considerably reduced (Fig. 8).

For higher angles the sputter rate again increases (Fig. 7d). A second but weaker minimum of the sputter rate due to channeling was observed near the $\langle 221 \rangle$ direction (Figs. 7e and 8). But even for incidence angles $\theta = 68^\circ$ (Fig. 7f) and 75° no distinct asymmetry of the spot emission could be found (Fig. 7f). An increase of the spot intensity in the forward direction, which has been observed by Chadderton et al.¹⁴ for 80keV ion energy, does not appear under our experimental conditions. The fraction of atoms sputtered by direct near-surface momentum transfer from the incident ions apparently is small compared with the fraction of atoms emitted by the mechanisms due to the focuson model and due to the surface model, where the incident ions after multiple scattering processes produce statistical collision cascades with some collision energy guided back to the surface. However, these indirect emission mechanisms do not produce any asymmetry in reference to the surface normal.

Conclusions

Investigations of the temperature dependence of the angular spread in sputtering spot patterns and of the symmetry of the spot patterns for oblique incidence of the ion beam indicate that the main mechanisms of the anisotropic atomic emission are focusing collisions along atomic chains and binary collisions between near-surface atoms induced by momentum transfer from the inner crystal. A direct momentum transfer from incident ions and sputtered surface atoms does not (or only scarcely) occur in the energy range around 20 keV.

References

1. G. K. Wehner, *J. Appl. Phys.* 26: 1056, 1955.
2. R. H. Silsbee, *J. Appl. Phys.* 28: 1246, 1957.
3. R. S. Nelson, M. W. Thompson, and W. Montgomery, *Phil. Mag.* 7: 1385, 1962.
4. C. Lehmann and P. Sigmund, *Phys. Stat. Sol.* 16: 507, 1966.
5. F. Schulz, Ph.D. thesis, TH München, 1967.
6. H.-P. Erlenwein, Ph.D. thesis, TU Berlin, D83, 1977.
7. H. Erlenwein, F.-J. Hohn, and H. Niedrig, *Optik* 49: 357, 1977.
8. H. Niedrig, *Opt. Acta* 24: 679, 1977; *J. Appl. Phys.* 53: R15, 1982.
9. J. Linders, H. Niedrig, and M. Sternberg, *Nucl. Instr. & Meth. in Phys. Res.* B2: 649, 1984.

10. M. Erdmann, J. Linders, H. Niedrig, and M. Sternberg, *Proc. XI ICEM*, Kyoto, I: 615, 1986.

11. P. Erlenwein and H. Niedrig, *Proc. VII Conf. Atomic Collisions in Solids*, Moscow 1977, II: 65 (Moscow State University Publishing House, 1980).

12. J. Linders, H. Niedrig, M. Sternberg, and M. Erdmann, *Scanning Microscopy* (Suppl.) 1: 23, 1987.

13. M. Sternberg, Ph.D. thesis, TU Berlin, D83, 1989.

14. L. T. Chadderton, A. Johansen, L. Sarholt-Kristensen, S. Steenstrup, and T. Wohlenberg, *Rad. Eff.* 13: 75, 1972.

LOW-ENERGY ELECTRON-INDUCED X-RAY SPECTROSCOPY (LEEIXS): AN EMERGING TECHNIQUE IN SURFACE AND THIN-FILM ANALYSIS

Marlène Charbonnier, M. J. Romand, and François Gaillard

Within the last two decades analysis and characterization of surfaces, interfaces, and very thin films have become of considerable importance in many fields of modern technology. This increasing demand has led to a rapid development of various surface and near-surface analytical techniques. Some of these methods, such as XPS, AES, SIMS, and ISS, have matured both with respect to instrumentation and methodology and therefore are now sufficiently well established. Others are still in their infancy but possess a large potential, which is the case of low-energy electron induced x-ray spectrometry (LEEIXS)^{1,2} discussed below.

Experimental

The instrument is a conventional wavelength-dispersive x-ray spectrometer in which the excitation source is an electronically stabilized gas-discharge tube working in the primary vacuum of the apparatus ($\sim 10^{-1}$ Torr). The quasi-monokinetic electron beam delivered by this source is not focused on the sample and the area analyzed is about 1 cm^2 . Typical operating conditions are in the range 0.5–5 keV with a current intensity of 0.1–0.5 mA. The probed depth, which is in the range 5 to 150 nm, is determined by the operator and depends mainly on the energy of the incident electrons, the threshold energy of the core-level involved, the wavelength of the x rays analyzed, and the nature of the matrix.³ Soft and ultrasoft x rays emitted in such conditions are dispersed by suitable flat crystals, pseudo-crystals, or synthetic multilayers, and are detected by a flow-proportional counter equipped with a thin aluminized polypropylene window (0.5 μm) and swept with a 90% Ar + 10% CH₄ gas mixture. LEEIXS uses the same mode of excitation as Auger electron spectrometry (AES) and electron probe microanalysis (EPMA). The energy of the electron beam is in the same range for AES and LEEIXS and the electron penetration depth is a few tens of nanometers. However, both techniques are quite different in their method of analysis. LEEIXS focuses on the products of the radiative decay processes after creating holes in atoms, whereas AES deals with the corresponding nonradiative processes. The former gives, in a nondestructive way, information about the near surface of materials (5–150 nm) because the escape depth of even soft x rays is large compared to the mean free path of outgoing

Auger electrons; the latter probes the top surface of materials (0.5–6 nm). As the electron beam energy used with EPMA is generally large (20 to 30 keV) the probed depth is much larger ($\sim 1 \mu\text{m}$) than in LEEIXS. Thus, as far as the excitation depth is concerned, LEEIXS occupies a unique and intermediary probing range between AES and EPMA. To continue the comparison between LEEIXS and EPMA, although the sampling depth in LEEIXS is about 10 times smaller, the volume in which x rays are created is at least 10^7 times greater. In such conditions, it is possible to use relatively high current intensities in LEEIXS while keeping low current densities (0.1 to 0.5 mA cm^{-2}), which considerably reduces sample damage and permits the analysis of insulating materials. By comparison, EPMA uses higher current densities (10 to 10^3 mA cm^{-2}). Furthermore, because of the relatively high current intensities used, LEEIXS has an important potential in low-energy x-ray emission and particularly in detection of characteristic radiations from low-Z elements,^{1,2} even though corresponding fluorescence yields are very low (e.g., 0.0085 for oxygen). In addition, LEEIXS is also well suited for obtaining some chemical information via fine structure and/or energy shifts of emission bands.¹

Results

Some examples are given hereafter concerning LEEIXS capabilities. The first one deals with Cr-N films synthesized on a Ni-Fe alloy substrate by reactive rf magnetron sputtering of a Cr target in various gas-mixtures (nitrogen and argon), which permits hard coatings of varying stoichiometry to be deposited. Chromium $L\alpha$ and β spectra (Fig. 1) recorded with a TiAP crystal show the effects of the Cr-N bonding on the $L\alpha/L\beta$ ratio on the one hand, and on the full width at half maximum of the Cr $L\alpha$ band and on the appearance of a nonresolved low-energy sub-band characteristic of CrN on the other. Some intensity measurements were carried out on Cr $L\alpha$ and N $K\alpha$ with a layered synthetic mirror (2d = 4.5 nm) used as the dispersing device. The energy of the incident electron beam was adjusted to excite each element on a similar depth (100 nm). Figure 2 shows Cr $L\alpha$ and N $K\alpha$ spectra recorded in the abovementioned conditions. We note in this figure the lack of resolution of the layered synthetic mirror, which is unable to separate chromium $L\alpha$ and $L\beta$ radiations. As against this disadvantage, its high reflecting power allows one to obtain high counting rates, especially for nitrogen. The Cr $L\alpha/\text{Cr } L\beta$ intensity ratios vs N $K\alpha/\text{Cr } L\alpha$

The authors are at the Laboratoire de Chimie Appliquée et de Génie Chimique, CNRS, URA 417, Université Claude Bernard--Lyon 1, F-69622 Villeurbanne Cédex, France.

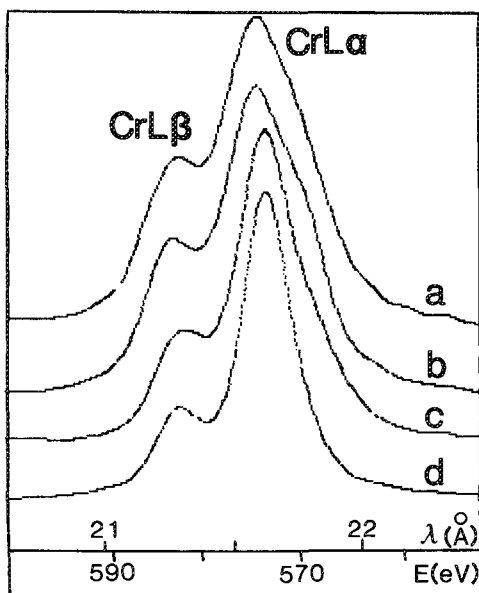


FIG. 1.--Cr $L\alpha, \beta$ spectra of (a) CrN and (d) Cr, and (b) and (c) nonstoichiometric nitrides recorded with TLAP analyzing crystal. Intensities are given in arbitrary units.

ratios for various samples are represented in Fig. 3; the value 1 for N $K\alpha$ /Cr $L\alpha$ corresponds to a CrN standard. The linearity of the curve shows that the Cr $L\alpha$ /Cr $L\beta$ ratio is characteristic of the stoichiometry. The oxygen traces detected on these samples that could participate in chromium oxide formation are negligible and thus cannot modify Cr $L\alpha, \beta$ bands.

To illustrate the capabilities of LEEIXS for the analysis of insulating samples, two examples are given. The first deals with polymeric films deposited on Al substrates from a plasma polymerization of an organic monomer (tetramethoxysilane) with an rf generator. The composition and density of the films obtained depends essentially on the tetramethoxysilane pressure in the vessel, and their thickness is governed by the deposition duration. LEEIXS measurements of C $K\alpha$ (OHM crystal), O $K\alpha$ (TLAP crystal), and Si $K\alpha$ (ADP 200 crystal) were carried out on polymers elaborated during variable times under two different pressure conditions. The excitation energy was calculated in order to probe each element within a 40 nm depth. The results of the measurements are shown in Fig. 4 in the form of Si $K\alpha$ /O $K\alpha$ and Si $K\alpha$ /C $K\alpha$ intensity ratios as a function of treatment duration. It appears that the samples prepared under low pressure show higher ratio values than those prepared under higher pressure. Thus, the higher the pressure the higher are the carbon and oxygen contents in the "polymer." The horizontal line in Fig. 4(a) represents the Si $K\alpha$ /O $K\alpha$ intensity ratio corresponding to a standard of SiO_2 . From these measurements, it can be concluded that the polymeric films mainly contain SiO_2 groups more or less linked by methyl groups. This conclusion is supported by Fig. 5, which shows the Si $K\beta$ spectrum on which the $K\beta'$ satellite characteristic of Si-O bonding appears

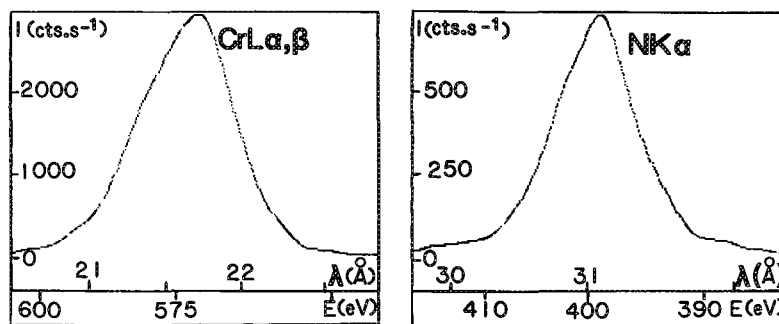


FIG. 2.--Cr $L\alpha, \beta$ and N $K\alpha$ spectra of nonstoichiometric chromium nitride, recorded with layered synthetic mirror ($2d = 4.5$ nm).

13.75 eV away from the $K\beta$ band.⁴

The other example concerning an insulating material analysis deals with polytetrafluoroethylene (PTFE) chemically treated in a sodium naphthalenide solution to improve its adhesion properties. An important modification of the surface composition can be seen from Fig. 6, which shows the intensity change of C $K\alpha$ (OHM crystal), F $K\alpha$, and O $K\alpha$ (TLAP crystal) between (a) an "as received" PTFE sample and (b) a chemically treated one. A brown carbonaceous layer appears on the surface of the latter. Figure 7 is characteristic of C $K\alpha$ normalized spectra relative to these samples. It shows a larger FWHM for PTFE (C-C and C-F bonds) (spectrum a) than for chemically treated PTFE (spectrum b), and for the latter shows only one kind of bond (C-C) characteristic of the defluorinated surface.

Conclusion

In dealing with these examples we demonstrate the capabilities of LEEIXS for analyzing conductive or insulating layers on various substrates for thicknesses intermediate between those probed by AES and EPMA. With respect to insulating materials, LEEIXS can be considered as a soft technique in terms of current density used for excitation. Furthermore, it can detect light elements (from their K radiation) with a high efficiency and, from the band structure examination, it can give some information on chemical bonding. In addition to the qualitative aspects presented here, LEEIXS is also well suited for providing quantitative analysis.^{1,2} It is therefore a well-adapted tool for controlling and optimizing thin-film depositions and surface treatment processes. In this context, an original application of LEEIXS has been proposed by Hecq.⁵ Finally, irrespective of the nature of the excitation source (electron gun, x-ray tube, synchrotron radiation), a great deal of research is in progress throughout the world (see, for example, Ref. 6) on the study of surfaces and very thin films by x-ray emission methods. LEEIXS constitutes one of the available tools.

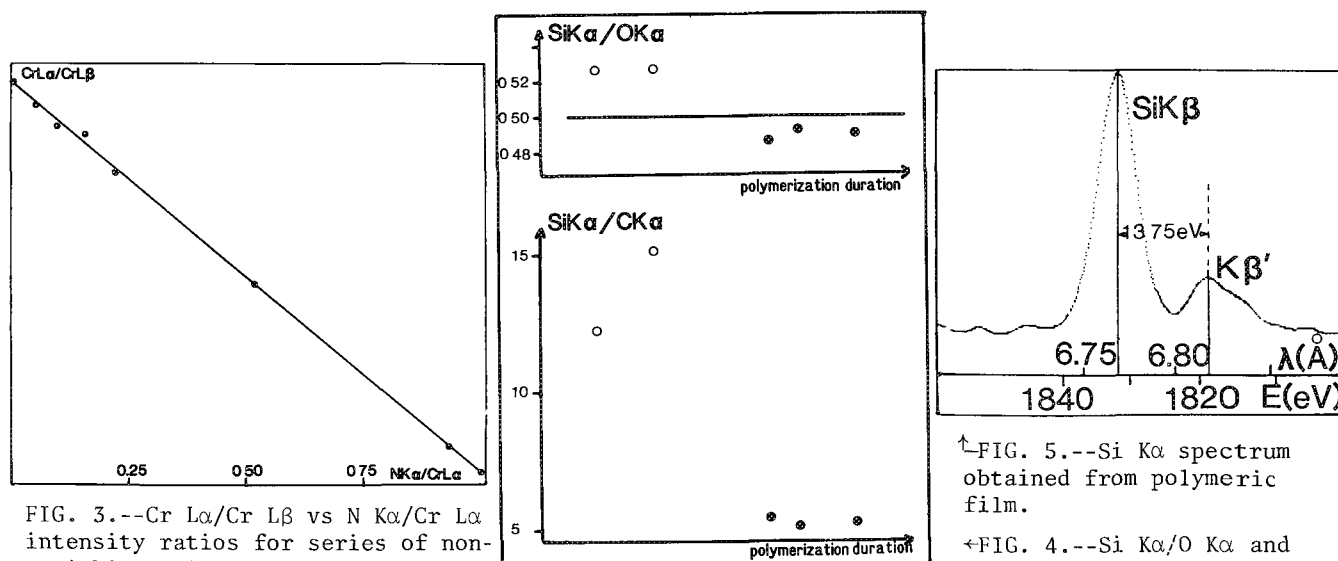


FIG. 3.--Cr $L\alpha$ /Cr $L\beta$ vs N $K\alpha$ /Cr $L\alpha$ intensity ratios for series of non-stoichiometric nitrides.

of series of polymeric films elaborated during various times and at different monomer pressures: (o) low pressure, (●) higher pressure.

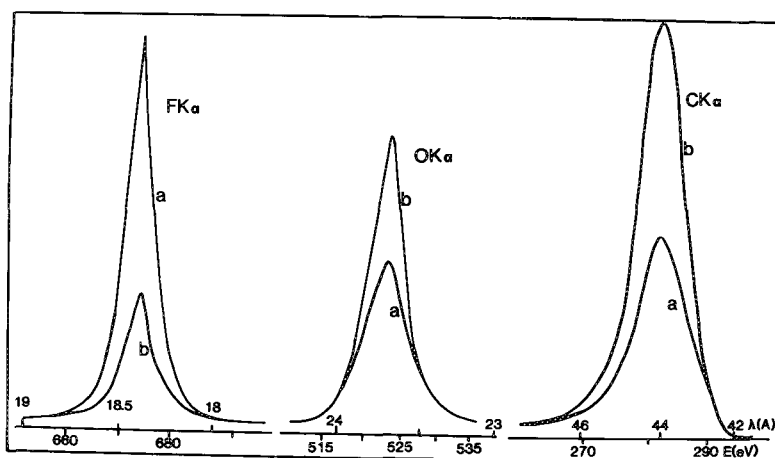


FIG. 6.--Relative intensities (in arbitrary units) of C $K\alpha$, O $K\alpha$, and F $K\alpha$ signals from (a) PTFE sample, (b) PTFE sample treated with solution of sodium naphthalenide.

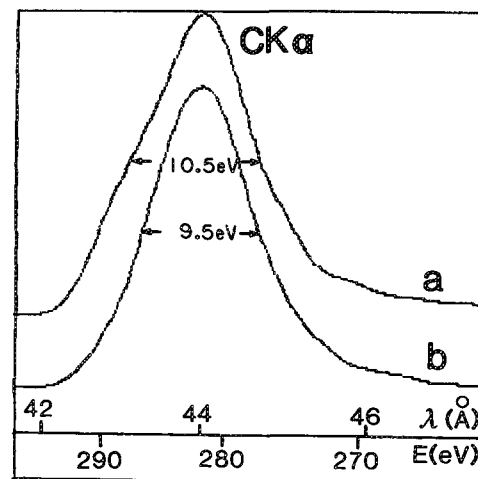


FIG. 7.--C $K\alpha$ spectra obtained with OHM analyzing crystal, from (a) PTFE, (b) chemically treated PTFE. Intensities are given in arbitrary units.

References

1. M. Romand, R. Bador, M. Charbonnier, and F. Gaillard, *X-ray Spectrometry* 16: 7-16, 1987.
2. M. Charbonnier, M. Romand, and F. Gaillard, *Analysis* 16: 17-23, 1988.
3. M. Romand, M. Charbonnier, and F. Gaillard, *J. de Physique* 48 (Suppl. 12): C9-87, 1987.
4. D. S. Urch, *J. Phys.* C3: 1275-1291, 1970.
5. M. Hecq and J. Leleux, *J. Vac. Sci. Technol.* A5: 1760, 1987.
6. G. Andermann, *Appl. Surf. Sci.* 31: 1, 1988.

ANGULAR RESOLVED ELECTRON SPECTROSCOPY WITH PARALLEL RECORDING

M. Huang, P. S. Flora, C. J. Harland, and J. A. Venables

A cylindrical mirror analyzer (CMA) has been built with a parallel recording detection system. It is being used for angular resolved electron spectroscopy (ARES) within a SEM. The CMA has been optimized for imaging applications; the inner cylinder contains a magnetically focused and scanned 30kV SEM electron-optical column, which is drawn to scale in Fig. 1. The CMA has a large inner radius (50.8 mm) and a large collection solid angle ($\Omega > 1$ sterad). The design and performance of the combination SEM/CMA instrument has been described previously;¹ the CMA and detector system has been used for low-voltage electron spectroscopy, where an energy resolution ($\Delta E/E$) of 1-2% has been achieved.² Here we discuss the use of the CMA for ARES and present some preliminary results.

The CMA has been designed for an axis-to-ring focus and uses an annular type detector. This detector consists of a channel-plate/YAG/mirror assembly which is optically coupled to either a photomultiplier for spectroscopy or a TV camera for parallel detection. The position of the detected electrons, as displayed on the TV image, contains both the radial (θ) and azimuthal (ϕ) angular information. The TV camera is connected to a video framestore for computer processing of the image. Figure 2 shows the calculated electron trajectories in the r, z plane in the region of the detector. The higher θ trajectories strike the detector at smaller radius r_d and vice versa. The energy transmission function $T(E)$ has been calculated by counting which trajectories pass through the energy selecting slits Fig. 3(a). The same trajectories, for given input angles θ , continued to the detector plane, give $T(r_d)$ as shown in Fig. 3(b). At this setting of the energy selecting slit that gives $\Delta E/E = 2\%$, the calculated radial angular resolution $\Delta\theta$ is 5-6°. When the slit is closed to improve $\Delta E/E$ to $\approx 1\%$, $\Delta\theta$ improves to ≈ 2.5 -3°. The ring detector also preserves the azimuthal (ϕ) information, and the CMA accepts ϕ between $\pm 150^\circ$. The angular azimuthal resolution is at present limited by the CMA input grids to $\Delta\phi \approx 5^\circ$.¹

An example of an angular resolved image from clean Si(111) is shown in Fig. 4. The pattern is brighter at larger radii where $\theta \approx 30^\circ$ and tails off at smaller radii at $\theta \approx 50^\circ$. The data

The authors are at the School of Mathematical and Physical Sciences, University of Sussex, Brighton, England BN1 9QH. (C. J. Flora's present address is Laboratoire de Physique des Solides, Bât. 510, F-91405 Orsay Cedex, France; J. A. Venables is also at the Department of Physics, Arizona State University, Tempe, AZ 85287.)

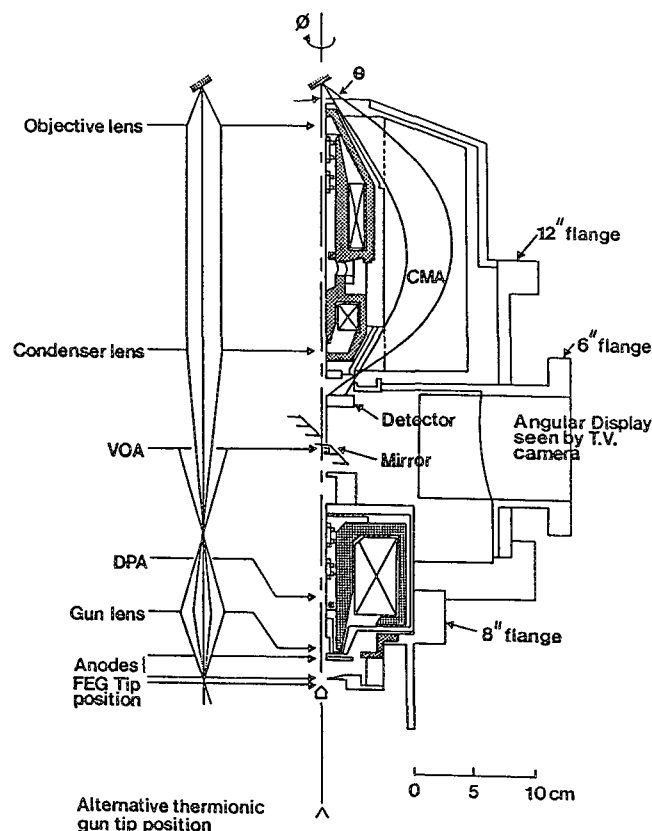


FIG. 1.--Cross section of electron optical column, showing electron paths, lens positions, and CMA. Angular scale of ray paths (left) is exaggerated.

extracted from the pie-shaped box ($-120^\circ < \phi < -90^\circ$) are analyzed in Fig. 5, which shows the integrated $N(E, \theta)$ signal at three energies around the Si Auger peak at 1620 eV, compared with the distribution expected for cosine emission. A comparison between the angular distribution obtained from Si(111) and from amorphous Si by back-scattered electrons is given in Fig. 6, which shows that the amorphous sample does give rise to a cosine distribution, and that the amorphous crystalline differences can be readily detected with our parallel recording system.

Future work is aimed at examining higher atomic number substrates, where we expect more marked angular variations, and at adsorbates on substrates to examine adsorption sites. It is also intended to explore angular effects as a means of nondestructive depth profiling. The ϕ structure in Fig. 4 is due to the grids at the exit slot in the inner

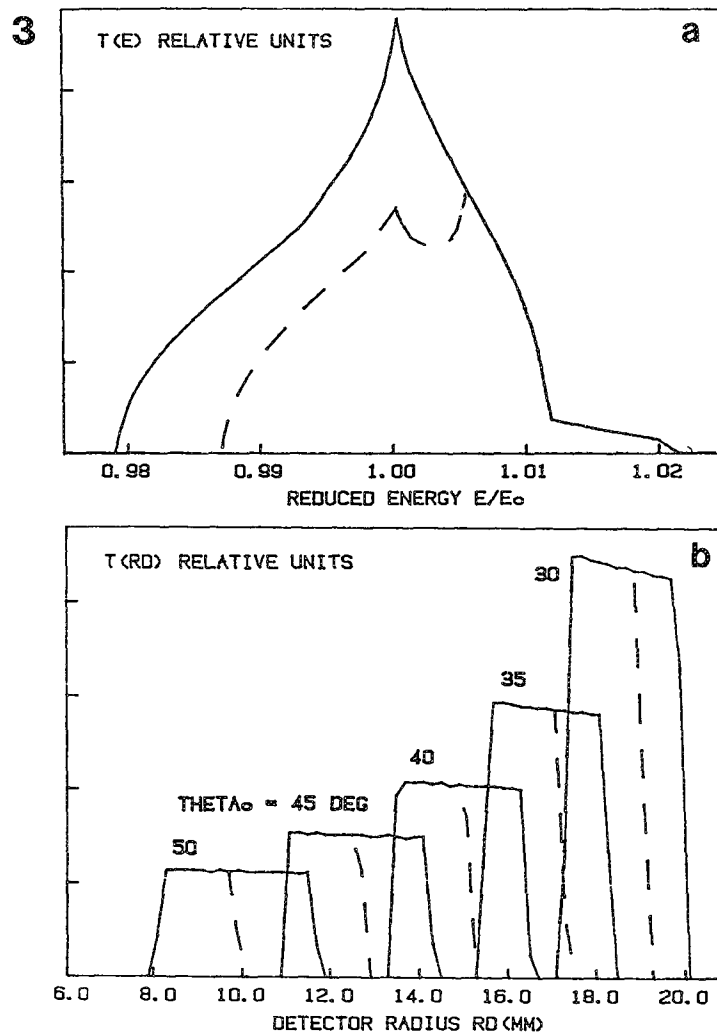
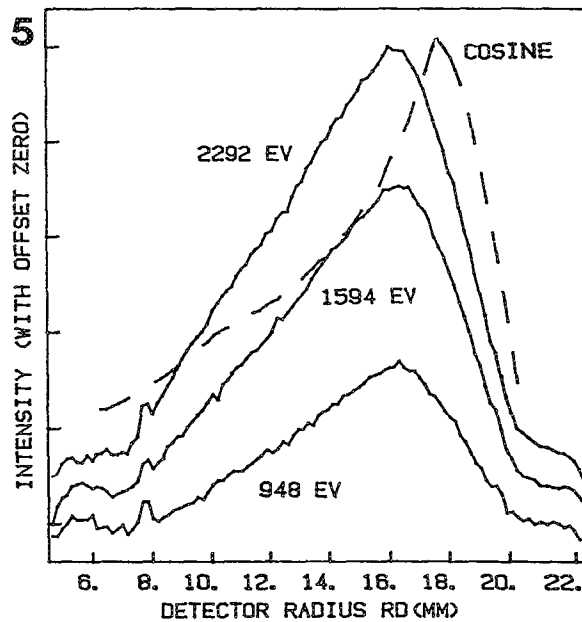
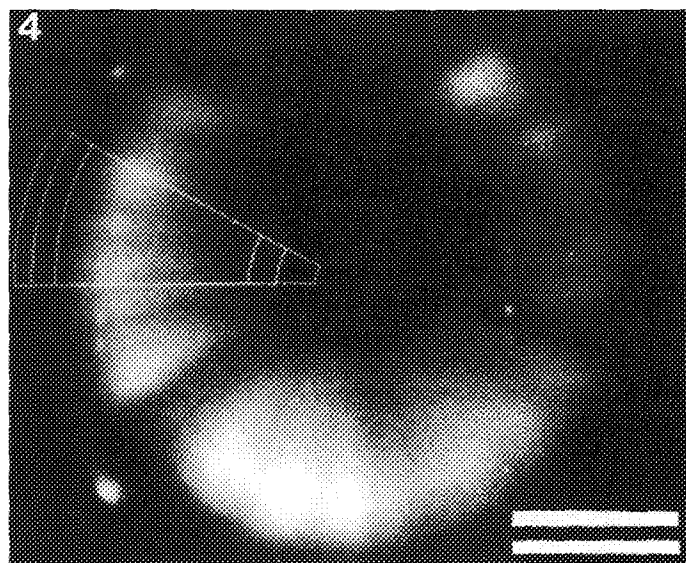


FIG. 3.--(a) Transmission function $T(E)$ for detector slit settings of 1.5 mm (full line) and zero (dashed line). (b) Corresponding angular transmission function $T(r_d)$ for incident angles $\theta_0 = 30-50^\circ$.

FIG. 4.--Angular resolved energy selected image of Si(111). (Bar = 10 mm.)

FIG. 5.--Data from pie-shaped box in Fig. 4.



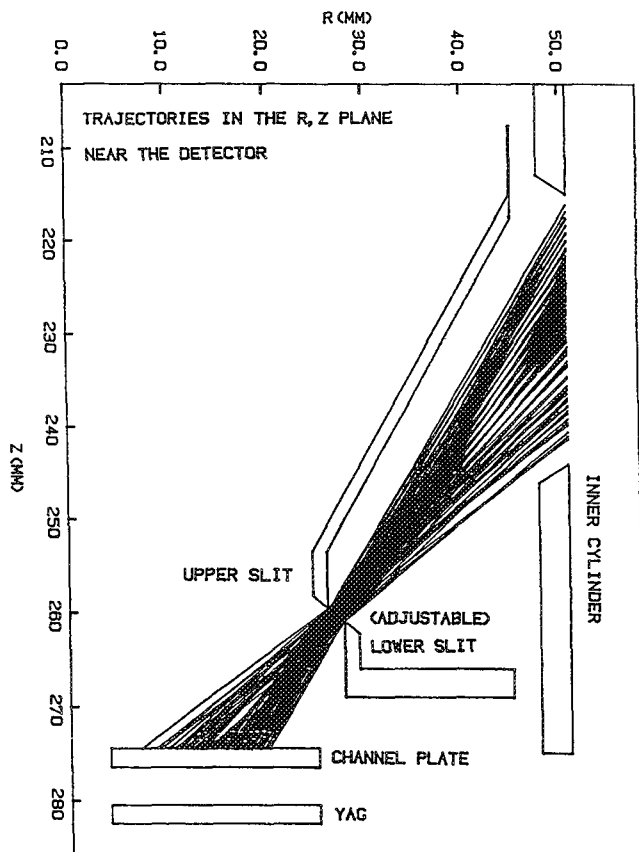


FIG. 2.--Trajectories in r, z plane near CMA detector. Three energies ($E/E_0 = 0.99, 1.00$ and 1.01) are shown at 1° angular intervals.

cylinder. We intend to eliminate these grids by a redesign of the electrodes in this area, and to record the angle-resolved and angle-integrated signals simultaneously. At this point we have demonstrated that we can record ARES information in an SEM using our parallel recording system, and that data from amorphous and crystalline samples can be distinguished.³

References

1. C. J. Harland, G. Cox, D. J. Fathers, P. S. Flora, M. Hardiman, G. Raynerd, M. Whitehouse-Yeo, and J. A. Venables, *Inst. Phys. Conf. Ser.* 90 (EMAG'87) 9-12.
2. P. S. Flora, Huang Min, C. J. Harland, and J. A. Venables, *Inst. Phys. Conf. Ser.* 98 (EMAG'89) 299-302.
3. This research is supported by SERC. M.Huang thanks the British Council for a scholarship.

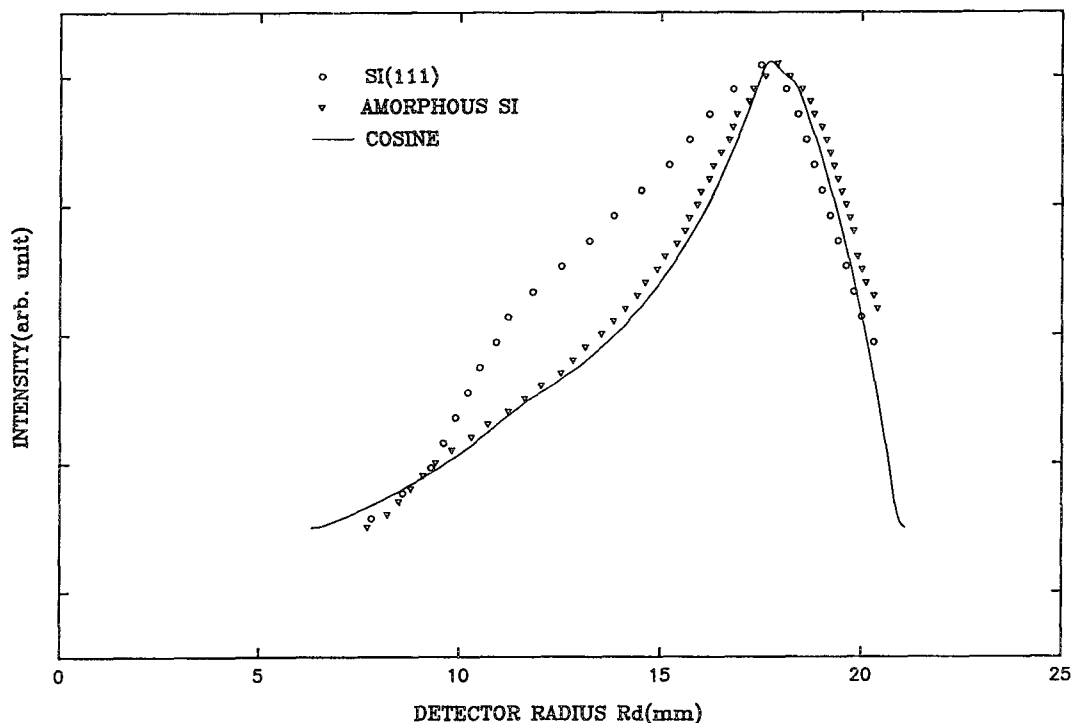


FIG. 6.-- $N(E, \theta)$ signal for $E = 3565$ eV from both amorphous Si and Si(111) samples compared with calculated values for a cosine distribution.

INTERFACE SEGREGATION IN A NICKEL BASE SUPERALLOY

M. C. Koopman and R. G. Thompson

Grain boundary chemistry has long been known to play a critical role in such varied phenomena as high-temperature stress rupture strength and microfissuring in the heat-affected zones of welds. Although intergranular segregation has been documented in nickel aluminides, the behavior and interaction of nonmetallic elements at grain boundaries is not fully understood in the high-nickel alloys. The present research is directed toward exploring the chemistry of interface surfaces in an alloy matrix similar to alloy 718 with controlled interstitial and substitutional additions.

Results

The base composition contained typical alloy 718 levels of Ni, Cr, Fe, Mo, Nb, Al, Ti, and less than 0.001% of S, B, C, P, Si, Zr, and Hf. Four modifications of this matrix were examined: 0.01 B and 0.1 Zr; 0.01 B, 0.01 C, 0.1 Hf, and 0.1 Zr; 0.01 B, 0.15 S, 0.15 P, and 0.1 Zr; and 0.01 B, 0.015 S, 0.15 P, and 0.1 C. Specimens were electrolytically charged with hydrogen to promote intergranular fracture. The specimens were fractured in the UH vacuum of the Auger microprobe, and exposed surfaces were analyzed by successive acquisition of spectra, sputtering with argon ions, and reacquisition of spectra. Figures 1 and 2 show grain boundary segregation of B, and of P and B, respectively. The B and Zr doped specimen fractured exposing 10-15 grain boundaries, and showed consistent B segregation within individual grains and between the three grains analyzed. The B, C, Hf, and Zr specimen fractured exposing 30-40 grain boundaries and showed little variation in B concentration within grain boundaries, but there was a factor of two variation in the Nb/B ratio between the five grain boundaries analyzed. The B, S, P, and Zr specimen fractured exposing three grain boundaries, and showed a factor of two variation in the Nb/B ratio within individual grain boundaries and between the three grain boundaries. A high variation in the P segregation within and between grain boundaries was also noted, as well as a small S peak on two of the boundaries. Sulfur was seen to segregate strongly to the surface between MC carbides and the matrix in this sample and in the B, S, P, and C sample (Fig. 3). The B, S, P, and C specimen fractured exposing 10-15 grain boundaries and showed trace concentrations of B on only a few grains. P and S were present on all six grains analyzed, and their concentrations were consistent within grains. The P concentration varied by a factor

The authors are at the Department of Materials Engineering, University of Alabama, Birmingham, AL 35294.

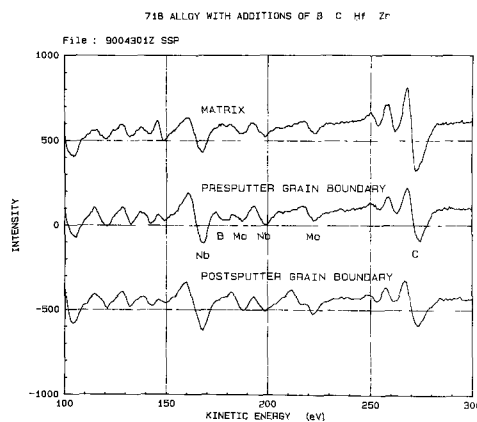


FIG. 1.--718 alloy with additions of B, C, Hf, and Zr showing segregation of B to grain boundaries.

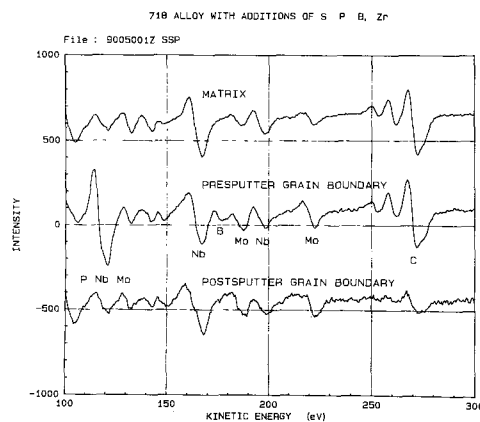


FIG. 2.--718 alloy with additions of S, P, B, and Zr showing segregation of P and B to grain boundaries.

of four between grains.

Although most of the specimens revealed smooth curving grain boundaries with slip lines intersecting the surface as the only topographic feature, the B, S, P, and Zr specimen showed indications of submicron phases at the grain boundaries. The spatial resolution of the beam during spectral acquisition may have overlapped these submicron phases, causing the variation in the B, S, and P concentrations. Sulfur-rich phases between 1 and 3 μm in size were found predominantly near MC carbides and may have played a role in the S segregation.

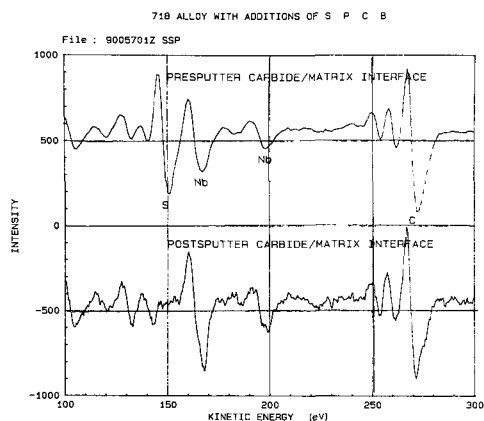


FIG. 3.--718 alloy with additions of S, P, C, and B showing segregation of S to carbide/matrix interface.

Conclusion

In summary, low-level B segregation was found in all samples doped with B. Undoped samples showed no B segregation. The highest B level was found in conjunction with large P segregation; however, significant evidence was not found for synergistic segregation of B and P. Sulfur was partitioned to the precipitate/matrix interface during solidification, where it remained during cooling. Work is continuing in this area. Special emphasis in future work will consider the effect of heat treatments on multi-element segregation of B, P, and S.

SPATIAL RESOLUTION AND DETECTABILITY LIMITS IN THIN-FILM X-RAY MICROANALYSIS

J. I. Goldstein, C. E. Lyman, and Jing Zhang

The major advantages of performing x-ray microanalysis in the analytical electron microscope (AEM) are the high compositional spatial resolution and the elemental analysis sensitivity. Unfortunately there is usually a trade-off between these two advantages. This paper discusses the factors involved in the optimization of both spatial resolution and sensitivity during x-ray microanalysis and shows the results of such optimization experiments for several AEM instruments.

X-ray Spatial Resolution

Spatial resolution R depends on the size d of the focused electron probe and the amount of electron beam broadening b in the thin foil specimen.^{1,2} Figure 1 shows schematically the concept of spatial resolution in thin-foil microanalysis. A focused electron probe is shown at the top of the thin foil. The incident electron probe is elastically scattered as it progresses through the thin foil and the beam is at maximum size at the bottom of the thin foil of thickness t . If we assume that x rays are generated throughout the scattering process, x-ray emission occurs from a volume which is a frustum of a right circular cone (Fig. 1). If the intensity in the probe is Gaussian and the electron distribution remains Gaussian while traversing the sample, Reed³ proposed that the total amount of broadening R_{\max} at the bottom of the thin foil is given by

$$R_{\max} = \sqrt{d^2 + b^2} \quad (1)$$

where b is the amount of beam broadening. As shown by Michael et al.,² the measured spatial resolution is an average of the electron probe size over the specimen thickness. In Fig. 1 we define the spatial resolution R as an average of the electron probe size from the top and the total beam broadening (Eq. 1) from the bottom. Thus, R is given by

$$R = \frac{d + \sqrt{d^2 + b^2}}{2} = \frac{d + R_{\max}}{2} \quad (2)$$

It is important to define the probe size and the resultant beam broadening in a consistent way. Recently, Michael and Williams⁴ proposed using the combination of the full-width at tenth maximum (FWTM) probe diameter d with the 90% beam broadening diameter b as determined by

The authors are at the Department of Materials Science and Engineering, Lehigh University, Bethlehem, PA 18015. The research was supported by Grant NAG 9-45. They also thank Dr. J. R. Michael of Sandia National Laboratories for his assistance with the HB501 microscope.

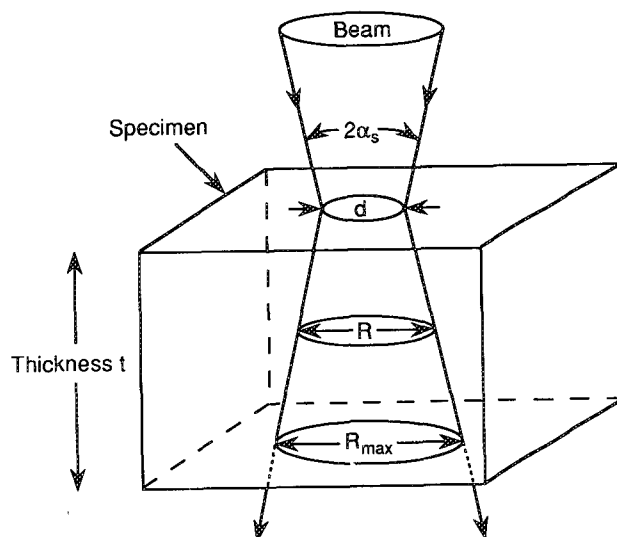


FIG. 1.--Definition of spatial resolution R in thin-foil microanalysis. (Older but commonly used value for spatial resolution in microanalysis is R_{\max} .)

Reed.³ In this way the probe and beam broadening diameters each contain 90% of the electrons and are combined in a consistent manner. Based on Reed's single scattering model,³ the beam broadening b is given in cm by

$$b = 7.21 \times 10^5 (\rho/A)^{1/2} (Z/E)t^{3/2} \quad (3)$$

where ρ , A , and Z are the average density, atomic weight, and atomic number of the specimen, respectively; E is the beam voltage in eV; and t is the specimen thickness in cm.

There are several ways to determine the probe size d at FWTM in an AEM for a given beam current and a specified operating voltage.^{2,4} One method to measure d is to scan the focused probe across a sharp edge on a thin specimen. Instead of a sharp discontinuous step, a smooth intensity profile is obtained. The width of this profile is a measure of the probe size under the assumption of a perfectly sharp edge. For a dedicated STEM, such as the Vacuum Generators HB-501, this is the only method available to measure the probe size. For a TEM/STEM system, it is also possible to image the probe directly on a photographic plate. If the exposure is controlled to remain within the linear range of the plate, the density level of the probe image on the film is a measure of the probe intensity. The intensity profile of the probe can be obtained and the probe size can be measured using a densitometer. In this study, the probe sizes for the Philips AEMs were measured by this method. Combining the calculation of b and a measurement of d at FWTM, one

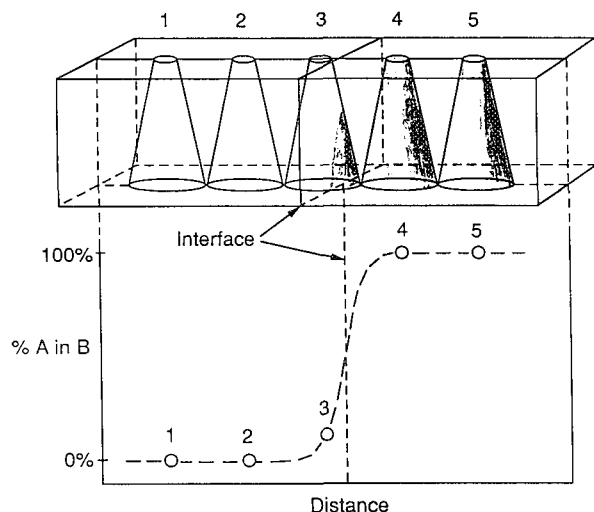


FIG. 2.--Schematic depiction of five x-ray excitation volumes near interface with step change in composition of element A.

can calculate the spatial resolution R using Eq. (2).

To optimize spatial resolution, one should use the smallest probe size d , most easily obtained by using a high-brightness field-emission gun (FEG). For thermionic sources the probe current is reduced to inadequate levels at probe sizes <10 nm. This reduction occurs because the probe current is proportional to $d^{8/3}$ for thermionic sources but not for FEG sources.⁵ In addition, specimens should be as thin as possible and the highest operating voltage should be used to minimize the beam broadening b .

One can determine the spatial resolution R experimentally by measuring composition profiles from specimens with abrupt concentration discontinuities.^{4,6} Figure 2 shows schematically how the x-ray excitation volume for a given element varies as the focused probe is stepped across an interface with an abrupt concentration change. The actual step size should be much less than the spatial resolution R so that the detailed concentration gradient across the interface can be measured. The measured concentration variation takes into account the finite x-ray spatial resolution, and the discontinuity is measured as an error function composition variation across the interface (Fig. 2).

As suggested by Michael et al.,² the FWTM distance of a Gaussian distribution R scanned across a composition step is a horizontal distance L that can be used to help measure the spatial resolution. If the concentration discontinuity is normalized to 100%, the FWTM across the apparent concentration variation is represented by L between the 2% and the 98% points on the compositional profile (Fig. 3). It may be easier to measure L from the full width at half maximum (FWHM), which is the distance between the 12% and the 88% points on the profile, and then to multiply that value by 1.82 to obtain L .

The geometry of the beam and specimen used

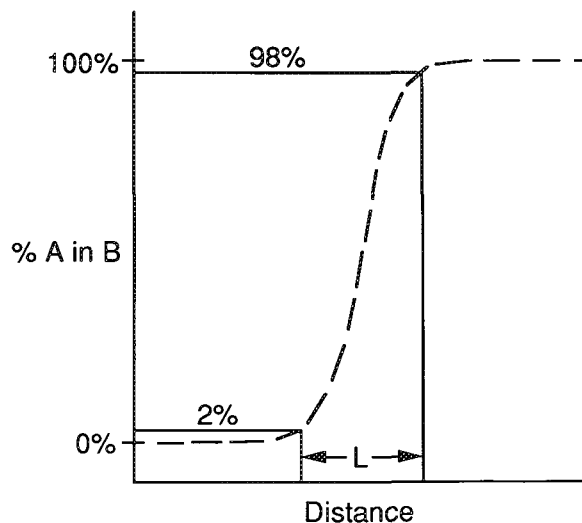


FIG. 3.--Schematic representation of measured profile for element A across step change in composition showing definition of L for FWTM.

to measure the spatial resolution across a concentration step is not the same as that shown in Fig. 1.² In the experimental setup, the scattering of electrons parallel to the boundary where the discontinuity is present occurs without a degradation of the spatial resolution in one dimension rather than in two dimensions as in Fig. 1. The spatial resolution R given in Eq. (2) can be obtained by multiplication of L , the FWTM across the error function, by $\sqrt{2}$.

Another test specimen for spatial resolution can be conceived as a right cylinder of a second phase in a thin foil. If such a cylindrical second phase could be obtained in various sizes, the spatial resolution would be given as the cylinder diameter where 90% of the the signal from the second phase may be obtained for a given probe diameter. Such a spatial-resolution specimen is not yet available.

Minimum Mass Fraction

The minimum mass fraction (MMF) is a measure of the elemental analysis sensitivity and represents the smallest concentration of an element that can be measured with a focused electron probe of size d under specified AEM operating conditions (kV, probe current, x-ray detector solid angle, counting time, etc.). The analyst can determine the MMF directly for a sample of known composition by making relatively simple measurements on the thin film. The approach used in this study to determine the MMF is to employ a thin film where element A is present and its concentration C_A in the sample is known. The analysis requirement is to detect significant differences between the sample and continuum background generated from the sample. For a single analysis,⁶ we can say that I_A is significantly larger than the background continuum radiation I_b for the sample if the value of I_A exceeds I_b by $3(21I_b)^{1/2}$. If we use a thin film where element A is present

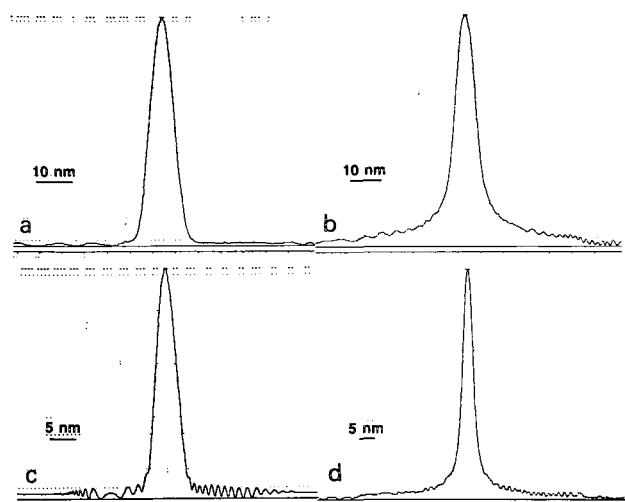


FIG. 4.--Measurement of the electron probe intensity profile for a Philips EM430T and a Philips EM400T AEM. (a) EM430T, 300kV, 50µm C2 aperture, spot size 4 setting; (b) EM400T, 120kV, 70µm C2 aperture, spot size 4 setting; (c) EM430T, spot size 5 setting; (d) EM400T, spot size 5 setting.

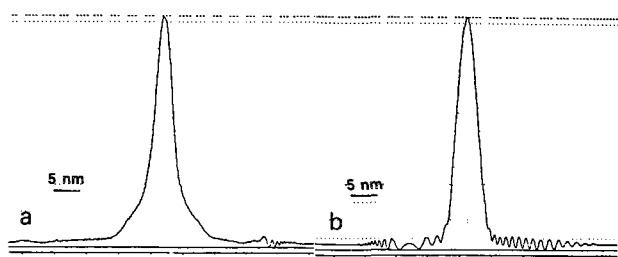


FIG. 5.--Electron probe intensity profiles of EM430T, spot size 5 setting at different objective lens focusing. (a) Small central peak with tail, (b) approximate Gaussian peak.

and its concentration C_A in the sample is known, then⁶

$$MMF = 3 \frac{\sqrt{2I_A^b}}{I_A - I_A^b} C_A \quad (4)$$

Since the x-ray yield I_A varies with film thickness, the value of MMF varies from one analysis point to the other. Therefore the MMF is not likely to be constant over an entire sample even for the same analysis conditions.

Ziebold⁷ showed that trace element sensitivity or MMF can also be expressed as

$$MMF \sim [P(P/B)T]^{-1/2} \quad (5)$$

where P is the pure element counting rate, P/B is the peak-to-background ratio of the pure element, and T is the counting time. One can decrease (improve) the MMF by increasing all three factors in Eq. (5). Thus, one may obtain improvements in MMF by increasing the electron current density and optimizing the x-ray detector configuration to increase P , by increasing

the operating voltage to increase P/B , and in increasing the analysis time T . Unfortunately, the analysis time is limited in most AEM instruments by contamination and specimen drift. In an AEM optimized for chemical sensitivity, the MMF is typically 0.1 to 0.2 wt% for elements near iron in atomic number. In this study the MMF was measured for Ni in a homogeneous thin foil of an Fe-25 wt% Ni alloy.

Results: Measurement of R and MMF

Measurements of the electron probe diameter for the Philips 400T at 120 kV and the Philips 430T at 300 kV were made by direct imaging of the probe and measurement of the intensity profile across the photographic negative by a densitometer. To image the electron probe, beam scanning was stopped and the microscope imaging system was switched from diffraction mode to image mode so that, instead of a scan raster, a magnified probe image was obtained on the microscope viewing screen. The objective focus was changed slightly to obtain a focused probe image. The error introduced in the probe diameter by variation of the objective focusing length was minimal. The advantage of using the microscope imaging mode was that at high magnification, the current density on the viewing screen falls within the linear range of the recording film. The intensity profiles of the magnified focused probe were measured with an LKB 222-020 Ultra Scan XL laser densitometer.

Measured probe diameters (FWHM and FWTM) and beam current for the Philips 400T and Philips 430T at various C2 apertures and probe forming conditions in STEM mode are listed in Table 1. For the 70µm C2 aperture used in the EM400T, the measured FWTM of the probe is larger than the calculated value for a Gaussian peak, $FWHM \times 1.82$. The larger FWTM probe size shows that the electron probe has a broad tail distribution because of the larger than optimum C2 aperture size available. For the EM430T with a 50µm C2 aperture, the electron probes are approximately Gaussian.

TABLE 1.--Experimentally measured electron probe parameters of the Philips EM430T and EM400T microscope in STEM mode.

STEM setting		EM430T 50 µm C2 aperture		EM400T 70 µm C2 aperture	
		diameter (nm)	current (nA)	diameter (nm)	current (nA)
Spot Size 4	FWHM	7.0	0.263	8.5	0.090
	FWTM	11.8	0.263	23.8	0.090
Spot Size 5	FWHM	4.0	0.062	3.9	0.030
	FWTM	6.8	0.062	11.6	0.030

Figure 4 shows the measured intensity profiles of the electron probes listed in Table 1, at optimum focusing conditions (smallest probe sizes with the minimum tails). For certain

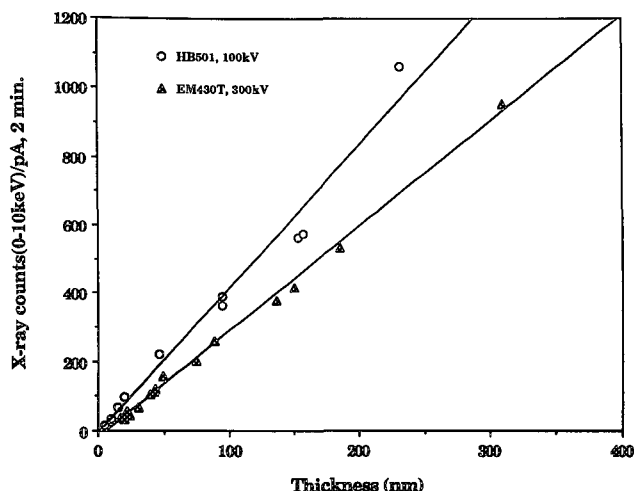


FIG. 6.--Calibration curve of 0-10keV x-ray counts per pA vs film thickness for Philips EM430T and Vacuum Generators HB501. Counting time, 120 s.

probe size and aperture combinations, the optimum probe for microanalysis was different from that which gives the best STEM image. An example is shown in Fig. 5. The probe in Fig. 5(a), which has a sharp central peak with a large tail will probably give a better STEM image. However, the probe in Fig. 5(b), which is approximately Gaussian and is underfocused by the objective lens by some 200 nm, will allow microanalysis at a higher spatial resolution, since it has no significant tail. As demonstrated previously by Cliff et al.,⁸ slightly underfocusing from the best STEM image condition improves the spatial resolution of x-ray analysis. For some experimental conditions, usually with large C2 apertures, it is not possible to achieve a Gaussian probe without a tail no matter what underfocusing is used.

The electron probe size of the HB-501 STEM was measured by Michael by use of a small MgO crystal.⁹ An optimum probe with FWTM of 1.8 nm was obtained with a 50 μ m virtual objective aperture. This probe size was used for the spatial resolution calculations for the VG STEM. In the calculation of the spatial resolution R of the Philips AEMs, we used the experimentally measured FWTM probe size when the electron probe was approximately Gaussian, and 1.82 times the experimentally measured FWHM probe size when the probe was not Gaussian. The spatial resolutions calculated in this study are the ideal values. The practically achievable spatial resolution may be worse due to factors such as specimen drift and other instabilities of the microscope, as well as nonideal electron probe characteristics as discussed above.

In order to calculate the amount of beam broadening from Eq. (3) one must measure the specimen thickness t at the analysis position. Direct foil thickness measurements were made by the EELS log-ratio technique.¹⁰⁻¹² This procedure involves measuring the ratio of the total area I_T under the electron energy loss spectrum from the Fe-Ni thin foil to the elastically scattered peak I_0 , where

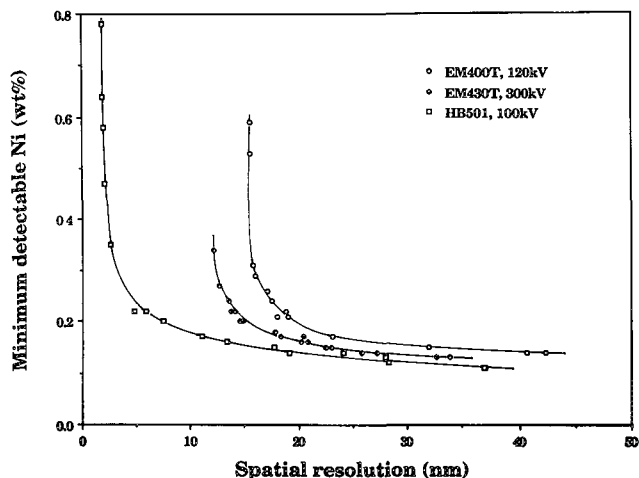


FIG. 7.--Relationship of spatial resolution and MMF measured for Ni in Fe-25 wt% Ni alloy by three AEM instruments. Operating conditions are (1) Philips EM400T: 120 kV, LaB₆ gun, spot size 4, 0.09nA beam current, 15.5nm probe diameter (1.82 times the measured FWHM); (2) Philips EM430T: 300 kV, LaB₆ gun, spot size 4, 0.26nA beam current, 11.8nm probe diameter (FWTM); (3) VG HB501: 100 kV, FEG, 0.3-0.35nA beam current, 1.8nm probe diameter (FWTM). Counting time, 120 s. Spatial resolution calculated from Eqs. (2) and (3); specimen thickness measured from calibration curves in Fig. 6.

$$t = \lambda \ln(I_T/I_0) \quad (6)$$

An equation for the total inelastic mean free path λ was derived by Malis based on experimentally measured values of λ for various materials.¹⁰ Absolute thickness can be determined to an accuracy of $\pm 20\%$. For a measurement of the relative specimen thickness at each analyzing position, the x-ray count method is the most convenient. To use this method, it is necessary to measure a calibration curve of x-ray counts vs thickness for a specimen of similar atomic number. The beam current must be measured by an independent method. In this study, a calibration curve of 0-10 keV x-ray counts per pA vs thickness was measured for a 120s counting time on an Fe-25 wt% Ni alloy for each of the AEM instruments used. The specimen thickness was measured by the EELS log-ratio technique.¹⁰ The calibration curves for the EM430T and HB-501 are shown in Fig. 6. These calibration curves are linear for film thicknesses up to at least 100 nm.

In the Philips 400T and 430T AEMs, the beam current from the LaB₆ filament was measured by means of a specimen holder electrically isolated from the microscope column and connected to a Keithley 480 picoammeter. The reading from the picoammeter was corrected for backscattering to obtain the direct beam current. The beam current was quite stable after an initial period when the beam current was decreasing. In the VG HB-501 STEM, the beam current was measured by insertion of an electrically

isolated slab of Mo into the beam path and accounting for backscatter. The beam current of the instrument was measured frequently during the experiment to obtain accurate and continuous information.

By combining the calculation of beam broadening b , using the measured thicknesses of the Fe-Ni thin foil and the measurement of d , we have calculated the x-ray spatial resolution R according to Eq. (2). Calculations of MMF were made from measurements of I_A and I_B at specific analysis points on the Fe-25 wt% Ni thin foil. Figure 7 shows the variation of MMF and spatial resolution R in the Fe-Ni alloy. The data are given for three AEM instruments: a Philips 430T, a Philips 400T, and a VG HB-501.

Discussion

The definition of the x-ray spatial resolution R has been stated in several different forms. We prefer the definition given by Eq. (2) and illustrated in Fig. 1 because the spatial resolution can be shown explicitly on a diagram (Fig. 1) and can be considered in such a way that the value of R is not tied directly to an experiment, for example a step in concentration at a planar interface. The spatial resolution given in Eq. (2) is about 40% larger than that defined by Michael et al.² for a planar interface and represents a more conservative value of R .

As noted in previous studies¹³ and in Fig. 7, the chemical spatial resolution and the MMF are not independent of one another. For the data shown in Fig. 7, the electron probe current and the probe diameter (FWTM) for each instrument is held constant. What is varied is the thickness of the Fe-25wt% Ni specimens from 20 to 250 nm. The spatial resolution R approaches the beam diameter d in the thinnest specimens. The MMF decreases continuously as the thickness (and spatial resolution) increases.

The measured electron probe current in the Philips 430T and VG HB-501 are almost the same (0.26 nA vs 0.3 nA). Although operating voltages and EDS collection angles are quite different, the MMF of both instruments is also quite similar, 0.15 to 0.20 wt% Ni. As shown in Fig. 7, the variation in optimum x-ray spatial resolution for the two instruments, however, is quite dramatic.

In order to improve the spatial resolution in AEMs with thermionic sources, one should use a small d , which minimizes the probe size, and also use a thinner specimen to minimize b . Both of these improvements degrade the MMF because a smaller x-ray intensity P is generated. At minimum specimen thickness, the spatial resolution is optimized and controlled by the probe size d . The MMF is optimized with thicker samples that force the spatial resolution to be 2 to 5 times optimum (Fig. 7). For this case the MMF is limited by the factors that control the number of x-ray counts collected (e.g., probe current, detector collection efficiency, and collecting time). The usefulness of the FEG is clearly illustrated in Fig. 7,

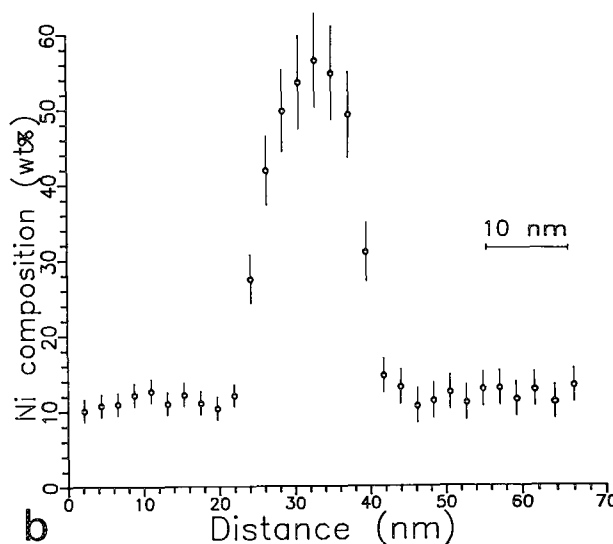


FIG. 8.--Ni composition profile for planar austenite (fcc) precipitate in plessite region of Grant meteorite: (a) STEM image, (b) Ni composition profile.

where spatial resolution R can be improved by almost an order of magnitude from ~ 15 to ~ 1.8 nm) without any loss of MMF.

Figure 8 shows a Ni composition profile across a planar 10nm-wide precipitate in the plessite region of the Grant iron meteorite.¹⁴ A spatial resolution of roughly 2.5-3.5 nm was obtained from a 20nm-thick sample analyzed in a Vacuum Generators HB-501 FEG AEM (electron probe diameter 1.8 nm FWTM). This spatial resolution is one of the best (smallest) measured in real specimens. Unfortunately, not enough data points were obtained to define accurately the error function composition curve and the value of L at FWTM (Fig. 3). The lack of an accurate L value leads to the uncertainty in the measured spatial resolution. Use of step sizes of the order of 0.2 L will lead to more accurate fitting of the error function composition variation through the measured data and hence a more accurate value of spatial resolution L . Such a small step size may not be practical due to specimen-borne contamination.

A modest amount of specimen drift was present during the measurement although a computer specimen drift correction program was used. This factor also led to an increase in the measured spatial resolution. Finally, the planar precipitate was probably not wide enough for the spatial resolution test, since a flat portion of the composition must be measured on both sides of the discontinuity in order to calculate the error function composition variation.

Prospects for improved spatial resolution and chemical sensitivity include combined use of intermediate voltages (300-400 kV) with the field-emission gun, optimization of x-ray intensity by use of higher collection angles and multiple x-ray detectors, longer counting times due to improved stage and electron beam stability, and the development of compact wavelength-dispersive spectrometers (WDS) to increase the peak-to-background of x-ray measurements.¹⁵ Some of these instrumental developments will soon be available. However, the employment of two or more EDS detectors will need to be carefully explored. Both detectors must see the same region of the sample. However, each detector will receive x rays absorbed along different specimen path lengths unless very special geometrical conditions are used.¹⁶

One can examine the effect of the instrumental improvements on the spatial resolution and MMF discussed above. Because of the higher brightness FEG, one will have available a 0.5nA beam current in a 1.0-1.5nm (FWTM) focused probe. With this small probe and high probe current, it should be possible to analyze thin foil specimens 10nm thick and obtain a spatial resolution of the order of the FWTM of the focused probe, 1.0 to 1.5 nm. With the use of a longer counting time (for example, 1200 s, due to increased stage and beam stability) and two EDS detectors at higher collection angles than available at present, it should be possible to obtain a MMF of 0.05 wt% with the improved spatial resolution discussed above. With the improved spatial resolution one should be able to measure x rays from about 1.5×10^{-19} g of material. With an MMF of 0.05 wt% for a given element, one could detect the presence of as little as 7.5×10^{-23} g of that element. In a specimen of an iron-base alloy, this spatial resolution and MMF allows the detection of as little as one atom of an element of interest in the iron-base alloy. The AEM would then be capable of single-atom analysis, a very exciting achievement. In specimens of average atomic number significantly lower than iron, the detection of single atoms of low atomic number in the analysis volume is more difficult.

Some concern must be raised about the effect of specimen preparation techniques on thin-specimen chemistry, electron-beam effects at high operating voltages, less than optimal vacuum at the specimen, and whether increased P/B can be achieved at higher voltage if the hole count becomes worse at such voltages.¹⁷ The hole count on current instruments has not prevented analysis, but for the very best values

of MMF it will have an effect since it will tend to reduce the peak-to-background ratio for an element in a local area. For example, the hole count tends to be a more serious problem as the atomic number of the specimen increases. Thus, it is likely that this effect of hole count on MMF will be worse for platinum in alumina than nickel in iron.¹⁷

Conclusions

This paper has shown detailed measurements of spatial resolution R and chemical sensitivity MMF from FEG and thermionic emission AEM instruments. For all these instruments there is a clear trade-off between R and MMF and an optimum value of R and MMF can be obtained. The FEG instrument is clearly superior, offering higher spatial resolution for comparable values of MMF. Future developments in instrumentation promise an improvement in both factors.

References

1. J. I. Goldstein et al., "Quantitative x-ray analysis in the electron microscope," *SEM/1977 I*, 315.
2. J. R. Michael et al., "The measurement and calculation of the x-ray spatial resolution obtained in the analytical electron microscope," *J. Microscopy* 60: 41, 1990.
3. S. J. B. Reed, "The single scattering model and spatial resolution in x-ray analysis of thin foils," *Ultramicroscopy* 147: 289, 1987.
4. J. R. Michael and D. B. Williams, "A consistent definition of probe size and spatial resolution in the analytical electron microscope," *J. Microscopy* 147: 289, 1987.
5. M. Troyan, "A survey of illuminating systems and electron guns in E.M.," *8th Eur. Cong. on Elect. Microsc.*, Budapest, 1984, I-11.
6. J. I. Goldstein et al., "Quantitative x-ray analysis," *Principles of Analytical Electron Microscopy*, New York: Plenum Press, 1986, 155.
7. T. O. Ziebold, "Precision and sensitivity in electron microprobe analysis," *Analytical Chemistry* 39: 858, 1967.
8. G. Cliff et al., "Monte Carlo deconvolution: The problems and pitfalls," *Analytical Electron Microscopy--1984*, 37.
9. J. R. Michael, "Probe size measurement in a field emission STEM," *Microbeam Analysis --1988*, 60.
10. T. Malis et al., "EELS log-ratio technique for specimen-thickness measurement in the TEM," *J. Elect. Mic. Techn.* 8: 193, 1988.
11. D. C. Joy et al., "Progress in the quantification of electron energy-loss spectra," *SEM/1979*, II, 817.
12. R. D. Leapman et al., "Mass thickness determination by electron energy-loss for quantitative x-ray microanalysis in biology," *J. Microscopy* 133: 239, 1983.
13. C. E. Lyman and J. R. Michael, "A sensitivity test for energy dispersive x-ray spectrometry in the analytical electron microscope," *Analytical Electron Microscopy--1987*, 231.

14. J. Zhang et al., "AEM investigation of the plessite structure of a IIIB iron meteorite --Grant," *Meteoritics* 23: 314, 1988.
15. J. I. Goldstein et al., "The wavelength dispersive spectrometer and its proposed use in the analytical electron microscope," *Ultramicroscopy* 28: 162, 1989.
16. R. W. Glitz et al., "Consideration of x-ray absorption for STEM x-ray analysis of Ni-Al foils," *Microbeam Analysis--1981*, 309.
17. C. E. Lyman et al., "The hole count test revisited: Effects of test specimen thickness," *Microbeam Analysis--1989*, 507.

APPLICATIONS OF HIGH-RESOLUTION X-RAY MAPPING

Anthony J. Garratt-Reed

It has been well established that x-ray imaging (mapping) of samples at high magnification in a field-emission analytical electron microscope is a viable technique when some form of correction is employed to compensate for the unavoidable image drift that occurs during the somewhat extended acquisition time of the images.^{1,2} It is the purpose of this paper to discuss x-ray mapping, and to present examples where high-resolution mapping provided data that were unique and essential to solving the problems under investigation.

Technique

The goal is to obtain a map containing the required information in the shortest possible time. As with all x-ray analysis problems, x-ray mapping depends on collecting a statistically significant set of data related to the sample. For most purposes, optimum results are obtained when the x-ray detector is operating at its maximum count rate, although one can, by compromising the count rate (and hence the precision of the chemical analysis), improve the spatial resolution of a system, a trade-off that applies to mapping exactly as to any other form of x-ray microanalysis.³

For the purpose of this discussion, we can differentiate two extreme conditions: (a) identification of areas of essentially pure elements, and (b) revelation of subtle changes in composition (including the presence or absence of an element at trace levels). In case (a), we can ignore the contribution of bremsstrahlung x-rays to the spectrum (for, in most cases, the bremsstrahlung in a window encompassing a peak is about 1% of the intensity of the peak), and conclude somewhat arbitrarily that the detection of three counts of an element indicates its presence, whereas the absence of the element leads to zero, or at most one count in a pixel. The x-ray system can count typically at 3000 cps, with about half this number (1500 cps) in a single elemental peak (for the K-line of a medium-atomic-weight element). Hence three counts are typically recorded in 2 ms, which may therefore be regarded as the shortest useful pixel dwell time for x-ray mapping.

At the other extreme, when attempting to map very low concentrations of an element, one must consider the peak-to-background ratio of the

x-ray spectrum. It has been shown that for K-lines of medium-atomic-weight materials, the peak-to-background ratio (for windows of equal and reasonable width) is about 100:1.³ Hence, when one looks for trace elements in the presence of a single dominant species, the bremsstrahlung count rate in the window for the trace element will be about 15 cps. If a 1% concentration of the trace element is present, it will also contribute 15 cps to the window, for a total of 30 cps. If we require each pixel to be significant without reference to its neighbors, the dwell time must be long enough to distinguish statistically between these cases. This condition is met with a 1.5 s acquisition, recording an average of 23 ± 10 counts from the bremsstrahlung or 45 ± 14 counts from the bremsstrahlung plus the trace element. Since a 128×128 pixel image contains 16 384 pixels, such an image would take about 25 000 s (or nearly 7 h) to acquire. In fact, in mapping, we almost always oversample (acquire overlapping pixels), and if we only require that any group of four pixels arranged in a square have a statistically significant number of counts, the required pixel dwell time becomes about 0.4 s and the image acquisition time becomes less than 2 h. We may regard that as a practical upper limit to the acquisition time (and, hence, 1% concentration as the minimum detectable by mapping), for, at least in microscopes with field-emission guns, the beam is not sufficiently stable for much longer acquisitions. If we can accept a minimum detectable concentration of 2%, the required dwell time becomes 0.1 s, and the image acquisition time is 0.5 h.

We can estimate the maximum useful magnification by considering the beam/specimen conditions that produce the maximum x-ray count rate.³ For a 100kV field-emission microscope, with a 0.078sr solid-angle x-ray detector, the optimum resolution (FWTM of the cylinder of x-ray production) is 3.8 nm. Since, by Shannon's theorem, we want to sample the data at twice the maximum frequency we wish to reproduce, the pixel spacing must be 1.9 nm and a line of 128 pixels covers 243 nm. If this line is reproduced on a CRT 8 cm wide (a typical value), the magnification will be about 330 000 \times . By a similar argument, the maximum useful magnification in a 300kV field-emission microscope with a detector of 0.3sr solid angle would be 1 000 000 \times . As was mentioned above, the maximum useful magnification would be increased if a higher-resolution, lower-sensitivity mode of analysis was being undertaken. Performing mapping at a magnification higher than the figures given above is statistically equivalent to mapping with a smaller number of

A. J. Garratt-Reed is at the MIT Center for Materials Science and Engineering, Cambridge, MA 02139. This work was sponsored in part by the National Science Foundation under Grant number DMR 87-19217. Certain samples were provided by K. Siebein, D. Bazyliniski, and K. Graham.

pixels, but with an increased dwell time; the result is to give an equivalent increase in the statistical significance of the data, and quite possibly a more pleasing picture. For example, a 128×128 map acquired at $600\ 000\times$ on the 100kV microscope at 0.1 s/pixel would contain the same information as a 64×64 map of the same area acquired at 0.4 s/pixel, but would appear to the eye as a "better" map. At the other extreme, one must also be wary of underscanning; that is, using a magnification so low that the beam samples only a very small fraction of the total area. An example will be given later.

Drift Correction

At the magnifications discussed above, and for the acquisition times mentioned, even very small drift rates (quite compatible with, for example, high-resolution imaging) can cause distortion of the images. Although providing adequate settling time for the sample and microscope to stabilize is critical, it is virtually impossible to eliminate drift altogether, and efforts have been made to apply computer-mediated compensating corrections.

The method employed by the commercial software provided by Link Systems is to identify a feature within the image, and, at predetermined intervals, to check the position of this feature. A correction based upon the drift so determined is then applied to the beam position. This method works well at moderately high magnifications, when suitable high-contrast features are discernible in the field of view. At very high magnifications, there is frequently no suitable image feature to use for a reference. To overcome this problem, Long and Glaisher have used a different method of drift correction.⁴ They acquired an image and maps without correction. They then used commercial image analysis software to transform the image to correct the distortion introduced by the drift, and performed the same transformation to correct the maps. This method depends on the drift being small and sensibly constant over the period of the acquisition, and also upon the image having suitable features to allow the transformation to be determined. They have applied it with good effect to the analysis of multilayer structures, for example.⁴

An interesting difficulty arises with the Link Systems software if the time between checks of the position is too short. It can happen that the drift detected is less than half a pixel, in which case no correction can be applied. However, the most recently acquired image of the reference point is saved as the new reference image, so on the next check, again less than half a pixel of drift is detected, and again no correction is applied. The remedy is to increase the time between checks of the reference point.

Examples

All experiments were performed in a VG Microscopes HB5 STEM. For most experiments, the

probe size was of the order of 2 nm, and the probe current was 0.2-0.4 nA. The x-ray detector was a Link Analytical LZ5 windowless energy-dispersive x-ray spectrometer with a resolution of 137 eV at 5.9 kV, subtending a solid angle of 0.078 sr at the sample. The x-ray spectra and images were acquired on a Link Analytical AN10000 analyzer running the Link Demon Plus operating system and version 5 of the Link program suite. Acquisition time varied according to the experiment, but was typically in the range 40-100 ms per pixel, for 128×128 pixel images.

Al-1%Si wire, 0.04-0.05 mm in diameter, is widely used in the electronics industry to form interconnections between IC chips and their headers. The microstructure of the wire consists of essentially pure Al with Si precipitates. The mechanical properties depend critically on the size and number density of the silicon particles, which in the best wire are a few tens of nanometers in diameter. Figure 1 shows a micrograph of such material. Some silicon particles are visible, but the structure of the foil potentially hides other precipitates. The Si image clearly shows all the silicon particles, and allows the number density to be estimated, as well as the size range.

For optimal performance, SiC whiskers used as reinforcement in composite materials require surface treatment. One such program involves coating the whisker with carbon, and then a further layer of SiC. The whiskers are of the order of micrometers in diameter and are not electron transparent. However, by examining the edge of the whisker, we hoped to study the coatings. Figure 2 shows a whisker as described above. Very little information can be deduced from the annular dark-field image. However, the maps of silicon and carbon show clearly that although the initial carbon layer is continuous and quite uniform, the overcoat of SiC is not a continuous film, but has separated into islands. The same conclusion could possibly have been reached by probing of the sample, but the map has an immediate and unambiguous visual impact. Incidentally, though not relevant to the investigation, the oxygen image clearly reveals the native oxide layer on the original SiC whisker, demonstrating the power of mapping even for thin layers of light elements.

Magnetotactic bacteria typically synthesize Fe_3O_4 .⁵ Some such organisms, however, which inhabit high-sulfur low-oxygen environments, synthesize instead iron sulfides. Figure 3 shows two magnetosomes from such an organism, with the Fe, S, and O maps. The particles appear larger in the Fe map than in the S map. From the O map it is clear that the particles have a thin coating of oxide. The significance of this observation is at present unknown, but it most certainly would not have been made without the map, since it would not have occurred to the operator to probe the edge of the particles.

Other applications of x-ray mapping in this

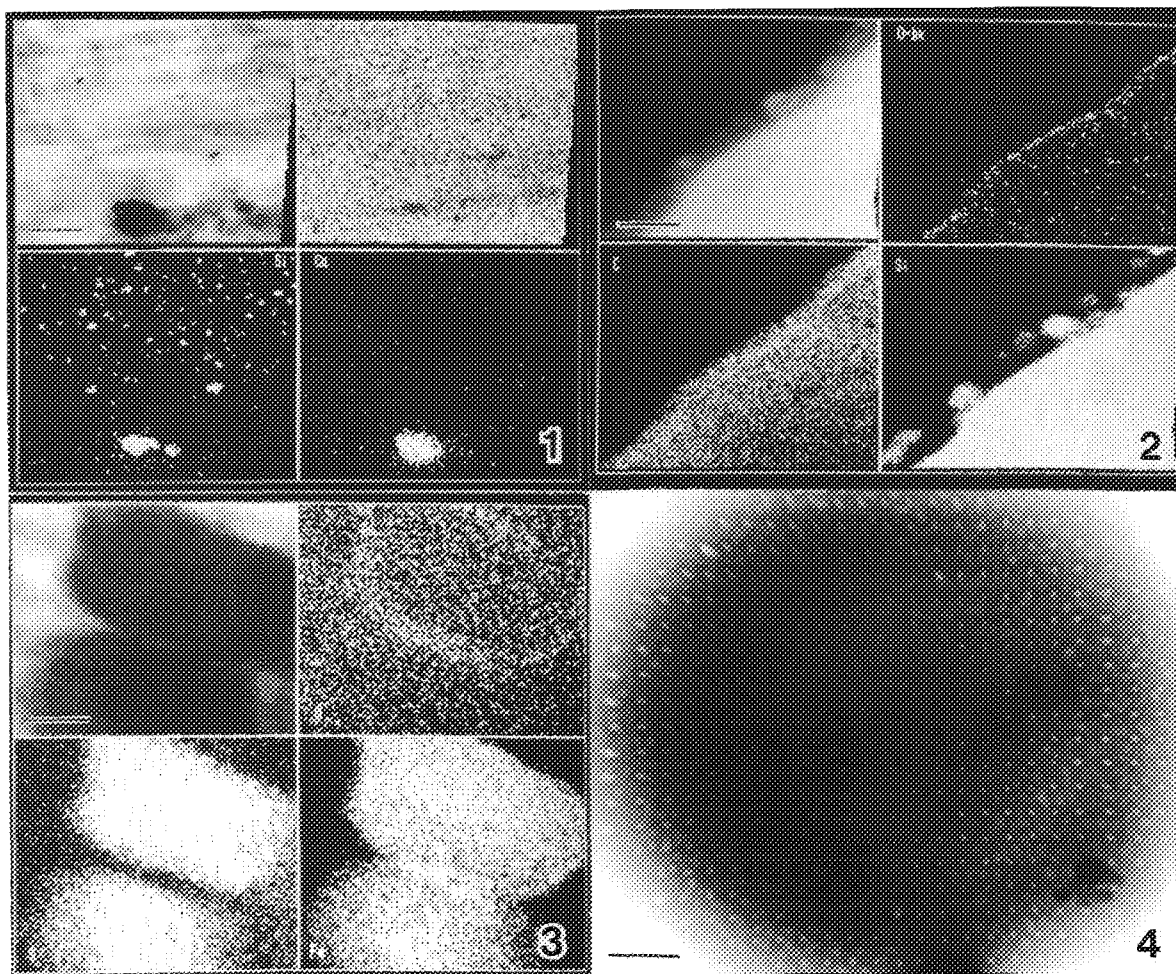


FIG. 1.--Image and Al, Si, and Cu maps of section of Al-1%Si wire. Bar = 1 μ m.

FIG. 2.--ADF image, and C, O, and Si maps of coated SiC whisker. Bar = 50 nm.

FIG. 3.--Image, with Fe, S, and O maps of two magnetosomes in magnetotactic bacterium. Bar = 25 nm.

FIG. 4.--Image of deposits from flue gas, showing positions of beam during earlier map acquisition. Bar = 100 nm.

laboratory have included studies of segregation in steels, metal distribution in metal-loaded polymers, elemental distributions in fly-ash, segregation in oxide scales, etc., and it has proved to be an invaluable powerful tool for the researcher.

A final example illustrates the problem of undersampling an area. The sample is a deposit from flue gas, which is highly beam sensitive. It had been mapped at low magnification, and the high-magnification image (Fig. 4) clearly shows the points at which the beam was positioned for each pixel acquisition. Some small particles in the sample have been entirely missed. The simplest way to overcome this deficiency is to defocus the probe, but a more satisfying method is to acquire the map with a larger number of pixels, and a correspondingly shorter dwell time.

References

1. S. H. Vale, *EMAG'87: Analytical Electron Microscopy*, 1987, 15.
2. C. E. Lyman et al., *Proc. 47th Ann. Meeting EMSA* 1989, 204.
3. A. J. Garratt-Reed, *SEM/85* 1, 21.
4. N. J. Long and R. W. Glaisher, *EMAG-Micro* 89 1, 277.
5. R. P. Blakemore and R. B. Frankel, *Scientific American* 245(6): 58, 1981.

APPLICATION OF PARALLEL COMPUTING TO THE MONTE CARLO SIMULATION OF ELECTRON SCATTERING IN SOLIDS: A RAPID METHOD FOR PROFILE DECONVOLUTION

A. D. Romig Jr., S. J. Plimpton, J. R. Michael, R. L. Myklebust, and D. E. Newbury

X-ray microanalysis by analytical electron microscopy (AEM) has proved to be a powerful tool for characterizing the spatial distribution of solute elements in materials. True compositional variations over spatial scales smaller than the actual resolution for microanalysis can be determined if the measured composition profile is deconvoluted. Explicit deconvolutions of such data, via conventional techniques such as Fourier transforms, are not possible owing to statistical noise in AEM microanalytical data. Hence, the method of choice is to accomplish the *deconvolution via iterative convolutions*.¹ In this method, a function describing the assumed true composition profile, calculated by physically permissible thermodynamic and kinetic modeling, is convoluted with the x-ray generation function and the result is compared with the measured composition profile. If the measured and calculated profiles agree within experimental error, it is assumed that the true compositional profile has been determined. If the measured and calculated composition profiles are in disagreement, the assumptions in the physical model are adjusted and the convolution process is repeated. To employ this procedure it is necessary to calculate the x-ray generation function explicitly. Although a variety of procedures are available for calculating this function,²⁻⁴ the most accurate procedure is to use Monte Carlo modeling of electron scattering.^{5,6}

Research Objectives

Monte Carlo simulations of electron scattering, and the calculation of the x-ray generation volume, in thin film and bulk specimens have been performed for many years. There are many uses of Monte Carlo simulations in electron microscopy and x-ray microanalysis; one very important application is to use it as a tool to investigate x-ray spatial resolution. The ideal application of the Monte Carlo simulation (once it is demonstrated that a particu-

lar Monte Carlo code actually models all aspects of electron scattering) is to explore a parameter space larger than one can conveniently explore experimentally. For example, if a Monte Carlo simulation accurately describes the spatial resolution for x-ray microanalysis in a thin film of some thickness, it is easier and more efficient to examine spatial resolution in specimens of other thicknesses by Monte Carlo simulation than by additional experiments. However, the widespread application of Monte Carlo modeling has never been realized in the microanalysis community for such problems because of the computation intensive nature of the Monte Carlo algorithm (e.g., many hours of computer time were required to run one simulation which might improve one's ability to interpret data; the time required was so large that it was not possible to use the calculations to improve experimental measurements in a time effective way). However, the development of parallel computation architectures has vastly improved the efficiency of Monte Carlo simulations. It was therefore the objective of this work to investigate the utility of the parallel-computation methodology for Monte Carlo simulations of electron scattering in solids as it applies to x-ray microanalysis in bulk and thin film specimens. To attain the objective, the NIST (National Institutes of Standards and Technology) Monte Carlo algorithm^{5,6} was modified to utilize a parallel architecture. The new parallel code was tested on a variety of microanalytical problems, in bulk and thin film specimens, to demonstrate its validity. An important result of the parallel Monte Carlo simulations was the significant reduction in computation time compared with Monte Carlo simulations run on a variety of traditional computers (from workstation to supercomputer). It was clearly shown that the time advantage in solving such problems with parallel computation methods is so significant that Monte Carlo modeling becomes a useful real-time tool for microanalysis. Specifically, it was demonstrated that parallel Monte Carlo calculations are a very rapid method for the deconvolution of composition profiles measured by AEM.

Monte Carlo Modeling

The basic principle of a Monte Carlo electron trajectory simulation is to calculate the path of each electron in a stepwise manner, accounting for both elastic and inelastic scattering.⁶ The distance between scattering events, the scattering angles, and the rate of energy loss with distance are calculated from physical models. Random numbers are used to

A. D. Romig Jr., S. J. Plimpton, and J. R. Michael are at the Sandia National Laboratories, Albuquerque, NM 87185; R. L. Myklebust and D. E. Newbury are at the National Institute of Standards and Technology, Gaithersburg, MD 20899. A portion of this work was performed at Sandia National Laboratories and supported by DOE contract DE-AC04-76DP00789. The computational methods used here were developed with the support of the Applied Mathematical Science Program, DOE Office of Energy Research. The National Institute of Standards and Technology is a U.S. Department of Commerce facility.

physical models. Random numbers are used to select the scattering angles so that, for a large number of electron trajectories, the resulting probability histogram closely resembles the actual angular distribution for single scattering events. To obtain physically meaningful results, a large number of electron trajectory simulations are required (usually of the order of 10^5). For electrons scattering in a solid, elastic scattering generally results in trajectory changes of less than 5° , but scattering through angles as large as 180° is possible. Elastic scattering events do not alter the energy of the electron. Inelastic scattering decreases the energy of the electron, but the scattering angle is very small, typically less than 0.1° . In this Monte Carlo model, the energy loss is described by the Bethe continuous energy loss function and any slight change in electron trajectory during an inelastic scattering event is ignored. For more detail, see the review paper in this volume.⁷

Parallel Computation of Monte Carlo Scattering

Monte Carlo simulations are obviously very computation intensive. Even in a thin film, a very large number of calculations is required to simulate the electron beam/specimen interaction for a single analysis point (i.e., 10^5 trajectories incident at a single point). For profile deconvolutions, as many as 100 incident points may be required to calculate the composition profiles and up to 10 iterations using various physical models may be required. Hence, up to 10^8 trajectories may be required to determine a single composition profile. The computation-intensive nature of Monte Carlo simulations and the fact that the scattering of each primary electron is independent of all other primary electrons suggests that such problems are ideally suited to computer simulations by machines with a parallel architecture.

The NCUBE 2 parallel computer used in this work has 1024 processors; hence 1024 trajectories (each with a unique starting random number) can be simulated simultaneously. The NCUBE 2 has a computing architecture well suited for this approach; it is a MIMD (multiple instruction-multiple data) machine where each processor (or node) executes a copy of the simulation program independently on its own data set. Messages can be passed between nodes at the end of the simulation to sum the results. Each of the 1024 nodes on the NCUBE 2 at Sandia has a ~ 1.0 Mflop CPU with ~ 1 Mbyte of memory. The nodes are interconnected in a hypercube topology.

Only two basic changes were necessary in adapting the original serial version of the Monte Carlo simulation to a parallel code. The first was a restructuring of the simulation so that the basic algorithm became the following: (1) input the simulation parameters for a run of N total trajectories and send a copy of the parameters to all P nodes, (2) simulate N/P trajectories on each node, (3) combine the binned simulation data by sending messages between nodes, and (4) output the results. Step 2 requires nearly all the computation time;

step 3 can be performed very quickly owing to the high connectivity of the hypercube architecture. This restructuring requires no modification of the basic physics routines by which the electron trajectories are calculated.

The second change was to alter the random-number generation scheme. In the typical serial Monte Carlo program, an initial random-number seed is supplied by the user. A sequence of random numbers is generated from the seed and used for successive trajectories; i.e., the first electron uses the first few random numbers, the next trajectory uses a few more, etc. The drawback is that one does not know a priori with which random number the n th trajectory will start. Hence, a parallel simulation cannot duplicate the serial results. This fact is important for both debugging/developing the simulation and because, in practice, programs can be run on the NCUBE 2 on any available power-of-two subset of nodes (up to 1024 maximum).

To overcome this drawback, a pseudo-random number tree scheme was implemented as discussed in Fox⁸ and detailed by Frederickson.⁹ It insures identical results independent of the number of processors on which the simulation runs. Each node is assigned one or more sets of $N/1024$ trajectories to simulate (e.g., for a run of 10 000 trajectories on 64 nodes, each node simulates 16 sets of 9 or 10 trajectories each). When each set is begun, a new random-number seed is used to restart the primary random-number generator. The new seeds come from a list of 1024 seeds each node calculates at the beginning of the simulation run from a second random-number generator. The second generator is started with the initial seed specified by the user; hence, one random-number seed is still sufficient to create all the trajectories. Since each node uses the same list of 1024 seeds and uses the appropriate seeds from the list for its own set(s) of $N/1024$ trajectories, the same trajectories are simulated regardless of which processors they run on. The accuracy of this method depends on the second generator producing seeds that are far apart in the sequence of random numbers created by the primary generator. As pointed out by Percus,¹⁰ this condition is not guaranteed for all choices of generators, but in practice satisfactory results were achieved; no statistical biases were seen in the Monte Carlo results. Evidence that the random-number generation scheme, or in fact the entire processes of parallelizing the code, did not affect the results of the Monte Carlo simulation is shown in Fig. 1. Here, backscatter electron coefficients in bulk targets at 20 keV vs atomic number are shown. The open circles represent the parallel computation results and the theoretical curve is a parametric fit to experimental data.¹¹ The agreement is excellent.

The timing results from the simulation on all 1024 nodes of the NCUBE 2 were compared with those from three conventional computers, a VAX 785, a DEC 3100 workstation, and one processor of a CRAY-XMP 4/16. The algorithm is

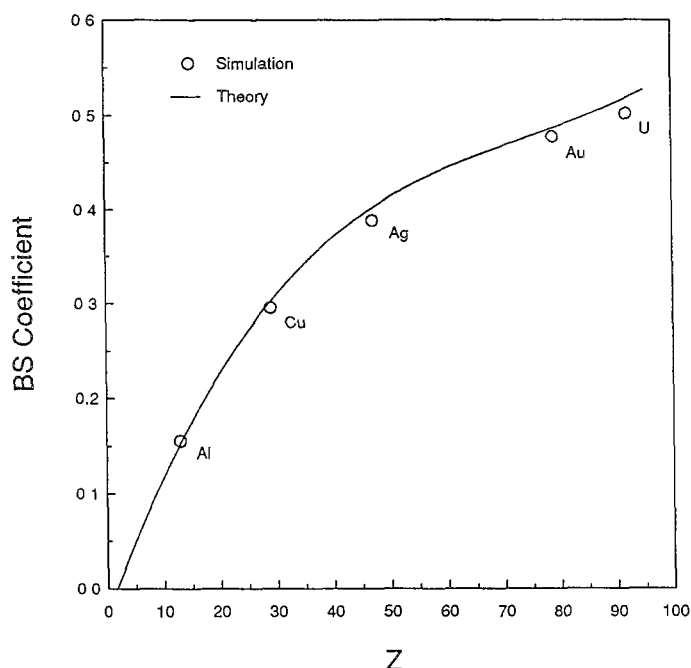


FIG. 1.--Comparison of backscatter electron coefficients for bulk targets at 20 keV, illustrating validity of new parallel simulation. Theory line is parametric fit to experimental data.¹¹

written in standard Fortran 77; all the codes were compiled by use of the best optimization level available on that machine. For a run of 100 000 electrons (20 keV) into bulk Cu, the timings (in seconds) were as follows: NCUBE = 32.1, VAX = 64 650, DEC = 23 900, CRAY = 4699. Thus, the NCUBE is 146 times faster than the CRAY for bulk simulations. The NCUBE was found to be 85% efficient for bulk simulations, meaning 1024 nodes are 870 times faster (0.85×1024) than a single node. The extra 15% is lost in the waiting that occurs because some nodes finish their trajectories a little sooner than others, and in the part of the simulation that is not performed in parallel (e.g., the input/output).

For thin film runs of 100 000 electrons into a Cr/Fe/Ni film (discussed in this paper), the timings (in seconds) were as follows: NCUBE = 4.81, VAX = 1350, DEC = 425, CRAY = 56.73. Here the NCUBE is 11.8 times faster than the CRAY. The difference between this and the bulk case is that in thin-film simulations there are a few high-angle scattering events that leave a high-energy secondary electron traversing the film parallel to the film surface. This event takes a much longer time to simulate than a typical trajectory where the primary electron passes quickly through the film. These anomalously long trajectories skew the computational balance so that 95% of the processors end up having to wait for the other 5% to finish. This skewing cut the parallel computing efficiency to 13% in this instance. However, some of this speed loss is recovered in practice, since (as in this paper), a thin-film simula-

tion is usually run on a series of spaced beam impact points (e.g., across an interface). The simulation assigns a subset of processors to the trajectories for each point and the whole set of impact points can then be run in parallel. This procedure has the effect of increasing the efficiency (and thus the overall speed for the simulation), since each processor simulates more trajectories and the run times of different processors became more uniformly balanced. For example, the same thin-film simulation on 16 incident points (100 000 electrons incident at each point) runs in 20.0 s on the NCUBE, which is 45 times faster than it runs on the CRAY.

Monte Carlo trajectory simulations such as this one can be vectorized for the CRAY. However, this step requires significant changes to the basic algorithm and data structures so that vectors of particles are followed simultaneously. Work on codes similar to this one have shown speed-ups on the order of $8\times$ can be achieved by such efforts.¹²

Simulation of Monolayer Impurity at a Grain Boundary.

This simulation considered the calculation of a composition profile in a thin film target. The target was a 25nm-thick film of Al, with a monolayer thick slab of Cu was oriented parallel to the incident electron beam. The results of two simulations are shown in Fig. 2. The first simulation is for a 1nm probe at 100 keV (typical of a modern cold field-emission analytical electron microscope). The apparent composition at the boundary is approximately 62 wt% Cu. Apparent compositions of less than approximately 0.1 wt% would be below the background and not measurable. Hence, at distances exceeding 3 nm from the boundary the Cu signal has essentially decreased to zero. The second simulation is for a 20nm probe at 200 keV, typical of a modern thermionic source (LaB₆) analytical electron microscope. The apparent composition at the boundary is approximately 4.9 wt% Cu. Apparent compositions of less than approximately 0.1 wt% would be below the background and not measurable. Hence, at distances exceeding 30 nm from the boundary the Cu signal has essentially decreased to zero. An interesting conclusion to be drawn from these simulations is the order in magnitude improvement in spatial resolution for microanalysis in field-emission electron microscopes even at 100 keV.

Comparison of Monte Carlo Simulation with Experimental Results

In order to verify the accuracy of the Monte Carlo electron trajectory simulation running on the parallel processor, the calculated results were compared with experimental measurements. Previously reported experimental data^{12, 14} are ideal for this comparison since the specimen thicknesses were known, the probe size had been accurately measured¹⁵ and the specimen was well characterized. A specimen of 40 wt% Ni-30 wt%

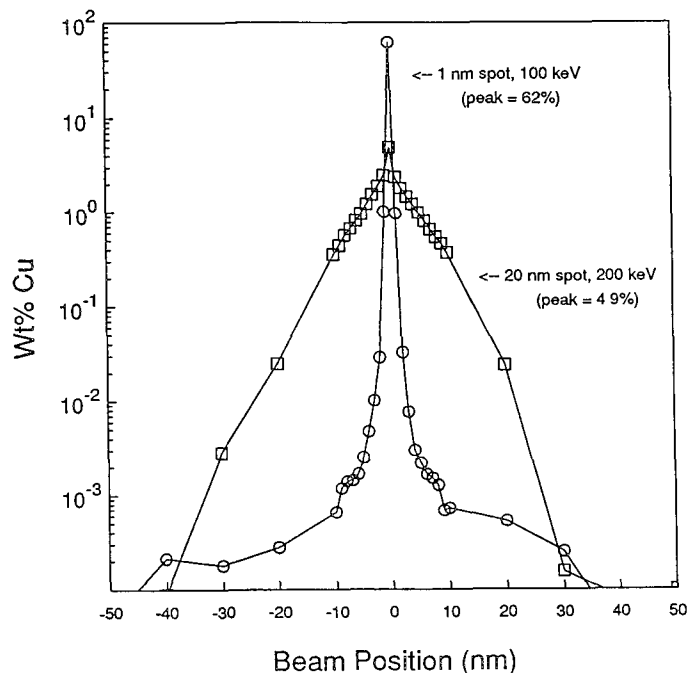


FIG. 2.--Calculation of spatial distribution of x rays from Al specimen 25 nm thick. Specimen contains one-monolayer (0.3nm-thick) Cu film oriented parallel to incident primary electron beam. Each point represents 10^5 electron trajectories. For 1nm probe at 100 keV, "measured" boundary composition is approximately 62 wt% Cu; for 20nm beam at 200 keV, approximately 4.9 wt% Cu. Distance at which boundary film can no longer be detected is 3 nm for 1nm probe, 30 nm for 20nm probe.

Cr-Fe, which had been heat treated to produce α precipitates (80-90wt% Cr) in a γ matrix (25-29 wt% Cr) was used to generate the experimental data.¹³ The α/γ interface was ideal for measuring concentration profiles, since these interfaces are very straight and atomically discrete.

The 1.0nm (full-width at half-maximum) electron probe was stepped across an α/γ interface while the x-ray spectrum obtained at each point was recorded. The specimen thicknesses were also measured for each profile. Four different specimen thicknesses were analyzed. As has been previously shown, the width of the concentration profiles is a measure of the amount of beam broadening that occurs as the electron probe traverses the specimen.¹⁶ If the composition change across the interface is normalized to 100%, the distance between the 12% and the 88% points on the profile represents the diameter that contains 50% of the incident electrons. The diameter that contains 90% of the incident electrons may be obtained by multiplication of the 50% diameter by 1.82. The 90% diameter is the most commonly used definition of x-ray spatial resolution.

Figure 3 shows an example of the actual experimental data.¹³ In this case the specimen was 112 nm thick. The analytical electron microscope was operated at 100 kV and the probe

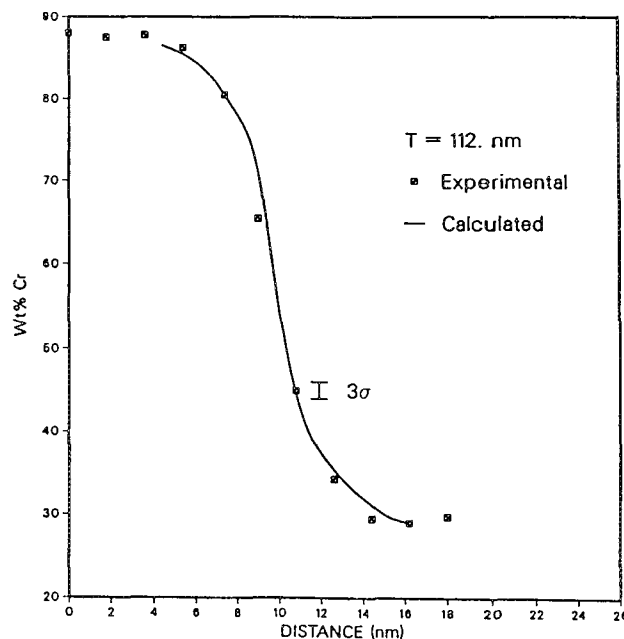


FIG. 3.--Experimental data for thin film in which precipitate phase containing 89.1 wt% Cr is in contact with matrix containing 26.2 wt% Cr.¹³ Film is 112 nm thick; 100keV electron probe size was 1 nm. A profile was measured across the phase interface. Experimental data are compared with Monte Carlo simulation.

size was 1 nm. The calculated curve was generated by Monte Carlo calculation. The excellent fit between the experimental data and Monte Carlo simulation is apparent.

The Monte Carlo simulation was used to model the same specimen thicknesses (55, 95, 112, and 150 nm) as in the experimental results with a 1.0 nm FWHM electron probe diameter. The 90% spatial resolutions were calculated in the same manner as those for the experimental profiles. The Monte Carlo simulations for the four specimen thicknesses are shown in Fig. 4. Table 1 compares the spatial resolutions determined by experimental measurements¹³ and the Monte Carlo simulation for the same four specimen thicknesses. All four curves calculated by the Monte Carlo simulation agree well with the measured data. A comparison of the measured profile width relative to the width determined from the Monte Carlo simulations is good. The 90% widths as determined by the Monte Carlo simulations are 2.7, 2.9, 6.7, and 10.3 nm for the four thicknesses. The measured values are 5.2, 6.6, 9.0, and 12.0 nm.

In all cases the Monte Carlo results underestimated the experimental measurements. This result is expected since the Monte Carlo calculations are not affected by experimental difficulties, which include the exact orientation of the interface parallel to the electron beam, specimen drift, and errors in probe placement. These results show that the Monte Carlo electron trajectory simulation can accurately model the electron trajectories in specimens of medium atomic number.

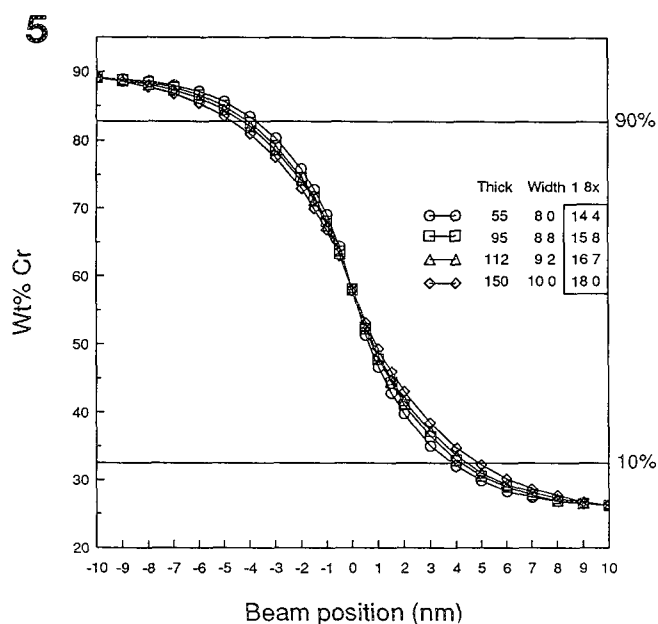
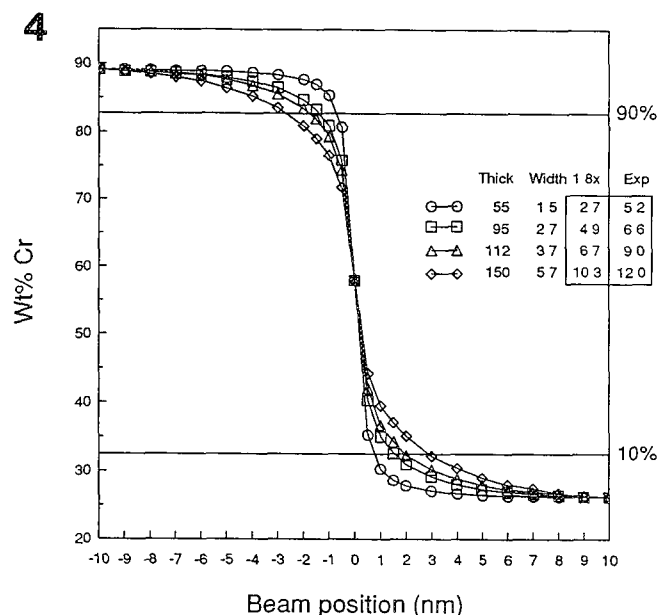


FIG. 4.--Comparison of composition profiles as a function of thickness in specimens as described in Fig. 3; 100keV electron probe size was 1 nm. Four specimen thickness (55, 95, 112, and 150 nm) are shown. 1.8 column shows measured spread of profile (for 90% of the electrons) as determined by the Monte Carlo simulation. Exp column are results of the experimental measurement.¹² Monte Carlo simulations consistently underestimate experimental data. All units in data table insert are in nm. FIG. 5.--Repeat of the numerical Monte Carlo simulations described in Fig. 4. In this case, 10nm electron probe is used. Comparison of results shown in Figs. 4 and 5 illustrate paramount importance of probe size in high-spatial-resolution x-ray microanalysis. All units in data table insert are in nm.

TABLE 1.--Comparison of x-ray spatial resolution at α/γ interface in an Fe-Ni-Cr alloy. The 90% x-ray spatial resolutions determined experimentally and by Monte Carlo calculation are compared for thin films of four different thicknesses.

Specimen Thickness (nm)	MC(nm)	Experimental (nm) ¹³
55.	3.6	5.2
95.	6.7	6.6
120.	7.2	9.0
150.	10.8	12.0

As a further numerical experiment, the same simulations were repeated with a 10nm probe, as shown in Fig. 5. In this case the effect of thickness on resolution is less dramatic. It clearly illustrates that probe size is the most important parameter for high resolution x-ray microanalysis in the analytical electron microscope.

Conclusions

The simulation of electron scattering in solids by Monte Carlo techniques is well suited to parallel computation. Significant gains in computation time are realized and make explicit calculation of convoluted composition profiles possible. Computation time is sufficiently shortened to enable such simulations to be used in a real-time experimental environment. Because such simulations break naturally into independent computational pieces that require little intercommunication, they are ideal candidates for fast parallel implementation on a MIMD machine such as the NCUBE 2. Similar performance gains should be possible for other kinds of Monte Carlo transport simulations (ion or photon), as well as codes modeling other electron-solid interactions, such as Auger electron production. Even on smaller and cheaper parallel machines, run times for such codes can be competitive with traditional supercomputers like the CRAY.

References

1. D. B. Williams and A. D. Romig Jr., "Studies of interfacial segregation in the analytical electron microscope: A brief review," *Ultramicroscopy* 30: 38, 1989.
2. J. I. Goldstein, J. L. Costley, G. W. Lorimer, and S. J. B. Reed, "Quantitative x-ray analysis in the electron microscope," *SEM/1977* I, 315.
3. A. D. Romig Jr. and M. J. Cieslak, "Solute segregation to phase interfaces and grain boundaries: Studies by analytical electron microscopy and profile deconvolution," *Analytical Electron Microscopy--1987*, 25.
4. P. Doig, D. Lonsdale, and P. E. J. Flewitt, "The spatial resolution of x-ray microanalysis in the scanning transmission electron microscope," *Phil. Mag.* 41A: 759, 1980.
5. D. E. Newbury, "Electron beam-specimen interactions in the analytical electron micro-

- scope," in D. C. Joy, A. D. Romig Jr., and J. I. Goldstein, Eds., *Profiles of Analytical Electron Microscopy*, New York: Plenum Press, 1986, 1.
6. D. E. Newbury and R. L. Myklebust, "Monte Carlo electron trajectory simulation of beam spreading in thin foil targets, *Ultramicroscopy* 3: 391, 1979.
7. D. E. Newbury and R. L. Myklebust, "Monte Carlo electron trajectory simulation of x-ray emission from films supported on substrates," *Microbeam Analysis--1990* (this volume).
8. G. Fox et al., *Solving Problems on Concurrent Processors*, New Jersey: Prentice-Hall, 1988, 210.
9. P. Fredrickson, R. Hiromoto and J. Larson, "A parallel Monte Carlo transport algorithm using a pseudo-random tree to guarantee reproducibility," *Parallel Computing* 4: 281, 1987.
10. P. Percus and M. Kalos, "Random number generators for MIMD parallel processors," *J. Parallel and Distributed Computing* 6: 477, 1989.
11. J. I. Goldstein et al., *Practical Scanning Electron Microscopy and Microanalysis*, New York: Plenum Press, 1981, 76.
12. K. Miura, "EGS4V: Vectorization of the Monte Carlo cascade shower simulation code EGS4," *Comp. Phys. Comm.* 45: 127, 1987.
13. J. R. Michael, D. B. Williams, C. F. Klien, and R. Ayer, "The measurement and calculation of the x-ray spatial resolution in the analytical electron microscope," *J. Microscopy* 160: 41, 1990.
14. J. R. Michael, "The effect of specimen thickness and electron probe characteristics on the x-ray spatial resolution in the analytical electron microscope," *Microbeam Analysis--1989*, 496.
15. J. R. Michael, "Probe size measurement in a field-emission STEM," *Microbeam Analysis--1988*, 60.
16. J. R. Michael and D. B. Williams, "A consistent definition of probe size and spatial resolution in the analytical electron microscope," *J. Microscopy* 147: 289, 1987.

COMPARISON OF EXPERIMENTAL AND THEORETICAL XEDS CROSS SECTIONS AND k-FACTORS AS A FUNCTION OF ACCELERATING VOLTAGE

N. J. Zaluzec

For nearly fifteen years k-factor measurements have been made by varying the composition of the standards at fixed accelerating voltage and reporting the change in the experimental k-factor with atomic number. An example is shown in Fig. 1(a), which compares recent data of Sheridan¹ with various k-factor calculations using cross section parameterizations by Mott and Massey (MM),² Green and Cosslett (GC),³ Brown (B),⁴ Powell (P),⁵ Schreiber and Wims (SW),⁶ and Zaluzec (Z).⁷ From these data a "best model" of the ionization cross section is frequently proposed for use in quantitative x-ray analysis in the AEM; however, it is valid only at that fixed voltage. It is usually difficult to judge the validity of the selection of cross section using this type of plot; difference plots (i.e., [Theory - Expt]/Expt) as shown in Fig. 1(b) are more useful for this purpose. These difference plots illustrate that the k-factor at a fixed voltage is not particularly sensitive for determination of the correct ionization cross-section parameterization owing to normalization effects inherent in its definition. In fact, calculations show that the relative errors between cross-section models as shown in the difference plot are of the same order of magnitude as those one would calculate, because of inaccuracy in the thickness of the various Si(Li) detector parameters (i.e., Be, Au, Si dead, Si active windows). For example, a variation in the Au thickness from 100 to 300 Å can shift the calculated k-factor difference curves by nearly 5%, which in some cases the difference between models at a fixed accelerating voltage (Fig. 1b). On the other hand few if any studies to date have sought to determine the systematic variation in the k-factor with accelerating voltage. In this paper experimental measurements of the absolute intensity variation of elemental standards are used to illustrate the differences cross-section models, which are subsequently compared with experimental variations in the k-factor with accelerating voltage. With the advent of medium-voltage analytical microscopes routinely available to the microscopy community, it becomes essential to understand how the k-factor varies with accelerating voltage in order that errors in quantitative analysis can be avoided, should experimental or theoretical k-factors from low-voltage instruments be applied to the medium-

N. J. Zaluzec is at the Electron Microscopy Center for Materials Research, Materials Science Division, Argonne National Laboratory, Argonne, IL 60439. This research was supported by DOE under contract BES MS W-31-109-Eng-38 at Argonne National Laboratory.

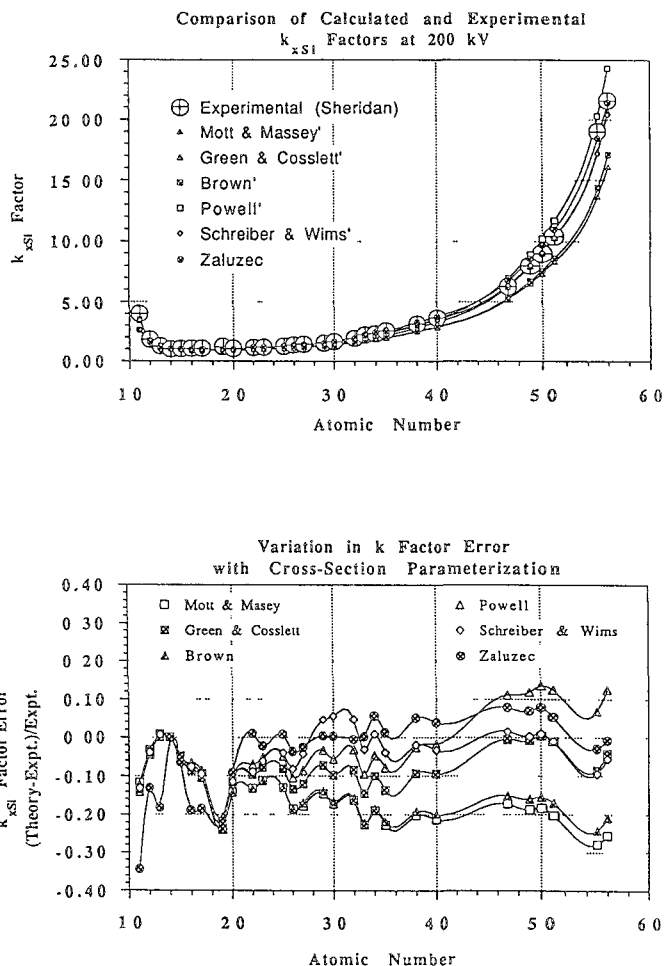


FIG. 1.--(a) Experimentally determined k-factors calculated from various cross-section models. (b) Difference plot [(Theory - Expt)/Expt] of k-factor showing relative errors.

voltage regime.

X-ray intensity measurements for five thicknesses of evaporated polycrystalline aluminum films (227, 415, 656, 1136, and 2083 ± 30 Å) were made from 50 to 300 kV in a Philips CM30T electron microscope equipped with a Be-Window Si(Li) detector interfaced to an EDAX 9900 energy-dispersive analysis system. Multiple measurements were taken of each of the specimens, which were mounted in a Gatan beryllium double-tilt liquid-nitrogen-cooled sample stage for the study. Hole count corrections were made to all spectra and were particularly important above 100 kV. Shown in Fig. 2(a) is the experimental Al K shell x-ray emission/nA as a function of thickness and replotted as:

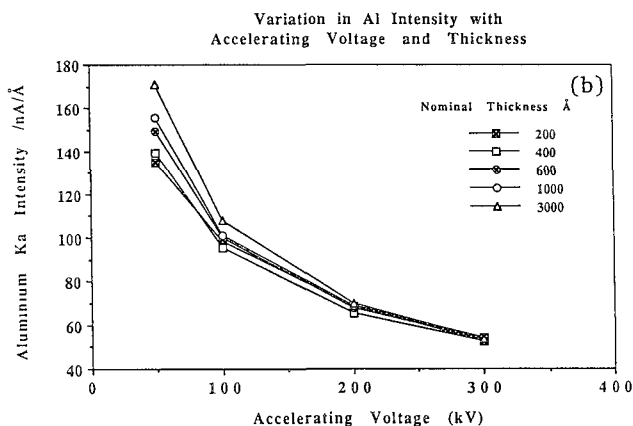
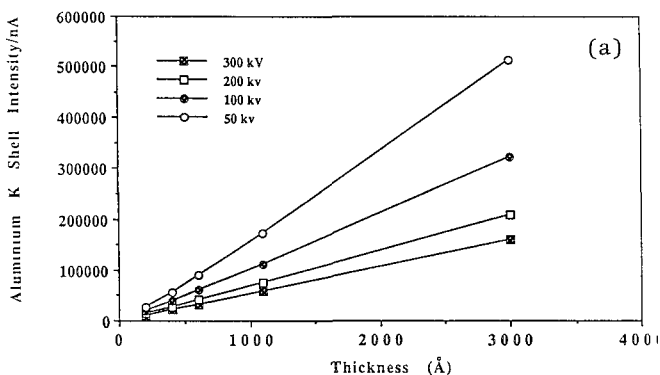


FIG. 2.--(a) Al K intensity/nA as a function of thickness for various voltages. (b) Al K intensity/(nA/Å) as a function of accelerating voltage for various specimen thicknesses.

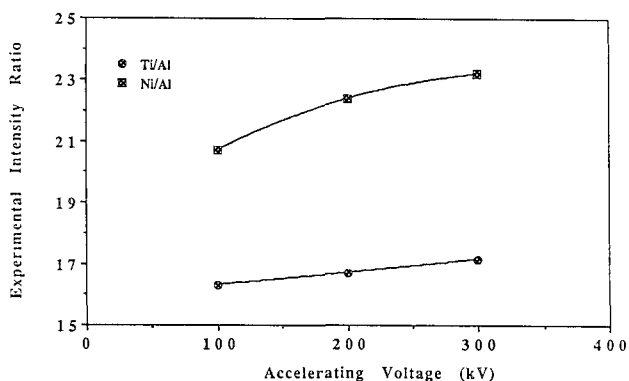


FIG. 4.--Experimental variation in Ni/Al and Ti/Al K shell x-ray intensity ratios as a function of accelerating voltage.

voltages, and in Fig. 2(b) the data are divided by the film thickness and replotted as a function of voltage to demonstrate multiple scattering effects on the x-ray intensity. Here we can see that as the thickness of the specimen increases above about 600 Å, the effects of multiple scattering give enhanced intensity over that of the thinner films, and hence cannot be directly used for cross-section comparison. In Fig. 3(a), the Al intensity/nA (which is now a direct measure of the ionization cross section) for the films 200 and 400 Å thick is normalized

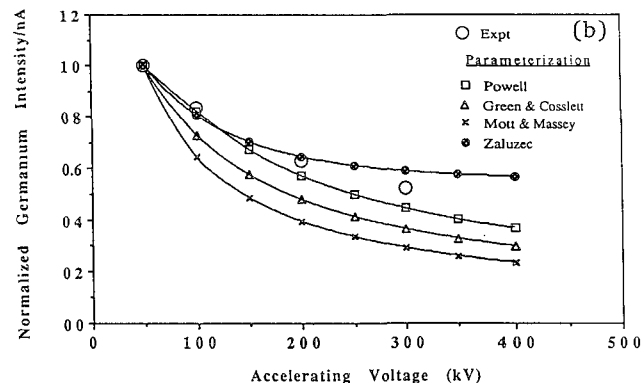
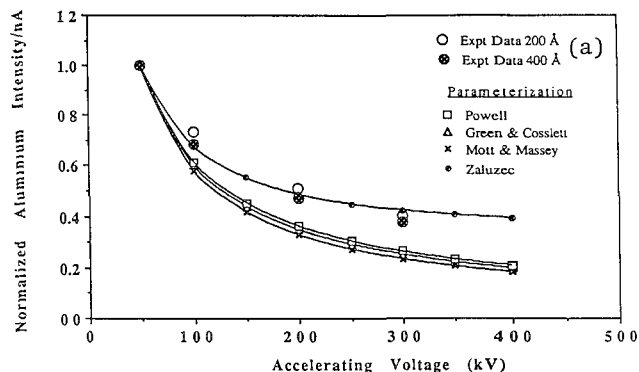


FIG. 3.--(a) Comparison of normalized Al intensity/nA with various cross-section parameterizations. (b) Comparison of normalized Ge intensity/nA with various cross-section parameterizations.

at 50 kV and compared to various theoretical calculations of the ionization cross section. Generally, the nonrelativistic models (MM, GC, P) severely underestimate the variation in cross section with voltage; the relativistic parameterization (Z) seems to follow the experimental data most closely. Figure 3(b) shows similar data and results from a thick (~600 Å) germanium evaporated film; again, as in the Al case, the nonrelativistic models underestimate the cross section. Here multiple scattering will, as in the case of Al, depress the normalized data at the higher voltage and hence the relativistic parameterization still appears to predict the voltage variation more closely.

In addition to the preceding evaporated elemental thin-film measurements, electropolished specimens of NiAl and TiAl were studied to determine the effect of accelerating voltage on the k-factor. Figure 4 shows the experimental variation of the Ni K α /Al K and Ti K α /Al K intensity ratios as a function of accelerating voltage from 100 to 300 kV. From Eq. (1), we can see that this ratio is a direct measure of the dependence of the k-factor and the ionization cross section σ with voltage, as σ is the only term that varies with electron energy:

$$\frac{I_A}{I_B} = \frac{\kappa_A \epsilon_A C_A}{\kappa_B \epsilon_B C_B} = \frac{1}{k_{AB}} \frac{C_A}{C_B} \quad (1)$$

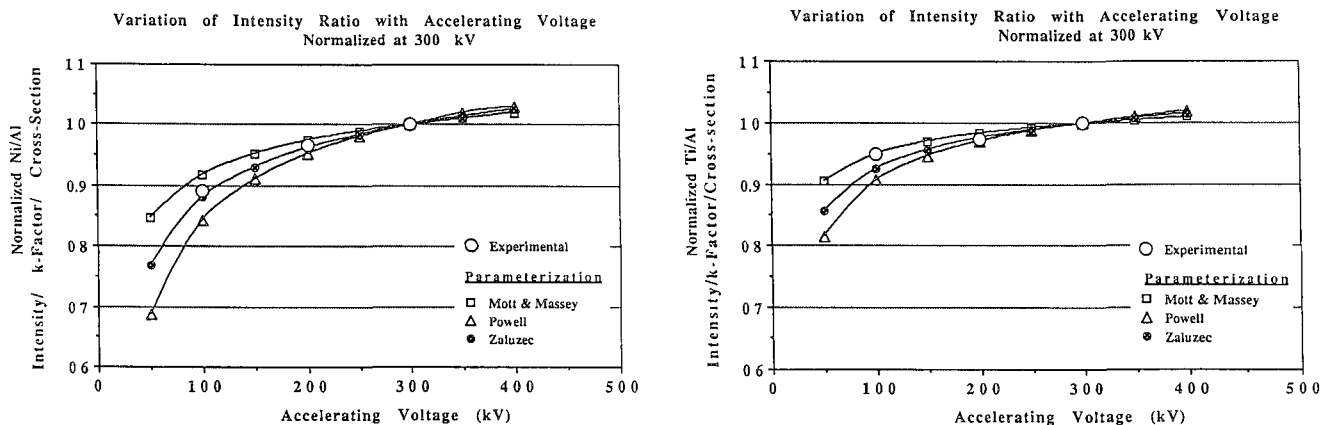


FIG. 5.--Comparison of calculated and experimental Ni/Al and Ti/Al intensity ratios as a function of accelerating voltage normalized at 300 kV.

where $\kappa_A = (\sigma_A \omega_A \Gamma_A) / W_A$ and σ_A , ω_A , Γ_A , W_A , ϵ_A , C_A , and I_A are respectively the ionization cross section, fluorescence yield, radiative partition function, atomic weight, detector efficiency, composition, and x-ray line intensity for the element A, and k_{AB} is the conventional k-factor. In Fig. 5, we compare these data with the theoretical variation in the ionization cross-section ratio for Ni K/Al K and Ti K/Al K shells, where all data are normalized at 300 kV.

These experiments illustrate that the k-factor can vary substantially with accelerating voltage and care must be taken when applying experimental and/or theoretical models determined at lower accelerating voltages to the intermediate voltage regime. Furthermore, relativistically corrected models for the ionization cross section can successfully predict the voltage dependence of both the relative intensity and the k-factor, within the limits of the thin-film approximation (no energy loss, absorption, and fluorescence). Further work is in progress to extend these measurements to higher atomic number materials to determine the applicability of the parameterized relativistic model more precisely.

References

1. P. J. Sheridan, *J. EM Technique* 11: 41-61, 1989.
2. N. F. Mott and H. S. W. Massey, *Theory of Atomic Collisions*, Oxford: Oxford University Press, 1940.
3. M. Green and V. E. Cosslett, *Proc. Phys. Soc.* 78: 1206-1212, 1961.
4. D. B. Brown, *Handbook of Spectroscopy*, Boca Raton, Fla.: CRC Press, 1974, vol. 1. 248.
5. C. J. Powell, *Rev. Mod. Phys.* A48: 33-47, 1976.
6. T. P. Schreiber and A. M. Wims, *Ultramicroscopy* 6: 323-334, 1981.
7. N. J. Zaluzec, *Analytical Electron Microscopy*--1984, 279.

DETECTION AND QUANTIFICATION PROBLEMS IN THE ANALYSIS OF LIGHT ELEMENTS WITH UTW DETECTORS

Gilles L'Espérance, Gianluigi Botton, and Mario Caron

Recent developments in windowless (WL) or ultrathin-window (UTW) detectors, improved energy resolution, larger angles of collection (0.15–0.2 sterad), and higher voltages (200–400 kV) make energy-dispersive spectrometry (EDS) more attractive for the analysis of low-Z elements both in SEM and TEM.¹ The spectrum in Fig. 1 obtained in the SEM from pure Be has a FWHM of 50 eV. Electron energy loss spectrometry (EELS) is the other technique that permits detection of light elements in TEM. Compared to EELS, EDS lends itself to faster, more routine analysis and offers in many cases the possibility of carrying out qualitative analysis for a wider range of materials thickness.² However, EELS has generally been recognized as having better sensitivities than EDS,^{3–5} except for some elements in biological materials as reported very recently by Leapman.⁵

This paper presents results and the performance of UTW detectors that can be achieved in materials microanalysis with both SEMs and TEMs, and difficulties in interpreting and quantifying the data. A comparison of sensitivity measurements made in EELS and EDS is also presented. All samples used are relevant to materials engineering.

Experimental

The EDS data in SEM were obtained with a JEOL 840 equipped with a Link LZ-4 detector. In TEM, the EDS analyses were done with a JEOL 2000FX equipped with a Link LZ-5 detector (solid angle ~ 0.16 sterad), and the EELS analyses were done on a Philips CM30 coupled to a Gatan (Model 666) parallel EELS.

Results

Both EDS detectors have a resolution of ~ 134 eV at 5.9 keV and allow the routine detection of boron x rays (0.185 keV) from pure B with the peak well resolved from the background and a peak/valley ratio of 8.2 in SEM and 12 in TEM (Fig. 2a–b).

The analysis of Mn, Fe, Co, and Ni transition metals showed the L α lines to be well resolved from the L α lines and the measured I L α /I L β ratio to be larger than that tabulated,

The authors are at the Ecole Polytechnique de Montréal, Centre for Characterization and Microscopy of Materials, Metallurgical Engineering Department, P.O. Box 6079, Station A, Montréal, Qué., Canada H3C 3A7. They thank R. Veillette and G. Guérin for preparing some of the samples and measuring the Ni L/Ni K ratio as a function of time, P. Hovington for the PEELS BN spectrum, J. Desrochers for preparing the figures, and Ms E. Campeau for typing the manuscript.

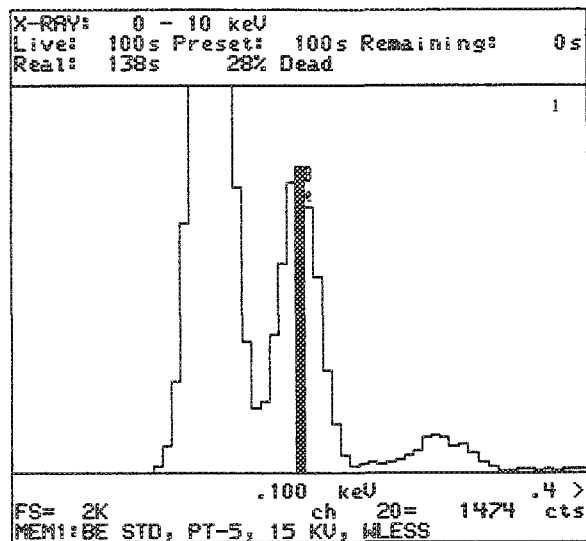


FIG. 1.--EDS spectrum of pure Be sample at 15 kV obtained in SEM. FWHM of peak is 50 eV.

e.g., 0.25 for Ni compared with a tabulated value of 0.09 (Fig. 3).⁶ The case of Cr analyzed in the SEM is particularly interesting. The (I L α /I L β) ratio observed appears to be close to 1.0 (Fig. 4a). However, a careful identification of the lines accounting for the slight shift (~ 2 channels) toward lower energies that we observe for the low-energy x rays, indicates that the peak to the left of the Cr L α line is not Cr L α only, but is constituted of a large contribution from O K. That oxygen was present was demonstrated by use of Auger electron spectroscopy (AES). Thus, Fig. 4(b) shows an AES spectrum obtained after ion-beam cleaning of the Cr sample in the Auger microscope prior to EDS analysis, and Fig. 4(c) shows an AES spectrum obtained from the same areas after EDS analysis. Clearly, oxygen was present on the surface of the nominally clean Cr sample after EDS. The oxygen may have come from the air during transfer of the sample from the Auger microscope to the SEM and back to the Auger microscope, and/or the formation in situ of a Cr oxide during the EDS analysis. In the case of this oxide layer, the intensity of the O K line might originate from primary ionization and from the fluorescence of the Cr L line through the oxidized layer. In SEM, however, for which the vacuum is not very good (7×10^{-7} Torr), the initial increase of the O K peak relative to that of the Cr L α has been observed to be very rapid (within a few seconds) after conditioning (see below) and exposure to the SEM chamber and the start of the analysis. This observation indicates that some O x rays have also come from the ice formed on

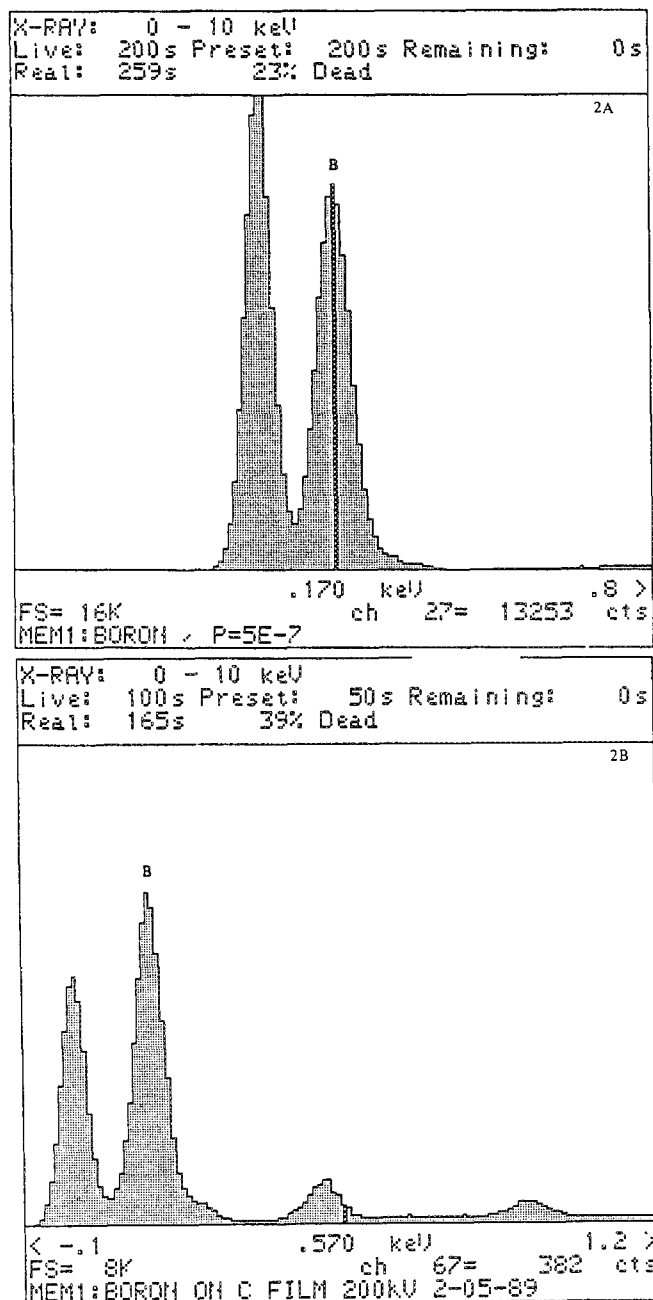


FIG. 2.--EDS spectra of pure boron obtained in SEM and TEM. (a) SEM, 15 kV, (b) TEM, 200 kV.

the surface of the Si detector and fluoresced by the Cr La line and the sample bremsstrahlung. Thus, Fig. 5 shows spectra obtained from Cr before and after conditioning and normalized to the Cr Ka lines. Clearly, the intensity of the (O Ka + Cr La) peak is reduced by its absorption in the ice. In addition, the intensity of O K is reduced relative to that of Cr La after conditioning, probably as a result of reduced fluorescence of oxygen from the ice. Whatever the origin of the O K x rays, it is clear that great care would have to be exercised to quantify the amount of Cr by use of Cr La lines.

In TEM, the Ni La/Ni Ka ratio is often used to follow the deposition of contaminants (ice

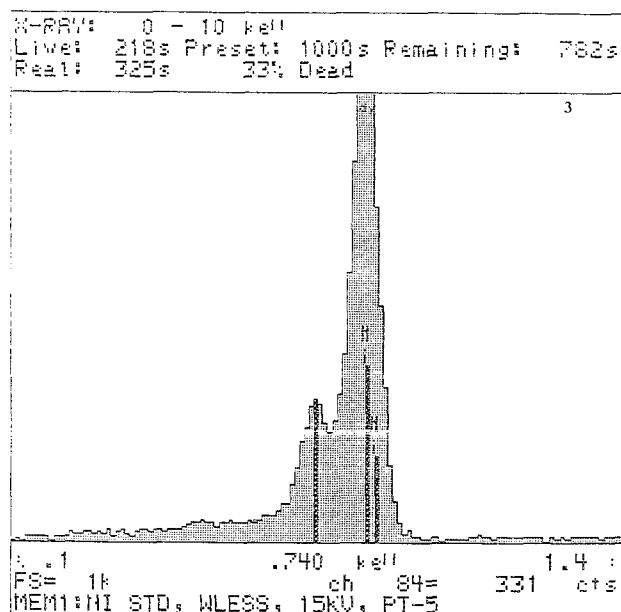


FIG. 3.--EDS spectrum of pure Ni obtained at 15 kV showing Li and La lines. Measured Li/La ratio is 0.25.

and/or possibly oil) on the surface of the detector as a function of time. With the Link system, it is possible to "condition" the detector to remove contaminants from the surface of the detector at regular intervals of time. Thus, Fig. 6 shows the Ni La/Ni Ka ratio plotted as a function of time after conditioning for successive "conditioning-operating" cycles of the detector during which the vacuum of the TEM column was never broken. As expected, the detector efficiency for relatively low-energy x rays steadily decreased with increasing time after each conditioning of the detector. Somewhat surprising, however, is the overall increase of the detector efficiency observed for an increasing number of successive conditioning treatments. Since the vacuum of the microscope column was not broken during the entire period of time taken by these successive "conditioning-operating" cycles, this increase may be explained by the fact that the more tenacious contaminants can be removed from the surface of the detector by conditioning only after that the detector has been exposed for a long time to the relatively good vacuum of the TEM column. Clearly, one must account for the variation in detector efficiency before attempting to quantify data involving light elements. In particular, it limits the usefulness of experimental k_{AB} factors used to quantify microanalyses in TEM if these factors are not obtained at approximately the same time as the analysis of the sample of unknown composition or with the detector in the same conditions (same efficiency).

Table 1 shows the minimum mass fractions (MMF) of various elements in various samples measured in EDS and EELS. Several interesting points are worth noting.

1. For light elements (B and N), PEELS

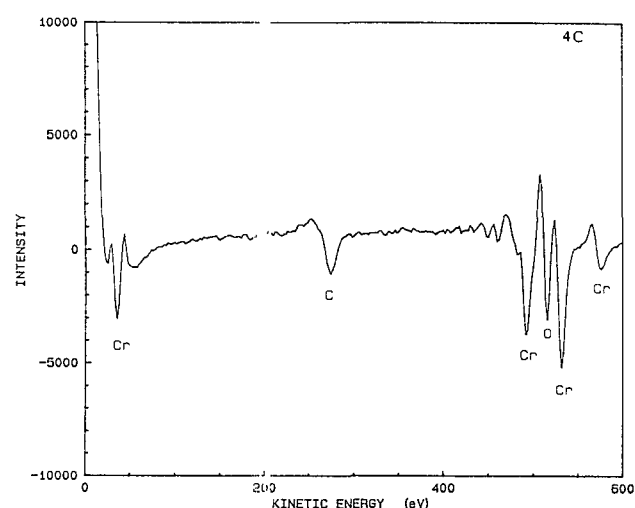
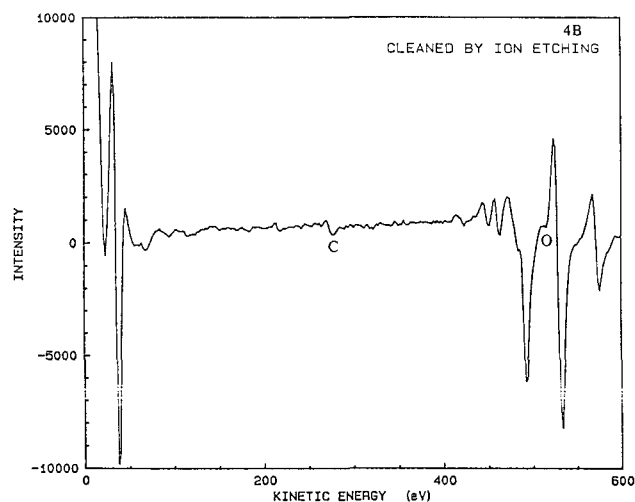
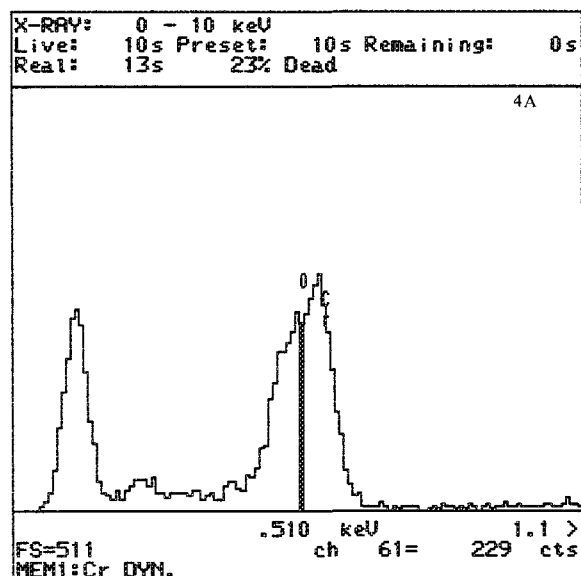


FIG. 4.--(a) EDS spectrum of pure Cr obtained at 15 kV; (b) AES spectrum of pure Cr after ion-beam cleaning in Auger microscope; (c) AES spectrum of nominally pure Cr after EDS in the SEM. Compared with 4(b), additional peaks of O and C are clearly visible.

TABLE 1.--Minimum mass fractions (MMF) measured in EDS and EELS. In EELS, the conditions were $\beta = 10$ mrad and the spectra were acquired in the image coupling mode (diffraction pattern on the screen).

Element	System	EDS		EELS (wt%)
		$I_p \gg 3/2BG$ (wt%)	Isaacson and Johnson ³ (wt%)	
B	Pure boron powder	1.1	0.5	too thick
B	BN flakes	5.1	2.4	0.094
B	Amorphous (RS) Fe ₃ B (thin foil)	B not detected		0.44
N	BN flakes	0.83	0.4	0.31
N	TiN particles on carbon film	not measured		0.78
N	Nb C ₃ N ₃ particles on carbon replica			
	- 50 nm particle	4.29	2.0	0.50
	- 60 nm particle			
Ti	TiN particles on carbon film			1.2
	25 nm particle			
	125 nm particle	0.15	0.072	
Fe	Amorphous (RS) Fe ₃ B (thin film)	0.4	0.2	6.9
Nb	Nb C ₃ N ₃ particles on carbon film			1.6
	10 nm particle $i=0.004$ nA, $J=2.2$ A/cm ²	6.18	2.91	
	50 nm particle	1.64	0.8	
	130 nm particle $i=0.250$ nA, $J=1.55$ A/cm ²	0.27	0.13	
	60 nm particle			

always gave better sensitivities than EDS, although sensitivities as low as 0.5% were achieved (by use of Isaacson and Johnson's criterion³) in EDS for both B and N combined with a light element. This was the case even for areas too thick to be analyzed by EELS. However, in the case of a relatively heavy matrix, such as B in Fe₃B, boron was not detected although the concentration (6.06 wt%) exceeds the MMF for B determined from pure B and BN spectra. This is probably the result of the large absorption of BK in Fe₃B; 9 nm is sufficient to absorb 10% of the BK x rays calculated using Henke and Ebisu's mass absorption coefficients. The large absorption of low energy x rays even for relatively thin samples (50 nm) is one of the major problems of EDS of light elements so that very thin samples are required, as is generally the case for EELS. As a matter of comparison, the value of 9 nm for 10% absorption of B in Fe₃B is smaller than that for which plural scattering begins to occur in EELS (~40 nm at 300 kV).

2. We did not attempt to measure a MMF of N (0.452 keV) in TiN due to the severe overlap

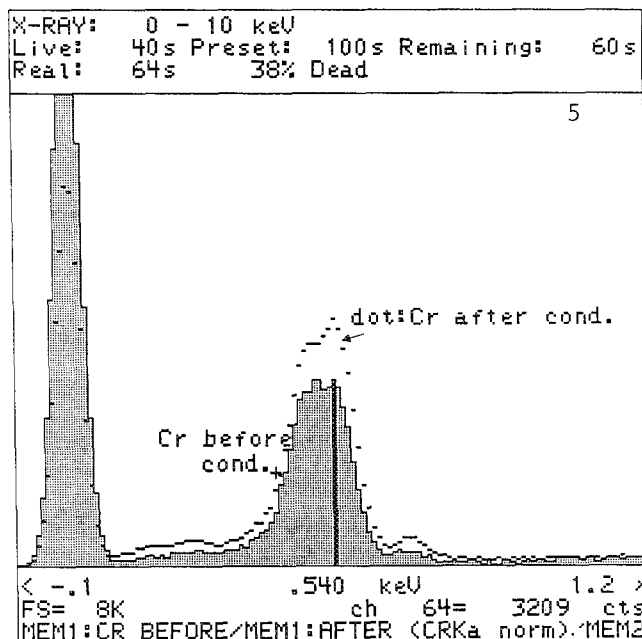
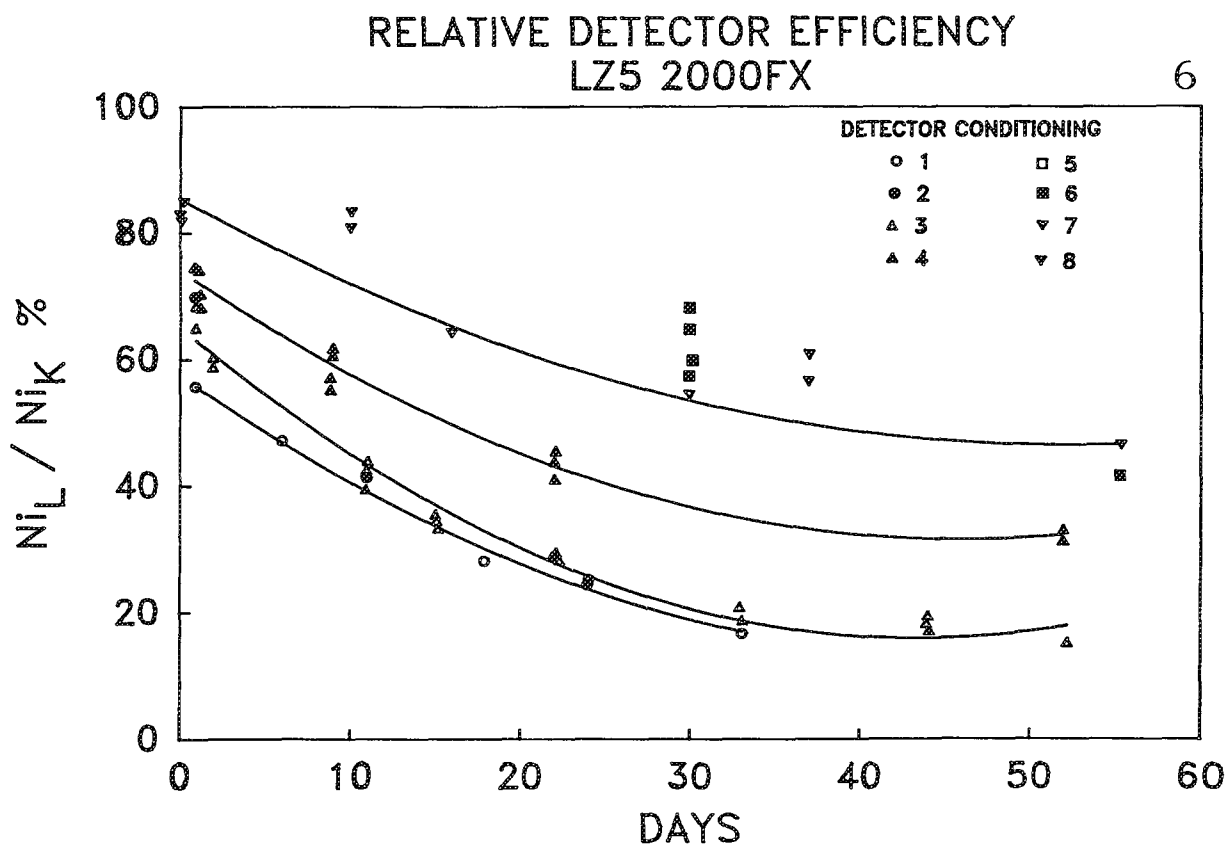


FIG. 5.--EDS spectrum from pure Cr sample showing O K and Cr L α line before (full spectrum) and after (dot spectrum) conditioning of the detector. SEM, 15 kV.

FIG. 6.--Ni L α /Ni K α ratio as a function of time after conditioning measured for successive "conditioning-operating" cycles of the detector. TEM, 200 kV.



between N K α (0.342 keV) and Ti L α (0.452 keV) lines and the possibility of fluorescence of the N K α line by the Ti L α line.

3. For relatively heavy elements (Ti in TiN, Fe in Fe₃B, and Nb in NbC_{0.5}N_{0.5}) lower sensitivities were achieved with EDS. Thus, for the systems studied here, EELS and EDS were complementary for the detection of small amounts of

elements in systems containing both light and relatively heavy elements.

4. The MMF in EDS of Nb in NbC_{0.5}N_{0.5} particles improved with increasing size of the particles analyzed. Since the probe size was increased to match the particle size, this improvement in MMF reflects the increase in probe current and of the interaction volume with in-

creasing particle size. In the context of characterizing particles as small as possible, on replicas, it is interesting to relate the lowest MMF (0.25 wt%) obtained with large particles to the smallest particles for which a signal was detected. For $\text{NbC}_{0.5}\text{N}_{0.5}$, Nb could be detected in particles ≥ 5 nm yielding a detected number of ~ 5000 atoms ($\sim 10^{-20}$ g); (assuming a FCC structure with $a = 0.45$ nm). If we assume that the crystal structure does not change in chemistry [Nb/(C + N) ratio] and convert the MMF of 0.27 wt% into a number of detectable atoms for a 5 nm particle, we obtain 500 atoms of Nb, reflecting the influence of poor counting statistics for small particles. In comparison, N was detected for particles bigger than 50 nm corresponding to 2.4×10^6 atoms ($\sim 5.6 \times 10^{-17}$ g).

Finally, we could not, using serial EELS, detect Nb or N in such small particles (< 50 nm). PEELS allowed the analysis of smaller particles (20 nm for Nb). However, first-difference methods of signal detection⁸ may improve this result. In this investigation, EDS allowed the analysis of the smallest particles (5 nm for Nb).

References

1. P. J. Statham, *Proc. ANRT Meeting on Microanalysis and Scanning Electron Microscopy*, Paris, 1985.
2. M. H. Loretto, *Ultramicroscopy* 28: 302-307, 1989.
3. M. Isaacson and D. Johnson, *Ultramicroscopy* 1: 33-52, 1975.
4. R. F. Egerton, *EELS in the Electron Microscope*, New York: Plenum Press, 1986, 22-23.
5. R. D. Leapman, *Proc. 47th Annual Meeting EMSA*, 1989, 400-401.
6. *CRC Handbook of Physics and Chemistry* (69th ed.), Boca Raton, Fla.: CRC Press, E-196.
7. B. L. Henke and E. S. Ebisu, *Advances in x-ray Analysis*, New York: Plenum Press, vol. 17, 150.
8. H. Shuman and A. P. Somlyo, *Ultramicroscopy* 21: 23-32, 1987.

EFFECT OF TILT ANGLE ON HOLE COUNT AND SECONDARY FLUORESCENCE IN X-RAY MICROANALYSIS

E. A. Kenik and J. Bentley

The spatial resolution and accuracy of x-ray microanalysis in an analytical electron microscope (AEM) are limited by a variety of factors, two of which are the hole count^{1,2} and secondary fluorescence.^{3,4} The hole count arises from uncollimated radiation, either electrons or x rays, which excite areas of the specimen other than that excited by the primary electron beam. This process can result in x-ray generation even when the probe does not hit the specimen; hence the name "hole count." Secondary fluorescence deals with x-ray generation resulting from radiation produced by the interaction of the incident probe with the specimen. This radiation may be either backscattered electrons spiraling in the magnetic field of the objective lens, diffracted electrons, or high-energy x rays, particularly forward-peaked bremsstrahlung. As the interaction of both the uncollimated radiation and the secondary radiation with the specimen can be influenced by the tilt angle of the specimen, the variation of the hole count and secondary fluorescence with specimen tilt was investigated.

Though methods for identifying the origins of both the hole count and secondary fluorescence and for reducing their magnitude have been available for a reasonable time,¹⁻⁴ there is still some confusion in the literature. Whereas several test specimens have been suggested,^{1,5-7} there is not a generally accepted test for comparing the performance of AEMs in x-ray microanalysis. The test specimen used in this study was a preliminary version of the standard proposed at the Giens workshop;⁷ a thin, holey chromium film supported on a molybdenum washer.

Experimental Procedures

The ~35nm-thick holey chromium film was prepared by evaporation of chromium on a holey Formvar film previously prepared on a glass slide. The chromium film was released from the slide by dissolution of the Formvar film in ethylene dichloride. Initially, the holey chromium films were supported directly across a small hole in a 0.3mm-thick, 3mm-diam molybdenum washer. As the films tended to crack when spanning the 1.0mm-diam holes in the washers, the films were supported by 75-mesh 3mm molyb-

denum grids, which were then spot-welded to the washers. The specimen was oriented in the AEM with the chromium film on the electron entrance side, supported by the grid, and then the washer. This arrangement prevents shadowing of the x-ray detector by the grid or the washer. Measurements were performed near the center of a grid square centered over the hole in the washer. A modified test specimen was made by placing a 40µm-thick copper sheet over one-half of the electron incidence side of the previous test specimen. The specimen was oriented so that when the specimen was tilted, the copper was either entirely upstream (nearer the electron gun) or downstream from the intersection of the electron probe with the chromium film.

Measurements of hole count and secondary fluorescence as a function of specimen tilt were performed in Philips EM400T/FEG, CM12/STEM, and CM30/STEM AEMs operating at 100, 120, and 300 kV, respectively, and each equipped with EDAX x-ray detectors (20° take-off angle) and 9100 or 9900 analyzers. The magnitudes of the hole count (HC) and secondary fluorescence (SF) were estimated as:

$$HC = I_h(Mo) / [I_f(Cr) - I_h(Cr)] \quad \text{and}$$

$$SF = [I_f(Mo) - I_h(Mo)] / [I_f(Cr) - I_h(Cr)]$$

where $I(A)$ is the integrated $K\alpha$ peak intensity for element A and the subscripts refer to the positioning of the probe on the film (f) or in a hole (h). Similar equations can be used for the $L\alpha$ line of molybdenum. Though these equations are not the usual definitions for hole count and secondary fluorescence, the normalization to the chromium signal is dictated by the nature of the test specimen.

Results

Figure 1 shows a typical area of the holey chromium film. The evaporated chromium was very fine-grained (<2nm in diam.) and randomly oriented. Therefore, x-ray generation was averaged over numerous grains and orientation effects such as channeling could be ignored. Holes sizes ranging from 0.1 to 10 µm were observed. When regions of similar mass thickness were selected, 2% variations in x-ray yield were observed in spot analyses indicating similar variations in film thickness.

Figures 2(a) and (b) show the dependence of HC and SF on specimen tilt measured for the Philips CM12 in the microprobe and nanoprobe modes, respectively. No attempt was made to optimize the hole count via choice of C_2 aperture, spot size, filament emission, etc., since the intent was to show the variation with

The authors are at the Oak Ridge National Laboratory (Metals and Ceramics Division), Oak Ridge, TN 37831-6376. The research was sponsored by the DOE Division of Materials Sciences under contract DE-AC05-84OR21400 with Martin Marietta Energy Systems, Inc. Specimen preparation by C. K. H. DuBose is gratefully acknowledged.

tilt angle. The probe current is ~25% higher in the nanoprobe mode than in the microprobe mode with the same C_1 excitation and condenser aperture. For Fig. 2, no corrections were made for the increase in $I_f(\text{Cr})$ with increasing tilt angle due to the increased projected film thickness. The hole count is lower in the nanoprobe mode than in the microprobe mode; it is interesting that the weak dependence of HC on tilt angle is in the opposite sense for the two modes. In contrast, the secondary fluorescence curves for the two operating modes superimpose exactly, which indicates that the process responsible for the effect is the same without regard to the operating mode, as expected. The increased secondary fluorescence at higher specimen tilt reflects the increased cross section presented by the specimen to the fluorescing radiation (x rays or electrons). A second effect may also contribute: more x rays may escape the thick washer as the specimen is tilted.

Measured Cr $K\alpha$ P/B ratios at 20° tilt were greater than 3000 under the Fiori definition of peak/background ratio (i.e., total integrated peak intensity divided by the average background intensity of a 10eV window).⁸ These results indicate that the x-ray microanalytical performance of the AEM is not seriously compromised by instrumental artifacts. P/B ratios at higher tilt angles were lower as SF of the grid bar and washer increased with an attendant increase in background from these components. Measurements below 10° tilt are not indicated in Fig. 2, as the beryllium specimen holder was cutting off a portion of the x rays (~12% of the Cr $K\alpha$ x rays at 0°). Such cutoff of x rays could be detected by a comparison of the corrected chromium intensity [$I_f(\text{Cr}) - I_h(\text{Cr})$] as a function of tilt angle with the expected $1/\cos \theta$ dependence. X-ray cutoff was not always observed at 0° tilt but appeared to depend on the location of the analyzed area in the specimen holder.

Figure 3 illustrates the dependence of HC and SF on the distance from the nearest grid bar. These measurements were performed in the Philips EM400T/FEG in the nanoprobe mode. Both HC and SF decrease as the distance increases. The HC measurements indicate that there is highly localized uncollimated radiation near the electron probe (<15 μm), presumably electron tails. The increased SF at small distances results from increased interaction of the secondary radiation (i.e., backscattered or diffracted electrons or forward-peaked bremsstrahlung) with the grid bar because of the close proximity. At the center of the 75-mesh support grid, the distance from all grid bars is >120 μm at 0°. On the basis of this result, it seems possible that a molybdenum washer with a smaller hole could be used as a support and the grid could be eliminated. This simpler geometry could aid in better understanding of the interaction of uncollimated and secondary radiation.

In an attempt to understand which radiation is responsible for secondary fluorescence, a modified test specimen (described above) was used with the copper either entirely upstream

(nearer the electron gun) or downstream from the intersection of the primary electron probe with the chromium film. Figure 4 shows the secondary fluorescence of copper and molybdenum from this composite specimen for the two orientations. Initially it was thought that if backscattered electrons were mainly responsible for secondary fluorescence, the copper signal would increase with increasing tilt and would be larger in Fig. 4(a) than in (b). Though molybdenum SF behavior is similar to that in Fig. 2, copper SF initially decreases and then rises slightly. When the copper is downstream (Fig. 4b), the molybdenum SF is decreased, but the copper SF is much larger than in Fig. 4(a) and increases with tilt angle. The low copper SF in Fig. 4(a) and the results in Fig. 4(b) indicate that forward-peaked secondary radiation is the primary source of secondary fluorescence for this microscope and specimen. Obviously, both high-energy bremsstrahlung and diffracted electrons are forward-peaked and are therefore possible secondary fluorescing radiation responsible for the results in Fig. 4. However, backscattered electrons (meaning high-energy electrons emerging from the electron incidence surface) can also explain these results. At zero tilt all backscattered electrons have a velocity component antiparallel to the incident beam, but as the specimen is tilted backscattered electrons with a forward velocity component (i.e., parallel to the incident beam) are produced in increasing numbers. Backscattered electrons with a forward velocity component spiraling in the magnetic field of the objective lens that collide with the specimen do so downstream from the point of emergence. Therefore, based on the qualitative behavior of the results from the copper-modified test specimen, all three types of secondary radiation ("backscattered" electrons, diffracted electrons, or bremsstrahlung) are possible causes of the observed secondary fluorescence.

In comparing the SF results for the three electron microscopes, it became apparent that the magnitude of the SF effect decreased with increasing accelerating voltage. At a fixed specimen tilt of 20°, the relative magnitudes were 1.00, 0.78, and 0.11 at 100, 120, and 300 kV, respectively. This decrease indicates that the secondary radiation becomes more forward-peaked as the incident electrons increase in energy and as such interacts less with the specimen. Unfortunately, all three possible secondary radiations would be expected to exhibit such behavior. This decreased influence of SF is an additional advantage of intermediate voltage AEMs for x-ray microanalysis over lower voltage instruments, other *potential* advantages being decreased beam spreading, increased x-ray yields, and higher P/B ratios. SF was normalized by the Cr x-ray yield from the film, which at constant probe current should decrease with increasing accelerating voltage. This decrease would be somewhat offset by the decreased interaction of higher-energy secondary radiation with the specimen.

Further studies aimed at identifying the radiations responsible for the hole count and secondary fluorescence based on the observed Mo L/K ratio and the Mo K P/B ratio are currently under way. Preliminary results indicate that electron excitation is chiefly responsible for both effects in the AEMs of the present investigation. More complete results and comparisons of HC and SF in several AEMs will be reported elsewhere.⁹

Conclusions

The utility of the holey chromium/molybdenum support test specimen has been demonstrated in the study of hole count, secondary fluorescence, and x-ray cutoff by the specimen holder. The hole count in the AEMs investigated shows a weak dependence on specimen tilt (if corrections for increased projected specimen thickness are not made), but also depends on operating mode. Conversely, secondary fluorescence is a strong function of specimen tilt, but is independent of operating mode. Both the hole count and secondary fluorescence depend on distance from the nearest thick material (grid bar). For the hole count, this result indicates that the uncollimated radiation flux is higher near the primary probe (e.g., electron tails). Secondary fluorescence increases with decreasing distance to the grid bar as a result of the increased "target" presented to the secondary radiation. Results of tests with the copper-modified test specimen indicate that secondary fluorescence in the AEMs studied occurs primarily downstream from the primary excited volume. The magnitude of secondary fluorescence decreases with increasing accelerating voltage. These last two results are consistent with forward-peaked radiation (backscattered electrons, diffracted electrons, or high-energy bremsstrahlung), which becomes more forward-peaked with higher accelerating voltage.

References

1. J. Bentley et al., *SEM/1979 II*, 581.
2. D. B. Williams, *Practical Analytical Electron Microscopy in Materials Science*, Mahwah, N.J.: Philips Electronic Instruments, 1984, 57.
3. J. Bentley, P. Angelini, and P. S. Sklad, *Analytical Electron Microscopy--1984*, 315.
4. P. Angelini and J. Bentley, *Proc. 42d Ann. EMSA Meeting*, 1984, 582.
5. L. F. Allard and D. F. Blake, *Analytical Electron Microscopy--1982*, 8.
6. C. E. Lyman et al., *Microbeam Analysis--1989*, 507.
7. Workshop on the future of electron microscopy (Organizers: J. A. Eades, C. Colliex, and P. Druit), Giens, France, 23-27 Sept. 1989.
8. C. E. Fiori et al., *Microbeam Analysis--1982*, 57.
9. E. A. Kenik and J. Bentley (to be published).

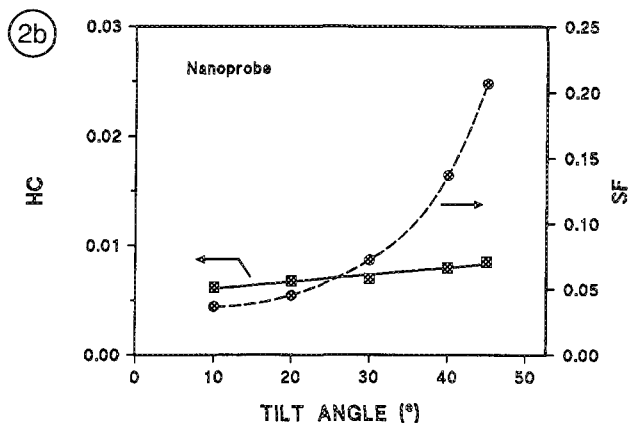
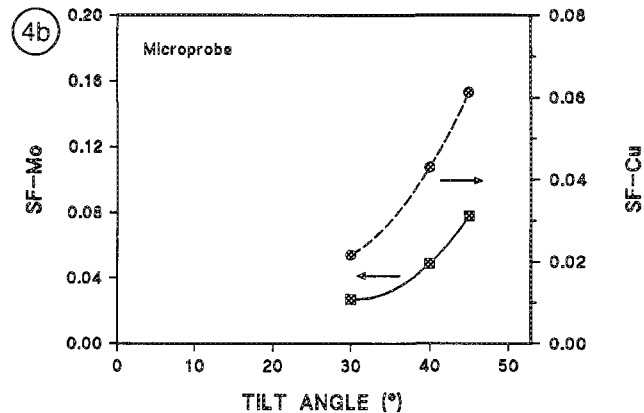
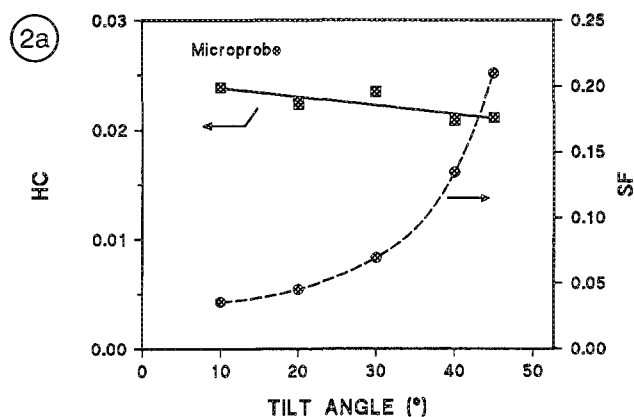
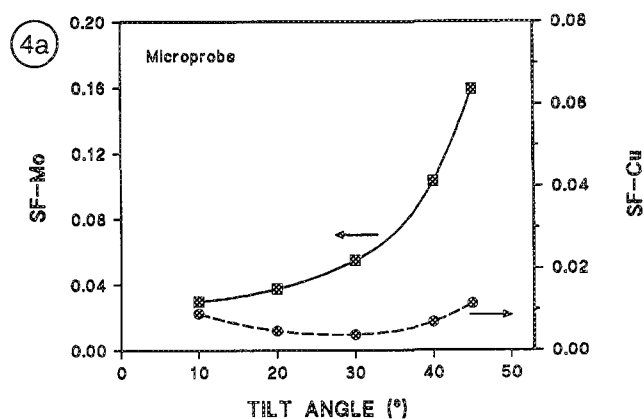
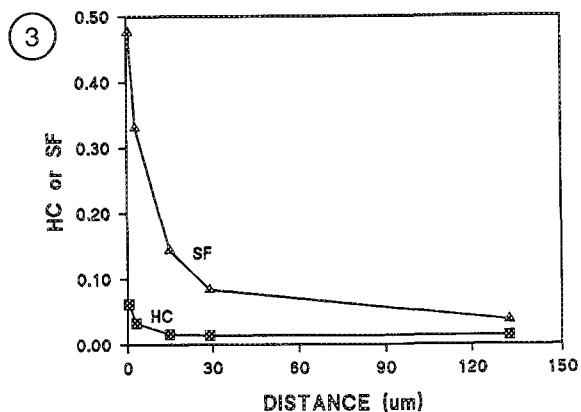
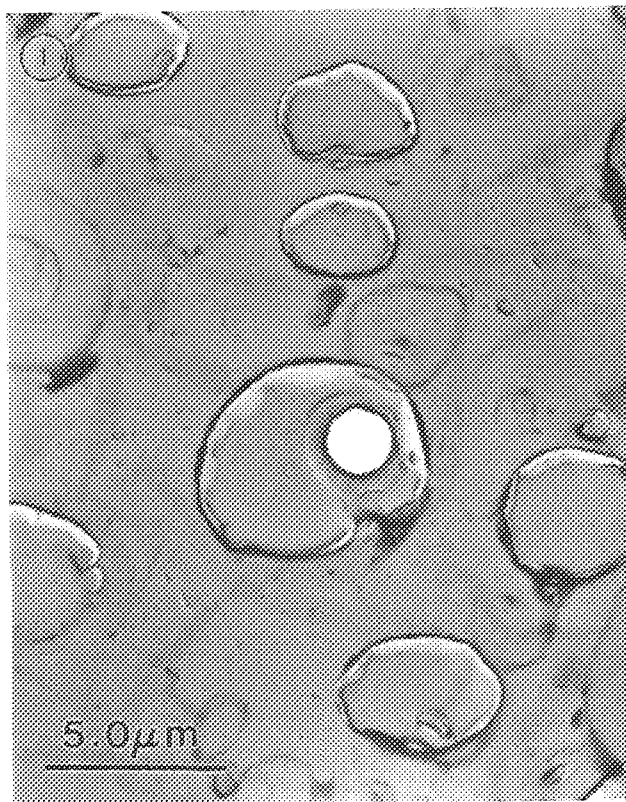


FIG. 1.--TEM image of holey chromium film used in this study.

FIG. 2.--Hole count (HC) and secondary fluorescence (SF) as function of specimen tilt measured in (a) microprobe and (b) nanoprobe modes on Philips CM12/STEM AEM.

FIG. 3.--Hole count (HC) and secondary fluorescence (SF) as function of distance to nearest grid bar measured in nanoprobe mode on Philips EM400T/FEG AEM at 10° tilt.

FIG. 4.--Secondary fluorescence of copper (SF-Cu) and molybdenum (SF-Mo) for modified test specimen as function of specimen tilt in microprobe mode (Philips CM12/STEM AEM) with copper sheet (a) upstream and (b) downstream from region excited by primary electron beam. Note in (b) copper sheet partially shadowed x-ray detector for tilts <30°.

ATOMIC SITE DETERMINATION OF Ti, Cr AND Co IN SENDUST (Fe-9.6wt%Si-5.5wt%Al) BY CHANNELING ENHANCED MICROANALYSIS

Kaoru Sato and Hirofumi Matsuhata

Sendust¹ (Fe-9.6wt%Si-5.5wt%Al) is a well-known soft magnetic material. Attempts have been made recently to improve the corrosion resistance of this alloy by adding a fourth and/or a fifth element. Since the excellent magnetic properties of Sendust have been reported to be strongly related to its crystal structure,² the DO₃ ordered structure, it is of vital importance to determine the crystallographic sites those additional elements occupy. In the present work we report the results obtained for the site occupation of Ti, Cr, and Co in Sendust alloys by the ALCHEMI (Atom Location by Channeling Enhanced Microanalysis) method.³

Experimental

Sendust alloys containing 4.0%Cr, 3.0%Co+0.5%Nb, and 2.0%Ti alloys were arc melted, then furnace-cooled from 1473 K with the cooling rate of 80°/h. TEM specimens were prepared in a twin jet electropolisher with 5% perchloric-acetic acid and the final thinning was done by an ion milling machine. The ALCHEMI experiment was performed in a Philips EM420T TEM equipped with an EDAX PV9900 energy-dispersive x-ray analytical system. The specimens were tilted about 20° toward the x-ray detector. The acquisition time was typically 200 s, so that the integrated x-ray intensity of Fe-K α (1.2 times that of the FWHM) was more than 100 000 counts. Background subtraction of x-ray spectra and the determination of the x-ray intensities were performed by an EDAX "thin" program. Planar ALCHEMI experiments were simulated with a Bloch-wave computer program.

Results

All specimens observed exhibited the diffraction spots associated with the DO₃-ordered structure. Dark-field micrographs obtained from these ordered reflections did not show antiphase domain boundaries, only uniform contrast, and thus the alloys appear to be in a highly ordered state. The DO₃ structure has three sublattices, A₁, A₂, and B (Fig. 1). Both the A₁ and A₂ sites are occupied by Fe; the B site is occupied by Al and Si. With Fe, Al, and Si as internal standards, the site location of Ti, Cr, and Co was determined. The site of Nb was not investigated because Nb-rich

precipitates were observed at the grain boundaries and thus the solubility of Nb in Sendust was found to be very low (<0.2%).

Typical x-ray spectra obtained by use of the 002 systematic excitation for each specimen are shown in Fig. 2. These spectra are normalized by the Fe-K α x-ray intensity. Relative x-ray intensities of Al and Si to that of Fe, I_{Al}/I_{Fe} , and I_{Si}/I_{Fe} , obtained at a deviation parameter $s < 0$ of the 002 reflection, are smaller than those obtained at $s > 0$, as expected from the DO₃ structure. This difference is not due to the variation of x-ray detection with specimen/detector geometry but to the channeling effect, because the spectra obtained from the same area with 002 and 00 $\bar{2}$ ALCHEMI showed the same tendency. The channeling effect was observed for the divergence semi-angles of both 1.6 mrad and 4.6 mrad. Therefore, the beam with a larger divergence was used for analysis to obtain higher x-ray counts. The ratio of the relative x-ray intensities, $R_X = (I_X/I_{Fe})_{s<0}/(I_X/I_{Fe})_{s>0}$ ($X = Al, Si, Co, Cr$, and Ti), are plotted in Fig. 3 for several areas of each specimen. I_{Al}/I_{Fe} and I_{Si}/I_{Fe} were 20-30% smaller for $s < 0$ than for $s > 0$; I_{Co}/I_{Fe} stays almost constant regardless of the diffraction condition, although the measurement in x-ray intensity of Co is subjected to large error because the Co-K α line overlaps with Fe-K α line and the Co-K β line is too weak to quantify. $R_{Co} \approx 1$ can result only when Co substitutes at the two Fe sites (the A₁ and A₂ sites) randomly. The preferential occupation of the A₁ site by Co atoms reported in a Mössbauer experiment⁴ was not observed in the present study. I_{Cr}/I_{Fe} at $s < 0$ was about 8% lower than that at $s > 0$. This result suggests that Cr weakly prefers the A₂ site to the A₁ site. However, the difference could be within the experimental error.

The result obtained for the Ti-bearing sample is shown in Fig. 2(b). Figure 3 shows that I_{Ti}/I_{Fe} is about 30% smaller when $s < 0$ than $s > 0$ and thus Ti tends to occupy the planes that contain the A₂ and B sites. In order to differentiate whether Ti occupies the A₂ or the B site, ALCHEMI experiments such as those using the (111) or the (113) planes (Fig. 4) would appear to be necessary because these planes can be resolved into layers of [A₁, A₂, A₁, B ...].

Computer simulation of the behavior of Bloch waves has to be performed to sort out suitable diffraction conditions for these systematic rows as well as for the (002) row for comparison. The calculation was performed by use of about 40 systematic reflections in each case under the accelerating voltage of 120 kV.

K. Sato is at the Steel Research Center, NKK Corp., 1-1 Minamiwatarida, Kawasaki 210; H. Matsuhata is at the Electrotechnical Laboratory, 1-1-4 Umezono, Tsukuba 305, Japan. The authors thank Mr. T. Nishimura for the provision of specimens and useful discussions and Mr. N. Simbu for technical assistance.

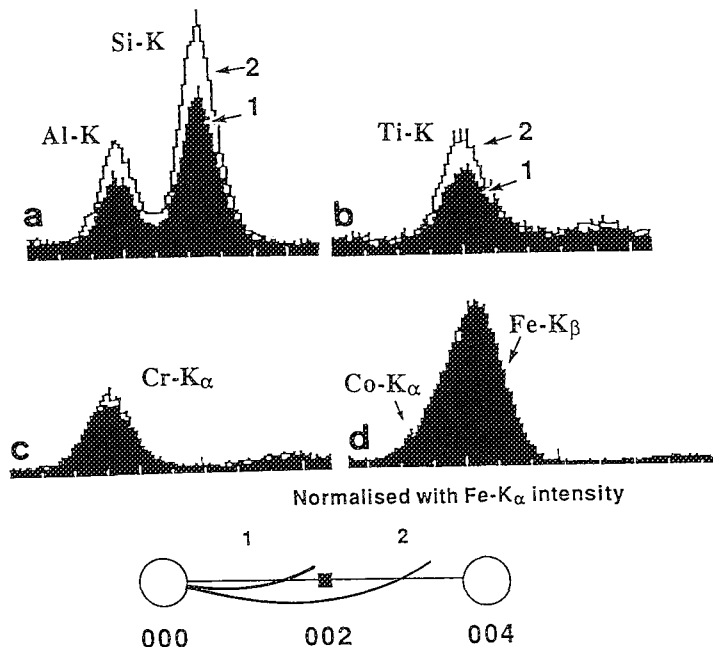
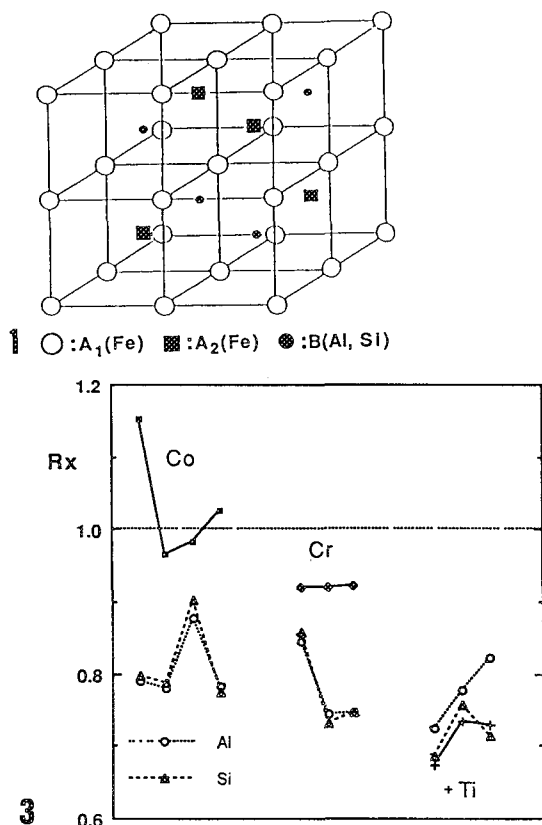


FIG. 1.--Three sublattices of DO₃ structure.
 FIG. 2.--EDXS spectra normalized with Fe-K α intensity obtained from each specimen, with $s < 0$ (1) and $s > 0$ (2) conditions for 002 reflections.
 FIG. 3.--Ratios of Al, Si, Cr, Co, and Ti intensities for $s < 0$ to those for $s > 0$ [$(I_X/I_{Fe})_{s<0}/(I_X/I_{Fe})_{s>0} \equiv R_X$] for (002) planar channeling.

FIG. 4.--(a) 110 projection of DO₃ structure and (b) diffraction conditions used in planar ALCHEMI experiments. Structure factor for each reflection is ○ $8f_{A_1} + 4f_{A_2} + 4f_B$; ■ $8f_{A_1} - 4f_{A_2} - 4f_B$; ● $4f_{A_2} - 4f_B$.

Fourier components of the inner potential V_g were calculated from atomic scattering factors given by Doyle and Turner.⁵ The imaginary part of the Fourier potential V_g' was chosen as $V_g' = 0.05V_g$. Thermal Debye parameters used were those tabulated in *International Table for X-ray Crystallography*.⁶ The elastic electron intensity for each branch across the unit cell, $|\psi(r)|^2$, is plotted. The intensity is normalized with that of the incident electron. The positions of the atomic planes A₁, A₂, and B are indicated. The numbers in the figure indicate the branches of Bloch waves. The diffraction conditions used in the simulation are de-

scribed by the parameter δ_g , which defines the position at which Ewald sphere intersects the systematic line. For example, $\delta_{002} = 1.4$ indicates that Ewald sphere intersects the position 001.4.

The channeling effect expected on the (002) plane is strong (Figs. 5a and b). Bloch wave 1, which localizes at the A₁(Fe) position, is dominant when $\delta_{002} = 1.4$, whereas Bloch wave 2 is dominant at $\delta_{002} = 3.4$; in this case electrons channel on the planes containing the A₂ and B sites. In both cases, the simulated behavior of Bloch waves explains the strong channeling effect observed in the (002) experiments.

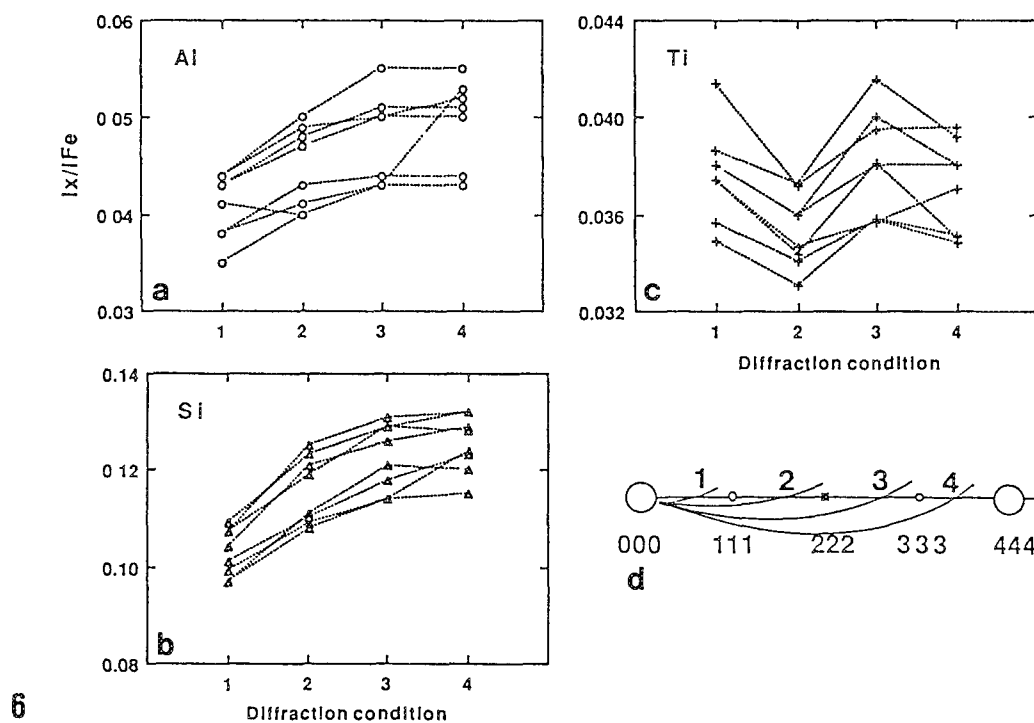
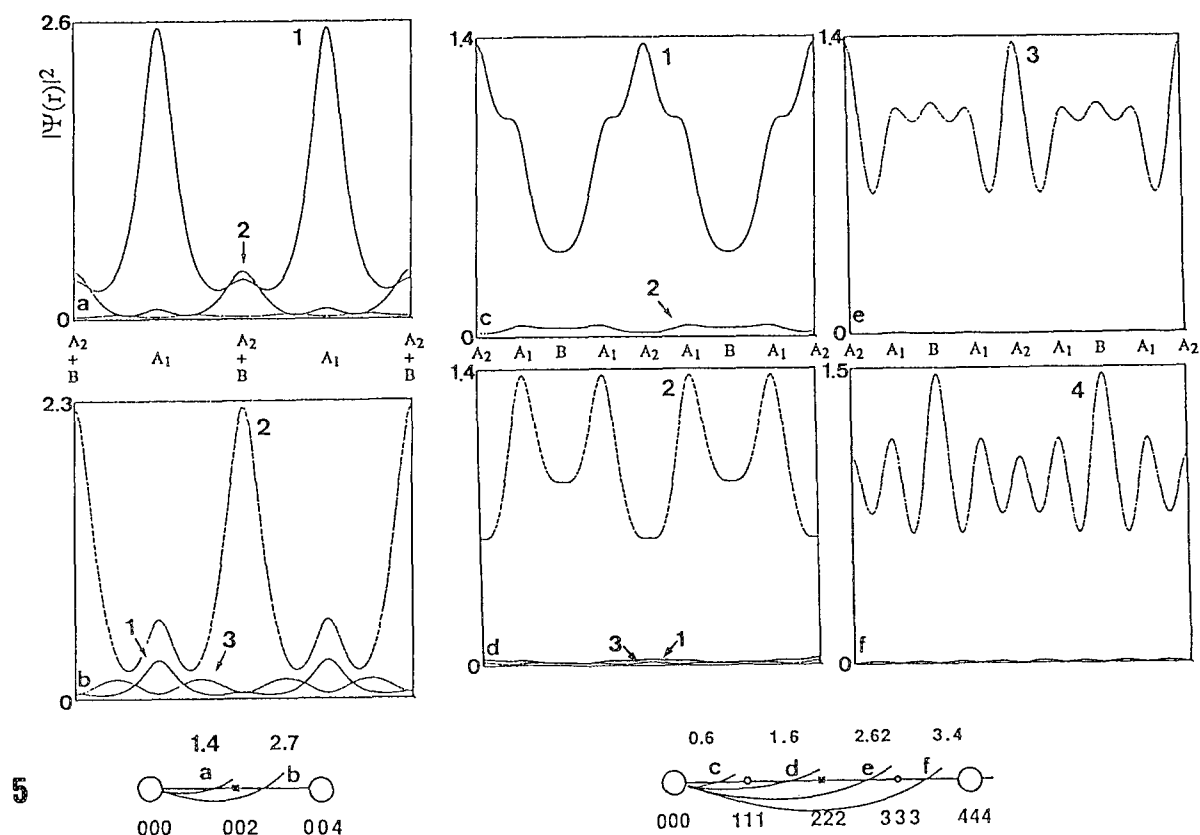


FIG. 5.--Calculated elastic electron intensity for each branch across unit cell, $|\psi(r)|^2$, for (a) and (b) 002 projection (c)-(f) 111 projection. Diffraction conditions assumed are also shown by positions of δ_g .
 FIG. 6.--Relative x-ray intensities of Al, Si, and Ti to Fe (I_x/I_{Fe}) for four 111 systematic diffraction conditions.

The computer simulations performed for the (111) ALCHEMI with $\delta_{111} = 0.6, 1.6, 2.62$, and 3.4 are shown in Figs. 4(c)-(f). Under these conditions, only one of the Bloch waves 1-4 is strongly excited. Although the channeling effect on (111) is weaker than that on (002), $|\psi(r)|^2$ has peaks at the $A_2(\text{Fe})$ planes for $\delta_{111} = 0.6$ and at the $A_1(\text{Fe})$ planes for $\delta_{111} = 1.6$. With $\delta_{111} = 2.62$ and 3.4 , Bloch waves 3 and 4 weakly localize at the $A_2(\text{Fe})$ and the B planes, respectively. It is also predicted that the intensity at the B site increases gradually as δ_{111} increases from 0.6 to 3.4.

Relative x-ray intensities I_X/I_{Fe} ($X = \text{Al, Si, Ti}$) as a function of diffraction conditions which were measured for the (111) systematic reflection from four different areas are plotted in Figs. 6(a)-(c). The diffraction conditions used are shown in Fig. 6(d). Both the hhh and $\bar{h}\bar{h}\bar{h}$ experiments are performed for each area. The scatter in I_X/I_{Fe} is not due to the local variation of the chemical compositions, but to the differences in thickness and diffraction condition including the accidental excitation of nonsystematic reflections. The behavior of $I_{\text{Al}}/I_{\text{Fe}}$ and $I_{\text{Si}}/I_{\text{Fe}}$ is consistent with the simulated behavior; they increase as δ_{111} increases. The behavior of $I_{\text{Ti}}/I_{\text{Fe}}$ is shown in Fig. 6(c). The measured $I_{\text{Ti}}/I_{\text{Fe}}$ is high for the two diffraction conditions, 1 and 3, where $|\psi(r)|^2$ at the A_2 planes is higher than those at the A_1 and B planes (Figs. 5c and e). Thus we conclude that Ti preferentially occupies the $A_2(\text{Fe})$ site. It is worth noting that $I_{\text{Ti}}/I_{\text{Fe}}$ for the diffraction condition 2 is the lowest in the four conditions used in the experiment, which indicates that two types of the Fe sites, A_1 and A_2 , as well as the A_2 and B sites can be distinguished in the (111) channeling.

The calculation shows that the channeling effect on the (113) planes should be too weak to be useful at 120 kV. The channeling effect observed was indeed weak partly because it was extremely difficult to avoid the excitation of nonsystematic reflections, which can change the electron channeling severely.

Conclusions

Atomic sites of Ti, Cr, Co in high corrosion-resistant Sendust (Fe-9.6%Si-5.5%Al) are determined by channeling enhanced x-ray microanalysis.

1. Strong channeling effect is observed for the (002) planar ALCHEMI, where distinction between the planes containing $A_1(\text{Fe})$ and those containing $A_2(\text{Fe})$ and B(Al, Si) is possible.

2. For the distinction of the A_2 site and the B site, the (111) and (113) planar ALCHEMI was tested. Computer simulation shows that the channeling effect expected is very weak for the (113) plane. However, it is predicted that the use of the (111) systematic condition can distinguish the three atomic sites, A_1 , A_2 , and B, although the channeling effect should be weaker than that for the (002) plane.

3. The (002) Planar ALCHEMI experiments re-

vealed that Cr and Co tend to occupy the A_1 and A_2 sites randomly, although Cr has a weak tendency to occupy the A_2 site preferentially.

4. The (002) and (111) planar ALCHEMI revealed that Ti preferentially occupies the A_2 site.

Burch et al.⁷ reported in their spin-echo experiment that impurity elements to the left of Fe in the periodic table enter the A_2 site and those beneath and to the right of Fe occupy the A_1 site in Fe_3Si . In the present work, preferential occupation of the A_2 site by Ti is observed, but Cr and Co exhibited the tendency to occupy the two Fe sites randomly in the (002) planar ALCHEMI. (111) ALCHEMI experiments on the Cr-bearing and Co-bearing Sendust are being carried out to see whether these elements prefer either of the two Fe sites. The magnetic and anticorrosion properties of the Sendust alloys described in the present studies will be discussed elsewhere.⁸

References

1. H. Masumoto and Y. Yamamoto, *Nippon Kinzoku Gakkaishi* 1: 127, 1937 (in Japanese).
2. See, for instance, M. Takahashi, S. Nishimaki, and T. Wakiyama, *J. Magn. Mat.* 66: 55, 1987.
3. J. Spence and J. Taftø, *J. Microsc.* 130(2): 147, 1983.
4. J. Suwalski et al., *Phys. Stat. Sol.* 53A: K195, 1979.
5. P. A. Doyle and P. S. Turner, *Acta Cryst.* A24: 390, 1968.
6. *International Tables for X-ray Crystallography*, vol. III, Birmingham: Kynoch Press, 1962, 234.
7. T. J. Burch, T. Litrenta, and J. I. Budnick, *Phys. Rev. Lett.* 33: 421, 1974.
8. Y. Nishimura and K. Sato (in preparation).

APPLICATION OF ALCHEMI TO INTERMETALLIC COMPOUNDS

P. R. Munroe and Ian Baker

Ternary substitutional elements are often added to binary intermetallic compounds. The effect of these ternary additions may depend on which lattice site they occupy; therefore, determination of the ternary lattice site is important. One method for determination of lattice site occupancy is a transmission electron microscope (TEM) technique called ALCHEMI,¹ or atom site location by channeling enhanced microanalysis. This paper presents the results of determinations of lattice site occupancy of ternary additions to a number of B2 and L1₂-structured intermetallic compounds by ALCHEMI. Site occupancy determinations by x-ray diffractometry (XRD) are also presented, providing a comparison of these two techniques for ternary atom site location.

Experimental

The following alloys were studied (all compositions are given in atomic %; their structures are given in parentheses): Ni-47Al-3V (B2); Ni-30Al-20Fe (B2); an alloy designated IC-77 with nominal composition Ni_{75.8}Al₂₂Hf_{2.0}B_{0.24} (L1₂); and an L1₂-structured phase with the approximate composition Al_{74.2}Ti₁₉Ni_{6.8}, designated a π phase, in an alloy with composition Al₆₉Ti₂₃Ni_{8.8}. Thin foils were prepared through established electropolishing routes.

For the ALCHEMI studies the thin foils were examined in a JEOL 2000FX TEM, furnished with a Tracor Northern 5500II EDS system. EDS data were recorded using an accelerating voltage of 80 kV, to minimize delocalization effects, using an incident beam divergence of ~ 5 mrad, spot sizes up to ~ 250 nm and acquisition times of up to 400 s. Pairs of data were obtained at two orientations, one in a strong channeling condition and the other in a "random" weak channeling condition. From these data the concentration C_X of an element X on the A atom sites was quantified according to the expression

$$C_X = \frac{(N_X^Z/N_X^R) - (N_B^Z/N_B^R)}{(N_A^Z/N_A^R) - (N_B^Z/N_B^R)}$$

where N_A^Z , N_B^Z , and N_X^Z are the characteristic x-ray intensities of elements A, B, and X in an AB + X or A₃B + X type of composition at the channeling position, and N_A^R , N_B^R , and N_X^R are the characteristic x-ray intensities A, B, and

X at the random position.² Results are the average of five measurements. The error quoted is the standard deviation of the five determinations.

Results

ALCHEMI was used to determine the site occupancy of vanadium in B2-structured Ni-47Al-3V. X-ray spectra were recorded by use of the {100} systematic row over a range of positive and negative values of the deviation parameter from the Bragg condition, S_g . The intensity of the vanadium $K\alpha$ peak, N_V , was ratioed to both the nickel $K\alpha$, N_{Ni} , and aluminum K , N_{Al} , peaks, and plotted as a function of S_g (Fig. 1). The N_V/N_{Al} ratio remains constant, whereas the N_V/N_{Ni} ratio varies with S_g , thus inferring that the V atoms occupy Al sites. However, quantification was more complex. For small deviations (e.g., ~ 0.02 nm⁻¹ positive and negative from the Bragg condition), the calculated fraction C of V atoms on the Al sublattice was $116 \pm 36\%$. When C was calculated from the "symmetry" position (i.e., where S_g is a minimum), and a "random" position (where S_g is large and positive, ~ 0.2 nm⁻¹), the fraction of V atoms on the Al sublattice was $96 \pm 5\%$. Clearly, quantification using spectra acquired at the "random" and at the "symmetry" positions is more accurate. The "symmetry" position can be set very accurately and reproducibly from convergent beam information, but the x-ray intensities at the "random" position vary little with small deviations in diffraction condition.

ALCHEMI studies of intermetallic compounds have been performed previously on compounds at, or near to, stoichiometry. In these cases it is assumed that there are no antisite defects. Yet in compounds which are far from stoichiometry, there may be A atoms on the B sublattice. For example, in Ni-45Al, 10% of the Al sublattice sites are occupied by Ni atoms. Thus if a nickel-rich NiAl thin foil is tilted to an orientation at which the x-ray intensity of the Al sublattice is enhanced, there will be a concomitant enhancement of the nickel x-ray intensity due to the Ni atoms located on the Al sublattice. It is not clear whether ALCHEMI may be applied to such compounds.

For the purposes of ALCHEMI studies on B2-structured Ni-30Al-20Fe it was assumed that Ni and Al sublattices were "perfect"; i.e., there were no antisite defects, which thus implies that all the Fe atoms are located on the Al sublattice. From spectra acquired from the {100} systematic row it was calculated that $70 \pm 5\%$ of the Fe atoms occupied the Al sublattice. That infers that the Fe atoms are

The authors are at Thayer School of Engineering, Dartmouth College, Hanover NH 03755. The research was funded by DOE under grant DE-FG02-87ER45311.

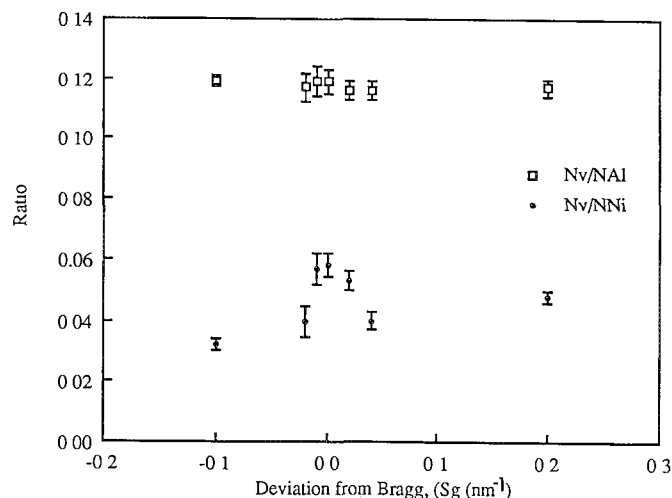


FIG. 1.--Ratios of N_V/N_{Al} and N_V/N_{Ni} as a function of S_g .

partitioned between both sublattices. If this alloy behaves in a similar manner to nickel-rich NiAl, the presence of Fe atoms on the Ni sublattice would result in excess Ni atoms located on the Al sublattice. Iteratively, that implies that the original assumption, that there is no Ni on the Al sublattice, is incorrect. Therefore, in orientations at which the x-ray intensity of Al is enhanced, there may also be some enhancement of the Ni x-ray intensity, so that the experimental data used in the above calculations are questionable. Alternatively, the deviation from stoichiometry through the presence of Fe on the Ni sublattice may be accommodated by constitutional vacancies on the Al sublattice. In this instance the quantified ALCHEMI data would be nominally correct. All one can therefore conclude is that all the Fe is not on the Al sublattice, and that some Fe atoms are located on the Ni sublattice, possibly with some Ni atoms located on the Al sublattice.

In contrast to B2 alloys, planar channeling may not be applied to $L1_2$ compounds, due to the absence of planes containing only A or B atoms. The $\langle 111 \rangle$ zone axis contains columns of A and B atoms well separated from each other, so that axial rather than planar channeling was performed. EDS spectra from IC-77 recorded at both $\langle 111 \rangle$ zone axis and at a weakly channeling "random" position $\sim 3^\circ$ away from the $\langle 111 \rangle$ zone axis are shown in Fig. 2. Quantification of the data showed that $66 \pm 5\%$ of the Hf atoms occupied the Al sublattice. The accuracy of this quantification may be affected by the slight peak overlap between the Al K and the Hf M peaks. Delocalization effects may also affect the accuracy of ALCHEMI quantifications, especially if the integrated intensities of low-energy peaks are used.^{3,4} These effects may be overcome by the use of delocalization correction factors. For example, the delocalization correction factor for the nickel L peak, F_{NiL} , may be calculated from

$$F_{NiL} = (Ni_L/Ni_K)_{\text{zone}} / (Ni_L/Ni_K)_{\text{random}}$$

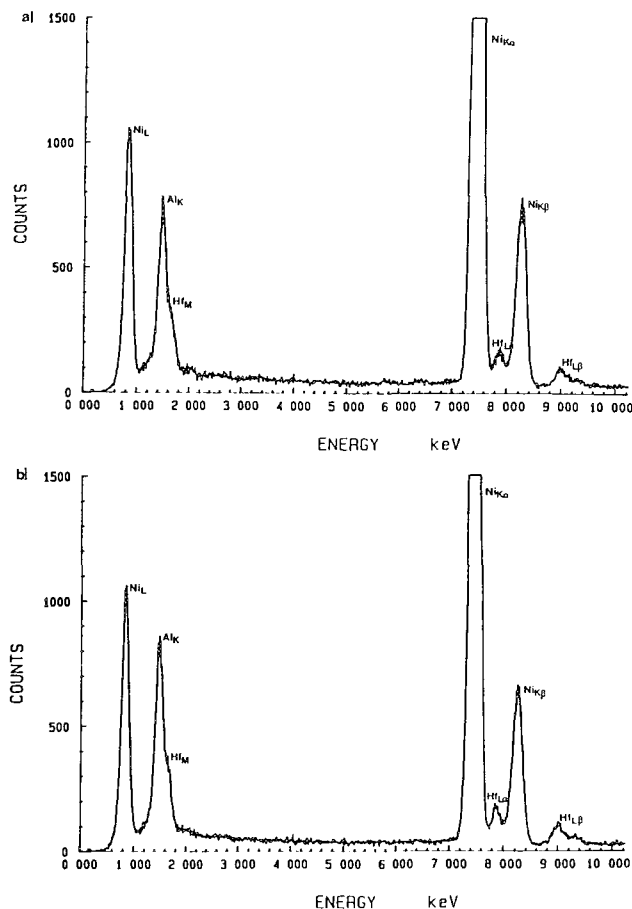


FIG. 2.--EDS spectrum from IC-77 recorded at (a) $\langle 111 \rangle$ zone axis, (b) $\sim 3^\circ$ away from $\langle 111 \rangle$ zone axis.

The expression for the concentration C_X of X atoms on the A sublattice may be modified to incorporate the delocalization correction factors,

$$C_X = \frac{\frac{1}{F_X}(N_X^Z/N_X^R) - \frac{1}{F_B}(N_B^Z/N_B^R)}{\frac{1}{F_A}(N_A^Z/N_A^R) - \frac{1}{F_B}(N_B^Z/N_B^R)}$$

where F_A , F_B , and F_X are the delocalization correction factors for elements A, B, and X in an $AB + X$ or $A_3B + X$ type of composition. For IC-77 a delocalization correction factor may not be directly calculated for aluminum since only the Al K peak is present. In a similar alloy, Bentley estimated a delocalization correction factor for Al K by interpolation between the calculated delocalization factors for the NiL and HfM peaks.⁴ In this study, F_{HfM} may not be readily calculated because of the peak overlap between the Al K and the Hf M peaks. However, spectra were recorded at an operating voltage of 80 kV where delocalization effects are reduced.^{3,5} F_{NiL} was calculated to be 0.85, which suggests that the delocalization correction factor for Al would be close to unity, and the corrected data would fall within the experimental error of the uncorrected data. Thus, the data at the $\langle 111 \rangle$ zone axis were not corrected for delocalization.

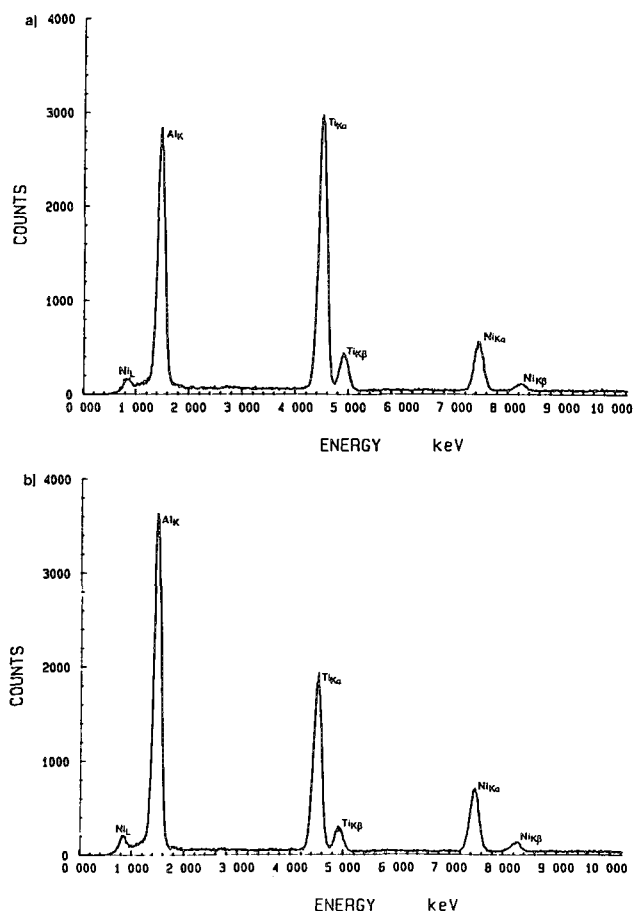


FIG. 3.--EDS spectrum from π phase recorded at (a) $\langle 111 \rangle$ zone axis, (b) $\sim 3^\circ$ away from $\langle 111 \rangle$ zone axis.

in the $L1_2$ -structured π phase of approximate composition $Al_{74.2}Ti_{19}Ni_{6.8}$. From spectra acquired from the $\langle 111 \rangle$ zone axis and the weakly channeling "random" orientation (Fig. 3), it was calculated that $6 \pm 1.5\%$ of the Ni atoms were located on the Ti lattice site. Again, a delocalization correction factor for Al could not be directly calculated, but F_{NiL} was estimated to be 0.9, which again suggests that the delocalization correction factor for aluminum would be close to unity, and the corrected data would fall within the experimental error of the uncorrected data.

X-ray diffractometry (XRD) was performed with unfiltered copper radiation on a Siemens D5000 diffractometer. A detailed description of both the theory and experimental methods used has been given elsewhere.⁶ XRD was performed on powders of the $Al_{69}Ti_{23}Ni_8$ alloy; the IC-77 was examined in the form of a sheet ~ 1 mm thick. Addition of a ternary addition to Ni_3Al , for example, increases or decreases intensity of the fundamental peaks, depending on the value of the atomic scattering factor relative to the atomic scattering factors of Ni and Al, independently of whether the ternary element sits on the Ni or Al sublattice. However, the superlattice peak intensity is strongly affected by both the atomic scattering factor and the site occupancy of the ternary element. Thus, by com-

paring measured (superlattice) intensities with theoretical calculations of intensities (based on an assumption of the ternary atom lattice site occupancy), one can determine on which lattice sites the ternary atoms sit.

For IC-77, the measured ratio I_{100}/I_{200} , by use of Cu $K\alpha$ radiation, was 0.049. A calculation of I_{100}/I_{200} was performed with the assumption that all the Hf, 1 at.% Ni and all the Al occupy the Al sublattice, giving a composition $(Ni_{25})_3(Al_{22}Hf_2Ni_1)$, yielded 0.053. The 8% difference between the calculated and measured values of I_{100}/I_{200} could theoretically be accommodated by having constitutional vacancies on the Ni sublattice, although this outcome seems unlikely given the nickel-rich composition of the alloy. Hf displacing Ni from the Ni sublattice is not a possibility since that would tend to make I_{100}/I_{200} larger. Another possibility is that the composition deviates slightly from the quoted value; for example, an error in the quoted Hf concentration of less than 0.2 at.% could account for the result. (The presence of boron was ignored, since it occupies interstitial lattice sites and thus does not displace any elements with a larger scattering factor, little was present, and it has an atomic scattering factor much lower than that of the other elements present.)

For the $L1_2$ -structured π phase, I_{100}/I_{200} was measured by use of Cu $K\alpha$ radiation; the result was 0.098. The composition suggests that the Ni atoms simply fill up the Al and Ti sublattices not occupied by the Al and Ti, respectively. However, calculation showed that this assumption could not yield the measured I_{100}/I_{200} values. In order to determine the site occupancy, the following calculation was performed. Ti was assumed to occupy only the Ti sublattice and no constitutional vacancies were assumed to be present. The Ni was assumed to partition between both sublattices with Al occupying the remaining sites. That is, a composition of the form

$$(Al_{68.2+6x} + Ni_{6.8-6x})(Ti_{19}Ni_{6x}Al_{6-6x})$$

was assumed, where x is the partitioning fraction (from 0 to 1) of Ni atoms on Ti sites. (The value of 0 still has 0.8 at.% Ni on the Al sublattice for no constitutional vacancies to be present.) The calculated value of I_{100}/I_{200} was set equal to the measured value to obtain x . The value of x obtained for Cu K was 0.49. Thus, the compound is approximately $(Al_{71.1}Ni_{3.9})(Ti_{19}Ni_{2.9}Al_{3.1})$, or 43% of the Ni is on the Ti sublattice. Again, errors in the composition (which was determined by EDS) would lead to changes in the calculated site occupancy.

Discussion

There are several sources of error in the ALCHEMI technique, some of which have been discussed by Bentley for $L1_2$ compounds.⁷ First, the poor energy resolution in EDS leads to

problems in peak overlap, which inhibits the accurate measurement of the integrated intensities of the peaks of interest. This was a problem for Hf in Ni₃Al in the present study. *Second*, small ternary additions (<0.5at%) will be either close to or below the detection limit for that element. Obtaining an accurate integrated intensity from a peak of a ternary addition may be difficult, and is likely to be a source of error. *Third*, delocalization effects, especially in low-energy lines, make quantification of data difficult. Since correction factors may not always be readily calculated, through interpolation for example, they must often be estimated, which can introduce a considerable error factor into any calculations. However, it has been demonstrated that delocalization effects are reduced by the use of lower accelerating voltages.^{3,5} *Fourth*, anti-site defects convolute ALCHEMI data, for example in the π phase it was found that the Ni atoms preferentially occupied the Al sublattice, which results in Al antisite defects on the titanium lattice. Under conditions where atoms on the Ti sublattice are strongly channeled, which leads to enhanced emission of Ti x-rays, there will also be enhancement of the Al x-ray intensity due to those Al antisite defects. This feature makes the experimental integrated x-ray intensities used in the ALCHEMI calculations questionable, and an accurate quantification of the number of Ni atoms on the Ti sublattice cannot be performed through this technique.

Only one of the above problems applies to atom location by XRD; a small amount of a ternary addition may have little effect on the x-ray peak intensities. Peak overlap may only be a problem in multiphase alloys, where peaks from other phases overlap peaks from the phase of interest. There are no delocalization problems; indeed, atom location of particularly light (and heavy elements) may be particularly accurate by this method, because their atomic scattering factors may differ significantly from those of transition metals for example. However, to perform the calculations some arbitrary, although possibly reasonable, assumptions were required. The determination of atom site location through XRD is ultimately limited by the accuracy with which the composition of the phase is known.

Conclusions

ALCHEMI experiments have been performed on a number of B2 and Ll₂-structured compounds. It has been demonstrated that ALCHEMI is easier to use for atom site location in B2 than Ll₂-structured compounds and in near, rather than non-stoichiometric compounds. Atom site location through XRD was found to be useful, although this technique also has experimental limitations.

References

1. J. C. H. Spence and J. Taftø, "A new technique for locating atoms in small crystals," *J. Microscopy* 130: 147, 1983.
2. K. M. Krishnan, "Site occupancy-valence measurements using channeling and related effects in microanalysis," *Mat. Sci. Eng.* B3: 397, 1989.
3. S. J. Pennycook, "Delocalization corrections for electron channeling analysis," *Ultramicroscopy* 26: 239, 1988.
4. J. Bentley, "Site occupations in Ll₂-ordered alloys by axial electron channeling microanalysis," *Proc. 44th EMSA*: 704, 1986.
5. P. R. Munroe and I. Baker, "The effect of delocalization in axial and planar channeling in ordered intermetallic compounds," *J. Mat. Res.* (in press).
6. P. R. Munroe and I. Baker, "Ternary atom site location in Ll₂-structured intermetallic compounds," *J. Mat. Res.* (in press).
7. J. Bentley, "Practical limitations of ALCHEMI on ordered intermetallic alloys," *EMAG-MICRO* 89, 285.

COMBINED MICROBEAM ANALYSIS APPLIED TO THE STUDY OF GOLD OCCURRENCE IN THE PRIMARY ORE OF CARLIN TYPE DEPOSITS IN SOUTHWESTERN CHINA

Yongkang Liu, Xianxian Ye, Zhenya Sun, Shirong Liu, Guanquan Wan, Lind Zhou,
Fangqiong Lu, M. L. Rivers, S. R. Sutton, Zhuoran Lin, and Jiliang Li

Since the mid-1960s many gold deposits of "Carlin" type have been discovered in Guizhou, Sichuan, Yunnan, and Guangxi in Southwest China. Knowledge about the occurrence of gold in Carlin type deposits, referred to as "invisible," has been an open question. In recent years, new results have been obtained with SXRF and AEM-EDX, but further overall work remains to be done for a better understanding of the occurrence and better solution to the recovery techniques of gold in this kind of ore. Our work in this direction has been successful owing to an analysis in which a complementary combination of SEM-EDS, AEM, EPMA, and SXRF is used. This paper reports the results of one study (among many others) of the Yata gold deposit showing the striking revelation of its occurrence which provides the key information for determination of the exploration and recovery method.

Geological

In China, Carlin-type gold deposits are referred to as "micrograined." Although various gold deposits are believed to differ from each other in terms of their petrography, tectonics and period of genesis, mineral association, and elemental constituent, behavior of adjoining rock alteration and occurrence of the gold ores are basically the same. The characteristics of the gold deposit of this kind have been generalized by (1) mostly very fine grain (a few nanometers to a few hundred nanometers), and only rarely with the coarse grain of natural gold up to 10 μm in oxidized ores; (2) ore bodies of irregular shapes, mainly lens shaped and vein shaped; (3) mineralization taking place mainly in fine grain detrital rocks, such as fine grain siltstone, clay rocks, partially in limestone, volcanic sedimentary rocks and tectonic breccia;

Y. and S. Liu, G. Wan, and L. Zhou are at the Institute of Geochemistry, Chinese Academy of Sciences, Wushan, Guangzhou 510640; X. Ye and Z. Sun are at Wukan University of Technology Center; F. Lu, M. L. Rivers, and S. R. Sutton are at the Department of Geophysical Science, University of Chicago, Chicago, IL 60673; and at the Applied Physics Division, Brookhaven National Laboratory, Upton, NY 11973; Z. Lin is at the Institute of Geology, State Seismology Bureau, Beijing 100029, China; and J. Li is at the Second Automobile Factory, Shiyang, Hubei, China. The work was supported by the State Gold Bureau of China and the Office of Gold Deposit Program, Chinese Academy of Sciences.

(4) closely related to the silicious process; and (5) intergrown with pyrite (arsenical pyrites), mispickel, zinniber, zinckenite, etc.

Ore Characteristics

Composition. The main composition consists of SiO_2 (more than 60%), Al_2O_3 (more than 15%), Fe_2O_3 , FeO , K_2O , CaO , MgO and S, with the desired Au as a trace concentration and As, Hg, Sb, and C as unwanted elements.

Mineral Association. Apart from the major associated quartz and clay minerals (kaolinite, montmorillonite, hydromica, etc.), various visible minerals pyrites (arsenical pyrites), polyopyrites, platyophthalmite, orpiment, to-waynite, etc., are associated as minor minerals.

Experimental

Analytical work was carried out with the application of a complementary combination of the following microbeam analysis techniques.

SEM-EDX. Polished sections of ore rock were observed by the backscattered electron image mode in a JEOL 35C SEM equipped with an EDX operating at accelerating voltage 20 kV. Possible gold grains were searched and identified according to their backscatter electron image brightness and EDX spectra.

AEM. Ore powder samples prepared by conventional procedure were observed under an H-600B TEM equipped with EDX.

EPMA. Some gold grains of bigger size were further analyzed with a JEOL JAX-733 electron microprobe analyzer with high-resolution WDX to facilitate better determination of the composition of both the gold grain and the intergrown minerals.

SXRF. Further analyses with high gold-detecting capability were carried out on gold-bearing arsenical pyrites and clay minerals by use of the SXRF facilities at the Brookhaven National Laboratory, USA.

Results: Occurrence of Gold

Through the combined analysis of complementary microbeam techniques, natural gold grains have been effectively found with the main minerals quartz, clays and arsenical pyrite of the ore-bearing rocks. The gold grains or aggregates are found embedded between grains of quartz or clays and inside the microcracks of quartz or clays. Many more gold grains have been found within the arsenical pyrite (regarded as a gold-bearing mineral) in the form of inclusions, but not isomorphous substitution or

so-called absorbed film.

The gold grain sizes in the unweathered original ore range from 7 nm to 0.2 μm . Gold grains larger than 1 μm are usually found in the weathered cracks. Occasionally 10 μm gold grains are found in the strongly weathered sites.

Some electron micrographs of SEM and TEM and spectra of EDX, EPMA, and SXRF are presented below to show the typical results.

Gold in Arsenical Pyrite. Photo 1 shows the EPMA result on a gold grain included in arsenical pyrite, giving the secondary electron image at the lower left, the Au $L\alpha$ x-ray image at the lower right, the As $K\alpha$ x-ray image at the upper left, and the Fe $K\alpha$ x-ray image at the upper right.

Figure 1 shows the EPMA x-ray spectra of the gold grain in Photo 1.

Photo 2 shows the EPMA backscattering electron image of an arsenical pyrite with an included natural gold grain in the center.

Figure 2 shows the EPMA x-ray spectra of the gold grain in Photo 2; note that the arsenic $K\alpha$ has appeared because of the spreading of the probe electron into the arsenical pyrite matrix.

Photos 3 and 4 are paired, showing a gold grain in arsenical pyrite and the Au $L\alpha$ x-ray intensity of linescan through the grain, giving a significant peak corresponding to the gold grain.

Figure 3 shows the result on SXRF analysis, providing further confirmation of gold existence in fine-grain arsenical pyrite.

Photo 5 shows the TEM micrograph of a gold grain in arsenical pyrite which is confirmed by the in situ EDX analysis result shown in Fig. 4.

Gold in Clays. Photo 6 is a TEM micrograph with 300 000 \times magnification, showing a gold grain smaller than 7 nm embedded in a kaolinite crystal, which has also been confirmed by in situ EDX analysis.

Photo 7 is a SEM micrograph showing a grain of natural gold embedded in the stratification of a clay, which is confirmed by in situ EDX analysis shown in Fig. 5 with significant peaks of Au, Si, Al, K, etc.

Figure 6 is the result of SXRF analysis on a clay crystal proper with no Au peak, showing that gold has been undetectable within the crystal of clay minerals. This does not mean that gold cannot exist as an interstitial between clay crystals.

Gold in Quartz. Photo 8 is an SEM micrograph showing a grain of natural gold embedded between grains of quartz, which is confirmed by in situ EDX analysis shown in Fig. 7.

References

1. J. R. Chen, E. C. T. Chao, J. A. Minkin, J. M. Back, W. C. Bagby, M. L. Rivers, S. R. Sutton, B. M. Gordon, A. L. Hanson, and K. W. Jones, *Nuclear Instruments and Methods in Physics Research* B22: 394-400, 1987.
2. J. A. Minkin, E. C. T. Chao, J. M. Back,

and J. R. Chen, *Microbeam Analysis--1987*, 329.

3. J. D. Well and T. E. Mullens, *Economic Geology* 68: 183, 1973.

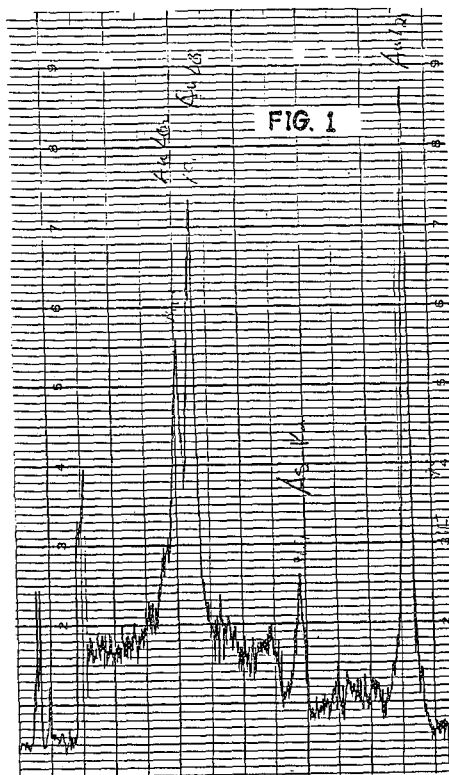


FIG. 1

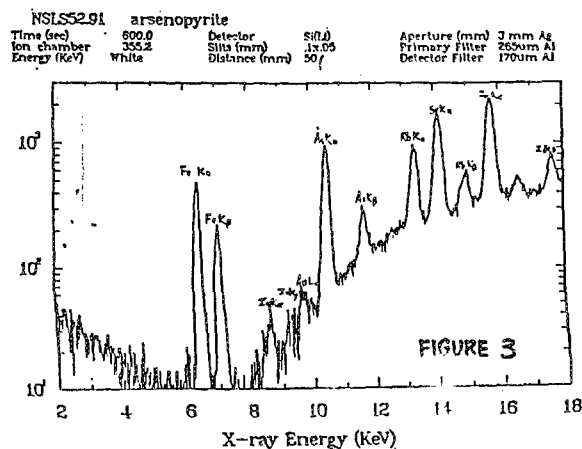


FIGURE 3

FIG. 2

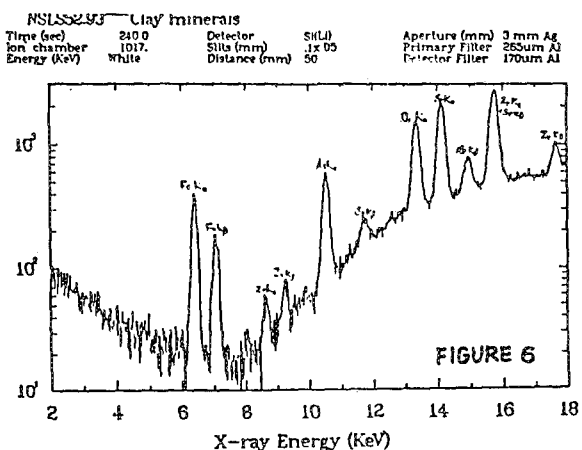


FIGURE 6

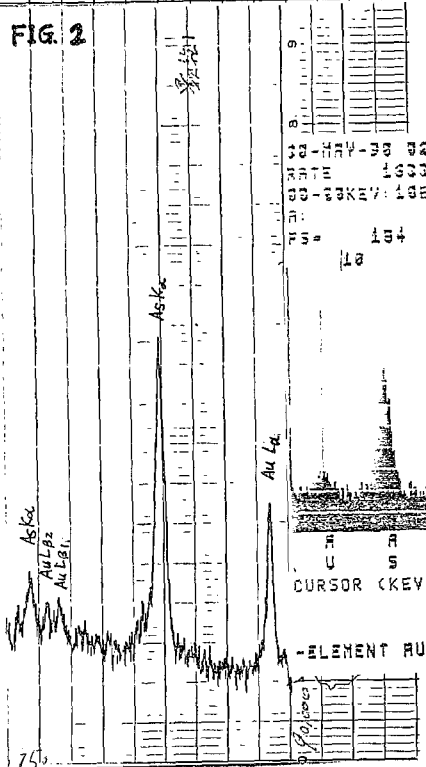


FIG. 4a

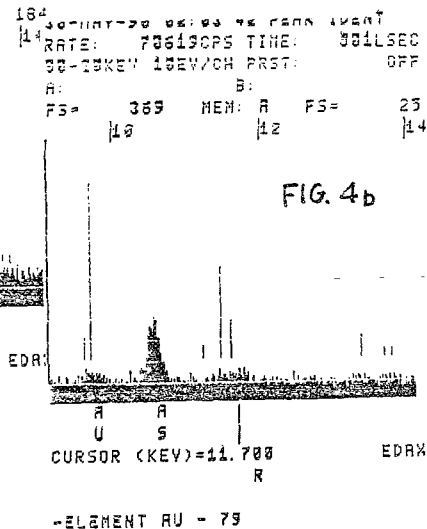
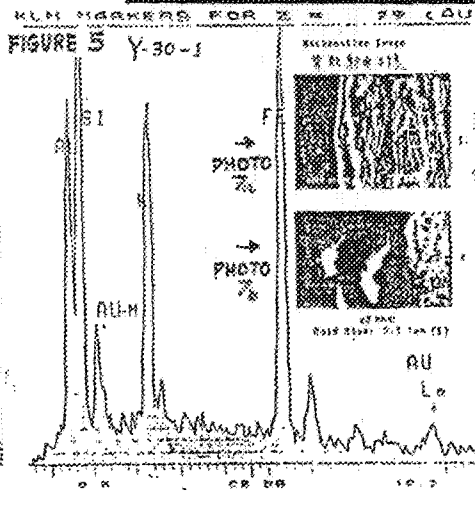
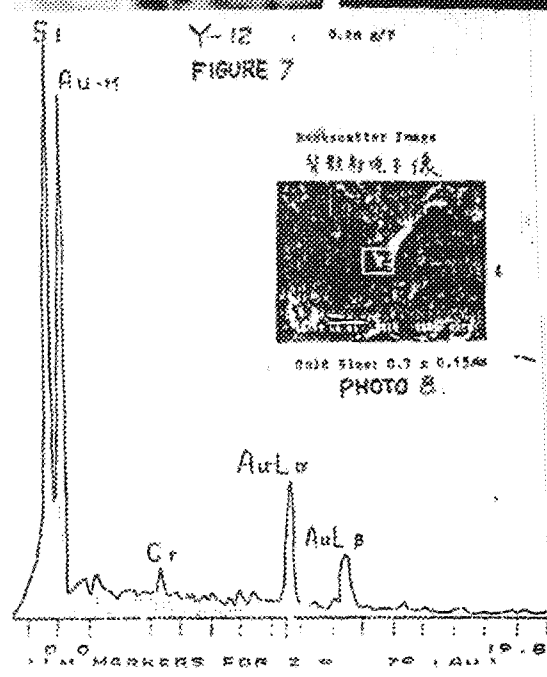
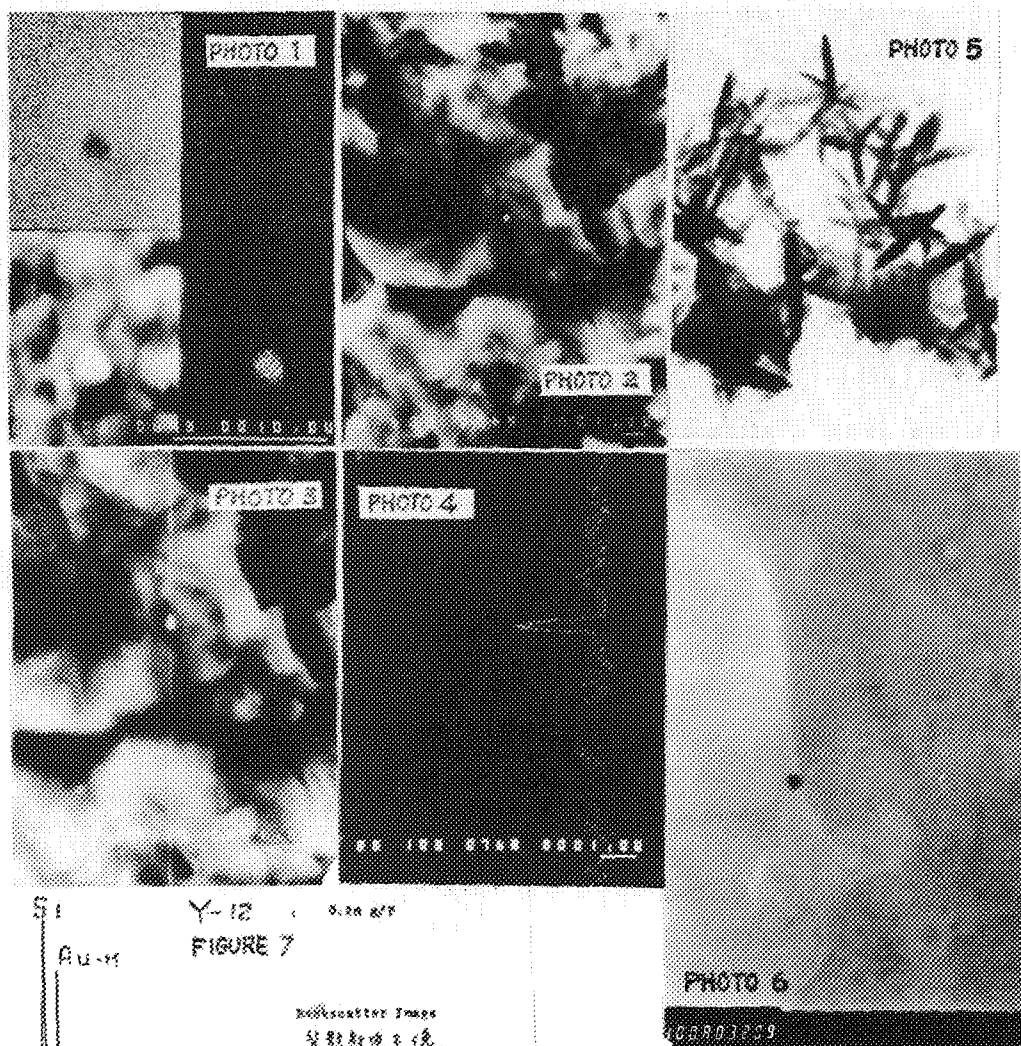


FIG. 4b



SITE OCCUPATION OF TERNARY ELEMENT IN AN AlTi COMPOUND BY ALCHEMI

Yunrong Ren, Ya Xu, Zuqing Sun, and Guoliang Chen

Site occupation of alloying addition in AlTi compounds is important for high-temperature alloy development. In this paper, we locate the ternary element Nb in an AlTi compound by the ALCHEMI technique. With the $L1_0$ -type structure, the planes of either (110) or (001) are composed of Al and Ti atoms alternately. A standing electron wave can be obtained when the incident beam is set to be nearly parallel to the (110) or (001) plane. Figures 1(a) and (b) show the $L1_0$ -type structure of the AlTi compound and its atomic arrangement. The standing electron waves were excited across (110) planes as shown in Fig. 1(c). The density of a standing wave has a maximum at the planes of Al atoms for $s > 0$ conditions and at the planes of Ti atoms for $s < 0$ conditions. Characteristic x-ray intensities depend directly on the density of the incident electrons at the atomic planes. Therefore, the ternary element dissolved in the AlTi compound can be easily located by the ALCHEMI technique.^{1,2}

Experiment

A specimen of 51.1at%Al-41.5at%Ti-7.4at%Nb alloy was used. The structure of this specimen is composed of AlTi, Ti_3Al , and other intermetallic compounds, which were examined by x-ray diffraction and electron diffraction. The electron micrograph of this specimen (Fig. 2) is of lamellae of the AlTi phase about 1 μm wide. An Nb-free specimen of AlTi was used in comparison with the Nb-containing sample. Experiments were performed with a Philips EM400T analytical electron microscope equipped with an EDAX 9100 EDS system at an accelerating voltage of 100 kV. The specimen was tilted to $\sim 30^\circ$. For ALCHEMI experiments, the incident electron beam was set to be nearly parallel to the (110) planes. The characteristic x-ray spectra were recorded from the crystal of AlTi under three diffraction conditions: at positive deviation ($s > 0$) from the exact Bragg diffraction condition, at negative deviation ($s < 0$) from the exact Bragg diffraction condition, and at a nonchanneling condition in which no low-order diffraction spots were excited. At the former conditions, the reflection (110) was excited. A spot size 400 nm in diameter in the microprobe was used. The beam convergence angle was about 1.2 mrad. X rays were collected for 100-200 s with a counting rate about 2000 cps.

Results

The x-ray spectra and the corresponding diffraction conditions are shown in Figs. 3-5.

The authors are at the University of Science and Technology Beijing, Beijing 100083, China.

Numerical data of the x-ray intensities of the spectra shown in Fig. 4 are listed in Table 1. From Fig. 3 we see clearly that the $L1_0$ -type structure is very sensitive to the electron channeling effect. Figure 4 shows that the ratio of the intensity of Ti and Nb peaks is approximately a constant under various diffraction conditions. It can be estimated that Nb atoms probably lie in Ti planes. The calculation was performed with the equation³

$$F_x = (1 - R_b)/(R_a - R_b)$$

where $R_a = (N_1^x/N_1^a)/(N_2^x/N_2^a)$, $R_b = (N_1^x/N_1^b)/(N_2^x/N_2^b)$, F_x is the fraction of ternary element on the site with A or B atoms, and N is the number of x-ray counts for atoms. Diffraction conditions were denoted by subscripts 1 and 2 for the nonchanneling and channeling spectrum, respectively. The combination of one channeling spectrum ($s > 0$ or $s < 0$) plus a nonchanneling spectrum was used for calculation. The results of the calculation of the fraction F_{Nb} with the data obtained from three different regions of the specimen are in the range of 102% to 106% with an average of $F_{Nb} = 104\%$. The reproducibility of this experimental value of F_{Nb} is acceptable.

TABLE 1.--Characteristic x-ray intensity (10^2 counts in peak).

	$s > 0$	$s < 0$	Nonchanneling
AlK	190.88	165.86	171.54
NbL	55.58	91.09	67.54
TiK	273.40	434.62	327.79

Conclusion

It can be concluded that approximately 100% Nb atoms lie in the planes of Nb atoms. We also noted that there was an error of $\sim 5\%$ in the F_{Nb} value in the present study, since the site-occupation determination by ALCHEMI is not fully quantitative. The accuracy of the ALCHEMI technique could be improved if a correction for the so-called localization effect were applied to the results obtained. This correction will be made in future studies.

References

1. J. C. H. Spence and J. Taftø, *Microsc.* 130: 147, 1983.
2. D. Shindo et al., *J. Electron Microsc.* 35: 4, 409, 1986.
3. M. T. Otten, *Philips Electron Optics Bulletin* 126: 21, 1989.

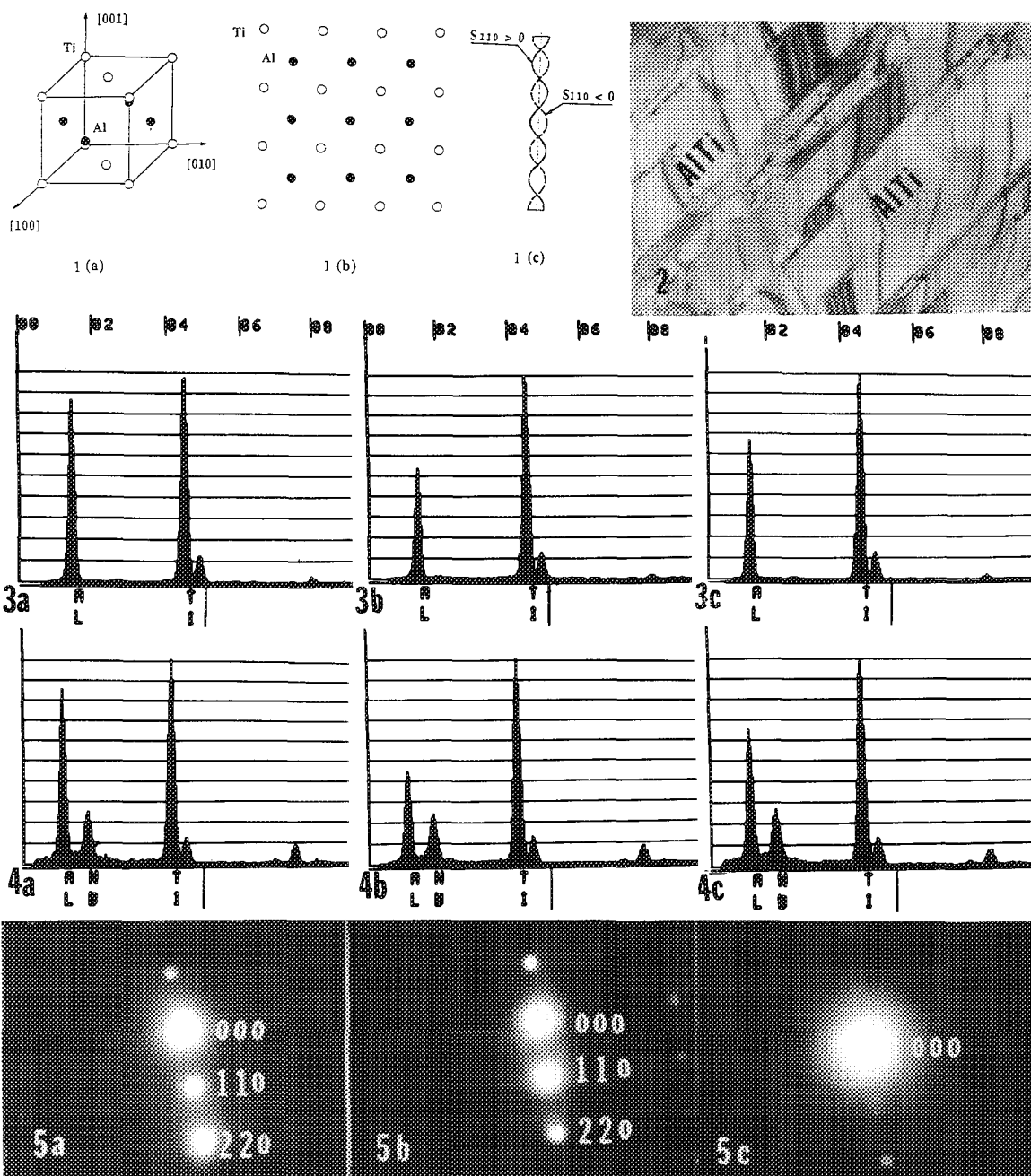


FIG. 1.--(a) Li_0 -type structure of AlTi , (b) atomic arrangement of AlTi projected along [001] direction, (c) standing-electron-wave schemes.

FIG. 2.--Transmission electron micrograph of AlTi compound with Nb. (Bar = 1 μm .)

FIG. 3.--Characteristic x-ray spectra of AlTi compound for (a) $s > 0$, (b) $s < 0$, (c) nonchanneling diffraction conditions.

FIG. 4.--Characteristic x-ray spectra of AlTi compound with Nb; diffraction conditions as in Fig. 3.

FIG. 5.--Electron diffraction patterns for (a) $s > 0$, (b) $s < 0$, (c) nonchanneling.

PRACTICAL IMPORTANCE OF SPATIAL RESOLUTION AND ANALYTICAL SENSITIVITY IN AEM X-RAY MICROANALYSIS

Jing Zhang, D. B. Williams, and J. I. Goldstein

Solutions to many materials science problems are based on the compositional analysis of components in multiphase microstructures that are often on a scale as fine as 10 to 100 nm. One of the most important advantages of the analytical electron microscope (AEM) is its ability to achieve high-spatial-resolution chemical analysis with x rays. Spatial resolution and analytical sensitivity are two fundamental parameters in AEM x-ray microanalysis. For many materials problems, especially when a nonequilibrium system is involved, it is very important that these two parameters are optimized. In this paper, we characterize these two parameters, using heat-treated Fe-Ni alloys for the determination of the low-temperature Fe-Ni phase diagram.

Spatial Resolution and Analytical Sensitivity

The spatial resolution of x-ray microanalysis is the size of the x-ray source, which is determined by the electron-probe diameter and the electron-beam broadening in the specimen.¹⁻³ Other factors such as specimen drift, stray radiation, and the geometry of the phases also affect the spatial resolution. Analytical sensitivity is the ability to distinguish, for a given element under given analysis conditions, two concentrations that are nearly equal. The analytical sensitivity is directly related to the number of peak x-ray counts collected and to the peak-to-background ratio, and therefore to the probe current, specimen thickness, and counting time.⁴ The spatial resolution and analytical sensitivity are interrelated. The use of a smaller probe size and a thinner specimen yields a higher spatial resolution. However, the resulting lower beam current and smaller x-ray excitation volume x-ray intensity and therefore degrades the analytical sensitivity.

Experimental

The diffusion of Ni in Fe-Ni alloys is extremely sluggish at low temperatures; for example the interdiffusion coefficient is $\sim 10^{-25}$ cm²/s in austenite at 400 C.⁵ As a result, it is practically impossible to expect significant atom movement in austenitic Fe-Ni alloys below 400 C. However, alloys containing <30wt% Ni

The authors are in the Department of Materials Science and Engineering, Lehigh University, Bethlehem, PA 18015. This research was supported by NASA Grant NAG 9-45. The technical aid of Drs. J. R. Michael (Sandia National Laboratory) and C. E. Lyman (Lehigh University) is gratefully acknowledged.

will transform to martensite and the diffusion coefficient of the martensite is at least six orders of magnitude larger than that of the austenite. The martensite will decompose into a two-phase structure during aging. Under the assumption of interface equilibrium, the interfacial composition of the two phases should represent the equilibrium on the nonequilibrium phase boundaries at the heat-treatment temperature. The difficulty in determining the low-temperature Fe-Ni phase diagram is due to the very fine two-phase structure resulting from the low diffusivity. The two-phase structure of the decomposed martensite Fe-Ni alloys investigated in this study is composed of a high-Ni fcc precipitate phase and a low-Ni bcc matrix phase. The width of the precipitates varies from roughly 100 nm at 400 C to 10 nm at 300 C for a one-year heat treatment.

A Philips EM430T TEM/STEM with a Link intrinsic Ge EDS detector and a Link AN10000 system, and a Vacuum Generators (VG) HB501 STEM with a Link Si(Li) windowless EDS detector and a Link AN10000 system were used for analysis. The electron probe diameter of the HB501 STEM (100 kV) used in this study was 1.8 nm (FWTM) and was measured by scanning the probe across a thin crystal of MgO.⁶ The beam current in this probe was 0.5-0.8 nA, which gave an analytical sensitivity of $\sim 5\%$ in 20nm-thick specimen regions for a 100s counting time. We measured the intensity distribution in the focused electron probe of the EM430T AEM (300kV) operating in the STEM mode by recording the probe image on a photographic plate and measuring the film density level using a densitometer. The smallest STEM condenser-lens setting that yields a minimum acceptable analytical sensitivity (5-10% for a 50-100nm specimen thickness and 2min counting time) is spot size setting 5. This probe has a 0.09nA beam current with a FWHM probe diameter of 4.0 nm and a FWTM probe diameter of 6.8 nm for a 50 μ m C2 aperture. Figure 1 shows the measured intensity profiles of this probe. Use of a large C2 aperture (100 μ m) results in a distorted probe shape with a major increase in the FWTM probe diameter (Fig. 1c). Hence the spatial resolution is degraded. The focusing condition of the probe forming lens (objective lens) for STEM imaging is different from the focusing condition for microanalysis for this probe size/C2 aperture combination. The electron probe shown in Fig. 1(a) has the smallest FWHM diameter and will probably give the best STEM image. However, the highest spatial resolution microanalysis will be achieved with the probe shown in Fig. 1(b), which is approximately Gaussian and has the smallest FWTM diameter. The objective

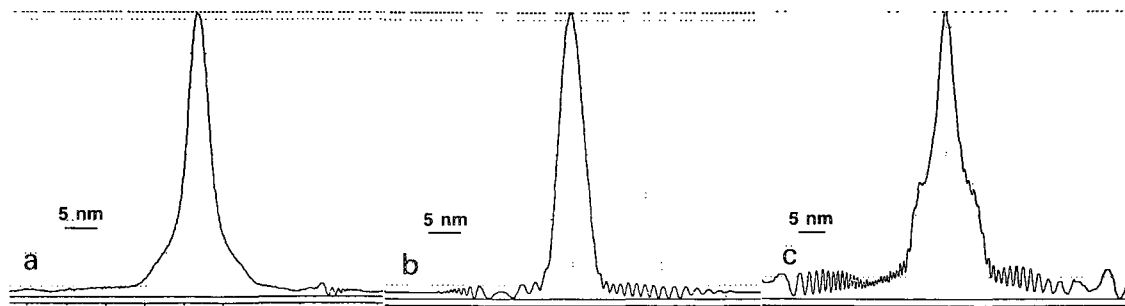


FIG. 1.--Densitometer intensity profiles of electron probe of EM430T operating at 300 kV and STEM mode, spot size setting 5. (a) and (b) 50 μm C2 aperture, different objective lens focusing (see text); (c) 100 μm C2 aperture.

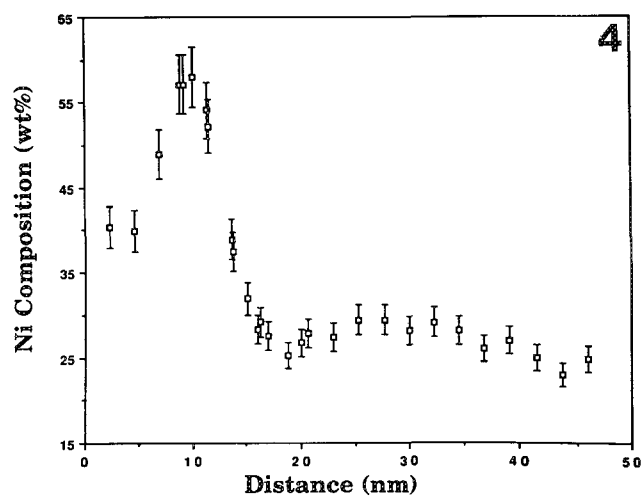
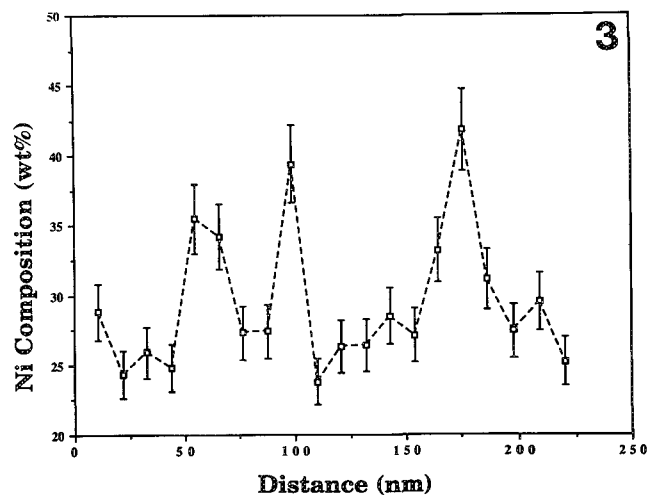
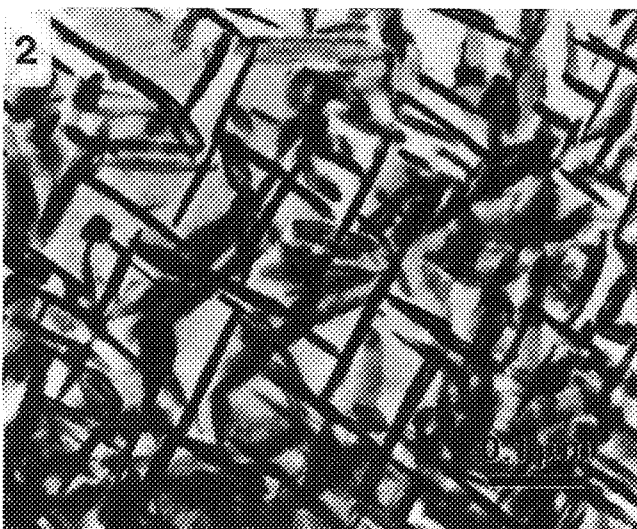


FIG. 2.--TEM BF image of Fe-30wt%Ni alloy heat treated at 300 C for 370 days. Precipitate phase (~ 10 nm wide) has fcc structure, matrix has bcc structure.

FIG. 3.--Ni composition profile across precipitates in Fe-30wt%Ni specimen measured using EM430T AEM. Spatial resolution was not high enough to permit accurate composition measurement.

FIG. 4.--Ni composition profile across one precipitate in Fe-30wt%Ni specimen measured with HB501 STEM.

FIG. 5.--TEM BF image of Fe-25wt%Ni alloy heat treated at 400 C for 362 days; fcc precipitates are about 50 to 100 nm wide.

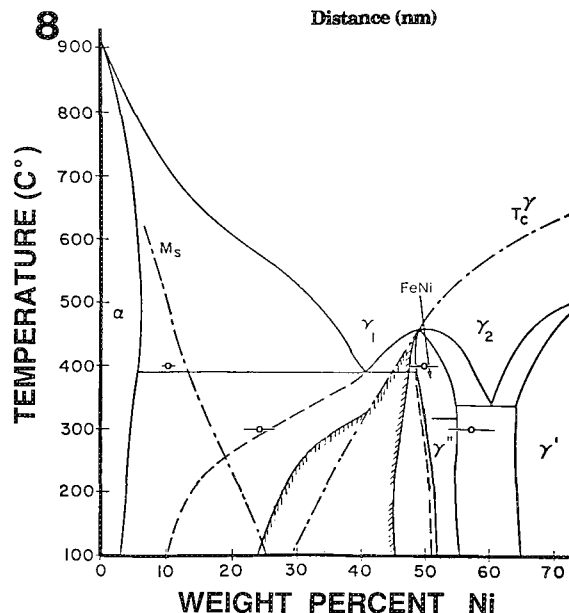
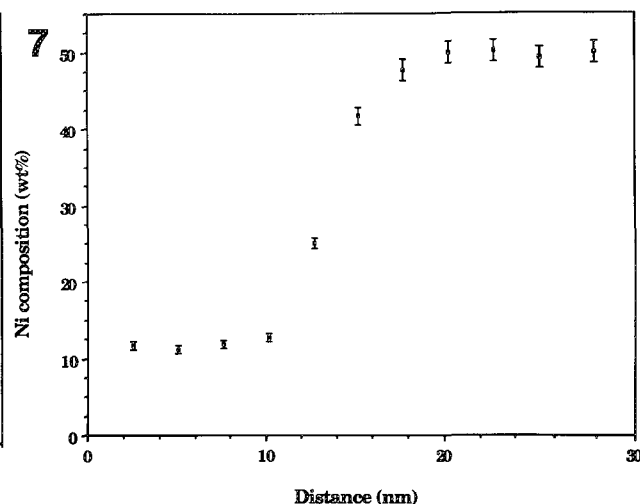
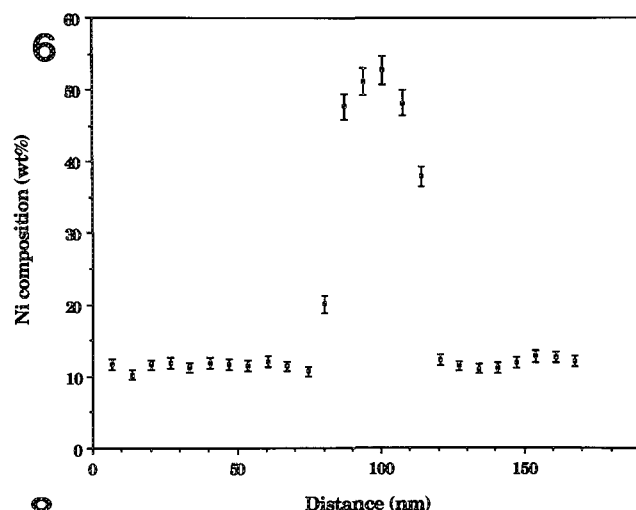


FIG. 6.--Ni composition profile across one precipitate in Fe-25wtNi specimen measured with EM430T AEM. Spatial resolution of EM430T was high enough to measure composition of precipitates in this specimen.

FIG. 7.--Ni composition profile of precipitate/matrix interface in Fe-25wtNi specimen measured with HB501 STEM. Result is consistent with those measured with EM430T.

FIG. 8.--Current Fe-Ni phase diagram.¹¹ Low-temperature portion (<400 C) was determined from iron meteorite data. -- indicates the measured Ni composition and error in this study.

Results and Discussion

lens focusing difference between the probe in Figs. 1(a) and (b) is 200 nm. This situation has been predicted by theoretical calculations.⁷ This problem does not exist for the large probe size setting (such as probe size STEM 4 and the same C2 aperture). In this case, the Gaussian probe has the smallest FWHM and FWTM diameter, and hence is the best electron probe for both STEM imaging and microanalysis.

The specimen thickness was estimated by the x-ray count method. A calibration curve of 0-10keV x-ray counts per pA in a fixed time period was measured for each AEM on an Fe-Ni specimen.⁸ The specimen thickness measured for the calibration curve was obtained by the EELS log-ratio method.⁹ The specimen drift was controlled during the analysis by Link software that automatically corrected for specimen drift. The spatial resolutions were calculated from the known probe size and beam broadening parameters that were calculated from the single-scattering mode.^{3,10} The error bars on the composition profiles shown in this study are obtained by combining the standard deviation for both elements at the 95% confidence level; i.e., $2(\sigma_{\text{Fe}}^2 + \sigma_{\text{Ni}}^2)^{1/2}$

Figure 2 is a TEM BF image of an Fe-30wt%Ni alloy which was heat treated at 300 C for 370 days and shows the morphology of the decomposed martensite structure. The intragranular precipitates are about 10 nm wide. EDS x-ray analysis was performed on regions near the edge of the specimen where no overlapping of the precipitates was observed. The composition profiles across the precipitates measured with both the EM430T and the HB501 are shown in Figs. 3 and 4, respectively. The specimen thickness of the regions where the two traces were measured was 35 nm (Fig. 3) and 27 nm (Fig. 4), respectively. The calculated spatial resolution was ~ 7 nm for the EM 430T and ~ 2 nm for the HB501. The calculated spatial resolution of EM430T is about the same as the width of the precipitate phase. However, the actual spatial resolution is worse due to the geometry of the precipitate and the specimen drift. Therefore, the measured composition of this specimen using the EM430T was not accurate. The VG STEM has a higher spatial resolution at the same analytical sensitivity level. Although the actual spatial resolution shown in Fig. 5 (~ 4 nm) is somewhat larger than the calculated value, it is still less than half the precipitate width. Therefore, the accuracy of the composition of this specimen measured by the VG STEM is limited only by analytical sensitivity.

Figure 5 is a TEM BF image of an Fe-25wt%Ni alloy which was heat treated at 400 C for 362 days showing the precipitates formed in the original martensite lath boundaries. The precipitates are about 50-100 nm wide. A Ni composition profile across a precipitate measured using the EM430T is shown in Fig. 6. The specimen thickness in this region was 51 nm and the calculated spatial resolution was ~8 nm. This spatial resolution should give an accurate measurement of the composition of this specimen, since the precipitate phase was much larger than the spatial resolution and no composition gradient was measured in matrix. This point is confirmed when the same specimen is measured by the VG STEM. Figure 7 shows such a VG STEM Ni composition profile of the specimen. The calculated spatial resolution of this measurement is 8 nm, although the step size in this measurement is much smaller.

The measured precipitate and matrix compositions are shown in the current Fe-Ni phase diagram (Fig. 8). The low-temperature portion (<400 C) of this phase diagram was determined according to the analytical data of the iron meteorites.¹¹ The 300 C data of this study seem to be on the boundaries of the miscibility gap. The Fe-Ni ordering observed in iron meteorites was not observed in this alloy. It is possible that the high-Ni side of the miscibility gap boundary is at ~57wt%Ni at 300 C. The 400 C data suggest that the proposed eutectoid temperature is above 400 C. The significant difference in matrix composition between the measured value and that predicted by the phase diagram has yet to be explained. Perhaps it is another metastable state of Fe-Ni alloy during the martensite decomposition.

Conclusion

Characterization of the instrument parameters that affect the spatial resolution is very important, especially for microanalysis at the top performance limit of the AEM instrument. The spatial resolution obtained is usually lower than the theoretical value, especially in the thinnest regions of the specimen. However, the calculated value gives a good estimation considering the fact that many sources of error are not counted.

The current Fe-Ni phase diagram determined from iron meteorite data needs to be revised with the addition of nonequilibrium features. In order to utilize the compositions measured through AEM microanalysis for phase diagram delineation, the spatial resolution and the analytical sensitivity conditions must be well known.

References

1. J. I. Goldstein, J. L. Costley, G. W. Lorimer, and S. J. B. Reed, "Quantitative x-ray analysis in the electron microscope," *SEM/1977* I, 315.
2. P. Doig, D. Lonsdale, and P. E. J. Flewitt, "Electron intensity distributions in STEM-EDS x-ray microanalysis of thin foils," in

M. H. Jacobs et al., Eds., *Quantitative Microanalysis with High Spatial Resolution*, London: Metals Soc., 1981, 41.

3. S. J. B. Reed, "The single-scattering model and spatial resolution in x-ray analysis of thin foils," *Ultramicroscopy* 7: 405, 1982.

4. D. B. Williams, *Practical Analytical Electron Microscopy in Materials Science*, Mahwah, N.J.: Philips, 1984, 82.

5. D. C. Dean and J. I. Goldstein, "Determination of the interdiffusion coefficients in the Fe-Ni and Fe-Ni-P systems below 900 C," *Met. Trans.* A17: 1131, 1986.

6. J. R. Michael, "Probe size measurement in a field-emission STEM," *Microbeam Analysis --1988*, 60.

7. G. Cliff and P. B. Kenway, "Fourier analysis of focused electron probes in STEM," *Inst. Phys. Conf. Ser.* 78: 113, 1985.

8. J. I. Goldstein, C. E. Lyman, and Jing Zhang, "Spatial resolution and detectability limits in thin film x-ray microanalysis," this volume.

9. T. Malis, S. C. Cheng, and R. F. Egerton, "EELS log-ratio technique for specimen-thickness measurement in the TEM," *J. Electron Microsc. Techn.* 8: 193, 1988.

10. J. R. Michael, D. B. Williams, C. F. Klein, and R. Ayer, "The measurement and calculation of the x-ray spatial resolution obtained in the analytical electron microscope," *J. Microscopy* (in press).

11. K. B. Reuter, D. B. Williams, and J. I. Goldstein, "Determination of the Fe-Ni phase diagram below 400 C," *Met. Trans.* A20: 719, 1989.

SIMULTANEOUS EVALUATION OF WEIGHT FACTORS AND k FACTORS FOR QUANTITATIVE X-RAY MICROANALYSIS OF THIN SPECIMENS

Y. M. Heng and G. T. Simon

Quantitative analyses of elemental content in thin specimens by x-ray energy-dispersive spectroscopy (XEDS) in the transmission electron microscope are commonly effected by the Cliff-Lorimer ratio approach or the Hall's peak-to-continuum normalization method.^{1,3} The former method is mainly used in metallurgy; the latter is favored in biology. These two methods require accurate proportionality factors in order to convert the characteristic x-ray intensities I_a and I_b , to the concentrations of the elements C_a and C_b . Nevertheless, both factors can be related as follows³:

$$\text{Hall's Weight factor} = W_a = C_a / (I_a / I_c) \quad (1)$$

$$\text{Cliff-Lorimer k factor} = k_{ab} = (C_a / C_b) (I_b / I_a) \quad (2)$$

$$\text{Therefore, } W_b = W_a k_{ba} \quad (3)$$

where I_c is the intensity of a fixed continuum region and Eq. (3) assumes that the Z^2 of the compositions of the two standards are not significantly different. This study evaluates the accuracy of the W_p and W_{Ca} , which were determined using standards. To accomplish this evaluation, these factors were used to determine kp_{Ca} , which was then compared to that measured from compounds of known stoichiometry, as well as that calculated theoretically. This procedure permitted an assessment of the reliability of applying theoretical k factors in Eq. (3) to calculate W_b .

Method

Preparations of Ca naphthenate and triphenylphosphine as absolute standards have been described previously.⁴ Resin-embedded $Ca_{10}(PO_4)_6 \cdot 2(H_2O)$ and $CaHPO_4$ were used as binary standards. Sections about 70 nm thick were analyzed on Cu grids. Analyses were performed with a JEOL 1200EX TEMSCAN operated at 80 kV, equipped with a Tracor-Northern Be window (Si(Li) detector and TN-5500 multichannel analyzer. Spectra were processed and the theoretical k factor was calculated by the BIOQ program in the TN-5500. Correction and mass loss were minimal under the present conditions.

Results

Figure 1 shows the calibration curves of peak-to-continuum ratios vs concentrations for calcium and phosphorus. Three continuum regions were analyzed and compared. Table 1 compares the weight factors determined from stan-

dards with those calculated from experimental and theoretical k factors. These k factors are listed in Table 2.

TABLE 1.--Weight factors determined from standards and from calculations based on experimental and theoretical k factors.

Method	Continuum Region		
	1.34-1.64keV	4.50-5.50keV	4.00-6.00keV
Calcium			
A	186 ±12	203 ±12	432 ±23
B	206 ±12	210 ±13	421 ±26
C	259	264	528
Phosphorus			
A	275 ±18	280 ±12	561 ±20
B	248 ±15	271 ±17	576 ±35
C	198	216	459

*Method A: Eqn(1)

B: Eqn.(3) with [k]-Exp

C: Eqn(3) with [k]-Theo

Note that + values are curve-fitting errors

TABLE 2.-- kp_{Ca} factors determined from Ca-P compounds, W_p/W_{Ca} , and theoretical calculation.

<u>Ca-P</u>	<u>W-P/W-Ca</u>			<u>BIOQ</u>
	<u>Continuum Regions(keV)</u>			
	<u>1.34-1.64</u>	<u>4.50-5.50</u>	<u>4.00-6.00</u>	
135 ±0.08	148 ±0.20	138 ±0.11	130 ±0.12	106
	141**		128***	

*Ca-P compounds **Ref.(3) ***Ref.(6)[5.5-6.5keV]

BIOQ = Tracor-Northern 'BIOQ' program

Conclusion

All three continuum regions gave satisfactory results. However, the narrow window of the lowest region may be subjected to statistical errors. Weight factors of Ca and P measured from resin-embedded standards were proved to be accurate. The kp_{Ca} factor calculated from Eq. (3) agrees well with the same factor determined independently but under the same analytical conditions. However, the theoretical kp_{Ca} factor deviated significantly from both experimental values. The theoretical factor

The authors are at the E. M. Facility, Faculty of Health Sciences, McMaster University, Hamilton, Ont., Canada.

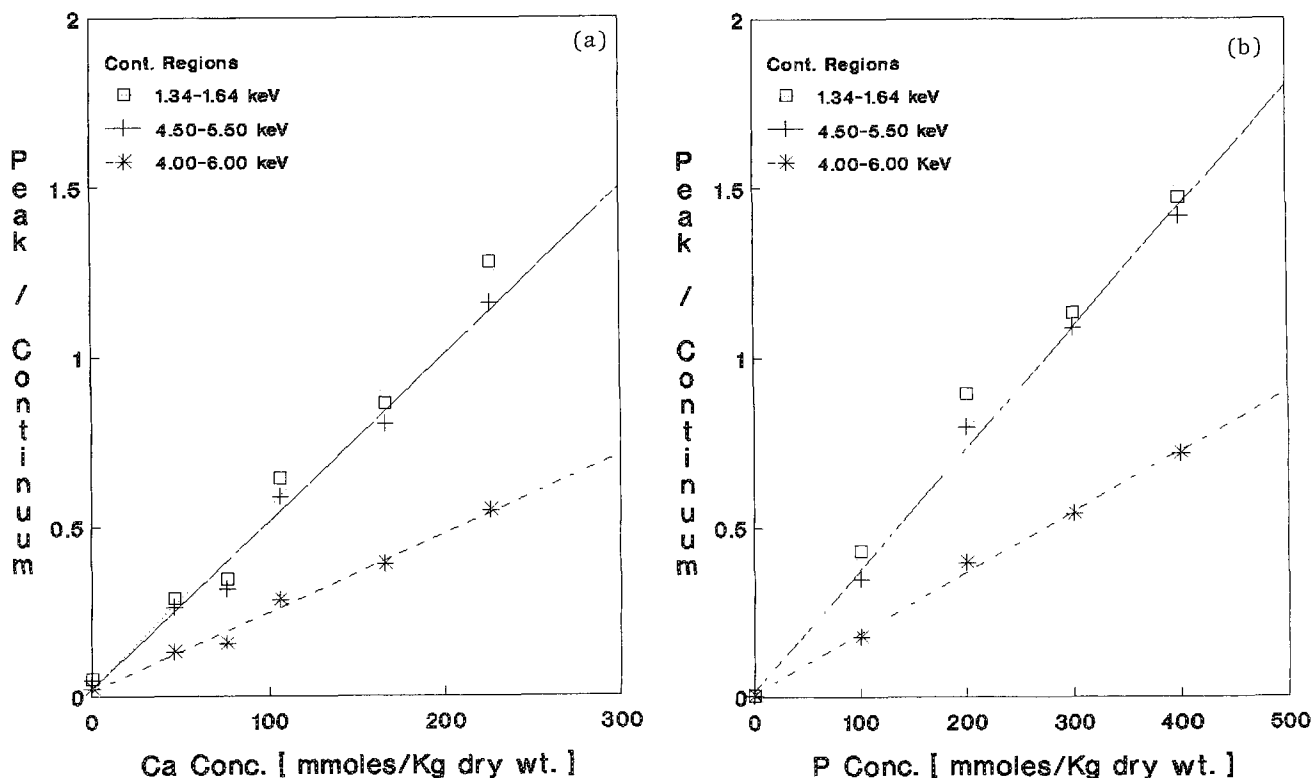


FIG. 1.--Calibration curve of (a) Ca, (b) P for Hall's method.

was shown to be inaccurate for this particular analytical setup because the cross-calculated weight factors were significantly higher for Ca or lower for P compared with the experimental weight factors. Since extrapolation of weight factors from one known factor is an indirect method, both known weight factor and k factor must be carefully assessed. It is therefore necessary that at least two weight factors must be measured directly from standards.

References

1. G. Cliff and G. W. Lorimer, *J. Microsc.* 103: 203, 1975.
2. T. A. Hall, in G. Osler, Ed., *Physical Techniques in Biological Research*, New York: Academic Press, 1971, 1A.
3. H. Shuman et al., *Ultramicroscopy* 1: 317, 1976.
4. G. T. Simon and Y. M. Heng, *Proc. XI ICXOM*, 1986, 416.
5. G. Roomans, *J. Electron Microsc. Tech.* 9: 19, 1988.
6. H. K. Hagler et al., *J. Microsc.* 131: 221, 1983.

LEACHED NUCLEAR WASTE GLASSES: ULTRAMICROTOMY AND ELECTRON MICROSCOPIC CHARACTERIZATION

J. P. Bradley and J. K. Bates

The containment of nuclear waste is a unique environmental problem because it requires a solution that remains technically valid on geological time scales. One disposal method that has been proposed is to incorporate radionuclides into borosilicate glasses followed by burial in a geological repository. Extensive experimental and computer modeling programs are in progress to evaluate the long-term stability of glasses in a terrestrial weathering environment.^{1,2} In the experimental program,^{1,3} glasses are reacted in a closed system (for between 3 and 1280 days) to simulate the effects of aqueous alteration (leaching). During leaching a layer of secondary phases, predominantly layer silicates, builds up on the glass surface. Determination of the mineralogy of leached layers is critical for evaluation of glass performance, but the layers are typically ultra-thin (1-50 μm), poorly crystallized, friable coatings that have eluded detailed characterization. Using ultramicrotomy, we have successfully prepared electron transparent thin sections of the glasses plus leached layers with minimal disturbance of their indigenous properties. Analytical electron microscopy has been employed to study the compositions, microstructures, and mineralogy of the leached layers. The results provide new insight into the mechanisms of glass reaction in an aqueous environment, and their suitability as media for long-term nuclear waste storage.

Sample Preparation

Polished thick-flats of the reacted glasses were initially prepared for examination of the leached layers in a scanning electron microscope (SEM) (Fig. 1). An ultramicrotome was then employed to prepare electron-transparent thin sections (50-100 nm thick) of the glasses for characterization by an analytical electron microscope (AEM) (Figs. 2-5). The ultramicrotomy procedure was developed specifically for preparation of thin sections of fine-grained geochemical specimens.⁴ Small fragments of the glass, together with the leached layer intact, were removed from a bulk specimen with a diamond blade. Care was taken to select fragments <100 μm with as little unreacted glass as possible in order to minimize fragmentation of the brittle glass during sectioning. The selected fragments were mounted in epoxy or acrylic resin in an orientation that would yield cross-sectional slices of the leached layers and un-

reacted glass. Multiple sections of each sample were cut and transferred to thin (<300Å) carbon films supported on 3mm copper TEM grids.

Results

Polished thick flats of the glasses were examined in an SEM to evaluate surface morphology, thickness, and degree of continuity of the reacted layers on the glass surface. Figure 1 shows a backscattered electron micrograph of a thick-flat section of glass that had been reacted in deionized water for 280 days. The thickness of the leached layer is of the order of 1 μm , so that the amount of structural and chemical information that can be obtained from the leached layer in the SEM is limited by spatial resolution. Figure 2 is a bright-field transmission electron micrograph of the same glass as shown in Fig. 1. A dramatic improvement in detail can be observed directly in an electron transparent section. The leached layer contains a zigzagging "backbone" of amorphous Fe-oxide. (In three dimensions this "backbone" forms a semicontinuous sheet over the surface of the reacted glass.) Layer silicates, predominantly smectite, cover both the upper and lower surfaces of the "backbone" (Figs. 2 and 3).

To elucidate reaction trends, a series of glasses reacted over an extended period were examined to monitor the development of the leached layers with time. Figure 6 shows electron micrographs of three different samples of the same glass reacted for 56, 91, and 280 days, respectively. After 56 days, the leached layer is 0.2-0.25 μm thick and remains firmly attached to the unreacted glass (Fig. 6a). Iron has begun to segregate toward the center of the reacted layer, where it forms a dark stain. After 91 days, iron has developed into the well-defined iron oxide "backbone" at the center of the reacted layer (Fig. 6b). The unreacted glass has retreated (by dissolution) away from the leached layer. The lower half of the leached layer retains textural (and compositional) characteristics of the 56 day sample (Fig. 6b), but the upper half is dominated by fibrous smectite. After 280 days, both the upper and lower sections of the leached layer are dominated by smectite (Fig. 6c).

Compositional variations within this series of glasses were investigated by quantitative x-ray energy-dispersive spectrometry. A thin-film correction procedure was used for data reduction.⁵ Thin-film standards were prepared by ultramicrotomy, by exactly the same procedures as those used for the glasses. Standards

J. P. Bradley is at McCrone Associates, Inc., Westmont, IL 60559; J. K. Bates is at Argonne National Laboratory, Argonne, IL 60439.

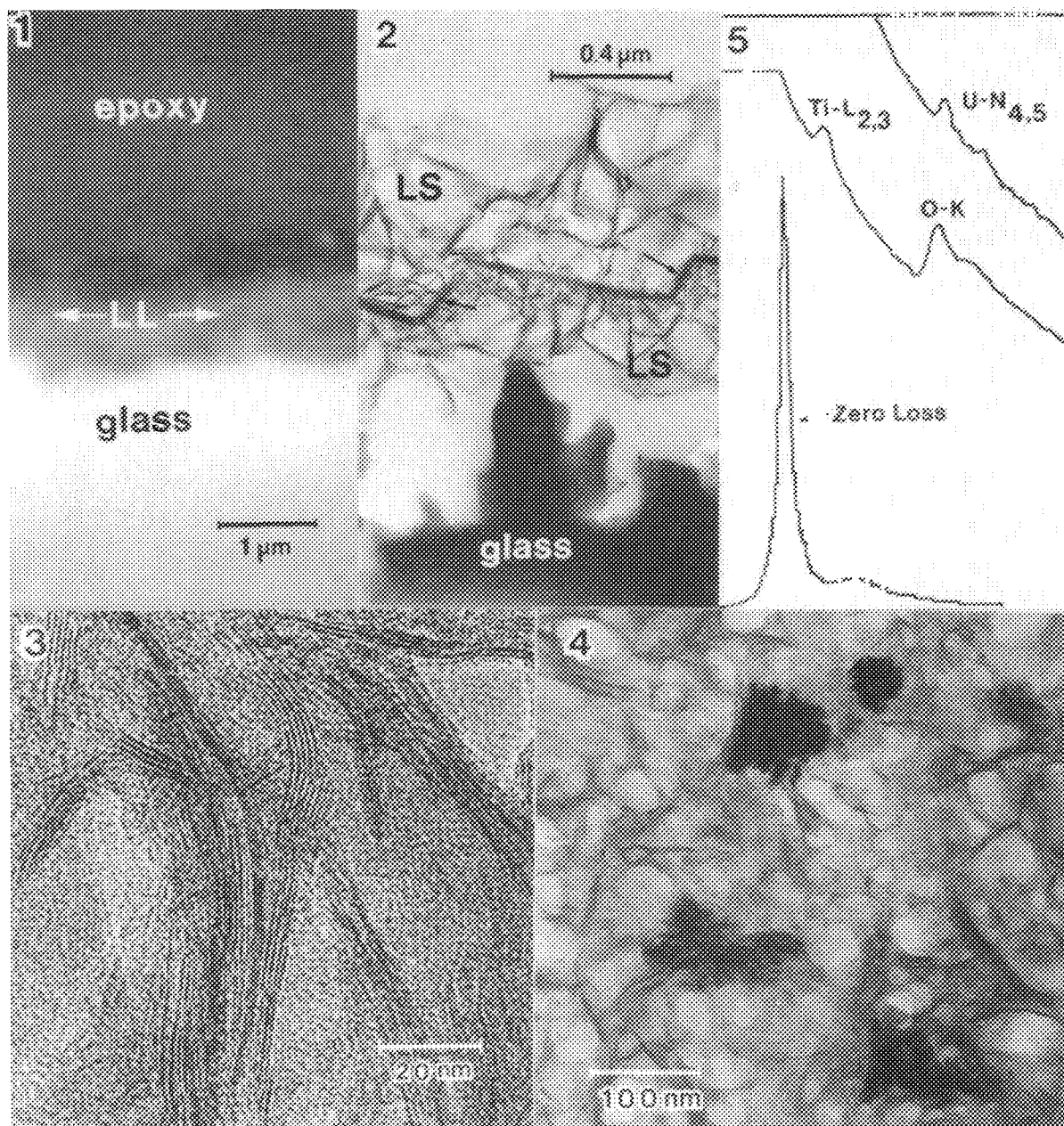


FIG. 1.--Backscattered electron micrograph of polished thick-flat of borosilicate glass. Leached layer (LL) on glass surface is $<1\ \mu\text{m}$ thick after 256 days.

FIG. 2.--Brightfield image of thin section ($\sim 50\ \text{nm}$ thick) of glass plus leached layer shown in FIG. 1. Leached layer contains iron oxide "backbone" (arrowed) and layer silicates (LS), predominantly smectite.

FIG. 3.--Lattice fringe image of layer silicates (LS) shown in Fig. 2. Basal lattice spacings are between 1.0 and 1.2 nm.

FIG. 4.--Precipitated U-Ti-O containing inclusions within leached layers of actinide-bearing glass.

FIG. 5.--Zero loss, plasmon, and core scattering edges from a U-rich inclusion. (Specimen thickness 40-50 nm, accelerating voltage 400 keV.)

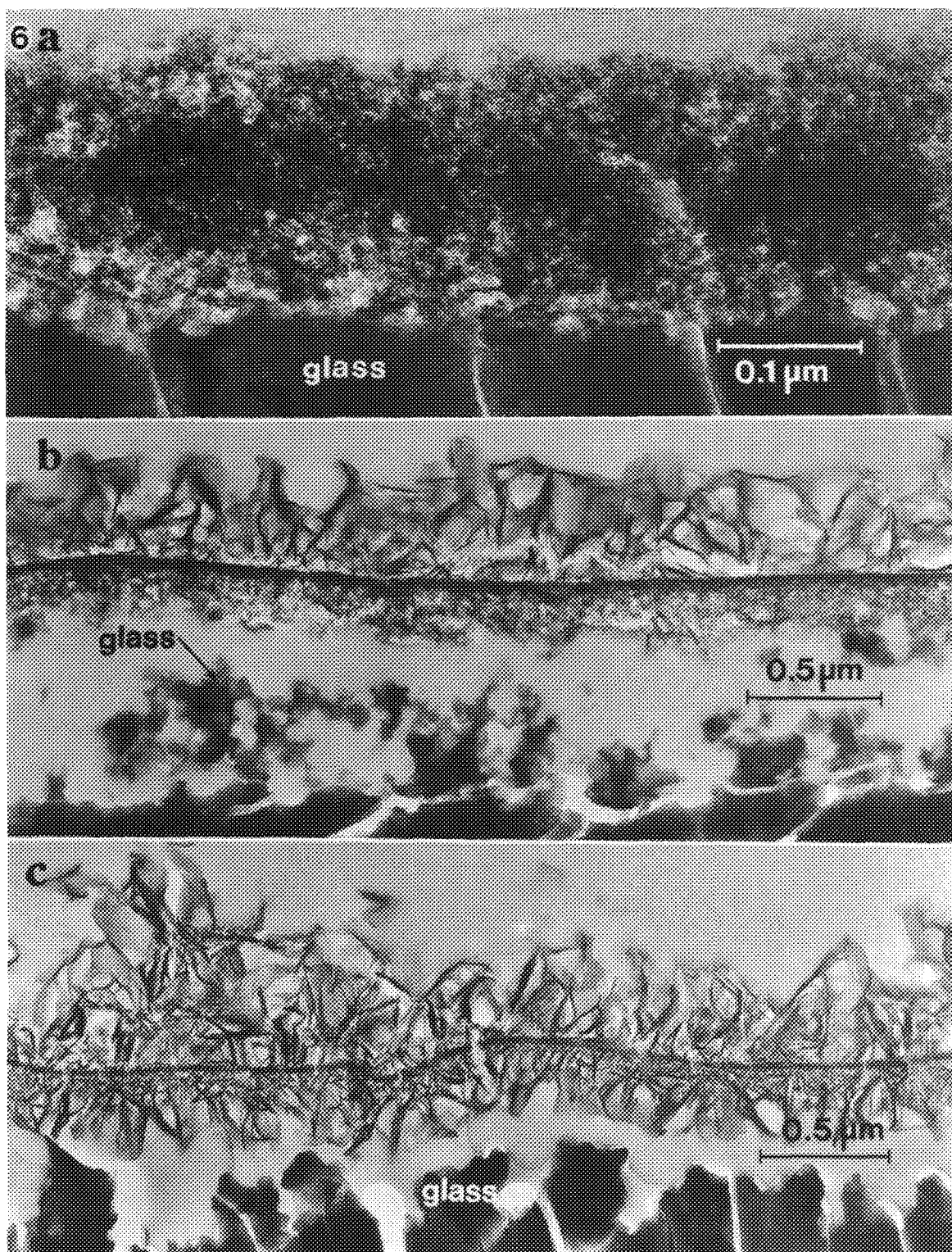


FIG. 6.--Brightfield electron micrographs of glass reacted for (a) 56 days, (b) 91 days, (c) 280 days. After 56 days leached layer is noncrystalline and firmly attached to unreacted glass substrate. After 91 days leached layer has segregated into three distinct structures, an upper smectite-rich layer, a central iron oxide "backbone," and a lower noncrystalline layer that remains morphologically similar to the 56-day sample. Leached layer is no longer attached to unreacted glass. After 256 days both upper and lower regions of leached layer are dominated by smectite.

TABLE 1.--Compositions of reacted layers on glasses leached for 56, 91, and 280 days (Element wt.% normalized).

	<u>1</u>	<u>2</u>	<u>3</u>	<u>4</u>	<u>5</u>	<u>6</u>	<u>7</u>
Mg	-	1.89	2.80	0.48	2.13	3.41	3.74
Al	8.24	12.68	13.85	12.51	13.40	14.94	15.65
Si	45.47	45.16	38.89	51.35	41.83	40.44	40.16
Ca	2.83	1.94	0.58	2.89	0.22	0.29	0.12
Ti	0.36	0.11	-	0.12	-	-	-
Mn	1.10	6.84	9.61	5.20	8.61	8.87	8.92
Fe	41.89	27.84	30.18	25.99	29.47	28.80	28.15
Ni	0.13	3.54	4.10	1.48	4.35	3.25	3.26

1. Bulk leached layer after 56 days (Fig. 6a)
2. Bulk leached layer after 91 days (Fig. 6b)
3. Bulk leached layer after 280 days (Fig. 6c)
4. Lower portion of leached layer after 91 days (Fig. 6b)
5. Upper portion of leached layer after 91 days (Fig. 6b)
6. Lower portion of leached layer after 280 days (Fig. 6c).
7. Upper portion of leached layer after 280 days (Fig. 6c).

included Kakanui hornblende,⁶ NIST thin-film glass SRM-2063, synthetic nickel silicate, Springwater olivine, and Johnstown pyroxene. Table 1 lists the compositions of the bulk glass and the reacted layers of the 56-, 91-, and 280-day samples shown in Fig. 6. (These analyses were obtained with a broad beam that encompassed the entire layer structures.) Mg and Ni are highly depleted (relative to the bulk glass) in the reacted layer at 56 days (column 1), but their abundances increase steadily thereafter (columns 2 and 3). Al and Mn also increase steadily; Fe fluctuates; and Si, Ca, and Ti decrease progressively from 56 through 280 days (columns 1-3).

Comparison of the compositions of the upper vs lower portions (i.e., above and below the "backbone") of the reacted layers in the 91- and 280-day samples suggest that element abundances correlate with the observed structural features (columns 4 through 7). For example, Mg, Mn, Fe, and Ni increase with layer silicate formation in the upper portion of the 91-day sample, whereas Si and Ca abundances decrease (cf. columns 4 and 5). These compositional trends continue with time. After 280 days, the lower portion of the leached layer has converted to layer silicates (Fig. 6c). As a result, Mg, Mn, and Ni abundances increase, and Si and Ca abundances decrease (cf. columns 4 and 6). At 280 days, both the appearance (Fig. 6c) and composition (Table 1, columns 6 and 7) of the upper and lower portion of the reacted layers are similar.

The fate of actinides during leaching is also critical for evaluation of glass performance. A different borosilicate glass from that described was reacted for 1280 days. This glass contained uranium; Fig. 4 shows U-rich inclusions that have nucleated within the leached layer. Since the inclusions are amorphous, it was not possible to identify a specific mineral phase. X-ray energy-dispersive analyses and electron energy-loss spectroscopy indicated that the inclusions contain U, Ti, and O (Fig. 5). The mineral brannerite (UTi_2O_6) may be an analog for the inclusions.⁷

Discussion

Despite the fragile nature and micrometer-scale thickness of the leached layers on borosilicate glasses, it is possible to prepare electron-transparent thin sections without seriously compromising indigenous microstructures or compositions. The sections enable acquisition of lattice fringe images, and electron microdiffraction, and x-ray, and electron energy loss spectroscopy (EELS), with optimum spatial resolution. Thin (<50 nm) sections are particularly useful for EELS applications, where they have enabled routine detection of light elements in heavy atom matrices (e.g., O in U). Analytical information derived from AEM studies, together with the (cation) concentrations of solutions in contact with the glasses, can be used to determine mechanisms of aqueous alteration in a reactive environment. This mechanistic information is critical input

for computer modeling programs designed to extrapolate glass stability over geological time scales. The observation of U-rich inclusions in the leached layers of an (actinide-bearing) glass indicates that uranium release was retarded by in situ precipitation. This observation suggests that stable actinide compound formation may be a viable mechanism for retarding radionuclide release into the environment during weathering in a geological repository.

References

1. W. L. Ebert, J. K. Bates, and T. S. Gerdling, "The reaction of glass during gamma irradiation of a saturated tuff environment, Part 4: SRL 165, ATM-1C, and ATM-8 glasses at 1E3 R/hr and 0 R/hr," Argonne National Lab. Report ANL-90/13, 1990.
2. W. L. Bourcier, "Geochemical modeling of radioactive waste glass dissolution using EQ3/6: Preliminary results and data needs," Lawrence Livermore Natl. Lab. Report UCRL-57012, 1989.
3. G. G. Wicks, J. A. Store, G. T. Chandler, and S. Williams, "Long term leaching behavior of simulated Savannah River Plant waste glass, Part 1: MEC-1 leachability results; four year leaching data," Savannah River Laboratory Report DP-1728, 1986.
4. J. P. Bradley, "Analysis of chondritic interplanetary dust thin-sections," *Geochim. Cosmochim. Acta* 52: 889, 1988.
5. J. I. Goldstein, "Principles of thin-film x-ray microanalysis," in J. J. Hren, J. I. Goldstein, and D. C. Joy, Eds., *Introduction to Analytical Electron Microscopy*, New York: Plenum Press, 1979, 83.
6. B. Mason and R. O. Allen, "Minor and trace elements in augite, hornblende, and pyrope megacrysts from Kakanui, New Zealand, *N. Z. J. Geol. Geophys.* 16: 935, 1973.
7. J. T. Szymanski and J. D. Scott, "A crystal structure refinement of synthetic brannerite (UTi_2O_6) and its bearing on rate of alkaline carbonate leaching of brannerite ore," *Can. Min.* 20: 271, 1982.

MICROSCOPY AND NANOANALYSIS OF A Cr-Mn AUSTENITIC STEEL α -BOMBARDED AT ROOM AND ELEVATED TEMPERATURE

G. Valdrè and E. Ruedl

The structural materials for nearer-term fusion reactors such as ITER and DEMO will likely be steels. During their operation, the radiation damage in the structural components will become very complex since the damage is produced simultaneously by high-energy neutrons, protons, and alpha particles. As long as no fusion device for material testing exists, data about the formation of radiation damage in candidate steels can only be obtained by simpler irradiating conditions such as by mixed energy spectra neutrons, protons, and/or alpha particles. The present work deals with a study of the Cr-Mn austenitic steel AMCR 0033, a material expected to produce less long-term waste than Ni-Cr steels. The steel was α -implanted, either at elevated temperature or at room temperature, and subsequently aged.

The composition of AMCR 0033, supplied by Creusot-Loire, is given in wt% as follows:

Fe	Mn	Cr	Ni	Si	C
71.2	17.5	10.4	0.09	0.53	0.11
N	Cu	Mo	S	P	
0.20	0.02	0.01	0.005	0.018	

Solution-annealed samples 3 mm in diameter and 150 μ m thick were uniformly implanted with 1000 appm He (displacement damage ~ 0.2 dpa, displacement rate $\sim 10^{-6}$ dpa \cdot sec $^{-1}$) in the Ispra cyclotron at 310 and 800 \pm 25 K (calibration by IR pyrometry). The samples implanted at low temperature were subsequently annealed at 773 K for 1000 h, at 973 K for 1 h, and at 1073 K for 100 h. The specimens were finally jet-electropolished for EM.

A Philips EM 400T electron microscope equipped with a field-emission gun, a GATAN 607 spectrometer for EELS, and an EDAX PV9900 system for EDS analysis as well as a JEOL 200 CX electron microscope were used.

The quantitative EELS analyses were performed (in the form of elemental at% ratios) by means of the SIGMAK and SIGMAL¹ programs; the EDS analyses were made by means of the program EDAX PV9900 THIN. The probe diameter for both type of analyses was about 10 nm.

Results and Discussion

The various treatments lead to a different microstructural evolution in the Mn-Cr austen-

G. Valdrè is a Dept. of Min. Sciences, P. Porta S. Donato 1, I-40100 Bologna and GNSM-CISM, INFN, Bologna University, Italy; E. Ruedl is at J.R.C. EEC, I-21020 Ispra (Va), Italy. G. V. thanks the Italian Ministry of Public Education (MPI) for financial support.

itic steel AMCR 0033.

Samples α -implanted at room temperature and subsequently annealed at 773 K for 1000 h show the formation of small dislocation loops (Fig. 1). Post aging at 973 K for 1 h leads to the formation of Frank interstitial loops of regular shape (Fig. 2) without detectable compositional change in their neighborhood, except for a slight increase of Si. In these samples there is no evidence of the presence of He bubbles and of precipitates on the loops.

Samples aged at 1073 K for 100 h show the presence of He bubbles whose surface is enriched with Cr, Mo, and N due to thermally induced phenomena (Figs. 3 and 4; Table 1).

TABLE 1.--Elemental at% ratios from EDS analysis obtained from He bubbles and surrounding matrix.

	Cr/Fe	Mn/Fe	Mo/Fe*	Ni/Fe
Bubbles	0.24	0.25	0.027	0.016
Matrix	0.19	0.24	0.015	0.016

*In region of enhanced Mo content.

Samples α -implanted at 800 \pm 25 K have developed Frank interstitial loops of "petular" shape (Fig. 5) apparently hindered in their growth by obstacles. Within and adjacent to the loop plane a high number of He bubbles (< 3 nm in diameter) are nucleated that affect the growth and shape of the loops (Fig. 6). EDS nanoanalysis shows enrichment of Fe and Si at the loops, whereas Mn and Cr are depleted as a consequence of radiation-induced segregation (Table 2).

TABLE 2.--Elemental wt% from EDS analysis obtained from loops seen edge-on and the surrounding matrix showing enrichments of Fe and Si and depletion of Cr and Mn at the loops.

Element	Loops	1	2	3	4	Matrix
Si		0.6	0.6	0.7	0.5	0.5
Cr		16.8	16.2	16.1	16.3	17.5
Mn		9.1	9.6	9.8	9.8	10.4
Fe		73.4	73.7	73.4	73.4	71.2

These compositional changes, except for Cr, are consistent with the microchemical changes observed in Fe-Mn-Cr alloys and steels at grain boundaries after electron irradiation^{2,3} and at voids after neutron irradiation.⁴

The implementation of morphological and structural investigations with microanalysis initiated some years ago^{5,6} provides a more complete and deeper insight into the study of

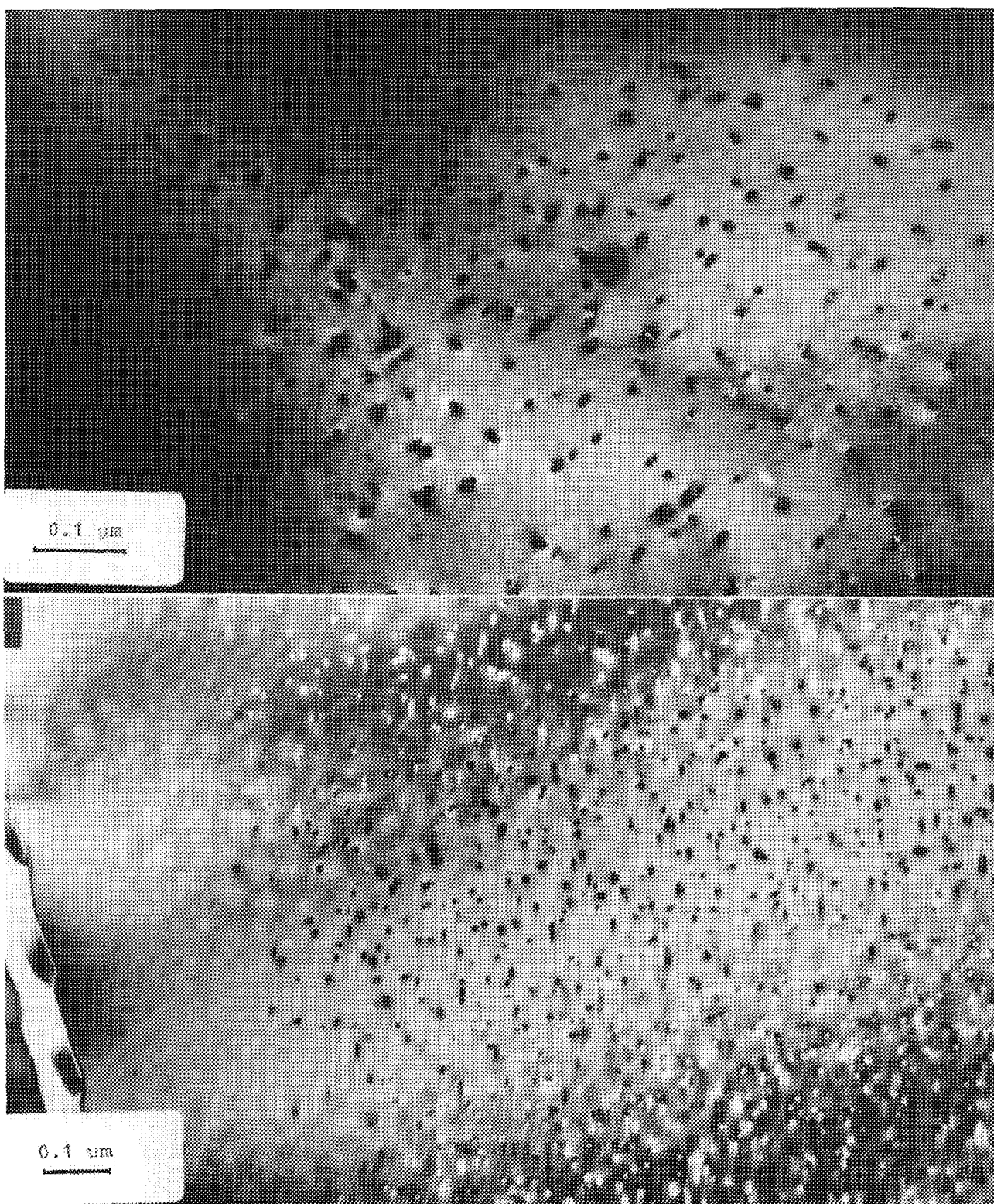


FIG. 1.--Sample α -implanted at R.T. and annealed at 773 K for 1000 h. (a) Area showing presence of small loops. (b) zone near grain boundary denuded of loops.

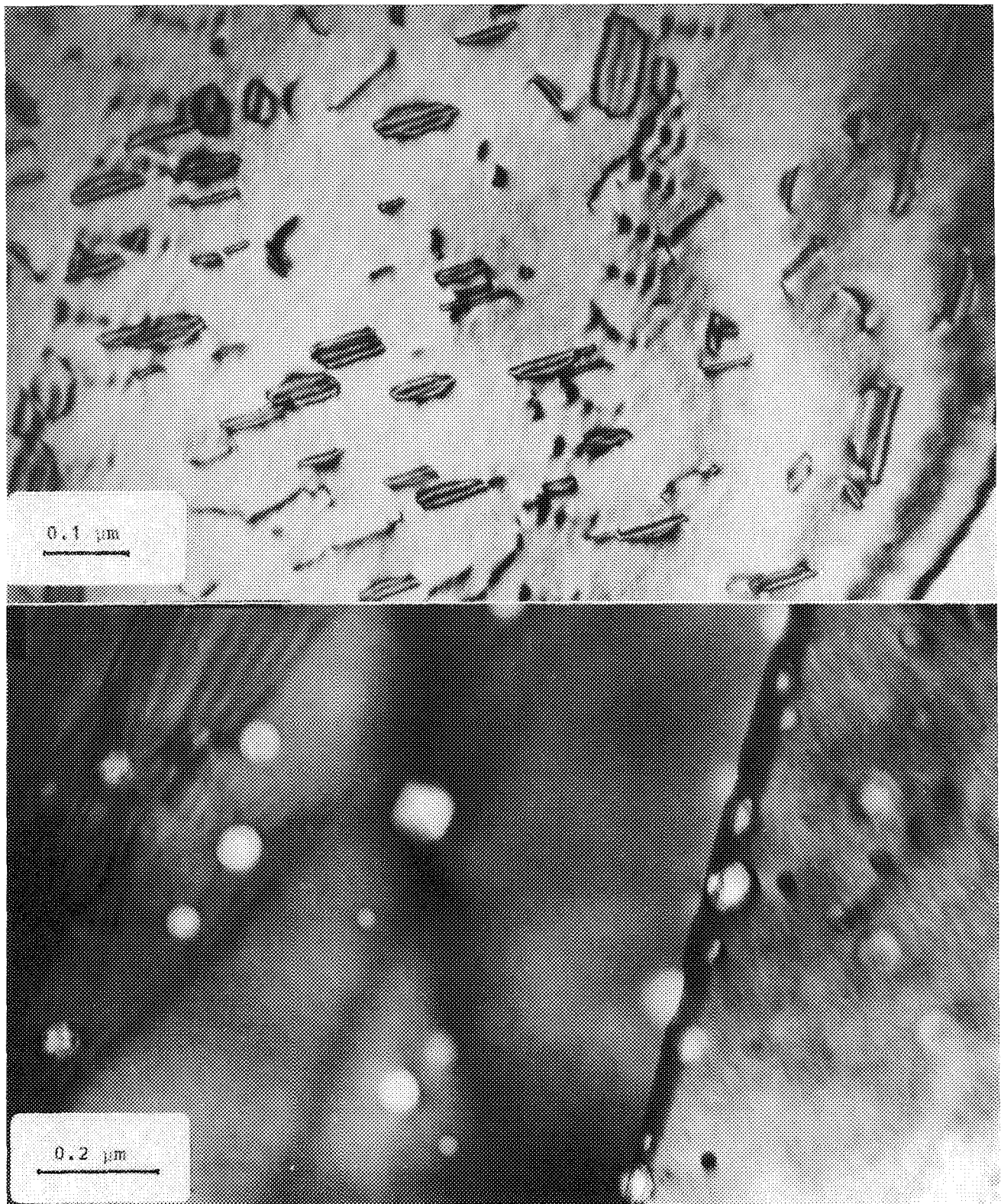


FIG. 2.--Formation of smooth-edged Frank interstitial dislocation loops. Sample R.T. α -implanted and post aged at 973 K for 1 h.
FIG. 3.--Sample α -implanted at R.T. and annealed at 1073 K for 100 h showing the presence of inter- and intragranular He bubbles.

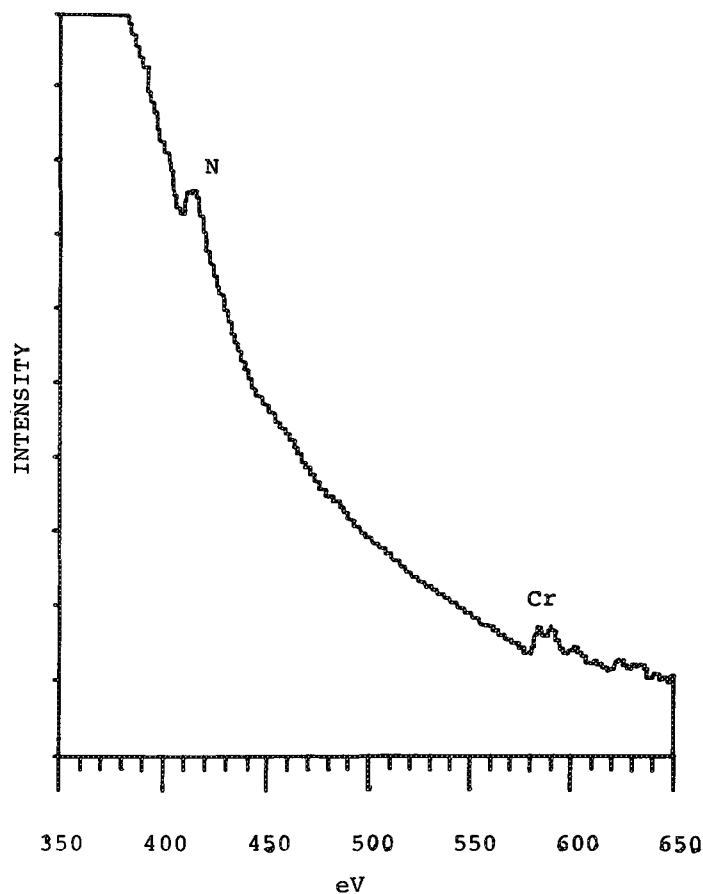


FIG. 4.--EELS spectrum from intragranular He bubbles showing enrichment of Cr and N near surface.

fusion materials and shows that improvement in the analytical spatial resolution leads to an increasingly complex radiation damage pattern for Cr-Mn steels, even for conditions simpler than those to be encountered in fusion reactor irradiation.

References

1. R. F. Egerton, *Electron Energy Loss Spectroscopy in the Electron Microscope*, New York: Plenum Press, 1986.
2. H. Takahashi, T. Takeyama, K. Tanikawa, and R. Miura, *J. Nucl. Mater.* 133 134: 566-570, 1985.
3. T. Kato, H. Takahashi, S. Ohnuki, K. Nakata, and J. Kuniya, *J. Nucl. Mater.* (in press).
4. J. M. McCarthy and F. A. Garner, *J. Nucl. Mater.* 155-157: 877, 1988.
5. E. Ruedl and G. Valdrè, *J. Mater. Sci.* 23: 3698-3705, 1988.
6. E. Ruedl and G. Valdrè, *J. Nucl. Mater.* 176, 1989.

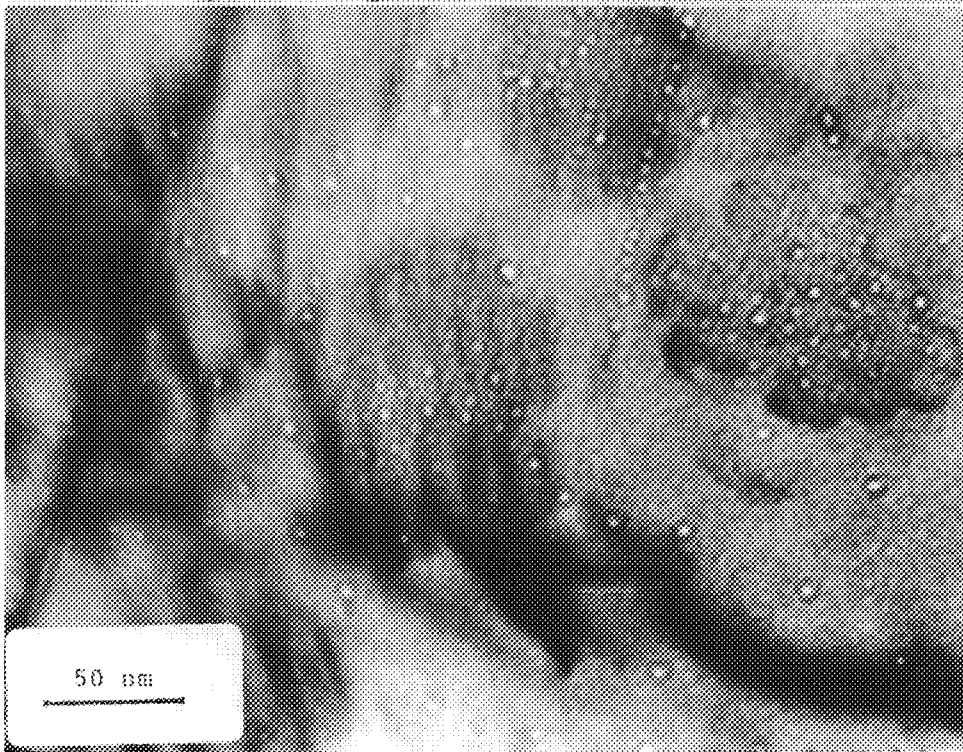


FIG. 5.--Sample α -implanted at 800 ± 25 K. Formation of Frank interstitial loops "petular" in shape lying in foil plane or seen edge-on with a high density of He bubbles visible on them. Smaller number of slightly larger bubbles are also present in surrounding matrix.
 FIG. 6.--High-magnification image of sample of Fig. 5 demonstrating formation of He bubble colonies within (or adjacent to) loop plane of Frank interstitial loops.

CROSS-SECTIONAL EXAMINATION OF SURFACE LAYERS ON ELECTROPOLISHED THIN SPECIMENS

Y. Wakaki, Y. Otsuka, Z. Horita, M. Nishimura, T. Sano, Y. Murata, and M. Nemoto

Surface layers often develop during electropolishing for preparation of electron-transparent thin specimens.¹⁻⁸ Because most of the layers have compositions different from the bulk, serious errors may arise in quantitative x-ray microanalysis using the analytical electron microscope (AEM), particularly at thin regions. To remove surface layers, ion beam sputtering was attempted,¹⁻⁸ but successful removal was reported only under well-controlled conditions.^{4,5,8}

For an examination of the layer structure underlying the specimen surface, Auger electron spectroscopy (AES) has been used.⁶⁻⁸ However, if it is possible to obtain a thin cross section of the specimen, the layer structure can be revealed more directly through the observation and microanalysis with the conventional transmission electron microscope (CTEM) and AEM. It was demonstrated that ultramicrotomy is a useful technique for obtaining such a thin cross section in metallic materials, although this technique is usually used for biological thin sections.⁹⁻¹¹

This study examines the structure of surface layers produced during electropolishing for preparation of electron-transparent thin specimens. The observation and microanalysis are first conducted in plan view of as-electropolished specimens with the AEM and secondary ion mass spectrometer (SIMS). Then, ultramicrotomy is used to obtain thin cross sections of as-electropolished specimens. The cross-sectional observation and microanalysis are performed with the high-resolution CTEM and AEM.

Experimental

Disks 3mm in diameter were punched from an Al-3.80wt%Cu sheet 0.06mm thick and were annealed at 813 K for 2 h under argon followed by

Y. Wakaki is at Thin Film Head Process Group, Magnetic Disk Media Engineering Department, Odawara Works, Hitachi Ltd., Kanagawa 256, Japan (formerly a graduate student in the Department of Metallurgy, Kyushu University); Y. Otsuka, M. Nishimura, and Y. Murata are at Morphological Research Laboratory, TORAY Research Center, Shiga 520, Japan; Z. Horita, T. Sano, and M. Nemoto are at the Department of Materials Science and Engineering, Faculty of Engineering, Kyushu University, Fukuoka 812, Japan. We are grateful to Mr. K. Wakasugi in the Department of Materials Science and Engineering, Kyushu University, for operation of a Hitachi IMA-2AS ion microanalyzer. This work was supported in part by Hyuga Fund in the Iron and Steel Institute of Japan.

quenching in iced water. They were thinned for electron microscopy with the twin-jet electropolishing technique. Two different electrolytes were used: one was a mixture of 15% perchloric acid, 10% glycerol, and 75% ethanol (hereafter the specimen prepared in this electrolyte is called the PA specimen) and the other of 30% nitric acid and 70% methanol (the NA specimen). The former electrolyte was cooled by ice in water and the latter by dry ice in methanol upon their use.

Observations and microanalyses in plan view of the specimens were conducted at the HVEM Laboratory of Kyushu University with a JEM-2000FX analytical electron microscope equipped with a Tracor Northern energy-dispersive Si(Li) x-ray detector with a Be window. The microscope was operated at 200 kV. The characteristic x rays of Al K α and Cu K α lines were acquired at different thicknesses, normally by positioning the beam near the edge of the specimen and moving the beam toward regions away from the edge.

As-electropolished thin specimens were also subjected to surface analysis with a Hitachi IMA-2AS ion microanalyzer. The primary O $_2^+$ beam was ~ 600 μ m in diameter and was placed on the specimen at an accelerating potential of 13 kV and a beam current of 0.1 μ A to monitor positive secondary ions. For comparison, bombardment by the O $_2^+$ beam was also attempted on a disk polished mechanically (hereafter called MC specimen).

For observations and microanalyses in cross-sectional view of the specimens, a Reichert-Nissel Ultracut N ultramicrotome at the TORAY Research Center was used to obtain thin cross sections. The procedure for preparing thin sections was essentially the same as that employed by Furneaux et al.⁹ An H-800 UHR electron microscope and an HB501 analytical electron microscope in the same research center were operated at 200 kV and 100 kV, respectively: the former was used for observations of structural variation near the specimen surface, the latter mainly for microanalyses of interest. The characteristic x-ray lines from O, Al, and Cu were measured with a KEVEX ultrathin window (UTW) type energy-dispersive Si(Li) detector interfaced to the HB501.

Results

Figure 1 shows the results of x-ray microanalyses obtained from the specimens in plan view. The intensity ratio I_{Cu}/I_{Al} was plotted against the Al K α intensity I_{Al} and also the thickness t , converted from I_{Al} . The conversion utilized a linear relationship of I_{Al} vs t constructed by measuring t by the convergent

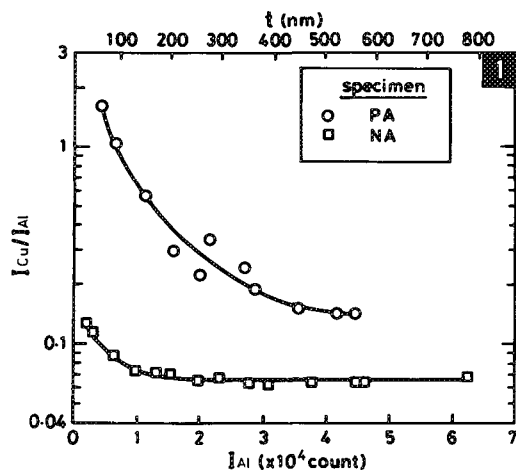


FIG. 1.--Plot of I_{Cu}/I_{Al} vs I_{Al} (or t) for PA and NA specimens.

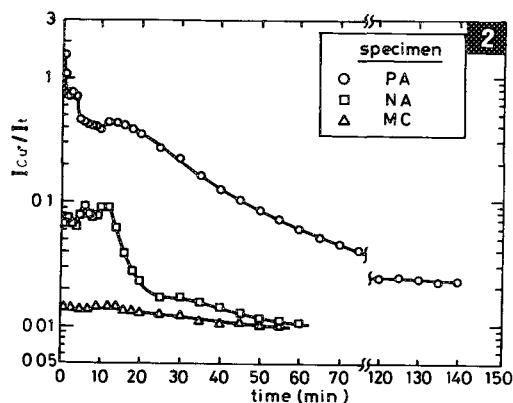


FIG. 2.--Plot of I_{Cu}/I_{Al} vs time of O_2 bombardment for PA, NA, and MC specimens.

beam electron diffraction (CBED) method¹² at an immediate neighbor of the point of analysis in NA specimen. Since the application of the CBED method was limited to the thickness below ~ 150 nm, the linear relationship was extended to larger thicknesses. This extension may be accepted because the absorption of the Al $K\alpha$ line in the specimen is estimated to be small ($\sim 8\%$ at $1\ \mu m$). However, the extension may involve some error due to the presence of surface layers formed on the specimens.

The results of Fig. 1 reveal that I_{Cu}/I_{Al} increases with a decrease in thickness for both PA and NA specimens, as observed by other investigators.¹⁻⁵ However, the extent of the increase in I_{Cu}/I_{Al} is much greater for the PA specimen than the NA specimen. This result suggests that the PA specimen is more enriched with Cu on its surface.

Figure 2 is the results monitoring the intensity of the secondary $^{63}Cu^+$, I_{Cu}^+ . Here, I_{Cu}^+ was normalized by the total ion intensity I_t , which excluded I_{Cu}^+ . It is seen that the production of $^{63}Cu^+$ decreases with time of O_2 bombardment for the PA and NA specimens, whereas it is almost invariant with time for MC specimen. This result indicates that a Cu-rich layer is present on the surfaces of the electropolished specimens and that the enrichment in Cu is more significant on the PA specimen than on the NA specimen. For the NA specimen, the production of $^{63}Cu^+$ reaches the level of the MC specimen in ~ 1 h, but for the PA specimen, it is well over the level of MC specimen even after 2h bombardment with O_2 . This trend is similar to that of the x-ray microanalysis shown in Fig. 1.

Figure 3 is an electron micrograph taken from a cross section of PA specimen. An electron beam of ~ 1 nm in diameter was positioned on four distinctive regions A to D in Fig. 3; the x-ray spectra obtained from these regions are shown in Figs. 4(A) to (D). Region A is composed of O, Al, and a minor amount of Cu. This layer was susceptible to beam damage during irradiation, and the beam was therefore moved

slowly to achieve continuous acquisition of x rays. In region B, the Cu peak is prominent. It is seen that this Cu rich layer consists of a number of particles. Region C contains O, Al, and some Cu as did region A, but no damage occurred during irradiation by a focused beam. When the beam was positioned from region C to region D, the peak heights of O and Cu relative to that of Al were lowered to the heights shown in Fig. 4(D) and no essential change in the relative peak heights was observed beyond region D. Evidently, the spectrum from region D can represent the bulk of the specimen. The O peak observed in the spectrum of region D may be due to the presence of an oxide layer formed on the surface of the ultramicrotomed thin section. The results shown in Figs. 3 and 4 are consistent with the surface observation by Morris et al. in plan view using the scanning electronic microscope (SEM)⁴; that the Cu-rich particles present in the oxide surface layer on an Al-4%Cu specimen polished in an electrolyte were similar to those in the present PA specimen.

A cross-sectional observation of NA specimen in Fig. 5 reveals that there are two types of surfaces: one is smooth as the left side in Fig. 5 and the other is complex as the right side. Figures 6(E) to (H) are the x-ray spectra obtained from regions E to H in Fig. 5, respectively. A comparison between the spectra from regions E and F indicates that there exists a layer enriched by Cu and O. The thickness of the layer is found to be ~ 5 -10 nm. Particles observed in region G are rich in Cu. These particles appear to form in the same way as the Cu-rich particles of region B in Fig. 4, although the size is small for those in region G. Region H exhibits the x-ray spectrum similar to region C in Fig. 4. Thus, the spectra from regions G and H suggest that the surface observed in the right side of Fig. 5 develops by the same mechanism as that in PA specimen.

Figure 7 shows a cross section of the MC specimen. The surface is irregular because the specimen was subjected to mechanical abrasion.

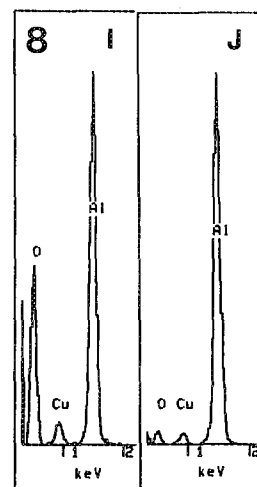
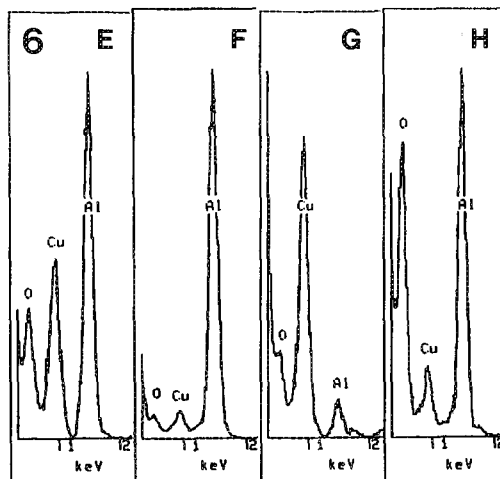
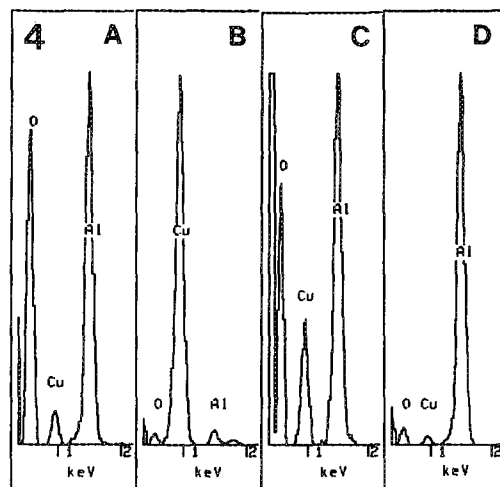
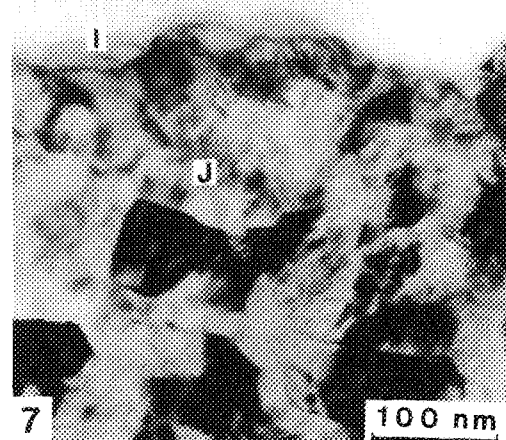
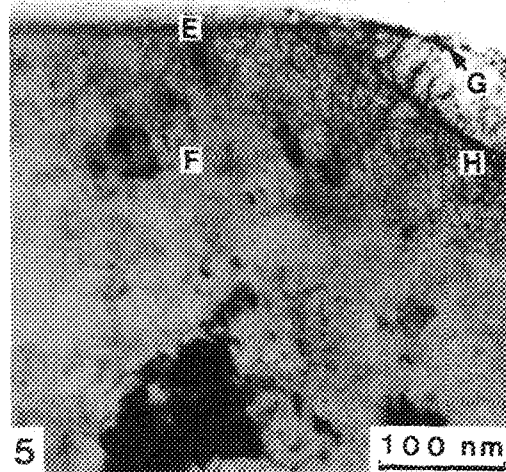
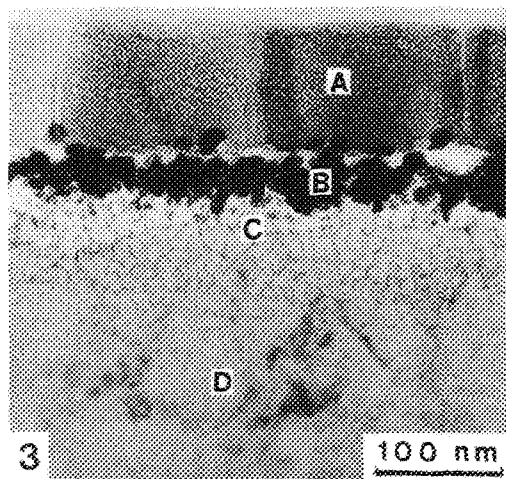


FIG. 3.--Micrograph taken from cross section of PA specimen.
 FIG. 4.--X-ray spectra (A)-(D) obtained from regions A to D in Fig. 3.
 FIG. 5.--Micrograph taken from cross section of NA specimen.
 FIG. 6.--X-ray spectra (E)-(H) obtained from regions E to H in Fig. 5.
 FIG. 7.--Micrograph taken from cross section of MC specimen.
 FIG. 8.--X-ray spectra (I) and (J) obtained from regions I and J in Fig. 7.

Figures 8(I) and (J) are the x-ray spectra from regions I and J in Fig. 7, respectively. The O peak is large in region I when compared with region J, which shows that an oxide layer exists on the MC specimen. However, no Cu-rich layers (or particles) were observed on this specimen.

Summary and Conclusion

Plan view analysis with the AEM and SIMS showed that a Cu-rich layer is present on both PA and NA specimens: the layer on the PA specimen is thicker than that on the NA specimen. This result was demonstrated more clearly by cross-sectional observations and microanalysis using high-resolution CTEM and AEM. The layer thickness was found to be ~ 50 nm for the PA specimen and $5\sim 10$ nm for the NA specimen.

Ultramicrotomy was shown to be useful for an examination of the layer structure underlying the specimen surface. No Cu-rich layers on the MC specimen suggest that ultramicrotomed thin sections can be suitable for microanalysis with the AEM compared with electropolished thin specimens.

References

1. M. N. Thompson, P. Doig, J. W. Edington, and P. E. J. Flewitt, *Phil. Mag.* 35: 1537, 1977.
2. P. Doig and P. E. J. Flewitt, *J. Microsc.* 110: 107, 1977.
3. K. J. Sawley, G. Cliff, and C. W. Hawthorth, *J. Phys.* D10: 1883, 1977.
4. P. L. Morris, N. C. Davies, and J. A. Treverton, *Inst. Phys. Conf. Ser.* 36, 377, 1977.
5. P. L. Morris and H. J. Lamb, *J. Phys.* D11: L73, 1978.
6. J. M. Pountney and M. H. Loretto, 7th *Eur. Cong. Electron Microscopy* 3: 180, 1980.
7. H. L. Fraser and J. P. McCarthy, *Microbeam Analysis--1982*, 93.
8. J. R. Michael and D. B. Williams, *Analytical Electron Microscopy--1984*, 61.
9. R. C. Furneaux, G. E. Thompson, and G. C. Wood, *Corrosion Science* 18: 853, 1978.
10. M. D. Ball, T. F. Malis and D. Steele, *Analytical Electron Microscopy--1984*, 189.
11. K. Shimizu, G. E. Thompson, G. C. Wood, and K. Kobayashi, *Phil. Mag. Letters* 61: 43, 1990.
12. P. M. Kelly, A. Jostsons, R. G. Blake, and J. P. Napier, *Phys. Stat. Sol.* A31: 771, 1975.

QUANTITATIVE ALCHEMI WITH ERROR ANALYSIS

C. J. Rossouw, P. S. Turner, T. J. White, and A. J. O'Connor

The ALCHEMI technique for determining the site distribution f_{ip} of impurity elements p ($= 1...P$) on host element lattice sites i ($= 1...I$) is well known.¹ Changes in x-ray emission from host atoms and intensities with crystal orientation are monitored under strong planar or axial diffraction conditions, and f_{ip} is derived via a ratio method.² However, ratio analysis involves count ratios (and ratios of ratios), leading to severe error amplification. Neglect of delocalization leads to further error.³

Theory

To overcome these inherent errors in the standard ALCHEMI method, we make the single assumption that the impurity count N_p^s for each of the spectra $s = 1...m$ may be written as a linear combination of the host atom counts N_i^s :

$$N_p^s = \sum_{i=1, I} \alpha_{ip} N_i^s \quad (1)$$

where the coefficients α_{ip} and their errors are determined by multivariate analysis.^{4,5} For m separate EDX spectra and $v = I, P$ fitted parameters α_i ($i = 1$ to v), the criterion $v \leq m$ must be satisfied to give $m - v$ degrees of freedom. The p th impurity atom concentration c_p and the distribution f_{ip} may be obtained from the coefficients α_{ip} :

$$c_p = \sum_{i=1, I} \frac{n_i \alpha_{ip}}{k_{ip} (1 + \sum_{q=1, P} \alpha_{iq} / k_{iq})} \quad (2)$$

where n_i is the number of host atoms of type i per unit cell, and k_{ip} the k-factor ratio k_i/k_p for host atoms i and impurity atoms p . The fractional partition f_{ip} of the impurity p onto site i is given by

$$f_{ip} = \frac{n_i \alpha_{ip}}{c_p k_{ip} (1 + \sum_{q=1, P} \alpha_{iq} / k_{iq})} \quad (3)$$

Uncertainties in both these quantities c_p and f_{ip} are derived from standard deviations α_{ip} yielded by the multivariate analysis.⁴⁻⁶

Results and Discussion

Diffraction patterns and the projected crystal structure of the spinel Cr_2MnO_4 for $\langle 100 \rangle$, $\langle 310 \rangle$, and $\langle 211 \rangle$ zone axes are shown in Fig. 1 (120keV electrons at 300 K and thickness of about 48 nm). In projection, each site is distinguishable along these zone axes. Iron impurities partition onto both Cr and Mn sites as Fe^{2+} or Fe^{3+} . Table 1 gives a summary of the site distribution obtained for each axial orientation from the theory described above. Note the improvement in error when all 49 spectra from each zone axis are subjected simultaneously to multivariate analysis.

When analyzed by the alternative "ratio" technique, 9 spectra had to be rejected as the partitioning was greater than or less than unity. Remaining spectra give $72 \pm 12\%$ partitioning onto Cr sites. Multivariate analysis, for the same data set and no data rejection, gives the partitioning onto Cr sites as $69 \pm 1.5\%$ as well as a concentration of $10.4 \pm 0.2\%$.

Figure 2 shows the fit of $\sum \alpha_{ip} N_i^s$ to N_p^s ; the linear behavior confirms the validity of the model for multivariate analysis. This approach yields impurity concentration as well as site distribution and quantitative uncertainties smaller than those obtained by ratio analysis. In addition, multivariate analysis is less sensitive to delocalization effects and numerical error propagation than the ratio technique. No data points are rejected, and an objective assessment of the model and errors is given in the standard deviations returned. The ratio method is similar to multivariate analysis with no degrees of freedom, given that the number of spectra necessary for analysis is equal to the number of distinguishable sites.

References

1. J. Taftø and J. C. H. Spence, *Ultramicroscopy* 9: 243, 1982.
2. J. Bentley, *Proc. EMSA* 44: 704, 1986.
3. S. J. Pennycook, *Ultramicroscopy* 26: 239, 1988.
4. C. J. Rossouw, P. S. Turner, T. J. White, and A. J. O'Connor, *Phil. Mag. Lett.* 60: 225, 1989.
5. P. S. Turner, T. J. White, A. J. O'Connor, and C. J. Rossouw, *J. Microscopy* (in press).
6. W. H. Press, B. P. Flannery, S. A. Teukolsky, and W. T. Vetterling, *Numerical Recipes*, London: Cambridge University Press, 1986, 498-526.

C. J. Rossouw is at the CSIRO Division of Materials Science and Technology, Clayton; P. S. Turner and A. J. O'Connor are at the Griffith University Division of Science and Technology, Nathan; and T. J. White is at the University of Queensland EM Centre, St. Lucia; all in Australia.

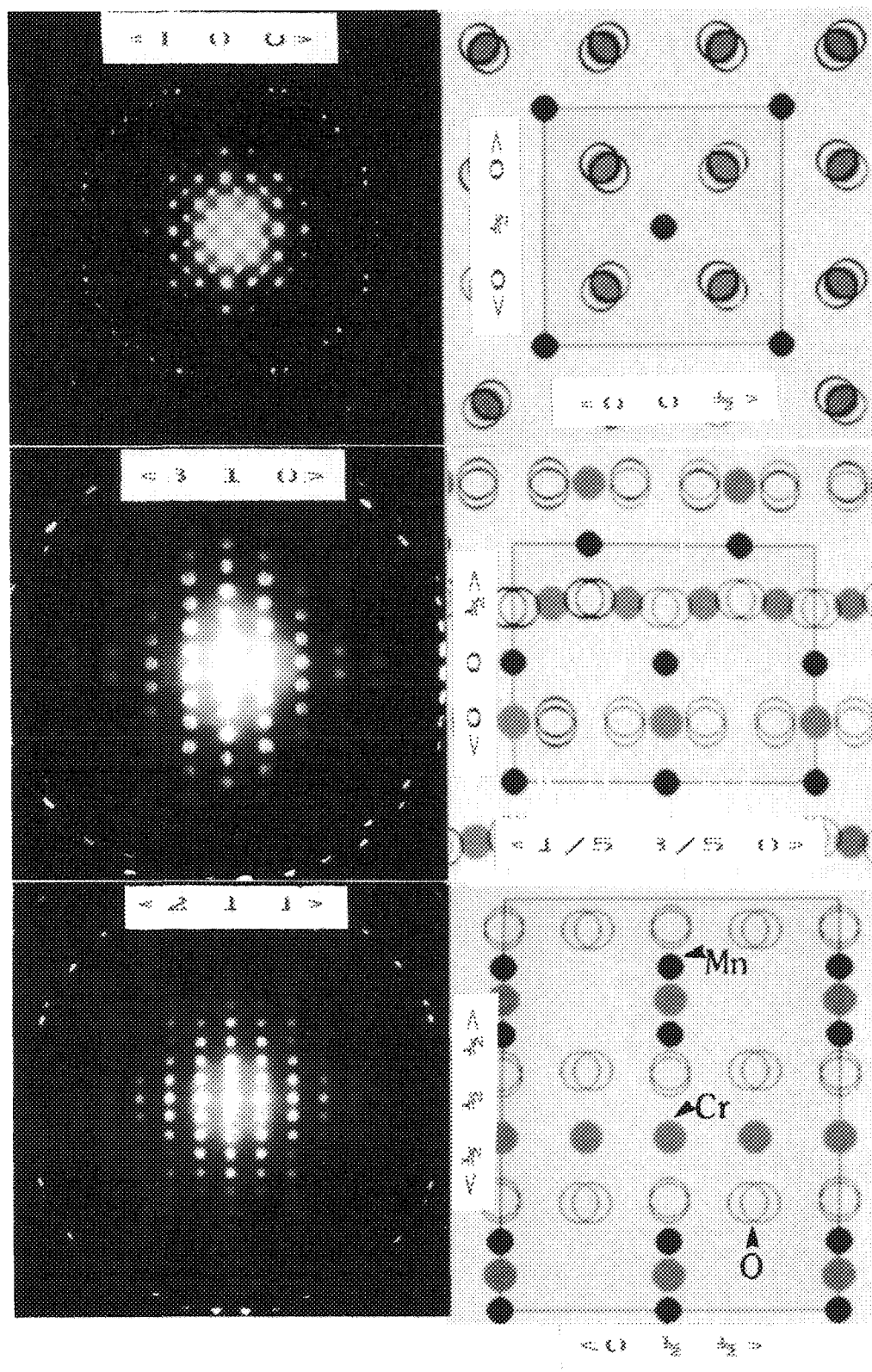


FIG. 1.--Zone axis diffraction patterns and projected structures for spinel.

TABLE 1.--Site distributions obtained from individual zone axes, analysis of all data, and comparison with ratio ALCHEMI analysis.

Zone	m - v	f_{Cr}	f_{Mn}
<100>	19	$.68 \pm .02$	$.32 \pm .01$
<310>	11	$.70 \pm .02$	$.30 \pm .02$
<211>	13	$.74 \pm .07$	$.26 \pm .06$
All Zones	47	$.69 \pm .015$	$.31 \pm .01$
Ratio analysis	49 spectra	$.72 \pm .12$	$.28 \pm .12$

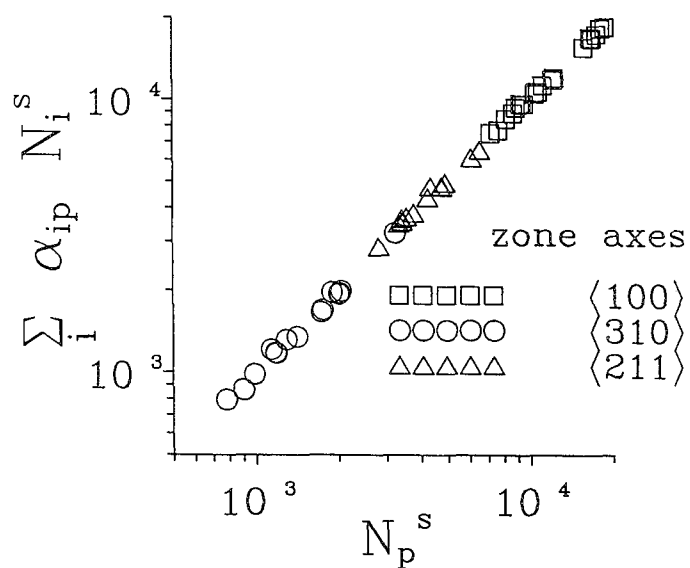


FIG. 2.--Fit of N_{Fe} to $\alpha_{Cr}N_{Cr} + \alpha_{Mn}N_{Mn}$ for all <100>, <310>, and <211> zone axis data.

EVOLUTIONARY DEVELOPMENTS IN X-RAY AND ELECTRON ENERGY LOSS MICROANALYSIS INSTRUMENTATION FOR THE ANALYTICAL ELECTRON MICROSCOPE

N. J. Zaluzec

Developments in instrumentation for both x-ray energy dispersive and electron energy loss spectroscopy (XEDS/EELS) over the past 10 years have given the experimentalist a greatly enhanced set of analytical tools for characterization. Microanalysts have waited nearly two decades for a true analytical microscope and the development of 300-400kV instruments should have allowed us to attain this goal. Unfortunately, that has not generally been the case. There have been some major improvements in the techniques, but there has also been some de-evolution in the modern AEM.

In XEDS, the majority of today's instruments are still plagued by the hole count effect, which was first described in detail over 15 years ago. The magnitude of this problem can still reach the 20% level for medium atomic number species in a conventional off-the-shelf intermediate-voltage AEM. This is an absurd situation and the manufacturers should be severely criticized. However, part of the blame also rests on the AEM community for not having come up with a universally agreed-upon standard test procedure. Fortunately, one is in the early stages of refinement. The proposed test specimen¹ consists of an evaporated Cr film ~500-1000 Å thick supported on a 3mm-diameter molybdenum 200µm aperture. The Cr film is mounted so that it partially covers the 200µm hole (Fig. 1). This specimen provides (1) a means of checking the detector and collimator alignment by x-ray mapping of the aperture, (2) hole-count measurements with a "thin" Cr film and "bulk" Mo signal, (3) peak/background evaluation with the Cr K α line, (4) background shape evaluations by comparison with the theoretical bremsstrahlung shape, (5) a nominal energy resolution at the FWHM of the Cr K α line, (6) a measure of near peak incomplete charge collection by a comparison of FWTM and FWHM measurements, (7) a measure of the relative collection efficiency of the particular detector if each film is calibrated at the supplier institution and the testing site can measure incident beam current, and (8) a nominal measure of the energy resolution of any electron spectrometer by a study of the Cr L $_3$ /L $_2$ edge profile. The specimen was designed to maximize any possible hole-count signal rather than minimize it. Thus, it is equally unfair to all manufacturers! When used as a hole-count test

N. J. Zaluzec is at the Electron Microscopy Center for Materials Research, Materials Science Division, Argonne National Laboratory, Argonne, IL 60439. This work was supported by DOE at ANL under contract BES-MS W-31-109-Eng-38.

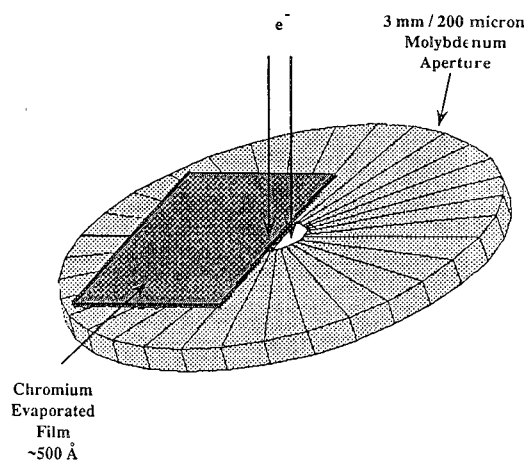


FIG. 1.--Proposed AEM/XEDS test specimen consisting of 500-1000Å thick evaporated Cr film supported on top of standard 3mm/200µm molybdenum aperture.

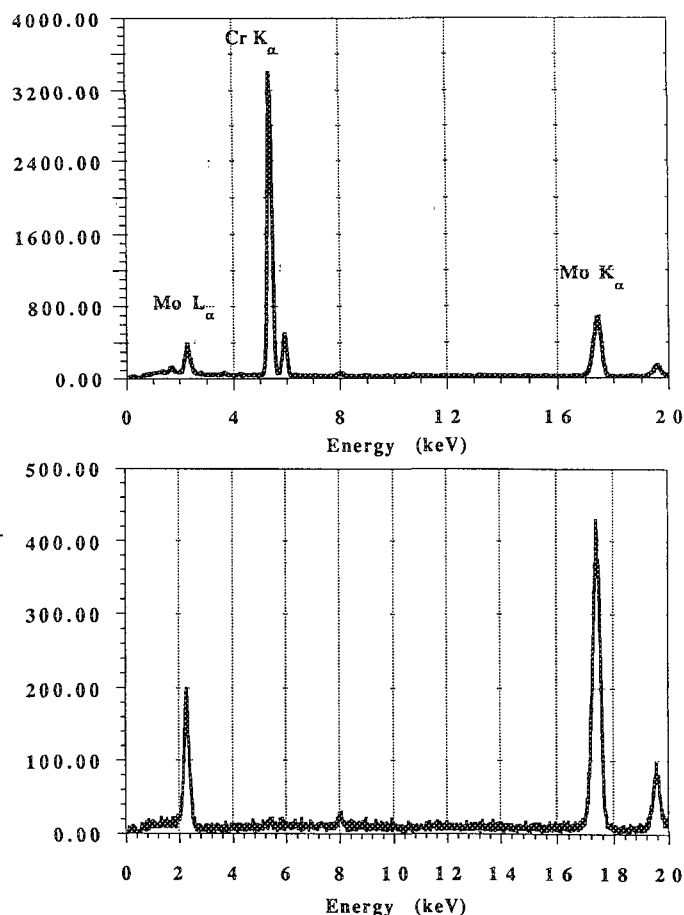


FIG. 2.--Examples of x-ray spectra from AEM/XEDS Cr/Mo test specimen: beam on specimen (top), beam in "hole" (bottom).

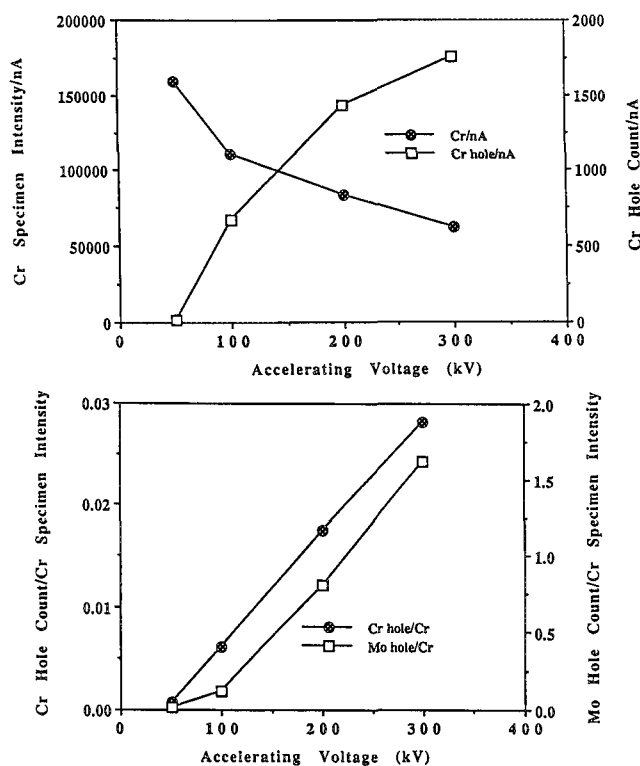


FIG. 3.--Experimental hole count information available from test specimen: (a) Cr and Cr-hole count/nA is used to identify source of uncollimated radiation, (b) magnitude of hole count signal is monitored by ratio of Mo-hole to Cr specimen intensity.

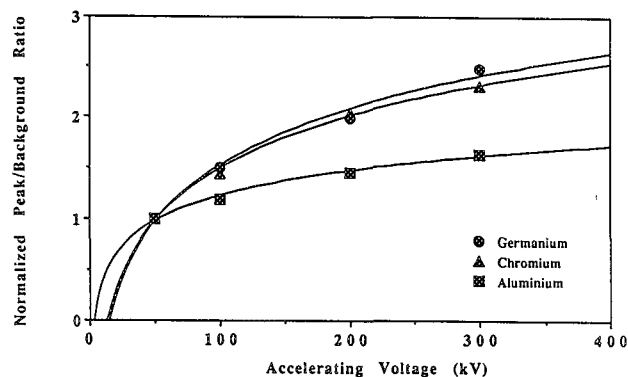


FIG. 4.--Experimental increase in peak/background ratio with accelerating voltage.

specimen, typical spectra (Fig. 2) would yield a Cr K x-ray series from the film, and Mo K and Mo L x-ray line series from uncollimated radiation striking and exciting emission from the aperture. When the electron beam is directed into the uncovered "hole," virtually no Cr signal is detected. However, a significant x-ray spectrum is still measured, which is due to uncollimated fluorescing radiation generated in the probe-forming system of the microscope. Figure 3(a) shows an example as a plot of the

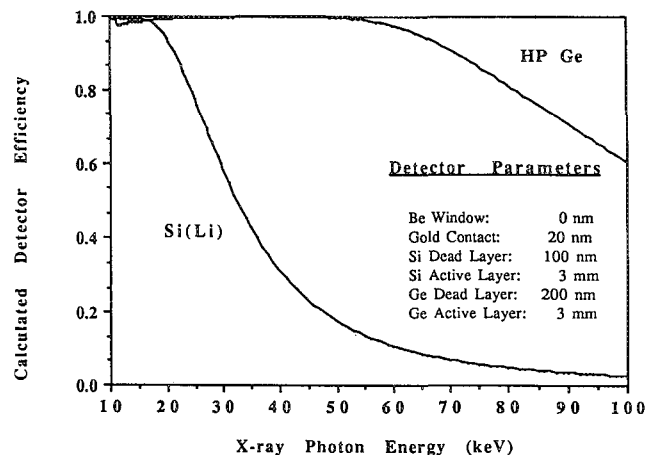
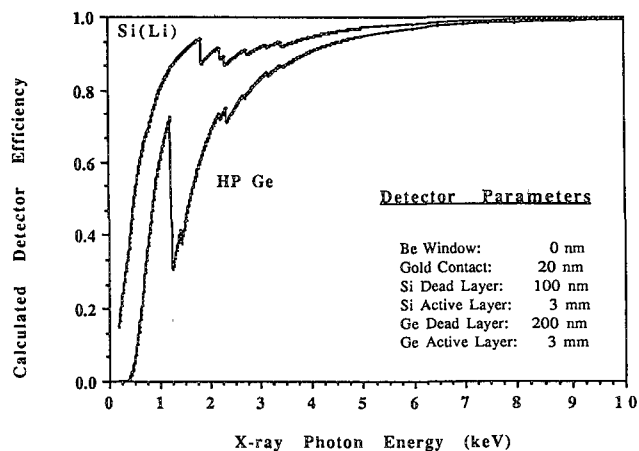


FIG. 5.--Calculated efficiency for windowless Si(Li) and HP Ge XEDS detectors.

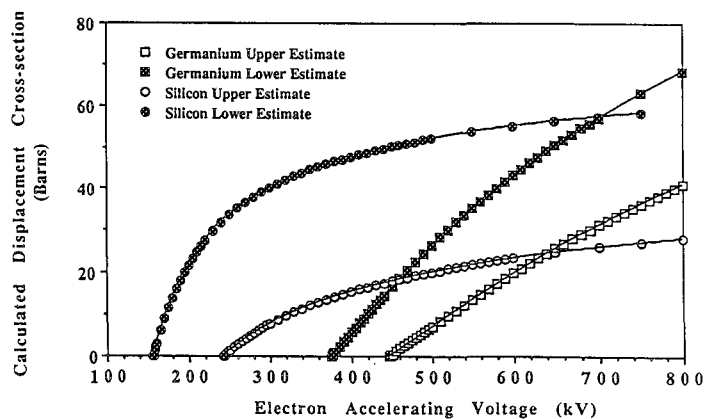


FIG. 6.--Calculated displacement cross sections in Si and Ge by electrons.

Cr/nA and Cr-hole/nA signals as a function of voltage from 50 to 300 kV. We see that the functional dependence of the Cr-hole count/nA on voltage is not the same as that of the Cr film signal. The Cr film signal follows a typical electron-excited cross-section dependence, whereas the Cr-hole signal increases monotonically with voltage, which suggests x-ray excitation generated in the condenser aperture system of the AEM as the probable source. In Fig. 3(b) we plot the Mo K and Cr hole intensity

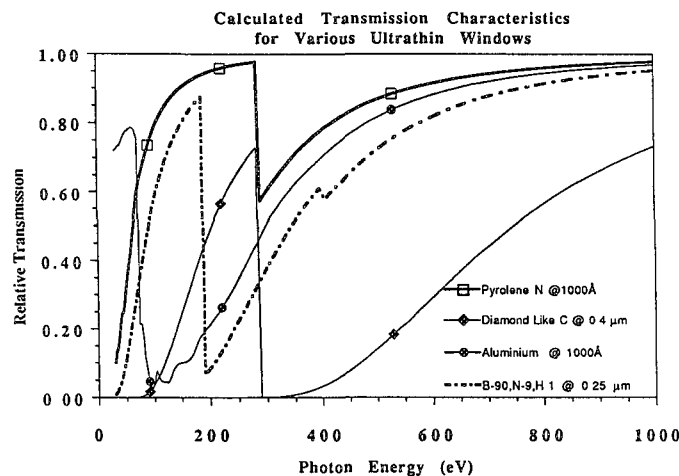


FIG. 7.--Calculated transmission efficiency of ultra thin windows of pyrolytic (ρ = 1.11 gm/cm³), diamond-like carbon (ρ = 3.5), aluminum (ρ = 2.7), and boron compound (ρ = 1.4).

measured when the electron beam is off the Cr film and in the "hole" of the aperture and ratio this to the Cr intensity measured with the beam on the film. As can be seen the Mo signal increases with voltage and from 200 kV and higher actually exceeds the signal produced by the electron beam hitting the Cr film! The existence of the hole count is a situation that can be cured by redesign of the instrument; however, that will not happen until sufficient numbers of analytical microscopists demand it, using a reproducible test specimen and procedure.

On the quantitative side, after corrections for the hole count, we understand the effects of the higher voltage on the intensity variation and hence to quantification.² K-factor calculations can be made generally to better than a ±10% relative error level, and for limited ranges of atomic numbers to less than 2%. The predictions by many authors as to the theoretical increase in the peak/background ratio with accelerating voltage have been realized (an example is shown in Fig. 4) and hence the predicted increased mass sensitivity of x-ray analysis with voltage in the AEM has been realized.

Windowless x-ray detector systems have opened up the low-energy light-element regime to the x-ray analyst (Fig. 5); however, spectral overlaps are a recurring problem in complex systems. The HPGe systems have extended the accessible high-energy x-ray analysis regime above 40 kV (Fig. 5), which permits us to study higher energy lines that were impractical with Si(Li) detectors. The energy resolution of Ge detectors is generally better than that of Si(Li) detectors, but if they are to make a substantial impact on the low-energy regime, attention must also be paid to the Ge dead layer absorption problem at ~1.3 keV (Fig. 5). This problem could also have an adverse effect on quantitative analysis, as it will greatly affect the accuracy of k-factor calculations owing to the errors in the detector efficiency calculations it could introduce. On the positive side, due

to its higher atomic number, germanium is less prone to electron displacement damage. Figure 6 is a plot of the estimated upper and lower limits of the calculated displacement cross section by electrons in both Si and Ge. As can be seen the Ge threshold is approximately 400 kV; hence in any modern medium-voltage instruments operating below 400 kV the Ge detectors should be nearly invulnerable (except of course to the inexperienced operator or student).

Recently various new windows for XEDS systems have been developed in which diamond-like carbon and/or boron compounds are used that (in contrast to Pyrolytic N or ultrathin Al) can withstand atmospheric pressure. In choosing such a window it is essential that one appreciates their transmission characteristics, particularly in the presence of severe absorption edge effects. Figure 7 shows the calculated transmission curve of these windows, which must be multiplied by the values in Fig. 5 to yield the relative detector efficiency curve. The important point evident from this figure is that not all ultrathin windows are the same. For example, the severe absorption edge at carbon makes it difficult for diamond-type windows significantly to detect nitrogen. Pyrolytic N still appears to be the best window from the efficiency standpoint, although it cannot withstand the differential pressure of 1 at. In the future, wavelength-dispersive systems may yet return to the AEM, but in which role they will participate is an open question. Overcoming the serial acquisition mode will be essential to making it a practical methodology. At present proposals at Lehigh University and Argonne National Laboratory seek to address these issues in the near future.

EELS has grown tremendously in the past five years. The major contributing factor is the successful commercialization of instrumentation for both serial and parallel data acquisition. The advent of higher-voltage AEMs has not affected the methodology adversely; in fact, the new medium-voltage systems have helped overcome multiple scattering effects. Spectral energy resolution has increased ten-fold in the past 15 years. We are now at the point where the energy width of the sources limits the performance of spectrometers, and values as low as 0.3 eV for field-emission sources are attainable. Photodiode and CCD arrays have made parallel EELS systems into viable analytical devices. No longer strapped by the time required to record serial data, we can expect significant results from these systems in the next few years; the quality of EELS data being produced now rivals that of synchrotron sources. Time-resolved EEL spectroscopy on commercial instruments has reached the millisecond regime and is down to the 10 μs range on research-grade instruments. On the horizon we should expect the development of two-dimensional imaging systems in which a magnetic sector spectrometer is followed by a series of multiple quadrupoles and sextupoles and large-area CCD arrays, providing energy-filtered imaging and

diffraction capabilities on all AEMs. Another likely area to see development in EELS is ultra-high energy resolution spectroscopy for applications in the meV regime. We may see the development of instruments with both prespecimen spectrometers to monochromate the incident electron probe, followed by high-resolution postspecimen spectrometers that will allow the materials scientist/physicist to explore the interesting physics and information now hidden in the ultralow-energy loss regime.

References

1. Standard proposed by the XEDS/AEM panel of the 1989 Higgs Meeting, Giens, France. Panel members (in alphabetical order): J. Bentley, J. Cazaux, A. Craven, R. Glas, J. J. Hren, P. Kruit, T. Malis, P. Rez, D. B. Williams, and N. J. Zaluzec.
2. N. J. Zaluzec, "Comparison of experimental and theoretical XEDS cross-sections and K-factors (this volume).

STACKING FAULTS IN THE α -AlMnSi CUBIC PHASE

S. J. Andersen, Y. X. Guo, and Ragnvald Høier

Owing to its strong relationship with the icosahedral quasicrystal (IQ) of a similar composition, the α -AlMnSi phase has been studied extensively in recent years. Its structure is largely described as a stacking of icosahedral atomic clusters, called MacKay Icosahedra (MIs). The IQ is believed to be constructed of a complicated, aperiodic stacking of similar clusters, held together by so-called "glue" atoms. The IQ may transform to the α -phase or to other phases containing icosahedral clusters, which indicates that such units are quite stable; yet there are few if any reports on the implications that such stability could have. We present a study of a stacking fault and the combination of such faults in a triple junction in the α phase, with displacements of the type $a\langle 1\tau 0 \rangle / 2\tau^2$, which has its origin with these clusters. Here a is the cube edge and $\tau = 2 \cos 36^\circ = \frac{1}{2}(1 + \sqrt{5})$ is the irrational number called the *golden mean*. The model we propose is found to be in very good agreement with the experimental results.

Experimental

Materials were prepared by the well-known melt-spinning technique. A conventional 6061 aluminum alloy, to which ~20% of $\text{Al}_{60}\text{Mn}_{25}\text{Cr}_8\text{Si}_7$ had been added to produce reasonably stable IQs in the 6061 matrix, was induction heated in a graphite crucible under argon atmosphere. A Cu wheel 200 mm in diameter was used at 2000 rpm. This produced a thin metal ribbon that as-quenched contained a dispersion of small IQs. Some ribbons were heat-treated at 450 C for 12 h. Specimens for the transmission electron microscope (TEM) were prepared by jet polishing at -25 C in an electrolyte of 33% vol. of HNO_3 in methanol. The specimens were investigated in a Philips EM 400T and a Philips CM30 TEM.

Results

The building block (MI) of the α phase (Fig. 1) consists of an inner Al-icosahedron surrounded by a Mn-icosahedron nearly twice as large. Just outside the thirty (2-fold) edges of the latter, there is a shell of thirty more Al-atoms. In the present case, Si and Cr atoms substitute some Al and Mn sites, respectively. This process is seen to equalize the clusters at the vertex and body center and produces a bcc phase of $a = 12.68 \text{ \AA}$. (The

pure α -AlMnSi version has a primitive cubic, nearly bcc structure.) Figure 2 illustrates the stacking of the α phase by these clusters, with the "glue" atoms neglected.^{2,3} In the following the α phase is represented by MIs drawn to the size of Mn-icosahedra, as in Fig. 2. Eight of the 20 triangular faces of the MIs have normals lying along the $\langle 111 \rangle$ directions. These faces are the bonding faces between MIs in the α phase. The remaining 12 faces of an MI have all normals pointing in incommensurate directions with respect to the cubic lattice. One example is $e_3 = [-\tau^2, 1, 0]/\tau\sqrt{3}$. All twelve 5-fold axes of the MIs point in directions found by cycling the vector $[\pm\tau, 0, \pm 1]$. Since τ is irrational, all 5-fold axes are also incommensurately directed. Figure 3 shows a $\langle 001 \rangle$ zone of the α phase. We have found that faults like the one observed in this figure are present for various compositions of this phase, i.e., with or without additions of Cr and Si. The fault boundary typically lies in a $\langle 110 \rangle$ plane. Careful measurements on such micrographs have revealed that the displacement along the boundary must be close to $\frac{1}{2}d_{110}$. In addition, an expansive displacement normal to the fault is experimentally found to be $\sim 0.08d_{110}$. The total displacement is found to be ~ 0.36 , in fraction of the edge. This fault is explained as follows: First, take each white spot of Fig. 3 to represent an MI, as visualized in Fig. 4. Here the $\langle 111 \rangle$ faces are indicated by smaller triangles. Two layers of MIs are shown. The lower layer has solid filled triangles and the upper layer has small open triangles on $\langle 111 \rangle$ faces. In the perfect bonding situation, hidden faces *below* unfilled triangles in the upper layer connect to faces marked with filled triangles in the lower layer (bonding between I-type faces). Notice that the four Vertical II-type faces of each MI have normals (3-fold axes) that lie in the paper plane. A stacking fault boundary shift distorts the bonding pattern. Across the fault boundary the bonds now exist only between pairs of faces of type II instead of I. The distance between pairs of type I and II are the same. However, there is an accompanying small increase in volume due to the fault.

In effect, this situation is as follows. Cleave the crystal along a (buckled) 110 plane without destroying any MIs. Then translate one of the halves along one 5-fold axis of the MIs until 3-fold axes across the fault coincide (Fig. 4). In the example shown an MI at position (000) with I-type bonds is moved in the $[001]$ plane to connect to an MI at position (100), to its $[-\tau^2, 1, 0]$ plane. The geometrically perfect total displacement is then

S. J. Andersen is at SINTEF Applied Physics, N-7034 Trondheim, Norway; his coauthors are at the Department of Physics, University of Trondheim-NTH, N-7034 Trondheim, Norway. This work was supported by Hydro Al A/S, Norway.

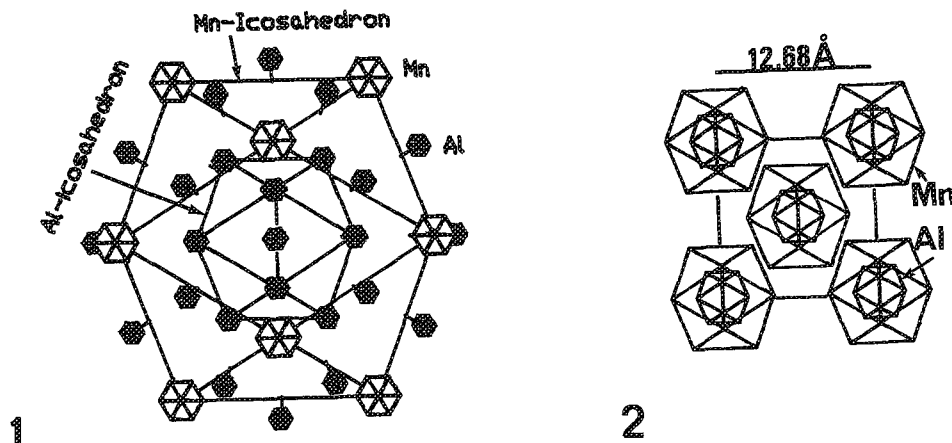


FIG. 1.--MI of α phase shown with Al and Mn icosahedra and shell of 30 Al atoms just outside 2-fold Mn icosahedron edges.

FIG. 2.--Visualization of α phase as packing of Mn icosahedra.

simply $a([100] + \frac{1}{2}\sqrt{3}e_3)$, or $a[1\tau 0]/2\tau^2$. (The length of the MI separation distance along a diagonal is $\frac{1}{2}a\sqrt{3}$, where a is the bcc edge.) The shift may be decomposed into $d_{110}/2$ along the fault (i.e., along $[110]$), plus $d_{110}/2\tau^3$ normal to the fault.⁴ A similar fault is found in the cubic R-phase of the Al-Li-Cu alloy.⁵

A more complicated case is shown in Fig. 5, which is a high-resolution micrograph of a junction of three α grains. The displacements in this junction may be understood according to the same mechanism as above (Figs. 6 and 7). In Fig. 6 the relative shift directions are shown for the case of a $[111]$ plane. We now see the decomposition of the shift along the $\langle 211 \rangle$ and $\langle 110 \rangle$ directions. The three shifts (Figs. 6 and 7) are determined to be $a[\tau 01]/2\tau^2$, $a[01\tau]/2\tau^2$, and $a[1\tau 0]/2\tau^2$. In Fig. 7 the small filled triangles on the triangular sides of each icosahedron indicate the bonding faces. The lower bonding faces of the icosahedron lie below faces without the small filled triangles. The stacking sequence is ..A B C A B C..; the bonds are indicated in the figure. Across the fault the stacking sequence has been interrupted to include bonding along 3-fold axes that are not commensurate with the lattice. One could say that this is a junction of three individual crystals connected through irrational directions. In a bcc phase there are six layers crossing one cell diagonal. The distance between two adjacent layers is therefore $d_{111}/2$. With respect to one of the individuals, the other two are shifted to an equal distance, $d_{111}/2$, along the $\langle 111 \rangle$ axis in opposite directions, which brings three icosahedra of type A (Fig. 7) closer together to the center. It is obvious that the unusual shift boundary described here is strong evidence for the stability of the MI clusters, which can be thought of as solid building blocks of the α phase. The shift boundary is found to lie on (110) planes, which are the most common glide planes in a bcc phase. A dislocation on such a glide plane will have a Burger's vector $a\langle 111 \rangle/2$. As inferred from the above, it is not possible to explain

the shift by such a Burger's vector, since the latter is 3 times the shift component observed along a $\langle 111 \rangle$ direction.

One might ask whether these stacking faults could play any part in the structure of the IQ. Since an IQ is believed to be realized through some subtle stacking of the MI, and since MIs are allowed to connect along any of their internal 3-fold axes, this question could indeed be important. One could imagine the IQ as produced by a more or less ordered stacking-fault mechanism. We believe that these stacking faults are a direct result of the transformation of the IQ. The IQ and the α phase have strong directional relationships,^{6,7} so that all $\langle 111 \rangle$ and $\langle 110 \rangle$ axes of the α phase fall exactly along some 3- and 2-fold axes of the IQ. The bcc phase can choose between 5 independent, relatively incommensurate base systems when it transforms from the IQ. When two such growth fronts meet, even with identical bases originating from the parent IQ, they nucleate at different positions and would be expected to produce some boundary faults.

Conclusions

A stacking fault in the bcc α -AlMnSi phase is found that cannot be explained by ordinary rational displacements of atoms or planes. It is shown that an irrational shift must exist across the boundary. A model is proposed that is found to be in good agreement with the experimental results. This model is extended to explain the relative shifts between individual grains in a triple junction. The results confirm the assumption that the MacKay icosahedra in the α phase are quite stable, and that they can have similar bonding properties in all twenty 3-fold directions and not only in the $\langle 111 \rangle$ directions. We have found that shift vectors associated with the faults discussed are always directed in one of the 12 internal 5-fold directions of the MI; i.e., of the type $a\langle 1\tau 0 \rangle/2\tau^2$. In the triple-junction case, if a $[111]$ axis is chosen as common, the three individual parts are shifted cyclically, with

total displacements $a[\tau 01]/2\tau^2$, $a[01\tau]/2\tau^2$, and $a[1\tau 0]/2\tau^2$.

References

1. H. Yamane et al., *Production of Al-based Ternary and Quaternary Icosahedral Phases*, Tech. Rep., ISSP, University of Tokyo, Ser. A, No. 1848, 1987.
2. P. Guyot and M. Audier, "A quasicrystal structure model for Al-Mn," *Phil. Mag.* B52: L15-19, 1985.
3. M. Audier and P. Guyot, "Al₄Mn quasicrystal atomic structure, diffraction data and Penrose tiling," *Phil. Mag.* B53: L43-51, 1986.
4. S. J. Andersen, *Quasicrystals and Inter-*

metallic Phases in Rapidly Quenched Aluminum Alloys, Ph.D. thesis, University of Trondheim-NTH, 1990, 13.

5. M. Audier et al., "Structural relationships in intermetallic compounds of the Al-Li-(Cu,Mg,Zn) systems," *Phil. Mag.* B60: 437-466, 1989.

6. Koskenmaki et al., "Coherent orientation relationship between an icosahedral phase and a cubic α -phase in melt-spun Al-Si-Mn," *Phys. Rev.* B33: 5328-5332, 1986.

7. M. Audier and P. Guyot, "Quasi-crystal structure models related to crystalline structures," in M. V. Jaric, Ed., *Aperiodicity and Order*, New York: Academic Press, 1989, 3: 1-36.

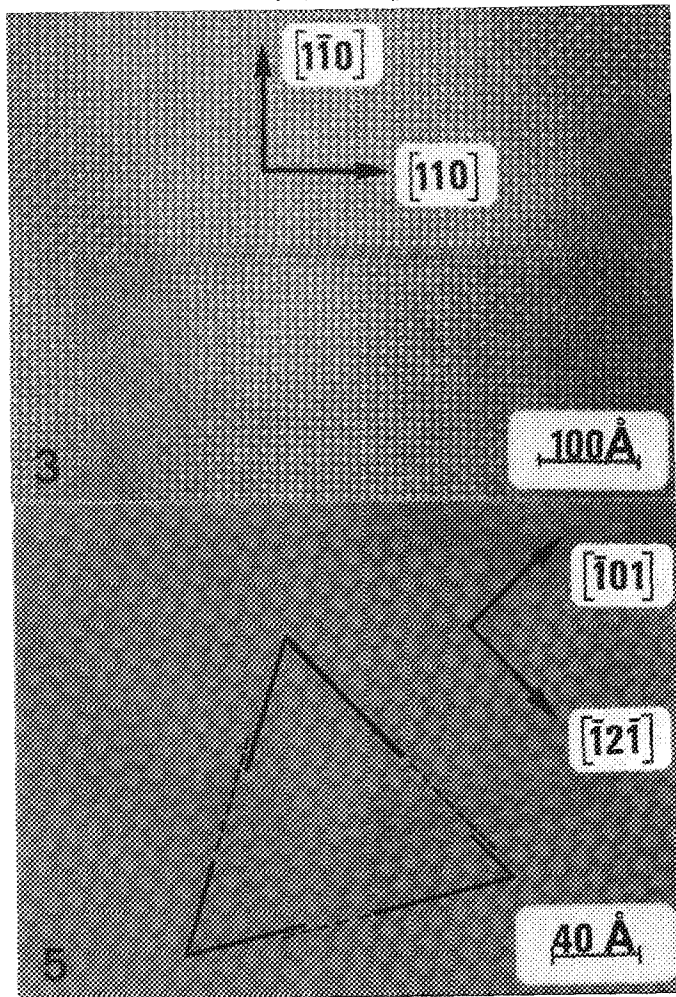


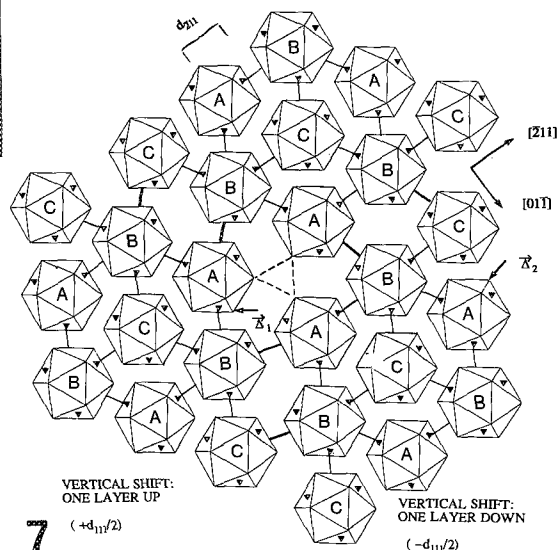
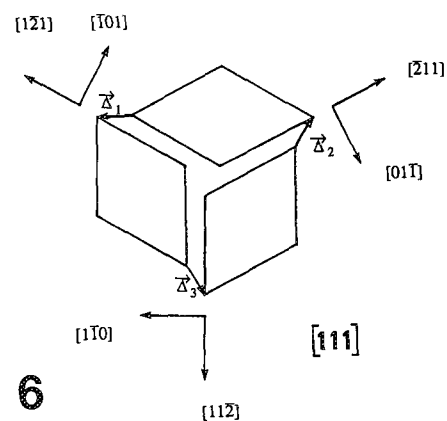
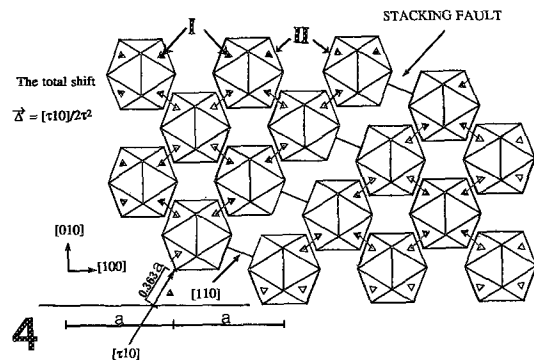
FIG. 3.--Typical stacking fault in [001] zone of phases.

FIG. 4.--Stacking fault modeled by shifted Mn icosahedra.

FIG. 5.--Junction of 3 α grains. Common [111] zone axis.

FIG. 6.--Illustration of relative shifts between grains of Fig. 5.

FIG. 7.--Junction in Fig. 5 visualized with Mn icosahedra. $\langle 111 \rangle$ bonding faces and shifts indicated. (Absolute shifts given in text.)



LACBED WITH QUANTITATIVE ANOMALOUS ABSORPTION CORRECTIONS

C. J. Rossouw, P. R. Miller, and L. J. Allen

Although Fourier coefficients V_g' for the absorptive potential due to thermal diffuse scattering (TDS) do not scale with elastic values V_g ,¹⁻⁴ it has been common practice to set $V_g' = \alpha V_g$ with a value 0.02-0.1 assigned to the phenomenological factor α . However, recent work⁵ has demonstrated why the α -model is inappropriate. It is preferable to describe absorption via an Einstein model for TDS⁴⁻⁹ by an imaginary component in the terms

$$V_{g-h} = \frac{h^2}{2\pi m V_c} [\text{site}] \cdot [f_{\beta n}(g-h) + if_{\beta n}'(g-h)] \quad (1)$$

where V_{g-h} is now the Fourier coefficient of the total scattering potential, $f_{\beta n}(g-h)$ the (thermally attenuated) atomic elastic scattering factors, and

$$[\text{site}] = \sum_{\beta n} \exp[i(g-h) \cdot \tau] \quad (2)$$

where $\tau_{\beta n}$ are the n sites of atom type β in the unit cell. The TDS absorptive component $f_{\beta n}'(g-h)$ is

$$f_{\beta n}'(g-h) = \frac{k}{4\pi^2 V_c} \cdot \int_0^{2\pi} d\phi \int_0^\pi d\theta \sin \theta f_{\beta}(q+g) f_{\beta}(q+h) [\text{TDS}] \quad (3)$$

where integration occurs over 4π steradians, and [TDS] describes coupled transitions between reciprocal lattice vectors g and h by

$$[\text{TDS}] = [\exp\{-M(g-h)\} - \exp\{-M(q+g) - M(q+h)\}] \quad (4)$$

where $M(g) = 0.5g^2 \langle U_{\beta n}^2 \rangle$ is the Debye-Waller factor. Eigenanalysis routines enable calculation of diffracted beam intensities with absorption included via perturbative or exact matrix methods.^{5,9}

Results

Figures 1(a) and (b) show kinematic mean free paths (mfp) λ_{kin} for TDS as a function of temperature T and incident beam energy E_0 for silicon and GaAs, derived from appropriate Debye temperatures θ_D .^{4,10} At 300 keV and 300 K, λ_{kin} is 1195 and 217 nm for Si and GaAs, respectively. An identical λ -value for the proportional model is obtained for GaAs with $\alpha = 0.0244$. The elastic potential $V(r)$ is compared with the Einstein potential $V'(r)$ in Figs. 1(c) and (d).

C. J. Rossouw and P. R. Miller are at CSIRO, Clayton, Australia; L. J. Allen is at Melbourne University, Parkville, Australia.

The full-width half-maximum of the TDS potential associated with each atomic site is roughly 4 times broader than $\langle u^2 \rangle$, the rms thermal displacement of individual atoms,⁴ and is highly localized about atomic sites with negligible values within empty crystal channels.

Figure 2 shows experimental and calculated $\langle 001 \rangle$ LACBEDs for silicon and GaAs. Differences within the central region for GaAs compared with Si are caused by the presence of Brillouin zone (BZ) boundaries due to additional $\{200\}$ difference reflections. Concentric ring contrast occurs within the first $\{220\}$ BZ boundaries for Si. GaAs exhibits a large increase in absorption near the exact zone axis orientation and is not thick enough for concentric ring contrast to be distinguishable within the $\{200\}$ BZ boundaries. Correlation between experiment and theory for Si is excellent, particularly in regions of strong contrast where $\{220\}$, $\{400\}$, and $\{660\}$ BZ boundaries intersect. There is some nonuniformity in crystal thickness, as evidenced by some distortion in the experimental contrast.

A comparison of experimental and calculated $\langle 111 \rangle$ LACBEDs for silicon and GaAs is shown in Fig. 3(a)-(d). Similar contrast is apparent for silicon and GaAs, since both crystals have diffracted beams with identical indices excited in the zeroth order Laue zone. Far stronger absorption within the $\{220\}$ channels occurs for GaAs than for Si.

Figures 3(e) and (f) compare changed in λ_{dyn} , the dynamical mfp, shown in terms of $\lambda_{kin}/\lambda_{dyn}$. These patterns are similar to those which map out fast electron probability density $\phi\phi^*$ on atomic species as a function of orientation, which is in turn related by reciprocity to the generation of Kikuchi band contrast from localized inelastic scattering events.¹¹ At very specific orientations, dynamical diffraction causes a severe decrease in localized inelastic scattering cross sections compared with kinematic values, in contrast to an increase in cross section at or close to a symmetrical zone axis orientation. This decrease is associated with orientations which force $\phi\phi^*$ to be peaked within empty crystal channels between atom positions, as opposed to exact zone axis orientations where $\phi\phi^*$ is predominantly superimposed on atomic columns. λ_{dyn} varies between 287 nm and 4135 nm for Si, and between 117 nm and 660 nm for GaAs. The dynamical mean free path may be increased by a factor of 4 in comparison with the kinematic (plane wave) result.

Calculations based on the Einstein and α -models are correlated in Fig. 4 with a densitometer line traces from the zeroth order beam

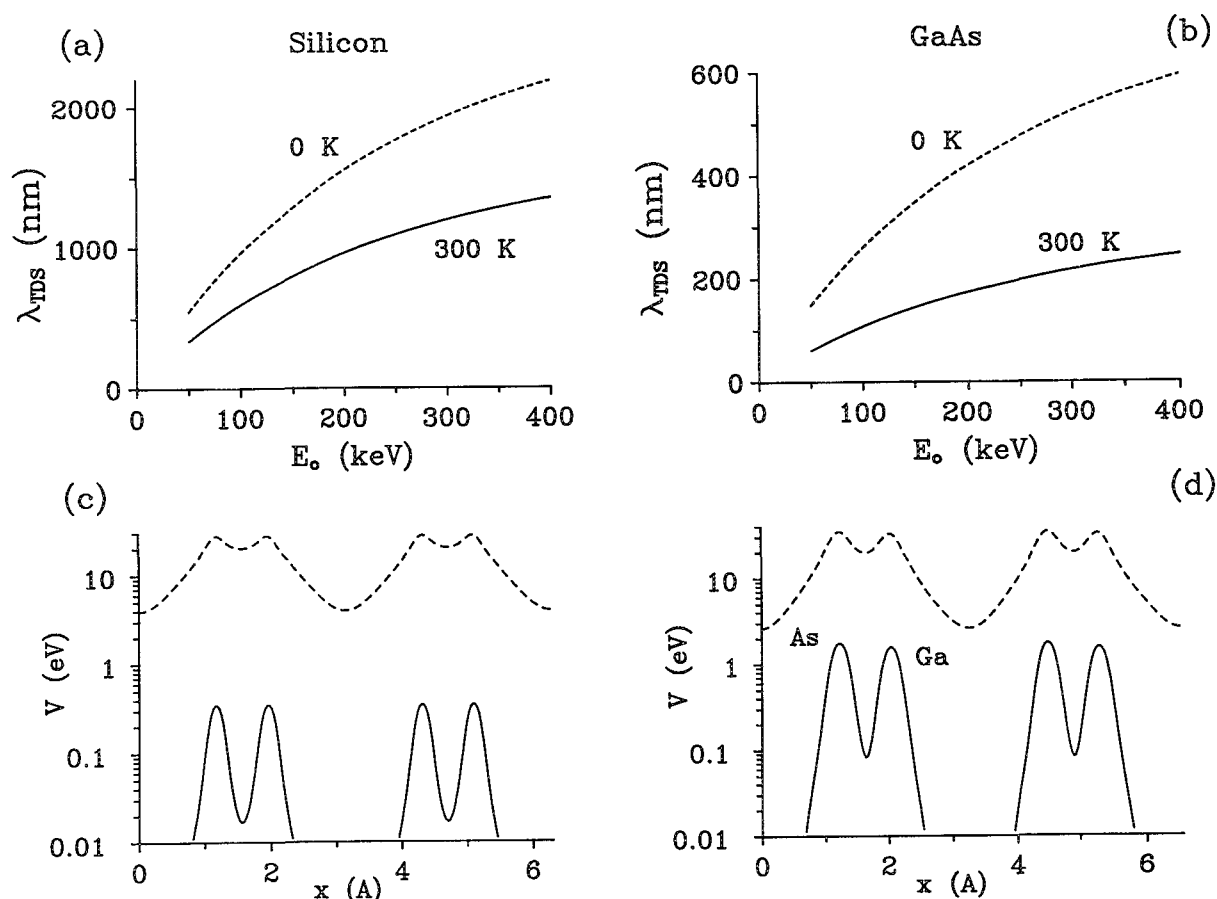


FIG. 1.-- λ_{TDS} for (a) Si, (b) GaAs for $T = 0$ K (dashed line) and 300 K (solid line) as a function of incident beam energy. Elastic (dashed) and TDS (solid) potentials along $\langle 111 \rangle$ for $E_0 = 300$ keV and $T = 300$ K is shown in (c) for silicon and in (d) for GaAs.

LACBED intensity, traced between positions X and Y as marked in Figs. 2(b) and 3(b). Note the lack of correlation produced by the α model, whereas overall agreement between the Einstein model and experiment is good. For the $\langle 001 \rangle$ zone, an increase in transmitted intensity is apparent between the 2nd and 4th $\{200\}$ BZ boundary due to a sharp increase in λ_{dyn} . This result is predicted by the Einstein model but not by the α model. The same phenomenon occurs between the 2nd and 4th $\{220\}$ BZ boundary for the $\langle 111 \rangle$ zone.

Discussion

The Einstein model for TDS enables mean and anomalous absorption coefficients on different Bloch wave dispersion surfaces to be determined from first principles.^{8,9} Diffraction contrast is defined solely by the Debye-Waller factor for each crystal atom; there are no open parameters in the formalism. We have shown that the α model cannot adequately describe anomalous absorption effects, whereas the Einstein model enables quantitative calculation of TDS absorption from first principles (totally defined by $\langle u^2 \rangle$ and incident beam energy E_0). A serious shortcoming of the α model is its inability to allow drastically enhanced transmission of the fast electron wavefunction for orientations

where the probability density is predominantly within open crystal channels, since the potential predicted by the α model is not negligible within these channels.

In contrast with high-resolution experiments, which require very thin crystals (< 30 nm thick) for quantitative interpretation, LACBED experiments are generally undertaken with relatively thick crystals, for three reasons. *First*, diffraction contrast needs to be sharpened by having relatively narrow rocking curves for each diffracted beam, which requires a thickness of order 100 nm. *Second*, since a relatively large crystal area is examined in the Tanaka techniques,¹² in which one uses the objective lens forefield in nanoprobe mode to produce a highly convergent beam, relative changes in thicknesses $\Delta t/t$ over the entire illuminated area may be minimized by a relatively large mean thickness t . *Third*, thick crystals are more rigid and minimize distortions due to bending over the illuminated area. However, for crystals of high atomic number and low λ_{TDS} , variations in dynamical absorption of the fast electron wave-function are strong for thicknesses in excess of 150 nm or so. It is for these situations, where $t/\lambda_{\text{TDS}} > \frac{1}{2}$, that the use of the quantitative Einstein model is extremely powerful, giving quantitative correlation where the α model is simply inappropriate.

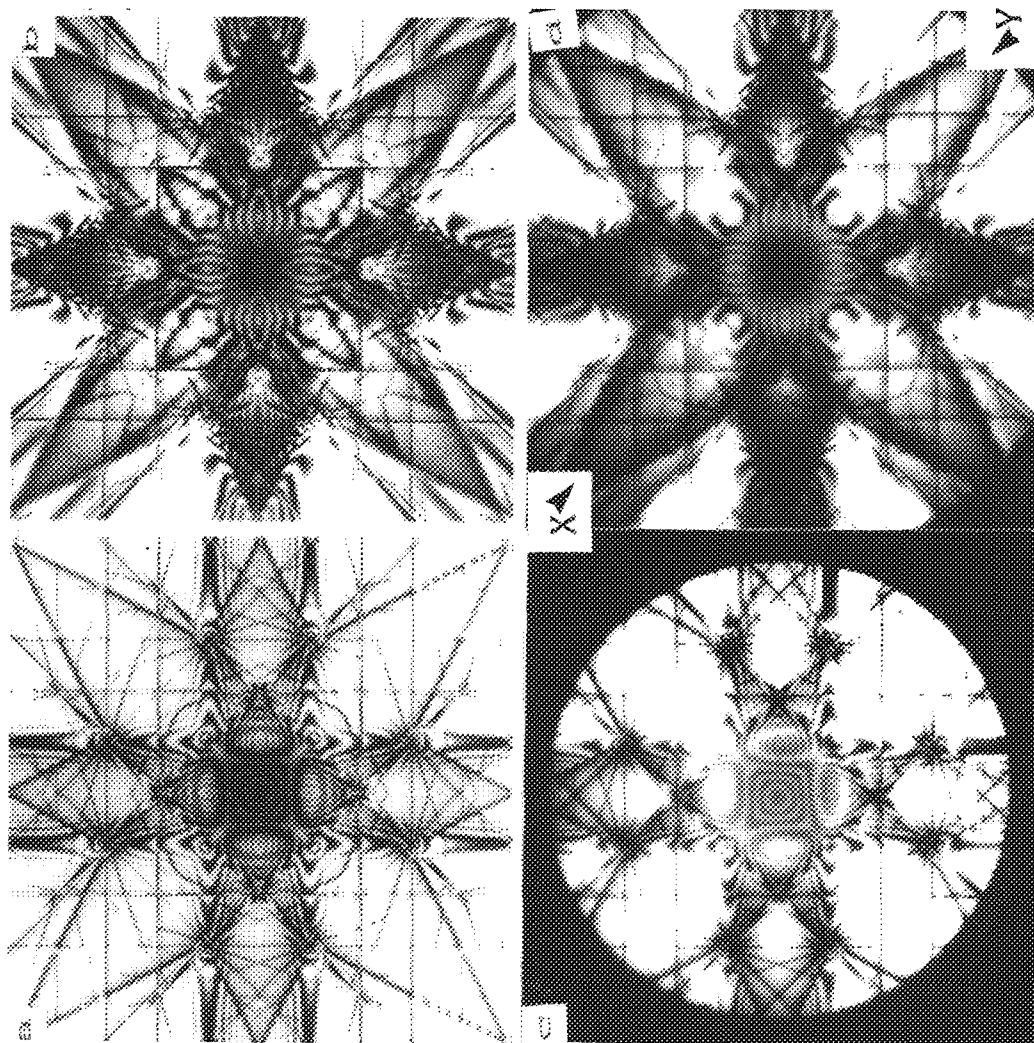


FIG. 2.--Comparison of calculated and experimental 300keV $\langle 001 \rangle$ zone axis LACBEDs for (a,c) Si (375 nm), (b,d) GaAs (300 nm).

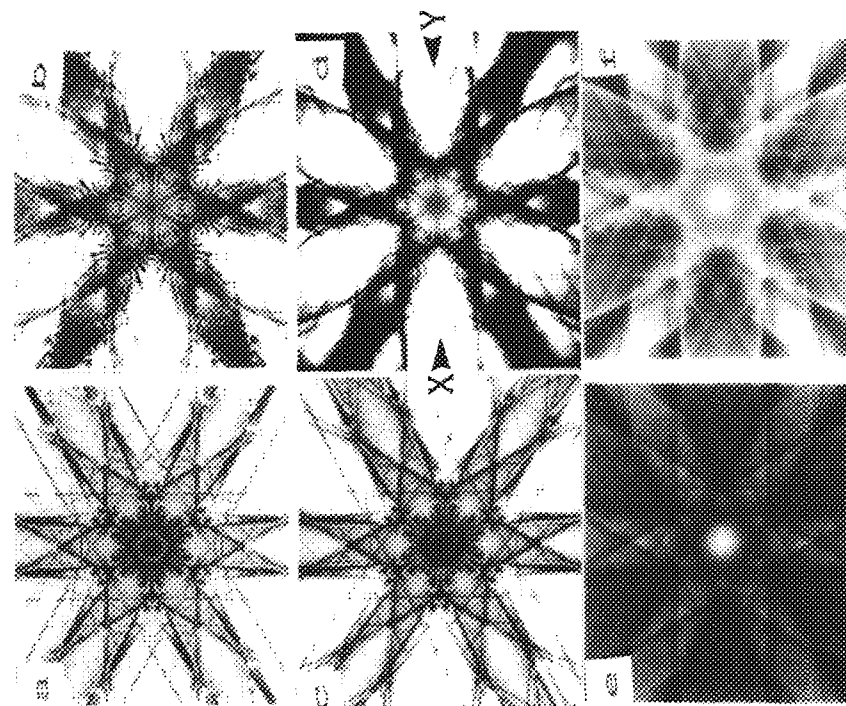


FIG. 3.--Comparison of calculated and experimental 300 keV $\langle 111 \rangle$ zone axis LACBEDs for (a,c) Si (260 nm), (b,d) GaAs (360 nm). $\lambda_{kin}/\lambda_{dyn}$ is given for (e) Si (max 4.17, min 0.29, $\lambda_{kin} = 1195$ nm), (f) for GaAs (max 1.84, min 0.33, $\lambda_{kin} = 217$ nm).

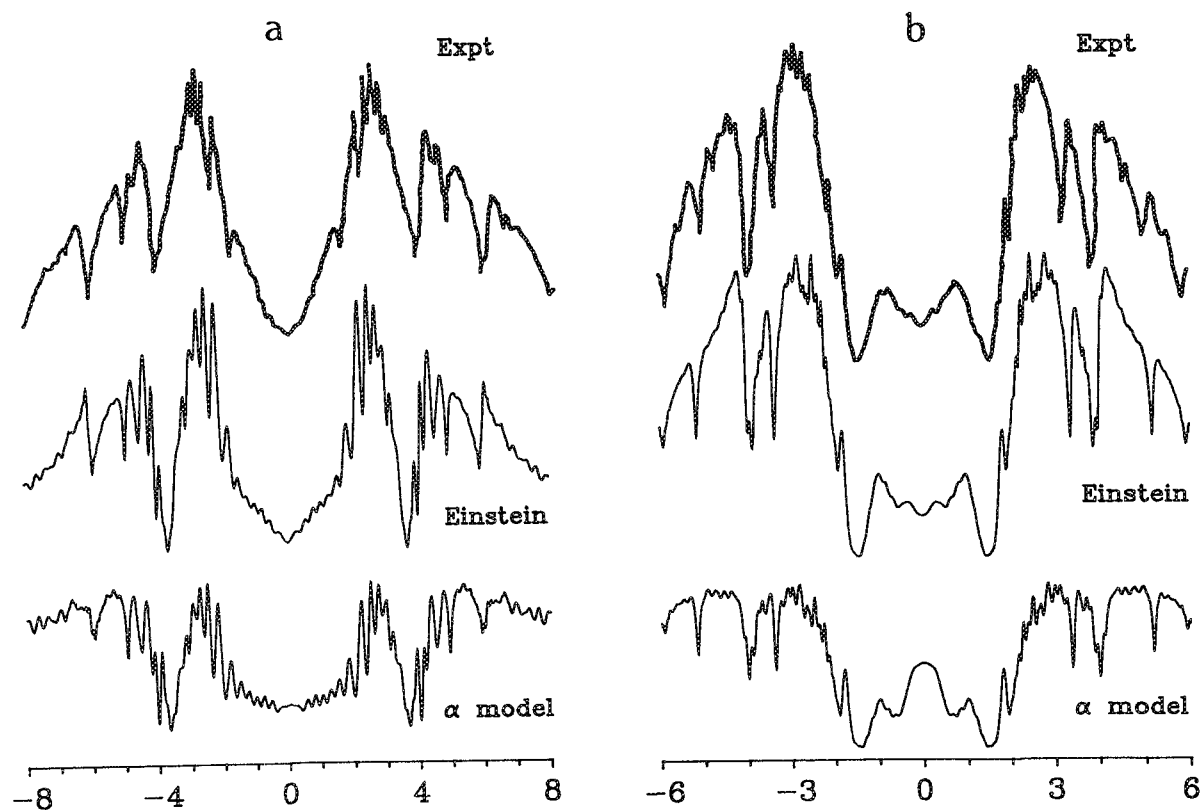


FIG. 4.--Comparison of α and TDS models with densitometer trace $X \rightarrow Y$ across (a) $\langle 001 \rangle$, (b) $\langle 111 \rangle$ LACBEDs as marked in Figs. 2(b) and 3(b) for GaAs; x axis is given in units of $\{200\}$ and $\{220\}$ BZ boundaries, respectively.

References

1. C. J. Humphreys and P. B. Hirsch, *Phil. Mag.* 18: 115, 1968.
2. G. Radi, *Acta Crystallogr.* A26: 41, 1970.
3. P. A. Doyle, *Acta Crystallogr.* A26: 133, 1970.
4. L. J. Allen and C. J. Rossouw, *Phys. Rev. B* (in press).
5. C. J. Rossouw, P. R. Miller, J. Drennan, and L. J. Allen, *Ultramicroscopy* (in press).
6. C. R. Hall and P. B. Hirsch, *Proc. Roy. Soc.* A286: 158, 1965.
7. C. J. Rossouw and L. A. Bursill, *Acta Crystallogr.* A41: 320, 1985.
8. L. J. Allen and C. J. Rossouw, *Phys. Rev. B*39: 8313, 1989.
9. D. M. Bird, *Acta Crystallogr.* A (in press).
10. J. S. Reid, *Acta Crystallogr.* A39: 1, 1983.
11. C. J. Rossouw and L. A. Bursill, *Proc. Roy. Soc.* A408: 149, 1986.
12. M. Tanaka, *J. Electron Microsc.* 35: 314, 1986.

A GROUP OF NEW EQUATIONS RELATED TO THE OPERATION OF TEM DOUBLE-TILT HOLDER AND THEIR APPLICATION TO TRANSMISSION ELECTRON MICROSCOPY

Liu Qing

A double-tilt holder is often used in a transmission electron microscope (TEM) to adjust the specimen orientation during the analysis of crystallographic problems. The operation of the holder results in a change of a crystallographic vector from one vector to another. In the present paper, the transformation matrices related to the above change are given. According to these matrices, new equations useful for studying some crystallographic problems in a simpler way are deduced, and some experimental examples are given to show the application of these equations.

Matrix Description of the Rotation About the Tilt axes

The relationship between a fixed-reference orthogonal coordinate system and the tilt axes of a double-tilt holder is shown in Fig. 1. The x-axis coincides with the longitudinal axis T_1 of the specimen holder, the z-axis lies along the optical axis of the microscope. The second tilt axis T_2 of the specimen holder lies in the yz plane; the exact position depends on the first tilt angle α_0 of the T_1 axis. When the specimen is tilted through an angle β about the T_2 axis (from β_0 to $\beta_0 + \beta$), followed by a tilt α about the T_1 axis (from α_0 to $\alpha_0 + \alpha$), the new position of a vector g is

$$g' = T_1 T_2 g \quad (1)$$

where T_1 and T_2 are the transformation matrices related to rotations around the T_1 - and T_2 -axes, respectively:

$$T_1 = \begin{pmatrix} 1 & 0 & 0 \\ 0 & \cos \alpha & -\sin \alpha \\ 0 & \sin \alpha & \cos \alpha \end{pmatrix} \quad (2)$$

$$T_2 = \begin{pmatrix} \cos \beta & -\sin \beta \sin \alpha_0 & \sin \beta \cos \alpha_0 \\ \sin \beta \sin \alpha_0 & \cos^2 \alpha_0 + \sin^2 \alpha_0 \cos \beta & \sin \alpha_0 \cos \alpha_0 (1 - \cos \beta) \\ -\sin \beta \cos \alpha_0 & \sin \alpha_0 \cos \alpha_0 (1 - \cos \beta) & \sin^2 \alpha_0 + \cos^2 \alpha_0 \cos \beta \end{pmatrix} \quad (3)$$

An Equation to Determine the Practical Tilt Angle of the Specimen

It is possible to determine the tilt angles of the two axes from the meter reading of the specimen holder. However, the practical tilt

angle of the specimen during the operation of the two tilt axes of the double-tilt holder may not be known. In Fig. 1, at the original position where the tilt angle about the T_1 axis is α_0 , a crystal direction $u_0 v_0 w_0$ coincides with the z axis, with the diffraction pattern of this zone axis shown on the fluorescent screen. When the specimen is tilted (from α_0 to $\alpha_0 + \alpha$ and from β_0 to $\beta_0 + \beta$) to bring the direction uvw into coincidence with the z axis by operation of the double-tilt holder, the new position of the vector $[uvw]$ (written as U) is

$$U' = \begin{bmatrix} 0 \\ 0 \\ 1 \end{bmatrix} \quad (4)$$

$$U' = T_1(\alpha) T_2(\beta) U \quad (5)$$

$$\gamma = \cos^{-1} [\sin(\alpha - \alpha_0) \sin \alpha_0 + \cos(\alpha - \alpha_0) \cos \beta] \quad (6)$$

From the geometrical relationship shown in Fig. 1, γ can be considered to be the practical tilt angle of the specimen during the operation of the double-tilt holder.

Calculation of Tilt Angles for the Specimen Orientation Adjustment

The Kikuchi map is normally used in practice as a type of "road map" to adjust the specimen from one orientation to another.¹ However, the Kikuchi map method has its difficulties. First, the specimen area of interest is often too thin to produce Kikuchi line pairs, second, for a severely strained specimen the visible Kikuchi line pairs are poorly defined; and third, for a small grain specimen, tilting of the specimen may cause loss of the corresponding diffraction pattern due to specimen shift. In these situations, adjustment of the crystal orientation to follow the Kikuchi map may be difficult or even impossible. A computer program to calculate the tilt angles for adjusting the specimen from one zone axis to another has been developed by Chou.² However, it was found in practice that the calculation was complex and time consuming. In this section we present a group of new equations that allow the rapid calculation of the tilt angles and orientation adjustment of the specimen to be achieved.

In Fig. 1, if the diffraction pattern of the zone axis $[uvw]$ is to be obtained from the original position; the angle between $[uvw]$ and $[u_0 v_0 w_0]$ is γ . The specimen should be tilted through the angle γ about the normal to the common crystallographic plane ($H_0 K_0 L_0$) to both

Liu Qing is at the Analysis and Measurement Centre, Harbin Institute of Technology, Harbin 150006, China.

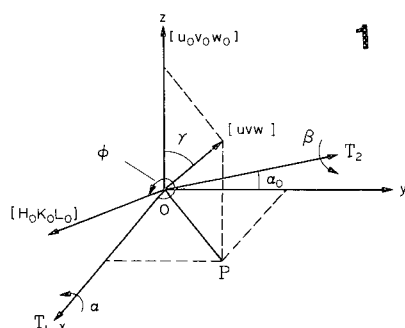


FIG. 1.--Geometry relationship of crystal specimen adjustment with double-tilt holder.

zones. The normal direction to the plane ($H_0K_0L_0$) is the direction of the line drawn from the central spot to the spot ($H_0K_0L_0$) in the diffraction pattern of the zone axis $[u_0v_0w_0]$. For a given camera length, the projection of the direction and sense of the x axis can be determined by observation of the movement of the Kikuchi pole as the T_1 axis is tilted. It follows that the angle ϕ between the normal to the plane ($H_0K_0L_0$) and the x axis can be measured on the fluorescent screen (Fig. 1). If we assume that the magnitude of the vector $|U|$ is unity, we can write U in the fixed reference orthogonal coordinate system shown in Fig. 1 as

$$U = \begin{bmatrix} \sin \gamma \cos(\phi - 270^\circ) \\ \sin \gamma \sin(\phi - 270^\circ) \\ \cos \gamma \end{bmatrix} = \begin{bmatrix} -\sin \gamma \sin \phi \\ \sin \gamma \cos \phi \\ \cos \gamma \end{bmatrix} \quad (7)$$

Use of Eqs. (2), (3), (4), and (7) in Eq. (5) leads to the equations

$$\alpha = \sin^{-1}(\sin \gamma \cos \phi \cos \alpha_0 + \sin \alpha_0 \cos \gamma) - \alpha_0 \quad (8a)$$

$$\beta = \tan^{-1}\left(\frac{\tan \gamma \sin \phi}{\cos \alpha_0 - \sin \alpha_0 \tan \gamma \cos \phi}\right) \quad (8b)$$

Having obtained the diffraction pattern of the zone axis $[u_0v_0w_0]$, in order to obtain the diffraction pattern of another zone axis, the angle ϕ between the normal to the common plane ($H_0K_0L_0$) and the x axis can be directly measured on the fluorescent screen by use of a beam-tilt technique described by Tambuyser.³ Thus, once we know the original angle α_0 of the T_1 axis from the meter reading and the angle γ between the two zone axes, we can readily calculate, from Eq. (8), the tilt angles for obtaining the diffraction pattern of any zone axis.

Table 1 shows an experimental example. A small hexagonal β -SiC whisker was used for the test as it was difficult to adjust the orientation following the Kikuchi map, since the diameter of the whisker was only 0.5 μm . The

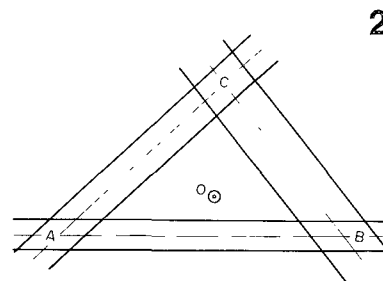


FIG. 2.--Illustration of three-Kikuchi pole method used to determine normal direction of TEM thin foil specimen.

original position was the zone axis $[0001]$ coincident with the beam direction; from the original position we obtained the diffraction patterns of the other eight zone axes by adjusting the specimen to the tilt angles calculated by Eq. (8). Table 1 shows the good agreement between the experimental and calculated tilt angles: the maximum error is $\leq 2.0^\circ$.

Determination of the Normal Direction of TEM Thin-foil Specimen

The three-Kikuchi pole method is frequently used to determine the normal orientation of a TEM thin-foil specimen (Fig. 2); the O is the central spot position where the specimen holder is at zero position. A , B , and C are three Kikuchi poles located nearby. It is necessary to record an image of the Kikuchi pattern since the angles $A^{\circ}O$, $B^{\circ}O$ and $C^{\circ}O$ have to be determined by measurement of the distances AO , BO , and CO from the Kikuchi pattern. However, we can adjust the specimen to obtain the exact zone axis pattern of the Kikuchi poles A , B , and C , and determine the corresponding tilt angles (α_A , β_A , α_B , β_B , α_C , and β_C) of the two axes of the double-tilt holder, respectively. It follows that the angles $A^{\circ}O$, $B^{\circ}O$, and $C^{\circ}O$ can be calculated from Eq. (6).

Figure 3 is a Kikuchi pattern of an Al alloy specimen which includes the three Kikuchi poles $[112]$, $[114]$, and $[215]$, where the specimen holder is at the zero position. Assuming that the normal direction of the thin foil is $[UVW]$, the angles between the three Kikuchi poles and $[UVW]$ can be calculated by the above method: 8.96° , 6.48° , and 7.57° . Then the normal direction of the thin-foil specimen can be determined by a method such as three Kikuchi-pole method to be $[0.316, 0.308, 0.898]$.

Determination of the Misorientation Between Two Grains

In order to determine the misorientation between two grains, the diffraction patterns

TABLE 1.--Experimental and calculated tilt angles for β -SIC whisker orientation adjustment, with double-tilt holder.

u v w	γ	$H_0 K_0 l_0 L_0$	ϕ	1st tilt angle		2nd tilt angle	
				α_{exp}	α_{cal}	β_{exp}	β_{cal}
0 0 0 1	0			9		12 4	
0 $\bar{1}$ 1 3	19 47	$\bar{2}$ 1 1 0	-10	28 0	28 14	10 3	8 64
0 2 2 3	35 26	2 $\bar{1}$ 1 0	170	-25 5	-25 71	20 7	18 79
1 1 0 3	19 47	1 1 2 0	-130	-4 0	-3 68	-1 5	-2 42
2 0 2 3	35 26	$\bar{1}$ 2 $\bar{1}$ 0	-70	17 0	18 83	-22 9	-22 57
0 $\bar{2}$ 2 3	35 26	2 1 1 0	-10	43 0	43 57	2 8	4 45
2 2 0 3	35 26	1 1 2 0	-130	-15 5	-13 81	-13 6	-14 69
1 $\bar{2}$ 1 6	17 02	$\bar{1}$ 0 1 0	20	24 0	24 91	17 5	18 74
$\bar{1}$ $\bar{1}$ 2 3	31 48	$\bar{1}$ 1 0 0	-40	30 2	31 91	-9 3	-10 89

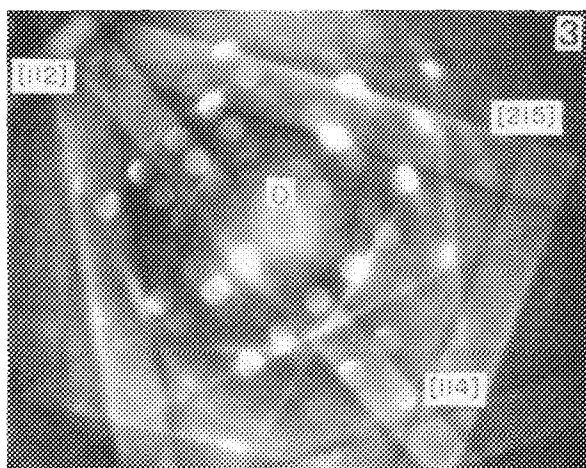


FIG. 3.--Kikuchi pattern of Al alloy specimen which includes three Kikuchi poles where specimen holder is at zero position.

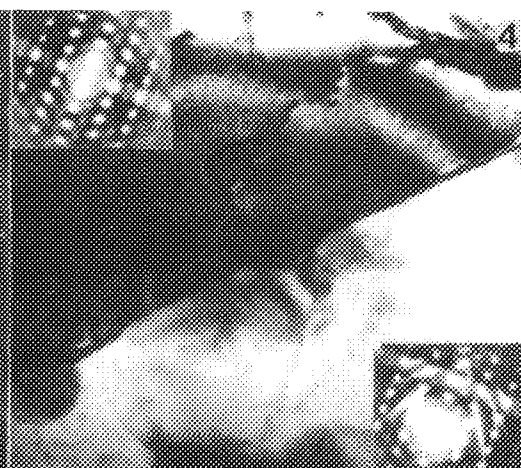


FIG. 4.--TEM image of grain boundary of Al alloy specimen together with corresponding diffraction patterns of two adjacent grains.

of the two grains are usually recorded separately when the specimen is at the same tilt position. Then the angle between the zone axes indexed from the diffraction patterns is calculated as the misorientation between the two grains. However, this method is complex and time consuming. In this section, a simpler and more convenient method is described.

First, an exact zone axis direction of one of the grains is aligned to the beam direction with reference to the Kikuchi pattern and the corresponding tilt angles α_1 and β_1 are obtained from the meter reading of the double-tilt holder. Then the same zone axis direction of another grain is aligned to the beam direction by operation of the double-tilt holder, and the tilt angles α_2 and β_2 are obtained. The angle between the zone axes of two grains can then be calculated from Eq. (6). The misorientation between the two grains is thus determined.

Figure 4 is a TEM image of a grain boundary of an Al alloy specimen and the corresponding diffraction of the two adjacent grains, where the zone axis $[112]$ of one of the grains coincides with the beam direction, and the tilt angles of the double-tilt holder are $\alpha_1 = 0.8^\circ$ and $\beta_1 = -5.3^\circ$. When the zone axis $[112]$ of another grain is tilted to coincide with the beam direction, the corresponding tilt angles are $\alpha_2 = 2.5^\circ$ and $\beta_2 = -4.1^\circ$. Thus the misorientation between the two grains is 2.1° .

Conclusions

One group of new equations related to the operation of the TEM double-tilt holder is deduced from matrix geometry. The orientation adjustment of a crystal specimen from the tilt angles calculated by these equations is considered to be more convenient and less time consuming than that following the Kikuchi map method, since the difficulty of orientation adjustment of severely strained and small grain size specimens is avoided. From the equations in this paper, the normal direction of a TEM thin-foil specimen and the misorientation between two grains can be determined without a need to record the Kikuchi pattern.

References

1. J. W. Edington, *Practical Electron Microscopy in Materials Science*, New York: Van Nostrand Reinhold, 1975, vol. 2.
2. C. T. Chou, "Computer software for specimen orientation adjustment using double-tilt and tilt-rotate holders," *J. Electron Microscope Technique* 7: 263, 1987.
3. P. Tambuyser, "A simple method for the direct measurement of diffraction patterns in the EM400T transmission electron microscope," *J. Phys.* E16: 483, 1983.

ON-LINE MEASUREMENT OF SPECIMEN THICKNESS BY CONVERGENT BEAM ELECTRON DIFFRACTION

M. T. Otten

In transmission electron microscopy, thickness measurements are important but rarely done because most measurement methods are difficult to perform and of notoriously poor accuracy. Convergent beam electron diffraction (CBED) provides an easy and accurate measurement method for crystalline specimens. Measurement can be done on-line on the Philips CM microscope with the aid of a remote-control computer program.

Experimental Conditions

For thickness measurement a CBED pattern is needed that contains a two-beam diffracting condition, with a dark Kikuchi line going through the center of the bright-field disk and the corresponding bright Kikuchi line through the center of a dark-field disk (Fig. 1). Parallel to the bright Kikuchi line, the dark-field disk contains a number of fringes whose distance from the Kikuchi line varies with specimen thickness.

The visibility of the fringes depends on the size of the diffraction disk (larger disks show more fringes) as well as the electron probe size used (larger probes illuminate larger areas that may contain defects or vary in thickness or orientation, which will smear out the fringes). The normal mode for CBED thickness determination is therefore the Nanoprobe mode, with a medium to large C2 aperture (as large as possible without overlap of the bright-field and dark-field disks).

Measurement Method

For measuring thickness through CBED the formula¹

$$s_i = (\lambda/d_{hkl}^2)(\Delta\theta_i/2\theta_B)$$

is used, where s_i is the so-called deviation parameter; λ is the electron wavelength; d_{hkl} is the d-spacing of the diffraction used; $\Delta\theta_i$ are the distances from the central bright fringe to the dark fringes 1, 2, etc.; and $2\theta_B$ is the distance in the pattern corresponding to the Bragg angle (Fig. 2).

Based on these data, a plot is made (Fig. 3) of $(s_i/n_i)^2$ against $(1/n_i)^2$, where n_i is the number of the dark fringe (1, 2, 3, ...). If n_i was chosen correctly, the plot would yield a straight line. If n_i is incorrect (with increasing thickness the fringes 1, 2, 3, ..., gradually merge with the Kikuchi line, so that the first dark fringe visible becomes 2, 3, 4, ...), the plot yields a curved line. The n_i numbers

are then increased until a straight-line plot is obtained. The intercept of the straight line corresponds to $(1/t^2)$ and thus yields the thickness t ; its slope is equivalent to $-(1/\zeta^2)$ and gives the extinction distance ζ . Instead of plots to determine the assignment of n_i , a linear regression can be used. Acceptance or rejection of the assignment can then be based on the correlation coefficient, which is -1 in the ideal case.

Computer-aided Measurement

Instead of doing the measurement calculation manually, a program can be prepared that will calculate the thickness. One such program, called CBEDOFF (short for OFF-line CBED thickness determination; also CMCBEDOFF²), takes the necessary input data, recalculates them, assigns an index to the fringes, fits the data to a straight line by linear regression, decides from the correlation coefficient which index assignment is correct, and from that assignment calculates the thickness and extinction distance.

Even more useful would be the possibility of direct on-line measurement on the microscope. In theory such a measurement can already be done by use of the CM microscope diffraction measuring function. The measuring function is based on calibrated shifts of the diffraction pattern by the image deflection coils. Since these coils are positioned right underneath the objective lens with its nearly constant current, the measurement is independent of the camera length and, through very accurate control of the deflection coils, highly accurate (better than 1%; compare with a reproducibility of 1.5% at best for the camera length). To make the measurement, one first shifts the transmitted beam and then two or more diffracted beams to a reference point (e.g., the beam stop) with the SHIFT X and Y knobs of the microscope. The results are directly given as d-spacings, and angle and ratio of d-spacings (Fig. 4). Inversion of the d-spacing output would give the distances in the diffraction pattern needed for thickness measurement.

However, in practice it is too difficult to use the diffraction measuring function directly for thickness measurement, because it is virtually impossible to shift accurately perpendicular to the fringes, since the fringes have no markers that make it possible to detect shifts parallel to the fringes. A remote-control computer program, called CBEDON (CMCBEDON²), has been therefore designed that provides on-line measurement by combining the internal measuring function with the remote-control capabilities of the CM microscope.

M. T. Otten is at Philips Analytical, Electron Optics Applications Laboratory, Building AAE, NL-5600 MD Eindhoven, The Netherlands.

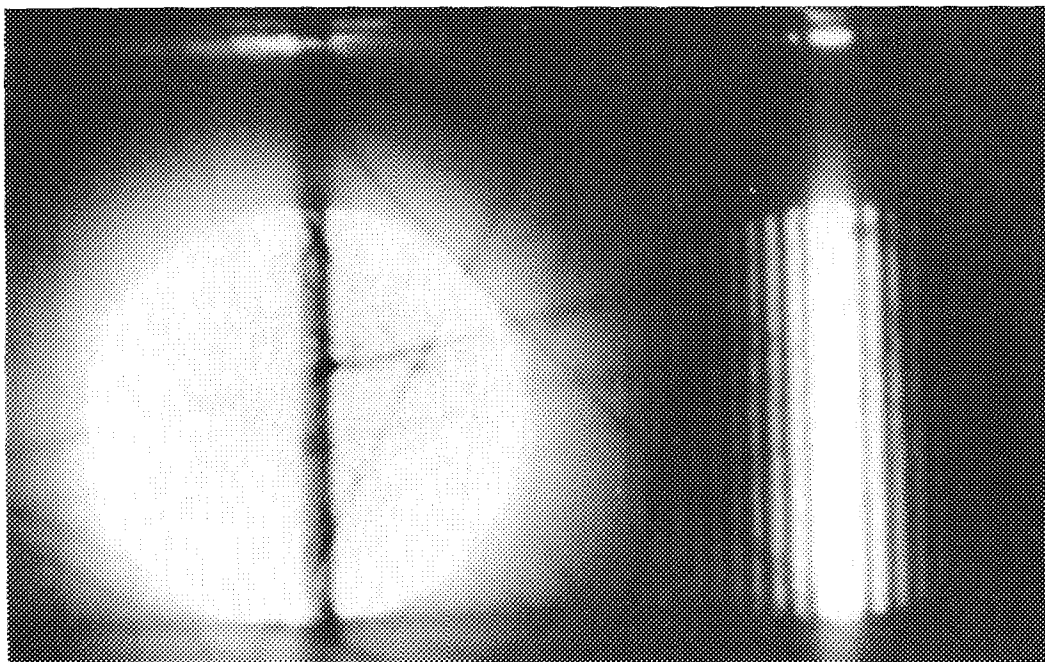


FIG. 1.--Typical CBED pattern used for thickness measurement. Kikuchi lines run through center of bright-field (left) and dark-field (right) disks, with thickness fringes running parallel to bright Kikuchi line in dark-field disk.

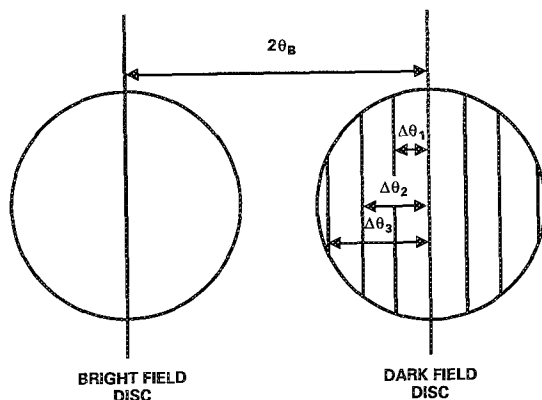


FIG. 2.--Data needed for CBED thickness measurement. The d-spacing is real-space value as normally determined in diffraction pattern analysis, in the same units as that of the electron wavelength; $2\theta_B$ and $\Delta\theta_i$ values are in the same arbitrary units (e.g., mm).

Program CBEDON retrieves the necessary data such as high tension and d-spacing directly from the microscope and guides the operator through the measurement procedure. The program starts with checking for the presence of the remote-control driver and connection with the microscope and instructs the operator to obtain a proper diffraction pattern. Through the logging facility (printout of data to the computer and storing in a disk file), the high tension and d-spacing are retrieved by the program. The program must therefore determine which PARAMETERS page contains the logging set-up (page 2 on a TEM, 4 on a STEM instrument) and insures that high tension and d-spacing are logged. The program then activates measuring

and instructs the operator to shift three key points to a reference point such as the beam stop: one intersection of the dark Kikuchi line with the edge of the bright-field disk and the two intersections of the bright Kikuchi line with the edges of the dark-field disk (Fig. 5). The shifting must be done with the keypad cursors of the computer, which in turn drive the SHIFT X and Y knobs through remote control. From the three key points the program determines the center positions of the two disks, which gives the combination of X and Y shifts necessary to shift along the fringe normal (i.e., the connecting line between the disk centers). The diffraction pattern is then shifted by the program to the center of the dark-field disk. Again with the keypad cursors the operator is asked to shift to the first fringe, second fringe, etc., to the reference point. At this stage the cursors will automatically produce a movement along the fringe normal by instructing the microscope to shift by the necessary combination of X and Y directions. Once the operator decides that a sufficient number of fringes have been measured (3 or 4 is usually sufficient), the program will fit the linear regression and produce the results.

Programs CBEDON and CBEDOFF are available as public domain software.²

Accuracy

CBED thickness measurement can be performed with high accuracy, in part because the position of the fringes changes rapidly with specimen thickness. The most important factor deciding the accuracy is the fact that the measurement depends mostly on the high-index

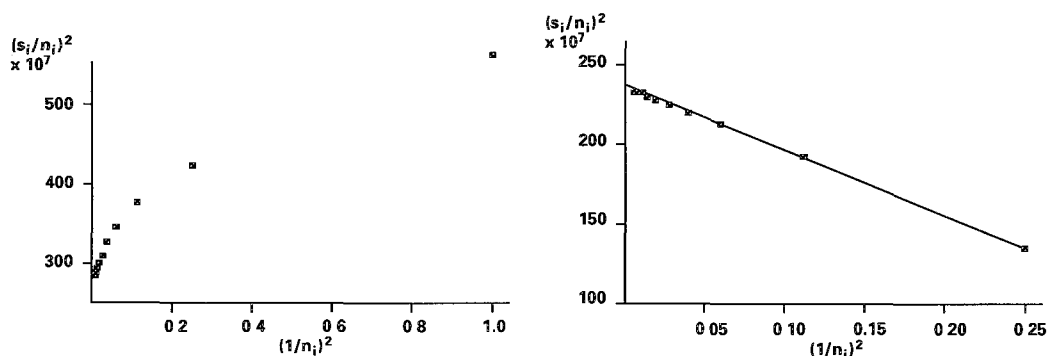


FIG. 3.--Plots of $(s_i/n_i)^2$ vs $(1/n_i)^2$ for indices starting with 1 (left) and for indices starting with 2 (right). Only for latter is it possible to fit straight line through data.

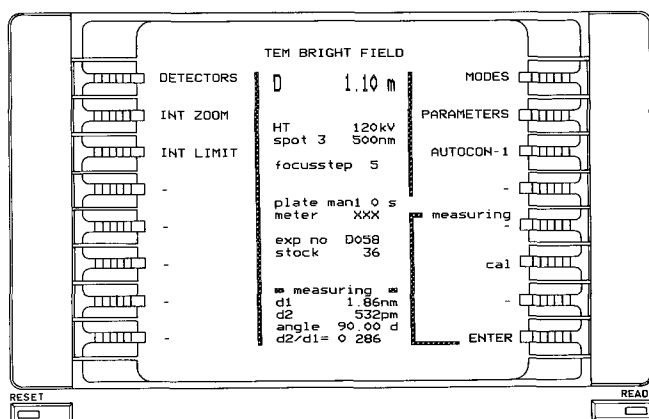


FIG. 4.--CM MICROCONTROLLER page showing diffraction measuring results (bottom of central information field).

fringes, since their $(s_i/n_i)^2$ values are very close to the intercept that gives the thickness. For these fringes the distance to the central Kikuchi line is the largest and thus the easiest to measure. In addition, absorption effects that could distort the measurement are smallest for these fringes. However, the measurement is sensitive to the accuracy in measuring the d-spacing of the diffraction used, as is easily seen from the fact that this parameter occurs squared in the formula for the deviation parameter.

The on-line measurement is less accurate than the off-line case because of a number of practical factors. Measurement with a ruler on a high-quality negative or print is inherently easier to perform. If deemed necessary, it is even possible to measure on a densitometer trace, allowing accurate location of the contrast minima. An inhibiting factor for on-line measurement is the fact that the contrast of the higher-index fringes is usually weak, so that they become difficult to observe. Beam damage or contamination can reduce the time available for measurement before the diffraction pattern fades out. The number of fringes measured on-line in practice is usually smaller than the number that would be measured off-line, and the fringes measured tend to be closer to

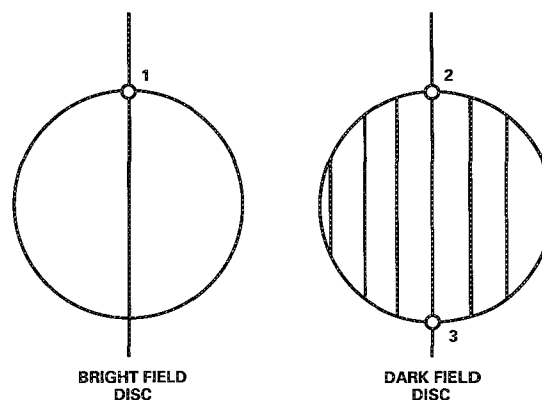


FIG. 5.--Three well-defined key points in measurement are intersections between Kikuchi lines and edges of diffraction disks.

the Kikuchi line and farther away from the intercept. Overall, however, the on-line measurement gives results within 10-15% of that obtained for off-line measurement.

References

1. P. M. Kelly, A. Jostsons, R. G. Blake, and J. G. Napier, "The determination of foil thickness by scanning transmission electron microscopy," *Phys. Stat. Sol.* A31: 771, 1975.
2. N. J. Zaluzec, "In the computer corner," *EMSA Bulletin* 19(2): 122, 1989.

A STRATEGY FOR QUANTITATIVE DETERMINATION OF STRUCTURE PARAMETERS BY COMPUTER SIMULATION OF CONVERGENT BEAM ELECTRON DIFFRACTION PATTERNS

Knut Marthinsen, L. N. Bakken, Ragnvald Høier, and Pål Runde

High-quality convergent beam electron diffraction (CBED) patterns from nanometer-size regions are now routinely obtained in almost every new TEM. Crystal structure studies are thus made possible on nanometer-sized crystals and on polycrystalline materials that have not been previously accessible by other structure-determination methods. However, whereas CBED has been widely used for determination of crystal symmetry, the application of quantitative CBED in crystal structure studies is so far much less developed. This situation is not due to a lack of theoretical models, but may reflect the generally involved numerical situation, which makes simple interpretations difficult.

So far most quantitative work on CBED has focused on effects and intensity variations that can be analyzed on a kinematic or two-beam like basis,^{1,2} or else the simpler one-dimensional intensity variation along a systematic row has been utilized.^{3,4} However, in focusing on an optimal use of CBED patterns, one should utilize the general two-dimensional dynamic intensity distribution in the disks; and a many-parameter fitting method has recently been suggested based on detailed simulations of the intensity variations observed.⁵ These simulations must in general be based on full dynamic many-beam calculations. Consequently, the number of refinable parameters (e.g., structure factor magnitudes and phases, absorption parameters, crystal thickness, wavelength, etc.) may in principle be large and the computer time long even on supercomputers. A relevant procedure for comparison of theory and experiment is thus much needed.

The present work is focused on this problem and a strategy for how to proceed is proposed. This strategy includes making use of the surface response methodology,⁶ which devises an effective way of searching in the many-parameter space for an acceptable fit between experiment and simulations. This method, which has been used with success in various fields of science since about 1950, is here illustrated by simulations on a theoretical four-beam example. It is shown that such a procedure strongly reduces the necessary number of diagonalizations and

thus makes realistic many-parameter determinations possible.

Experiments

As an example the 0,0,0; 7,1,-3; 7,1,-5; 0,0,-8 nonsystematic four-beam case in the [1,-7,0] zone of the noncentrosymmetric crystal InP has been investigated. Crushed samples on holey-carbon grids have been studied in a Philips CM-30 electron microscope. The resulting CBED patterns for the 7,1,-n (n = 1,3,5,7) disks are shown in Fig. 1. They show typical intensity variations in strongly coupled reflections with split lines and intensity maxima and minima reflecting the magnitudes and phases of the reflections involved.⁷ For example, in the 7,1,-3 disk the upper left gap is governed by the strong 0,0,4 coupling to the 7,1,-7 disk. A similar splitting in the 7,1,-7 disk is seen at a position corresponding to the coupling vector 0,0,4. The lower right line splitting is mainly governed by the 0,0,2 coupling to the 7,1,-5 reflection, but is heavily perturbed by coupling to other reflections that are accidentally at or near the Bragg condition. A more detailed discussion of this kind of many-beam effects and their strong dependence on the structure factor magnitudes and phases of the reflections involved may be found elsewhere.^{5,7} However, it is these strong parameter dependences that make these effects suitable for quantitative structure parameter determinations.

Simulation of the CBED patterns is based on the Bloch-wave formulation of high-energy dynamic electron diffraction, where we have made use of the FORTRAN code of Zuo, Gjønnes, and Spence.⁸ Here absorption is included by diagonalization of the full complex non-Hermitian structure matrix. However, a small refinement has been made to allow for the inclusion of absorptive form factors from Bird and King.⁹ They include only the thermal diffuse scattering contribution to the absorption potential, but in this way one takes into account that the absorptive potential and the real part of the potential in principle have a different spatial distribution, which in general gives different phases for the Fourier coefficients of the real and imaginary parts of the potential. This feature may be important in quantitative work from noncentrosymmetric crystals.

Simulated CBED patterns for the 7,1,-3 and 7,1,-5 disks at 2000 Å corresponding to the same incident beam directions as in Fig. 1 are shown in Fig. 2: 18 beams are included in the simulations, including accidental HOLZ lines that were identified in the experimental pat-

K. Marthinsen is at SINTEF Applied Physics, N-7034 Trondheim, Norway; his coauthors are at the Department of Physics, University of Trondheim-NTH, N-7034 Trondheim, Norway. Financial support from The Norwegian Council for Technical and Industrial Research (NTNF) to one of us (K.M.) and a grant to L.N.B. from The Norwegian Council for Science and Humanities (NAVF) are gratefully acknowledged.

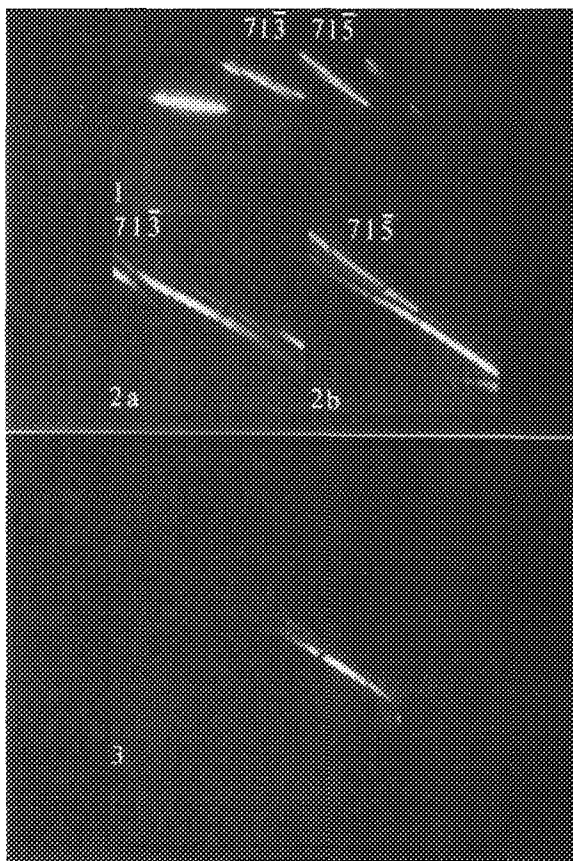


FIG. 4.--Possible response surface in two-parameter example, with points shown for one-variable-at-a-time approach and arrow indicating path of steepest descent from point O.

terns. They show remarkable similarity with the corresponding observed disk intensities in Fig. 1, including most of the details, and support the fact that it should be possible to simulate observed CBED patterns with high accuracy.

Comparison of Theory and Experiment

A quantitative determination of unknown parameters cannot be based on visual comparisons of calculated patterns as a very large number of patterns are involved. We therefore need a method that utilizes computer comparisons. The first step is therefore to get the 2-dimensional observed intensity in the disks digitized and read into the computer. That can be done via film, a transilluminator, and a CCD camera, but preferably directly in the microscope by use of EELS. So far only film-based data have been available in our laboratory. The experimental pattern in Fig. 1 is acquired by a CCD camera from film, stored on the SYNOPTICS Synapse image processing framestore, and re-displayed on a monitor with the image processing language SEMPER 6.

To compare theory and experiment in the computer it is convenient to define a normalized fit index based on the intensity differences in each pixel, i.e.

$$R = \sum_i |I_{\text{exp}} - I_{\text{the}}| / \sum_i I_{\text{exp}} \quad (1)$$

Here the intensity distribution in a general disk h is a function of numerous parameters, including for example all the structure factors

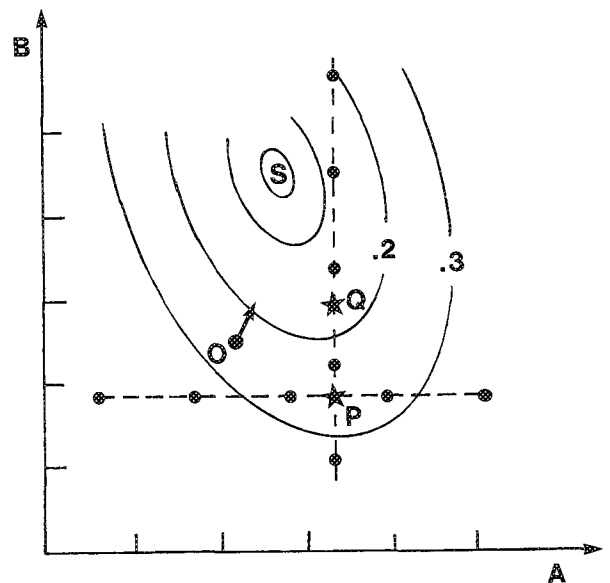


FIG. 1.--Observed CBED pattern from InP showing split lines and intensity variations in 7,1,-n disks; [1,-7,0] zone; 150 keV

FIG. 2.--Calculations for InP corresponding to Fig. 1, thickness 2000 Å, (a) 7,1,-3 disk, (b) 7,1,-5 disk.

FIG. 3.--Difference map as compared with 7,1,-5 disk intensity in Fig. 2(b) when ϕ_{002} is changed by 5° .

U_1 ($l = h, g, h - g, \dots$) involved, i.e., both their magnitudes $|U_1|$, their phases ϕ_1 and their absorptive parts U_1' , the thickness t of the specimen, the instrument voltage m/m_0 , and the incident beam direction:

$$I_h = f(|U_1|, \phi_1, U_1', t, m/m_0, \dots) \quad (2)$$

The idea is now to start with an arbitrary set of unknown parameters to minimize the fit index R with respect to these parameters thereby determining them. However, although some of these parameters may be known beforehand (e.g., the thickness and the voltage), or others from other structure determination methods, there may still be a large number of parameters to be determined; and as each position in the pattern necessitates one diagonalization of the general non-Hermitian structure matrix, such many-parameter fitting is a formidable task in terms of computation time.

However, it is obvious that the refinement need not be done on the whole disk but may be limited to regions within the disks where the important intensity variations are. In fact, it has been shown that much can be learned by fitting performed on very limited regions. As an example, consider the difference map of Fig. 3, which represents the intensity differences in the 7,1,-5 disk with respect to that of Fig. 2(b) when the structure factor ϕ_{002} has been changed by 5° . It is clearly seen that the main intensity differences is found to the right and below the center of Fig. 3. Limiting the refinement to this region would greatly

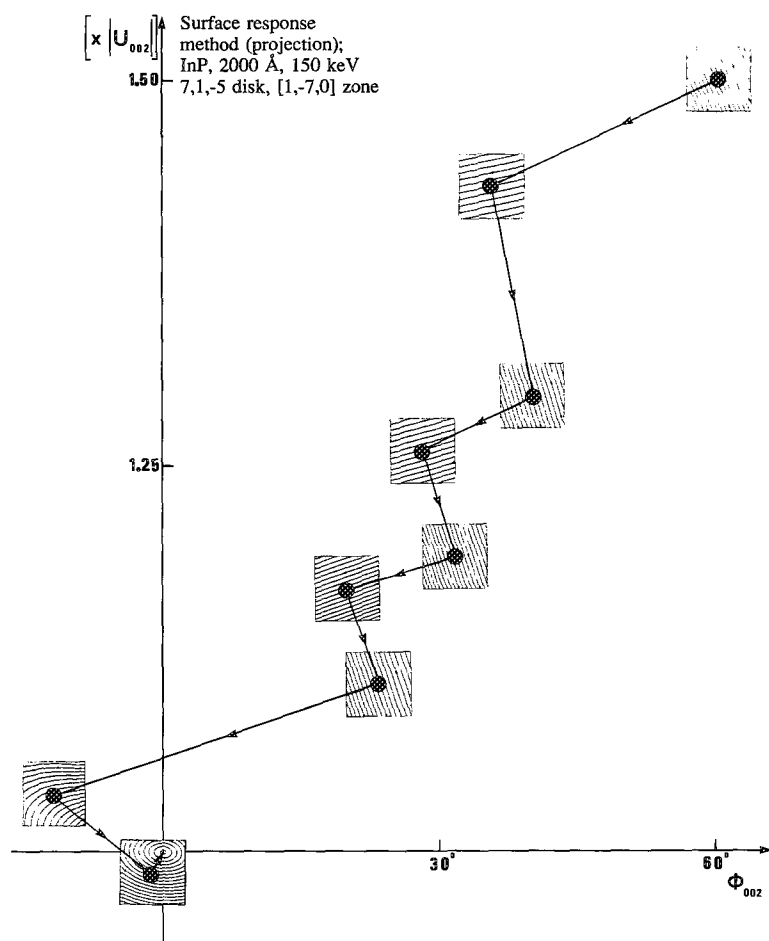


FIG. 5.--Response surface method, two-parameter example, applied to disk intensity of Fig. 2(b), $|U_{002}|$ and ϕ_{002} taken as variable parameters.

an unsurmountable task and a better procedure for fitting the unknown parameters is needed.

The Surface Response Method

The surface response method⁶ devises an alternative way, usually better, to do these fitting of parameters. It is based on finding first a representation of the local response surface and then the path of steepest descent (or ascent if one seeks a response function maximum) to indicate in which direction the parameters should be varied. This approach is illustrated in Fig. 4, where following the path of steepest descent from an arbitrary point O immediately leads us in the right direction. The crucial point here, in contrast to the one-variable-at-a-time strategy, is that the parameters are varied together.

In general the principle is as follows. Start from a point in the many-parameter space corresponding to the best guess of the unknown parameters. The response function is then determined in a carefully chosen set of points around the center point to allow for efficient least-square fitting and checking of a first-degree polynomial model. As the starting values are somewhat away from the true minimum, it is likely that the predominant local characteristics of the response surface is its gradient and that the local surface can be roughly represented by a planar model. However, if lack of fit of the first-order model is found, the design of test points to fit the local response surface has to be augmented to make fitting of a second-order model possible. Anyway, having found an acceptable local representation of the response surface, one continues the procedure by exploring in the direction of steepest descent. In this way a new minimum is found and the procedure described above starts all over again and is repeated until the true minimum is reached and the unknown parameters are thus determined.

In the present work the surface response method will be illustrated by a theoretical four-beam example (the one described in Fig. 1). The intensity in the 7,1,-5 disk in Fig. 2(b) is taken as the theoretical "correct" pattern, and it is assumed that the only two unknown parameters are the magnitude and the phase of the structure factor U_{002} , i.e., the coupling reflection between the 7,1,-3 and 7,1,-5 reflections. Starting with $|U_{002}|$ 1.5 times the correct value and $\phi_{002} = 60^\circ$

reduce the necessary computing time. If necessary, the whole disk could be included in a final refinement. The difference map in Fig. 3 also illustrates the strong intensity variations that occur when only one structure factor phase is changed.

The next step then is how to vary the unknown parameters to make a fit possible. The classical way of attacking this problem is to use the one-variable-at-a-time strategy. This means that only one parameter at the time is varied while the others are kept constant, and when a one-parameter minimum is found the parameter in question is fixed at the value giving this minimum. This procedure is repeated until all parameters are fixed. However, this procedure has its disadvantages, as illustrated by Fig. 4. It shows a possible response surface in a simple two-parameter example. If we now follow the one-variable-at-a-time strategy by first varying the parameter A along the horizontal dashed line, we would be led to an optimum at P; fixing A at this value and then varying B would lead us to a final optimum at Q, which is still somewhat away from the true optimum at S. Such a procedure would only work adequately if the variables were truly independent. This is rather an exception than the rule and will thus generally not lead us to the correct minimum unless the whole many-parameter room is run through. In our case this would be

(the true value being 0°), a two-parameter fitting following the response surface methodology has been carried out. The result is shown in Fig. 5. It is seen that despite some zig-zagging the unknown parameters approach the correct values relatively fast; only 9 steps were needed. In the first 7 steps a first-order polynomial sufficed to represent the local response surface; a second-order equation was needed in the final two steps. It is clear that such a procedure will greatly reduce the computer time as compared with the classical one-parameter-at-a-time strategy if we demand the same degree of fit.

Conclusions

It is clear that the method discussed has a large potential for quantitative determination of structure parameters. The complicated 2-dimensional intensity distributions in CBED disks are ideal from a simulation point of view and with the strong parameter dependences that exist particularly in nonsystematic many-beam cases, quantitative parameter determinations should be possible. To compare theory and experiment, computer comparisons are necessary and a fit index based on the pixel-by-pixel intensity difference between the 2-dimensional digitized intensity in the disks and simulations may be used. To minimize this fit index and thus determine the unknown parameters a fitting procedure like the surface response method has to be used. Although this method is illustrated here only by a two-parameter example, it has general applicability to the determination of global minima for an arbitrary number of unknown parameters. This procedure will greatly reduce the number of necessary diagonalizations, and thereby make many-parameter fittings possible.

References

1. D. M. Bird, R. James, and A. R. Preston, "Direct measurement of crystallographic phase by electron diffraction," *Phys. Rev. Letters* 59: 1216, 1987.
2. R. Vincent and D. J. Exelby, "Crystal structure determination by convergent beam electron diffraction," *Proc. 47th Ann. Meet. EMSA*, 1989, 476.
3. K. Gjønnes et al., "Two-beam features in electron diffraction patterns: Application of refinement of low-order structure factors in GaAs," *Acta Cryst.* A44: 810, 1988.
4. J. M. Zuo, J. C. H. Spence, and R. Høier, "Accurate structure-factor phase determination by electron diffraction in noncentrosymmetric crystals," *Phys. Rev. Letters* 62: 547, 1989.
5. R. Høier et al., "Determination of structure factor phase invariants from nonsystematic many-beam effects in convergent-beam patterns," *Ultramicroscopy* 26: 25, 1988.
6. G. E. P. Box, W. G. Hunter, and J. S. Hunter, *Statistics for Experimenters*, New York: Wiley, 1978.
7. J. M. Zuo, R. Høier, and J. C. H. Spence, "Three-beam and many-beam theory in electron

diffraction and its use for structure-factor phase determination in noncentrosymmetric crystal structures," *Acta Cryst.* A45: 839, 1989.

8. J. M. Zuo, K. Gjønnes, and J. C. H. Spence, "FORTRAN source listing for simulating three-dimensional convergent beam patterns with absorption by the Bloch wave method," *J. Electron Microsc. Tech.* 12: 29, 1989.

9. D. M. Bird and Q. A. King, "Absorptive form factors for high-energy electron diffraction," *Acta Cryst.* A46: 202, 1990.

CONVERGENT BEAM ELECTRON DIFFRACTION ZONE AXIS PATTERN MAP OF ZIRCONIUM

E. G. Silva and R. A. Scozia

Convergent beam electron diffraction (CBED) is a very useful technique for crystallographic analysis. A zone axis CBED pattern map (ZAP map) available for a given material provides a quick and reliable tool to identify crystalline phases and crystallographic directions, even in very small areas of samples (~ 1 nm in diameter). In the present work, a CBED ZAP map of Zr is shown. Patterns were obtained with a Philips EM300 transmission electron microscope set up to carry out this technique.

Experimental

Thin foils were prepared by conventional jet electropolishing technique from a Zr single crystal grown in the [0001] direction.¹ A convergent objective upper polepiece for STEM and some electronic modifications in the lens circuits were required (recommended by Philips for the STEM system). Furthermore, the microscope vacuum system and column were carefully cleaned with high-purity chemicals and it was operated at a very good vacuum. Contamination of the specimen was reduced by surrounding the sample with a cold trap at liquid nitrogen temperature and flooding the specimen for a few minutes with a high electron flux before observation.² A double tilt holder was used in the goniometer stage.

CBED patterns were observed in D + I mode with suitable conditions of the first and second condenser lenses. Current was fixed at 6.0 A for the objective and at a very low value for the intermediate lens. The objective aperture was out of the beam and the appropriate C2 aperture was used. Kossel lines were used to tilt the sample to the required zone axis. CBED patterns in the Zr ZAP map consist of zero layer disks, showing fine details within them that correspond to an intersecting set of higher-order Laue zone (HOLZ) deficiency lines. The position of these lines is very sensitive to changes in voltage, among other parameters. This fact allowed the precise voltage at which CBED patterns were taken to be determined, by comparing them with computer simulations of direct disks HOLZ lines. To aid in the interpretation

of patterns from the zone axis of Zr, results of a previous study were applied.³

Results

The CBED ZAP map of Zr covering a basic 30° sector of the hexagonal crystal system extends to about 28° from the [0001] to the $[\bar{2}113]$ and $[\bar{1}012]$ directions. ZAP [4223] also appears (Fig. 1). ZAPs such as $[\bar{1}015]$, $[\bar{1}014]$, $[\bar{1}013]$, and $[\bar{1}012]$ are observed on the (1210) plane, as well as ZAPs $[\bar{2}119]$, $[\bar{2}116]$, $[\bar{4}229]$, $[\bar{2}113]$, and $[\bar{4}223]$ along the (0 $\bar{1}$ 10) plane. Patterns present their zero layer containing direct and dark-field disks. In some patterns such as $[\bar{2}119]$, $[\bar{1}015]$, and $[\bar{1}014]$, HOLZ lines are visible. Enlarged central disks of these ZAPs are shown in Figs. 2-4. Computer simulations of direct disks HOLZ lines corresponding to these ZAPs were drawn by a Calcomp plotter. A simulation program improved to fit experimental results was used.⁴ An accelerating voltage of 84 kV was taken as input for the program, which produced best results in matching experimental HOLZ lines with those simulated for each of the ZAPs mentioned above (Figs. 5-7).

Conclusions

It was possible to attain CBED with a Philips EM300 TEM after performing the modifications for STEM. The ZAP map for Zr taken at 84 kV is useful for subsequent "fingerprint" identification of Zr in precipitates, alloy phases, and crystallographic directions determination. A single CBED pattern would suffice for this purpose.

References

1. D. O. Northwood and R. W. Gilbert, "Comments on the preparation of thin foils of zirconium and zirconium alloys for electron microscopy," *J. Aust. Inst. Met.* 18: 158, 1973.
2. J. W. Steeds, *Introduction to Analytical Electron Microscopy*, New York: Plenum, 1979, 387.
3. E. Silva and J. W. Robinson, "Experimental and computed zone axis pattern maps from zirconium monocrystal in the [0001] direction," *Materials Characterization* 24: 69, 1990.
4. J. F. Mansfield, *The Diffraction Suite*, Argonne National Laboratory, Illinois, 1987.

The authors are at the Departamento de Física, Facultad de Ciencias Físicas y Matemáticas, Universidad de Chile, Santiago. Financial support from Departamento Técnico de Investigación, U. de Chile, E2858/8923, is acknowledged. Thanks are due to Dr. J. F. Mansfield for valuable help and suggestions, to Mr. J. W. Robinson for samples preparation, to Mr. M. Rodriguez for microscope maintenance, and to Prof. J. Grez for electronic modifications supervision of the EM300.

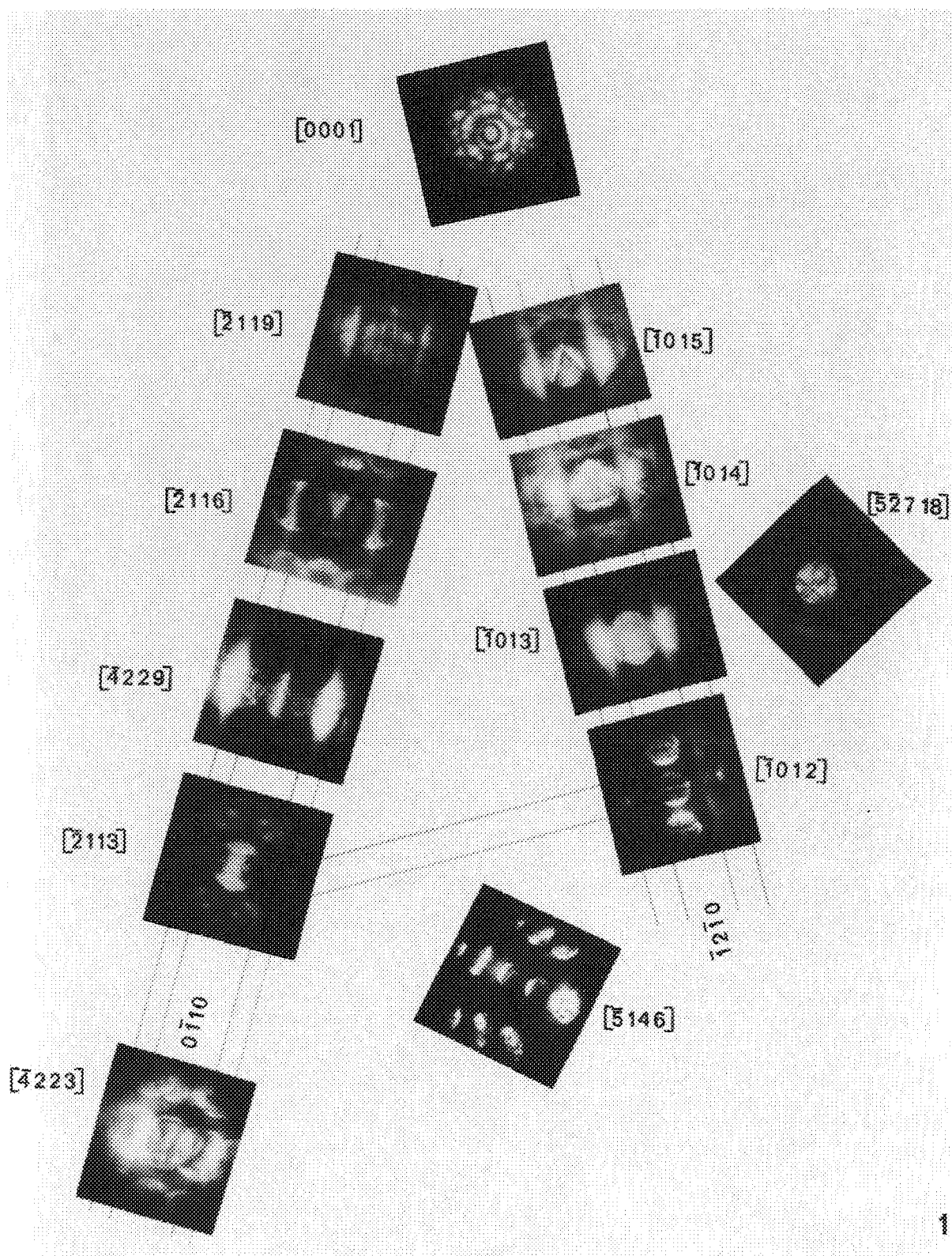
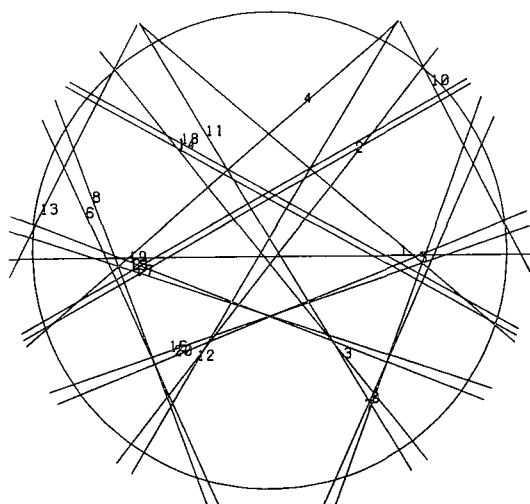
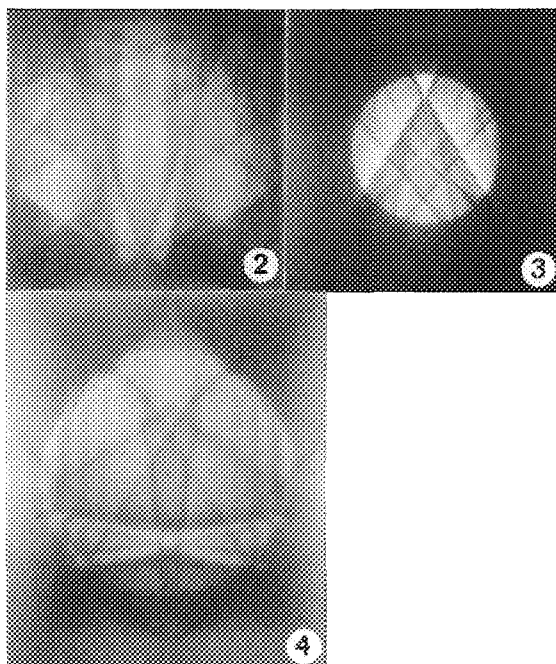
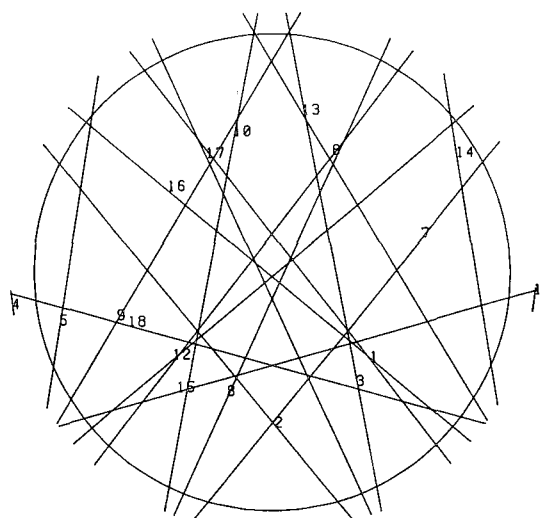


FIG. 1.--CBED pattern ZAP map of Zr at 84 kV.



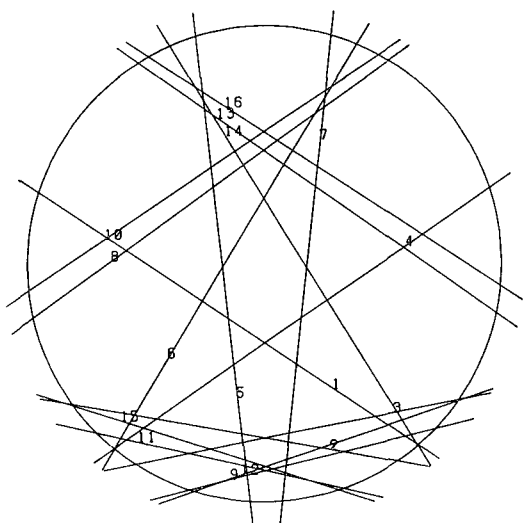
11-844-2
21-5-38-1
31-58-3-1
41-4-15-1
51-45-1-1
612-531
7123-51
813-962
9136-92
1014-952
1114-642
12144-82
13145-92
1415-502
1515-4-12
1615-1-42
17150-52
1817-703
1917-6-13
2017-1-63
21178-73

5



11-761-1
21-651-1
31-46-20
41-35-20
51-38-51
61-1-67-1
71-1-56-1
81-18-72
9104-41
1012-640
1112-530
12124-62
1314-401
1415-831
15152-73
1616-4-22
1717-812
1817-2-53

6



11-743-2
21-514-2
31-4-15-2
41-3-47-2
51-35-20
6106-62
712-530
8123-52
9131-42
10134-73
1114-1-32
12142-63
1315-3-22
1416-602
1516-2-43
1617-4-33

7

FIG. 2.--Enlarged central disk of CBED pattern from Zr at $[2119]$.

FIG. 3.--Enlarged central disk of CBED pattern from Zr at $[1015]$.

FIG. 4.--Enlarged central disk of CBED pattern from Zr at $[1014]$.

FIG. 5.--Computer simulation for ZAP of Fig. 2.

FIG. 6.--Computer simulation for ZAP of Fig. 3.

FIG. 7.--Computer simulation for ZAP of Fig. 4.

APPLICATIONS OF CBED TECHNIQUES TO THE STRUCTURAL CHARACTERIZATION OF CRYSTALLINE DEFECTS

R. Pérez

In recent years, CBED techniques have been mainly used for the symmetry characterization of perfect crystals. However, the studies of defective crystals by CBED have received little attention in the literature.¹⁻⁴ The results presented in this communication explore some of the image contrast characteristics obtained in theoretical simulations of zero-order Laue zone (ZOLZ) reflections. The theoretical simulations are based on the multibeam form of the dynamical theory.⁵ These calculations have been carried out for perfect crystals and crystals with dislocations or stacking faults. Some of the parameters that affect image contrast strongly have been explored, including specimen thickness, multibeam effects, nature of the defect, etc. The calculations are carried out for an operating voltage of 100 kV. In the past, methods for the characteristics of the nature of stacking faults (SF) and dislocations based on CBED techniques, have been developed.¹ These methods are mainly based on the results predicted by the two-beam form of the dynamical theory. We also explore the consequences of multibeam effects on these methods.

Theoretical Background

In the dynamical theory of electron diffraction the high-energy electrons in the crystalline specimen can be described by Bloch waves of the form

$$b^{(i)} = \exp(2\pi i \vec{k}^{(i)} \cdot \vec{r}) \sum_g C_g^{(i)} \exp(2\pi i \vec{g} \cdot \vec{r})$$

The Fourier coefficients $C_g^{(i)}$ and the Bloch wavevectors $\vec{k}^{(i)}$ can be found from a solution of the eigenvalue equation

$$AC^{(i)} = \gamma^{(i)} C^{(i)}$$

where $C^{(i)}$ is a column vector whose elements are $C_g^{(i)}$ and $\gamma^{(i)} = (k_z^{(i)} - K_z)$, where K_z is the z-component of the incident wave vector after the effects of the mean inner potential of the lattice are allowed for. A is a matrix whose off-diagonal elements are proportional to the Fourier coefficients of the lattice poten-

tial V_g through the relation $A_{gh} = U_{g-h}/2K$, where $U_g = 2m_e V_g/h^2$ and the diagonal elements are related to the crystalline orientation. The diffracted beam amplitude can be expressed as

$$\phi_g = \sum_i C_0^{(i)} C_g^{(i)} \exp(2\pi i \vec{\gamma}^{(i)} \cdot \vec{r})$$

where $\vec{\gamma}^{(i)} = \vec{k}^{(i)} - \vec{K}$. The directly transmitted beam intensity can therefore be written as

$$I_0(\delta) = \sum_i C_0^{(i)4}(\delta) + 2 \sum_{i,j} C_0^{(i)2}(\delta) C_0^{(j)2}(\delta) \cos(2\pi z / \xi_{ij}(\delta))$$

where ξ_{ij} is the inverse of the gap between the branches i and j of the dispersion surfaces for the orientation δ .

CBED Reflections from Perfect Crystals

To investigate the multibeam effects on the image contrast obtained in ZOLZ reflections, theoretical calculations of CBED disks have been carried out. In these calculations, the number of beams and the type of elements have been varied (Figs. 1 and 2). Figures 1(A) and 1(B) show the directly transmitted disk for a specimen of Al ($Z = 13$) 200 nm thick along the (100) zone axis and correspond to the 9-beam and 25-beam theoretical simulations, respectively. No appreciable differences between the two images can be seen. However, Figs. 2(A) and 2(B) show the directly transmitted disk for a specimen of Au ($Z = 79$) under similar conditions as in Fig. 1. In this case strong differences between the 9-beam and the 25-beam cases can clearly be seen.

CBED Reflections from Crystalline Specimens with Defects

The study of crystalline defects with CBED techniques is very limited in the literature. One of the most systematic studies of this topic has been carried out by Tanaka et al.,¹ who have studied intensity profiles from both lower- and higher-order reflections in CBED patterns of specimens with stacking faults and dislocations. The experimental results are compared with the predictions of the two-beam theory. The results presented in the next sections are based on the multibeam form of the dynamic theory with Doyle and Turner atomic scattering factors.⁶ The Fourier coefficients are Debye-Waller corrected in all cases. In the calculations, the column approximation is assumed to prevail. The standard geometric

R. Pérez is at the Cuernavaca Laboratory of the National Autonomous University of Mexico Physics Institute, A.P. 319-B, 62191 Cuernavaca Mor., Mexico. The author thanks Prof. K. Urban, who provided the facilities to carry out this investigation; to the Alexander von Humboldt Foundation for financial support; and to the KFA Forschungszentrum Jülich in Germany for allowing him to stay one year working in its facilities.

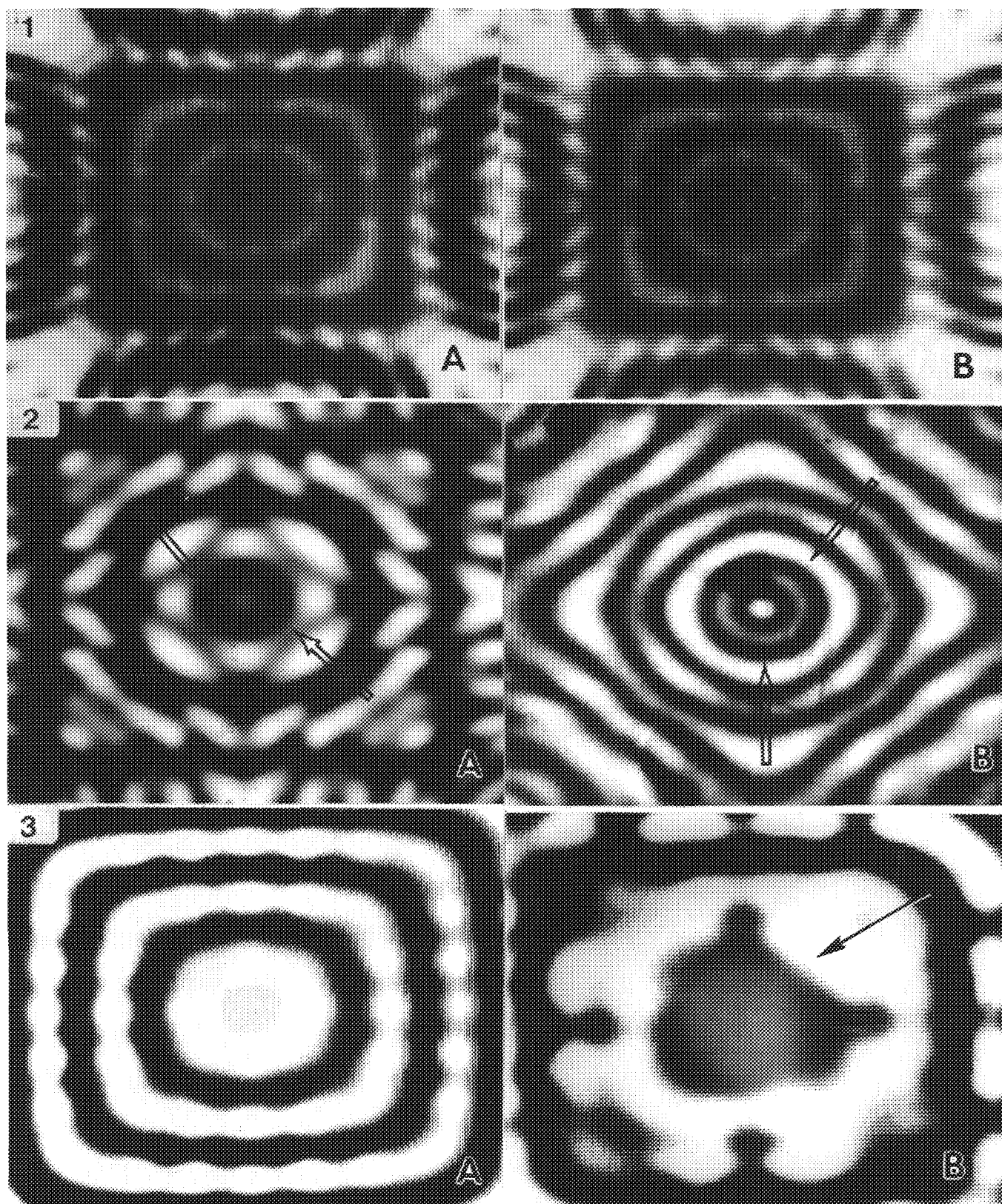


FIG. 1.--CBED disks for Al specimen 200 nm thick obtained along (100) zone axis: (A) 9-beam calculation, (B) 25-beam calculation.
 FIG. 2.--CBED disks for Au specimen 200 nm thick obtained along (100) zone axis: (A) 25-beam calculation, (B) 9-beam calculation.
 FIG. 3.--CB transmitted disk for Si specimen along (100) zone axis: (A) perfect crystal 200 nm thick, (B) same crystalline specimen with transverse SF at middle of slab.

arrangement of the crystalline specimen with a dislocation or a stacking fault is also assumed.⁵

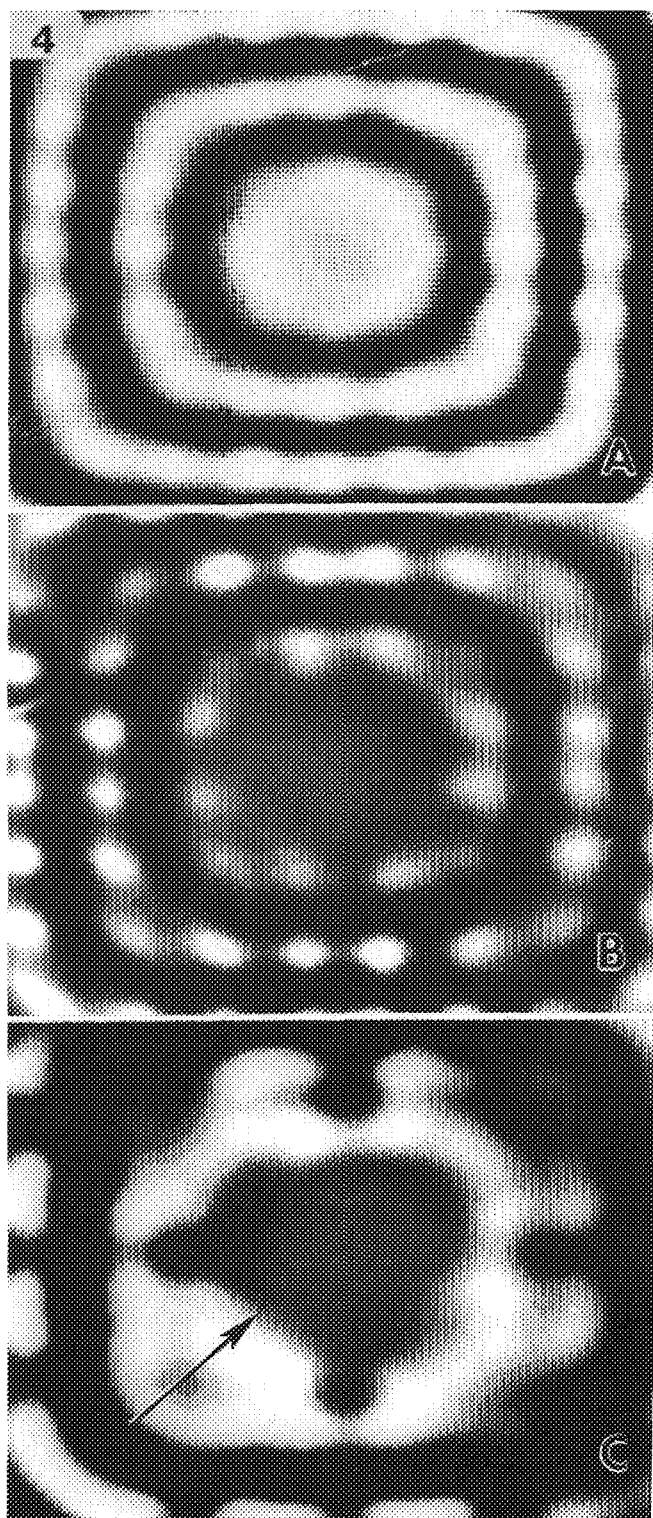


FIG. 4.--CB transmitted disk for Si specimen along (100) zone axis: (A) perfect crystal 200 nm thick, (B) crystal with transverse SF at 10 nm depth, (C) crystal with transverse SF at 100 nm depth.

Directly Transmitted Disks from Crystals with Stacking Faults. In the past, a result that has been commonly found in the studies of transverse SF by CBED is related to the breakdown of the symmetry in the defected crystals. For example, Fung has found that a transverse SF lowers the symmetry of the crystalline specimen from 6mm to 3m.⁴ This effect can also be obtained in simulations of CBED disks. Thus, for example, Fig. 3(A) shows the simulation of a transmitted disk along the (100) zone axis in Si; Fig. 3(B) shows the simulation of the same crystalline specimen but with an SF at the middle of the slab. This figure clearly illustrates the breakdown of the symmetry of the perfect crystal.

The image contrast obtained from CB disks of crystals with SFs depends strongly on the depth of the SF plane in the specimen. Figure 4(A) shows the CB disks for a perfect crystal

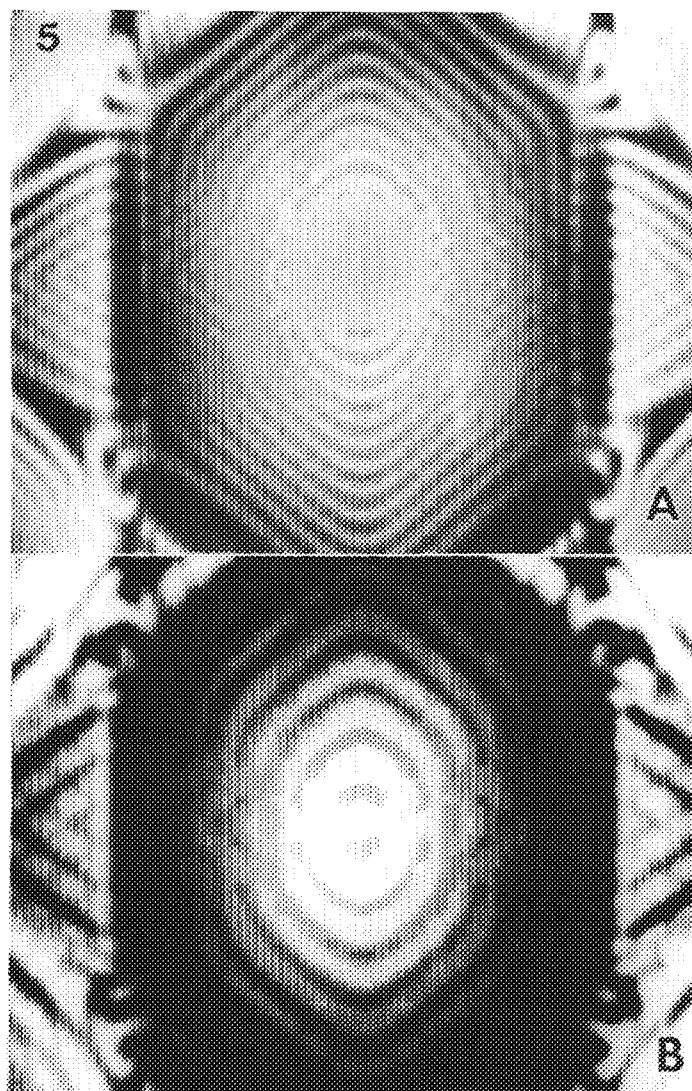


FIG. 5.--CBED disks for Al specimen 200 nm thick obtained along (111) zone axis: (A) perfect crystal, (B) transverse SF at middle of slab.

of Si of 200 nm; Fig. 4(B) shows the CB disk for a faulted crystal with an SF plane 10 nm deep, and Fig. 4(C) corresponds to the case of an SF plane 100 nm deep. The most pronounced changes in image contrast are obtained in Fig. 4(C). In some cases the presence of an SF does not give rise to pronounced effects on image contrast. In Fig. 4, a (111) zone axis CB transmitted disks for perfect and faulted crystals are displayed. Both patterns in these images show similar characteristics.

Directly Transmitted Disks from Crystals with Dislocations. The presence of dislocations can also break the original symmetry of the perfect crystal. Figure 6(A) shows the perfect crystal case and Fig. 6(B) illustrates the case of a crystal with a screw dislocation. The nucleus of the dislocation lies in the middle of the crystalline slab. This figure clearly illustrates the breakdown of the origi-

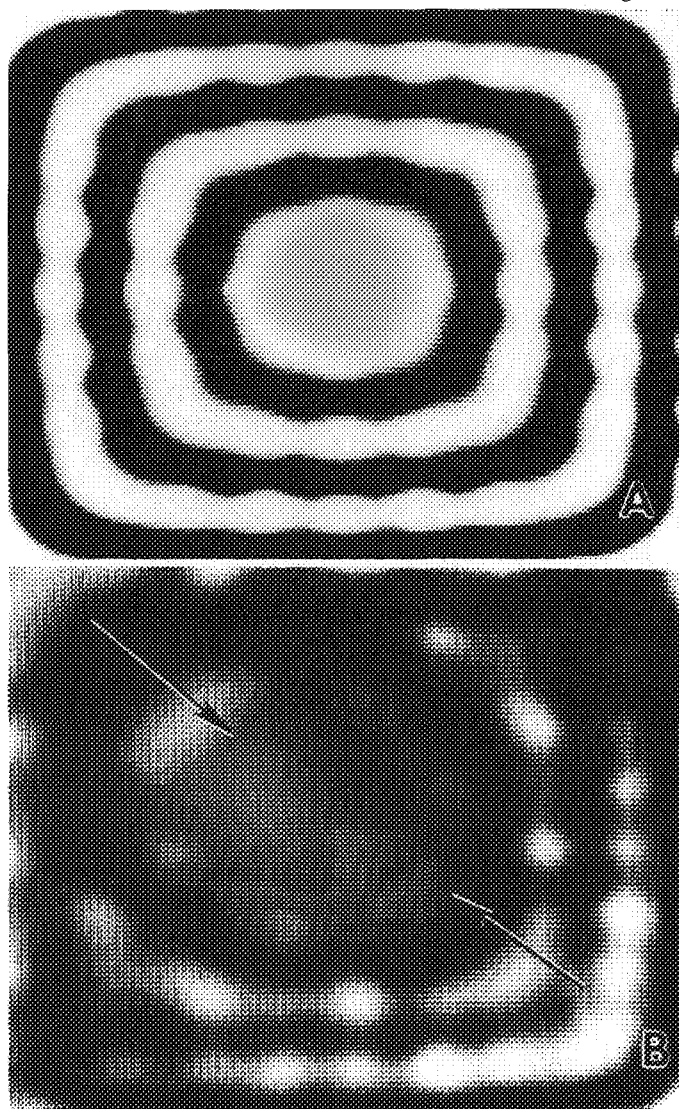


FIG. 6.--CB transmitted disks for Si specimen 200 nm thick along (100) zone axis: (A) perfect crystal, (B) crystal with screw dislocation where nucleus of dislocation lies at middle of slab.

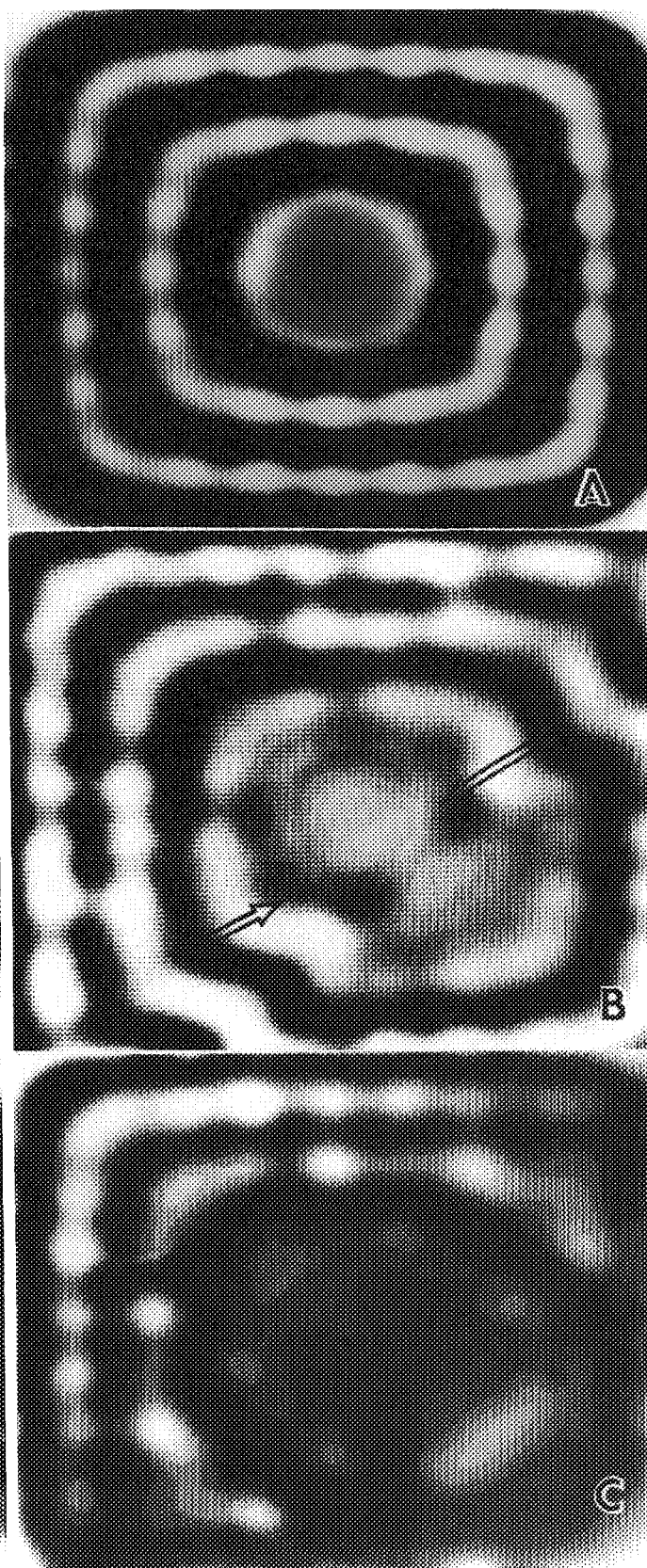


FIG. 7.--CB transmitted disk for Si specimen along 100 zone axis: (A) perfect crystal 200 nm thick, (B) crystal with screw dislocation at 10 nm depth, (C) crystal with screw dislocation 100 nm depth.

nal symmetry. There is also a strong dependence of the image contrast obtained in the CB disk and the depth of the nucleus of the dislocation. Figure 7 shows the perfect crystal, with the nucleus at 10 nm and 100 nm deep in an Si specimen 200 nm thick. Furthermore, the image contrast obtained in the CB disk also depends strongly on the horizontal distance from the nucleus of the dislocation along the top surface of the specimen. Thus, for example, Fig. 8(A) shows the CB disk of a crystal with a screw dislocation. This CB disk is obtained at a horizontal distance of 5 nm from the nucleus of the dislocation. However, Fig. 8(B) shows the CB disk obtained at a horizontal distance of 50 nm from the nucleus. It is clear from these images that the CB disk obtained at large distances from the dislocation are similar to the perfect crystal case.

Characterization of the Nature of Dislocation by CBED Reflections. Recently, methods to

identify the nature of dislocations from CBED patterns have been developed.¹ These methods are based on the image contrast displayed by rocking curves obtained close to the dislocation line. Thus, for example, Fig. 9 shows the dark field (DF) reflections for a specimen of Si with a screw dislocation. The specimen thickness is 20 nm and the dislocation nucleus is 10 nm deep. The abscissa and the ordinate in these figures correspond to the excitation

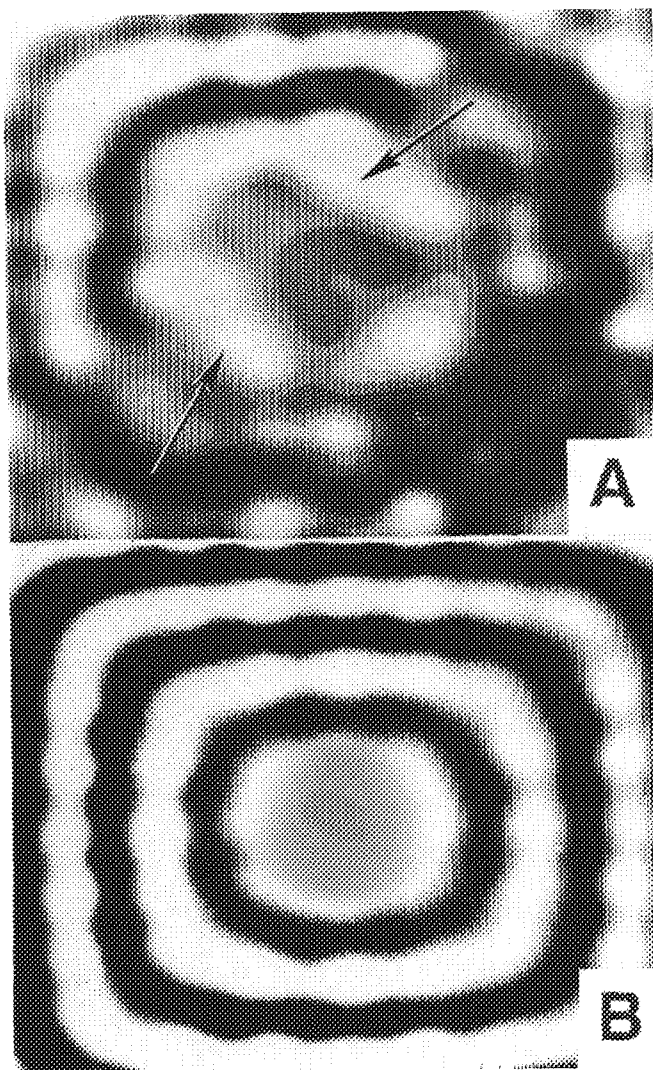


FIG. 8.--CB disks from Si specimen 200 nm thick with screw dislocation; pattern obtained at horizontal distance of (A) 5 nm from dislocation, (B) 50 nm from nucleus of dislocation.

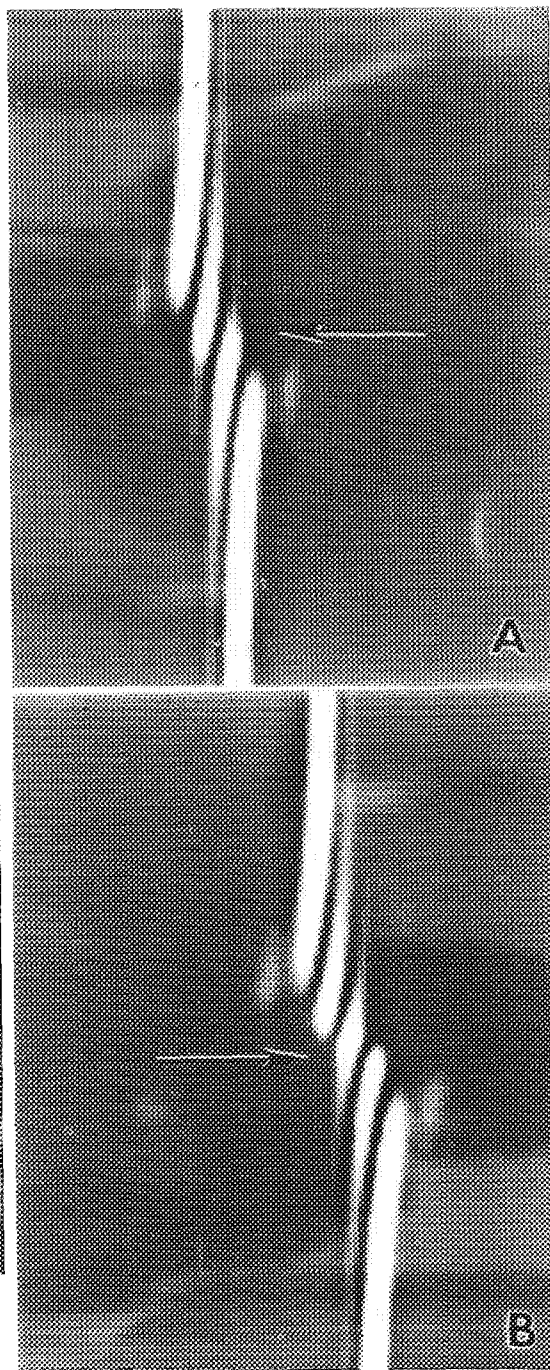


FIG. 9.--Dark-field CB reflections for Si specimen with screw dislocation. Specimen is 20 nm thick and dislocation nucleus is at 10 nm depth (15-beam calculation). (A) $g \cdot b = 3$, (B) $g \cdot b = 4$.

error and the horizontal distance from the dislocation line, respectively. Figure 9 shows the case where $g \cdot b = n = 3$ and 4, respectively; for $n = 1$, the reflection line splits into two lines, for $n = 2$ the reflection line splits into 3, etc. This image contrast characteristic has been used in the determination of the Burgers vector. However, there is a strong dependence of this particular kind of image contrast on various parameters. In Fig. 10,

the dark field disks of Co with a screw dislocation and $g \cdot b = 4$ are displayed: Fig. 10(A) corresponds to the two-beam calculation, Fig. 10(B) shows the DF disk when a nonsystematic reflection is included. The two figures show appreciable differences. The two-beam case (Fig. 10A) splits the reflection line into five segments. However, in the three-beam case only four segments can be clearly seen (Fig. 10B). Systematic reflections have small

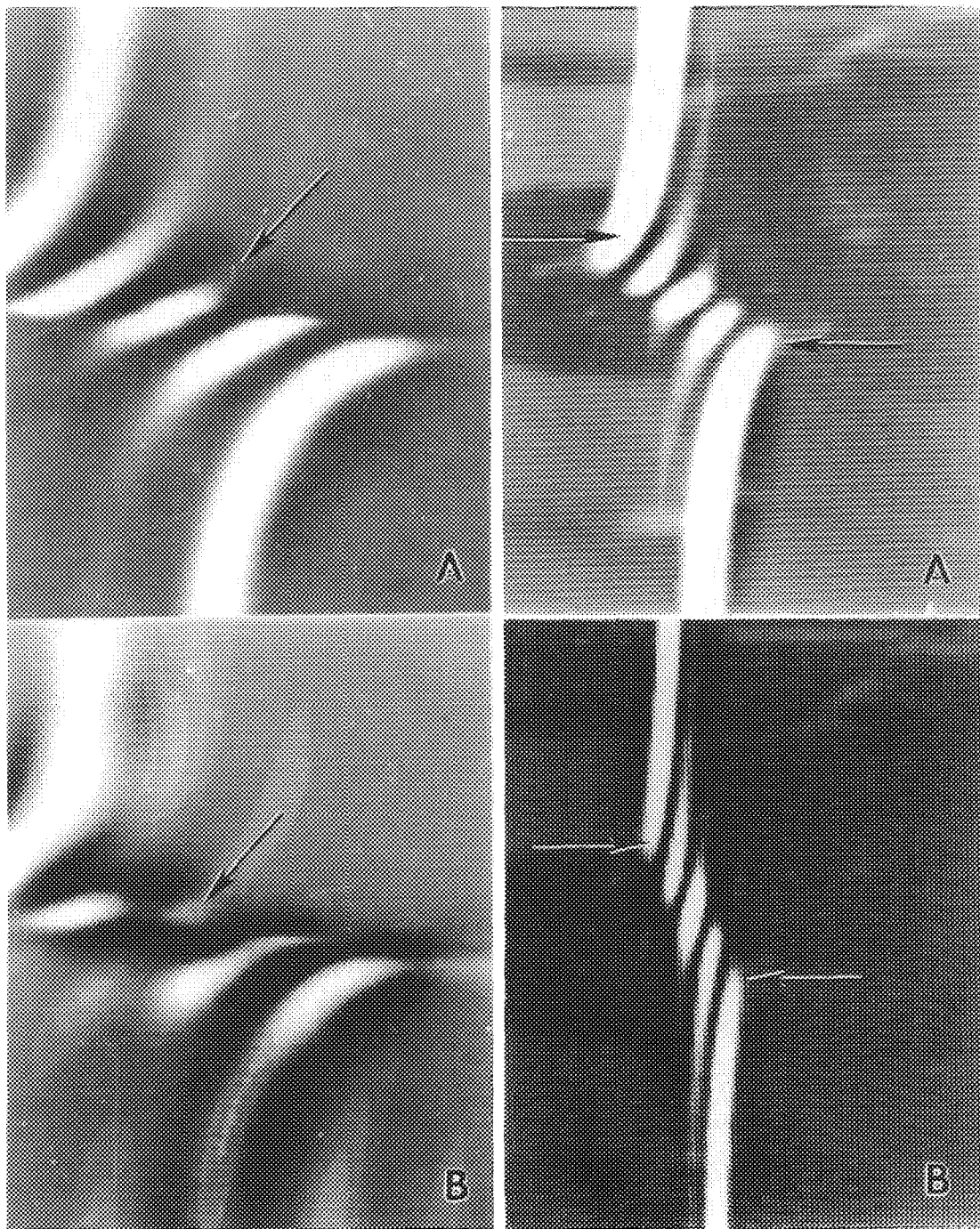


FIG. 10.--Dark-field disk for Co specimen with screw dislocation. (A) 2-beam calculation, (B) 3-beam calculation including nonsystematic reflection close to its Bragg condition.

FIG. 11.--CB dark-field disk from Si specimen with screw dislocation ($g \cdot b = 4$). (A) 2-beam calculation, (B) 15-beam calculation including only systematic reflections.

image contrast effects, as shown in Fig. 11, where DF disks obtained from a Si specimen with a screw dislocation is displayed. Figures 11(A) and (B) correspond to the two-beam and 15-beam calculation, including only systematic reflections. There are only small differences between these images. The specimen thickness also has a strong effect on the image contrast obtained in CB disks. Figures 12(A) and (B) show the dark-field disks for an Si specimen of 50 and 100 nm, respectively.

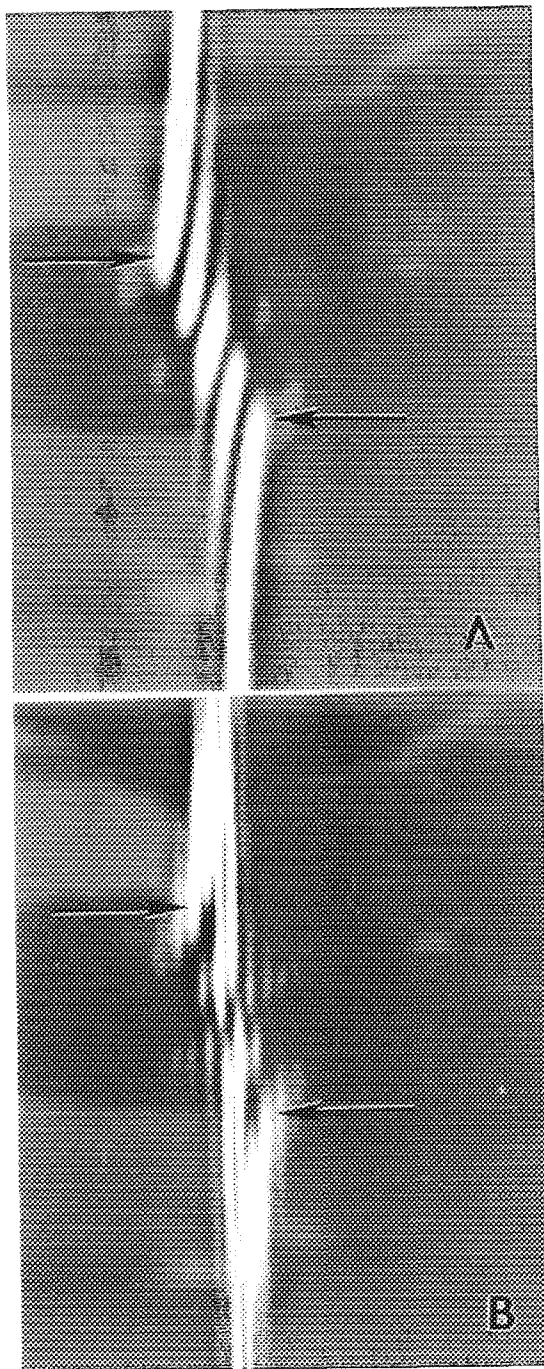


FIG. 12.--CB dark-field disk from Si specimen with screw dislocation ($g \cdot b = 4$). (A) Specimen 50 nm thick, (B) specimen 100 nm thick.

Appreciable differences in image contrast can clearly be seen suggesting that the identification method can be properly applied only in thin regions of the crystalline specimen. The effect of thickness is more pronounced for higher atomic number elements. Figure 13 shows the DF disks for specimens of Al and Au 40 nm thick and with a screw dislocation. The image contrast obtained in the gold case (Fig. 13B) does not fit with the main image contrast characteristics for defect identification.

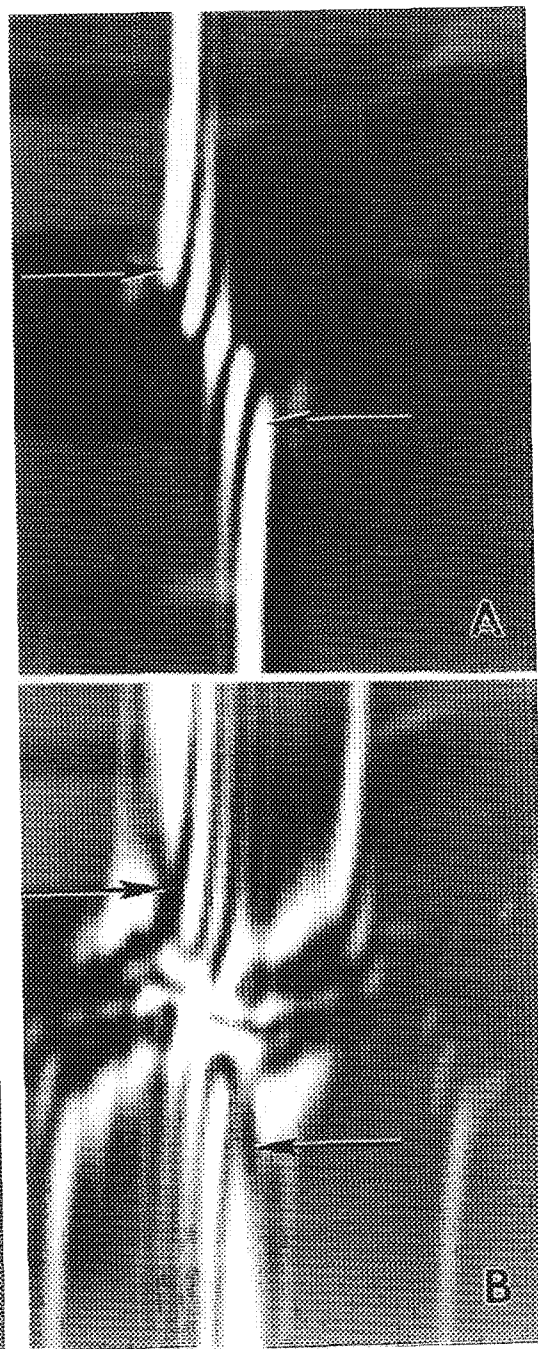


FIG. 13.--CB dark-field disk from crystalline specimen with screw dislocation of $g \cdot b = 4$. (A) Al 40 nm thick, (B) Au 40 nm thick.

Characterization of the Nature of Stacking Faults from CBED Reflections. The method to identify the nature of SFs from CBED reflections is based on the image contrast displayed by rocking curves obtained from specimens with transverse SF. In the past, the theoretical simulations have only been based on the two-beam approximation of the dynamic theory. In

experimental situations it is always difficult to avoid the effect of systematic and (in some cases) nonsystematic reflections. The importance of these kinds of reflections is illustrated in Fig. 14. This figure shows the rocking curves obtained from an Si specimen 300 nm thick. The crystal has a transverse stacking fault with a phase angle of $2\pi/3$. Figure 14(A)

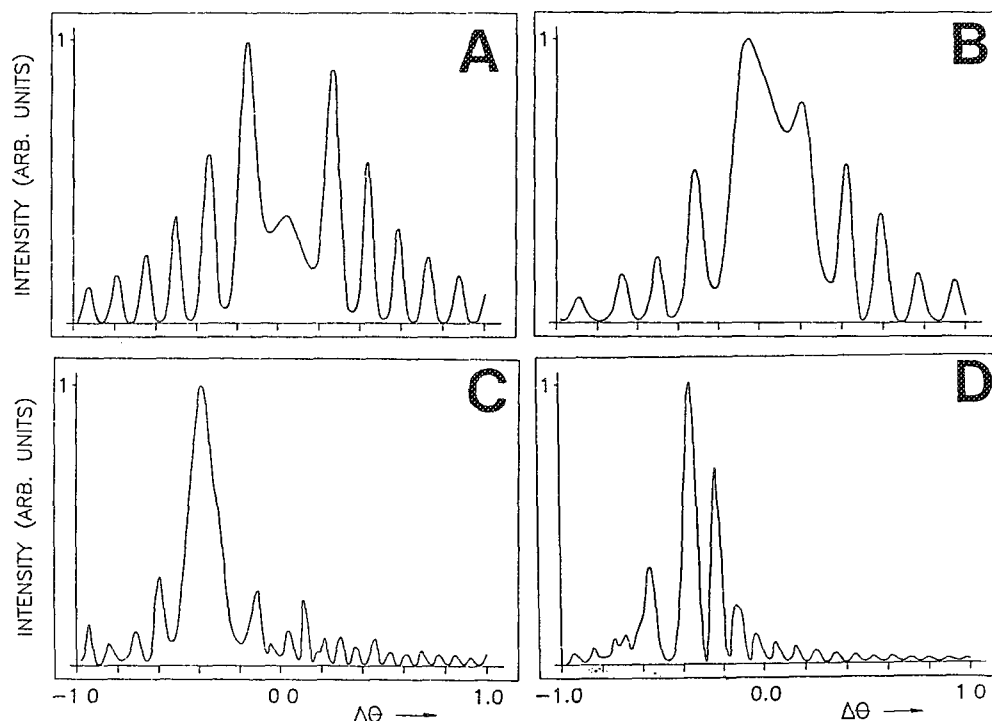


FIG. 14.--Rocking curves obtained from 300nm Si specimen with SF phase angle of $2\pi/3$. (A) 2-beam calculation, (B)-(D) 3-beam calculations including nonsystematic reflection that approaches Bragg condition from (B) to (D).

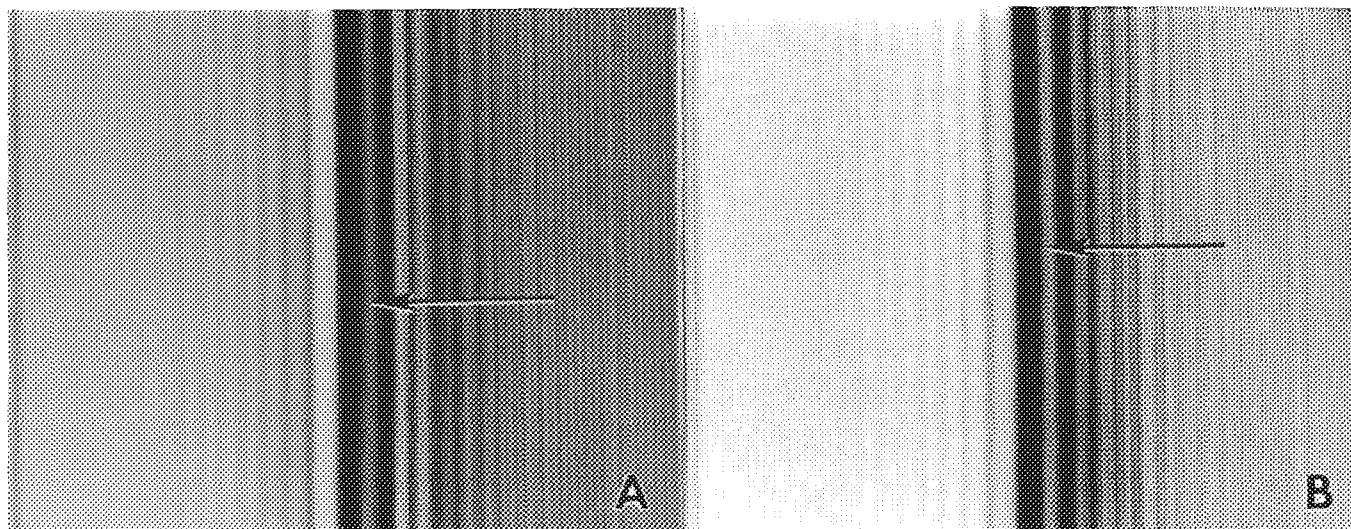


FIG. 15.--Directly transmitted disk for Al specimen with SF plane at 10 nm. (A) Phase angle $2\pi/3$, (B) phase angle $-2\pi/3$.

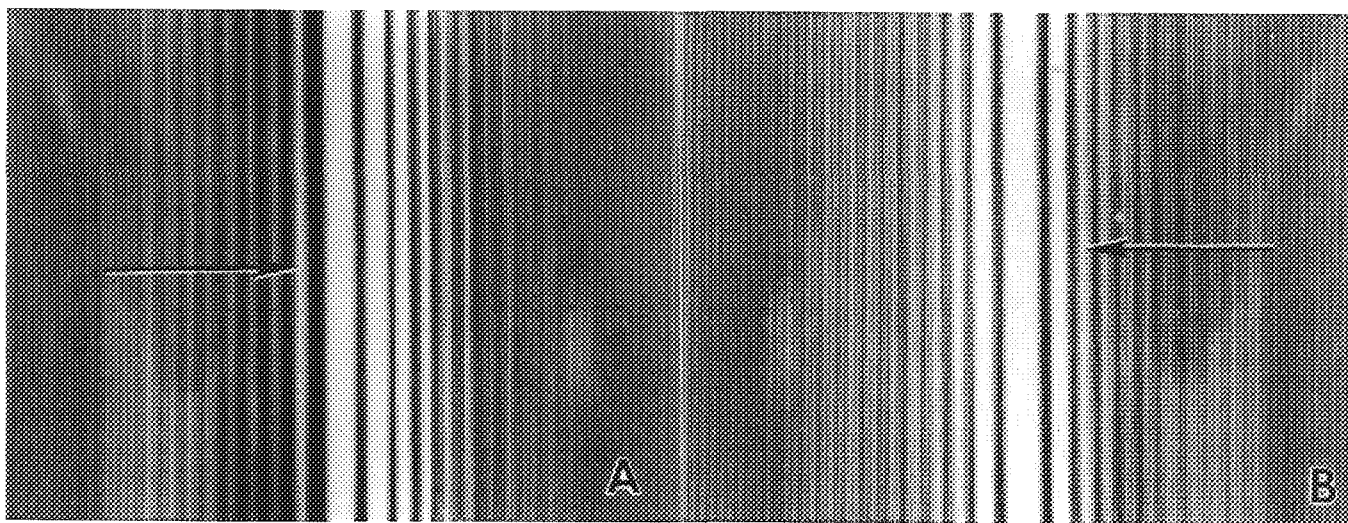


FIG. 16.--Dark-field disk for Al specimen with SF plane at 10 nm. Specimen thickness is 200 nm and phase angle is (A) $2\pi/3$, (B) $-2\pi/3$.

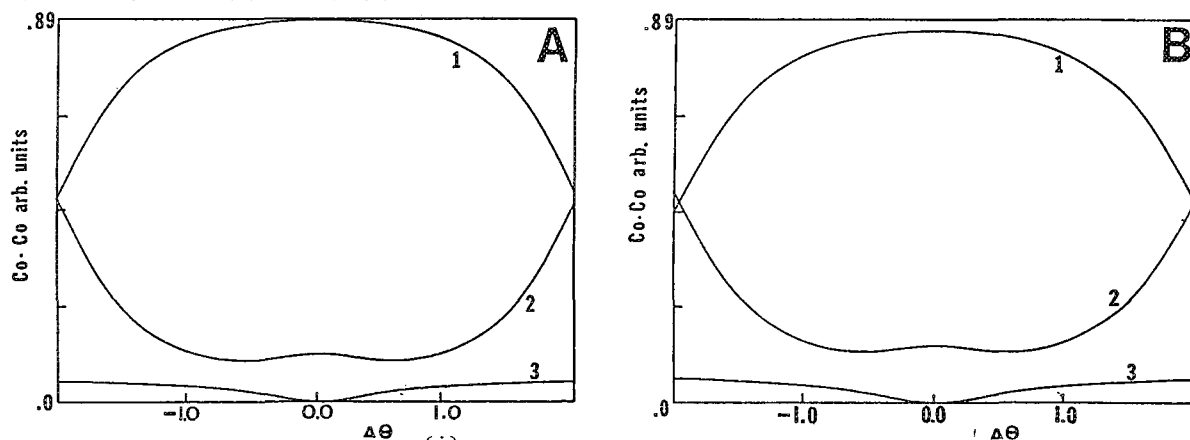


FIG. 17.--Bloch wave parameters $\phi_0^{(j)}$ as a function of crystalline orientation $\Delta\theta$, from $-2g$ at Bragg position to $2g$ at Bragg $g = 0 - 2.2$. (A) 9-beam calculation, (B) 25-beam calculation.

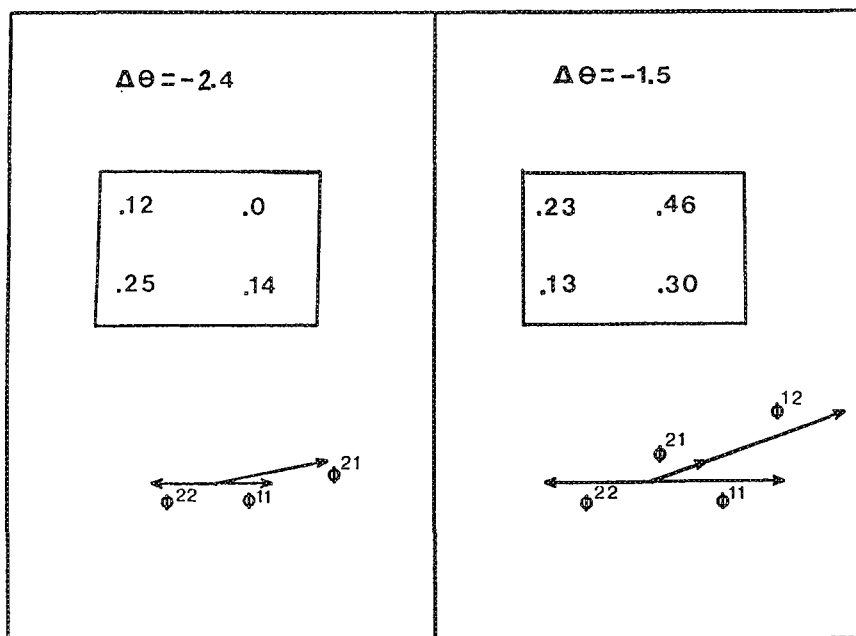


FIG. 18.--Contributions of interbranch and intrabranch scattering terms to diffracted beam amplitude for $\alpha = 2\pi/3$ fault (Fig. 15) for two crystalline orientations: (A) $\Delta\theta = -2.4$, (B) -1.5 .

assumes a two-beam situation; Figs. 14(B), (C), and (D) take into account a nonsystematic reflection with diffraction condition successively closer to its Bragg condition. Pronounced changes can clearly be seen from these profiles. On the other hand, the method used in the past to identify the nature of SFs by CB reflections is mainly based on the intrinsic asymmetry obtained in the overall image contrast of CB disks from specimens with these kinds of faults. The method involves the use of microdensitometer traces to be compared with the two-beam theoretical profiles. The same kind of information can be obtained by comparing the directly transmitted disk and one of the diffracted disks simultaneously. Figure 15(A) shows the directly transmitted disk for an Al specimen with an SF plane 10 nm deep. The phase angle is $2\pi/3$ and the thickness of the specimen is 200 nm. Figure 15(B) shows the same situation at a phase angle of $-2\pi/3$. The image contrast obtained from these disks is similar, so that no information can be obtained on the nature of the SF. However, the dark-field disks (Fig. 16) show appreciable differences in the image contrast characteristics. Thus, for example, the $2\pi/3$ case shows high intensity for negative values of the excitation errors, but in the $-2\pi/3$ case the high values of intensity corresponds to positive values of the excitation error. If we compare the BF and DF disks (Figs. 15 and 16), we see that the high-intensity regions are in opposite ranges of the excitation errors for $2\pi/3$ and in the same range for $-2\pi/3$. It is therefore clear that a simple comparison of the BF and DF disks could provide part of the information required for SF identification.

Discussion

The results of the calculations reported in this communication can be understood by following the behavior of the Bloch wave parameters as a function of the crystalline orientation. The importance of the contribution of Bloch wave j to the rocking curve profiles can therefore be determined by a plot $\phi_0(j) = (C_0(j))^2$ as a function of the rocking angle. Thus, for example, Fig. 1 shows no appreciable differences between the 25-beam and 9-beam disks in Al, but Fig. 17 shows a $\phi_0(j)$ profile ($-2g$ to $2g$) for 9-beam and 25-beam calculations. There are no important differences between these two plots. There are only two important Bloch waves in each case and therefore the image contrast of these CB disks are similar. The intrinsic asymmetry obtained in CB disks from crystals with stacking faults can also be understood from the behavior of the inter- and intra-branch scattering terms that are responsible for the image contrast in crystalline specimens containing SFs.⁵ The diffracted beam amplitude at the exit surface of the faulted (SF) crystal can be written as⁷

$$\phi_g = \sum_i \sum_j \phi_g^{ij}$$

The term ϕ_g^{ij} represents the contribution of the diffracted beam amplitude of the inter-branch scattering from Bloch wave j to Bloch wave i . (If $i = j$, the scattering is referred to as intrabranch.) Thus, for example, the asymmetry shown in Fig. 18 can be understood from a calculation of the magnitudes and phases of ϕ_g^{ij} (Fig. 18).

Conclusions

The results presented in this communication show that image contrast obtained in CBED disks in ZOLZ depends strongly on the diffraction conditions. Thus, for example, the presence of nonsystematic reflections closed to its respective Bragg condition can destroy the image contrast features used for defect identification. The thickness of the specimen also has strong effects on image contrast, which is of particular importance for defect identification.

References

1. M. Tanaka, M. Terauchi, and T. Kaneyama, *Convergent-beam Electron Diffraction II*, JEOL Ltd., 1989.
2. R. W. Carpenter and J. C. H. Spence, *Acta Cryst.* A45: 428, 1989.
3. R. Wang and J. Wen, *Acta Cryst.* A45: 428, 1989.
4. K. K. Fung, *Ultramicroscopy* 17: 81, 1985.
5. P. B. Hirsch et al., *Electron Microscopy of Thin Crystals*, New York: Krieger, 1977.
6. P. A. Doyle and P. S. Turner, *Acta Cryst.* A24: 390, 1968.
7. S. S. Sheinin and K. Z. Botros, *Phys. Stat. Sol.* 13A: 585, 1972.

PARTICULATE MAGNETIC MEDIA CONTAMINATION: LARGE DEFECTS

Evelyn R. Ackerman and Gerald Kimmel

The density of information stored on magnetic disks is increasing rapidly. The size of the recorded bit is getting smaller and the width of the track of the bits is becoming narrower. To achieve the increased density, the thickness of the recording medium is decreasing, and the distance between the disk and the read/write head (the flying height) is decreasing. Medium thickness of less than 100 nm and flying height of about 12 microinches are common. With these decreasing dimensions come increasing problems with particle contamination on the disks. Figure 1 shows a comparison of the flying height to the size of several typical particle contaminants. If the head encounters one of these particles resident on the disk, it is easy to see that catastrophic damage to the recording medium is possible. A particle may prevent the recording of a bit by causing the head to fly too high above the disk. If the head collides with the particle, the particles may gouge the medium and remove a bit. In either case some information is lost. Part of the quality assurance at Storage Technology Corp. is the prevention of the accumulation of particles on the disk before, during, and after assembly of the head-disk assembly (HDA).

Head/disk interference (HDI) occurs when contamination on the disk and/or recording media/substrate defects interfere with the head and cause head flight instability. HDI can range from a loss of a single bit of data to complete loss of data (head crash). This study includes the photographic documentation of the surface characteristics of recording/medium substrate defects and HDIs caused by particulate contamination by a scanning electron microscope (SEM).

Medium/substrate defects can cause the removal of the recording medium and leave a void and exposing the substrate. Figure 2 shows an example of a void that occurred as the result of the polishing operation done on the recording medium. A void can also occur when a contaminant is trapped in the medium and is pulled out (Fig. 3). Sometimes deposited contaminants are not pulled out, but remain trapped in the medium (Fig. 4). The agglomeration in Fig. 4, which contained human contaminants, possibly was deposited in the medium while it was still wet. The removal of the recording medium or contaminants that remain trapped in the media can affect the magnetic characteristics of the medium and result in the loss of data.

Particles introduced into an HDA during an assembly process or resulting from the wear of parts can cause HDIs of various magnitudes.

Figure 5 shows silicon-rich particles, marked by arrows, embedded in excess medium at the end of its path. The inset shows (at low magnification) the same particles dragged across the disk surface. Particles can also be dragged across the surface and shattered as a result of contact with the head (Fig. 6). The inset shows the path of the HDI on the disk.

Loose airborne particles can graze the surface of a disk at high velocity causing a gouge-like mark in the recording medium (ballistic-type defects). Figure 7 shows a ballistic-type defect generated outside the head flight zone. The medium was displaced (as shown by the arrow) and the substrate was exposed, which resulted in a mound of material. A similar ballistic-type defect in the head flight zone (Fig. 8) would result in the removal and displacement of the mound of material. The displaced material is burnished down because of repeated head/disk interferences (HDI). Measurement of the defect (Fig. 9) by an optical profilometer indicated that it was burnished down to approximately flying height level.

By use of the Ferrofluid developing technique (Ferrofluidics Corp., Nashua, N. H.), the scanning electron microscope can be a valuable tool in accessing the damage caused by an HDI (Ref. 1). The developed data tracks are represented as white rectangles on recording media. Figure 10 shows the path of a particle of an HDI which resulted in the damage of the recording medium and caused a 100% loss of data. The HDI (Fig. 11) is a mass of contamination that was transferred to the disk from the head during flight. As a result of the contamination, a multitrack and multibit defect occurred. Data also can be lost in a subtle way. Figure 12 shows a particle shoved into the substrate that resulted in the loss of two bits of data. The loss of one or two bits of data can be as detrimental to data retrieval as a multibit or multitrack failure.

These techniques help to determine the root causes of large defects by furthering an understanding of their formation and what materials are present, and will insure minimal impact to our users.

References

1. R. D. Weiss and J. Schifter, *J. Appl. Phys.* 57: 4274-4276, 1985.

The authors are at Storage Technology Corp., Louisville, CO 80028-2166.

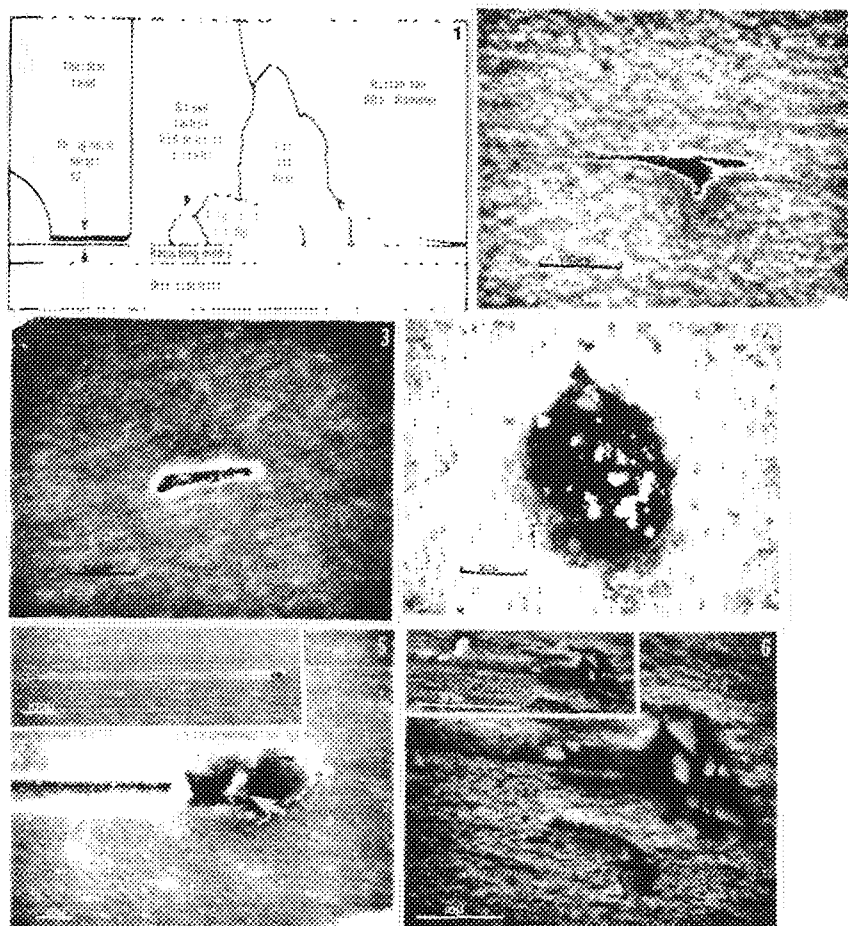


FIG. 1.--Comparison of head flying height with respect to human contaminants and airborne dust.
 FIG. 2.--Void in recording medium result of polishing operation done on the media.
 FIG. 3.--Void in recording medium result of contaminant being pulled out.
 FIG. 4.--Agglomeration deposited on medium while it was still wet.
 FIG. 5.--Silicon-rich particles embedded in excess medium (arrows). Inset shows path of particles.
 FIG. 6.--Silicon-rich particles shattered by contact with head. Inset shows path of particles.

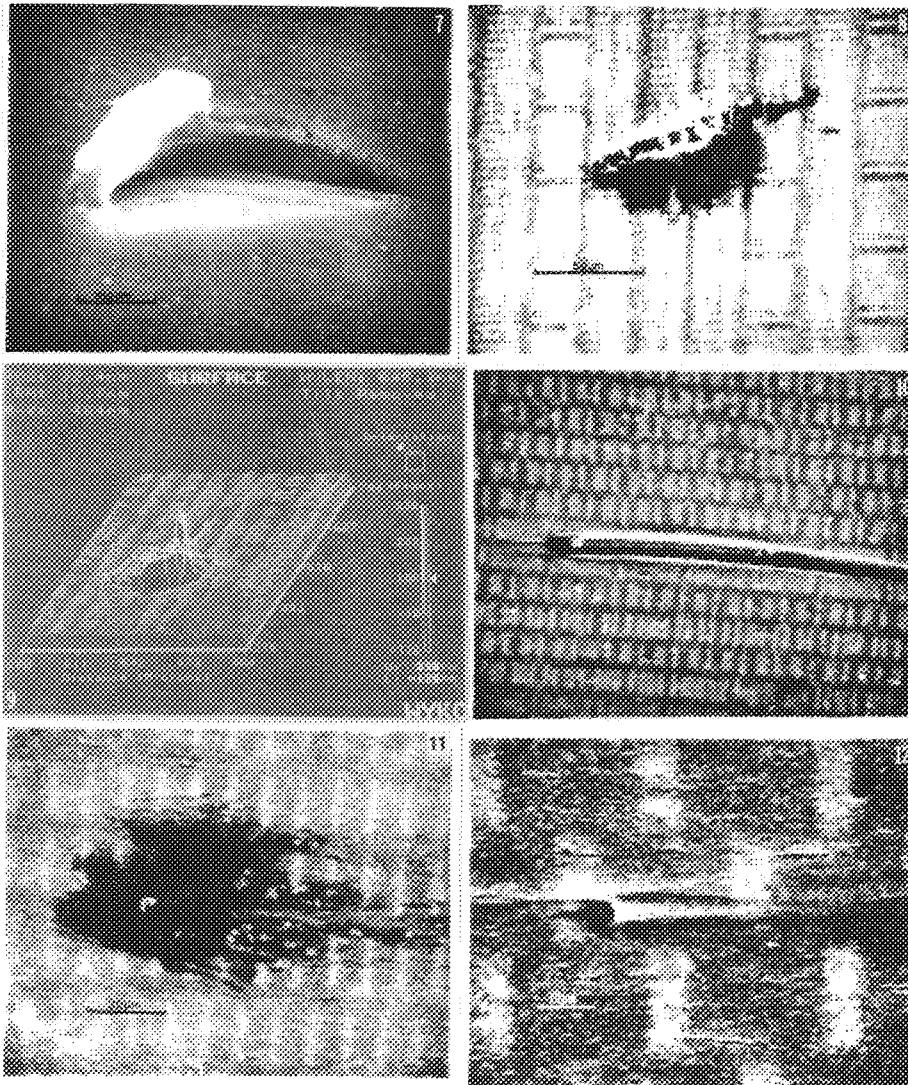


FIG. 7.--Ballistic-type defect outside head flight zone.
 FIG. 8.--Ballistic-type defect inside head flight zone.
 FIG. 9.--3-D optical profilometer graph of ballistic-type defect in Fig. 8.
 FIG. 10.--Developed recording medium showing 100% loss of data.
 FIG. 11.--Developed recording medium showing multitrack, multibit error.
 FIG. 12.--Developed recording medium showing two-bit error.

USE OF METAL BLACKS FOR CAPTURE OF LOW-VELOCITY (<200 m/s) PARTICLES

G. H. Bearman, J. G. Bradley and S. G. Davidson

Collection of low-velocity (~ 50 -200 m/s) micron-size dust particles is an upcoming challenge for dust instruments aboard NASA's Comet Rendezvous and Asteroid Flyby (CRAF) mission, scheduled for launch in 1995. The scanning electron microscope and particle analyzer (SEMPA) is one of the CRAF dust analysis instruments.¹ The work reported here examines particle capture in light of SEMPA's particular functional requirements. These requirements include particle visibility for imaging and x-ray analysis, high contrast, no interfering x-ray lines, and collection without size or velocity discrimination. Collection techniques have been tested in our laboratory with dust from a free-expansion gas-drag dust gun that accelerates micron-size dust to ~ 50 -200 m/s, the expected relative velocity of the spacecraft and the dust at the comet. The dust capture experiments were performed with two types of particles: round ceramic spheres, ~ 2 -10 μm in diameter, and 5-15 μm aluminum oxide grains. The density of the ceramic spheres is $\sim 2.6 \text{ g/cm}^3$; that of the grains, $\sim 4 \text{ gm/cm}^3$. Irregularly shaped grains were used, as they more closely resemble the morphology of comet dust. Although it would be desirable to use fluffy agglomerates like those expected among the cometary dust, we know of no way to make them.

Capture of a micron-size particle at 50-200 m/s requires slowing the particle down to where mechanical or electrostatic adhesive forces pin it to a substrate. The use of metal blacks as a collection substrate was suggested by Frisch and Igenbergs,² although for use at higher velocities, 500 m/s. Particles stop in the metal black by breaking or crushing the filamentary structures of the metal black, much like a collapsible car bumper. We have investigated metal blacks made by evaporation of metals at several hundred millitorr of pressure onto a substrate. Experiments have demonstrated that the stopping power is related to the bulk density and structure of the black.

The metal blacks are made by evaporating the metal in a static 200-700 millitorr pressure of argon in a belljar. Metal evaporation at these pressures allows formation of particles in the 10-50 nm range by nucleation. These particles are carried upward and outward by convection current and eventually precipitate onto nearby surfaces. The blacks are prepared on silicon wafers placed ~ 2 -4 cm above the level of the

evaporator boat; there is no line of sight to the boat to avoid thermal radiation from the boat that would otherwise remelt or sinter the blacks. Both the morphology and volumetric density of the metal black are a strong function of the vertical and horizontal distance from the boat. The most effective capture coatings in our experiments were made at 4 cm above the boat and 4 cm horizontal from the boat.

Copper blacks were investigated initially and were moderately successful at particle capture. However, the black had to be relatively thick, 10 μm , for effective retention. As a result, the particles tended to bury themselves below the surface and were analytically inaccessible, especially for samples with low bulk density. Gold blacks were also examined, partly because, like copper, they do not pose a serious interference for x-ray analysis for the elements of interest in cometary dust. Gold was used also because it was felt that the larger mass/unit area would be more effective in absorbing energy from the impacting dust. Gold black yields the best results, with consistent and reproducible capture rates of $\sim 80\%$ for particles 1-7 μm in diameter. The particles were retained on or slightly below the surface, permitting x-ray analysis without difficulty. Capture efficiency is calculated by counting particles and bounces in a visual field; bounces of even 1 μm particles leave easily observed impact craters. Figures 1 and 2 show some particles captured by the gold blacks.

These initial tests have provided evidence that particle capture is related to the metal black density and structure; an overly dense or solid network bounces the particles off the surface, and a very spongy one collapses completely and allows the particles to impact the substrate and again bounce. Profile views of the metal blacks demonstrate a clear connection between the morphology of the black and capture efficiency. A clean edge for imaging the profile is obtained after deposition by cleaving the silicon substrate; high-resolution SEM photos show that this procedure cleaves the metal black as well. Figure 3 shows what is called a "spongy" structure and Fig. 4 is a top view of the same after exposure in the dust gun. The dust particles are either deeply embedded or have created impact craters from hitting the silicon substrate and rebounding. Figure 5 is a side view of a different sample; the metal black appears to have grown in a "columnar" arrangement. Figure 1 is that sample as a dust collector; for the visual field of this sample the capture rate is $\sim 100\%$. The correlation between morphology and dust capture is strong

The authors are at the Jet Propulsion Laboratory, California Institute of Technology, Pasadena, CA 91109. The work described in this paper was performed in part by the Jet Propulsion Laboratory and was sponsored by the National Aeronautics and Space Administration.

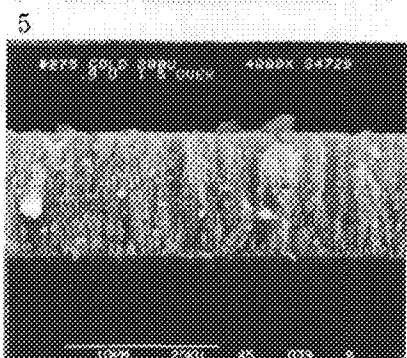
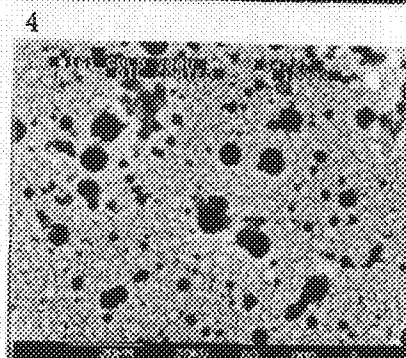
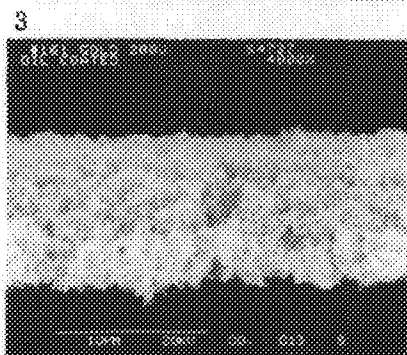
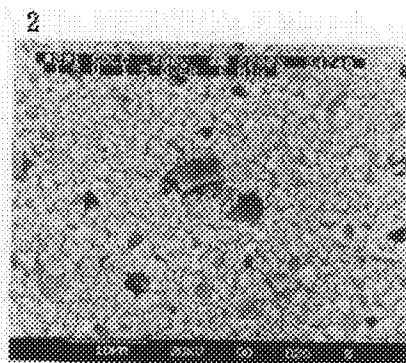
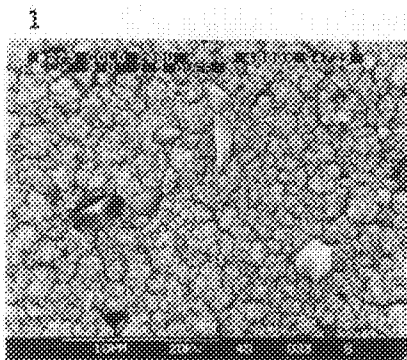


FIG. 1.--50-200 m/s Al_2O_3 grains captured on gold black. There are 24 captured particles and one impact crater.
 FIG. 2.--50-200 m/s Al_2O_3 grains captured on gold black. There are 53 captured particles and 8 impact craters.
 FIG. 3.--Side view of a "spongy" gold black.
 FIG. 4.--Top view of sample in Fig. 3 after exposure in dust gun. Very few of the particles have been captured; craters from particles bouncing off substrate are very visible.
 FIG. 5.--Side view of sample of Fig. 1; note vertical or "columnar" structure of metal black.

enough to permit the use of side views as predictors of capture efficiency.

Metal blacks have been demonstrated to be efficient collectors of low-velocity dust, typical of what is expected on the CRAF mission. Particles captured on the best blacks are analytically accessible, as they are on or only slightly below the surface; however, particle contrast on the substrate is poor. There may be some size discrimination for a given collection substrate, although the effect in the tested range of 1-7 μm seems small. Testing for velocity discrimination is more difficult and has not yet been done. The behavior of this capture technique in an airstream is unknown, but it may have value in aerosol capture systems where rare particles must be captured and every one examined without handling.

References

1. J. M. Conley et al., "Development of a miniature scanning electron microscope for in-flight analysis of comet dust, *Microbeam Analysis--1983*, 177.

2. W. Frisch and E. Igenbergs, "Metallic dust collectors for low-velocity impacts," *Adv. Space Res.* 6: 213, 1986.

AUTOMATION OF GUNSHOT-RESIDUE ANALYSIS BY FUNCTIONAL INTEGRATION OF A SCANNING ELECTRON MICROSCOPE AND AN ENERGY DISPERSIVE MICROANALYSIS SYSTEM

M. H. Peeters, J. Antoine, V. Lamothe, and A. Viala

Over the past ten years, the combination of scanning electron microscopy and energy dispersive analysis has proved to be a good and reliable tool for characterization of the different components of gunshot residue.^{1,2} The method reported has evolved from a qualitative technique, involving a large amount of operator involvement, to a higher degree of quantification and automation allowing unattended analysis of gunshot residue samples. Most systems currently in use are restricted to detection of rather large ($>2\text{ }\mu\text{m}$) particles.³ As a consequence rather large surfaces (approximately 1 cm^2) have to be analyzed in order to yield sufficient statistical validity of the results. The system described here overcomes this limitation and is geared to high-speed automated unattended analysis, particularly suited to applications such as gunshot-residue analysis.

Equipment

The system (PHAX-Scan) is based on a Philips scanning electron microscope and an EDAX PV9900 energy dispersive microanalyzer in combination with highly optimized software. The system makes use of the dual processor structure of the EDAX analyzer and of the bus structure of the Philips scanning electron microscopes. It is designed such that it performs a fully quantitative data reduction, including background subtraction, and ZAF correction in (typically) 100 ms. This improvement in data processing time (previously typically 10 to 40 s) makes it practical to perform high-speed high-volume particle classifications. The high-precision motor stage of the scanning electron microscope allows detection and later retrieval and review of submicron size particles.

Method

A particle search is first performed on digital images of 1000×800 pixels. In order to be able to detect a particle, it must occupy at least a few pixels. The field width is therefore selected according to the minimum particle size to be detected. Fields of $16\text{ }\mu\text{m}$ up to 1 mm can be covered in one digital image. The number of seek fields required for the full analysis will be defined by the magnification at which the SEM is set at the start of the unattended run.

M. H. Peeters is at Philips Analytical, Electron Optics Applications Laboratory, Building AAE, NL-5600 MD Eindhoven, The Netherlands; his co-authors are at the Laboratoire Interrégional de Police Scientifique de Marseille, 2 Rue Becker, F-18002 Marseille, France.

The stage is moved to the first seek field and the magnification is adjusted automatically. The beam is scanned over the specimen with a resolution of 1000×800 pixels. A binary image is then formed of particles with a selected range of mean atomic number, as represented by the backscattered response. The binary image is searched for particles. As soon as a particle is detected, its size and shape are determined. During this process a preliminary spectrum is collected. The analysis of this spectrum allows the determination whether one or more of the elements typical for gunshot residue is present. The particles containing barium, lead, or antimony whose size and shape fall within the limits set by the user are accepted and their position is recorded. The beam moves to the center of the particle and an x-ray analysis is performed during a user-selectable time (for gunshot residue analysis typically 4 s).

The results of this quantitative analysis are compared to a user-defined library of compositions. Since the library is based on absolute concentrations rather than k-values or relative intensities, it can be compiled from results obtained under totally different conditions. This procedure is repeated for each particle until the seek field is completed. The stage is then moved to the next seek field and a new image is collected. This is done until the whole area to be analyzed is covered. For each class, the number of detected particles as well as the average area and particle size are printed out. Since all the data relevant to each accepted particle are stored on disk, further studies can be made by sorting the results on library class, particle size, or shape by calculating averages on subpopulations.

For each accepted particle all relevant data can be called back and the particle can be displayed on the microscope screen so that it can be analyzed in more detail if required.

Experimental

Gunshot residue has been collected from four different types of arms. The shots were fired on an outdoor shooting stand. Two hand weapons (.357 magnum, .22 LR pistol), a pump gun, and a .22 LR carbine were used. The residue was collected with double-sided adhesive tape (1 cm in diameter), mounted on an aluminum stub. The specimens were carbon coated. The stubs were mounted on a multispecimen holder and analyzed with a Phax-Scan system consisting of a Philips SEM525M and an EDAX PV9900 analyzer. A surface of about 20% of each stub has

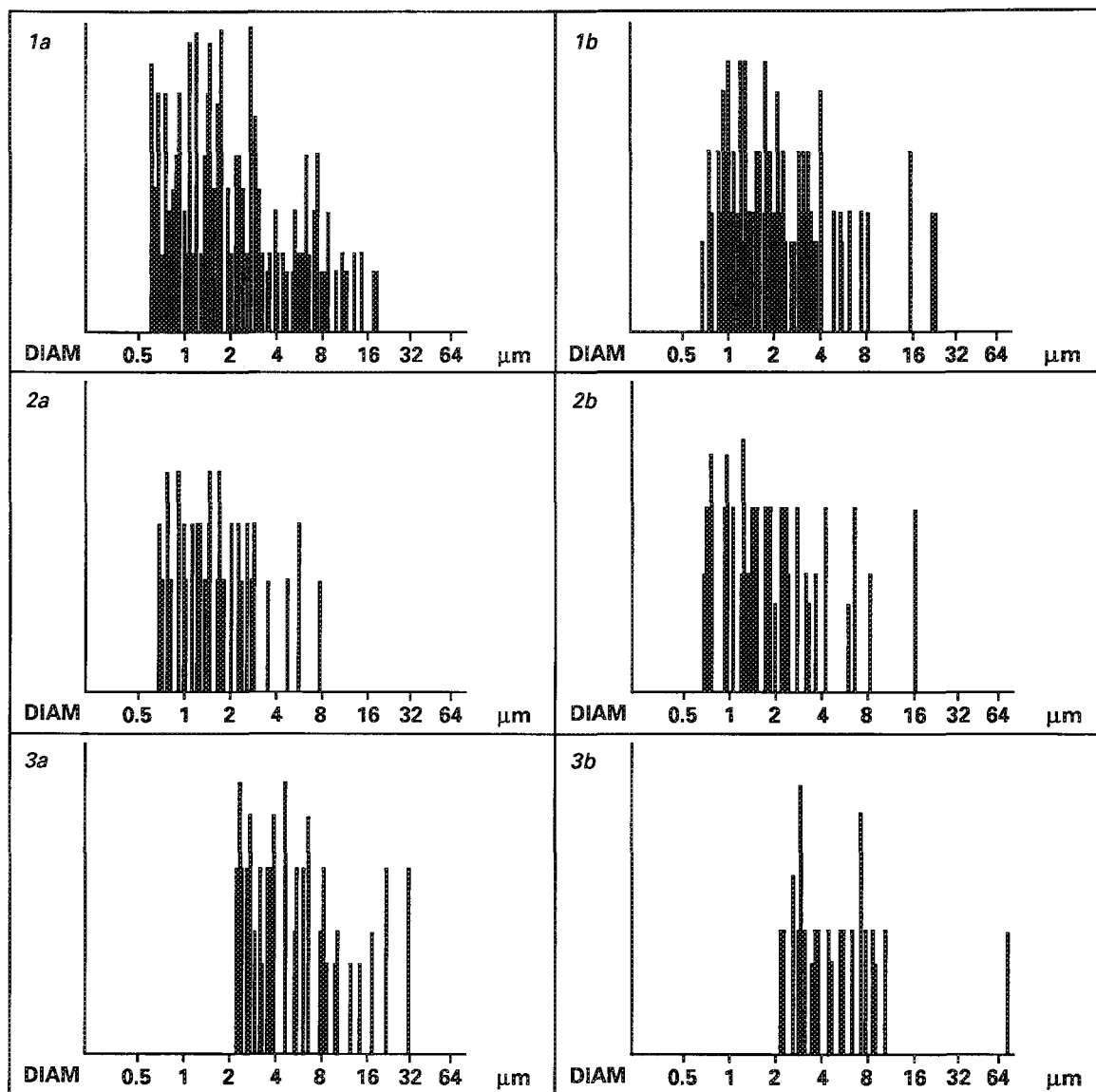


FIG. 1.--Accepted particle size distributions of various weapon types: (a) .22 LR pistol, (b) pump gun.

FIG. 2.--Positive gunshot residue particle size distributions. (a) .22 LR pistol, (b) pump gun.

FIG. 3.--Accepted particle size distributions of various weapons. Particle search for particles > 2 μm . (a) .22 LR pistol, (b) pump gun.

been analyzed for particles with diameters between 0.75 and 30 μm .

Results

Table 1 shows the number of detected and accepted particles for each analysis. The total analysis time is also indicated.

The population of gunshot residue varies considerably as a function of the weapon type, but also as a function of firing conditions and type of ammunition used. In our case, it was necessary to analyze 20% of the stub to identify only few particles emitted by a .22 LR carbine. However, for other weapons more than sufficient particles are identified on this surface, so one could shorten the analysis time even further by reducing the analyzed area, with the preset

particle count facility.

Figure 1 shows size distribution histograms of the accepted particles (containing one or more element typical for gunshot residue). Figure 2 shows the distribution of particles containing Ba, Pb, and Sb. It is clear that the average size of the gunshot residue particles (PbBaSb) are smaller in diameter than the average accepted particle. Figure 3 shows the size distributions of the accepted particles when only particles with a diameter bigger than 2 μm were searched for. It is clear (cf. Fig. 1) that this procedure limits the chance of detecting gunshot residue considerably.

Conclusions

The Phax-Scan system allows the detection

TABLE 1.--Number of particles and analysis time for various weapons.

Weapon	Time of analysis	Detected particles	Accepted particles	PbBaSb particles
.357 Magnum	3h27min	513	49	27
.22 LR pistol	3h42min	834	222	155
Pump gun	3h36min	1430	139	106
.22 LR carbine	3h12min	547	31	11

and identification of gunshot residue particles on a big surface in a time compatible with the needs of a police investigation. The majority of gunshot residue particles have a small dimension (below 2 μm). It is therefore necessary to concentrate future investigations on these smaller particles.

References

1. G. M. Wolten, R. S. Nessbit, A. R. Callo-way, et al., *Final Report on Particle Analysis for Gunshot Residue Detection Corp*, El Segundo, Calif., 1977, 13-22.
2. A. Svensson, O. Wendell, and A. Fisher, *Techniques of Crime Scene Investigation*, 3d ed., New York: Elsevier, 1981, 240.
3. W. Tillman, "Automated gunshot residue particle search and characterization," *J. Forensic Sciences* (JFSCA) 32(1): 62-71, 1987.

CORRELATION OF PERMEABILITY TO PORE STRUCTURE BY SEM-IMAGE ANALYSIS

C. A. Callender, W. C. Dawson, and J. J. Funk

The geometric structure of pore space in some carbonate reservoir rocks can be correlated to petrophysical properties such as permeability (measure of fluid flow rate) by a quantitative analysis of pore structures in binaries generated from SEM images. Reservoir rocks with similar porosities can have markedly different permeabilities. Image analysis identifies which characteristics of a rock are responsible for permeability differences. Imaging data can explain unusual fluid flow patterns which, in turn, can improve oil production simulation models.

Sample Suite

Our sampling consists of 30 Middle East carbonates having porosities ranging from 21 to 28% and permeabilities from 92 to 2153 md (millidarcies; the unit measurement of permeability). Although it is generally assumed that rocks with higher porosities have greater permeability, in this sample suite engineering tests reveal the lack of a consistent relationship between porosity and permeability (Fig. 1). The analytical scheme of this study was designed to identify attributes of the pore system that influence the flow rate, because total porosity does not relate well to permeability.¹

Analytical Scheme

Thirty finely polished thin sections (30 μ m-thick slices of rock, mounted on a glass slide) were studied petrographically to determine rock texture. Four petrographically distinct rock types (microfacies) were identified (Table 2).² The thin sections were then analyzed for pore structure characteristics by a Tracor Northern 5500 EDS analyzer (IPP and SIA software programs) and a 80386 microprocessor-based imaging system (Perception and Decisions Systems software). Between 30 and 50 SEM-generated back-scattered electron frames were collected (GW Electronics, Type 30 solid state BSE detector) per thin section. Because pore size varies markedly within individual thin sections, BSE frames were taken at several scales. Magnification combinations of 50 \times , 100 \times , 500 \times , 1000 \times , 1500 \times , and 2000 \times include views of micropores (1-5 μ m diameters) up to pores exceeding 1000 μ m. At least 15-20 frames were collected at each scale.

Binaries of the pores were created by isolation of the gray level in the BSE image that represents only the pore space. The TN IPP/SIA

program was run on about 1200 different binaries representing the four different microfacies. The resulting SEM-IA calculated total porosities were then compared with conventionally measured total porosities from the same core plug. X-ray computed tomography (CT) was also performed every 2 mm along the length of the core plugs. These CT inspections helped identify extremely heterogeneous samples and confirm the belief that samples whose calculated porosities did not match actual measured porosities are indeed heterogeneous (i.e., comprised of more than one microfacies).

TABLE 1.--Microfacies.

- A. Compacted, well-sorted, foraminiferal, peloidal, ooid grainstone.
- B. Compacted, moderately well-sorted, intraclastic foraminiferal, peloidal grainstone.
- C. Compacted, poorly sorted, dolomitized, foraminiferal, peloidal, intraclastic grainstone.
- D. Well-sorted, foraminiferal, ooid, peloidal grainstone with drusy rim cement.

Discussion: Pore System Typing

Results of this study indicate that certain types of pore systems are associated with certain ranges of permeability. Samples A and B have relatively high and low porosity values, respectively (Table 2); however, they both have high permeabilities. A comparison of each sample's pore space binary (Figs. 3a and b) reveals that both samples are dominated by *channeled* pore structures. Other samples, which possess similar porosity and pore size distributions but lack channels, have much lower permeabilities (sample C; Table 2; Figs. 3c and 5); these pore structures are *compartmentalized*. Compartmentalized porosity occurs where effective pores, commonly enlarged by dissolution (Fig. 5), are isolated or poorly connected to matrix porosity, thereby limiting effective pathways and reducing flow rates. Small *pore size* has the potential effect of lowering permeability. For example, sample D has high porosity, yet very low permeability (Table 2; Figs. 3d and 6). Pore size distribution centers in the small size range, and the pore throat size distribution is skewed toward small sizes.

TABLE 2.--Petrophysical measurements.

Sample	Porosity (%)	Permeability (md)
A	28.2	1060
B	23.5	961
C	28.0	495
D	28.5	212

The authors are at Texaco's Exploration and Production Technology Division. This work has been requested and supported by the Saudi Arabian Oil Company.

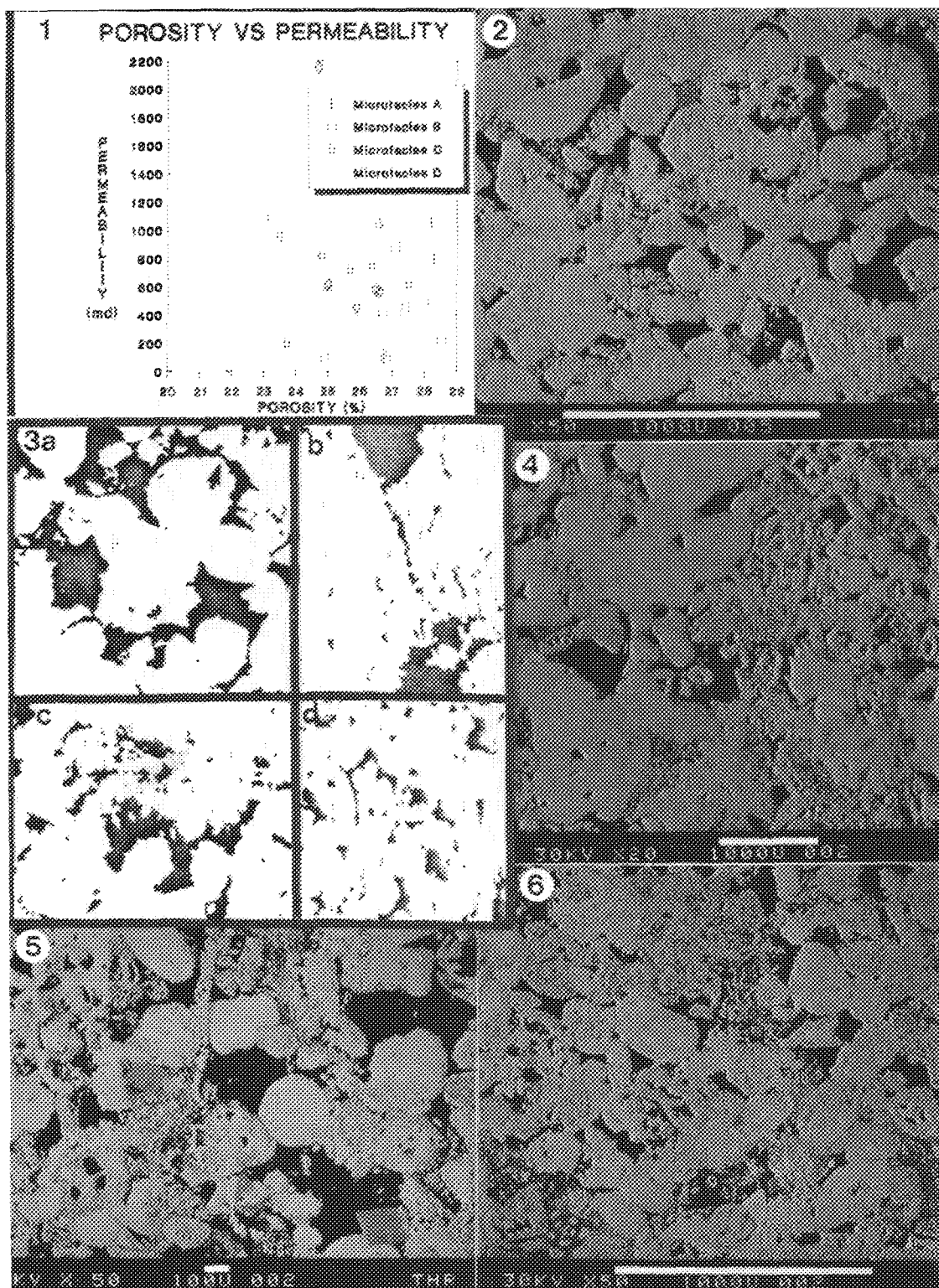


FIG. 1.--Plot shows lack of predictable relationship between porosity and permeability.

FIG. 2.--BSE image of sample A (microfacies A).

FIG. 3.--(a) Binary of sample A: arrow indicates channelized pores; (b) binary of sample B: microchannels connect large pores; (c) binary of sample C: isolated, compartmentalized pores; (d) binary of sample D: small, poorly connected pores.

FIG. 4.--BSE image of sample B (microfacies C).

FIG. 5.--BSE image of sample C (microfacies B).

FIG. 6.--BSE image of sample D (microfacies B).

Results

Pore connectivity, rather than absolute pore size, is the principal factor influencing permeability. Pore size distributions can affect permeability through compartmentalization (isolated pore types). Pores, enlarged by dissolution, or microchannels produce fairways (channelization) that increase permeability. Pore systems can be classified (pore system typing) and correlated to flow patterns and permeability ranges.

References

1. J. J. Funk, M. C. Choinski, B. B. Saxman and C. A. Callender, *Characterization of Carbonate Porosity Using Petrophysical Properties and Image Analysis*: SPE 17943, SPE Middle East Oil Technical Conference, March 11, 1989.
2. R. J. Dunham, *Classification of carbonate rocks according to depositional texture*, in W. E. Ham, Ed., *Classification of Carbonate Rocks--a Symposium*, AAPG Memoir 1, 108-121, 1962.

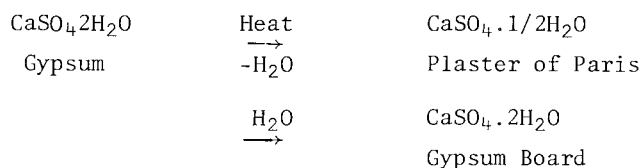
AN ELECTRON MICROSCOPICAL STUDY OF SILICONE HYDROPHOBICITY IN COMMERCIAL GYPSUM WALLBOARD

H. A. Freeman and Y. A. Peters

Trimethyl endblocked methylhydrogen polysiloxane, *Experimental*

DOW CORNING 1107 Fluid, is used to make moisture-resistant gypsum board, marketed as Dens Shield by the Georgia-Pacific Corp. in Decatur, Ga. The moisture-resistant board is produced as one of two types: sheathing or tile backer board. They differ in that the sheathing must have less than a 10% water pick-up and tile backer less than 5% water pick-up.

The general production scheme is as follows: Gypsum is rehydrated $\text{CaSO}_4 \cdot 2\text{H}_2\text{O}$. Gypsum is mined, calcined, and then rehydrated as in the following reaction:



The hemi-hydrate as part of a slurry is dropped onto paper face stock. Typically, the slurry consists of three separate mixtures which are mixed in a pin mixer for a few minutes before being applied to the paper. The three components are (1) a water/fiber glass mixture, (2) an asphalt wax emulsion, and (3) a water, surfactant, and starch mixture. The slurry is dropped on the paper; a top sheet is added; and, as the gypsum rehydrates, the board "sets up." The board is cut and then dried in a hot oven, about 550 F, after which it is wrapped and stacked.

Asphalt wax has been traditionally used but has several drawbacks. It has a short life and must be shipped, stored, and used at 110-130 F. It also tends to weaken the board. DOW CORNING 1107 has no temperature restrictions and a long shelf life. Its use does not detract from the strength of the board and may in fact strengthen the overall gypsum structure. Several different silicone types were evaluated to provide the best combination of hydrophobicity and structural integrity of the gypsum board product. Conclusions from these studies demonstrated that the methylhydrogen polysiloxane type of silicone was preferred. However, it remained unknown where the silicone became localized to achieve this effect. Microanalyses were therefore performed in the analytical electron microscope to define the distribution of silicone in commercial gypsum wallboard samples.

Gypsum samples were obtained which included those containing silicone and others to which no silicone had been added during manufacture. Analyses were performed in a JEM 2000FX analytical microscope operated at 200 keV and equipped with Noran Instruments Micro-ZHV and Microtrace energy dispersive x-ray spectrometers. Scanning (SEM), transmission (TEM), and scanning transmission (STEM) images were correlated with the mapped distributions of as many as six different elements acquired simultaneously. Low-Z substrates and tilting specimen holders effectively minimized incorporation of spurious x rays in the final spectra. Initial SEM examination of comparatively thick sections showed large open voids surrounded by a porous matrix of recrystallized tabular gypsum crystals (Fig. 1). Dimple polished specimens from the same untreated control board showed a typical microstructure (Fig. 2a). Substantial Si occurred in electron dense particles scattered throughout the gypsum matrix (Fig. 2b). At first, it was felt that this Si content may have obscured the detection of Si derived from silicone in subsequent examination of treated samples. However, similar areas in the silicone-containing wallboard (Fig. 3a) showed not only analogous Si concentration in these discrete particles, but increased carbon and a moderate Si content in narrow zones around open voids (Fig. 3b). Images of these void linings (Fig. 4) demonstrated an increased electron opacity compared to that in the untreated wallboard (Fig. 2a). Moreover, spectra from these void linings showed no evidence of Al and K, both of which appeared prominently in spectra obtained from the discrete particles (Fig. 5). This association of elements allowed distinction between silicone and a probable silicate impurity within the gypsum microstructure.

Results

Results of this investigation showed that the silicone in the treated wallboard was preferentially localized discontinuously around the periphery of large, roughly spherical voids in the commercial gypsum product. It was concluded that this silicone distribution effectively sealed the wallboard interior from penetration by external moisture during subsequent use.

References

1. H. H. Steinbach and M. Reider, *Production of Water Repellant Moldings from Plaster*,

The authors are with the Research and Development division of Dow Corning Corp., Midland, MI 48686-0994.

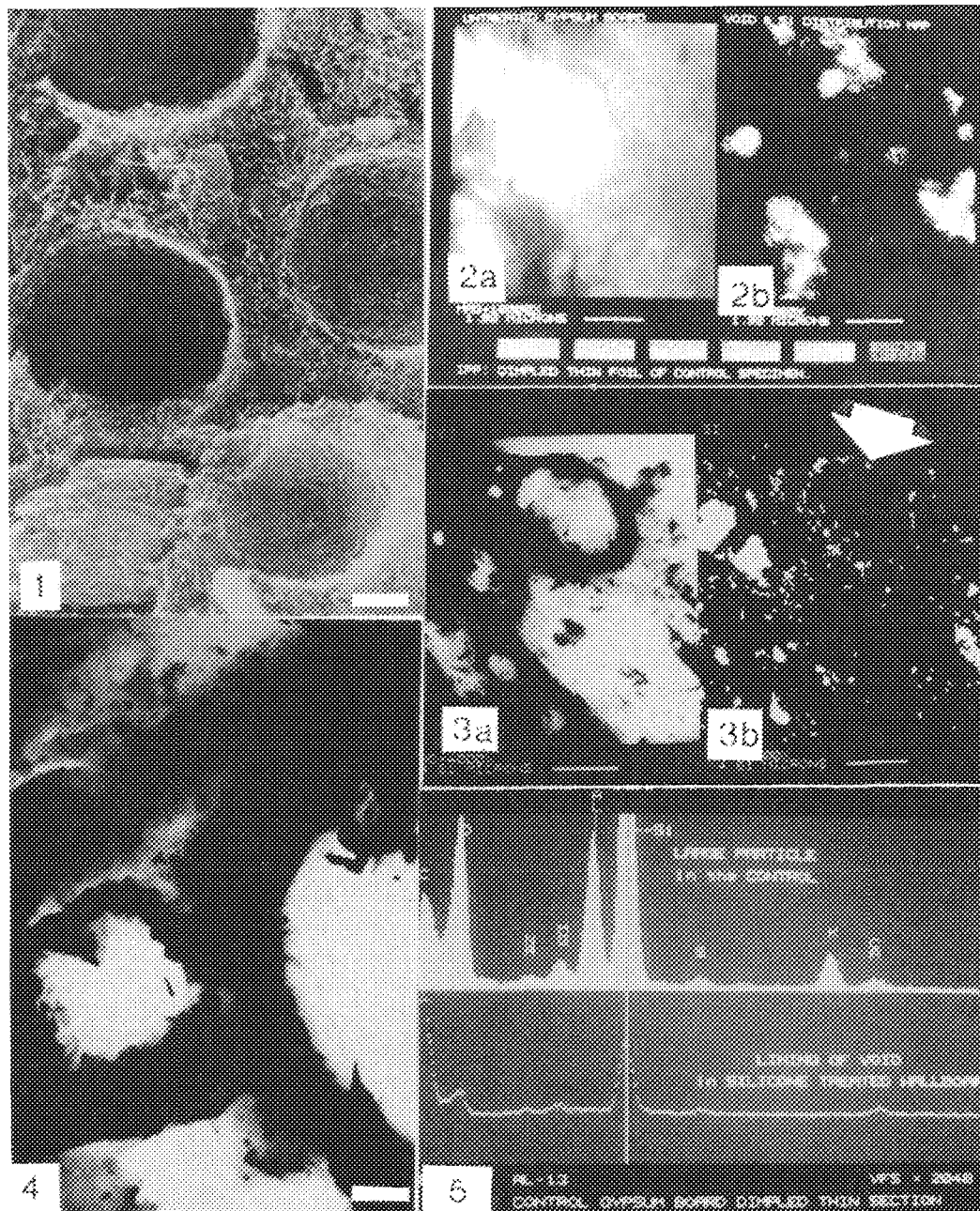


FIG. 1.--SEM micrograph of untreated gypsum wallboard fractured interior. Bar = 10 μm .

FIG. 2.--Dimple-thinned gypsum wallboard without silicone: (a) STEM image around void, (b) corresponding Si distribution. Bar = 1.9 μm .

FIG. 3.--Dimple-thinned gypsum wallboard containing silicone: (a) STEM image at void with dark electron dense lining, (b) Si distribution from silicone at arrow. Bar = 1.9 μm .

FIG. 4.--TEM micrograph of voids and matrix in gypsum wallboard containing silicone. Bar = 0.5 μm .

FIG. 5.--EDS spectra showing distinction between elemental content of large, discrete particle in control and void lining resulting from silicone incorporation in wallboard, upper and lower spectra, respectively.

U.S. Patent 4 643 771, 17 February 1987.

2. H. A. Freeman and R. L. Durall, "Microscopical characterization," in A. L. Smith, Ed., *Analytical Chemistry of Silicones*, Krieger Pub. Co. (in press).

USING AN IRON OVERLAYER TO ENHANCE CONTRAST IN SEMPA

Raymond Browning, Thomas VanZandt, and Martin Landolt

Thin iron overlayers on ferromagnetic samples are shown to be nonintrusive probes of the magnetization of the underlying sample when one uses secondary electron microscopy with polarization analysis (SEMPA) for domain microscopy. Domain images of the iron overlayer show that the local magnetization direction is indicative of that in the sample. However, the magnitude of the spin polarization reflects the magnetization of the iron overlayer. Thus, for materials with low spin polarization, the iron overlayer provides a large signal enhancement.

SEMPA of Magnetic Media

The spin polarization of low-energy secondary electrons, emitted from a ferromagnetic sample, has a vectorial direction that is highly correlated with the magnetization of the sample surface.^{1,2} SEMPA^{3,5} uses a scanning electron microscope with an electron spin analyzer to image the surface magnetization. However, many systems of interest to the magnetic recording industry have a low secondary electron spin polarization, either because the material's magnetization is low (as with Co alloy films) or because surface treatments such as oxidation have reduced the spin polarization. The low spin polarized contrast from these samples means that detailed study of the characteristics of a recorded field is very time consuming. Typically tens of minutes are needed to collect a single image that may cover a very small part of a sample. As a result, it is difficult to provide sufficient information over the range of length scales needed to characterize the magnetic distribution.

In this paper we report the development of a new surface preparation technique for SEMPA imaging that is easily implemented and that should remove some of the difficulties associated with low contrast surfaces. The technique involves the in situ evaporation of a thin Fe overlayer onto the sample before SEMPA imaging. This technique is somewhat analogous to the well-known Bitter decoration method⁶ in that an external feature on the magnetized surface is imaged. The technique differs from the Bitter method in the use of a thin homogeneous marker film. The film thickness is of decisive importance. The film should be thick enough to be ferromagnetically ordered with a bulk-like Curie temperature, i.e., thicker than approxi-

mately 5 layers,⁷ but thin enough so that the contribution of the film to the magnetic free energy of the entire system can be neglected. Otherwise the sample's domain structure will change upon absorption of the marker film.

In the instrument used for these studies, the sample must be moved out of the imaging position to deposit an Fe film. Thus, to demonstrate that the magnetization in an Fe overlayer film is a faithful representation of the sample surface magnetization, we have used a single-crystal Fe whisker as a simple, identifiable magnetic system. The domain structure at the end of the whisker can be imaged in relation to a clear SEM signal. We can therefore return repeatedly to the same sample position. Spin-polarized images after ion cleaning, oxidation, and evaporation of an Fe overlayer can be referenced to one another very simply. Finally, we show an application of the Fe overlayer technique to a system of magnetic bits written in a Co-Ni alloy.

Instrumental

The experiments were performed with a recently constructed ultrahigh-vacuum (UHV) spin-polarized electron microscope.⁸ This instrument consists of a modified scanning Auger microprobe and a high-energy Mott analyzer (Sherman function approximately 0.11 at 50 keV). The spatial resolution of the instrument for spin-polarized imaging is 50 nm. The sample is mounted with its surface normal to the electron beam and the instrument detects two components of polarization in the plane of the sample's surface. The sample can be lifted out of the microscope manipulator and moved around to different preparation stations. One station faces an ion gun; another, through a load lock, an Fe filament source.

The two detected components of in-plane polarization are orthogonal, P_x and P_y , and can be plotted as a vector on a Cartesian plot. When the end points of the vectors are plotted for each picture element (pixel) in an image, the result is a scatter plot with lobes showing the main directions and magnitudes of the polarization (Fig. 1). The lobes in the scatter plot can be windowed with a software-generated graphics window, and the pixels within a window can be colored to produce a false-color image of the main directions of magnetization in a sample. These false-colored images are reproduced here in monochrome.

Results from an Fe<100> Whisker Surface

The sample is a single-crystal Fe whisker of approximate dimensions $0.3 \times 0.3 \times 30$ mm, aligned along the <100> direction. The whisker

Raymond Browning is with the Center for Integrated Systems, and Thomas VanZandt is with the Department of Applied Physics at Stanford University, Stanford, CA 94305. Martin Landolt is with Laboratorium für Festkörperphysik, ETH, CH-8093, Zurich, Switzerland. This work was supported by the IBM Almaden Research Center.

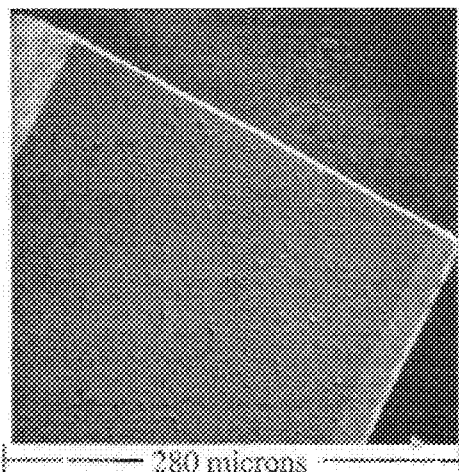


FIG. 1.--SEM micrograph of end of Fe single crystal whisker.

was mounted on a nonmagnetic aluminum holder with one $\langle 100 \rangle$ face normal to the electron beam. An SEM of the whisker is shown in Fig. 1

The experiment proceeded in three steps. First, the whisker was cleaned by use of a 500eV Ar ion beam and placed in the microscope stage for imaging. Second, the Fe whisker surface was oxidized in situ and re-imaged. Third, 2 nm of Fe was deposited on the oxidized whisker, and the whisker was again imaged.

Figure 2 shows the spin-polarized image information, plotted as scatter diagrams of the polarization direction and magnitude with the respective images.³ Figure 2(a) shows the image information after initial cleaning of the Fe whisker with 500eV argon ions. The argon ion cleaned surface shows a high-spin polarized signal ($\pm 31\%$), and the various directions of magnetization in the closure domains at the end of the whisker appear as well-separated lobes in the scatter diagram. The central region near zero polarization is from the nonmagnetic microscope stub. The spin-polarized image (Fig. 2b) is displayed as a false-color image which shows the spatial distribution of the magnetization; it is reproduced here in monochrome. Oxidization of the whisker surface in situ with 500L of oxygen produces a low-contrast surface. The scatter diagram of the image (Fig. 2c) shows very little separation. Figure 2(d) shows the result of evaporating 2.5 nm of Fe on the oxidized surface. It can be seen that the full contrast of Fig. 2(a) is very nearly restored. Also, the corresponding false color image Fig. 2(f) is nearly identical with that of Fig. 2(b) and the polarization is $\pm 27\%$. Deposition of nonmagnetic films of Au on the whisker removes the correlation between Fe overlayer and whisker. This result suggests that short-range exchange forces through the oxide are responsible for the overlayer/substrate interaction. In this case the enhanced image is expected to follow the magnetic structure of

the substrate even at very high spatial resolution.

Application to a Co-Ni Hard Disk

The Fe overlay method will have its greatest application on samples that have inherently low spin polarization. Many of these materials have a higher coercive force than Fe, so that it is most likely that the Fe overlayer will only weakly disturb the magnetic system and effectively act as a nonintrusive probe. We tested this assumption with a high-resolution image from a Co-Ni alloy hard disk.⁹ The sample is initially saturated in one direction (DC erased), and then a series of bits are written in which the magnetization is reversed with respect to the background. Initially the sample is cleaned with 500eV Argon ions, which gives a typical value of $\pm 7.5\%$ polarization between the two directions of magnetization. The sample is then exposed to 10^3 L of oxygen, which reduces the spin polarization below the detection limit. We evaporate 2.5 nm of Fe onto the sample before imaging. Figure 3 shows the scatter diagram and false-color image for a typical area showing a written track. These are raw unsmoothed data and show a polarization contrast of $\pm 22\%$. From the DC-erased part of the disk it can be shown that the magnetization directions are the same as found on the ion-cleaned directions, so that the coupling mechanism may be the same for both the oxidized Fe whisker and the Co-Ni alloy. The mark space ratio within the track is 1:1, and the ripples at the edges of the bits, which are due to the demagnetizing fields associated with forming of the bit patterns, can clearly be seen. Thus, there is no evident for any modification of the magnetic structure on the part of the Fe marker film.

Conclusion

The evaporation of a thin film of Fe as method of enhancing the spin-polarized contrast in SEMPA is shown to be a nonintrusive probe of the magnetic structure of recording media. The enhancement can lead to an order-of-magnitude increase in the imaging speed.¹⁰

References

1. G. Chrobok and M. Hofman, *Phys. Lett.* 57A: 257, 1976.
2. J. Unguris, D. T. Pierce, A. Galejs, and R. J. Celotta, *Phys. Rev. Lett.* 49:72, 1982.
3. K. Koike and K. Hayakawa, *Appl. Phys. Lett.* 45: 585, 1984.
4. G. G. Hembree, J. Unguris, R. J. Celotta, and D. T. Pierce, *Scanning Microsc. Suppl.* 1:229, 1987.
5. H. P. Oepen and J. Kirschner, *Phys. Rev. Lett.* 62: 849, 1989.
6. F. Bitter, *Phys. Rev.* 38: 1903, 1931.
7. W. Durr, M. Taborelli, O. Paul, R. Germar, W. Gudat, D. Pescia, and M. Landolt, *Phys. Rev. Lett.* 62: 206, 1989.

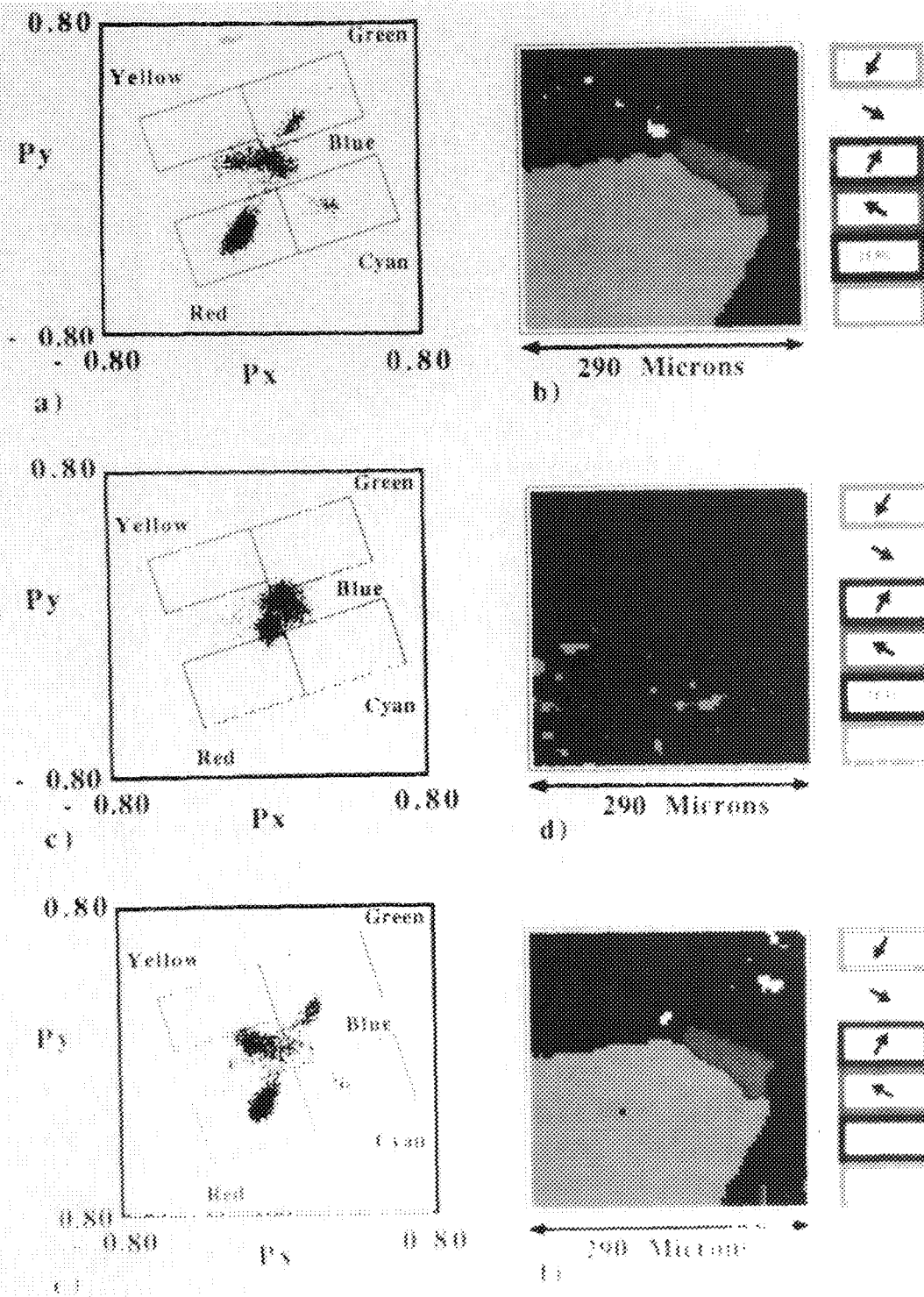


FIG. 2.--(a) Scatter diagram of polarization data from spin-polarized image of ion-cleaned Fe whisker; (b) monochrome reproduction of false-color image produced by assigning colors to regions of scatter diagram; image size, 290 μ m microns. (c) and (d) Scatter diagram and false color image of whisker following oxidation (e) and (f) Scatter diagram and false color image obtained after evaporation of 2.5 nm of Fe onto oxidized whisker surface.

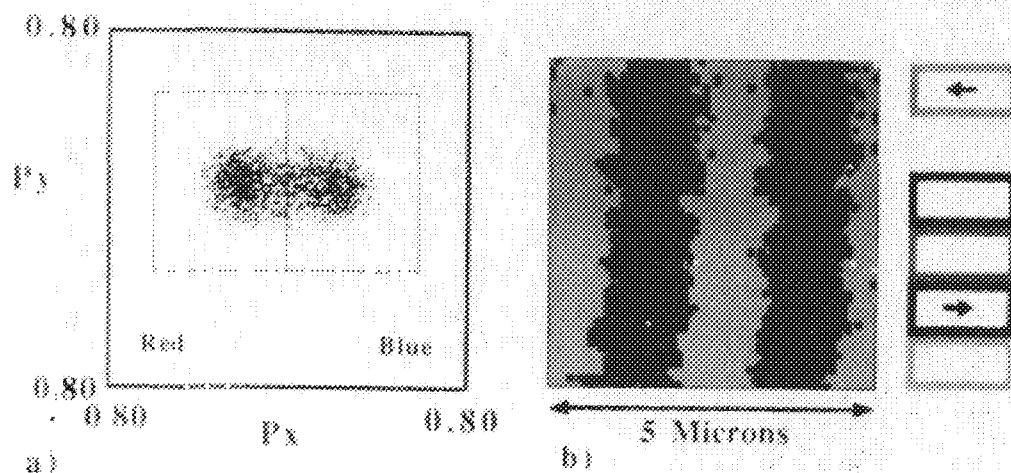


FIG. 3.--Spin polarized image of magnetic bits written in Co-Ni alloy. Sample preparation used 2.5 nm of evaporated Fe. (a) Scatter diagram of polarized image data; (b) monochrome reproduction of false color image produced by windowing lobes in scatter diagram. Image size, approximately 5 μm .

8. R. Browning, T. VanZandt, C. R. Helms, H. Poppa, and M. Landolt, *J. Elec. Spectros. and Related Phenom.* 51: 315, 1990.

9. The Co-Ni alloy sample was provided by M. Khan of Seagate Magnetics, Fremont, CA.

ELECTRON BEAM INDUCED CURRENT STUDY OF MULTILAYER STRUCTURES

Z. J. Radzinski, A. Buczkowski, J. C. Russ, and G. A. Rozgonyi

The electron beam induced current (EBIC) technique is a well-recognized method for characterization of semiconductor materials.^{1,2} The current generated by the electron beam and collected by a p-n junction or Schottky contact depends on many factors, such as the energy of incident electrons, the thickness of "dead" layer, space-charge region width, carrier diffusion length, etc. For bulk uniform semiconductor material with diffusion length much larger than the electron beam penetration depth, a high ratio of the collected current to the electron beam current can be achieved. For keV electrons the ratio may be of the order of several thousand, which makes this technique a very sensitive tool for studying electric-field distributions and defect-related phenomena. However, in modern device structures a reduced volume of active semiconductor is available, e.g., in silicon on insulator (SOI) or in thin multicomponent heterostructures. In these cases the total EBIC current may be significantly reduced if the structure thickness is smaller than the penetration depth of electron beam, in comparison with bulk material.

Since the energy loss distribution of the primary beam is not uniform and varies with beam energy, it is not straightforward to predict the optimum imaging conditions for using this technique. Moreover, the energy losses in an ohmic or Schottky contact (which can be of the same order of magnitude or higher than within active device region) complicate this prediction. Generally, none of the common analytical models, which are based on an assumption of a point-like region of electron beam generation,^{3,4} can be used satisfactorily for multi-layered and/or SOI structures, and a limited number of data has been published on this subject.⁵ In this report we describe a Monte Carlo technique that simulates the electron-beam interactions in thin multilayer structures. This approach can be satisfactorily used to optimize the experimental conditions to obtain the highest signal-to-noise ratio, and predict precisely the information depth for these conditions. Both the theoretical and experimental data for EBIC gain are used to illustrate this optimization process.

Monte Carlo Program

The Monte Carlo program used in this work is based on earlier single scattering programs developed by Shimizu,⁶ Myklebust,⁷ and Joy⁸ and

The authors are at the Department of Materials Science and Engineering, North Carolina State University, Raleigh, NC 27695-7916.

their co-workers. The program, written in Pascal, was modified to provide a simulation of the electron beam interactions with thin multilayer structures.⁹ The program has been successfully applied to structures with internal variations in composition or density and/or surface irregularities,¹⁰ which are not generally dealt with in Monte Carlo programs.

The additions provide the following capabilities:

1. Arbitrary regions may be defined as polygons in the X-Z plane. These define volumes that extend indefinitely in the Y direction (parallel to the specimen surface). The polygons may have any number of sides, and so may approximate curved surfaces. If overlapping regions are defined, the program uses whichever is the highest numbered. This makes it easy to insert regions within larger ones, to assemble complex structures.

2. The regions may be beneath, at, or above the specimen surface. This allows the specimen surface to be irregular and composed of different regions, for example, a space charge region, or other regions with different diffusion length.

3. Each region's composition can be entered in weight percent, consisting of any number of elements, for example, Schottky contact metal, silicon dioxide or silicon.

The EBIC current was calculated for a simple one-dimensional geometry, i.e., the depletion layer separating electron-hole pairs spreads out to infinity in the x- and y-directions. A point-type generation function whose location is the actual location of an incident electron energy loss event has been assumed. The collection efficiency of electron-hole pairs was assumed to be 100% for carriers generated within the depletion layer. Outside this layer an inverse exponential function of depth was assumed with the effective diffusion length as a parameter. The carriers generated within ohmic or Schottky contacts, in any insulator layer and beneath this layer, were not taken into account.

Results and Discussion

The Monte Carlo calculations were conducted for three different semiconductor structures with a Schottky contact (200 Å of Al). In the first sample a contact of variable thickness was assumed to be on bare silicon. The second was a layered structure deposited on substances with different diffusion lengths, and the third one a silicon on insulator structure. If the multilayer heterostructure consists of several layers, each with approximately the same

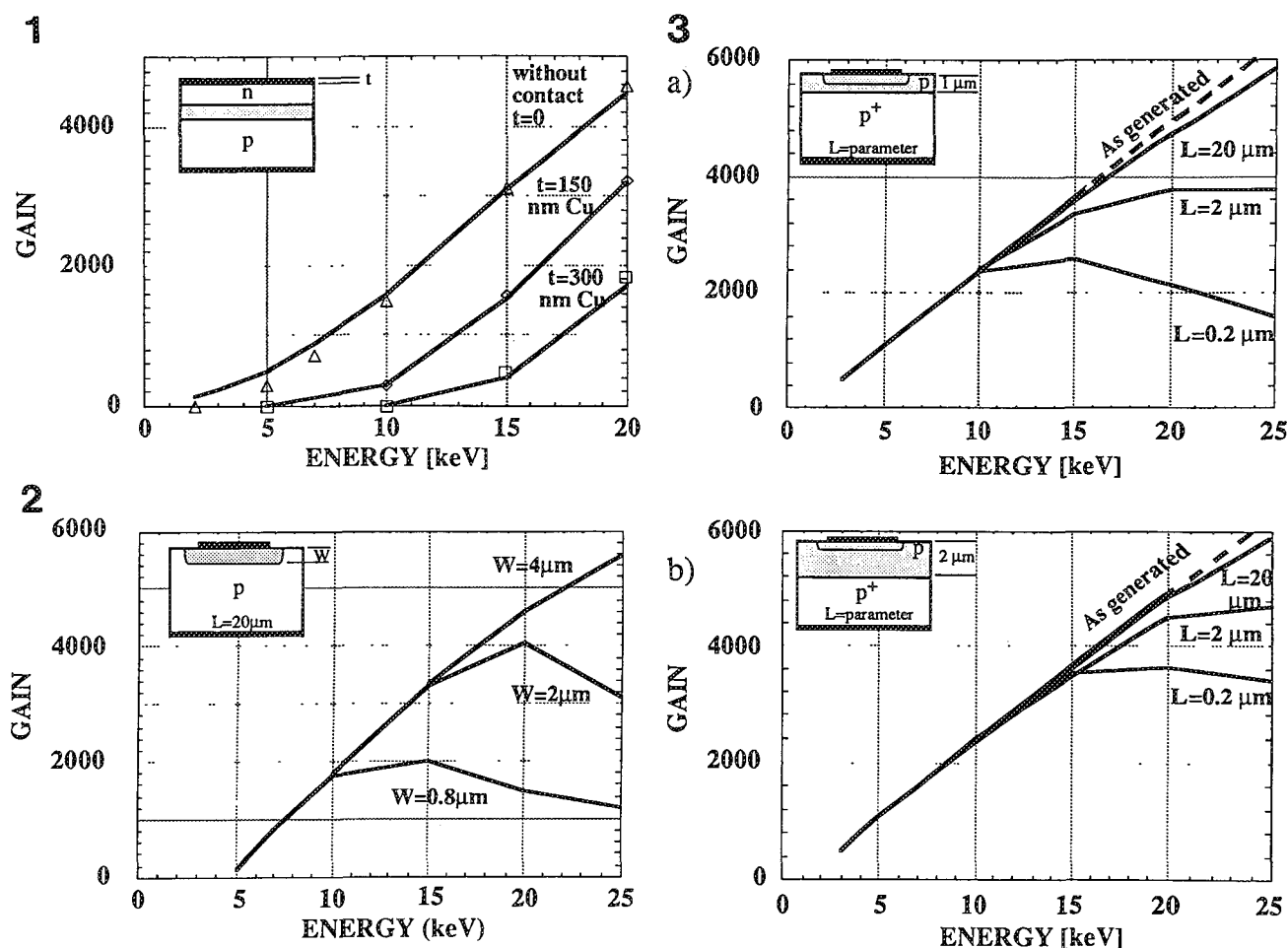


FIG. 1.--Comparison between simulated and measured gain for p-n junction diode as a function of accelerating voltage for various thicknesses of ohmic contact metal. Substrate: bulk silicon, diffusion length, 50 μ m; junction depth, 1 μ m.

FIG. 2.--Simulated gain vs electron beam energy for a Schottky type diode for various space charge region widths. Substrate: bulk silicon, diffusion length, 20 μ m.

FIG. 3.--Simulated gain vs electron beam energy for a layered structure with a Schottky type diode, and substrate diffusion length as the parameter. Top layer thickness: (a) 1 μ m, (b) 2 μ m; diffusion length of layer, 20 μ m.

diffusion length, such a sample may be considered as a bulk silicon. The EBIC signal in this case increases with energy if the diffusion length is much larger than the penetration of an electron beam, both in p-n junction and Schottky type contacts. The simulation data for a 1 μ m deep junction fabricated in silicon with 50 μ m diffusion length (the parameters of device studied experimentally) are shown in Fig. 1. However, gain depends strongly on the contact thickness, as shown on the same figure for a Cu contact 150 and 300 nm thickness. The theoretical data are in good agreement with the experimental results.

The experimental values of gain were calculated as the ratio of EBIC current to the incident beam current measured with a Faraday cage. The beam current was kept low

(tens of picoamperes) to maintain low injection conditions.

Generally the gain increases monotonically with electron beam energy if the diffusion length is much larger than the beam penetration depth. In this case one can also easily predict the information depth of EBIC technique, which is approximately equal to the maximum penetration depth of primary electrons. The other factor to be taken into account is the space charge region (SCR) width W. The SCR is the most effective region for charge collection (100%). If the width of this region is comparable to the beam penetration depth, then most of the generated carriers contributes to the EBIC current (see (Fig. 2 for a 4 μ m-wide SCR of a Schottky contact. For a very narrow SCR (the case of highly

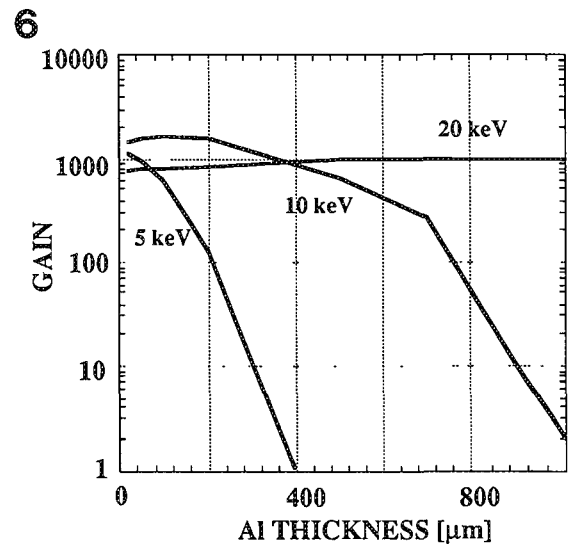
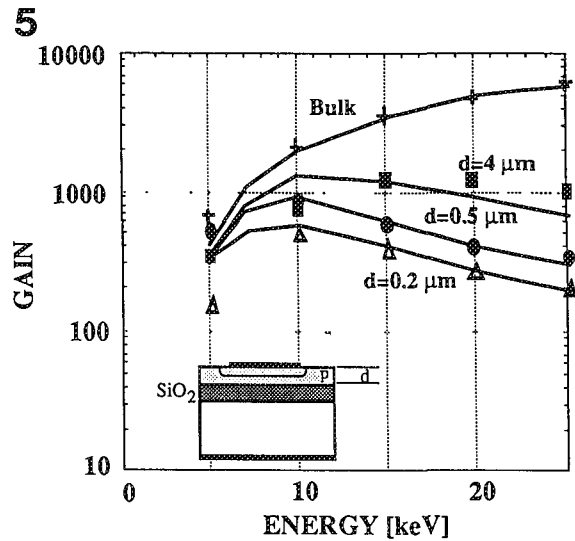
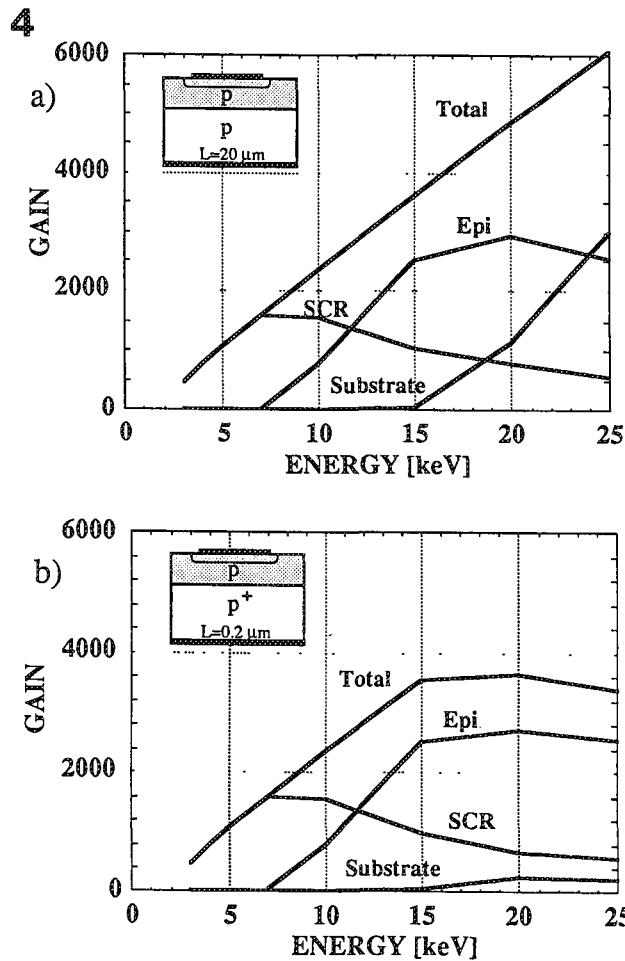


FIG. 4.--Simulated contribution to EBIC signal from various regions of layered structures with Schottky type diode. Substrate diffusion length, (a) 20 μm , (b) 0.2 μm , layer thickness, 2 μm , diffusion length of layer, 20 μm .

FIG. 5.--Comparison between simulated and measured gain for a 200A Al Schottky diodes fabricated on silicon-on-insulator substrates as a function of electron beam energy, with superficial layer thickness as parameter.

FIG. 6.--Simulated gain as function of Schottky contact thickness for silicon-on-insulator substrate. Effective diffusion length of top layer, 0.2 μm ; layer thickness, 0.2 μm .

doped sample) the collection efficiency decreases when the penetration depth is much larger than SCR width. That is also true for materials with long diffusion lengths. The example is shown in Fig. 2 for $W = 0.2 \mu\text{m}$ and substrate with $L = 20 \mu\text{m}$.

In thin multicomponent heterostructures both parameters, diffusion length and SCR width, have to be carefully considered in order to optimize the electron beam for maximum EBIC signal and accurate estimation of the information depth, especially when the layers differ significantly in electrical properties, in terms of diffusion length. The total EBIC signal may be significant smaller (e.g., a thin layer on a highly doped substrate) because of the reduced carrier diffusion from the substrate toward the surface

Schottky contact. The simplified case of a structure having a top layer with 20 μm diffusion length and two different thicknesses (1 and 2 μm), deposited on substrates with $L = 20, 2, 0.2 \mu\text{m}$ (i.e., low, medium, and high doping concentrations, respectively) has been studied. The simulated data are shown in Fig. 3. The case when L is 20 μm for both layer and substrate can be considered as uniform bulk silicon. When the diffusion length of the substrate is much smaller than the penetration depth of the electron beam, the gain is significantly reduced. As expected, the gain is smaller for a 1 μm -thick layer in comparison with a 2 μm layer. For the 1 μm layer deposited on a highly doped substrate (with $L = 0.2 \mu\text{m}$) there is an optimum energy, between 10 and

15 keV, at which the highest gain can be obtained. For higher energies the maximum generation of carriers occurs in the substrate, from which the carriers have limited possibility of reaching the surface space charge region.

The contribution of carriers generated in each layer to the total EBIC signal can be easily addressed by Monte Carlo simulation. In this way the information depth can be precisely predicted. In this paper the contribution to gain was calculated for three regions: space-charge region, active top layer, and substrate, for the structure in Fig. 3(b), which has a 2 μm -thick epilayer and a 20 μm diffusion length. Two configurations were assumed: the first one is a low doped substrate with $L = 20\ \mu\text{m}$; the second, $L = 0.2\ \mu\text{m}$. The first structure can be considered as uniform bulk silicon. The theoretical data for both structures are shown in Fig. 4. The gain for each structure is predicted to be the same up to the energy at which the maximum carrier generation occurs in the top layer. The gain vs energy dependence reaches a maximum at 15 keV for substrates with $L = 0.2\ \mu\text{m}$ and remains constant for higher energies, since the carriers generated in the substrate, having short diffusion lengths, cannot reach the SCR. Therefore, the information depth of EBIC remains the same for accelerating voltages higher than 15 keV.

Another interesting case is for a semiconductor isolated from its substrate by a thin insulator layer (SOI). The geometries used for simulations were chosen to match the samples actually used in the experimental part of this work. The theoretical data presented in Fig. 5 show how significantly the gain decreases with a decrease in superficial layer thickness. For thicknesses of a top semiconductor layer smaller than the penetration depth of the electron beam, only a small portion of the incident electron energy that is lost in the top layer contributes to the electron beam induced current. Moreover, there is an optimum beam energy at which the gain reaches its maximum value for a particular silicon thickness.

To verify these data experimentally a series of Al Schottky contacts, $\sim 50\ \text{nm}$ thick were fabricated on SOI structures and bulk silicon. The SOI substrates were prepared by oxygen implantation, which produces a 0.2 μm superficial silicon layer separated from the silicon substrate by 0.4 μm of buried silicon dioxide. The 0.5 and 4 μm -thick superficial layers were obtained by a subsequent epilayer growth. The final geometrical configuration of the samples, which were essential for comparison with theoretical calculations, was determined by angle polishing and interface delineation. (For details of material and sample preparation see Ref. 11.) Schottky depletion widths, required for Monte Carlo simulations, were determined from capacitance vs voltage curves. The diffusion length of the bulk silicon sample was measured by a laser beam induced current (LBIC) technique, and an effective diffusion length was taken for the SOI layer. The experimental data (Fig. 5) are in excellent agreement with the Monte Carlo simulations. Some discrepancy

between the experimental and theoretical data was observed at low beam energy (5 keV), where the gain is very sensitive to the Al contact thickness, as shown theoretically in Fig. 6. The data presented in Figs. 5 and 6 indicate that the optimum conditions for an EBIC study of thin SOI structures require that not only the beam energy but also metal contact thickness be carefully selected. The optimum metal contact does not have to be the thinnest one, as in the case of bulk silicon.

Conclusions

The optimization of the imaging and test conditions to study the electrical properties of thin multilayer heterostructure by the EBIC technique is very important, and the analytical approaches known for uniform bulk semiconductor materials cannot be applied. In the multilayer semiconductor structures the EBIC signal and the information depth depend strongly on the thickness and diffusion length of each layer. The Monte Carlo method is a very valuable tool to study this problem theoretically, because it permits a proper definition of the energy dissipation function for multilayer structure, and carrier diffusion mechanism through semiconductor layers of various electrical properties. Using this method one can sample the contribution of different layers to the total gain and in this way also define the "real" information depth.

A series of simulations were performed for layered structures with the active layer placed on semiconductor as well as insulator substrates. The collection efficiency was discussed as a function of metal contact thickness, top active layer thickness, and diffusion length of substrate and layer for various energies of primary electrons. Although we have illustrated the application of the Monte Carlo method for relatively simple structures, it can be used satisfactorily to predict the EBIC signal in any combination of electrically active and nonactive layers.

References

1. H. J. Leamy, *J. Appl. Phys.* 53: R51, 1982.
2. J. F. Bresse, *SEM/1982 IV*, 1497.
3. C. Donolato and H. Klann, *J. Appl. Phys.* 51: 1624, 1980.
4. A. Jakubowicz, *Scanning Microscopy* 1: 515, 1987.
5. E. Napchan and D. B. Holt, *Inst. Phys. Conf. Ser.* 87: Sec. 11, 1989.
6. R. Shimizu and K. Murata, *J. Appl. Phys.* 42: 387-394, 1971.
7. R. L. Myklebust, D. E. Newbury, and H. Yakowitz, *Use of Monte Carlo Calculations in EP Microanalysis and SEM*, NBS Spec. Publ. 460, 105.
8. D. C. Joy, *J. Microsc.* 147: 51, 1976.
9. J. C. Russ, Z. J. Radzinski, A. Buczkowski, and L. Maynard, *J. Computer Assisted Microscopy* (in press).
10. Z. J. Radzinski and J. C. Russ, *J. Computer Assisted Microscopy* 1: 181, 1990.
11. A. Buczkowski, Z. J. Radzinski, and G. A. Rozgonyi, *ECS Proc.* 90b: 351, 1990.

MONTE CARLO MODELING OF SECONDARY ELECTRON YIELD FROM ROUGH SURFACES

John C. Russ

Monte Carlo programs are well recognized for their ability to model electron beam interactions with samples, and to incorporate boundary conditions such as compositional or surface variations that are difficult to handle analytically. This success has been especially powerful for modeling x-ray emission and the backscattering of high-energy electrons. Secondary electron emission has proved to be somewhat more difficult, since the diffusion of the generated secondaries to the surface is strongly geometry dependent, and requires analytical calculations as well as material parameters. Modeling of secondary electron yield within a Monte Carlo framework has been done by use of multiple scattering programs, but is not readily adapted to the moderately complex geometries associated with samples such as microelectronic devices, etc.¹⁻³

This paper reports results based on a different approach, in which simplifying assumptions are made to permit direct and easy estimation of the secondary electron signal from samples of arbitrary complexity. The single-scattering program that performs the basic Monte Carlo simulation (and is also used for backscattered electron and EBIC simulation) allows multiple regions to be defined within the sample, each with boundaries formed by a polygon of any number of sides.⁴ The regions may be below, at, or above the nominal specimen surface, and need not be convex. Each region may be given any desired elemental composition, expressed in atomic percent.

In addition to the regions comprising the primary structure of the sample, a series of thin regions are defined along the surface(s) in which the total energy loss of the primary electron is summed. This energy loss is assumed to be proportional to the generated secondary electron signal that would be emitted from the sample. The only adjustable variable is the thickness of the region, which plays the same role as the mean free path of the secondary electrons in an analytical calculation. This is treated as an empirical factor, similar in many respects to the λ and ϵ parameters in the Joy Model.¹⁻³

One can determine the value for the appropriate thickness of the surface region for a particular material composition can be done by generating curves of total deposited energy as

a function of accelerating voltage and thickness, and comparing them to the measured secondary electron yield curves for planar surfaces. Figure 1 shows these results for silicon; comparison to measured data³ shows that a region about 150 Å thick in silicon matches the empirical results rather well; the peak lies near 1 keV, and changes in the layer thickness as small as 25 Å shift the peak higher or lower.

The program reads a disk file containing the specimen geometry (including the surface layers) and repeats the Monte Carlo simulation for a user-selected number of electrons as the beam incidence point is traversed across the specimen in small steps. The resulting calculated secondary electron yield values are saved in disk file, and are subsequently plotted to show the predicted signal profile for the device geometry and beam voltage chosen.

By comparing measured secondary electron signal profiles on actual devices with the simulated data, we have found that for materials ranging from SiO₂ and photoresist to metallization of aluminum and gold, region thicknesses in the range from 100 to 200 Å produce fair agreement. Figure 2 shows an example in which profiles across the edge of a metallized aluminum strip on SiO₂ were measured in a Hitachi S-6000 SEM at low accelerating voltages (1-2 keV). Figure 3 shows the simulated profiles for the same geometry. The model predicts (and the measured profiles show) a reduction in contrast and variation in the shape of the signal along the highly sloped sidewall as the accelerating voltage is varied.

Figure 4 shows simulated data for a secondary electron signal profile across the edge of a line of SiO₂ on silicon. It is interesting (and potentially very important if secondary electron profiles are to be used for device metrology) to note that the extrema and inflection points in the profile do not align with the corners of the actual structure, and that this displacement is a function of voltage.

This model appears to produce acceptable results for investigating the effect of measurement conditions, specimen geometry and composition, and data-reduction algorithms on the accuracy of SEM metrology values. It may also be possible in the future to extend it to include the effects of charging within the samples, which is a particular problem even at low accelerating voltages with resist and some oxide structures.

The Monte Carlo program discussed here is written in Pascal to run on Macintosh computers, and is available from the author. (To receive source code, please send a formatted disk and return envelope.)

John C. Russ is at the Materials Science and Engineering Department, North Carolina State University, Box 7907, Raleigh, NC 27695. Support for this work was provided by the Microelectronics Center of North Carolina. Lorraine Maynard, at MCNC, measured the SEM signal profiles.

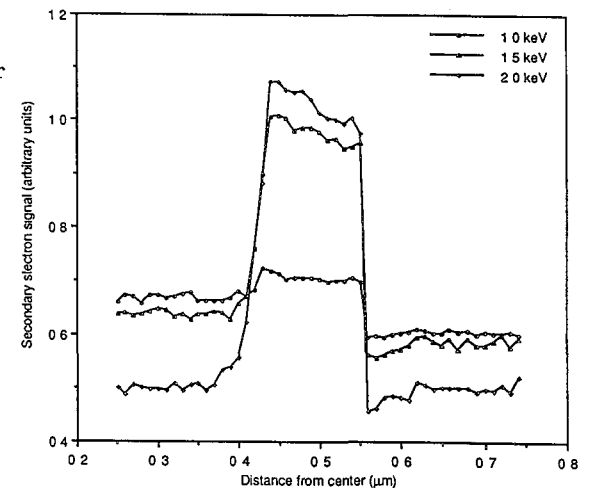
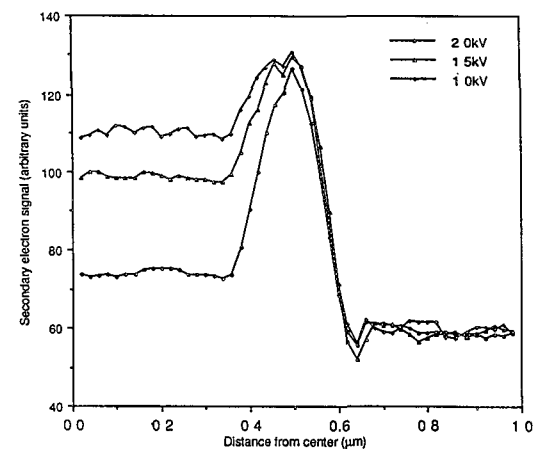
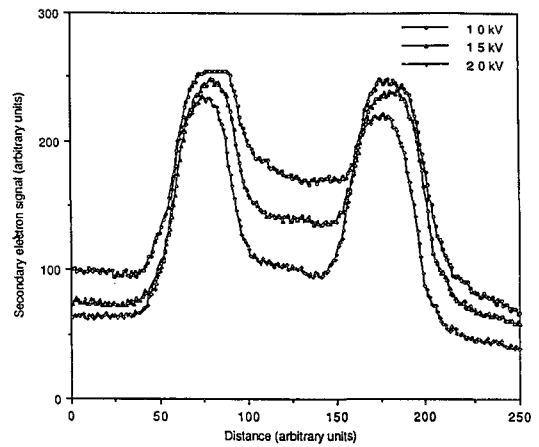
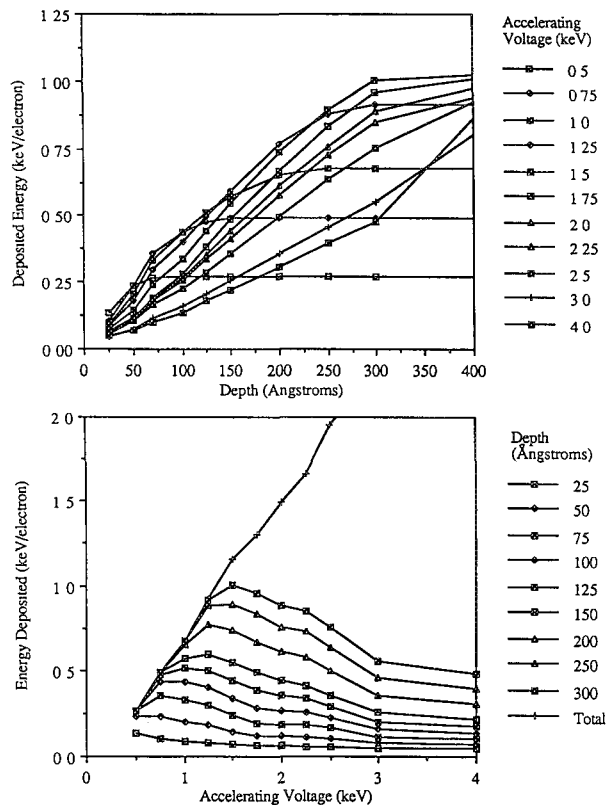


FIG. 1.--Effect of variation in depth of surface layer used to estimate secondary electron yield on total modeled signal from silicon as electron accelerating voltage is varied.

FIG. 2.--Measured secondary electron signal on trace of aluminum on silicon oxide.

FIG. 3.--Simulated secondary electron profile across edge of trace of aluminum on silicon oxide.

FIG. 4.--Simulated secondary electron profile across edge of 0.5μm high trace of SiO₂ on silicon.

References

1. D. C. Joy, "A model for calculating secondary and backscattered electron yields," *J. Microscopy* 147: 51-64, 1987.
2. M. T. Postek, W. J. Keery, and R. D. Larabee, "The relationship between accelerating voltage and electron detection modes to line width measurement in an SEM," *Scanning* 10: 10-18, 1987.
3. D. C. Joy, *Low-voltage Scanning Electron Microscopy*, Hitachi Tech. Rept., 1989.
4. J. C. Russ and Z. J. Radzinski, "Monte-Carlo modelling of electron signals from heterogeneous samples with non-planar surfaces," *J. Computer-assisted Microscopy* (in press).

Quantitative Microanalysis in Biology

COMPARISON OF QUANTITATIVE X-RAY IMAGING AND RASTER PROBING IN HEART CELLS EXPOSED TO SODIUM-FREE MEDIA

Mary Carney, Ann LeFurgey, L. A. Hawkey, Peter Ingram, and Melvyn Lieberman

Quantitative biological electron probe x-ray microanalysis (EPXMA) can make use of two approaches to examine samples: static raster probing and quantitative x-ray imaging.¹ Efficient use of microanalytical equipment requires intelligent decisions on the appropriate strategy to optimize data collection. A low resolution, short dwell time map (for example, 64×64 pixels \times 2 s) may survey one to several cells at low magnification and provide adequate statistics for many structures and elements. However, low concentrations of elements present within cells or subcellular compartments (e.g., Ca) may require the acquisition equivalent of long static raster probes, increased numbers of images from low-resolution maps, higher-resolution maps, longer dwell-time maps, or a combination of these options. Available instrumentation permits two approaches. Differences between the two approaches are reflected in the total area sampled and the amount of signal collection time. In the mapping case the x-ray signal from a single acquisition site or group of pixels may be acquired for few to many seconds. The number of sites sampled depends on the magnification and the pixel resolution chosen. In investigations incorporating both static probe and map data, it is appropriate to verify that probe values and map values are comparable. In addition, by examination of different regions of the same mapped organelle, the homogeneity of that organelle can be evaluated in a fashion that is not practical with static probing.

Within heart muscle cells, mitochondria, nucleus, cytoplasm, and sarcoplasmic reticulum have been viewed as subcellular compartments. In addition to fulfilling a characteristic function in the cell, these compartments play a role in maintaining the ionic homeostasis of the cell.² A knowledge of the compartmental content is fundamental to the understanding of the physiological mechanisms associated with ion and water transport. We examined results obtained from raster probe and mapped images of cultured heart cells. In these cells EPXMA can be used to observe the results of ion gradient perturbations, brought about by incubating cells in low-Na or Na-free media.^{3,4} Such experiments contribute to the characterization of coupled transport mechanisms, e.g., Na-Ca exchange.

The authors are with the Department of Cell Biology, Duke University Medical Center, Durham, NC 27710, except Peter Ingram, who is with the oEsearch Triangle Institute, Research Triangle Park, NC 27709. The work is supported in part by NIH grants HL17670 and HL27105.

Sample Preparation

Cell Culture. Aggregates of heart muscle cells were obtained from muscle-enriched cells of 11-day-old embryonic chick hearts.⁵ The cultures were incubated at 37 C in a humidified chamber containing 4% CO₂ and 96% air. Cells cultured under identical conditions for 3-4 days were then transferred to either modified Earle's balanced salt solution (MEBSS) or MEBSS in which all sodium was replaced with trimethyl-ammonium chloride and choline bicarbonate.⁶

Cryopreservation. After incubation for 4 min in the above solutions, the cultures were observed by light microscopy and small (50-100 μ m) spontaneously beating aggregates were chosen for rapid freezing. Aggregates of cells were withdrawn from the medium into a pipette attached to a syringe and placed on a cryomicrotome specimen stub precoated with a drop of 20% gelatin solution. The aggregate on the specimen stub was rapidly plunged into liquid nitrogen-cooled liquid propane and then stored under liquid nitrogen. Average time from withdrawal of the aggregates from the culture dish to freezing was < 20 s. Frozen aggregates from each experiment were then cryosectioned at <-140 C. The samples were freeze dried and carbon coated prior to EPXMA.

X-ray Data Acquisition

Instrumentation. Energy-dispersive spectra were acquired by a transmission electron microscope equipped with a scanning module (STEM). The microscope (JEOL JEM 1200EX) was operated with a lanthanum hexaboride filament at 80 keV in the STEM mode. The condenser lenses were set to obtain probe currents of approximately 1 nA in the probe mode and 10 nA in the mapping mode. The STEM was equipped with an energy-dispersive x-ray detector (Tracor Northern), which was mounted normal to the beam direction (side entry configuration) and contained a 30mm²Si(Li) crystal. The coldstage was eucentrically tilted at 35° from the horizontal toward the energy-dispersive detector, which was placed close to the sample such that the solid angle subtended was as large as possible, i.e., approximately 0.13 sr.

Spectral Acquisition. Freeze-dried cryosections (<100 nm thick) were analyzed on the STEM. The sections were mounted on 200-mesh fine bar nickel grids, within a low background cryotransfer stage (Gatan 626). A micro-computer (Macintosh II) controlled the on-line acquisition, spectral processing, and display of data and images.⁷ Mitochondria were ideal

test regions among organelles because an individual mitochondrion can usually be recognized, and with allowances made for orientation changes, an area of a mitochondrion could be relocated repeatedly. X-ray maps and raster probes were obtained for physiologically important elements. The maps were acquired at 8000-10 000 \times , 19 C, 4 s dwell time per pixel, and a pixel resolution of 128 \times 128. The 500s raster probes were obtained at 100 000 \times at -119 C from an $\sim 0.5\mu\text{m}^2$ raster area within a previously mapped mitochondrion. The positions of the mapped and probed mitochondria were noted on a photograph to facilitate positive identification of the paired mapped and probed structures. Spectra from probes and maps were analyzed by the Hall procedure for ultrathin specimens⁸ and quantitation was done by a multiple-least-squares fitting routine on filtered x-ray spectra,⁹ which incorporated derivative correction procedures for K-Ca peak deconvolution.¹⁰

Results

A map of a control heart cell aggregate is shown in Fig. 1. A portion of the first panel (STEM), a STEM image with a nucleus and mitochondria, is enlarged in the adjacent panel (STEM-ZOOM). The remaining images are quantitative elemental maps of the elements assayed. The sodium, magnesium, phosphorus, sulfur, chlorine, and potassium maps are shown. All areas of the image may be analyzed for concentration values. The content value of all elements within an outlined region is obtained by enlarging ("zooming") and then outlining the various regions of a mitochondrion. In seven mitochondria, opposite ends (referred to as the "top" and "bottom" regions) were sampled. Elemental content from equally sized areas (6 pixels) were obtained for the top and bottom regions (Table 1). The sodium content of mapped and probed mitochondria from both control and experimental cells is presented in Table 2. A 500s raster probe acquisition time contrasts with a maximum 96s acquisition time of a mapped mitochondrion.

Discussion

With mapping it is possible to sample organelles (here, mitochondrial) more thoroughly than is realistically possible in static raster probes. The digital nature of the map is evident in the enlarged region of Fig. 1 (STEM-ZOOM). It is possible to obtain content measurements from a single pixel, several pixels, or the entire mitochondrion. The "top" and "bottom" regions of the mitochondrion are not statistically different. The top and bottom values are the average of 6-pixel regions acquired at 4 s per pixel; thus, a total top or bottom counting time of 24 s. When the elemental contents of the regions are compared with the contents of mapped whole mitochondria (data not shown), no differences are found. The whole mitochondria value was obtained by outlining the entire mitochondrion. The whole value was thus based on 13-24 pixels (depending

on the size of the mitochondrion) and a total counting time of 52 to 96 s. The mapped and probed comparisons of experimentally manipulated cells show the experimental mitochondrial sodium values to be 7% (probe) or 10% (map) of control values. The probe sodium control value is higher than the mapped control value, but not significantly so by unpaired Student's *t* test. The low sodium values are similar to each other.

The sodium response to reversal of the sodium gradient follows the same trend as in the quantitative values reported previously for cultured heart cells¹¹ and rabbit papillary muscles.⁴ The 4 min exposure of heart aggregates to zero sodium conditions lowered sodium in cytoplasm (data not shown) as well as in all analyzed mitochondria. Mapping permits the simultaneous observation of all organelles/compartments in a manipulation. EPXMA observations of the magnitude and direction of elemental changes within an organelle, and of the interorganelle rates of elemental changes (e.g., cytoplasm rates vs mitochondrial rates) enhance the understanding of cellular ion movement. Mitochondria are convenient organelles to track in combined probe/mapping studies. In examining various regions of mitochondria, the elemental contents of the mapped regions were similar to each other and to the entire mapped mitochondrion. In proceeding with EPXMA-directed questions involving perturbation of the ion gradients and efforts at characterization of coupled transport mechanisms, it is necessary to know how, on a working basis, the map and probe modes compare and how their similarities can be optimized.

References

1. C. E. Fiori, *Microbeam Analysis--1986*, 183.
2. B. L. Gupta et al., *Transport of Ions and Water in Animals* New York: Academic Press, 1977, 83.
3. A. LeFurgey et al., *Microbeam Analysis--1987* 267.
4. E. S. Wheeler-Clark and J. McD Tormey, *Microbeam Analysis--1985* 116.
5. L. Ebihara et al., *J. Gen Physiol.* 75: 437, 1980.
6. R. Jacob et al., *J. Physiol.* 387: 549, 1987.
7. P. Ingram et al., *Microbeam Analysis--1988* 433.
8. T. Hall, *J. Microscopy* 117: 45, 1979.
9. H. Shuman et al., *Ultramicroscopy* 1: 317, 1976.
10. T. Kitazawa et al., *Ultramicroscopy* 11: 251, 1983.
11. A. LeFurgey et al., *J. Mol. Cell Cardiol.* 20: S30, 1988.

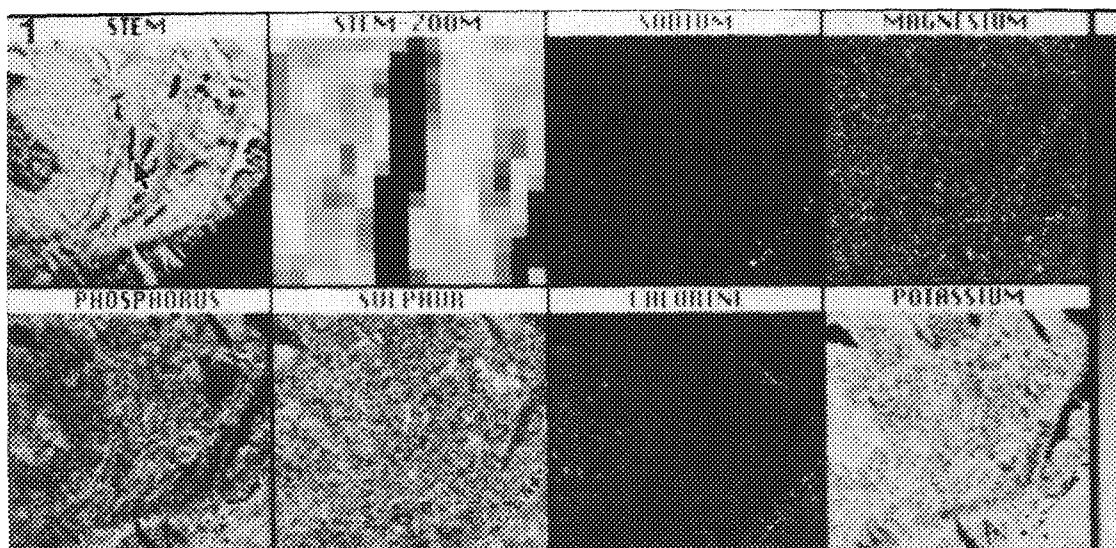


FIG. 1.--Scanning transmission electron micrograph and quantitative energy-dispersive x-ray images of control heart aggregate cryosection. Gray scale is relative to each element: Na, P, Cl, and K maps are scaled with a low (black) of 0 and a high (white) of 700 mmol/kg dry weight. Mg is scaled from 0 to 200mmol/kg dry weight; and S, from 0 to 300mmol/kg dry weight. Arrow on STEM image indicates mitochondrion which is zoomed in adjacent panel.

TABLE 1.--Elemental content from opposite ends ("top" and "bottom") of paired control mitochondria. Content (mmol/kg dry wt) of cultured heart cell mitochondria as determined by EPXMA.

	Na	K	P
TOP	86 ± 10	705 ± 22	464 ± 17
BOTTOM	67 ± 10	697 ± 30	448 ± 19

Values are the average ± SEM, n = 7, of 6-pixel mapped analysis sites. No significant differences were found within an element.

TABLE 2.--Sodium content (mmol/kg dry weight) in cultured heart cell mitochondria during control and zero Na conditions as determined by EPXMA raster probes and quantitative images.

	PROBE	MAP
CONTROL	116 ± 10.7 n = 38	86.5 ± 10.0 n = 7
0 Na	8.6 ± 2.2* n = 19	8.7 ± 6.8* n = 18

n = number of raster probes (500 s) or number of mapped analysis sites ± standard error of the mean.

*Significantly different relative to control as determined by Student's test (p<0.001).

ATRIAL SPECIFIC GRANULES: THE CYTOPLASMIC CALCIUM STORE

C. Zhong, Z. Yu, W. Yu, and Y. Ling

It is well known that certain organelles in cytosol contain high Ca concentration, and some cell activities are dependent on the release of Ca from the intracellular Ca stores. The question whether the atrial specific granule (ASG) contains high Ca concentration is a top priority in elucidating the role of Ca in the stimulus-secretion coupling of atrial specific granules. The present study was designed to determine Ca in ASGs with the techniques of quantitative electron probe microanalysis (EPMA) and Ca^{2+} -ATPase cytochemical localization.

Materials and Methods

Adult Sprague Dawley rats weighing 200 ± 50 g were used. The auricle samples were prepared and determined in the following procedures.

Preparation of Ultrathin Cryosections. The rat was sacrificed by decapitation, and its heart was excised immediately. In the 37°C Ringer-Krebs's solution with bubbles of 95% O_2 + 5% CO_2 , the inner surface of the auricle was turned out and then the auricle was wrapped on the top of a sectioning pin. After being immersed in 4% bovine serum albumin, the auricle with the pin was thrown rapidly into supercooling Freon 12 (melting point -164°C) for frozen fixation. The fixed auricle was cut into ultrathin cryosections 100–200 nm thick by Reichert Ultracut E microtome fitted with a FC4D cryosystem. The cryosection was mounted on the grid and freeze-dried in a high-vacuum evaporator. Then the section was covered with a thin film of carbon and stored in a desiccator.¹

Quantitative Electron Probe X-ray Microanalysis. The analysis was carried out with a JEM 1200EX electron microscope equipped with a Link AN 10000 energy-dispersive x-ray spectroscopy (EDS). The resolution of the 10mm² Si(Li) detector was better than 155 eV. The TEM mode of image was used for the analysis in the conditions of accelerating voltage of 80 kV, emission current 5–10 μA , grid holder tilted 35° to the horizontal entry x-ray detector, and probe diameter of about 0.5 μm . During analysis, the electron beam was focused on the ASG and the x-ray count rate was adjusted to 1000 cps with the collecting time of 300 s to form the energy spectra. The spectra were then processed by the

Link Quantum/FLS quantitative analysis software designed by the multiple least-squares fitting routine for showing the concentration values in mM/kg dry weight of the analyzed elements.^{2,3}

Cyt chemical Localization of Ca^{2+} -ATPase. Rats anesthetized intraperitoneally with sodium pentobarbital (40 mg/kg) were perfused through the left ventricle with 2% paraformaldehyde in 0.1 M cacodylate buffer of pH 7.4. The auricle was then taken out and dissected into small pieces, which were immersed in the same solution at 4°C for fixation for not longer than 30 min in all. After fixation the specimen was washed in the same buffer solution containing 0.25 M sucrose for more than 30 min. The tissue block was cut into sections 40 μm thick by a Microslicer (Dosaka EM Co. Ltd.). The composition of the cytochemical Ca^{2+} -ATPase reaction medium, which was developed by Fujimoto and Ogawa, was as follows: 250 mM glycine buffer, pH 9.0; 3mM ATP-2Na (Sigma Chem. Co.); 10mM CaCl_2 ; 10mM lead citrate; 2.5 mM levamisole (nonspecific alkaline phosphatase inhibitor, Sigma Chem. Co.). The sections were incubated in the medium for 10 min at 37°C.

Results

Ca Analysis of ASG. The ultrathin cryosections were observed under the electron microscope. It was shown that the atrial cardiocytes were arranged regularly, myofibrils lined up with clear striations, mitochondria located between myofibrils, the ovape nucleus located in the middle of a cardiocyte, and a lot of ASGs located in both poles of the nucleus (Fig. 1). When the electron beam was focused on the ASG, an energy spectrum including Na K α , Mg K α , P K α , S K α , Cl K α , K K α , K K β , and Ca K α elemental characteristic peaks was acquired (Fig. 2). It was demonstrated that the K K β peak overlapped with Ca K α peak. When the K peaks were subtracted from spectrum 1 (Fig. 2), spectrum 2 (Fig. 3) was obtained, which showed a prominent Ca K α peak. When the x-ray counts of spectrum 1 were processed with the software, the concentrations of the elements were given in mM/kg dry wt. The results indicated that the Ca concentration in ASG was 81 mM/kg dry wt., much higher than that in the cytoplasm (Table 1).

Cytochemical Localization of Ca^{2+} -ATPase. The reaction products were localized at the myofibrils and the matrix of mitochondria. Besides, they were localized on the membrane of the ASG, but not inside the ASG. The reaction products were more coarse at the myofibrils and the matrix of mitochondria, and finer on the

The authors are at the Department of Biophysics, Shanghai Medical University, Shanghai 200032, P. R. China. This work was supported by grant 38970254 from National Science Foundation of China. The aid of Dr. K. Ogawa of Kyoto University and Drs. A. P. Somlyo and A. V. Somlyo of the University of Virginia is gratefully acknowledged.

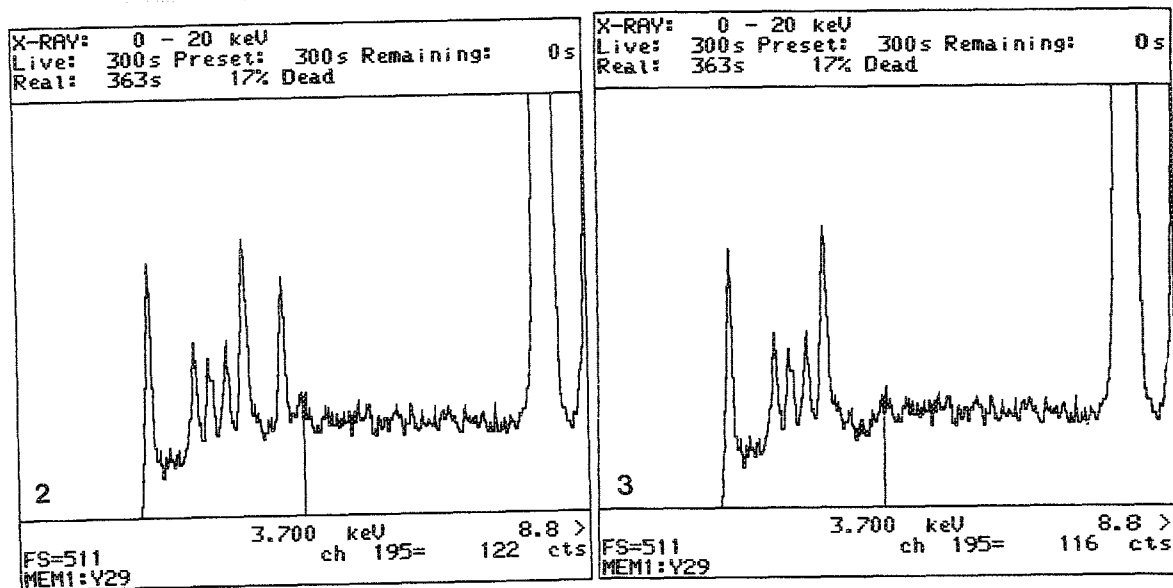
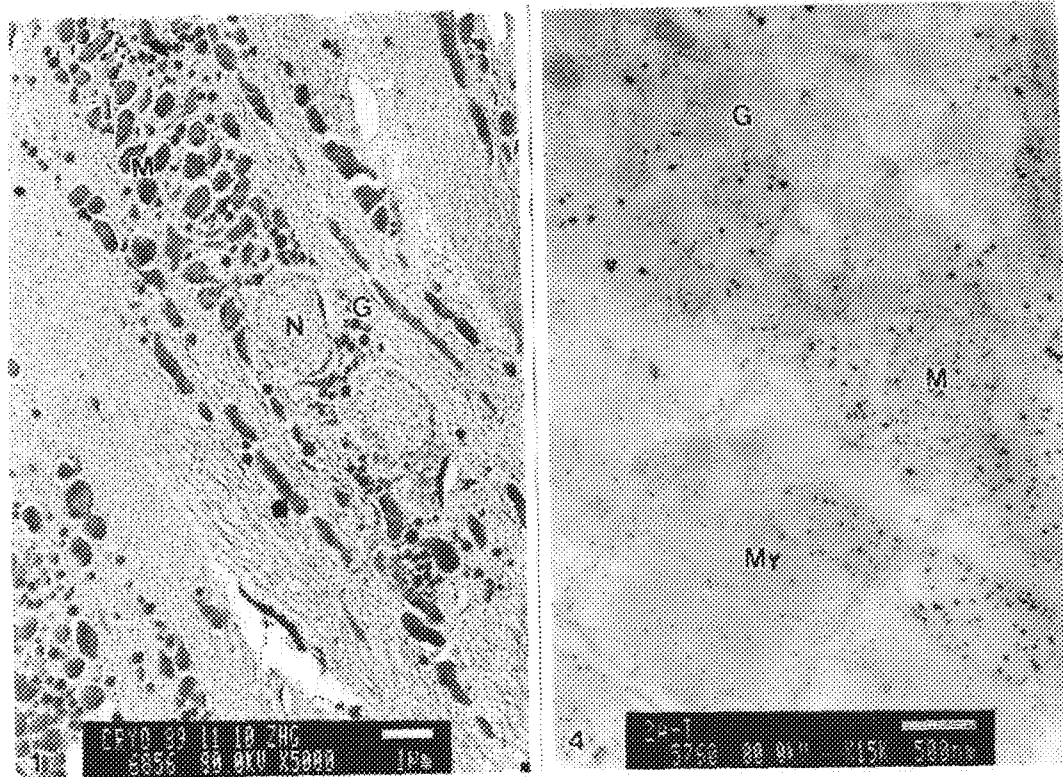


FIG. 1.--Ultrathin cryosection of atrial cardiocyte, showing nucleus N, atrial specific granules G, and mitochondria M.

FIG. 2.--Spectrum of atrial specific granule in cryosection, showing prominent Ca K α peak and K K α , Cl K α , S K α , P K α , Mg K α , Na K α peaks.

FIG. 3.--Same as Fig. 2, except K K α and K K β peaks subtracted by computer.

FIG. 4.--Cytochemical localization of Ca²⁺-ATPase, showing reaction products at myofibrils M, matrix of mitochondria M, and membrane of atrial specific granules G.

TABLE 1.--Composition of atrial specific granules in cryosection, mM/kg dry wt. (mean \pm S.E.).

Group	n	Na	Mg	P	S	Cl	K	Ca
ASG	10	13 \pm 4	19 \pm 6	391 \pm 44	405 \pm 41	471 \pm 42	341 \pm 25	81 \pm 15
Cytoplasm ⁵	20	36 \pm 6	9 \pm 3	467 \pm 37	476 \pm 53	292 \pm 29	443 \pm 44	<1

membrane of ASG (Fig. 4). The control specimen incubated in the substrate-free medium did not show any reaction products.

Discussion

Kish reported the presence of a great number of specific granules in atrial cardiocytes.⁶ They were named atrial specific granules and divided later on into three types, A, B, and D, morphologically.⁷ The crude extract of the rat atria had powerful natriuretic and diuretic effects.^{8,9} In the ASG, a potent peptide, which was designated atrial natriuretic peptide (ANP), was determined immunocytochemically.¹⁰ However, the immunocytochemical markers did not show any differences among the three types of ASG. Recently, more attention has been paid to isolating, sequencing, and synthesizing the ANP, and applying it to clinical practice.¹¹ However, the mechanism of ANP secretion from the ASG and the role of Ca in the secretion are not fully understood.

Eucaryotic cells contained a low concentration of Ca in their cytosol ($\leq 10^{-7}$ M) in the face of a much higher extracellular Ca concentration ($\sim 10^{-3}$ M). A few organelles in the cytosol contained high concentration of Ca to the extent of 18 mM, and were named intracellular Ca store, such as the sarcoplasmic reticulum. Somlyo determined a high calcium concentration of 70 mM/kg dry wt. in the rat ASG with the techniques of the rapid frozen auricle, ultrathin cryosectioning, and quantitative EPMA. From the present work on ultrathin cryosections of rapidly frozen rat auricles, the Ca concentration in the ASG was 81 mM/kg dry wt., which was approximately equal to Somlyo's.¹

With the Ca^{2+} -ATPase cytochemical technique, we further observed that Ca^{2+} -ATPase activities were localized on the membrane of the ASG. It was postulated that the Ca^{2+} -ATPase pumps Ca^{2+} from the cytosol into the ASG and maintains a high Ca concentration inside the ASG; therefore, the ASG is considered to be a Ca store in atrial cardiocytes (which has not been reported in the literature), just like sarcoplasmic reticulum in striated myocytes. It is reasonable to further postulate that the secretion of ANP is related to the release of Ca from the ASG. We are going to test this postulation in future work.

References

1. A. V. Somlyo et al., "Atrial-specific granules in situ have high calcium content, are acidic, and maintain anion gradients," *Proc. Natl. Acad. Sci. USA* 85: 6222, 1988.
2. Z. Yu et al., "Quantitative electron probe microanalysis of biological thin section," *Acta Academiae Medicinae Shanghai* 15: 436, 1988.
3. H. Shuman et al., Quantitative electron probe microanalysis of biological thin sections: Methods and validity," *Ultramicroscopy* 1: 317, 1976.
4. K. Fujimoto and K. Ogawa, "Enzyme cytochemical study of rat cardiac muscle: II.

Ca^{2+} -ATPase and ouabain-sensitive, K^{+} -dependent p-nitrophenyl-phosphate," *Acta Histochem. Cytochem.* 15: 338, 1982.

5. Y. Ling et al., "Electron probe microanalysis of calcium in ischemia-like lesions of rat myocardiocytes," *Proc. 12th ICXOM*, Cracow, Poland, 1989, 611.

6. B. Kisch, "Electron microscopy of the atrium of heart: I. Guinea pig," *Exp. Med. Surg.* 14: 99, 1956.

7. M. Cantin et al., "Ultrastructural cytochemistry of atrial muscle cells: VI. Comparative study of specific granules in right and left atrium of various animal species," *Anat. Rec.* 193: 55, 1979.

8. H. Sonnenberg et al., "Rapid and potent natriuretic response to intravenous injections of atrial myocardial extract in rats," *Physiol. ogist* 23: 13, 1980.

9. R. Garcia et al., "Relationship of specific granules to the natriuretic and diuretic activity of rat atria," *Experientia* 38: 1071, 1982.

10. M. Cantin et al., "Immunocytochemical localization of atrial natriuretic factor in the heart and salivary glands," *Histochemistry* 80: 113, 1984.

11. N. G. Seidak et al., "Amino acid sequence of homologous rat atrial peptides: Natriuretic activity of native and synthetic forms," *Proc. Natl. Acad. Sci. USA* 81: 2640, 1984.

QUANTITATIVE EPXMA IMAGING OF RAPIDLY FROZEN KIDNEY PROXIMAL TUBULE PRIMARY CULTURES

A. J. Spencer, L. A. Hawkey, Ann LeFurgey, K. G. Dickman, L. J. Mandel, and Peter Ingram

The role of ions (elements), particularly calcium, in processes such as renal cell injury is equivocal. A variety of techniques are required not only to assess the total cell element content or cytoplasmic free ion concentration, but also to identify the sites involved in binding, uptake and release of those ions/elements. The need to correlate such changes with alterations in cell metabolism has given rise to the use of in vitro models; for example, isolated nephron segments in suspension have been employed to study the effects of anoxia/hypoxia in the absence of any hemodynamic effects.¹ Our previous studies have shown that changes in Ca compartmentation in isolated rabbit proximal tubules after short-term anoxia appear to be subtle.² However, the effects of longer periods of anoxia and/or recovery have not been studied due to lack of an in vitro model. A preparation of primary kidney proximal tubule cultures has been recently described, which accurately reflects the in vivo metabolic features of proximal tubules, for extended periods of time in vitro.³ We have therefore applied ultrarapid freezing and electron-probe x-ray microanalysis (EPXMA) imaging to characterize the ultrastructure and subcellular element composition of these new primary proximal tubule cultures.

Methods

Primary cultures of rabbit proximal tubules were obtained as previously described.³ Tubules were then maintained under shaking conditions, during which the cells retain the metabolic characteristics of oxidative rather than glycolytic metabolism for at least 24 h.³ In this initial characterization of primary cultures, tubules were preincubated at 37°C and gassed with 95% O₂/5% CO₂ for 60 min before samples were taken for further processing. Small aliquots of tubule suspension were rapidly ultracentrifuged (~3 s) to concentrate the tubules and the loose pellet pipetted onto a previously prepared aluminum planchet, mounted on the freezing head. The freezing head was then transferred to the quick freezing device (Cryopress, Med Vac Inc.) and the sample slam-frozen against a liquid helium-cooled polished copper block. Time from taking tubules from incubating suspension to freezing averaged 30 s. Samples were stored in liquid nitrogen and subsequently freeze-substituted to assess the

quality of freezing,⁴ or ultrathin cryosectioned, placed onto carbon films on nickel grids, freeze dried, and carbon-coated for EPXMA. Low resolution quantitative elemental images (64 × 64 pixel arrays; 2 s dwell time per pixel) of freeze dried cryosections were obtained as previously described.^{5,6}

Results

Examination of the primary kidney proximal tubule preparation revealed tubule fragments with the typical ultrastructure of the S1 and S2 fragments of the proximal tubule.⁷ Assessment of the quality of freezing of the cells that impacted the copper block first (point of first impact, PFI) by freeze substitution revealed tubules that were separated from each other and had minimal ice crystal damage, patent lumens, and a well-preserved brush border (Fig. 1). As the distance from the PFI increased, tubules became more compacted and exhibited ice crystal damage of increasing magnitude (not shown).

Cryosections taken *en face* from very close to the PFI exhibited minimal contrast; as with freeze-substituted tubules, there was little evidence of ice crystal damage (Fig. 2). Brush border at the apical region of the cells could be positively identified. However, no distinction could be made between intracellular organelles such as mitochondria and lysosomes. In addition to *en face* cryosections taken near the surface of the frozen tissue block, specimens were mounted and trimmed in order to obtain very large, nominally 100 nm-thick hydrated cryosections, perpendicular to the block face. These sections typically contained many tens of cells. Following freeze-drying, a clear gradient of freezing could be seen, from cells near the PFI with excellent freezing and low contrast, through cells with relatively little ice crystal damage and easily identifiable intracellular morphology, to cells with gross ice crystal reticulations.

Although it was difficult to determine intracellular morphology in low-contrast cryosections, organelles could be identified by their element content in quantitative elemental maps. Figure 3 shows an example of an EPXMA image of such a low-contrast cryosection. Although in this case it is possible to identify the nuclear region in the scanning transmission (STEM) image, the nucleus is more clearly delineated in the P image, as well as in the K and Na images. In contrast, S-rich lysosomes are easily identifiable in the S image, but not in the STEM image.

The results of EPXMA imaging of primary

The authors are with Department of Cell Biology, Duke University Medical Center, Durham, NC 27710, except Peter Ingram, who is with Research Triangle Institute, Research Triangle Park, NC 27709.

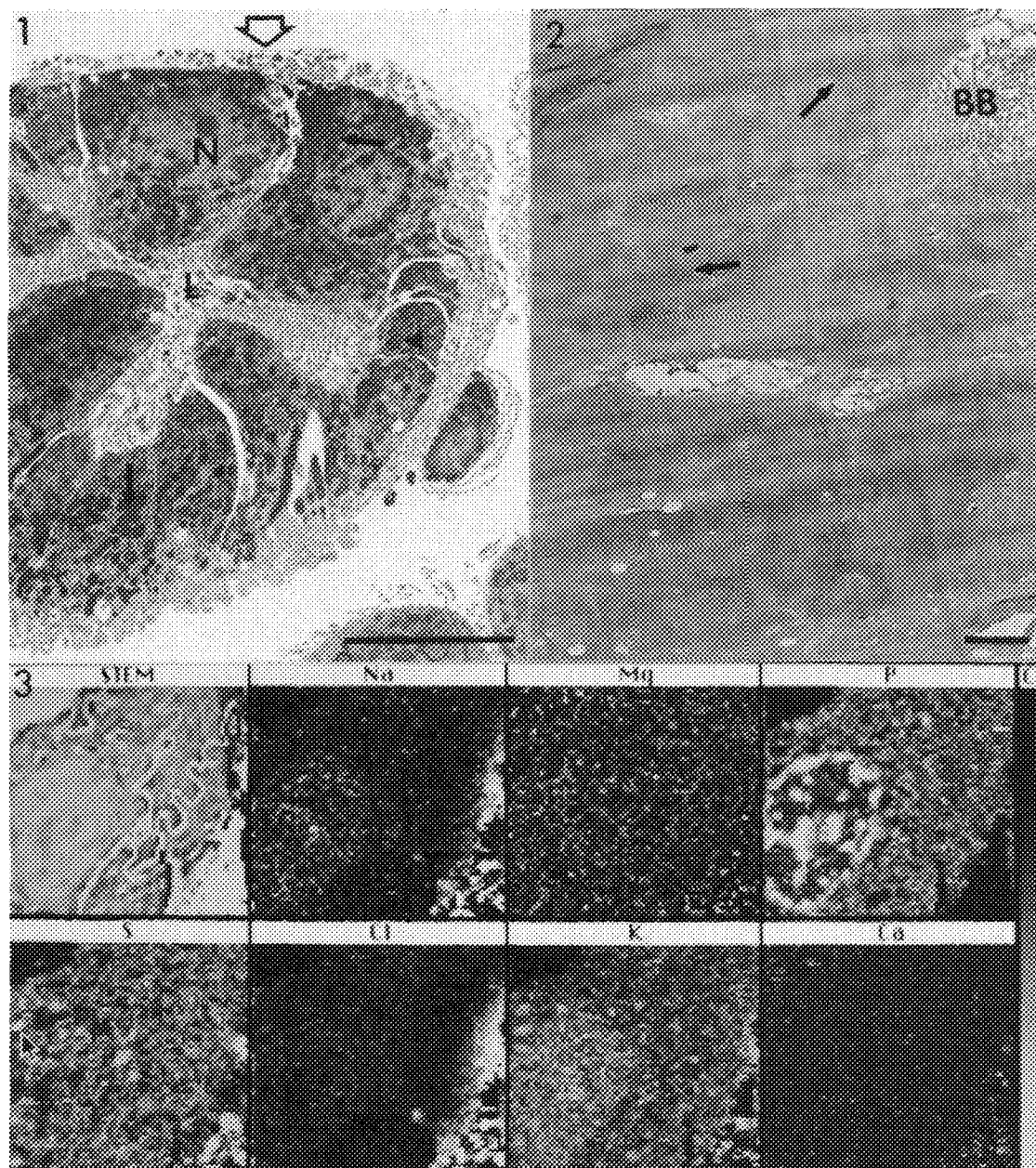


FIG. 1.--TEM of slam-frozen, freeze-substituted kidney proximal tubule. Large open arrow indicates point of first impact; nucleus N, lumen L, mitochondria (arrows), lysosomes (arrowhead), are easily identifiable. Scale bar = 5 μ m.

FIG. 2.--TEM of cryosection taken *en face* close to PFI. Brush border BB, intracellular organelles (arrows). Scale bar = 1 μ m.

FIG. 3.--STEM image and quantitative elemental images for Na, Mg, P, S, Cl, K, Ca of freeze-dried cryosection of rabbit kidney proximal tubule cell, cultured under control conditions. Elemental images are scaled on gray scale to right of figure as follows (in nmol/mg dry weight): Na, P, Cl, K: -100 to 600; Mg, Ca: -100 to 200; S: -100 to 350. Note high S content of lysosomes in S image (arrow).

kidney proximal tubule cultures maintained under shaking culture conditions are summarized in Table 1. Mean cell cytoplasmic K/Na ratio was variable (overall mean 3.1/1), with no correlation between K and Na content ($R = 0.296$). As borne out by the images, nuclear Na, K, and P content were significantly higher than in other subcellular compartments. Mitochondria con-

tained significantly lower Na, Mg, P, and K and higher S than cytoplasm and nucleus on a dry-weight basis. Lysosomes contained significantly higher S and lower P, in comparison with all other compartments, and higher Cl than cytoplasm and mitochondria.

TABLE 1.--Quantitative EPXMA data for proximal tubule cells cultured under control conditions. Data are mean \pm SEM. N, n₁, n₂ are numbers of rabbits, cells, and regions analyzed, respectively. Nucleus data are for whole nucleus region; p values calculated from nested ANOVA by use of Games-Howell procedure for differences among organelles.

	N	n ₁	n ₂	Na	Mg	P	S	Cl	K	Ca
Cytoplasm	5	25	250	177 \pm 5	30 \pm 2	432 \pm 7	75 \pm 2	135 \pm 5	437 \pm 9	8.6 \pm 1.3
Mitochondria	5	25	250	146 \pm 4	19 \pm 1	377 \pm 6	111 \pm 3	144 \pm 5	374 \pm 7	5.8 \pm 1.1
Nucleus	5	11	11	248 \pm 18	34 \pm 3	547 \pm 31	60 \pm 9	144 \pm 22	581 \pm 51	4.2 \pm 1.9
Lysosomes	5	8	22	161 \pm 21	13 \pm 8	276 \pm 20	315 \pm 11	179 \pm 12	358 \pm 23	5.1 \pm 2.4
Cyto vs Mito				p<0.01	p<0.01	p<0.01	p<0.01	ns	p<0.01	ns
Cyto vs Nuc				p<0.01	ns	p<0.05	ns	ns	p<0.05	ns
Cyto vs Lyso				ns	ns	p<0.01	p<0.01	p<0.01	p<0.05	ns
Mito vs Nuc				p<0.01	p<0.01	p<0.01	p<0.01	ns	p<0.01	ns
Mito vs Lyso				ns	ns	p<0.01	p<0.01	p<0.05	ns	ns
Lyso vs Nuc				p<0.05	ns	p<0.01	p<0.01	ns	p<0.01	ns

Discussion

Quantitative electron-probe x ray micro-analysis (EPXMA) imaging facilitates assessment of cell ultrastructure and measurement of total element content with high lateral spatial resolution.^{5,6,8} The first and most critical step in attempting to determine the distribution of elements in biological specimens is the freezing process. The liquid helium-cooled copper block method (slam freezing) meets the criteria for rapid arrest of physiological processes and minimal ice crystal distortion of the outer regions of the tissue in question.^{9,10} Primary kidney proximal tubule cultures frozen by this procedure exhibited well-preserved ultrastructure in freeze-substituted samples, minimal ice crystal damage in freeze-dried cryosections taken from close to the PFI, and gradients for diffusible ions across plasma and organelle membranes in EPXMA images.

Quantitative elemental data were similar to those obtained previously in short-term cultures of rabbit proximal tubules.^{11,12} Although K/Na (often used as an indicator of cell viability) was variable among cells, the overall mean was within the range of values established by other investigators for renal cell cytoplasm (as determined by EPXMA) or whole cell (bulk measurement) in a variety of in vivo or in vitro preparations.^{13,15} The Na content of isolated proximal tubules in which the lumen has collapsed is lower than that measured in the current study, due to reduced Na transport across the cells.¹⁶ The Na data from the present study are therefore consistent with availability of Na for transport from open lumens of tubules in shaking culture. The difference in Na reabsorptive capacity along the length of the proximal tubule (which decreases from S1 to S2 segments) is well documented.¹⁷ Variability in Na content may therefore reflect differences in the transport capacity of adjacent cells within distinct segments of the proximal tubule or a heterogeneity of Na transport capacity between different segments of the proximal tubule. However, variability in Na and K content are not due to incorporation of extracellular space

in cytoplasmic regions chosen for data acquisition, since any Na and K gradients due to basolateral interdigitations are easily identifiable in quantitative EPXMA images.

The visual perception of elemental distribution afforded by EPXMA images is not easily obtainable by analysis of thicker freeze-dried cryosections or by static probe methods alone.^{5,6} The ability to distinguish intracellular organelles such as lysosomes from mitochondria and to detect cell-to-cell heterogeneity by EPXMA imaging has been described previously.^{18,19} The use of slam-frozen specimens to obtain very large, ultra-thin cryosections enables the acquisition of low-magnification, low-resolution EPXMA images to help determine the cell-to-cell and tubule-to-tubule variation in elemental content in these primary tubule cultures. In addition, since these cryosections also contain areas of tissue with minimal ice crystal damage and easily identifiable intracellular morphology, the option also exists to perform very high resolution EPXMA imaging with longer dwell times, combined with static probes when necessary, in order to obtain the statistical accuracy for quantitation of elements present in low concentrations. Ultimately, the ability to resolve smaller structures such as endoplasmic reticulum will be limited by the size of the electron beam.²⁰ This primary proximal tubule preparation will be utilized for longer-term studies of anoxia/recovery in the future.

References

1. T. Takano et al., "Intracellular respiratory dysfunction and cell injury in short-term anoxia of rabbit proximal tubules," *J. Clin. Invest.* 76: 2377, 1985.
2. A. J. Spencer et al., "Anoxia-induced changes in elemental compartmentation in renal proximal tubules as studied by high resolution x ray imaging," *Kidney Int.* 37: 485, 1990.
3. K. Dickman and L. J. Mandel, "Glycolytic and oxidative metabolism in primary renal proximal tubule cultures," *Am. J. Physiol.* 257 (Cell Physiol. 26): C333, 1990.
4. R. Nassar et al., "The quick freezing of

single intact skeletal muscle fibers at known time intervals following electrical stimulation," *Scanning Microscopy* 1: 309, 1986.

5. P. Ingram et al., "Real-time quantitative elemental analysis imaging in cells," *Analytical Electron Microscopy--1987*, 179.

6. P. Ingram et al., "Quantitative elemental x ray imaging of biological cryosections," *Microbeam Analysis--1988*: 433.

7. B. Kaissling and W. Kriz, "Structural analysis of the rabbit kidney, *Adv. in Anatomy, Embryol. and Cell Biol.* 56: 1, 1979.

8. A. V. Somlyo et al., "Atrial-specific granules *in situ* have high calcium content, are acidic and maintain anion gradients," *Proc. Natl. Acad. Sci. USA* 85: 6222, 1988.

9. J. Heuser et al., "Synaptic vesicle exocytosis captured by quick freezing and correlated with quantal transmitter release," *J. Cell Biol.* 81: 275, 1979.

10. P. Ingram et al., "Quantitative x ray elemental mapping of dynamic physiologic events in skeletal muscle," in K. Zierold and H. K. Hagler, Eds., *Electron Probe Microanalysis*, Berlin: Springer-Verlag, 1989, 251.

11. A. LeFurgey, P. Ingram, and L. J. Mandel, "Heterogeneity of calcium compartmentation: Electron probe analysis of renal tubules," *J. Membr. Biol.* 94: 191, 1986.

12. A. LeFurgey et al., "Elemental microanalysis of organelles in proximal tubules. I. Alterations in transport and metabolism," *J. Am. Soc. Nephrol.* (in press).

13. F. Beck et al., "Element concentrations of renal and hepatic cells under potassium depletion," *Kidney Int.* 22: 250, 1982.

14. A. J. Saubermann et al., "Simultaneous comparison of techniques for x-ray analysis of proximal tubule cells," *Kidney Int.* 29: 682, 1986.

15. J. Grantham et al., "Effect of hypotonic medium on K and Na content of proximal renal tubules," *Am. J. Physiol.* 232: F42, 1977.

16. L. Rome et al., "Proximal tubule volume regulation in hyperosmotic media: Intracellular K^+ , Na^+ and Cl^- ," *Am. J. Physiol.* 257:C1093, 1989.

17. M. B. Burg, "Renal handling of sodium, chloride, water, amino acids, and glucose," in B. M. Brenner and F. C. Rector, Eds., *The Kidney*, (3rd ed), 1986, 145.

18. A. LeFurgey et al., "Alterations in calcium and sulfur compartmentation during anoxia in kidney proximal tubules," *Microbeam Analysis--1989*, 69.

19. M. E. Cantino et al., "Heterogeneity in elemental images of cells and tissues," *Microbeam Analysis--1989*, 73.

20. J. I. Goldstein et al., "Spatial resolution and detectability limits in thin-film x ray microanalysis," *Proc. XII ICEM* 2: 450, 1990.

SYSTEMATIC CHANGES IN CORNEOCYTE ELEMENT CONCENTRATIONS IN SKIN INNER STRATUM CORNEUM

R. R. Warner

The outer layer of skin, the stratum corneum (SC), is usually considered to be homogeneous in its structure and physical properties.¹ Previously we showed the *outer* SC was not homogeneous in its composition, but contained steep gradients of the physiological inorganic elements Na, K and Cl.² Here we show there is considerable elemental heterogeneity in the *inner* SC, with dramatic systematic changes in composition occurring with cell position within the SC.

The SC is the 15µm-thick outer layer of skin that constitutes the major barrier to desiccation and bacterial attack and allows our existence on land. This layer is formed by skin keratinocytes that mature during transit through the viable layers of the epidermis, and then abruptly form the condensed, flattened, dead organelle-free cells called corneocytes that are the primary constituents of the SC. The SC is generally considered to be homogeneous in structure and barrier properties,¹ and is often shown schematically as a brick wall,³ the "bricks" being the corneocytes, the "mortar" being intercellular lipid. The concept that the SC is a homogeneous structure is increasingly difficult to reconcile with mounting evidence for chemical heterogeneity across the SC. Differences between the inner and outer SC are known to exist for water, protein (e.g., filaggrin⁴) and lipid (e.g., cholesterol⁵). Recently we showed the outer SC itself was not homogeneous in composition, but contained steep gradients for Na, K, and Cl that probably originated from sweat salts (Fig. 1). Figure 1 also shows that large elemental changes occur in the inner SC (ISC). This report describes the ISC elemental changes in greater detail.

Materials and Methods

Methods have been described previously.⁶ Briefly, human skin biopsies were taken from the lower leg of individuals with both "good" and "dry" skin and plunged into a stirred, liquid nitrogen-cooled 20/80 mixture of isopentane and propane. Cryosections 1µm thick were obtained at -110°C and freeze-dried overnight. Analysis was with a modified Hitachi H500 TEM/STEM⁷ equipped with a Tracor Northern 5500 EDS system and a high-angle detector. Analytical conditions were 100 kV and 0.5 nA.

Results

Figure 2 shows a STEM image and x-ray maps of the ISC (and some of the underlying granular

cell layer). As shown in the lower x-ray maps of this figure, the cellular Na and S concentrations (per unit volume of tissue) do not undergo major alterations in transit across the ISC and tend to reflect simply an increasing concentration (per unit volume) due to an increase in cell density as the corneocyte water content decreases (see water profile of Fig. 1). However, other elements undergo dramatic changes in elemental composition as the corneocytes advance through the ISC. Phosphorus is present at a reduced concentration in the first SC cell layer, and then falls to negligible levels. The cellular K concentration is somewhat reduced in the first SC layer, drops dramatically across the subsequent layer, and then drops to negligible levels. In contrast, the cellular chloride (Cl) concentration increases in the innermost corneocyte layer, increases further in the subsequent layer or two (as K declines), and then decreases to values comparable to those in the innermost corneocyte. The Cl, K, and P profiles are shown more graphically in the linescan of Fig. 3, which shows that the decline in P occurs very abruptly, that K continues much further into the ISC, and that the decrease in K generally correlates with an increase in Cl. Chloride subsequently decreases, but remains at a substantially elevated level. Note that a decrease in K and increase in Cl within a corneocyte defies charge balance. The increase in Cl within the SC is also observed when concentrations are expressed per unit dry weight, as shown in Table 1, and thus cannot be explained simply by cell water loss.

Discussion

We have shown that the ISC is not homogeneous in elemental composition. The composition changes in the SC are systematic, with P decreasing prior to K, and Cl increasing as K decreases. The position-dependent alterations in corneocyte elemental composition may reflect sequential maturation changes occurring intracellularly during SC transit. In particular, the SC cell K/Cl charge imbalance may be due to enzymatic formation of intracellular fixed positive charges.

If the SC is not homogeneous in its composition, then it is very possible that the SC is not homogeneous in its physical properties. This conclusion could imply that, contrary to current thought,^{1,8} the SC does not constitute a uniform and homogeneous barrier.

R. R. Warner is at the Miami Valley Laboratories, Procter & Gamble Co., Cincinnati, OH 45239.

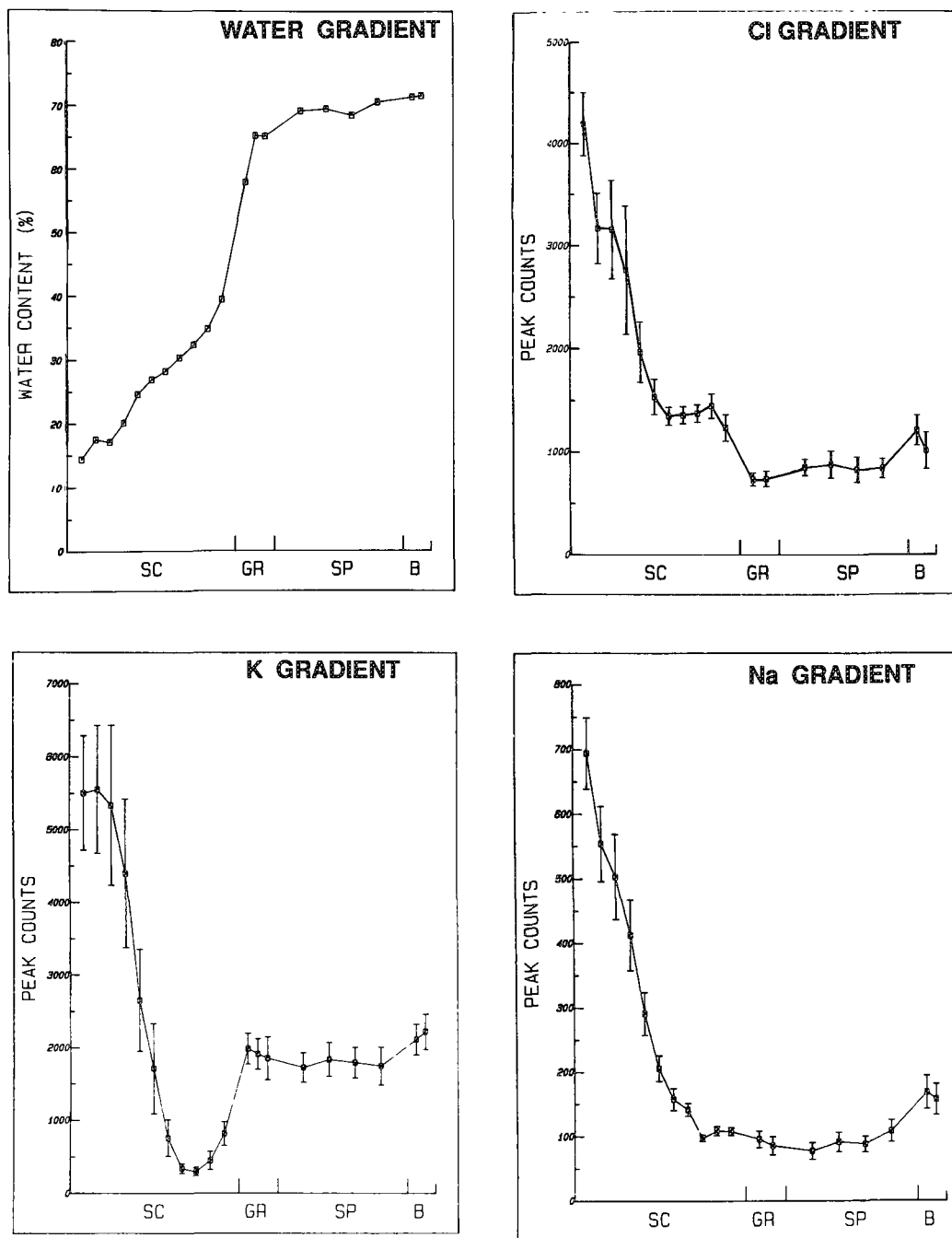


FIG. 1.--Water, Cl, K, and Na profiles across human skin. Horizontal axis represents position across skin epithelium (not drawn to scale); SC = stratum corneum, GR = stratum granulosum, SP = stratum spinosum, B = basal cell layer. (From Refs. 3 and 6.)

References

1. A. M. Kligman, "The biology of the stratum corneum," in W. Montagna and W. C. Lobitz, Eds., *The Epidermis*, New York: Academic Press, 1964, 387-433.
2. R. R. Warner, M. C. Myers, and D. A. Taylor, "Electron probe analysis of human skin: Element concentration profiles," *J. Invest. Dermatol.* 90: 78-85, 1988.
3. A. S. Michaels, S. K. Chandrasekaran, and J. E. Shaw, "Drug permeation through human skin: Theory and in vitro experimental measurement," *AIChE J.* 21: 985-996, 1975.
4. I. R. Scott, C. R. Harding, and J. B. Barrett, "Histidine-rich protein of the kerato-

hyalin granules: Source of the free amino acids, urocanic acid and pyrrolidone carboxylic acid in mammalian stratum corneum," *Biochim. Biophys. Acta* 719: 110-117, 1982.

5. G. M. Gray et al., "Lipid composition of the superficial stratum corneum cells of pig epidermis," *Br. J. Dermatol.* 106: 59-63, 1982.

6. R. R. Warner, M. C. Myers, and D. A. Taylor, "Electron probe analysis of human skin: Determination of the water concentration profile," *J. Invest. Dermatol.* 90: 218-224, 1988.

7. R. R. Warner, M. C. Myers, and D. A. Taylor, "Inaccuracies with the Hall technique due to continuum variation in the analytical micro-

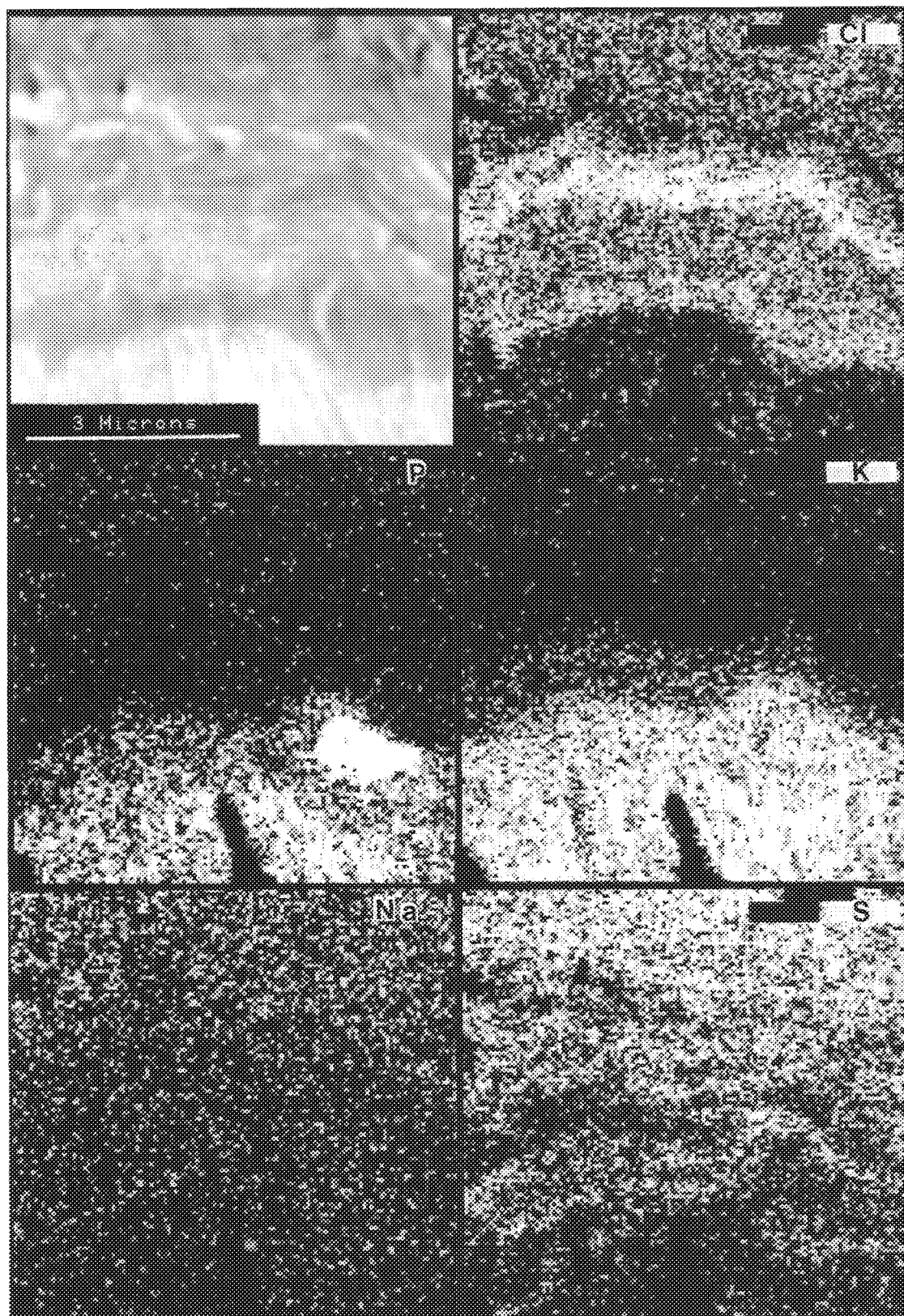


FIG. 2.--STEM image (upper right) and corresponding Cl, P, K, Na, and S x-ray maps. Lowest region of STEM image is from granular layer, the uppermost living cell layer. Overlying 5-6 cell layers are ISC corneocytes.

scope," *J. Microsc.* 138: 43-52, 1985.

8. B. Idson, "Percutaneous absorption," *J. Pharm. Sci.* 64: 901-904, 1975.

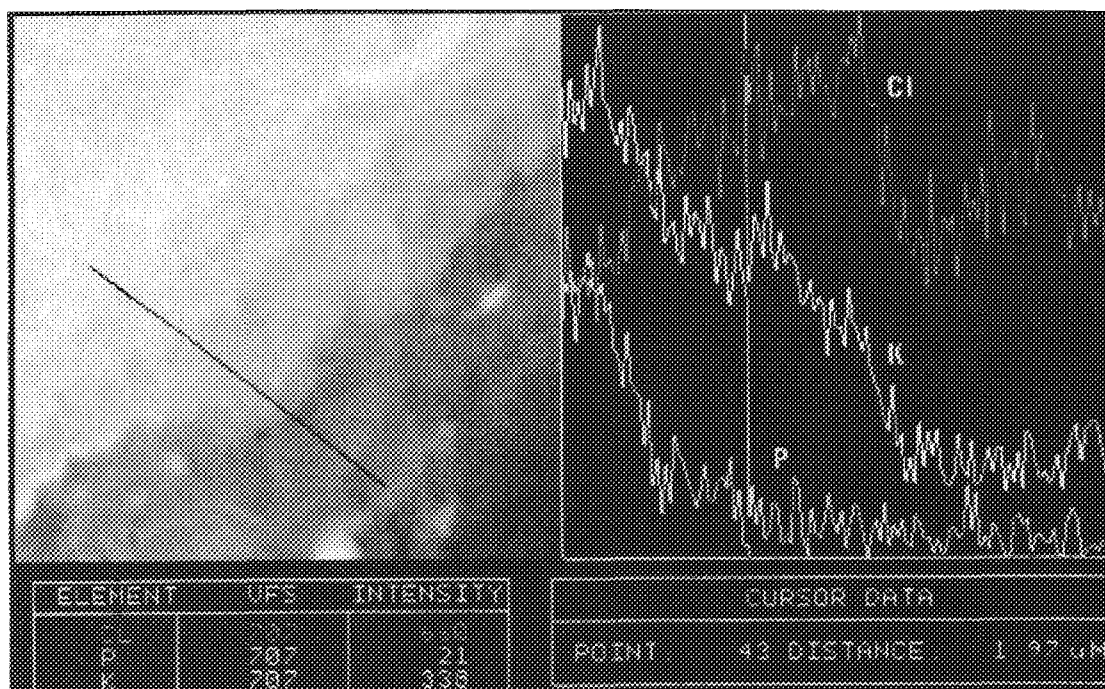


FIG. 3.--STEM image and corresponding line profiles for Cl, K, and P. Position of vertical cursor superimposed on line profiles correlates with position marked + on displayed scan line in STEM image.

TABLE 1.--Intracellular point analysis: Concentration (mM/kg dry weight) (Mean \pm s.e., n = 6).

	Na	P	K	Cl
GR1	111 + 33	263 + 43	284 + 40	179 + 30
GR2	98 + 24	204 + 33	242 + 36	165 + 19
SC1	68 + 30	102 + 27	103 + 17	134 + 22
SC2	48 + 25	28 + 7	80 + 28	204 + 28
SC3	39 + 11	6 + 2	38 + 13	148 + 15
SC4	36 + 8	8 + 2	10 + 2	107 + 11

GR = Granular layer Cell
SC = Stratum Corneum Cell

BIOMEDICAL ELEMENTAL ANALYSIS AND IMAGING USING SYNCHROTRON X-RAY MICROSCOPY

K. W. Jones, B. M. Gordon, George Schidlovsky, Per Spanne,
Xue Dejun, R. S. Bockman, and A. J. Saubermann

The application of synchrotron x-ray microscopy to biomedical research is currently in progress at the Brookhaven National Synchrotron Light Source (NSLS). The current status of the x-ray microscope (XRM) is reviewed from a technical standpoint. Some of the items considered are photon flux, spatial resolution, quantitation, minimum detection limits, and beam-induced specimen damage. Images can be produced by measurement of fluorescent x rays or of the attenuation of the incident beam by the specimen. Maps of the elemental distributions or linear attenuation coefficients can be made by scanning of the specimen past the beam. Computed microtomography (CMT) can be used for nondestructive images through the specimen in either the emission or absorption mode. Examples of measurements made with XRM are given.

The Brookhaven XRM uses continuous-energy bending-magnet radiation produced at the NSLS as the x-ray source. The electron ring operates at an energy of 2.5 GeV and a stored electron current of about 225 mA at the beginning of a fill and a current of about 100 mA at the end of the fill. The lifetime of a fill is approximately 24 h, but there can be large fluctuations in this value depending on ring conditions. The x-ray beam flux at the XRM specimen position is shown in Fig. 1 at a ring current of 100 mA.

Emphasis is placed on retaining flexibility in the arrangement of the components in designing the XRM beam line. A monochromator prior to a focusing mirror can be used, if desired, to produce an image of the x-ray source with a demagnification of the source size by about a factor of two. The final beam size at the specimen is controlled by a set of x-y adjustable slits and/or a pinhole. A set of four stepper-motor driven tantalum slits can be used to produce collimated beams from a size of about 40 mm in the horizontal and about 10 mm in the vertical (consistent with the vertical opening angle of the source) down to a size of about 40 μm set by the geometry of the source, pinhole, and specimen. A fixed geometry pinhole collimator placed 3.5 cm from the specimen

is used to define x-ray beams down to 1 μm in size. Collimators of different sizes are used to cover the spatial range below 40 μm . It is sometimes desirable to replace the final collimator with a channel-cut silicon monochromator. It can be used for simple experiments to produce monoenergetic beams with energies below the absorption edge for a major element or for chemical speciation by use of x-ray absorption near-edge spectroscopy (XANES).

The photon flux is maximized by location of the XRM as close to the x-ray source as possible (9 m). Flux values of about 3×10^8 photons/(s- μm^2) integrated over the energy distribution of the synchrotron x-ray source are obtained with a 100mA current of electrons in the storage ring. The specimen is moved with respect to the photon beam by use of computer-controlled stepping motors. The fluorescent x rays are detected with a 30mm² Si(Li) x-ray detector placed at 90° to the incident beam to minimize Compton scattering. (The high-degree of polarization of the synchrotron x-ray source makes this arrangement possible.)

Some work has also been done with a Kirkpatrick-Baez microscope produced by Giauque et al.¹ This instrument uses multilayer coatings to obtain high-throughput monoenergetic beams with energies from 6 to 14 keV. Spatial resolutions and photon fluxes obtained are very similar to the values mentioned above for collimated continuous radiation. To date, the use of the collimated XRM has the advantage of simplicity and broad range detection capability over the focused probe.

The sensitivity of the XRM for detection of characteristic x rays is found by use of specimens of known composition. For example, National Institute of Standards and Technology (NIST) Standard Reference Materials (SRM) 3171 and 3172 are multielement standards in liquid form. After deposition on filter paper,² the fluorescent x-ray spectra are analyzed to correlate the known elemental concentrations in units of mM/kg with the number of characteristic x rays for given conditions of ring current, absorber thicknesses, detector solid angle, and efficiency. The measured values can be compared to calculations based on the theoretical values for photon flux produced by the synchrotron radiation method and known geometrical factors of the XRM. The results of sensitivity determinations made using the two methods are shown in Fig. 2. The calculated and experimental values are normalized at the maximum of the K x-ray curve. The calculated values are higher by about a factor of 4 in absolute value. This agreement is reasonable when the uncertainties in collimator area and

The authors are at the Atomic and Applied Physics Group, Brookhaven National Laboratory, Upton, NY 11973, except R. S. Bockman, who is at the Hospital for Special Surgery, 535 East 70th Street, New York, NY 10021; and A. J. Saubermann, who is at the SUNY Department of Anesthesiology, School of Medicine, Health Sciences Center, Stony Brook, NY 11794. This work was supported by NIH Biotechnology Research Resource grant P41RR01838 and DOE contract DE-AC02-76CH00016.

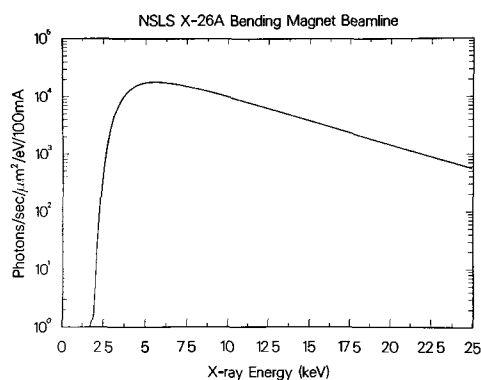


FIG. 1.--Flux of x rays produced by NSLS bending-magnet source is shown as a function of x-ray energy. Units are number of x rays produced by stored current of 100 mA that fall on $1 \mu\text{m} \times 1 \mu\text{m}$ area at 9 m from x-ray source. Values are given for constant bandwidth of 1 eV. Effects of beryllium windows used to separate XRM from vacuum conditions of ring are shown.

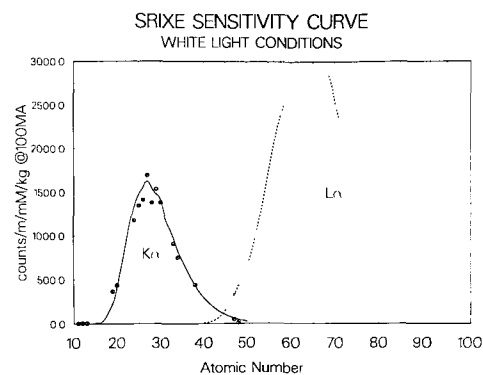


FIG. 2.--Minimum detection limits for K and L x-ray detection as a function of atomic number Z . Values scaled from those reported by B. M. Gordon and K. W. Jones, *Nucl. Instrum. Methods* B10/11: 293, 1985, are given to indicate agreement with calculations for focusing XRM. Proton curve shows values attained with proton microprobe and proton-induced x-ray emission (PIXE).

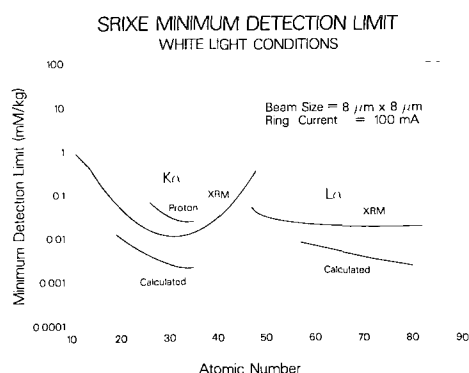


FIG. 3.--Sensitivity for elemental concentrations from XRM is shown as a function of atomic number. Beam size, $8 \mu\text{m} \times 8 \mu\text{m}$; ring current, 100 mA. Experimental points were determined from thin standards. Curve was calculated from knowledge of photon flux and experimental parameters. Detector solid angle was 1.2×10^{-3} sr.

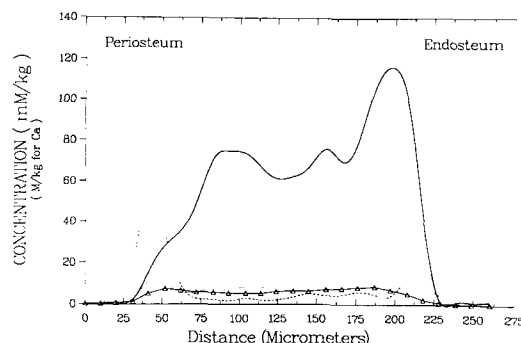


FIG. 4.--Line scan across rat femur section from rachitic rat treated with Vitamin D and gallium. Beam size, $\sim 5 \mu\text{m} \times 8 \mu\text{m}$. In this case concentration values are referenced to average calcium value taken as 20% of bone's wet mass. Values for Ca (triangles), Fe (dashes), Zn (dots), and Ga (solid line) are given.

alignment, as well as photon flux and energy distribution, are considered.

The specimen areal density is measured by comparison of the scattered radiation intensity from the specimen with that from a standard of known thickness and similar composition. For work with tissue sections, a calibration curve is established by measurement of the scattered radiation from a set of polyimide foils of known areal density and then deduction of the areal density of the unknown from this curve. The concentration values for the elements in the unknown are then easily found in units of g/g, mM/kg, etc. The same procedures are followed for specimens of bone where substantial amounts of Ca and P are present, although other types of standards have to be used. Absorp-

tion of the x rays in thick samples is accounted for using a modified version of the NRLXRF program.³ The accuracy of the concentration assignments is estimated at ± 10 -15%; repeated runs on a single point show variation of $< \pm 5\%$.

Detection limits assigned for tissue sections are < 0.02 mM/kg for elements around iron. These limits increase for lighter elements such as calcium. The detection limits for K and L x-ray detection are given in Fig. 3. We have investigated the detection limit for calcium by measuring a response curve in thin PVP sections with concentrations down to 12.5 mM/kg. From the spectra obtained, a value for the calcium detection limit of less than 0.1 mM/kg is obtained for a 300s exposure, at the cost of great loss in spatial

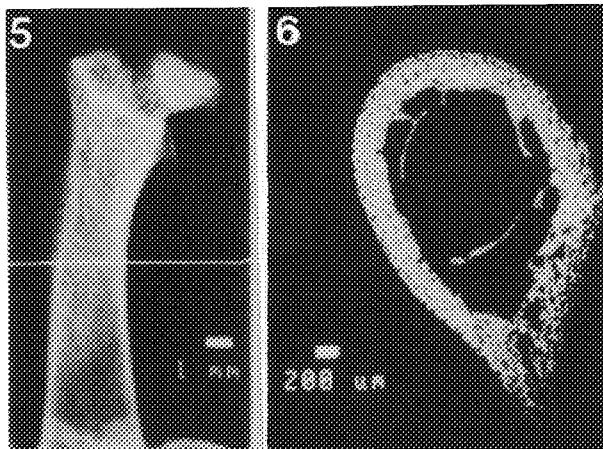


FIG. 5.--X-ray projection image of rat femur generated with 20keV synchrotron x rays.

FIG. 6.--X-ray absorption tomogram of rat femur imaged with 20keV synchrotron x rays. Matrix size, 285 \times 285; pixel size, 15 μ m \times 15 μ m.

resolution. Furthermore, the sensitivity of EPMA would also be better at higher count rates. The present detection limits show that the XRM substantially improves on the limits attainable by electron-probe microanalysis. Furthermore, several changes can be made in the existing apparatus that will improve detection conditions and reduce the detection limit.

The XRM is equipped with instrumentation and computer programs, which makes computed tomography with spatial resolution in the micrometer range possible.⁶⁻⁹ Measurements made by using CMT are based either on fluorescent x rays or on differences in sample x-ray linear attenuation coefficients. Two types of CMT scanners have been developed. One is a high-resolution first-generation scanner with a pencil beam⁶ and a single radiation detector; the other is a third-generation scanner with a wide radiation field defined by a narrow slit and a photodiode array and a scintillator for the detection of x rays. The third-generation scanner allows us to produce images with a spatial resolution of the order of 100 μ m at present, but has potential for resolutions down to about 25 μ m. The first-generation scanner is used for imaging with much higher spatial resolutions. To date we have been able to generate a tomogram with a spatial resolution of approximately 1 μ m by defining a 1 μ m x-ray beam with a collimator of the same type as is used for the fluorescence measurements. It is possible to produce such a small field at the sample position because the collimator can be placed as close to the sample as 1 mm during tomography, and the source to sample distance is of the order of 9 m. The CMT system is therefore not source-size limited at present. The CMT system can be used both for absorption tomography mapping the distributions of the linear attenuation coefficient in unsectioned samples and for elemental mapping by fluorescent x rays excited by the first-generation pencil beam.

The use of synchrotron x rays for CMT has several advantages, mostly related to the very

high flux of photons available. The high flux makes the use of monochromators for x rays possible, which has several interesting advantages compared to the broad x-ray spectra from conventional rotating anode x-ray tubes. The energy choice is important in minimizing the imaging time⁸ and gives the possibility for elemental mapping by use of photoelectric absorption edges or multiple energy CMT.

The interaction of high-flux beams with the specimen can cause damage to the specimen. We have looked at changes in the specimen morphology and in the change of x-ray yield as a function of total fluence. For thin nylon foils severe damage is seen for a 300s run, and a measurable decrease in scattered intensity is also observed for other types of plastic films.⁴ The measurable effects on biological materials are not found to be serious at present fluence levels, but they need to be carefully evaluated for individual specimens.

The use of the XRM to study the distribution of elements in a thin section of rat tibia or to measure the density distribution in a complete rat femur illustrates how the XRM can be applied in biological experiments. In particular, gallium nitrate is a therapeutic agent used to treat hypercalcemia in cancer patients. The mechanisms by which gallium acts to inhibit calcium release from bone is not known. Hence, knowledge of the distribution of the gallium in the bone and the bone density is important.

Bockman et al. used the XRM to map the distribution of gallium in the tibia of rats and showed that it accumulated preferentially in areas of highest bone metabolism.⁵ The work has been extended to study rachitic rats treated with gallium and vitamin D. Determinations were made of the concentrations of calcium, iron, zinc, and gallium in line scans across the tibial shaft. A typical result from such a scan (Fig. 4) for a rat that has been treated with both vitamin D and gallium shows that there is a strong spatial variation in the trace elements across the diaphysis. The systematics of the changes and the dependence of the trace element values on gallium concentration can be found from such data. Detailed interpretation of the results obtained in this animal study is now in progress.

In vivo serial measurements of the bone density of the rat femur as a function of treatment would be very useful for study of the gallium treatment. In principle, such measurements can be made by the use of CMT. A tomogram was made of a normal whole rat femur specimen to demonstrate the approach. Bone studies by CMT on living animals are contemplated for the near future.

A channel-cut Si monochromator in which diffraction off the (220) plane is used was mounted in the NSLS X-26C microprobe beam line between a four-jaw slit assembly and a Ta collimator with an opening of approximately 20 \times 20 μ m². If the monochromator is placed before the collimator, x rays diffracted from planes other than the (220) plane can be prevented

from reaching the sample and the detector. The monochromator was rotated by a remotely controlled stepper-motor-driven rotator. The diffraction angle was set to an energy of 10 keV. The energy was verified by use of an Mo foil (K absorption edge at 20.0 keV) and rotation of the collimator while the x rays transmitted through the foil were counted. A 1mm-thick CaF_2 (Eu) scintillation detector operated in current mode was used for the detection of the x rays transmitted through the sample. The sample, a formalin-fixed femur from a normal rat, was placed on a sample stage consisting of two orthogonal stepper-motor-driven translators carrying a rotator (cf. Spanne and Rivers⁶). A $10 \times 20 \mu\text{m}^2$ radiation field was produced by tilting of the Ta collimator relative to the x-ray beam's direction of travel. Both the horizontal and the vertical dimensions of the beam were determined by scanning of a 25 μm -thick Cu foil through the beam while the number of x rays reaching the detector was measured. This procedure gives the edge spread functions in two directions for the system. The data collected during a translate/rotate motion scheme of the sample through the x-ray beam were reconstructed by means of a filtered back projection algorithm.¹⁰

Figure 5 shows a projection image of the whole femur with the plane of the tomogram marked. This image was generated for orientation purposes. Figure 6 shows the computed tomogram at the position marked in Fig. 5. The transverse spatial resolution in this image is approximately 10 μm ; the imaged slice is 20 μm thick. The image shows the fine structure in the bone in detail. In the original image, small remains of bone marrow can also be seen, but this not visible in the reproduction shown in Fig. 6. By sorting of the pixel values in the tomogram into a histogram, a frequency function for the linear attenuation coefficient in the pixels can be produced and used for a further comparison of bones from rats that have been subjected to various diseases and therapies. In wet samples multiple energy allows a more definite separation of soft and bone tissues.

The XRM instrument described above is now being used for elemental analysis and imaging of a number of biological systems. For example, the distribution of essential trace elements (Fe, Cu, Zn, etc.), toxic elements (Pb, Cd, etc.), and therapeutic elements such as Ga is currently being studied in bone, teeth, hair, and soft tissues in the dry state at room temperature and pressure. Provisions to study live tissue culture cells are being made. A facility to keep specimens at liquid nitrogen temperatures for study of low-Z diffusible elements is in the planning stage.

References

1. R. D. Giaume et al., "Measurement of femtogram quantities of trace elements using an x-ray microprobe," *Anal. Chem.* 60: 855, 1988.
2. B. M. Gordon et al., "The application of synchrotron radiation to microprobe trace element analysis of biological samples," *Nucl. Instrum. Methods* B45: 527, 1990.
3. J. W. Criss, *NRLXRF, A Fortran Program for Fluorescence Analysis: Users' Reference Manual and General Documentation*, Cosmic Program #DOD-00065, University of Georgia Office of Computing and Information Services, Athens, GA 30602.
4. K. Themner et al., "Mass loss during x-ray microanalysis," *Nucl. Instrum. Methods* B49: 52, 1990.
5. R. S. Bockman et al., "Distribution of trace levels of therapeutic gallium in bone as mapped by synchrotron x-ray microscopy," *Proc. Natl. Acad. Sci. USA* 87: 4149, 1990.
6. P. Spanne and M. L. Rivers, "Computerized microtomography using synchrotron radiation from the NSLS," *Nucl. Instrum. Methods* B24/25: 1063, 1987.
7. P. Spanne and M. L. Rivers, "Microscopy and elemental analysis in tissue samples using computed microtomography with synchrotron x-rays," *BioSci. Abs.* 1: 101, 1988.
8. P. Spanne, "Microanalysis using computed microtomography and synchrotron x-rays," Presented at BioScience 90, Malmö, Sweden, April, 1990, *BioSci. Abs.* 3.
9. K. W. Jones et al., "Biomedical applications of synchrotron x-ray microscopy," in R. Moro and R. Cesareo, Eds., *Proc. 2nd International Workshop on XRF and PIXE Applications in Life Science, Capri, June 1989*, Singapore, World Scientific Publishing Co., 1990, 163.
10. G. T. Herman, in *Image Reconstruction from Projections: The Fundamentals of Computerized Tomography*, New York: Academic Press, 1980.

CALCIUM IMAGING WITH MONOCHROMATIC X RAYS

B. J. Panessa-Warren, G. T. Tortora, R. L. Stears, and J. B. Warren

By using soft x rays (1-10nm wavelength) to try and image biological materials, one can image unstained and hydrated cells at spatial resolutions approaching 5-10 nm.^{1,2} Unlike imaging cells with electrons and photons in the visible light spectrum, with soft x-ray exposures radiation damage (and to a lesser extent heat damage) is less, in part because the exposure time may range from 60 ns to a few minutes.^{3,4} Samples can also be examined in an hydrated environment at atmospheric pressure.^{5,6} Soft x rays exhibit numerous absorption edges which can be exploited to provide elemental information about biological samples, without the need for specimen preparation. In recent years, with the further development of synchrotron sources and their increased accessibility, it has been possible to obtain high-brightness, intense, tunable monochromatic x rays for biological absorption-edge experiments. This paper analyzes the biological x-ray contact microscopy absorption edge image in light of its biological content in comparison to conventional light and electron microscopic data using genetically identical specimens. X-ray contact microscopy calcium absorption edge and nitrogen absorption edge images of the bacterial endospores *B. subtilis*, *B. thuringiensis*, and *Clostridium sporogenes* were compared to data obtained by light microscopy; fixed, routinely prepared scanning and transmission electron microscopy; and histochemistry, in order to interpret the absorption-edge replicas in terms of their ultrastructural and elemental fidelity. Soft x-ray absorption-edge images made above the calcium LIII absorption edge produced sharp calcium elemental information about each of the biological specimens that was faithful to the elemental data obtained by conventional histochemical methods, and matched the x-ray microanalytical data of Stewart et al. obtained from cryo-thin sections of endospores from similar bacteria.^{7,8}

Materials and Methods

Three varieties of spores were chosen because each has a high calcium content. *Bacil-*

B. J. Panessa-Warren is at the SUNY Department of Allied Health Resources, G. T. Tortora is at the SUNY Department of Medical Technology/Clinical Microbiology, and R. L. Stears is at the SUNY Department of Cell and Developmental Biology, all at Stony Brook, NY 11794; J. B. Warren is at the Brookhaven National Laboratory, Upton, NY 11973. The authors are deeply indebted to Neal Temple and Myron Ledbetter at Brookhaven, without whom this study could not have been completed. This research was sponsored under DOE contract DE-AC02-76CH00016.

lus sp. bacteria were grown aerobically on AK sporulating agar no. 2; and *Clostridium sporogenes* was grown in cooked-meat media. After maximal sporulation, the spores were harvested, heated sporulation, the spores were harvested, heated to 80 C for 20 min to kill any remaining vegetative cells, and washed three times with deionized sterile water for storage at 2-8 C.

For routine scanning electron microscopy (SEM) spores were fixed on an aluminum polished stub in an equal volume of 3% glutaraldehyde in 0.1 M cacodylate buffer (pH 7.2), washed in buffer, postfixed in 1% aqueous osmium tetroxide, dehydrated in acetone, dried by the critical-point method, coated with gold/palladium, and examined at 20 kV accelerating voltage with an AMRay 1000A at Brookhaven National Laboratory, Upton, N. Y. For transmission electron microscopy, isolated spores were layered into warm 2% agar, fixed in 3% glutaraldehyde, buffer washed, postfixed, dehydrated in acetone, embedded in Epon 812, sectioned, and examined at 80 kV on a Philips 300 at Brookhaven National Laboratory. Lanthanum histochemistry was done by either fixing of endospores in 3% glutaraldehyde were washed in water and postfixed in 1% aqueous osmium tetroxide in 1% lanthanum chloride. Spores were also fixed in 1% osmium tetroxide containing 2% potassium pyroantimonate for 1 h to localize calcium.⁹ These agar blocks were prepared for transmission electron microscopy as previously described.

Small aliquots of spore suspension were placed on polymethyl methacrylate coated silicon chips and allowed to settle. The exposures were done at the U 15 beamline of the 750MeV VUV storage ring at the National Synchrotron Light Source, Brookhaven National Laboratory. A calcium sulfate standard was used to map the calcium absorption edge and identify the optimum wavelengths for imaging. Because the endospores are rich in nitrogen, nitrogen absorption-edge images were made of each specimen to obtain general morphology images and for orientation. Following x-ray exposure, the entire biological sample was removed and the photoresist developed in 1:1 methyl isobutyl ketone/isopropanol. The developed resist was coated with gold palladium and examined by SEM.

Results

Figure 1(a) shows the soft x-ray image of the calcium sulfate test specimen/standard above the calcium absorption edge. Each island of salt is clearly outlined with intricate surface structure. Figure 1(b) shows the same calcium sulfate standard imaged below the calcium absorption edge. Here the islands of

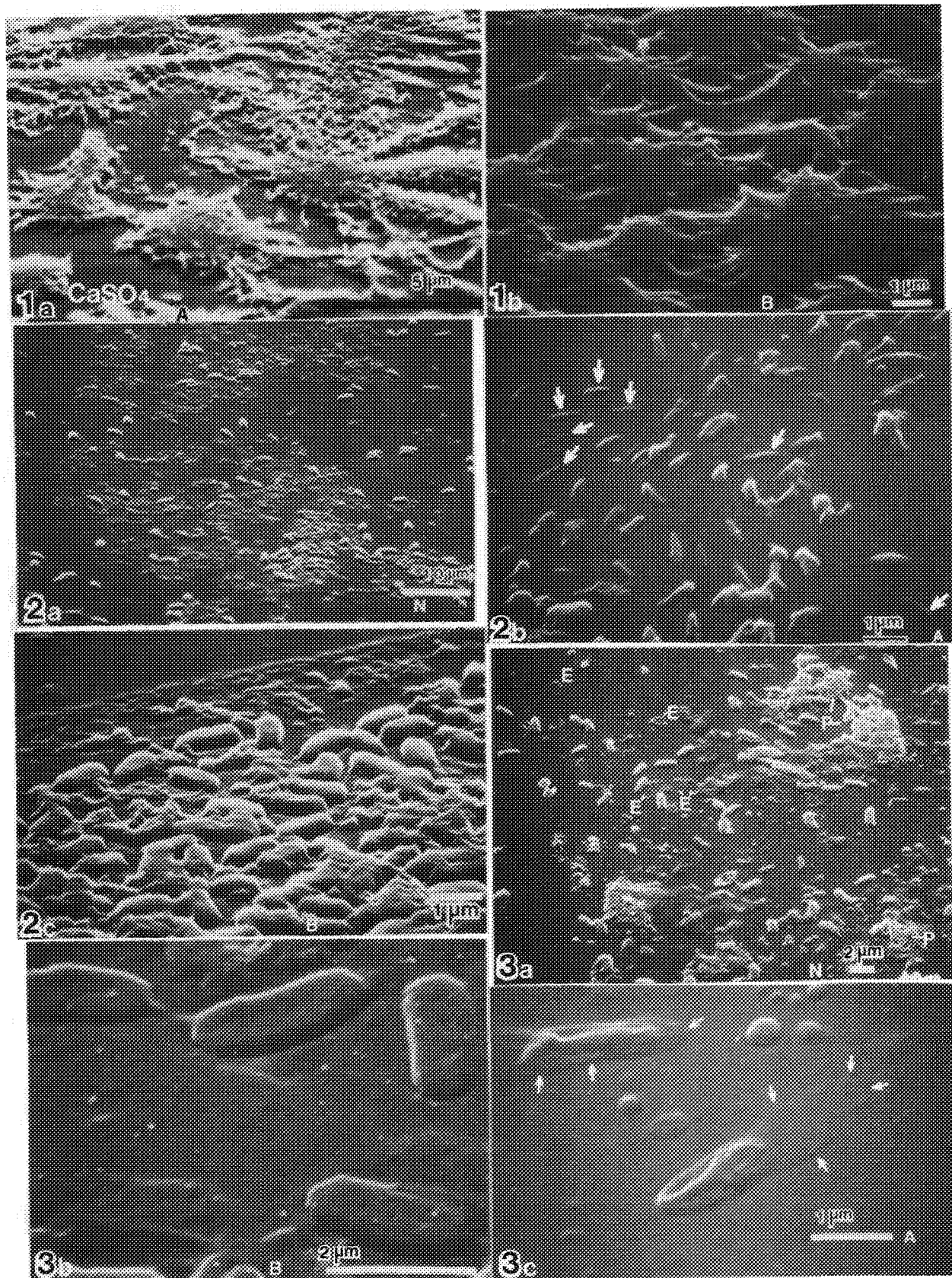


FIG. 1.--(a) X-ray replica of CaSO_4 made above calcium absorption edge (A). (b) Same specimen imaged below absorption edge.
 FIG. 2.--*B. subtilis* spores imaged (a) at nitrogen absorption edge (N), (b) above calcium absorption edge, (c) below calcium edge. Arrows in 2(b) identify alternate form of spores seen.
 FIG. 3.--(a) *B. thuringiensis* endospores imaged at the nitrogen edge (N), (b) below calcium edge, (c) above calcium edge, where the delicate exosporium (white arrows) can be seen enveloping the centrally located spore. E, exosporia; P, protein.

dried salt can also be seen, but they are more softly outlined with virtually no surface detail.

Nitrogen absorption edge images of *B. subtilis* endospores showed x-ray replicas with clearly outline, 3-dimensional rod-shaped spores (Fig. 2a). After tilt-angle correction, the nitrogen image of the spores was identical in morphology to control SEM images of critical point dried samples. The debris around the spores represents the protein-rich contents of lysed spores. In all of the spores examined, images made above the Ca L_{III} absorption edge produced clear crisp spore replicas that revealed fine structure where high levels of calcium were localized histochemically (Figs. 2b and 3c). Nitrogen absorption edge images (Figs. 2a and 3a) all showed plump endospores surrounded by nitrogenous background. Soft x-ray absorption-edge images made below the Ca L_{III} absorption edge revealed a low-relief, flattened outline of the spores in a thick background material (Figs. 2c and 3b). Histochemical data demonstrated that the calcium deposit within the spores is variable depending on the maturation stage of the spore. Similarly, the x-ray images made above the Ca L_{III} edge clearly imaged areas with high calcium preferentially. Below the calcium absorption edge, all imaging of the spores was in low relief with no fine structural details (Figs. 2c and 3b).

References

1. R. Feder et al., "High resolution soft x-ray microscopy," *Science* 197: 259, 1977.
2. B. Panessa-Warren et al., "Imaging unstained proteoglycan aggregates by soft x-ray contact microscopy," *Ultramicros.* 5: 267, 1980.
3. R. McCorkle, "Soft x-ray emission by an electron beam sliding spark device," *Atom. Molec. Phys.* BII: L407, 1978.
4. B. Panessa-Warren, G. Tortora, and J. B. Warren, "Absorption edge imaging of bacterial endospores with synchrotron radiation," *Ultramicros.* 27: 151, 1989.
5. J. Kirz and D. Sayre, "Soft x-ray microscopy of biological specimens," in H. Winick and S. Doniach, Eds., *Synchrotron Radiation Research*, New York: Plenum Press, 1980, 277.
6. B. Panessa-Warren et al., "A wet cell for high resolution imaging of hydrated biological specimens and dynamic processes," *Scanning* 4: 21, 1981.
7. M. Stewart et al., "Scanning electron probe x-ray microanalysis of elemental distributions in freeze dried cryosections of *Bacillus coagulans* spores," *J. Bact.* 147: 670, 1981.
8. M. Stewart et al., "Distribution of calcium and other elements in cryosectioned *Bacillus cereus* T. spores, determined by high resolution scanning electron probe x-ray microanalysis," *J. Bact.* 143: 481, 1980.
9. S. Atsumi and H. Sugi, "Localization of calcium accumulating structures in the anterior byssal retractor muscle of *Mytilus edulis*," *J. Physiol.* 257: 59, 1976.

PATHOPHYSIOLOGICAL FUNCTION OF THE MITOCHONDRIA AS A CALCIUM RESERVOIR: QUANTITATIVE X-RAY MICROANALYSIS

N. Kaneko, K. Teraoka, Y. Horikawa, T. Uchida, R. Matsuda, S. Hosoda, and S. Nakamura

It is generally known that irreversible injury of the myocardium induced by ischemic conditions is accompanied by the accumulation of calcium in the mitochondria.¹⁻³ However, the physiological significance of this phenomenon, and the possible role of the mitochondria under such conditions of calcium loading, has not been well understood. In this investigation, in order to gain more insight into the relationship between calcium loading and mitochondrial calcium accumulation, calcium loading was carried out in rat myocardium, and x-ray analysis was employed in the determination of cytosolic and mitochondrial calcium levels.

Perfusion was carried out as in the classical Langendorff method; a change in the concentration of calcium in the perfusate from 2 mM CaCl_2 to 5.5 mM CaCl_2 produced an immediate rise in left ventricular systolic pressure. Within 1 min following the commencement of calcium loading, there was a clear increase in mitochondrial calcium; further increases were seen with time. In tissue samples freeze-dried under vacuum, sectioned, and observed by electron microscopy, mitochondrial calcium uptake was manifested by the appearance of electron-dense granules.

Materials and Methods

Perfusion. Twelve pure-bred Wistar rats (17 weeks old) were employed. Rats were sacrificed by cervical dislocation, after which hearts were quickly excised and immersed in perfusate solution chilled to 40°C. For each heart, a catheter was inserted into the ascending aorta, and retrograde perfusion was carried out as in the Langendorff method. Perfusate solution consisted of Krebs-Henseleit buffer, containing (in mM), NaCl (120), KCl (4.7), MgSO_4 (1.2), KH_2PO_4 (1.2), NaHCO_3 (25), and glucose(5), gassed with 95% O_2 and 5% CO_2 . Perfusate calcium concentration in the control group was 2mM CaCl_2 , and for the calcium-loading group, it was 5.5mM CaCl_2 . Pacing leads were inserted into the right atrium and apex, and pacing was

The authors at the Department of Cardiology (except R. Matsuda, who is at the Department of Biochemistry), Tokyo Women's Medical College, Tokyo, Japan; and except S. Nakamura, who is at Nissei Sangyo Corp. This research was supported in part by a grant from the Ministry of Education, Science and Culture, Japan, and an Open Research Grant from the Japan Research Promotion Society for Cardiovascular Diseases. We also thank Marcy N. Wilder, University of Tokyo, for translation assistance in the preparation of the manuscript.

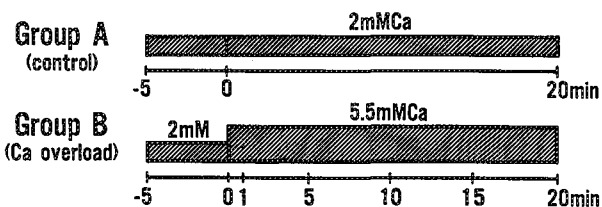


FIG. 1.--Experimental protocol.

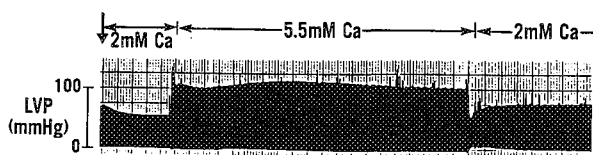


FIG. 2.--Recording of left ventricular pressure during calcium-overload.

carried out at 330/min. Perfusate temperature was maintained at 37°C during time. In addition, 4 rats were inserted with balloons in the left ventricle, and left ventricular pressure was monitored and recorded.

Experimental Design. Experimental protocol is delineated in Fig. 1. Two animal groups were employed; in both groups, 2 mM CaCl_2 was perfused for an initial 5 min. Group A (control) was perfused in this manner for an additional 20 min. Group B (calcium-overload) was switched to 5.5 mM CaCl_2 , and hearts in this group were perfused for up to 1, 5, 10, or 20 min and then removed from the perfusion apparatus. In both groups, tissue from the left ventricular papillary muscle was utilized in the determination of intracellular calcium. One to 3 papillary muscles were dissected out per rat.

Cytosolic Mitochondrial Calcium Determination by X-ray Analysis. Papillary muscle tissue specimens were halved longitudinally and attached by the endocardium layer to tissue mounting pins; subsequently, tissue was quick-frozen in a Reichert-Jung KF 80/MM 80 and copper blocks chilled under liquid nitrogen. Cryoultramicrotomy was performed on a Reichert-Jung Ultracut N Fc-4E, and the resulting sections were attached to collodium-carbon coated 200-mesh grids and freeze-dried (-100°C, 10^{-5} Torr) in a JEOL FD7000. Last, a JEOL 1200 EX and an energy-dispersive x-ray analyzer were used in the determination of

calcium levels in the cytosol and mitochondria.

Results

1. Increasing calcium concentrations in the perfusate from 2 to 5.5 mM produced an immediate rise in systolic pressure of the left ventricle when concentrations were returned to 2mM, systolic pressure once again decreased to basal levels. Pressure changes under calcium loading are shown in Fig. 2.

2. Calcium concentrations in the cytosol and mitochondria determined by x-ray microanalysis are shown in Table 1. In the control group, cytosolic and mitochondrial concentrations were 15.8 ± 11.4 and 19.0 ± 15.0 mmol/kg dry wt, respectively. In the calcium-loading group, within 1 min after the commencement of 5.5 mM perfusion, an immediate increase in mitochondrial calcium concentrations to 95.9 ± 32.7 mmol/kg was seen, but cytosolic calcium remained low at 17.0 ± 2.4 mmol/kg. Further increases in mitochondrial calcium levels were seen with time; after 10 and 20 min of calcium-loading, concentrations reached 569.2 ± 221.5 and 562.0 ± 331.1 mmol/kg dry wt. However, regarding the cytosol, no significant differences in calcium concentration were observed between the control and calcium-loading group at any point during perfusion.

3. Tissue samples in both groups were freeze-dried and cryoultrasectioned. The presence of electron-dense granules in calcium-loaded myocardium was revealed by electron microscopy. In the control group, such granules were not present (Fig. 3). X-ray spectra of the cytosol and mitochondria used in calcium determination are shown in Figs. 4(a) and (b)

TABLE 1.--Calcium content of mitochondria and cytosol (mmol/kg dry weight).

	Cytosol	Mitochondria
Group A (control)	15.8 ± 11.4	19.0 ± 15.0
Group B (Ca overload)		
1 min	17.0 ± 2.4	95.9 ± 32.7
5 min	23.7 ± 8.3	250.0 ± 92.0
10 min	23.2 ± 10.3	569.2 ± 221.5
20 min	16.6 ± 18.9	562.0 ± 331.1

(Ca-overload group). A clear calcium peak appears in the spectrum corresponding to calcium-loaded mitochondria only.

Discussion and Conclusions

It has recently become possible to determine intracellular calcium concentration at the level of electron microscopy by employing quick-freezing techniques together with x-ray microanalysis. Jennings et al. have reported that calcium uptake by mitochondria can be stimulated by reperfusion in ischemic myocardium,¹ but there are as yet few reports addressing the physiological significance of this phenomenon^{4,5} and the possible role of the mitochondria in intracellular calcium regulation.⁶ That calcium ion is extremely important in excitation-contraction coupling of the myocardium is well

established; on the other hand, investigations on catecholamine-induced myocardial injury have revealed that an excess influx of calcium into the myocytes is a cause of myocardial damage. Fleckenstein et al.⁷ have shown that massive dosages of isoproterenol (30 mg/kg) result in rapid uptake of Ca^{45} by the myocytes; through these results, they have demonstrated the involvement of extreme calcium ion influx into the myocytes in the development of myocardial necrosis. In our previous investigations, we have shown that the selective administration of calcium chloride into the coronary artery results in myocardial necrosis resembling that ordinarily seen with myocardial infarction.⁸ Such results have suggested that increases in intracellular calcium are highly significant in bringing about cell damage and necrosis. In the present investigation, we examined the effects of calcium loading on ventricular pressure and mitochondrial functioning via Langendorff perfusion and x-ray microanalysis. It was observed that in hearts perfused initially with 2 mM CaCl_2 , with conditions changing from that of calcium loading (5.5 mM CaCl_2), systolic pressure immediately increased. These changes in pressure were reversible upon restoration of initial conditions of perfusion. In a related investigation, we have determined that the release of creatine phosphokinase (CPK) and decreases in ATP levels did not occur during calcium loading; correspondingly, by electron and light microscopy, we have also observed that no significant histological changes resulted in the myocardium.⁹ From the above results encompassing several investigations, we conclude that

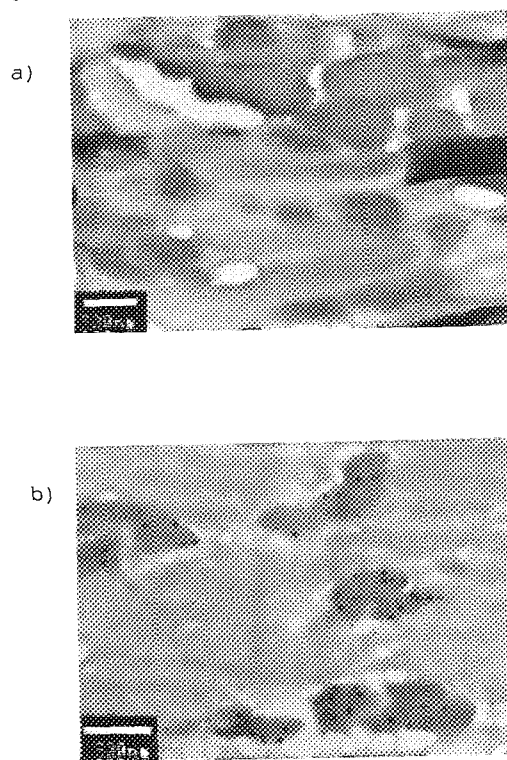


FIG. 3.--Transmission electron micrograph. (a) control, (b) calcium overload (5 min following 5.5 mM calcium perfusion). Presence of electron-dense granules was observed in calcium-overloaded mitochondria.

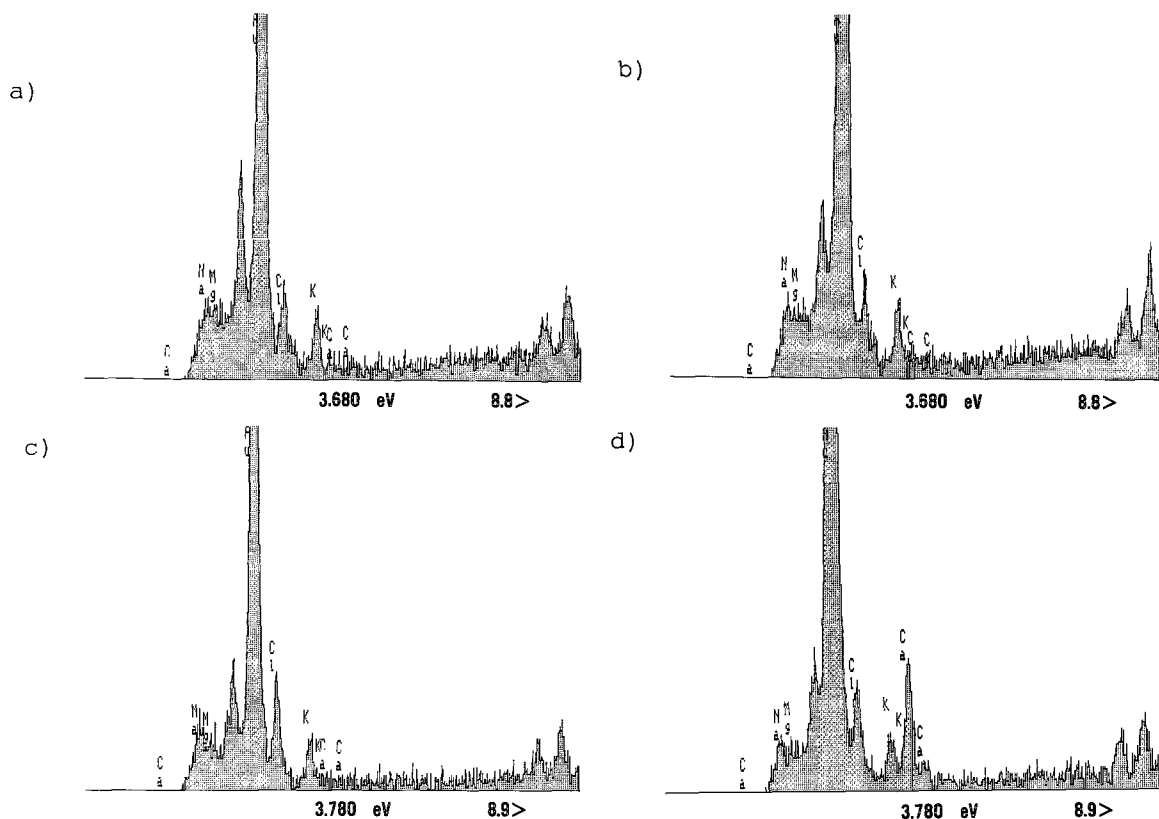


FIG. 4.--X-ray spectrum. (a) Cytosol in control group; (b) mitochondria in control group; (c) cytosol in calcium overload (5 min); (d) mitochondria in calcium overload (5 min) with clear calcium peak observed in mitochondria following calcium overload.

under observation of our experimental protocol.

Through the present investigation, we have revealed that mitochondrial calcium uptake during calcium loading is rapid and immediate. The data have indicated that calcium accumulation in the mitochondria is manifest within 1 min of the commencement of experimental calcium loading, which was observed as an increase from basal levels of 19.0 ± 15.0 to 95.9 ± 32.7 mmol/kg dry wt. As these levels were seen to have increased nearly 6-fold during a 20min duration of perfusion, our results suggest that as intracellular calcium increases, the mitochondria in response actively take up calcium. Regarding the physiological significance of this phenomenon, it may be likely that the mitochondria function as a calcium reservoir in the myocytes in order to maintain intracellular calcium at normal levels and thereby circumvent cell injury.

References

1. R. B. Jennings et al., *Circ. Res.* 34 (Suppl. III): 156-172, 1974.
2. D. J. Hearse et al., *J. Mol. Cell. Cardiol.* 10: 641, 1978.
3. N. S. Dhalla et al., *Basic Res. Cardiol.* 77: 117, 1982.
4. R. Ferrari et al., *European Heart J.* 7: 3, 1986.
5. W. G. Nayler et al., *J. Mol. Cell. Cardiol.* 20(Suppl. 2): 41, 1988.
6. D. J. Miller, *Nature* 313: 638, 1985.
7. A. Fleckenstein et al., in E. Bajusz et al., Eds., *Cardiomyopathies*, Baltimore: University Park Press, vol. 2, 1973, 455.
8. N. Kaneko et al., *European Heart J.* 10(Suppl.): 393, 1989.
9. N. Kaneko et al., *Jpn. Cir. J., Proc. 54th Ann. Meet. Fukuoka*, 1990, 43-44.

SUBCELLULAR CALCIUM CONTENT OF MYOCARDIUM AFTER ISCHEMIA AND REPERFUSION: X-RAY MICROANALYSIS

Yoshifumi Horikawa, Noboru Kaneko, Kunihiro Teraoka, Tatsuroh Uchida,
Saichi Hosoda, and Ryuhko Matsuda

We have reported previously on the calcium accumulation in mitochondria following ischemia,¹ and other authors have confirmed these observations.²⁻⁴ It is generally agreed that calcium accumulation within the mitochondria is the result of irreversible injury.^{5,6} However, there are some reports^{7,8} that mitochondria play a role in intracellular calcium regulation. If calcium accumulated in the mitochondria following ischemia were to be decreased by reperfusion, it would suggest that mitochondria may play a part in intracellular calcium regulation. The goal of this study is to clarify whether calcium content in the mitochondria after a 30 min period of ischemia is altered by reperfusion for 60 min.

Rat hearts were circulated with the control (95%O₂, 80cmH₂O) or the ischemic (50%O₂, 15cmH₂O) Krebs-Henseleit solution by the Langendorff method. They were divided to the control group, the ischemia group, and the reperfusion group. The papillary muscles were rapidly frozen by the metal contact method and cryo-ultrasectioned. After freeze-drying, calcium content was measured by energy-dispersive x-ray microanalysis. Mitochondrial calcium accumulation was observed in the ischemia and reperfusion groups. However, the mitochondrial calcium content of the reperfusion group was significantly decreased when compared to the ischemia group. These results suggest that mitochondrial calcium accumulation is reversible and that the mitochondria may play a part in intracellular calcium regulation.

Material

Nine adult male Wistar rats were killed by cervical dislocation. The heart was quickly removed and immediately chilled to 4 C. The aorta was cannulated and the heart was circulated by the Langendorff method. The heart was stimulated to 330 beats/min by a pacemaker. The experiments were performed at 37 C. The perfusate was Krebs-Henseleit solution containing (in mmol/L): NaCl 120, KCl 4.7, MgSO₄ 1.2, KH₂PO₄ 1.2, CaCl₂ 2.0, NaHCO₃ 25, and glucose 5.0. The hearts were divided into three groups.

1. Control group. This group was perfused for 30 min with a Krebs-Henseleit solution bubbled by a 95%O₂ + 5%CO₂ gas mixture at a pressure of 80 cm water.

2. Ischemia group. This group was perfused for 30 min with a Krebs-Henseleit solution bubbled by a 50%O₂ + 45%N₂ + 5%CO₂ gas mixture at a pressure of 15 cm water.

3. Reperfusion group. Following the 30min period of ischemia, this group was perfused for 60 min with a Krebs-Henseleit solution bubbled by a 95%O₂ + 5%CO₂ gas mixture at a pressure of 80 cm water.

Method

Specimens were taken from the papillary muscles of the left ventricle immediately after perfusion. These specimens were quickly mounted on tissue-mounting pins and fired onto a liquid nitrogen cooled copper block. The specimens were frozen by use of a Reichert-Jung KF 80/MM 80. These pins with specimens were mounted in the arm of a Reichert-Jung Ultracut N FC4E and specimens were cryo-ultrasectioned. The specimens and the knife were set and maintained between -140 and -160 C. Sections were cut to a thickness of approximately 90 nm. These sections were transferred to 400-mesh copper grids coated with collodion-carbon. The grid with sections was placed in a JEOL FD7000 and freeze-dried at -100 C in 10⁻⁵ Torr. After freeze-drying, they were observed in an electron microscope (JEOL 1200EX); the calcium content was measured by an energy-dispersive x-ray microanalyzer and calculated by the peak-to-continuum ratio, proportional concentration as described by Hall et al.⁹ (Link AN 10000S). The microscope was operated in the TEM mode at 80 keV and measurements were made for 100 s.

Statistical Analysis

Data was expressed as mean values ± standard deviation. For statistical analysis, the unpaired t-test was performed between groups.

Results

Transmission electron microscopy of the papillary muscles after they were freeze-substituted in osmium acetone was performed to evaluate the general quality of tissue preservation following rapid freezing. The cardiac cells below 5 to 10 μm from the endocardium demonstrated virtually no ice crystal formation. We used sections for x-ray microanalysis below 5 μm from the endocardium. Transmission electron micrographs of freeze-dried papillary muscle were obtained of the control group (Fig. 1), the ischemia group (Fig. 2), and the reperfusion group (Fig. 3).

The authors are at the Department of Cardiology (except R. Matsuda, who is at the Department of Biochemistry), Tokyo Women's Medical College, Tokyo, Japan.

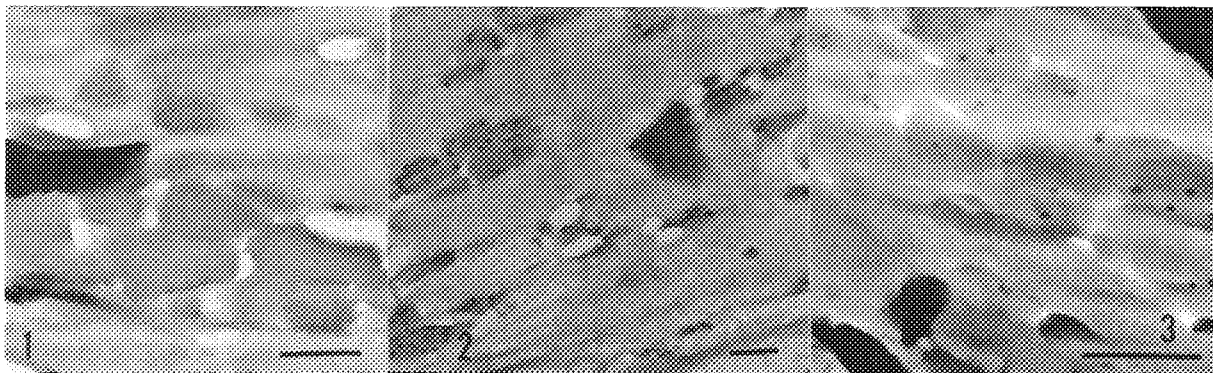


FIG. 1.--Transmission electron micrograph of freeze-dried papillary muscle of control group. Mitochondria have no electron-dense inclusions. Bar: 500 nm.

FIG. 2.--Transmission electron micrograph of freeze-dried papillary muscle of ischemia group. Mitochondria have electron-dense inclusions. Bar: 500 nm.

FIG. 3.--Transmission electron micrograph of freeze-dried papillary muscle of reperfusion group. Mitochondria also have electron-dense inclusions; however, more inclusions are noted in ischemia group than in reperfusion group. Bar: 500 nm.

The muscle cells had dense ovoid structures with the size and distribution of mitochondria. In these pictures, no other ultrastructural element was identifiable. In the ischemia and reperfusion groups, the mitochondria had electron-dense inclusions, but in the control group, no such inclusions were observed. More inclusions were noted in the ischemia group than in the reperfusion group. Mitochondria and cytosol calcium content was measured by energy-dispersive x-ray microanalysis. The spectra of the control group were obtained. The characteristic calcium peak is not observed in either the mitochondria (Fig. 4) or the cytosol (Fig. 5). The spectra of the ischemia group demonstrate a prominent calcium peak in the mitochondria (Fig. 6), but not in the cytosol (Fig. 7). In the spectra of the reperfusion group, the calcium peak is also observed in the mitochondria (Fig. 8), but not in the cytosol (Fig. 9). However, the mitochondrial calcium peak of the reperfusion group is lower than the calcium peak of the ischemia group. The calcium content was calculated from each spectrum, and the graph of the change in the calcium content of the mitochondria and the cytosol was plotted (Fig. 10). The calcium was remarkably accumulated into the mitochondria following ischemia (202.3 ± 51.9 mmol/kg dry weight, control 3.8 ± 1.6 , $p < 0.01$). Also, the calcium accumulation into the mitochondria was observed in the reperfusion group (103.6 ± 16.4). However, the calcium content of the mitochondria of the reperfusion after 30 min of ischemia was significantly reduced when compared to the ischemia group ($p < 0.01$). No significant changes were observed in the cytosol calcium concentration among the three groups.

Discussion

It was demonstrated by x-ray microanalysis that calcium was accumulated into the mito-

chondria during ischemia, and the calcium was significantly reduced by a 60min reperfusion period. From these results, it is thought that calcium accumulation into the mitochondria is at least partially reversible and that the mitochondria takes up calcium in an attempt to prevent the increase in intracellular calcium concentration and irreversible cell injury.

It is generally thought that the free calcium concentration in the cytosol is increased during ischemia and immediately after reperfusion by indo 1¹⁰ and aequorin.¹¹ An increase in calcium concentration was not observed in the cytosol by x-ray microanalysis. Measurements of low calcium concentration in the cytosol are limited by the accuracy of x-ray microanalysis. We look forward to the development of more accurate x-ray microanalysis. Recently, it has been suggested that calcium concentration increases immediately after reperfusion.¹²⁻¹⁴ This study was designed to address the reversibility of calcium accumulation. Although we did not measure the calcium content immediately after reperfusion, we hypothesize that more calcium may be accumulated into the mitochondria immediately following reperfusion than after 30 min of ischemia.

We concluded that calcium accumulation into the mitochondria is reversible to some degree, and that mitochondria may play a part in intracellular calcium regulation.

References

1. Y. Horikawa et al., *European Heart J.* 10: 268, 1989.
2. A. V. Somlyo et al., *Proc. 33th Ann. Meet. EMSA*, 532, 1975.
3. L. M. Buja et al., *Circulation* 68: 872, 1983.
4. H. K. Haguler et al., *Annals New York Acad. Sci.* 428: 68, 1984.

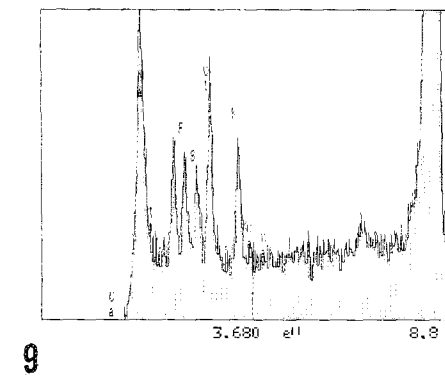
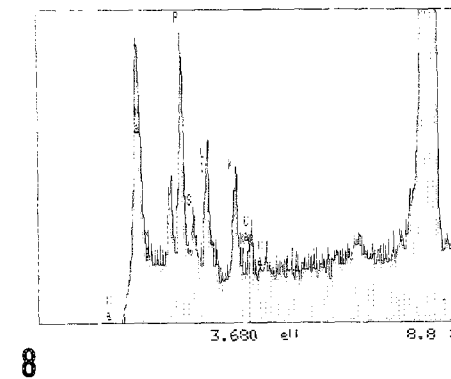
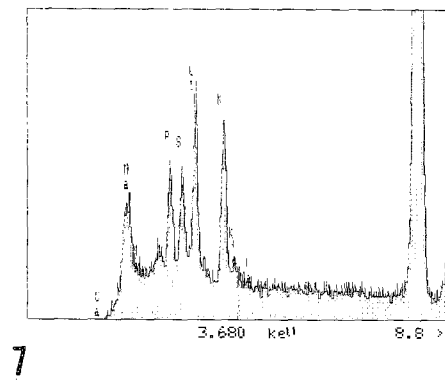
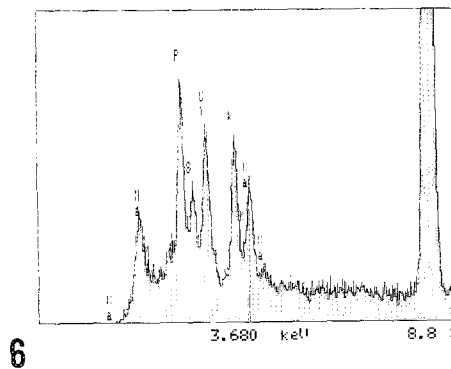
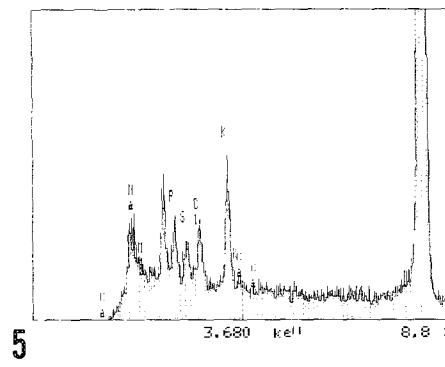
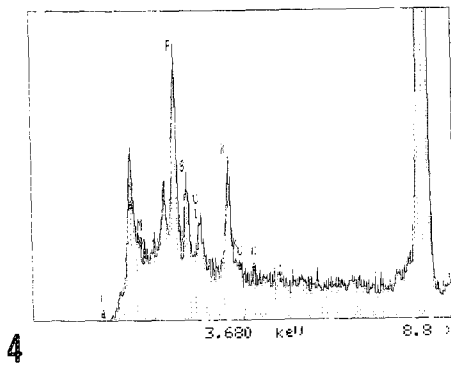


FIG. 4.--Spectrum of mitochondria in control group.

FIG. 5.--Spectrum of cytosol in control group.

FIG. 6.--Spectrum of mitochondria in ischemia group. Note prominent calcium peak.

FIG. 7.--Spectrum of cytosol in ischemia group.

FIG. 8.--Spectrum of mitochondria in reperfusion group. Calcium peak is also observed; however, calcium peak of reperfusion group is lower than that of ischemia group.

FIG. 9.--Spectrum of cytosol in reperfusion group.

5. D. J. Hearse et al., *J. Mol. Cell. Cardiology* 10: 641, 1978.
6. N. S. Dhalla et al., *Basic Res. Cardiol.* 77: 117, 1982.
7. A. L. Lehninger et al., in *Calcium and Phosphate Transport Across Biomembranes*, New York: Academic Press, 1981, 73.
8. D. J. Miller, *Nature* 313: 638, 1985.
9. T. A. Hall et al., *Physical Techniques in Biological Research*, vol. 1, 1971, 157.
10. Hoh-Chi Lee et al., *Circulation* 78: 1047, 1988.
11. A. Ashley et al., *Biochem. J.* 244: 381, 1987.
12. R. Ferrari et al., *European Heart J.* 7: 3, 1986.

13. D. Stone et al., *J. Mol. Cell. Cardiol.* 21: 963, 1989.

14. W. G. Nayler et al., *J. Mol. Cell. Cardiol.* 20(suppl 2): 41, 1988.

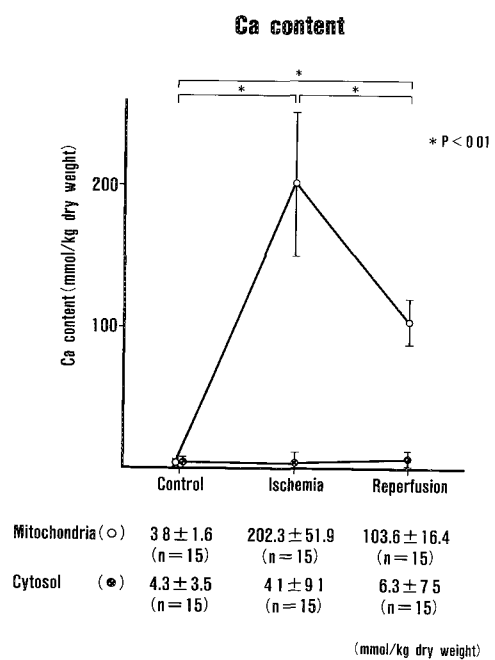


FIG. 10.--Change in calcium content of mitochondria and cytosol.

HIGH-EFFICIENCY X-RAY MONOCHROMATOR FOR MEASUREMENT OF Ca IN THE TEM

Songquan Sun, J. McD. Tormey, and D. B. Wittry

A novel miniature wavelength dispersive (WDS) monochromator with an LiF crystal has been developed for use in a transmission electron microscope (JEOL 100CX). Our goal has been to improve on the limited sensitivity available when energy-dispersive spectrometry (EDS) is used to measure low concentrations of Ca in biological tissues. This paper presents the calculated performance, design features, and experimental results.

Limitations of EDS

When EDS is used to measure biological Ca in an electron column instrument, precision is severely limited by counting statistics. EDS was used by Tormey to quantify Ca in cardiac muscle, employing procedures similar to those used by Shuman et al.¹ In a typical application, myofibrillar Ca increased from 1.4 ± 0.2 to 2.6 ± 0.3 mmol/kg dry wt when going from rest to contracture.² This precision (\pm standard error of mean) was the result of 125 measurements in each condition. Since each individual measurement took 400 s live time, this result required over 30 h of acquisition time. The situation under which these measurements were made was nearly ideal. Furthermore, an analysis of variance showed that this result was obtained with minimal biological variation and fluctuations in systematic errors.²

The inherent error in each 400 sec measurement is accounted for by Poisson counting statistics. The expected error in Ca peak counts is $\sqrt{(S + B) + B}$, where S is signal counts and B is background counts. A typical peak (FWHM 130 eV) consists of 65 signal counts in a 240eV-wide window containing 4000 counts. Half the background is bremsstrahlung and the rest is overlap from the neighboring potassium peak. (The concentration of potassium in these cells is typically 500 times greater than that of calcium.) The expected error evaluates to ± 89 counts and is in good agreement with independent estimates from least squares fitting statistics.

Expected Improvement with WDS

A comparison of WDS and EDS can be made based on the minimum detection limits as a function of the signal to background ratio, the signal, and the measurement time. The detection limit is given by Curie³:

$$C_{MD} = 3.29 C_s \sqrt{\eta B / S} \quad (1)$$

where C_s is the mass fraction of a standard specimen and η varies between 1 and 2 depending on the accuracy of background determination. In EDS the full signal is spread over many channels. It has been suggested when the peak-to-background ratio is very small, the optimum window size would be $1.82 \times \text{FWHM}$.⁴ We therefore use all the background in a 240eV-wide window to calculate C_{MD} for EDS. In WDS, however, if the natural line width is narrow, a monochromator collects all the signal when set at the peak. Hence, only the background that would be passed by a fixed monochromator is used to calculate C_{MD} for WDS.

The key part of a monochromator is the diffractor. A doubly curved diffractor with point-to-point focusing could theoretically have high collection efficiency and energy resolution as shown by Wittry and Sun.⁵ The new WDS monochromator used LiF(111) single crystal material (from Harshaw crystal distributor, Englehard Corp.) which is doubly curved to the point-to-point focusing geometry for a Bragg angle 46.26° . This geometry has a toroidally curved surface and toroidally curved planes equivalent to rotation of the Johansson geometry about a line passing through the source and image points. If the crystal is well bent, the whole surface of this diffractor diffracts the Ca $K\alpha$ incident x rays; the elliptically shaped diffractor measuring $5.0 \text{ cm} \times 3.5 \text{ cm}$ subtends approximately the same solid angle as the EDS detector, namely, 0.075 sr . The diffracting efficiency of the diffractor could be 25% to 33%, considering polarization effects, along with effects of absorption, strains, and dislocations in the crystal. To find the appropriate polarization effect it is helpful to note that when x rays are diffracted, the component K_\perp whose electric vector is perpendicular to the plane containing the incident and diffracted ray is not affected, but the parallel component K_\parallel reduced by a factor of $\cos 2\theta$ for a perfect crystal or $\cos^2 2\theta$ for a mosaic crystal.⁶ In our case, since the incident radiation is unpolarized, each component has the relative value of $1/2$, and also the diffractor is mosaic; the maximum intensity I_m is

$$I_m = \left[\frac{1}{2} + \cos^2(2\theta)/2 \right] \times I_0 \quad (2)$$

where I_0 is the incident intensity. For $\theta = 46.26^\circ$, $I_m \sim 0.5 I_0$. The efficiency loss due to strains and dislocations could not be calculated because it is determined by bending and surface conditions.

Assuming the EDS detector is 100% efficient,

S. Sun and D. B. Wittry are at the USC Department of Materials Science, Los Angeles, CA 90089-0241; J. McD. Tormey is at the Department of Physiology, UCLA School of Medicine, Los Angeles, CA 90024-1751. This work was supported in part by NIH grant HL31249 to J. McD. T.

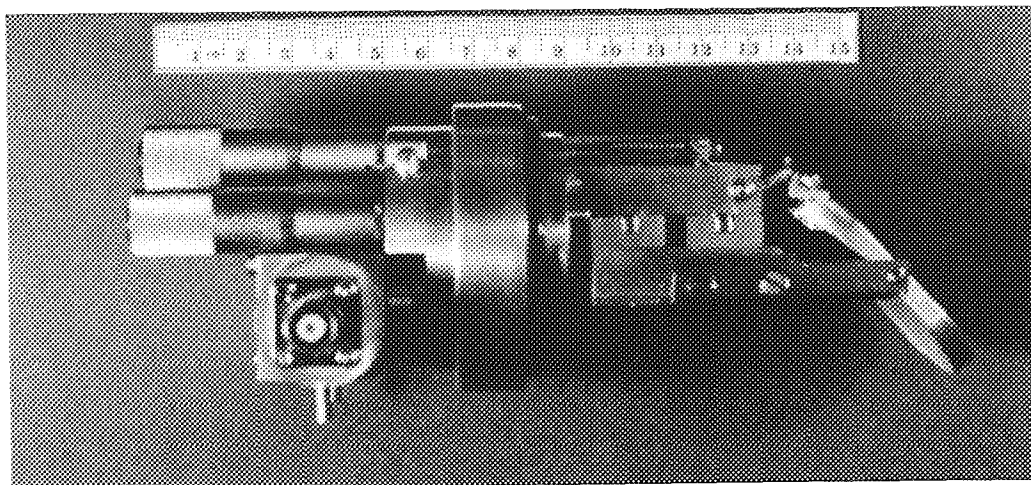


FIG. 1.--WDS monochromator.

the signal-to-background ratio for WDS would be 78-fold higher than for EDS; this assumes the WDS resolution to be 6 eV FWHM. Half the improvement would arise from elimination of the overlap between potassium $K\beta$ (3589 eV) and calcium $K\alpha$ (3690 eV) peaks; these peaks correspond to Bragg angles of 47.98° and 46.26° respectively. The rest of the improvement is due to reduced bremsstrahlung transmitted by the monochromator's narrow bandpass. The ratio of detection limits for WDS vs EDS based on Curie's definition would be 1/5. This corresponds to a 25-fold reduction of measurement time for the same detection limits. The calculation of these results are given as follows:

$$\frac{(S/B)_{EDS}}{(S/B)_{WDS}} = \frac{(FWHM)_{WDS}}{1.82 \times 2 \times (FWHM)_{EDS}}$$

$$= \frac{6}{1.82 \times 2 \times 130} = \frac{1}{78} \quad (3)$$

The ratio of detection limits for WDS and EDS is

$$\frac{(C_{MD})_{WDS}}{(C_{MD})_{EDS}} = \frac{\sqrt{B_{EDS}} \times (S/B)_{EDS}}{\sqrt{B_{WDS}} \times (S/B)_{WDS}} = \frac{1}{5} \quad (4)$$

Since the measurement time is inversely proportional to the square of minimum detection limits, a 25-fold reduction of measurement time for the same detection limits could be obtained from the result of Eq. (4).

Design Features

Figure 1 shows the monochromator; Fig. 2 is a schematic diagram. The crystal diffractor is fabricated by double bending of a cylindrically cut 0.25mm-thick LiF crystal lamella. To make a good LiF diffractor, about 20 fabrication steps (including all cutting, grinding, polishing, bending, and final preparation) are needed. The detailed description of the fabrication of this type of diffractor was given by Golijanin, Wittry, and Sun.⁷

Figure 3 shows the overall geometric conditions, as follows: (1) $2d \sin \theta_B = \lambda$, where d is the spacing of crystal planes, λ is the wave-

length of incident x rays, and θ_B is Bragg angle; (2) $MI = MS = 2R_1 \sin \theta_B$, where MS and MI is the distance between the midpoint of the diffractor and the sample and the image on the window of detector respectively, and R_1 is the radius of focal circle; (3) the focal circle passes through points S , M , and I ; (4) the curvature of the diffractor surface in a direction perpendicular to the plane of focal circle is R_2 , where $R_2 = 2R_1 \sin^2 \theta_B$.

Therefore we have designed and constructed a mechanism that provides three angular alignments θ , ϕ , and δ . The θ alignment ($46 \pm 2.5^\circ$) is used for Bragg angle scanning and the ϕ alignment ($0 \pm 3^\circ$) is utilized so the diffractor will be symmetrical about a line through the source and image points. It is necessary to have a small rotation of the whole assembly ($\delta = \pm 0.5^\circ$) with respect to the plane containing focal circle to allow for fabrication errors and possible slight misalignment of (111) planes of the block of LiF used.

The detector is a flow proportional counter using P-10 gas and has a window of aluminized mylar film 5.08 μm on top of an aluminum foil 1.27 μm thick. The efficiency of this detector is calculated to be 66%, taking account of the calculated absorption by the argon (95%), experimentally determined transmission of the window (77%), and calculated net counts after including the escape peak effects (90.4%).

The escape peak reduces the detector efficiency because its pulse height is proportional to the difference between energy of incident x-ray photon and energy of the argon $K\alpha$ photon.

Fortuitously, the JEOL 100CX instrument has space for the diffractor above the specimen and a port in the front wall for the diffracted beam, so that no modifications to the electron microscope are required. Therefore, the LiF crystal diffractor, alignment mechanism, and detector are all contained in a compact assembly that fits through the existing port above the objective polepiece assembly.

Preliminary Experimental Results

Initial bench tests were first carried out

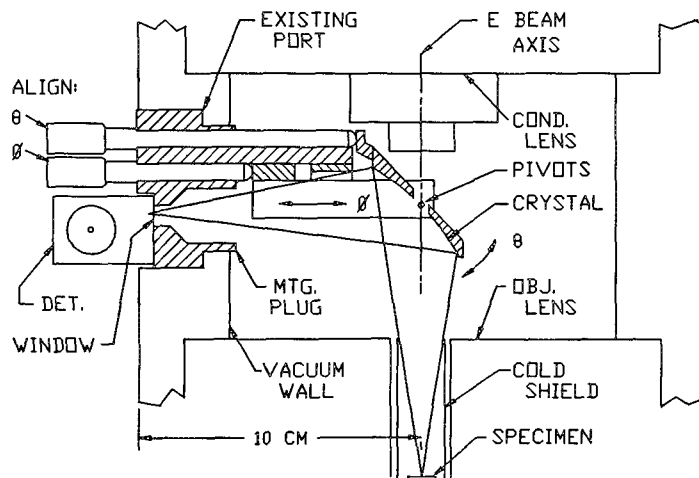


FIG. 2.--Schematic diagram of WDS monochromator.

using a pure Ca target in a microfocus x-ray unit that was constructed from parts from the EMX-SM electron probe microanalyzer; then the monochromator was put into the electron microscope.

A 10% diffracting efficiency was obtained based on the ratio of intensity of diffracted beam to the intensity of direct beam in the bench test. However, measurements in the JEOL 100CX with simultaneous detection by EDS indicated a much lower efficiency ($\sim 1\%$). It is thought that the discrepancy is due to an error in the bench test that resulted from dead time effects in the detector, since it was subsequently found to be operating outside the proportional region.

In the JEOL 100CX TEM, three targets were used: pure calcium; pure titanium; and a potassium compound, orthoclase (KAlSi_3O_8). These targets could be placed on the Rowland circle passing through the LiF diffractor by adjusting the microscope sample stage in the x-y direction. The Z adjustment of sample stage and θ , ϕ , and δ adjustments of the monochromator were used with the monochromator in the TEM column to obtain a precise alignment.

The pure calcium target was used for alignment and measurement of efficiency. However, we cannot measure the background accurately by detuning the diffractor with this particular geometry since the collection efficiency changes with the θ adjustment. Hence the pure titanium target was used to determine background from the continuum, since Ca and Ti have similar atomic number. The potassium compound target was used to study the $\text{K}\beta$ peak and background to evaluate the sensitivity of the spectrometer at wavelengths different from the Ca $\text{K}\alpha$ radiation.

In order to achieve the estimated improvements in acquisition time, it will be necessary to use WDS to measure the Ca peak while using EDS to evaluate the background. This is a possible procedure because the WDS system does not interfere with the simultaneous use of the EDS system. So far, 10 700 cps was obtained using EDS with Si(Li) detector and Link AN10000 system, and 70 cps using WDS with an ORTEC-490B

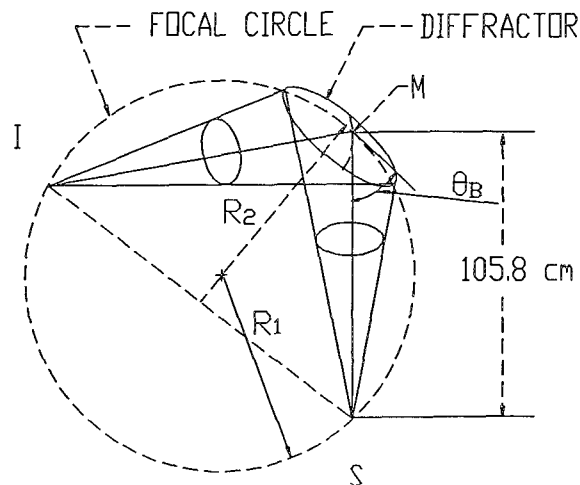


FIG. 3.--Geometry of monochromator optics.

single-channel analyzer and Anadex-CF204 timer and scaler; taking into account the 66% detector efficiency, the diffractor efficiency was about 1%.

Discussion

Up to now, the experiment is still in progress. The preliminary results are quite different from theoretical estimates; the discrepancy between the anticipated efficiency and experimental results may be attributed to the following.

1. The raw LiF block material was misaligned to some extent, which caused the (111) plane to be slightly tilted with respect to the surface. This misalignment was confirmed by a topograph of the bulk LiF material used for making the diffractor.
2. The diffractor was imperfectly bent and had an incorrect surface treatment.
3. The solid angle of collection by the diffractor was less than 0.075 sr because about 10% of area was lost due to some avoidable obstruction by the diffractor mounting.

Imperfect bending is the dominant factor, and improvement is expected with refinement of the bending procedures. A very promising approach to this goal would be to use a stepped diffractor geometry,⁸ which could provide point-to-point focusing with minimum plastic deformation. Since the fabrication of a stepped diffractor will reduce or completely eliminate the undesirable distortion of the crystal lattice, it has the advantages of higher diffracting efficiency and ease of control of its performance.

From the theoretical considerations and the preliminary results from the operation of the miniature spectrometer and the performance of a stepped mica diffractor, it is apparent that the monochromator with a doubly curved diffractor has promise for greatly improving the quantitation of Ca in biological specimens. Specifically, it promises to reduce the time it now takes to achieve useful results with EDS by more than an order of magnitude.

References

1. H. Shuman, A. V. Somlyo, and A. P. Somlyo, *Ultramicroscopy* 1: 317-339, 1976.
2. J. McD. Tormey, *Microbeam Analysis--1984*, 271-276.
3. A. Curie, *Anal. Chem.* 40: 586-593, 1968.
4. K. Heydorn and W. Lada, *Anal. Chem.* 44: 2313-2317, 1972.
5. D. B. Wittry and S. Sun, *J. Appl. Phys.* 67: 1633, 1990.
6. A. Guinier, *X-ray Diffraction* (transl. by P. Lovarian and D. Lovarian), San Francisco: Freeman, 1963, 11.
7. D. M. Golijanin et al., *Microbeam Analysis --1989*, 186-190.
8. D. B. Wittry and S. Sun, *Proc. XII ICEM*, 1990, vol. 2, 114-115.

ELEMENT CONCENTRATIONS IN CARDIAC MYOCYTES ISOLATED FROM CONTROL AND POTASSIUM DEPLETED RABBITS STUDIED BY X-RAY MICROANALYSIS

Alice Warley and J. P. T. Ward

Previous studies have shown that, in the rabbit, the myocardium adapts to K depletion by an increase in density of the sarcolemmal Na K pump. although this finding has been questioned.^{1,2} Any changes in the properties of the sarcolemma should be reflected in these cells when isolated. Here, we report results obtained from x-ray microanalysis of cardiac myocytes isolated from control and K-depleted rabbits. The isolated cells show changes in element concentration on exposure to various media, which are consistent with an increased Na K pump density.

Methods

Adult male NZW rabbits were fed either a standard diet or a diet deficient in K. The period of K depletion was 4 weeks. The animals were anesthetized, the hearts were removed, and myocytes were isolated by collagenase disaggregation.³ Cells from control animals were maintained in a Hepes buffered medium pH 7.3 containing 144 mM NaCl, 0.3 mM NaH_2PO_4 , 4 mM KCl, 1 mM MgCl_2 , and 0.5 mM CaCl_2 . Cells from the K-depleted animals were maintained either in the same buffer, or one in which K was reduced to 2 mM. The different concentrations of K were used to mimic serum concentrations of this element in control and depleted animals. Isolated cells were incubated for a minimum of 20 min at 37 °C. The cells were concentrated by centrifugation, the supernatant was removed, and drops of the pellet were quenched frozen by plunging into liquefied propane. Cryosections 200 nm thick were cut on a Reichert cryoultramicrotome and placed on Pioloform coated Ni grids (100 mesh). The sections were freeze dried overnight and coated with carbon before analysis. Analysis was carried out in a Philips CM12 electron microscope operating at 80 keV in STEM mode. The areas analyzed were large areas of the cell (probe 4–5 μm^2). Spectra were collected for 100–150 s live time and processed with EDAX 9800 software.

Results and Discussion

Morphology. Isolated cardiac myocytes form two populations of cells morphologically

The authors are at the departments of Biochemistry and Medicine, U.M.D.S. of Guy's and St. Thomas's Hospitals, London, England SE1 7EH. The work was funded by The Garfield Weston Foundation. The authors thank Philips Scientific (Cambridge, England) for the use of their CM12 microscope and EDAX analytical system.

distinct in the light microscope, termed round and rod shaped cells. Our previous x-ray microanalysis studies confirmed that high concentrations of Na and Cl (often > 500 mmol/kg) are associated with the round (dead) cells.⁴ In this study only cells showing elongated rod-shaped outlines were studied (Fig. 1). Subcellular details such as mitochondria, A bands, and Z lines could be clearly seen in cells from both control and K-depleted animals.

X-ray Microanalysis. Elemental concentrations in cells from control animals and K-depleted animals maintained at 2 mM external K concentration and 4 mM external K concentration are shown in Table 1. The control cells had a mean K/Na ratio of 5.1 ± 4.4 (S.D.); individual values ranged from 2 to 20 with a median value of 4.4. The mean value for K/Na is lower than would be expected owing to relatively high concentrations of Na in some of the individual cells. High concentrations of Na reported by x-ray microanalysis could be due to technical problems such as inadvertent redistribution of this element, or possibly an error in quantitation. Care was taken when the frozen sections were handled to insure that redistribution of Na did not occur. The finding of lower concentrations of Na in cells from the experimental animals handled under the same conditions suggests that technical problems were not the cause. High concentrations of Na have now been reported in a number of freshly isolated cells; therefore, increased permeability of the sarcolemma during isolation is a likely explanation of the increased Na concentration.⁵ These results indicate that there is some heterogeneity, even in the rod-shaped myocytes, and for functional studies a method of selection of cells by use of criteria other than morphology is needed.

The concentration of Na and the overall K/Na ratio (5.4 ± 4) were not changed in cells isolated from K-depleted animals despite an increase in the concentration of K. However, exposure of myocytes isolated from depleted animals to an external concentration of 4 mM K resulted in a significant ($p < 0.001$) decrease in intracellular Na concentration, and a significant increase ($p < 0.001$) in K concentration. The K/Na ratio in these myocytes was also increased to 9.9 ± 3.8 (range 5–21). A highly significant decrease in Cl concentration was also found. The decrease in Cl can be clearly seen in the spectra from the various cells (Fig. 2). The concentration of Na was lower and less variable in the cells from

TABLE 1.--Elemental concentrations in isolated cardiac myocytes (mmol/kg dry weight \pm S.E.).

	n	Na	Mg	P	S	Cl	K
Control	34	107 \pm 9	49 \pm 2	382 \pm 10	201 \pm 8	236 \pm 16	445 \pm 11
2mM K	38	116 \pm 9	66 \pm 3	452 \pm 12	166 \pm 6	223 \pm 10	502 \pm 15
4mM K	31	61 \pm 4	33 \pm 4	256 \pm 20	163 \pm 6	43 \pm 4	546 \pm 16

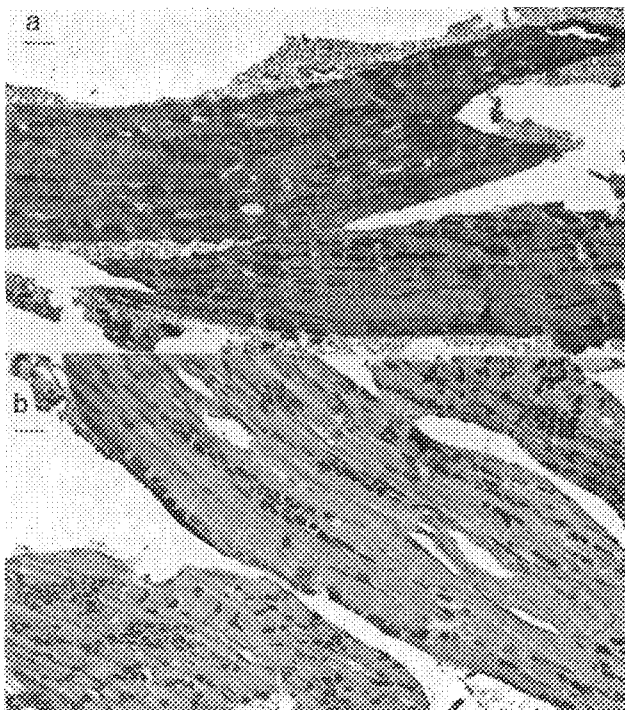


FIG. 1.--Freeze-dried frozen section of cardiac myocytes isolated from (a) K-depleted rabbits isolated in presence of medium containing 4 mM external K, (b) control rabbits; subcellular detail such as nuclei, mitochondria and z lines can be clearly seen in these cells. Marker = 3 μ m.

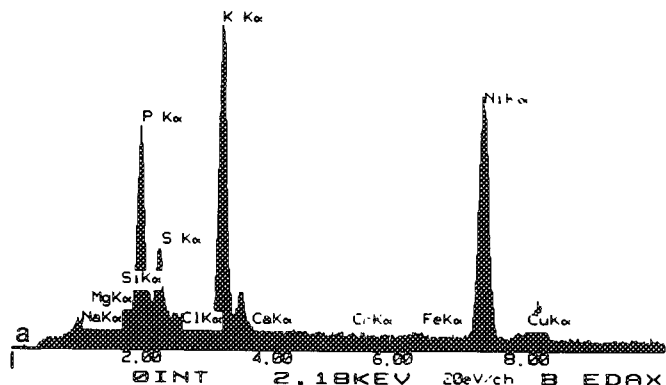
K-depleted animals maintained at 4mM external K. The coefficient of variation for Na was 34% compared to 54% in the control cells. Concentrations of Mg, P, and S were variable among the different groups of cells.

A finding of no change in Na concentration in the cells from the depleted animals is consistent with bulk analytical studies that showed no change in the ventricular concentration of this element, although the increase in K in the isolated cells was unexpected. The results from the cells from K-depleted animals maintained in the presence of 4mM external K (increased concentrations of K and lowered concentrations of Na) are in complete agreement with the bulk analytical studies, and are consistent with an increase in Na pump density in the sarcolemma of the K-depleted animals.

References

1. J. P. T. Ward and I. R. Cameron,

RATE= 567CPS TIME= 100LSEC
FS= 1373CNT PRST= 100LSEC
B =CFB CELL 7 WHOLE CELL



RATE= 561CPS TIME= 100LSEC
FS= 1138/ 1138 PRST= 100LSEC
B =CF12 CELLS WHOLE AREA

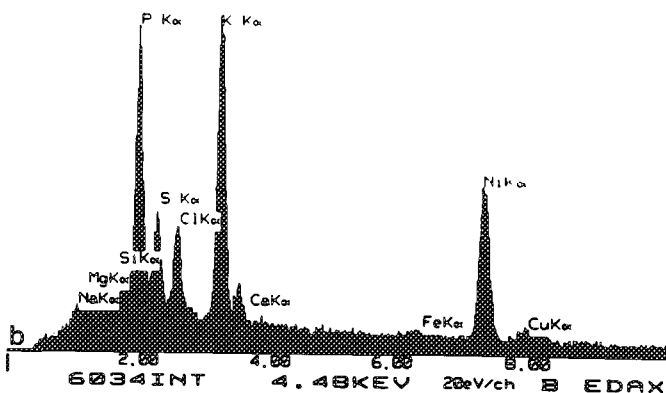


FIG. 2.--Spectra taken from (a) cell from K-depleted rabbit isolated in the presence of 4 mM external K, (b) cell from control rabbit. Note decrease in Cl in cell from experimental animal.

"Adaptation of the cardiac muscle sodium pump to chronic potassium deficiency," *Cardiovas. Res.* 18: 257-263, 1984.

2. L. Brown et al., "Ouabain binding and inotropy in acute potassium depletion in quinea pigs," *Cardiovas. Res.* 20: 286-293, 1986.

3. C. H. Fry et al., "Net calcium exchange in adult ventricular myocytes: An assessment of mitochondrial calcium accumulating capacity," *Proc. Roy. Soc. Lond.* B223: 223-238, 1984.

4. J. P. T. Ward and A. Warley, "X-ray microanalysis of myocytes isolated from rabbit heart," *J. Physiol.* 414: 54:, 1989.

5. Z. Szallasi et al. "Effect of enzymic (collagenase) harvesting on the intracellular Na/K ratio of Swiss/3T3 cells as revealed by x-ray microanalysis," *J. Cell Sci.* 90: 99-104, 1988.

Techniques for Microanalysis in Medicine

EFFECTS OF VIP SECRETORY STIMULATION ON CYTOPLASMIC ION CONCENTRATIONS IN MOUSE INTESTINAL CRYPT CELLS

T. von Zglinicki and G. M. Roomans

Agents that cause a rise of intracellular concentrations of cAMP in intestinal crypt cells also stimulate electrolyte and water secretion in the gut. It is believed that an increase of the Cl permeability of the apical membrane resembles the primary event in stimulated secretion.¹ A decrease of intracellular Cl concentrations down to electrochemical equivalent might therefore be expected in actively secreting cells. However, cAMP stimulates both basolateral Cl influx (probably via a NaKCl-cotransport mechanism) and K efflux. In fact, both apical Cl permeability, Cl entry, the Na exit step, and the K efflux must be stimulated and remain in a state of increased activity once secretion is stimulated.¹ Depending on the cell type studied and the drug used for stimulation, different ion transport systems could be rate-limiting.¹

Changes of Na, K, and Cl concentrations in secreting cells indicate the relative efficiency of the respective transport systems after stimulation. Intracellular ion concentrations in the mouse intestinal mucosa were measured by x-ray microanalysis.² Vasoactive intestinal polypeptide (VIP) was used as a potent and fast stimulator of electrolyte secretion in the intestine.^{3,4}

Experimental

Five female mice weighing 20-25 g were injected intraperitoneally with 5 mg VIP in 0.2 ml physiological salt solution plus 0.1% albumin. Increased water and Cl secretion a few minutes after VIP stimulation, both in vitro and in vivo, is well documented.⁵ After 5 min, mice were killed by cervical dislocation and samples from the proximal part of the jejunum were taken by a cryobiological technique.⁶ Sections about 0.2-0.5 μ m thick were cut in a LKB Cryonova at about 160 K, cryotransferred, and freeze-dried in a Phillips EM 400 electron microscope. The cytoplasm of the following cell types was analyzed at 100 kV: smooth muscle cells, Paneth cells, crypt A cells, and crypt B cells. It has been shown previously that the so-called undifferentiated crypt enterocytes can be discriminated into one subgroup of cells containing small secretion granula and rather low K concentrations under control conditions (crypt A cells) and a second group of enterocytes lacking secretion granula, but with significantly higher cytoplasmic K

(crypt B cells).² X-ray microanalysis was performed as previously described.²

Results

Concentrations of Cl, Na, K, Mg, and Ca in the respective cells of controls and VIP-stimulated mice are given in Figs. 1-4. Control data were similar to those obtained in earlier studies.^{2,7}

Following stimulation with VIP, a significant increase in cytoplasmic Na and Ca concentrations was found as a common pattern in both subtypes of crypt enterocytes. Decreases of cytoplasmic K concentrations were seen in both cell types, but were not significant at the 5% level. Cl concentrations increased after stimulation in crypt A cells, but tended to decrease in crypt B cells (Figs. 1a and b).

Probably both cell types participate in stimulated secretion. Since luminal Cl exit is stimulated by VIP, the results suggest that Cl entry is also increased. This basolateral Cl entry is coupled to Na and, possibly, to K.¹ Na is extruded from the cells via the basolateral Na/K-ATPase. However, because K concentrations are not increased in stimulated crypt enterocytes, it appears that basolateral K conductance is not the rate-limiting step. Instead, the capacity of the Na/K-ATPase seems to be rate limiting with respect to Na extrusion. In terms of Cl transport, the rate-limiting step is the exit pathway in crypt A cells, but might rather be the basolateral Cl inward transport in crypt B cells. However, since changes in Cl concentrations are considerably smaller than those of Na, it might be concluded that the activity of the Na/K-ATPase sets the practical limit to electrolyte secretion in crypt enterocytes under VIP stimulation.

Ca concentrations in crypt A and B cells were significantly increased after VIP stimulation. The Ca measured is evidently bound in Ca-sequestering organelles such as the endoplasmic reticulum, which was not discriminated from the cytoplasm in the frozen-dried cryosections examined. This result supports the idea of an interrelationship of cAMP and Ca as second messengers in VIP-stimulated secretion.¹

There was an increase of cytoplasmic Na and K concentrations in Paneth cells after stimulation (Fig. 1c). Two reasons appear possible for that increase: First, Paneth cells might be involved in stimulated secretion. In this case, the activity of the basolateral Cl entrance mechanism would even be higher than the luminal Cl conductance after stimulation. In fact, because Na and K

T. von Zglinicki is at the Institute of Pathology, Charité, Berlin; G. M. Roomans is at the Institute of Anatomy, University of Uppsala, Sweden.

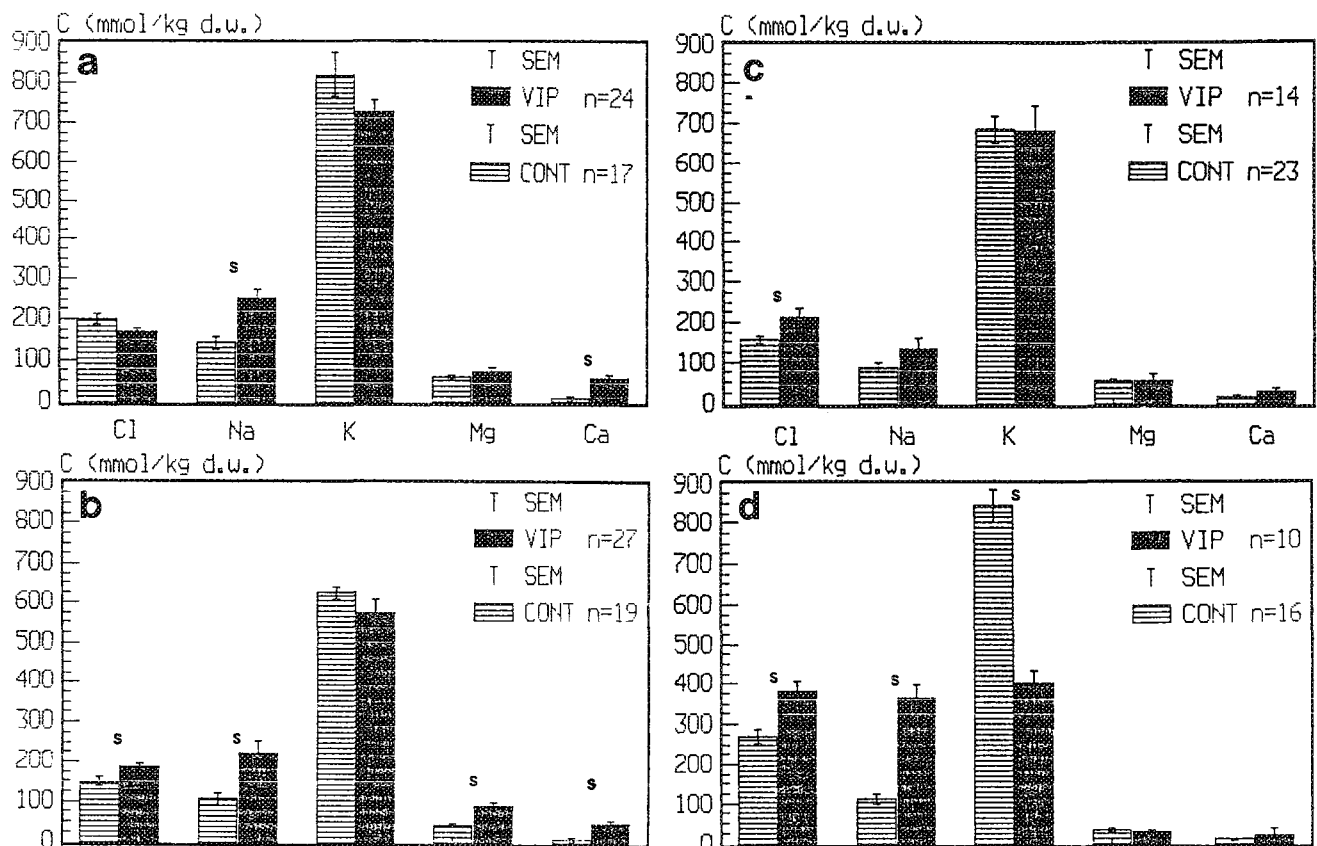


FIG. 1.--Concentrations of Cl, Na, K, Mg, and Ca (in mmol/kg dry weight) in the cytoplasm of (a) crypt B cells, (b) crypt A cells, (c) Paneth cells, (d) smooth muscle cells, under control conditions (CONT) and 5 min after VIP stimulation (VIP). Data are given as mean \pm SEM. Number n of cells measured is indicated. Significant differences (at 5% level) are indicated by s.

concentrations were not significantly altered, apical Cl conductance would represent the rate-limiting step of VIP-stimulated electrolyte secretion in Paneth cells. Conversely, it is not clear whether Paneth cells are involved in secretion at all. Results obtained in muscle cells (Fig. 1d) show that VIP treatment depolarizes these nonsecreting cells, leading to Na and Cl influx and a highly significant K efflux. A similar mechanism (i.e., depolarization) not including net ion transport may also be possible in Paneth cells.

Conclusions

Changes in the cytoplasmic ion concentrations in the major epithelial cells of the intestinal crypts after VIP-induced stimulation were measured and compared with those occurring in smooth muscle cells as a nonsecreting cell type. VIP not only increases the luminal Cl conductance in secreting cells, it also stimulates different basolateral ion transport systems. The relative amount of stimulation of these transport systems is cell specific. The contributions of any given cell type to the overall secretion could be estimated only if the activity of at least one of the systems were measured by some other technique. In addition to secretory stimulation, VIP had a depolarizing effect in nonsecreting cells.

The results presented are obtained from measurements performed on dried sections, i.e., from measurements of ion concentrations per dry mass of cytoplasm. The conclusions could

be somewhat different if VIP treatment changed the water content of the cells. Water content measurements of the cells of the intestine are therefore under way.

References

1. M. Donowitz and M. J. Welsh, "Regulation of mammalian small intestinal electrolyte secretion," in L. R. Johnson, Ed., *Physiology of the Gastrointestinal Tract*. 2nd ed., New York: Raven Press, 1987, 1351.
2. T. von Zglinicki and G. M. Roomans, "Element concentrations in the intestinal mucosa of the mouse as measured by x-ray microanalysis," *Scann. Microsc.* 3: 483, 1989.
3. G. J. Krejs et al., "Intestinal secretion induced by vasoactive intestinal polypeptide," *J. Clin Invest.* 61: 1337, 1978.
4. S. Eklund et al., "Effects of vasoactive intestinal polypeptide on blood flow, motility and fluid transport in the gastrointestinal tract of the cat," *Acta Physiol. Scand.* 105: 461, 1979.
5. G. J. Krejs, "Intestinal anion secretion in animal and man," in E. Skadhauge and K. Heintze, Eds., *Intestinal Absorption and Secretion*, Lancaster: MTP Press, 1984, 369.
6. T. von Zglinicki et al., "Fast cryofixation technique for x-ray microanalysis," *J. Microsc.* 141: 79, 1986.
7. T. von Zglinicki and G. M. Roomans, "Sodium, potassium and chlorine in electrolyte secreting cells in the intestine," *Microbeam Analysis--1989*, 105.

CROSS-SECTIONAL IMAGING OF COATED DRUG GRANULES

M. P. Mawn and R. W. Linton

Coatings on pharmaceutical products serve many purposes such as hiding an unpalatable drug taste, giving increased stability, and providing controlled-release dosage. An alternate approach to pharmaceutical drug coating characterization is reported here. Individual drug granule coatings are imaged as a complement to bulk studies such as dissolution tests, stability tests, and sieve analysis.^{1,2} Microscopy and microanalysis of granule coatings provides information on the effects of manufacturing conditions on microstructural features that influence dissolution behavior and drug bioavailability.^{3,4} Successful cross-sectional imaging required the development of a sample preparation technique suitable for optical, electron, and ion microscopies. Preliminary studies on the characterization of chemical components found within the drug granule were performed by time-of-flight secondary ion mass spectrometry (TOF-SIMS).

Experimental

The granules were produced by a wet granulation process and contain approximately 13% antibiotic drug (MW 510), 4% cornstarch, and 83% sucrose.⁵ This inner granule (200-250 μm) was then coated (10 μm) with an hydrogenated cotton seed oil in a spray congealing microencapsulating process.⁶

An Anatech LTD Hummer VII sputter coater was used to deposit a 400nm Au/Pd coating onto the granules with intermittent shaking to expose all surfaces. The inner granules were then extracted in 9 M sulfuric acid for at least 12 h. A drop of the acid, which usually contains 5-10 extracted granules in suspension, was then placed into a size 00 cylindrical tip (hemi-hyperboloid) BEEM capsule. The capsule was cut and fitted with a 200-mesh Ni TEM grid. Distilled water was then added to remove remaining acid and to trap the granules against the grid during drainage. The embedding material (JB-4 Plus) was added dropwise (under N₂ conditions) to infiltrate the granules and to prevent the low-density extracted drug coatings from floating. This procedure insures that all granules, irrespective of their coating thicknesses, are sectioned during microtoming. To prevent fracture during TEM grid removal, the tip was sanded flush with the grid before the grid was peeled back from the sample. The stub was microtomed with a Sorvall MT-I ultramicrotome and glass knife, to approximately the midpoint of

the granules. Subsequently, 1-2 μm -thick sections were obtained and mounted on a microscope slide for optical microscopy and carbon coated prior to SEM investigation.

Two sets of samples were also prepared for TOF-SIMS analysis. Both positive and negative ion spectra were acquired by use of a 12keV Ar ion beam on the TOF I static SIMS instrument developed at the University of Münster.⁷ Set A consisted of a series of pure component drug granule (drug, sucrose, cornstarch, and wax coating) as well as extracted granules embedded in JB-4 Plus, sectioned to 1-2 μm and supported on pure Si wafer substrates. Set B consisted of the pure granule components (except cornstarch) dissolved in a 1mg/mL solution (with water used for sucrose and methylene chloride for the dissolution of drug and wax coating components) and 2 μL was deposited on roughened Ag substrates. A solvent for the cornstarch granules could not be found and consequently a spectrum was not acquired for this minor granule component. (The cornstarch comprises of only 4% of the inner granule.) For a 70mm² monolayer coverage area of the drug, this corresponded to approximately 3.4×10^{13} molecules/mm². The greatest ion dose in any of the spectra for set A or B was 2×10^9 primary ions. Considering that the bombarded area was 1 mm², this corresponded to a dose density of 2×10^{11} ions/cm², well within the static SIMS regime of $<1 \times 10^{13}$ ions/cm² to assure minimal beam damage to surface molecules.

Results

The coated drug granules presented several obstacles to successful cross sectioning and microscopic imaging of the wax coating. Initial attempts to cross section embedded granules were only partly successful because the inner granule (composed of drug, sucrose, and cornstarch particles) is brittle and sometimes crumbles out of the thin section. Extraction of the inner granule before embedding, leaving only the wax coating, was found to facilitate sectioning. Unfortunately, the remaining wax coating is less dense than the embedding medium and therefore required the use of the BEEM capsule-TEM grid configuration to align the coatings against the grid for microtoming. An advantage of this approach is that sampling bias does not occur when samples with differing densities need to be embedded. This sample preparation regimen is also flexible in that various mesh TEM grids can be used depending on the embedding material, particle size, and sample/embedding material density differences. A requirement for the embedding material is that it should have a quick cure time to lessen the

The authors are at the Department of Chemistry, University of North Carolina, Chapel Hill, NC 27599-3290. Support was provided by Glaxo Inc., Analytical Chem. Dept., Research Triangle Park, NC 27709.

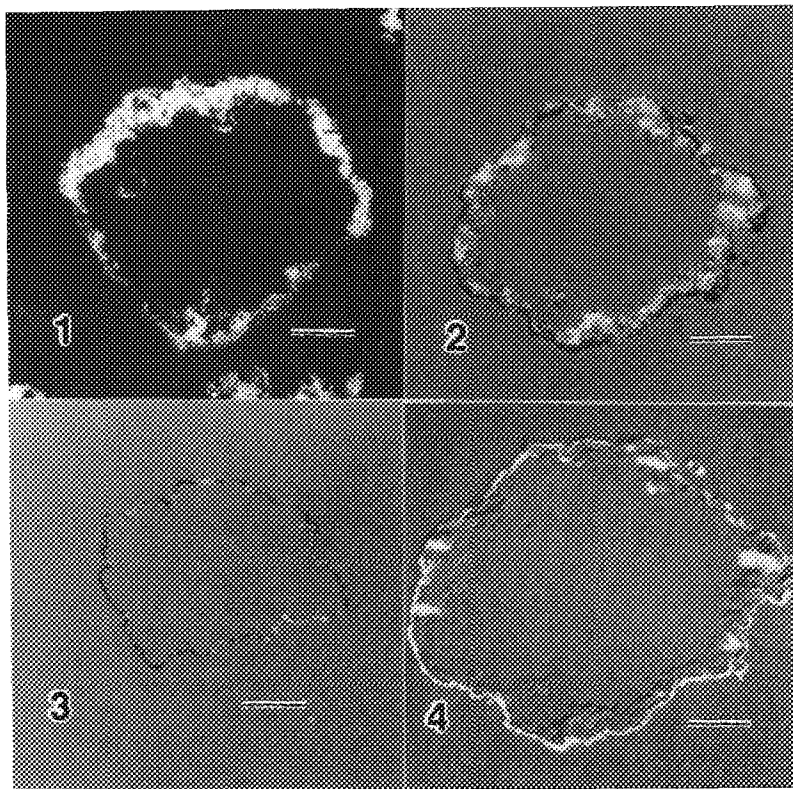


FIG. 1.--Polarized light micrograph (LM) of extracted granule coating after embedding and sectioning. Bar = 49 μ m.

FIG. 2.--LM of Au/Pd-coated granule after extraction showing complete granule boundaries. Bar = 49 μ m.

FIG. 3.--LM of Au/Pd-coated control granule without a wax coating, which leaves only Au/Pd shell after extraction. Bar = 49 μ m.

FIG. 4.--SEM of granule in Fig. 2 highlighting Au/Pd coating and porous wax coating (backscattered electron image). Bar = 40 μ m.

burden of addition of the embedding material dropwise until its viscosity is high enough to prevent further drainage. Various embedding materials were tried to optimize embedding, sectioning, and mounting the granule coatings. JB-4 Plus was found best suited for embedding since the wax coating appears insoluble in this material and also provides quick cure times. One disadvantage is that swelling occurs while mounting the sections with water, as observed by comparison of the section to the block face.

Figures 1-3 are cross-polarized light micrographs of various extracted drug granule coatings. The coatings include regions of discontinuous coverage and a porous structure (Fig. 1). These defects must affect dissolution behavior. Application of a 400nm Au/Pd sputter film prior to extraction defines the particle surface in discontinuous coating coverage areas, which is essential for quantitative image analysis (Fig. 2). The Au/Pd film also identifies uncoated granules that would otherwise completely extract away, as illustrated for an uncoated control granule in Fig. 3. A correlative backscattered electron micrograph in Fig. 4 provides better definition of the Au/Pd coating for the coated granule (previously shown in Fig. 2). The porous nature of the wax coating also is more apparent owing to the unique backscatter electron yields of the exposed glass slide, which appears as the intermediate gray level between the darker organic components and the brighter Au/Pd coating.

The cross-sectioned wax coating appears to entrap portions of the inner granule during microencapsulation instead of uniformly covering the example's surface. This result is consis-

tent with the observation that the coating material is much more brittle during sectioning of the extracted drug granules than pure coating material. Also, the coating thickness measured by microscopy is thicker than expected from calculated results based on the average granule size and weight percent of wax applied. Typical average measured coating thicknesses are approximately 20 μ m, well above the predicted 10 μ m thickness.

Attempts were made to stain individual drug granule components preferentially to identify trapped material within the coating by optical and electron microscopy, but the number of possible stains was limited owing to the differing solubilities of the drug granule components. The coating is soluble in less polar organic solvents, whereas the sucrose in the inner granule is soluble in polar solvents. Vapors of osmium tetroxide and iodine were successful in staining the wax coating, but highly selective staining of individual components could not be achieved.

Chemical speciation of the trapped material was also investigated by TOF-SIMS. It was hoped that static SIMS could be used to generate secondary-ion images reflecting the distribution of each of the molecular components in the drug granule. However, significant differences were not found between the cornstarch, sucrose, and drug spectra reflecting relatively poor ion yields for both the molecular and characteristic fragment ions (sample Set A).

A more suitable SIMS sample preparation (sample Set B) was used to take advantage of enhanced ion yields from monolayer depositions on an underlying Ag substrate. The Ag serves

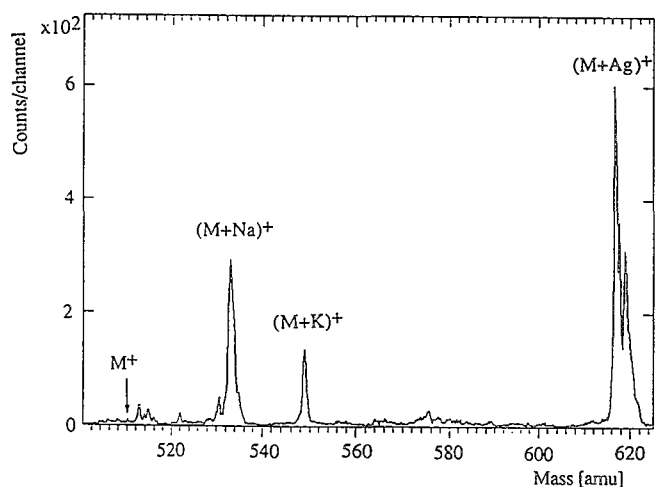


FIG. 5.--Static SIMS spectrum of pure drug component deposited on Ag substrate in monolayer coverage.

to provide a source of metal ions to enhance the detection of molecules as adduct ions $(M + Ag)^+$. Sodium and potassium were present in sufficient abundance to provide additional adduct formation.

Figure 5 is the positive ion spectrum of the drug, which was dissolved in methylene chloride, and deposited onto an Ag substrate. The spectrum was ratioed to a Ag blank, which removed plasticizer peaks (memory effects in the TOF-SIMS I). The parent molecular ion (MW 510) for the drug is not abundant. However, Na^+ , K^+ , and Ag^+ adducts at masses 533, 549, and 617/619, respectively, are prominent. The addition of Na or K to cross-sectioned extracted granules may enhance ion yields and adduct formation sufficiently to allow chemical ion mapping to be performed. A list of secondary ions, with assignments and ion dose corrected peak intensities, is given in Table 1. The list includes promising candidates to perform ion mapping of the spatial distributions of the individual components. The large dynamic range of SIMS allows large peak intensity differences, which are apparent for each of the $(M - H)^-$ and $(M + Metal)^+$ ions relative to the other components (Table 1). For example, the ions at masses 283, 365, and 533 are highly specific to the wax, sucrose, and drug components, respectively. Using the integrated intensities of the drug + Ag^{107} and drug + Ag^{109} adducts, and assuming similar ion yields can be achieved for an alkali ion adduct for the embedded drug granules, one can make an estimate for the resolution attainable for the drug in a static (1×10^{13} primary ions/cm²) ion map $(M3 + Na)^+$. The (drug + Ag)⁺ combined isotope integrated intensity was 1.4×10^6 counts for a primary ion dose of 2.2×10^9 ions in a 1mm² area. For 10% precision (100 counts), a resolution in the 1μm² range should be achievable with a focused liquid-metal ion source.

Conclusions

A novel sample preparation method was devel-

TABLE 1.--Ion dose-corrected peak intensities for drug granule components deposited on roughened Ag substrates in approximately monolayer coverages.

M1a= PALMITIC ACID (WAX COATING)

M1b= STEARIC ACID (WAX COATING)

M2 = SUCROSE

M3 = DRUG

MASS	COMPONENT	M1	M2	M3
255.4	(M1a-H) ⁻	15970	6244	1317
283.5	(M1b-H) ⁻	38974	1658	589
341.3	(M2-H) ⁻	585	15552	429
365.3	(M2+Na) ⁺	97	261077	10363
381.3	(M2+K) ⁺	82	6253	3295
449.2	(M2+Ag ¹⁰⁷) ⁺	79	115702	5859
509.1	(M3-H) ⁻	524	239	2999
533.1	(M3+Na) ⁺	62	2434	130668
549.1	(M3+K) ⁺	112	1370	71256
617.1	(M3+Ag ¹⁰⁷) ⁺	75	797	102224

oped to image directly drug granule coatings by optical, electron, and ion microscopy. Examination of the drug coatings suggests that some inner granule material is entrapped within the coating, and that the coatings show considerable variations in thickness and porosity. Such defects will influence the biological activity of the drug as will be assessed quantitatively by correlation of morphometry measurements with dissolution tests. Molecular imaging of the individual components within the drug granule cross sections will be attempted by use of static SIMS. The incorporation of alkali metals into the cross sections may help improve detection sensitivity by use of metal ion adducts of the molecular species, as suggested by the Na and K adduct formation observed from monolayer coverages of pure components deposited on Ag substrates.

References

1. S. Kaura et al., "A study of the effects of sucrose concentration, lacquer concentration and coating time on the formulation of stable and effective carbenicillin indanyl sodium microcapsules," *Drug Devel. Ind. Pharm.* 14: 925, 1988.
2. A. K. Singla and Alka Nagrath, "Stability of ascorbic acid-zinc sulphate tablets," *Drug Devel. Ind. Pharm.* 14: 1471, 1988.
3. M. R. Brophy and P. B. Deasy, "Application of the Higuchi model for drug release from dispersed matrices to particles of general shape," *Int. J. Pharm.* 37: 41, 1987.
4. J. M. Conra and J. R. Robinson, *Pharmaceutical Dosage Forms: Tablets*, New York: Marcel Dekker, Inc., 1982, vol. III, 149.

5. H. M. Unvala, "The effect of the wet granulation process on drug dissolution," *Drug Devel. Ind. Pharm.* 14: 1327, 1988.
6. P. L. Madan, "Methods of preparing microcapsules: Mechanical methods," *Pharm. Technol.* 2(8): 24, 1978.
7. P. Steffens et al., "A time-of-flight mass spectrometer for static SIMS applications," *J. Vac. Sci. Technol.* A3(3), May/June, 1985.

PREPARATION OF FREEZE-DRIED SECTIONS OF HUMAN BIOPSIES FOR X-RAY MICROANALYSIS

K. E. Tvedt, Jostein Halgunset, Gunnar Kopstad, and Asbjørn Nordby

The benefit of cryoultramicrotomy as a preparative technique for x-ray microanalysis is two-fold: cryofixation retains soluble components that would have been otherwise lost or displaced, and thin sections provide optimal spatial resolution. Such sections, if kept frozen-hydrated or if carefully freeze-dried, may preserve the elemental gradients present at the moment of freezing.

This paper presents a method for rapid and convenient preparation of human tissue obtained by needle biopsies. The method has been used to perform elemental analysis of various compartments in prostatic and mammary epithelial cells. Even if the manipulation of the tissue specimen as well as the time lapse between the biopsy taking and the freezing have been reduced to a minimum, the data indicate that some redistribution of the more mobile elements may occur.

Experimental

Prostatic tissue cylinders (2 mm in diameter) were obtained from ten patients with Tru-Cut® disposable needles. Mammary tissue cylinders (1.2 mm in diameter) were obtained from four patients with Biopsy Cut® equipment.

The tissue cylinder was transferred to a Formvar film supported by a polystyrene frame, and quickly frozen by the firm pressure of a pair of pliers (Fig. 1), precooled in liquid nitrogen.¹ After freezing, the tissue block was kept submerged in liquid nitrogen until sectioning. The frozen specimen was mounted into the flat specimen holder of a Reichert-Jung Ultracut/FC4 Cryosystem.® Thin sections were cut at -130°C and collected onto Formvar coated grids, situated inside a transportable press (Fig. 1).² The press was flushed with cold nitrogen gas during transport to an external freeze-drier. After freeze-drying overnight, a Formvar film was mounted on top of the grid/retainer assembly. X-ray microanalysis was performed with a Kevex 7000 energy-dispersive spectrometer in combination with a JEOL 100 CX electron microscope with a scanning equipment. X-ray counts were converted into concentrations (mmol/kg dry weight) by procedures described in detail elsewhere.²

Results

The flat specimen obtained with the described freezing method proved to be particularly useful in these types of specimens, since both the human prostate and the mammary gland contain large areas of stromal components, which often

makes it necessary to perform several sectioning sessions in order to produce suitable sections of epithelial cells. The homogeneous sectioning properties of the flat specimens were therefore of great advantage.

The morphological resolution was sufficient to permit easy recognition of the main cellular and tissue structures. (Figs. 2 and 3). In breast tissue, the intralobular stroma was clearly distinguished from the extralobular, which typically contains thick bundles of collagen fibers. It was therefore often possible to confirm the light microscopical diagnosis determined from adjacent pieces of tissue.

Organelles containing large amounts of calcium, zinc, and magnesium were found in the cytoplasm of prostatic epithelial cells (Fig. 4). The concentration of calcium was negatively correlated to phosphorus (Fig. 5). High concentrations of calcium were also found in organelles in the cytoplasm of epithelial cells of the mammary gland. However, in contrast to the prostate, most of the mammary cells revealed severe membrane leakage. Na:K-ratios close to extracellular values were commonly encountered (Table 1).

Conclusions

Needle biopsies represent a rich source of human material for x-ray microanalysis. The freezing method presented represents a modification of a method introduced by Hagler et al.³ When supported by Formvar film even small and delicate pieces of tissue are easily frozen, and the subsequent sectioning can be usually performed without difficulty.

The loss of blood supply after the excision of a biopsy causes a leakage of ions. It is therefore important to freeze the tissue as quickly as possible. Local enrichment of calcium in intracellular compartments may be caused by leakage of calcium ions into the cytoplasm, where they precipitate as calcium phosphate. However, in most prostatic glands we found a significant negative correlation between calcium and phosphorus, which may indicate protein binding of the ion. Furthermore, the sequestration of zinc and magnesium as well as calcium in these compartments indicates strongly that these structures represent secretory granules rather than artifacts. In the data from the mammary gland, on the other hand, there is clear evidence that massive leakage has taken place (Table 1). Some of the epithelial cells show Na:K ratios close to the extracellular value. Another remarkable result is the consistently lower Na:K ratio in the small, electron-dense,

K. E. Tvedt is at the Norske Radiumhospital, Montebello, N-0310 Oslo 3, Norway; his coauthors are at the University of Trondheim.

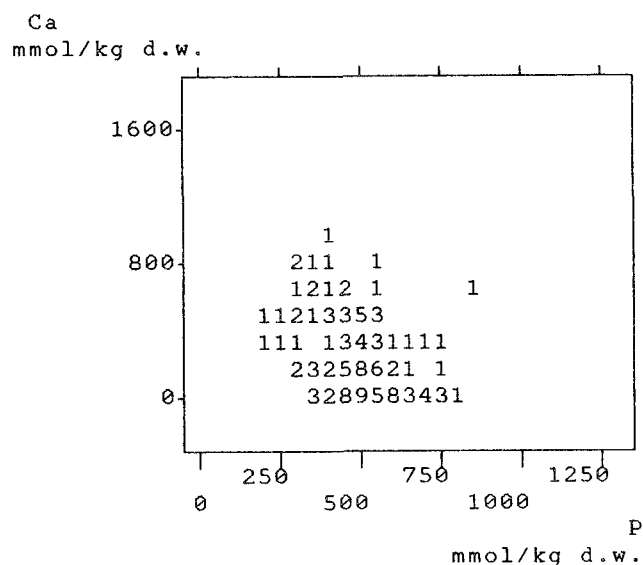


FIG. 5.--Plot of calcium with phosphorus demonstrating negative correlation ($r = -0.348$, $p < 0.01$, $n = 127$) in electron-dense cytoplasmic organelles (prostatic epithelium). Concentrations in mmol/kg dry weight.

TABLE 1.--X-ray microanalytical data from mammary epithelial cells in biopsies from four patients. Elemental composition of nucleus and electron-dense cytoplasmic organelles.

P ^a	C ^b	Na:K ^c	Na ^d	Mg	P	S	Cl	K	Ca	n ^e	age
#1	Nuc ^f	1.11 0.15	742 100	78 7	1237 60	192 15	519 53	778 45	6 2	30	27
	Cyt ^g	0.94 0.06	273 19	48 1	604 17	116 4	186 11	347 13	45 6	86	
#2	Nuc	8.83 0.45	786 34	26 3	656 47	93 6	491 28	107 18	19 2	23	37
	Cyt	4.79 0.26	571 22	38 2	540 23	109 3	392 13	132 6	54 5	56	
#3	Nuc	6.98 0.36	790 19	31 3	731 36	109 3	419 12	121 9	15 3	18	37
	Cyt	2.75 0.25	423 27	48 3	545 21	114 4	248 17	169 6	110 19	49	
#4	Nuc	9.81 0.43	637 29	7 4	648 26	112 4	461 17	66 3	26 2	22	41
	Cyt	3.63 0.29	373 22	27 4	537 21	105 3	274 13	111 4	122 17	36	

^aPatient. ^bCompartment. ^cMolar ratios.
^dConcentrations in mmol/kg dry weight. ^eNumber of analyses. ^fNucleus. ^gElectron-dense cytoplasmic organelles.

calcium-containing organelles in the cytoplasm (Table 1). Most likely, these electron dense structures represent membrane bound organelles less prone to leakage than the plasma membrane.

The marked difference in behavior between the prostate and the mammary gland may be due to difference in vulnerability to the mechanical trauma induced by the biopsy procedure. The

fact that different types of biopsy needles of different caliber were used to collect the tissues may also have played a role. The prostatic tissue cylinders (2 mm in diameter) were much thicker than the mammary tissue cylinders, which were collected with a needle only 1.2 mm in diameter. Thus, the harmful effect of mechanical trauma, as well as the duration of ischemia, should be taken into consideration when evaluating preparation methods for x-ray microanalysis of biopsy material.

References

1. K. E. Tvedt et al., "Rapid freezing of small biopsies for cryosectioning and x-ray microanalysis," *Am. J. Clin. Path.* 92: 51, 1989.
2. K. E. Tvedt et al., "Intracellular distribution of calcium and zinc in normal, hyperplastic, and neoplastic human prostate: x-ray microanalysis of freeze-dried cryosections," *The Prostate* 15: 41, 1989.
3. H. K. Hagler et al., "Standards for quantitative energy dispersive x-ray microanalysis of biological cryosections: Validation and application to studies of myocardium." *J. Microsc.* 131: 221, 1983.

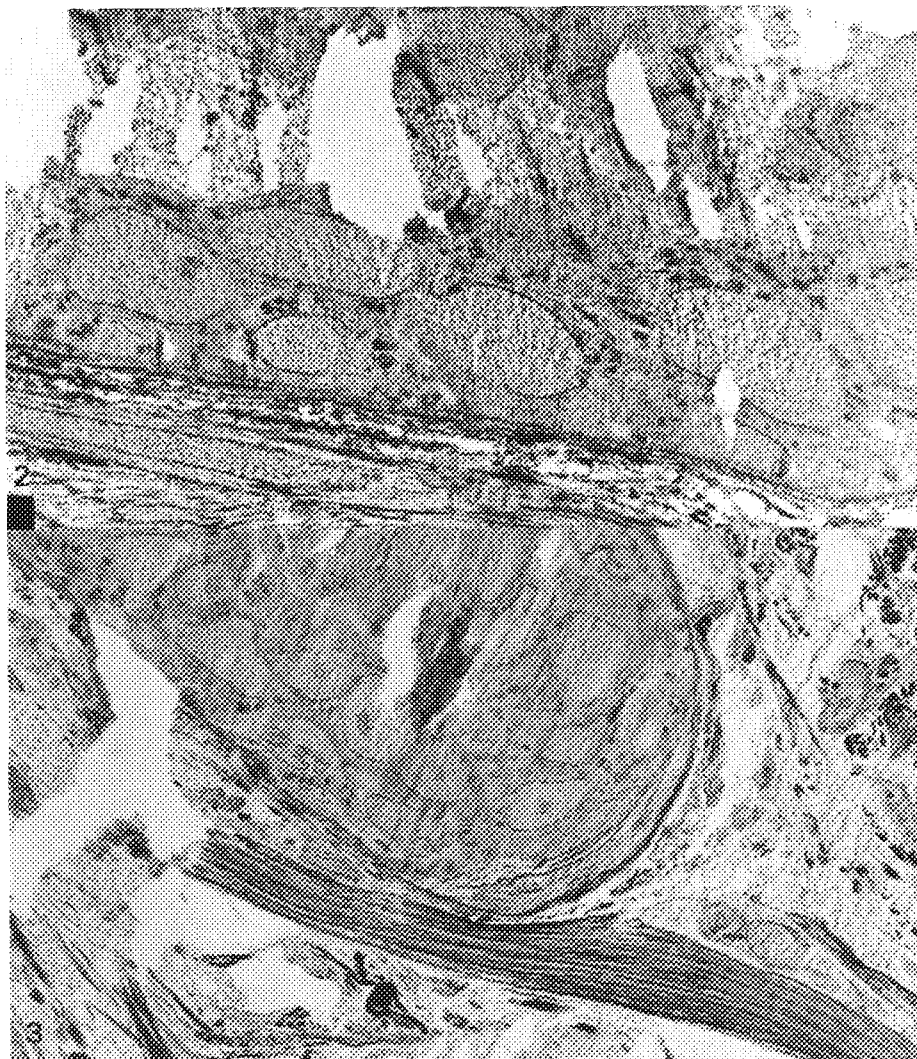
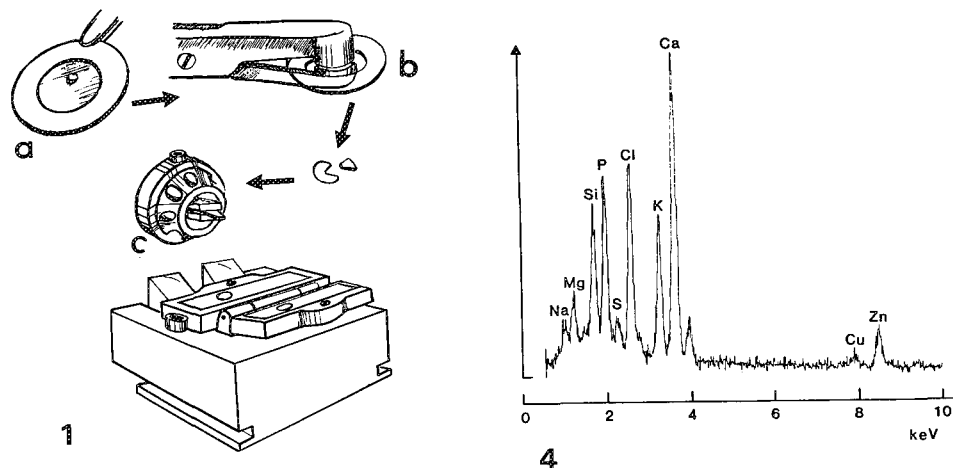


FIG. 1.--Illustration of freezing procedure. (a) Specimen is placed on Formvar film supported by a circular frame. (b) Freezing is performed by firmly clamping of specimen with a pair of pliers pre-cooled in liquid nitrogen. (c) A piece of frozen specimen is mounted in the flat specimen holder.

FIG. 2.--TEM of prostatic tissue, showing acinar cells, stromal components (lower part), and luminal secretion (upper part). Magnification 4200 \times .

FIG. 3.--TEM of mammary tissue, showing acinar cells and intralobular stroma with thick bundle of collagen. Magnification 3000 \times .

FIG. 4.--X-ray spectrum demonstrating elemental composition of secretory granule (prostatic epithelial cell), showing high concentrations of calcium, zinc, and magnesium.

APPLICATIONS OF X-RAY MICROANALYSIS TO THE STUDY OF DRUG DISTRIBUTIONS IN CULTURED CELLS

R. G. Kirk, Ping Lee, and M. J. Reasor

A potentially important application of the technique of x-ray microanalysis is the study of the transport of drugs and the determination of sites of their accumulation in cells of treated animals or humans. In order for a drug to be distinguished by x-ray techniques, it has to contain an element not normally present in the cell. If such an element is absent in the structure of the drug, labeling has to be carried out to identify the molecule. Studies using this approach have been carried out by several investigators with the iodine-containing antiarrhythmic drug amiodarone¹⁻³ and the bromine-containing anesthetic halothane.⁴ In these studies it was shown that the drugs tend to concentrate in specific organelles of the cells (e.g., amiodarone in lipid lamellar bodies and halothane in mitochondria). Since drugs may not bind irreversibly with intracellular components, histological procedures used in conventional electron microscopy may not preserve the drug molecules in their original intracellular location. Rapid freezing combined with cryomicrotomy is a method that preserves the distribution of the diffusible molecules.

We have previously reported our results on the use of x-ray microanalysis to measure quantitatively the subcellular distribution of iodine in alveolar macrophages of rats treated with amiodarone.⁶ Amiodarone is a cationic amphiphilic compound that is very effective for the treatment of ventricular arrhythmia. One major problem with this drug is that it can cause cellular lipidosis and pulmonary toxicity.⁶ Structurally, the drug contains two atoms of iodine per molecule (Fig. 1). Therefore, it can be followed by the x-ray microanalysis technique. We found small amounts of iodine throughout the alveolar macrophages following a single administration of the drug. The major accumulations were observed in the lipid lamellar structures, which were of lysosomal origin and appeared as amorphous bodies in freeze-dried cryosections. More recently we have examined the effects of 1-week and 9-week treatments with amiodarone to assess the drug dis-

tribution with longer-term administration. Severe lipidosis in the alveolar macrophages occurred after the 1-week treatment with amiodarone. Substantial changes in iodine distribution occurred in cells with increasing length of drug treatment. In addition to the high concentrations of iodine in the lamellar bodies, the iodine levels in the nuclei slowly increased with the length of treatment, and after 9 weeks of treatment approached the high levels found in the lamellar bodies. From HPLC analysis of the metabolites present in the cells after amiodarone treatment, it is thought that this accumulation of iodine in the nuclei is due to the presence of polar metabolites. Because x-ray microanalysis measures only the iodine signal, we were not able to distinguish amiodarone and its metabolites in the cells. In *in vitro* cultures of alveolar macrophages, neither amiodarone nor its major metabolite, desethylamiodarone, is metabolized.⁷ This observation allows us to study the accumulation of each drug independent of one another. In this paper we report our results on the differential accumulation of amiodarone and desethylamiodarone by alveolar macrophages in culture.

Methods

Cell Culture. Alveolar macrophages were collected from untreated or chloropheniramine-treated (30 mg/kg, *i.p.* for 3 days) male Fischer 344 rats (250-300 g, Hilltop Laboratories, Scottsdale, Pa.) by pulmonary lavage under sterile conditions using eight 5 ml aliquots of warm, filtered calcium-free Hanks' balanced salt solution (HBSS), pH 7.4. The collected fluid samples were centrifuged at 500 g for 7 min. The cell pellet containing alveolar macrophages was resuspended in a sterile growth medium (RPMI 1640 medium with L-glutamine, 10% fetal bovine serum, gentamicin sulfate (10

The authors are at the West Virginia University Health Science Center, Morgantown, WV 26506: R. G. Kirk at the Department of Anatomy, P. Lee at the Department of Physiology, and M. J. Reasor at the Department of Pharmacology and Toxicology. This research was supported by NSF grant DCB 8818863 and by a grant-in-aid from the American Heart Association. The authors are grateful to Laura Knopf and Candace Ogle for expert technical assistance, and Sanofi Recherches Centre and Wyeth Laboratories for their generous gifts of drugs.

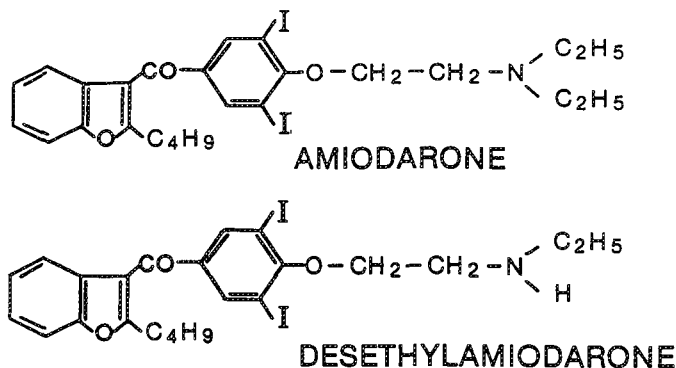


FIG. 1.--Structures of amiodarone and its primary metabolite, desethylamiodarone.

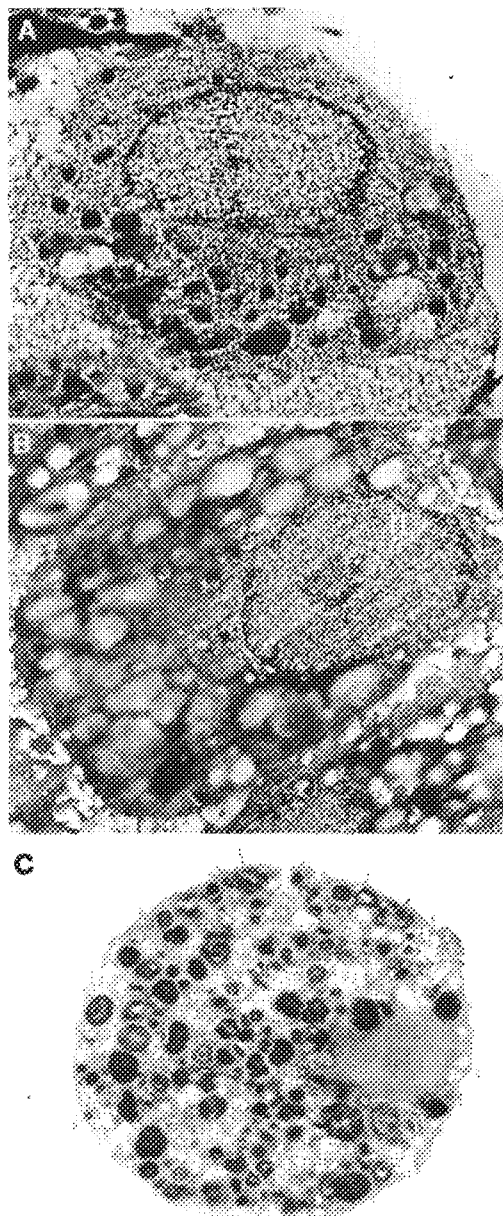


FIG. 2.--Transmission electron micrographs of rat alveolar macrophages. (A) Freeze-dried cryosection without chemical fixation or stain of cell from rat treated with amiodarone for 9 weeks. Lighter inclusions are amorphous bodies. (B) Freeze-dried cryosection of cultured cell exposed to desethylamiodarone for 42 h. Large number of dark, small inclusions are dense granules and the few lighter, larger inclusions are amorphous bodies. (C) Plastic section with chemical fixation and staining of cell from rat treated with amiodarone for 9 weeks.

mg/ml), and 2-mercaptoethanol (10 mmol in 0.02 KOH). Cells were plated at a concentration of 0.5×10^6 cells/ml in tissue culture plates or wells. Prior to treatment with drugs the cells were allowed to equilibrate for 1 h at 37°C in a tissue culture incubator containing air and 5% CO₂. Amiodarone or desethylamiodarone was added to the culture to a final drug concentration of 7.5 μ M. Control cultures were treated with

the 50% ethanol vehicle (0.1% final concentration). After 42 h, the conditioned medium was removed from the plates and centrifuged to remove floating cells. The adherent cells were washed gently with saline three times, then scraped into 0.5 ml of saline and processed for cryofixation. A sample was also processed for HPLC measurement to determine the purity of the original drug.

Embedding Plastic for Conventional Microscope. The procedure used has been described previously by Reasor et al.¹² Cells were fixed for 1 h at 4°C in 3% glutaraldehyde in Dulbecco's PBS (pH 7.4). After having been in PBS, the cells were postfixed in 1% OsO₄ in PBS for 1 h at room temperature. To preserve the lipid lamellar structure of the cells, they were incubated in 0.5% tannic acid in PBS for another hour. The cells were then dehydrated with a series of ethanol solutions of increasing concentrations, infiltrated in propylene oxide, and embedded in Epon 812. Sections were cut and stained with 3% uranyl acetate for 20 min followed by Reynold's lead citrate for 5 min.

Cryofixation and Cryosectioning. To prepare cells for freeze preservation, the cells were centrifuged at 500 g for 10 min at 4°C and resuspended in plasma. Plasma is necessary to provide energy for metabolism and to aid in cryosectioning. In order to allow recovery of their cellular potassium, the cells were warmed to 37°C for 15 min and centrifuged in a Beckman Microfuge (Model B) at 4000 g for 10 s to obtain a pellet. A portion of this pellet was used for x-ray microanalysis. Small drops of packed cells were deposited on wooden dowels (4 mm in length, 1.5 mm in diameter) and rapidly frozen in precooled liquid propane stirred to maintain a low fluid temperature (-190°C). Sections were cut at -110°C with glass knives in an Ultracut E41 microtome equipped with a low-temperature sectioning system (FC4C, Reichert). Sections were then transferred in the dry cold (-110°C) atmosphere of the chamber onto the center of a nitrocellulose film about twice the size of an electron microscope grid. A nickel grid (100 mesh) covered with nitrocellulose was carefully placed on top of the sections so that the sections were sandwiched between two nitrocellulose films. During freeze-drying, cold small brass containers were used to protect samples. The sections were freeze-dried in a vacuum evaporator (Denton Vacuum, Cherry Hill, N.J.) equipped with a turbomolecular pump (Balzers, Asslar, Germany). These containers were allowed to warm to room temperature in a vacuum. The sections were then coated with a thin film of carbon in the evaporator before being used for x-ray microanalysis. Dry nitrogen was vented into the evaporator to prevent rehydration of the samples after the coating procedure.

X-ray Microanalysis. The procedure for x-ray microanalysis has been described previously.^{2,5} A Kevex 7000 spectrometer (Kevex Corp., San Carlos, Calif.) interfaced to a PDP 1123

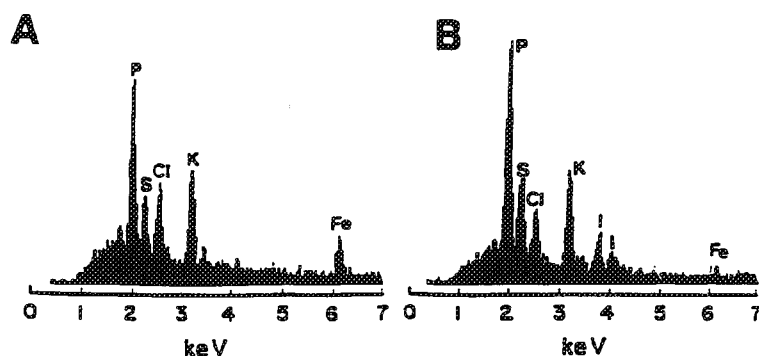


FIG. 3.--X-ray spectra of amorphous bodies from (A) untreated alveolar macrophages, (B) cultured alveolar macrophages exposed to desethylamiodarone for 42 h.

computer (DEC, Maynard, Mass.) was used in conjunction with a JEOL 100 CX electron microscope to collect the x-ray data. Sections on nickel grids were transferred to the microscope carbon sample holder in the dry nitrogen atmosphere of the desiccator. The samples were analyzed for 50 s at an accelerating voltage of 80 kV and a beam current of 1 nA. Our quantitation procedure consists of measuring the mass from the continuum and fitting the characteristic x-ray peaks from the standards with those from the samples by multiple least-squares method.⁸⁻¹⁰

Results

Extensive accumulation of lipid lamellar structures occurs in cells that have been exposed to amiodarone for extended periods.³ Figure 2(A) shows a freeze-dried cryosection of a cell from a rat treated with amiodarone for 9 weeks.³ Sufficient morphological detail is present in the cryosectioned sample to allow identification of the various subcellular structures. An alveolar macrophage treated in culture with amiodarone for 42 h is shown in Fig. 2(B). It contains some amorphous bodies, but primarily dense granules. These seemingly amorphous bodies are in fact lipid lamellar structures, which can be seen in plastic sections prepared by chemical fixation and staining techniques (Fig. 2C).

Typical x-ray spectra of amorphous bodies from control and desethylamiodarone-treated cultured cells are shown in Fig. 3. Similar spectra are obtained with exposure of the alveolar macrophages to amiodarone, except that the iodine peaks are somewhat depressed. The iodine concentrations in the desethylamiodarone-treated cells are higher than in amiodarone-treated ones. This finding is true for all the analyzed regions including nucleus, cytosol, dense granules, and lipid amorphous bodies (Table 1). The dense granules and the lipid amorphous bodies apparently are of lysosomal origin. The concentration of amiodarone is uniform among the amorphous bodies, whereas a much more heterogeneous pattern is seen in desethylamiodarone-treated cells. The desethylamiodarone concentrations in the amorphous bodies cover a

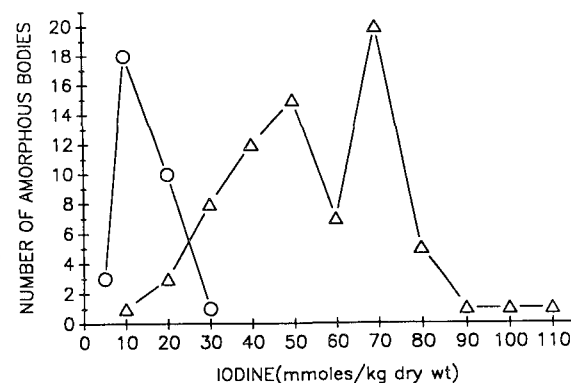


FIG. 4.--Distribution of iodine in amorphous bodies from macrophages treated in culture with amiodarone (circles) or desethylamiodarone (triangles).

broader range than that of amiodarone concentrations, and a bimodal distribution is seen (Fig. 4).

TABLE 1.--Distribution of iodine in alveolar macrophages in culture.

Cellular Compartment	Iodine Concentration (mmol/kg dry wt.)	
	Treated with Amiodarone ^a	Treated with Desethylamiodarone ^a
Nucleus	7±1 (50) ^b	29±1 (42)
Cytosol	8±1 (50)	31±1 (45)
Amorphous bodies	13±1 (50)	56±4 (35)
Dense granules	10±1 (50)	50±5 (22)

^aAlveolar macrophages were exposed to amiodarone or desethylamiodarone (7.5 μM) for 42 h.

^bData are given as mean ± SEM (n), where n is the number of analyses.

In order to study the effects of preexisting lipidotic condition in cells on the accumulation of the drugs, we have produced lipidotic alveolar macrophages by treating rats with chlorphentermine.¹¹ This treatment resulted in a massive accumulation of amorphous bodies in cells. When these cells were exposed to amiodarone and desethylamiodarone in culture, we observed the same preferential accumulation of desethylamiodarone over amiodarone in these lipid-filled cells, although the difference between the two drugs was not as great as in those without preexisting lipidosis. Within an individual amorphous body, the concentration of iodine also appeared to vary depending on which part of the structure was analyzed. There was a higher concentration of the iodine at the dark edges of the amorphous bodies than in their lighter centers (Table 2). Apparently the drug is not able to penetrate

into the deepest part of the lipid lamellar structure.

TABLE 2.--Distribution of iodine in alveolar macrophages from chlorphentermine-treated rats exposed to amiodarone or desethylamiodarone in culture.^a

Cellular Compartment	Iodine concentration (mmoles/kg dry wt.)	
	Treated with Amiodarone ^b	Treated with Desethylamiodarone ^b
Nucleus	6±1 (43) ^c	10±2 (33)
Amorphous bodies		
Edge	6±1 (41)	21±2 (50)
Center	4±1 (40)	6±1 (50)

^aRats were treated with chlorphentermine (30 mg/kg, i.p.) for 3 days.

^bAlveolar macrophages were exposed to amiodarone or desethylamiodarone (7.5 M) for 42 h.

^cData are given as mean ± SEM (n), where n is the number of analyses.

Discussion

It is clear from these results presented that x-ray microanalysis can be usefully exploited to study drug accumulation if suitable conditions exist. A problem with this analysis is that the label has to be present in millimolar concentrations in order to be measured with reasonable accuracy. The reason amiodarone and desethylamiodarone can be successfully detected in the alveolar macrophages is that these drugs bind with phospholipid and accumulate in the lysosomal lamellar structures in relatively high concentrations. Another handicap of the x-ray microanalysis technique is its inability to distinguish the chemical forms of the molecule that contain the element of interest. In our previous *in vivo* experiments with amiodarone,^{2,4} the high iodine signal detected in the dense granules and lamellar structures clearly did not come from amiodarone alone because the drug is metabolized in the liver and desethylamiodarone and bis-desethylamiodarone must also have contributed to the signal.¹² There is no way to tell the relative amount of each metabolite in the various structures. *In vitro* cultures of alveolar macrophages circumvent this difficulty. The fact that alveolar macrophages metabolize neither amiodarone nor desethylamiodarone makes it possible to study the intracellular distribution of the two drugs in cultured cells by x-ray microanalysis and to examine the differential accumulation in the cell. Alveolar macrophages exposed to either amiodarone or desethylamiodarone accumulated significant levels of the drug during 42 h in culture. In both cases, iodine, which serves as a marker for the drugs, was distributed into all compartments that were analyzed. The iodine lev-

els are higher in amorphous bodies and dense granules than in the cytosol and nucleus.

Desethylamiodarone is clearly taken up into all compartments of the cells to higher levels than is amiodarone. In particular, desethylamiodarone is markedly higher in amorphous bodies than is amiodarone. This higher accumulation of the desethylamiodarone is apparently due to its higher binding capability to phospholipids. We have no proven explanation for the broad distribution of desethylamiodarone.

In order to test how preformed lipid lamellar structures affect the accumulation of the drugs, we produced lipidotic alveolar macrophages by treating rats with chlorphentermine. Again, the desethylamiodarone concentration in the lamellar structures was higher than the amiodarone, but the concentration of the drug was lower than that found with no preexisting lipid structures. When the total amount of drug present in the cell is measured by use of HPLC, we have found that the lipidotic cells contain much greater amounts of the drugs than the non-lipidotic cells. Because of the preponderance of lipid structures in the cell, it is not difficult to see that the total amount of drugs in the cell is higher, though the concentrations in the organelles are lower than that found in normal alveolar macrophages when exposed to the drugs. The difficulty of the drugs in penetrating the inner portion of the lamellar structure is clearly shown by the finding of relatively high iodine signal found at the edges as opposed to the center of the lamellar structure. In summary, we have shown that by using *in vitro* culture of cells we were able to investigate intracellular accumulation of amiodarone and desethylamiodarone independent of one another.

References

1. J. W. Trimble, D. S. Mendelson, B. F. Fetter, P. Ingram, J. J. Gallagher, and J. D. Shelburne, "Cutaneous pigmentation secondary to amiodarone therapy," *Arch. Dermatology* 119: 914, 1983.
2. R. G. Kirk, M. J. Reasor, and Ping Lee, "Iodine in rat alveolar macrophages following amiodarone treatment: Quantitative x-ray microanalysis," *Exptl. Molec. Path.* 49: 339, 1988.
3. R. G. Kirk, Ping Lee, and M. J. Reasor, "Quantitative x-ray microanalysis of alveolar macrophages after long-term treatment with amiodarone," *Exptl. Molec. Path.* 52: 122, 1990.
4. R. G. Eckenroff and H. Shuman, "Subcellular distribution of anesthetic *in situ*," *Proc. Natl. Acad. Sci.* "Drug distribution in cells using x-ray microanalysis," in P. E. Russell, Ed., *Microbeam Analysis--1989*, 31.
5. J. W. Mason, "Medical intelligence: Drug therapy, amiodarone," *N. Engl. J. Med.* 316: 465, 1987.
6. C. L. Ogle and M. J. Reasor, "Response of alveolar macrophages to amiodarone and desethylamiodarone, *in vitro*," *Toxicology* 62: 227, 1990.
7. T. A. Hall, "The microprobe assay of

chemical elements," in G. Oster, Ed., *Physical Techniques in Biological Research*, New York: Academic Press, 1A: 157, 1971.

9. F. H. Schamber, "A modification of the linear least-squares fitting methods which provides continuum suppression," in T. G. Dzubay, Ed., *X-ray Fluorescence Analysis of Environmental Samples*, Ann Arbor, Mich.: Ann Arbor Science, 1977, 241.

10. H. Shuman, A. V. Somlyo, and A. P. Somlyo, "Quantitative electron probe microanalysis of biological thin sections: Method and validity," *Ultramicroscopy* 1: 317, 1976.

11. M. J. Reasor, R. A. Koshut, and V. Castronova, "Biochemical characteristics of rat alveolar macrophages with chlorphentermine-induced phospholipids: Variations with increasing cell size," *Exp. Molec. Pathol.* 31: 297, 1979.

12. M. J. Reasor, C. L. Ogle, E. R. Walker, and S. Kacew, "Amiodarone-induced phospholipidosis in rat alveolar macrophages," *Am. Rev. Respir. Dis.* 137: 510, 1988.

Analysis of Environmental Toxicants

HEXACHLOROBENZENE TOXICITY IN THE MONEKY OVARY: II. ULTRASTRUCTURE INDUCED BY MEDIUM (1.0 mg/kg) DOSE EXPOSURE

A. Singh, D. E. Sims, J. Jarrell, and D. C. Villeneuve

Hexachlorobenzene (HCB), a persistent organochlorine pesticide, is known to occur in the environment^{1,2} and is produced as a byproduct during the manufacture of chlorinated solvents.³ HCB has been shown to be present in human serum and follicular fluid. An objective of the present study was to detect the cytologic effects of HCB on ovarian follicles in a primate model. This report is part of a larger investigation to study the ovarian toxicity of HCB.

Experimental

Eight cynomolgus monkeys were housed under controlled conditions at the Animal Facility of Health Protection Branch, Ottawa.⁴ Animals were orally administered gelatin capsules containing HCB mixed with glucose in daily dosages of 0.0 or 1.0 mg/kg body weight for 90 days; the former was the control group. On the menstrual period following completion of dosing, the animals were induced to superovulate by use of pregnol and HCG, and then humanely killed. At necropsy, one ovary from each animal was diced into 2-3mm cubed specimens that were fixed by immersion in 2.5% glutaraldehyde in 0.1 M cacodylate buffer (pH 7.3); specimens were post-fixed in 2% osmium tetroxide prepared in the same buffer, followed by conventional processing procedures for transmission electron microscopy.⁵ Thin sections were examined in a Hitachi H-7000 electron microscope at 75 kV. The term follicle was used in the same context as defined by Haney.⁶

Results

Images of ovaries from animals of the control group were characteristic of normal monkey ovary (Figs. 1 and 2). In early follicles, nuclei of developing ova were vesicular and ooplasm mitochondria were distributed typically in several clusters. A layer of follicular cells in early follicles that was composed of simple flat or squamous epithelium rested on basal lamina which separated the cells from theca folliculi (Figs. 1 and 2). In the treated group, follicles at various stages of development manifested morphologic lesions. Degenerative changes were observed in developing ova,

follicular cells, and theca folliculi (Figs. 3 and 4). Nuclei of many developing ova had lost chromatin; some of these nuclei contained pyknotic nucleoli. Ooplasm in early follicles was most severely affected (Fig. 3). Mitochondria had electron-lucent matrices, had lost their characteristic distribution pattern, and were gathered as a single heap in the cytoplasm. Ooplasm in primordial follicles had heightened number of lysosomal elements (Fig. 3). Basal lamina in these follicles had thickened. Follicular cells showed degenerative lesions (compare Fig. 2 with Fig. 4). Cells of the theca folliculi contained necrotic cytoplasm (Fig. 4); some primordial follicles were denuded of this layer (Fig. 4). Ovarian stroma exhibited a paucity of cells, giving it a fibrous appearance.

Discussion

The ovary from cynomolgus monkeys fed 1.0 mg/kg of HCB exhibited follicle and stromal lesions and was consistent with architectural alterations in the ovary that were recorded in animals dosed with a 0.1 mg/kg body weight of HCB.⁴ The described alterations in the present study of follicles and stroma from ovary of monkeys fed HCB might have occurred due to atresia, a normal physiological phenomenon, but atresia of follicles in the monkey is heralded by changes which occur first in follicular (granulosa) cells that show pyknotic nuclei.⁷ Follicular cells in the examined follicles from treated group had vesicular nuclei (Fig. 4). The presence of electron-lucent mitochondria in our study may be indicative of water and solute influx into the cell, and therefore of an abnormal cell. Altered morphology of mitochondria may result from any injury-causing entry of solutes into cells or its organelles.⁸

In the present work, cytoplasm of developing ova contained an augmented number of lysosomal elements which is suggestive of increased intracellular digestive activity presumably due to cell injury as a result of chemical insult. Autophagy is exaggerated in cells affected by sublethal injury.^{8,9} The breakdown of follicular cells observed in our work may allow greater exposure to the chemical, and thus cause degeneration of developing ova. A fibrous appearance of ovarian stroma may have been caused by degeneration of cells in the interfollicular region.

A light-microscopic study documents changes in monkey ovary surface epithelium where a much higher dose than in the present study of HCB was given.¹⁰ However, even at the 1.0mg/kg HCB level, surface epithelium of monkey ovary

A. Singh and D. E. Sims are at the Atlantic Veterinary College, Charlottetown, PE, Canada C1A 4P3; J. Jarrell is at the University Foot-hills Hospital, 1403 29th Street, N.W., Calgary, AB, Canada T2N 2T9; D. C. Villeneuve is at the Environmental Health Directorate, Tunney's Pasture, Ottawa, ON, Canada K1O 0L2. Ms. Anna Dykeman provided indispensable aid.

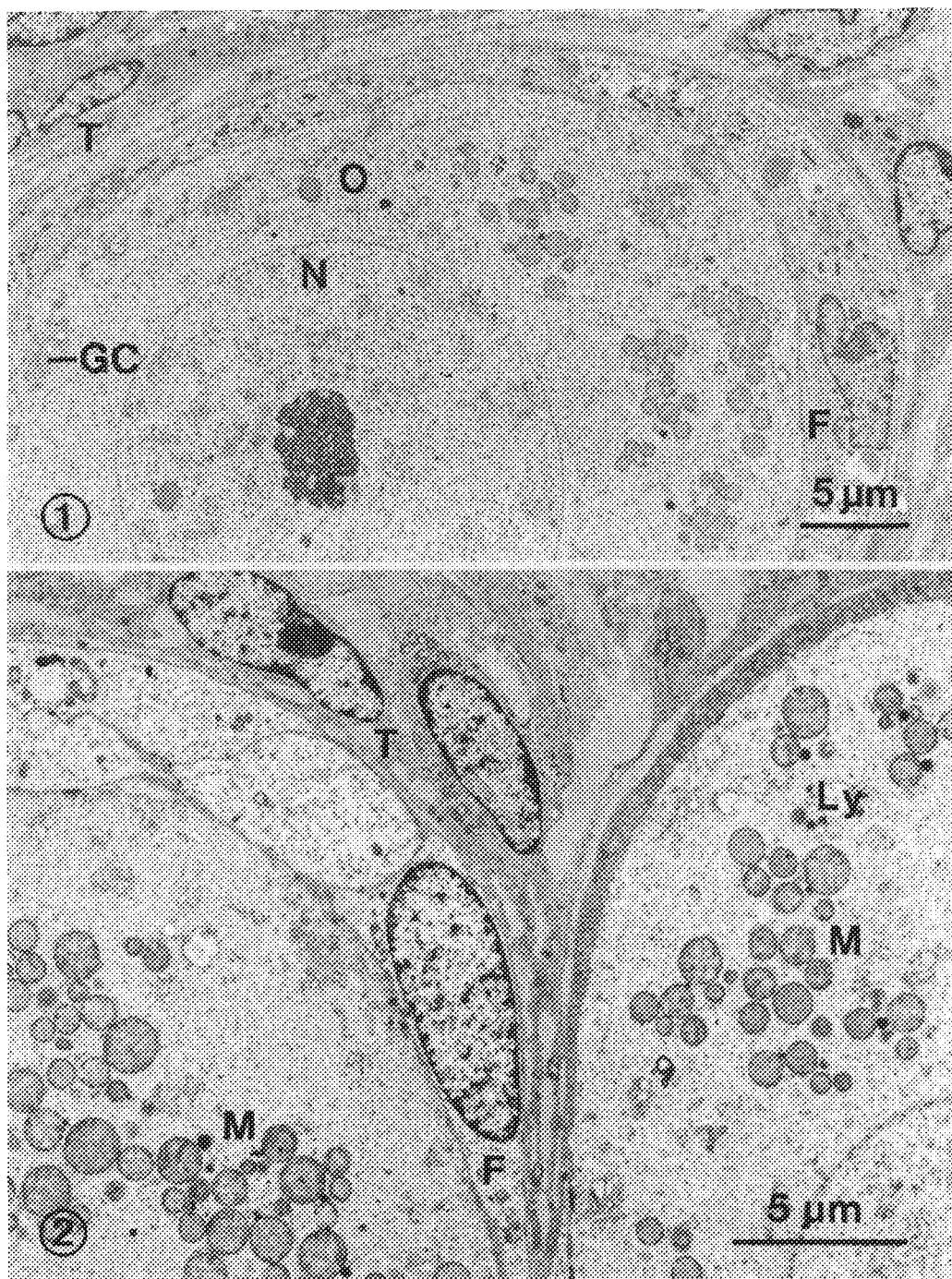


FIG. 1.--Portion of primordial follicle from cynomolgus monkey of control group. F = follicular cell; GC = Golgi complex; N = nucleus; O = ooplasm; T = theca folliculi.

FIG. 2.--Portions of two primordial follicles from another monkey of control group to depict characteristic accumulations of mitochondria (M) in developing ovum cytoplasm. F = follicular cell; Ly = lysosomal elements; T = theca folliculi.

was altered¹¹ in one of our other studies on toxicity of the compound on monkey ovary (Babineau et al., manuscript submitted for publication). A combined effect of discussed alterations in the follicles, stroma, and surface epithelium would lead to failure of ovarian function and disruption of dynamic hormonal equilibrium, since these structures must func-

tion in concert to realize the process of reproduction.

References

1. D. Krewski et al., "Environmental risk assessment: Hexachlorobenzene," in C. R. Morris and J. R. P. Cabral, Eds., *Hexachlorobenzene*, Lyon: Int. Agency Res. Cancer, 1986, 621.

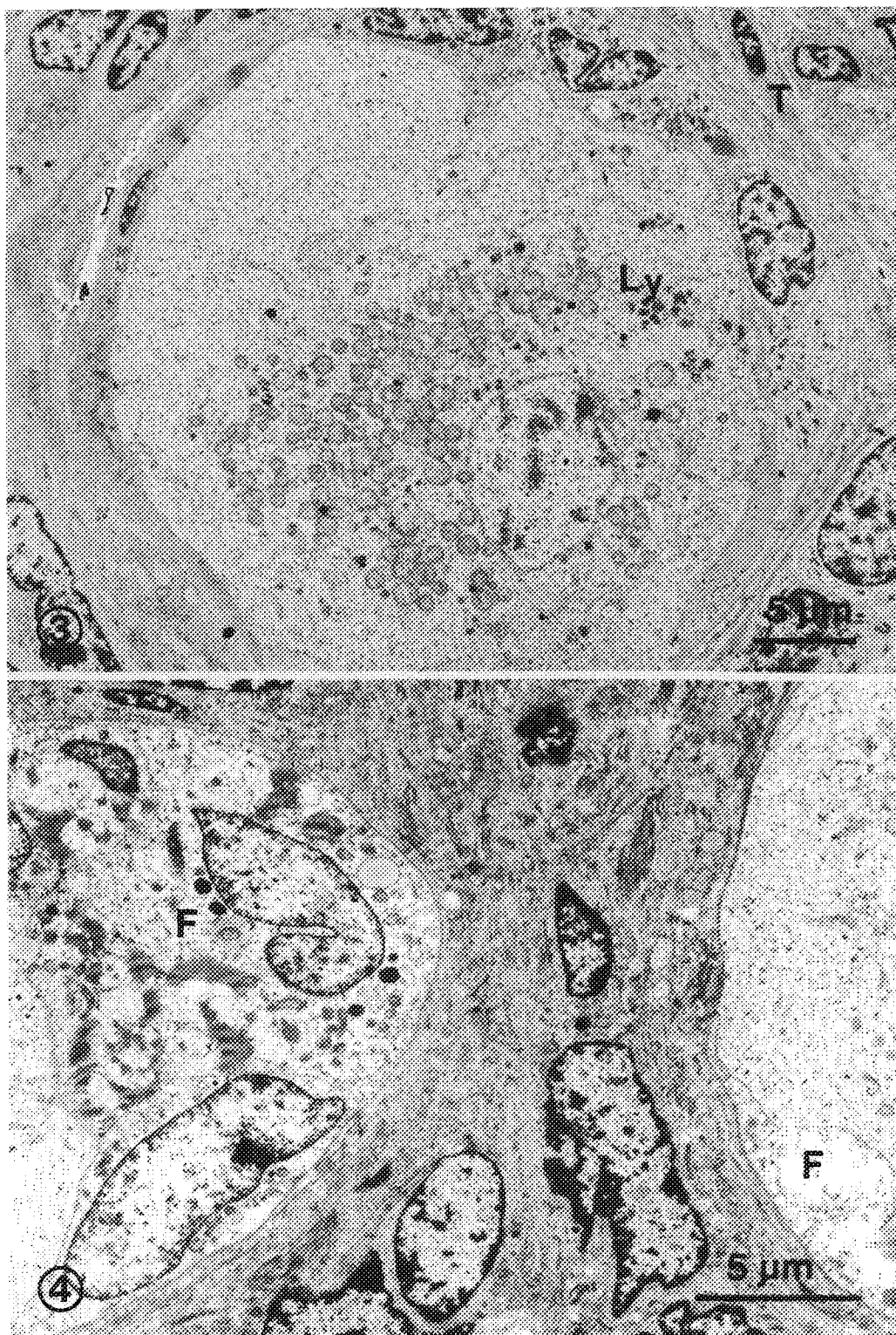


FIG. 3.--Similar follicle as illustrated in Fig. 1 but from HCB-exposed animal. Note abnormal number of lysosomal elements (Ly) and irregular collection of mitochondria in degenerating ovum. T = theca folliculi.

FIG. 4.--Portions of two early follicles from HCB-exposed animal are mostly denuded of theca folliculi, with severely altered follicular cells from HCB-exposed animal. F = follicular cell.

2. A. Nair and M. K. K. Pillai, "Monitoring of hexachlorobenzene residues in Delhi and Faridabad, India," *Bull. Environ. Contam. Toxicol.* 42: 682, 1989.

3. P. Tobin, "Known and potential sources of hexachlorobenzene," in C. R. Morris and J. R. P. Cabral, Eds., Ref. 1, 3.

4. A. Singh et al., "Hexachlorobenzene tox-

icity in the monkey ovary. 1. Ultrastructure induced by low (0.1 mg/kg) dose exposure," *Proc. XII Meet. ICEM II*: 282, 1990.

5. A. Singh et al., "Ultrastructural alterations in the liver of rats fed Photomirex (8-monohydromirex)," *Pathology* 13: 487, 1981.

6. A. F. Haney, "Endocrine and anatomical correlations in human ovarian pathology,"

Environ. Hlth. Perspect. 73: 5, 1987.

7. M. J. Koering, "Comparative morphology of the primate ovary," *Contrib. Primat.* 3: 38, 1974.

8. N. F. Cheville, *Cell Pathology*, Ames: Iowa State University Press, 1983, Ch. 2, 3, 9.

9. F. N. Ghadially, *Ultrastructural Pathology of the Cell and Matrix*, 3rd ed., London: Butterworths, 1988.

10. M. J. Iatropoulos et al., "Morphological effects of hexachlorobenzene toxicity in female rhesus monkeys," *Toxicol. Appl. Pharmacol.* 37: 433, 1976.

11. K. Babineau et al., "Effects of hexachlorobenzene feeding on surface epithelium of primate ovary: An ultrastructural study," *Research Rostrum*, 42nd Meet. Can. Vet. Med. Assoc., Halifax, NS, 1990, 10.

HEPATOTOXICITY OF RUBBER VULCANIZATION FUMES IN RATS

Konrad Rydzynski, Barbara Opalska, Slawomir Czerczak, and Jan Stetkiewicz

Epidemiological studies identified the presence of many hazards in the working environment of the rubber industry.¹ Rubber vulcanization fumes are one of the hazardous agents that occur in the workplace atmosphere in the rubber factories. Vulcanization processes generate a whole spectrum of vapors and gases, which contain, among others, benzene, trichloroethylene, benzo[a]pyrene, and nitrozamines.¹

The mutagenic activity of airborne particulate material and of several rubber additives and vulcanization fumes was demonstrated.²⁻⁴ Moreover, a higher prevalence of lung cancer and chronic bronchitis was detected among rubber industry workers.^{1,5,6} In guinea pigs exposed to rubber vulcanization fumes parenchymal infiltrations with inflammatory cells and increased numbers of mast cells were observed in the lungs.⁷ Dermatological effects resulting from exposure to rubber and/or rubber chemicals are also documented.⁸ However, little is known about effects on the liver of combined exposure to the mixture of gases, fumes, and particulates emitted in the vulcanization processes. The present study has been aimed at the evaluation of potential hepatotoxic effects of acute and subchronic inhalatory exposures in rats. We have shown that short exposure to rubber vulcanization fumes at high concentrations induced reversible liver steatosis. Subchronic 28-day exposure to the fumes at lower concentration led to hepatotoxic effect concerning mainly mitochondria and peroxisomes.

Experimental

Wistar rats were exposed to rubber vulcanization fumes in dynamic inhalation chambers for 4 h at a fumes concentration of 2-3 mg/l (acute exposure); and for 5 h daily, five times a week, for 28 days, at a fumes concentration of 0.1 mg/l (subchronic exposure). Controls inhaled the air under the same conditions. Liver samples were taken from rats immediately after termination of both exposure types, and at days 2 and 14 after termination of acute exposure to study recovery processes. The samples were fixed, dehydrated, and embedded according to conventional EM procedures. The numbers of fat-storing cells (FSC) and Kupffer cells were estimated directly on JEOL JEM100C fluorescence

screen at magnification of 2600× (measured area 7500 μm^2). Relative volume of lipid droplets in the liver parenchyma and, separately, in hepatocytes and FSC were determined on toluidine blue-stained semithin sections by means of computer image analyzing system (CLIP, Technical University of Lodz) and expressed as a $\mu\text{m}^3/\mu\text{m}^3$ of liver tissue. The single examined area was 8464 μm^2 , whereas the resolution was 0.36 $\mu\text{m}/\text{pixel}$. In addition, relative volume of lipid droplets in FSC cytoplasm was determined on electron micrographs by point-counting analysis according to Wiebel⁹ and expressed as a percent volume of FSC cytoplasm occupied by lipid droplets.

Results

In the liver of animals subjected to acute exposure, immediately after termination and on the 2nd day after exposure, fatty degeneration and proliferation of smooth endoplasmic reticulum, mainly in peripheral zone hepatocytes were observed. In some hepatocytes focal cytoplasmic degradation was seen. Results of morphometric investigations on liver lipids in acute exposure are presented in Table 1. Relative volume of total lipid content increased from 0.39 ± 0.02 to as high as $6.39 \pm 1 \mu\text{m}^3/\mu\text{m}^3$ liver tissue on the 2nd day after acute exposure, and remained still higher than normal on the 14th day; $1.17 \pm 0.13 \mu\text{m}^3/\mu\text{m}^3$ liver tissue. Relative volume of hepatocyte lipids followed these patterns, whereas the volume occupied by FSC lipids was the same on the 2nd day as in the controls; 0.30 and $0.33 \mu\text{m}^3/\mu\text{m}^3$ liver tissue, respectively, increasing to $0.89 \pm 0.04 \mu\text{m}^3/\mu\text{m}^3$ liver tissue on the 14th day after exposure. The liver FSC counts in unexposed rats amounted to a mean number of 124 ± 11 cells/ mm^2 . After acute exposure to rubber vulcanization fumes, the FSC number decreased on the 2nd day to 97 ± 8 cells/ mm^2 , then increased to 142 ± 35 cells/ mm^2 , but the changes were not statistically significant for $p < 0.05$. However, relative volume of lipid droplets in FSC cytoplasm increased after 2 days by $\sim 80\%$ (Figs. 1 and 2, Table 1).

After subchronic exposure to rubber vulcanization fumes no fatty degeneration was observed. The numbers of FSC and their lipid content were similar to those in the controls. The swelling of mitochondria, disruption of mitochondrial cristae, and increased number of autophagolysosome and peroxisomes were found in hepatocytes (Figs. 3 and 4).

Discussion

Our findings revealed that acute exposure to rubber vulcanization fumes at high concentra-

The authors are at the Department of Pathomorphology, Nofer Institute of Occupational Medicine, P.O. Box 199, 8 Teresy St., 90-950 Lodz, Poland. An IFSEM travel grant for one of us (K.R.) to attend XII ICEM, and additional financial support from Balzers Union AG is gratefully acknowledged. The work was supported by a CPBR grants 11.11.6.1 and 11.11.1.13.

TABLE 1.--Effects of acute exposure to rubber vulcanization fumes (4 h, concentration of 2-3 mg/1) on rat liver lipids. Data show relative volume of lipid droplets in whole liver (Total), hepatocytes (Hepatocyte), and fat-storing cells (FSC). Results are expressed as mean \pm standard error of mean. Statistical significance ($p < 0.05$) between controls and experimental groups marked by asterisk.

Group	Total	Hepatocyte	FSC	FSC/Total	FSC cytoplasm	FSC number
of rats	$\mu\text{m}^3/\mu\text{m}^3$ liver parenchyma			in %	in % vol	per mm^2 liver
Controls	0.39 ± 0.02	0.06 ± 0.01	0.33 ± 0.01	85.5 ± 2.18	34.7 ± 7.25	124 ± 11
2 days	$6.39 \pm 1.00^*$	$6.09 \pm 1.00^*$	0.30 ± 0.02	$7.0 \pm 2.0^*$	$59.2 \pm 5.2^*$	97 ± 8
14 days	$1.17 \pm 0.13^*$	$0.28 \pm 0.11^*$	$0.89 \pm 0.04^*$	81.2 ± 4.6	$52.8 \pm 4.78^*$	142 ± 35

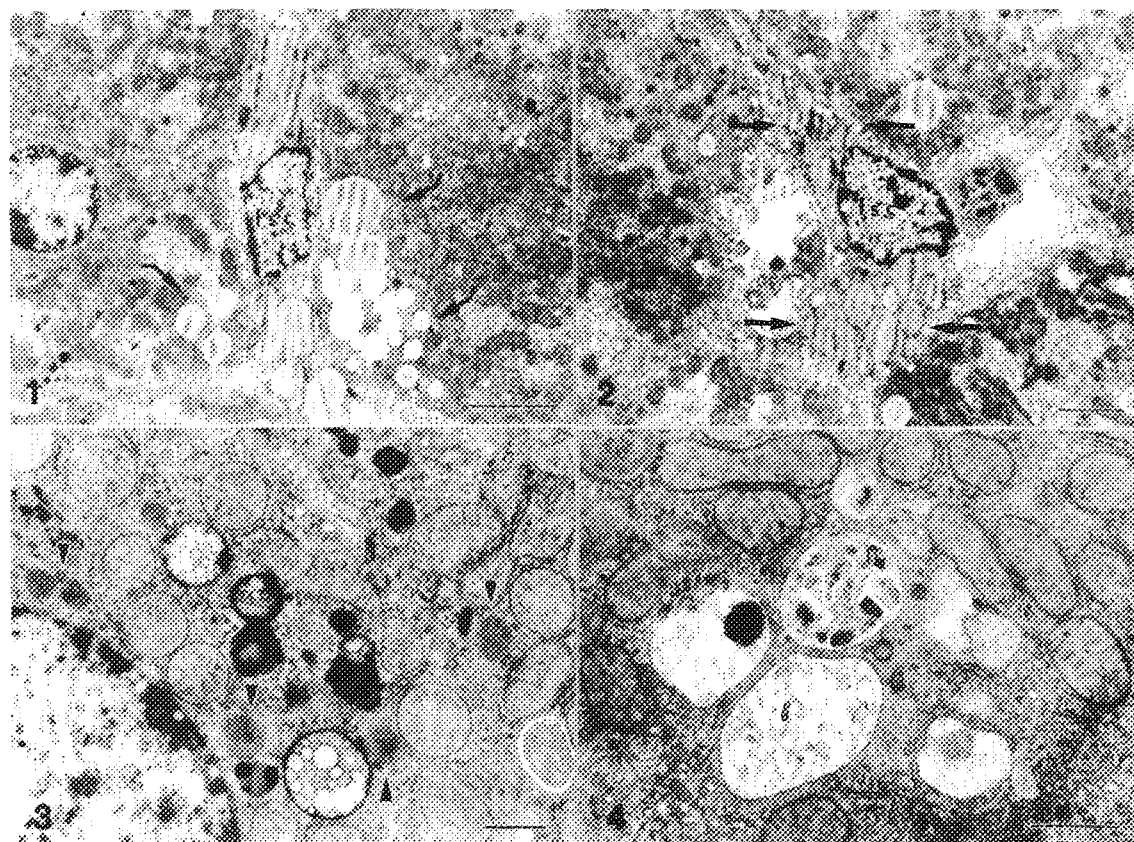


FIG. 1.--Lipid accumulation in hepatocytes 2 days after acute exposure to rubber vulcanization fumes (arrows). Note also fat-storing cell (FSC) with lipid droplets. (Bar = 5 μm .)

FIG. 2.--Lipid accumulation in FSC 14 days after acute exposure (arrows). (Bar = 5 μm .)

FIG. 3.--Secondary lysosomes in perinuclear region of hepatocytes after subacute exposure to rubber vulcanization fumes. Note also increased number of peroxisomes (arrowheads). (Bar = 1 μm .)

FIG. 4.--Injured mitochondria in hepatocytes after subacute exposure. (Bar = 1 μm .)

tions induce reversible fatty degeneration (steatosis) in the liver. A large number of chemical agents can produce fatty liver. The type observed after acute exposure to rubber vulcanization fumes may be described briefly as peripheral microvesicular steatosis. This type tends to occur after treatment with chemicals primarily affecting protein synthesis.¹⁰ There are various potential mechanisms by which these processes may be affected by chemicals presented in rubber vulcanization fumes. For example, dimethylnitrosamine is postulated to act by alkylation of DNA and RNA;¹¹ others, like trichloroethylene, are thought to be converted to highly active metabolites which can interact with hepatic proteins to form alkylated derivatives.¹² However, specific steatogenic molecular mechanisms are unknown for the most of steatogens.¹⁰ Fat-storing cells account for 1.4% in the total volume of the liver,¹³ but we have shown here that 85% of normal liver lipid droplets are found in these cells (Table 1). Proliferation of FSCs was described in fatty degeneration due to alcoholic hepatitis, CCl₄ intoxication, and vinylchloride poisoning.¹³ After acute exposure to rubber vulcanization fumes we have found that the numbers of FSC varied, showing the decrease after 2 days and the increase after 14 days. The observed changes in FSCs number were not statistically significant, but they might be caused by great variations in their numbers between animals even in the controls. Our observation that FSCs contain 80% more lipid droplets in their cytoplasm on the 14th day after exposure even if the lipid contents in hepatocytes approaching normal level, indicate that FSCs might play an important role in restoring lipid metabolism in the liver to the norm.

Subchronic 28-day exposure to the vulcanization fumes at much lower concentrations led to changes concerning mainly mitochondria and peroxisomes. There is little doubt that mitochondrial swelling, fragmentation, and disruption of their cristae membranes are caused by chemical injury. However, all those changes may occur in response to a variety of forms of injury, including anoxia, and also may be artifactual.^{14,15} Peroxisomes appear to protect against peroxidative injury, and are involved in lipid metabolism. They increase in number in response to a number of drugs and chemicals.^{14,15} Whether the increase in peroxisomes is an adaptative response or evidence of injury is still uncertain.

References

1. IARC, *Monographs on the evaluation of the carcinogenic risk of chemicals to humans: The rubber industry*. IARC 28, Lyons, France, 1982.
2. A. Hedenstedt, C. Ramel, and C. A. Wachtmeister, "Mutagenicity of rubber vulcanization gases in *Salmonella typhimurium*," *J. Toxicol. Environ. Health* 8: 805, 1981.
3. M. Donner, K. Husgafvel-Purianen, D. Jenssen, and A. Rannug, "Mutagenicity of rubber additives and curing fumes," *J. Work Environ. Health* 9: 27, 1983.
4. B. Baranski, J. Indulski, E. Janik-Spiechowicz, and J. Palus, "Mutagenicity of airborne particulates in the rubber industry," *J. Appl. Toxicol.* 9: 389, 1989.
5. H. L. Fine and J. M. Peters, "Respiratory morbidity in rubber workers: I. Prevalence of respiratory symptoms and disease in curing workers," *Arch. Environ. Health* 31: 5, 1976.
6. T. Sorahan, H. G. Parces, C. A. Veys, and J. Waterhouse, "Cancer mortality in the British rubber industry: 1946-1980," *Br. J. Ind. Med.* 43: 363, 1986.
7. K. Rydzynski, A. Domanska, S. Czerczak, and B. Krysiak, "Effect of subchronic exposure to the rubber vulcanization fumes on the guinea pig lungs," *Polish J. Occupat. Med.* (in press).
8. E. Cronin, *Contact Dermatitis*, Edinburgh: Churchill Livingstone, 1980, 714.
9. E. R. Weibel and D. M. Gomez, "A principle of counting tissue structures on random sections," *J. Appl. Physiol.* 17: 343, 1962.
10. J. R. Glaister, *Principles of Toxicological Pathology*, London and Philadelphia: Taylor and Francis, 1986, 81.
11. J. R. Gillette, "Mechanisms of hepatic necrosis induced by halogenated aromatic hydrocarbons," in D. Keppler, Ed., *The Pathogenesis and Mechanisms of Liver Cell Necrosis*, Lancaster, England: MTP, 1975, 239.
12. H. Allemand, D. Passayre, V. Desca-toire, C. Degott, G. Feldman, and J. Benhamou, "Metabolic activation of trichloroethylene into a chemically reactive metabolite toxic to the liver," *J. Pharmacol. Exp. Ther.* 204: 714, 1978.
13. H. David and P. Reinke, "The concept of the 'perisinusoidal functional unit' of the liver: Importance to pathological processes," *Exp. Pathol.* 32: 193, 1987.
14. B. A. Fowler, G. W. Lucier, and A. W. Hayes, "Organelles as tools in toxicology," in A. W. Hayes, Ed., *Principle and Methods in Toxicology*, New York: Raven Press, 1989, 815.
15. A. M. Jezequel, "Ultrastructural changes induced by drugs on the liver," in W. Taylor, Ed., *The Hepatobiliary System: Fundamental and Pathological Mechanisms*, New York: Plenum Press, 1976, 179.

MICROANALYSIS OF ASBESTOS FIBERS BY FT-IR MICROSCOPY

J. A. Reffner and W. T. Wihlborg

Identification of asbestos fibers in bulk and airborne samples can be made by Fourier transform infrared (FT-IR) microscopy. Since asbestos fibers have been shown to be a health hazard, it is important to identify their presence in environment samples.¹ Infrared (IR) spectroscopy has been used to characterize asbestos and asbestos containing materials.² However, these classic IR methods do not provide information on sample morphology. Asbestos minerals require both chemical and morphological data for their identification.^{3,4} Since only the fibrous forms of asbestos have been shown to be health hazards, it is critical that the analytical technique employed permit the observation of sample morphology. The FT-IR microscopical method presented here uses light microscopy to observe the sample's morphology and IR spectroscopy to determine the chemical identity of microscopical fibers.

FT-IR microscopy can be used to identify asbestos fibers and morphologically similar materials. Full range mid-infrared spectra (4000-600 cm^{-1}) provide a positive qualitative analysis of all six asbestos minerals. IR microbeam analysis can also confirm the presence of asbestos fibers in samples prepared for polarized light microscopy (PLM) identification or phase contrast counting. A detection limit of 220 pg was established for airborne chrysotile fibers collected on cellulose ester filters.

Experimental

Instrumentation. The IR spectra presented here were obtained by means of an IRus[™] infrared microspectrometer system.^{5,6} (The IRus fully integrated FT-IR microscope is described elsewhere in this volume.)⁶ The IRus' diffraction limited, high numerical aperture optics, 15X, 0.58 N.A. and 32X, 0.65 N.A. objectives and 10X, 0.71 N.A. condenser were used. A dry, CO_2 free, air purge, which is critical for the evaluation of asbestos materials smaller than $5 \times 50 \text{ m}$, was used. Spectra were collected within the range 4000-600 cm^{-1} (2.4 to 16.7 μm) at a spectral resolution of either 4 or 2 cm^{-1} . Data collection was 2 min for all samples except where noted.

Sample Preparation. Four sample preparation techniques were utilized for IR microanalysis. To obtain full range mid-infrared spectra of asbestos standards^{7,8} and morphologically similar materials,^{9,10} the samples were mounted between two IR transmitting windows (NaCl) and placed in a $\mu\text{Sample Plan}^{\text{™}}$ compression cell. Bulk asbestos samples were prepared by two dif-

ferent methods. The first entailed preparing the sample for PLM. The bulk samples were dispersed in Cytoseal 60[™] mounting medium or Cargille np 1.550 HD oil on glass microscope slides and covered with a glass coverslip. The second method, which was applied to samples of roofing material and floor tile, involved soaking the matrix in methylene chloride, placing a drop of the suspension on a NaCl window, and allowing it to evaporate forming a thin film. Finally, airborne fibers collected on cellulose ester filters were prepared for analysis by the NIOSH 7400 method. A portion of the filter was placed onto a glass slide and then exposed to acetone vapors to collapse the filter's structure. When the filter cleared, a drop of triacetin was used to optically couple the coverslip.

Results and Discussion

The IR spectra of the six asbestos minerals actinolite, amosite, anthophyllite, chrysotile, crocidolite, and tremolite) are reported in Fig. 1. Although all six asbestos minerals have strong bands centered near 1000 cm^{-1} (Si-O bands), the intensities and positions of these bands are characteristic of the particular asbestos mineral and they are readily distinguished. Figure 2 shows the IR spectra of Kevlar®, polypropylene, cellulose, wollastonite, and vermiculite, which are morphologically similar to asbestos fibers. Comparison of the IR spectra of these materials with the IR spectra of the six asbestos minerals reveals that they are significantly different and should not be confused spectroscopically.

IR spectra of bulk asbestos samples prepared for PLM are shown in Fig. 3. Note that due to the strong absorbance of the glass substrate in the region below 2300 cm^{-1} only the region between 4000-2300 cm^{-1} can be used. In this narrow region the spectra of the asbestos minerals are not unique enough to enable specific mineral identification. The IR spectra of actinolite and tremolite reveal a pair of bands at 3676 and 3662 cm^{-1} and are indistinguishable since these are isostructural minerals 3). Crocidolite and amosite are also difficult to distinguish in this narrow range. IR spectra of asbestos fibers mounted on glass are not specific enough to identify individual mineral fibers, but they are useful to confirm PLM analysis. Figure 4 illustrates the sensitivity of this technique. The IR spectrum of an $\sim 220\text{pg}$ ($12 \times 3 \text{ m}$) fiber of chrysotile mounted for PLM shows the characteristic doublet associated with the OH bands from chrysotile.

The identification of asbestos in building materials is of paramount importance. One pre-

The authors are at Spectra-Tech Inc., Stamford, CT 06906.

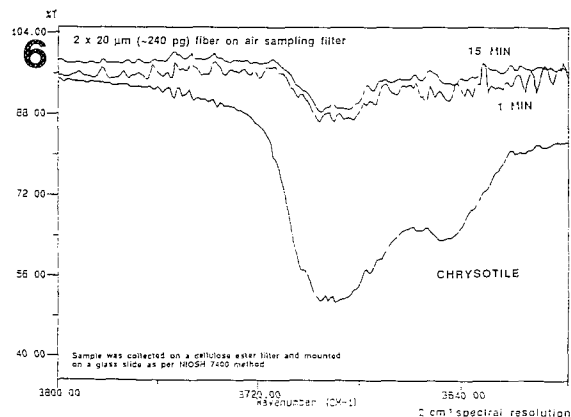
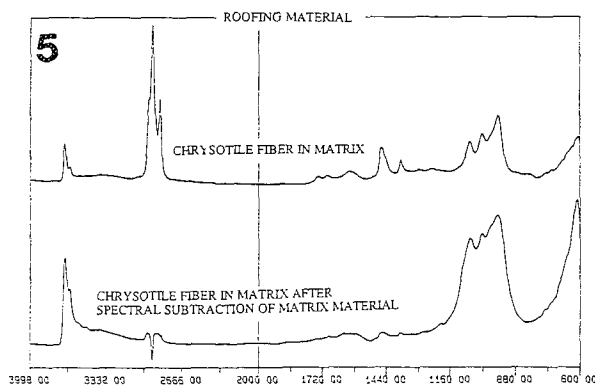
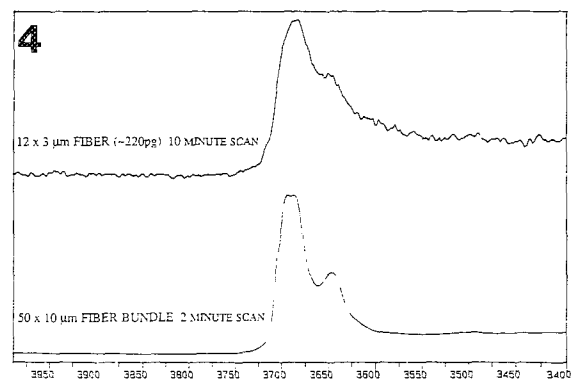
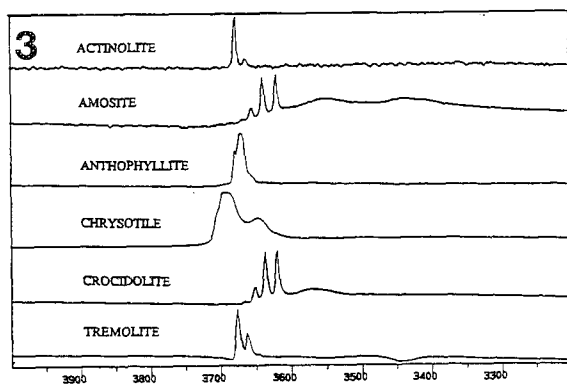
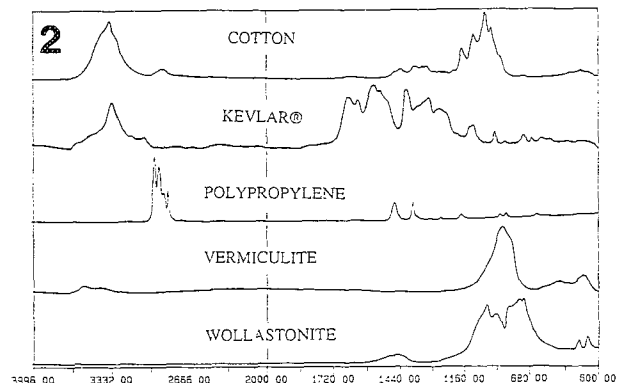
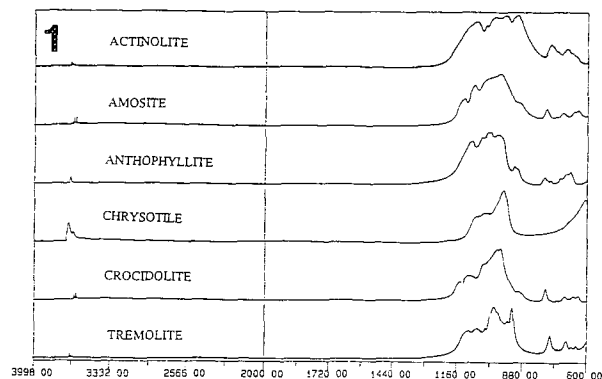


FIG. 1.--Mid-IR absorption spectra of six standard asbestos mineral fibers.

FIG. 2.--Mid-IR absorption spectra of materials morphologically similar to asbestos fibers.

FIG. 3.--IR absorption spectra of asbestos fibers in glass mounts.

FIG. 4.--IR absorption spectra of chrysotile fibers; top: single fiber, approaching detection limit; bottom: fiber bundle.

FIG. 5.--Mid-IR absorption spectra of asbestos in roofing material; top: chrysotile fibers in matrix, bottom: chrysotile fiber after matrix is subtracted.

FIG. 6.--IR transmission spectra of chrysotile fiber on cellulose ester filter. Sample was collected on cellulose ester filter and mounted on glass slide as per NIOSH 7400 method.

pared friable ACMs for FT-IR microscopy by either placing fibers between two IR transmitting windows (NaCl) or by mounting on glass for PLM as previously described. Nonfriable asbestos containing materials such as floor tiles and roofing materials are analyzed via FT-IR microscopy by first separating the fibers from the binding medium. Typically an organic solvent is used to dissolve the binding material which creates a suspension of fibers. The suspension is then transferred to a NaCl window and allowed to evaporate, which leaves

behind both fibers and dilute binding matrix. Complete separation of asbestos from the binding matrix is not necessary to identify fibers as asbestos. The IR spectrum of a fiber in a roofing material (Fig. 5, top spectrum) shows the characteristic chrysotile bands at 3691, 3647, 958, and 608 cm^{-1} , as well as bands due to the binding matrix. Spectral subtraction of pure binding material from the fiber yields a spectrum that matches chrysotile (Fig. 5, bottom spectrum).

Airborne particles collected on cellulose

ester filters are the most challenging samples for the FT-IR microscope. Fibers collected via this method are extremely small and difficult to find without use of phase contrast. Small fibers of chrysotile were used to establish a detection limit for airborne fibers (Fig. 6). For a 1 min collection time at spectral resolution of 2 cm^{-1} , the detection limit was $\sim 220\text{ pg}$ ($2 \times 20\text{ m}$ fiber). Optimizing the IRus system for the $4000\text{--}3500\text{ cm}^{-1}$ spectral range is expected to lower this detection limit.

References

1. W. C. Cooper, *Asbestos: The Need for and Feasibility of Air Pollution Controls*. Committee on Biological Effects of Atmosphere Pollutants (1971) Div. Medical Sciences/National Research Council, Washington, D.C.
2. G. A. Luoma, L. K. Lee, and R. Rowland, *Anal. Chem.* 54: 2140-2142, 1982.
3. H. G. Siegrist and A. G. Wylie, *Environ. Res.* 23: 348, 1980.
4. A. Marconi, E. Menichini, and L. Paoletti, *Ann. Occup. Hyg.* 26: 321, 1984.
5. IRus is a grademark of Spectra-Tech Inc., Stamford, Conn., U.S.A.
6. J. A. Reffner and W. T. Wihlborg, "FT-IR molecular microanalysis system" (this volume).
7. U.I.C.C. Standard reference asbestos samples, Duke Scientific Corp., Palo Alto, Calif.
8. Ward's Natural Science Establishment Inc., Rochester, N.Y.
9. Testfabrics Inc., Middlesex, N.J.
10. Ward's Natural Science.

THE ANALYSES OF ANTHROPOGENIC ATMOSPHERIC PARTICULATES BY ELECTRON MICROSCOPY

P. A. Russell

With the exception of NO_2 , visibility degradation in the atmosphere is caused by suspended particles. The visibility is affected by either optical absorption or scattering. Optical absorption is mainly affected by (1) the cross-sectional area of the particles between the light source and optical receptor, and (2) the light-absorption characteristics of the particles. Optical scattering is most pronounced for "fine" particles in the size range ~ 0.1 – 3.0 μm and is also a function of size distribution and refractive index.^{1,2} Particles in approximately the same size range (~ 0.1 – 10 μm) are also preferentially deposited deep within mammalian lungs where they can be in intimate physical and chemical contact with lung tissue.

Because of the importance of airborne particles in producing visibility degradation and health problems, it is imperative that the particles causing the effect be as completely characterized as possible to (1) understand the possible interactions with the deposition interface/substrate; (2) determine where the particles were generated; and (3) understand the chemical/physical reactions or changes that have taken place between the particle source and receptor sites. Bulk particle analyses are relatively easy to perform and provide information about the particles of interest, including qualitative and quantitative elemental and ionic composition. However, bulk analyses must make assumptions about the degree of homogeneity, and physical and chemical characteristics of the individual particles collected. Discrete-particle analyses can measure more variables of each distinct population of particles being observed, including average size, size distribution, shape, shape variation, internal and external physical structure, chemistry, chemical variation, relative thermal stability, crystallography, ionic composition, and optical properties.

Methods and Materials

The two best tools for examining "fine" discrete atmospheric particles are the scanning electron microscope (SEM) equipped with an energy-dispersive x-ray spectrometer (EDS) and the transmission electron microscope (TEM) equipped to perform selected area electron diffraction (SAED).^{3–5} The SEM/EDS combination has a resolution of ~ 6 nm and can be used to determine the morphological and chemical nature of individual particles. This process can be automated⁶ but is less effective for smaller particles, complex shapes, or particles with

low atomic numbers. Sample preparation can be simple, but samples must be subjected to a vacuum during sample preparation and examination. The TEM produces resolution of ~ 0.4 nm but sample preparation is more difficult and samples must also be subjected to a vacuum during sample preparation and examination. With SAED, it is possible to obtain crystallographic information about individual particles. The optical microscope (OM), especially if it is equipped with an optical or infrared spectrometer, is a useful instrument for the initial examination of particles, but lacks the requisite resolution for the detailed examination of "fine" particles.

For SEM or TEM analyses, particles must be collected on an inert, relatively flat surface. For SEM examination this surface, with adhering particles, is usually transferred to a metal substrate suitable for insertion into a SEM and coated with a thin layer of conductive metal while in a vacuum. For TEM analysis, the particles need to be transferred to an electron-transparent film of metal (or carbon); the particles are usually covered with a very thin film of metal or carbon while on the original collection substrate, and then the original collection substrate is dissolved away and the thin film containing the particles (or replica) is transferred to a previously prepared TEM substrate. It is also possible to collect particles directly onto a thin carbon or metal TEM film. Particles may be collected on chemically reactive substrates for true in situ analysis.⁷

Sample collection of particles may be achieved by filtration, impaction, virtual impaction, electrostatic precipitation, or thermal precipitation. Usually filtration is preferred because of its simplicity. Polycarbonate (e.g., Nucleopore™) filters are preferred for SEM or TEM analysis because of their flat surface and well-defined round pores. Two Nucleopore™ filters of differing pore size may be used in sequence to produce excellent particle size separation. Cellulose acetate (e.g., Millipore™) filters may also be used but are somewhat less desirable because of their convoluted surface and the possible distribution of the smallest particles to hidden depths within the filter. For TEM analyses, cellulose acetate filters must be dissolved with acetone or amyl acetate; polycarbonate filters are dissolved with chloroform. Fluorohydrocarbon filters are preferred for most of the chemical mass balance (CMB) method of bulk analysis, but this method can also use cellulose acetate or polycarbonate filters.

Sample collection may range from simple collection on an open filter to the collection

P. A. Russell is president of Rocky Mountain SEM Consulting, 1551 E. Cornell Ave., Englewood CO 80110-3010.

with virtual impactors equipped with gas-scanning apparatus at the air flow entrance. Novel techniques that employ balloon-borne sampling methods⁸ have been used to collect samples from various sources by multiple samplers simultaneously at variable heights.

When collecting and preparing samples one must take precautions to prevent chemical reactions or physical changes on the filter. The presence of ammonia or high humidity may cause physical and/or chemical changes to collected particles, particularly for sulfate and nitrate particles. Ammonium sulfate particles have even been observed on the back side of filters and as large secondary growths on the front side of filters.

With care and a little imagination, virtually any type of discrete particle can be examined. With a combination of chemical and physical analyses by SEM/EDS (windowless, which permits elemental identification of elements with atomic number ≥ 6) and the TEM with SAED, it should be possible to quantify discrete nitrate and sulfate particles chemically. It is also possible to coat collection substrates with reactive chemicals that react instantly, or later under controlled conditions, to permit further refinement of the chemical identification of discrete liquid or soluble particles.⁹

Other instruments that might have application for discrete particle analysis would include (1) scanning Auger spectroscopy, which could provide high sensitivity for elements, including elements of low atomic number, on particle surfaces; (2) "microspot" x-ray photoelectron spectroscopy (XPS), which would produce sensitive information on elements and chemical bonds; and (3) scanning secondary ion mass spectroscopy (SIMS), which would produce extremely sensitive information on ionic composition, including isotopes. These instruments have generally not been used for the examination of atmospheric particles because of their high use costs, difficult sample preparation, and limited availability. Scanning Tunneling Microscopy (STM) is a relatively new but potentially very useful microscopic technique that offers spatial resolution better than a TEM, is low in cost, and does not require a vacuum. However, its use in examining anthropogenic particles has not been evaluated and it currently cannot provide chemical or crystallographic information.

Results

Since 1973 discrete particles from various locations and sources (including Denver, Colo.; Henderson, Nev.; Provo, Utah; Montezuma's Castle National Monument, Ariz.; Heyden, Colo.; Tampa Bay, Fla.; upstate New York; Los Angeles and San Joaquin Valley, Calif.; and Point Barrow, Alaska) have been examined by SEM/EDS and TEM/SAED. In all those observations, discrete particles rich in sulfate (or nitrate) have rarely been observed. What is usually observed are relatively large concentrations of carbon black particles. If sulfur (nitrates, organics,

etc.) is observed to be present, it is in the form of sulfur chemically/physically adsorbed into the structure of the carbon black. The size, shape, and structure of the carbon black particles are not significantly altered.¹⁰⁻¹⁸ Examples of representative carbon black particles are illustrated in Fig. 1.

Discussion and Conclusions

Carbon black (soot, elemental carbon, inorganic carbon, etc.) is a major component of fine particulate air pollution and has characteristics that make it ideal in affecting optical absorption and scattering. It is also capable of being transported great distances. Carbon black is almost always the location of anthropogenic sulfur collected at receptor sites. The sulfur is adsorbed in the carbon black particles and does not appear to change the physical size or optical characteristics of the carbon black. Carbon black also readily adsorbs other ions and gases.

A current method of bulk analyses of air-borne particles is chemical mass balance (CMB), which quantifies bulk source and receptor samples.¹⁹⁻²¹ It utilizes x-ray excited x-ray fluorescence, ion chromatography, and pyrolysis to determine bulk concentrations of elements, ions, and organic types collected on a filter substrate. It permits the analysis of a relatively large number of air-pollution particulate samples at a relatively low cost and is currently the most refined method for apportioning sources of atmospheric chemical components to sources. Like all bulk analyses, CMB has limitations:

1. It must assume collected samples are homogeneous when they may be in fact a complex mixture of particles of varying size and composition.
2. Bulk x-ray analysis of virtual impactor samples has a bias favoring larger particles because the amount of x rays produced by a "fine" particle is proportional to its mass and volume, and because size segregation by aerodynamic selection always includes some particles larger than the specified limit.
3. The particles segregated by aerodynamic sizes may not be representative of the particle population(s) that are most responsible for optical scattering and absorption, or health problems.
4. Source apportionment of carbon particles among various carbon sources is difficult and, at present, unrefined. The CMB method depends on potassium to differentiate "biological" vs "fossil" carbon in source apportionment. But even though potassium is one of the major elements associated with combustion of biological material, it is also a major component of various mineral particles and flyash, and a minor component of other source emissions including diesel engines. There are also other sources of carbon black (e.g., aircraft, refineries, charcoal burning, restaurants, forest fires, inefficient natural gas combustion, etc.) that have not been profiled. It is also possible that the potassium particle species produced by

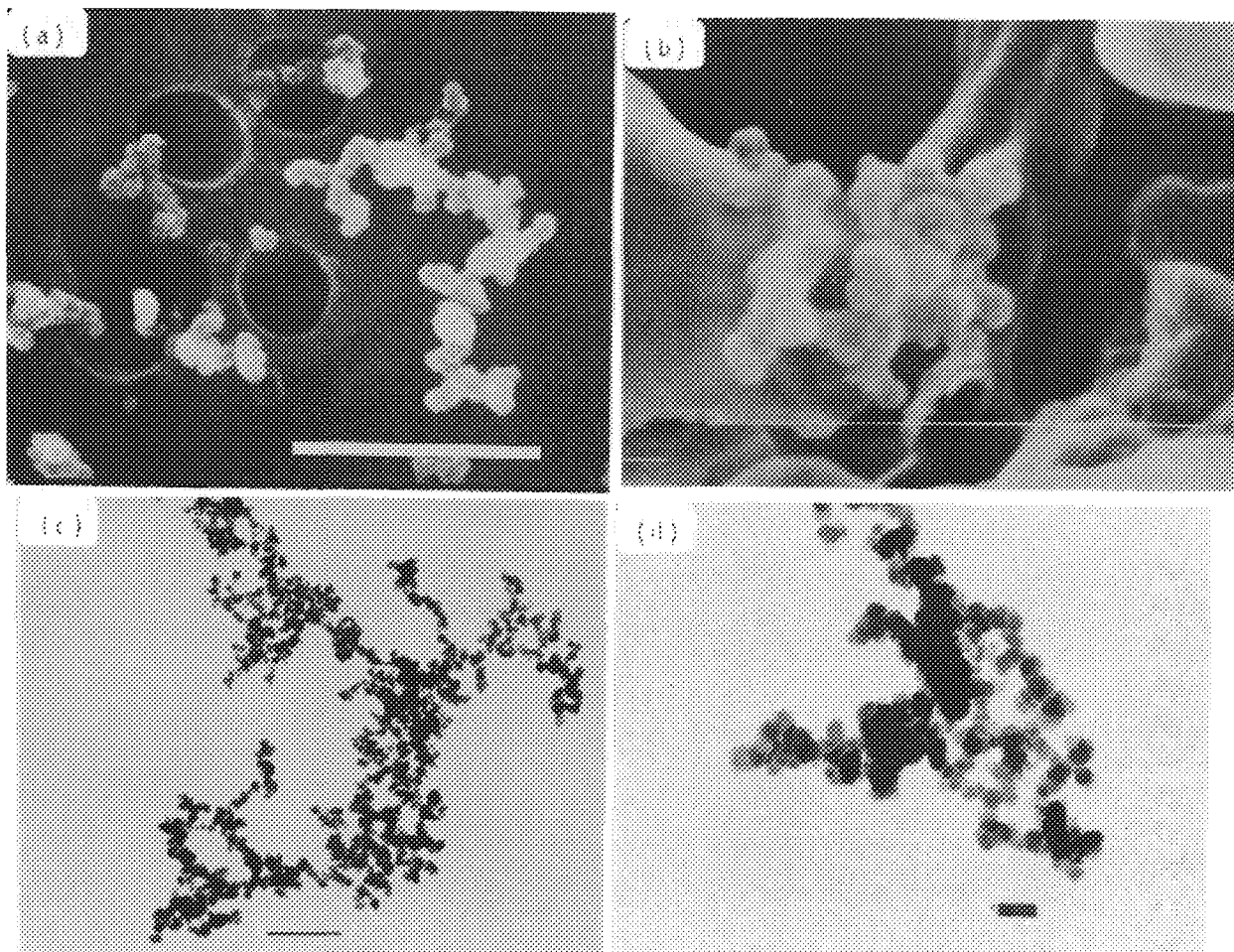


FIG. 1.--(a) SEM micrograph of carbon black particle collected in Denver, Colo., 25 May 1990; bar = 1 μm . (b) SEM micrograph of carbon black particle collected at Barrow, Alaska, 1979; bar = 1 μm . (c) TEM micrograph of relatively large carbon black agglomerate collected in Denver, Colo., 1973, bar = 1 μm . (d) TEM micrograph of smaller carbon black particle collected in Denver, Colo., 1973; bar = 0.1 μm .

burning wood may be discrete particles, different in size from the carbon black particles they are supposed to trace.

The problem of not utilizing the information provided by discrete particle analysis is demonstrated in the results of a 1988-1989 Winter study of Denver's urban plume. An extensive CMB study²² concluded that visibility could be apportioned to 28% carbon produced by mobile sources, 22% carbon produced by vegetative combustion, 9% secondary sulfure, 23% secondary nitrate, 8% minerals, and 10% to other factors including Rayleigh scattering and NO_2 . The analytical results are excellent but the final source apportionment, based on assumptions that are not validated by discrete particle analysis, are in error. What is observed about the discrete fine particles in the Denver "brown cloud" is that (1) no discrete particles of sulfate or nitrate are present, and (2) the predominant fine-particle species are carbon black particles with adsorbed sulfur, etc. It is also known that the adsorbed material has little effect on the physical nature and optical properties of the carbon black particles. However, when these particles are analyzed by bulk XRF and ion chromatography they are chemically indistinguishable from discrete sulfate and nitrate particles. The importance is, that if the sulfate and nitrate sources contributing to Den-

ver's "brown cloud" are reduced or eliminated and the carbon black particle sources are not reduced, no visibility reduction can be expected. From the results from the CMB study and discrete particle analysis it becomes apparent that Denver's visible "brown cloud" is produced mainly by carbon black particles that are the product of automobile emissions²³ and other sources of incomplete combustion. The accuracy of the differentiation between fossil and non-fossil carbon black is also subject to question, considering that carbon black is a predominant component of Denver's particular air pollution all year round.

In conclusion, discrete particle analysis has demonstrated that the fine particles responsible for visibility degradation in the atmosphere may be very different from what theoretical chemical models and bulk analytical techniques suggest. More studies are obviously needed on sulfur (and other chemicals) and its interaction with carbon black in the atmosphere.²⁴ The abundance of anthropogenic carbon black, and its chemical and physical adsorption must also be taken into account when the health effects of inhaled fine particles are modeled. Theoretical chemical models predict that sulfates and other ionic species should be formed as discrete particles from emissions of SO_2 , NH_3 , etc., but these studies have generally ignored or minimized the impact of carbon black

in their estimates of what reaches receptor sites. Therefore, bulk analytical techniques have assumed that their measurements of elements, ions, and ion ratios are produced by discrete particles. However, observations of discrete particles collected from the atmosphere conclude that particles of sulfate and nitrate are rare and that the "fine" particle fraction is usually dominated by carbon black particles containing adsorbed inorganic (and organic) materials. Until chemical modeling, bulk empirical analyses, and discrete particle analyses can be co-validated, serious errors may be made in mitigating air pollution or estimating health effects caused by suspended "fine" anthropogenic particles.

References

1. R. D. Cadle, *The Measurement of Airborne Particles*, New York: Wiley, 1975.
2. W. C. Hinds, *Aerosol Technology: Properties, and Measurement of Airborne Particles*, New York: Wiley, 1982.
3. M. Grasserbauer, "Characterization of individual airborne particles by light microscopy, electron and ion probe microanalysis, and electron microscopy," in H. Malissa, Ed., *Analysis of Airborne Particulates by Physical Methods*, West Palm Beach, Fla.: CRS Press, 1978, 125-178.
4. P. A. Russell, "Analyses of atmospheric sulfur-containing particles by electron microscopy," in P. A. Russell and A. E. Hutchings, Eds., *Electron Microscopy and X-ray Applications to Environmental and Health Analysis*, Ann Arbor, Mich.: Ann Arbor Sciences Publishers, 1978, vol. 1, 205-210.
5. J. T. Armstrong and P. R. Buseck, "Applications in air pollution research of quantitative analysis of individual microparticles with electron beam instruments," *ibid.*, vol. 1, 211-228.
6. G. S. Casuccio, P. B. Janocko, R. J. Lee, J. F. Kelly, S. L. Dattner, and J. S. Mgebroff, "The use of computer controlled scanning electron microscopy in environmental studies," *JAPCA* 33: 937-943, 1983.
7. Y. Mamane, *A Quantitative Method for the Detection of Individual Submicron Sulfate Particles*, Ph.D. thesis, Pennsylvania State University, 1977.
8. J. A. Armstrong, P. A. Russell, L. E. Sparks, and D. Drechsel, "Tethered balloon sampling systems for monitoring air pollution," *JAPCA* 31: 735-743, 1980.
9. Y. Mamane and R. F. Pueschel, "A method for the detection of individual nitrate particles," *Atmos. Environ.* 24: 629, 1980.
10. P. A. Russell, "The analyses of discrete atmospheric particulates: Implications for source/receptor analyses," *Proc. AWMA/EPA Conf. on Visibility and Fine Particles*, Estes Park, Colo. (in press).
11. P. A. Russell, Ed., *Denver Air Pollution Study--1973*, EPA publication 600/9-76-007a, NTIS, Springfield, Va., 1976, vol. 1.
12. *Ibid.*, vol. 2.
13. P. A. Russell and C. O. Rund, "An analysis of particulates from the Denver urban plume using scanning electron microscopy and energy dispersive x-ray analysis," *ibid.*, vol. 1, 165-233.
14. P. A. Russell, "Particulate characterization and source/receptor analysis: U.S. Steel Corp. Geneva plant," *Proc. Fourth Symp. Fugitive Emissions*, EPA publication 600/9-80-041, 1989, 179-207.
15. P. A. Russell, *Aerosol Particles Collected at Montezuma's Castle, Arizona*, Report submitted to Environmental Monitoring and Support Laboratory, 1981.
16. J. A. Armstrong and P. A. Russell, in F. P. Venditti, J. A. Armstrong, and M. Durham, Eds., "The monitoring of particulates using a balloon-borne sampler," *Proc. Symposium on the Transfer and Utilization of Particulate Control Technology* (vol. 4: Fugitive Dusts and Sampling, Analysis and Characterization of Aerosols), EPA 600/7-79-49d, NTIS, Springfield, Va., 1979.
17. J. A. Armstrong and P. A. Russell, "Particle production from surface mining: Part 1. Particle measurements," Ref. 14, 37-63.
18. J. A. Armstrong, P. A. Russell, M. N. Plooster, and L. E. Sparks, "Tethered Balloon sampling of a Portland cement plant," presented at the Third Symp. Transfer and Utilization of Particulate Control Technology, Orlando, Fla., 1981.
19. J. G. Watson, *Chemical Element Balance Receptor Model Methodology for Assessing the Sources of Fine and Total Suspended Particulate Matter in Portland, Oregon*, Ph.D. Thesis, Oregon Graduate Center, Beaverton, Ore., 1980.
20. T. G. Dzuby, "Chemical element balance method applied to dichotomous sampler data," *Annals N. Y. Acad. of Sci.* 338: 126-144, 1980.
21. J. A. Cooper and J. G. Watson, "Receptor oriented methods of air particulate source apportionment," *JAPCA* 30: 1116-1125, 1980.
22. J. G. Watson, J. C. Chow, L. W. Richards, W. D. Neff, S. R. Anderson, D. L. Dietrich, and I. Olmez, *The 1987-88 Metro Denver Brown Cloud Study*, Desert Research Institute, Reno, Nev., DRI Document No. 8810 1F1, 2, & 3, 1988.
23. W. R. Pierson and P. A. Russell, "Aerosol carbon in the Denver area in November, 1973," *Atmos. Environ.* 13: 1623-1628, 1979.
24. J. H. Seinfeld, "Urban air pollution: State of the science," *Science* 243: 745-752, 1989.

AN INTEGRATED SCREENING METHOD FOR EVALUATING THE PULMONARY TOXICITY OF INHALED PARTICULATES: ROLE OF MICROSCOPIC TECHNIQUES IN ASSESSING PULMONARY MACROPHAGE CLEARANCE FUNCTIONS

D. B. Warheit, D. K. Rennix, K. A. Moore, and L. A. Belcher

There is a great need for a rapid and reliable bioassay to evaluate the pulmonary toxicity of inhaled particles. We have developed a comprehensive approach to lung toxicity studies. To validate the method, rats were exposed for 6 h or 3 days to various aerosol concentrations of silica or carbonyl iron (CI) particles. Cells and fluids from groups of sham and dust-exposed animals were recovered by bronchoalveolar lavage (BAL) fluids and measured for biochemical markers of lung injury at several time points postexposure. Cell differentials were counted and pulmonary macrophages (PM) were cultured and studied for morphology, chemotaxis, and phagocytosis by scanning electron microscopy. The lungs of additional exposed animals were processed for histopathology (LM) scanning and transmission electron microscopy. Our results showed that brief doses of silica elicited a sustained granulocytic inflammatory response (primarily neutrophils) with concomitant increases in BAL levels of biochemical markers, i.e., fibronectin, alkaline phosphatase, LDH, and protein ($p < 0.01$). In addition, pulmonary macrophage (PM) phagocytic and chemotactic activities in vitro were depressed ($p < 0.05$) in cells recovered from silica-exposed rats when compared to sham controls. Histopathological analysis showed that exposure of rats to silica for 3 days produced a chronically active pulmonary inflammatory response characterized by hyperplasia of Type II alveolar epithelial cells, the infiltration of PM and neutrophils into interstitial tissues and alveoli, and lipid-filled, foamy PM. The lesions were progressive and led to a granulomatous pneumonitis within 2 months postexposure. In contrast to the alterations in pulmonary tissues produced by silica, PM function in carbonyl iron-exposed rats was not significantly different from sham controls. Furthermore, no CI-related lesions were detected at any time postexposure. The data presented in this report demonstrate that silica inhalation produces inflammation and alters macrophage phagocytic functions; the effects of CI particles are similar to other nuisance dusts.

Experimental

General Experimental Design. Groups of male Crl:CD®BR rats (8 weeks old, Charles River Breeding Laboratories, Kingston, N.Y.) were exposed to crystalline silica (α -quartz) or carbonyl iron (CI) particles for 6 h or 3 days

The authors are at the Haskell Laboratory, E.I. du Pont de Nemours & Co., Newark, DE 19714.

at exposure concentrations of 100 mg/m³. Following exposure, dust-exposed animals and aged-matched sham controls were evaluated at several time points postexposure (i.e., 0, 24, and 48 h, 8 days, and 1, 2, and/or 3 months).

Pulmonary Lavage and Preparation of Macrophage Monolayers. Bronchoalveolar lavage procedures were conducted according to methods previously described.^{1,2} Lavaged fluids recovered from sham and dust-exposed rats were centrifuged, and the supernatant was removed and processed for biochemical studies. The cell pellet containing primarily pulmonary macrophages was processed for cell differential analysis and morphological, phagocytosis, and chemotaxis studies. Pulmonary macrophage cell culture and phagocytosis assays have been previously reported.^{1,2} For the phagocytic assay, a suspension of carbonyl iron particles was added to the macrophage monolayers. Phagocytosis of iron particles was carried out at 37°C in a CO₂ incubator for 1 h and then fixed in Karnovsky's solution before processing for scanning electron microscopy (SEM), as described below. Specimens were prepared according to standard methods and examined with a JEOL 840 scanning electron microscope. Studies of morphology and in vitro phagocytosis were implemented by use of SEM of randomly selected cultured cells as previously described.¹ In vivo and in vitro phagocytosis were assessed in carbonyl iron and silica-exposed macrophages by means of secondary and backscatter electron imaging in concert with x-ray energy spectrometry. For in vitro phagocytosis of carbonyl iron (CI) beads, the numbers of interiorized CI beads were counted in individual macrophages.

For light and electron microscopy of tissue, the lungs of carbonyl iron, silica, or sham control rats were prepared for light or electron microscopy at recovery periods of 0, 24, 48 h, 8 days, and/or 1, 2, or 3 months following aerosol exposure. After anesthesia, lungs of rats were fixed either through the vasculature (vascular perfusion) or intratracheally (airway infusion). Sagittal sections of the left lung were made with a razor blade. Tissue blocks were dissected from upper, middle, and lower regions of the lung, and were subsequently prepared for light microscopy as well as for scanning and transmission electron microscopy (see below).

Transmission Electron Microscopy. Selected fixed lung tissues were post-fixed with OsO₄; subsequently, pulmonary tissue blocks from sham, silica, or carbonyl iron-exposed rats were

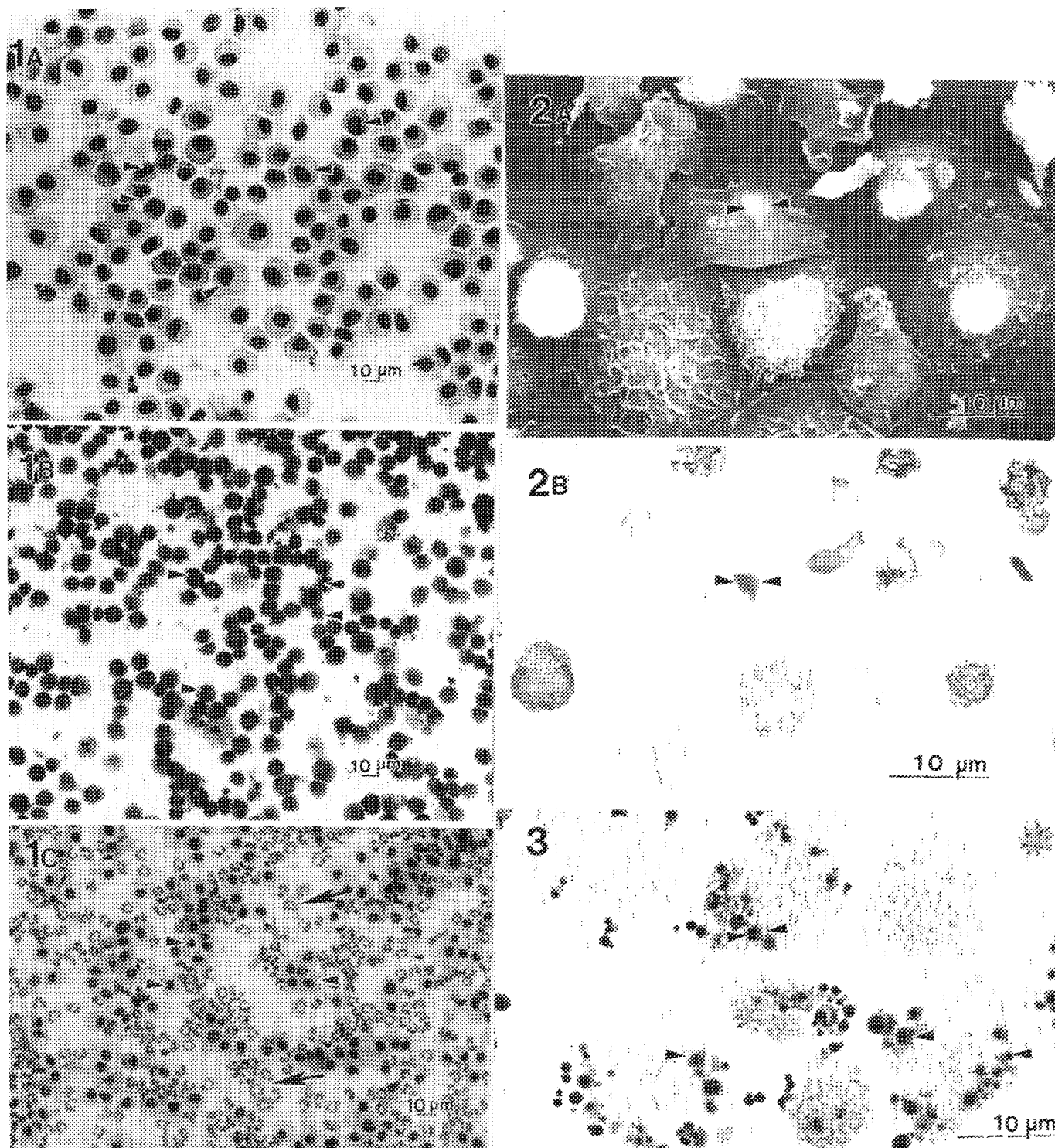


FIG. 1.--Light micrographs of cytocentrifuge preparation of cells recovered from lungs of (A) sham, (B) carbonyl iron, and (C) silica-exposed rats. More than 95% of cells were PMs (arrowheads) in sham and CI-exposed animals. In contrast, significant numbers of neutrophils (arrows) were recovered from lungs of silica-exposed rats.

FIG. 2.--SEM of lavaged-recovered rat pulmonary macrophages (M) exposed to silica particles in vivo in (A) secondary and (B) backscatter electron images. Silica particle (arrowheads) is contained within a PM 1 month after exposure.

FIG. 3.--In vitro phagocytosis of carbonyl iron particles (arrowheads) by pulmonary macrophages.

dehydrated through ethanol and propylene oxide, infiltrated with graded propylene oxide-Epon solutions, and finally embedded in Epon® 812. Ultrathin sections were cut and placed on copper grids. Sections were then stained with uranyl acetate and lead citrate and examined with a Zeiss EM 10 electron microscope.

Results and Conclusions

Carbonyl iron exposures did not produce inflammatory responses in the lungs of exposed rats. However, inflammation, as evidenced by the increased numbers of neutrophils, was a prominent feature in the lungs of silica-exposed rats (Fig. 1). In addition, fibronectin levels were substantially higher in lavaged fluids recovered from silica-exposed rats when compared to controls. SEM techniques were utilized to assess morphologic characteristics as well as in vivo and in vitro phagocytic capacities of lavage-recovered PM exposed to either silica or carbonyl iron particles. Forty-seven percent of the macrophages recovered immediately after a 3-day exposure to silica contained particles, and the percentages of silica-containing macrophages remained steady through 1 month post-exposure (Table 1, Fig. 2). In contrast, more than 80% of PM recovered immediately after a 3-day exposure to carbonyl iron-containing particles. In addition, the percentages of ruffled macrophages recovered from silica or carbonyl iron-exposed rats were not significantly different from sham controls at any postexposure period. The in vitro phagocytic capacities of macrophages recovered from carbonyl iron-exposed animals were not significantly different from sham controls (Table 1, Fig. 3). In contrast, in vitro phagocytosis by silica-exposed PM was decreased compared to sham controls (Table 1).

Pulmonary lesions caused by exposure to silica were evaluated microscopically over a 3-month postexposure period at 1-month intervals following exposures. Lesions in animals exposed to silica for 3 days were present at 1 month and became progressively more severe with time. Hyperplastic and hypertrophic type II cells were common features of silica-induced epithelial alterations along with inflammation of the airspaces. In addition, lipid-laden (foamy) alveolar macrophages often filled alveoli and alveolar ducts (Fig. 4). In contrast to the development of granulomatous-type lesions observed in silica-exposed rats, no pulmonary lesions were detected at any time postexposure in sham-exposed control rats or in rats exposed to carbonyl iron particles for 6 h or 3 days (Fig. 5).

A short-term inhalation screening program to assess the toxicity of inhaled materials has been developed by a multidisciplinary approach. Silica and carbonyl iron particles were selected for study because they represent reference points of the toxicological spectrum; i.e., silica is fibrogenic and iron is "nuisance-like." The results presented here support the differences in toxicity between silica and carbonyl

TABLE 1.--Morphology and phagocytosis of carbonyl iron and silica-exposed pulmonary macrophages.

Time after 3-Day exposure					
In Vivo Phagocytosis Percentages of Phagocytic Pulmonary Macrophages					
	Sham	0H	48H	8D	1M
CI	---	81(5)	75(6)	73(11)	63(6)
SILICA	---	47(9)	48(13)	42(3)	53(19)

Morphology & Ruffled Cells					
CI	79(6)	76(5)	74(9)	75(6)	74(11)
SILICA	76(5)	75(12)	70(13)	67(7)	75(6)

In Vitro Phagocytosis & Response of Sham Control					
CI	100	95	97	105	108
SILICA	100	51	82	95	98

Numbers in parentheses represent standard deviations					

iron and affirm the utility of this method as a predictive short-term bioassay to evaluate pulmonary toxicity of inhaled particulates. The true value of a predictive screen lies in its ability to accurately estimate the potential effects of materials for which little or no available toxicological information exists. Accordingly, studies are in progress to test the pulmonary effects of both reference materials as well as untested particles and fibers.

References

1. D. B. Warheit, L. H. Hill, and A. R. Brody, "Pulmonary macrophage phagocytosis: Quantification by secondary and backscattered electron imaging," *SEM/1983 I*, 431.
2. D. B. Warheit et al., "Pulmonary macrophage accumulation and asbestos-induced lesions at sites of fiber deposition," *Am. Rev. Respir. Dis.* 129: 301, 1984.

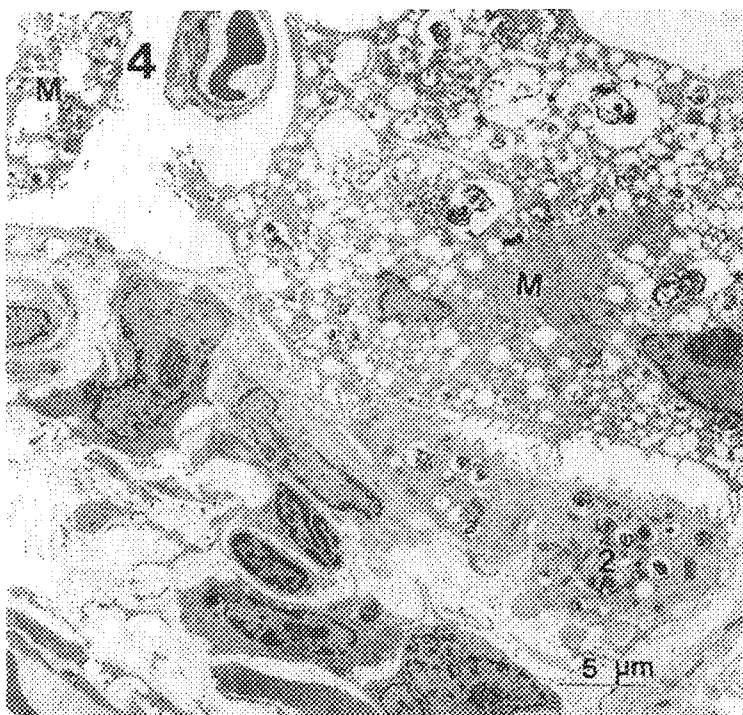


FIG. 4.--TEM of lung section in rat 3 months post-silica exposure, demonstrating hyperplastic type II (2) epithelial responses and lipid-filled (arrowheads) foamy pulmonary macrophage (M).

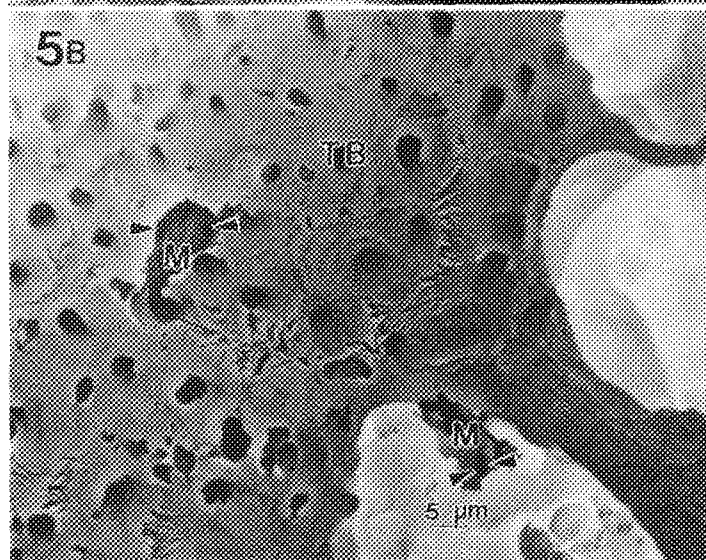
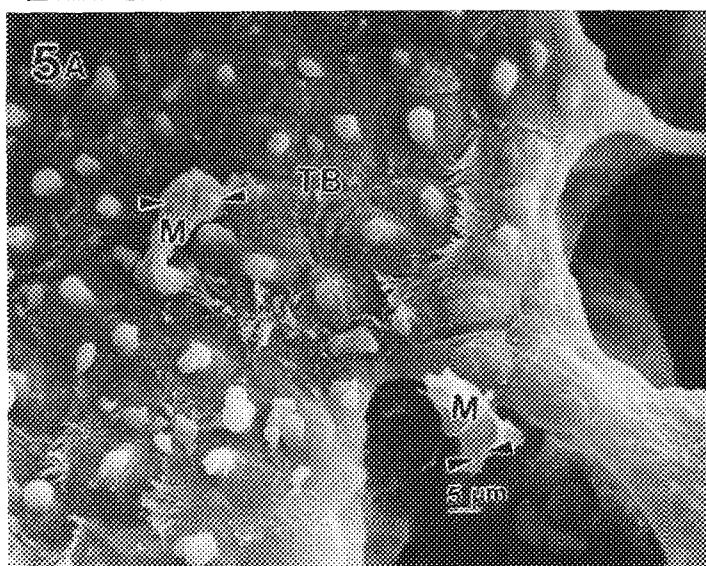


FIG. 5.--SEM of pulmonary macrophages (M), that have traveled from alveolar regions to terminal bronchiolar surfaces (TB). Phagocytes are exiting the lung via the mucociliary escalator. Two macrophages (M) contain iron particles (arrowheads) viewed in (a) secondary, and (b) backscatter electron images.

EFFECTS OF ENDOTOXIN-INDUCED NEUTROPHIL INFLUX ON THE MORPHOLOGY OF SECRETORY CELLS AND INTRAEPITHELIAL MUCOSUBSTANCES IN CANINE BRONCHI

J. R. Harkema, J. A. Hotchkiss, M. D. Hoover, and B. A. Muggenburg
(with technical assistance from L. K. Herrera and P. C. Lawson)

Endotoxins are lipopolysaccharide-protein molecules released from the walls of gram-negative bacteria. Although they are not chemotactic for neutrophils,^{1,2} endotoxins induce neutrophil emigration more potently, on a per molar basis, than do all other chemotactic factors so far tested,³ and are one of the major bacterial constituents responsible for inducing pulmonary injury in gram-negative sepsis and gram-negative, bacterial bronchopneumonia.⁴ Pulmonary airway infections caused by gram-negative bacteria containing endotoxin account for 40-60% of hospital-associated pneumonias; the mortality of these bacterial pneumonias hovers around 50%.^{5,6}

Airway inflammation induced by endotoxin-laden, gram-negative bacteria is often characterized by an increased production and hypersecretion of mucus from surface epithelium and subepithelial glands and by infiltration of airways by inflammatory leukocytes (i.e., neutrophils). Both the inflammatory exudate and the hypersecretion of mucus are thought to be important factors in the pathogenesis of not only bacterial pneumonias, but of other obstructive disorders, such as cystic fibrosis⁷ and chronic bronchitis.⁸ Although inhaled endotoxin is known to induce acute airway inflammation in laboratory animals,⁹ its effects on the ciliated respiratory epithelium and the mucus-secretory apparatus lining the bronchial airway have not been thoroughly investigated. For a better understanding of the pathogenesis of inflammatory airway disorders, it is important to determine which changes in the mucous-secretory apparatus are due to the induced inflammatory process and which are due to the inhaled bacteria or other etiologic agents. It has been previously demonstrated that transepithelial migration of neutrophils stimulates hypersecretion of mucus from the nasal airway secretory cells.¹⁰ The purpose of the present study was to determine whether a single instillation of endotoxin in intrapulmonary bronchi would elicit a similar neutrophil-dependent hypersecretory response.

Materials and Methods

Eighteen 2-4-yr-old beagle dogs from the Institute's colony were used for this study.

The authors are at the Inhalation Toxicology Research Institute, Albuquerque, NM 87185. The research was sponsored by U.S.D.O.E. under contract DE-AC04-76EV01013 in facilities fully accredited by the American Association of Laboratory Animal Care

Each dog in the study was transiently anesthetized with halothane and a fiberoptic bronchoscope was used to instill various amounts of lipopolysaccharide (endotoxin) from *Escherichia coli* 0111:B4 (Sigma Chemical Co., St. Louis, MO) in specifically designated bronchial airways. A stainless-steel radial microsyringe, 1 mm in diameter and 3 mm long, with eight, 150- μ m-diameter openings around the circumference of its distal end, was used to spray radially 100 μ l of saline containing 500 μ g of endotoxin onto the luminal surface of the major intrapulmonary bronchus of the left cardiac lobe (airway generation 2), 100 μ l of saline containing 250 μ g of endotoxin onto the luminal surface of the major intrapulmonary bronchus of the right diaphragmatic lobe (generation 3), and 100 μ l of saline containing 125 μ g of endotoxin onto the luminal surface of the minor intrapulmonary bronchus of the left diaphragmatic lobe. Complimentary airway locations in the left lung lobes were sprayed with 100 μ l of saline alone (control airways).

Six of the dogs were injected intravenously with hydroxyurea, 200 mg/kg, in 5 ml saline, daily, for 8 days prior to the intrabronchial instillations of endotoxin. The remaining 12 dogs in the study received daily intravenous injections of saline alone, 5 ml/d, for 8 days prior to the bronchial instillations. Hydroxyurea-injected animals were sacrificed 6 h after bronchial instillations. Half of the saline-injected dogs were sacrificed 6 h after the instillations and the other half were sacrificed 18 h later (24 h after the instillations).

At the designated time of sacrifice, the dogs were anesthetized with barbiturate and killed by exsanguination through the heart. Immediately after death, the trachea, extrapulmonary bronchi and lungs were excised intact from the thoracic cavity and perfused intratracheally with a modified Karnovsky's fixative, 0.6% glutaraldehyde/0.45% paraformaldehyde in cacodylate buffer (pH of 7.4) at 30 mm of fixative pressure for 2 h.

After fixing the lungs, we microdissected the bronchial airway segments that had been sprayed with endotoxin, according to the method of Plopper.¹¹ One half of each segment was embedded in glycol methacrylate (GMA) and sectioned at 2 μ m. We stained the sections with toluidine blue to morphologically identify epithelial cells and neutrophils or with Alcian Blue (pH 2.5)/Periodic Acid-Schiff sequence (AB/PAS), to demonstrate acidic and neutral mucosubstances by light microscopy (LM). Quantitative estimates of the numbers of neutrophils and epithelial cells per mm of basal

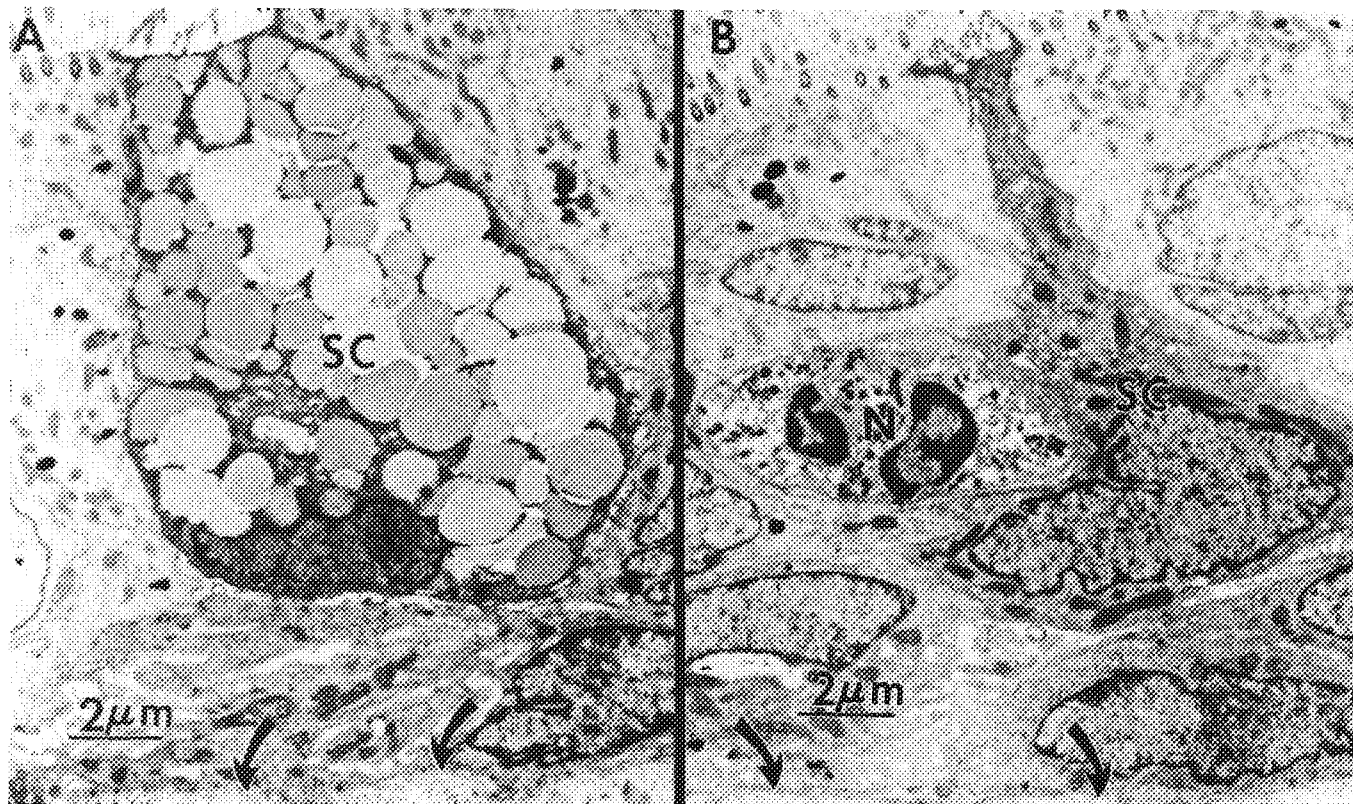


FIG. 1.--Composite of two transmission electron photomicrographs of surface epithelium in bronchi obtained 6 h after exposure to only saline (A) or endotoxin (B). Photomicrograph A shows secretory cell (sc) filled with incytoplasmic granules. Photomicrograph B shows secretory cell containing few intracytoplasmic mucous granules, and a neutrophil (N). Arrow = epithelial basal lamina; CC = ciliated epithelial cell.

lamina, and the amounts of stainable intraepithelial mucosubstances within these bronchial sections were made by the standard morphometric techniques previously described.¹⁰

Only the complementary halves of the airway segments from the cardiac lobes were processed for transmission electron microscopy (TEM). Tissues for TEM were post-fixed in 1% osmium tetroxide, dehydrated in a graded series of alcohol solutions, infiltrated with propylene oxide solutions, then embedded in epon araldite, and thin-sectioned with a diamond knife on an Ultracut E ultramicrotome (Reichert-Jung, Cambridge Instruments, Inc., Deerfield, IL). These sections were mounted on Formvar-coated, slotted grids, stained with uranyl acetate and lead citrate, and examined with a Hitachi H7000 scanning transmission electron microscope (Hitachi Ltd., Tokyo, Japan). TEM montages of the entire bronchial epithelial section were prepared at a final magnification of 3900 \times . Differential cell counts were based on counts of all nuclear profiles within the intact epithelium visible on these montages. We determined the number of nuclear profiles per basal lamina length. We counted approximately 200-500 cells per montage, representing basal lamina lengths of 300-1000 μ m per montage.

The natural logarithms of the data were used for statistical analyses. We used an unpaired Student's t-test with a Bonferroni correction for multiple comparisons to test the equality of the group means. The criterion for statistical significance was set at $p \leq 0.05$.

Results

In all cases, the bronchial epithelium from airways instilled with saline contained no (or only a few) neutrophils, but did contain numerous secretory cells that were distended with copious amounts of AB/PAS-stained mucosubstances (Fig. 1). In contrast, marked intraepithelial infiltration of neutrophils was evident in bronchial epithelium exposed to 500, 250, or 125 μ g of endotoxin from dogs that were injected IV with saline and killed 6 h after the bronchial instillations. There was a concurrent decrease in stored mucosubstances within the secretory cells of endotoxin-exposed epithelium, compared to cells from the saline-control airways (Fig. 1). There were no significant differences in the number of intraepithelial neutrophils or amounts of mucosubstances among the airways exposed to the high, medium, or low concentrations of endotoxin. Therefore, all data from these endotoxin-instilled airways were combined and presented as a single group. There was no evidence of epithelial cell necrosis or exfoliation in any of the endotoxin-exposed epithelia from dogs killed 6 h after instillation. In addition, there were no significant changes in either the numbers of total epithelial cells or of specific cell types (e.g., mucous goblet cells) per mm of basal lamina.

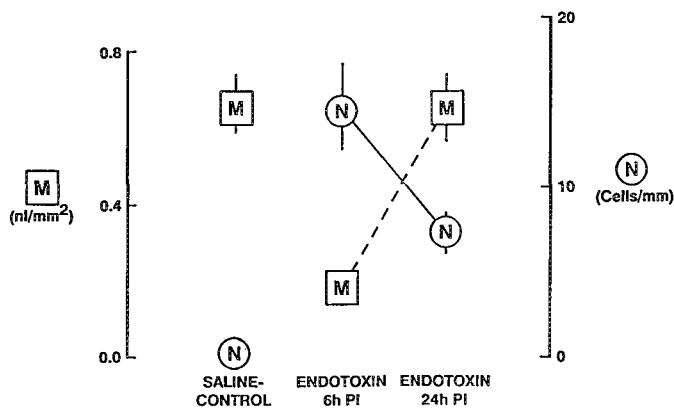


FIG. 2.--Effects of endotoxin on number of neutrophils (N) and amounts of mucosubstances (m) in bronchial epithelium 6 and 24h post-instillation (PI).

As we observed for airway tissues taken 6 h after endotoxin instillation, there were no concentration-dependent differences in intraepithelial responses 24 h after endotoxin instillation. Therefore, all data for these endotoxin-instilled airways were combined and presented as a single group. For saline injected dogs killed 24 h after endotoxin instillation, the number of neutrophils in the endotoxin-exposed bronchial epithelium was greater than in control airways, but was markedly reduced from the numbers observed in endotoxin-exposed airways from dogs killed 6 h after instillation. In contrast, the amount of intraepithelial mucosubstances in the endotoxin-exposed airways 24 h after instillation was significantly greater than at 6 h after instillation. There were no differences in the numbers of total epithelial or secretory cells observed per mm of basal lamina 24 h after instillation for endotoxin-exposed, compared to saline-exposed, airways. Figure 2 summarizes the changes in the number of intraepithelial neutrophils and the amounts of mucosubstances 6 and 24 h after endotoxin instillation.

Hydroxyurea-treated dogs had less than 10% of the circulating blood neutrophils observed in the blood of saline-injected animals both prior to endotoxin instillation and 6 h after endotoxin instillation. In nonhydroxyurea-treated dogs, endotoxin induced a marked neutrophilia 24 h after instillation. Endotoxin-instilled airways from dogs treated with hydroxyurea had fewer than one fourth the number of intraepithelial neutrophils (3 ± 1 neutrophils/mm of basal lamina compared to 14 ± 3 neutrophils/mm of basal lamina) and three times the amount of intraepithelial mucosubstances (0.57 ± 0.20 nl/mm² compared to 0.18 ± 0.04 nl/mm²) compared to the epithelia of endotoxin-instilled airways from dogs not treated with hydroxyurea. The amounts of intraepithelial mucosubstances and neutrophils in saline-control airways of hydroxyurea-treated and nonhydroxyurea-treated dogs were not significantly different. In addition, there were no significant differences in the numbers of secretory cells,

or any other epithelial cell types per mm of basal lamina between the endotoxin- or saline-instilled airways of either hydroxyurea-treated or nonhydroxyurea-treated dogs.

Discussion

The results of this study suggest that neutrophils migrating intraepithelially, or substances released from neutrophils during the course of epithelial migration, cause a transient depletion of mucosubstances stored in canine bronchial epithelium. The peak, endotoxin-induced influx of neutrophils into the respiratory epithelium lining the bronchi was associated with a marked attenuation of the amount of histochemically identifiable mucosubstance within this surface epithelium of the dog bronchial epithelium. The transient depletion of epithelially stored mucosubstance, associated with the inflammatory cell influx occurring 6 h after intrabronchial endotoxin instillation, suggest that during this post-exposure period the rate of mucous secretion exceeded the rate of synthesis. Because no epithelial cell necrosis or exfoliation, or changes in the numbers of secretory cells were evident during this post-instillation period, we conclude that the depletion of mucosubstance was not due to a loss of secretory cells, but was due to increased secretion of mucosubstances from the cytoplasm of these airway lining cells. The restoration of mucosubstances within the bronchial epithelium concurrent with the conspicuous absence of neutrophils also suggests that there is a functional relationship between neutrophil influx and hypersecretion of mucus from respiratory epithelium. The significant increase in stored mucosubstance that we observed between 6 and 24 h after instillation of endotoxin could have been due to decreased secretion and/or increased production of these glycoproteins by the bronchial epithelium. Neutra and Leblond¹² have demonstrated that the time between the incorporation of glucose into colonic mucous goblet cells and its discharge in secreted mucus is approximately 4 h. If the bronchial secretory cell behaves in a manner similar to that of the colonic mucous goblet cell, the 18 h between the 6 and 24h observation points should be adequate for restoring normal amounts of mucosubstances without changing the "normal" rate of mucous production.

We were able to demonstrate the close relationship between neutrophil influx and hypersecretion by using hydroxyurea to attenuate the number of neutrophils entering the endotoxin-exposed bronchial epithelium. The neutropenia induced by hydroxyurea treatment accounted for the marked reduction in intraepithelial influx of neutrophils into the endotoxin-instilled airways. The simultaneous lack of mucosubstance diminution in the endotoxin-exposed epithelium demonstrated that these granular leukocytes played a key role in the transient hypersecretion of mucus in the endotoxin-instilled bronchial airways. It also

demonstrated that endotoxin is not in itself a direct secretagogue for bronchial airway mucus.

Mucous hypersecretion and neutrophil influx are characteristic features of bronchopneumonias induced by gram-negative, endotoxin-laden bacteria. Our findings suggest that neutrophilic infiltration induced by endotoxin exposure provides a stimulus for increased secretion of mucus by the respiratory epithelium lining canine bronchi. The results of previous in vitro studies suggest that neutrophils release secretagogues (i.e., proteases, oxygen free radicals, and arachidonic acid metabolites) that could mediate the hypersecretory response in vivo. Furthermore, the physical movement of migrating leukocytes within the epithelium cannot yet be discounted as a possible stimulatory mechanism for mucous secretion.

References

1. R. Snyderman, H. Gewurz, and S. E. Mergenhagen, "Interactions of the complement system with endotoxin lipopolysaccharide: Generation of a factor chemotactic for polymorphonuclear leukocytes," *J. Exp. Med.* 128: 269, 1969.
2. A. C. Issekutz and S. Bhimji, "Role of endotoxin in the leukocyte infiltration accompanying *Escherichia coli* inflammation," *Infect. Immun.* 36: 558, 1982.
3. I. G. Colditz and H. Z. Movat, "Kinetics of neutrophil accumulation in acute inflammatory lesions induced by chemotaxins and chemotaxinogens," *J. Immunol.* 133: 2169, 1984.
4. K. L. Brigham and B. Meyrick, "Endotoxin and lung injury," *Am. Rev. Respir. Dis.* 133: 813, 1986.
5. M. P. Reyes, "The aerobic gram-negative bacillary pneumonias," *Med. Clin. North Am.* 64: 363, 1980.
6. J. R. Tillotson and A. M. Lerner, "Pneumonias caused by gram negative bacilli," *Medicine* 45: 65, 1986.
7. D. Lamb and L. Reid, "The tracheobronchial submucosal glands in cystic fibrosis," *Br. J. Dis. Chest* 66: 230, 1972.
8. R. DeHaller and L. Reid, "Adult chronic bronchitis: Morphology, histochemistry, and vascularization of the bronchial mucous glands," *Med. Thoracic* 22: 549, 1965.
9. A. R. Hudson, K. H. Kilburn, G. M. Halprin, and W. N. McKenzie, "Granulocyte recruitment to airways exposed to endotoxin aerosols," *Am. Rev. Respir. Dis.* 115: 89, 1975.
10. J. R. Harkema, J. A. Hotchkiss, A. G. Harmsen, and R. F. Henderson, "In vivo effects of transient neutrophil influx on nasal respiratory epithelial mucosubstances," *Am. J. Pathol.* 130: 605, 1988.
11. C. G. Plopper, A. T. Mariassy, and L. O. Lollini, "Structure as revealed by airway dissection," *Am. Rev. Respir. Dis.* 128: S4, 1983.
12. M. Neutra and C. P. Leblond, "Synthesis of the carbohydrate of mucus in the golgi complex as shown by electron microscope radioautography of goblet cells from rats injected with glucose- H^3 ," *J. Cell Biol.* 30: 119, 1966.

METHODS TO STUDY INTERACTIONS BETWEEN INHALED SUBSTANCES AND EPITHELIUM OF THE RESPIRATORY TRACT IN VITRO

Jianngwu Lee, N. J. Akley, T. M. Krunkosky, and K. B. Adler

Epithelium lining the tracheobronchial tree represents the first cells with which particulates, gases, microbes, etc., come into contact upon inhalation. Thus, interactions between such inhaled substances and epithelial cells probably are integral to the pathogenesis of several occupational or environmental-related pulmonary lesions, yet such interactions have not yet been elucidated fully. Many published studies have described patterns of deposition within extra- and intrapulmonary airways and alveolar ducts, and histologic and ultrastructural changes in epithelium *in vivo* in response to inhalation and deposition.¹ However, our knowledge of specific structural and functional responses of airway epithelium *on a cellular level* is limited, since exposures of animals *in vivo* or even tissues *in situ* do not allow for studying intracellular responses, especially subtle sublytic alterations that could be the basis for subsequent pathogenic responses.

For this reason, investigators have utilized *cell culture* systems to examine intracellular mechanisms related to responses of respiratory epithelium to deleterious substances which may be inhaled in an occupational or environmental setting. However, a recurring problem with most airway epithelial cell culture systems is the great disparity between the structure and function of cells in culture and *in vivo*.

Thus, to elucidate cellular mechanisms related to interactions with inhaled deleterious substances, it would be a great advantage to have available a cell culture system that mimics to the greatest extent possible the structure and function of epithelium *in situ*, especially one that maintains vital intercellular interactions which undoubtedly influence responses. We have developed and described previously a unique air/liquid interface culture system in which guinea pig tracheobronchial epithelial cells are isolated enzymatically and plated onto a collagen-coated filter. In our system, the collagen-coated filter is immersed into serum-free medium in such a way that the cells contact the medium from the basal side only; the apical surfaces of the cells are exposed only to a humidified 95% air/5% CO₂ environment. When cultured in this manner, the

cells proliferate and differentiate so as to resemble greatly guinea pig pseudostratified columnar epithelium as observed *in situ*.²

Experimental

Analysis of Cell Cultures. We examined this cell culture system using ultrastructural morphometry of fixed and embedded cultures, and compared several morphometric parameters of the cultures with those of guinea pig airways removed directly from the animal and fixed immediately. In addition, several biochemical characteristics of high molecular weight glycoconjugates released by these cell cultures were analyzed to determine whether this material was mucin-like. The specific experimental procedures have been described previously.³

Effects of Oxidant Stress on Airway Epithelial Cells. It is known that interactions of pulmonary cells with a variety of deleterious inhaled materials results in production in the lung and airways of oxygen-free radicals and other toxic oxygen metabolites.⁴ We generated oxygen metabolites by combining xanthine oxidase with purine in the cell cultures as described previously.⁵ We examined effects of oxidant stress on epithelial cells *in vitro* on the following parameters.

1. *Mucin secretion.* Cells were incubated with tritiated glucosamine for an 18h period, then placed in fresh medium for a 2h (baseline) time period followed by a 1h (test) period during which the cells were exposed to chemically generated oxygen metabolites or to control medium not containing oxidants. At the end of each period (baseline and test) released mucins were collected from the medium and apical surfaces of the cell cultures and subjected to digestion with hyaluronidase before being separated on Sepharose CL-4B columns. Mucin secretion was measured as the radioactivity in the void volume fractions and expressed as a ratio of test/baseline values. These procedures have been described in detail previously.⁵

2. *Metabolism of arachidonic acid.* Cells were incubated with tritiated arachidonic acid for 2 h, then placed into fresh medium and exposed to oxidant stress or solvent control for another 2 h. Media were subjected to reverse-phase high-performance liquid chromatography (HPLC) as described previously⁵ to measure both cyclooxygenase and lipoyxygenase arachidonate metabolites formed in response to oxidant stress.

3. *Hydrolysis of membrane inositol phospholipids.* Cells were incubated with tritiated

The authors are at the Department of Anatomy, Physiological Sciences, and Radiology, College of Veterinary Medicine, North Carolina State University, Raleigh, NC 27606. The research was supported by NIH grants HL37636 and HL36982, a grant from the State of North Carolina, and a grant from Hoffmann La-Roche, Inc., Nutley, N.J. Dr. Adler is an Established Investigator of the American Heart Association.

myo-inositol for 48 h, at which time they were placed in new medium containing 5 mM LiCl and exposed to oxidant stress for periods of time ranging from 5 s to 15 min. At each time point, the reaction was stopped by addition of ice-cold methanol and the cells were scraped off. After separation of the organic and soluble phases with chloroform, the water-soluble phase was eluted through Dowex anion exchange columns sequentially with deionized water (free inositol), 5 mM sodium borate (glycerophosphoinositol), 5 mM Na borate/0.1 M formic acid plus, 0.2 M ammonium formate (IP), 0.4 M ammonium formate (IP₂), and 1 M ammonium formate (IP₃). Fractions were counted by liquid scintillation.

4. *Production of extracellular matrix (ECM) components.* Cells were incubated with radio-labeled cysteine, then exposed to oxidant stress or controls for 2 h. After an additional 4 h, cell lysates and media were analyzed by immunoprecipitation for the ECM components fibronectin and laminin.

Results

Analysis of Cell Cultures. The cellular content of the cultures was very similar to that of intact epithelium, with the volume densities V_V of ciliated, secretory, and basal cells almost identical to those of the same cells within intact airway segments. In addition, various characteristics of the high-molecular-weight glycoconjugates (mucins) released by intact airway segments and cell cultures, such as amino acid composition, proteoglycan content, buoyant density, and alkaline borohydride elimination patterns, were almost identical. These combined ultrastructural morphometric and biochemical results further support the validity of this air/liquid interface culture as a model system for studying cellular mechanisms of response of airway epithelium to inhaled substances.³

Effects of Oxidant Stress on Airway Epithelial Cells. Ultrastructural examination of the cell cultures failed to reveal obvious signs of cell injury, yet the cell cultures, in response to sublytic oxidant stress and in a dose-dependent manner:

- (1) increased mucin secretion;
- (2) increased metabolism of arachidonic acid, producing elevated amounts of PGF_{2a} and hydroxyeicosatetrenoic acids (HETES);
- (3) activated phospholipase C, as reflected by a significant rise in total intracellular inositol polyphosphates;
- (4) produced altered ECM components: a faster migrating band in the dimeric region of fibronectin, suggesting production of a lower molecular weight molecule; and a molecular species in the B subunit of laminin that was not observed in control cells;
- (5) appeared to produce additional intracellular oxygen radicals and lipid peroxides. In a related effect, low concentrations of the airborne pollutant gas ozone enhanced mucin secretion, an effect attenuated by the cyclooxy-

genase inhibitor indomethacin. (Since additional studies revealed similar dose-dependent increases in mucin secretion and cyclooxygenase metabolism after exposure of cell cultures to the organic hydroperoxide, t-bu-OOH, lipid peroxidation might be a key event in the response of airway epithelial cells to oxidant stress.)

Conclusions

This air/liquid interface airway cell culture system allows for measurement of subtle alterations following interactions of airway epithelium with sublytic concentrations of particulate or gaseous materials that might be inhaled directly, or to inflammatory mediators (e.g., oxygen free radicals) known to be generated after inhalation of a number of potentially harmful materials. In conjunction with data regarding deposition patterns and observable morphological effects on pulmonary cells, studies on subtle ultrastructural and biochemical alterations in epithelial cells in vitro may be invaluable in elucidating intracellular mechanisms governing toxic or subtoxic responses to inhaled materials that may relate to subsequent pathological alterations.

References

1. A. R. Brody, "Inhaled particles in human disease and animal models: Use of electron beam instrumentation," *Environ. Health Perspectives* 56: 149, 1984.
2. K. B. Adler, J. E. Schwarz, J. M. Whitcutt, and R. Wu, "A new chamber system for maintaining differentiated guinea pig respiratory epithelial cells between air and liquid phases," *Biotechniques* 5: 462, 1987.
3. K. B. Adler, P-W. Cheng, and K. C. Kim, "Characterization of guinea pig tracheal epithelial cells maintained in biphasic organotypic culture: Cellular composition and biochemical analysis of released glycoconjugates," *Am. J. Resp. Cell Molec. Biol.* 2: 145, 1990.
4. I. P. Gormley, M. J. Kowolik, and R. T. Cullen, "The chemiluminescent response of human phagocytic cells to mineral dusts," *Br. J. Exp. Pathol.* 66: 409, 1985.
5. K. B. Adler, W. J. Holden-Stauffer, and J. E. Repine, "Oxygen metabolites stimulate release of high molecular weight glycoconjugates by cell and organ cultures of rodent respiratory epithelium via an arachidonic acid-dependent mechanism," *J. Clin. Invest.* 85: 75, 1990.

Specimen Preparation Methods

DESIGN OF AN ULTRACLEAN COMPUTER-CONTROLLED FREEZE DRYER FOR BIOLOGICAL SPECIMENS

R. R. Flenniken, Ann LeFurgey, Peter Ingram, and D. A. Kopf

Electron probe x-ray microanalysis (EPXMA) requires accurate and consistent preparation of samples to obtain meaningful quantitative data. For biological specimens it is critical that the morphological state and elemental content of individual subcellular compartments be preserved. An excellent choice in obtaining preserved samples without using chemical fixatives or cryo-protectants is the process of quick-freezing, cryosectioning, and freeze drying. To produce high-quality samples, it is necessary to understand the physical processes involved in the steps of preparation, particularly in the case of freeze drying which can be a source of severe ultrastructural change and elemental redistribution. Examination of these processes and related problems in dehydration of samples has led to the design for an ultraclean freeze dryer aimed at reducing specimen alterations inherent to many freeze drying systems.^{1,2}

Methods of cryofixing tissue involve rapid removal of heat through contact with a cryogen or a cryogen-cooled surface. Simpler procedures involve manual immersion of specimens in liquid propane or ethane at 77 K. One very effective technique consists of slamming the sample onto a liquid helium-cooled copper block (4 K) by use of an electrically controlled mechanism which provides cooling rates approaching 10^5 K/s.^{3,4} Another method is high pressure freezing, where the tissue is exposed to pressures of the order of 2.1 kbar as it is cooled. Although complex, this method increases freezing depth at lower cooling rates.¹ However, theoretically, when a high enough rate of cooling is obtained, the water in the sample will be solidified to a noncrystalline vitreous state. Commonly the water is frozen to a microcrystalline cubic form which can be mistaken as vitrified if x-ray diffraction of limited resolution is used to determine crystallinity.⁵ Regardless of the actual form the water has taken upon fixing the sample, faster cooling rates produce better preservation.^{1,3}

A well-fixed sample may have a 1-10 μm region of vitreous or microcrystalline tissue with another 40-50 μm of adequately frozen material.^{3,6} Cryosectioning of these regions is performed at temperatures below 125 K, in addition to performance of transfers under liquid nitrogen (LN_2), to avoid alterations caused by phase changes. Once sectioned, the 0.1 μm -thick samples are

freeze dried. Freeze-dried tissue can be analyzed to determine mmol/kg dry weight concentrations of elements in subcellular compartments. Dehydrated tissue is also easily stored in a desiccator for an extended time.⁷

In the dehydration of samples, several factors must be considered for the design of an effective sample preparation system. First, sample temperature must be precisely controlled over the warming cycle of the dehydration. The water, if vitreous, will devitrify and recrystallize in the 130 K to 140 K range; if microcrystalline, the water will have volume-changing state changes and increased crystal growth as it is warmed.⁸ Lowering the

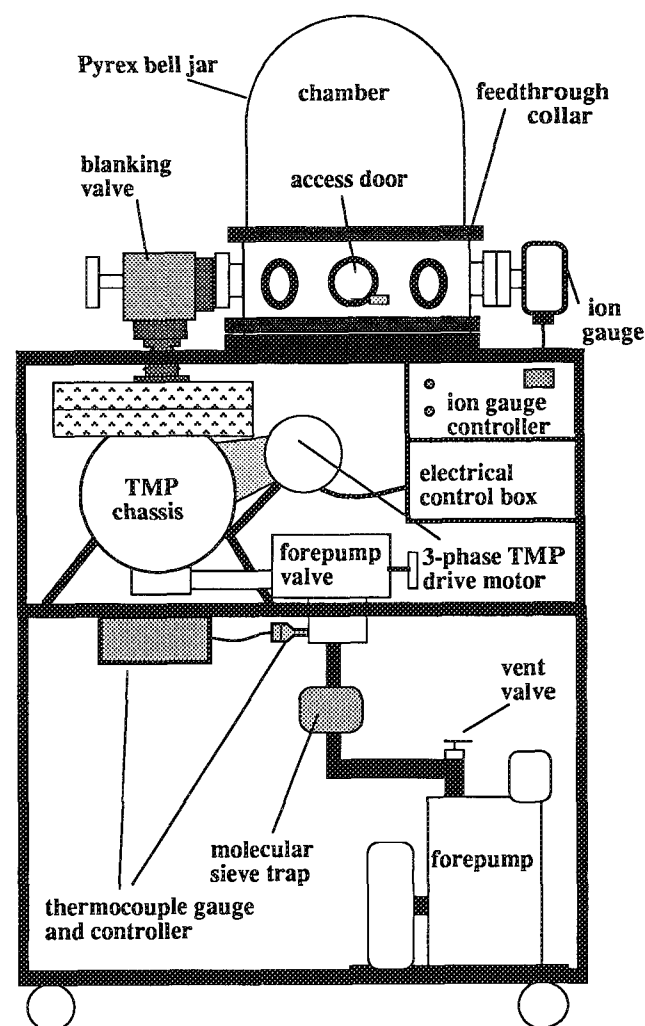
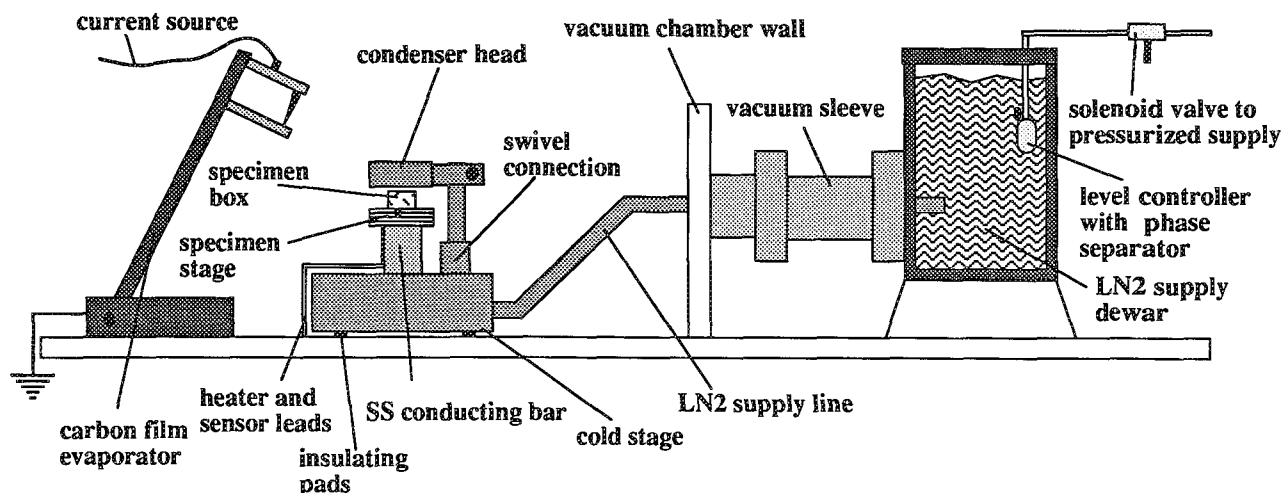


FIG. 1.--Ultraclean vacuum system for freeze dryer.

R. R. Flenniken and Ann LeFurgey are with the Department of Cell Biology, Duke University Medical Center, Durham, NC 27710; Peter Ingram is with the Research Triangle Institute, Durham, NC 27709; D. A. Kopf is with the Department of Physics, Duke University, Durham, NC 27706.



rate of these changes is paramount to decreasing the damage to the tissue; however, the actual temperatures of these transitions in biological specimens of variable water and protein content are found only through experimentation.⁵

A second consideration is minimization of the exposure of the dehydrated sample to (humid) room air during transfer to the microscope. Freeze drying in the microscope itself would circumvent this problem, but would usually not permit evaporation of a conductive layer of carbon on the sample. In addition, microscope use would be expended primarily for freeze drying, rather than for EPXMA data acquisition; with time and repeated drying procedures, sublimed water could become a significant component of column partial pressure.

Third, contaminants arising within the freeze dryer, backstreamed from the vacuum pump or leaked into the system, must be kept from the sample. The initially cold sample will attract molecules from these sources before they are pumped. Molecules condensed on the sample can thus lead to compromised EPXMA data.

The foundation of our system that deals with the above problems is the high-vacuum turbomolecular pump (Fig. 1). Its hydrocarbon-free nature makes it an excellent choice in providing clean vacuum to $\sim 10^{-6}$ Torr.¹ The forepump is trapped by a heatable molecular sieve with synthetic zeolite for prevention of hydrocarbon backstreaming. Stainless-steel components and a minimum of Viton seals allow heating the system to ~ 473 K. A pyrex belljar provides optimal viewing during all stages of operation. Conflat flanges on the feedthrough collar allow for easy connections and compatibility with residual gas analyzers, temperature sensors, and other laboratory instruments. A connection to an extra dry nitrogen gas tank provides positive pressure when the system is open to atmosphere, thereby reducing flow of contaminating room air into the system. Samples are entered into the system through a 3.8cm feedthrough so that the belljar need not be removed, which also reduces sample exposure to room air. For

faster operation, the seal for this connection requires the tightening of only a single bolt. An ultrahigh-vacuum ion gauge is mounted in the chamber and a thermocouple gauge is mounted at the forepump to measure foreline vacuum. Isolation of the chamber from the pumping system is accomplished with the blanking valve.

The system requires temperature control on the order of ± 0.1 K over the range of 77 to 305 K. A two-stage design (Fig. 2) has been chosen in order to minimize LN₂ consumption and meet the accuracy requirement. The aluminum cold stage (10cm dia., 4cm ht.) is cooled by an insulated supply line (1cm dia.) from an external dewar. This dewar is kept filled by an LN₂ level controller attached to a large pressurized dewar. A phase separator at the end of the controller line lowers LN₂ usage by reducing splashing as the small dewar is refilled. The supply line is surrounded by a vacuum sleeve to prevent heat absorption and extensive frost build-up.

At equilibrium the cold stage surface temperature is just above 77 K. A stainless-steel (SS) cylinder (2cm dia., 3cm ht.) extends above the aluminum cold stage. The SS bar connects to the copper specimen stage (3.5cm dia., 1cm ht.). Aluminum is chosen for its high thermal conductivity (~ 150 W/m²K) and low heat capacity, which allow it to cool rapidly at the beginning of the drying cycle. The SS bar has a lower thermal conductivity (~ 12 W/m²K) than deoxidized copper (~ 190 W/m²K), which gives the specimen stage a faster response to warming, while keeping the specimen thermally linked to the cold stage. The specimen stage is heated by a nichrome wire coiled around the stage. Temperature is monitored by a silicon diode sensor embedded on the top surface of the stage for the most accurate measurement of the sample. The relatively small mass of the specimen stage is easily controlled with less power than would be needed for the larger aluminum cold stage connected directly to the LN₂ supply. The sensor and heater leads are fed through a teflon tube to the electrical feedthrough.

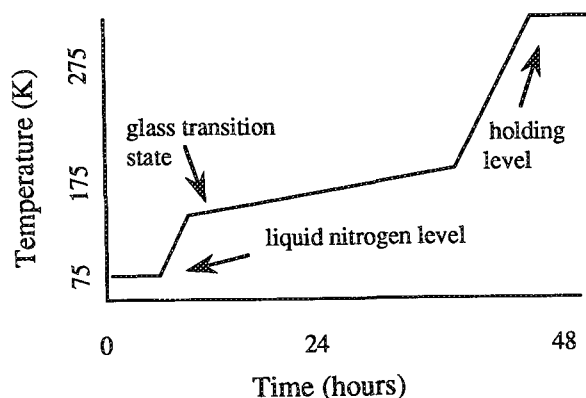


FIG. 3.--Temperature profile for freeze drying specimen.

To obtain the worst-case situation of radiative absorption between the cold stage and belljar, the cooling system is modeled as one large block of aluminum at 77 K. With the belljar at room temperature (0.9 emissivity) an influx of 0.20 W is calculated from the Stefan-Boltzmann law, which translates to ~ 5 ml/h LN_2 consumption.⁹ This low value precludes the construction of a copper radiation shield around the cold stage components.

A laboratory software package (LabView, National Instruments) on a microcomputer (Macintosh II, Apple Computer) with a controller card (NBI)-16, National Instruments), allows full programmability of the warming cycle. Figure 3 shows a typical warming cycle for a specimen. Warming to 125 K from 77 K at several deg/h is safely performed as water is not sublimed at these low temperatures. The rate of warming is lowered to 1 K/h as the glass transition temperature of pure water (~ 140 K), where significant crystal growth begins, is approached. In this example the 1K/h rate is continued for several hours until most of the water has been removed from the sample.^{2,6,10} At the end of the cycle the sample is maintained at several degrees above room temperature until it is removed from the instrument.

For protection against contamination, a vapor condenser has been designed which is placed above the sample during dehydration. This aluminum bar is mounted to the cold stage by a swivel and rises up and over the specimen stage. Water vapor from the sample (as well as any other molecules near the sample) is collected here and slowly pumped away. The head of the condenser is vertically adjustable in order to determine the best height above the sample. Although placement 14 mm above the specimen has been reported,¹⁰ individual system variances require experimental determination of optimum positioning. Close placement to the tissue will better protect the sample; however, the cool head may absorb by radiation all the heat produced in the stage and never allow the specimen to warm properly.¹¹

The sample is contained in a small copper box with a lid at LN_2 temperature when placed in the chamber. By use of the manipulator, the condenser is rotated over the sample which

pushes the lid off the box and exposes the condenser. At the end of the drying cycle the condenser is rotated away from the sample by using the manipulator. Without a break in chamber vacuum, the sample is then evaporatively coated with a layer of carbon for the dual purpose of protection from rehydration during transfer to the microscope and prevention of charging in the microscope.^{3,10,12} The carbon coater consists of an aluminum stand for mounting an ultrapure carbon rod and a connection to a high power copper feedthrough. The feedthrough connects to a manually controlled 3kW power source.¹²

The components of this system have been designed to work together according to the protocol below:

- (a) cold stage is precooled under vacuum
- (b) chamber is isolated and backfilled with nitrogen gas
- (c) sample is entered into chamber and placed on specimen stage
- (d) chamber is opened to vacuum and condenser is rotated over specimen
- (e) warming cycle is initiated
- (f) condenser is rotated away from dried sample
- (g) specimen is evaporatively carbon coated
- (h) with sample above room temperature, chamber is backfilled with nitrogen gas
- (i) sample is removed to microscope under a N_2 atmosphere or stored in a dessicator

In summary, this system:

- (1) automatically warms the sample through a programmable curve that minimizes elemental shifts due to devitrification and crystal growth;
- (2) reduces sample contamination by using a clean turbopumped system and providing a vapor condenser that prevents molecules from absorbing onto the sample;
- (3) minimizes contamination and rehydration during transfer between instruments by carbon coating.

Using these features in conjunction with a residual gas analyzer, one can perform extensive studies of the effects of freeze drying for various time/temperature profiles on an array of biological specimens. The data will provide information on ultrastructural changes and, more important, any elemental redistribution as determined by EPXMA.

References

1. A. W. Robards and U. B. Sleytr, "Low-temperature methods in biological microscopy," in *Practical Methods in Electron Microscopy*, New York: Elsevier, 1985, 12-21.
2. J. Pawley and H. Ris, *J. Microscopy* 145: 319-332, 1987.
3. A. LeFurgey, M. Bond, and P. Ingram, *Ultramicroscopy* 24: 185-220, 1988.
4. A. LeFurgey and P. Ingram, *Environmental Health Perspectives* 84: 57-73, 1990.
5. F. Franks, Ed., *Water: A Comprehensive*

Treatise, vol. 7, New York: Plenum, 1982, 309-315.

6. J. G. Linner, S. A. Livesey, D. S. Harrison, and A. L. Steiner, *J. Histochemistry and Cytochemistry* 34: 1123-1135, 1986.

7. D. Johnson, K. Izutsu, and M. Cantino, *Ultramicroscopy* 24: 221-226, 1988.

8. H.-G. Heide and E. Zeitler, *Ultramicroscopy* 16: 151-160, 1985.

9. G. K. White, *Experimental Techniques in Low-temperature Physics*, Bristol: Oxford, 213-217, 1968.

10. P. Ingram, R. Nassar, A. LeFurgey, S. Davilla, and J. Sommer, in K. Zierold and H. K. Hagler, Eds., *Electron Probe Microanalysis Applications in Biology and Medicine*, Berlin: Springer-Verlag, 1988.

11. H. Elder, personal communication.

12. M. K. Lamvik, D. Voreades, P. Norton, A. LeFurgey, and P. Ingram, *J. Electron Microscopy Technique* 5: 153-157, 1987.

PREPARATION OF BARLEY EPIDERMIS FOR X-RAY MICROANALYSIS

G. G. Ahlstrand, R. J. Zeyen, and T. L. W. Carver

Numerous plant pathological investigators have determined and compared elemental differences between healthy and diseased plant tissues using bulk specimens, scanning electron microscopy (SEM), and energy-dispersive x-ray microanalysis (EDX). In these studies effects of specimen preparation procedures are largely ignored.^{1,2} This study compares bulk specimen preparation procedures to determine their advantages and disadvantages for EDX of intact epidermal cells of barley, *Hordeum vulgare* L. Our objective was to establish a baseline for the distribution of elements in normal epidermal cells for use in later pathological investigations.

Experimental

Three tissue preparation procedures were compared: (1) frozen-hydrated (FH) tissues were used to maintain soluble and insoluble elements as they exist in situ; (2) freeze-dried (FD) tissues that maintain soluble and insoluble elements, but perhaps not in their precise in situ locations,³ were used to allow deeper electron beam penetration than did FH materials;^{4,5} and (3) critical-point dried (CD) materials were used to determine which elements were soluble or insoluble in two chemical fixatives; formalin/acetic acid/ethanol (FAA) and unbuffered glutaraldehyde (GLUT). For CD, ethanol was the dehydrating agent and CO₂ the critical point drying fluid.

We prepared specimen mounts by coating aluminum SEM stubs with colloidal graphite, leaving a small Al margin for electron beam calibrations; and FH specimens by attaching 0.5 cm² pieces of living leaf to stubs using additional colloidal graphite to anchor tissue edges. Mounted specimens were immediately transferred to a vacuum evaporator (1×10^{-4} Torr) for nickel coating. Immediately after nickel evaporation (ca. 5 min) stubs were clamped on a pre-cooled (-150 C) SEM cold stage where leaf surfaces reached -150 C within 2 min. The SEM chamber was purged with a small amount of dried N₂ gas to sublimate surface frost; during this process specimen surface temperatures never exceeded -120 C.

We prepared FD specimens by mounting living leaf squares on stubs as above, transferring the stubs to a brass block (mass 675 g)

cooled to liquid N₂ temperature (-196 C). The brass block and stubs were placed on an insulated platform in a continual 5×10^{-2} Torr vacuum for 16 h and allowed to warm to 25 C.

For CD specimens, 1 cm whole leaf segments were fixed in sodium phosphate buffered FAA for 2-6 weeks or 2.5% unbuffered glutaraldehyde for 24 h. Fixed leaf segments (ca 0.5 cm²) were dehydrated in ethanol, CO₂ critical-point dried, and mounted on graphite coated stubs. FD and CD specimens were made electrically conductive by nickel evaporative coating.

A Philips 500X SEM operated at 12 kV and fitted with an EDAX International System 711F energy-dispersive x-ray microanalysis unit was used. The x-ray take-off angle was 31°; working distance from specimen to objective lens was 21 mm. For standardization, Al K α x rays were collected from the stub margin and beam-current adjusted with the spot size control to a count rate of 3000/s. To excite and accumulate x rays from epidermal cells, a 2.5 μ m raster (obtained at 15 000 \times magnification) was centered on the cell surface for 100 s (Fig. 1). Approximately 100-140 cells were analyzed for each specimen preparation method, except for GLUT fixed materials, where only 20 cells were used. K-shell x rays of Na, Mg, Si, P, S, Cl, K, Ca (Ca corrected for K β overlap), and Mn were collected with a Si(Li) detector with a 7.5 μ m Be window. Net elemental intensities (total counts/100 s) were determined by automatic background subtraction for bulk specimens (EDAX Corp. FDEM Software, BULK program).

Minimum detectable limits (MDL) were defined as net peak intensity divided by local background equal to 0.05 (P/B = 0.05). In practice, any net intensity less than 150 counts/100 s was assigned zero value. All net intensities for each element were combined to obtain mean and mean deviation values. In this study it was deemed unnecessary to factor the detector efficiency correction into each elemental intensity. Consequently, direct inter-element comparisons of relative amounts should not be made; however, comparisons of relative amounts of specific elements present can be made.

Results

FH samples showed no collapse or distortion of thin-walled, turgid epidermal cells (Fig. 1). Evidently barley leaf tissue is unaffected by the 1×10^{-4} Torr vacuum used for ca 5 min during evaporative nickel coating and subsequent cold stage freezing. This relatively slow freezing process gave better results than a quick quench in liquid nitrogen, which resulted in blistering distortions of epidermal

The authors are at the Electron Optical Facility of the Minnesota Agricultural Experiment Station and the Department of Plant Pathology, University of Minnesota, MN 55108. T. L. W. Carver is with the Welsh Plant Breeding Station, Plas Gogerddan, Aberystwyth, Dyfed, Wales, United Kingdom, SY23 3EB.

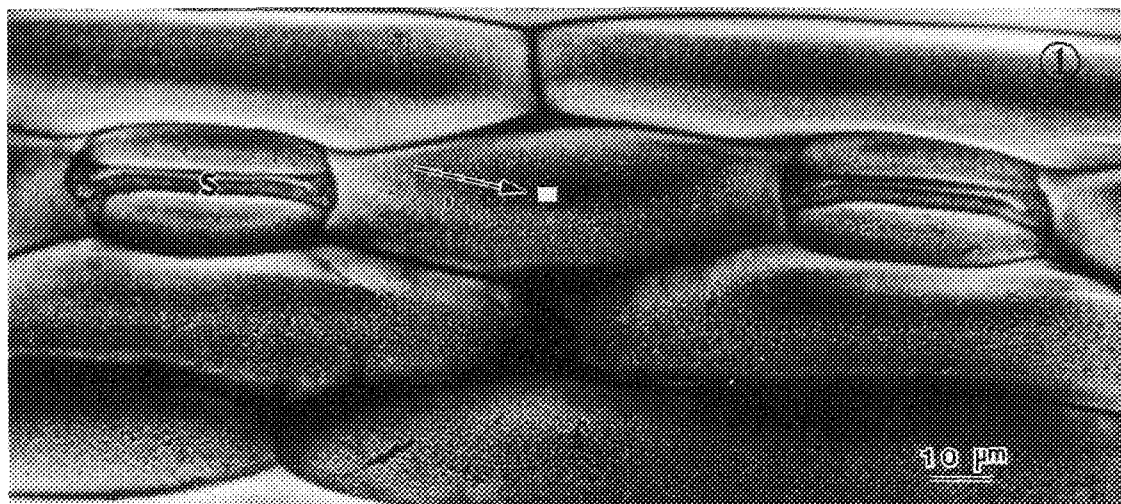


FIG. 1.--SEM micrograph of frozen-hydrated barley leaf epidermal surface cells. White square (arrow) indicates size and placement of typical electron beam raster used to excite x-ray emission. S = stomata or gas exchange areas that are now closed.

cell surfaces (not shown). FD and CD samples showed some distortion and partial collapse of epidermal cells, as expected (not shown).

Averaged net elemental intensities for each preparation are plotted against a log scale of counts for comparison (Fig. 2). FD prepared specimens yielded the highest measured intensities for all elements of interest, except for Na and Mg, which are highest for CD-FAA and CD-GLUT samples, respectively. FH prepared specimens yielded second highest intensities for Si, Cl, K, and Ca, but gave zero measurements for Na, Mg, P, and S. CD-FAA specimens yielded the lowest intensity for Ca and zero for Mg, Si, Cl, and K. Compared with CD-FAA specimens, CD-GLUT specimens yielded significantly higher levels of Mg, P, Cl, K and Ca; no Na; and nearly the same level of S. Mn was undetected in barley epidermal cells.

CD specimens fixed in liquid fixatives and dehydrated in ethanol indicate which elements exist as soluble forms in epidermal cells. Mg, Si, Cl, K, and Ca are obviously soluble, being abundant in FH and FD preparations, but are zero or at low levels in CD-FAA preparations. Phosphorous appears partially soluble in CD-FAA preparations when compared with P intensities from FD preparations, which are five times higher (Fig. 2). As liquid-fixed preparations, CD-GLUT specimens retained more Mg, P, Cl, K, and Ca than did CD-FAA specimens, a difference that is possibly due to the following: (1) CD-FAA samples were stored in FAA for 2-6 weeks, whereas CD-GLUT samples were stored in GLUT for only 24 h before ethanol dehydration and critical point drying. Thus, more time existed for soluble elements to leach from CD-FAA samples. (2) Glutaraldehyde used in the CD-GLUT procedure cross links and stabilizes proteins, whereas the formaldehyde component of FAA is less effective at forming cross linkages. Cross linkage of proteins may result in retention of elements enclosed or closely associated with pro-

teins in epidermal cells. (3) The FAA fixative components of acetic acid and ethanol may form a more efficient solvent for removal of soluble elements than does the weakly bipolar, aqueous medium of the GLUT fixative.

In contrast to elemental loss when liquid fixatives are used, the sodium phosphate buffered FAA might be expected to elevate levels of Na and P above those in aqueous nonbuffered CD-GLUT samples by contaminating cells, but our results are ambiguous. Na is found in FAA-fixed samples and in no other preparation, but P is much lower in CD-FAA than in CD-GLUT treated specimens. In fact Mg, P, and S levels in CD-GLUT specimens compare favorably with FD samples, which shows that 24 h in unbuffered aqueous glutaraldehyde fixative removes insignificant amounts of these elements from epidermal cells (Fig. 2).

In FH specimens, Na, Mg, P, and S levels are zero compared to FD or CD specimens; and Cl, K, and Ca levels, although substantial, are significantly lower than for FD specimens (Fig. 2). This phenomenon is easily explained if penetration of the 12kV electron beam into FH specimens is limited by ice, and only penetrates into the highly hydrated cell wall region (noncytoplasmic region) which surrounds and protects the cytoplasm. The best evidence for restricted beam penetration occurs with the elements P and S, which are absent in FH spectra. Both P and S are essential cytoplasmic constituents of cells; S is associated with protein structure, P with nucleic acids and metabolic activity. Their absence from FH spectra indicates that beam penetration in FH specimens does not reach the cytoplasmic contents of epidermal cells. The combined thickness of epidermal cell wall, cuticle, and wax layer in cross sections of FH barley cells was found to be 2.5-3.0 μm . This thickness range fits the expected beam penetration for FH materials based on the equation of Anderson and

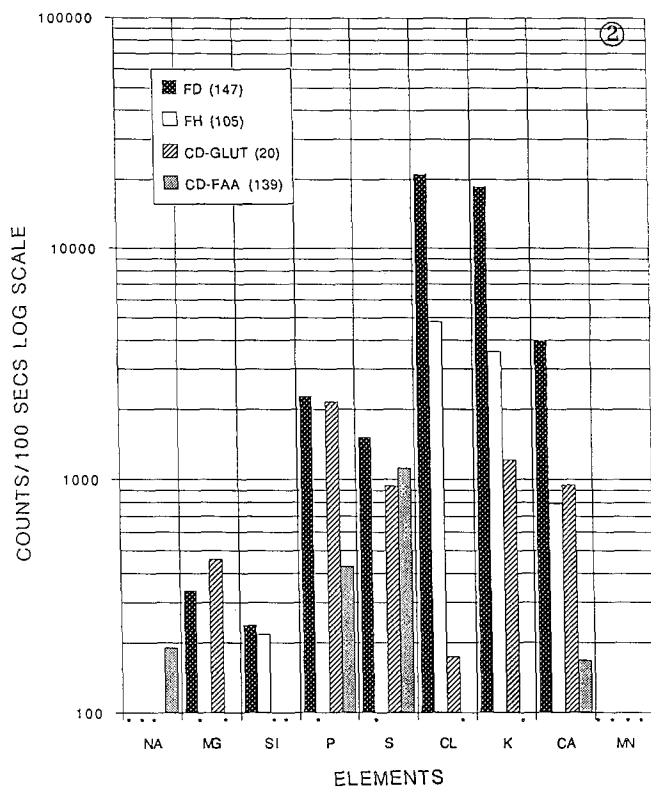


FIG. 2.--Elemental levels detected in barley epidermal cells from frozen hydrated (FH), freeze dried (FD) and critical point dried (CD) preparations. Number of cells measured for each preparation procedure is indicated in parentheses. Asterisks indicate elemental levels below 150 counts/100 s.

Hasler.^{5,6} If we assume a density of 1.20 gm/cm³ for FH plant materials⁵ and apply the equation for maximum depth of x-ray generation,⁶ a 12kV electron beam should excite K-shell x rays from Na to Ca at maximum depths between 3.4 and 2.9 μ m, respectively. For P and S the maximum depth of excitation in FH materials would be 3.2 μ m; thus, the 12kV beam would be sufficient to excite P and S found at greater depths in the FH specimen cytoplasm.

The removal of water and ice in CD and FD preparations, respectively, decreases the average density in dehydrated cells and increases the depth of electron beam penetration. For a density of 0.5 gm/cm³ for FD and CD plant materials,^{5,6} the range of maximum depths for K-shell x-ray generation for the elements Na to Ca increases to 8.2 to 7.0 μ m, respectively, and has a value of 7.8 μ m for S and P. At these depths of penetration, a 12kV beam should excite high levels of S and P in CD and FD preparations, which is indeed the case (Fig. 2). It follows that S and P, and also Mg, are associated with these deeper cytoplasmic regions (FD and CD-GLUT data) but not cell wall regions (FH data). Similarly Si, Cl, K, and Ca are present in epidermal cell wall (FH data) and in cytoplasmic regions of cells (FD data). Another consequence of water or ice removal from epidermal

cells is to increase the mass fraction of each element remaining in the dehydrated mass, assuming no loss of mass other than water. If the mass fraction of elements in FD cells increases, higher levels of characteristic x rays would be expected in FD than in FH specimens; this effect is evident in the levels of Cl, K, and Ca (FH and FD data, Fig. 2).

Conclusions

The limitations in applying EDX to botanical materials are not intrinsic to EDX technology but rather center on specimen preparation procedures.^{1,2,9} EDX remains the best technology for detecting elements of interest in situ. However, methods of specimen preparation must be evaluated if EDX is to reach its promise in biological work.⁹ We sought to compare specimen preparation procedures on well-defined plant materials with procedures that are relatively easy to use and require a minimum of specialized equipment.

The only advantage of using CD materials is that the procedure results in a reasonable preservation of morphological features. CD samples prepared with liquid chemical fixatives and dehydrated with ethanol demonstrated significant loss of soluble elements. CD preparations are only suitable when elements of interest are known to be bound and insoluble.^{1,2,7} If there is no alternative to liquid fixation of botanical specimens for EDX, then our limited data indicate that glutaraldehyde used in an aqueous medium for the shortest time compatible with fixation of structure appears to be the fixative of choice.

FH specimens, prepared with our relatively slow freezing method, show excellent preservation of surface morphology (Fig. 1) and retain soluble elements within tissues. However, for EDX, beam penetration is limited to the cell wall region when compared to FD and CD preparations. Therefore EDX of FH materials is most appropriate for studies of chemical changes on plant cell surfaces or changes occurring in the cell wall of epidermal cells; e.g., pathological processes, pesticide or herbicide applications, and pollution deposition.^{1,2,7} For whole-cell or unfractured-tissue preservation, the use of FH plant materials is limited primarily by beam penetration considerations.

Because of deeper beam penetration and conservation of soluble elements, FD plant materials probably represent the best compromise for EDX of bulk samples. FD samples can be used at ambient temperatures and do not require specialized freezing SEM stages.^{2,3,8} However, spectral interpretation can be problematic owing to greater depth of beam penetration and a larger x-ray generation volume, and the possibility of exciting x rays from subtending structures not visible from the surface. In addition, FD may cause specimen distortion and collapse.

References

1. R. J. Zeyen, "Applications of in situ microanalysis in understanding disease: X-ray microanalysis," *Ann. Rev. of Phytopathology* 20: 119-142, 1982.
2. R. J. Zeyen, "Analytical electron microscopy in plant pathology: X-ray microanalysis and energy loss spectroscopy," in K. Mendgen, Ed., *Electron Microscopy of Plant Pathogens*, Berlin: Springer-Verlag (in press).
3. D. M. R. Harvey, "Applications of x-ray microanalysis in botanical research," *SEM/1986* III, 953-979.
4. A. T. Marshall, "Progress in quantitative x-ray microanalysis of frozen hydrated bulk biological samples," *J. Electron Microscopy Technique* 9: 57-64, 1988.
5. P. Echlin, C. E. Lai, T. L. Hayes, and G. Hook, "Elemental analysis of frozen-hydrated differentiating phloem parenchyma in roots of *Lemna minor* L., *SEM/1980* II, 383-394.
6. C. A. Anderson and M. F. Hasler, "Extension of electron microprobe techniques to biochemistry by the use of long wavelength x rays," *4th Intern. Congr. X-ray Optics and Microanalysis*, Paris, 1966, 310-327.
7. H. Koga, R. J. Zeyen, W. R. Bushnell, and G. G. Ahlstrand, "Hypersensitive cell death, autofluorescence, and insoluble silicon accumulation in barley leaf epidermal cells under attack by *Erysiphe graminis* f. sp. *hordei*," *Physiol. and Mol. Plant Pathology* 32: 395-409, 1988.
8. P. Echlin, "Ambient-temperature chemical specimen preparation for biological x-ray microanalysis," *Microbeam Analysis--1988*, 1-8.
9. P. Echlin, "Biological electron-probe x-ray microanalysis: An unfulfilled promise?" *Microbeam Analysis--1988*, 451-455.

AUTHOR INDEX

- Ackerman, E. R., 364
 Adler, K. B., 457
 Ahlstrand, G. G., 463
 Ahn, C. C., 56
 Akley, N. J., 457
 Ales, M. W., 79
 Allen, L. J., 337
 Ammann, N., 21, 150
 Andersen, S. J., 334
 Antoine, J., 369
 Asher, S. E., 97

 Baird, R. J., 209
 Baker, I., 297
 Bakken, L. N., 347
 Barkan, S., 139
 Bastin, G. F., 159
 Bearman, G. H., 367
 Belcher, L. A., 449
 Bentley, J., 289
 Bergin, F. J., 235
 Boivin, D., 120
 Botton, G., 284
 Bradley, J. G., 367
 Bright, D. S., 73, 190
 Brown, J. D., 115
 Browning, R., 195, 199, 377
 Buczkowski, A., 381
 Burilla, C. T., 169

 Callender, C. A., 372
 Carney, M., 387
 Caron, M., 284
 Carver, T. L. W., 463
 Chabala, J. M., 93, 105
 Chambers, W. F., 155, 193
 Chang, W. Z., 69
 Charbonnier, M., 257
 Chen, G., 305
 Chodos, A. A., 155
 Chou, I.-M., 228
 Czerczak, S., 439

 Davidson, S. G., 367

 Dawson, W. C., 372
 de Bruijn, W. C., 32
 Delhay, D., 220
 Dhamelin-court, P., 220
 Dickman, K. G., 393
 Dijkstra, J. M., 159
 Ding, Z.-J., 6
 Donovan, J. J., 66
 Doyle, J. H., 193
 Duncumb, P., 1

 Elthon, D., 185
 Etz, E. S., 89, 243

 Fiori, C. E., 147
 Flenniken, R. R., 454
 Fletcher, R. A., 89
 Flora, P. S., 263
 Freeman, H. A., 212, 375
 Fultz, B., 56
 Funk, J. J., 372

 Gaillard, F., 257
 Garratt-Reed, A. J., 272
 Goldstein, J. I., 265, 307
 Gordon, B. M., 401
 Griffin, B. J., 203
 Griffis, D. P., 101
 Guo, Y. X., 334

 Hagan, R. C., 155
 Halgunset, J., 427
 Handwerker, C. A., 190
 Harkema, J. R., 453
 Harland, C. J., 263
 Hartmann, A., 43
 Hawkey, L. A., 387, 393
 Heijligers, H. J. M., 159
 Heinrich, K. H. J., 146
 Hembree, G. G., 249
 Henderson, C. E., 215
 Heng, Y. M., 311
 Heyman, R. V., 185
 Hoeft, S., 89

 Hofer, F., 48
 Høier, R., 334, 347
 Hoover, M. D., 453
 Horikawa, Y., 408, 411
 Horita, Z., 323
 Hosoda, S., 408, 411
 Hotchkiss, J. A., 453
 Hssein, K., 35
 Huang, M., 263
 Hunter, J. L., Jr., 101

 Ingram, P., 393, 387, 454

 Jarrell, J., 435
 Jonas, P., 51
 Jones, K. W., 401

 Kaneko, N., 408, 411
 Karduck, P., 21, 150
 Kenik, E. A., 289
 Kimmel, G., 364
 King, P. L., 195, 199
 Kirk, R., 430
 Koerner, G. S., 93
 Koopman, M. C., 260
 Kopf, D. A., 454
 Kopstad, G., 427
 Krunkosky, T. M., 457

 Laabs, F. C., 217
 Lábár, J. L., 29
 la Barré, S., 43
 Lamothe, V., 369
 Lampert, J. K., 93
 Landolt, M., 377
 LeFurgey, A., 387, 393, 454
 Lee, J., 457
 Lee, J.-J., 101
 Lee, P., 430
 L'Espérance, 284
 Levi-Setti, R., 93, 105
 Lieberman, M., 387
 Lin, W.-J., 101
 Ling, Y., 390

- Linton, R. W., 101, 423
 Liu, D. R., 209
 Luo, F. C. H., 249
 Lyman, C. E., 265

 Macaoay, J. M., 93
 McCarthy, J. J., 79
 McKay, G., 167
 Mackenzie, A., 165
 McMillan, D. J., 79
 Mandel, L. J., 393
 Mao, S., 206
 Marinenko, R. B., 190
 Mathinsen, K., 347
 Matsuda, R., 408, 411
 Mawn, M. P., 423
 Mecholsky, J. J., Jr., 190
 Michael, J. R., 275
 Miller, P. R., 337
 Moore, K. A., 449
 Muggenburg, B. A., 453
 Munroe, P. R., 297
 Murata, Y., 323
 Myklebust, R. L., 127, 146, 147, 275

 Nakamura, S., 408
 Nassiopoulos, A. G., 161
 Nemoto, M., 323
 Newbury, D. E., 105, 127, 147, 275
 Niedrig, H., 43
 Nishimura, M., 323
 Nordby, A., 427

 O'Connor, A. J., 327
 Ogilvie, R. E., 174
 Okamoto, J. K., 56
 Opalska, B., 439
 Otsuka, Y., 323
 Otten, M. T., 344

 Panessa-Warren, B. J., 405
 Paque, J. M., 195, 199
 Pasteris, J. D., 228
 Peeters, M. H., 369
 Pérez, R., 354

 Peters, Y. A., 375
 Pianetta, P., 195, 199
 Pichoir, F., 120
 Plimpton, S. J., 275
 Pouchou, J.-L., 120
 Powell, C. J., 13

 Qing, L., 339
 Quandt, E., 43

 Rabe, J. A., 212
 Radzimski, Z. J., 381
 Reasor, M. J., 430
 Reed, S. J. B., 109, 181
 Reffner, J. A., 240, 442
 Rehbach, W. P., 21
 Ren, Y., 305
 Rennix, D. K., 449
 Rivers, M. L., 66
 Romand, M. J., 257
 Romig, A. D., Jr., 275
 Roomans, G. M., 421
 Ross, D. K., 185
 Rossouw, C. J., 327, 337
 Rozgonyi, G. A., 381
 Ruedl, E., 318
 Runde, P., 347
 Russ, J. C., 381, 385
 Russell, P. A., 445
 Rydzynski, K., 439

 Sano, T., 323
 Saubermann, A. J., 401
 Schattschneider, P., 48, 51, 53
 Schidlovsky, G., 401
 Schiffman, K., 177
 Schroeder, T. D., 243
 Scozia, R. A., 351
 Seitz, J. C., 228
 Serin, V., 35
 Sévely, J., 35
 Shimizu, R., 6
 Shinozaki, S. S., 209
 Silva, E. G., 351
 Simon, G. T., 311
 Sims, D. E., 435
 Singh, A., 435

 Soni, K. K., 105
 Sorber, L. W. J., 32
 Spanne, P., 401
 Spencer, A. J., 393
 Statham, P. J., 85
 Stears, R. L., 405
 Steel, E. B., 127
 Stetkiewicz, J., 439
 Su, D., 53
 Sun, S., 69, 415
 Sun, Z., 305

 Teraoka, K., 408, 411
 Thompson, R. G., 260
 Tormet, J. M., 415
 Tortora, G. T., 405
 Turner, P. S., 327
 Tvedt, K. E., 427

 Uchida, T., 408, 411

 Valamontes, E., 161
 Valdrè, G., 318
 VanZandt, T., 377
 VENABLES, J. A., 249, 263
 Viala, A., 369
 Villeneuve, D. C., 435

 Wagstaff, J., 167
 Wakaki, Y., 323
 Ward, J. P. T., 419
 Warheit, D. B., 449
 Warley, A., 419
 Warner, R. R., 397
 Warren, J. B., 405
 Warsinski, R. G., 209
 White, T. J., 327
 Wihlborg, W. T., 240, 442
 Williams, D. B., 105, 307
 Willich, P., 177
 Wilson, A. R., 39
 Wittry, D. B., 69, 415
 Wong-Ng, W., 243
 Wopenka, B., 228

 Xu, Y., 305
 Xue, D., 401

Yang, S. V., 167

Yu, W., 390

Yu, Z., 390

Zaluzec, N. J., 281, 330

Zanchi, G., 35

Zeyen, R. J., 463

Zglinicki, T. von, 421

Zhang, J., 265, 307

Zhong, C., 390

